

mann  
Ulrich

ADA258805

1

ULTRASTRUCTURE PROCESSING

# ULTRASTRUCTURE PROCESSING — OF — ADVANCED MATERIALS



Donald R. Uhlmann  
Donald R. Ulrich

This document contains information that is not to be distributed outside the organization.



LEY-  
CIENCE

BEST  
AVAILABLE COPY

REPORT DOCUMENTATION PAGE			Form Approved OMB No. 0704-0182	
<small>Public report (GPO) for the collection of information and statistical data for the U.S. Air Force, including the time for reviewing instructions, searching existing data sources, gathering and maintaining the data needed, and completing and reviewing the collection of information, send comments regarding this burden estimate or any other aspect of this collection of information, including suggestions for reducing this burden to Washington Headquarters Services, Directorate for Information Operations and Reports, 1215 Jefferson Davis Highway, Suite 1204, Arlington, VA 22202-4302, and to the Office of Management and Budget, Paperwork Reduction Project (0704-0182), Washington, DC 20503.</small>				
1. AGENCY USE ONLY (Leave blank)	2. REPORT DATE November 1992	3. REPORT TYPE AND DATES COVERED Final Report 2/15/89 - 08/14/92		
4. TITLE AND SUBTITLE The Fourth International Conference on Ultrastructure Processing of Ceramics, Glasses and Composites		5. FUNDING NUMBERS  61102F 2303 A3		
6. AUTHOR(S)  Donald R. Uhlmann				
7. PERFORMING ORGANIZATION NAME(S) AND ADDRESS(ES)  Univ of Arizona 2030 E. Speedway Tucson, AZ 85721		8. PERFORMING ORGANIZATION REPORT NUMBER  AFOSR-TR- 92 0977		
9. SPONSORING/MONITORING AGENCY NAME(S) AND ADDRESS(ES)  AFOSR/NC Building 410, Bolling AFB DC 20332-6448		10. SPONSORING/MONITORING AGENCY REPORT NUMBER  AFOSR-89-0236		
11. SUPPLEMENTARY NOTES				
12a. DISTRIBUTION/AVAILABILITY STATEMENT  APPROVED FOR PUBLIC RELEASE; DISTRIBUTION IS UNLIMITED.		12b. DISTRIBUTION CODE		
13. ABSTRACT (Maximum 200 words)  This book contains the proceedings of the Fourth International Conference on Ultrastructure Processing of Ceramics, Glasses and Composites, held February 20-24, 1989, in Tucson, Arizona. The conference was sponsored by the Department of Materials Science and Engineering, College of Engineering and Mines, University of Arizona, and supported by the Directorate of Chemical and Atmospheric Sciences of the Air Force Office of Scientific Research (AFOSR). More than 250 scientists and engineers from university, industry, and government laboratories attended and included participants from the United States, Great Britain, Japan, France, Italy, Germany, Canada, Brazil, and Spain. Forty-two papers were presented, orally, and an additional seventy-three papers were presented at a poster session.				
14. SUBJECT TERMS		15. NUMBER OF PAGES 723		
		16. PRICE CODE		
17. SECURITY CLASSIFICATION OF REPORT UNCLASSIFIED	18. SECURITY CLASSIFICATION OF THIS PAGE UNCLASSIFIED	19. SECURITY CLASSIFICATION OF ABSTRACT UNCLASSIFIED	20. LIMITATION OF ABSTRACT	

AD-A258 805



# ULTRASTRUCTURE PROCESSING OF ADVANCED MATERIALS

Accession for	
NTIS Cross	<input checked="" type="checkbox"/>
DTIC T-2	<input type="checkbox"/>
U. announced	<input type="checkbox"/>
Justification	
By	
Distribution /	
Availability /	
Dist	
A-1	

DTIC QUALITY INSPECTED 2

92 1 021

92-30769



033800

75086

# **ULTRASTRUCTURE PROCESSING OF ADVANCED MATERIALS**

EDITED BY  
DONALD R. UHLMANN  
DONALD R. ULRICH



A WILEY-INTERSCIENCE PUBLICATION  
**JOHN WILEY & SONS, INC.**  
NEW YORK / CHICHESTER / BRISBANE / TORONTO / SINGAPORE



In recognition of the importance of preserving what has been written, it is a policy of John Wiley & Sons, Inc., to have books of enduring value published in the United States printed on acid-free paper, and we exert our best efforts to that end.

Copyright © 1992 by John Wiley & Sons, Inc.

All rights reserved. Published simultaneously in Canada.

Reproduction or translation of any part of this work beyond that permitted by Section 107 or 108 of the 1976 United States Copyright Act without the permission of the copyright owner is unlawful. Requests for permission or further information should be addressed to the Permissions Department, John Wiley & Sons, Inc.

***Library of Congress Cataloging in Publication Data:***

Ultrastructure Processing of Advanced Materials

edited by Donald R. Uhlmann, Donald R. Ulrich.

p. cm.

"Proceedings of the Fourth International Conference on Ultrastructure Processing of Ceramics, Glasses and Composites, held February 20-24, 1989 in Tucson, AZ ... sponsored by the Department of Materials Science and Engineering, College of Engineering and Mines, University of Arizona"--Pref.

Includes bibliographical references.

ISBN 0-471-52986-9

1. Ceramics--Congresses. 2. Glass--Congresses. 3. Composite materials--Congresses. I. Uhlmann, D. R. (Donald R.) II. Ulrich, Donald R. III. International Conference on Ultrastructure Processing of Ceramics, Glasses, and Composites (4th : 1989 : Tucson, Ariz.) IV. University of Arizona. College of Engineering and Mines. Dept. of Materials Science and Engineering.

TP785.U46 1992

666--dc20

91-23612

CIP

Printed and bound in the United States of America by Braun-Brumfield, Inc.

10 9 8 7 6 5 4 3 2 1

## DEDICATION

The present volume is dedicated to the memory of Dr. Donald R. Ulrich, whose vision, determination, and insight were critical to the development of ultra-structure processing.

After receiving his doctorate in ceramics from Rutgers, Don joined the staff of the General Electric Company in Valley Forge, Pennsylvania, where he made notable contributions to scientific understanding in areas ranging from compound semiconductors to lunar rocks. He found his real métier, however, when he joined the Directorate of Chemical and Atmospheric Sciences of the Air Force Office of Scientific Research (AFOSR) in 1975. He was fortunate to have Don Ball as a director, who immediately recognized Don's talent and imagination and was willing to provide him with wide operating latitude and to support his initiatives.

Early in his tenure at AFOSR, Don Ulrich recognized the importance of improved chemical and structural insight to developments in the field of polymers, and he undertook a range of new initiatives in the area. This interest continued throughout his career at AFOSR and is reflected in his support of pioneering efforts in areas ranging from the structure of amorphous polymers and models of gelation to copolymer systems, blends, and molecular composites.

Long before it became fashionable, Don recognized the potential of wet chemical processing for the synthesis of ceramic materials and launched a major initiative to exploit the potential of such processing. Thanks to his imagination,



vital new links were forged between chemists and ceramists; and a veritable explosion in activity and creativity ensued. This in turn led to the concept of marrying chemistry and processing science to tailor the structure of materials on a scale of tens to thousands of angstroms; and the science of ultrastructure processing was launched.

Don was also among the first to recognize the importance of materials in optical applications and the central role played by chemistry in designing and synthesizing new materials for such applications, and again he launched major initiatives to address these opportunities. Yet another area of Don's special interests was the development of multifunctional materials; and again Don's support and encouragement were critical to activities in the field.

In each of these areas—and the listing is by no means complete—Don displayed an almost uncanny ability to anticipate the course of future developments, identify subjects of great scientific and technological potential that lay at the interfaces between established disciplines, locate individuals who could make significant contributions at such interfaces, and provide the encouragement and support to ensure their active participation.

Besides his technical insight and talent for launching major new initiatives, Don was also a great proponent of communication and collaboration. He launched and nurtured numerous major international conferences, including the present series on ultrastructure processing and the Materials Research Society meetings on Better Ceramics through Chemistry. In each case, Don was not a passive source of financial support, but an active contributor to the organization, with knowledge of who was carrying out definitive work and who had made recent breakthroughs.

Don's encouragement of collaboration and communication did not stop at the borders of the United States. He was an active participant in technical meetings in countries around the world and played a key role in establishing collaborative research programs between American research teams and their counterparts in England, France, Germany, Canada, and Japan. These activities not only advanced the level of scientific understanding, but also promoted personal and social interactions among researchers around the world.

In addition to his role as a driver of modern chemical/materials research, Don was an active participant in the Air Force Reserve. Here again he made important contributions, rose to the rank of full colonel, and, in the this writer's judgment, seemed headed for a general's star.

Beyond any and all of these professional activities, Don was a dedicated family man, a devoted husband, and father. His beloved Eleanor was always first in his heart—a trusted confidant and companion, the most loyal of friends, and the source of great inspiration.

Don was taken from us while this volume was in press, and it is a pleasure to dedicate it to his memory. He had a myriad of friends; and some of us were fortunate to feel we were part of his extended family. He will be sorely missed.

## CONTRIBUTORS

ABRAMOFF, B.  
Rutgers-The State University of  
New Jersey, Ceramics  
Department, Piscataway, New  
Jersey

ADAMS, W. W.  
Materials Laboratory, Wright-  
Patterson Air Force Base, Ohio

AEGERTER, M. A.  
Instituto de Fisica e Quimica de  
Sao Carlos, University of Sao  
Paulo, Sao Carlos, Brazil

AKSAY, I. A.  
Department of Materials Science  
and Engineering FB-10, and the  
Advanced Materials Technology  
Program, University of  
Washington, Seattle, Washington

ASHLEY, C. S.  
Sandia National Laboratories,  
Albuquerque, New Mexico

BAILEY, J. K.  
Department of Chemical  
Engineering and Materials  
Science, University of Minnesota,  
Minneapolis, Minnesota

BALABAN, C.  
GELTECH, Inc., Alachua, Florida

BALAVOINE, G. A.  
Institut de Chimie Moleculaire  
D'Orsay, Universite de Paris-  
Sud, Paris, France

BARRERA-SOLANO, C.  
Department of Structure and  
Properties of Materials, Faculty  
Science, University of Cadiz,  
Spain

BARRINGER, E. A.  
Massachusetts Institute of  
Technology, Cambridge,  
Massachusetts

- BERRY, G. C.  
Department of Chemistry,  
Carnegie-Mellon University,  
Pittsburgh, Pennsylvania
- BIRNIE, D. P. III  
Department of Materials Science  
and Engineering, University of  
Arizona, Tucson, Arizona
- BOLT, J. D.  
E. I. duPont de Nemours &  
Company, Wilmington, Delaware
- BOULTON, J. M.  
Department of Materials Science  
and Engineering, University of  
Arizona, Tucson, Arizona
- BOWEN, H. K.  
Massachusetts Institute of  
Technology, Cambridge,  
Massachusetts
- BOYER, R. D.  
B.P. America Research and  
Development, Cleveland, Ohio
- BRADLEY, D. C.  
Department of Chemistry, Queen  
Mary College, London, United  
Kingdom
- BRENNAN, A. B.  
Department of Chemical  
Engineering, Polymer Materials  
and Interfaces Laboratory,  
Virginia Polytechnic Institute  
and State University, Blacksburg,  
Virginia
- BRINKER, C. J.  
Sandia National Laboratories,  
Albuquerque, New Mexico
- BUCKELY, A.  
Hoechst Celanese Science and  
Technology Company, Robert L.  
Mitchell Technical Center,  
Summit, New Jersey
- BURGGRAF, L. W.  
Air Force Office of Scientific  
Research, Bolling Air Force Base,  
Washington, DC
- CALUNDANN, G. W.  
Hoechst Celanese Science and  
Technology Company, Robert L.  
Mitchell Technical Center,  
Summit, New Jersey
- CALVERT, P.  
Department of Materials Science  
and Engineering, Arizona  
Materials Laboratory, University  
of Arizona, Tucson, Arizona
- CHARBONNEAU, L. F.  
Hoechst Celanese Science and  
Technology Company, Robert L.  
Mitchell Technical Center,  
Summit, New Jersey
- CHARBOUILLOT, Y.  
Instituto de Fisica e Quimica de  
Sao Carlos, University of Sao  
Paulo, Sao Carlos, Brazil
- CHENG, Y.-C.  
Advanced Materials Research  
Center, University of Florida,  
Alachua, Florida
- CHICK, L. A.  
Battelle Pacific Northwest  
Laboratories, Richland,  
Washington

## CONTRIBUTORS

ix

CLAUSEN, E. M.  
Advanced Materials Research  
Center, University of Florida,  
Gainesville, Florida

COLTRIAN, B. K.  
Corporate Research Laboratories,  
Eastman Kodak Company,  
Rochester, New York

CUMBRERA, F. L.  
Department of Physics of  
Condensed Matter, Faculty of  
Physics, University of Sevilla,  
Spain

DAVIS, L. P.  
Air Force Office of Scientific  
Research, Bolling Air Force Base,  
Washington, DC

DE LA ROSA-FOX, N.  
Department of Structure and  
Properties of Materials, Faculty  
Science, University of Cadiz,  
Spain

DE GODOY, L. H.  
Instituto de Fisica e Quimica de  
Sao Carlos, University of Sao  
Paulo, Sao Carlos, Brazil

DUNN, B.  
Department of Materials Science  
and Engineering, University of  
California, Los Angeles,  
California

DYNYS, J.  
IBM/East Fishkill, Hopewell  
Junction, New York

EAST, A. J.  
Hoechst Celanese Science and  
Technology Company, Robert L.  
Mitchell Technical Center,  
Summit, New Jersey

EICHORST, D. J.  
Department of Materials Science  
and Engineering and Materials  
Research Laboratory, University  
of Illinois at Urbana-Champaign,  
Urbana, Illinois

ENGEL, B. N.  
Optical Sciences Center and  
Department of Physics,  
University of Arizona, Tucson,  
Arizona

ESQUIVIAS, L.  
Department of Structure and  
Properties of Materials, Faculty  
Science, University of Cadiz,  
Spain

FALCO, C. M.  
Optical Sciences Center and  
Department of Physics,  
University of Arizona, Tucson,  
Arizona

FEATHERSTONE, M.  
Department of Chemistry,  
Carnegie-Mellon University,  
Pittsburgh, Pennsylvania

FLEMING, S. A.  
AT&T Bell Laboratories, Murray  
Hill, New Jersey

FLEMING, J. W.  
AT&T Bell Laboratories, Murray  
Hill, New Jersey

FOX, J. R.  
B.P. America Research and  
Development, Cleveland, Ohio

FRICKE, J.  
Physikalisches Institut der  
Universität, Germany

FRYE, G. C.  
Sandia National Laboratories,  
Albuquerque, New Mexico

FUQUA, P. D.  
Department of Materials Science  
and Engineering, University of  
California, Los Angeles,  
California

GLASER, R. H.  
Department of Chemical  
Engineering, Polymer Materials  
and Interfaces Laboratory,  
Virginia Polytechnic Institute  
and State University, Blacksburg,  
Virginia

GORDON, M. S.  
North Dakota State University,  
Fargo, North Dakota

HAN, K. H.  
Rutgers, The State University of  
New Jersey, G. N. Howatt  
Laboratory, Piscataway, New  
Jersey

HARDY, A. B.  
Massachusetts Institute of  
Technology, Cambridge,  
Massachusetts

HENCH, L. L.  
Advanced Materials Research  
Center, University of Florida,  
Alachua, Florida

HENRY, M.  
Laboratoire de Chimie de la  
Matière Condensée, Université P.  
et M. Curie, Paris, France

HOWARD, K. E.  
Department of Materials Science  
and Engineering and Materials  
Research Laboratory, University  
of Illinois at Urbana-Champaign,  
Urbana, Illinois

HU, H. S.-W.  
The Johns Hopkins University  
Applied Physics Laboratory,  
Laurel, Maryland

HUANG, H.  
Department of Chemical  
Engineering, Polymer Materials  
and Interfaces Laboratory,  
Virginia Polytechnic Institute  
and State University, Blacksburg,  
Virginia

HURD, A. J.  
Sandia National Laboratories,  
Albuquerque, New Mexico

JANAVICIUS, L. V.  
Massachusetts Institute of  
Technology, Cambridge,  
Massachusetts

JIAN, L.  
Department of Chemistry and the  
Polymer Research Center,  
University of Cincinnati,  
Cincinnati, Ohio

JIANG, C.-Y.  
Department of Chemistry and the  
Polymer Research Center,  
University of Cincinnati,  
Cincinnati, Ohio

## CONTRIBUTORS

xi

JOLIVET, J. P.  
Laboratoire de Chimie de la  
Matiere Condensee, Universite P.  
et M. Curie, Paris, France

JONAS, J.  
School of Chemical Sciences,  
University of Illinois, Urbana,  
Illinois

KELLY, D.  
AT&T Bell Laboratories, Murray  
Hill, New Jersey

KENNISH, R. A.  
Department of Materials Science  
and Engineering, and the  
Polymeric Materials Laboratory  
of the Washington Technology  
Center, University of  
Washington, Seattle, Washington

KLEIN, L. C.  
Ritagers-The State University of  
New Jersey, Ceramics  
Department, Piscataway, New  
Jersey

KNOBBE, E. T.  
Department of Materials Science  
and Engineering, University of  
California, Los Angeles,  
California

KOZUKA, H.  
Institute for Chemical Research,  
Kyoto University, Kyoto, Japan

KUMAR, S.  
School of Textile and Fiber  
Engineering, Georgia Institute of  
Technology, Atlanta, Georgia

KUMTA, P. N.  
Department of Materials Science  
and Engineering and Arizona  
Materials Laboratory, University  
of Arizona, Tucson, Arizona

LAINE, R. M.  
Department of Materials Science  
and Engineering, and the  
Polymeric Materials Laboratory  
of the Washington Technology  
Center, University of  
Washington, Seattle, Washington

LANG, H.  
Department of Chemistry,  
Massachusetts Institute of  
Technology, Cambridge,  
Massachusetts

LING, H. C.  
AT&T Bell Laboratories,  
Princeton, New Jersey

LISHAWA, C. R.  
Department of Physics, Utica  
College of Syracuse University,  
Utica, New York

LIVAGE, J.  
Laboratoire de Chimie de la  
Matiere Condensee, Universite P.  
et M. Curie, Paris, France

MACKENZIE, J. D.  
Department of Materials Science  
and Engineering, University of  
California, Los Angeles,  
California

MARK, J. E.  
Department of Chemistry and the  
Polymer Research Center,  
University of Cincinnati,  
Cincinnati, Ohio



- MATJEVIC, E.  
Department of Chemistry, Clarkson  
University, Potsdam, New York
- MCCARTHY, D.  
Department of Chemistry and the  
Polymer Research Center,  
University of Cincinnati,  
Cincinnati, Ohio
- MECARTNEY, M. L.  
Department of Chemical  
Engineering and Materials  
Science, University of Minnesota,  
Minneapolis, Minnesota
- MELPOLDER, S. M.  
Corporate Research Laboratories,  
Eastman Kodak Company,  
Rochester, New York
- MOHALLEM, N.  
Instituto de Fisica e Quimica de  
Sao Carlos, University of Sao  
Paulo, Sao Carlos, Brazil
- MURATAKE, R.  
Faculty of Science and Technology,  
Keio University, Yokohama,  
Japan
- MURPHY, R. A.  
The Johns Hopkins University  
Applied Physics Laboratory,  
Laurel, Maryland
- NAZERI-ESHGHI, A.  
Department of Materials Science  
and Engineering, University of  
California, Los Angeles,  
California
- NING, Y.-P.  
Department of Chemistry and the  
Polymer Research Center,  
University of Cincinnati,  
Cincinnati, Ohio
- NIRASHIMA, H.  
Faculty of Science and Technology,  
Keio University, Yokohama,  
Japan
- NISHIDA, F.  
Department of Materials Science  
and Engineering, University of  
California, Los Angeles,  
California
- NOGUÈS, J. L.  
GELTECH, Inc., Alachua, Florida
- PANTANO, C. G.  
Department of Materials Science  
and Engineering, The  
Pennsylvania State University,  
University Park, Pennsylvania
- PARKER, A.  
Department of Chemistry,  
Colorado State University, Fort  
Collins, Colorado
- PAYNE, D. A.  
Department of Materials Science  
and Engineering and Materials  
Research Laboratory, University  
of Illinois at Urbana-Champaign,  
Urbana, Illinois
- PEKALA, R. W.  
Lawrence Livermore National  
Laboratory, Livermore,  
California

## CONTRIBUTORS

xiii

PHILLIPS, R. J.  
University of Pittsburgh,  
Department of Materials Science  
and Engineering, Pittsburgh,  
Pennsylvania

PHULE, P. P.  
Department of Materials Science  
and Engineering and Arizona  
Materials Laboratory, University  
of Arizona, Tucson, Arizona

PIERRE, A. C.  
Department of Mining,  
Metallurgical and Petroleum  
Engineering, the University of  
Alberta, Edmonton, Alberta,  
Canada

POTEMBER, R. S.  
The Johns Hopkins University  
Applied Physics Laboratory,  
Laurel, Maryland

POTTER, B. G.  
Advanced Materials Research  
Center, University of Florida,  
Gainesville, Florida

PRASAD, P. N.  
Photonics Research Laboratory,  
Department of Chemistry, State  
University of New York at  
Buffalo, Buffalo, New York

RAHN, J. A.  
Department of Materials Science  
and Engineering, and the  
Polymeric Materials Laboratory  
of the Washington Technology  
Center, University of  
Washington, Seattle, Washington

RIMAN, R. E.  
Rutgers, The State University of  
New Jersey, G. N. Howatt  
Laboratory, Piscataway, New  
Jersey

RISBUD, S. H.  
Department of Materials Science  
and Engineering and Arizona  
Materials Laboratory, University  
of Arizona, Tucson, Arizona

RODRIGUES, D.  
Department of Chemical  
Engineering, Polymer Materials  
and Interfaces Laboratory,  
Virginia Polytechnic Institute  
and State University, Blacksburg,  
Virginia

RONCONE, R. L.  
Optical Sciences Center, University  
of Arizona, Tucson, Arizona

SAFARI, A.  
Rutgers, The State University of  
New Jersey, G. N. Howatt  
Laboratory, Piscataway, New  
Jersey

SAKKA, S.  
Institute for Chemical Research,  
Kyoto University, Kyoto, Japan

SALVA, J. M.  
Corporate Research Laboratories,  
Eastman Kodak Company,  
Rochester, New York

SAWHILL, H. T.  
E.I. DuPont de Nemours,  
Experimental Station,  
Wilmington, Delaware

SCHAEFER, D. W.  
Sandia National Laboratory,  
Albuquerque, New Mexico

SCHERER, G. W.  
E.I. duPont de Nemours &  
Company, Central R&D  
Department, Wilmington,  
Delaware

SCHMIDT, H.  
Fraunhofer-Institut für  
Silicidforschung, Germany

SCHUTTE, C. L.  
Massachusetts Institute of  
Technology, Cambridge,  
Massachusetts

SEYFERTH, D.  
Department of Chemistry,  
Massachusetts Institute of  
Technology, Cambridge,  
Massachusetts

SHANE, M. J.  
University of Pittsburgh,  
Department of Materials Science  
and Engineering, Pittsburgh,  
Pennsylvania

SHOUP, R. D.  
Corning Glass Works, Corning,  
New York

SIMMONS, C. J.  
Advanced Materials Research  
Center, University of Florida,  
Gainesville, Florida

SIMMONS, J. H.  
Advanced Materials Research  
Center, University of Florida,  
Gainesville, Florida

SLAUGHTER, J. M.  
Optical Sciences Center and  
Department of Physics,  
University of Arizona, Tucson,  
Arizona

SOGA, N.  
Department of Industrial  
Chemistry, Kyoto University,  
Kyoto, Japan

SPECK, K. R.  
The Johns Hopkins University  
Applied Physics Laboratory,  
Laurel, Maryland

SPOONER, S.  
Oak Ridge National Laboratory,  
Oak Ridge, Tennessee

STILLE, J. K.  
Department of Chemistry,  
Colorado State University, Fort  
Collins, Colorado

SUBRAMONEY, S.  
Department of Materials Science  
and Engineering, University of  
Arizona, Tucson, Arizona

SUN, C.-C.  
Department of Chemistry and the  
Polymer Research Center,  
University of Cincinnati,  
Cincinnati, Ohio

SWITZER, J. A.  
University of Pittsburgh,  
Department of Materials Science  
and Engineering, Pittsburgh,  
Pennsylvania

TILLEY, T. D.  
Chemistry, Department, University  
of California at San Diego, La  
Jolla, California

## CONTRIBUTORS

xv

TSANG, J.  
Department of Chemistry,  
Colorado State University, Fort  
Collins, Colorado

TSUKIMI, K.  
Faculty of Science and Technology,  
Keio University, Yokohama,  
Japan

UHLMANN, D. R.  
Department of Materials Science  
and Engineering, University of  
Arizona, Tucson, Arizona

VINEY, C.  
Department of Materials Science  
and Engineering FB-10, and the  
Advanced Materials Technology  
Program, University of  
Washington, Seattle, Washington

WALLACE, S.  
Advanced Materials Research  
Center, University of Florida,  
Alachua, Florida

WARD, K. J.  
Sandia National Laboratories,  
Albuquerque, New Mexico

WEBER, M. J.  
Lawrence Livermore National  
Laboratory, University of  
California, Livermore, California

WELLER-BROPHY, L. A.  
Optical Sciences Center, University  
of Arizona, Tucson, Arizona

WEST, J. K.  
Advanced Materials Research  
Center, University of Florida,  
Alachua, Florida

WHEELER, G. E.  
The Metropolitan Museum of Art,  
Objects Conservation  
Department, New York, New  
York

WILCOXON, J. P.  
Sandia National Laboratory,  
Albuquerque, New Mexico

WILKES, G. L.  
Department of Chemical  
Engineering, Polymer Materials  
and Interfaces Laboratory,  
Virginia Polytechnic Institute  
and State University, Blacksburg,  
Virginia

WILSON, M. J. R.  
Advanced Materials Research  
Center, University of Florida,  
Alachua, Florida

WOO, H.-G.  
Chemistry Department, University  
of California at San Diego, La  
Jolla, California

YAMANE, M.  
Department of Inorganic Materials,  
Tokyo Institute of Technology,  
Tokyo, Japan

YOUNGDAHL, K. A.  
Department of Materials Science  
and Engineering, and the  
Polymeric Materials Laboratory  
of the Washington Technology  
Center, University of  
Washington, Seattle, Washington

ZARZYCKI, J.  
Laboratory of Science of Vitreous  
Materials, University of  
Montpellier 2, France

ZELINSKI, B. J. J.  
Department of Materials Science  
and Engineering, University of  
Arizona, Tucson, Arizona

ZHANG, H.  
Department of Materials Science  
and Engineering, The  
Pennsylvania State University,  
University Park, Pennsylvania

ZHENG, H.  
Department of Materials Science  
and Engineering, University of  
California, Los Angeles,  
California

ZINK, J. I.  
Department of Chemistry,  
University of California, Los  
Angeles, California

## PREFACE

This book contains the proceedings of the Fourth International Conference on Ultrastructure Processing of Ceramics, Glasses and Composites, held February 20-24, 1989, in Tucson, Arizona. The conference was sponsored by the Department of Materials Science and Engineering, College of Engineering and Mines, University of Arizona, and supported by the Directorate of Chemical and Atmospheric Sciences of the Air Force Office of Scientific Research (AFOSR). More than 250 scientists and engineers from university, industry, and government laboratories attended and included participants from the United States, Great Britain, Japan, France, Italy, Germany, Canada, Brazil, and Spain. Forty-two papers were presented orally, and an additional seventy-three papers were presented at a poster session.

Advanced ceramics and composites continue to be of great technological importance and represent vital elements of many emerging technologies. The key to the effective utilization of such materials lies in the control of molecular architecture and microstructure; and the ability to effect such control depends in turn upon the art and science of processing.

The past decade has seen the emergence of the new science of *ultrastructure processing*, where understanding and control of phenomena are provided at the level of *ultrastructure*, that is, on the scale of tens to thousands of angstroms. Developments in the area are well documented in the proceedings of previous conferences in this series. The papers in these proceedings illustrate well the central role played by chemistry in the development of new materials with novel combinations of properties. This role is reflected in the use of tailored metalorganic precursors, in the control of structural evolution beginning at the molecular level, in the development of new processes that take advantage of the chemistry and structure to produce shaped bodies (including films) with controlled ultrastructure, and in the use of later-stage (as postgelation) chemical treatments to modify further the performance characteristics.

The present conference included all phases of advanced research in these areas. Participants include recognized leaders of the scientific community who

are playing active roles in the development of the science of ultrastructure processing. Their contributions are reflected in the chapters that follow, which have been organized into six sections:

1. Precursors, chemistry, and structure development in ultrastructure processing.
2. Processing.
3. Powders, films, and monoliths.
4. Composites including organic modified ceramics.
5. Optical and electrical applications.
6. Organometallic precursors, polymers, and aerogels.

When the present volume is compared with its predecessors, it will be observed that the principles of ultrastructure processing are now being actively applied to the synthesis of novel composite materials and to the preparation of new materials with exciting optical and electrical properties. The editors expect these thrusts to continue during the coming years.

This volume presents a comprehensive treatment of recent advances in all aspects of ultrastructure processing and provides perspective on the current state of the field. We hope it will become, like previous volumes in the series, a standard reference for scientists and engineers who are concerned with modern chemical processing of materials. We also anticipate its importance as a source book for researchers entering the field and for individuals who are interested in utilizing this emerging science for products and applications. More generally, it is hoped that the volume will become de rigueur for chemists desiring to learn more about modern materials and for materials scientists who want perspective on the increasing importance of chemistry in their lives.

The local organizing committee of Professor M. C. Weinberg and Professor Subhash Risbud as cochairs and Ms. M. York, Ms. M. Cromwell, Mrs. G. Champagne, Mrs. R. Evans, and Mrs. K. North deserve much credit and praise for their outstanding services that made the conference successful and the publication of this book possible.

DONALD R. UHLMANN  
DONALD R. ULRICH

*Tucson, Arizona*  
*Washington, D.C.*  
*May, 1992*

# CONTENTS

<b>PART 1</b>	<b>PRECURSORS, CHEMISTRY, AND STRUCTURE DEVELOPMENT IN ULTRASTRUCTURE PROCESSING</b>	<b>1</b>
<b>1</b>	<b>Chemistry and Reactions of Metal Alkoxides</b> <i>D. C. Bradley</i>	<b>3</b>
<b>2</b>	<b>Molecular-Level Understanding of the Sol-Gel Process</b> <i>J. Jonas</i>	<b>13</b>
<b>3</b>	<b>Role of Complexation in the Sol-Gel Chemistry of Metal Oxides</b> <i>M. Henry, J. P. Jolivet, and J. Livage</i>	<b>23</b>
<b>4</b>	<b>Neutral and Anionic Hypervalent Silicon Complexes in Silanol Polymerization</b> <i>L. W. Burggraf, L. P. Davis, and M. S. Gordon</i>	<b>47</b>
<b>5</b>	<b>Characterization of Structural Development in Sol- Gel Systems by Cryogenic Transmission Electron Microscopy</b> <i>J. K. Bailey and M. L. Mecartney</i>	<b>57</b>
<b>6</b>	<b>Effect of Hydrogen Ion Concentration on Gelation of Tetrafunctional Silicate Sol-Gel Systems</b> <i>B. K. Coltrain, S. M. Melpolder, and J. M. Salva</i>	<b>69</b>



<b>7</b>	<b>Calorimetric Study of Sol and Gel Formation</b>	<b>77</b>
	<i>J. W. Fleming, S. A. Fleming, and D. Kelly</i>	
<b>8</b>	<b>Nuclear Magnetic Resonance Investigations of Lithium Niobium Alkoxide Solutions</b>	<b>87</b>
	<i>D. J. Eichorst, K. E. Howard, and D. A. Payne</i>	
<b>9</b>	<b>Initial Evidence for Si-O-Ti Bond Formation in Organically Modified Silicon Titanates by Solid-State <sup>29</sup>Si Nuclear Magnetic Resonance Spectroscopy</b>	<b>95</b>
	<i>C. L. Schutte, J. R. Fox, R. D. Boyer, and D. R. Uhlmann</i>	
<b>10</b>	<b>The Gelation of Colloidal Gels and the D.L.V.O. Theory</b>	<b>103</b>
	<i>A. C. Pierre</i>	
<b>11</b>	<b>Quantum Calculations on Sol-Gel Silica Clusters</b>	<b>111</b>
	<i>J. K. West, S. Wallace, L. L. Hench, and C. R. Lishawa</i>	
<b>PART 2</b>	<b>PROCESSING</b>	<b>119</b>
<b>12</b>	<b>Ultrastructure Processing of Shaped Ceramic Bodies from Liquids</b>	<b>121</b>
	<i>J. D. Mackenzie</i>	
<b>13</b>	<b>Sonogels—Development and Perspectives</b>	<b>135</b>
	<i>J. Zarzycki</i>	
<b>14</b>	<b>Biomimetic Processing of Ceramics and Composites</b>	<b>149</b>
	<i>P. Calvert</i>	
<b>15</b>	<b>Sol-Gel Processing of Large Silica Optics</b>	<b>159</b>
	<i>L. L. Hench, M. J. R. Wilson, C. Balaban, and J. L. Noguès</i>	
<b>16</b>	<b>Physics of Drying</b>	<b>179</b>
	<i>G. W. Scherer</i>	
<b>17</b>	<b>Phase Separation and Clustering in Systems of Rodlike Particles</b>	<b>201</b>
	<i>L. A. Chick, C. Viney, and I. A. Aksay</i>	

# CONTENTS

xxi

<b>18 Sol-Gel Processing of Controlled Pore Films</b>	<b>211</b>
<i>C. J. Brinker, G. C. Frye, A. J. Hurd, K. J. Ward, and C. S. Ashley</i>	
<b>19 Sol-Gel Processing of Oxycarbide Glasses and Glass Matrix Composites</b>	<b>223</b>
<i>H. Zhang and C. G. Pantano</i>	
<b>20 Seeded Transformation of Aluminum Chlorohydrate Gels</b>	<b>233</b>
<i>J. M. Boulton, S. Subramoney and D. R. Uhlmann</i>	
<b>21 Photoelectrochemical Deposition of Thallium(III) Oxide Thin Films onto <i>n</i>-Silicon</b>	<b>239</b>
<i>J. A. Switzer, R. J. Phillips, and M. J. Shane</i>	
<b>22 Real Time Monitoring of Silica Gel Drying Behavior</b>	<b>247</b>
<i>M. J. R. Wilson and L. L. Hench</i>	
 <b>PART 3 POWDERS, FILMS, AND MONOLITHS</b>	 <b>255</b>
<b>23 The Science of Ultrafine Powders: Well-Defined Composite and Coated Particles</b>	<b>257</b>
<i>E. Matijević</i>	
<b>24 Preparation of Narrow-Site-Distribution Borosilicate Powders by Alkoxide Hydrolysis</b>	<b>269</b>
<i>L. V. Janavicius, E. A. Barringer, A. B. Hardy, H. K. Bowen, and J. Dynys</i>	
<b>25 Synthesis and Processing of Alkaline Earth Metal, Titanate Gels, Powders, and Thin Films</b>	<b>277</b>
<i>P. P. Phule and S. H. Risbud</i>	
<b>26 Formation of <math>V_2O_5</math> Gels from Vanadyl Alkoxides</b>	<b>285</b>
<i>H. Hirashima, K. Tsukimi and R. Muratake</i>	
<b>27 Properties of Alkali Silicate Gels and Their Sintered Fused Silica Glasses</b>	<b>291</b>
<i>R. D. Shoup</i>	

<b>28</b>	<b>Effects of Ultrastructure on Elastic and Thermal Properties of Glass</b>	<b>303</b>
	<i>N. Soga</i>	
<b>29</b>	<b>Determination of the Skeletal Density of Silica Gels from Wide-Angle X-Ray Diffraction</b>	<b>315</b>
	<i>L. Esquivias, C. Barrera-Solano, N. de la Rosa-Fox, F. L. Cumbreira, and J. Zarzycki</i>	
<b>30</b>	<b>Modulus of Rupture for Room-Temperature Gels Derived from Methyltrimethoxsilane</b>	<b>327</b>
	<i>G. E. Wheeler and S. A. Fleming</i>	
<b>31</b>	<b>Sol-Gel-Derived Titania-Silica Gel-Glasses</b>	<b>333</b>
	<i>Y.-C. Cheng and L. L. Hench</i>	
<b>PART 4 COMPOSITES INCLUDING ORGANIC-MODIFIED CERAMICS</b>		<b>341</b>
<b>32</b>	<b>Conventional and Molecular Composites—Past, Present, and Future</b>	<b>343</b>
	<i>W. W. Adams and S. Kumar</i>	
<b>33</b>	<b>Structure-Property Relationships in Silica-Siloxane Molecular Composites</b>	<b>361</b>
	<i>D. W. Schaefer, J. E. Mark, L. Jian, C.-C. Sun, D. McCarthy, C.-Y. Jiang, Y.-P. Ning, and S. Spooner</i>	
<b>34</b>	<b>Preparation of <math>(\text{Pb}_{0.5}\text{Bi}_{0.5})(\text{Ti}_{0.5}\text{Fe}_{0.5})\text{O}_3</math> Ceramic Powder from Metal Organic Precursors for 0-3 Ceramic-Polymer Composites</b>	<b>377</b>
	<i>K. H. Han, R. E. Riman, and A. Safari</i>	
<b>35</b>	<b>Sol-Gel Synthesis of Alumina-Zirconia and Mullite-Zirconia</b>	<b>385</b>
	<i>J. M. Boulton, S. Subramoney, and D. R. Uhlmann</i>	
<b>36</b>	<b>Densification of Silica-Cubic Boron Nitride Composites: I</b>	<b>393</b>
	<i>A. Nazeri-Eshghi and J. D. Mackenzie</i>	

## CONTENTS

xxiii

37	<b>Mechanical Behavior of (Poly)methylmethacrylate-Impregnated Silica Gels</b> <i>B. Abramoff and L. C. Klein</i>	401
38	<b>Organically Modified Ceramics—Materials with “History” or “Future”?</b> <i>H. Schmidt</i>	409
39	<b>Structure–Property Study of Hybrid Materials Incorporating Organic Oligomers into Sol–Gel Systems</b> <i>H. Huang, R. H. Glaser, A. B. Brennan, D. Rodrigues, and G. L. Wilkes</i>	425
40	<b>Structure–Property Investigations in Heat-Treated Polyquinoline Fibers</b> <i>S. Subramoney, D. R. Uhlmann, M. Featherstone, G. C. Berry, A. Parker, J. Tsang, and J. K. Stille</i>	439
<b>PART 5 OPTICAL AND ELECTRICAL APPLICATIONS</b>		445
41	<b>Recent Optical Studies of the Local Environment of Rare Earth Ions in Glass</b> <i>M. J. Weber</i>	447
42	<b>Nonlinear Optical Processes in Polymers and Sol–Gel Glass Composites</b> <i>P. N. Prasad</i>	461
43	<b>Phase Change Materials for Optical Data Storage</b> <i>D. P. Birnie III</i>	475
44	<b>Structure-Dependent Optical Properties of Composite Materials</b> <i>B. G. Potter, E. M. Clausen, C. J. Simmons, and J. J. Simmons</i>	491
45	<b>Gradient-Index Materials by the Sol–Gel Process</b> <i>M. Yamane</i>	509

<b>46</b>	<b>Laser Behavior and Nonlinear Optical Properties in Organic Dye-Doped Sol-Gel Materials</b>	<b>519</b>
	<i>E. T. Knobbe, B. Dunn, P. D. Fuqua, F. Nishida, and J. I. Zink</i>	
<b>47</b>	<b>Optical Properties of Artificially Structured Metals</b>	<b>531</b>
	<i>C. M. Falco, J. M. Slaughter, and B. N. Engel</i>	
<b>48</b>	<b>Sol-Gel Synthesis of Planar Optical Waveguides and Integrated Components</b>	<b>545</b>
	<i>R. L. Roncone, L. A. Weller-Brophy, and B. J. J. Zelinski</i>	
<b>49</b>	<b>Chemical Synthesis of Lanthanum Sesquisulfide Powders for Infrared Optical Applications</b>	<b>555</b>
	<i>P. N. Kumata and S. H. Risbud</i>	
<b>50</b>	<b>Fabrication of Superconducting Oxide Coatings Films and Fibers by the Sol-Gel Method</b>	<b>565</b>
	<i>S. Sakka and H. Kozuka</i>	
<b>51</b>	<b>Superconductivity and Microstructure in Lead-Substituted Bi-Sr-Ca-Cu-O Ceramics</b>	<b>579</b>
	<i>H. C. Ling</i>	
<b>52</b>	<b>Ultrastructure Processing of Ceramics in Electronics Packaging</b>	<b>599</b>
	<i>H. T. Sawhill</i>	
<b>53</b>	<b>Synthesis, Characterization, and Applications of Lead and Barium Titanate Materials Prepared by the Sol-Gel Method</b>	<b>613</b>
	<i>M. A. Aegerter, Y. Charbouillot, N. Mohallem, and L. H. de Godoy</i>	
<b>54</b>	<b>A Novel Process for Fabrication of Bi-Ca-Sr-Cu-O High- <math>T_c</math> Superconductors—A Glass-to-Ceramic Process</b>	<b>629</b>
	<i>H. Zheng and J. D. Mackenzie</i>	
<b>55</b>	<b>Sol-Gel Growth of Vanadium Dioxide Phase Transition Materials</b>	<b>641</b>
	<i>K. R. Speck, H. S.-W. Hu, R. A. Murphy, and R. S. Potember</i>	

## CONTENTS

xxv

<b>PART 6 ORGANOMETALLIC PRECURSORS- POLYMERS, AND AEROGELS</b>	<b>649</b>
<b>56 Transition Metal-Catalyzed Routes to Polysilane Polymers</b>	<b>651</b>
<i>H.-G. Woo and T. D. Tilley</i>	
<b>57 Polycarbosilanes as Silicon Carbide Precursors</b>	<b>667</b>
<i>D. Seyferth and H. Lang</i>	
<b>58 Preparation of Aluminum Nitride Fibers</b>	<b>675</b>
<i>J. D. Bolt</i>	
<b>59 Structure-Reactivity Relationships of Polysilazane Preceramics</b>	<b>681</b>
<i>K. A. Youngdahl, J. A. Rahn, R. M. Laine, R. A. Kennish, and G. A. Balavoine</i>	
<b>60 Multifunctional Macromolecular Materials</b>	<b>687</b>
<i>A. Buckley, G. W. Calundann, L. F. Charbonneau, and A. J. East</i>	
<b>61 The Microstructure of Aerogels and Its Effect on Properties</b>	<b>699</b>
<i>J. Fricke</i>	
<b>62 Aerogels and Xerogels from Organic Precursors</b>	<b>711</b>
<i>R. W. Pekala</i>	
<b>Index</b>	<b>719</b>

# **ULTRASTRUCTURE PROCESSING OF ADVANCED MATERIALS**

## PART 1

# **Precursors, Chemistry, and Structure Development in Ultrastructure Processing**



# 1

## CHEMISTRY AND REACTIONS OF METAL ALKOXIDES

D. C. BRADLEY

### 1.1. INTRODUCTION

The metal alkoxides  $[M(OR)_x]_n$ , where  $M$  is a metal of valency  $x$  and  $R$  is an alkyl group, have been known for more than a century but it was not until 1978 that a monograph was published on this topic [1], although a number of review articles had appeared before then. Interestingly there has been a resurgence of interest in the metal alkoxides in recent years primarily because it has at last been recognized that they are excellent precursor molecules for the deposition of metal oxides by either metallo-organic chemical vapor deposition (MOCVD) or sol-gel processes. The driving force for this activity has been due to the important role played by metal oxides in the electronics, ceramics, and glass industries.

Because the basic features of the chemistry of metal alkoxides have been comprehensively described [1], this Chapter will give only a brief review of the topic with an emphasis on new developments since 1978.

---

*Ultrastructure Processing of Advanced Materials.*

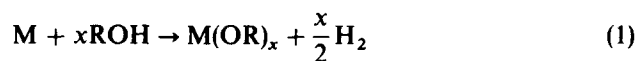
Edited by Donald R. Uhlmann and Donald R. Ulrich (deceased).

ISBN 0-471-52986-9 © 1992 John Wiley & Sons, Inc.

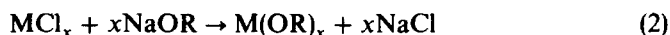
## 1.2. SYNTHETIC METHODS

1.2.1. The Preparation of Binary Metal Alkoxides  $M(OR)_x$ 

A variety of methods is available and the choice is determined mainly by the electropositive nature of the metal or by any specific requirements concerning purity. Thus, the alkoxides of the alkali metals, the alkaline earths, and the trivalent metals can all be synthesized by the direct reaction between metal and alcohol.



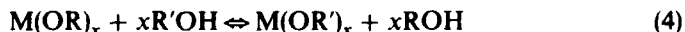
However, in the case of divalent or trivalent metals, the use of a catalyst (either  $I_2$  or  $HgCl_2$ ) is required to initiate the reaction. Because the catalyst may introduce undesirable impurities, it may be necessary to use an alternative route. For the trivalent and higher valent metals, the chloride method is usually satisfactory.



There are two main limitations to this method. If the metal alkoxide is insoluble (e.g., some methoxides) then there will be problems of separation from the sodium chloride (Eq. 2). This can be overcome by using the lithium alkoxide in place of the sodium alkoxide, because lithium chloride can usually be extracted out of the insoluble metal alkoxide. The second problem arises when there is the formation of a stable ternary metal alkoxide (or double alkoxide) involving the sodium and the other metal [e.g.,  $NaZr_2(OR)_9$ ]. The use of anhydrous ammonia usually solves this problem.

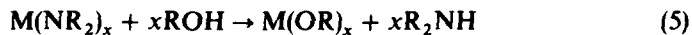


Yet another method involves alcohol interchange:



Provided that the alcohol  $R'OH$  has a higher boiling point than  $ROH$ , the reaction can be driven quantitatively to the right-hand side by fractional distillation. This method is very useful when the alcohol  $R'OH$  is in short supply or is liable to cause side reactions in Eq. 3. There are some limitations when  $R'OH$  involves a bulky  $R'$  group.

Another specialized method makes use of the reactivity of metal dialkylamides:



Finally, one should mention the electrochemical synthesis using the metal as a sacrificial anode. This method has recently been shown to give high yields of the alkoxides of Sc, Y, Ti, Zr, Nb, Ta, Ga, and Ge [2].

### 1.2.2. The Preparation of Heterometal Alkoxides (Ternary and Quaternary Compounds)

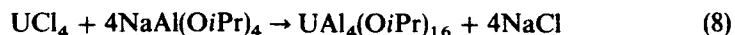
The ternary metal alkoxides (double alkoxides)  $M_aM'_b(OR)_x$  have been known for many years [1] and can be prepared by various methods. The simplest method is to combine the two binary alkoxides in the correct proportions.



If M is an alkali metal and M' a less electropositive (higher valency) metal, then the reaction can be carried out as a titration. Alternatively the electropositive metal M can be made to react with  $M'(OR)_y$  in the parent alcohol.



Another method uses the reaction between a metal chloride and a ternary metal alkoxide:



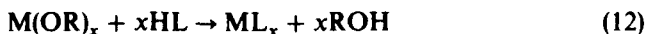
Recently Dubey et al. [3, 4] have developed interesting syntheses of heterometal alkoxides containing three or even four different metals.



The heterometal alkoxides are clearly of immense interest because of their potential as precursors for depositing heterometal oxides.

## 1.3. CHEMICAL PROPERTIES

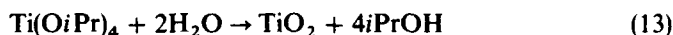
The metal alkoxides are characterized by their ability to undergo reactions with protic ligands HL in a general reaction that liberates the alcohol:



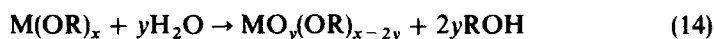
Depending on the ligand L, a variety of compounds such as alkoxides

## 6 CHEMISTRY AND REACTIONS OF METAL ALKOXIDES

(L = OR'),  $\beta$ -diketonates (L = RCOCHCOR), carboxylates (L = RCO<sub>2</sub>), or halides (L = X) may be formed. However, the most important reaction is hydrolysis (L = OH), because this leads directly to the metal oxide



For most metal alkoxides, hydrolysis is a facile reaction, and its mechanism has not been unraveled, although it has been shown by controlled hydrolysis that the intermediate metal oxide alkoxides may be isolated.

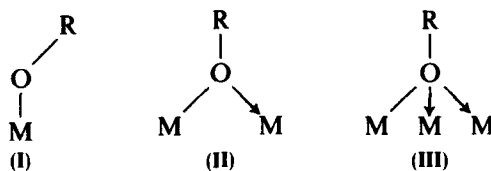


These compounds are interesting from the structural point of view in forming a link between the oligomeric metal alkoxides  $[\text{M}(\text{OR})_x]_n$  and the three-dimensional macromolecular metal oxides.

### 1.4. PHYSICAL PROPERTIES

#### 1.4.1. Structures

Another common property of the metal alkoxides is their oligomeric nature due to the tendency of the metal to expand its coordination number by utilizing the bridging capability of the alkoxide oxygen that may bond to two (II) or three (III) metals [1].



Generally the metal coordination number will reflect the typical chemistry of that metal in forming complex compounds. Thus the tetrameric form of aluminium isopropoxide is interesting in that it contains a central octahedrally coordinated aluminium joined to three tetrahedrally coordinated aluminiums by bridging ( $\mu_2$ ) alkoxides (Fig. 1.1). Similarly, niobium and tantalum pentaalkoxides are dimeric with octahedrally coordinated metals joined by bridging ( $\mu_2$ ) alkoxides (Fig. 1.2). The tetrameric structure of titanium tetraalkoxides is extremely interesting, because both bridging modes ( $\mu_2$  and  $\mu_3$ ) are present in this centrosymmetric molecule that contains distorted octahedrally coordinated titaniums in an edge-shared structure (Fig. 1.3).

Some structural information on oligomeric metal alkoxides has been derived from nuclear magnetic resonance (NMR) spectroscopy [1]. Thus the structure of  $\text{Al}_4(\text{Oi-Pr})_{12}$  (Fig. 1.1), which was originally postulated in 1959 [5], was

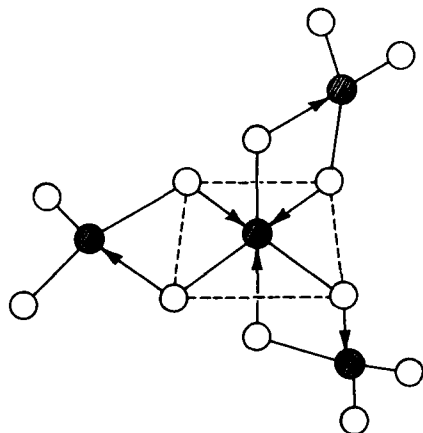


Figure 1.1. Structure of  $\text{Al}_4(\text{OR})_{12}$  (R groups omitted).

confirmed by  $^1\text{H}$ -NMR by Shiner et al. [6] before the X-ray crystal structure was determined [7]. The  $^1\text{H}$ -NMR spectra of lanthanide aluminium alkoxides  $\text{LnAl}_3(\text{O}i\text{-Pr})_{12}$  ( $\text{Ln}$  = lanthanide) suggested a similar structure for these compounds with the larger lanthanide atom occupying the octahedral site [8]. Variable-temperature NMR spectroscopy has also been used to demonstrate the fluxional behavior of metal alkoxide oligomers in which the terminal and bridging alkoxide groups undergo rapid exchange. Thus, the edge-shared bioctahedral structure of the dimeric pentaalkoxides  $\text{M}_2(\text{OR})_{10}$  (Fig. 1.2) was established by  $^1\text{H}$ -NMR [9] before the determination of the X-ray crystal structure [10]. However, the ethoxide groups in  $\text{Ti}_4(\text{OEt})_{16}$  were too labile even at very low temperatures to allow a structural determination by NMR and an X-ray crystal structure was required [1]. Interestingly, Chisholm et al. [11] found that  $\text{W}_4(\text{OEt})_{16}$ , which has a similar structure, was stereochemically rigid

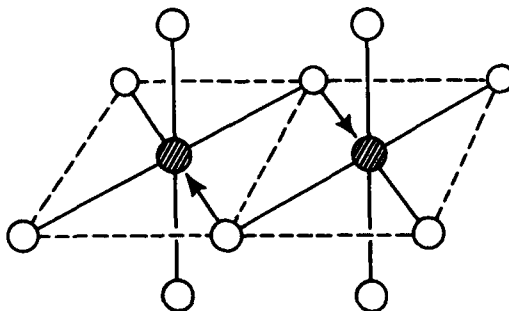


Figure 1.2. Structure of  $\text{M}_2(\text{OR})_{10}$  (R groups omitted).

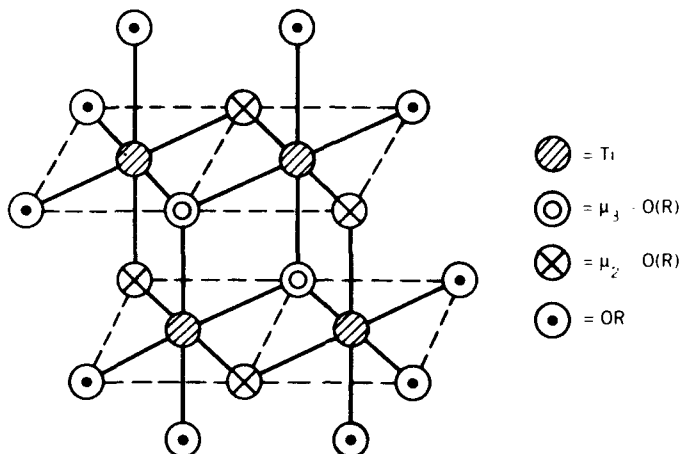


Figure 1.3. Structure of  $\text{Ti}_4(\text{OR})_{16}$  (R groups omitted).

due to the presence of tungsten-tungsten bonding involving the  $5d^2$  orbitals of  $\text{W(IV)}$  [cf.  $\text{Ti(IV)} d^0$ ].

Relatively few structures are known for metal oxide alkoxides  $[\text{M}_x\text{O}_y(\text{OR})_{x-2y}]$  with the first X-ray crystal structure being carried out on  $\text{Ti}_7\text{O}_4(\text{OEt})_{20}$  [12], which contains titanium in distorted octahedral configuration. Similarly the niobium(V) was shown to exhibit very distorted octahedral configurations in  $\text{Nb}_8\text{O}_{10}(\text{OEt})_{20}$  [13]. Recently, Chisholm et al. have isolated and characterized by X-ray crystallography a number of interesting new molybdenum oxoalkoxides  $[\text{Mo}_3(\mu_3\text{-O})(\mu_3\text{-OR})(\mu_2\text{-OR})_3(\text{OR})_6]$  [14],  $[\text{Mo}_4\text{O}_4(\mu_2\text{-O})_2(\mu_3\text{-O})_2(\mu_2\text{-Oi-Pr})_2(\text{Oi-Pr})_2(\text{pyridine})_4]$  [11], and  $[\text{Mo}_6\text{O}_{10}(\text{Oi-Pr})_{12}]$  [15]. These and related compounds were reviewed by Chisholm [16] under the heading of Metal Alkoxides: Models for Metal Oxides. The only structurally characterized species containing transition metals in coordination numbers higher than 6 is the trideca zirconium oxide methoxide  $\text{Zr}_{13}\text{O}_8(\text{OMe})_{36}$  reported by Morosin [17]. This complex structure contains a central 8-coordinated zirconium bonded to the oxo ligands, which also bridge the 12 peripheral 7-coordinated zirconiums, which are each bonded to two oxo ligands, four bridging methoxides, and one terminal methoxide.

A few structures of nontransition metal oxide alkoxides are known. From the partial hydrolysis of lead diisopropoxide, Yanovskii et al. [18] obtained the hexanuclear compound  $[\text{Pb}_6(\mu_3\text{-O})_4(\mu_3\text{-Oi-Pr})_8]$  in which each lead atom is bonded to two  $\mu_3\text{-O}$  ligands and two  $\mu_3\text{-Oi-Pr}$  ligands.

In attempting to prepare  $\text{In(Oi-Pr)}_3$  from the reaction of indium trichloride and sodium isopropoxide, we were surprised to isolate a crystalline complex  $[\text{In}_5(\mu_5\text{-O})(\mu_3\text{-Oi-Pr})_4(\mu_2\text{-Oi-Pr})_4(\text{Oi-Pr})_5]$  (Fig. 1.4) which comprises an unique  $\mu_5\text{-O}$  ligand bonded to five indiums in a tetragonal pyramidal configuration. Each indium is bonded to one terminal isopropoxide trans to the  $\mu_5\text{-O}$  and two  $\mu_3\text{-isopropoxides}$  and two  $\mu_2\text{-isopropoxides}$  giving a distorted octahedral

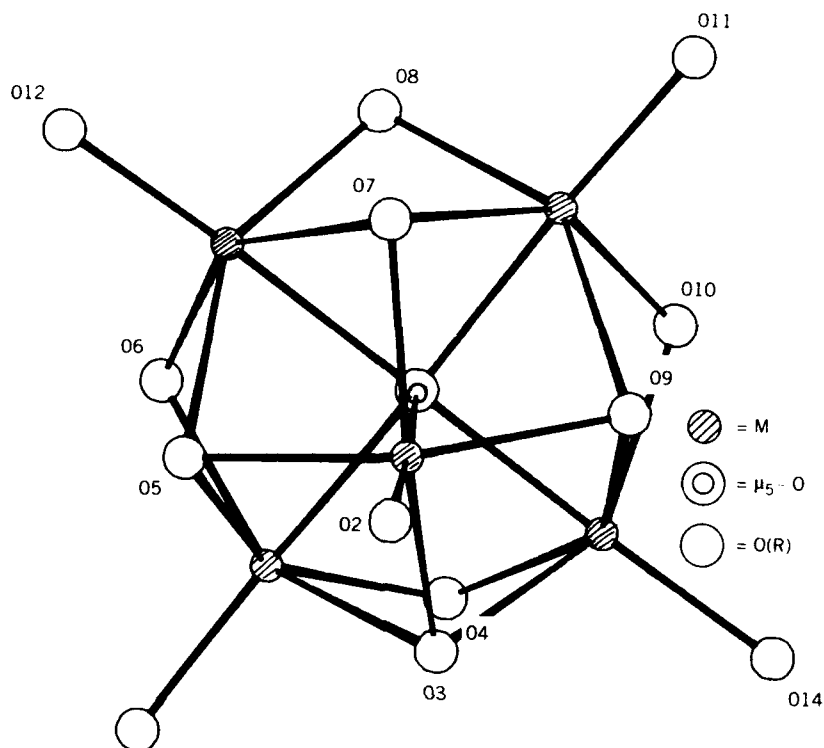


Figure 1.4. Structure of  $M_5(\mu_5-O)(\mu_3-OR)_4(\mu_2-OR)_4(OR)_5$  (R groups omitted).

configuration [19]. The low-temperature  $^1\text{H}$ - and  $^{13}\text{C}$ -NMR spectra showed that this structure was maintained in toluene solution. We have also found that scandium, yttrium, and ytterbium all give similar complexes with the formula  $[M_5(\mu_5-O)(\mu_3\text{-O}i\text{-Pr})_4(\mu_2\text{-O}i\text{-Pr})_4(\text{O}i\text{-Pr})_5]$ , which can be sublimed in vacuo and give mass spectra demonstrating the survival of the pentanuclear cluster in the gas phase [19]. Because the earlier literature reported straightforward preparations of the triisopropoxides  $M(\text{O}i\text{-Pr})_3$  of all of these metals [1], we are currently reinvestigating this field.

#### 1.4.2. Volatility

Metal alkoxides with the lower alkyl groups (e.g., methyl, ethyl) tend to be relatively nonvolatile due to their oligomeric structure involving the bridging alkoxide group [1]. In these compounds, the enthalpy of vaporization  $\Delta H_v$  will be large due either to the energy required to depolymerize the structure to liberate monomeric gas molecules or, if the oligomer structure is very stable, to

the much greater intermolecular forces involved in the condensed phase of the larger molecules.

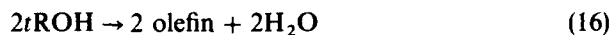
We found that a dramatic increase in volatility could be engineered by using the steric effect of bulky alkoxy groups to prevent the formation of oligomers [1]. Thus in the case of zirconium tetraalkoxides  $[\text{Zr}(\text{OR})_4]_n$ , the highly polymeric tetramethoxide sublimed at  $280^\circ\text{C}/10^{-4}$  torr, the tetrameric tetraethoxide sublimed at  $180^\circ\text{C}/10^{-4}$  torr, the trimeric tetraisopropoxide distilled at  $160^\circ\text{C}/0.1$  torr, and the mobile liquid monomeric tetratertiary butoxide distilled at  $54^\circ\text{C}/0.1$  torr. The latter compound has a measurable vapor pressure at room temperature and produces a fog of zirconium dioxide on exposure to moist air. Extensive studies on a large number of metal alkoxides established that the tertiary alkoxides were the most effective in screening the central metal atom and that the larger the metal atom, the larger was the tertiary alkoxide required to produce a mononuclear metal alkoxide. This use of steric hindrance to prevent oligomerization is most effective for metals in higher valence states (e.g., 4, 5, and 6). For the lower valences (e.g., 1, 2, and 3), it becomes difficult, if not impossible, to produce monomeric metal alkoxides. Thus lithium tertiary butoxide (sublimes  $110^\circ\text{C}/0.1$  torr) is hexameric  $\text{Li}_6(\text{Ot-Bu})_6$  and beryllium ditertiary butoxide (sublimed  $100^\circ\text{C}/10^{-3}$  torr) is trimeric  $\text{Be}_3(\text{Ot-Bu})_6$ . The use of the bulkier tertiary heptyloxy group  $\text{OC}(\text{C}_2\text{H}_5)_3$  resulted in the formation of a more volatile ( $50\text{--}70^\circ\text{C}/10^{-3}$  torr) dimeric beryllium compound. For trivalent iron and aluminium, the tertiary butoxides are dimeric and can be distilled at  $136^\circ\text{C}/0.1$  torr and  $134^\circ\text{C}/0.2$  torr. Our current work using much bulkier tertiary alkoxide groups suggests that more volatile derivatives of yttrium and other trivalent metal alkoxides  $\text{M}(\text{OR})_3$  can be obtained especially when  $\text{CF}_3$  groups are used in place of  $\text{CH}_3$  groups.

#### 1.4.3. Thermal Stability and Metal–Oxygen Bond Strengths for Metal Alkoxides

For many years the ease of hydrolysis of metal alkoxides had been explained in terms of weak metal–oxygen bonds, although there was no direct evidence to support this. Some of the earlier work also claimed a low thermal stability for metal alkoxides. However, from our reaction calorimetry on titanium tetraalkoxides [20], we calculated high average bond dissociation energies  $\bar{D}$  of  $104 \pm 2$  kcal/mol for several compounds. For the  $3d^0$ ,  $3d^1$ ,  $3d^2$  tetrahedrally coordinated metal alkoxides  $\text{Ti}(\text{Ot-Bu})_4$ ,  $\text{V}(\text{Ot-Bu})_4$ , and  $\text{Cr}(\text{Ot-Bu})_4$ , the values of  $\bar{D}$  were 102, 87.5, and 73 kcal/mol [21]. The ease of hydrolysis of  $d^0$  transition metal alkoxides is presumably a consequence of the presence of low-energy unfilled d orbitals, which offer a facile substitution mechanism, and is not due to the presence of weak  $\text{M-OR}$  bonds. Similarly our studies on the thermal stability of zirconium tetraalkoxides [22] showed that when pure these compounds have high thermal stability and that primary alkoxides are more stable than secondary alkoxides, which are more stable than tertiary alkoxides. In fact, the facile decomposition of the tertiary alkoxides is due to a hydrolytic



mechanism, which is caused by the heterogeneous dehydration of the tertiary alcohol, which sets up a chain reaction [23].



The apparent stability of the metal alkoxide then depends on how much care is taken to eliminate residual water in the system. It seems probable that this hydrolytic mechanism is responsible for the ease with which zirconium dioxide can be deposited by thermolysis at a relatively low temperature (e.g., 180°C).

Further evidence of the intrinsic stability of the metal-oxygen bonds in metal alkoxides can be found in the mass spectra of a range of monomeric and oligomeric metal alkoxides that show parent molecular ions and very strong fragment ions caused by the loss of alkyl groups rather than alkoxo ligands [1].

## 4.5 INDUSTRIAL APPLICATIONS

Metal alkoxides are ubiquitous compounds that have found a variety of applications in industry, such as catalysts for organic reactions, components of heat resisting paints, water-repellent treatments for fabrics, and paint and ink drying agents and as precursors for the deposition of metal oxides, glasses, and ceramics [1]. The volatile metal alkoxides are especially useful for depositing metal oxide films by the MOCVD technique. Not only binary metal oxides  $\text{Al}_2\text{O}_3$ ,  $\text{TiO}_2$ ,  $\text{ZrO}_2$ ,  $\text{HfO}_2$ ,  $\text{Ta}_2\text{O}_5$ , and so on, but also ternary oxides, such as  $\text{BaTiO}_3$ ,  $\text{LiNbO}_3$ , and  $\text{PbTiO}_3$ , and quaternary oxides, such as  $\text{PbSc}_{0.5}\text{Ta}_{0.5}\text{O}_3$ , have been deposited by MOCVD [24]. These materials are of considerable importance to the electronics industry due to their range of electrical and electrooptical properties. For bulk production of speciality glasses and ceramic oxides, the sol-gel technique has found widespread use. In this technique the metal alkoxides are dissolved in a suitable solvent, and the solution is hydrolyzed under controlled conditions to produce a gel of the hydrated metal oxide. After drying and compacting, the solid can be fired at a relatively low temperature to produce the glass or ceramic [25].

## REFERENCES

1. D. C. Bradley, R. C. Mehrotra, and D. P. Gaur, *Metal Alkoxides* Academic Press, London New York San Francisco (1978).
2. V. A. Shreider, E. P. Turevskaya, N. I. Koslova, and N. Ya. Turova, *Inorg. Chim. Acta*, **53**, L73 (1981).
3. R. K. Dubey, A. Shah, A. Singh, and R. C. Mehrotra, *Rec. Trav. Chim.*, **107**, 237 (1988).
4. R. K. Dubey, A. Singh, and R. C. Mehrotra, *J. Organomet. Chem.*, **341**, 569 (1988).

## 12 CHEMISTRY AND REACTIONS OF METAL ALKOXIDES

5. D. C. Bradley, *Advan. Chem. Ser.*, **23**, 10 (1959).
6. V. J. Shiner, D. Whittaker, and V. P. Fernandez, *J. Amer. Chem. Soc.*, **85**, 2318 (1963).
7. N. Ya Turova, V. A. Kozunov, A. I. Yanovskii, N. G. Bokii, Yu. T. Struchkov, and B. L. Tarnopol'skii, *J. Inorg. Nucl. Chem.*, **41**, 5 (1979).
8. R. C. Mehrotra and M. M. Agrawal, *J. Chem. Soc., Chem. Commun.*, 469, (1968).
9. D. C. Bradley and C. E. Holloway, *J. Chem. Soc. (A)*, 219 (1968); C. E. Holloway, *J. Coord. Chem.*, **1**, 253 (1972).
10. A. A. Pinkerton, D. Schwarzenbach, L. G. Hubert-Pfalzgraf, and J. G. Riess, *Inorg. Chem.*, **15**, 1196 (1976).
11. M. H. Chisholm, J. C. Huffman, C. C. Kirkpatrick, J. Leonelli, and K. Folting, *J. Amer. Chem. Soc.*, **103**, 6093 (1981).
12. K. Watenpaugh and C. N. Caughlan, *J. Chem. Soc., Chem. Commun.*, 76 (1967).
13. D. C. Bradley, M. B. Hursthouse, and P. F. Rodesiler, *J. Chem. Soc., Chem. Commun.*, 1112 (1968).
14. M. H. Chisholm, K. Folting, J. C. Huffman, and C. C. Kirkpatrick, *J. Amer. Chem. Soc.*, **103**, 5967 (1981).
15. M. H. Chisholm, K. Folting, J. C. Huffman, and C. C. Kirkpatrick, *Inorg. Chem.*, **23**, 1021 (1984).
16. M. H. Chisholm, *Inorganic Chemistry: Toward the 21st Century*, Vol. 16, p. 243, American Chemical Society, Washington D.C. (1983).
17. B. Morosin, *Acta Crystallogr., Sect. B*, **33**, 303 (1977).
18. A. I. Yanovskii, N. Ya. Turova, E. P. Turevskaya, and Yu. T. Struchkov, *Koord. Khim.*, **8**, 153 (1982).
19. D. C. Bradley, H. Chudzynska, D. M. Frigo, and M. A. Mazid, *J. Chem. Soc., Chem. Commun.*, 1258 (1988).
20. D. C. Bradley and M. J. Hillyer, *Trans. Farad. Soc.*, **62**, 2367, (1966).
21. D. C. Bradley and M. J. Hillyer, *Trans. Farad. Soc.*, **62**, 2374 (1966).
22. D. C. Bradley and M. M. Faktor, *J. Applied Chem.*, **9**, 5425 (1959).
23. D. C. Bradley and M. M. Faktor, *Trans. Farad. Soc.*, **55**, 2117 (1959).
24. D. C. Bradley, *Chem. Rev.*, **89**, 1317 (1989).
25. J. F. Campion, D. A. Payne, H. K. Chae, J. K. Maurin and S. R. Wilson, *Inorg. Chem.* **30**, 3244 (1991).

## 2

# MOLECULAR-LEVEL UNDERSTANDING OF THE SOL-GEL PROCESS

JIRI JONAS

## 2.1. INTRODUCTION

As a continuation of our efforts to improve the molecular level understanding of the sol-gel process, we have recently carried out several studies dealing with the tetramethylorthosilicate (TMOS)/CH<sub>3</sub>OH/H<sub>2</sub>O system. This report reviews some of the main results obtained in these experiments.

It has been shown that the fluoride anion F<sup>-</sup> is one of the most effective catalysts [1] in accelerating the gelation process. For example, a concentration of  $1.25 \times 10^{-4}$  M NaF in TMOS at neutral pH and room temperature reduces the gelation time,  $t_{\text{gel}}$ , from 33 to 10 h. By employing <sup>29</sup>Si-NMR and Raman spectroscopy [2], we were able to study the early stages of the polymerization process of uncatalyzed and fluoride-catalyzed TMOS sols. In addition, we carried out a detailed characterization of surface properties of dried gels (xerogels) by using the Brunaur-Emmett-Teller (BET) technique [3]. The surface area, pore volume, average pore radius and pore size distribution were discussed as a function of fluoride concentration. It has been found that addition of NaF to TMOS sols leads to a large increase in pore size, and the pore distribution becomes narrower.

*Ultrastructure Processing of Advanced Materials.*

Edited by Donald R. Uhlmann and Donald R. Ulrich (deceased).

ISBN 0-471-52986-9 © 1992 John Wiley & Sons, Inc.

**TABLE 2.1. Experimental Techniques Used to Study the Gelation Point**

---

NMR relaxation times
Fluorescence polarization
Turbidity
Low-frequency Raman spectra
Static and dynamic light scattering
Shear viscosity

---

In order to obtain information about the growth process and structural evolution in the course of the sol-gel transition, we applied the small-angle neutron scattering (SANS) technique [4] to study uncatalyzed and  $F^-$ -catalyzed TMOS sols. It has been well established [5-11] that both SAXS and SANS techniques can be used to follow the evolution of structure of gels. The purpose of our work was to characterize the structural properties of these systems from the formation of the sol to the final gel and to elucidate how this process is affected by the addition of NaF.

In the course of these experiments, we realized that there is a great need to provide more information on the gelation point and to search for more quantitative ways to determine the gelation time. The most common way of determining the gelation time is to observe when the meniscus of a sol in a container no longer remains horizontal when the container is tilted. This method also used in our experiments is somewhat arbitrary because we recognize that the gelation time depends on the volume of the sample.

This provided motivation for our work in progress [12] aimed at a better definition of the gelation point. Various experimental techniques, as listed in Table 2.1, are employed in these experiments dealing both with microscopic and macroscopic characterizations of the gelation point [13-15]. Several specific results discussed in this Chapter will illustrate the scope of our systematic studies in progress.

## 2.2. EXPERIMENTAL

The sol-gel samples were prepared by a dropwise addition of a  $H_2O/CH_3OH$  mixture to the silicon-alkoxide tetramethylorthosilicate (TMOS),  $Si(OCH_3)_4$  (Aldrich Chemical Company) which was diluted in  $CH_3OH$ . Concentration of the reagents were adjusted to yield a final mole ratio  $TMOS:CH_3OH:H_2O = 1:4:4$ . The initial pH value of these solutions was about 6.4, which was measured with a digital pH meter with a glass electrode. The samples were maintained at room temperature (23°C) throughout the whole study.

The experimental procedures were given in detail elsewhere [2-4, 12]. The

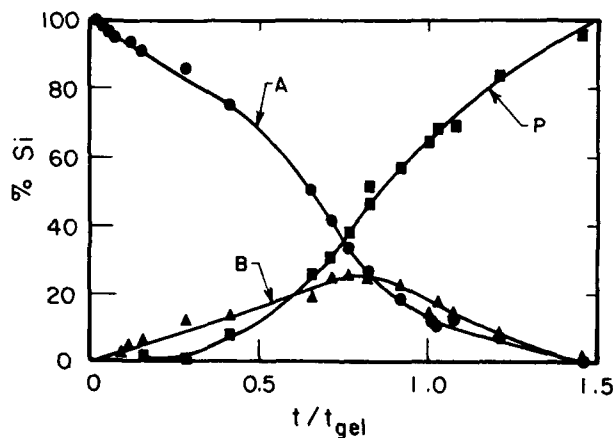
following fluorescent probes were used: 2,3-(diphenylhexatriene)propanoyl-3-palmitoyl-L- $\alpha$ -phosphatidylcholine (DPHPC); 2-aminonaphthalene-8-sulfonate (ANS), and the laser dye, rhodamine 6G.

## 2.3. RESULTS AND DISCUSSION

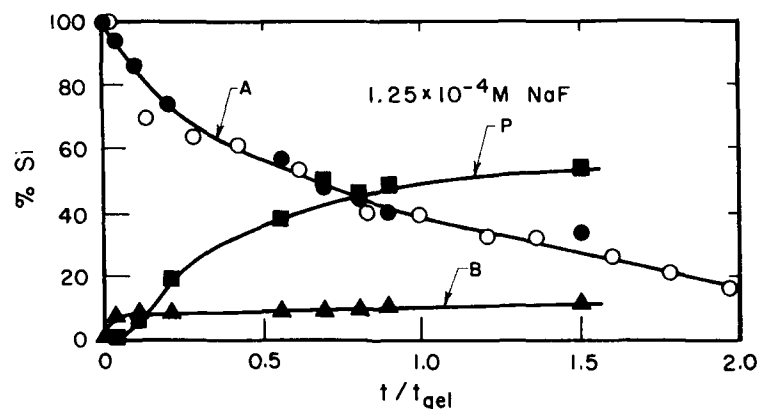
### 2.3.1. The Effect of Fluoride on the Sol-Gel Process

Natural abundance  $^{29}\text{Si}$ -NMR spectroscopy and laser Raman scattering experiments [2] were employed to investigate the effects of the fluoride ion on the gelation process in TMOS at pH 6.4. The hydrolysis and condensation reactions responsible for gelation can be followed by the appearance and disappearance of spectroscopic signals arising from the different species detected during this process.

Figures 2.1 and 2.2 depict the relative concentration (in %Si) of the monomers (A), dimers and trimers (B), and higher-branched silicon species (C-F, shortly abbreviated as P in the following) for solution without a catalyst (solution I) and for solution containing  $1.25 \cdot 10^{-4} \text{ M NaF}$  (solution II) as a function of time  $t$ , normalized to the gelation time  $t_{\text{gel}}$ . At the gelation point of solution I (without NaF), there are still about 13% monomers and 18% of dimers and trimers present. During the course of the polymerization, the dimers and trimers form as an intermediate state, their intensity reaches a maximum at about  $t/t_{\text{gel}} = 0.8$  and decreases to zero at  $t/t_{\text{gel}} = 1.5$ . At this time, all the monomers, dimers, and trimers have disappeared. In comparison, fluoride-



**Figure 2.1.** The time evolution of monomeric (A), dimeric and trimeric (B), and higher-branched (P) silicon groups for solution without catalyst as determined by natural abundance  $^{29}\text{Si}$ -NMR ( $t_{\text{gel}} = 33 \text{ h}$ ). Maximum error: 10% in %Si; 5% in  $t/t_{\text{gel}}$ .



**Figure 2.2.** The time evolution of monomeric (A), dimeric and trimeric (B), and higher-branched (P) silicon groups for fluoride-containing solution containing  $1.25 \times 10^{-4} M$  NaF; as determined by natural abundance  $^{29}\text{Si}$ -NMR ( $t_{gel} = 13$  h). Maximum error: 10% in %Si; 5% in  $t/t_{gel}$ . Closed symbols: NMR results; open circles: Raman results.

containing solution II contains still about 40% monomers at the gelation point, and it appears that the amount of dimers and trimers is almost constant 10% over the whole time scale. Also, in contrast to solution I, the monomer concentration in the fluoride-containing solution decreases more rapidly from the beginning, thus leading to a strong increase of higher-branched silicon species P. These data indicate that the dimers and trimers do not play a significant role as intermediate species in the polymerization process catalyzed by fluoride ions. In the case with added NaF, the experimental data indicate that the polymerization proceeds via the formation of higher-branched polymers from the very beginning of the process.

Similar to the NMR case, no specific changes in the spectral features of the Raman spectra are observed upon addition of NaF. Only a distinct difference between the intensities of the individual bands in solutions I and II is found. In particular, the intensity of the monomer TMOS band is very low at the gelation point in solution I, whereas the same band in solution II exhibits a rather high intensity, even at times  $t/t_{gel} = 1.5$ . A further difference is that the intensities of the hydrolyzed monomer species decrease with the increasing fluoride concentration.

A quantitative analysis of the Raman experiments can be obtained, because the peak intensities are proportional to the concentration of the scattering species. After calculating the intensity of the entire band between  $600$  and  $740\text{ cm}^{-1}$ , followed by subtraction of the background and normalization to the intensity of the methanol peak [16, 17], the total concentration of the monomer species  $C(t)$  at any time  $t$  can be obtained by  $C(t) = C(0) \cdot I(t)/I(0)$ , where  $I(t)$  is the normalized intensity at time  $t$ ,  $I(0)$  and  $C(0)$  are the corresponding values for the intensity and concentration at a time very close to the preparation time ( $t \approx 0$ ). As an example, Fig. 2.2 shows the relative concentration of the total

monomer species A for fluoride-containing solution II as obtained from the Raman experiment (open circles) together with the NMR results (closed circles). The agreement between these two experimental methods is very good.

Under our experimental conditions ( $\text{pH} = 6.4$ ), we observed no Si-O-Si network vibration at  $830\text{ cm}^{-1}$  during the course of the gelation reaction. This might be due to the formation of a very irregular structure of the wet gel in terms of a significant variation of O-Si-O bond angles and possibly also bond lengths. Such a structural feature can be explained by the presence of a relatively large amount of organic  $-\text{OCH}_3$  groups in the silica network, which will lead to an irregular and relatively open structure.

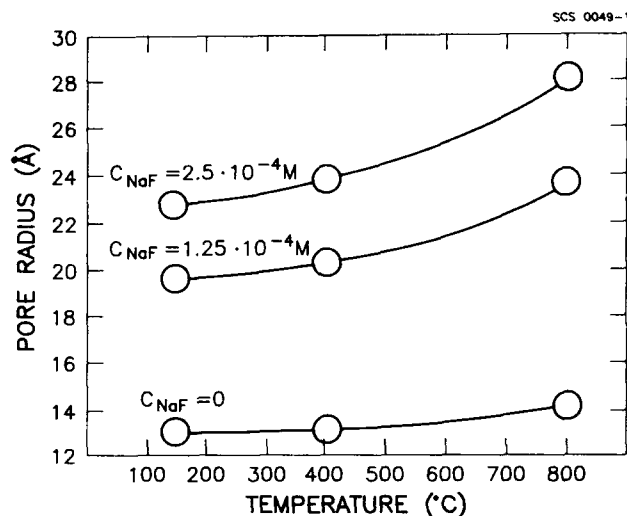
In order to test this suggestion, we performed the pore analysis of dried gels without and with NaF ( $2.5 \cdot 10^{-4}\text{ M NaF}$ ) using the BET technique [3]. Here we assumed that either the pore structure does not change significantly during the drying process or that the pore structure changes are comparable for the various samples prepared.

The overall surface area of pores increases slightly with the addition of fluoride. The most striking result of the pore analysis is the increase in total pore volume and average pore radius  $R$  due to the addition of fluoride. At the same time, the micropore ( $R < 10\text{ \AA}$ ) area decreases, and the mesopore ( $10\text{ \AA} \leq R \leq 250\text{ \AA}$ ) area increases. These findings support the interpretation that the presence of a certain amount of organic  $-\text{OCH}_3$  groups leads to the formation of a loose and relatively open silica network with a large fraction of mesopores and also containing a large amount of monomer species inside the large pores, even at times well after gelation.

The effect of the drying temperature on the average pore radius in samples with and without the fluoride anion is shown in Fig. 2.3. Due to the sintering process, the total pore volume decreases, and the average pore radius increases. The most interesting feature is that the micropores are gradually eliminated with increasing temperature, thus leading to a rather narrow distribution of mesopores at  $800^\circ\text{C}$ . The smaller pores collapse first at lower temperatures because of their higher surface energies. During the sintering process, residual  $\equiv\text{Si}-\text{OR}$  and  $\equiv\text{Si}-\text{OH}$  groups condense to  $\equiv\text{Si}-\text{O}-\text{Si}\equiv$  bonds. Thus, at these higher heating temperatures of about  $800^\circ\text{C}$ , narrow pore sizes can be obtained whose average pore radius can be tuned between 14 and  $28\text{ \AA}$  by changing the fluoride concentration. For still higher temperatures ( $T > 900^\circ\text{C}$ ), the mesopores will also collapse by viscous sintering, which leads to the formation of poreless dense silica glass [17-20].

Only a few comments are made on the results of the SANS experiments [4] on the uncatalyzed and fluoride-catalyzed TMOS gels. The analysis of the Guinier and Porod regions of the scattering curves yielded valuable information about the particle size, the structural evolution, and the growth process of these systems.

Let us focus on the question of fractal dimension that can be obtained from the analysis of the diffraction curves in the Porod region. For random objects, such as polymer structures, the concept of fractal geometry provides a valuable



**Figure 2.3.** The average pore radius  $R$  of uncatalyzed and fluoride-catalyzed gels as a function of heating temperature.

means of quantitatively describing the average structure of these objects by the relation  $M \propto R^D$ , where  $M$  is the mass of the object and  $D$  is the mass fractal dimension [21–23]. The intensity  $I(Q)$  scattered at higher angles ( $QR_g > 1$ ) in diffraction experiments can be analyzed in terms of a power law

$$I(Q) = Q^{-\mu} \quad (1)$$

using  $\ln I(Q)$  versus  $\ln Q$  plots. It has been shown [21–24] that  $\mu$  is related to the fractal dimension characteristics of the particles. For mass fractals of dimension  $1 < D < 3$ ,  $D = -\mu$ . In agreement with observations in similar silica systems [8], we observed no significant changes in the scattering profile or the  $D$  value at the gel point even though drastic changes in dynamic properties such as viscosity [15] are observed at the transition from the sol to the rigid gel. The fractal dimension was found to increase with time even after the time of gelling and reached a constant value only close to  $t/t_{gel} = 3$ . The time dependences of  $I_0$  and  $D$  clearly demonstrated that the local structure of the polymer network is changing a long time after gelation. The  $D$  value indicated that the scattering particles in the system are mass fractals over the entire time scale. Figure 2.4 compares the evolution of  $D$  for an uncatalyzed sample with that of a sample containing  $1.25 \times 10^{-4} M$  NaF up to  $t/t_{gel} = 1.0$ . The time dependence of  $D$  is similar for both systems, and at  $t/t_{gel} = 1$  the fractal dimension  $D = 1.6$  was obtained. From the Porod region, a fractal dimension  $D = 2.2 \pm 1$  was obtained at  $t \gg t_{gel}$ .

In the original study, we discussed in detail the analysis of the scattering data and compared the experimental results to predictions of theoretical models. The



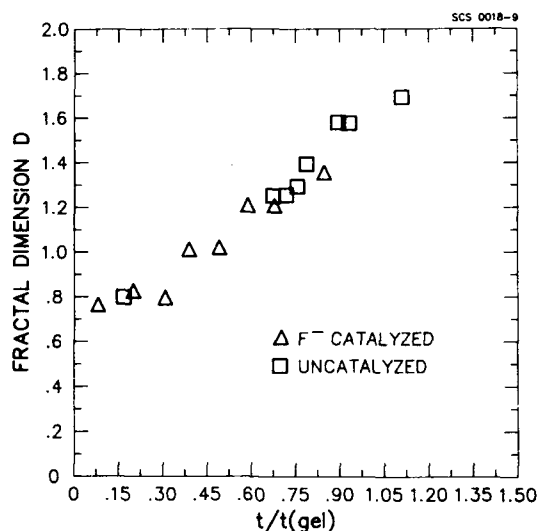


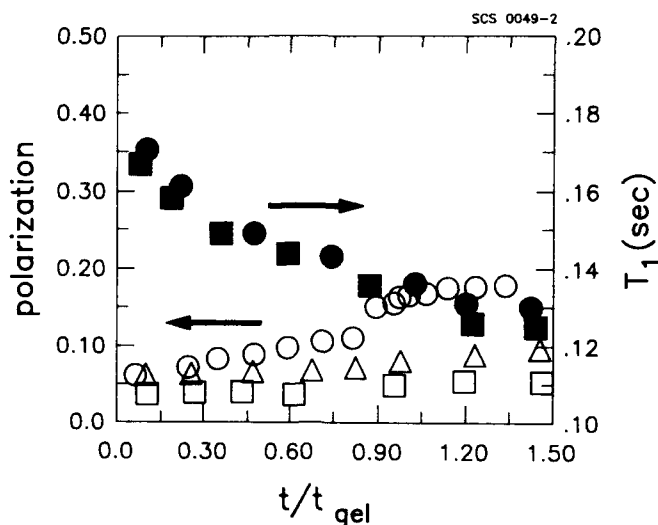
Figure 2.4. The time evolution of the fractal dimension  $D$  for uncatalyzed and fluoride-catalyzed samples.

experimentally observed value of  $D = 2.2$  found both for uncatalyzed and fluoride-catalyzed gels at  $t/t_{gel} \gg 1$  is quite close to that predicted for the chemical reaction-limited cluster-cluster growth model [13, 22, 25, 26].

### 2.3.2. Systematic Studies of the Gelation Point

As indicated in the Introduction, we have recently started systematic experiments [12] employing a variety of experimental techniques in order to obtain more quantitative information about the gelation point. Several preliminary results dealing with NMR relaxation studies, fluorescence polarization, and viscosity measurements will be discussed.

Both the NMR relaxation experiments and fluorescence polarization experiments show that the motional dynamics of small molecules such as  $D_2O$  and  $CD_3OD$  or various fluorescence probes show small changes in motional dynamics at  $t/t_{gel} = 1$  due to the fact that the pores in the wet gel are large enough to allow for relatively unhindered motion of the small molecules. This contrasts to the behavior of shear viscosity [15], which exhibits divergence when approaching the gelation point. Figure 2.5 compares the time dependence of deuterium NMR spin-lattice relaxation time in  $D_2O$  and  $CD_3OH$  with the polarization changes of various fluorescence probes of different size. One can see that the changes at  $t/t_{gel}$  for the microscopic probes are very small and the rotational motions are relatively free even after gelation, reflecting the existence of large pores filled with  $CD_3OH$  and  $D_2O$  in the gel network. The theoretical analysis of the viscosity and intrinsic viscosity measurements will be presented in



**Figure 2.5.** Comparison of rotational motion of various probes of different size during gelation. Fluorescent probes:  $\circ$ , DPHPC;  $\Delta$ , ANS;  $\square$ , Rhodamine 6G. NMR probes:  $\bullet$ ,  $\text{CD}_3\text{OH}$ ;  $\blacksquare$ ,  $\text{D}_2\text{O}$ . Because only the general change of  $T_1$  with time is of interest, the  $T_1$  scale for  $\text{CD}_3\text{OH}$  probe was set to coincide with the  $T_1$  values obtained for  $\text{D}_2\text{O}$ .

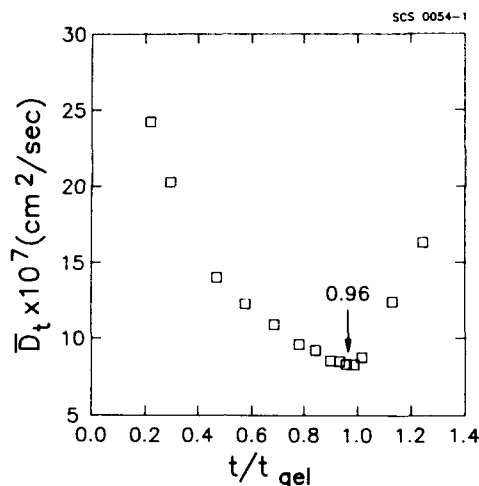
detail elsewhere [12] and compared with the recent results obtained by Pope and Mackenzie [15, 27].

In connection with the NMR experiments, it is interesting to note the deuterium isotope effect [12] on the gelation time. For the TMOS/ $\text{CH}_3\text{OH}/\text{H}_2\text{O}$  system, the gelation time was 36 h for pH 6.4 and  $23^\circ\text{C}$ ;  $t_{\text{gel}}$  increased to 58 h for TMOS/ $\text{CH}_3\text{OH}/\text{D}_2\text{O}$  under the same experimental conditions. The gelation time further increased to 65 h for the TMOS/ $\text{CD}_3\text{OD}/\text{D}_2\text{O}$  system.

At the present time, measurements using static (SLS) and dynamic light scattering (DLS) techniques are in progress. In addition to information on particle size and translational diffusion coefficient, the SLS data will enable us to test the scaling law behavior of the radius of gyration and the average molecular weight.

It is interesting to mention the preliminary result of the determination of the average translational diffusion coefficient  $D_t$  during gelation by the DLS method. The correlation function of the scattered light intensity is determined by the motional state of the scattering particles in the DLS experiment [28]. For a polydisperse sol-gel system one has to use a cumulant fit in order to obtain the average decay constant  $\Gamma$  of the correlation function  $G(t)$ .  $\Gamma$  is related to the average translational diffusion coefficient [29]

$$\Gamma = D_t q^2 \quad (2)$$



**Figure 2.6.** Time evolution of the average translational diffusion coefficient  $D_t$  for the TMOS gel as obtained by the dynamic light scattering experiment.

where  $q$  is the wave vector defined as  $q = (4\pi n/\lambda)\sin \theta/2$ ,  $\lambda$  is the wavelength of the incident light,  $n$  is the refractive index of the sol-gel (1.348), and  $\theta$  is  $90^\circ$ .

$\Gamma$  was obtained by fitting the experimental correlation functions for different reduced time  $t/t_{gel}$  with a third-order polynomial. The calculated  $D_t$  as a function of  $t/t_{gel}$  is shown in Fig. 2.6. It is clearly seen that the  $D_t$  versus  $t/t_{gel}$  plot can be used to indicate the gelation point for the sol-gel system. One observed a minimum in  $D_t$  versus  $t/t_{gel}$  at  $t/t_{gel} = 0.96$ . First, one sees the decrease in the effective diffusion coefficient reflecting a more restricted motion due to growth of particles, and after gelation, the increase in  $D_t$  may be due to further polymerization (aging) of the gel resulting in a more rigid gel. Similar results were obtained by Hwang and Cummings [30] in their DLS study on gelation of gels with added formaldehyde for which the decay rate of the correlation function continuously increased in time as the gel became increasingly rigid. A detailed theoretical analysis of the experimental DLS and SLS data is in progress [12]. One should add that of particular promise are the low-frequency Raman scattering experiments [31, 32] which together with the SANS experiments will lead to a better understanding of the structural development during the gelation process.

In conclusion, we observed no drastic changes in the structures at the gelation point, and the polymer network continues to change after gelation. Systematic experiments using various experimental techniques are necessary to improve our molecular-level understanding of the gelation process.

## ACKNOWLEDGMENTS

This work was partially supported by the Air Force Office of Scientific Research under Grant AFOSR 85-0345.

## REFERENCES

1. E. J. A. Pope and J. D. Mackenzie, *J. Non-Cryst. Solids*, **87**, 185 (1986).
2. R. Winter, J.-B. Chan, R. Frattini, and J. Jonas, *J. Non-Cryst. Solids*, **105**, 214 (1988).
3. J.-B. Chan, D.-W. Hua, R. Winter, and J. Jonas, *J. Mat. Res.*, **4**, 693 (1989).
4. R. Winter, D.-W. Hua, P. Thiagarajan, and J. Jonas, *J. Non-Cryst. Solids*, **108**, 137 (1989).
5. C. J. Brinker, K. D. Keefer, D. W. Schaeffer, R. A. Assink, B. D. Kay, and C. S. Ashley, *J. Non-Cryst. Solids*, **63**, 45 (1984).
6. G. Orcel, R. W. Gould and L. L. Hench, in *Mat. Res. Soc. Symp. Proc.*, **73**, 289 (1986).
7. K. D. Keefer, in *Mat. Res. Soc. Symp. Proc.*, **73**, 295 (1986).
8. J. C. Pouxviel, J. P. Boilot, A. Lecomte, and A. Dager, *J. Phys. (Paris)*, **48**, 921 (1987).
9. B. Cabane, M. Dubois, and R. Duplessix, *J. Phys. (Paris)*, **48**, 2131 (1987).
10. T. Lours, J. Zarzycki, A. Craievich, D. I. Dos Santos, and M. Aegerter, *J. Non-Cryst. Solids*, **100**, 207 (1988).
11. E. Bouchaud, M. Delsanti, M. Adam, M. Daoud, and D. Durand, *J. Phys. (Paris)*, **47**, 1273 (1986).
12. D.-W. Hua, R. Winter, W. Mantulin, and J. Jonas, manuscript in preparation.
13. P. Meakin, in: R. Pynn and T. Riste, Eds., *Time Dependent Effects in Disordered Materials*, Plenum Press, New York (1987).
14. D. Stauffer, A. Coniglio, and M. Adam, *Adv. Polymer Sci.*, **44**, 103 (1982).
15. E. J. A. Pope and J. D. Mackenzie, *J. Non-Cryst. Solids*, **101**, 198 (1988).
16. I. Artaki, M. Bradley, T. W. Zerda, and J. Jonas, *J. Phys. Chem.*, **89**, 4399 (1985).
17. T. W. Zerda, M. Bradley, and J. Jonas, *Mat. Lett.*, **3**, 124 (1985).
18. R. K. Iler, *The Chemistry of Silica*, Wiley, New York (1979).
19. D. M. Krol and J. G. Van Lierop, *J. Non-Cryst. Solids*, **63**, 131 (1984).
20. M. Nogami and Y. Moriya, *J. Non-Cryst. Solids*, **37**, 191 (1980).
21. J. E. Martin and B. J. Ackerson, *Phys. Rev. A*, **31**, 1180 (1985).
22. D. W. Schaefer and K. D. Keefer, in *Mat. Res. Soc. Symp. Proc.*, **73**, 277 (1986).
23. J. E. Martin and K. D. Keefer, *Phys. Rev. A*, **34**, 4988 (1986).
24. J. E. Martin, J. Wilcoxon, and D. Adolf, *Phys. Rev. A*, **36**, 1803 (1987).
25. C. J. Brinker, *J. Non-Cryst. Solids*, **100**, 31 (1988).
26. W. B. Brown and R. C. Ball, *J. Phys. A*, **18**, L517 (1985).
27. Ren Xu, E. J. A. Pope, and J. D. Mackenzie, *J. Non-Cryst. Solids* **106**, 242 (1988).
28. B. J. Berne and R. Pecora, *Dynamic Light Scattering*, Wiley, New York (1976).
29. J. E. Martin and F. Leyoraz, *Phys. Rev. A*, **34**, 2346 (1986).
30. J. S. Hwang and H. Z. Cummings, *J. Chem. Phys.*, **79**, 5188 (1983).
31. A. Boukenter, B. Champagnon, E. Duval, J. Dumas, J. F. Quinson, and J. Serughetti, *Phys. Rev. Lett.*, **57**, 2391 (1986).
32. A. Boukenter, B. Champagnon, J. Dumas, E. Duval, J. F. Quinson, and J. Serughetti, *J. Non-Cryst. Solids*, **96**, 1189 (1987).

# 3

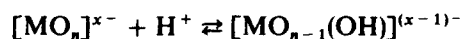
## ROLE OF COMPLEXATION IN THE SOL-GEL CHEMISTRY OF METAL OXIDES

M. HENRY, J. P. JOLIVET, AND J. LIVAGE

### 3.1. INTRODUCTION

The sol-gel process is based on inorganic polymerization chemistry. Starting from molecular precursors, oxide networks are obtained via hydroxylation-condensation reactions [1]. Two routes are usually described in the literature, depending on whether the precursor is an inorganic salt in aqueous solution or an alkoxide in organic solvent [2].

In the first case, hydroxylation of inorganic precursors is performed via pH modification of the aqueous solution [3]. This leads to the protonation of anionic oxo ions:



or to the deprotonation of cationic aquo ions:



*Ultrastructure Processing of Advanced Materials.*

Edited by Donald R. Uhlmann and Donald R. Ulrich (deceased).

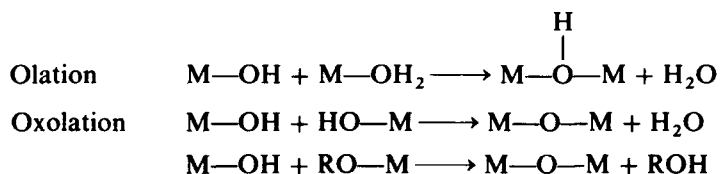
ISBN 0-471-52986-9 © 1992 John Wiley & Sons, Inc.

## 24 ROLE OF COMPLEXATION IN THE SOL-GEL CHEMISTRY

In the second case, the hydroxylation of metal alkoxides occurs upon addition of water:



Condensation then follows via



Such a description of the sol-gel chemistry is actually much too simplified. Other chemical species are almost always present in the solution. They are sometimes added in order to improve the process such as catalysts [4], stabilizing additives [5], or drying control chemical agents [6]. More often, they are just present as counterions when metallic salts are used as precursors or when the pH is modified by adding a base or an acid. Such foreign species are almost never taken into account in the chemical description of hydroxylation-condensation reactions. However, they appear to play a decisive role during the course of the sol-gel process.

The gelation time of silicon alkoxides decreases significantly upon acid catalysis. This can be explained by the protonation of the leaving OR group that makes the nucleophilic substitution easier. However, acids such as HF or  $CH_3COOH$  have a more pronounced effect despite the fact that they are rather weak acids [4]. Indeed, highly nucleophilic  $F^-$  and  $CH_3COO^-$  anions have been shown to react with the metal alkoxide [7,8], changing the rate of hydrolysis and condensation.

Anions are often used in order to control the shape and size of colloidal particles. A large number of examples can be found in the work of Matijević et al. [9, 10]. Spherical hematite ( $\alpha-Fe_2O_3$ ) particles are obtained by heating  $FeCl_3$  solutions, whereas spindle-type particles are produced from ferric nitrate solutions in the presence of small quantities of phosphate ions [9].

The crystalline structure of the precipitated particles also depends on the nature of the anions:  $\alpha-FeOOH$  (goethite) precipitates from ferric nitrate or perchlorate solutions, whereas  $\beta-FeOOH$  (akaganeite) is produced in the presence of  $Cl^-$  ions [11]. The thermohydrolytic precipitation of Ti(IV) from sulfuric acid solutions produces only titanium oxide with the anatase structure. In HCl or  $HNO_3$  solutions, both anatase and rutile structures can be obtained [12].

Even the chemical composition of the solid phase can be modified by the presence of some anions. Heating ferric chloride solutions in the presence of HCl leads to  $\alpha-Fe_2O_3$  or  $\beta-FeO(OH)$ , depending on the experimental procedure. In

the presence of sulfate ions, either hexagonal  $\text{Fe}_3(\text{SO}_4)_2(\text{OH})_5 \cdot 5\text{H}_2\text{O}$  or monoclinic  $\text{Fe}_4(\text{SO}_4)(\text{OH})_{10}$  are formed [9].

Some anions remain strongly bonded to the metal cation and thus end up in the solid phase giving basic salts, whereas others are released during the hydrolysis process or can be simply removed by leaching.

This Chapter presents an analysis of the role of complexation during the sol-gel synthesis of metal oxides. Foreign species can be involved at two levels during the nucleation-growth process. As chemical additives, they are able to coordinate metal cations leading to a chemical modification of the precursor at a molecular level. Because both the reactivity and the functionality of the precursor are changed, hydroxylation-condensation reactions are modified. As charged species, they change the ionic strength of the solution and are involved in the formation of the double layer around the colloidal particles. Aggregation processes are then also modified. In the following discussion, we will focus on the first aspect only.

### 3.2. THE PARTIAL CHARGE MODEL

It will be assumed that the chemical role of additives L depends on their ability to form stable M—L bonds during the course of hydroxylation-condensation reactions. Therefore, the question arises to give clear evidence of such bonds and to be able to predict in which cases complexation occurs. The chemical role of these species will be tentatively described according to the experimental results of the literature. However, rather few experiments are available. Therefore, a theoretical analysis will be suggested, based on the so-called partial charge model (PCM). This model is applicable to any chemical compound carrying a global charge  $z$  and a mean electronegativity  $\bar{\chi}$  given by the relationship [13]

$$\bar{\chi} = \left( \sum_{i=1}^n \sqrt{\chi_i} + 1.36z \right) / \left( \sum_{i=1}^n 1/\sqrt{\chi_i} \right) \quad (1)$$

where  $n$  is the total number of atoms  $i$  having a Pauling electronegativity  $\chi_i$ . From  $\bar{\chi}$ , the partial charge  $\delta_i$  on any atom  $i$  in the compound is given by

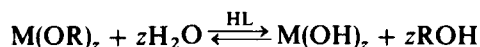
$$\delta_i = (\bar{\chi} - \chi_i)/(1.36\sqrt{\chi_i}) \quad (2)$$

Once a partial charge distribution  $\delta_i$  ( $i = 1, \dots, n$ ) is known, the aim of the PCM is to look for simple criteria based on electrostatic grounds and that can help to predict whether reactions such as hydrolysis, condensation, or complexation should occur or not. Usually, one selects a chemical group X of particular interest within the compound, calculates its partial charge in the complex  $\delta_c(X)$  by direct summation according to the formula  $\delta_c(X) = \sum_j \delta_j$ , and compares this partial charge to the integer charge  $x$  that X usually bears in a free state without chemical interaction. A critical state is always reached when

$\delta_C(X) = x$ , which defines a criterion of occurrence for the chemical process in which the X group is involved (elimination, nucleophilic attack, etc.). These criteria are usually expressed in terms of critical electronegativities  $\chi^*$  or hydrolysis ratio  $h^*$  found by solving the charge conservation equation ( $\sum_i \delta_i = z$ ) with the constraint  $\delta_C(X) = x$ . We have already shown [13] how modilization of both hydrolysis and condensation reactions could be made by selecting  $x = 0$  and  $X = OH, H, H_2O$ . In the following we try to show that some interesting conclusions on complexing properties of anionic species could be reached by choosing  $x = -1$  and  $X = CH_3COO, CH_3COCHCOCH_3, ClO_4, NO_3, Cl, HSO_4, HCO_3, HCrO_4$ , and  $H_2PO_4$ .

### 3.3. ALKOXIDE PRECURSORS

It is well known that protic species HL are able to react with metal alkoxides [14]. Highly electronegative species ( $L = Cl^-, NO_3^-, ClO_4^-$ ) increase the rate of hydrolysis:



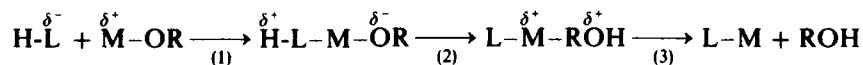
Hydrolysis of titanium alkoxides with pure water leads to the precipitation of amorphous hydrated oxide  $TiO_2 \cdot nH_2O$ . Acid hydrolysis in the presence of HCl directly leads to crystalline  $TiO_2$  either in the anatase or rutile form (Fig. 3.1a).

When L is less electronegative, such as acetate (OAc) or acetylacetonate (Acac), chemical modification of the molecular precursor occurs:



These reactions can be described in terms of associative nucleophilic substitutions. A three-step process may be suggested for modelization:

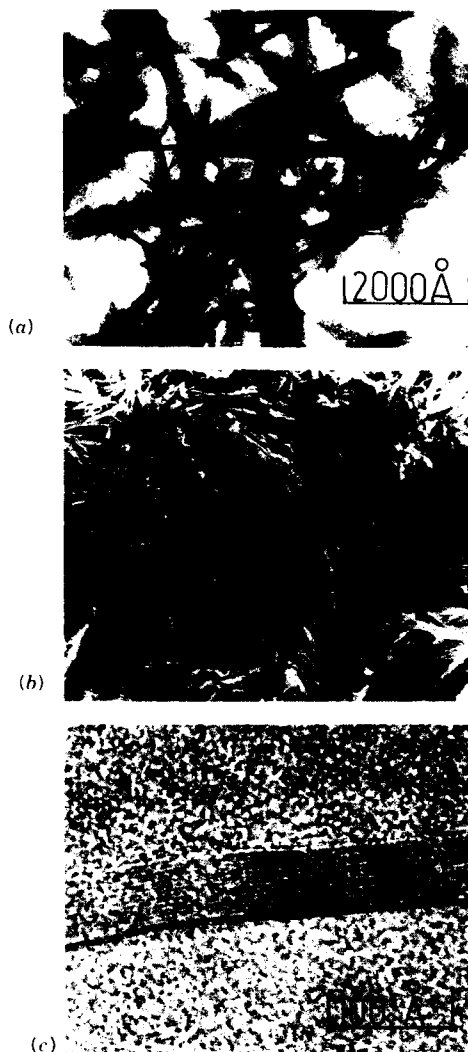
1. Nucleophilic addition of HL onto the positively charged metal atom.
2. Proton transfer within the transition state from the entering molecule toward an alkoxy group.
3. Departure of the positively charged protonated species.



The whole process depends on charge distribution in the alkoxide and the transition states. As a simple criterion, both the metal atom M and the leaving group ROH have to be positively charged to ensure repulsion.

An estimate of the charge distribution can be deduced from the PCM [13]. Calculations performed in the case of  $Ti(Oi-Pr)_4$  ( $i-Pr = {}^iC_3H_7$ ) and acetic acid show that in the transition state  $\delta(AcOH) = -0.7$ , while  $\delta(i-PrOH) = +0.1$ .





**Figure 3.1.** Morphology of  $\text{TiO}_2$  sols and gels obtained through hydrolysis of  $\text{Ti}(\text{O}i\text{-Pr})_4$  with various protic additives. (a) Transmission electron micrograph of crystalline rutile particles formed through the hydrolysis in  $i\text{-Pr OH}$  with  $\text{HCl}$  ( $\text{pH} = 1.5$ ). Acicular crystals are roughly 6 nm wide and 130 nm long. (b) Scanning electron micrograph of amorphous fibrous titanium oxoacetate xerogels ( $\approx \text{TiO}(\text{OAc})_2$ ) formed from  $\text{Ti}(\text{O}i\text{-Pr})_4$  in glacial acetic acid. The aggregated fibers have a diameter close to 100 nm and can be 4  $\mu\text{m}$  long. (c) Transmission electron micrograph of semicrystalline linear polymers ( $\approx \text{TiO}(\text{Acac})_2$ ) formed upon hydrolysis of  $[\text{Ti}(\text{O}i\text{-Pr})_4 + 2\text{AcacH}]$  in  $i\text{-Pr OH}$  with  $\text{H}_2\text{O}/\text{EtOH}$  mixture. The ribbons are 0.7 to 4 nm wide and roughly 0.1  $\mu\text{m}$  long.

## 28 ROLE OF COMPLEXATION IN THE SOL-GEL CHEMISTRY



The positively charged alcohol molecule will then be removed, while the negatively charged acetate group remains bonded to titanium. The nucleophilic substitution is therefore possible in agreement with experimental results [15]. X-Ray absorption, NMR, and infrared spectra show that acetate groups behave as bidentate-bridging ligands, leading to the formation of dimeric species  $\text{Ti}_2(\text{OR})_6(\text{OAc})_2$ .

A new molecular precursor is thus obtained and the whole hydrolysis-condensation process is modified. Alkoxy groups are hydrolyzed faster than acetate groups, and polymeric chains can even be obtained when a large amount of acetic acid is added (Fig. 3.1b).

The complexing ability of organic species does not depend only on their nucleophilic character. Chelating ligands, such as acetylacetone, are often used in order to stabilize highly reactive alkoxides such as  $\text{Ti}(\text{OR})_4$ ,  $\text{Zr}(\text{OR})_4$ , or  $\text{Al}(\text{OR})_3$ . Calculations performed in the case of  $\text{Ti}(\text{O}i\text{-Pr})_4$  and acetylacetone (AcacH) show that in the transition state  $\delta(\text{AcacH}) = -0.46$ , while  $\delta(i\text{-PrOH}) = +0.09$ .



Again, the positively charged alcohol molecule will be removed. Experimental results [15] show that Acac behaves as a chelating ligand, leading to monomeric species  $\text{Ti}(\text{Acac})(\text{O}i\text{-Pr})_3$ . Acetylacetonate is strongly bonded to the metal atom and cannot be removed upon hydrolysis. The functionality of the molecular precursor therefore decreases, leading to the formation of anisotropic condensed species (Fig. 3.1c).

In the last two examples, substitution occurs because both acetic acid ( $\bar{\chi} = 2.49$ ) and acetylacetone ( $\bar{\chi} = 2.38$ ) are more electronegative than isopropanol ( $\bar{\chi} = 2.29$ ). If a less electronegative organic compound such as diethylamine  $\text{HNEt}_2$  ( $\bar{\chi} = 2.24$ ) is used, calculations lead to  $\delta(\text{HNEt}_2) = +0.19$ , whereas  $\delta(i\text{-PrOH}) = -0.12$ .

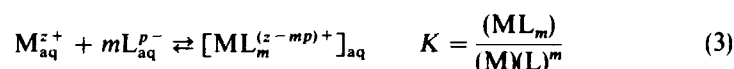


Consequently, transformation of alkoxides into dialkylamides is not possible, whereas alcoholysis of dialkylamides easily occurs in agreement with experimental results [14].

### 3.4. AQUEOUS PRECURSORS

Anions play a decisive role in the homogeneous precipitation of metal oxides from aqueous solutions [9]. As for organic phases, it may be assumed that

chemical modification occurs when anions are able to form soluble complexes. Usually the complexing ability of a given anion  $L^{p-}$  on a metal cation  $M^{z+}$  is simply measured by the equilibrium constant  $K$  corresponding to the formation of  $ML$  species.



However, in an aqueous medium, the  $ML_m$  concentration strongly depends on the pH of the solution. Side reactions may occur:

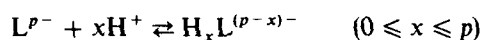
- Increasing the pH leads to the deprotonation of metal aquo ions:



and to further condensation of hydroxo aquo precursors:



- Protonation of anions  $X^{y-}$  can also be observed when the pH decreases:

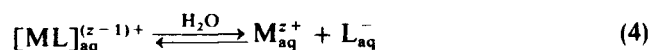


As a result of these side reactions, equilibrium 3 is displaced toward the left, and the observed equilibrium constant decreases. An "apparent constant"  $K'$  has then to be introduced taking into account all side reactions [16]. It varies with pH and goes through a maximum for a given pH when complexation is the most effective.

Efficient complexation, therefore, occurs only over a given range of pH. Outside of this range, side reactions become important enough to lead to the dissociation of the complex. Apparent constants can be computed from the literature [16]. However, complexation constants for condensed species are rather difficult to obtain. Therefore it would be useful to introduce simpler criteria in order to be able to predict whether complexation has to be taken into account or not.

In order to find which factors govern complexation, let us consider what could happen to any M-L bond in aqueous solution. For simplification we will in a first time assume that L is a monovalent ligand ( $p = 1$ ) complexing a nonhydrolyzed metal cation (aquo ion  $M_{aq}^{z+}$ ). Water plays a double role:

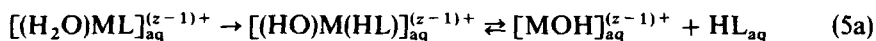
1. Owing to its high dielectric constant ( $\epsilon = 80$ ), dissociation of any purely ionic bond can readily occur:



### 30 ROLE OF COMPLEXATION IN THE SOL-GEL CHEMISTRY

A simple criterion of complete ionicity of the M-L bond is easily found from the PCM through the condition  $\delta_c(L) < -1$ . Indeed,  $\delta_c(L) > -1$  means that some charge transfer has occurred from  $L^-$  to M (within a molecular orbital, for example). In such a case the M-L bond having some covalent character cannot be broken anymore. A criterion of stability against this ionic dissociation would thus be:  $\delta_c(L) = \delta(L_{aq}^-) = -1$ .

Owing to its filled  $3a^1$  orbital, the water molecule is able to coordinate to metal cations setting a  $\sigma$  charge transfer that makes protons more acidic. Prototropic transfers toward other free water molecules (hydrolysis) or alternatively toward neighboring L ligands may thus occur:



As already discussed for alkoxide precursors, removal of the HL molecule is expected to occur as soon as  $\delta_c(HL) > 0$ . If  $\delta_c(HL) < 0$ , the proton can go back toward the OH group because the HL molecule is able to stay in the vicinity of the hydrolyzed complex, ensuring stability. A second criterion of stability against hydrolytic dissociation (assisted nucleophilic substitution) is thus found by setting  $\delta_c(HL) = \delta(HL_{aq}) = 0$ . Notice that the net result of this hydrolytic dissociation depends on the acid-base properties of the HL molecule in aqueous solution. With highly acidic ligands, such as HCl, equilibrium 5b is strongly shifted to the right leading to the formation of an aquo ion with  $Cl^-$  as a counterion (cf. reaction 4), despite the highly covalent nature of the M-Cl bond. On the other hand with weakly acidic molecules such as alcohols ROH, equilibrium 5b is strongly shifted to the left leading to the formation of an hydrolyzed precursor as in hydrolysis of alkoxide. Finally, with molecules having a measurable  $pK$  in aqueous solution (AcOH, AcacH), an aquo ion or a hydrolyzed precursor is obtained depending on the pH.

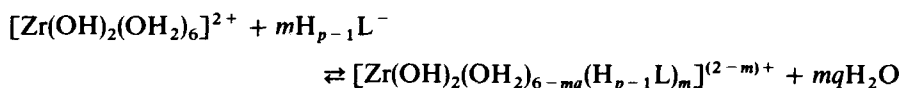
If we turn now our attention toward multivalent ligands such as phosphate ( $p = 3$ ), four main forms are to be considered, namely,  $PO_4^{3-}$ ,  $HPO_4^{2-}$ ,  $H_2PO_4^-$ , and  $H_3PO_4$ . For the  $H_xPO_4^{(3-x)-}$  ions ( $x = 0, 1$ ), stability against ionic dissociation requires  $\delta_c(PO_4) > -3$  for  $x = 0$  and  $\delta_c(HPO_4) > -2$  for  $x = 1$ . Hydrolysis by water molecules leads to the formation of  $HPO_4$  ( $x = 0$ ) and  $H_2PO_4$  ( $x = 1$ ) ligands, which again have to be stable against ionic dissociation:  $\delta_c(HPO_4) > -2$  for  $x = 0$  and  $\delta_c(H_2PO_4) > -1$  for  $x = 1$ . If we recall that  $\delta_c(H) < 1$  in any chemical compound, the two above conditions will always be fulfilled as soon as  $\delta_c(H_2PO_4) > -1$ . Consequently, stability against ionic as well as hydrolytic dissociation requires  $\delta_c(H_xPO_4) > -1$  ( $\forall x \leq 1$ ). For  $x = 2$ , the same condition applies, but hydrolysis of  $H_2PO_4$  ligand leads to  $H_3PO_4$ . Stability for this ligand then requires  $\delta(H_3PO_4) < 0$ .

To sum up this section, strong complexation for any  $p$ -valent  $H_xL$  ligand

( $x < p - 1$ ) is expected if both conditions  $\delta_C(H_{p-1}L) > -1$  and  $\delta_C(H_pL) < 0$  are simultaneously fulfilled in any protic solvent such as water. If  $\delta_C(H_pL) > 0$  hydrolysis by water molecules may occur while if  $\delta_C(H_{p-1}L) < -1$ , ionic dissociation becomes possible. Two criteria,  $\delta_C(H_pL) = 0$  and  $\delta_C(H_{p-1}L) = -1$ , have then to be considered in order to define electronegativity ranges where complexation is most likely to occur.

### 3.5. COMPLEXING ABILITY OF ANIONS

Let us consider the so-called zirconyl cation  $ZrO^{2+}$ , which on stereochemical grounds must be written  $[Zr(OH)_2(OH_2)_6]^{2+}$ , because the zirconium atom is very often coordinated by eight ( $n = 8$ ) oxygen atoms. Complexation of this inorganic precursor ( $h = 2$ ) by  $H_{p-1}L^-$  anions leads to the following equilibrium:



where  $q$  is the number of water molecules displaced by complexation ( $q = 1$  for a monodentate anion, whereas  $q = 2$  for a bidentate one). Charge conservation in the complexed precursor leads to

$$\delta_C(Zr) + (8-mx)\delta_C(H_2O) - 2\delta_C(H) + m\delta_C(H_{p-1}L) = 2 - m$$

from which critical electronegativities for ionic  $\bar{\chi}_D$  and hydrolytic  $\bar{\chi}_H$  dissociation may be calculated by setting  $\delta_C(H_{p-1}L) = -1$  and  $\delta_C(H_pL) = 0$ , respectively:

$$\begin{aligned} \delta_C(H_{p-1}L) = -1 &\Rightarrow \bar{\chi}_D(m, q) = \bar{\chi}[ZrO_{8-mq}H_{14-2mq}^{2+}] \\ \delta_C(H_pL) = 0 &\Rightarrow \delta_C(H_{p-1}L) = -\delta_C(H) \Rightarrow \bar{\chi}_H(m, q) = \bar{\chi}[ZrO_{8-mq}H_{14-m(2q+1)}^{(2-m)+}] \end{aligned} \quad (6)$$

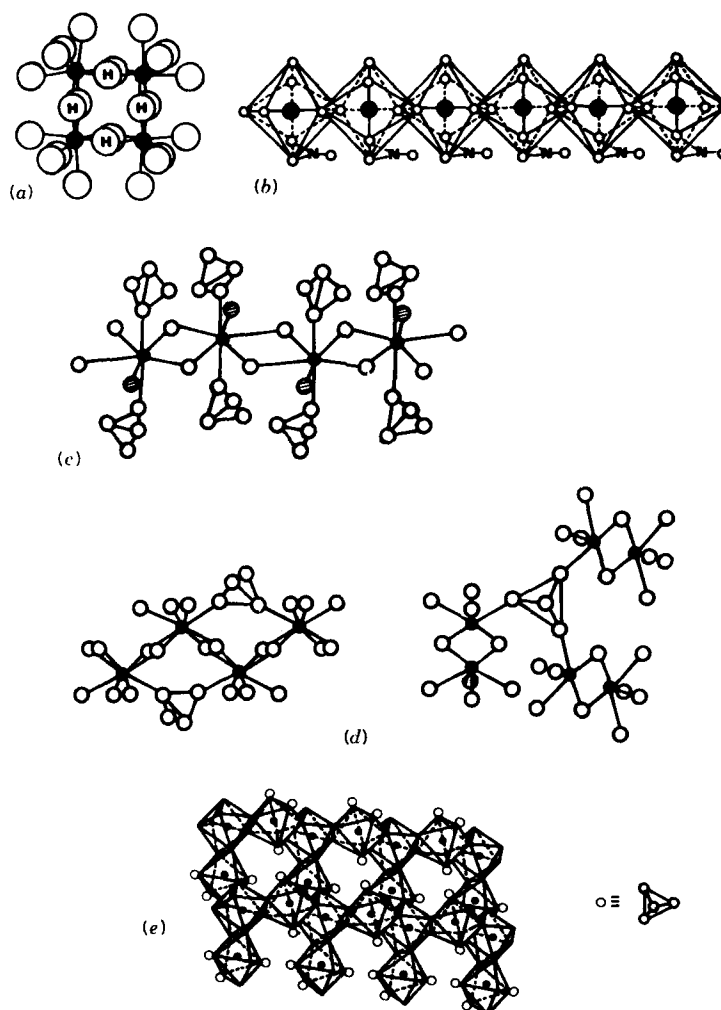
from which Table 3.1 can be computed. From the results of last section, stability requires simultaneously  $\bar{\chi}(H_{p-1}L) < \bar{\chi}_D$  and  $\bar{\chi}(H_pL) > \bar{\chi}_H$ . Anions can then be separated into three classes.

**TABLE 3.1. Critical Electronegativities Corresponding to Ionic ( $\chi_D$ ) and Hydrolytic ( $\chi_H$ ) Dissociation Deduced from the Partial Charge Model applied to the Zirconyl Cation  $ZrO^{2+}$  ( $h = 2$ )**

$x$	$\bar{\chi}_H(1, x)$	$\bar{\chi}_D(1, x)$	$\bar{\chi}_H(2, x)$	$\bar{\chi}_D(2, x)$
1	2.58	2.66	2.49	2.69
2	2.60	2.69	2.50	2.80

## 32 ROLE OF COMPLEXATION IN THE SOL-GEL CHEMISTRY

1. *Counterions.* They are not able to form a stable Zr-X bond in aqueous solution and would therefore not be involved in the formation of condensed species. Highly electronegative anions such as  $\text{ClO}_4^-$  ( $\bar{\chi} = 2.86$ ) belong to this class as  $\bar{\chi} > \bar{\chi}_D(m, q)$  whatever the coordination mode (mono- or bidentate). Anions with a low electronegativity such as  $\text{Cl}^-$  belong also to this class as  $\bar{\chi}(\text{HCl}) = 2.44 < \bar{\chi}_H(m, q)$ , again whatever the coordination mode. Consequent-



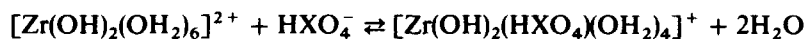
**Figure 3.2.** X-ray structures of some basic salts of zirconium with  $\text{OH/Zr} = 2$  ratio (zirconyl ion  $\text{ZrO}^{2+}$ ). (a) Cyclic tetramer of  $\text{ZrOCl}_2 \cdot 8\text{H}_2\text{O} \equiv [\text{Zr}_4(\text{OH})_8(\text{OH}_2)_{16}]^{8+} \cdot 8[\text{Cl}(\text{H}_2\text{O})_3]^-$ . (b) Dodecahedral chain of  $\text{ZrO}(\text{NO}_3)_2 \cdot 5\text{H}_2\text{O} \equiv [\text{Zr}(\text{OH})_2(\text{NO}_3)(\text{OH}_2)_2]^{4+} \cdot \text{NO}_3^- \cdot 2\text{H}_2\text{O}$ . (c) Pentagonal bipyramidal chain of  $\text{ZrOSO}_4 \cdot 2\text{H}_2\text{O} \equiv [\text{Zr}(\text{OH})_2(\text{OH}_2)(\text{SO}_4)]$ . (d) Square antiprismatic chain of  $\text{ZrOSO}_4 \cdot \text{H}_2\text{O} \equiv [\text{Zr}(\text{OH})_2(\text{SO}_4)]$ . (e) Dodecahedral sheets of  $\text{ZrOCrO}_4 \cdot \text{H}_2\text{O} \equiv [\text{Zr}(\text{OH})_2(\text{CrO}_4)]$ .

ly, both in solid zirconyl chloride  $\text{ZrOCl}_2 \cdot 8\text{H}_2\text{O}$ , and in its aqueous solutions, zirconium is present mainly as tetrameric species  $[\text{Zr}_4(\text{OH})_8(\text{OH}_2)_{16}]^{8+}$  (Fig. 3.2a). Zirconium atoms are linked by four bridging OH groups and have four water molecules giving an eightfold coordination (square antiprism) [17, 18].

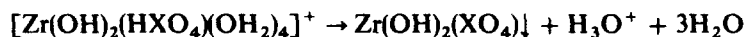
Solutions of these species are known to polymerize upon heating or neutralization and to yield a hydrous oxide  $\text{ZrO}_2 \cdot n\text{H}_2\text{O}$  containing such tetrameric units linked by hydroxo and oxo bridges [19].

2. *Weakly complexing anions.* They are able to substitute water molecules and could therefore be involved in the formation of condensed species such as basic salts. From Table 3.1, nitrate ions  $\text{NO}_3^-$  ( $\bar{\chi} = 2.76$ ) are expected to show some weak complexing ability toward zirconium for  $\text{NO}_3/\text{Zr} = m = 2$  if they behave as bidentate ligands. In agreement, crystals of composition  $\text{Zr}(\text{OH})_2(\text{NO}_3)_2(\text{OH}_2)_4$  can be isolated, where  $\text{NO}_3^-$  behave as a chelating ligand substituting two water molecules [20]. The crystal structure is built from infinite zig-zag chains of composition  $[\text{Zr}(\text{OH})_2(\text{NO}_3)(\text{OH}_2)]_n^+$ , where the zirconium atoms in eightfold coordination are linked together by four bridging OH groups [20] (Fig. 3.2b).

3. *Strong complexing anions.* They are able to act as bridging ligands and thus behave as network formers in basic salts. Sulfate ( $\bar{\chi}[\text{HSO}_4^-] = 2.64$ ), phosphate ( $\bar{\chi}[\text{H}_2\text{PO}_4^-] = 2.49$ ), and chromate ( $\bar{\chi}[\text{HCrO}_4^-] = 2.44$ ) ions are typical examples of such a behavior as their electronegativity always lies below  $\bar{\chi}_D(m, q)$  or above  $\bar{\chi}_H(m, q)$  ( $\bar{\chi}[\text{H}_2\text{SO}_4] = 2.88$ ,  $\bar{\chi}[\text{H}_3\text{PO}_4] = 2.71$ , and  $\bar{\chi}[\text{H}_2\text{CrO}_4] = 2.70$ ). In agreement, the structure of basic salts  $\text{Zr}(\text{OH})_2\text{SO}_4$  and  $\text{Zr}(\text{OH})_2\text{SO}_4 \cdot \text{H}_2\text{O}$  is made of  $[\text{Zr}(\text{OH})_2]_n^{2n+}$  chains held together by sulfate tetrahedra [21, 22] (Figs. 3.2c and d). With the more covalent chromate anion, similar basic salts  $\text{Zr}(\text{OH})_2\text{CrO}_4$  can be obtained, but in this case, infinite networks of composition  $[\text{Zr}_3(\text{OH})_6(\text{CrO}_4)]_n^{4n+}$  are held together by chromate groups [23]. All these basic salts can be nucleated from the following inorganic precursor ( $X = \text{S}, \text{Cr}$ ):



which appears to be stable in an aqueous solution. As evidenced from X-ray structures, crystal growth involves a deprotonation process in order to form the  $\text{XO}_4^{2-}$  ligand:



This reaction can be induced through thermohydrolysis of the aqueous solution. With  $\text{H}_2\text{PO}_4^-$ , basic salts are also formed, but precipitation occurs at room temperature leading to  $\text{Zr}(\text{OH})_2(\text{H}_2\text{PO}_4)_2$  rather than  $\text{Zr}(\text{OH})_2(\text{HPO}_4)$  [24]. The structure of this polymeric compound has not yet been established.

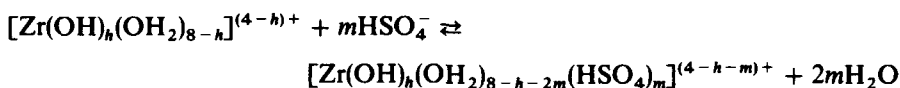
### 34 ROLE OF COMPLEXATION IN THE SOL-GEL CHEMISTRY

The same considerations apply to any hydrolyzed metal cation  $[M(OH)_h(OH_2)_{n-h}]^{(z-h)+}$  having a coordination number  $n$  and a Pauling electronegativity  $\chi_M$ . In this more general case, it is an easy matter to show that relation 6 becomes

$$\begin{aligned}\delta_C(H_{p-1}L) &= -1 \Rightarrow \bar{\chi}_D(z, n, h, m, q, \chi_M) = \bar{\chi}[M(OH)_h(OH_2)_{n-h-mq}^{(z-h)+}] \\ \delta_C(H_pL) &= 0 \Rightarrow \bar{\chi}_H(z, n, h, m, q, \chi_M) = \bar{\chi}[M(OH)_{h+m}(OH_2)_{n-h-m(q+1)}^{(z-h-m)+}]\end{aligned}\quad (7)$$

### 3.6. COMPLEXING ABILITY AND HYDROLYSIS RATIO

In the previous section we have shown how different anions are able to nucleate basic salts from aqueous solutions of a  $h = 2$  hydrolyzed cation. We will now turn our attention to the structural modification induced by a ligand such as sulfate as a function of the hydrolysis ratio for the same metal cation Zr(IV) ( $z = 4$ ,  $n = 8$ , and  $\chi_M = 1.29$ ):



Sulfate ions are supposed to behave as bidentate ligands ( $q = 2$ ). The condition  $\delta(HSO_4) > -1$  and charge conservation lead to

$$\delta_C(Zr) + (8 - 2m)\delta_C(H_2O) - h\delta_C(H) < 4 - h$$

from which a critical value  $h_D^*$  for ionic dissociation can be defined:

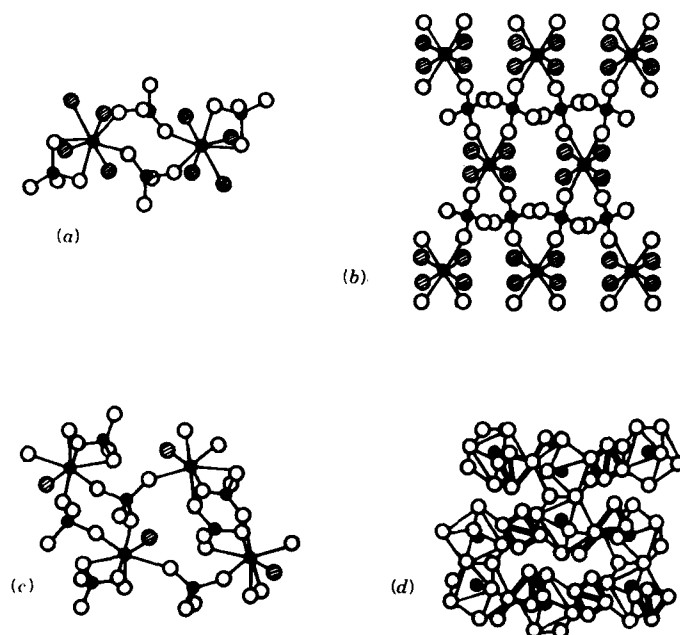
$$h < \frac{1}{1 - \delta_C(H)} [4 - (8 - 2m)\delta_C(H_2O) - \delta_C(Zr)] \equiv h_D^* \quad (8)$$

Because  $\bar{\chi} = \bar{\chi}(HSO_4^-) = 2.641 \Rightarrow h_D^* = 1.98 + 0.58m$ .

Complexation of Zr(IV) with sulfate is expected when  $m = 1$  for  $h \leq 2$ , whereas for  $m = 2$  it will be  $h \leq 3$ . Therefore, owing to the stability of the Zr-SO<sub>4</sub> bond in aqueous solution for  $h \leq 3$ , evaporation or thermohydrolysis of sulfate solutions are expected to form a lattice where the Zr(IV) cation will be coordinated by sulfate tetrahedra. Experimental evidence of such a behavior is provided by the X-ray structures of neutral or basic salts of Zr(IV).

A survey of the literature shows that many neutral salts  $Zr(SO_4)_2 \cdot yH_2O$  ( $m = 2$ ) can be obtained from aqueous solutions ( $y \geq 4$ ). Isolated dimeric complexes of composition  $Zr_2(SO_4)_2(H_2O)_8$  are found if  $y = 5$  or 7 [25-27] (Figure 3.3a). For  $y = 4$ , a layered structure is obtained as the stable form at room temperature (Fig. 3.3b) [28]. In both structures, SO<sub>4</sub> tetrahedra bridge two zirconium atoms surrounded by water molecules in order to reach an eightfold coordination. These crystals may be nucleated from soluble complexes





**Figure 3.3.** Crystal structures of zirconium sulfates as a function of the hydrolysis ratio  $h = \text{OH}/\text{Zr}$ . (a)  $h = 0$ : Dodecahedral dimers formed in  $\text{Zr}(\text{SO}_4)_2 \cdot 7\text{H}_2\text{O} \equiv [\text{Zr}_2(\text{SO}_4)_4(\text{OH}_2)_8] \cdot 6\text{H}_2\text{O}$  and  $\text{Zr}(\text{SO}_4)_2 \cdot 5\text{H}_2\text{O} \equiv [\text{Zr}_2(\text{SO}_4)_4(\text{OH}_2)_8] \cdot 2\text{H}_2\text{O}$ . (b)  $h = 0$ : Square antiprismatic layers formed in  $\text{Zr}(\text{SO}_4)_2 \cdot 4\text{H}_2\text{O}$ . (c)  $h = 0$ : Sheets formed in  $\text{Zr}(\text{SO}_4)_2 \cdot \text{H}_2\text{O}$ , where Zr is in sevenfold coordination as in  $\text{ZrO}_2$  monoclinic. (d)  $h = 1$ : Dodecahedral sheets found in  $\text{Zr}_2\text{O}(\text{SO}_4)_3 \cdot 5\text{H}_2\text{O} \equiv [\text{Zr}_2(\text{OH})_2(\text{SO}_4)_3(\text{OH}_2)_4]$ . This structure can be viewed as being composed of dimers  $[\text{Zr}_2(\text{OH})_2]^{6+}$  linked by sulfate tetrahedra.  $h = 2$ : See Figs. 3.2c and d for  $[\text{Zr}(\text{OH})_2(\text{OH}_2)(\text{SO}_4)]$  and  $[\text{Zr}(\text{OH})_2(\text{SO}_4)]$ .

such as



Hydroxo groups are converted into aquo ligands by a prototropic transfer from  $\text{HSO}_4$  ligands within the coordination sphere of  $\text{Zr}(\text{IV})$ . Another much less probable pathway involving  $h = 0$  precursors can also be imagined:



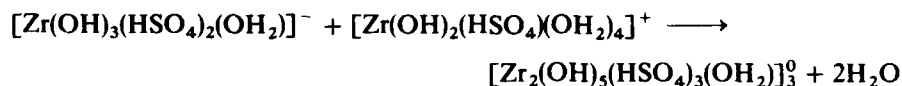
The structural relationship between the tetrahydrate and higher hydrates can be understood as a competition between bridging sulfate and water molecules around the  $\text{Zr}(\text{IV})$  cation. At a low temperature, water molecules are able to break some sulfate bridges in the layered structure of the tetrahydrate leading to dimeric species as found in the penta- and heptahydrates. When temperature increases ( $T = 100^\circ\text{C}$ ), sulfate groups can displace water molecules from the

### 36 ROLE OF COMPLEXATION IN THE SOL-GEL CHEMISTRY

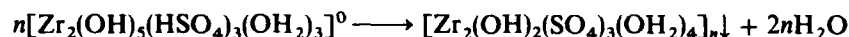
coordination sphere of Zr(IV) leading to several monohydrates ( $y = 1$ ) made of layers  $[\text{Zr}(\text{SO}_4)_2 \cdot \text{H}_2\text{O}]$  held together by hydrogen bonds. Each Zr(IV) is surrounded by six oxygen atoms belonging to bridging sulfate groups and one water molecule (Fig. 3.3c). At a higher temperature ( $T > 300^\circ\text{C}$ ), anhydrous  $\text{Zr}(\text{SO}_4)_2$  is obtained, and each zirconium atom is bonded to seven bridging sulfate groups forming a three-dimensional network.

Basic sulfates can be obtained by thermohydrolysis of zirconium sulfates aqueous solutions. A crystalline compound with the composition  $\text{Zr}_2(\text{OH})_2(\text{SO}_4)_3(\text{H}_2\text{O})_4$  can be obtained by aging sulfuric solutions of Zr(IV) between  $100^\circ\text{C}$  and  $150^\circ\text{C}$  [32]. The structure is built up of dimeric  $\text{Zr}_2(\text{OH})_2^{6+}$  species forming layers in which each zirconium is connected to four other Zr by bridging sulfate groups. Two water molecules complete the eightfold coordination (dodecahedron) (Fig. 3.3d).

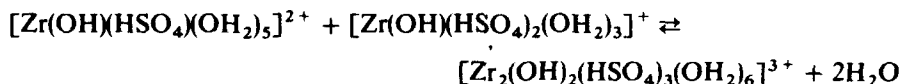
The nucleation of such a structure can be described via an olation process between two complexed inorganic Zr(IV) precursors, respectively, ( $h = 3, m = 2$ ) and ( $h = 2, m = 1$ ):



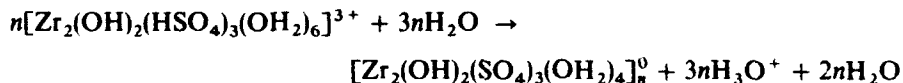
Prototropic transfers between  $\text{HSO}_4$  groups and nonbridging OH groups lead to the formation of highly nucleophilic  $\text{SO}_4$  ligands, which are able to substitute two water molecules in order to form the previously described layers:



Another possibility is the reaction between the ( $h = 1, m = 1$ ) and ( $h = 1, m = 2$ ) precursors:

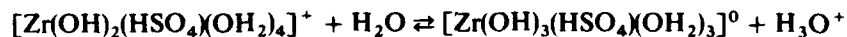


Prototropic transfers now occur toward free water molecules leading to



On the basis of purely electrostatic arguments, the first reaction, forming a neutral dimeric precursor, seems to be highly probable.

When the hydrolysis temperature increases beyond  $T = 200^\circ\text{C}$ , the following equilibrium

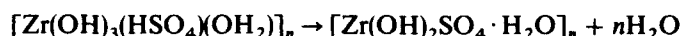


is strongly displaced toward the right. Direct nucleation of chain polymers based on double OH bridges is possible leading to the well-known polymeric  $\text{Zr}(\text{OH})_2\text{SO}_4 \cdot x\text{H}_2\text{O}$  ( $x = 0, 1$ ) basic salts [21, 22] (Figs. 3.2c and d). An olation growth mechanism can be suggested, giving rise to chain polymers as follows:



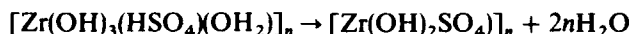
These polymers are able to give more condensed species through sulfate bridges by simultaneous prototropic transfers and water elimination.

1. When sulfates bridge two chains only, hydrated basic salts are obtained:



In this structure Zr(IV) is in sevenfold coordination (pentagonal bipyramid).

2. When sulfate tetrahedra are allowed to bridge three polymeric chains, bridging sulfates must be present inside every chain and all the water molecules are removed from the coordination sphere:

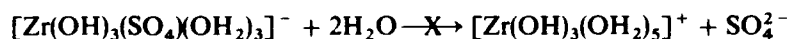


Zr(IV) remains in an eightfold coordination (square antiprism).

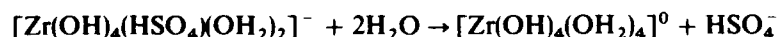
For  $h > 3$ ,  $\delta(\text{HSO}_4) < -1$ , sulfate groups are no more able to coordinate the zirconium atom (purely ionic bond), and no basic salts are expected. Amorphous zirconium oxide  $\text{ZrO}_2 \cdot n\text{H}_2\text{O}$  is obtained. Sulfates are no longer present in the solid network, but still play an important role during the nucleation-growth processes. Thermal hydrolysis of hydrochloric solutions leads to  $\text{ZrO}_2$  particles irregular in morphology, whereas monodispersed spherical particles are obtained in the presence of  $\text{K}_2\text{SO}_4$  [33]. Metastable sulfate complexes such as  $[\text{Zr}(\text{OH})_3(\text{SO}_4)(\text{OH}_2)_3]^-$  could be involved controlling the local concentration of the active  $h = 4$  precursor through an intramolecular prototropic transfer:



The complex at the left appears to be stable against ionic dissociation:



In this case,  $\bar{\chi} = 2$ ,  $53 \Rightarrow \delta(\text{SO}_4) = -1.47 > -2$ . This is no more valid for the complex at the right, formed after prototropic transfer. For the same mean electronegativity,  $\delta(\text{HSO}_4) = -1.25 < -1$ . Ionic dissociation readily occurs:



### 38 ROLE OF COMPLEXATION IN THE SOL-GEL CHEMISTRY

and the active  $h = 4$  precursor appears in solution. Consequently, depending on the prototropic transfer ability (as a function of the pH) and on the concentration of  $\text{SO}_4^{2-}$  in solution, optimum concentration of the  $h = 4$  precursor in solution could be attained giving rise to monodispersed spherical particles. Such a mechanism with  $\text{Cl}^-$  ions is not possible due to their monovalent charge and their low complexing ability.

Table 3.2 shows how computed partial charges vary when the mean electronegativity decreases. Note that as long as  $\delta(\text{SO}_4) \geq -1$ , sulfate is able to bridge three or four zirconium atoms. When  $\delta(\text{SO}_4) < -1$ , sulfates cannot bridge more than two zirconium atoms, and no complexation occurs when  $\delta(\text{HSO}_4) < -1$ . This decrease in the coordination ability of the sulfate group seems to be correlated to an increase of the ionicity of the  $\text{M}-\text{OSO}_3$  bond.

Generalization of relation 8 to any hydrolyzed metal cation as well as any ligand  $\text{H}_{p-1}\text{L}$  is straightforward and leads to

$$h < \frac{1}{1 - \delta_{\text{C}}(\text{H})} [z - (n - mq)\delta_{\text{C}}(\text{H}_2\text{O}) - \delta_{\text{C}}(\text{M})] \equiv h_{\text{D}}^* \quad \text{with} \\ \bar{\chi} = \bar{\chi}[\text{H}_{p-1}\text{L}^-] \quad (9)$$

giving in the case of sulfate ions ( $\bar{\chi} = 2.641$ )

$$h_{\text{D}}^*(\text{HSO}_4^-) = 1.38z - 0.29(n - mq) - (2.641 - \chi_{\text{M}})/\sqrt{\chi_{\text{M}}}$$

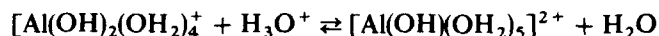
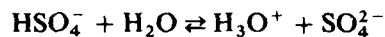
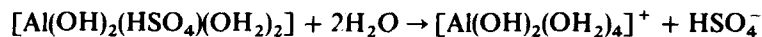
Let these relations be now applied to aluminum for which  $n = 6$ ,  $z = 3$ , and  $\chi_{\text{M}} = 1.47$ .

Relation 9 with  $m = 1$  gives  $h_{\text{D}}^* = 1.43 + 0.29q$ . Consequently,  $\text{Al}^{3+}$  polycations can be precipitated by sulfates for  $h \geq 2$ , these ions acting only as counterions rather than network formers as with  $\text{Zr(IV)}$ . For  $h = 2$ , sulfates can behave in two ways:

**TABLE 3.2. Partial Charges of Sulfate Groups in Some Crystalline Zirconium Sulfates**

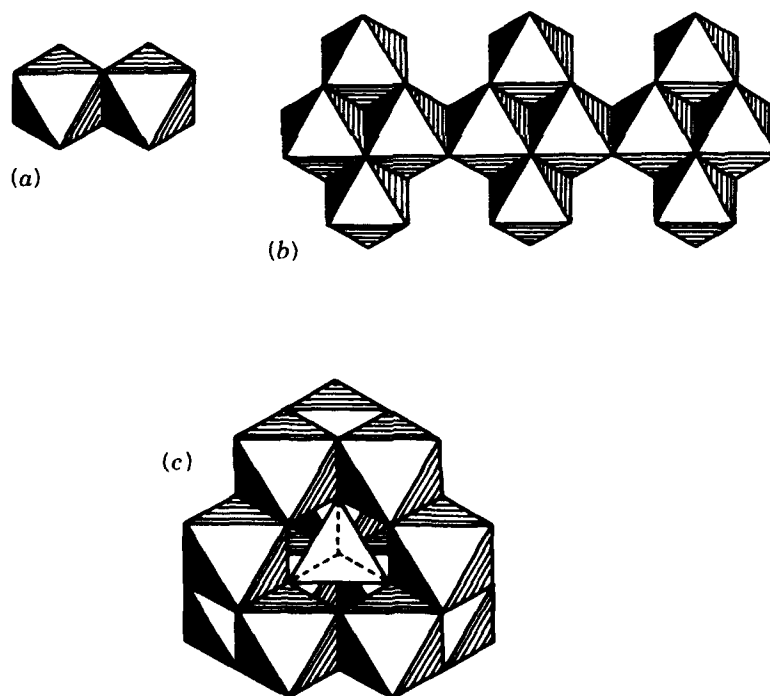
Compound	$\bar{\chi}$	$\delta(\text{SO}_4)$	$\delta(\text{HSO}_4)$
$\text{Zr}(\text{SO}_4)_2$	2.996	-0.53	—
$\text{Zr}(\text{SO}_4)_2 \cdot \text{H}_2\text{O}$	2.880	-0.77	-0.37
$\text{Zr}(\text{OH})_2\text{SO}_4$	2.758	-1.02	-0.68
$\text{Zr}_2(\text{OH})_2(\text{SO}_4)_3(\text{H}_2\text{O})_4$	2.732	-1.07	-0.75
$\text{Zr}(\text{SO}_4)_2 \cdot 4\text{H}_2\text{O}$	2.721	-1.09	-0.78
$\text{Zr}(\text{OH})_2\text{SO}_4 \cdot \text{H}_2\text{O}$	2.695	-1.15	-0.84
$\text{Zr}(\text{SO}_4)_2 \cdot 5\text{H}_2\text{O}$	2.694	-1.15	-0.85
$\text{Zr}(\text{SO}_4)_2 \cdot 7\text{H}_2\text{O}$	2.654	-1.23	-0.95
$\text{Zr}(\text{OH})_3\text{SO}_4(\text{OH}_2)_3^-$	2.532	-1.47	-1.25

1. Direct elimination of  $\text{HSO}_4^-$  followed by the protonation of the hydrolyzed precursor:



A dimerization of this last uncomplexed precursor then occurs giving rise to octahedral dimers sharing an edge  $[\text{Al}_2(\text{OH})_2(\text{OH}_2)_8]^{4+}$ . This polycation has been isolated. It does not show any evidence of chemical bond between Al and  $\text{SO}_4$  (Fig. 3.4a) [34].

2. Direct elimination of  $\text{HSO}_4^-$  with no protonation of the precursor. The resulting  $h = 2$  precursor is able to form a chainlike polycation based on  $[\text{Al}_4(\text{OH})_8(\text{OH}_2)_6]^{4+}$  tetramers sharing two edges (Fig. 3.4b) [35]. These chains are further associated with  $\text{SO}_4^{2-}$  tetrahedra and water molecules, again without complexation of aluminum by sulfate ions.



**Figure 3.4.** Crystal structures of basic aluminium sulfates. (a) Octahedral dimers  $[\text{Al}_2(\text{OH})_2(\text{OH}_2)_8]^{4+}$  found in  $[\text{Al}_2(\text{OH})_2(\text{OH}_2)_8](\text{SO}_4)_2 \cdot 2\text{H}_2\text{O}$ . (b) Octahedral chain  $[\text{Al}_4(\text{OH})_8(\text{OH}_2)_6]^{4+}$  found in  $[\text{Al}_4(\text{OH})_8(\text{OH}_2)_6](\text{SO}_4)_2 \cdot 4\text{H}_2\text{O}$ . (c) Complex octahedral and tetrahedral ions  $[\text{Al}_{13}\text{O}_4(\text{OH})_{24}(\text{OH}_2)_{12}](\text{SO}_4)_4 \cdot 13\text{H}_2\text{O}$ . In all three structures,  $\text{SO}_4^{2-}$  acts as mere counterion (compare with those in Figure 3.3).

TABLE 3.3. Partial Charge of Sulfate Groups in Some Crystalline Aluminium Sulfates

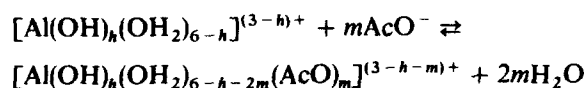
Compound	$\bar{\chi}(\text{SO}_4)$	$\delta(\text{SO}_4)$	$\delta(\text{HSO}_4)$
$[\text{Al}_2(\text{OH})_2(\text{OH}_2)_8](\text{SO}_4)_2 \cdot 2\text{H}_2\text{O}$	2.600	-1.34	-1.09
$[\text{Al}_2(\text{OH})_4(\text{OH}_2)_3]\text{SO}_4 \cdot 4\text{H}_2\text{O}$	2.559	-1.42	-1.19
$\text{Na}[\text{Al}_{13}\text{O}_4(\text{OH})_{24}(\text{H}_2\text{O})_{12}](\text{SO}_4)_4$	2.553	-1.44	-1.22

For  $h > 2$ , the well-known globular polycation  $[\text{Al}_{13}\text{O}_4(\text{OH})_{24}(\text{OH}_2)_{12}]^{7+}$  is formed (Fig. 3.4c) [36] and may be precipitated by  $\text{SO}_4^{2-}$  ions, which are still not involved in the coordination sphere of aluminum.

Finally, the clear difference between basic aluminium sulfates ( $\text{SO}_4^{2-}$  acts as a counterion) and basic zirconium sulfates ( $\text{SO}_4^{2-}$  acts as a network former) can thus be attributed to the ionic character of the  $\text{M}-\text{SO}_4$  bond, which increases from  $\text{M} = \text{Zr(IV)}$  to  $\text{M} = \text{Al}^{3+}$  (Table 3.3).

### 3.7. COMPLEXING ABILITY AGAINST HYDROLYSIS

In the previous section we have considered in detail strongly ionic bonds such as  $\text{M}-\text{OSO}_3$  and found critical hydrolysis ratio for ionic dissociation  $h_{\text{H}}^*$ . In this section we will consider more covalent bonds that can be formed between acetate ion and aluminum, for example. In this case the other condition  $\delta_{\text{C}}(\text{AcOH}) = 0$  must be used and new critical hydrolysis ratio  $h_{\text{H}}^*$  can be computed. For inorganic precursors of aluminum we have to consider the following complexation reaction:



if acetate ions act as bidentate ligands. The condition  $\delta_{\text{C}}(\text{AcOH}) < 0$  and charge conservation lead to

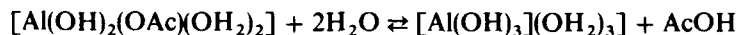
$$\delta_{\text{C}}(\text{Al}) + (6-m)\delta_{\text{C}}(\text{H}_2\text{O}) - (h+m)\delta_{\text{C}}(\text{H}) > 3-h-m$$

from which the critical value  $h_{\text{H}}^*$  may be defined:

$$h > \frac{1}{1 - \delta_{\text{C}}(\text{H})} [3 - (6-m)\delta_{\text{C}}(\text{H}_2\text{O}) - \delta_{\text{C}}(\text{Al})] \equiv h_{\text{H}}^* \quad (10)$$

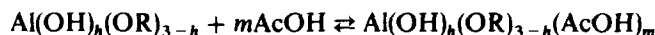
Because  $\bar{\chi} = \bar{\chi}(\text{AcOH}) = 2.493$  and  $\chi_{\text{M}} = 1.47$ , it becomes  $h_{\text{H}}^*(\text{AcOH}) = 2.97 - m$ .

With  $m = 1$ ,  $h_H^* = 1.97$ . Consequently, complexation with acetate appears to be possible only if  $h \geq 2$ , whereas hydrolysis of acetate groups is expected for  $h < 2$ . Aluminium monoacetate  $[\text{Al}(\text{OH})_2(\text{OAc})(\text{OH}_2)_2]$  could therefore be formed in aqueous solutions. However, as  $h$  is close to  $h_H^*$  ( $\bar{\chi} = 2.489 \Rightarrow \delta(\text{AcOH}) = -0.02$ ), the following reaction has also to be taken into account:



This equilibrium can be shifted toward the left via the substitution of coordinated water molecules by donor molecules such as dimethylformamide (DMF) [5]. Accordingly, a compound such as  $\text{Al}(\text{OH})_2(\text{OAc}) \cdot \text{DMF}$  ( $\text{DMF} = \text{C}_3\text{H}_7\text{NO}$ ) appears to be quite stable as now  $\bar{\chi} = 2.425 \Rightarrow \delta(\text{AcOH}) = -0.26$ . Other additives may be used in place of DMF [5].

Because complexation of precursors  $h < 2$  by acetate groups is impossible in aqueous solution, one must turn toward alkoxide precursors, which are much better electron donors than hydroxoquo ions. The equilibrium that must now be considered is



Charge conservation and  $\delta(\text{AcOH}) < 0$  condition lead to

$$\delta_c(\text{Al}) + h\delta_c(\text{OH}) + (3-h)\delta_c(\text{OR}) > 0$$

from which another critical value  $h_A^*$  can be deduced:

$$h < \frac{1}{\delta_c(\text{R}) - \delta_c(\text{H})} [3\delta_c(\text{OR}) + \delta_c(\text{Al})] \equiv h_A^* \quad (11)$$

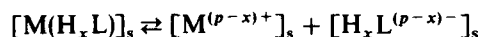
With  $\bar{\chi} = \bar{\chi}[\text{AcOH}] = 2.493$  and  $\text{R} = \text{C}_4\text{H}_9$ , it becomes  $h_A^* = 3.02$  showing that all precursors such as  $h \leq 3$  can be complexed by acetic acid in agreement with reference 37.

Generalization of relations 10 and 11 to any metal cation or ligand  $\text{H}_p\text{L}$  is again straightforward, giving

$$\begin{aligned} h &> \frac{1}{1 - \delta_c(\text{H})} [z - (n - mq + m)\delta_c(\text{H}_2\text{O}) - \delta_c(\text{M})] - m \equiv h_H^* \\ h &< \frac{1}{\delta_c(\text{R}) - \delta_c(\text{H})} [z\delta_c(\text{OR}) + \delta_c(\text{M})] \equiv h_A^* \end{aligned} \quad \bar{\chi} = \bar{\chi}[\text{H}_p\text{L}] \quad (12)$$

## 3.8. DISCUSSION

It appears that criteria as simple as  $\delta(H_{p-1}L) > -1$  or  $\delta(H_pL) < 0$  can be used to predict the complexing ability of any ligand toward any metal atom without direct reference to an equilibrium constant. This could be understood by looking at the nature of the chemical bond between M and L. Let us consider the following dissociation reaction in a given solvent S:



$RT \ln K$  is roughly proportional to  $E_f^s[M(H_xL)]_s$ , where  $E_f^s[M(H_xL)]_s$  is the free energy of formation of the M-LH<sub>x</sub> bond in the solvent S. This last quantity can be evaluated using the partial charge model. Following Sanderson [38], the M-L bond can be described as intermediate between a pure covalent bond ( $\delta(H_xL) = 0$ ) and a pure ionic one ( $\delta(H_xL) = x - p$ ). The total energy  $E$  of the M-L bond can thus be expressed as the sum of a covalent contribution that vanishes for  $\delta(H_xL) = x - p$  and an ionic contribution that vanishes for  $\delta(H_xL) = 0$ .

The covalent contribution depends on the fraction  $\beta$  of bonding electrons shared in a molecular orbital between M and H<sub>x</sub>L. If  $\delta(H_xL)$  is the partial charge of the ligand in the complex, this fraction  $\beta$  could be estimated as  $\beta = 1 + \delta(H_xL)/(p - x)$ . If now the energy of a purely covalent M-L bond  $E_{cov} < 0$  is known, the covalent contribution to  $E_f^s$  would be  $\beta E_{cov}$ .

The ionic contribution to the bond energy could simply be expressed as the coulombic energy attraction of partial charges  $\delta(M)$  and  $\delta(H_xL)$  separated by a mean distance  $r_{ML}$  in a medium of dielectric constant  $\epsilon$ :

$$E_{ion} \propto \delta(H_xL)\delta(M)/\epsilon$$

The total bond energy and the equilibrium constant  $K$  can thus be written as follows:

$$RT \ln K \propto E_f^s[M(H_xL)]_s \propto \beta E_{cov} + E_i$$

Two cases have to be considered:

1.  $x \neq p$  means that the H<sub>x</sub>L ligand has one or several unpaired electrons to share with M. In highly polar solvents, such as water or short-chain alcohols ( $\epsilon > 40$ ), the leading term is the covalent one. Complexation occurs if  $\ln K < 0$  and as  $E_{cov}$  is always strongly negative, stability requires  $1 + \delta(H_xL)/(p - x) > 0$ , that is to say,  $\delta(H_xL) > (x - p)$ . The less negative  $\delta(H_xL)$ , the more negative  $\ln K$  will be and the more the equilibrium is displaced toward the left. If  $\delta(H_xL) < (x - p)$ ,  $\ln K$  becomes positive and equilibrium shifts toward the right. The condition  $\delta(H_xL) = (x - p)$  is thus a critical point for



complexation reactions in solvents of high dielectric constant. It can be used to estimate the stability of the complex against ionic dissociation.

In apolar solvents such as toluene ( $\epsilon < 10$ ), both contributions are important. In such a case  $\ln K$  is always strongly negative, and it would be difficult to differentiate complexation and strong ion-pairing without referring to partial charge calculations.

2.  $x = p$  means that the  $H_pL$  ligand is a molecule that can share only lone pairs of electrons with M through a coordination bond. If  $E_{cov}$  is weakly negative (no crystal field stabilization for example), the sign of  $\ln K$  depends on the sign of  $\delta(H_pL)$  as  $\delta(M)$  is always strongly positive. In order to have  $\ln K < 0$ ,  $\delta(H_pL)$  must then be negative too, whereas instability ( $\ln K > 0$ ) is expected if  $\delta(H_pL) > 0$ . Consequently, the condition  $\delta(H_pL) = 0$  corresponds to another critical point for complexation reactions, particularly in low dielectric constant solvents. It can be used to characterize the stability of a complex against solvolysis. In high dielectric constant solvents (water) both terms are close to zero and neutral molecules always show poor complexing ability. This may explain why anions play such a dominant role in aqueous sol-gel chemistry, whereas neutral protic molecules play the same dominant role in nonaqueous sol-gel chemistry (chemical modification of alkoxide precursors).

### 3.9. CONCLUSION

This Chapter shows that an alternative formalism based on the electronegativity equalization principle can be used to discuss the complexation of both inorganic and organic molecular precursors. Several critical conditions  $\delta(H_xL) = (x - p)$  have been introduced for any multivalent ligand. These criteria can be used to find simple analytical expressions where all parameters that can affect the complexing ability are explicitly taken into account:

The chemical nature of the entering ligand through  $\bar{\chi}[H_{p-1}L^-]$  and  $\bar{\chi}[H_pL]$ .

The coordination mode  $q$  of the ligand (mono- or bidentate).

The number  $m$  of coordinating ligands within the coordination sphere of M.

The hydroxylation ratio  $h = OH/M$ .

The oxidation state  $z$  of M.

The coordination number  $n$  of M.

The Pauling electronegativity  $\chi_M$  of M.

The chemical nature of R groups when alkoxides are used.

Electronegativity ranges of complexation, as well as critical hydrolysis ratio, can then be easily evaluated without direct reference to an equilibrium constant for any type of ligand and metal cation. Such relations apply to monomeric as well as polymeric species and could provide a powerful tool for the sol-gel chemists in order to predict basic salt versus hydrous oxide formation:

#### 44      ROLE OF COMPLEXATION IN THE SOL-GEL CHEMISTRY

1. Because of the high dielectric constant of water, electronegative anions appear to play a major role in aqueous sol-gel chemistry. They are able, through complexation, to affect both particle composition and morphology, depending on their complexing power. Weakly electronegative anions ( $\text{AcO}^-$ ,  $\text{Acac}^-$ ,  $\text{Cl}^-$ , etc.) do not play a major role because they form highly covalent bonds that can be easily broken through prototropic transfers leading to neutral molecules that show little complexing ability.

2. These same neutral molecules have a quite different behavior in organic sol-gel chemistry involving metal alkoxides. Here, a low  $\epsilon$  value together with a great decrease in electronegativity of the molecular precursors when  $\text{OH}_2$  molecules are replaced by  $\text{RO}^-$  ligands lead to a strong chemical modification. Water acts as a reagent rather than a solvent and orientation of hydrolysis/condensation reactions becomes possible.

The only difference between both routes lies in the availability of electrons. In aqueous sol-gel chemistry, metal cations are highly electronegative. Only highly electronegative anions can lead to stable complexes. In organic sol-gel chemistry, metal alkoxides are much less electronegative, which renders electronic clouds much more polarizable. Stable complexes may be formed with moderately electronegative ligands, which allow a greater versatility, because soft ligands are much more abundant than hard ones.

#### REFERENCES

1. L. C. Klein, *Annu. Rev. Mater. Sci.*, **15**, 227 (1985).
2. B. J. J. Zelinski and D. R. Uhlmann, *J. Phys. Chem. Solids*, **45**, 1069 (1984).
3. J. Livage, *J. Solid State Chem.*, **64**, 322 (1986).
4. E. J. A. Pope and J. D. Mackenzie, *J. Non-Cryst. Solids*, **87**, 185 (1986).
5. G. F. Everitt, in: J. D. Mackenzie and D. R. Ulrich, Eds., *Ultrastructure Processing of Advanced Ceramics*, p. 493, Wiley, New York (1988).
6. G. Ortel and L. L. Hench, in: C. J. Brinker, D. E. Clark, and D. R. Ulrich, Eds., *Better Ceramics through Chemistry*, Mat. Res. Soc. 32, p. 79, Elsevier, New York (1985).
7. R. Winter, J. B. Chan, R. Frattini, and J. Jonas, *J. Non-Cryst. Solids*, **105**, 214 (1988).
8. A. Campero, R. Arroyo, C. Sanchez, and J. Livage, in: J. D. Mackenzie and D. R. Ulrich, Eds., *Ultrastructure Processing of Advanced Ceramics*, p. 327, Wiley, New York (1988).
9. E. Matijević, *Annu. Rev. Mater. Sci.*, **15**, 483 (1985).
10. E. Matijević, *Langmuir*, **2**, 12 (1986).
11. C. M. Flynn, Jr., *Chem. Rev.*, **84**, 31 (1984).
12. L. I. Bekkerman, I. P. Dobrovolskii, and A. A. Ivakin, *Russian J. Inorg. Chem.*, **21**, 223 (1976).
13. J. Livage and M. Henry, in: J. D. Mackenzie and D. R. Ulrich, Eds., *Ultrastructure Processing of Advanced Ceramics*, p. 183, Wiley, New York (1988).
14. D. C. Bradley, R. C. Mehrotra, and D. P. Gaur, *Metal Alkoxides*, Academic Press, London (1978).
15. C. Sanchez, F. Babonneau, S. Dœuff, and A. Leautaud, in: J. D. Mackenzie and D. R. Ulrich, Eds., *Ultrastructure Processing of Advanced Ceramics*, p. 77, Wiley, New York (1988).

16. A. Ringböm, *Complexation in Analytical Chemistry*, Interscience, New York (1963).
17. A. Clearfield and P. A. Vaughan, *Acta Crystallogr.*, **9** 555 (1956).
18. T. C. W. Mak, *Can. J. Chem.*, **46**, 3493 (1968).
19. A. Clearfield, *Rev. Pure Appl. Chem.*, **14**, 91 (1964).
20. D. B. McWhan and G. Lundgren, *Acta Crystallogr.*, **16**, A36 (1963).
21. M. Brahim, J. Durand, and L. Cot, *Eur. J. Solid State Inorg. Chem.*, **25**, 185 (1988).
22. M. Hansson, *Acta Chem. Scand.*, **27**, 2614 (1973).
23. W. Mark, *Acta Chem. Scand.*, **26**, 3744 (1972).
24. L. Baetsle and J. Pelsmaekers, *J. Inorg. Nucl. Chem.*, **21**, 124 (1961).
25. I. J. Bear and W. G. Mumme, *Acta Crystallogr., Sect. B*, **25**, 1566 (1969).
26. I. J. Bear and W. G. Mumme, *Acta Crystallogr., Sect. B*, **25**, 1572 (1969).
27. I. J. Bear and W. G. Mumme, *Acta Crystallogr., Sect. B*, **25**, 1558 (1969).
28. J. Singer and D. T. Cromer, *Acta Crystallogr.*, **12**, 719 (1959).
29. I. J. Bear and W. G. Mumme, *Acta Crystallogr., Sect. B*, **26**, 1131 (1970).
30. I. J. Bear and W. G. Mumme, *Acta Crystallogr., Sect. B*, **26**, 1125 (1970).
31. I. J. Bear and W. G. Mumme, *Acta Crystallogr., Sect. B*, **26**, 1140 (1970).
32. S. B. McWhan and G. Lundgren, *Inorg. Chem.*, **5** 284 (1966).
33. M. A. Blesa, A. J. G. Maroto, S. I. Passagio, N. E. Figliolia, and G. Rigotti, *J. Mater. Sci.*, **20**, 4601 (1985).
34. G. Johansson, *Acta Chem. Scand.*, **16**, 401 (1962).
35. C. Sabelli and R. T. Ferroni, *Acta Crystallogr., Sect. B*, **34**, 2407 (1978).
36. G. Johansson, *Arkiv Kemi*, **20**, 321 (1963).
37. A. Ayral, J. Phalippou, and J. C. Droguet, in: *Better Ceramics through Chemistry III*, p. 239, M.R.S., Pittsburgh (1988).
38. R. T. Sanderson, *J. Am. Chem. Soc.*, **105**, 2259 (1983).

# 4

## NEUTRAL AND ANIONIC HYPERVALENT SILICON COMPLEXES IN SILANOL POLYMERIZATION

LARRY W. BURGGRAF, LARRY P. DAVIS,  
AND MARK S. GORDON

### 4.1. INTRODUCTION

Silanol polymerization chemistry is the basis of technologies like sol-gel processing, zeolite synthesis, and siloxane adhesive bonding. Silica materials are especially versatile in such applications because of the wide variety of stable microstructures that can be created using siloxane bonds. Synthesis of novel silica microstructures is limited only by the control we can exercise over silanol polymerization chemistry. Molecular orbital calculations permit us to explore the reaction surfaces for gas-phase condensation of monosilicic acid to disilicic acid and higher oligomers. Our goal is to construct theoretical models for silanol polymerization in order to better understand and employ this interesting chemistry.

In previous work we have proposed mechanisms for anionic silanol polymerization in which participation of hypervalent siliconates is important [1]. Hypervalent silicon is an obvious candidate as an intermediate in this chemistry. Strong anionic nucleophiles have been shown to form pentacoordinate complexes with silanes without activation in the gas phase [2]. Certain pentacoordinate siliconates are readily stabilized in solution [3]. Although

*Ultrastructure Processing of Advanced Materials.*

Edited by Donald R. Uhlmann and Donald R. Ulrich (deceased).

ISBN 0-471-52986-9 © 1992 John Wiley & Sons, Inc.

## 48 NEUTRAL AND ANIONIC HYPERVALENT SILICON COMPLEXES

hypervalent species have not yet been detected in silanol polymerization experiments, our calculations implicate pentacoordinate siliconates as reactive intermediates in anionic silanol polymerization.

An important key to understanding silanol polymerization chemistry is identifying how water is eliminated as the polymerization proceeds. Our calculations suggest that water is more readily eliminated from hypervalent siliconates than tetravalent silicates in hydroxide-catalyzed silanol polymerization. However, accurate predictions of the entire process of water elimination using the MNDO method is difficult, because MNDO overestimates dissociative activation energies and does not model hydrogen-bonding interactions. These faults are due to overestimation of core-core repulsions between atoms when they are separated by approximately van der Waals's distances. The AM1 semiempirical program has largely overcome this drawback. We are modeling silicic acid reactions using AM1 to predict siliconate elimination reactions as influenced by other nucleophilic species that can complex to form hypervalent intermediates.

In this research we have applied semiempirical molecular orbital calculations to examine the formation of pentacoordinate silicic acid complexes with hydroxide and fluoride ions, as well as neutral adducts with hydrogen fluoride, ammonia, and formamide. We also have calculated reaction paths for water elimination from silicic acid complexes with hydroxide and fluoride ions and hydrogen fluoride. We quantify the qualitative semiempirical picture of the reaction surface by employing high-level *ab initio* calculations for selected intermediates and transition state structures. The adducts studied were chosen because of their potential as catalysts or drying control agents in sol-gel-processing chemistry. For example, formamide is used as a drying control additive for sol-gel chemistry to control the ratio of rates of siloxane hydrolysis and silanol polymerization [4].

### 4.2. CALCULATIONS

Semiempirical methods used in this research are all part of the MOPAC program available from Quantum Chemistry Program Exchange.<sup>5</sup> Semiempirical molecular orbital calculations were performed using MNDO [6] and AM1 [7] methods developed by Dewar and co-workers. Revised silicon parameters were used for MNDO calculations [8]. All stationary points on the potential surfaces were fully optimized using procedures of the MOPAC program. Force constant calculations and intrinsic reaction coordinate calculations were performed for each stationary point to determine the nature and connectivity of the potential surface.

*Ab initio* calculations were performed using the GAUSSIAN86 program and basis sets it contains [9]. All *ab initio* calculations in this work were single-point calculations at AM1 geometries. Estimates of energies at the MP2/6-31++G(d) level [10] were calculated by assuming correlation effects and polarization

effects are additive [11]. Comparisons of *ab initio* results and semiempirical results are used to establish a quantitative benchmark for semiempirical energies in order to solve problems that are too large for high-level *ab initio* methods [12].

### 4.3. RESULTS AND DISCUSSION

For reaction of any nucleophile with silicic acid, two possible outcomes are addition and abstraction. In gas-phase silanol polymerization, reactive anions may be formed by addition or abstraction. For example, our previous calculations have shown that a hydroxide ion may react with monomeric silicic acid to form a tetravalent silicate anion by proton abstraction, or it may add to form a pentacoordinate anion. The pentacoordinate anion is formed without activation as is generally the case for siliconate adducts. Direct abstraction of a silanol proton by hydroxide proceeds through a transition state complex also requiring little or no activation energy. Either anionic product can then add without activation to silicic acid to form a larger anion. In either case a hypercoordinate intermediate is involved in the process.

For the polymerization process to continue, at some point water must be eliminated from the hypercoordinated anion either directly or as a hydrated anion. Elimination of water requires energy, generally less energy for more overcoordinated structures. We have found that elimination of water involves a transition-state structure resembling a partially dissociated hypervalent adduct having large negative charge localized on the leaving group. The leaving anion then plucks a proton from a neighboring hydroxyl group followed by elimination [12].

As the size of the anion grows larger, more complicated reactions are possible. For example, the cyclic dimer anion formed by reaction of monomeric silicic acid and monosilicate anion is found to be particularly stable. This dimer can add a silicic acid unit expanding to a trimeric anion in a mechanism involving a tricoordinate oxygen bridge requiring about 16 kcal/mol of activation energy. This process may be followed by a low-energy elimination of pentacoordinate siliconate anion to give neutral dimeric silicic acid [13].

It is tempting to compare the energetics of these mechanisms with experimental measurements for aqueous solution. (The calculated heat of reaction for dimerization is -15 kcal/mol by MNDO and -11 kcal/mol by AM1 in approximate agreement with experimental estimates of about -8 kcal/mol. The experimental activation energy for polymerization is approximately 15 kcal/mol for base catalysis [14].) An apparent shortcoming of this approach is that solvent hydrogen-bonding and dipole interactions may preferentially stabilize anions or transition states. We have begun AM1 calculations of hydrated clusters to address this problem.

Calculations of reaction entropy for addition and abstraction reaction paths of the silicic acid-hydroxide ion system show that the entropy contribution is

## 50 NEUTRAL AND ANIONIC HYPERVALENT SILICON COMPLEXES

small. We need not consider entropic effects unless the reaction enthalpy changes by less than 5 kcal/mol.

To understand this chemistry we must determine the minimum energy reaction path for possible reactions of a given nucleophile. Clearly water elimination reactions are reasonable initial choices for making these comparisons. To obtain a better quantitative view of the silicic acid-hydroxide potential surface we have repeated these calculations using the AM1 method and *ab initio* calculations for selected structures. The results of the AM1 reaction coordinate calculations are shown in Fig. 4.1. Comparisons of AM1 predictions with those of MNDO and *ab initio* methods are shown in Table 4.1. As expected, AM1 results agree better with the *ab initio* calculations than do MNDO results. However, AM1 energies for the monosilicate anion and for the external abstraction transition state are too high by more than 20 kcal/mol, because in these species substantial negative charge is localized on a single oxygen atom. MNDO and AM1 exhibit this same energy overestimation for small anions. The limited basis set of these models does not contain sufficiently diffuse functions to appropriately accommodate this localized electron density. These situations must be recognized when interpreting AM1 and MNDO results.

The AM1 reaction path calculations for the silicic acid-hydroxide system are shown in Fig. 4.1. They qualitatively agree with our previous MNDO predictions. Stabilization of the pentacoordinate intermediate produces a large activation barrier to water elimination. Direct proton abstraction is the low-energy pathway. Note the formation of distinct hydrogen-bonded intermediates stabilized by about 15 kcal/mol relative to the separated reactants or products. Both reaction paths lead through the hydrated silicate anion.

A comparison of activation energy calculations for water elimination by

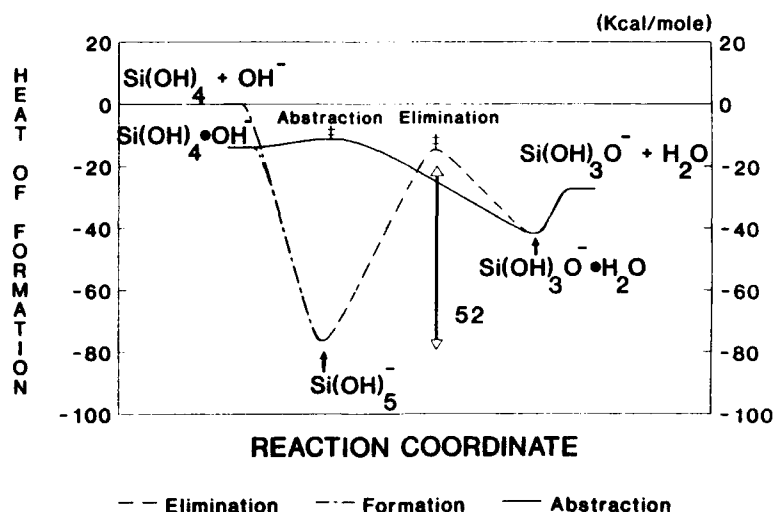


Figure 4.1. The reaction profile for the silicic acid-hydroxide system.

TABLE 4.1. Energetics for Silicic Acid + Hydroxide System

Species	Relative Energy (kcal/mol)		
	MNDO	AM1	Ab Initio <sup>a</sup>
Si(OH) <sub>4</sub> + OH <sup>-</sup>	0.0	0.0	0.0
Si(OH) <sub>5</sub> <sup>-</sup>	-37.7	-76.4	-73.3
Si(OH) <sub>3</sub> O <sup>-</sup> + H <sub>2</sub> O	-8.3	-27.4	-51.6
Internal abstraction transition state	29.9	-24.7	-37.1
External abstraction transition state	11.9	-11.3	-43.3
Si(OH) <sub>4</sub> · OH <sup>-</sup>	—	-13.9	—
Si(OH) <sub>3</sub> O <sup>-</sup> · H <sub>2</sub> O	—	-41.8	—

<sup>a</sup>MP2/6-31 + + G(d)//AM1.

abstraction and internal elimination for the silicic acid-hydroxide ion system is shown in Table 4.2. MNDO calculations predict that the activation energy for water elimination from the dimer silicate anion is substantially less than that for elimination from the monomer silicate anion. This result is confirmed by the AM1 method. Internal elimination of water from the dimeric anion is about 20 kcal/mol more favorable than elimination from the monomeric anion. The reason for this large difference is that the doubly bridged dimer can sustain hypervalent coordination at the losing silicon through a hydroxide bridge. The AM1 and *ab initio* activation energies for proton abstraction from monomeric silicic acid suggest that the reaction proceeds without activation.

The reaction profile for the silicic acid-fluoride ion system calculated using

TABLE 4.2. Activation Energies for Water Elimination

Reaction	Activation Energy (kcal/mol)		
	Semiempirical MNDO	AM1	Ab Initio <sup>a</sup>
External elimination from monomer	11.9	-11.3	-43.3
Internal elimination from monomer	67.6	51.7	36.2
Internal elimination from dimer	49.6	34.3	—

<sup>a</sup>MP2/6-31 + + G(d)//AM1.



## 52 NEUTRAL AND ANIONIC HYPERVALENT SILICON COMPLEXES

AM1 is shown in Fig. 4.2. Comparison with the silicic acid-hydroxide profile in Fig. 4.1 shows many similarities. The pentacoordinate anion is stabilized nearly as much with fluoride ion as with hydroxide ion. Again, most of that stabilization energy is spent forming the hydrated monosilicate anion. A substantial transition state energy is calculated for proton abstraction by fluoride. As before, this activation energy is too large by at least 20 kcal/mol because of the charge localization problem mentioned earlier. Probably there is little or no barrier to proton abstraction, in which case the pentacoordinate intermediate can also eliminate hydrogen fluoride. AM1 predicts that water is more readily eliminated than is hydrogen fluoride.

Illustrative of the facility by which fluoride forms silicon-bridged structures, hydrogen fluoride forms a stable neutral pentacoordinate adduct with silicic acid as is shown in the reaction profile in Fig. 4.3. Although its stability is less than that of fluoride or hydroxide ion adducts the silicic acid, hydrogen fluoride complex is more stable than that for any other small neutral adduct such as water, ammonia, and hydrogen chloride. Elimination of water is much easier by internal abstraction of the HF proton than by abstraction of an OH proton. The difference is due to the strongly nucleophilic fluoride ligand stabilizing the transition state and product for the HF-abstraction path compared to the weakly nucleophilic hydrogen fluoride ligand stabilizing the transition state and product in the OH-abstraction path. The products of this reaction are complexes with water occupying the axial position of the trigonal bipyramid opposed to the fluoride-containing ligand. There are very small energy differences between the pentacoordinate water adducts and the corresponding hydrogen-bonded water adducts.

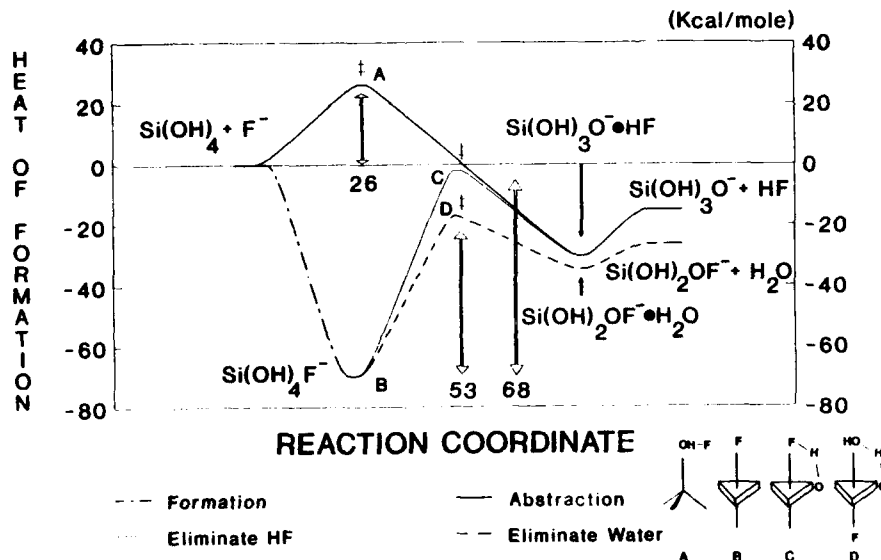


Figure 4.2. The reaction profile for the silicic acid-fluoride system.

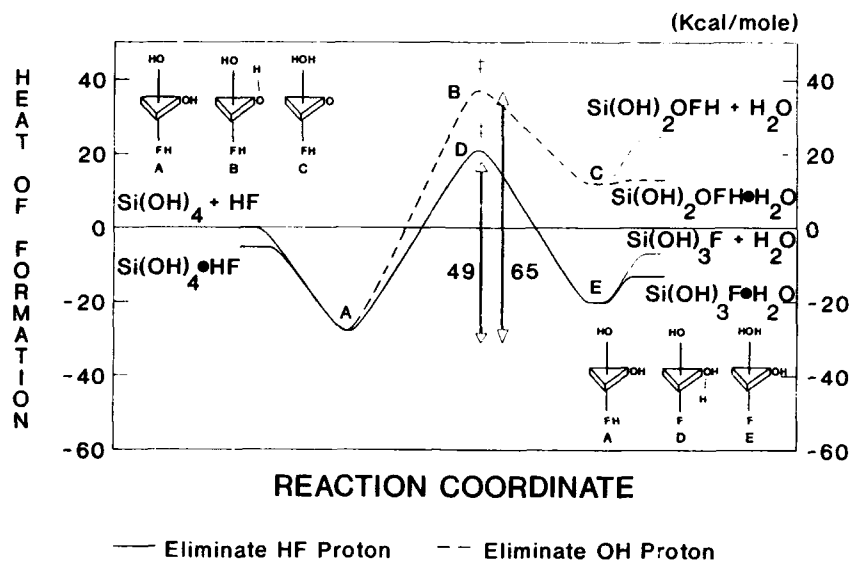


Figure 4.3. The reaction profile for the silicic acid-hydrogen fluoride system.

Applying bond order conservation principles to hypervalent siliconates, we expect that intramolecular elimination of a hydroxide opposed to a ligand that strongly binds will require less activation energy than for an opposed ligand that weakly binds. It is interesting to observe that fluoride and hydroxide influence the pentacoordinate reaction path in a similar way in that both add strongly to silicic acid to form complexes of comparable stability. Also, for both adducts the activation energy requirement to intramolecularly eliminate water is nearly the same. On the other hand, hydrogen fluoride bonds less strongly to form the pentacoordinate adduct, and a much larger activation energy is required for intramolecular water elimination by the silanol path than for the fluoride or hydroxide complexes. This analysis suggests that the intramolecular water elimination path for pentacoordinate siliconates will be facilitated by more strongly binding adducts.

Molecular orbital calculations predict that ammonia and formamide form a series of complexes with silicic acid by hydrogen bonding and by addition to silicon. The differences in energy between adduct and hydrogen-bonding forms are not as great as for hydroxide and fluoride adducts because of the decreased ionic bonding contribution to adduct bonding. Table 4.3 shows the relative energies of silicic acid-ammonia complexes. AM1 calculations suggest that ammonia forms a stable hydrogen-bonded species binding ammonia through two ammonia hydrogen bridges to a single oxygen and by a silanol hydrogen on another silanol to the nitrogen. The axial ammonia adduct is stabilized by comparable energy. The equatorial adduct predicted by the AM1 calculation is probably not stable.

## 54 NEUTRAL AND ANIONIC HYPERVALENT SILICON COMPLEXES

TABLE 4.3. Stabilization of Ammonia with  $\text{Si(OH)}_4$

Structure	Relative Energy (kcal/mol)		
	AM1	Ab Initio	
		6-31 <sup>a</sup>	MP2/6-31 <sup>b</sup>
$\text{Si(OH)}_4 + \text{NH}_3$	0.0	0.0	0.0
Hydrogen bonded $\text{Si(OH)}_4 \cdot \text{NH}_3$	-3.7	-4.1	-6.4
Pentacoordinate $\text{Si(OH)}_4\text{NH}_3 \cdot \text{NH}_3$ axial	-12.0	0.6	-5.7
Pentacoordinate $\text{Si(OH)}_4\text{NH}_3 \cdot \text{NH}_3$ equatorial	-8.5	20.8	13.4

<sup>a</sup>6-31G(d)//AM1.

<sup>b</sup>MP2/6-31 + G(d)//AM1.

Formamide adducts to silicic acid are more complex. AM1 calculations indicate that combinations of hydrogen bonding and addition occur for formamide. A complex, doubly hydrogen bonded through amide hydrogens, is stabilized by 3.4 kcal/mol. AM1 calculations yield two stable nitrogen adducts complexes having one and three hydrogen bonds stabilized by 2.5 and 3.9 kcal/mol, respectively. Adducts that are bonded through the formamide oxygen are predicted to be more stable than nitrogen adducts. Four forms of oxygen adducts are found to be stabilized by between 9.5 and 12 kcal/mol. Two of these adducts are hydrogen bonded through an aldehyde proton and two are hydrogen bonded through an amide proton. The significant difference between like adducts is the oxygen takes on either a long or a short bond distance. The structures having long silicon-oxygen bond distance permit a more favorable hydrogen-bonding interaction. This is an example of molecular bistability.

### 4.4. CONCLUSIONS

The AM1 model is useful for modeling hydrogen-bonded species important to silanol polymerization. Comparisons with *ab initio* calculations show that AM1 results are reliable for anionic silicates and transition state silicate structures except when substantial negative charge is localized on an atom. The enthalpies of such silicate species are overestimated by 20 kcal/mol or more.

Water elimination from hypercoordinated silicates is expected to be a key to understanding silanol polymerization chemistry. Reaction profiles for water elimination were calculated for hydroxide and fluoride ions and hydrogen fluoride adducts with silicic acid. Hydroxide ion and fluoride ion form very stable pentacoordinate adducts with silicic acid without activation. Most of that

stabilization energy is required to achieve the activated complex to eliminating water. In an alternative reaction path hydroxide ion and fluoride ion may abstract a proton from silicic acid to directly form the hydrated tetracoordinate silicate with little or no activation requirement. Hydrogen fluoride can also form pentacoordinate adduct with silicic acid. This requires more activation energy to eliminate water than does the fluoride adduct. However intramolecular elimination of water by proton abstraction from the HF ligand has an activation energy requirement comparable to that for the fluoride adduct.

Ammonia and formamide form adducts with silicic acid involving hydrogen bonding and addition to silicon. Formamide is predicted to bond by hydrogen bonding and addition to silicon in bistable forms in which the oxygen-silicon bond distance is either short or long. The structures having long oxygen-silicon bond distances permit more favorable hydrogen-bonding interactions.

## REFERENCES

1. L. P. Davis, and L. W. Burggraf, *Ultrastructure Processing of Advanced Ceramics*, pp. 367-378, Wiley, New York (1988). L. W. Burggraf and L. P. Davis, *Chemically Modified Surfaces*, Vol. 1, pp. 157-187, Gordon and Breach Science. L. P. Davis and L. W. Burggraf, *Science of Ceramic Chemical Processing*, pp. 400-411, Wiley, New York (1986). L. W. Burggraf and L. P. Davis, *Mater. Res. Soc. Symp. Proc.*, **73**, 529-542 (1986).
2. R. Damrauer, L. W. Burggraf, L. P. Davis, and M. S. Gordon, *J. Am. Chem. Soc.*, **110**, 6601 (1988).
3. S. N. Tandura, M. G. Voronkov, and N. V. Alekseev, *Top. Current Chem.*, **131**, 99 (1986).
4. Private communication, Prof. Larry L. Hench, University of Florida, 1989.
5. J. J. P. Stewart, Quantum Chemistry Program Exchange, Program 455, Department of Chemistry, Indiana University, Bloomington, IN 47405.
6. M. J. S. Dewar and W. Thiel, *J. Am. Chem. Soc.*, **99**, 4899 (1977).
7. M. J. S. Dewar, E. G. Zoebisch, E. F. Healy, and J. J. P. Stewart, *J. Am. Chem. Soc.*, **107**, 3902 (1985).
8. M. J. S. Dewar, J. Friedhaim, G. Grady, E. F. Healy, and J. J. P. Stewart, *Organometallics*, **5**, 375 (1986).
9. M. J. Frisch, J. S. Binkley, H. B. Schlegel, K. Raghavachari, C. F. Melium, R. L. Martin, J. J. P. Stewart, F. W. Brobrowicz, C. M. Rohlfing, L. R. Kahn, D. J. DeFrees, R. Seeger, R. A. Whiteside, D. J. Fox, E. M. Fluder, S. Topiol, J. A. Pople, GAUSSIAN86, Carnegie-Mellon Quantum Chemistry Publishing Unit, Pittsburgh, PA 15213.
10. R. Krishnan and J. A. Pople, *Int. J. Quantum Chem.*, **14**, 91 (1978).
11. T. A. Holme, M. S. Gordon, S. Yabushita, and M. W. Schmidt, *Organometallics*, **3**, 583 (1984). M. S. Gordon, *J. Am. Chem. Soc.*, **104**, 4352 (1982). M. L. McKee and W. N. Lipscomb, *J. Am. Chem. Soc.*, **103**, 4673 (1981).
12. L. P. Davis, L. W. Burggraf, and M. S. Gordon, *J. Am. Chem. Soc.*, **110**, 3056 (1988).
13. L. P. Davis and L. W. Burggraf, *Ultrastructure Processing of Advanced Ceramics*, pp. 367-378, Wiley, New York (1988).
14. R. K. Iler, *The Chemistry of Silica*, pp. 248-251, Wiley, New York (1979).

## **5**

# **CHARACTERIZATION OF STRUCTURAL DEVELOPMENT IN SOL-GEL SYSTEMS BY CRYOGENIC TRANSMISSION ELECTRON MICROSCOPY**

**JOSEPH K. BAILEY AND MARTHA L. MECARTNEY**

### **5.1. INTRODUCTION**

The key to optimizing the properties of sol-gel ceramics lies in being able to design the structure of these materials from the atomic scale on up. Control of the gel structure is of paramount importance, because the gel structure influences the flow, drying, and sintering behaviors and, hence, will affect the final material properties [1]. A critical first step to optimizing the structure, however, is to understand the structural evolution of the gel during the different stages of processing and to determine how this structural development can be modified.

#### **5.1.1. Gelation of Alkoxide Sols**

Alkoxysilanes are the most prominently studied starting materials for sol-gel synthesis of ceramics. Tetraethoxysilane (TEOS) undergoes gelation through

---

*Ultrastructure Processing of Advanced Materials.*

Edited by Donald R. Uhlmann and Donald R. Ulrich (deceased).

ISBN 0-471-52986-9 © 1992 John Wiley & Sons, Inc.

hydrolysis and condensation reactions. Brinker and Scherer [2] and Sakka and Kamiya [3] have proposed that at low pH with stoichiometric water content the sols are polymeric, but if processed with a high pH and excess water, the structure is similar to that of a colloidal gel, only with highly branched clusters in place of dense particles. Small-angle scattering work by Schaefer and Keefer [4] has shown that the gels are fractal in nature. However, seemingly conflicting theories and models ascribe the structures to different growth mechanisms. Keefer [5] proposed a poisoned Eden growth model based on monomer addition that demonstrates a single growth model can generate the entire range of observed fractal dimensions. Zarzycki [6] has suggested that small particles form which gel by clustered aggregation kinetics, which also explains the observed bimodal pore distributions. Himmel et al. [7] using small-angle X-ray scattering found evidence for a dense silica primary particle of 5 to 10-Å radius, which indicates that the monomer for gel growth might not be a TEOS molecule. While small-angle scattering studies are useful for obtaining structural information, such as fractal dimensions and correlation lengths for size scales of 10 to 1000 Å, the results are subject to various interpretations, leading to differing models of gelation.

#### 5.1.2. Gelation of Colloidal Sols

For colloidal sol-gel systems, small-angle scattering work has been the primary means performed to determine the structures and gelation mechanisms. Small-angle scattering results have indicated that the gel structures for spherical colloidal silica are fractal with a fractal dimension of 2.1 [8]. Growth mechanisms for the colloidal silica aggregation is governed by aggregation kinetics and has been modeled by Lin et al. [9]. The structure of colloidal boehmite gels, composed of colloids that are flat hexagonal platelets, have been less well studied [10].

#### 5.1.3. Growth of Colloidal Particles

Preparation of monodisperse, high-purity powders via colloidal processing is also of great interest in chemical processing of ceramics. One method of preparing colloidal particles of silica is the process of Stöber et al. [11] in which a dilute solution of TEOS is reacted with water in a highly basic medium. Bugosh and Zukoski [12, 13] have developed an aggregation model of growth for this system, in which the primary nuclei form and aggregate into larger particles. The larger particles, due to the highly basic medium, are colloiddally stable and do not aggregate, but still can grow by addition of the primary nuclei. The main source of evidence for this growth model, in which small nuclei form early in the reaction, has been transmission electron microscopy (TEM) of dried sol samples [12].

#### 5.1.4. Structural Characterization

Many methods have been used to characterize the structures that form in sols and in the gel state, including NMR spectroscopy [14–16], small-angle scattering [4, 7–9], and electron microscopy [17–23]. NMR spectroscopy is limited to providing local chemical information, and small-angle scattering is indirect with the interpretation model dependent. In contrast, electron microscopy can provide direct visualization of the microstructure and thus potentially offers the most direct technique for characterization of the microstructures of sols and gels.

##### 5.1.4.1. Characterization by TEM

Although TEM can offer images with near atomic resolution, one important caveat must be offered here, which is that the value of the information obtained by electron microscopy is dependent on sample preparation technique. Preparing a sample that can withstand the high vacuum inside the electron microscope can induce structural changes in the sample.

Various techniques used to prepare samples for electron microscopy studies of sol and gel microstructures include desiccation [17, 18], freeze-fracture replication [19, 20], and thin liquid film vitrification [21–23]. Desiccated samples are prepared by placing a drop of the sol or gel on a support grid and allowing the solvent to evaporate. The dried structures are then viewed in the electron microscope. Desiccation of the solvent produces drying stresses within the sample and can rearrange the microstructure. Another sample preparation method is freeze-fracture replication, in which a sample is frozen and the frozen material is then fractured. The fracture surface is coated with carbon and/or platinum, the frozen sample is removed, and the replica is viewed in the TEM. This technique only allows the observation of the fracture surface.

A third method of sample preparation that avoids creating artifacts caused by desiccating the sample and also allows observation of the entire microstructure is vitrification of thin liquid samples [21, 24]. This technique involves fast freezing a thin liquid sample and viewing the frozen sample in the transmission electron microscope using a cold stage (cryo-TEM), a process that allows the vitrified sample to be viewed directly. This Chapter summarizes the important contributions made by using cryo-TEM to study sol–gel systems.

## 5.2. EXPERIMENTAL

### 5.2.1. Cryo-TEM Sample Preparation

Samples are prepared by using a holey carbon film as a support. A drop of the sol is placed on the grid and the sample is blotted to produce a thin liquid film that spans the holes (much like a soap bubble). This sample is prepared in a

controlled environmental chamber [24] that is saturated in order to prevent evaporation of the solvent. At the appropriate time, the sample is then rapidly plunged into liquid ethane. The freezing rate is greater than 10,000 K/sec. This rapid freezing rate prevents crystallization of the solvent and produces solid amorphous (vitreous) solvent that traps the structure of the liquid state in place. The sample is then transferred under liquid nitrogen to a liquid nitrogen cold stage and then placed into the electron microscope. Structural development can be tracked as gelation proceeds by preparing samples at successive times in the reaction.

For this work, a JEOL 100CX microscope was used with Kodak SO-163 film. This high sensitivity film was selected to allow short exposure times, which minimizes damage to the sample caused by the electron beam. A defocus of 1 to 3  $\mu\text{m}$  underfocus was used to enhance phase contrast.

### 5.2.2. Sol Preparation

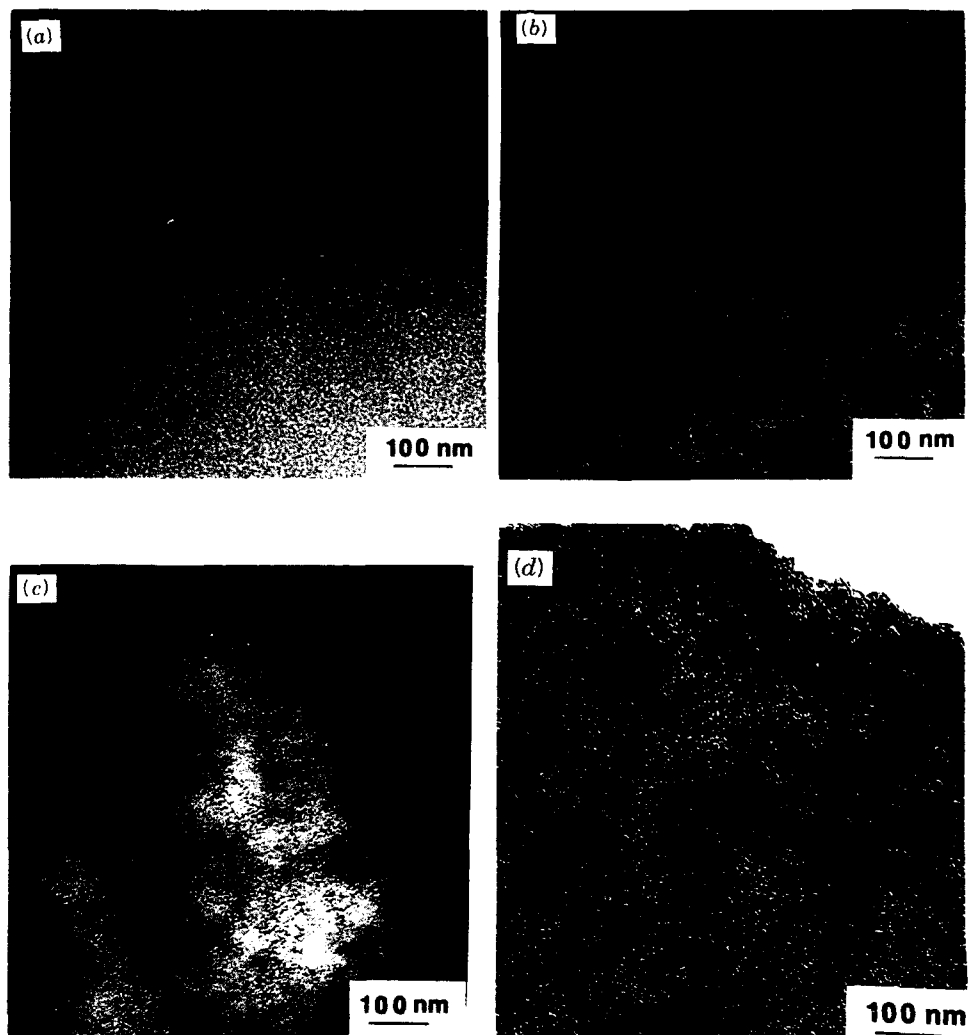
The sols investigated were Ludox colloidal silica (HS-40), colloidal boehmite [Disperal  $\text{AlO}(\text{OH})$ ], and TEOS gelled under acidic and basic conditions. The Ludox was gelled using NaCl solutions and was diluted to a 5 wt % concentration before observation in the TEM. The boehmite was dispersed in water using nitric acid for stabilization. When diluted with pure water, the samples began to gel and were diluted to a 2 wt % concentration before observation in the TEM. The acidic TEOS gels were prepared using a 1:3:3:0.07 mole ratio of TEOS: $\text{H}_2\text{O}$ :*n*-propanol:HCl. The sols were diluted to 0.14 M TEOS before observation. The base-catalyzed TEOS gels were prepared using the two-step method of Brinker et al. [17]. The final ratio was 1:5:5:0.25 mole ratio of TEOS: $\text{H}_2\text{O}$ :*n*-propanol: $\text{NH}_4\text{OH}$ . The base-catalyzed sols were also diluted to 0.14 M TEOS before observation. In addition, silica colloids were grown via the Stöber et al. process in which a dilute solution of TEOS is reacted with water in a highly basic medium [11]. For these experiments, the solutions contained 0.17 M TEOS, 1.0 M  $\text{H}_2\text{O}$ , and 1.0 M  $\text{NH}_3$ . This solution took approximately 30 min to turn turbid.

## 5.3. RESULTS AND DISCUSSION

### 5.3.1. Gelation of TEOS

Previous TEM work on TEOS gels has been conducted using dried gel samples [17,18]. These methods collapse the structure and cannot give direct observation of the wet state structure. Cryo-TEM of vitrified liquid films, however, does give direct visualization of the structure and has been used to observe the structure in the wet state. The most striking example of structural evolution during gelation of alkoxides viewed by cryo-TEM is from base-catalyzed TEOS. Figure 5.1a shows the sol. No distinct structures are visible in the vitreous





**Figure 5.1.** Structural development during the gelation of base-catalyzed TEOS. (a) Initial sol. (b) Sol at 50% of the gel time. (c) Sol at 90% of the gelation time. (d) Xerogel (dried gel).

solvent. The sol at one-half the gel time is shown in Fig. 5.1*b*, and small dark spots appear in the vitreous solvent indicating that the silica has formed small clusters. These clusters are approximately 40 Å in diameter. When the gel state is neared, these clusters apparently link together to form a network. Figure 5.1*c* shows the sol at 90% of the gelation time. Here, chains of the small silica clusters have linked together to form network structures. For comparison, Figure 5.1*d* shows the structure of a base-catalyzed TEOS gel that has been dried before viewing in the TEM. The pores have collapsed, and the detail about the connectivity of the primary clusters has been lost.

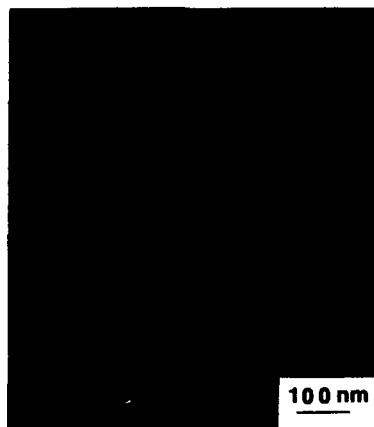


Figure 5.2. Acid-catalyzed TEOS sol at 90% of gelation.

Although the base-catalyzed sol gels by the formation of clusters and their subsequent aggregation, the acid-catalyzed TEOS sols gel distinctly differently. Figure 5.2 shows an acid-catalyzed sol at 90% of gelation at the same concentration as the base-catalyzed sol of Figure 5.1c. This micrograph shows a homogeneous structure in which no primary particles are visible. This indicates that there are no silica-rich clusters larger than approximately 2 nm in the solution. Furthermore, if there are small silica clusters less than 2 nm, they must link up in chains, because large aggregates of small clusters would be visible. From the cryo-TEM micrographs, it is evident that the base-catalyzed sols do form small clusters that aggregate during gelation, but the acid-catalyzed sols form structures with at least one dimension smaller than 2 nm.

The cryo-TEM results indicate that the method of gelation proposed by Brinker and Scherer [2] is qualitatively accurate. Initially, small silica clusters form and subsequently link together. For the acid-catalyzed gelation, there is not the random aggregation seen in the base-catalyzed gels. Large aggregates of small particles would be seen in the cryo-TEM results if they existed. The homogeneity seen in the cryo-TEM micrographs supports 'polymeric' or chain growth models of gelation for acid-catalyzed TEOS.

### 5.3.2. Colloidal Silica and Boehmite Gels

We have determined the gel structures using cryo-TEM and have found aggregated structures for colloidal silica (Figure 5.3) and for colloidal boehmite (Figure 5.4). The structures shown are the structures in the wet state of the material. The colloidal silica appears to be similar to the fractal silica clusters observed by Schaefer et al. [8]. The boehmite sample indicates that not only face-to-face aggregation, but also edge-to-edge aggregation occurs during gelation. Cryo-TEM micrographs allow the structure to be determined as the

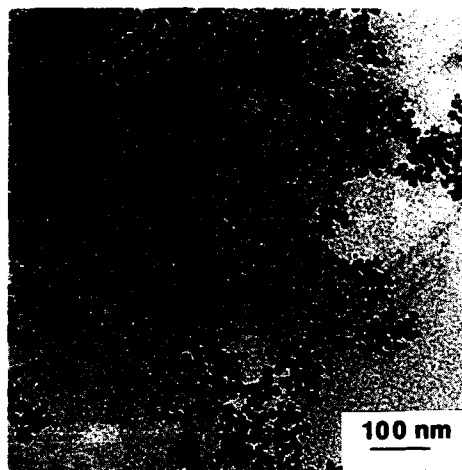


Figure 5.3. Colloidal silica gel structure.

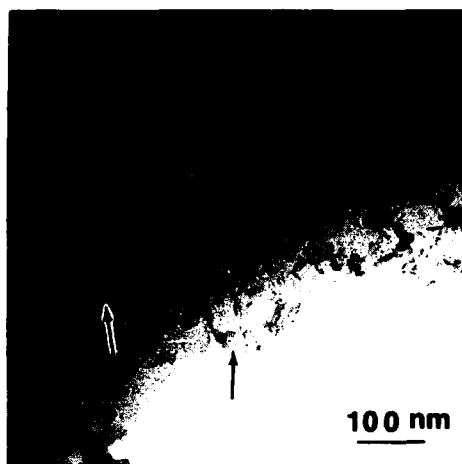
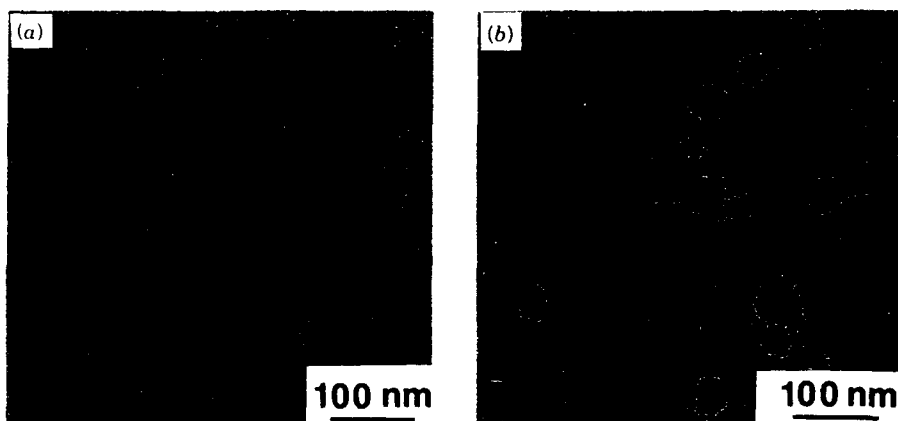


Figure 5.4. Colloidal boehmite structure at the onset of gelation. Note both edge-to-edge and face-to-face aggregation.

gelation proceeds, and we have also begun efforts to correlate the structure with the rheological properties of the sols [23].

### 5.3.3. Growth of Colloidal Silica Particles

The model proposed by Bogush and Zukoski [12, 13] for silica colloid growth during the Stöber et al. process supposes that small primary nuclei (approx-



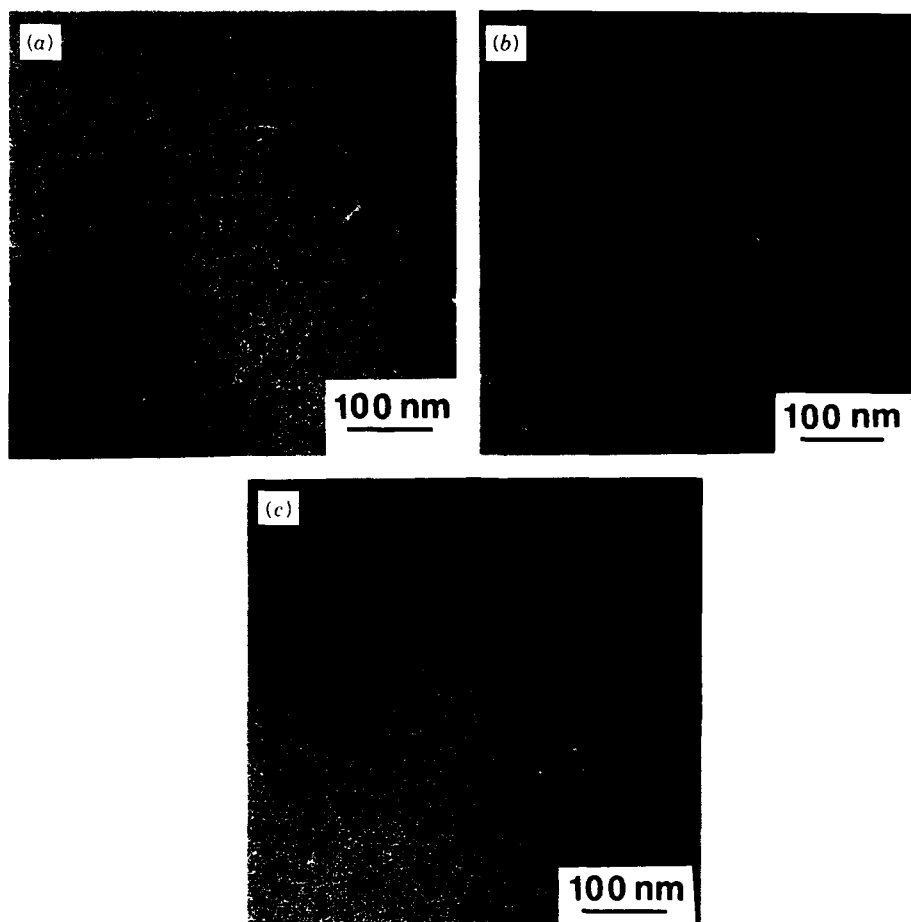
**Figure 5.5.** Dried silica colloids grown by the process of Stöber et al. [11]. (a) Two min into the reaction. (b) Twenty-five minutes into the reaction.

imately 4–6 nm) form early in the reaction then aggregate and grow. TEM micrographs of dried sols do appear to support this hypothesis. Figure 5.5a shows a dried sample 2 min into the reaction and small particles of approximate size 6 nm are seen. Later in the reaction, large primary particles appear to grow by addition of the small clusters (Fig. 5.5b).

Cryo-TEM micrographs of the solutions, however, show no evidence for the formation of small nuclei early in the reaction. Figure 5.6a, a cryo-TEM micrograph taken 6 min into the reaction, shows that the sol still has a uniform contrast and no small nuclei are visible. After 16 min into the reaction, low contrast, diffuse particles appear in the cryo-TEM samples (Figure 5.6b). At a later time, smaller particles, which are more distinct and have a higher contrast, are seen by cryo-TEM (Fig. 5.6c). Subsequent pictures in this sequence show normal growth of the colloids.

These results indicate that the primary nuclei particles seen in the dried TEM micrographs may be artifacts of sample preparation, forming and aggregating as the solvent evaporates and the solution becomes more concentrated. The alkoxysilane polymers may be soluble at low molecular weights, but if they are dried or grow to a critical size, they collapse. An analogy can be found in organic polymers, where higher-molecular-weight species are insoluble [25]. Solubilized particles observed in solution have low contrast, because the density of the particle is reduced due to inclusion of the solvent. Therefore, before growing to a critical size, the silica particles appear diffuse and expanded (Fig. 5.6b), but after reaching a critical size, they collapse and form denser particles with a higher contrast (Fig. 5.6c). An alternative explanation would be that loosely aggregated flocs of very small silica particles (1–2 nm) form initially and when the floc reaches a critical mass, it collapses into a dense particle.

One important unanswered question about the growth of these colloids is



**Figure 5.6.** Sequence of cryo-TEM micrographs illustrating the early stages of growth for silica colloids *in solution*. (a) Six minutes into the reaction. (b) Sixteen minutes into the reaction. (c) Twenty-four minutes into the reaction.

why they grow more or less uniformly as spheres. One would not expect random aggregation of particles to produce uniform spherical particles without surface rearrangement of the particles. Bogush and Zukoski attribute the uniform spherical growth to the larger particles being colloidally stable with respect to each other while the smaller ones are not [12]. Therefore the larger particles sweep out the smaller particles from the solution; however, this type of mechanism would not necessarily lead to uniform growth. An attractive feature of the solubilized silica explanation is that the low-molecular-weight species that are solubilized in solution could coat the growing silica colloids, collapsing onto the surface of the particle and contributing to the growth of the colloids as spheres.

### 5.4. CONCLUSIONS

These results show the utility of the cryo-TEM technique. It is a valuable tool that can be used to directly observe the structure of sols and gels in the wet state. It eliminates the structural rearrangement that can occur to samples as they are dried and allows the three-dimensional structures of the gels to be observed with stereo tilt microscopy. The current resolution allows observation of structures that are on the order of 2 nm, which is mainly limited by the stability of the sample to the electron beam. The potential of this cryo-TEM technique lies in its ability to reveal the structure of liquid sols and wet gels by direct imaging and hence verify or confute proposed models and mechanisms of particle growth and gelation.

### ACKNOWLEDGMENTS

The authors would like to acknowledge the 3M Foundation and AFOSR Contract AF/F49620-89-C-0050 for support for gel network formation studies and Sandia National Laboratories, Contract 05-3976, for support for the colloid growth studies. Professors H. T. Davis and L. E. Scriven are thanked for access to the controlled-environment vitrification system.

### REFERENCES

1. D. R. Ulrich, *J. Non-Cryst. Solids*, **100**, 174 (1988).
2. C. J. Brinker and G. W. Scherer, *J. Non-Cryst. Solids*, **70**, 301 (1985).
3. S. Sakka and K. Kamiya, *J. Non-Cryst. Solids*, **48**, 31 (1982).
4. D. W. Schaefer and K. D. Keefer, in: C. J. Brinker, D. E. Clark, and D. R. Ulrich, Eds., *Better Ceramics Through Chemistry*, Elsevier Science, New York, (1984). pp. 1-14.
5. K. D. Keefer, in: L. L. Hench and D. R. Ulrich, Eds., *Science of Ceramic Chemical Processing*, p. 131, Wiley, New York (1986).
6. J. Zarzycki, in: L. L. Hench and D. R. Ulrich, Eds., *Science of Ceramic Chemical Processing*, pp. 21-36, Wiley, New York (1986).
7. B. Himmel, Th. Gerber, and H. Bürger, *J. Non-Cryst. Solids*, **91**, 122 (1987).
8. D. W. Schaefer, J. E. Martin, P. Wiltzius, and D. S. Cannell, *Phys. Rev. Lett.* **52**, 2371 (1984).
9. M. Y. Lin, H. M. Lindsay, D. A. Weitz, R. C. Ball, R. Klein, and P. Meakin, *Proc. R. Soc. London, Ser. A*, **423**, 71 (1989).
10. M. G. Schwabel, *Am. Ceram. Soc. Bull.*, **62**, 872 (1983).
11. W. Stöber, A. Fink, and E. Bohn, *J. Colloid Interface Sci.*, **26**, 62 (1968).
12. G. H. Bogush and C. F. Zukoski, *Ceramic Microstructures 1986*, eds. J. A. Pask and A. G. Evans (Plenum, New York, 1987) 477.
13. G. H. Bogush, M. A. Tracy, and C. F. Zukoski, *J. Non-Cryst. Solids*, **104**, 95 (1988).
14. W. G. Klemperer, V. V. Mainz, S. D. Ramamurthi, and F. S. Rosenberg, in: C. J. Brinker, D. E. Clark, and D. R. Ulrich, Eds., *Better Ceramics Through Chemistry*, Vol. III, p. 15 *Mat. Res. Soc. Proc.*, **121**, 1988).

15. L. W. Kelts and N. J. Armstrong, *J. Mater. Res.*, **4**, 423 (1989).
16. B. D. Kay and R. A. Assink, in: C. J. Brinker, D. E. Clark, and D. R. Ulrich, Eds., *Better Ceramics Through Chemistry*, Vol. II, p. 157, (*Mater. Res. Soc. Proc.*, **73**, 1986).
17. C. J. Brinker, K. D. Keefer, D. W. Schaefer, and C. S. Ashley, *J. Non-Cryst. Solids*, **48**, 47 (1982).
18. C. A. M. Mulder, B. Van Leeuwen-Stienstra, J. G. van Lierop, and J. P. Woerdman, *J. Non-Cryst. Solids*, **82**, 148 (1986).
19. G. C. Ruben and M. W. Shafer, in: C. J. Brinker, D. E. Clark, and D. R. Ulrich, Eds., *Better Ceramics Through Chemistry*, Vol. II, p. 207 (*Mater. Res. Soc. Proc.*, **73**, 1986).
20. R. B. Matthews, P. H. Teware, and T. P. Copps, *J. Colloid Interface Sci.*, **68**, 260 (1979).
21. J. K. Bailey, J. R. Bellare, and M. L. Mecartney, in: J. C. Bravman, R. M. Anderson, and M. L. McDonald, Eds., *Specimen Preparation for Transmission Electron Microscopy of Materials*, p. 69, (*Mater. Res. Soc. Proc.*, **115**, 1988).
22. J. Bellare, J. K. Bailey, and M. L. Mecartney, in: J. D. Mackenzie and D. R. Ulrich, Eds., *Ultrastructure Processing of Advanced Ceramics*, p. 835, Wiley, New York (1988).
23. J. K. Bailey, T. Nagase, S. M. Broberg, and M. L. Mecartney, *J. Non-Cryst. Solids*, **109**, 198 (1989).
24. J. R. Bellare, H. T. Davis, L. E. Scriven, and Y. Talmon, *J. Electron Microscopy Technique*, **10**, 87 (1988).
25. P. C. Heimenz, *Polymer Chemistry*, Marcel Dekker, New York (1984).

## 6

# EFFECT OF HYDROGEN ION CONCENTRATION ON GELATION OF TETRAFUNCTIONAL SILICATE SOL-GEL SYSTEMS

BRADLEY K. COLTRAIN, SHARON M. MELPOLDER,  
AND JOHN M. SALVA

The role of specific acid anion and its concentration on the gel time of tetraethoxysilane (TEOS) was investigated by varying molarity and acid counterion. The gel time of the various acid-catalyzed sol-gel solutions correlated with the pH\* value and was independent of the counterion. Acid- and base-catalyzed tetramethoxysilane (TMOS) sol-gels at time =  $0.5t_{\text{gel}}$  were diluted to 2% solids and adjusted to similar pH values while maintaining a constant ionic strength in an aqueous solvent. The gel time of these two-step hydrolyzed solutions depended upon the surface charge of the polymerizing sol. This charge was determined by the final rather than the initial pH conditions.

## 6.1. INTRODUCTION

A number of studies have focused on the effects of acid or base on hydrolysis rates, gel times, and final properties of sol-gel systems [1-8]. It is well known that solution pH, the water-to-alkoxide ratio, and the solvent, as well as a

*Ultrastructure Processing of Advanced Materials.*

Edited by Donald R. Uhlmann and Donald R. Ulrich (deceased).

ISBN 0-471-52986-9 © 1992 John Wiley & Sons, Inc.



number of other variables, greatly affect the gelation processes. It has been shown that properties such as melting point, viscosity, and strength can be altered by changing the connectivity or structure of the initially formed polymers [9, 10]. It seems apparent that by understanding the mechanisms of the hydrolysis and condensation reactions and the effects of pH on properties such as gel times and polymer structure, it should be possible to control reactions in such a manner as to selectively dictate polymer structures and properties.

As recently reported by Pope and Mackenzie [6], the particular effect of the catalyst on the gelation behavior has not been systematically studied even though it is well recognized that pH has a tremendous effect on the material's final properties. A systematic, controlled study of the effects of various acid catalysts on the gel times of TEOS-based sol-gels was initiated. In this Chapter the effect of various acids on gel times and clarification of pH measurement in the sol-gel reaction mixtures are shown. Additionally, the surface charges of the growing silicate particles generated by the hydrolysis and condensation of TMOS under acidic and basic conditions have been studied and correlated with the aqueous solution gel times.

## 6.2. EXPERIMENTAL

TEOS and TMOS were obtained from Fluka and were used as received. Ethanol, 200 proof, was obtained from US Industrial Company and was used as received. Water was distilled and deionized by passing through a Millipore Milli-Q-Plus Model ZD4011584-4 four-cartridge system. The various acids that were employed, hydrochloric (HCl), *p*-toluenesulfonic (PTSA), nitric ( $\text{HNO}_3$ ), acetic (HOAc), and trifluoroacetic (TFA), were reagent grade and were used as received.

A standardized procedure was employed for all of the solutions in order to provide a systematic study. Typically, 14.33 ml (0.064 mol) of TEOS and 14.33 ml (0.246 mol) of ethanol were stirred for 30 min at room temperature before 4.67 ml (0.259 mol) of the acid solution was added dropwise. The resulting solution was stirred 1 h at room temperature and then placed in a 60°C bath until gelation. All gel times are reported relative to the time of water addition and were defined as the point of no detectable flow upon inverting the flask.

All pH measurements were done on an Orion Research Model 231 digital pH meter using an Orion lab-grade combination glass electrode. The reported pH values were determined by measuring the aqueous acid solutions that were added to the reaction. The reported pH\* values were obtained 1 h after placing the reaction flask in a 60°C bath.

The gel time for the acid and base TMOS sol-gels were determined by monitoring the viscosity of the reacting system. The particle size growth for both systems was monitored by inelastic light scattering techniques [11]. To 200 ml of deionized water 25 g of  $\text{NH}_4\text{OH}$ ,  $\text{NH}_4\text{NO}_3$ , or  $\text{HNO}_3$  was added and mixed.

At time =  $0.5t_{gel}$  for each reacting system, 50 ml of the polymerizing TMOS sol-gel was added, mixed, and immediately analyzed using the Matec ESA System to determine the pH and electrokinetic sonic amplitude (ESA). The ESA effect is generated by the application of an alternating electric field and results in relative motion between particles and liquid, generating a sound wave at the frequency of the applied field. Each particle vibrating in the electric field radiates sounds that sum up to a coherent sound wave when many particles are present. This effect, which was discovered at Matec, is expressed as the pressure amplitude per unit electric field generated by the particles and has SI units of pascals per volt per meter [12]. Knowing the particle size and other parameters, the ESA unit can be reexpressed in terms of mobility or  $\zeta$  potential. The gel times for the two-step hydrolyzed TMOS sol-gel reacting systems incubated at 24°C in capped Nalgene containers were defined as previously described in the pH/pH\* experiment.

### 6.3. RESULTS AND DISCUSSION

Virtually all previous literature reports on the effects of acids on gel times focused on single acid concentrations. Recognizing that many of these acids have greatly different  $pK_a$  values (acetic acid and HCl, for example), this work spanned a variety of concentrations so that similar pH values could be studied. Table 6.1 shows the various acids and concentrations that were studied, as well as the measured gel times and pH and pH\*; Fig. 6.1 shows plots of the gel times versus pH.

As clearly seen in Fig. 6.1, all of the acids yield sigmoidal-shaped curves for gel time versus pH. This behavior has been previously reported by Iler for the condensation of  $\text{Si}(\text{OH})_4$  [13] and by Pope and Mackenzie for the HCl-catalyzed reactions of TEOS [6]. The gel times were longest near pH 2 and shortest near pH 3.5. Iler has noted that pH 2 corresponds to the isoelectric point of silica and represents the slowest point in the condensation reactions [13]. As was reported by Pope and Mackenzie, a sharp increase in gel time is observed near pH 4, which has been associated with decreased hydrolysis rates [6]. It is well known that the hydrolysis rate of TEOS is slowest at pH 7 [1, 2].

A close look at Fig. 6.1 reveals that the carboxylic acids, TFA and HOAc, exhibit different behavior from the other acids, particularly near pH 2. The gel time maxima are clearly shifted from pH 2 for these two acids, which is difficult to explain based on the isoelectric point of silica. A comparison of the gel times for HOAc and HCl sols at 1 M concentrations, for example, shows that HOAc sols gel about three faster than do the HCl sols. Such behavior could lead to the conclusion that catalysis by the acetate anion is occurring.

It is important to recognize that the data in Fig. 6.1 represents the pH of the aqueous solution that was added to the sol-gel mixture. The data are reported this way to avoid the problem of defining pH in a nonaqueous solution.

Because the data from the pH plots suggested possible interactions of the acid

TABLE 6.1. Gel Times, pH, and pH\*

Acid	Molarity	Gel Time (hr)	pH	pH*
HCl	1	27.5 ± 2.5	0.16	0.02
	0.15	40.5 ± 4.5	0.90	1.16
	0.05	80.8 ± 2.8	1.36	1.37
	0.02	88.3 ± 4.8	1.75	1.76
	0.004	56.9 ± 2.9	2.43	2.15
	3.1 × 10 <sup>-4</sup>	9.9 ± 2.4	3.51	3.55
	3.1 × 10 <sup>-5</sup>	17.8 ± 1.8	4.50	4.94
<i>p</i> -Toluenesulfonic acid	1	32.6 ± 2.4	0.21	0.30
	0.1	91.0 ± 1.0	1.14	1.17
	1 × 10 <sup>-2</sup>	85.9 ± 4.2	2.06	2.13
	1 × 10 <sup>-3</sup>	13.1 ± 0.7	3.34	3.20
	1 × 10 <sup>-4</sup>	15.2 ± 0.8	4.44	4.60
	1 × 10 <sup>-5</sup>	20.9 ± 1.6	5.33	5.60
HNO <sub>3</sub>	1	39.7 ± 5.0	0.20	0.20
	0.1	83.4 ± 5.6	1.19	0.92
	1 × 10 <sup>-2</sup>	76.6 ± 1.6	2.15	1.69
	1 × 10 <sup>-3</sup>	26.9 ± 1.1	3.07	2.63
	1 × 10 <sup>-4</sup>	15.5 ± 4.8	4.05	4.43
	1 × 10 <sup>-5</sup>	47.5 ± 1.3	4.92	7.09
Trifluoroacetic acid	1	83.0 ± 5.5	0.32	1.17
	0.1	75.0 ± 7.0	1.14	1.74
	1 × 10 <sup>-2</sup>	50.9 ± 7.6	2.04	2.13
	1 × 10 <sup>-3</sup>	17.9 ± 1.9	3.00	2.85
	1 × 10 <sup>-4</sup>	9.8 ± 2.4	3.97	4.09
	1 × 10 <sup>-5</sup>	23.5 ± 1.0	5.42	6.75
HOAc	5	40.5 ± 5.0	1.75	2.80
	1	9.6 ± 2.6	2.31	3.44
	0.1	14.0 ± 1.5	2.86	4.13
	1 × 10 <sup>-2</sup>	17.0 ± 4.0	3.37	4.90
	1 × 10 <sup>-3</sup>	25.4 ± 1.6	3.91	6.27
	1 × 10 <sup>-4</sup>	52.8 ± 1.5	5.43	7.70

anions, a means was sought to accurately determine the true  $[H^+]$  in the sols. Although there has been a great deal of effort directed at understanding pH in nonaqueous systems, no universal pH scale has been developed [14]. It is clear that relative acid strengths can vary in different solvents, and great care must be exercised when making comparisons in different media. Bates and Schwarzenbach have noted that relative  $H^+$  activities can be determined in aqueous alcoholic solvents using a pH meter and glass electrode, because many glass electrodes display nearly theoretical responses to  $H^+$  at least to 90% ethanol [15]. They also note that the pH\* scale can be used in many mixed solvents.

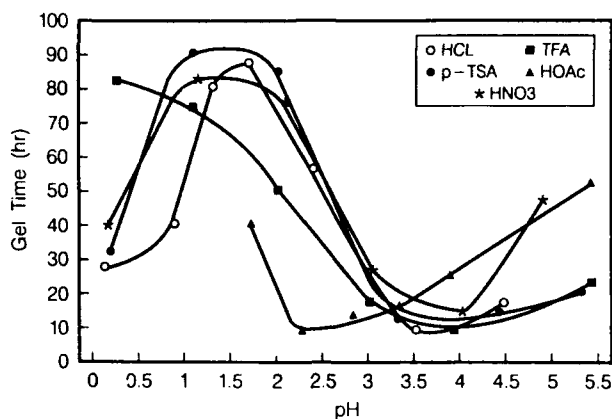


Figure 6.1. Gel time versus pH for sols catalyzed by various acids.

Based on this,  $\text{pH}^*$  values for the sol-gel solutions were determined 1 h after mixing using a glass electrode, and the data are plotted in Fig. 6.2. Clearly the carboxylic acid sols correlate well with the other acids using the  $\text{pH}^*$  scale, although small differences remain near the isoelectric point. It is also evident that the gel times correlate with  $[\text{H}^+]$  with little or no evidence for acid anion catalysis.

The apparent discrepancy between the pH and  $\text{pH}^*$  data can be clarified by the work of Bates and Schwarzenbach who have studied acidity functions in ethanol-water mixtures. They have shown that HOAc acts as a much weaker acid as the mole fraction of ethanol is increased, whereas HCl acts as slightly stronger acid, but with a less pronounced dependence on the ethanol concentration [14, 15]. pH and  $\text{pH}^*$  would be expected to be similar for acids like HCl,

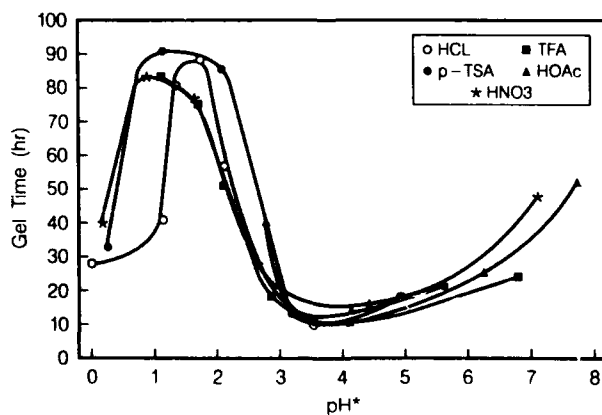


Figure 6.2. Gel time versus  $\text{pH}^*$  for sols catalyzed by various acids.

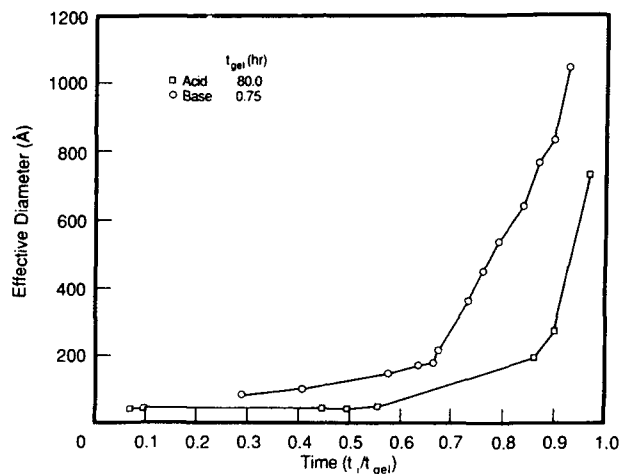


Figure 6.3. Particle diameter versus time for acid- and base-catalyzed reactions of TMOS.

whereas  $pH^*$  would be expected to be higher than  $pH$  for acids like HOAc. The apparent shift in the gel time curves is due to the fact that more HOAc is required to produce a given  $[H^+]$  than would be expected. Thus, care must be taken in drawing conclusions from gel times for 1 M HCl and 1 M HOAc, for example, because the solution  $[H^+]$  is totally different, and different portions of the gel time versus  $pH^*$  curves are being compared. Clearly an understanding of acid  $pK_a$  values and solvent effects on acid strengths must be taken into account if one intends to generate sol-gels at given  $[H^+]$ . It is also clear that  $pH^*$  is the best measure of  $H^+$  affinity and that the gel times are dependent primarily on the  $[H^*]$  with the acid anion accounting having little if any effect.

The gel time for the initially base-catalyzed TMOS system,  $7.5 \times 10^{-3}$  M  $NH_4OH$ , is 45 min and for the acid system,  $3.1 \times 10^{-4}$  M HCl, is 80 h. A plot of effective diameter versus dimensionless time for both catalysis conditions is

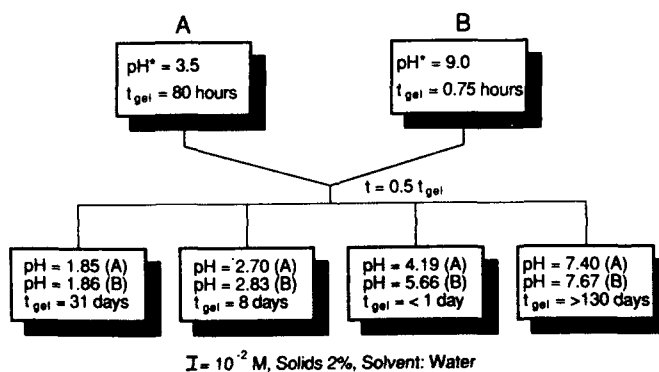


Figure 6.4. Experimental conditions for sol-gel preparation.

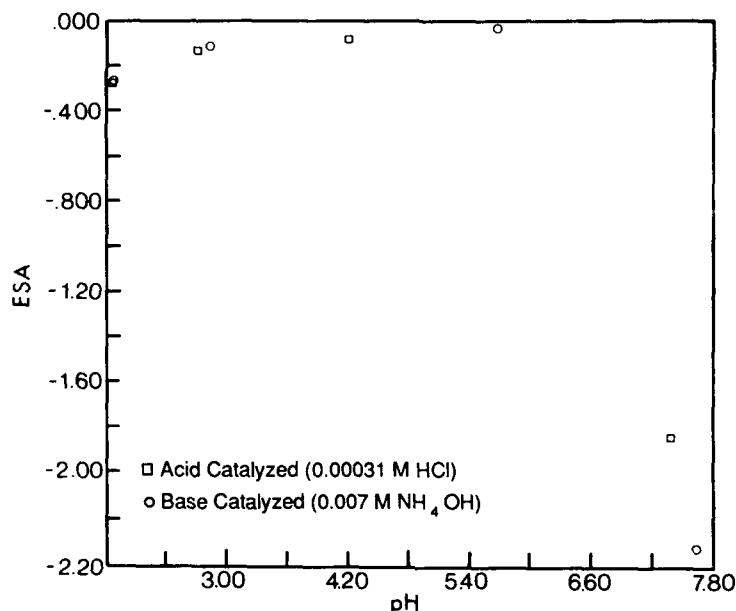


Figure 6.5. ESA versus pH for acid- and base-catalyzed sols.

shown in Fig. 6.3. The actual structure of the polymerizing silicon species has been described by Kelts et al. [16]. It is seen that at  $t = 0.5t_{gel}$  the microstructure and extent of hydrolysis and condensation reactions for the acid- and base-catalyzed TMOS systems have proceeded differently as shown by  $^{29}\text{Si}$ -NMR. At pH 1.86 the particle charge of either the initially acid- or base-catalyzed two-step hydrolyzed systems was found to have a small, but negative charge. At pH 5.66, the lowest particle charge and least stable system or shortest time to gelation were observed. The particle charge and time to gelation of the reacting systems both increased as the pH was adjusted to pH 7.67. The most stable sol had the highest measured surface charge under these conditions. The gel times for these aqueous sol-gels were seen to correlate with the measured ESA particle charge of the reacting systems and the data are presented in Figs. 6.4 and 6.5.

#### 6.4. CONCLUSIONS

This work has shown that  $[\text{H}^+]$  is of critical importance to sol-gel systems and that  $\text{pH}^*$  is the best measure to use. It has also been demonstrated that the acid counterion has little effect on the gel time. In the two-step hydrolyzed TMOS systems, the gel time correlated with the particle surface charge of the reacting system. This effect was dominated by the final pH of the reacting sol-gel system

rather than the initial microstructural differences that were determined by the initial acid or base catalysis conditions.

### ACKNOWLEDGMENT

The authors would like to thank R. A. Guistina for helpful discussions and insight on pH and pH\* determination.

### REFERENCES

1. R. Aelion, A. Loebel, and F. Eirich, *Am. Chem. Soc. J.*, **72**, 124 (1950).
2. R. Aelion, A. Loebel, and F. Eirich, *Recoil*, **69**, 61 (1950).
3. Y. Paoting, L. Hsiaoming, and W. Yuguang, *J. Non-Cryst. Solids*, **52**, 511 (1982).
4. M. Nogami and Y. Moriya, *J. Non-Cryst. Solids*, **37**, 191 (1980).
5. L. C. Klein and G. J. Garvey, *J. Non-Cryst. Solids*, **38/39**, 45 (1980).
6. E. J. A. Pope and J. D. Mackenzie, *J. Non-Cryst. Solids*, **87**, 185 (1986).
7. T. W. Zerda, I. Artaki, and J. Jonas, *J. Non-Cryst. Solids*, **81**, 365 (1986).
8. B. Himmel, T. Gerber, and H. Burger, *J. Non-Cryst. Solids*, **91**, 122 (1987).
9. B. E. Yoldas, *J. Non-Cryst. Solids*, **51**, 105 (1982).
10. S. P. Mukherjee, *J. Non-Cryst. Solids*, **42**, 477 (1980).
11. S. M. Melpolder and B. K. Coltrain, in: C. J. Brinker, D. E. Clark, and D. R. Ulrich, Eds., *Better Ceramics Through Chemistry*, Vol. III, *Mater. Res. Soc. Symp. Proc.*, **131**, 811 (1988).
12. Robert O. James, personal communication, 1987.
13. R. K. Iler, *The Chemistry of Silica*, Wiley, New York (1979).
14. R. G. Bates, *Determination of pH*, Wiley, New York (1973).
15. R. G. Bates and G. Schwarzenbach, *Helv. Chim. Acta*, **38**, 699 (1955).
16. L. W. Kelts, N. J. Emlinger, and S. M. Melpolder, *J. Non-Cryst. Solids*, **83**, 353 (1986).

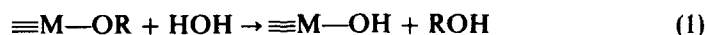
# 7

## CALORIMETRIC STUDY OF SOL AND GEL FORMATION

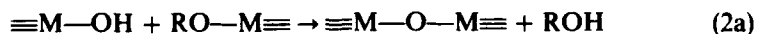
J. W. FLEMING, S. A. FLEMING,  
AND D. KELLY

### 7.1. INTRODUCTION

This study examines the early stages of sol and gel formation using calorimetric analysis of the reactions from their initiation. The objective is to see if calorimetric data can help to explain the large variation in sol-gel behavior between alkoxide derived sols. In the early stages of the formation of a gel derived from metal alkoxides, alcohol, and water, the principal chemical reactions expected to occur are the hydrolysis of metal alkoxides to form metal hydroxides and alcohol as follows:



These products react to form metal-oxygen-metal bonds according to reaction 2 eventually leading to particles that may link together by some bonding mechanism to occlude the liquid phase forming a gel or, more often, form a precipitate that settles out of the sol.



*Ultrastructure Processing of Advanced Materials.*

Edited by Donald R. Uhlmann and Donald R. Ulrich (deceased).

ISBN 0-471-52986-9 © 1992 John Wiley & Sons, Inc.



Exactly what happens during the initial stages when the reactants are mixed together is not entirely understood. For example, it is not clear from previous investigations at what point in time the various stages commence. Many investigators have attempted to examine this period in the formation of gels with spectroscopic techniques sensitive to bond formation and particle growth. Of particular value are NMR studies of  $\text{SiO}_2$  gels. Several excellent reviews of the subject are currently available [1-3]. No consensus exists among investigators as to the nature of the reactions. A factor that makes the  $\text{SiO}_2$  gel more interesting is that most other metal alkoxide precursors will form precipitates immediately when combined with the same quantities of water, catalyst, and alcohol as in the silica organometallic case. The sol formed of this latter material may not gel for several weeks or months, may gel in a few minutes, or may form a precipitate depending on the sol chemistry.

Calorimetric analysis is a method thought to provide useful information about the events occurring in the initial stages of sol formation. Because chemical reactions are involved with their associated heats of reaction being signatures of the events, it was thought that a calorimetric approach to their observation might yield further understanding of the reactions comprising sol and gel formation.

## 7.2. EXPERIMENTAL

Specimens were made containing a constant molar quantity of a given alkoxide in a fixed amount of alcohol present as a mutual solvent for the water. Tetraethylorthosilicate (TEOS) and tetraethylorthogermanate (TEOG) were the alkoxides studied. These were combined with equal volume amounts of ethanol to make a solution with a volume of approximately 8 ml for each experiment. In a separate vessel, water in amounts equivalent to molar ratios of 0.25, 0.5, 1.0, 2.0, 4.0, and 16.0 was mixed with an amount of HCl or  $\text{NH}_4\text{OH}$  equivalent to 0.5% by volume of the total solution. The resultant pH was 1.3 and 12.7, respectively. Mixing was performed at room temperature in fused silica test tubes suitable to fit in the analysis port of the calorimeter.

The Setaram HT 1000 calorimeter used in this study functions according to the principle of heat flow isothermal calorimeters. The sample is in direct contact with the calorimetric chamber and is equilibrated to its temperature. The measured calorimetric output is the thermal power that flows into or out of the sample to the thermostated chamber. The measurement is made using a heat flow detector. This consists of a multitude of identical thermocouples oriented around the sample such that it is reasonable to assume all the heat flowing from the sample must pass through the thermocouples. Because the sample is at thermal equilibrium with the surrounding chamber, the enthalpies of reaction are measured directly, and it is not necessary to know the heat capacity of the sample under observation. Isothermal measurements can continue for very long times, and it is thus applicable to slow and fast reactions. However, reaction

rates cannot be determined directly. Two completely symmetrical calorimetric heat flow detectors are connected in opposition and seated symmetrically in the calorimetric unit. This provides autocompensation for thermal instability and results in much higher measurement resolution. The calorimetric detectors are attached to massive Kanthal blocks, which serve as heat sources or sinks depending on the thermal response of the sample. In the experiments performed herein the resolution of energy detection was about 0.001 cal.

The experiments were performed as follows. The calorimeter was equilibrated to a temperature of 35°C and held isothermally for the duration of each test. The mixed alkoxide-alcohol solution was placed in the sample cell with a stirring plunger of Teflon, which fit the bore of the sample tube with fractions of a millimeter to spare. Stirring consisted of moving the plunger up and down through the fluid at a frequency of about 1 cycle every 5 sec. The water and catalyst containing solution was placed in the reference section. Within this sample holder a syringe was also present for subsequent transfer of the liquid to the sample cell. Calorimetric data collection began with the initial signal observed as shown in Fig. 7.1 being the response of the calorimeter to the change in temperature of the cells due to the introduction of the cooler samples. The operator monitored the signal until it returned to zero. At this point the syringe was used to transfer the water and acid solution to the alkoxide-alcohol vessel and stirring commenced immediately thereafter. The result was an instantaneous power output signal as shown in Fig. 7.1. Stirring was continued through the period of exothermic reaction shown in Fig. 7.1 terminating when the signal had substantially returned to zero.

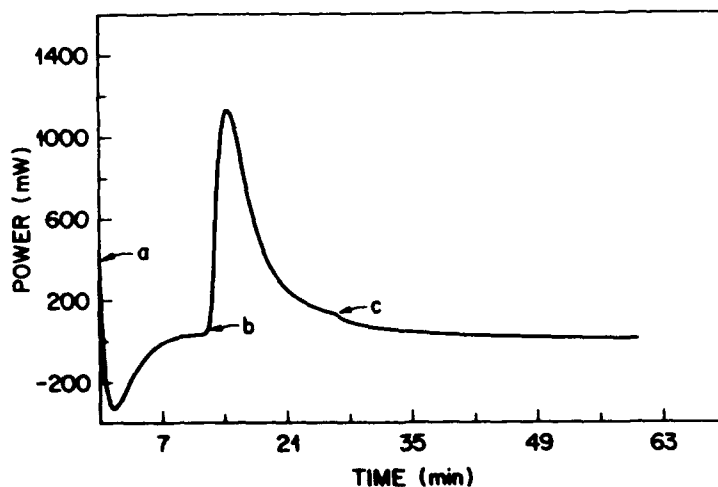


Figure 7.1. Exemplary graph showing the various stages in the collection of calorimetric data. a, Time zero reactant in separate chambers of calorimeter; b, Reactants combined and stirring commenced; c, Stirring stopped.

The power signal observed for each run was then integrated to yield the total energy released by the reaction. Each experiment was replicated three or four times in order to discern the standard error associated with the measurement.

### 7.3. RESULTS AND DISCUSSION

The intent of the study is to observe the changes in the energy released in the reaction of the alkoxide solution and the water solution as the levels of the various factors were changed. A strictly quantitative examination of the energy release is not possible in these experiments, because associated with the reactions of interest (hydrolysis and condensation) are other side reactions that also have thermodynamic effects. The most prominent we are aware of is the reaction of water with alcohol. This enthalpy is approximately 25% of the magnitude of the reaction when viewed separately in the 16:1 experiments.

#### 7.3.1. Acid Catalyzed Sols

The total calorimetric output of the acid-catalyzed sol experiments in which TEOS was the alkoxide and the water content was varied is shown in Fig. 7.2. As indicated in this figure,  $\text{H}_2\text{O}/\text{TEOS}$  molar ratio is a statistically significant factor affecting calorimetric output. An analysis of variance performed on the complete data set shows that over the range of water contents examined in the study, the water-to-alkoxide ratio has a strong effect on the energy released. An interesting observation is that there is a strong dependence below 2  $\text{H}_2\text{O}/\text{TEOS}$ , but no statistically significant dependence from 2 through 16. Some of the

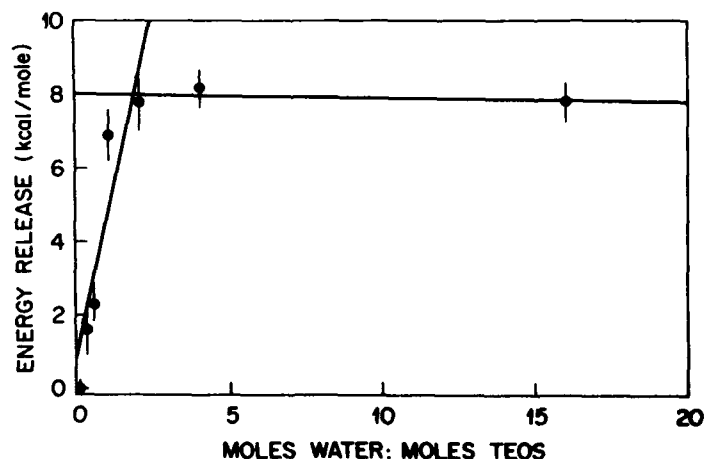


Figure 7.2. Average calorimetric output in kilocalories per mole of  $\text{SiO}_2$  for acid-catalyzed TEOS as a function of  $\text{H}_2\text{O}/\text{TEOS}$  ratio.

experiments were monitored for 15 days with no evidence of heat change in the sols. One explanation for this is that hydrolysis is essentially complete by 2 H<sub>2</sub>O/TEOS with further water addition having no calorimetric effect on the calorimetric by-product of hydrolysis. It follows that a ratio of 4, which would balance the reaction, is not required for complete hydrolysis. The additional water for hydrolysis could be supplied by the condensation reaction of the hydrolyzed species, Eq. 3, which is happening within our measurement time frame, which is approximately 15 min.



The data suggest that condensation occurs rapidly in this system. The region between 1 and 2 H<sub>2</sub>O/TEOS appears to be critical. The molar ratio of 2 would be the one expected to yield the maximum in energy release given the hydrolysis reaction is the primary exothermic reaction in the sol. This is supported by Le Chatlier's principle and the fact that with up to 2 mol H<sub>2</sub>O/TEOS the water is completely consumed in the formation of alcohol. A significant difficulty with the above argument is that while condensation certainly is suggested, it is unreasonable to support 2 H<sub>2</sub>O/TEOS as the transition point, because there is certainly some OH bonded to the silica network.

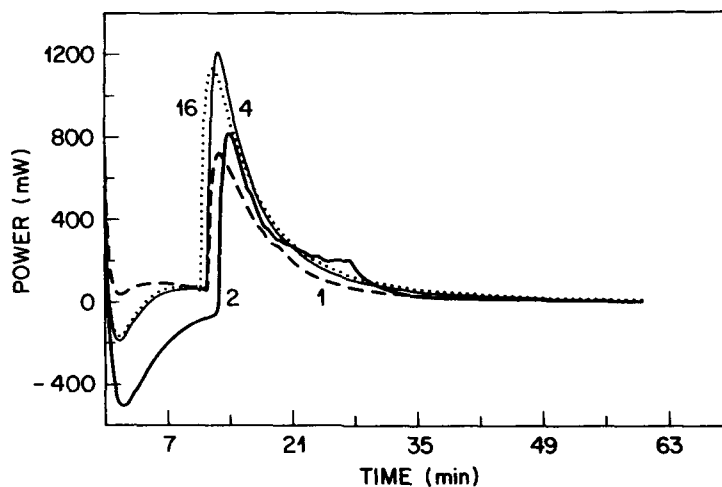
The above arguments are consistent with the general theory of gel formation presented by Iler [4]; the observations of Aelion et al. [5], who indicated that the condensation reaction rate was so high it was immeasurable; and several other investigators [6-8]. The NMR data of several investigators also indicate substantial condensation is occurring very early in sol formation [9].

Above 4 H<sub>2</sub>O/TEOS condensation reactions need not occur to achieve complete hydrolysis. However, it is expected that except for the dilution factor there is no reason to assume that condensation would not occur as readily as it does at lower H<sub>2</sub>O/TEOS ratios. Dilution may inhibit condensation and particle growth by decreasing the probability of molecular interaction.

The samples did not gel for 15 to 21 days. During this period there was no detectable energy change in the sol system of selected samples evaluated for the extended period. These results are consistent with those of other investigators. There seems to be no enthalpic signature associated with the growth of the gel network. Further refinement of the measurement technique is planned to search for energy release in the period from approximately 15 min after sol formation to gelation.

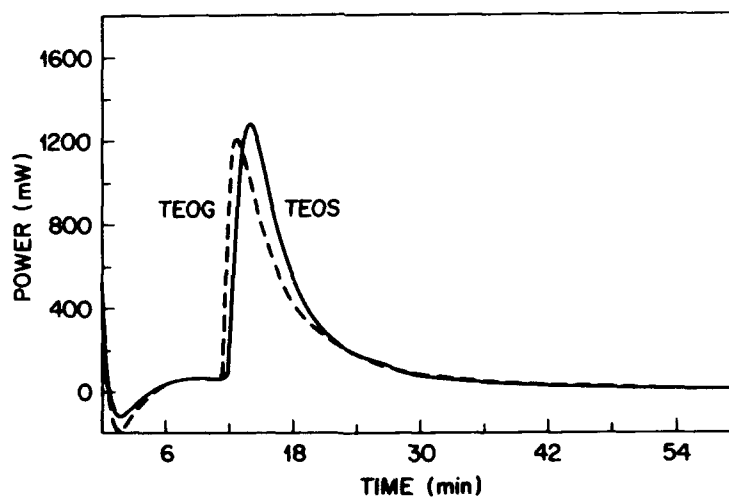
Experiments performed with TEOG in place of TEOS with all other factors remaining the same showed similar magnitudes of energy release for the different water-to-alkoxide ratios, and again statistically there is strong evidence to indicate the ratio is a significant factor in determining the energy release. In Fig. 7.3 the calorimetric output signature for the TEOG acid-catalyzed experiments are shown. One difference is that the data indicate an increase in the energy release after the 2 molar ratio is obtained. This may be a result of the fact that the experiments were confounded by the rapid, almost instantaneous,

## 82 CALORIMETRIC STUDY OF SOL AND GEL FORMATION



**Figure 7.3.** Calorimetric output for selected TEOG experiments where acid catalysis was employed and  $H_2O/TEOG$  varied from 0.25 to 16.

formation of  $GeO_2$  particles in the test vessels which clogged test tubes and inhibited stirring and thus prevented uniform mixing of the sol. However, there is also no additional exothermic heat associated with the reactions than exhibited in the TEOS experiments. Additionally, the calorimetric output from a given molar ratio for each alkoxide appear quite similar (see Fig. 7.4). This is support of the contention that condensation reactions in TEOS are happening



**Figure 7.4.** Comparison of energy release from TEOS and TEOG experiments both at molar ratios of  $2 H_2O/alkoxide$ .

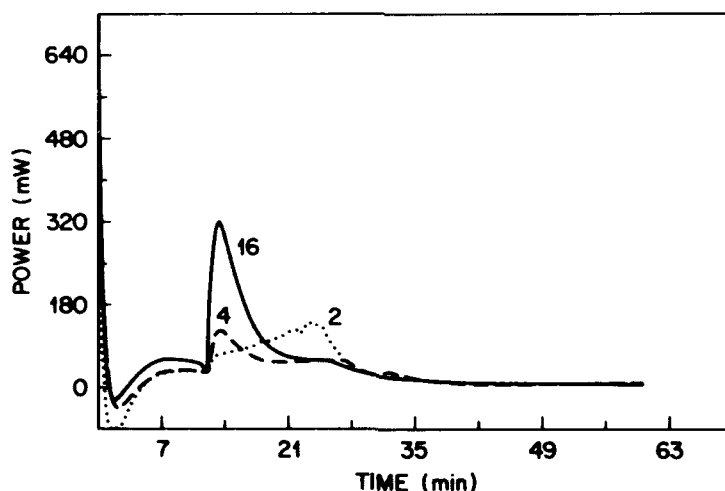
in the same time frame as hydrolysis. In the TEOG experiments, one has visible evidence of oxide particle formation. The apparent difference between the two alkoxide sols is related to the rate of particle growth and not hydrolysis and condensation.

The above experiments were also performed again in the same way with the calorimeter set at 60°C. The results were statistically the same as the 35°C experiments.

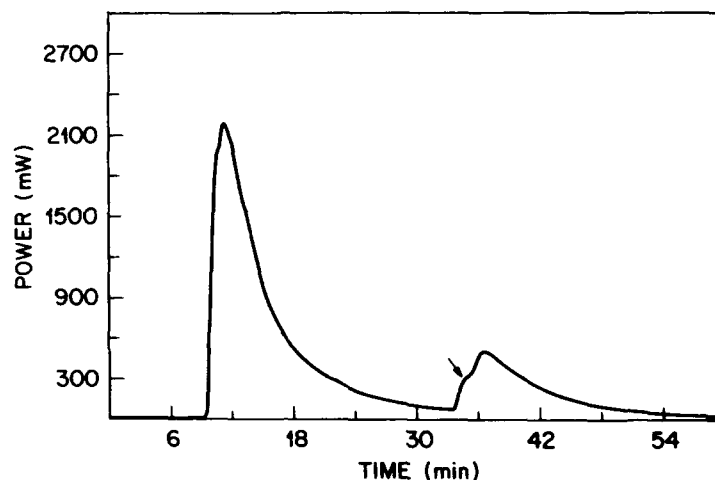
### 7.3.2. Base Hydrolysis

It is generally accepted that the hydrolysis reaction can be catalyzed by either acidic or basic conditions. Ammonium hydroxide was used as a catalyst to study the enthalpy of the base-catalyzed TEOS sol system. Figure 7.5 shows the calorimetric response of several characteristic samples at different  $H_2O$ /alkoxide ratios. There is no statistically significant dependence of calorimetric response on water content. Typically, the calorimetric output is a factor of 5 less than that observed in the acid-catalyzed experiments and is actually in the same range as measured for the combination of ethanol and water. It has been suggested by previous investigators that base hydrolysis is much slower than acid hydrolysis [5]. The calorimetric results could be spread over a broader time. Additionally, as in other experiments, particles are observed to form in the sol, which suggests complications in such reactions.

As in the acid case, these specimens do not gel for weeks. Again there is no calorimetric response associated with gelation. There is observable clouding of



**Figure 7.5.** Calorimetric response of several characteristic samples at different  $H_2O$ /TEOS ratios for base-catalyzed sols.



**Figure 7.6.** Calorimetric response of an experiment in which an acidic sol was formed and permitted to hydrolyze and condense, and then the sol was made basic by addition of  $\text{NH}_4\text{OH}$  and water at the arrow the sol gelled.

the sol occurring as a result of the precipitate formation in the initial stages of sol formation.

If particles are formed rapidly in acid-catalyzed TEOS sols and their growth in base-catalyzed TEOS sols is enhanced as is evident from early signs of a precipitate, further evidence of condensation and particle growth might be obtained by combining the two experiments. First a sol was formed using acid catalysis followed by addition of base to render the solution basic. The calorimetric output of this experiment is shown in Fig. 7.6. As in the other experiments, the ethanol and alkoxide of a 2:1 trial were combined with water and acid after the temperature of the separated components was equilibrated with the calorimeter. The resultant calorimetric output similar to that seen previously is indicated by the first peak in the figure. After the calorimetric output substantially subsided, base mixed in a small quantity of water was introduced into the cell with the resultant calorimetric response being the second peak. Sufficient base was added to bring the pH from 1.3 to 11.

An important result of this experiment is the following. At the point of the inflection on the left side of the second peak in Fig. 7.6, the sample had already gelled. This is less than 30 sec after the addition of base. Other trials indicated that with sufficient base, gelation could be made effectively instantaneous. This is taken as strong evidence that the first reactions must have included condensation reactions and significant particle formation and that the addition of base helps the growth of these particles toward gel formation.

The reverse experiment in which base catalysis was followed by acidification of the sol resulted in immediate formation of a thick, white powder.

#### 7.4. CONCLUSION

The sol-gel transition was studied for several alkoxide systems using calorimetry. These experiments support the hypothesis that hydrolysis in acid-catalyzed TEOS sols and condensation occur simultaneously and that gelation time is a function of the growth and flocculation of the condensation particles. The resultant product formed from the sol is dependent upon the initial chemistry of the sol. For example, acid-catalyzed sols will form small particles during condensation, which will percolate into a gel as compared to base catalysis, which results in larger particles and a milky sol. The pH of the sol both before and after hydrolysis and condensation affects the final gel and gelling time. Additionally, the type of alkoxide used will affect the result. Statistically significant to all sols studied is the  $H_2O$ /alkoxide ratio. Having enough water present for hydrolysis and condensation is critical, but any additional water will only dilute the sol and affect gelation time.

#### REFERENCES

1. S. A. Pardenek, Masters Thesis, Rutgers University, 1987, Mechanical properties of wet silica gels.
2. G. W. Scherer, *J. Jap. Ceram. Soc.*, **95**, 21 (1987).
3. K. D. Keefer, in: C. J. Brinker, D. E. Clark, and D. R. Ulrich, Eds., *Better Ceramics Through Chemistry*, North-Holland, New York (1984).
4. R. K. Iler, *The Chemistry of Silica*, Wiley, New York (1979).
5. R. Aelion, A. Loebel and F. Eirich, *J. Am. Chem. Soc.*, **72**, 5705 (1950).
6. B. E. Yoldas, *J. Mater. Sci.*, **14**, 1843 (1979).
7. J. Zarzycki, M. Prassas, and J. Phalippou, *J. Mater. Sci.*, **17**, 3371 (1982).
8. C. J. Brinker and G. W. Scherer, *J. Non-Cryst. Sol.*, **502**, 70, 301 (1985).
9. L. W. Kells and N. J. Armstrong, in: C. J. Brinker, D. E. Clark, and D. R. Ulrich, Eds., *Better Ceramics Through Chemistry III*, *Mater. Res. Soc. Proc.*, **121**, 519 (1988).



## 8

# NMR INVESTIGATIONS OF LITHIUM NIOBIUM ALKOXIDE SOLUTIONS

D. J. EICHORST, K. E. HOWARD,  
AND D. A. PAYNE

### 8.1. INTRODUCTION

Lithium niobate,  $\text{LiNbO}_3$ , is an acentric dielectric that has a large electrooptic coefficient making it suitable for applications that include optical modulation [1]. Homogeneous material is required to eliminate refractive index and electrical property fluctuations that are commonly present in melt-grown material. Recently, sol-gel processing of lithium niobate has been investigated as a method of producing high-purity, homogeneous material of stoichiometric composition [2-6]. However, the influence of solution chemistry on structure development and dependent properties is poorly understood.

Additions of water and/or catalysts have been demonstrated to produce differences in the amorphous gel structure and crystallization behavior of other sol-gel-derived materials [7,8]. Similar effects may be expected during the processing of amorphous lithium niobate. Therefore, so as to develop a better understanding of the effects of solution chemistry on the processing of lithium niobate, a systematic investigation has been undertaken of the effects of solution chemistry on structure development. This Chapter describes the investigation of structural changes occurring in the solution stage for ethanol and 2-methoxyethanol-based lithium niobium alkoxide solutions.

*Ultrastructure Processing of Advanced Materials.*

Edited by Donald R. Uhlmann and Donald R. Ulrich (deceased).

ISBN 0-471-52986-9 © 1992 John Wiley & Sons, Inc.

Sol-gel processing of lithium niobate typically involves the preparation of an alcoholic solution containing a *double alkoxide* or *mixed-metal alkoxide* (i.e.,  $\text{LiNb}(\text{OEt})_6$ ) [2-4]. The formation and isolation of such a complex suggests a method of producing stoichiometric  $\text{LiNbO}_3$ , which has proven difficult using traditional ceramic processing routes. However, the existence of such a structure has not been established. The structure of the resultant mixed-metal alkoxide and the structural rearrangements that occur during processing ultimately result in the formation of the lithium niobate crystal structure. Hydrolysis of the alcoholic solution results in the formation of a gel that may be converted to crystalline  $\text{LiNbO}_3$  by heat treatment. The interaction between lithium ethoxide and niobium ethoxide was investigated using  $^7\text{Li}$ - and  $^{93}\text{Nb}$ -NMR to explore chemical changes that evolve during hydrolysis and gelation.

## 8.2. EXPERIMENTAL

### 8.2.1. Solution Preparation

All reactions were carried out under an inert atmosphere using standard Schlenk techniques. Ethanol was dried and distilled from magnesium and stored under  $\text{N}_2$  over molecular sieves. High-performance liquid chromatography grade 2-methoxyethanol (Aldrich) was used as received. Niobium ethoxide was synthesized and further purified according to the method of Bradley et al. [9]. Niobium 2-methoxyethoxide was formed by an alcohol exchange reaction between niobium ethoxide and 2-methoxyethanol [2]. Lithium alkoxides were prepared by the addition of lithium metal to the parent alcohols.

Alkoxide mixtures were prepared by addition of equimolar lithium and niobium alkoxide solutions at room temperature. NMR spectra were obtained immediately after mixing the alkoxides. Mixed-metal alkoxides were prepared by mixing the respective alkoxides, refluxing for 24 h and concentrating to 1 M stock solutions [3]. Hydrolyzed samples were formed by dilution with deionized water and alcohol to form 0.25 M lithium niobium 2-methoxyethoxide solutions. The gelation study was carried out on a 0.5 M lithium niobium methoxyethoxide solution with 3.25 mol water/Nb. Catalyzed samples were prepared by the addition of nitric acid or ammonium hydroxide to give a 0.1 mol catalyst/Nb ratio.

### 8.2.2. NMR Characterization

Spectra were acquired using an IBM AF-100 NMR spectrometer equipped with a digital multinuclear probe (Doty Scientific). Samples for gelation studies were analyzed in situ. The remaining samples were diluted with deuterated benzene as a lock solvent (2 ml sample-1 ml  $\text{C}_6\text{D}_6$ ).

$^{13}\text{C}$  spectra were acquired at 25.178 MHz ( $^1\text{H}$  = 100.13 MHz) with a 4- $\mu\text{sec}$

pulse width and 5000-Hz sweep width using nuclear Overhauser enhancement with no relaxation delay. An acquisition time of 1.638 msec was used. The reported spectra required 11,400 scans of 16 K block size with 0.1 Hz line broadening. Carbon spectra were referenced to tetramethylsilane resonating at 0.000 ppm.

$^7\text{Li}$  spectra were acquired at 38.915 MHz ( $^1\text{H} = 100.13$  MHz) with a 15- $\mu\text{sec}$  pulse width and 10,000-Hz sweep width. An acquisition time of 0.819 msec and a 0.5-sec relaxation time were used. The reported spectra required 256 scans with a 16K block size with no line broadening applied. The spectra were referenced to  $\text{LiCl}$  in  $\text{D}_2\text{O}$  resonating at 0.000 ppm [10].

$^{93}\text{Nb}$  spectra were acquired at 24.507 MHz ( $^1\text{H} = 100.13$  MHz) with a 15- $\mu\text{sec}$  pulse and 50,000-Hz sweep width. An acquisition time of 0.164 msec with a 0.1-sec relaxation delay was used. Spectra required 100,000 scans of 16K block size. No line broadening was used. Niobium spectra were referenced to the  $\text{NbCl}_6^-$  resonance ( $\omega_{1/2} \approx 30$  Hz) of  $\text{NbCl}_5$  in "wet"  $\text{CH}_3\text{CN}$  [10].

### 8.3. RESULTS

#### 8.3.1. Niobium Ethoxide

Figure 8.1 shows the  $^{13}\text{C}$  spectrum of as-prepared niobium ethoxide. The quartets centered at 19.23 and 18.14 ppm correspond to the methyl carbons of terminal and bridging alkoxy groups, respectively. The triplets centered at 69.12

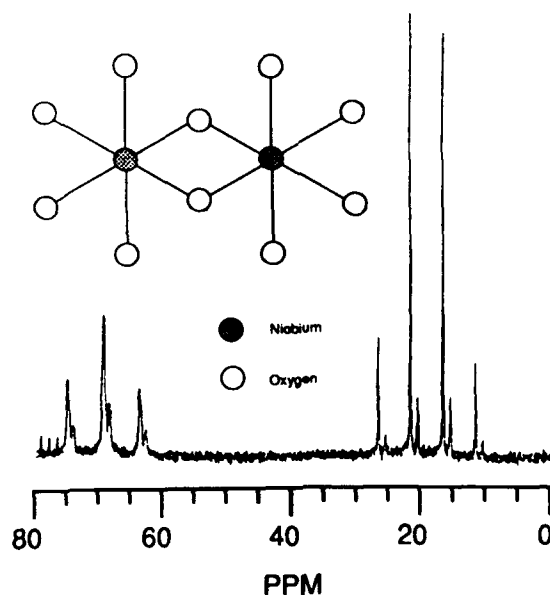


Figure 8.1. Structure and  $^{13}\text{C}$  spectrum of niobium ethoxide.

and 68.24 ppm correspond to the methylene carbons of the terminal and bridging groups. The integrated intensity ratio of terminal-bridging groups (4-1) confirms the dimeric nature of niobium ethoxide illustrated in Fig. 8.1.

### 8.3.2. Lithium and Niobium Alkoxides

A comparison of the  $^7\text{Li}$  spectra for lithium ethoxide, a mixture of lithium ethoxide and niobium ethoxide, and a refluxed solution is given in Fig. 8.2. The broad peak of lithium ethoxide suggests considerable solvent exchange that occurs on the NMR time scale. Upon addition of niobium ethoxide, the peak shifts from  $-1.90$  to  $-2.56$  ppm, and the linewidth narrows. The identical spectrum was obtained for the refluxed mixture, indicating that refluxing does not change the chemical nature of the mixture. Furthermore, if a mixed-metal alkoxide is formed, the reaction appears to be nearly instantaneous ( $< 2$  min) at room temperature. Similar results were obtained for the 2-methoxyethanol system with a shift from  $-2.66$  ( $\text{LiOEtOMe}$ ) to  $-3.17$  ppm for the refluxed solution  $\text{LiNb}(\text{OEtOMe})_6$ .

The  $^7\text{Li}$  peak shift observed is not definitive evidence for the formation of a mixed-metal alkoxide, but could result from the addition of, but not reaction with, the niobium ethoxide. The above data suggest either immediate formation of a mixed-metal alkoxide or that no reaction occurred under the conditions used. Cooling a concentrated solution of  $\text{LiNb}(\text{OEt})_6$  resulted in crystal formation. The  $^7\text{Li}$  spectrum for crystals redissolved in ethanol was identical to the refluxed solution, giving further evidence of a mixed-metal alkoxide formation.

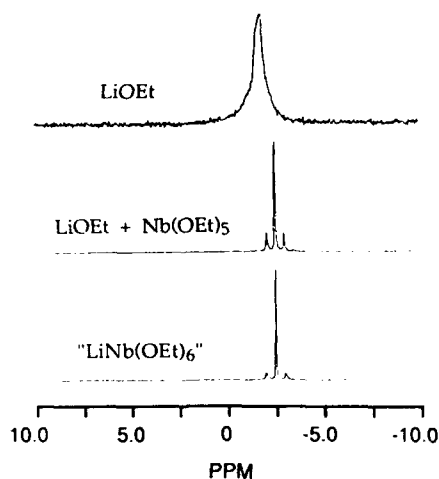


Figure 8.2.  $^7\text{Li}$  spectra of lithium ethoxide, lithium ethoxide mixed with niobium ethoxide, and a refluxed mixture of lithium ethoxide with niobium ethoxide.

### 8.3.3. Effect of Water Additions

NMR spectra of solutions with varying water concentrations were obtained to determine if the chemical environment changed with increasing water content. A continuous shift in peak position and increase in peak width were observed with increasing water content for the 0.25 M lithium niobium methoxyethoxide solutions (Fig. 8.3). The data indicate a continuous change in the lithium signal with increasing water content. However, as the amount of water reached the stoichiometric quantity required for complete hydrolysis (i.e., 3 mol water/LiNb(OR)<sub>6</sub>) changes in the <sup>7</sup>Li-NMR resonance became less dramatic, suggesting a limit to structural development (i.e., a fully condensed structure).

Lithium niobium methoxyethoxide solutions (0.5 M) hydrolyzed with 3.25 mol H<sub>2</sub>O/mol Nb were found to form gels. The resonance was found to occur at -2.79 ppm compared with -3.17 ppm for the anhydrous alkoxide mixture that had been refluxed for 24 h. Furthermore, the peak position remained constant throughout the experiment indicating that hydrolysis resul-

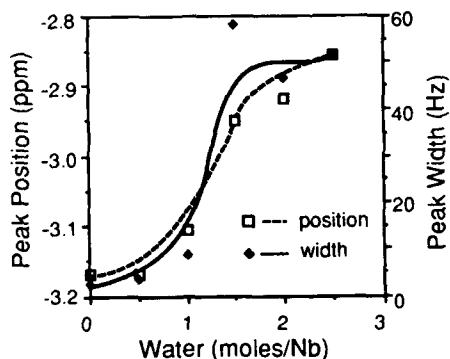


Figure 8.3. NMR study of the hydrolysis of 0.25 M methoxyethanol solutions.

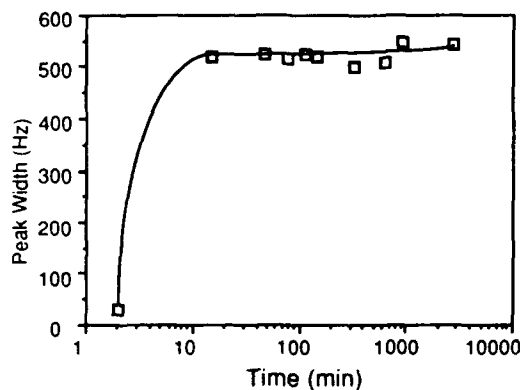


Figure 8.4. NMR study of the gelation of a 0.5 M methoxyethanol solution hydrolyzed with 3.25 mol H<sub>2</sub>O/Nb.

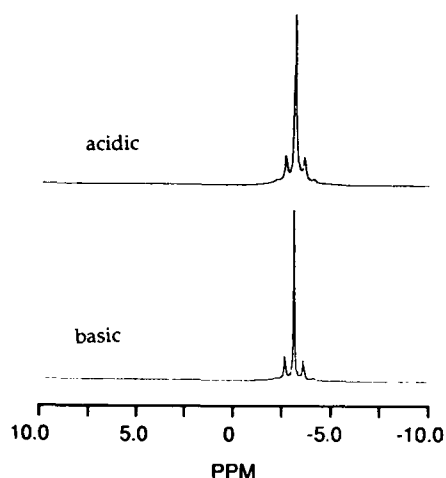


Figure 8.5.  $^7\text{Li}$  spectra of acid and base-catalyzed methoxyethanol solutions hydrolyzed with 1 mol water/Nb.

ted in an immediate change of the lithium signal. A similarly prepared test sample gelled after 20 h; however, the  $^7\text{Li}$  spectra show no significant change in linewidth after an initial 15-min period as shown in Fig. 8.4. These results indicate that although immediate changes were observed in the chemical shift (2 min) and linewidth (15 min) of the  $^7\text{Li}$  resonance, gelation was not complete for several hours (ca. 20 hr).

#### 8.3.4. Effects of Acid or Base Catalysis

The effects of 0.1 M acid ( $\text{HNO}_3$ ) or base ( $\text{NH}_4\text{OH}$ ) on the NMR resonances of Li and Nb for the methoxyethanol solutions (1 mol water/Nb) are illustrated in Figs. 8.5 and 8.6, respectively. The lithium environment as seen by  $^7\text{Li}$ -NMR, was nearly independent of catalyst. However, an approximate 125-ppm shift in peak position is observed in the  $^{93}\text{Nb}$  spectra. The NMR results suggest significant structural change in the niobium environment, whereas the Li environment remained relatively unaffected.

### 8.4. DISCUSSION OF RESULTS

The condensation reactions of niobium ethoxide have previously been shown to result in polymeric niobium oxyalkoxides of which  $\text{Nb}_8\text{O}_{10}(\text{OEt})_{20}$  was isolated and found to possess a cage structure [11]. During the hydrolysis of lithium niobium alkoxides, similar cage structures may develop in which lithium ions occupy central positions in the cage structures. Gelation may then occur through further condensation of the cage units. The proposed mechanism accounts for the rapid attainment of an "equilibrium" lithium environment prior to the onset of gelation with little effect observed in the  $^7\text{Li}$  signal as gelation

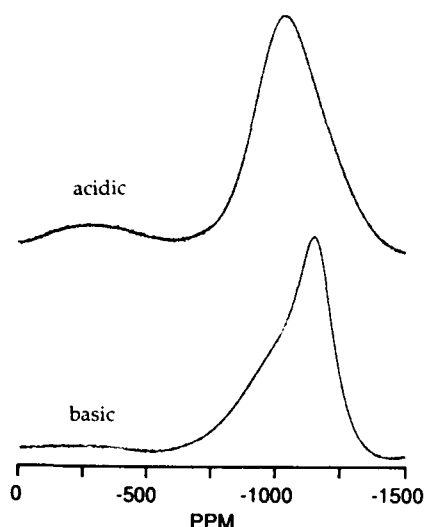


Figure 8.6.  $^{93}\text{Nb}$  spectra of acid- and base-catalyzed methoxyethanol solutions hydrolyzed with 1 mol water/Nb.

proceeds. Catalyst additions may result in changes of the Nb–O cage network through different polycondensation mechanisms, whereas the cage interior ( $\text{Li}^+$  environment) remains relatively unchanged. Rearrangement of the Nb–O cage structure during heat treatment results in the development of the lithium niobate crystal structure. Distortion of the amorphous gel structure may result upon the addition of catalysts. Differences in the crystallization behavior of catalyzed gels have been observed and were attributed to variations in gel structure and rearrangement processes resulting from catalyst conditions [12]. Acid ( $\text{HNO}_3$ )-catalyzed gels crystallized approximately  $20^\circ\text{C}$  lower and had lower crystallization enthalpies than base ( $\text{NH}_4\text{OH}$ )-catalyzed samples. Differences in crystallization behavior suggest acid-catalyzed samples allowed more facile structural rearrangement during heat treatment. The results indicate a continuous influence of solution chemistry on molecular structure from the solution state to the solid crystalline material.

## 8.5. SUMMARY

This Chapter demonstrates the usefulness of  $^7\text{Li}$ - and  $^{93}\text{Nb}$ -NMR spectroscopy in probing the effects of various chemical changes that occur during the sol–gel processing of  $\text{LiNbO}_3$ . The dimeric structure of niobium ethoxide was confirmed by  $^{13}\text{C}$ -NMR spectroscopy. The addition of niobium ethoxide to lithium ethoxide (or vice versa) resulted in an immediate shift of the  $^7\text{Li}$ - and  $^{93}\text{Nb}$ -NMR resonances. The  $^7\text{Li}$ -NMR spectra of mixtures prepared at room temperature and those refluxed for 24 h were identical. Hydrolysis reactions apparently occurred instantaneously. A continuous change in the  $^7\text{Li}$  signal was observed for increasing water content. Changes in the lithium environment

during hydrolysis appeared to be complete well before the gel point was reached. Additions of catalyst resulted in significant changes of the niobium resonance with no change in the lithium spectrum. A cage structure model was proposed that accounts for the differences observed in the niobium and lithium behavior. The actual Nb-O cage network may be greatly influenced by the catalyst conditions, whereas the lithium ion positions are apparently unaffected. Different network structures may have different crystallization temperatures resulting from different rearrangement processes. The results indicate that solution chemistry has an effect on the evolution of structure in the sol-gel processing of lithium niobate.

### ACKNOWLEDGMENTS

We acknowledge the support of an IBM Fellowship on Materials and Processing Sciences and the support of the U.S. Department of Energy, Division of Materials Sciences, under Contract DE-AC02-76ER01198.

### REFERENCES

1. R. S. Weis and T. K. Gaylord, *Appl. Phys. A*, **37**, 191 (1985).
2. D. J. Eichorst and D. A. Payne, in: *Better Ceramics Through Chemistry*, Vol. III, *Mater. Res. Soc. Symp. Proc.*, **121**, 773 (1988).
3. S. Hirano, *Ceramic Powder Science, Proceedings of the International Conference on Ceramic Powder Processing Sci.* p. 171 (1987).
4. A. P. Leonov et al., *Izv. Akad. Nauk SSSR, Neorg. Mater.*, **21**, 1935 (1985).
5. D. P. Partlow and J. Gregg, *J. Mater. Res.*, **2**, 595 (1987).
6. N. Puyôo-Castaings, F. Duboudin, and J. Ravez, *J. Mater. Res.*, **3**, 557 (1988).
7. K. D. Budd, S. K. Dey, and D. A. Payne, in: *Better Ceramics Through Chemistry*, Vol. II, *Mater. Res. Soc. Symp. Proc.*, **73**, 711 (1986).
8. S. Sakka, H. Kozuka, and S. Kim, *Ultrastructure Processing of Advanced Ceramics, Proceedings of the III International Conference on Ultrastructure Processing of Ceramics, Glasses, and Composites*, p. 161 (1988).
9. D. C. Bradley, B. N. Chakravarti, and W. Wardlaw, *J. Chem. Soc.*, p. 2381 (1956).
10. J. Mason, *Multinuclear NMR*, Plenum Press, New York (1987).
11. D. C. Bradley, *Coord. Chem. Rev.*, **2**, 299 (1967).
12. D. J. Eichorst, D. A. Payne, and A. N. A. Wragg, "Ceramic Thick and Thin Films," ed. B. Hiremath, *Am. Ceram. Soc.*, 375-384 (1990).



# INITIAL EVIDENCE FOR Si-O-Ti BOND FORMATION IN ORGANICALLY MODIFIED SILICON TITANATES BY SOLID-STATE $^{29}\text{Si}$ NUCLEAR MAGNETIC RESONANCE SPECTROSCOPY

CAROL L. SCHUTTE, JOSEPH R. FOX, ROBERT D. BOYER,  
AND D. R. UHLMANN

## 9.1. INTRODUCTION

Organically modified silicates synthesized by the sol-gel route represent a new class of materials that consolidate organic with inorganic functionality; these new materials have found a wide variety of applications [1]. Varying the organic groups attached to the inorganic network is one way of affecting their properties [1]. Another way to alter the chemical and physical properties is to incorporate other metal alkoxides. The preparation and thermal characterization of polydimethylsiloxane (PDMS)-modified  $\text{SiO}_2$ - $\text{TiO}_2$  glasses has been described previously [2]. In continuing studies, we have found that solid-state  $^{29}\text{Si}$  nuclear magnetic resonance (NMR) appears to be a useful tool for the characterization of these materials. The goal of this work was to apply solid state  $^{29}\text{Si}$ -NMR to determine whether the formation of Si-O-Ti bonds in organically modified sol-gel-derived silicon titanates could be detected.

*Ultrastructure Processing of Advanced Materials.*

Edited by Donald R. Uhlmann and Donald R. Ulrich (deceased).

ISBN 0-471-52986-9 © 1992 John Wiley & Sons, Inc.

The sol-gel approach allows for the synthesis of many pure single- and multicomponent glasses [3]. Because the reagents, typically liquid metal alkoxides, can be mixed in solution prior to reaction, the multicomponent glasses are believed to be more homogeneous on a molecular scale than conventional glasses. However, because of either gross imbalances in their relative chemical reactivities or the insolubility of one of the reagents during the course of the reaction, these components may not stay homogeneously distributed. In this study, the issue of homogeneously incorporating Ti alkoxides into organically modified  $\text{SiO}_2$ - $\text{TiO}_2$  glasses is addressed. Titanium alkoxides are significantly more reactive than dimethyl-substituted silicon alkoxides,  $(\text{CH}_3)_2\text{Si}(\text{OR})_2$ , toward hydrolysis and condensation reactions [2], making the degree of homogeneity on a molecular scale of a composite of these species highly dependent upon the choice of starting materials and reaction conditions. In this study, a bulky and therefore less reactive titanium alkoxide, titanium(IV)butoxide  $[\text{Ti}(\text{On-Bu})_4]$  [4], was coreacted with a preformed telechelic hydroxy-terminated PDMS polymer ( $\text{HO-PDMS-OH}$ ), as well as the monomeric silicon compounds dimethyldimethoxysilane  $[(\text{CH}_3)_2\text{Si}(\text{OCH}_3)_2]$  and dimethyldiacetoxysilane  $[(\text{CH}_3)_2\text{Si}(\text{OOCCH}_3)_2]$  to form composite glasses. We have found that the characterization of these samples by solution and solid-state  $^{29}\text{Si}$ -NMR yields information on the formation of Si-O-Ti bonds. Furthermore, we have illustrated that the degree of intimate incorporation of these species is a function of the relative chemical reactivities of the starting materials.

## 9.2. EXPERIMENTAL

All silicon starting materials and the model compounds  $\text{Si}[\text{OSi}(\text{CH}_3)_3]_4$  and  $\text{Ti}[\text{OSi}(\text{CH}_3)_3]_4$  were used as received from Petrarch; the  $\text{Ti}(\text{On-Bu})_4$  and *p*-toluenesulfonic acid were purchased from Alfa. The telechelic hydroxy-terminated PDMS oligomer (molecular weight, 1700) was treated with  $\text{Ti}(\text{On-Bu})_4$  ( $\text{SiOH/Ti}$  mole ratio, 1/1) in tetrahydrofuran (0.06 *N*) at room temperature. This solution quickly became viscous and was transferred into an aluminum drying pan, covered with parafilm, and allowed to air dry for 1 week under ambient conditions.

The monomeric compounds,  $(\text{CH}_3)_2\text{SiX}_2$  [ $\text{X} = \text{OCH}_3, \text{OOCCH}_3$ ], were prehydrolyzed by adding distilled water ( $\text{SiX}/\text{H}_2\text{O}$ , 1/1) in tetrahydrofuran [0.15 *N*] with *p*-toluenesulfonic acid catalyst (0.14 mol %) and refluxing overnight (18 hr).  $(\text{CH}_3)_2\text{SiX}_2$  samples that were not reacted with the titanium reagent were air dried at this stage. Prehydrolysis of the Si alkoxide was necessary prior to the addition of the Ti alkoxide, because the presence of excess water results in the precipitation of  $\text{TiO}/\text{OH}$  species.  $\text{Ti}(\text{On-Bu})_4$  ( $\text{SiX/Ti}(\text{OR})_4$ , 1/1) was added, and the solution was heated to reflux temperature (18 hr). The solution was cooled, poured into an aluminum dish, covered with parafilm, and allowed to air dry at room temperature.

The solution  $^{29}\text{Si}$ -NMR spectra were obtained in chloroform at 79.4 MHz on a Varian VXR 400 spectrometer using a silicon-free Cryomagnetics Systems probe. The solid-state  $^{29}\text{Si}$ -NMR spectra were obtained using cross-polarization magic angle spinning (CP/MAS) conditions at 39.7 MHz on a Nicolet NT200 spectrometer with a Chemagnetics solids probe. The solid samples were spun at approximately 3 KHz. The chemical shifts are plotted in parts per million (ppm) relative to tetramethylsilane. Zeolite Na-A ( $-89.4$  ppm) was employed as the external reference. The high field side of tetramethylsilane was taken to be negative.

### 9.3. RESULTS AND DISCUSSION

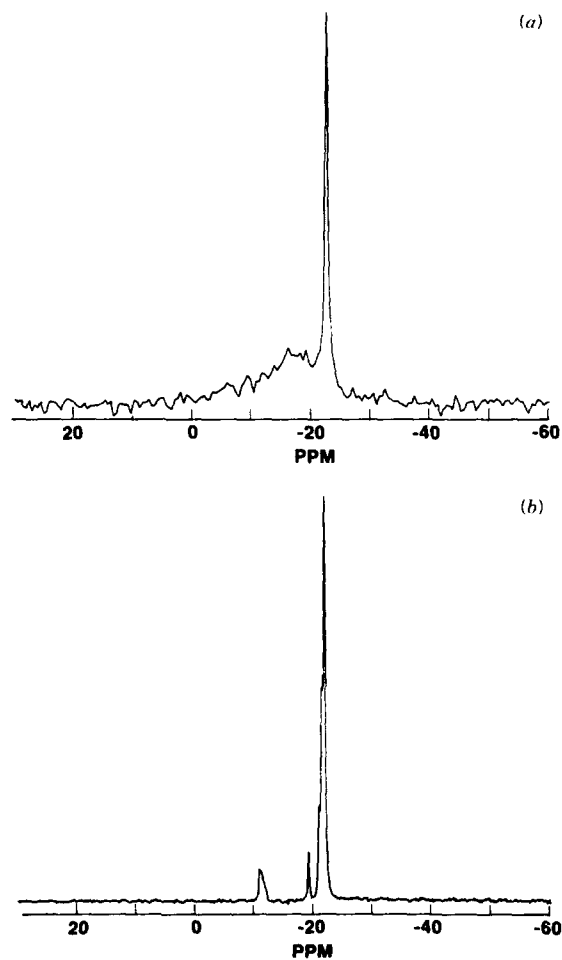
Figure 9.1a shows the solid-state  $^{29}\text{Si}$ -NMR spectrum of the reaction product of the preformed PDMS polymer and  $\text{Ti}(\text{On-Bu})_4$ . The sharp resonance at  $-23$  ppm is characteristic of Si atoms in the linear dimethylsiloxane polymer backbone [5]. A similar resonance appears in the solution  $^{29}\text{Si}$ -NMR spectrum of the starting polymer (Fig. 9.1b). In this spectrum, the fairly broad resonance at  $-11$  ppm is attributed to silicon atoms in the hydroxy-terminated end groups of the polymer [5]. The sharp resonances at  $-19$  ppm and at  $-21$  and  $-22$  ppm are attributed to cyclic tetramers, pentamers, and dimethylsiloxane units near the end of the linear polymer chains or cyclic hexamers, respectively [5]. A broad resonance between  $-10$  and  $-20$  ppm is also observed in Fig. 9.1a.

The solid-state  $^{29}\text{Si}$ -NMR spectrum of the product of prehydrolyzed  $(\text{CH}_3)_2\text{Si}(\text{OOCCH}_3)_2$  and  $\text{Ti}(\text{On-Bu})_4$  is given in Fig. 9.2a. The resonance at  $-23$  ppm, corresponding to linear  $-\text{Si}(\text{CH}_3)_2\text{O}-$  units, indicates that extensive Si-O-Si bond formation has occurred. There is also a weaker resonance observed at  $-21$  ppm which is quite sharp. Because the spectrum is very similar to the solution  $^{29}\text{Si}$ -NMR spectrum shown in Fig. 9.2b for the product prepared from  $(\text{CH}_3)_2\text{Si}(\text{OOCCH}_3)_2$  without any added Ti reagent, the weaker resonance is also attributed to silicon-only-containing species.

The solid-state  $^{29}\text{Si}$ -NMR spectrum of the product of  $(\text{CH}_3)_2\text{Si}(\text{OCH}_3)_2$  and  $\text{Ti}(\text{On-Bu})_4$  is shown in Fig. 9.3a. The spectrum contains a sharp resonance characteristic of the linear dimethylsiloxane at  $-23$  ppm, but there are also very broad resonances centered at  $-17$  and  $-8$  ppm. The peak at  $-8$  ppm is somewhat weaker than that at  $-17$  ppm. In contrast, the solution  $^{29}\text{Si}$ -NMR spectrum of the product obtained from  $(\text{CH}_3)_2\text{Si}(\text{OCH}_3)_2$  without any added Ti species (Fig. 9.3b) shows a strong resonance for linear dimethylsiloxane units at  $-23$  ppm with perhaps a small amount of cyclics, but no broad, strong resonances appear at either  $-17$  or  $-8$  ppm as in Fig. 9.3a.

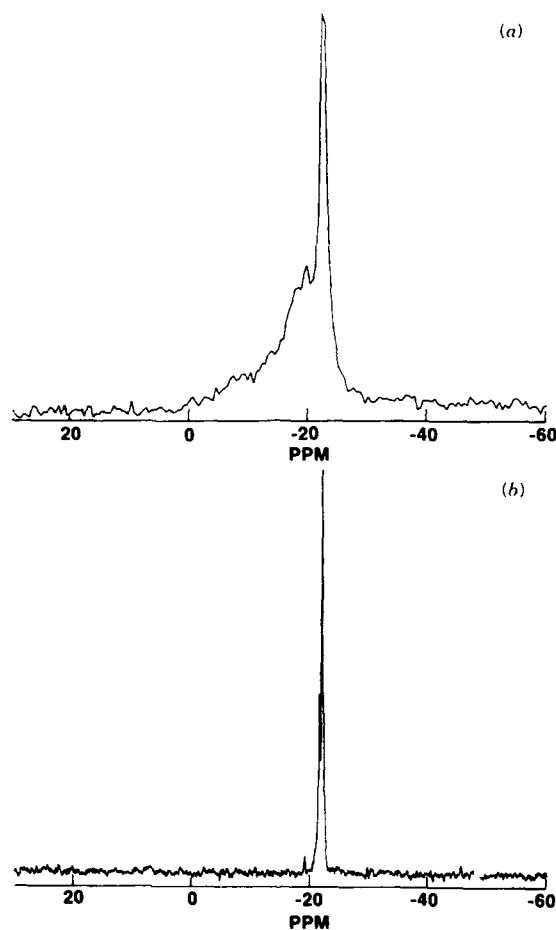
The solid-state  $^{29}\text{Si}$ -NMR spectra for the product of  $(\text{CH}_3)_2\text{Si}(\text{OOCCH}_3)_2$  and  $\text{Ti}(\text{On-Bu})_4$  with no added water is given in Fig. 9.4. A sharp resonance at  $-23$  ppm, characteristic of linear dimethylsiloxane, as well as a broad resonance at  $-17$  ppm are present.

The solid-state  $^{29}\text{Si}$ -NMR spectra for the organically modified silicon



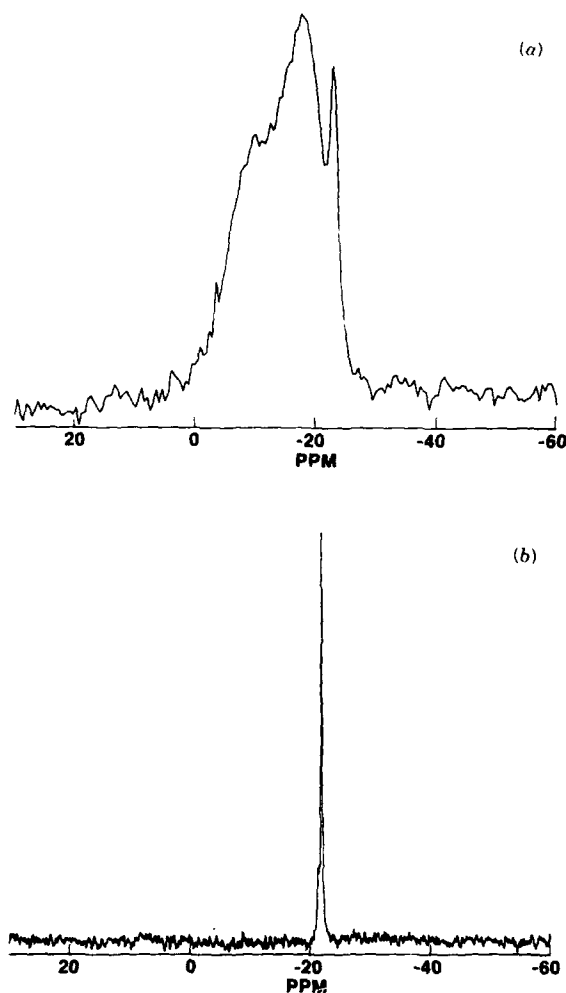
**Figure 9.1.** (a) Solid-state  $^{29}\text{Si}$ -NMR spectrum of the product obtained from the reaction of  $\text{Ti}(\text{On-Bu})_4$  and the preformed PDMS polymer. (b) Solution  $^{29}\text{Si}$ -NMR spectrum of the starting PDMS polymer (molecular weight, 1700).

titanates, prepared from the reaction of  $\text{Ti}(\text{On-Bu})_4$  with polymeric PDMS and the monomeric organosilanes, indicate that the environment of the silicon atom is different in the product obtained with  $(\text{CH}_3)_2\text{Si}(\text{OCH}_3)_2$  from that in the other materials. Comparing Figs. 9.3a and b, we attribute the resonances at -17 and -8 ppm to Si shifted downfield as a result of bonding to Ti, possibly due to  $-\text{O}(\text{CH}_3)_2\text{SiO}-$  units bonded to one and two Ti atoms, respectively. With this interpretation, it appears that extensive Si-O-Ti bond formation has occurred in this product. The assignment of these resonances is supported by the solution  $^{29}\text{Si}$ -NMR spectra of the model compounds  $\text{Si}[\text{OSi}(\text{CH}_3)_3]_4$  and



**Figure 9.2.** (a) Solid-state  $^{29}\text{Si}$ -NMR spectrum of the product obtained from the reaction of  $\text{Ti}(\text{On-Bu})_4$  and  $(\text{CH}_3)_2\text{Si}(\text{OOCCH}_3)_2$ . (b) Solution  $^{29}\text{Si}$ -NMR spectrum of the product prepared without  $\text{Ti}(\text{On-Bu})_4$ .

$\text{Ti}[\text{OSi}(\text{CH}_3)_3]_4$ , where the resonance for the Si atom in the trimethylsilyl group was shifted downfield approximately 5 ppm, from 8.3 to 13 ppm, in the titanium-containing compound. Downfield shifts from the resonance at  $-23$  ppm of similar magnitude occur in Fig. 9.3a. Similar stepwise shifts of 6–7 ppm for silicon chemically bound to aluminum oxide atoms are observed for aluminosilicates as well [6]. The resonances assigned to Si atoms bonded to Ti in the solid-state spectrum are quite broad compared to the resonances for the Si cyclic species which appear in the same region. This broadening could be due to one of several effects: quadrupolar coupling with the Ti atoms, the presence of a distribution of atoms in the outer coordination sphere of the Si resulting in a



**Figure 9.3.** (a) Solid-state  $^{29}\text{Si}$ -NMR spectrum of the product obtained from the reaction of  $\text{Ti}(\text{On-Bu})_4$  and  $(\text{CH}_3)_2\text{Si}(\text{OCH}_3)_2$ . (b) Solution  $^{29}\text{Si}$ -NMR spectrum of the product prepared without  $\text{Ti}(\text{On-Bu})_4$ .

distribution of parts per million values, or dynamic effects whereby the relative mobility of the Si species are approaching the time scale of the experiment.

In contrast, the product of  $(\text{CH}_3)_2\text{Si}(\text{OOCCH}_3)_2$  and  $\text{Ti}(\text{On-Bu})_4$  (Fig. 9.2a) shows little, if any, Si-O-Ti bond formation. Rather, the spectrum in Fig. 9.2a is similar to that in Fig. 9.1a, where substantial Si-O-Si bond formation is present in the precursor before reaction with the titanium species. Figure 9.1a contains some broad absorptions between -10 and -20 ppm; however, these resonances are weak, and we conclude that this sample also shows no strong

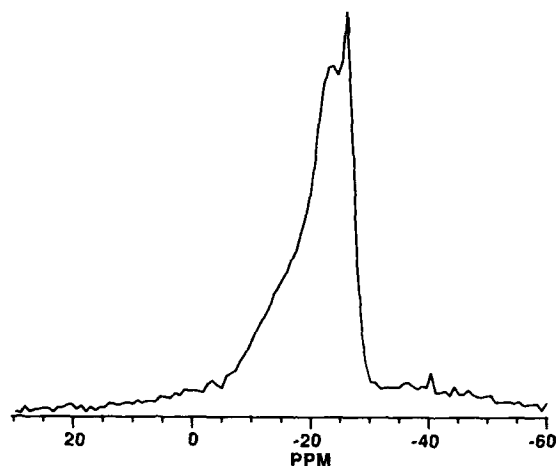


Figure 9.4. Solid-state  $^{29}\text{Si}$ -NMR spectrum of the product obtained from the reaction of  $\text{Ti}(\text{On-Bu})_4$  and  $(\text{CH}_3)_2\text{Si}(\text{OOCCH}_3)_2$ .

evidence for Si–O–Ti bond formation. This result is not surprising, because only the Si atoms in the end groups and in the cyclic species, through ring opening polymerization, are available for reaction with the Ti alkoxide, and Fig. 9.1b indicates that the concentration of these species are low.

The difference between the spectra in Figs. 9.2a and 9.3a can be explained by the fact that  $(\text{CH}_3)_2\text{Si}(\text{OOCCH}_3)_2$  is a more reactive monomer toward hydrolysis and condensation than  $(\text{CH}_3)_2\text{Si}(\text{OCH}_3)_2$  [7]. The acetic acid produced upon hydrolysis can replace butoxy groups on the titanium, providing bidentate acetate ligands that reduce the reactivity of the titanium toward condensation [8,9]. Solid-state  $^{13}\text{C}$ -NMR revealed that acetate was present in the product prepared with  $(\text{CH}_3)_2\text{Si}(\text{OOCCH}_3)_2$ . Infrared spectrometric analysis revealed that the frequency difference between the symmetric and asymmetric stretch was less than  $130\text{ cm}^{-1}$ , which is indicative of bidentate acetate bonded to titanium [9].

Figure 9.3a clearly shows that with  $(\text{CH}_3)_2\text{Si}(\text{OCH}_3)_2$ , condensation to form Si–O–Si bonds has not proceeded as far as in the  $(\text{CH}_3)_2\text{Si}(\text{OOCCH}_3)_2$  system. Instead, hydrolysis of the slower-reacting alkoxy groups has produced monomeric and oligomeric Si species with Si–OH groups, which readily reacted with  $\text{Ti}(\text{On-Bu})_4$  to form Si–O–Ti bonds. The relative concentration of the Si–OH species in the  $(\text{CH}_3)_2\text{Si}(\text{OCH}_3)_2$  sample must be higher than for the hydroxy-terminated PDMS, which contains a Si/OH ratio of about 11.5/1, in order for more reaction to occur with Ti. When  $\text{Ti}(\text{On-Bu})_4$  is added directly to  $(\text{CH}_3)_2\text{Si}(\text{OOCCH}_3)_2$ , under anhydrous conditions, the solid state  $^{29}\text{Si}$ -NMR of the product in Fig. 9.4 shows the same type of broadening as in Fig. 9.3a. More Si–O acetate is available to react with the Ti alkoxide, and more Si–O–Ti bond formation can occur than in the prehydrolyzed case in Fig. 9.2a.

### 9.4. CONCLUSIONS

Several research groups, which cite work with mixtures of metal alkoxides [3, 10], note that the less reactive alkoxide should be prehydrolyzed to maximize mixed metal-oxygen-metal bond formation. In this Chapter, we have presented initial results of NMR evidence for heterocondensation of Si-O-Ti and have shown that this can vary with Si monomer reactivity. We have shown that solid-state NMR has the potential for monitoring the formation of Si-O-Ti bonds in sol-gel-derived materials and that the selection of sol-gel monomers, based on their relative reactivities under the given chemical reaction conditions, is essential for the maximum homogeneity of the final material.

The extent of Si-O-Ti bond formation is dictated by the choice of starting materials and the reaction conditions, such as temperature, time, order of addition, reagent concentration, and catalyst. Studies are underway to elucidate the understanding of the effects of these variables.

### ACKNOWLEDGMENTS

This work was partially supported by the Air Force Office of Scientific Research. C.L.S. would like to acknowledge the American Association of University Women for financial support. Dr. Louis Scarmoutzos is gratefully acknowledged for helpful discussions.

### REFERENCES

1. H. Schmidt and B. Seiferling, in: C. J. Brinker, D. E. Clark and D. R. Ulrich, Eds., *Better Ceramics Through Chemistry*, Vol. II, *Mater. Res. Soc. Symp. Proc.*, **73**, 739 (1986).
2. C. S. Parkhurst, W. F. Doyle, L. A. Silverman, S. Singh, M. P. Andersen, D. McClurg, G. E. Wnek, and D. R. Uhlmann, in: C. J. Brinker, D. E. Clark, and D. R. Ulrich, Eds., *Better Ceramics Through Chemistry*, Vol. II, *Mater. Res. Soc. Symp. Proc.*, **73**, 769 (1986).
3. M. Yamane, S. Inoue, and K. Nakasawa, *J. Non-Cryst. Solids*, **48**, 153 (1982).
4. D. C. Bradley, R. C. Mehrotra, and D. P. Gaur, *Metal Alkoxides*, p. 160, Academic Press, New York (1978).
5. A. L. Smith, *Analysis of Silicones* p. 319, Wiley, New York (1974).
6. C. A. Fyfe, J. M. Thomas, J. Klinowski, and G. C. Gobbi, *Angew. Chem. Int. Ed. Engl.*, **22**, 259 (1983).
7. R. K. Iler, *The Chemistry of Silica*, p. 177, Wiley, New York (1979).
8. C. Sanchez, J. Livage, M. Henry, and F. Babanneau, *J. Non-Cryst. Solids*, **100**, 65 (1988).
9. S. Doeuff, M. Henry, C. Sanchez, and J. Livage, *J. Non-Cryst. Solids*, **89**, 206 (1987).
10. K. Kamiya and S. Sakka, *J. Mater. Sci. Lett.*, **15**, 2937 (1980).



# 10

## THE GELATION OF COLLOIDAL GELS AND THE DERJAGUIN–LANDAU– VERWEY–OVERBEEK (OR DVLO) THEORY

A. C. PIERRE

### 10.1. INTRODUCTION

Although coagulation is one type of aggregation of primary particles into compact structures, gelation is experimentally known as being another type of aggregation in which linear structures are built. The latter behavior has been observed under the microscope by Thomas and McCorkle [1] for  $\text{ThO}_2$  sols and mentioned, but not explained, by Verwey and Overbeek [2]. When a nonpotential determining electrolyte is added, a critical gelation concentration  $C_g$  has been observed experimentally by Prakash and Dhar [3], which is similar, but lower than the classical coagulation concentration  $C_c$ . A theoretical work by Thomas and McCorkle [1] on linear aggregation has been carried out by numerical computation, which does not allow to discriminate easily the effect of particle size and double-layer thickness, and by assuming the interaction with a string of spheres can be considered as a sum of isolated sphere interactions, which is shown here to be incorrect in the case where linear aggregation occurs.

Linear gelation is addressed differently and analytically here as a development of a proposition made in a previous publication [4] for the first linking

*Ultrastructure Processing of Advanced Materials.*

Edited by Donald R. Uhlmann and Donald R. Ulrich (deceased).

ISBN 0-471-52986-9 © 1992 John Wiley & Sons, Inc.

between a few spheres. It differs from fractal growth such as resulting from diffusion limited aggregation, which concerns latter stages involving a larger number (i.e., having statistical significance) of spheres.

## 10.2. THE DLVO THEORY FOR TWO SPHERICAL PARTICLES

The DLVO theory addresses the total interaction between two particles through a mechanical potential  $\Phi$  that is the sum of two terms:

$$\Phi = \Phi_{\text{vdw}} + \Phi_{\text{el}} \quad (1)$$

The van der Waals interaction term  $\Phi_{\text{vdw}}$  is attractive except at very close separation distances, where "hard contact" occurs, and expressions for this term are known [2]. The electrostatic interaction term  $\Phi_{\text{el}}$  is repulsive: It results from charges of same sign on the surface of the particles, progressively attenuated by the counterions at increasing distances. Its knowledge requires first the determination of the electric potential  $\Psi^{\text{sph}}$  around the spherical particle of radius  $R$  and must be obtained by solving a Poisson's equation in spherical coordinates. Unfortunately, an approximate analytical expression can only be obtained for low electric potentials  $\Psi_0$  (Debye Hückel approximation):

$$\Psi^{\text{sph}} = \Psi_0 \left( \frac{R}{R+S} \right) \exp(-\kappa S) \quad (2)$$

where  $R$  is the radius of the sphere;  $S$ , the distance from the surface of the particle;  $\Psi_0$  the surface electric potential; and  $\kappa^{-1}$  is homogeneous to a dimension that is called the *double-layer thickness*. For  $z+z-$  nonpotential determining electrolytes, with the same concentration  $n_0$  of positive and negative ions with the same absolute charges  $z$  far from the particles,  $\kappa$  is given by

$$\kappa^2 = \frac{2n_0 z^2 e^2}{\epsilon_0 \epsilon k T} \quad (3)$$

where  $\epsilon_0$  is the dielectric constant of vacuum, and  $\epsilon$ , the relative dielectric constant of the liquid. Comparing the electric potentials  $\Psi^{\text{sph}}$  from a sphere of radius  $R$  and  $\Psi^{\text{pl}}$  from a flat plane (corresponding to  $R = \infty$  in Eq. 3) at a distance  $S = \kappa^{-1}$ , one finds

$$\Psi^{\text{sph}} = \frac{R}{R + \kappa^{-1}} \Psi^{\text{pl}} = \frac{R\kappa}{R\kappa + 1} \Psi^{\text{pl}} \quad (4)$$

Equation 4 shows that if  $R < \kappa^{-1}$ , the electric potential decreases appreciably faster with increasing distance from a sphere than from a flat surface. This is due to the fact that the counterions that attenuate the surface charge can be

found in a volume increasing with a spherical divergence, hence on a shorter distance. A measure of the upper bound of the particle size where this difference remains appreciable is given by  $\kappa^{-1}$ . For 1:1 nonpotential determining electrolytes of molarities 0.001, 0.01, and 0.1, this is respectively 96, 30, and 9.6 Å. However, most often in sol-gel processing of oxides, only a potential determining electrolyte is used, which is either an acid or a base. For pH values 2, 3, 4, and 5 obtained with a monovalent acid or base, the value  $\kappa^{-1}$  is then, respectively, 30, 96, 300, and 960 Å. In fact, this situation is fulfilled in many of the oxide sol-gel studies. Unfortunately, under these conditions the mathematical expressions for the electrostatic interaction term are complex [2].

On the contrary, in the case  $R > \kappa^{-1}$ , the electric potential around a sphere does not differ much from that of a flat plate, and it becomes possible to use a general expression for the electric potential given by the Gouy-Chapman model for a flat surface. It is not restricted to low surface electric potential  $\Psi_0$ , nonetheless a simple expression for the electrostatic interaction term per unit area between the two plates  $\Phi_{el}^{pl}$  can be obtained only for a "large enough" separation distance  $S_0$ . The latter condition is fulfilled only if the electric potential at middistance is a small fraction of the surface value  $\Psi_0$ . It leads to

$$\Phi_{el}^{pl} = \frac{64n_0kT\gamma_0^2}{\kappa} \exp(-\kappa S_0) \quad (5)$$

Returning to identical spherical particles with smallest separation distance  $S_0$ , the electrostatic interaction term becomes noticeable at a separation distance  $S_0$  small by comparison with the sphere radius, but large enough for Eq. 5 to be applicable. The well-known method of Derjaguin [5] consists in approximating a sphere by a succession of planar rings of area  $dA_i^{sph} = 2\pi h dh$  and integrating with the approximation  $h/R \ll 1$ . This is justified by the fact that the repulsion decreases exponentially with the distance, and only the closest parts of each sphere contribute appreciably to the repulsion. Under these conditions,

$$\Phi_{el}^{sph} = \pi R \kappa^{-1} \Phi_{el}^{pl} \quad (6)$$

For  $R < \kappa^{-1}$ , numerical plots show that the repulsion according to the flat plate solution is overestimated, but qualitatively the shape of the curves remains [2], and at short distances the whole cross sections of the spheres interact in a nonnegligible manner.

### 10.3. STRING OF SPHERES AND A PLANAR ARRAY OF SPHERES

If one considers a string of spheres, several linking sites are possible for an additional sphere. Sphere 1 in Fig. 10.1 may approach near an extremity in A or near any side location between B and C. In configuration B, sphere 1 is

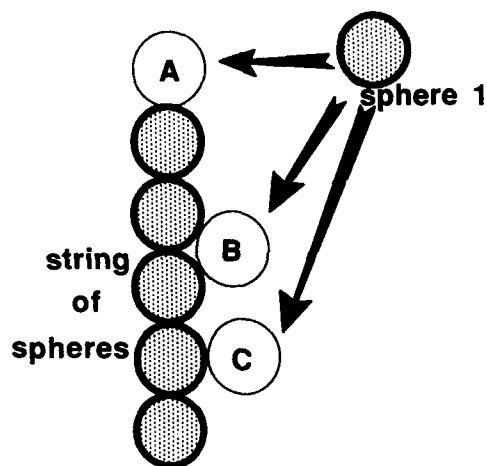


Figure 10.1. Possible linking sites between a single sphere and a string of spheres.

submitted to two van der Waals interactions and two electrostatic interactions of the types in configuration A. Under conditions where an energy barrier ( $\Phi_{\max} = \Phi_{\text{vdw}} + \Phi_{\text{el}} > 0$ ) has to be overcome by thermal motion, this barrier is in all cases (thick or thin double layer) of a higher magnitude in configuration B than in configuration A. Stated differently, sphere 1 has a much higher probability to keep building the string. A similar set of situations can be described for a sphere approaching a planar array of identical spheres (Fig. 10.2), the probability of linking being higher in position A than in position B, or C itself higher than in position D.

Considering the isolated sphere 1 approaching a string of spheres (Fig. 10.1),

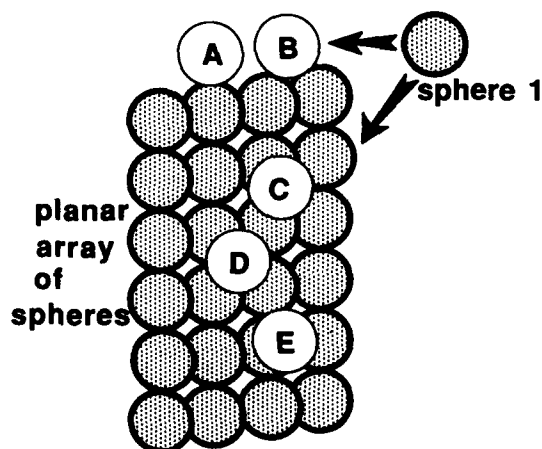


Figure 10.2. Possible linking sites between a single sphere and a planar array of spheres.

it is now necessary to compare the difficulty of approaching in position C with that of position B or A. At a large separation distance from the string surface, the surfaces of constant electric potential  $\Psi$  are cylinders (Fig. 10.3). The fluctuations in the equipotential surfaces resulting from the necks become sensible at closer distance. If one considers a neck between two particles in the string, a local concave wedge surface is present instead of a convex surface for one single sphere. The electric potential  $\Psi_{el}^{neck}$  is therefore stronger than for a flat face term  $\Psi_{el}^{pl}$  by opposition with the sphere electric potential  $\Psi_{el}^{sph}$ , which is lower. In terms of magnitude, the difference can be expected to be appreciable in similar conditions, that is to say when the double-layer thickness  $\kappa^{-1}$  is at least of a size comparable with the sphere's radius, and as we have seen this is the case with most of the sol-gel hydrous colloidal oxides. Qualitatively this can be related to the fact that near the neck two surfaces of the same charge are close to each other, excluding an important volume for thick double layers where the counterions cannot go because of the presence of the neighbor sphere. Moreover an important overlapping volume occurs. The counterions are therefore rejected in the liquid wedge of the neck where they build a thicker double layer. Under these conditions, summing up the interactions derived from isolated spheres at distances of the order of the double layer thickness, such as done by Thomas and McCorkle [1], is incorrect.

The situation is nonetheless such that the string of spheres appears to a sphere I coming laterally like a cylinder with a thick double layer. The latter can be described in a first approximation by a "smoothed" surface potential  $\Psi_s$  at a distance close to the radius  $R$  from the string axis, somewhat like in Stern's model. A similar approximation holds for a planar array, and indeed for secondary particles, which are themselves agglomerates of smaller primary particles, the same hypothesis is always implicitly admitted.

To obtain an order of magnitude of the *curvature effect* on the electrostatic interaction term, the technique of Derjaguin, which is really valid for  $R > \kappa^{-1}$ , can be extended to the interactions between a sphere and a flat surface or a cylinder. For the electrostatic interaction term  $\Phi_{el}^{sph/pl}$  between a sphere of radius

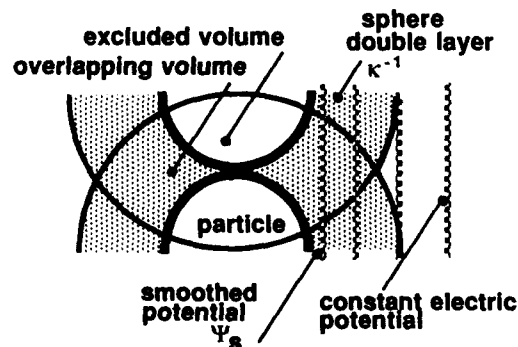
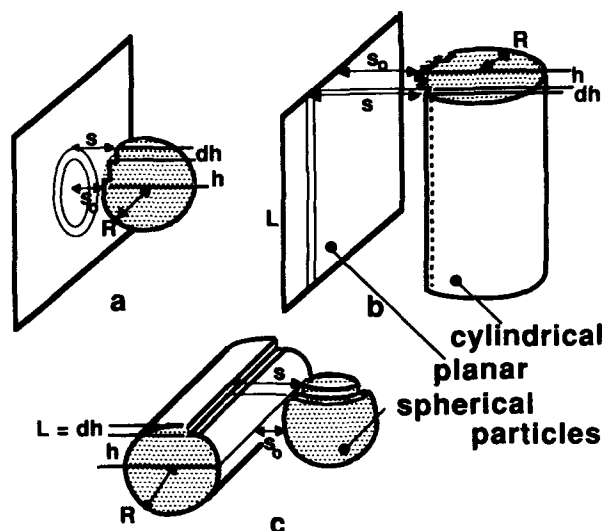


Figure 10.3. Smoothed electric potential near a spherical wedge for a thick double layer.



**Figure 10.4.** Derjaguin method for the calculation of the electrostatic repulsion between (a) a sphere and a flat surface, (b) a cylinder and a flat surface, and (c) a sphere and a cylinder.

$R$  and a flat surface, one may decompose the sphere in elementary disks of width  $dh$  and radius  $h$  (Fig. 10.4a), and it becomes

$$\Phi_{el}^{sph/pl} = 2\Phi_{el}^{sph} \quad (7)$$

For the interaction between a cylinder of radius  $R$  parallel to a flat plane, one may decompose the cylinder into planar strips parallel to the plane (Fig. 10.4b), which for a length  $L$  gives

$$\Phi_{el}^{cy/pl} = L \frac{64n_0kT\gamma_0^2}{\kappa} \sqrt{\frac{2R}{\kappa}} \int_{-\infty}^{\infty} \exp\left(-\frac{\kappa}{2R}h^2\right) dh = L \sqrt{\frac{2\pi R^2}{R\kappa}} \Phi_{el}^{pl} \quad (8)$$

The interaction between a sphere and a cylinder can be obtained by decomposing the sphere and the cylinder into strips of length  $L = dh$  (Fig. 10.4c), leading to

$$\Phi_{el}^{sph/cy} = \sqrt{\frac{2\pi R^2}{R\kappa}} \Phi_{el}^{pl} \int_{-\infty}^{\infty} \exp\left(-\frac{\kappa}{2R}h^2\right) dh \quad (9)$$

or

$$\Phi_{el}^{sph/cy} = \frac{\pi R^2}{R\kappa} \sqrt{2} \Phi_{el}^{pl} = \sqrt{2} \Phi_{el}^{sph} \quad (10)$$

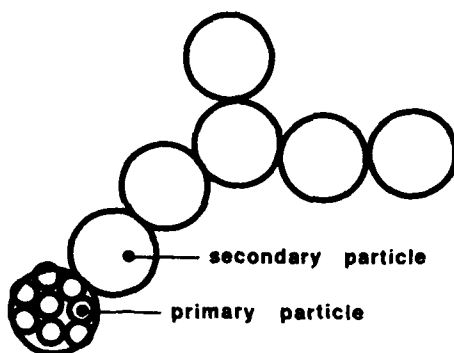


Figure 10.5. Possible structure of a gel as a result of electrostatic interactions.

#### 10.4. CONCLUSIONS: POSSIBLE GELATION OF COLLOIDAL HYDROUS OXIDE SOLS

Under conditions where most hydrous oxide sols and gels are made, the double layer is of a thickness comparable with the colloidal dimensions of the particles. This has the effect of (1) smoothing out the surface roughness of an aggregate in terms of electrostatic repulsion and (2) amplifying the effect of the smoothed curvature (i.e., the repulsion decreasing from a smoothed planar surface to a smoothed cylindrical surface to a smoothed spherical surface). Simultaneously it leaves unchanged the van der Waals interaction, which comes from bulk matter.

With respect to aggregation, a good indication of the stability of a sol is given by the factor  $W \cong \exp(\Phi_{\max}/kT)$ , where  $\Phi_{\max}$  must exceed 15 kT for the sol to be stable on an appreciable time scale [2]. However,  $\Phi_{\max}$  decreases with radius  $R$ , for instance, for 1-nm primary particles with a surface potential of 27.5 mV at pH 3 it is 2.85 and 4 kT, respectively for linear and lateral linkage. Both are therefore quite probable, so that the primary particles agglomerate into secondary spherical particles.

If these secondary particles reach a size comparable to the double-layer thickness, for instance, 5 nm, the repulsion barriers increase to 15 and 21 kT, respectively, for linear and lateral linkage. These secondary particles will therefore slowly link linearly.

In conclusion, an overall picture of the gel network as a result of the DLVO theory (Fig. 10.5) can be quite close to that described by Fricke [6] for silica gels.

#### REFERENCES

1. J. L. Thomas and K. H. McCorkle, *J. Colloid Interf. Sc.*, **36**, 110 (1971).
2. E. J. W. Verwey and J. Th. G. Overbeek, *Theory of the Stability of Lyophobic Colloids*, Elsevier, Amsterdam (1948).

3. S. Prakash and N. R. Dhar, *J. Ind. Chem. Soc.*, **7**, 417 (1930).
4. A. C. Pierre and D. R. Uhlmann, in: *Better Ceramics Through Chemistry, Mat. Res. Soc. Symp. Proc.*, **121**, 207 (1988).
5. B. Derjaguin and L. D. Landau, *Acta Physicochim. USSR*, **14**, 633 (1941).
6. J. Fricke, *J. Non-Cryst. Solids*, **10**, 169 (1988).



## QUANTUM CALCULATIONS ON SOL-GEL SILICA CLUSTERS

J. K. WEST, S. WALLACE, L. L. HENCH, AND C. R.  
LISHAWA

### 11.1. INTRODUCTION

Recent developments in sol-gel optics have produced type V amorphous silica monoliths with extremely wide optical transmission bands [1,2]. Laser-densified optical waveguide tracks have been produced in porous type VI silica [3]. Optically transparent soda-silica monoliths with good UV cutoff wavelengths have also been made [4] at substantially lower densification temperatures than the pure silica system.

These developments and others increase the importance of understanding the structural models of sol-gel silica and the theoretical grounds for the UV cutoff of silica optics. Thus, semiempirical quantum calculations have been initiated using Hückel molecular orbital (HMO) [5] and intermediate neglect of differential overlap (INDO) molecular orbital models. The INDO program was made available by the Quantum Theory Project at the University of Florida [6].

### 11.2. MODEL STRUCTURES

The structures evaluated contain from one to six silica tetrahedra. In each model two bridging oxygens and two nonbridging oxygens are bonded to each silicon.

*Ultrastructure Processing of Advanced Materials.*

Edited by Donald R. Uhlmann and Donald R. Ulrich (deceased).

ISBN 0-471-52986-9 © 1992 John Wiley & Sons, Inc.

One hydrogen is bonded to each of the nonbridging oxygens to terminate the structure and balance charge. Both ring and chain cluster models of silica tetrahedra were evaluated and their energies compared. Figure 11.1 shows the two-dimensional projection of a geometrically optimized INDO chain and ring structure for four silica tetrahedra. These projections are typical of the hydroxylated silica structures modeled in this study.

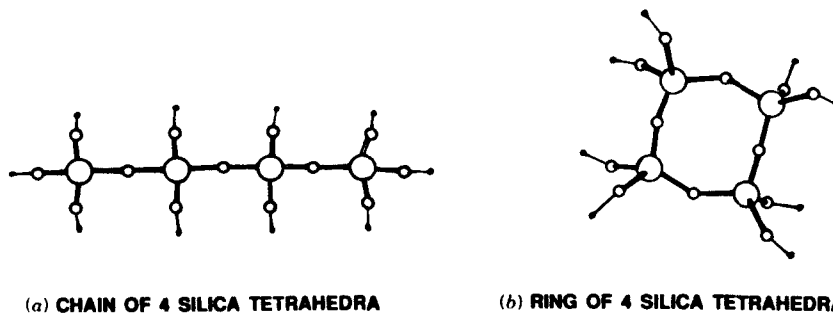
The clusters were each optimized for the minimum energy using a molecular mechanics (MM2) [7] routine. The molecular orbitals were calculated first using HMO then using geometrically optimized INDO calculations. The molecular energies were evaluated and compared to establish the relative stability of each structure. The energy gap between the highest occupied molecular orbital (HOMO) and the lowest unoccupied molecular orbital (LUMO) for the single states and the corresponding UV cutoff wavelength were determined.

The heteroatom parameters,  $k$  and  $h$ , which are used to modify the Hamiltonian matrix for the HMO calculations, were adjusted to compensate for the differences in the bonding orbitals between carbon and silicon. In HMO theory the matrix diagonal represents the ionization potentials,  $\sigma_i$ , of the valence electrons for carbon  $i$ , where  $h = 1$ , and the off diagonal matrix elements represent the bond interactions,  $\beta_{ij}$ , between carbon atoms  $i$  and  $j$ , where  $k = 1$ :

$$\sigma_i = -11.26 \times h_i (\text{eV}) \quad (1)$$

$$\beta_{ij} = -2.5 \times k_{ij} (\text{eV}) \quad (2)$$

The HOMO-LUMO gap for a single silica tetrahedra was set at 8.2 eV, and the parameters were determined. Thus, the relative energies of the various structures were determined without further adjustment of the parameters by comparison to a single silica tetrahedra. Table 11.1 shows the results of the empirical determination of the  $k$  and  $h$  parameters for silicon [8], carbon, oxygen, and nitrogen [5].



**Figure 11.1.** The two dimensional projection of a geometrically optimized INDO chain and ring structure for four silica tetrahedra.

TABLE 11.1. Heteroatom Parameters

Bond	k parameter	Reference No.	Atom	h parameter	Reference No.
C—C	1.00	5	C	1.00	5
C—O	0.80	5	O	1.00	5
C—N	0.80	5	N	1.50	5
C=C	1.00	5	Si	0.80	8
C=O	1.414	5			
C=N	1.0	5			
C=Si	0.72	8			
O=Si	1.4	8			

### 11.3. RESULTS AND DISCUSSION

Table 11.2 summarizes the HMO calculations of these silica structures. The Hückel energy (HE) is the total molecular energy for each structure. The relative stability of each structure can be compared using the HE per silica tetrahedra. In Table 11.3, summarizing the INDO calculations, a similar calculation is shown to compare the relative stability of the INDO structures. The more negative the energy, the more stable the structure.

Figure 11.2 shows the INDO energy per silica tetrahedra for rings and chains as a function of the number of tetrahedra and suggests that the chain structures are more stable than the rings. This has been observed experimentally using

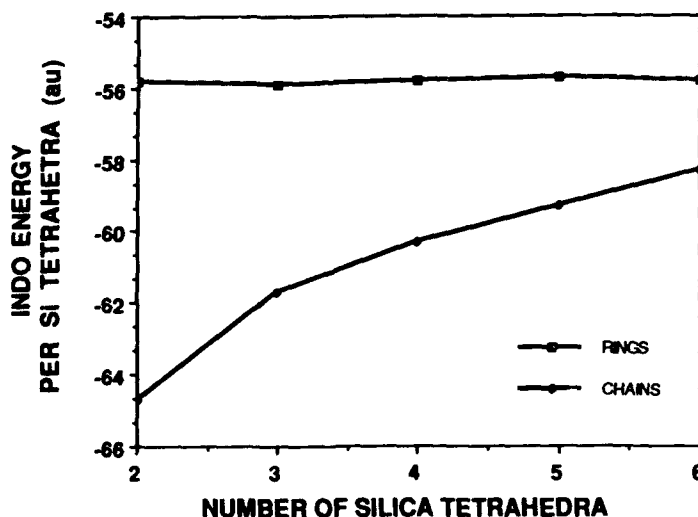


Figure 11.2. INDO energy per silica tetrahedra for rings and chains as a function of the number of tetrahedra.

TABLE 11.2. Hückel Calculations for Silica Structures

Number of Silica Tetrahedra	Structure	Resonance Energy (eV)	HE <sup>a</sup> per Tetrahedra (eV)	HOMO-LUMO <sup>a</sup> Bandgap (eV)	UV <sup>a</sup> Cutoff Wavelength (nm)
1	Tetrahedra	14.3	-67.8	8.22	151.1
2	Chain	-25.2	-94.4	7.22	172.1
2	Ring	39.0	-69.5	7.29	170.2
3	Chain	41.9	-60.6	6.87	180.8
3	Ring	11.9	-70.4	7.29	170.3
4	Chain	46.3	-58.5	5.16	240.7
4	Ring	56.2	-56.7	6.20	200.3
5	Chain	70.0	-59.0	6.52	190.5
5	Ring	-18.9	-76.7	7.60	163.4
6	Chain	-11.6	-75.2	8.80	141.1
6	Ring	84.3	-70.8	6.19	200.5

<sup>a</sup> Abbreviations used: HE, Hückel energy; HOMO, highest occupied molecular orbital; LUMO, lowest unoccupied molecular orbital; UV, ultraviolet.

TABLE 11.3. INDO Calculations for Silica Structures

Number of Silica Tetrahedra	Structure	Dopant [mol %]	INDO <sup>a</sup> Energy per Tetrahedra (a.u.)	HOMO-LUMO <sup>a</sup> Bandgap (a.u.)	UV <sup>a</sup> Cutoff Wavelength (nm)
1	Tetrahedra	0.00	-73.82	0.6201	87.1
2	Chain	0.00	-64.72	0.4129	130.7
2	Chain-Na	6.25	-64.46	0.3195	168.1
2	Chain-OH	5.88	-73.39	0.1561	345.9
2	Chain-water	5.88	-73.78	0.3950	136.7
2	Ring	0.00	-55.82	0.4786	112.8
3	Chain	0.00	-61.74	0.4069	132.7
3	Ring	0.00	-55.86	0.5082	106.2
4	Chain	0.00	-60.25	0.3867	139.6
4	Ring	0.00	-55.80	0.4725	114.3
4	Ring-Na	4.00	-55.62	0.3319	162.6
4	Ring-OH	3.85	-60.28	Degenerate	N/A
5	Chain	0.00	-59.35	0.4024	134.2
5	Ring	0.00	-55.76	0.3740	144.3
6	Chain	0.00	-58.55	0.3974	135.8
6	Ring	0.00	-55.79	0.4696	114.1
6	Ring-Na	2.78	-55.69	0.3564	151.5
6	Ring-OH	2.70	-58.73	Degenerate	N/A

<sup>a</sup> Abbreviations used: INDO, intermediate neglect of differential overlap; HOMO, highest occupied molecular orbital; LUMO, lowest unoccupied molecular orbital; UV, ultraviolet; N/A, not applicable.

NMR spectroscopy [9], where a linear, as opposed to a ring, growth model most consistently interprets the experimental structural evidence prior to gelation.

Investigators [10,11] have proposed models for the structure of acid-catalyzed silica gels containing two levels of structure formed before gelation. These models propose the formation of primary particles of diameter 1–2 nm that agglomerate to form secondary particles of about 4–6 nm before drying. The secondary particles give rise to the pore structure after drying.

Table 11.4 shows the differences in the INDO structural energies between chains and rings. The relative stability of chains compared to rings decreases as the number of silica tetrahedra increases, as shown in Fig. 11.3 by the decrease in the difference between their calculated INDO energies. The difference is estimated to reach zero as the number of tetrahedra reaches about 10 or 12,

TABLE 11.4. Energy Difference between Chains and Rings

Number of Silica Tetrahedra	Cluster Size (Å)		INDO <sup>a</sup> (Chain-ring) (a.u.)	Hückel (Chain-ring) (eV)
	Rings	Chains		
2	6.567	9.090	8.90	24.86
3	7.143	12.671	5.88	−9.84
4	9.293	16.253	4.45	1.79
5	11.319	19.832	3.59	−17.67
6	11.88	23.414	2.76	4.44
...				
12		44.823	0.00	(Estimate)

<sup>a</sup>Abbreviation used: INDO, intermediate neglect of differential overlap.

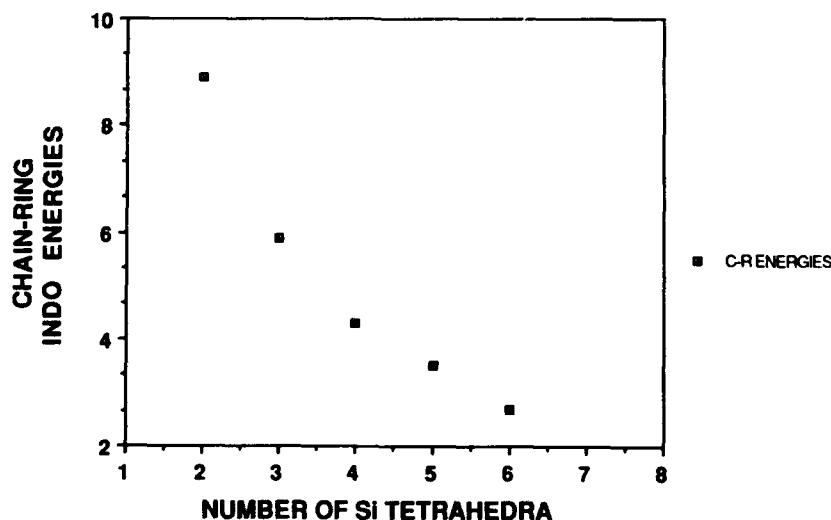


Figure 11.3. The relative stability of chains compared to rings as a function of the number of silica tetrahedra.

when the driving force for rings becomes more favorable than for chains. This result is similar to the size range where primary particle growth stops in acidic silica sols [10, 11]. Acid catalysis ensures complete hydrolysis of the silica tetrahedra, as used in these calculations. The size of the INDO calculated rings or clusters for 10–12 tetrahedra appears to fall within the range of the radius of gyration of the primary particles calculated from small angle X-ray scattering analysis of acid-catalyzed silica sols [10, 11].

As gelation occurs, the crosslinking of the structure becomes more dominant. Statistical analysis indicates that chain growth is limited by this process, and rings must be formed [12]. The energy differences in the ring structures in the INDO model are very small. This indicates that a broad distribution of ring sizes may be possible in a gel as they become energetically more favorable.

Tables 11.2 and 11.3 show the HOMO–LUMO bandgap energy and the associated theoretical UV cutoff. In both models the ring structures tend to yield a lower UV cutoff than the chain structures. Experimental UV cutoff values of dense dehydrated gel–silica are close to those predicted by the calculated ring structures [13] involving five tetrahedra per ring.

The effect of dopants on the UV cutoff is significant. The hydroxyl radical seems to have the most impact. The degenerate HOMO–LUMO bandgaps indicate that absorption is complete. In the case of the sodium dopant, this result tracks the experimental results of sol–gel soda–silica systems [4]. When the concentration of soda was increased from 0 to 7%, the UV cutoff increased by 105 nm from 200 nm to 305 nm. In the INDO model, as the sodium dopant was increased from 0 to 6.25%, the UV cutoff increased by 54.6 nm. Hydrogen-bonded water also increased the UV cutoff, as seen experimentally.

#### 11.4. CONCLUSIONS

The HMO molecular orbital model is relatively simple and can be run on personal computers. The INDO model is more sophisticated and consequently more accurate; it also requires larger computational power, for example, Sun Microsystems. The differences in the INDO structural energies between rings and chains indicate that chain structures are the most stable up to about 10–12 silica tetrahedra. The calculated UV cutoffs in the pure silica is lower than the experimental values, however, ring structures with 5 tetrahedra are close to experimental values of pure gel–silica optics. Small concentration of hydroxyl, sodium, or water increases the UV cutoff wavelength, as expected.

#### ACKNOWLEDGMENTS

The authors acknowledge the US-AFOSR (Contract F49620-88-C-0073) and the Quantum Theory Project at the University of Florida for their support of this research.

## REFERENCES

1. L. L. Hench, S. H. Wang, and J. L. Noques, *Multifunctional Materials*, SPIE Vol. 878, 76 (1988).
2. S. H. Wang, C. Campbell, and L. L. Hench, in: J. D. Mackenzie and D. R. Ulrich, Eds., *Ultrastructure Processing of Advanced Ceramics*, p. 145, Wiley, New York (1988).
3. R. V. Ramaswamy, T. Chia, R. Srivastava, A. Miliou, and J. West, *Multifunctional Materials*, SPIE Vol. 878, 86 (1988).
4. R. N. Li and L. L. Hench, in: C. J. Brinker, D. E. Clark, and D. R. Ulrich, Eds., *Better Ceramics Through Chemistry*, Vol. III, *Mat. Res. Soc. Symp. Proc.*, 589 (1988).
5. K. Sarnow, *Molecular Matters*, 80 Micro, pp. 100-107 (October 1983).
6. M. Zerner et al., Quantum Theory Project, Gainesville, FL, Program No. 010183.
7. N. L. Allinger et al., QCPE, Bloomington, Indiana, Program No. 318.
8. L. L. Hench and J. K. West, in: *Principles of Electronic Ceramics*, Wiley, New York (in press).
9. L. W. Kelts, N. J. Effinger, and S. M. Melpolder, *J. Non-Cryst. Solids*, **83**, 353 (1986).
10. G. Orcel, L. L. Hench, I. Artaki, J. Jonas, and T. W. Zerda, *J. Non-Cryst. Solids*, **105**, 223 (1988).
11. B. Himmel, Th. Gerber, and H. Burger, *J. Non-Cryst. Solids*, **91**, 122 (1987).
12. J. Zarzycki, in: L. L. Hench and D. R. Ulrich, Eds., *Science of Ceramic Chemical Processing*, p. 215, Wiley, New York (1986).
13. L. L. Hench, in: *Proceedings 4th Ultrastructure Processing Conference, Tucson, AZ, February 1989*.



## PART 2

# **Processing**

# **12**

## **ULTRASTRUCTURE PROCESSING OF SHAPED CERAMIC BODIES FROM LIQUIDS**

**JOHN D. MACKENZIE**

### **12.1. INTRODUCTION**

The fabrication of a ceramic into some specific shape is generally much more difficult than for a metal or an organic polymer. This is primarily due to the brittleness of ceramics, which makes machining difficult. If near-net-shape structures can be formed, fracture during machining is minimized. Glass-forming oxide systems are, of course, widely utilized for the fabrication of all types of complex shapes. Second, for some very limited numbers of systems, a shaped glass body can be converted into a fine-grained glass-ceramic. However, most ceramic systems do not form glass readily. One then has to use the powder process via the slip-cast or sintering route. It has been emphasized that because even fine powders are of micrometer dimensions, the attainment of ultrahomogeneity is practically impossible with a powder process [1].

For electronic ceramics, ultrahomogeneity is of particular importance. The powder process is thus not desirable. Vapor deposition is frequently difficult to control for multicomponent ceramic systems, because the chemical composition and sticking coefficients of the depositing species are different. Second, for large objects and/or complex-shaped objects, vapor deposition is generally not practical. One is then left with the liquid route. At present, there are two low-

---

*Ultrastructure Processing of Advanced Materials.*

Edited by Donald R. Uhlmann and Donald R. Ulrich (deceased).

ISBN 0-471-52986-9 © 1992 John Wiley & Sons, Inc.

temperature liquid routes that appear to be highly promising for the fabrication of shaped ceramic bodies. One is the metal-organic polymer route, which has been used principally for the fabrication of ceramic carbide fibers [2]. The second one is the so-called sol-gel route, which is primarily utilized for oxide ceramics. In this Chapter, only the processing of oxides will be treated, especially processes based on sol-gel-related liquids.

There are some examples of the successful preparation of shaped ceramic objects from sol-gel-related liquid systems. These will be reviewed in a later section. Because of the many subtle complexities associated with the use of low-temperature liquids, some of these will be critically reviewed before a discussion of specific examples.

## 12.2. SOME IMPORTANT CONSIDERATIONS FOR FABRICATION

### 12.2.1. The Ideal End Product

The end product of the fabrication process, be it a fiber, a film, a sphere or a rod, can be either a single crystal, a polycrystal, or a noncrystalline solid. The successful preparation of an oxide single crystal based on the use of sol-gel-type liquids is not known. Polycrystalline and noncrystalline oxides, however, have been successfully prepared in specific shapes. The ideal end product should be chemically homogeneous on a molecular scale and for a polycrystalline ceramic should have controllable grain size and practically zero porosity. For a porous ceramic, the pore size and size distribution should be controllable. For both polycrystalline or noncrystalline bodies, there should be negligible residual stresses. Prior to the adaptation of the low-temperature liquid method for fabrication, considerations should be given as to the probability of attaining such goals. These questions cannot be answered unless the various complexities associated with the sol-gel process are known. We will therefore first consider the evolutions of simple and complex oxide systems.

### 12.2.2. The Sol-Gel Process for a One-Oxide System

The sol-gel process ideally begins with a homogeneous liquid of low viscosity based on alkoxides. The viscosity increases with time as depicted in Fig. 12.1 and when it reaches a suitable value, fibers can be drawn and heat treated. Because the viscosity increases rapidly with time in the high-viscosity range and in a complex manner dependent on many factors, its precise control is difficult. The liquid then becomes a wet gel, which is a porous and mechanically weak solid whose pores are filled with a liquid mixture comprising of unreacted alkoxides, alcohol, and perhaps water. As condensation proceeds, more M-O-M bonds are formed. As the polymeric gel grows, it also shrinks, and liquid is expelled from the pores. The process is known as *syneresis*. The porosity and micro-

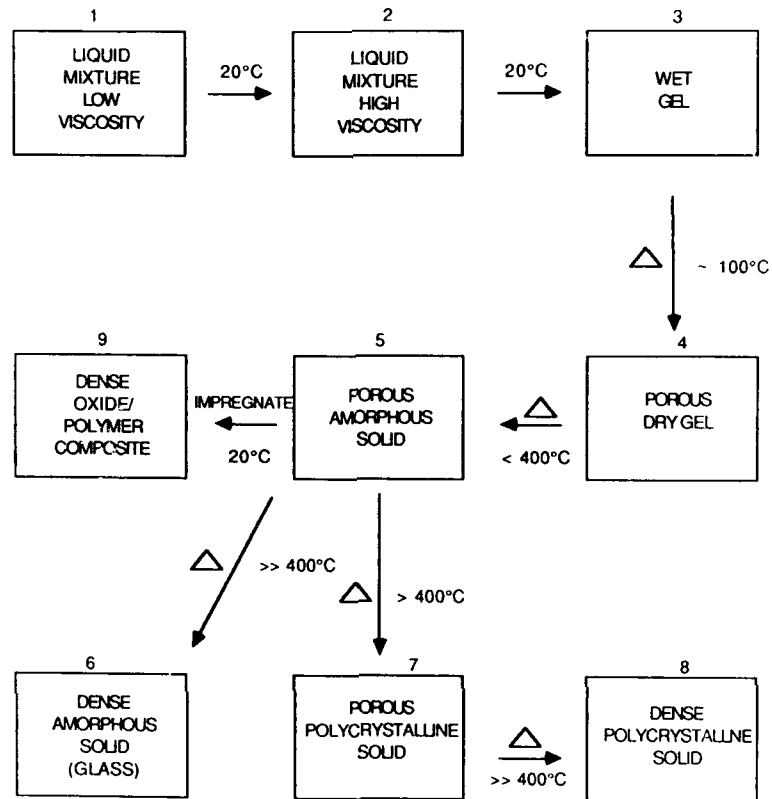


Figure 12.1. Evolution of the sol-gel-type liquid process from liquid to solids.

structure of the wet gel are dependent on numerous factors [3]. The mechanical strength of the wet gel is highly dependent on the structure of the oxide "skeleton," which is governed by the completeness of the condensation reaction to form M-O-M bonds. It is also dependent on the microstructure such as chains versus three-dimensional networks. Assuming sufficient water is present to permit complete hydrolysis, then at gelation, the bonds present are M-O-M, M-OH, and M-OR. The energy of the M-O-M bond is of the order of 100 kcal versus the 1 kcal of hydrogen bonds. The total number of M-O-M bonds in a wet gel have a greater effect on mechanical properties than the porosity. For instance, the elastic modulus of a fired ceramic of 85% porosity can be approximately calculated from [4]

$$E = E_0 \exp[-(bP + cP^2)] \quad (1)$$

to be  $\sim 0.03E_0$ . For silica,  $E$  is  $\sim 3 \times 10^5$  lb/in.<sup>2</sup>. The measured values of  $E$  for wet silica gels range only from 0.02 to 4 lb/in.<sup>2</sup> [5, 6]. It is assumed that the wet gel porosity is also  $\sim 85\%$ . The measured tensile strength of a silicate foamed

glass of 90% porosity is  $\sim 150 \text{ lb/in.}^2$  [7]. That of a wet silica gel is  $\sim 1 \text{ lb/in.}^2$  [6]. The wet gel is again assumed to have the approximately similar porosity. Although there are some uncertainties concerning the porosities of the wet gels studied, these comparisons leave little doubt that the completeness of the condensation process is of utmost importance if a strong wet gel is desired. The drying of the wet gel (steps 3 and 4 of Fig. 12.1) is usually accompanied by large changes of volume ( $\sim 50\%$ , say) and frequently by fracture. This is probably the most serious barrier to the fabrication of large bodies. Various approaches have been used to suppress fracture. Because the capillary pressure  $P$  is the likely cause of fracture when the liquid within the pores evaporate, and

$$P = 2\gamma \cos \theta / r \quad (2)$$

where  $\gamma$  is the vapor liquid surface tension,  $\theta$  is the wetting angle, and  $r$  is the pore radius, an increase of  $r$  would lower  $P$ . This has been achieved by Shoup in the fabrication of silica bodies [8]. The addition of chemical agents (drying control chemical additive) also increases the average pore size, but, more importantly, decreases pore size distribution [9]. Hypercritical drying has also been successfully used to suppress fracture during drying [10]. This approach, however, necessitates the use of high-pressure equipment. It should also be mentioned that silica optical fibers have also been drawn from porous preforms obtained from wet gels without hypercritical drying. For an excellent treatment of the theories of aging and drying of gels, the reader is referred to the work of Scherer [11].

When the porous dry gel is further heated to  $\sim 400^\circ\text{C}$ , most of the unreacted components are driven off and a fairly strong porous amorphous oxide results (Fig. 12.1, step 5). The pores are mainly small and continuous. This porous amorphous solid can be used as ceramic ultrafilters or can be impregnated with organic polymers to form transparent composites (Fig. 12.1, step 9). Porous amorphous solids can be conveniently divided into two types [12]. Type A would crystallize readily on further heating to give a porous polycrystalline solid (Fig. 12.1, step 7). This includes common oxides such as  $\text{TiO}_2$ ,  $\text{Al}_2\text{O}_3$ , and  $\text{ZrO}_2$ . At even higher temperatures the ceramic would become denser. Type B can be heat treated without crystallization to give dense amorphous solids that have properties indistinguishable from those of melt-formed glasses. This includes  $\text{SiO}_2$ ,  $\text{B}_2\text{O}_3$ , and  $\text{GeO}_2$ . From the porous dry gel to the fully dense non-crystalline (glasslike) or polycrystalline solid, all oxides are brittle. Thermal stresses must be minimized at each step to prevent fracture during heat treatment. Although considerable success has been achieved in the fabrication of relatively large, dense silica objects of various shapes, there is little information of similar successes for polycrystalline ceramics.

### 12.2.3. The Sol-Gel Process for Polycomponent Oxide Systems

Based on the above considerations, it is not difficult to expect that the fabrication of shaped oxide bodies containing two or more components must

become even more complex. It is not commonly recognized that a very well-mixed liquid solution does not necessarily result in a truly homogeneous gel. An example of this is the attempted preparation of an ultra-low expansion, glasslike solid based on  $\text{TiO}_2$  and  $\text{SiO}_2$ . If a silicon alkoxide and a titanium alkoxide are dissolved in an alcoholic solvent to form a homogeneous liquid mixture and exposed to  $\text{H}_2\text{O}$ , each alkoxide has its own reaction tendency and reaction rate. The titanium alkoxide would more readily form a titanium oxide gel than the silicon alkoxide. The net result could be the formation of a two-phase gel. On heating, the titanium oxide could crystallize with small inclusions of amorphous  $\text{SiO}_2$ . Because of the high-melting temperature of  $\text{TiO}_2$  and the high viscosity of  $\text{SiO}_2$ , it is unlikely that an ultrahomogeneous glasslike  $\text{TiO}_2$ - $\text{SiO}_2$  solid can be easily fabricated by such a method. Inhomogeneity on a microscopic scale would also generate internal stresses during heat treatment. A large stress-free and homogeneous body is thus practically impossible to produce unless the homogeneity is preserved at every step.

The same logic is applicable to the fabrication of a polycrystalline two-component oxide body such as  $\text{BaTiO}_3$ . In this case, it is again assumed that both barium alkoxide and titanium alkoxide are available and can form a homogeneous liquid solution. Even if  $\text{Ti-O-Ba}$  linkages are formed in the wet gel, because the  $\text{Ba-O}$  bond is mostly ionic, and the heat-treatment process can lead to the dissociation of organic groups,  $\text{BaCO}_3$  crystals can form at relatively low temperatures [1] ( $\sim 300^\circ\text{C}$ ). Such crystals can rapidly grow to dimensions in excess of a few thousand angstroms. The dried gel has thus become a mixture of fine oxide powders. The main advantage of the sol-gel method to prepare ultrahomogeneous solids is now lost. For a three-component oxide system such as  $\text{PbZrTiO}_3$ , the complexities are obviously much greater, even if all the metals are introduced as alkoxides.

For multicomponent glass-forming systems such as those based on  $\text{Na}_2\text{O-B}_2\text{O}_3\text{-SiO}_2$ , even if a homogeneous, pore-free, glasslike solid is produced from the sol-gel liquid route, prolonged heat treatment can result in liquid-liquid phase separation similar to that observed for melt-formed glasses [13].

#### 12.2.4. The Use of Salt Solutions

The use of alkoxides as raw materials to fabricate shaped objects offers a number of important advantages. One obvious advantage is that  $\text{M-O-M}$  bonds are formed in the liquid state, which in turn leads to the increase of viscosity with time. Although the control of viscosity is difficult, it can be done. This then permits the fabrication of fibers and tapes and objects of other shapes. For fibers, viscosities of the order of 100 to 1000 P are desirable and such values pose no problems for alkoxide-based solutions. Frequently, metal alkoxides are not readily available, and even if they are available, some alkoxides do not form concentrated miscible solutions easily. For a multicomponent oxide system such as  $\text{YBa}_2\text{Cu}_3\text{O}_7$ , one is tempted to replace alkoxides with salts. In Table 12.1, it is seen that despite the very high concentrations of metal salts in aqueous solutions, the viscosities remain in the range of only 1 to  $10 \times 10^{-2}$  P versus the

TABLE 12.1. The Viscosity and Solubility of Selected Compounds

Compounds	Weight Percent in Solution	Viscosity (cP)	Solubility
BaCl <sub>2</sub>	0.50	0.8966	37% hw
	26.00	1.3356	
CaCl <sub>2</sub>	0.50	0.9020	43% cw
	40.00	7.9945	
CuSO <sub>4</sub>	0.50	0.9038	24% cw
	18.00	2.1761	
Pb(NO <sub>3</sub> ) <sub>2</sub>	0.50	0.8931	27% cw
	34.00	1.2991	
AgNO <sub>3</sub>	0.50	0.8913	55% cw
	40.00	1.2136	
NaAc	0.50	0.9073	54% cw
	30.00	4.3897	
Na <sub>3</sub> C <sub>6</sub> H <sub>5</sub> O <sub>7</sub>	1.00	0.9269	42% cw
Sodium citrate	36.00	8.6974	

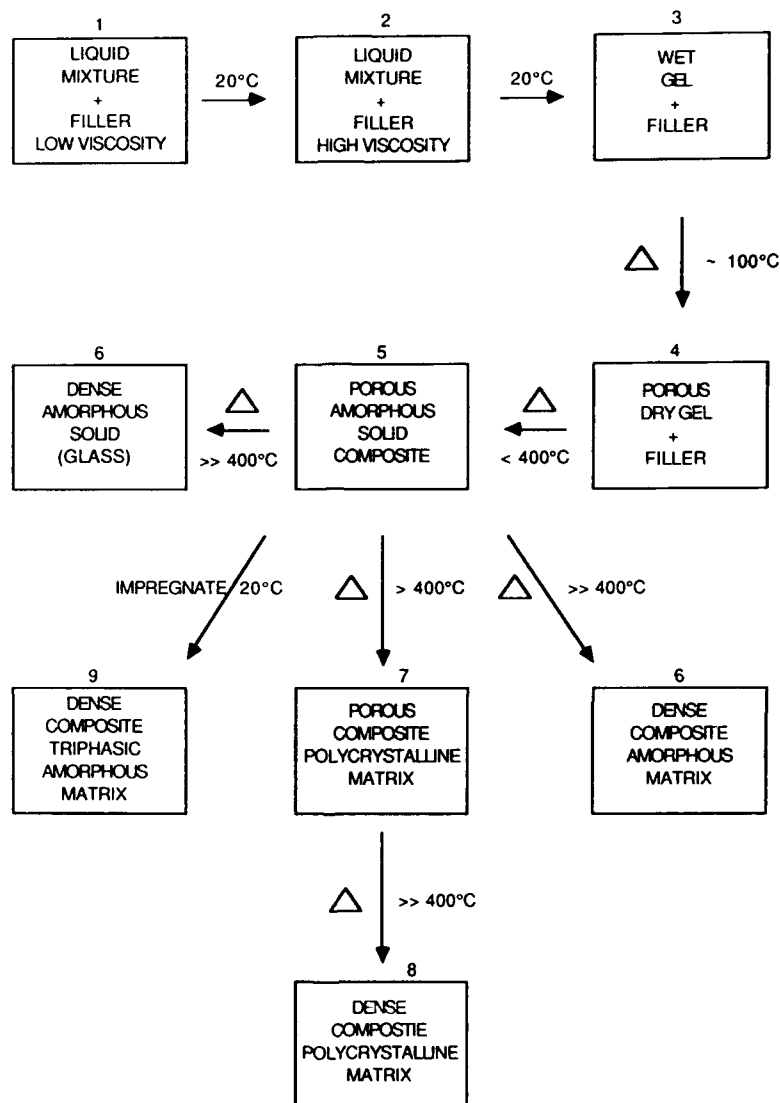
Abbreviations: hw, hot water; cw, cold water.

100 to 1000 P needed for fiberization. It may be argued that such aqueous solutions based on metal salts are at least applicable to the formation of thin films if their viscosities do not permit fiber or tape drawing. However, even for thin films, as the solvent evaporates, one salt could precipitate first while the others are still in solution. This would obviously lead to inhomogeneity. Third, whereas M-O-M bonds are formed at low temperatures for alkoxide-based solutions, mixtures of nitrates or sulfates do not form oxides until very high temperatures are reached. It is uncertain if even thin films can be prepared without reactions with the substrate and/or the creation of uneven film thickness. Partial replacement of alkoxides with salts such as the use of two alkoxides and one salt may permit the formation of viscous solution. However, the dissociation of the salt is still necessary for the formation of oxides. It thus appears that for "ideal"-shaped objects from liquids, the use of metal salts is not recommended.

#### 12.2.5. The Use of Fillers

Because the sol-gel process begins with liquids of low viscosity, fillers can be readily dispersed to form composites. The evolution of various types of composites is shown in Fig. 12.2. In addition to the fabrication of composites such as SiC-SiO<sub>2</sub> [14], the filler can be of the same chemical composition as the gel matrix, for example, colloidal silica in a silica gel. The presence of the filler

# SOME IMPORTANT CONSIDERATIONS FOR FABRICATION 127



**Figure 12.2.** Evolution of the sol-gel-type liquid process from liquid to composites.

not only has a beneficial effect on pore size, but it also reduces overall shrinkage. Dense glasslike solids have been prepared by this method [8]. In general, large objects can be fabricated with composites than for single-phase systems. In addition to increasing the apparent viscosity of the liquid, inert fillers can also affect the microstructure of the gels as illustrated by the example of cubic BN in  $\text{SiO}_2$  to be discussed later. The difference of the thermal expansion coefficients between filler and matrix is obviously of importance in the fabrication of a



shaped object. Depending on the nature of the filler and its shape, surface structure, and thermal history, adsorbed gases can nucleate, and microbubbles can subsequently be trapped during the evolution of the composite microstructure. The removal of such small bubbles after the matrix is partially densified can be a serious problem. The removal of macropores that originate from the shrinkage of a porous gel containing rigid fillers is also a difficult barrier to overcome.

### 12.3. SOME SUCCESSFUL EXAMPLES

Despite the many complexities of the use of sol-gel-type liquids to fabricate shaped objects, there are many successful examples, especially for glasslike silica bodies. Workers of the Seiko Epson Corporation of Japan were able to fabricate dense silica glass sheet as large as  $420 \times 290 \text{ mm}^2$  in 1988 [15]. Recently, the company announced that even larger samples have been prepared. Silica glass tubes 1000 mm in length, with an outside diameter of 25 mm and an inside diameter of 13 mm have also been produced by the same group of workers [16]. Large silica glass preforms and tubes that were used to fabricate high-purity optical fibers were made by Rabinovich and co-workers in 1984 [17]. Shoup has developed an innovative technique based on alkali silicate solutions to fabricate complex fused silica objects [8]. The sol-gel solution route is not only advantageous for the fabrication of silica glass objects at relatively low temperatures. It has also permitted Hench and co-workers to fabricate silica plates with optical properties that are far superior to silica glass prepared by other methods [18]. Following the pioneering of Sakka [19], the Asahi Glass Company of Japan was successful in the development of a continuous process for the manufacture of silica glass fibers in 1987.

There is little doubt that the many successes in fabricating shaped objects based on silica is primarily due to the very extensive research on silica sol-gel science in the past decade. It is probably equally true that because relatively little fundamental research has been carried out on other sol-gel systems, the number of successes are minimal with other oxide systems. With the exception of thin films, most successful fabrications involve glass-forming systems. Large and/or complex shaped objects of polycrystalline oxides fabricated by sol-gel-type liquids are not known, especially for ceramics of low porosity. Frequently, this is because the T-T-T curves for the transformation of the porous amorphous solid to the porous polycrystalline solid (Fig. 12.1, steps 5 to 7) are not available. Second, there has been little research on the transformations of wet gels to non-glass-forming porous dry gels (Fig. 12.1, steps 3 and 4). For an introduction to sol-gel technology for thin films and other specialty objects, the reader is referred to a recent text by L. C. Klein [20]. Even more recent advances are treated elsewhere in this text.

## 12.4. EXAMPLES OF CURRENT RESEARCH

Research is being conducted in this author's laboratory to fabricate various oxides into specific shapes from the sol-gel liquid route with varying degrees of success. These examples should be of interest to those who are not concerned with various shapes of silica glass.

### 12.4.1. Fabrication of a Superconducting $\text{YBa}_2\text{Cu}_3\text{O}_7$ Ceramic

The goals were to fabricate a small rectangular piece of the ceramic with dimensions of  $5 \times 10 \times 1 \text{ cm}^3$  and also to draw continuous fiber. The finished

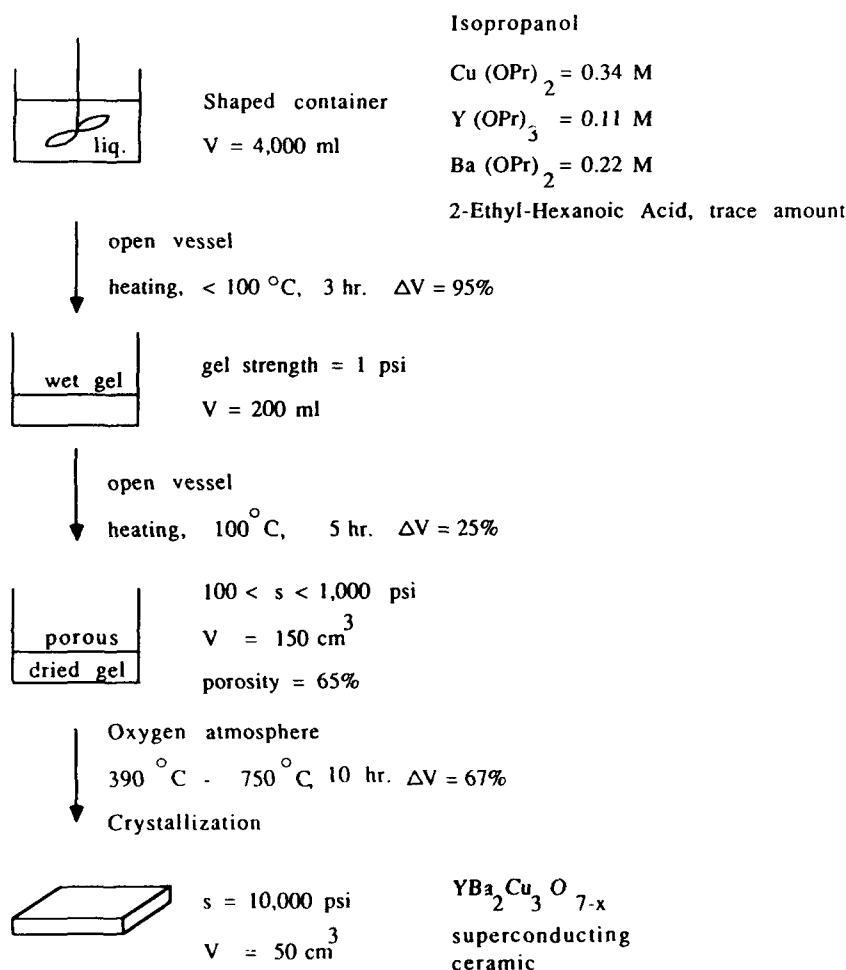


Figure 12.3. Simplified processing steps for the fabrication of a superconducting  $\text{YBa}_2\text{Cu}_3\text{O}_7$  ceramic monolith.

superconducting ceramic should be  $>95\%$  dense. The process for the monolith is illustrated in Fig. 12.3. The first task was to prepare a homogeneous solution based on alkoxides. Viscous solutions are necessary for continuous fibers. Because of the limited solubility of the alkoxides, a initial solution volume of 4000 ml had to be used. Gelation was accompanied by the evaporation of solvent. The wet gel so formed had a volume of only 200 ml. The wet gel then converted to a porous dried gel with further shrinkage. The most difficult task was then to convert this porous amorphous solid into the  $\text{YBaCu}_3\text{O}_7$  compound without the formation of intermediate crystalline phases. T-T-T curves had to be obtained. Finally the porous ceramic was densified to a final volume of 50 ml. The ceramic was a superconductor.

#### 12.4.2. Fabrication of a Superabrasive Disc

The goal was to fabricate a superabrasive disc which was a composite of cubic BN fine particles in a hard oxide matrix. The process is schematically shown in Fig. 12.4. It was not possible to predict the shrinkage behavior of a porous silica matrix containing different concentrations of cubic BN power with dimensions from 0.5 to 10  $\mu\text{m}$ . Figure 12.5 shows the shrinkage of some of these samples.

##### Silica-40vol% Cubic Boron Nitride(CBN) Composite

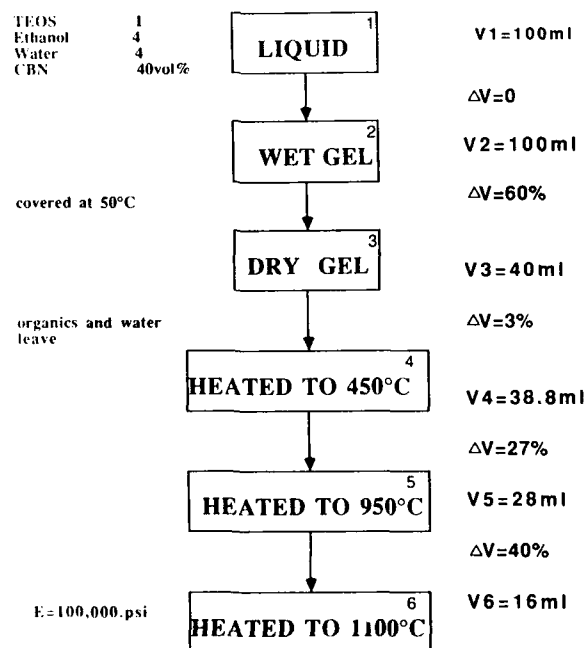


Figure 12.4. Flow sheet for the fabrication of a cubic BN-SiO<sub>2</sub> superabrasive disc.

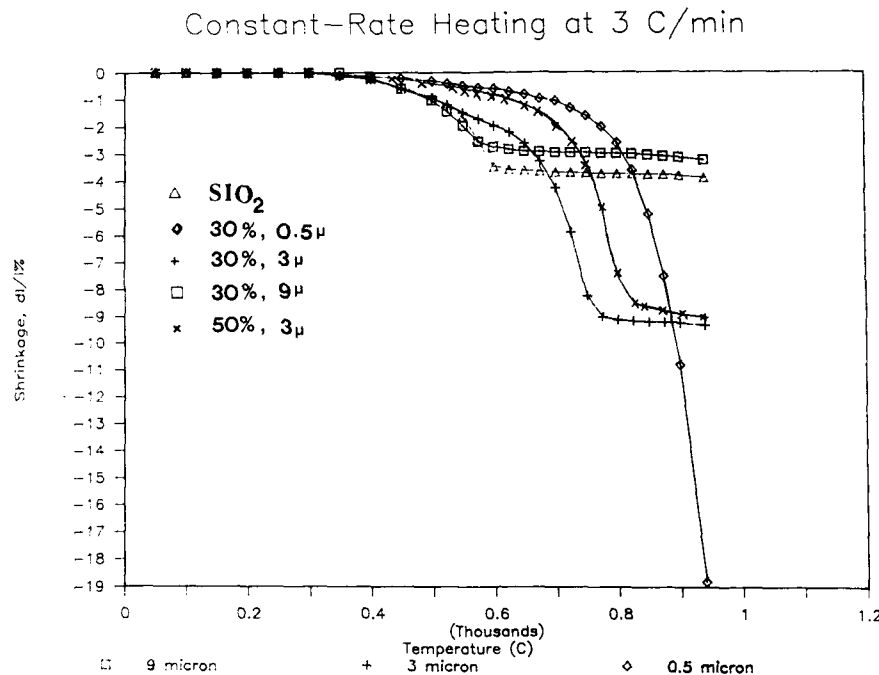


Figure 12.5. Shrinkage behavior of composites based on cubic BN powder dispersed in  $\text{SiO}_2$ .

The dispersion of apparently inert cubic BN powder in the gel resulted in significant changes in the microstructure of the gel and hence its shrinkage characteristic. One remaining problem was the presence of macropores even after heating at  $1100^\circ\text{C}$ .

#### 12.4.3. Fabrication of a Zirconia Porous Bead with 1- $\mu\text{m}$ -Diameter Continuous Pores

The goal was to fabricate an inert sphere for ultrafiltration of contaminated water. Figure 12.6 shows the processing steps leading from liquid to a ceramic porous  $\text{ZrO}_2$  sphere with a diameter of  $\sim 1 \mu\text{m}$ . Because of the geometry and the small size, stress-induced fracture was not a problem. The control of uniform porosity and the suppression of the formation of an impermeable skin on the surface, however, became a difficult problem to solve.

### 12.5. CONCLUSIONS

1. The successful fabrication of silica glass into complex and/or large shapes has been achieved by many workers despite the complexities of the sol-gel

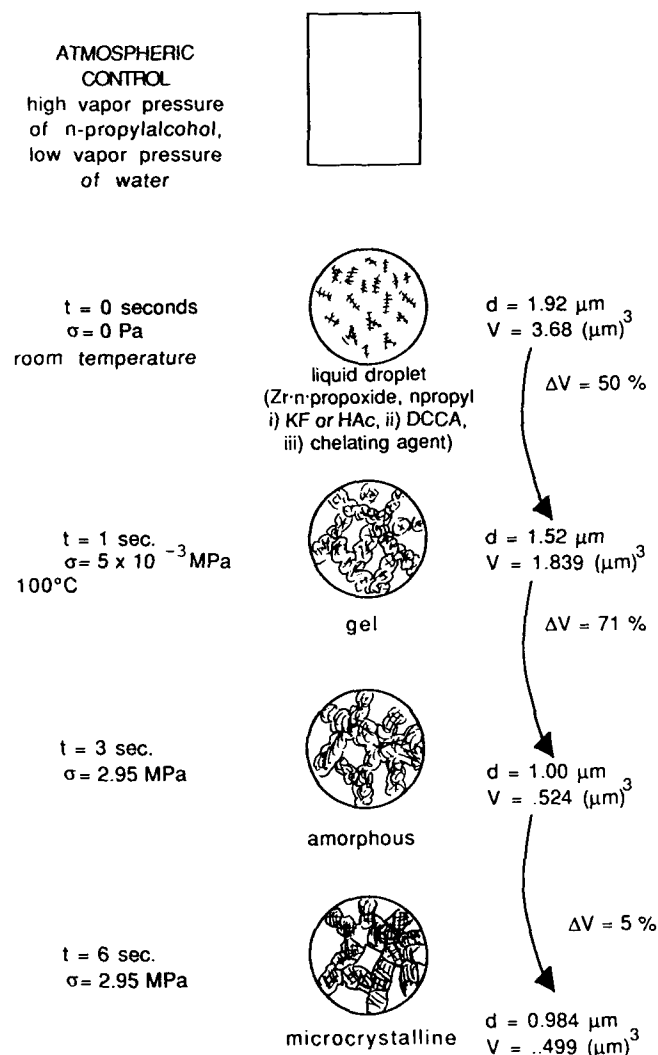


Figure 12.6. Critical steps in the fabrication of a porous  $\text{ZrO}_2$  microsphere.

process. These successes are attributable to the extensive amount of fundamental research on the gelation of silica.

2. There are very few examples of the fabrication of crystalline oxides via the sol-gel liquid route into large and/or complex shapes with the exception of thin films and, perhaps, fibers. This is primarily due to the lack of basic research regarding the evolution of the sol-gel process from gel to ceramic and the chemistry of liquid mixtures used.

## ACKNOWLEDGMENTS

The support of the Directorate of Chemical and Atmospheric Sciences of the Air Force Office of Scientific Research and especially the encouragements of Drs. Donald Ball and Donald Ulrich are gratefully acknowledged. This Chapter was prepared with the assistance of and after many stimulating discussions with Mary Colby, Edward Pope, Azar Nazeri-Eshghi, and Ren Xu.

## REFERENCES

1. E. Wu, K. C. Chen, and J. D. Mackenzie, in C. J. Brinker, D. E. Clark, and D. R. Ulrich, Eds., *Better Ceramics Through Chemistry*, pp. 169-174, North-Holland, New York (1984).
2. S. Yajima, Y. Hasegawa, J. Hayashi, and M. Iimura, *J. Mater. Sci.* **13**, 2569-2567 (1978).
3. J. D. Mackenzie, in L. L. Hench and D. R. Ulrich, Eds., *Science of Ceramic Chemical Processing*, Chap. 12, Wiley, New York (1986).
4. J. C. Wang, *J. Mater. Sci.* **19**, 801-806 (1984).
5. S. A. Khan et al., in C. J. Brinker, D. E. Clark, and D. R. Ulrich, Eds., *Better Ceramics Through Chemistry*, Vol. III, *Mater. Res. Soc. Symp. Proc.*, 73-80 (1988).
6. S. A. Pardenmek, J. W. Fleming, and L. C. Klein, in J. D. Mackenzie and D. R. Ulrich, Eds., *Ultrastructure Processing of Advanced Ceramics*, Chap. 28, Wiley, New York (1988).
7. J. C. Crandall, "Strength porosity relationship of foamed glass." M.S. Thesis, University of California, Los Angeles (1976).
8. R. D. Shoup, in J. D. Mackenzie and D. R. Ulrich, Eds., *Ultrastructure Processing of Advanced Ceramics*, Chap. 25, Wiley, New York (1988).
9. L. L. Hench, in L. L. Hench and D. R. Ulrich, Eds., *Science of Ceramic Chemical Processing*, Chap. 4, Wiley, New York (1986).
10. S. P. Mukherjee, in J. D. Mackenzie and D. R. Ulrich, Eds., *Ultrastructure Processing of Advanced Ceramics*, Chap. 57, Wiley, New York (1988).
11. G. W. Scherer, *J. Non-Cryst. Solids*, **100**, 77-92 (1988).
12. J. D. Mackenzie, in J. D. Mackenzie and D. R. Ulrich, Eds., *Ultrastructure Processing of Advanced Ceramics*, Chap. 43, Wiley, New York (1988).
13. N. Tohge, G. S. Moore, and J. D. Mackenzie, *J. Non-Cryst. Solids*, **63**, 95-103 (1984).
14. E. J. A. Pope and J. D. Mackenzie, in C. J. Brinker, D. E. Clark, and D. R. Ulrich, Eds., *Better Ceramics Through Chemistry*, Vol. II, *Mater. Res. Soc. Symp. Proc.*, 809-814 (1988).
15. M. Toki et al., *J. Non-Cryst. Solids*, **100**, 479-482 (1988).
16. Y. Moru et al., *J. Non-Cryst. Solids*, **100**, 523-525 (1988).
17. E. M. Rabinovich et al., *J. Non-Cryst. Solids*, **63**, 155-161 (1984).
18. L. L. Hench, S. H. Wang, and J. L. Nogués, *SPIE Proc.*, **878**, 76-86 (1988).
19. S. Sakka, *Am. Ceram. Soc. Bull.*, **64**, 1463-1466 (1985).
20. L. C. Klein, Ed., *Sol-Gel Technology for Thin Films, Fibers, Preforms, Electronics and Specialty Shapes*, Noyes Publications, N.J. (1988).

# 13

## SONOGELS—DEVELOPMENT AND PERSPECTIVES

J. ZARZYCKI

Ultrasonic irradiation can be used to promote hydrolysis and polycondensation of alkoxide + water mixtures without the need to add a common solvent. Various analyses show that the *sonogels* obtained in this way differ from classical gels. The dose of ultrasound delivered to the system during the sonocatalytic treatment influences the degree of reticulation of the gel network. The study of mechanical properties of wet gels (Young's modulus,  $K_{IC}$ , and fracture surface energy) constitutes a sensitive way of detecting structural differences that arise from different ultrasonic treatments and following their evolution with time during syneresis. Sonocatalysis offers additional parameters for controlling the time of gelation and thus is potentially interesting in particular for the preparation of dense matrices for various composites by the sol-gel method.

### 13.1. HISTORICAL OUTLINE

The most usual way of preparing gels for the sol-gel process is based on hydrolysis and polycondensation reactions of metal alkoxides. In the case of pure silica, tetramethoxysilane  $\text{Si}(\text{OCH}_3)_4$  (TMOS) or tetraethoxysilane  $\text{Si}(\text{OC}_2\text{H}_5)_4$  (TEOS) are hydrolyzed in the presence of an acid or basic catalyst.

---

*Ultrastructure Processing of Advanced Materials.*

Edited by Donald R. Uhlmann and Donald R. Ulrich (deceased).

ISBN 0-471-52986-9 © 1992 John Wiley & Sons, Inc.

However, because these compounds and water are immiscible, they are dissolved in a common solvent, generally, methyl or ethyl alcohol.

It was reported by Tarasevich [1, 2] that it was possible to avoid the use of this common solvent by submitting the mixture to intense ultrasonic radiation that initiates the reaction when an acid catalyst is added. He gave the name of *sonogels* to gels prepared in this way.

Our group has since undertaken a systematic study of this process in order to understand the possible mechanism and to compare the physicochemical and structural characteristics of sonogels to those of classical gels prepared in the presence of an alcoholic solvent. The systems studied were pure  $\text{SiO}_2$  [3], the binaries  $\text{SiO}_2\text{--B}_2\text{O}_3$  and  $\text{SiO}_2\text{--P}_2\text{O}_5$  [4, 5], and recently the system  $\text{SiO}_2\text{--TiO}_2$  [6], as well as  $\text{SiO}_2\text{--SiO}_2$  composites introducing fine silica particles (Aerosil) [7].

The problem of the solventless preparation of gels has since interested other laboratories; it has been reported [8] that gels can be prepared under magnetic stirring of TMOS–water mixtures. Other ways were proposed that eliminated the need of an alcoholic solvent: hydrolysis of TEOS under high dilution in water, followed by quick-setting by change of pH [9] or hydrolysis of  $\text{SiCl}_4$  vapor in a water bath [10]. The last two methods do not require mechanical agitation, they operate in the presence of an excess of  $\text{H}_2\text{O}$ , which necessitates a syneresis stage to condense the structure and are thus not likely to be used in cases where small shrinkage is required, for example, as in composite matrix synthesis.

Our early investigations of  $\text{SiO}_2$ -based sonogels were mainly directed toward the characterization of the resulting gels and their behavior under oxidation and densification treatments. Systematic studies combining differential thermal analysis, thermogravimetric analysis, Brunaur–Emmett–Teller, and infrared spectroscopy have clearly shown that the behavior of sonogels during heat treatment differs from that of classic gels. The release of OH and of organic residues is more spread out in time, and the sequences observed point to the presence of several kinds of sites possibly linked with a very fine porosity of sonogels. The density of the sonogels has been shown to be higher than that of corresponding classic gels, which is normal in view of the initial absence of a solvent.

The porosity can be exceedingly fine as is revealed by small-angle X-ray scattering measurements [11], the size of the pores being of the order of 10–20 Å. These gels do not possess, after drying, a structure that would justify the use of “fractal” concepts. The density of the matrix at the elementary grain level (30 Å) deduced from combined small-angle X-ray scattering and Brunaur–Emmett–Teller data is also higher than that of the classic gels. In the case of multicomponent systems  $\text{SiO}_2\text{--B}_2\text{O}_3$  and  $\text{SiO}_2\text{--P}_2\text{O}_5$  the losses of the more volatile components  $\text{B}_2\text{O}_3$  or  $\text{P}_2\text{O}_5$  are smaller compared to the classic counterparts, which indicates a more intimate incorporation into the structure. This was confirmed by programmed thermal decomposition analysis coupled with mass spectroscopy. These losses are smaller both in the wet preparation



stage and during hypercritical solvent evacuation when aerogels are prepared [4].

The conversion into glasses of the aerogels obtained from sonogels is quicker, due to the larger surface associated with the exceedingly fine porosity, but necessitates prior careful oxidation and elimination treatments to eliminate the last firmly entrapped residues that may sometimes prove more difficult than for classic gels.

### 13.2. SONOCATALYSIS

The study of the gelation process as a function of the ultrasonic irradiation dose and at stabilized temperatures was undertaken in an attempt to better understand the mechanism at work. The action of ultrasound undoubtedly produces an atomization effect, emulsifying the water-alkoxide mixture and provoking a release of alcohol, which in turn accelerates the homogenization process. A simple mixing may be effective in the case of TMOS-water mixture [8], but is insufficient for the less reactive TEOS.

An additional effect is provided by cavitation phenomena, which has been studied in various polymerization and depolymerization reactions. Cavitation produces extreme pressures and hot spots in the liquid during the collapse of vapor bubbles in the liquid submitted to the ultrasonic waves.

Two theories were proposed: one based on the presence of resonating bubbles [12], the other on the transient collapse of bubbles [13, 14]. Basically, as an ultrasonic wave propagates, a microcavity is formed in the low-pressure phase at a nucleus, which may be constituted, for example, by a gas bubble. This cavity expands quasi-isothermally and becomes filled with the vapors of the reactants. At some point during the high-pressure phase, the cavity suddenly collapses adiabatically, which leads to an extremely high temperature increase (hot spots). At this point the reaction takes place in the gas phase inside the collapsing bubble. Although the concept of "temperature" must be considered here with care, local hot spot temperatures up to several thousand degrees have been calculated using these models. In water-containing solutions, one of the reactions is the production of radicals, as in numerous organic systems reactions are not obtained when water is not present.

Cavitation phenomena are notoriously enhanced by the presence of foreign particles that act as vapor nucleation sites. We have observed that the sonocatalytic process is indeed speeded up by the presence of fine silica particles such as Aerosil and also by dissolved gases. A very high-speed (20,000 T/min) rotary blender (which also induces cavitation effects) may be used to promote homogenization of TEOS + H<sub>2</sub>O mixture, although the effects are less regular and less easy to control than with ultrasound [15].

Detailed ultrasonic studies have shown [5] that at constant temperature the time for gelation  $t_G$  is directly related to the sonication dose  $U_s$ , or energy delivered to the system.

A threshold for gelation was observed at  $U_s \approx 270 \text{ J/cm}^3$ , and for  $U_s \geq 1200 \text{ J/cm}^3$  gelation took place in the container during insonation. Experiments have further shown that two regimes are present, separated by a level  $U_s \approx 600 \text{ J/cm}^3$  (Fig. 13.1). The activation energies for the process are around 12 kcal/mol for lower doses and 15–18 kcal/mol for doses higher than  $600 \text{ J/cm}^3$ .

These two regimes were correlated on the basis of infrared spectroscopic studies with respectively predominant hydrolysis and polycondensation stages [4]. At the highest irradiation doses, a reesterification mechanism could also be operating.

These studies have clearly shown that the irradiation dose  $U_s$  constitutes an additional parameter that can be used to control the textures of the resulting gels. In particular, the degree of reticulation closely depends on  $U_s$ , as can be seen from the studies of the elastic properties of wet gels.

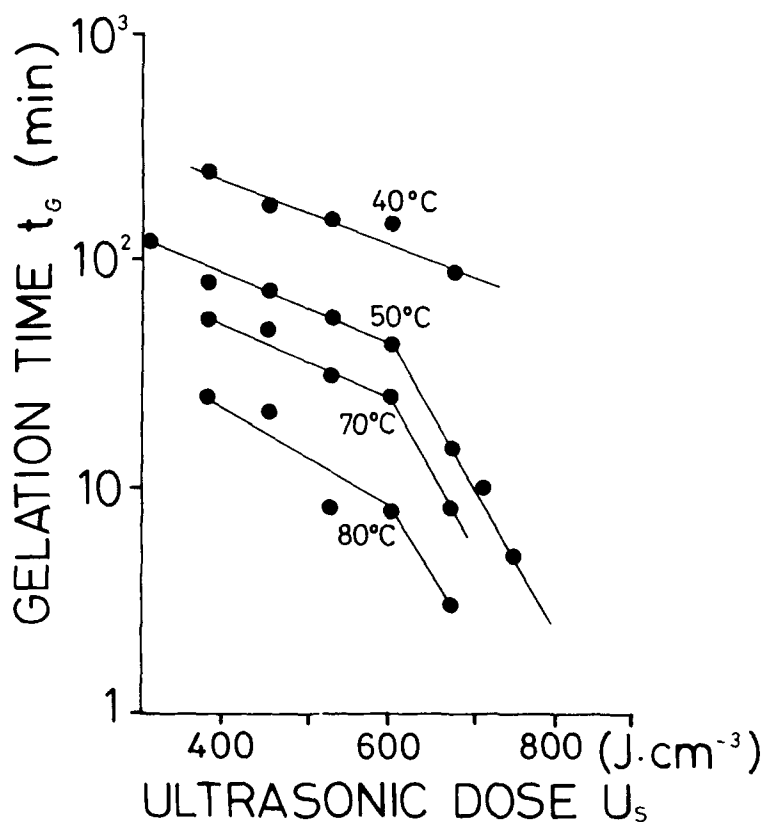


Figure 13.1. Evolution of the gelation time  $t_g$  for  $n = [\text{H}_2\text{O}]/[\text{TEOS}] = 4$  mixtures as a function of irradiation dose  $U_s$  for various temperatures. (After [5], corrected\*).

## 13.3. VISCOELASTIC PROPERTIES OF WET SONOGELS

The study of viscoelastic and fracture properties of wet gels have been systematically undertaken as preliminary studies [16] showed that these characteristics are very sensitive to the way in which the gel is prepared and can directly reveal variations in the initial state of reticulation of the wet gel before any subsequent drying processes can alter the structure.

The elastic modulus was measured by a method based on the Hertzian contact of a sphere pressed under a known load on the surface of the gel. In this way the quantity  $E' = E/(1 - \nu^2)$ , where  $E$  is Young's modulus and  $\nu$ , the Poisson's ratio, can be obtained [5].

Figure 13.2 shows the variation of  $E'$  as a function of time for  $\text{SiO}_2$  sonogels obtained with different  $n = [\text{H}_2\text{O}]/[\text{TEOS}]$  ratios and submitted to various sonication doses  $U_s$ .

It can be seen that while  $E'$  varies strongly with time (1 to 2 orders of magnitude) due to continuing crosslinking and syneresis effects, the limiting levels attained are functions both of  $n$  and  $U_s$ , and a direct comparison of the

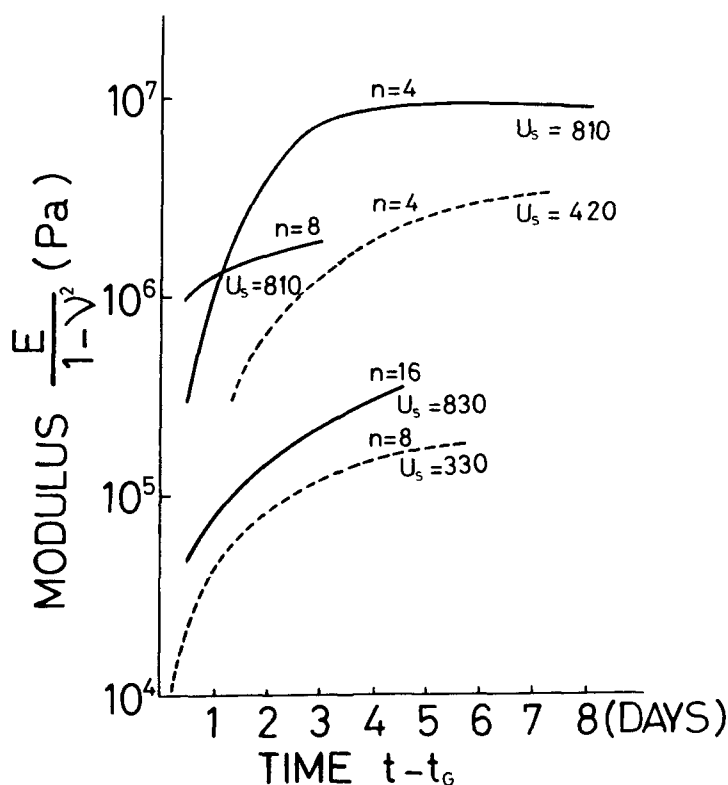


Figure 13.2. Evolution of the elasticity modulus  $E/(1 - \nu^2)$  as a function of time for  $\text{SiO}_2$  gels with different  $n = [\text{H}_2\text{O}]/[\text{TEOS}]$  ratios and for different irradiation doses  $U_s$ . (After [5], corrected \*).

effects of these two parameters is possible. Increased water content ( $n$  higher) promotes a more complete hydrolysis and polycondensation. For a fixed water content a similar effect can be brought about by increasing the irradiation dose. This is reflected in the elastic properties of the resulting gel: The final level of the modulus  $E'$  is seen to increase. It can be seen that the order of magnitude of  $E'$  depends on the  $U_s/n$  ratio: 5 days after gelling  $E'$  attains  $10^5$ -,  $10^6$ -, and  $10^7$ -Pa levels for  $U_s/n$  ratios approximately equal to 50, 100, or 200, respectively.

Critical stress intensity factors  $K_{IC}$  of wet  $\text{SiO}_2$  sonogels were measured by a specially designed method using a notched bar tested in tension [16].  $K_{IC}$  values thus obtained have also shown dependence on the irradiation dose.

Drying chemical control additives (DCCA) are generally used to facilitate drying of gels in a monolithic state [17]. Other additives are necessary in cases where modification of rheological characteristics is essential, for example, in fine patterning of surfaces obtained by the sol-gel method [18].

We have recently undertaken a general study to evaluate the influence of ultrasound on these systems. TEOS- or TMOS-based systems containing formamide, glycerol, polyethylene glycol, and so on in various concentrations were studied for various ultrasonic irradiation doses. In all cases a definite influence of the irradiation dose on resulting properties was detected. As an

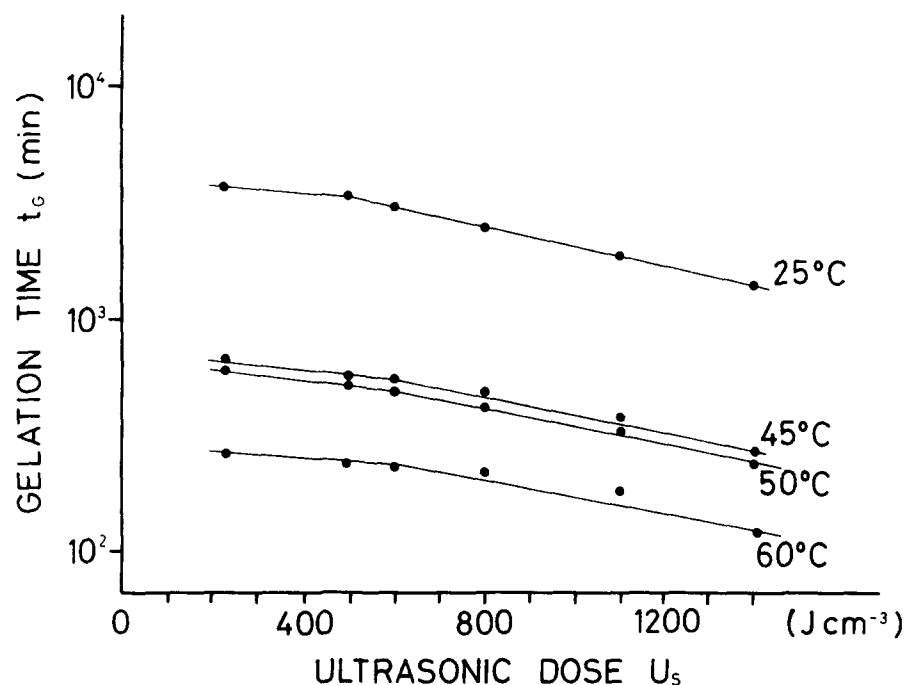


Figure 13.3. Evolution of the gelation time  $t_G$  for mixtures with  $[\text{H}_2\text{O}]/[\text{TEOS}] = 4$  and  $[\text{glycerol}]/[\text{TEOS}] = 2.5$  ratios at different temperatures as a function of the irradiation dose  $U_s$ .

example some results of the study of TEOS-glycerol series will be presented. A full experimental account will be published elsewhere [19]. In all the cases presented here the molar ratios were

$$[\text{glycerol}]/[\text{TEOS}] = 2.5 \quad \text{and} \quad [\text{H}_2\text{O}]/[\text{TEOS}] = 4$$

with pH of added water equal to 1.5.

Figure 13.3 shows the influence of the irradiation dose  $U_s$  on the gelling time  $t_G$  at various temperatures. The results are similar to those of pure TEOS already presented and show distinctly two regions for  $U_s < 600 \text{ J/cm}^3$  and  $U_s > 600 \text{ J/cm}^3$ . However, the magnitude of the ultrasonic effect on  $t_G$  is less pronounced here than for pure TEOS certainly due to the dilution effect by the additive.

The average activation energy of the gelling process is close to 14 kcal/mol for the different  $U_s$  values as shown in Fig. 13.4. The density of the wet gels shows a regular increase with  $U_s$  (Fig. 13.5), the important scatter being attributable to various aging levels.

To quantify the effect of ultrasound, a study of Young's modulus was used that definitely shows (Fig. 13.6) that the insonation dose  $U_s$  determines both the speed of evolution of the modulus during aging and the final level attained by  $E'$ , which is evidently correlated to the degree of crosslinking of the solid phase.

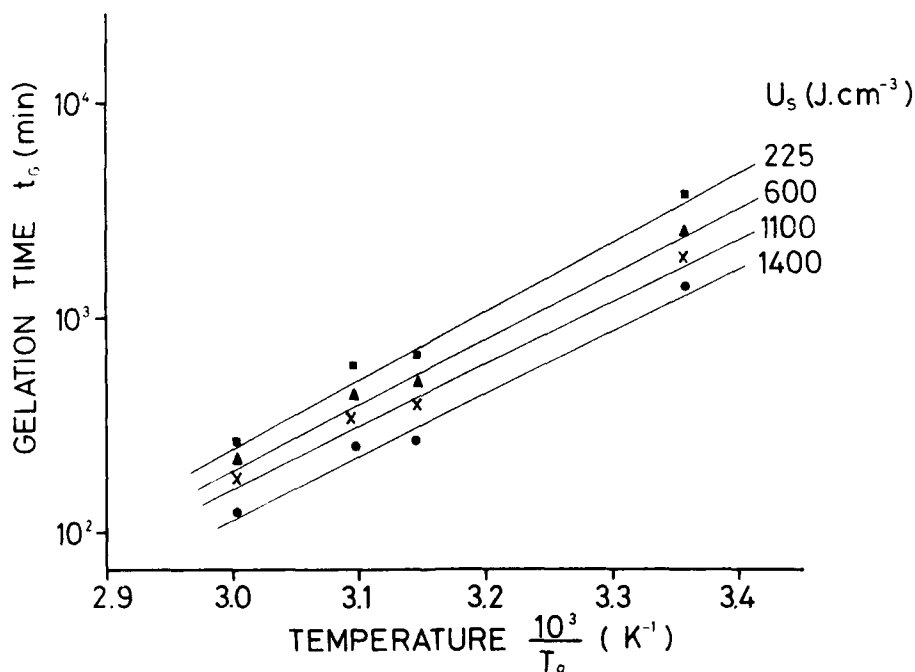


Figure 13.4. Gelation time  $t_G$  as a function of temperature for gels in Fig. 13.3.

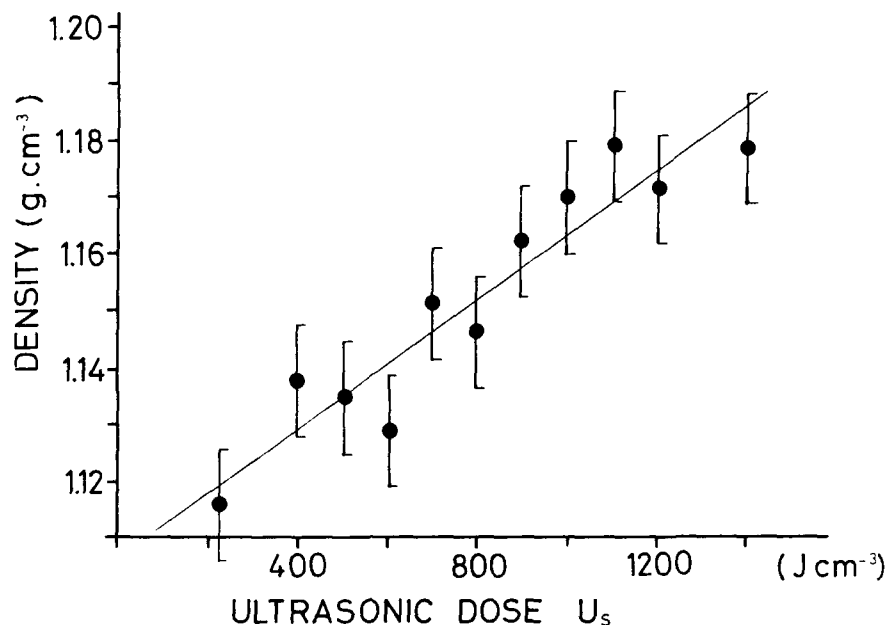


Figure 13.5. Density of wet gels obtained with  $[H_2O]/[TEOS] = 4$  and  $[glycerol]/[TEOS] = 2.5$  ratios as a function of the irradiation dose  $U_s$ .

The corresponding evaluation of  $K_{IC}$  factors at different stages of aging similarly shows the influence of  $U_s$  on the toughness of the wet gels. The fracture surface energy  $\Gamma$ , which can be obtained from the preceding measurements by the classic relation

$$\Gamma = \frac{K_{IC}^2(1-\nu^2)}{2E} = \frac{K_{IC}^2}{2E'}$$

is shown in Fig. 13.7 as a function of  $E'$ , which constitutes a convenient parameter characterizing the degree of aging.

It can be seen that  $\Gamma$  decreases during aging and levels off to a constant value for  $E' > 10^6$  Pa. The higher initial values of  $\Gamma$  are attributable to a strong anelastic component that diminishes with aging. The freshly prepared gels show initially a sticky behavior, then a rubberlike stage, after which brittleness sets in definitively.

The limiting values of the fracture surface energy  $\Gamma$  are seen to tend on average toward

$$\Gamma = 0.025 \pm 0.01\ J/m^2$$

As the final  $\Gamma$  values were shown to be correlated with the hydration energy of the solid fraction exposed during fracture [16], this indirectly demonstrates

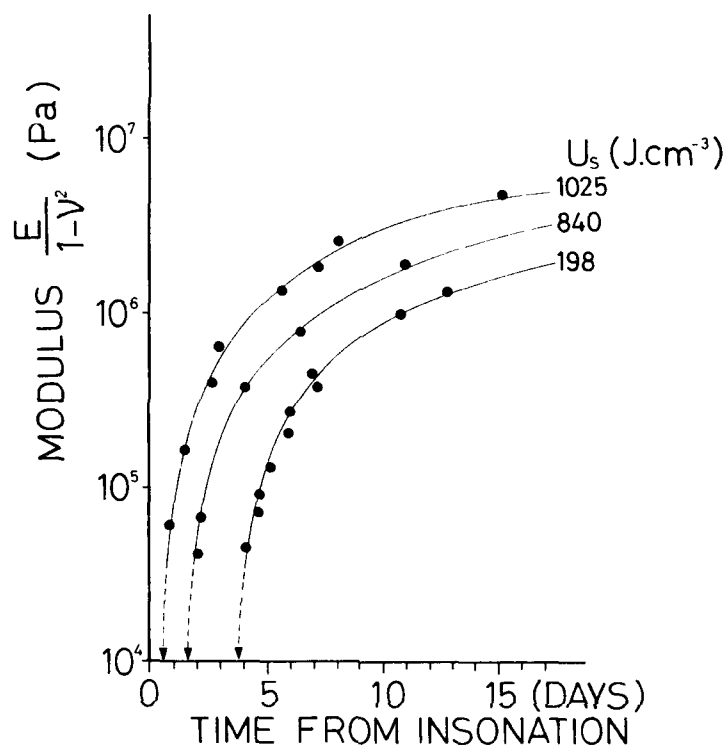


Figure 13.6. Evolution of the elastic modulus  $E/(1-\nu^2)$  for  $\text{SiO}_2$  gels obtained from  $[\text{H}_2\text{O}]/[\text{TEOS}] = 4$  and  $[\text{glycerol}]/[\text{TEOS}] = 2.5$  mixtures as a function of time after insonation for different irradiation doses  $U_s$ .

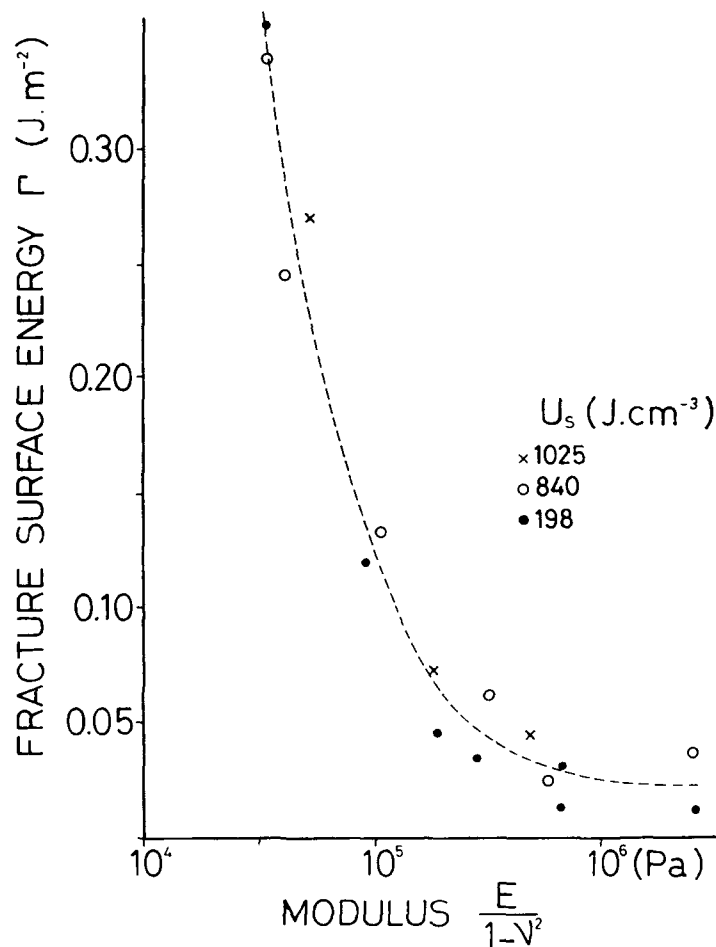
the higher degree of final crosslinking attained for samples having experienced larger  $U_s$  doses and that is not much modified during subsequent aging. The solid-phase fraction of these wet gels can be estimated at  $x = 0.1$  to  $0.15$ . For the values of surface energy of the  $\text{SiO}_2/\text{H}_2\text{O}$  interface  $\gamma \approx 0.129$  to  $0.142 \text{ J/m}^2$  given by Iler [20], this would correspond to values of  $\Gamma = x\gamma$  ranging from  $0.013$  to  $0.022 \text{ J/m}^2$ , which is in good agreement with the experimentally found average.

In spite of the inevitable scatter it can be seen that the final level of  $\Gamma$  seems to depend on the initial irradiation dose  $U_s$ , the lowest values of  $\Gamma$  corresponding to lower irradiation doses  $U_s$ .

A more complete study of the evolution of the rheological characteristics was undertaken with the spherical penetrometer already used for  $E'$  determinations. Under constant load  $P$  the wet gel shows a deformation  $\delta(t)$  function of time, which can be used to measure the compliance  $J(t)$  from an expression

$$J(t) = KR^{\frac{1}{2}}P^{-1}\delta^{\frac{1}{2}}$$

where  $R$  is the radius of the sphere and  $K$ , a constant.



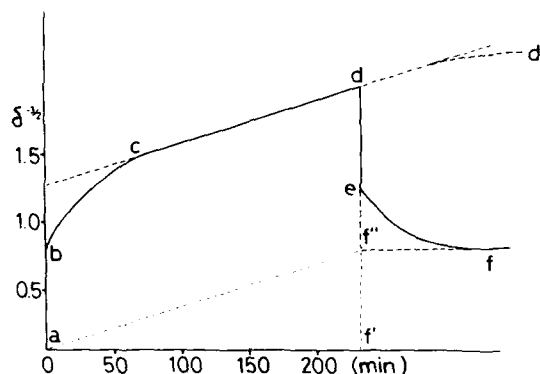
**Figure 13.7.** Evolution of the fracture surface energy  $\Gamma$  for SiO<sub>2</sub> gels obtained from [H<sub>2</sub>O]/[TEOS] = 4 and [glycerol]/[TEOS] = 2.5 mixtures as a function of elastic modulus  $E' = E/(1 - \nu^2)$  for different irradiation doses  $U_s$ .

A typical experimental result for the preceding gels is shown in Fig. 13.8. Upon application of the load the instantaneous elastic deformation (*ab*) is followed by an anelastic transition (*bc*) and a viscous flow deformation (*cd*), where  $\delta_1$  is seen to vary linearly with time.

For prolonged holdings (depending on the age of the gel) after the linear portion (*cd*) a curved portion (*dd'*) is observed with a continuously decreasing slope, which shows a secondary relaxation mechanism. Upon unloading, the gel shows an instantaneous elastic recovery (*de*) followed by an anelastic recovery (*ef*), which leaves a permanent deformation (*f'f''*).

This type of creep curve can be interpreted by a viscoelastic model of a liquid.





**Figure 13.8.** A typical creep curve obtained for a silica-glycerol gel ( $\delta^2$  in relative values). *ab*, instantaneous elastic deformation; *bc*, anelastic deformation; *cd*, viscous flow; *de*, elastic recovery; *ef*, anelastic recovery; *f'f''*, permanent deformation due to viscous flow.

From the steady-state slope of the initial linear portion (*cd*) (or of the parallel of ") the viscosity of the gel can be evaluated.

In the case of gels the measurements are complicated by the fact that the system is composed of a solid network phase filled with liquid. For instantaneous solicitation the system behaves as if it were incompressible (i.e.,  $\nu = \frac{1}{2}$ ) while for static situations  $\nu \sim 0$  [21, 22]. This effect has been taken into account in the calculation of the axial viscosity  $F$  shown in Fig. 13.9 and of the axial relaxation time  $\tau_a = F/E$  shown in Fig. 13.10.

Figure 13.9 shows the evolution  $F$  as a function of time, which corresponds to the values of  $E' = E/(1 - \nu^2)$  already shown in Fig. 13.6 for different values of the insonation dose  $U_s$ . It can be seen that viscosity follows the evolution of  $E'$ , but if the relaxation time is considered (Fig. 13.10) the difference in behavior appears quite distinctly according to the initial insonation dose. For a high dose ( $U_s = 1025 \text{ J/cm}^3$ ) the relaxation time steadily increases with time, which reveals a progressive strengthening of the network, whereas for a low dose ( $U_s = 198 \text{ J/cm}^3$ ) the system quickly reaches a constant level, which does not seem to evolve with age.

These smaller  $\tau_a$  values correspond to a lesser reticulation state of the wet gel, which is seen to persist even after prolonged aging.

### 13.4. CONCLUSION

The various methods examined clearly indicate that the structure of wet sonogels and their viscoelastic behavior depend on the insonation dose used in sonocatalysis. Besides the gelling time, the density, degree of syneresis, elastic, and viscoelastic parameters can be readily modified by this method by varying the ultrasonic energy delivered to the system. The insonation dose thus represents an additional parameter that can be used together with temperature

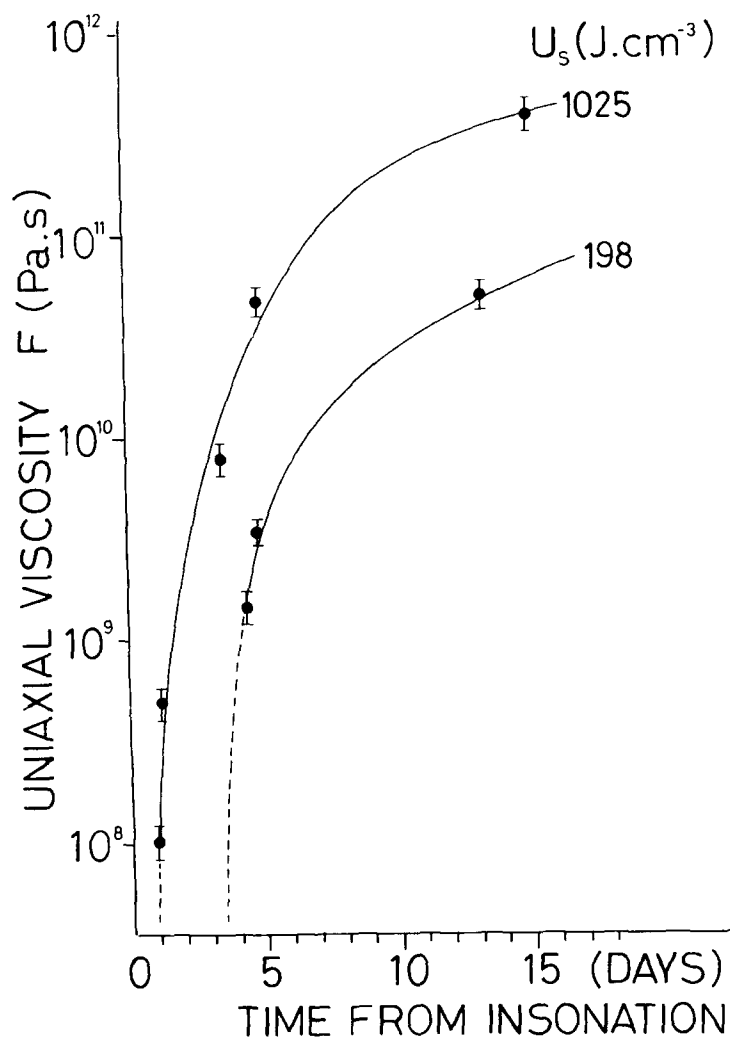
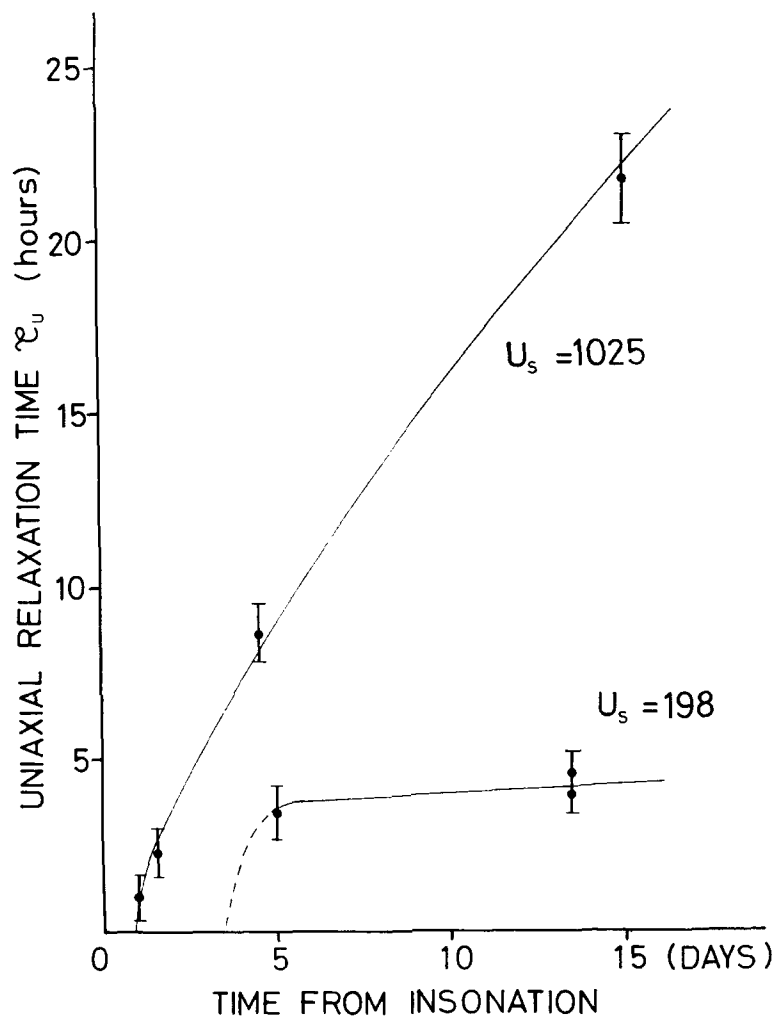


Fig. 13.9. Evolution of the uniaxial viscosity  $F$  with time calculated from the linear portion of the creep curve (assuming  $\nu = 0$  for Poisson's ratio) for  $\text{SiO}_2$ -glycerol gels obtained with different irradiation doses  $U_s$ .

and pH to modify both the gelling kinetics and the resulting viscoelastic properties of a given gel.

In view of the potential value of sonocatalysis in the preparation of gels where their properties must be tailored for particular techniques, it is important to evaluate quantitatively the insonation effects starting with the gels in the wet stage. We have shown that this is possible using fairly simple methods.



**Figure 13.10.** Evolution of the uniaxial relaxation time  $\tau_u = F/E$  for  $\text{SiO}_2$ -glycerol gels obtained with different irradiation doses  $U_s$ .

## REFERENCES

1. M. Tarasevich, in: *86 Annual Meeting of the American Ceramic Society*, Pittsburgh, May 2, 1984. *Cer. Bull.*, **63**, 500 (1984) (abstract).
2. M. Tarasevich, 3rd International Conference on Ultrastructure Processing of Ceramics, Glasses and Composites, Palm Coast, FL, February, 1985 (poster).
3. L. Esquivias and J. Zarzycki, Study of silica gels obtained by ultrasonic treatment of silicon alkoxide, in: M. D. Baro and N. Clavaguera, Eds., *Current Topics on Non-Crystalline Solids*, pp. 409-414, World Scientific, Singapore (1986).

4. L. Esquivias and J. Zarzycki, Sonogels: An alternative method in sol-gel processing, in: J. D. Mackenzie and D. R. Ulrich, Eds., *Ultrastructure Processing of Advanced Ceramics*, Proc. Conf. February 23–27, 1987, San Diego, Calif., pp. 255–270, Wiley, New York (1988).
- 5.\* N. de la Rosa-Fox, L. Esquivias, and J. Zarzycki, Glasses from sonogels, in: R. A. Weeks and D. L. Kinser, Eds., *Effects of Modes of Formation on the Structure of Glass*, 2nd International Conference, Nashville, Tenn., June 8–11, 1987, pp. 363–373, Trans. Tech. Publ., Switzerland (1987) (see note \*).
6. M. Ramirez, L. Esquivias, N. de la Rosa Fox and J. Zarzycki, *J. Non-Cryst. Solids* **121**, 84 (1990).
7. M. Atik, Ph.D Thesis, University of Montpellier (1990).
8. D. Avnir and V. R. Kaufman, *J. Non-Cryst. Solids*, **192**, 180–182 (1987).
9. W. M. Jones and D. B. Fischbach, *J. Non-Cryst. Solids*, **101**, 123–126 (1988).
10. J. W. Flemming and S. A. Flemming, Vapogel a new glass-forming technique, presented at Materials Research Society Meeting, April 5–9, 1988, Reno, Nev.
11. N. de la Rosa Fox, L. Esquivias, and J. Zarzycki, *J. Mater. Sci. Lett.*, **10**, 1237 (1991).
12. M. E. Fitzgerald, V. Griffing, and J. Sullivan, *J. Chem. Phys.*, **25**, 926 (1974).
13. B. E. Nolting and E. A. Nepiras, *Proc. Phys. Soc.*, **B-63**, 674 (1950).
14. D. J. Donaldson, M. D. Farrington, and P. Kruss, *J. Phys. Chem.*, **83**, 3130 (1979).
15. M. Ramirez, N. de la Rosa Fox, L. Esquivias, and J. Zarzycki, *J. Non-Cryst. Solids*, **121**, 40 (1990).
16. J. Zarzycki, *J. Non-Cryst. Solids*, **100**, 359–363 (1988).
17. L. L. Hench, Use of drying control chemical additives (DCCA's) in controlling sol-gel processing, in: L. L. Hench and D. R. Ulrich, Eds., *Science of Chemical Processing*, pp. 52–64, Wiley, New York.
18. N. Tohge, A. Matsuda, T. Minami, Y. Matsuno, S. Katayama, and Y. Ikeda, *J. Non-Cryst. Solids*, **100**, 501–505 (1988).
19. J. Zarzycki. Submitted for publication.
20. R. K. Iler, *The Chemistry of Silica*, Wiley, New York (1979).
21. T. Tanaka, L. O. Hocker, and G. B. Benedek, *J. Chem. Phys.*, **59**, 5151 (1973).
22. G. W. Scherer, S. A. Pardenek, and R. M. Swiatek, *J. Non-Cryst. Solids*, **107**, 14–22 (1988).

\*Note. In Reference 5 the  $U_s(J/cm^3)$  values are incorrect and must be multiplied by 50.

# 14

## BIOMIMETIC PROCESSING OF CERAMICS AND COMPOSITES

PAUL CALVERT

### 14.1. INTRODUCTION

Biological systems have been in existence for around 4.1 billion years. Materials issues were presumably not important for single-celled organisms, but became crucial to survival for larger creatures, particularly since the appearance of the invertebrates 600 million years ago. In looking at the structures of organisms we could be surprised at the limited range of materials that are used and at the diversity of microstructure. Thus most plants are built out of cellulose and all vertebrates rely on collagen to withstand tensile forces. However, there is in each case a great variety of forms of the material. Collagen appears as a pure tensile fiber in tendon, a reinforcement for an elastic sheet in skin, and a mineral-reinforced matrix in bone. Biology seems to have displayed little versatility in the chemistry of structural materials, but shows great subtlety in processing to obtain different properties. Manufactured materials have tended to follow the opposite track. There are now almost as many "engineering" thermoplastics as there are applications, but most are used pure or with a simple reinforcement.

The biological approach to structural materials and to materials for sensors and actuators is different to the synthetic approach. What follows is a brief description of a number of biological materials, an attempt to extract some general principles from these examples, and a discussion of our own efforts to

---

*Ultrastructure Processing of Advanced Materials.*

Edited by Donald R. Uhlmann and Donald R. Ulrich (deceased).

ISBN 0-471-52986-9 © 1992 John Wiley & Sons, Inc.

## **150 BIOMIMETIC PROCESSING OF CERAMICS AND COMPOSITES**

duplicate biological processing methods. This Chapter focuses on ceramics and composites, but polymeric materials could be treated similarly.

### **14.2. EXAMPLES OF BIOLOGICAL MATERIALS**

#### **14.2.1. Magnetic Bacteria**

In 1975 Blakemore [1] described magnetotactic, which live in the substantially anaerobic mud of marine and lake beds. A chain of magnetite particles allows these organisms to orient themselves along the earth's magnetic field and so, presumably, to be able to swim back downward to their low-oxygen habitat if they are displaced. The magnetite particles are each 40–100 nm in diameter and form a chain down the axis of the bacterium [2]. They are surrounded by a membrane. The details are unclear of the deposition of the particles, but probably involves uptake of chelated  $\text{Fe}^{3+}$  iron by the cell and reduction to  $\text{Fe}^{2+}$  at the membrane surrounding the magnetic organelle to allow transport through the membrane and then reoxidation and precipitation of ferrihydrite within. Subsequent reduction of some of the iron converts the soft ferrihydrite gel to magnetite [3].

#### **14.2.2. Sponge Spicules**

The skeletons of the sponges are formed from elongated spicules of various complex shapes [4]. These form within a space surrounded by a membrane, the silicalemma. Electron microscopy shows the presence of small silica particles inside the membrane, suggesting that silica may be formed on the outer membrane surface and then transported through as colloidal particles, which diffuse across the space to deposit on the growing spicule.

The core of the spicule contains a thread of polymer, either polysaccharide or protein, of about  $0.1\text{ }\mu\text{m}$  in diameter and in the shape of the final spicule. Apparently this acts as a former on which the silica is deposited. Subsequent growth would then be by preferential deposition on the outer surface. This implies that by control of the concentration and pH nanoparticles of silica can be used to grow complex structures on a patterned substrate.

#### **14.2.3. Mollusc Shell**

Mollusc shell is calcium carbonate with a small quantity of protein surrounding each of the crystallites. There are various designs that seem to be appropriate for protection from the main predators of each species of mollusc. Both calcite and aragonite are found in different arrangements of fibers, rods, and plates. Aragonite does not form during any synthetic precipitations. Nacreous shell is the most spectacularly ordered form with parallel layers of aragonite plates of about  $0.5\text{ }\mu\text{m}$  thick and a few micrometers in diameter. In some species there are

also common  $a$  and  $b$  axes within the layers. From micrographs of Nakahara [5] the shell apparently grows by nucleation of each plate at a site on the compartment membrane. As each plate grows within its compartment, it is apparently surrounded by another membrane. It should be remembered, however, that it is exceedingly difficult to prepare electron micrographs of biological tissue without artifacts. The nucleation of the aragonite is discussed below.

What we see from this structure is that it is possible to form essentially fully dense ceramic shapes by direct precipitation. Further, the particles need not be equiaxed, but may be highly elongated for greater toughness. It is also possible to use polymeric nucleation catalysts to promote deposition of unusual polymorphs and to define a point of nucleation. Further the polymer structure can define an epitaxial relationship with the crystal.

#### 14.2.4. Bone

Bone is a highly developed material with very different microstructure at different sites. In essence it is collagen reinforced by hydroxyapatite. Aspects of interest to materials scientists include its piezoelectric properties, its ability to absorb and reform to counteract the highest levels of stress, the transitions from narrow dense shafts to broad porous heads to allow efficient transfer of stress at articular joints, and the directional porosity, which allows blood vessels to penetrate the structure without severely weakening it. This is a good example of how microstructure and design should be integrated throughout a component.

Our own interest has focused on mimicking possible growth mechanisms of bone. There is still considerable uncertainty about the biological mechanism, but the following outline seems feasible. Long bones grow by the movement of a mineralization zone (the growth plate) into preexisting cartilage. Blood supply to the cartilage transports in the needed calcium, and phosphate. In the growth zone there appear matrix vesicles, which are rich in phosphate and may be satellites of the chondrocytes. There is also an enhanced activity of phosphatase in the region. Within or around the matrix vesicles form randomly arranged hydroxyapatite crystals. The phosphatase may be removing pyrophosphate or other crystallization inhibitors. There is a strong tendency for dead tissue to calcify, suggesting that continuous pyrophosphate (or other inhibitor) production is necessary to prevent hydroxyapatite deposition in normal tissue. In fully developed bone the mineral is aligned parallel to the direction of the collagen fibers, suggesting an epitaxial nucleation role for the collagen. There are studies that discuss the nature of this relation and the possibility of nucleation within the gaps at the end of individual collagen fibrils within the fiber. The evidence for initial random nucleation and for resorption mechanisms suggests that this relation develops during a ripening process involving dissolution and regrowth rather than being a product of nucleation. The crystals in bone are typically

## **152 BIOMIMETIC PROCESSING OF CERAMICS AND COMPOSITES**

plates 10 nm thick by 50 nm wide. Those in tooth enamel are much larger, and synthetic hydroxyapatite crystals are generally larger still.

It is clear from this that the organic cartilaginous bone matrix is exerting considerable control on the precipitation of the crystals within it, both in terms of orientation and size. These mechanisms must be duplicable synthetically, but do not fall naturally within our current understanding of nucleation and growth control.

### **14.2.5. Macadamia Shells**

The macadamia nut is notoriously difficult to crack and there has been much research on improved methods for shelling [6]. The structure of the nut shell is essentially a dense fibrous mass, an isotropic wood with a density of  $1.3 \text{ g/cm}^3$ . The fibers are arranged into bundles with the bundles randomly oriented so as to fill 100% of the volume. As a result there is a great potential for crack deflection, but no easy crack path. It would be most interesting to duplicate this structure with ceramic fibers, but it is apparently impossible as long as we start with fibers and try to pack them. Rather, we must arrange to grow the fibers in place to form a ceramic green body.

## **14.3. UNDERLYING MECHANISMS**

The sections above describe a number of biological materials that have lessons to teach us about how synthetic materials may be improved in ways that are not obviously extensions of current lines of development. The particular examples and interpretations are rather personal; many others could be chosen. In considering how we might mimic these natural materials and what might be gained, we need to move the argument to a level of principles of materials science rather than particular materials. In the following sections a number of the principles underlying the above examples are discussed further.

### **14.3.1. Strengths of Bioceramics**

If we consider a mollusc shell or a tooth as a ceramic, it is interesting to compare its strength with synthetic ceramics. Table 14.1 gives values for strength and work of fracture for a number of mineralized tissues in comparison with good alumina ceramic. The strengths of the natural materials are not truly very high. However, calcium carbonate does not have the bond strength of alumina and therefore would not be expected to reach such high strength values. Unfortunately we do not have strengths of synthetic calcium carbonate or hydroxyapatite to compare with the biological materials. This may be clarified by current work on synthetic hydroxyapatite. The components of ceramic strength are intrinsic strength, which is related to lattice energy, the size of flaws, and toughening mechanisms that increase crack growth energy.

The strength of alumina is limited by the flaws left after processing. Even the



TABLE 14.1. Mechanical Properties of Biological Composites

Material	Volume % Mineral	Work of Fracture (J/m <sup>2</sup> )	Bend Strength (MPa)
Enamel	92	200(p11), 13(perp)	76
Whale ear bulla	66	200	33
Dentine	48	550(p11), 270(perp)	250
Bone	41	1700	270
Antler	31	6200	179
Macadamia shell		100-1000	25-80
Hydroxyapatite	100		6
Alumina	100	50	1000

best samples have flaws of 20–100  $\mu\text{m}$ , which act as stress concentrators for crack formation. In recent years research has made considerable progress in reducing flaw size and has now shifted to increasing the toughness (and resistance to crack propagation) of ceramics. Biological ceramics do not rely on being flaw-free. This is probably reasonable in a world where shells will be subjected to various kinds of battering that could form surface defects. Also many structures are required to have flaws. Thus bones must have channels for blood supply, and tooth enamel has a porosity that seems to be intrinsic to its growth behavior.

One characteristic of biological ceramics is the polymer content. They might be described as ceramics with polymeric grain boundaries. This might appear to be an effective toughening mechanism, but is probably not. While proteins are intrinsically very tough, it is not clear that they are still capable of large amounts of energy absorption when they are constrained as thin layers around ceramic grains. It is clear from Table 14.1 that toughness does rise dramatically as the protein content increases from tooth enamel to antler, but the effect of a small amount of polymer is probably small. This is a point that we cannot test without a way to reach polymer-ceramic composites with ceramic packing densities of greater than 90 vol %.

Another characteristic of the biological systems is their exploitation of toughening mechanisms based on highly oriented fibrous or platey microstructures with local variations in orientation direction. Similar toughness is also seen in other fibrous ceramics such as jades. These structures depend on the grains being formed in place, because there is no known way of inducing micrometer-sized rods to pack to high densities.

A final point is that the strength and hardness of a tooth is apparently optimized by a hard surface superimposed on a tougher substructure, such as enamel over dentine. This principle is familiar as case hardening of metals, but I am not aware of synthetic ceramic examples.

In summary, it is clear that biology values toughness more than strength.

## 154 BIOMIMETIC PROCESSING OF CERAMICS AND COMPOSITES

Given self-repairing constructions, it makes sense that the primary goal should be to avoid catastrophic failure rather than maximum strength. The obvious goals of biomimetic ceramics should be dense, sinterable fibrous, or platey green bodies; polymer-ceramic composites at high mineral content; and gradient structures with hard surfaces and tough interiors. There remains the question as to how this could actually be achieved.

### 14.3.2. Growth within Membrane

The synthetic approach to ceramics and composites is generally to form particles or fibers and then pack them into the required shape. The biological approach is to grow the particles at or close to their final site. The problem then becomes one of how to concentrate the reagents for precipitation in the mineralization region without precipitation taking place at the organelle that is actually transporting the reagents.

In part this is achieved by a membrane separating the deposition site from the surrounding tissue. Reagents can be transported through the membrane and precipitation induced by a change of pH or other conditions inside. This method is suitable to the growth of isolated particles such as sponge spicules or bacterial magnetite.

A second part of this mechanism that is seen in the sponge spicules and in nacreous shell is the presence of nucleating polymer surfaces. Heterogeneous nucleation is frequently discussed in terms of epitaxial relationships between the growing crystal and the substrate. This does not seem to be appropriate for the precipitation of silica onto polysaccharide in the sponge. There has been extensive discussion of possible relationships between hydroxyapatite and collagen [7]. The nucleation of aragonite in nacre depends on the presence of water-soluble acid proteoglycans, which may be attached to the nucleating sites [8]. These would be expected to bind calcium and so may form a favorable surface for crystal growth. The preferred *a-b* (in-plane) orientation of the aragonite found in some species has been attributed to the influence of the underlying layer of the crystalline polysaccharide chitin. It has been suggested that nucleating effects of these surfaces may arise from attachment of submicrometer particles of amorphous calcium carbonate, which are then induced to crystallize [9]. The nucleating effect does not seem to be specific. Dentine phosphoprotein is capable of nucleating calcite when attached to the surface of agarose beads. All that is clear at this point is that biological surfaces are capable of inducing precipitation, but this effect may be more related to surface energy than to any specific structural spacing match.

A third part of the mechanism controlling mineralization is growth inhibition. The human body is supersaturated with respect to both calcium carbonate and hydroxyapatite. It also contains many ionic and polymeric species that are effective growth poisons for these crystals. The same acidic proteoglycans from molluscs that enhance nucleation on surfaces are able to inhibit nucleation in solution [10].

A final factor that may be important is that the initial precipitate, at least in bone, is capable of substantial recrystallization into conformity with the matrix. Hence, early micrographs of bone mineralization show randomly oriented hydroxyapatite crystals surrounding matrix vesicles, and X-ray diffraction in the early stages of bone formation shows a largely amorphous precipitate. Fully mineralized bone has highly aligned plates of hydroxyapatite. The driving force for this recrystallization is presumably a lowered free energy due to surface interactions with the collagen fibrils.

The conclusion from this discussion is that there are many interactions between a polymeric or gel matrix and crystals growing within it. If we try to emulate biological systems by forming composites by in situ precipitation, we will also want to learn how to exploit these effects.

#### 14.4. SYNTHETIC EFFORTS

A recent review covers work on the preparation of composite materials by the growth of organic or inorganic particles in polymer matrices [11].

The closest approach to crystals growth within a membrane is the precipitation of inorganic particles such as cadmium and cobalt sulfides, iron, and silver oxides within liposomes. For instance, Mann and Hannington [12] have prepared liposomes from solutions of metal salts and then transferred these to base. As the base diffuses into the liposome, a precipitate forms. The liposomes are of the order of 20–30 nm internally and the particles typically about 5 nm. The starting solutions were rather dilute (100 mM) and so the particle content of the liposomes was low, about 0.1 vol %. Much higher concentrations would be needed if this were to be a viable route to preparing ceramic particles. It is an attractive route, because the particles are prepacked in an organic layer that prevents agglomeration. There have been related studies on the use of emulsions to produce ceramic particles [13]. In this case alkoxides were dispersed in polar organic solvents with various emulsifiers and hydrolyzed by the slow addition of water. The emulsifier layer and the liposome bilayer are two examples of a potentially wide range of membrane analogues.

Crystal growth in gels has long been studied by Henisch [14]. The silica gel or organic gel acts as a medium controlling reagent transport and preventing particle collision and agglomeration. The main goal of this work has been the growth of single crystals. Recently work has been reported on the precipitation of silica in polyacrylamide gels [15]. The gels were swollen with water and silicon tetraethoxide allows to diffuse in. The amide function of the gel may catalyze the hydrolysis reaction.

Wang and Mark [16] have prepared composites of silicone rubbers and polyisobutylene containing silica and titania by allowing the rubber to swell in metal alkoxide and then hydrolyzing the sample by exposure to moist air. We have prepared polymer films containing titanium alkoxides and then induced precipitation of amorphous titania particles by treatment of the film with water.

## 156 BIOMIMETIC PROCESSING OF CERAMICS AND COMPOSITES

A similar procedure has been used to prepare polymer films containing magnetic iron oxides [17], iron metal [18], and barium titanate [19]. The barium titanate could be induced to crystallize within the polymer and could be fired to a ceramic film.

Questions arising from this work concern the factors that control whether particles form in the polymer or the reagent is eluted, whether the precipitation is at the surface or uniform throughout, and the factors that control particle size. We have generally observed particles in the range of 1  $\mu\text{m}$  by scanning electron microscopy, although when these crystallize the primary particle is of the order of 2 nm as seen in transmission electron microscopy or by X-ray diffraction linewidth analysis.

These studies all involve the precipitation of equiaxed particles from amorphous polymers. In the case of organic crystals growing from a polymer, finer crystals can be grown from a crystalline polymer where the polymer morphology can restrict the extension of the organic crystal. This is of interest because very fine precipitates can yield transparent composites [20] that we have been studying as potential materials for nonlinear optical applications. By growing the organic crystals in a previously oriented polymer, we can also get highly oriented precipitates.

### 14.5. FUTURE POSSIBILITIES

The work on synthetic systems described here has been aimed largely at composite materials for structural, optical, or electronic applications. The polymer usually plays a passive role in controlling reagent diffusion and preventing particle aggregation. One goal that we have to pursue is to understand the mechanisms by which biological polymers exert more active control of particle formation, shape, orientation, and size. We also need to find synthetic systems that can duplicate these effects.

This level of control will open up the possibility of much more complex three-dimensional synthetic structures being grown using gel-state growth processes, similar to the vapor phase growth processes of integrated circuit manufacture. This will allow the design of "intelligent composites" in the sense that sensor materials, transport materials, and transducers can be incorporated into a single composite structure.

One characteristic of biological materials when compared to synthetic ones is that they form relatively slowly. In the natural world the limiting factor was normally the supply of nutrients so that precipitation kinetics were not limiting. The synthetic methods discussed here are also relatively slow because they rely on gel-state diffusion and that limits the production of bulk pieces of material, but not the production of films or fibers. As we move to greater sophistication, these factors of cost and time will become less limiting in the possible industrial application of biomimetic materials.

## REFERENCES

1. R. P. Blakemore, *Science*, **190**, 377 (1975).
2. R. B. Frankel and R. P. Blakemore, *J. Magnetism Magn. Mat.*, **15-18**, 1562 (1980).
3. R. B. Frankel, G. C. Papaefthymiou, R. P. Blakemore, and W. O'Brien, *Biochim. Biophys. Acta*, **763**, 147 (1983).
4. B. E. Volcani, in: P. Westbroek and E. W. de Jong, Eds., *Biom mineralization and Biological Metal Accumulation*, D. Reidel, Dordrecht (1983) pp. 389-405.
5. H. Nakahara, in: P. Westbroek and E. W. de Jong, Eds., *Biom mineralization and Biological Metal Accumulation*, D. Reidel, Dordrecht (1983) pp. 225-230.
6. J. S. Jennings and N. H. Macmillan, *J. Mater. Sci.*, **18**, 2081 (1983).
7. P. Koutsoukos and G. H. Nancollas, *Colloids Surfaces*, **28**, 95 (1987).
8. E. M. Greenfield, D. C. Wilson, and M. A. Crenshaw, *Am. Zoologist*, **24**, 925 (1984).
9. P. C. Rieke, in: I. A. Aksay, G. L. McVay, T. G. Stoebe, and J. F. Wager, Eds., *Atomic and Molecular Processing of Electronic and Ceramic Materials*, Mater. Res. Soc. (1987) p. 109.
10. A. Berman, L. Addadi, and S. Weiner, *Nature*, **331**, 546 (1988).
11. P. Calvert and S. Mann, *J. Mater. Sci.*, **23**, 3801 (1988).
12. S. Mann and J. P. Hannington, *J. Colloid Interface Sci.*, **122**, 326 (1988).
13. A. Hardy, Synthesis of Ceramic Powders by Emulsion Processing, Ph.D. Thesis, MIT Ceramics Processing Research Lab. (1988).
14. H. K. Henisch, *Crystals in Gels and Liesegang Rings* (1988).
15. B. J. Tarasevich, I. A. Aksay, and M. Sarikaya, in: I. A. Aksay, G. L. McVay, T. G. Stoebe, and J. F. Wager, Eds., *Atomic and Molecular Processing of Electronic and Ceramic Materials*, Mater. Res. Soc. (1987) p. 115.
16. S. B. Wang and J. E. Mark, *Polym. Bull.*, **17**, 271 (1987). S. Liu and J. E. Mark, *Polym. Bull.*, **18**, 33 (1987).
17. C. A. Sobon, H. K. Bowen, A. Broad, and P. D. Calvert, *J. Mater. Sci. Lett.*, **6**, 901 (1987).
18. P. D. Calvert, A. Broad, and G. Cloke, *Polymer Preprints*, **29**(2), 246 (1988).
19. P. Calvert and R. A. Broad, "Routes to composites and ceramics by in-situ precipitation in polymers," in *Contemporary Topics in Polymer Science*, Vol. 6. W. Culbertson, Ed. Plenum, (1989) p. 95.
20. P. Calvert, B. Moyle, and N. Azoz, in: "Organic Materials for Non-Linear Optics" eds. R. A. Hann, D. Bloor, *Royal Soc. Chem. Spec. Pub.* 69, RSC, London 1989 pp. 308-314; B. D. Moyle, R. E. Ellul, and P. D. Calvert, Eds., *J. Mater. Sci.* **6**, 167 (1987).

# **15**

## **SOL-GEL PROCESSING OF LARGE SILICA OPTICS**

**L.L. HENCH, M. J. R. WILSON, C. BALABAN, AND J. L.  
NOGUÈS**

### **15.1. INTRODUCTION**

In the first Ultrastructure Processing Conference in 1983, J. D. Mackenzie summarized numerous potential advantages and disadvantages of sol-gel processing [1]. The advantages cited were largely based upon the intimate mixing possible with chemically based processing compared with powder processing. The disadvantages primarily centered around the difficulties in controlling this new generation of molecular-based processing and potential costs.

The objective of this Chapter is to summarize and present, 6 years later, the progress made in achieving the advantages and minimizing the disadvantages in the sol-gel processing of one important application, sol-gel-derived silica optics. The potential advantages discussed are homogeneity, purity, coefficient of thermal expansion, As-cast shapes and surface features, and unique properties of silica ultrastructures, such as for doping applications and laser-enhanced densification.

The possible disadvantages discussed in this Chapter are inherent to size scaleup. They can be in most cases overcome by well-defined processing including control of drying, elimination of casting defects, and precise at-

---

*Ultrastructure Processing of Advanced Materials.*

Edited by Donald R. Uhlmann and Donald R. Ulrich (deceased).

ISBN 0-471-52986-9 © 1992 John Wiley & Sons, Inc.

mosphere control. The consequence of overcoming most of these problem areas is the ability to make new types of silica optics with sizes of 100 mm and larger using organometallic-based sol-gel silica processing.

## 15.2. SILICA OPTICS PROCESSING

Silica optics are preferred for many optical systems, such as intracavity laser optics, because of the characteristics listed in Table 15.1. Development of a successful sol-gel-derived process for making silica optics requires achieving all the features listed in this table. It also requires achieving significant improvements in at least some of the most important properties over what is presently produced commercially.

There are presently four major methods of manufacturing silica optics, as summarized in Table 15.2 [2,3]. The first two processes involve melting naturally occurring quartz crystals at high temperatures. The resulting materials are termed *fused quartz*. Deficiencies of fused quartz optics can include: substantial amounts of cation impurities (type I), hydroxyl impurities (type II), inhomogeneities, seeds, bubbles, inclusions, and microcrystallites. The relative extent of these defects depends on the grade of fused quartz. The higher the grade, the fewer the defects, but the higher the cost and the more difficult the production of large optics.

Both types III and IV are termed *synthetic fused silica*. The cation impurity content of fused silica optics is substantially lower than fused quartz optics due to the higher purity of the raw materials [3]. It is difficult for the chemical reactions indicated in Table 15.2 for these types of silica to go to completion, consequently water contents up to a few thousand parts per million are present in type III silica, and Cl ion contents of a few hundred parts per million can be retained as an unreacted residue in both type III and type IV silicas. Other defects are somewhat lower for fused silicas than for fused quartz [3]. The nature of the chemical processes involved in the production of types III and IV silicas

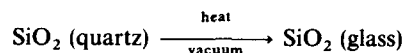
TABLE 15.1. Features of Silica Optics

1. Excellent optical transmission from the ultraviolet (160 nm) to near infrared wavelengths (3600 nm)
2. Excellent refractive index homogeneity.
3. Isotropic optical properties.
4. Small strain birefringence.
5. Very low coefficient of thermal expansion of about  $0.55 \times 10^{-6}/^{\circ}\text{C}$ .
6. Very high thermal stability.
7. Very high chemical durability.
8. Small numbers of bubbles or inclusions.
9. Ability to be polished to high standards.

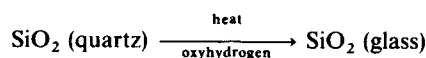
TABLE 15.2. Methods of Silica Optics Manufacture

*Fused Quartz*

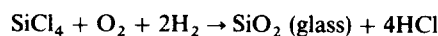
Type I: Electric melting of natural quartz crystals



Type II: Flame fusion of natural quartz crystals

*Fused Silica*

Type III: Vapor-phase hydrolysis of pure silicon tetrachloride carried out in a flame

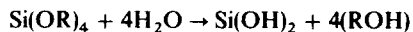


Type IV: Oxidation of pure silicon tetrachloride, which is fused electrically or by means of a plasma

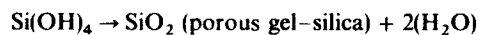
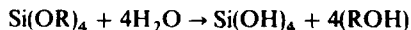
*Gel-Silica*

Type V: Gelation of alkali silicate colloidal solutions with fully densification (1500 to 1720°C), or

Hydrolysis and condensation of organometallic precursor with fully densification (1150 to 1200°C)



Type VI: Hydrolysis and condensation of organometallic precursor with partial densification (600 to 950°C)



makes the direct manufacture of near net shape optics impossible. Price increases considerably as the quality of fused silica and the size of the optics increase.

During the last few years chemically based sol-gel processes have been developed and lead to the manufacture of types V and VI silicas as described in Table 15.2 [3-6]. These processes offer the potential for improving many



features of silica optics listed in Table 15.1. Additional advantages over types I to IV silicas are also possible, as described in Table 15.3.

Two primary sol-gel processing methods for silica optics have reached commercialization: (1) hydrolysis and condensation of an organometallic precursor [3-5] and (2) gelation of a colloidal alkali silicate powder suspension [6]. The silicas resulting from these sol-gel processes are termed *type V* when the final product is fully dense with no residual porosity. If the densification process is not accomplished entirely, the organometallic method produces a porous optical material named *type VI silica*.

The ultrastructure of the gel and the final densification conditions are considerably different for the organometallic versus the colloidal methods of manufacture of sol-gel silicas, as summarized in Fig. 15.1. An organometallic-based sol-gel silica, such as Gelsil<sup>TM†</sup>, has a totally interconnected porosity with a dried bulk density of 1.2 g/cm<sup>3</sup>, an average pore diameter of 2.5 nm, and a specific surface area of 700-800 m<sup>2</sup>/g prior to densification [3]. Because of the very small pore size and the very narrow distribution of pores, the gel is optically

**TABLE 15.3. Potential Advantages of Gel-Silica Optics**

---

*Net Shape/Surface Casting*

Complex geometries  
Light weight optics  
Aspheric optics  
Surface replication (e.g., Fresnel lenses)  
Internal structures  
Reduced grinding  
Reduced polishing

*Improved Physical Properties (Type V)*

Lower coefficient of thermal expansion  
Lower vacuum ultraviolet cutoff wavelength  
Higher optical transmission  
No absorption due to H<sub>2</sub>O or OH bands  
Lower solarization  
Higher homogeneity  
Fewer defects

*Transparent Porous Structures (Type VI)*

Impregnation with organic polymers  
Graded refractive index lenses  
Laser-enhanced densification  
Controlled chemical doping  
Control of variable oxidation states of dopants

---

<sup>†</sup>Gelsil<sup>TM</sup> is a trademark of GELTECH, Inc.

## Gel-Silica Glass Process Sequence

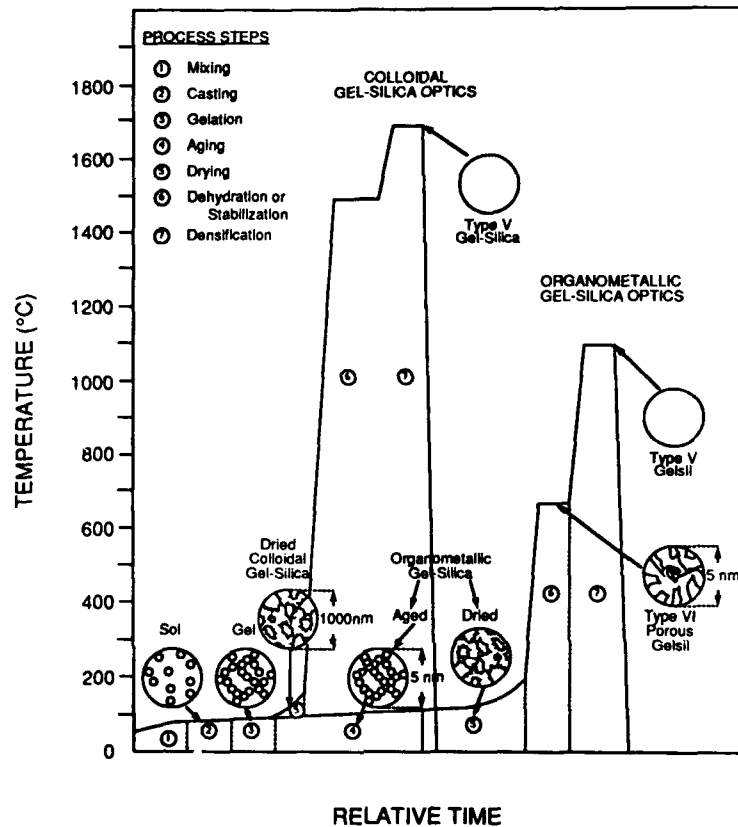


Figure 15.1. Processing sequence for sol-gel silica optics.

transparent. The uniformity of the ultrastructure results in densification at a very low temperature, 1150°C, without a change in mean pore radius. Densification takes place almost entirely by decreasing the connectivity (genus) of the uniform pore network [7] and is very sensitive to pore size, as shown in Fig. 15.2.

Because there is no pore growth by Ostwald ripening, the organometallic derived monoliths remain optically transparent throughout the processing schedule shown in Fig. 15.1, after they pass the opaque stage in drying (Chapter 22). Examples of a large 100-mm organometallic sol-gel-derived optical silica monolith after drying is shown in Fig. 15.3a. Samples of organometallic-derived type VI and type V silica plano-plano optical components are shown in Figs. 15.3b and c, respectively.

The colloidal sol-gel optics process developed by Shoup [6] involves nucleation and polymerization of potassium silicate by colloidal silica in the presence of a hydrolytic organic reagent. By varying the ratio of colloidal species

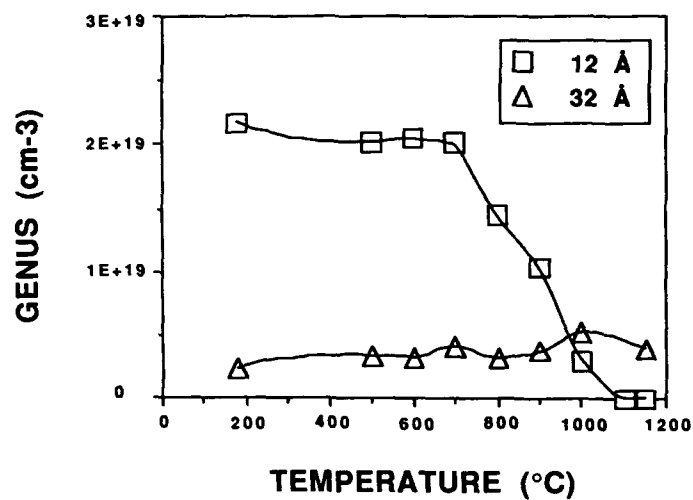


Figure 15.2. Temperature dependence on pore network connectivity of organometallic gel-silicas with differing mean pore radii. (Data courtesy of W. Vasconcelos, University of Florida.)

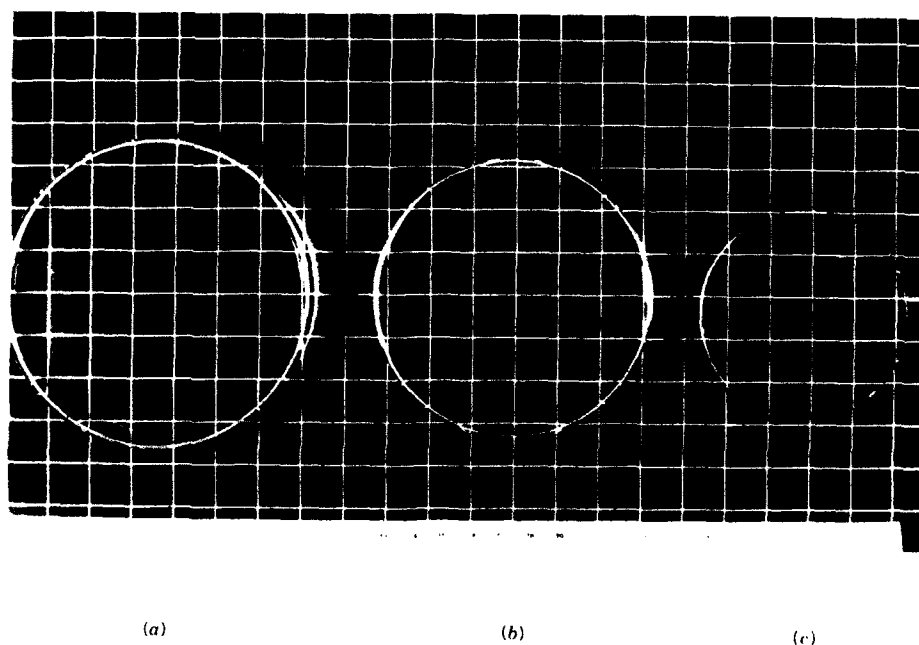
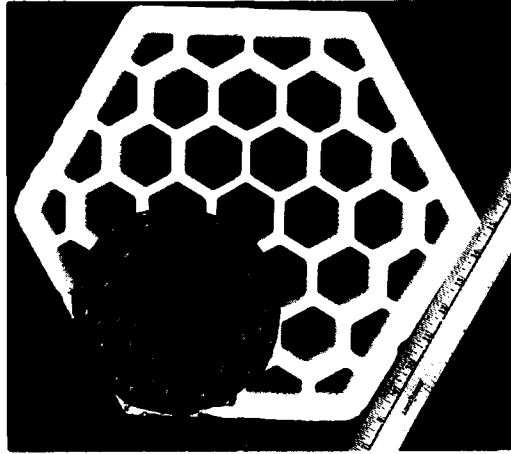


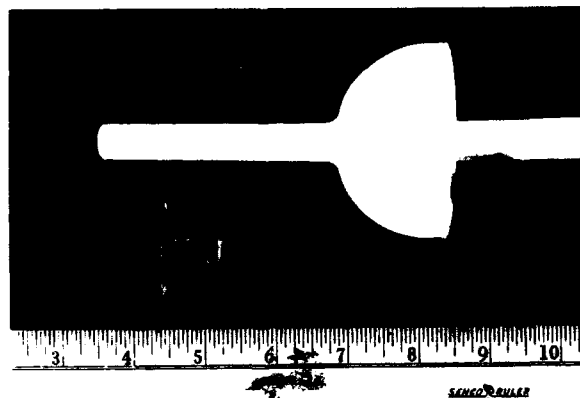
Figure 15.3. Organometallic sol-gel silica monoliths: (a) dried, (b) porous plano-plano optical component (type VI Gelsil™), (c) fully dense plano-plano optical component (type V Gelsil™).



**Figure 15.4.** Lightweight mirror backing made by colloidal gel-silica process: (a) after drying, (b) after densification. (Photo courtesy of R. D. Shoup, Corning Glass Works.)

to soluble silicate, the gel pore diameter can be controlled between 10 and 300 nm with a relatively narrow size distribution. As a result, strong silica gel structures are formed by the colloidal process with large pores,  $>200$  nm diameter, that can resist capillary pressures encountered during drying. Microwave drying can be used for these  $\geq 80\%$  porous colloidal gels in minutes to hours, depending on body dimensions, without cracking.

The large-pore structures produced in the colloidal sol-gel method help in the removal of alkali ions by an aqueous dealcalization process. The large pores also facilitate gaseous removal of chemisorbed impurities prior to densification, yielding low water levels and alkali and transition metal impurity of a few



**Figure 15.5.** Near net-shape colloidal gel-silica component: (a) after drying, (b) after densification. (Photo courtesy of R. D. Shoup Corning Glass Works.)

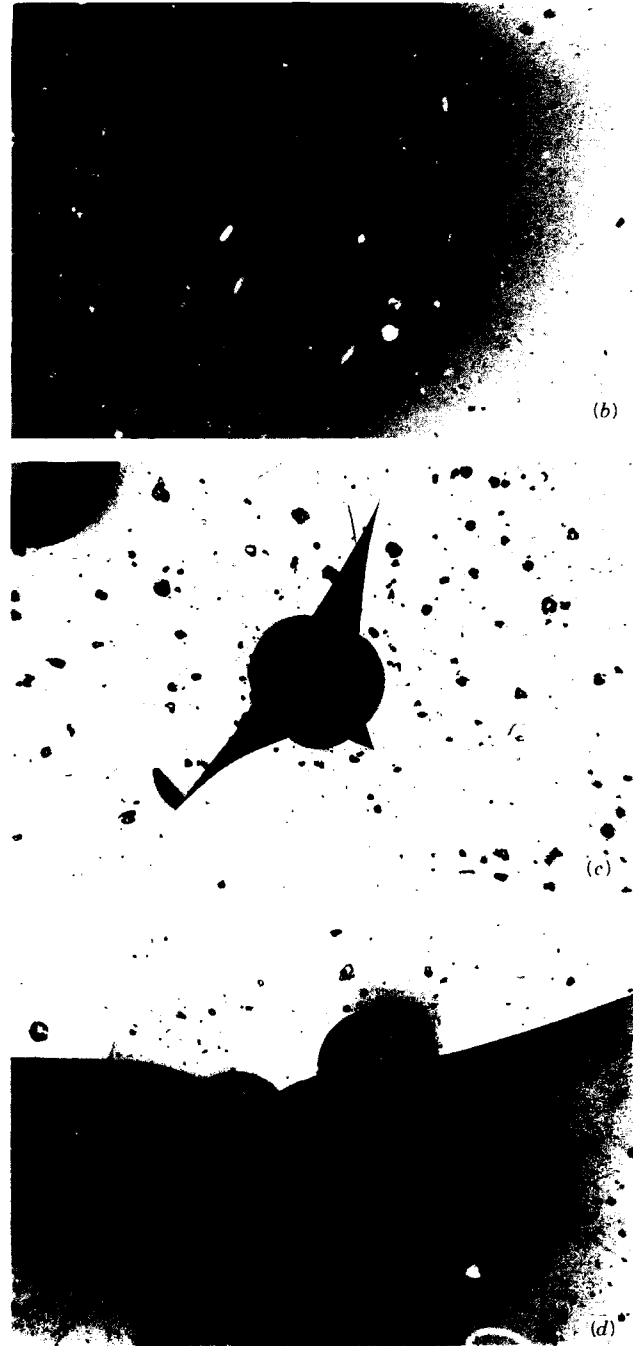
hundred parts per million. Total density is achieved after 30 min at 1500°C and high-quality optical silica is achieved after 10 min at 1720°C. Examples of type V silica glasses made by the colloidal gel-silica process are shown in Figs. 15.4 and 15.5.

### 15.3. FACTORS IN SIZE SCALEUP

Scaleup of sol-gel processing has been considered potentially one of the greatest uncertainties. In order to achieve large optical components by the sol-gel route it is essential to control: (1) drying rates, (2) defects in the as-cast gel monoliths, and (3) removal of chemisorbed water prior to pore closure in densification. Control of these factors is less sensitive in the colloidal method because of the large pores in the structure.

1. *Drying Control.* A critical step in the drying of organometallic-derived sol-gel optics is the rate of removal of water during the "opaque stage." As shown by Wilson and Hench in this text (Chapter 22), it is during the transition between filled pores and pore emptying that substantial bulk strains are developed in the gel monoliths. The rate of water removal must be slowed during this critical period to avoid cracking. The gel monolith is relatively insensitive to the rate of drying prior to and after the opaque stage.
2. *Defect Control.* Imperfections in a gel will cause stress risers during drying and further processings steps. Consequently, even if a gel monolith has sufficient strength to withstand a given level of bulk strain, the presence of stress risers will induce fracture. These imperfections can take many forms and are usually created during casting of the sol and are incorporated in the solid when gelation occurs. Several examples of bubbles, which are particularly damaging stress risers, are shown in Fig. 15.6. In Fig. 15.6a, a





**Figure 15.6.** Bubbles in a gel-silica monolith: (a) acting as a stress riser, (b) initiating a crack, (c) initiating three cracks, and (d) initiating a complex crack front.

stress field is beginning to develop around the bubble; in Fig. 15.6b, we can see a crack initiating from a bubble; in Fig. 15.6c, three cracks have initiated; and in Fig. 15.6d, a complex crack front originates from the interaction of stress fields around two bubbles.

Elimination of bubbles involves careful deaeration of the sol prior to casting, using a casting technique that does not introduce air, avoiding gas generating chemical additives in the sol formula, and avoiding containers that nucleate bubbles at the interface.

3. *Atmosphere Control.* Tightly bound hydroxyl ions on the surface of pores must be removed prior to pore closure during densification for both organometallic and colloidal sol-gel silicas. Surface dehydroxylation occurs from 200 to 1000°C for organometallic-derived gels and up to 1300°C for colloidal silica monoliths. It is usually necessary to enhance the dehydroxylation process by flowing halogen-containing gases through the pore network before closure. In this particular case the atmosphere control treatment should include the removal of any halogen left in the structure of the glass. If densification is attempted without hydroxyl removal, foaming and bloating result due to expansion of the gases formed and trapped in the closed pores. Because of the very small size of pores in organometallic-derived gels and the absence of pore growth during densification, it is especially critical to have complete hydroxyl removal for these materials if they are to achieve full density. It is important to recognize that more internal SiOH groups are retained in an acid-catalyzed organometallic-derived gels at high temperature than base-catalyzed gels [8]. The internal SiOH groups polarize the silica tetrahedra [9], which probably is responsible for a decrease in the viscosity of the silica gel network. Consequently viscous flow, responsible for pore closure and reduction of pore network connectivity, takes place at a lower temperature. Thus, it is essential to optimize hydroxyl removal for acid-catalyzed gels when the pore network has as large a connectivity as possible, such as at as low a temperature as possible, for example, below 900°C for small pore organometallic-derived gels (Fig. 15.2).

Control of drying rates, elimination of casting defects, and rigorous atmosphere control can yield large sol-gel silica optical components as shown in Figs. 15.3 to 15.5.

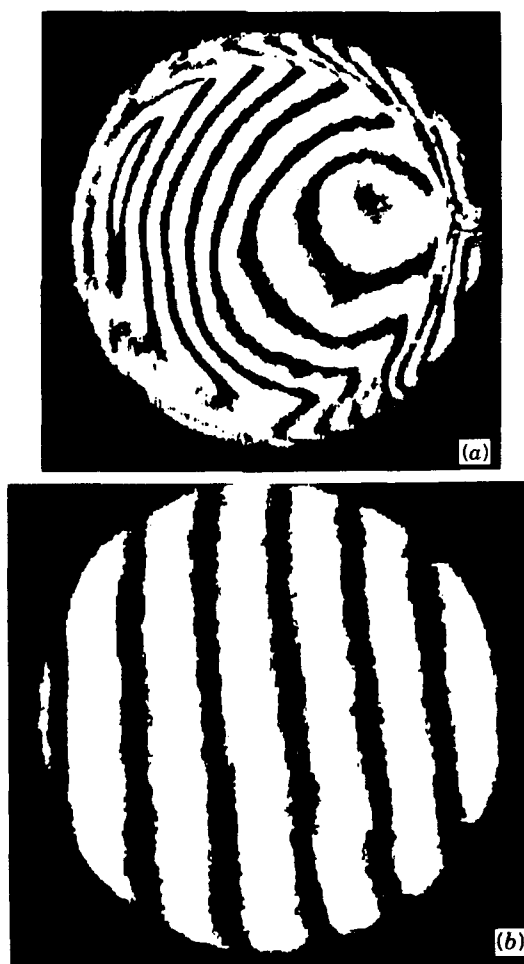
## 15.4. POTENTIAL ADVANTAGES OF SOL-GEL SILICA OPTICS

### 15.4.1. Homogeneity

One of the primary incentives for use of chemically based ultrastructure processing of materials is improvement of homogeneity. The fact that or-

ganometallic precursors can be hydrolyzed with water on a molecular scale of mixing yields the possibility that the glass structure derived from an organometallic gel may have a molecular level of homogeneity. However, as indicated above macroscopic defects must be eliminated first in order to achieve high levels of homogeneity. Also, processing controls must be developed to eliminate fluctuations in the density and index of refraction during densification.

Successful processing controls have been achieved for organometallic-derived optics up to 75 mm for type V silica and 100 mm for type VI silica (Fig. 15.3). Results from optical property measurements show no evidence of bubbles, no striae, a superior index of refraction homogeneity of about  $1-6 \times 10^{-6}$ , and very low strain birefringence of 4-6 nm/cm. These characteristics of organometallic-



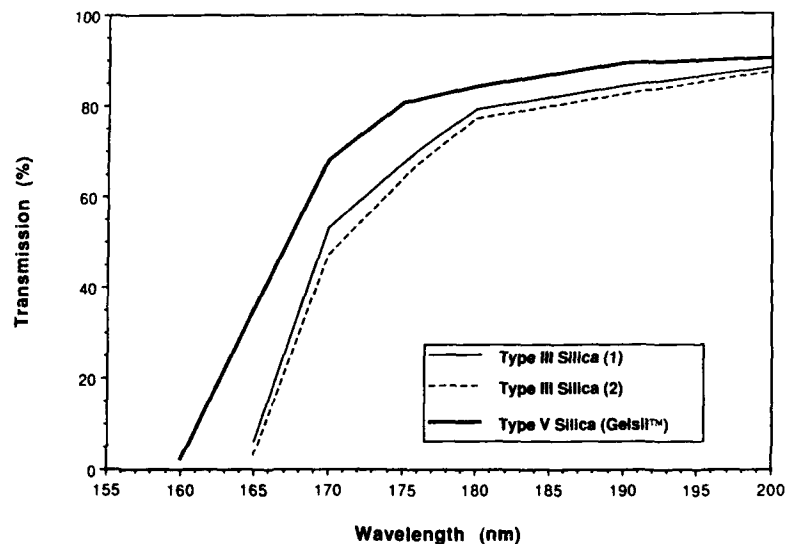
**Figure 15.7.** Interferometry analysis of dense organometallic gel-silicas (type V Gelsil<sup>TM</sup>): (a) improperly densified with severe index gradients, (b) ideal densification with good homogeneity.



derived sol-gel silica (Gelsil<sup>TM</sup>) are equal or superior to types I to IV optical silicas. Figure 15.7a is an example of an earlier generation organometallic gel-silica monolith that was homogeneous as a gel, but developed large index of refraction gradients during densification. This type of inhomogeneity can be eliminated, as shown in Fig. 15.7b.

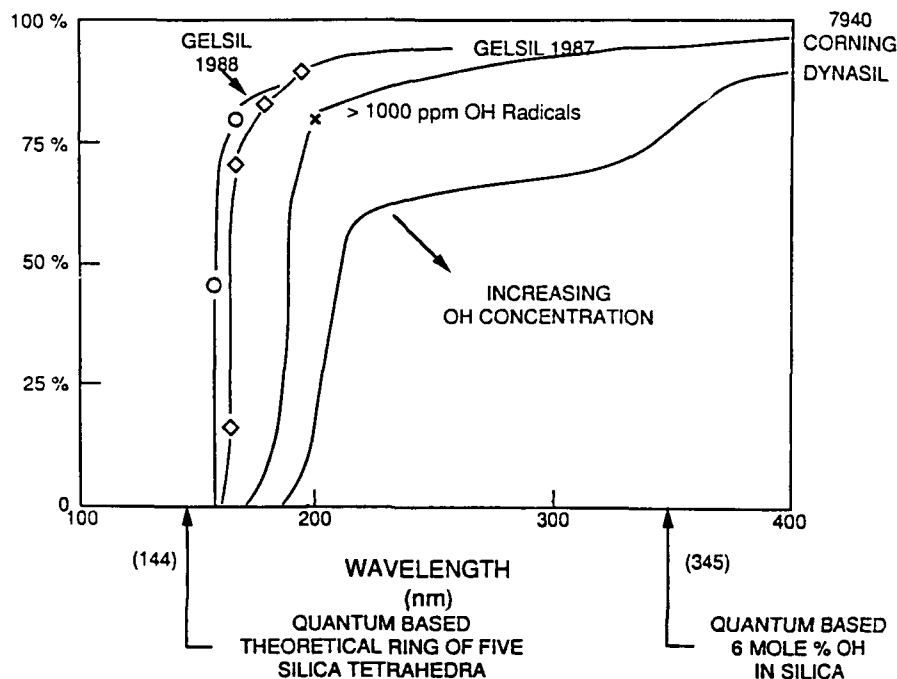
#### 15.4.2. Purity and Properties

Another major incentive for low-temperature, chemically based processing is achieving a higher level of purity than traditional glass and ceramic-processing methods. The organometallic sol-gel glasses have very few cation and hydroxyl impurities. An important consequence of the elimination of impurities is the improvement of transmission throughout the optical spectrum. Figure 15.8 compares the ultraviolet optical transmission of two commercial ultraviolet (UV)-grade optical silicas (type III) with a typical spectrum from an organometallic-derived gel-silica (type V). The vacuum UV cutoff wavelength is substantially improved for the gel-silica material. Recent quantum mechanical calculations of West et al. have shown that the greater transmission in the UV can be attributed to a lower alkali and OH radical content in the gel-silica (Chapter 11). Results from the quantum mechanics calculations are compared in Fig. 15.9 with the improvement in gel-silica transmission over the last three Ultrastructure Processing Conferences, as the OH radical content of the gel-silica glasses has been progressively eliminated. The ultraviolet transmission of



**Figure 15.8.** Ultraviolet optical transmission of a dense organometallic gel-silica (type V Gelsil<sup>TM</sup>) compared with two commercial type III silicas.

## UV TRANSMISSION



**Figure 15.9.** Improvements in UV transmission of organometallic gel-silicas with time compared with quantum mechanics predictions of UV cutoff wavelength.

colloidal based silica is poorer than organometallic-derived gel-silica due to a higher level of impurity inherent to the alkali-silicate-based colloidal process.

Elimination of OH radicals from gel-silica optics also results in elimination of absorption bands in the near infrared, as shown in Fig. 15.10. This figure shows the difference between type V gel-silica and type III silica, which exhibits absorption bands at 1400 and 2200 nm, and a very broad absorption band at 2730 nm. Reliability of production of low OH radical content in type V gel-silicas (Gelsil™) has also been recently achieved.

#### 15.4.3. Coefficient of Thermal Expansion

A very low coefficient of thermal expansion (CTE) is an especially important physical characteristic of optical silica. The organometallic process leads to the production of a type V silica having a lower CTE than other types of silica. Figures 15.11 and 15.12 compare the thermal expansion and the CTE values of a type V silica (Gelsil™) optics with the NBS silica reference and type III and IV commercial silicas over the temperature range of 25 to 700°C. The organometal-

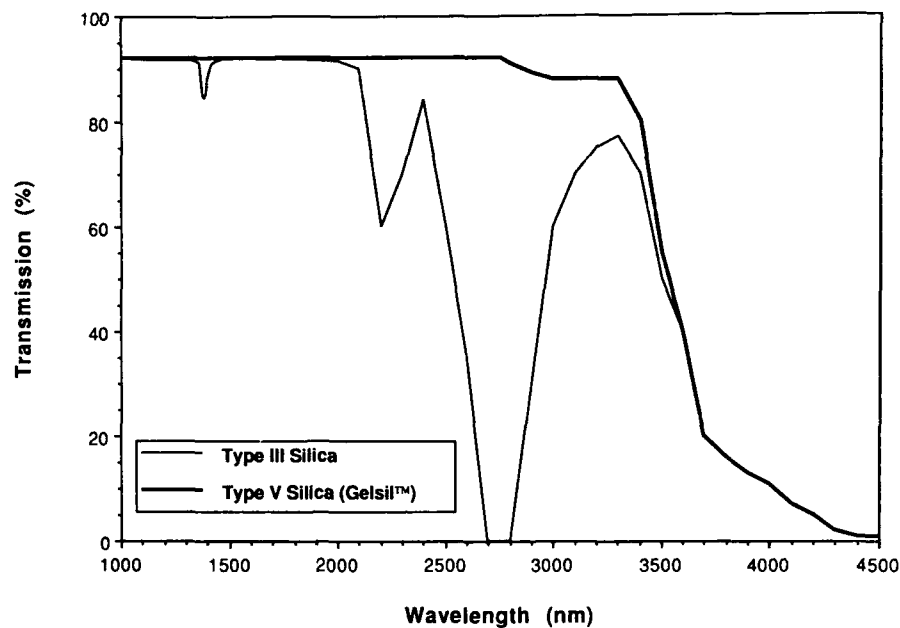


Figure 15.10. Near infrared transmission of a dense organometallic gel-silica (type V Gelsil™) compared with a type III silica.

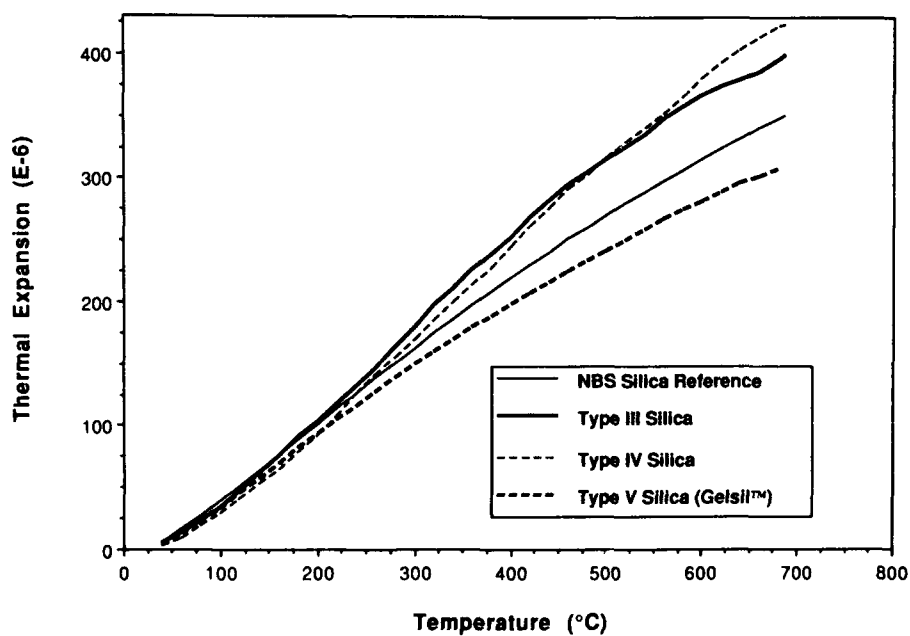
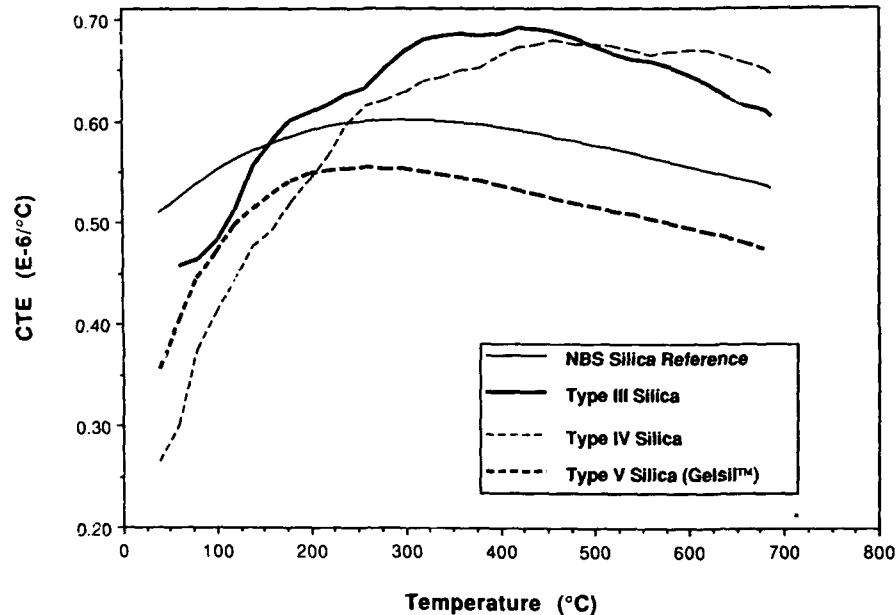


Figure 15.11. Thermal expansion of a dense organometallic gel-silica (type V Gelsil™) compared with NBS silica reference and types III and IV silicas.



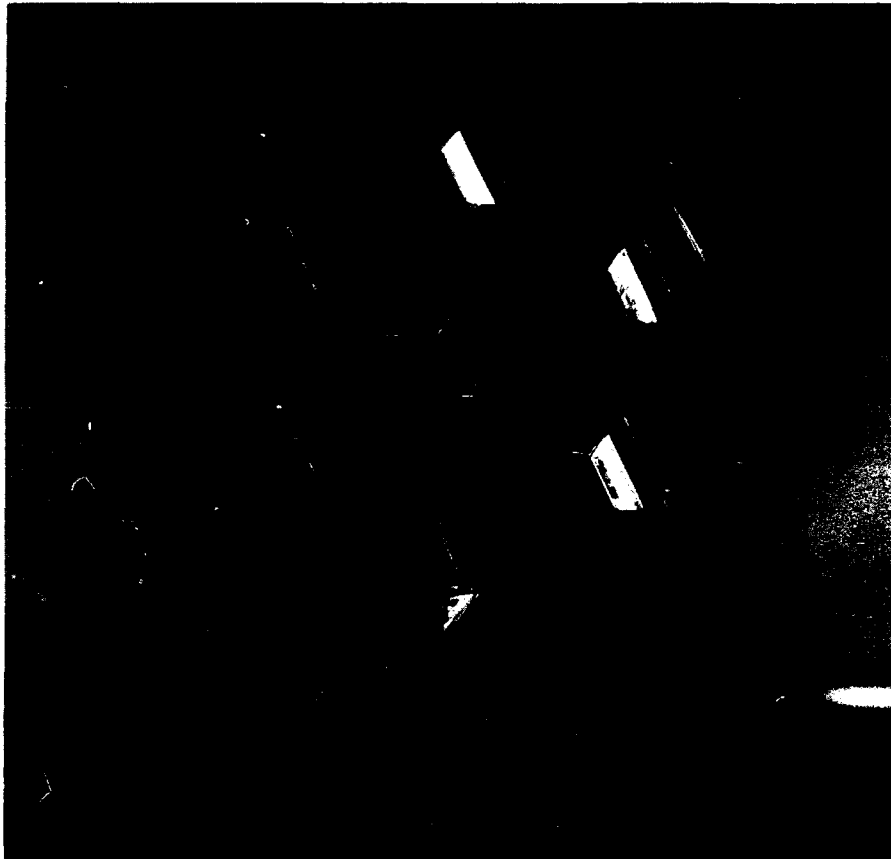
**Figure 15.12.** Coefficient of thermal expansion (CTE) of a dense organometallic gel-silica (type V Gelsil™) compared with NBS silica reference and types III and IV silicas.

lic sol-gel optical silica have lower values of thermal expansion and CTE than the other types of silica [10].

#### 15.4.4. As-Cast Shapes and Surface Features

Another area of potential advantage of sol-gel optics processing is that of obtaining net shapes and surfaces or at least near-net shapes and surfaces through casting sols at low temperature into molds of predetermined configurations. Advantages offered by this type of processing are listed in Table 15.3. A lightweight mirror with integrally cast face plate and honeycomb backing made by gelation of silica organometallic precursor is shown in Fig. 15.13. This configuration has been successfully dried and a sample of similar size (75 mm in diameter) and shape has been successfully densified. A net shape honeycomb mirror backing made by the colloidal route is shown in Fig. 15.4 and a complex mold casting of colloidal silica gel-glass is shown in Fig. 15.5.

Another application of net shape casting is the replication of specific surface features. For example, Fig. 15.14 shows the surface characteristic graphs obtained on a Sloan Dektak/FLM profilometer of a plastic Fresnel lens master and the corresponding gel-silica Fresnel lens. The lens master was machined in a polymer and the organometallic sol-gel silica positive replica was made by direct casting against it. Figure 15.15 shows a microscope photograph of a dry organometallic sol-gel silica part. It can be seen from this photograph and the

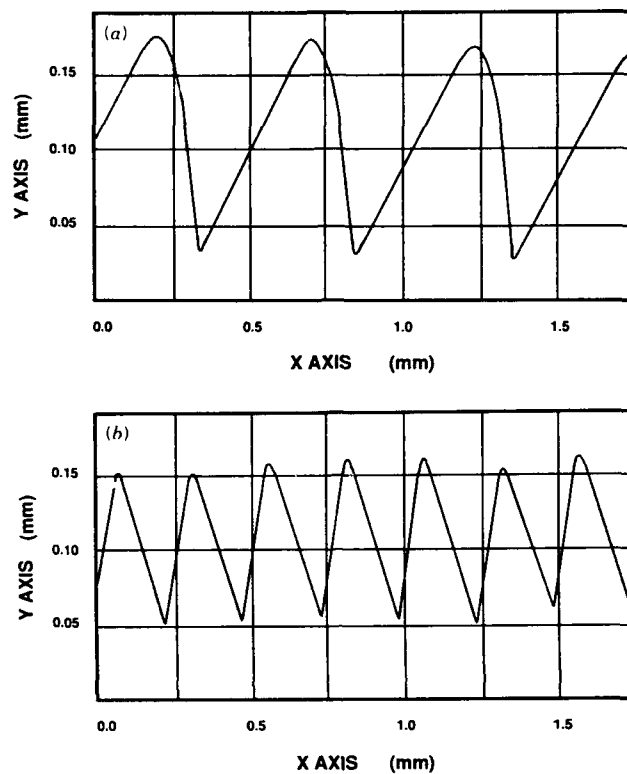


**Figure 15.13.** Lightweight sol-gel silica mirror with integral faceplate made by the organometallic route. (Photo courtesy of J. West, M. J. R. Wilson, J. Parramore, and B. F. Zhu, University of Florida).

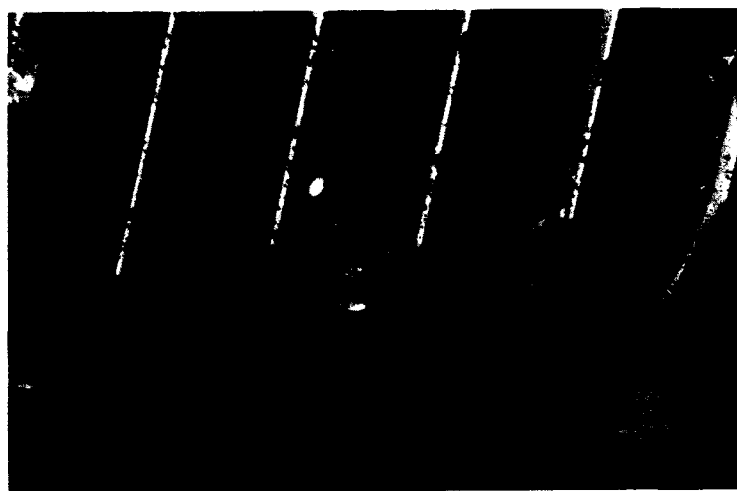
profilometry graphs that the replication of the surface details is very good. The precision of the master was maintained through densification into a type V gel-silica. The advantages of the silica Fresnel lens over a polymer lens is the very low thermal expansion coefficient and the thermal and radiation stability of the silica compared to a polymer.

#### **15.4.5. Porous Type VI Gel-Silica and Applications**

The extremely small scale of interconnected porosity in organometallic derived gel-silica results in optical transparency to UV wavelengths as far as 250 nm. The transparent porous structure can be impregnated with a second phase thereby achieving an optical composite. Examples of optical polymers that have been put into type VI silica (porous Gelsil<sup>TM</sup>) are shown in Table 15.4. Results



**Figure 15.14.** Profilometry graphs of Fresnel lenses: (a) polymer master, (b) replication in organometallic gel-silica.



**Figure 15.15.** Microscope photograph of a dry organometallic gel-silica Fresnel lens.

TABLE 15.4. Optical Composite Made from Type VI Silica (Porous Gelsil™)

---

*Non-linear Optical Polymers*

Phenylenebenzobisthiazole  
2-Methyl-4-nitroaniline

*Organic Fluors*

2-(4'-*t*-Butylphenyl)-5-(4''-biphenyl)-1,3,4-oxadiazole  
*p*-Terphenyl  
*p*-Quaterphenyl

*Wavelength Shifter*

3-Hydroxyflavone

*Other Organics*

Laser dyes  
Liquid crystals

---

from some of these studies have been discussed elsewhere [3, 11]. The colloidal-based silica processing produces gels with large pore size that are not optically transparent and therefore cannot be used to make type VI optical silica.

Another unique application of the type VI structure is to use it as the substrate for laser densification. Optical waveguides have been made using laser writing of higher-density tracks on the porous gel-silica substrate [12]. The higher-density tracks have a greater index of refraction than the porous matrix and therefore can serve as a planar waveguide. The prime advantage of the laser-written waveguide is that it matches the index of refraction of silica fiber optics, which is not the case for ion-exchanged or diffusion-based waveguides.

## 15.5. CONCLUSIONS

Since the first Ultrastructure Processing Conference, the progress made in sol-gel science allowed the development of two new types of optical silica. A fully dense sol-gel-derived silica, termed *type V gel-silica*, can be made either with a colloidal process or an organometallic process. The colloidal method results in optically opaque gels to large pores of  $>200$  nm in diameter with  $\geq 80\%$  porosity requiring 1500 to 1720°C densification temperatures. The organometallic process results in optically transparent gels with 45% pores of only 2.5 nm in diameter and require a densification temperature of only 1150°C. An optically transparent sol-gel-derived porous silica, termed *type VI gel-silica*, can be made by the organometallic route. This new type of silica can be used for applications such as an optical element with a second phase impregnated within the pores or as a substrate for laser-written waveguides.

The major progress was made in size scaleup. This was achieved by (1) developing an understanding of the chemical mechanisms involved in each of the seven sol-gel-glass processing steps and (2) establishing careful process controls for each processing step. It is the precise control over the chemical mechanisms and rates of reactions that allows the production of optics of 75 and 100 mm in diameter or larger for both type V and type VI silicas, respectively.

The physical properties of the organometallic-derived type V gel-silica are equal or superior to types I to IV optical silicas and include short UV cutoff, low optical absorption throughout the spectrum, high homogeneity, very few defects, low strain birefringence, and low coefficient of thermal expansion.

Both the colloidal and the organometallic methods of optical gel-silica manufacture can be used to produce complex net shapes by direct casting at ambient temperature. This unique property of the sol-gel process can be used to make optics with special shapes and surface features, such as lightweight mirrors, Fresnel lenses, and aspheric optical components.

### ACKNOWLEDGMENTS

The authors gratefully acknowledge financial support of Air Force Office of Scientific Research Contracts F49620-88-C-0073, F49620-85-C-0079, and F49620-86-C-0120 and the encouragement of D. R. Ulrich throughout this research. Two of the authors (L.L.H. and M.J.R.W.) also acknowledge financial assistance of the State of Florida High Tech and Industries Council.

### REFERENCES

1. J. D. Mackenzie, in: L. L. Hench and D. R. Ulrich, Eds., *Ultrastructure Processing of Ceramics, Glasses, and Composites*, p. 15, Wiley, New York (1984).
2. M. Grayson, Ed., *Encyclopedia of Glass, Ceramics, Clays and Cement*, Wiley, New York (1985).
3. L. L. Hench, S. H. Wang, and J. L. Noguès, *SPIE Proc.*, **878**, 76 (1988).
4. S. H. Wang, C. Campbell, and L. L. Hench, in: J. D. Mackenzie and D. R. Ulrich, Eds., *Ultrastructure Processing of Advanced Ceramics*, p. 145, Wiley, New York (1988).
5. L. L. Hench, G. Ortel, and J. L. Noguès, in: C. J. Brinker, D. E. Clark, and D. R. Ulrich, Eds., *Better Ceramics Through Chemistry, Mater. Res. Soc. Symp. Proc.*, **73** (1986).
6. R. D. Shoup, in: J. D. Mackenzie and D. R. Ulrich, Eds., *Ultrastructure Processing of Advanced Ceramics*, p. 347, Wiley, New York (1988).
7. W. Vasconcelos and L. L. Hench, in: *Proceedings 4th Ultrastructure Processing Conference*, Tucson, AZ, February 1989.
8. G. Ortel, J. Phalippou, and L. L. Hench, *J. Non-Cryst. Solids*, **88** 114 (1986).
9. J. K. West, personal communication, 1987.
10. L. L. Hench and S. H. Wang, *Phase Transitions*, **24-26**, 785 (1990).
11. J. L. Noguès, S. Majewski, J. K. Walker, M. Bowen, R. Wojcik, and W. V. Moreshead, *J. Am. Ceram. Soc.*, **71**, 1159 (1988).
12. R. V. Ramaswamy, T. Chia, R. Srivastava, A. Miliou, and J. K. West, *SPIE Proc.*, **878**, 86 (1988).



# **16**

## **PHYSICS OF DRYING**

**GEORGE W. SCHERER**

### **16.1. INTRODUCTION**

This Chapter presents a brief review of the driving forces and transport mechanisms that are important during drying of gels. The driving forces for shrinkage include chemical effects, such as condensation reactions, and physical effects, such as capillary pressure. Fluid transport can occur by flow down a pressure gradient or diffusion down a chemical potential gradient, and deformation of the network may involve elastic, plastic, or viscoelastic strains. As liquid is removed by evaporation, tension that develops in the pores produces contraction of the network; when the pressure is not uniform (as is often the case), warping and cracking of the gel can result. The interaction of the pressure in the pore liquid and the shrinkage of the network has been thoroughly examined theoretically, and the results are reviewed. These topics are discussed in detail elsewhere [1].

### **16.2. DRIVING FORCES**

#### **16.2.1. Chemical Reactions**

The shrinkage of gels during aging is attributable to ongoing condensation reactions between M-OH groups [2]. The total contraction resulting from condensation can be enormous, as in the titania gels made by Yoldas [3], but in

*Ultrastructure Processing of Advanced Materials.*

Edited by Donald R. Uhlmann and Donald R. Ulrich (deceased).

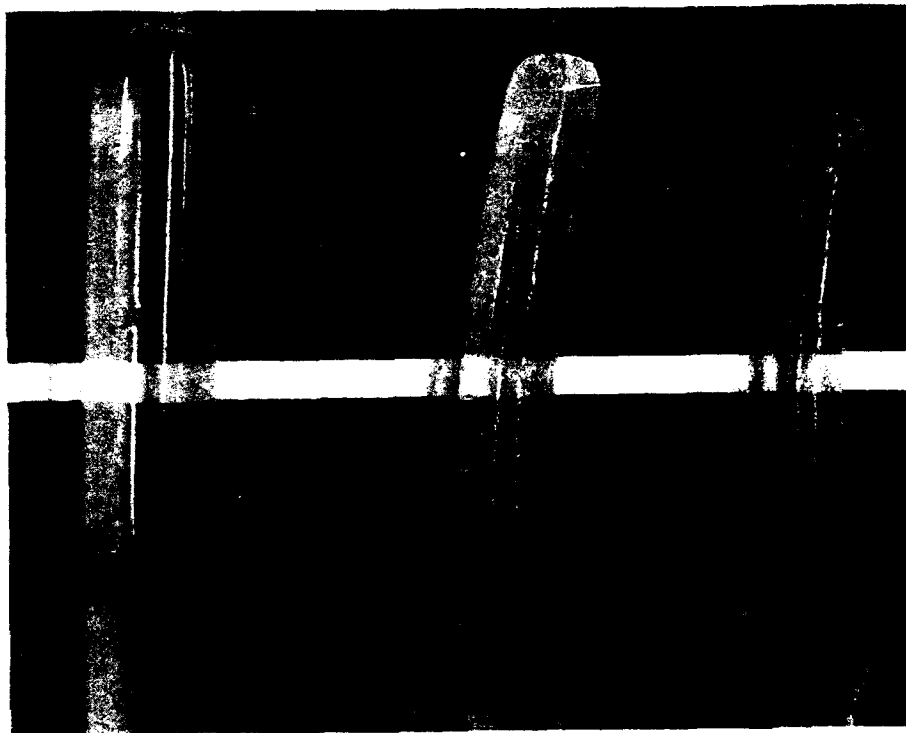
ISBN 0-471-52986-9 © 1992 John Wiley & Sons, Inc.

more typical cases is on the order of 10% (linear). For example, after a year of syneresis, a base-catalyzed silica gel was found to have contracted  $\sim 8\%$  in diameter, but it shrinks several times as much in a few days if evaporation is permitted [4]. Thus, the driving force for shrinkage provided by chemical reactions is small compared to the other factors operating during evaporation. On the other hand, the mechanical properties of gels are profoundly affected by the formation of new bridging bonds. The modulus and viscosity of the gel increase during aging and rise even faster during drying-induced shrinkage. It seems likely that the contraction brings reactive M-OH groups into proximity so that further condensation is possible, and the shrinkage is irreversible. This process is also influenced by adsorbed organics: in alcohol/acetone solutions, where condensation is inhibited by adsorption, it was found that the modulus of silica gel does not increase during aging [4]. Thus chemical reactions are less important for their contribution to the driving force for shrinkage than for their impact on the rheology of the gel.

#### 16.2.2. Osmosis

*Osmosis* is a process of diffusion driven by a concentration gradient. For example, if pure liquid is separated from a salt solution by a membrane that is permeable to liquid, but not to salt, pure liquid will diffuse into the salt-rich side. This type of transport occurs in general when liquid A and B are separated by a membrane permeable only to B. A dramatic example is shown in Fig. 16.1: Yoldas [5] prepared a sol of alumina in water, placed it into a bag made from a dialysis membrane, and immersed the bag in alcohol; as the water diffused out of the sol into the alcohol bath, the sol contracted and finally gelled. Beyond the gel point it is not necessary to have a membrane to have osmotic flow, because the network of the gel serves the same function: if a gel is immersed in a salt solution, liquid diffuses out of the pores into the bath; counterflow is inhibited by the low permeability of the network, so there is a net shrinkage of the gel. If the permeability of the network were high, no tension would develop in the pores, because liquid would flow in from the bath; without tension (and corresponding compressive force on the network) there would be no shrinkage of the gel. A typical situation that arises during drying of a gel with a solution of alcohol and water in its pores is that the alcohol evaporates preferentially, creating a concentration gradient of alcohol in water that induces interdiffusion of the liquids. This phenomenon may be exploited to reduce drying stresses [6].

In organic polymers it is recognized that there is a difference in the affinity of polymer chains for one another and of the chains for the solvent; if the concentration of chains changes (e.g., by evaporation of solvent) or if the quality of the solvent changes, the change in chemical potential of the chains will induce diffusion of the solvent. This phenomenon contributes to the enormous volume changes seen in polyacrylamide gels upon a change in the ratio of acetone to water in the pore liquid [7]. For silicate gels there is no report of swelling upon immersion in any liquid. The rate of *shrinkage* may change when a gel is



**Figure 16.1.** Sample on left is dialysis bag containing fresh sol ( $\sim 5\%$  solids in water) of alkoxyde-derived alumina; bag was suspended in an alcohol bath, allowing the water to diffuse out of the bath. Loss of water caused the sample to gel (middle sample); further loss caused more shrinkage (right sample). After removal from the bath, the sample was completely dried by exposure to air, but little further shrinkage occurred. The shrinkage in the bath occurred in a matter of hours. (From Ref. 5.)

transferred from one liquid to another, but the change is always in the direction expected from the effect of the new liquid on the rate of condensation reactions [8]. Quinson et al. [9] reported microsyreresis in a titania gel that increased the pore size by a factor of 3. This resulted in only a 1–3% increase in volume when the gel was transferred into pure decane; the volume returned to the original value when the sample was immersed in pure water. This small effect was produced by liquids that represent the extremes of polar and nonpolar behavior, so it is not surprising that osmotic swelling has not been observed in polymeric inorganic gels in alcohol/water systems. On the other hand, osmotic forces are important in clays [10] and transition metal gels [11], which consist of covalently bonded sheets held together by ions. Water tends to invade the space between the sheets and build a layer of hydration around the ions, which pushes the sheets apart. As a result, such materials may swell and even disperse when immersed in liquid.

### 16.2.3. Disjoining Forces

*Disjoining forces* are a class of short-range forces resulting from the presence of a solid/liquid interface. The most important examples are double-layer repulsion between charged surfaces and interactions caused by structure created in the liquid by dispersion forces. Liquid molecules, especially water [12, 13], tend to adopt a special structure in the vicinity of a solid surface. The interaction with the surface is so strong that the adsorbed layers resist freezing. Brun et al. [14], using a calorimetric method, found a noncrystallizing layer with a thickness of 0.8 nm for water and 1.3 nm for benzene. Water in the pores of silica gel is also found to have a higher thermal expansion coefficient and density than bulk water [15]. These *structured layers* inhibit close approach of surfaces, as they resist overlapping. The effect of adsorption forces on the mobility of molecules near solid surfaces is discussed in section 16.3.2.

At low concentrations of electrolyte, the force between surfaces is found to obey the DLVO theory until the separation is  $\sim 1.5$  nm; then the force oscillates as individual layers of molecules are displaced. The same behavior is observed in a wide range of nonaqueous liquids. In water containing high concentrations of electrolytes, ions adsorbed on the solid surface develop a layer of hydration that creates an additional component of repulsion that decays exponentially over the range of  $\sim 1.5$  to 4 nm (decay length  $\sim 0.6$  to 1.1 nm). This monotonic component results from hydration forces, not ordering of molecules, and is not observed in liquids other than water [13].

As evaporation occurs and solid surfaces are brought together, repulsive forces arising from electrostatic repulsion, hydration forces, and solvent structure resist contraction of the gel. The pore liquid will diffuse or flow from the swollen interior of the gel toward the exterior to allow the surfaces to move farther apart. The disjoining forces thus produce an osmotic flow, because transport is driven by a gradient in concentration of the solid phase. Because these forces become important when the separation between surfaces is small, they are most likely to be important near the end of drying, when the pore diameter may approach 2 nm.

### 16.2.4. Capillary Forces

The capillary pressure in an unsaturated porous body can be predicted by a simple argument [16, 17], if the pore size is uniform. Suppose that the liquid in the saturated portion of the body is suddenly subjected to a negative pressure of  $P_c$  (as if the interfacial energies were just now "turned on"). It will cause the solid network to contract so that the pore space in the saturated region decreases by  $\Delta V$ , forcing that volume of liquid to redistribute into the previously unsaturated region. The liquid will cover an area equal to  $\Delta V S_p / V_p$ , where  $S_p / V_p$  is the surface-to-volume ratio of the empty pores, so the redistribution process will yield energy equal to  $(\gamma_{sv} - \gamma_{sl}) \Delta V S_p / V_p$ ;  $\gamma_{sv}$  and  $\gamma_{sl}$  are the solid/vapor and solid/liquid interfacial energies, respectively. The work done by the liquid to

cause that contraction is simply  $P_c \Delta V$ , so balancing these energies we find that the capillary pressure is

$$P_c = -\frac{(\gamma_{sv} - \gamma_{sl})S_p}{V_p} = -\frac{\gamma_{lv} \cos(\theta)S_p}{V_p} \quad (1)$$

where  $\gamma_{lv}$  is the liquid/vapor interfacial energy and  $\theta$  is the contact angle. The specific surface area of a porous body (interfacial area per gram of solid phase),  $S$ , is related to the surface to volume ratio by [17]

$$\frac{S_p}{V_p} = \frac{S\rho_s\rho}{1-\rho} \quad (2)$$

where  $\rho$  is the *relative density*,  $\rho = \rho_b/\rho_s$ ,  $\rho_b$  is the *bulk density* of the solid network (not counting the mass of the liquid), and  $\rho_s$  is the density of the solid skeleton (the *skeletal density*).

The preceding analysis is strictly valid only if the pore size of the body is uniform. Otherwise, the liquid will preferentially invade the smaller pores in which the capillary suction is greatest; that is, the liquid will invade the pores with the greatest surface-to-volume ratio, because that route will yield the greatest reduction in the energy of the system. One might think that the pores would fill in order, from smallest to largest, so that the pressure could be predicted as a function of volume fraction of liquid, if the pore size distribution were known. That may not be true in general, however, because the pores of a given size might not be connected with one another. For example, the smallest pores might be separated by much larger ones that the liquid would not tend to enter, so some intermediate pores would fill before all of the smallest ones could. This is a problem of percolation [18], because it depends on the connectivity of randomly distributed pores.

The vapor pressure of the liquid,  $p_v$ , is related to the capillary pressure by the *Gibbs-Thompson* (or *Kelvin*) equation,

$$p_v = p_0 \exp\left(\frac{V_m P_c}{R_g T}\right) = p_0 \exp\left(\frac{V_m \kappa \gamma_{lv}}{R_g T}\right) \quad (3)$$

where  $p_0$  is the vapor pressure over a flat liquid surface,  $V_m$  is the molar volume of the liquid,  $R_g$  is the ideal gas constant, and  $\kappa$  is the curvature of the liquid/vapor interface. Recalling that  $P_c$  and  $\kappa$  are negative, we see that the vapor pressure is reduced over a concave interface. It is easy to understand intuitively that molecules are less likely to leave when tension (suction) already exists in the liquid phase. Because the pore diameters in gels are typically in the range of 2 to 10 nm, significant reductions in  $p_v$  can occur.

It is obvious that Eq. 3 must cease to be valid when the radius of the pore approaches atomic dimensions, because the concepts of interfacial energy and contact angle lose their meaning. This equation has been subjected to direct

tests [19–21], and it has been shown that the relation between liquid pressure and vapor pressure is valid for radii as small as 1 nm for organic liquids such as cyclohexane, *n*-hexane, and benzene. For water, one study [21] concludes that Eq. 3 is valid for vapor pressures as low as  $p_v/p_0 \geq 0.7$ , corresponding to a radius of curvature  $\geq 1.5$  nm; another [20] finds departures exceeding 10% when  $p_v/p_0 < 0.9$ , when the radius of curvature drops below  $\sim 5$  nm. The difference between the behavior of water and the organic liquids is attributed to the long range hydration forces in water, which could influence the surface tension in films less than 5 nm thick [20]. These studies indicate that the concepts of bulk thermodynamics can be applied without serious error even on the scale of sizes of interest in inorganic gels.

The importance of capillary pressure to the drying of gels is not its effect on the vapor pressure, but its effect on the solid phase. The tension in the liquid is supported by the solid phase (for example, the walls of a simple capillary tube are subjected to a tensile stress equal to  $-P_c$  that pulls them radially inward). The gel contracts as the liquid evaporates from its pores, because of the huge stresses generated by the menisci in the tiny pores. In ordinary ceramic materials, where the pore diameters are on the order of millimeters, these stresses are relatively small, but in gels they can exceed the strength of the network by a considerable margin. If the pressure is uniformly applied on the network (i.e., if it is placed under hydrostatic compression by the liquid), it will shrink uniformly and have no tendency to crack. However, as we shall see, large pressure gradients can develop through the thickness of the gel, such that the network is compressed more at the exterior surface than in the interior or the body, and this differential strain causes cracking. Such pressure gradients are quickly relaxed by fluid flow in materials with large pores, but flow is difficult within gels, so the gradients persist.

#### 16.2.5. Moisture Stress

*Moisture stress* or *moisture potential*,  $\psi$ , is the partial specific Gibbs free energy (J/g) of liquid in a porous medium and is given by [22]

$$\psi = \left( \frac{R_g T}{\rho_L V_m} \right) \ln \left( \frac{p_v}{p_0} \right) \quad (4)$$

where  $\rho_L$  is the density of the liquid. In soil science [23] it is conventional to define the moisture potential in terms of the height to which it would draw a column of water, so a factor of  $g$  (the gravitational acceleration) would be included in the denominator on the right side of Eq. 4. Comparison of Eqs. 4 and 3 reveals that  $\psi$  is equivalent to  $P_c/\rho_L$  when only capillary forces are acting (or, according to the alternative definition,  $\psi = P_c/\rho_L g$ ). However, the moisture potential is quite general, because the vapor pressure is depressed by other factors, including osmotic pressure, hydration forces, and adsorption forces. Thus, moisture potential subsumes all of the driving forces discussed above and

can be obtained by measuring the vapor pressure of the liquid in the system. For that reason, Zarzycki [24] recommends it as the appropriate potential driving shrinkage of gels during drying. The difficulty in implementing that suggestion is that capillary pressure gradients produce bulk flow, whereas concentration gradients (that produce osmotic pressure) cause diffusion, so it is necessary to apply portions of the total potential to different transport processes. In soil science, it is customary to assume that bulk flow is driven by the gradient in moisture potential, but it is done with the understanding that factors other than capillary pressure and gravitation are negligible [23].

### 16.3. LIQUID TRANSPORT

#### 16.3.1. Darcy's Law

Fluid flow through porous media obeys *Darcy's law* [25, 26], which states that the flux of liquid,  $J$ , is proportional to the gradient in pressure in the liquid,  $\nabla P_L$ :

$$J = - \frac{D}{\eta_L} \nabla P_L \quad (5)$$

The flux is in units of volume per area of the porous body (*not* the area occupied by the liquid) per time (m/s),  $P_L$  is the force per unit area of the liquid (Pa),  $\eta_L$  is the viscosity of the liquid (Pa · s), and  $D$  is called the *permeability* and has units of area (m<sup>2</sup>). Positive flux moves in the direction of increasingly negative pressure (i.e., the flow is toward regions of greater tension in the liquid). Equation 5 is an empirical equation derived from observation of flow of water through soil [27], but it is analogous to *Poiseuille's law* for flow of liquid through a straight circular pipe. This has naturally led to many models for the permeability of porous media based on representations of the pores by arrays of tubes, resulting in equations of the form

$$D = (1 - \rho)r_h^2/f_s f_T \quad (6)$$

where  $1 - \rho$  is the porosity, and  $f_s$  and  $f_T$  are two finagle factors accounting for the noncircular cross section and the nonlinear path, respectively, of the actual pores;  $f_T$  is called the *tortuosity*. The *hydraulic radius*,  $r_h$ , is defined as the ratio of pore volume to surface area.  $r_h = S_p/V_p$ ; for a circular capillary of radius  $a$ ,  $r_h = a/2$ . A number of these models are discussed in the excellent texts by Scheidegger [25] and Dullien [26]; van Brakel [28] offers a critical review of over 300 such models. Every conceivable shape and distribution of pores has been considered, including tubes with various cross-sectional shapes, with and without constrictions and intersections along their length; some represent the solid phase by isolated solid objects and analyze the flow around them. The most popular model, because of its simplicity and accuracy, is the *Carman-*

*Kozeny equation*, which gives the permeability in terms of the relative density and specific surface area:

$$D = \frac{(1 - \rho)^3}{5(\rho S \rho_s)^2} \quad (7)$$

The factor of 5 is an estimate of the shape and tortuosity factors of the "tube" based on experimental results. This equation is reasonably successful for many types of granular materials, but it often fails and should be applied with caution.

Very little is known about the permeability of inorganic gels, but the importance of microstructure is revealed by studies of polyacrylamide gels. Phase separation occurs when PA gels are cooled to  $-17^\circ\text{C}$ , whereupon the polymer chains cluster together (as in Fig. 6.3) leaving relatively large pores. Using a light scattering technique, Tanaka et al. [29] found that phase separation resulted in an increase in permeability of more than an order of magnitude. Weiss et al. [30] found that the permeability of PA gels increased by orders of magnitude when the crosslink density was increased at a fixed concentration of monomer. This was attributed to the heterogeneous distribution of crosslinks, resulting in segregation into regions of dense polymer and open pores. By analogy, we would expect base-catalyzed silica gels to be more permeable than acid-catalyzed gels with the same concentration of silica, because the "granular" nature of the former systems implies the existence of larger pores. This idea is supported by data presented in section 16.3.2.

### 16.3.2. Flow in Small Pores

The pores of inorganic gels are so small that solvent structure can extend throughout the volume of the liquid, so the permeability of the gel can be controlled by liquid whose viscosity is different from that of the bulk liquid. There is abundant evidence that the mobility of liquid molecules is lowered in the vicinity of a solid surface. For example, nuclear magnetic resonance reveals that the reorientation time of water molecules is longer than for bulk liquid [31]; this phenomenon is used to estimate the surface area of porous materials by determining the relative amounts of rapidly and slowly relaxing solvent molecules [32]. Warnock et al. [33, 34] examined the mobility of nitrobenzene (a planar, polar molecule) and carbon disulfide (linear, nonpolar) within the pores of two types of silica gel, one derived from alkoxides and the other by Shoup's method [35] from potassium silicate. Using an optical spectroscopic technique, they found that nitrobenzene in a gel with 4.4-nm pores exhibited two reorientation times, one characteristic of the bulk liquid and one three times slower that was attributed to the molecules adjacent to the solid surface. If the gel was esterified by boiling in alcohol, the slow reorientation time was not observed; carbon disulfide showed only bulk behavior. These results imply that



the viscosity of the polar molecule is increased by a factor of  $\sim 3$  in the vicinity of the hydroxylated surface of the gel, but the mobility is unaffected if the surface or the molecule is nonpolar.

Chan and Horn [36] and Israelachvili [37] have reported contradictory results for the viscosity of liquid between two mica sheets at very small separations. It was subsequently recognized [38] that the technique used in both of those studies gives misleading results. Because the mica surfaces are curved, the measurement examines liquid in a gap of varying width; in fact, the measured viscosity is dominated by liquid in regions where separation of the surfaces is large (compared to the point of closest approach). Thus there are no reliable direct measurements of viscosity very close to solid surfaces.

There are very few direct measurements of flow through inorganic gels. Debye and Cleland [39] studied the permeability of a related material, VYCOR<sup>®</sup> porous glass, which has 5 to 10-nm pores and porosity of  $\sim 35\%$ . In accordance with Darcy's law, the flux was found to be proportional to the pressure drop through the sample. The permeability was in the range  $D \approx 0.02$ – $0.04 \text{ nm}^2$  (which means that a pressure drop of 1 atm through a plate 1 mm thick would allow water to flow at a rate of  $10^{-7} \text{ cm}^3/\text{cm}^2 \cdot \text{s}$ !); the Carman-Kozeny equation predicts  $D \approx 0.09 \text{ nm}^2$ . When the temperature was changed, the flux did not change at the same rate as the viscosity of the bulk liquid. This indicates that the temperature dependence of the liquid in the pores is different from that of the bulk liquid and/or that the thickness of the adsorbed (structured) layer changes with temperature. (Note that an underestimate of  $\eta_L$  would produce a corresponding underestimate of  $D$ ; if the pore liquid is more viscous than the bulk liquid, then  $D$  is smaller than indicated above, and the Carman-Kozeny equation is in error by more than the indicated factor of  $\sim 3$ .)

Scherer and Swiatek [40] measured the permeability of silica gels made from tetraethoxysilane (TEOS) using acid catalysis and  $R = (\text{moles water})/(\text{moles TEOS}) = 16$  (gel A), or two-step acid/base catalysis with  $R = 3.7$  (gel B2). The flux was found to be roughly proportional to the applied pressure in keeping with Darcy's law. Given the permeability of  $\sim 1 \text{ nm}^2$  for gel A and the relative density of  $\rho \approx 0.1$ , the surface area found from Eq. 7 is  $\sim 1400 \text{ m}^2/\text{g}$ , which is  $\sim 2.5$  times as large as the Brunaur-Emmett-Teller area of the corresponding xerogel. This could mean that  $\eta_L$  is 2.5 times as great as for the bulk liquid. The base-catalyzed gel B2 had a permeability  $\sim 10$  times greater than that of gel A, as expected (qualitatively) from its coarser pore structure.

These studies indicate that flow through gels obeys Darcy's law to the extent that the flux is proportional to the pressure gradient in the liquid. Further, it appears that  $D/\eta_L$  is within a factor of  $\sim 3$  of the value predicted by using the Carman-Kozeny equation and the bulk viscosity. However, the flow process is more complicated than in materials with larger pores, and it is probably not appropriate to assume that  $\eta_L$  is the same as for the bulk liquid (differences being likely in absolute value and temperature dependence). The errors are likely to increase as the gel shrinks during drying, as a larger proportion of the liquid in the pores is in structured layers.

### 16.3.3. Unsaturated Media

An *unsaturated* body contains both gas and liquid in its pores. Gels become unsaturated near the end of drying, when shrinkage stops and the meniscus recedes into the pores. The liquid is said to be in the *pendular* state when it is trapped in isolated pockets; at higher liquid contents, the pockets become contiguous and are said to be in the *funicular* state. In the pendular state, liquid is transported only by diffusion of the vapor, but funicular liquid can still be transported by flow, and the flux can be related to the gradient in capillary pressure by Darcy's law [25, 41]. The permeability is a strong function of liquid content and shows considerable hysteresis as the liquid content is raised and lowered.

### 16.3.4. Diffusive Transport

*Diffusion* is a random-walk process by which material is transported down a gradient in concentration. According to *Fick's law*, the diffusive flux,  $J_D$  (moles/cm<sup>2</sup> · s), is proportional to the gradient,  $\nabla C$  [42]:

$$J_D = -D_c \nabla C \quad (8)$$

where  $D_c$  is the chemical diffusion coefficient (cm<sup>2</sup>/s), and  $C$  is the concentration (mol/cm<sup>3</sup>). It was shown in section 16.1 that diffusion contributes to the shrinkage of gels in special cases (e.g., when the gel is immersed in a salt solution) and may be important during evaporative drying, if a concentration gradient develops in the pores by preferential evaporation of one component of the pore liquid.

In organic gels, a gradient in polymer concentration can produce osmotic flow. For example, Tanaka and Fillmore [43] found that spheres of polyacrylamide gel swelled by 10–14% linearly when transferred from paraffin oil into water; the infinite quantity of water in the bath then floods into the water-starved (concentrated) polymer. An analogous process in inorganic systems is the swelling of clay in water [44]. Rather than assuming that fluid transport occurred by diffusion, Tanaka and Fillmore [43] analyzed the rate of swelling by assuming that the network was effectively stretched by the *osmotic pressure*,  $\Pi$ , which created suction in the pore liquid and induced fluid flow (according to Darcy's law) into the gel. The kinetics of swelling were shown to depend on the elastic modulus and permeability of the gel network. Given that a pressure gradient exists,<sup>†</sup> it is interesting to see in what circumstances bulk flow will dominate over diffusive transport. The chemical potential,  $\mu$ , can be written in

<sup>†</sup>Actually, this is a controversial idea. Tanaka and Fillmore [43] image that the osmotic pressure "inflates" the network as if there were a gas pressure in the pores, but it is generally argued [45] that there is no actual pressure. It is hard to argue with the fact that the swelling kinetics were in agreement with independently measured values of the elastic modulus and permeability of the gel, but the validity of the approach is theoretically disputable.

terms of the concentration as

$$\Delta\mu = R_g T \ln(\gamma C) \quad (9)$$

where  $\gamma$  is the activity coefficient, so the potential gradient is

$$\nabla\mu = \frac{R_g T}{\gamma C} \nabla(\gamma C) \approx \frac{R_g T}{C} \nabla(C) \quad (10)$$

(the approximation is exact if Henry's law [45] applies). Fick's law can be written as

$$J_D = -\frac{D_c C}{R_g T} \nabla\mu = \frac{D_c C V_m}{R_g T} \nabla\Pi \quad (11)$$

where the second equality follows from the definition of the osmotic pressure,

$$\Delta\mu = -\Pi V_m \quad (12)$$

Note that  $C V_m = 1 - \rho$  is the volume fraction of liquid in the gel. We want to know when the volume flux from Darcy's law,  $J$ , exceeds that from diffusion,  $J_D V_m$ . From Eqs. 8 and 11 we find that fluid flow dominates when

$$\frac{D}{\eta_L} > \frac{D_c (1 - \rho) V_m}{R_g T} \quad (13)$$

The chemical diffusion coefficient can be related to the viscosity of the liquid by the Stokes-Einstein equation [46]

$$D_c = \frac{R_g T}{6\pi N_A r_m \eta_L} \quad (14)$$

where  $N_A$  is Avogadro's number, and  $r_m$  is the radius of the diffusing molecule. With Eqs. 6 and 14, Eq. 13 becomes

$$r_h > 2r_m \quad (15)$$

This means that flow dominates whenever the pore size is larger than a few times the molecular dimension. Of course, Darcy's law and the Carman-Kozeny equation cannot be expected to apply to such small pores, so the result must be taken as an order-of-magnitude estimate. Nevertheless, this is a physically appealing conclusion: diffusion dominates in dense objects (as in the initial swelling of a polymer by a solvent), but flow takes over whenever channels are present that are much larger than the diffusing molecules (as in osmotic swelling of gels). Pierre and Uhlmann [47] argue that diffusion is the dominant transport

process during drying of materials such as alumina gels, where osmotic forces are important. However, Dwivedi [48] found that the drying rate of alumina gels was too rapid to be explained by diffusion with a diffusion coefficient on the order of  $10^{-5} \text{ cm}^2/\text{s}$ . The latter conclusion is consistent with the preceding analysis.

Note that flow can relieve a gradient in polymer concentration by swelling the network, but cannot reduce a concentration gradient in the liquid phase. For example, if a gel is immersed in a salt solution, flow of the solution into the pores does not affect the difference in salt concentration between the bath and the original pore liquid; that can be achieved only by diffusion. Similarly, if evaporation creates a concentration gradient in the pore liquid, flow from the interior of the gel cannot eliminate it, only interdiffusion within the pores can do so. Therefore, the analysis given above applies only to situations such as the swelling experiment by Tanaka et al. and to flow within a clay body (where tension in the liquid is produced by disjoining forces), where there is a gradient in concentration of solid phase.

Fluid flow is the principal transport mechanism in both saturated and unsaturated media, but diffusion of vapor becomes increasingly important as the liquid content of the pores decreases. After the pendular state is reached, liquid can be removed from the gel only by diffusion of its vapor. Isolated pockets of liquid actually participate in the transport process, as shown by Philip and de Vries [49], because the gradient in vapor concentration causes liquid to condense on one side of the pocket and evaporate from the other; as a result, the flux through the liquid is the same as that through the vapor in the open pores. Whittaker [50] has analyzed the coupled flows of mass and heat during drying of unsaturated bodies, using the same principle of local averaging that is implicit in Darcy's law. That is, the transport parameters are assumed to be uniform on a scale large compared to the pores, but small compared to the drying body. His model has been successfully used to describe the temperature distribution and evaporation rate from porous sandstone [51, 52], for example.

#### 16.4. RHEOLOGY OF THE GEL

In this section we discuss a theoretical model for the deformation of a gel network. It is convenient to imagine that the properties of the liquid and solid are independent, but it should be kept in mind that this is an approximation, because (as Johnson [53] points out) disjoining forces may contribute to the rigidity of the gel. The *network* may be elastic, viscoelastic, or plastic, but we assume that the liquid and solid phases are incompressible; that is, stresses can deform the network, but cannot change the volume of the constituents. (For example, there might be  $10 \text{ cm}^3$  of polymeric material in  $100 \text{ cm}^3$  of dry sponge; when you crush it in your hand, the volume of the sponge might decrease to  $20 \text{ cm}^3$ , but there would still be very nearly  $10 \text{ cm}^3$  of polymer. The compressibility of the network is orders of magnitude greater than that of the solid phase.)

It has been shown that alkoxide-derived silica gels are viscoelastic [54], and that is the behavior that we will concentrate upon in the following discussion. It should be noted, however, that other types of behavior are seen in related materials. For example, particulate gels may be plastic [55] and may even redisperse when agitated [56]; other plastic materials include clay, soil [57], and wood [58].

In a classic series of papers, Biot developed a theory for the deformation of saturated and unsaturated porous media, assuming the solid skeleton to be homogeneous and elastic [59], homogeneous but anisotropic and viscoelastic [60, 61]; or heterogeneous, anisotropic, and viscoelastic [62]. The model was tailored to describe propagation of acoustic waves through soil [63], but could also be applied to consolidation and drying of soil. It allowed for compressibility of the solid and liquid phases, and for dissipation of energy within both phases, as well as by their relative movement. A number of other workers (e.g., [64–66]) have developed related models, but Johnson and Chandler [53, 67] have shown that the correct ones are special cases of, or approximations to, Biot's. The model discussed in this chapter [68, 69] is also closely related, but is particularly adapted to the case of drying of gels in that it allows for syneresis and for simple viscoelastic behavior.<sup>†</sup>

#### 16.4.1. Continuity

The *equation of continuity* (conservation of matter) is found to be [68]

$$\dot{\epsilon} = -\nabla \cdot J = -\nabla \cdot \left( \frac{D}{\eta_L} \nabla P \right) \quad (16)$$

where  $\dot{\epsilon}$  is the volumetric strain rate of the gel network. We need to express  $\dot{\epsilon}$  in terms of the stress in the liquid using a constitutive equation. Various authors have done this by using empirical (nonlinear elastic) equations [23, 70], by assuming elastic behavior with the solid and liquid phases compressible [59, 64] or incompressible [65, 71], or allowing the network to be purely viscous [69] or viscoelastic [60, 61, 62, 72, 73]. When the network is assumed to be elastic, Eq. 16 has the mathematical form of the diffusion equation. Philip [23] discusses at length the methods for solving the nonlinear version of that equation that results when the permeability and elastic properties vary with the porosity (and therefore with position in the body).

If the pores contain a solution of liquids with intrinsic diffusion coefficients  $D_1$  and  $D_2$ , then diffusion contributes to transport and the diffusion term must be added to the flow term. Then Eq. 16 becomes

$$\dot{\epsilon} = -\nabla \cdot \left( \frac{D}{\eta_L} \nabla P \right) + (1 - \rho) \nabla \cdot [V_{m1}(D_1 - D_2) \nabla C_1] \quad (17)$$

<sup>†</sup>Several mistakes in the original treatment [69] are discussed and corrected in Ref. 68.

Note that diffusion has no influence if the intrinsic diffusion coefficients of the two liquids are equal, because the diffusive volume fluxes are then equal and opposite (i.e., diffusion produces no volume flow). It has been shown that drying stresses can be reduced considerably when the diffusion term is significant.

#### 16.4.2. Finite Deformation

During drying of a gel, there is a huge change in volume (often 1 or 2 orders of magnitude), which is not explicitly allowed for in the analysis given in section 16.4.1. There are two ways of handling the contraction of the network: the *Eulerian* [74] and the *Langrangian* methods [75-77]. The Eulerian approach uses a coordinate system fixed in the frame of reference of the laboratory and takes account of the velocity of the body relative to that frame as the volume of the body changes. The Langrangian method uses a coordinate system fixed in the gel, such that a fixed volume of solid phase is contained in any volume element. The solution is obtained in terms of the *material coordinate*,  $m$ , where

$$dm = \rho \, dx \quad (18)$$

when the shrinkage is uniaxial (in the  $x$  direction). This approach is simpler than the Eulerian, but still leads to a nonlinear differential equation that must be solved by numerical methods, except in special cases. A Langrangian coordinate system was used implicitly in the derivation of Eq. 16. If the shrinkage varies strongly with position in the gel, then  $\rho = \rho(x)$ , and Eq. 18 indicates that the Langrangian coordinate is not linearly proportional to a coordinate fixed in the frame of the laboratory. However, if the volumetric contraction is nearly uniform throughout the gel, solutions obtained from Eq. 16 are valid regardless of the amount of shrinkage that has occurred.

#### 16.4.3. Drying Stress

As liquid evaporates from the gel, the network becomes exposed and a solid/vapor interface appears where a solid/liquid interface had been. This raises the energy of the system, because  $\gamma_{sv} > \gamma_{sl}$ , so liquid tends to flow from the interior of the gel to cover the exposed solid. As it stretches toward the exterior, the liquid goes into tension, and this has two consequences: (1) liquid tends to flow from the interior along the pressure gradient, according to Darcy's law and (2) the tension is balanced by compressive stress in the network that causes shrinkage. The lower the permeability, the more difficult it is to draw liquid from the inside of the gel, and therefore the greater the pressure gradient that develops. As the pressure gradient increases, so does the variation in free strain rate, with the surface tending to contract faster than the interior. It is the *differential strain* [i.e., the spatial variation in strain (for an elastic material) or strain rate (for a viscous material)] that produces stress.

As the stress in the liquid increases, the vapor pressure decreases according to

Eq. 3 with  $P_c = -P$ . However, during most of the drying process the pressure is too small to have a significant effect on the evaporation rate. In that case, we can find the pressure and stress distributions in a drying plate by solving Eq. 16 subject to the boundary condition that the flux at the exterior surface is constant:

$$\left. \frac{D}{\eta_L} \frac{dP}{dz} \right|_{z=L} = \dot{V}_E \quad (19)$$

where  $\dot{V}_E$  is the constant evaporation rate ( $\text{cm}^3/\text{cm}^2$  of gel/sec). When the permeability of the gel is not too low, the stress in the plane of a drying plate of gel is found to be [68]

$$\sigma_x \approx C_N \left( \frac{L\eta_L \dot{V}_E}{2D} \right) \left( \frac{z^2}{L^2} - \frac{1}{3} \right) \quad (\alpha \leq 1) \quad (20)$$

where the surfaces of the plate are at  $z = \pm L$ , and the constant  $C_N \approx 1$ . Thus there is a parabolic distribution of stress, with the greatest tension appearing at the drying surface,  $z = L$ . The stress increases in proportion to the thickness of the plate and the rate of evaporation and in inverse proportion to the permeability, that is, the stress is increased by those factors that steepen the pressure gradient. Comparing the stress at the surface of a drying plate, cylinder, and sphere, it is found [78] that the tension decreases in the ratio plate/cylinder/sphere  $= \frac{1}{3}/\frac{1}{4}/\frac{1}{5}$ . The lower stress reflects the shallower pressure gradients in the cylinder and sphere, where the liquid flowing from the interior passes through a volume that increases as  $r^2$  and  $r^3$ , respectively. Because these results are derived from Eq. 16, they are only valid as long as the pores remain filled with liquid. At some point the network will stop shrinking and the meniscus will retreat into the gel; then Eq. 20 will apply only within the saturated pores inside the gel.

Whereas the stress in the plate comes from the internal pressure distribution, the stress in a film results principally from the external constraint of the substrate. No strain can occur in the plane of the film, because it is too thin to deform the substrate. The stress in the film is [68, 79] approximately  $\sigma_x \approx P$ , which means that the stress in the film can be as large as the capillary stress in the liquid. The remarkable fact, discussed in the next section, is that this enormous stress does not cause fracture of thin films of gel.

## 16.5. AVOIDING FRACTURE

We have seen that drying produces a pressure gradient in the liquid phase of a gel, which leads to differential shrinkage of the network. When the exterior of the gel tries to shrink faster than the interior, tensile stresses arise that tend to fracture the network at the exterior. The material on either side of the crack can

contract more freely, so it is favorable for the crack to grow into the drying surface. It may seem odd that *compression* of the network by the liquid causes fracture. In fact, if the pressure in the liquid were uniform, the whole network would be isotropically compressed and the gel would shrink without risk of cracking. However, the higher tension in the liquid at the exterior causes greater contraction of the network in that region. Because that contraction is inhibited by the slower-contracting interior (where the tension in the liquid is less), the network at the exterior is effectively *stretched* (prevented from contracting), and this promotes cracking. Thus, it is the differential contraction that produces macroscopic tension in the network and causes cracking.<sup>†</sup>

Cracking occurs when the stress in the network exceeds its strength. Since the classic work of Griffith [80], it has been understood that fracture of brittle materials depends on the presence of flaws that amplify the stress applied to the body. That is, if a uniform stress  $\sigma_x$  is applied to a body containing a crack with a length of  $c$ , the stress at the tip of the crack is proportional to  $\sigma_x\sqrt{c}$ , and failure occurs when that stress exceeds the strength of the material. The theory of linear elastic fracture mechanics, which is discussed in several excellent textbooks [81–83], indicates that catastrophic crack propagation occurs when

$$\sigma_x\sqrt{\pi\gamma} \geq K_{IC} \quad (21)$$

where  $K_{IC}$  is a material property called the *critical stress intensity factor*, and  $\sigma_x$  represents the applied stress.

Unfortunately, there is only one report of measurement of  $K_{IC}$  for an alkoxide-derived gel. Zarzycki [55] determined  $K_{IC}$  as a function of aging time for two particulate gels and a sonogel (prepared by ultrasonic mixing of TEOS and water [84]); for the latter,  $K_{IC}$  was in the range of 160–270 Pa $\sqrt{m}$ , increasing slightly with age. If the full capillary pressure ( $P_R > 10$  MPa) were applied to that material, Eq. 21 indicates that any flaw with  $c > 0.1$  nm would grow uncontrollably. This unrealistically small size for the critical flaw size accounts for the instantaneous failure of gels when suddenly exposed to the atmosphere. In fact, the stress developed during slow drying, given by Eq. 20, is much smaller than  $P_R$ . The strength (i.e., the stress that causes fracture in a bending test) of similar gels is found to be  $\sim 0.1$  MPa [54]; with Zarzycki's data, this corresponds to a critical flaw size of  $c \approx 1\text{--}2$   $\mu\text{m}$ . Flaws of that size are inevitable, unless the mold is highly polished, and the sample is handled with the greatest care, so the drying stresses must be kept well below the maximum (viz.,  $\sigma_x = P_R$ ).

Cracking is sometimes attributed to the existence of a pore size distribution in

<sup>†</sup>An analogous argument can be offered in the case of thermal stress. One could say that a body contracts on cooling because of an effective compressive force that drives atom centers toward one another as the temperature decreases. If a temperature gradient exists in a body such that the surface is cooler, the atoms at the surface are being "compressed" more strongly, but they cannot freely move toward one another because they are bound to the warmer interior of the plate. The interior effectively stretches the surface beyond its equilibrium interatomic spacing, and cracking may result. Then the atoms on either side of the crack can move closer together.



the gel [85, 86]. That possibility is discussed and criticized in Ref. 2. The analysis presented here indicates that dangerous stresses can be developed even if the pore size distribution is perfectly uniform, so efforts to avoid fracture by controlling the breadth of the pore size distribution are futile.

A variety of strategies have been employed to avoid fracture from drying stresses, including: developing gels with larger pores (having lower capillary stress and higher permeability); aging to increase the strength of the gel, as well as increasing the pore size; using chemical additives to lower interfacial energies or encourage diffusion within the pores; supercritical drying to eliminate entirely the liquid/vapor interfacial energy, thereby preventing fracture and reducing shrinkage. These methods are discussed in Refs. 1 and 2.

As explained in section 16.4.3, the stress in a film is approximately equal to the tension in the liquid,  $\sigma_x \approx P$ . Therefore, as the film becomes rigid, the tension in the film becomes equal to the capillary stress,  $\sigma_x \approx P_R$ , which would shatter a macroscopic gel. There is no indication that the capillary stress is absent in a film; on the contrary, it seems sufficient to cause complete collapse of the porosity in some cases [87], as predicted [88] for a material with a very compliant matrix. The fascinating observation is that inorganic films thinner than  $\sim 0.5 \mu\text{m}$  do not crack, regardless of the drying rate, whereas films thicker than  $\sim 1 \mu\text{m}$  are virtually impossible to dry without cracks (see, e.g. [89-93]).

This behavior may be analogous [79] to crack growth in composites containing inclusions, where thermal expansion mismatch causes cracks to appear near large inclusions, but not near small ones. The explanation [94] is that the energy that drives the growth comes from relief of stress in a volume proportional to the size of the inclusion, whereas the energy invested to grow the crack is proportional to the surface area created. When the inclusion is small, this surface-to-volume ratio becomes a barrier to growth of the crack; that is, the energy invested to extend the crack is greater than the energy gained from relief of stresses near the inclusion. This line of argument is supported by the work of Thouless [95], who investigated the conditions for growth of flaws of the type shown in Fig. 16.2. It was shown that the energy release rate,  $G$ , for such flaws is approximately proportional to the thickness of the film,  $G \approx L$  (when  $R/a \approx 1$ ); there is also a very weak dependence on flaw size ( $G \sim R^{0.1}$ ). The stress intensity,  $K_I$ , at the tip of the crack is given by

$$K_I \propto \sqrt{G} \propto \sqrt{L} \quad (22)$$

so as  $L \rightarrow 0$ , it inevitably falls below the critical stress intensity of the material,  $K_{IC}$ . Unfortunately, we cannot apply this result to see whether it accounts quantitatively for the observed limit of  $\sim 1 \mu\text{m}$  for films, because the physical properties of the film are not known.

Two exceptions to the micrometer rule should be noted. Schmidt et al. [96] were able to dry films  $20 \mu\text{m}$  thick by using a silicon precursor with two nonhydrolyzing phenyl substituents. This evidently provided sufficient compliance (rubberiness) to prevent fracture. Cracking did occur when the organics

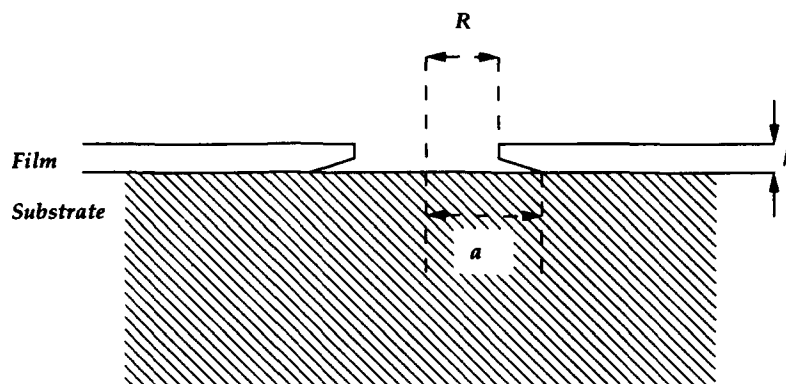


Figure 16.2. Pinhole of radius  $R$  in film extends to radius  $a$  along interface; film thickness  $h$  is much less than the thickness of the substrate. (After Ref. 95.)

were burned out, but large (compared to  $L$ ) areas remained intact. This appears to be a promising route to preparation of thicker films. Another remarkable exception to the rule was produced by Schlichting [97], who made dense films  $\sim 10\text{ }\mu\text{m}$  thick from alkoxides. It appears that he dipped the substrates in *unhydrolyzed* alkoxides and allowed hydrolysis to occur in the air, then heated the samples slowly ( $37^\circ\text{C/hr}$ ) to  $700\text{--}900^\circ\text{C}$ . Perhaps these mild conditions left a substantial fraction of ligands unhydrolyzed during drying (as contrived deliberately by Schmidt et al.), allowing the rubbery film to remain intact. This remarkably simple approach deserves to be reexamined.

## 16.6. CONCLUSIONS

The principal factors driving shrinkage of drying gels are capillary pressure and osmotic pressure. The pores in inorganic gels are so small that thermodynamic properties such as the liquid/vapor interfacial energy begin to depart from their bulk values; however, significant deviations are not expected for pores larger than  $\sim 2\text{ nm}$ . Therefore, the pressures can be reasonably estimated for most gels. Liquid is transported to the surface of the gel by Darcy flow and/or diffusion. The latter is expected to be important only if a concentration gradient exists within the liquid phase *and* the components of the solution have different intrinsic diffusion coefficients, but it is not known how generally that occurs. The viscosity controlling the rate of flow may be substantially higher than the bulk viscosity, especially when the pore liquid is water, when the pore diameter is  $< 5\text{ nm}$ . The limited data presently available indicate that Darcy's law is obeyed: The flux through the gel is proportional to the pressure gradient.

The existence of a pressure gradient in the pore liquid gives rise to stresses that cause cracking of drying gels. Several strategies that reduce the capillary pressure or raise the strength of the gel have been successfully employed. In

films, the stress is always high (approximately equal to the capillary stress), but cracks do not form if the film is thin (typically  $<0.5 \mu\text{m}$ ). This is attributed to the small amount of elastic energy stored in the film, which is incapable of causing propagation of existing flaws.

There is a critical need for experimental studies of transport processes (measurement of permeability of the gel network, viscosity of the pore liquid), rheology of the network (viscosity, modulus, yield stress), fracture mechanics of gels, and direct measurements of stresses and strains developed during drying. The theory clearly indicates the essential properties, but virtually no data are currently available to test the predictions of drying stresses.

## REFERENCES

1. C. J. Brinker and G. W. Scherer, *Sol-Gel Science* (Academic Press, New York (1989).
2. G. W. Scherer, *J. Non-Cryst. Solids*, **100**, 77-92 (1988).
3. B. E. Yoldas, *J. Mater. Sci.*, **21**, 1087-1092 (1986).
4. G. W. Scherer, *J. Non-Cryst. Solids*, **109**, 183-190 (1989).
5. B. E. Yoldas, private communication, Westinghouse Co., Pittsburgh, Pa.
6. G. W. Scherer, *J. Non-Cryst. Solids*, in press.
7. T. Tanaka, *Sci. Am.*, **244**, 124-138 (1981).
8. G. W. Scherer, in: C. J. Brinker, D. E. Clark, and D. R. Ulrich, Eds, *Better Ceramics Through Chemistry*, Vol. III, *Mater. Res. Soc. Symp. Proc.*, 179-186 (1988).
9. J. F. Quinson, N. Tchikam, J. Dumas, C. Bovier, J. Serughetti, C. Guizard, A. Larbot, and L. Cot, *J. Non-Cryst. Solids*, **99** 151-159 (1988).
10. H. van Olphen, *Introduction to Clay Colloid Chemistry*, Interscience, London (1977).
11. J. Livage, *J. Solid State Chem.*, **64**, 322-330 (1986).
12. K. J. Packer, *Phil. Trans. R. Soc. London, Ser. B*, **278**, 59-87 (1977).
13. J. N. Israelachvili, *Chem. Scr.*, **25**, 7-14 (1985).
14. M. Brun, A. Lallemand, J. F. Quinson, and C. Eyraud, *Thermochimica Acta*, **21** 59-88 (1977).
15. B. V. Derjaguin, V. V. Karasev, and E. N. Khromova, *J. Colloid Interface Sci.*, **109**, 586-587 (1986).
16. L. R. White, *J. Colloid Interface Sci.*, **90**, 536-538 (1982).
17. G. W. Scherer, *J. Non-Cryst. Solids*, **92**, 375-382 (1987).
18. R. Zallen, *The Physics of Amorphous Solids*, Chap. 4, Wiley, New York (1983).
19. L. R. Fisher and J. N. Israelachvili, *J. Colloid Interface Sci.*, **80**, 528-541 (1981).
20. L. R. Fisher and J. N. Israelachvili, *Colloids Surfaces*, **3**, 303-319 (1981).
21. H. K. Christenson, *J. Colloid Interface Sci.*, **121**, 170-178 (1988).
22. R. Q. Packard, *J. Am. Ceram. Soc.*, **50**, 223-229 (1967).
23. J. R. Philip, *Hydroscience*, **5**, 215-296 (1969).
24. J. Zarzycki, in: L. L. Hench and D. R. Ulrich, Eds., *Ultrastructure Processing of Ceramics, Glasses, and Composites*, pp. 27-42, Wiley, New York (1984).
25. A. E. Scheidegger, *The Physics of Flow Through Porous Media*, 3d ed., Univ. Toronto Press, Toronto, Canada (1974).
26. F. A. L. Dullien, *Porous Media — Fluid Transport and Pore Structure*, Academic Press, New York (1979).

27. H. Darcy, *Les Fontaines Publiques de la Ville de Dijon*, Librairie des Corps Impériaux des Ponts et Chaussées et des Mines, Paris (1856).
28. J. van Brakel, *Powder Technol.*, **11**, 205–236 (1975).
29. T. Tanaka, S. Ishiwata, and C. Ishimoto, *Phys. Rev. Lett.*, **38**, 771–774 (1977).
30. N. Weiss, T. van Vliet, and A. Silberberg, *J. Polym. Sci., Polym. Phys. Ed.*, **17**, 2229–2240 (1979).
31. K. J. Packer, *Phil. Trans. R. Soc. London, Ser. B*, **278**, 59–87 (1977).
32. C. L. Glaves, C. J. Brinker, D. M. Smith, and P. J. Davis, *Chem. Mater.*, **1**, 34 (1989).
33. J. Warnock, D. D. Awschalom, and M. W. Shafer, *Phys. Rev. B*, **34**, 475–478 (1986).
34. M. W. Shafer, D. D. Awschalom, J. Warnock, and G. Ruben, *J. Appl. Phys.*, **61**, 5438–5446 (1987).
35. R. D. Shoup, *Colloid and Interface Science*, Vol. III, pp. 63–69, Academic Press, New York (1976).
36. D. Y. C. Chan and R. G. Horn, *J. Chem. Phys.*, **83**, 5311–5324 (1985).
37. J. N. Israelachvili, *J. Colloid Interface Sci.*, **110**, 263–271 (1986).
38. J. van Alsten, S. Granick, and J. N. Israelachvili, *J. Colloid Interface Sci.*, **125**, 739–740 (1988).
39. P. Debye and R. L. Cleland, *J. Appl. Phys.*, **30**, 843–849 (1959).
40. G. W. Scherer and R. M. Swiatek, *J. Non-Cryst. Solids*, in press.
41. K. K. Watson, *Water Resources Res.*, **2**, 709–715 (1966).
42. J. Crank, *Mathematics of Diffusion*, Clarendon Press, Oxford (1975).
43. T. Tanaka and D. J. Fillmore, *J. Chem. Phys.*, **70**, 1214–1218 (1979).
44. H. van Olphen, *Introduction to Clay Colloid Chemistry*, Interscience, London (1977).
45. K. Denbigh, *The Principles of Chemical Equilibrium*, Cambridge Univ. Press, Cambridge (1968).
46. R. B. Bird, W. E. Stewart, and E. N. Lightfoot, *Transport Phenomena*, Wiley, New York (1960).
47. A. C. Pierre and D. R. Uhlmann, in: C. J. Brinker, D. E. Clark, and D. R. Ulrich, Eds., *Better Ceramics Through Chemistry*, Vol. III, *Mater. Res. Soc., Symp. Proc.*, **121**, 207–212 (1988).
48. R. K. Dwivedi, *J. Mater. Sci. Lett.*, **5**, 373–376 (1986).
49. J. R. Philip and D. A. de Vries, *Trans. Am. Geophys. Union*, **38**, 222–232 (1957) (1957) (erratum, p. 594).
50. S. Whitaker, *Adv. Heat Transfer*, **13**, 119–203 (1977).
51. C. K. Wei, H. T. Davis, E. A. Davis, and J. Gordon, *AIChE J.*, **31**, 1338–1348 (1985).
52. C. K. Wei, H. T. Davis, E. A. Davis, and J. Gordon, *AIChE J.*, **31**, 842–848 (1985).
53. D. L. Johnson, *J. Chem. Phys.*, **77**, 1531–1539 (1982).
54. G. W. Scherer, S. A. Pardenek, and R. M. Swiatek, *J. Non-Cryst. Solids*, **107**, 14–22 (1988).
55. J. Zarzycki, *J. Non-Cryst. Solids*, **100**, 359–363 (1988).
56. E. M. Rabinovich, in: L. C. Klein, Ed., *Sol-Gel Technology for Thin Films, Fibers, Preforms, Electronics, and Speciality Shapes* pp. 260–294, Noyes, Park Ridge, N.J. (1988).
57. L. D. Baver, W. H. Gardner, and W. R. Gardner, *Soil Physics*, 4th ed., Wiley, New York (1972).
58. P. F. Lesse, *Wood Sci. Technol.*, **6**, 204–214; 272–283 (1972).
59. M. A. Biot, *J. Appl. Phys.*, **12**, 155–164 (1941).
60. M. A. Biot, *J. Appl. Phys.*, **25**, 1385–1391 (1954).
61. M. A. Biot, *J. Acoustical Soc. Am.*, **34**, 1254–1264 (1962).
62. M. A. Biot, *J. Appl. Phys.*, **33**, 1482–1498 (1962).
63. M. A. Biot, *J. Acoust. Soc. Am.*, **28**, 168–178; 179–191 (1956).
64. J. Geertsma, *J. Mech. Phys. Solids*, **6**, 13–16 (1957).
65. T. Tanaka, L. O. Hocker, and G. B. Benedek, *J. Chem. Phys.*, **59**, 5151–5159 (1973).
66. J. R. Rice and M. P. Clearly, *Rev. Geophys. Space Phys.*, **14**, 227–241 (1976).

67. R. N. Chandler and D. L. Johnson, *J. Appl. Phys.*, **52**, 3391-3395 (1981).
68. G. W. Scherer, *Non-Cryst. Solids*, **109**, 171-182 (1989).
69. G. W. Scherer, *J. Non-Cryst. Solids*, **87**, 199-225 (1986).
70. H. H. Macey, *Trans. B. Ceram. Soc.*, **41**, 73-121 (1942).
71. G. W. Scherer, *J. Non-Cryst. Solids*, **92**, 122-144 (1987).
72. G. W. Scherer, *J. Non-Cryst. Solids*, **99**, 324-358 (1988).
73. P. J. Banks, in: R. Toei and A. S. Mujumdar, Eds., *Drying '85*, pp. 102-108, Hemisphere, New York (1985).
74. J. R. Philip, *Aust. J. Soil Res.*, **6**, 249-267 (1968).
75. J. R. Philip and D. E. Smiles, *Aust. J. Soil Res.*, **7**, 1-19 (1969).
76. J. R. Philip, *Fundamentals of Transport Phenomena in Porous Media*, pp. 341-355, Elsevier, New York (1972).
77. H. J. M. van Dijk, P. Walstra, and J. Schenk, *Chem. Eng. J.*, **28**, B43-B50 (1984).
78. G. W. Scherer, *J. Non-Cryst. Solids*, **91**, 101-121 (1987).
79. G. W. Scherer, *J. Non-Cryst. Solids*, **89**, 217-238 (1987).
80. A. A. Griffith, *Phil. Trans. R. Soc. London, Ser. A*, **221**, 163-198 (1920).
81. B. R. Lawn and T. R. Wilshaw, *Fracture of Brittle Solids*, Cambridge Univ. Press, Cambridge (1975).
82. H. L. Ewalds and R. J. H. Wanhill, *Fracture Mechanics*, Edward Arnold, Victoria, Australia (1984).
83. G. P. Cherepanov, *Mechanics of Brittle Fracture*, McGraw-Hill, New York (1979).
84. L. Esquivias and J. Zarzycki, in: J. D. Mackenzie and D. R. Ulrich, Eds., *Ultrastructure Processing of Advanced Ceramics*, pp. 255-270, Wiley, New York (1988).
85. J. Zarzycki, M. Prassas, and J. Phalippou, *J. Mater. Sci.*, **17**, 3371-3379 (1982).
86. L. L. Hench, in: L. L. Hench and D. R. Ulrich, Eds., *Science of Ceramic Chemical Processing*, pp. 52-64, Wiley, New York (1986).
87. G. C. Frye, A. J. Ricco, S. J. Martin, and C. J. Brinker, in: C. J. Brinker, D. E. Clark, and D. R. Ulrich, Eds., *Better Ceramics Through Chemistry*, Vol. III, pp. 349-354, *Mater. Res. Soc. Symp. Proc.* (1988).
88. W. H. Banks and W. W. Barkas, *Nature*, **158**, 341-342 (1946).
89. H. Schroeder, in: G. Hass, Ed., *Physics of Thin Films*, pp. 87-141, Academic Press, New York (1969).
90. H. Dislich, in: L. C. Klein, Ed., *Sol-Gel Technology for Thin Films, Fibers, Preforms, Electronics, and Specialty Shapes*, pp. 50-79, Noyes, Park Ridge, N.J. (1988).
91. S. Sakka, K. Kamiya, K. Makita, and Y. Yamamoto, *J. Non-Cryst. Solids*, **63**, 223-235 (1984).
92. I. Strawbridge and P. F. James, *J. Non-Cryst. Solids*, **82**, 366-372 (1986).
93. I. Strawbridge and P. F. James, *J. Non-Cryst. Solids*, **86**, 381-392 (1986).
94. F. F. Lange, in: R. C. Bradt, D. P. H. Hasselman, and F. F. Lange, Eds., *Fracture Mechanics of Ceramics*, Vol. 2, *Microstructure, Materials, and Applications*, pp. 599-609, Plenum, New York (1974).
95. M. D. Thouless, *Acta Metall.*, **36**, 3131-3135 (1988).
96. H. Schmidt, G. Rinn, R. Nass, and D. Sporn, in: C. J. Brinker, D. E. Clark, and D. R. Ulrich, Eds., *Better Ceramics Through Chemistry*, Vol. III, *Mater. Res. Soc. Symp. Proc.*, 743-754 (1988).
97. J. Schlichting, *J. Non-Cryst. Solids*, **63**, 173-181 (1984).

# 17

## PHASE SEPARATION AND CLUSTERING IN SYSTEMS OF RODLIKE PARTICLES

LARRY A. CHICK, CHRISTOPHER VINEY,  
AND ILHAN A. AKSAY

### 17.1. INTRODUCTION

Although a few investigators [1,2] have reported maximum packing concentrations for randomly oriented, rodlike reinforcing media, we have found no published studies dealing with the local arrangement of such rods. Milewski's [1] empirical studies of randomly oriented macroscopic rods (wooden sticks) established an inverse relationship between the axial ratio and the maximum packing fraction. Evans and Gibson [2] used free-volume concepts to model the maximum packing fraction. These free-volume arguments were originally developed to model the liquid crystalline phase behavior of rodlike molecules. However, it is reasonable to expect the packing of macroscopic rods (sticks), microscopic rods (fibers and whiskers), and molecular rods to follow the same pattern. Figure 17.1 compares Milewski's results with the upper concentration limit of stability for pure random phase predicted by Flory [3,4] for an athermal system of rodlike molecules. At concentrations greater than those indicated by the phase boundary, rodlike molecules phase-separate into an aligned (ordered; anisotropic) phase and a randomly oriented (disordered; isotropic) phase. This

*Ultrastructure Processing of Advanced Materials.*

Edited by Donald R. Uhlmann and Donald R. Ulrich (deceased).

ISBN 0-471-52986-9 © 1992 John Wiley & Sons, Inc.

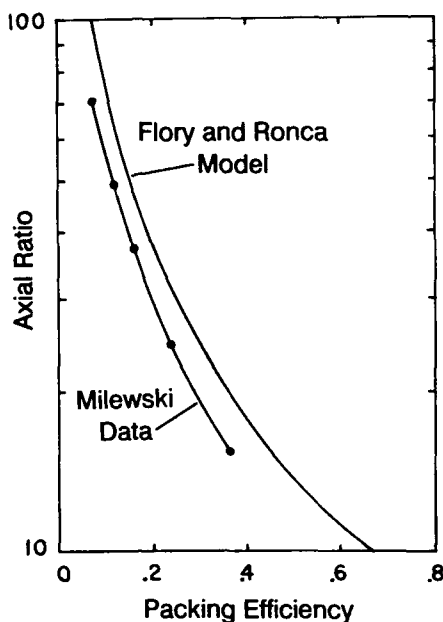


Figure 17.1. Comparison of Milewski's data for wooden rods and glass fibers [1] with the boundary of the pure random phase from Flory and Ronca's model for rigid-rod liquid crystals [4].

transition is spontaneous if the molecules undergo sufficient thermal agitation. Evans and Gibson [2] assume that randomly oriented macroscopic and microscopic rods would not exhibit the transition to an aligned phase, because they are too large to be agitated sufficiently. Yet, it is easily demonstrated that, when packed to high concentration, macroscopic rods do form into clusters with a high degree of internal alignment (Fig. 17.2). We suggest that many processing operations that are used in fabricating composites, for example, high-shear blending and sonication, provide sufficient agitation to allow at least partial transition to an aligned state.

In investigating similarities between the packing of macroscopic rods and the phase behavior of rigid, rodlike molecules, we began with two-dimensional systems. It is simpler to observe the arrangement of rods in a monolayer than in the bulk of a three-dimensional system. Also, practical composites are frequently built up by laminating sheets that individually contain two-dimensional distributions of fibers. Our first task has been to establish a phase diagram for two-dimensional systems of rods. Several investigators [5-7] have studied two-dimensional configurations of rods by using lattice-based Monte Carlo simulations. However, these calculations restricted the rods to two distinct orthogonal orientations and to distinct positions determined by the lattice; none produced a phase diagram. We also employed Monte Carlo techniques, but utilized continuously varying position and orientation.



**Figure 17.2.** Clustering caused by mechanical vibration of wooden rods (axial ratio of 16) in a beaker.

## 17.2. THE MODEL

Our approach is directed by the well-accepted three-dimensional model of Flory and Ronca [4], which is derived for athermal systems, that is, for rods that exhibit neither attraction nor repulsion with respect to the solvent or each other. In such systems, the free energy is determined solely by entropy, which is composed of a translational and an orientational component. Flory and Ronca approximated the translational entropy on the basis of a lattice model and the orientational entropy by using an equation derived from combinatorial analysis. It is possible to formulate their model in two dimensions by redefining the parameters that describe rod orientation. However, the model adapted in this way does not predict any phase separation [8]. Some further refinements are therefore necessary. We chose to measure the translational entropy directly from our Monte Carlo simulations and to calculate the orientational entropy by using the exact combinatorial equation from which Flory and Ronca's approximation was derived.

The Flory-Ronca approach stipulates that the translational (combinatory) partition function is given by

$$Z_c = \frac{1}{n_x!} \prod_{j=1}^{n_x} v_j \quad (1)$$



where  $n_x$  is the total number of rods (with axial ratio  $x$ ) in the lattice, and  $v_j$  is the number of vacant positions available to the  $j$ th rod when  $j - 1$  rods have already been placed in the lattice. This relation should apply equally well to two- or three-dimensional systems, as long as the  $v_j$  factors reflect placement in the system of appropriate dimension. We claim that  $v_j$  can be measured from our Monte Carlo data by using

$$v_j = \frac{K}{\langle T_j \rangle} \quad (2)$$

where  $\langle T_j \rangle$  is the average number of tries required for the Monte Carlo algorithm to find a vacant position, within the existing configuration, in which to place the  $j$ th rod.  $K$  is a mathematically arbitrary constant of proportionality; it does not affect the outcome of subsequent calculations. The algorithm first randomly chooses an orientation for the  $j$ th rod and then tries sets of randomly generated positional coordinates until the appropriate space is found. As more rods are added to the configuration,  $\langle T_j \rangle$  increases, reflecting the increasing difficulty of happening upon an appropriate vacant site by choosing candidate positions at random. For the isotropic (randomly oriented) phase, rod orientations are evenly distributed between  $0^\circ$  and  $180^\circ$ . For the aligned phase, the orientations are generated to fill a normal distribution with a preset standard deviation. (Flory and Ronca [4] assumed that the shape of the distribution of rod orientations within the aligned phase would have little effect on the results. They based their calculations on an even distribution. However, we have found that a normal distribution has significantly lower free energy than an even distribution with the same average angular deviation.) Data for the number of tries per rod are collected from several Monte Carlo runs simulating a given system. The number of tries for the  $i$ th rod is averaged over the several runs, and the averaged data are fitted to an empirical relation of the form

$$\ln \langle T \rangle = AF_x^2 + BF_x \quad (3)$$

where  $F_x$  is the area fraction (concentration) of rods, and  $A$  and  $B$  are fitted coefficients. This relation is used with Eqs. 2 and 1 to yield  $\ln Z_c$ . We have found that averaging the number-of-tries data from nine Monte Carlo runs is sufficient to determine the phase boundaries to within a few percent.

We calculate the orientational partition function by randomly generating large sets of angles with the appropriate distribution. The distribution is divided into a sufficiently large number of increments, and the partition function is calculated as

$$Z_0 = \frac{n_x!}{n_1!(n_x - n_1)!} \times \frac{(n_x - n_1)!}{n_2!(n_x - n_1 - n_2)!} \times \frac{(n_x - n_1 - n_2)!}{n_3!(n_x - n_1 - n_2 - n_3)!} \times \dots \quad (4)$$

where  $n_1, n_2, n_3, \dots$  are the numbers of rods falling within the respective increments. Each factor represents the number of ways of choosing the  $n_i$  rods within the  $i$ th increment from among the remaining  $(n_x - \sum_{i=1}^{i-1} n_p)$  rods. As the number of increments is increased, the calculation converges at approximately 90 increments. For each phase, be it randomly, evenly, or normally distributed, the orientational entropy decreases linearly with increasing rod concentration.

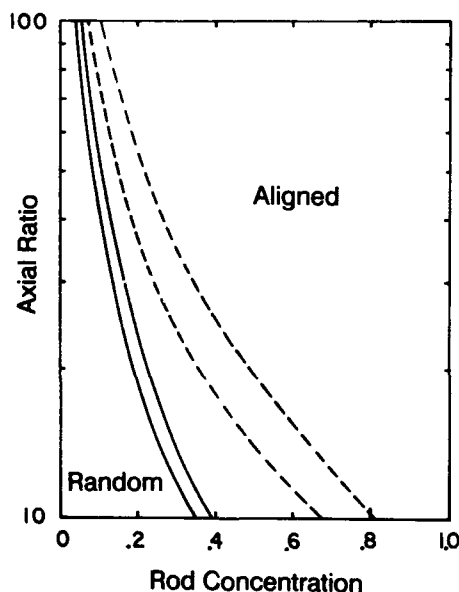
The total entropy of the configuration,  $Z_m$ , is given by

$$-\ln Z_m = -\ln Z_c - \ln Z_0 \quad (5)$$

Phase equilibria are determined by finding the common tangent to the free energy curves for the random and aligned phases.

### 17.3. RESULTS AND DISCUSSION

Our preliminary phase diagram for two-dimensional systems of rods, with axial ratios from 10 to 100, is shown in Fig. 17.3. For comparison, Fig. 17.3 also shows Flory and Ronca's [4] phase diagram for three-dimensional systems. In each case, the lines represent the boundaries of the two-phase region. It is evident that

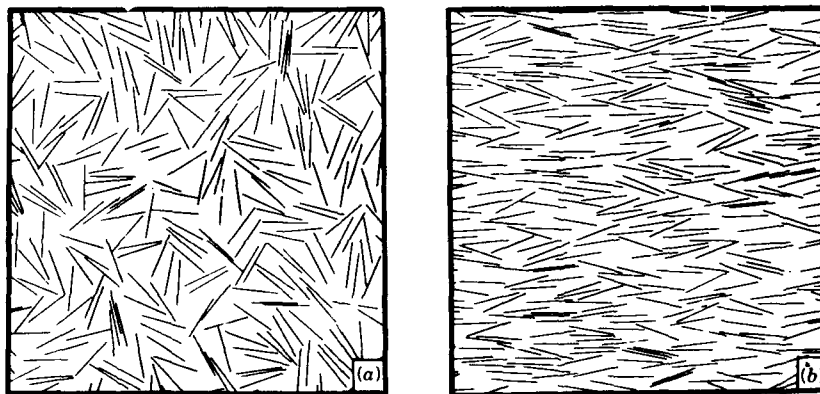


**Figure 17.3.** Phase diagrams for rodlike particles. Solid lines enclose two-phase region for rods in two dimensions from our analysis. Broken lines enclose two-phase region for rods in three dimensions from the model of Flory and Ronca [4].

separation occurs at lower rod concentrations in two dimensions, which seems reasonable on the basis that orientational freedom is more restricted in two dimensions than in three.

Because the free energy of the aligned phase varies with the spread in rod orientations, it is necessary to determine which standard deviation gives the lowest free energy when compared to the random phase. The aligned phase having this particular standard deviation will achieve equilibrium with the random phase at the lowest possible overall concentration. At an axial ratio of 25, the first normally distributed aligned phase to appear as the concentration is increased has a standard deviation of approximately  $12.5^\circ$ . Investigation of the equilibria *between aligned phases* with various standard deviations indicates that, as the concentration is increased above the upper boundary of the two-phase region, aligned phases with progressively decreasing standard deviation have the lowest free energies. In other words, as the rod concentration is increased above the point at which the random phase disappears, the aligned phase gradually becomes more perfectly aligned.

Figures 17.4a and b are computer-generated drawings of the random and normally distributed aligned phases that are in equilibrium for an axial ratio of 25. As the concentration is increased above that of the random phase shown, the translational freedom of the rods becomes so restricted that the total entropy can be decreased if clusters of aligned rods are formed. Thus maximum orientational entropy is sacrificed for increased translational entropy as the aligned phase appears and increases in area fraction. At the upper boundary of the two-phase region, given sufficient agitation, the entire configuration will transform to the aligned phase. This aligned phase will contain many "packing defects," but will attain more perfect alignment as the concentration is increased further.



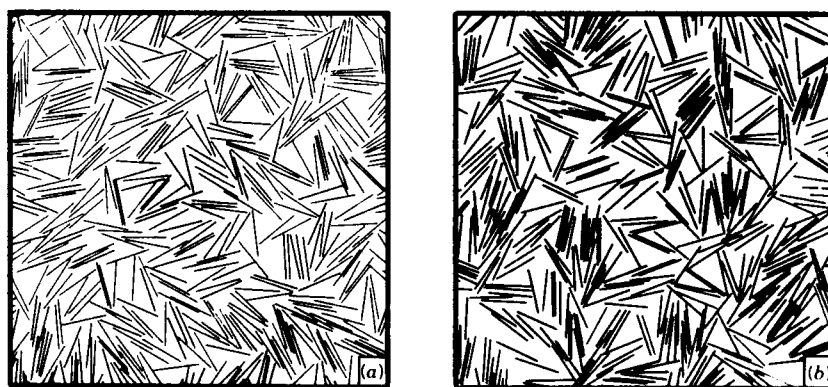
**Figure 17.4.** Computer-generated rod configurations for an axial ratio of 25. (a) Randomly oriented phase at maximum (equilibrium) rod concentration (area fraction of 0.158). (b) Normally distributed aligned phase in equilibrium with the random phase (area fraction of 0.192; standard deviation of  $12.5^\circ$ ).

The phase diagram (Fig. 17.3) predicts area fractions of the phases present at equilibrium. It does *not* predict the *scale* of the microstructure. For example, above the two-phase region we know that the entire configuration will tend to transform to an aligned state with a predictable standard deviation of rod orientations, but the phase diagram does not predict the resulting cluster (domain) size.

#### 17.4. IMPLICATIONS FOR COMPOSITE ENGINEERING

The discussion so far has assumed that the rods are sufficiently agitated, either by thermal or mechanical means, so that they can attain a configuration characterized by maximum total entropy. The degree to which they approach that equilibrium state is a matter of kinetics and is therefore difficult to predict, especially for larger-scale rods that have no thermally activated motion. Furthermore, in ceramic and metal composite processing, the motion of the fibers or whiskers is restricted by the presence of the matrix phase. However, the phase diagram does predict the critical concentrations above which the rods in a system will tend to form an aligned phase.

Also, our analysis establishes the minimum incidence of clustering present at a given concentration of rods. By way of illustration, consider the configuration in Fig. 17.5a, produced by running the Monte Carlo algorithm for the random distribution well beyond the upper boundary of the two-phase region. This disordered configuration necessarily is unstable and is expected to transform to an aligned phase, given sufficient agitation. However, the Monte Carlo algorithm allows no movement of a rod once it is placed successfully. Because no movement has taken place, and the configuration has a random distribution of



**Figure 17.5.** Metastable rod configurations at high concentration (area fraction of 0.263; axial ratio of 25). (a) Randomly oriented, computer-generated configuration obtained by running Monte Carlo for an extended period. (b) Photograph of wooden rods vibrated until all lay flat on a horizontal substrate.

rod orientations, the free energy of the configuration is given by the extrapolation of the random phase free energy curve. This configuration therefore represents the condition of minimum possible entropy at this concentration. Yet, there are definitely clusters of rods present. The clusters that appear at high concentrations in the random phase arise due to space-filling constraints. Simply put, the majority of the available vacant positions for new rods are next to and aligned with respect to existing rods. The most probable way to squeeze in more rods is to add to the clusters. It is reasonable to expect that the microstructure in Fig. 17.5a would coarsen if the configuration were annealed.

Figure 17.5b shows wooden rods with an aspect ratio of 25 at the same concentration as the computer-generated configuration of Fig. 17.5a. The wooden rods were scattered at random onto a substrate and gently vibrated until all lay flat on the surface. The rods that were originally stacked on top of others tended to "push" their way onto the surface, thereby displacing rods that were already laying flat. Therefore, some limited rod movement was allowed during the development of this configuration. It is evident that rods in some of the resulting clusters tend to be more perfectly aligned with somewhat larger vacant spaces between clusters than in Fig. 17.5a. Due to the limited motion allowed, the wooden rods have begun the transition to a minimum free energy (coarsened and more perfect) aligned phase.

In summary, the developers of composite materials should be aware that fibers or whiskers will inevitably form clusters even when no interrod attractive forces are present. Average cluster size will increase as the concentration of rods is increased. Above the critical concentration at which random alignment disappears, predicted by the phase diagram for the aspect ratio in question, the microstructure will tend to coarsen and the degree of alignment within clusters will increase. The degree of transformation attained will be governed by the extent of mechanical agitation used and by the properties of the matrix phase. Previously reported maximum packing fractions represent process-dependent kinetic barriers that will be surpassed for processes utilizing a high degree of mechanical agitation. These findings should apply to three-dimensional configurations as well, although the phase boundaries will occur at higher rod fractions. Mechanical models for fiber- and whisker-reinforced composites currently assume a simpler scenario in which the rods are independently as well as randomly oriented; the effect of clustering at high concentration has not been taken into account.

## ACKNOWLEDGMENTS

We are grateful to Professor B. E. Eichinger for stimulating discussions. This work was sponsored by the Air Force Office of Scientific Research (AFOSR) and the Defense Advanced Research Projects Agency (DARPA) and was monitored by AFOSR under Grant. AFOSR-87-0114. Work performed by L. Chick was sponsored by the Advanced Education and Training Program from Battelle

Pacific Northwest Laboratory in Richland, Washington. We also acknowledge the IBM Corporation for its support of this research as part of a block grant on the microdesigning of ceramics and polymer/ceramic composites.

## REFERENCES

1. J. V. Milewski, *Advan. Ceramic Mater.*, **1**, 36 (1986).
2. K. E. Evans and A. G. Gibson, *Composites Sci. Technol.*, **25**, 149 (1986).
3. P. J. Flory, *Proc. R. Soc. Ser. A*, **234**, 73 (1956).
4. P. J. Flory and G. Ronca, *Molec. Cryst. Liquid Cryst.*, **54**, 289 (1979).
5. H. Okamoto, *J. Chem. Phys.*, **64**, 2686 (1976).
6. F. L. McCrackin, *J. Chem. Phys.*, **69**, 5419 (1978).
7. A. Baumgartner, *J. Chem. Phys.*, **84**, 1905 (1985).
8. L. A. Chick, C. Viney, and I. A. Aksay, in: W. W. Adams, R. K. Eby, and D. E. McLemore, Eds., *The Materials Science and Engineering of Rigid Rod Polymers*, Materials Research Society, Pittsburgh, Pa, **134**, 27-32 (1989).

## SOL-GEL PROCESSING OF CONTROLLED PORE FILMS

C. J. BRINKER, G. C. FRYE, A. J. HURD, K. J. WARD,  
AND C. S. ASHLEY

### 18.1. INTRODUCTION

During sol-gel thin film formation via dipping or spinning, oligomeric or polymeric precursor species often described by mass or surface fractal dimensions,  $D$  or  $D_s$ <sup>†</sup> [1], are rapidly aggregated on the substrate surface by gravitational or centrifugal draining accompanied by vigorous solvent evaporation and continued condensation reactions. Our previous research [2] has shown that the film porosity (calculated from the refractive index on the basis of the Lorentz-Lorenz relationship) depends on the compactness ( $D$ ,  $D_s$ ) and extent of branching of the precursors prior to deposition and the relative rates of condensation and evaporation during deposition. Precursor structure dictates steric constraints according to [3]

$$M_{1,2} \propto R^{D_1 + D_2 - d} \quad (1)$$

where  $M_{1,2}$  is the probability of intersection of two mass fractal objects of size  $R$

<sup>†</sup>The mass fractal dimension,  $D$ , relates the mass of an object,  $M$ , to its radius  $r$ :  $M \sim r^D$ . The surface fractal dimension,  $D_s$ , varies from 2 for a smooth surface to 3 for a surface so convoluted that it fills space.

*Ultrastructure Processing of Advanced Materials.*

Edited by Donald R. Uhlmann and Donald R. Ulrich (deceased).

ISBN 0-471-52986-9 © 1992 John Wiley & Sons, Inc.

and mass fractal (or Euclidian) dimensions,  $D_1$  and  $D_2$ , placed independently of each other in the same region of space, and  $d$  is the dimension of space, 3. When  $D_1$  and  $D_2$  are  $\leq 1.5$ ,  $M_{1,2}$  decreases indefinitely as the polymer size increases: The structures are mutually transparent and should interpenetrate as their concentration is increased, leading to dense films. de Gennes [4] envisioned such networks as "entangled worms." If  $D_1$  and  $D_2$  are greater than 1.5, the probability of intersection increases algebraically with  $R$ : The structures, although often porous, are "mutually opaque," similar to an assemblage of tumbleweeds.

The above discussion assumes that all intersections result in irreversible condensation reactions (sticking probability = 1) and that the precursor structures are completely rigid. In reality the structures are more or less compliant, because, for example, the elastic moduli of fractal objects decrease with  $R$  [5]. Furthermore, the sticking probability is  $\ll 1$  and is a sensitive function of pH as indicated by the pH dependence of gel times in aqueous and alcoholic silicate solutions [6] (see Chapter 6). These factors mitigate the criteria for mutual transparency, because few intersections result in condensation, and the compliancy of the structures reduces the effectiveness of screening according to Eq. 1.

The relative rates of condensation and evaporation dictate chemical constraints. During film formation, a competition is established between evaporation and continuing condensation reactions. Evaporation tends to compact the film structure first by concentration and later by the capillary pressure exerted as the liquid-vapor interface recedes into the film interior. Condensation reactions at points of intersection inhibit interpenetration, according to the concepts of mutual opacity, and stiffen the structure, consequently increasing its resistance to compaction by the capillary pressure. For reacting systems, both increasing the condensation rate and reducing the evaporation rate allow more condensation reactions to occur during the brief time of film formation,<sup>†</sup> resulting in more porous films. Conversely, reducing the condensation rate and/or increasing the evaporation rate reduce the number of condensation reactions that occur during film formation leading to denser films. We will show, however, that for nonreacting systems of repulsive particles, increasing the drying time allows ordering to occur, leading to denser films.

This Chapter explores how precursor structure and deposition conditions influence the porosity of thin sol-gel films prepared by dipping. This study extends our previous work [2] by providing a measure of the pore size and surface area of the deposited films in addition to the pore volume. We show that the pore size can be precisely tailored, suggesting applications as materials for sensors, filtration, or separation processes.

<sup>†</sup>The time of film formation is generally several seconds comprising aging, gelation, and drying that convert the wet layer at the reservoir surface to a completely dry film normally a few centimeters above the reservoir surface.



## 18.2. EXPERIMENTAL

Three classes of precursors were prepared:

1. Rather weakly branched silicates (composition A2 in Ref. 7) characterized by  $D = 1.9$ , deposited near pH 2.
2. More highly branched, compact clusters (prepared according to Ref. 8) characterized by  $D = 2.4$ , deposited between pH 3.5 and 1.
3. Dense colloidal particles (nonfractal) synthesized by variations of the Stöber process [9] and deposited above pH 10.

Films were deposited at room temperature on polished  $\langle 100 \rangle$  single-crystal silicon (ellipsometry experiments); ST-cut crystalline quartz (SAW experiments); MYLAR or  $v\text{-SiO}_2$  (small-angle X-ray scattering, SAXS, experiments); or Au-coated glass substrates (Fourier transform infrared, FTIR, experiments). Subsequent measurements employed room temperature-dried films or films heated to  $400^\circ\text{C}$  for 5 min. (Note: Prior to SAW measurements films were reheated to  $160^\circ\text{C}$  for 2 hr.)

Prior to deposition the solutions were characterized by SAXS, quasielastic light scattering (QELS) or FTIR. Scattering data were analyzed in the Porod regime [10] to obtain structural information. Film structure was investigated in situ during deposition using imaging ellipsometry [11] or FTIR microscopy [12]. The structure of the deposited films was investigated by ellipsometry to obtain thickness and refractive index data and by performing  $\text{N}_2$  adsorption experiments using a SAW technique [13] to obtain surface area and pore size information.

## 18.3. RESULTS AND DISCUSSION

### 18.3.1. Weakly Branched System

Our previous work [2] indicated that weakly branched precursors deposited near the isoelectric point of silica (pH 1–2, Chapter 6) yielded dense films with  $n \geq 1.425$  (corresponding to  $< 5\%$  porosity based on the refractive index of  $v\text{-SiO}_2$ , namely, 1.458) regardless of the precursor size, which was varied by over 1 order of magnitude. Consistent with these results the corresponding  $\text{N}_2$  adsorption isotherm (Fig. 18.1a) is a type II isotherm [14], indicating adsorption on a nonporous surface. Thus any porosity that exists has openings smaller than the kinetic radius of  $\text{N}_2$  ( $\sim 0.2\text{ nm}$ ). The measured surface area,  $S = 0.95\text{ cm}^2/\text{cm}^2$ , corresponds approximately to the geometric area of the film surface,  $1\text{ cm}^2/\text{cm}^2$ .

Several factors contribute to the high density of these films:

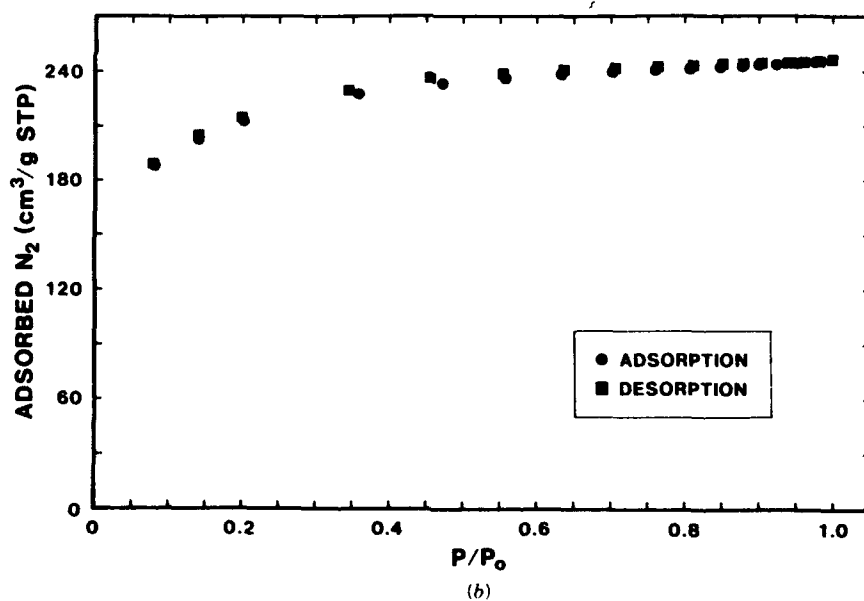
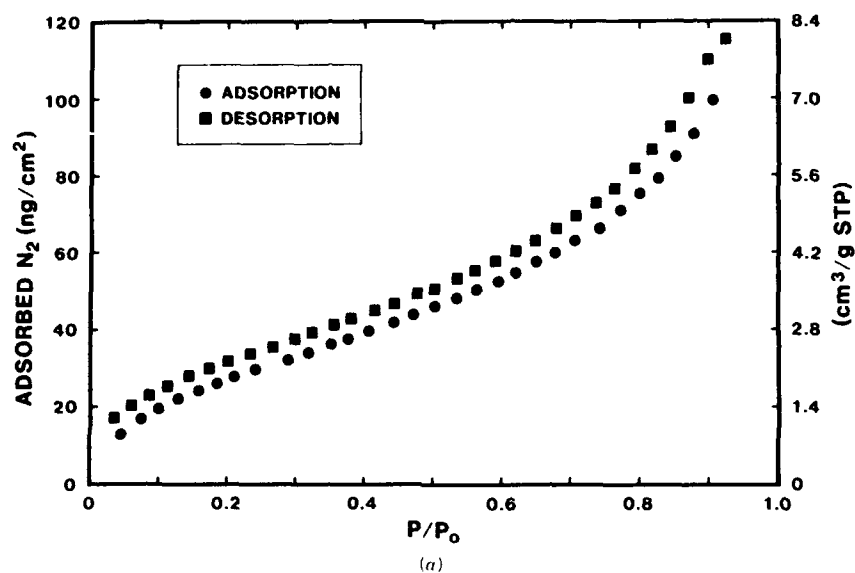
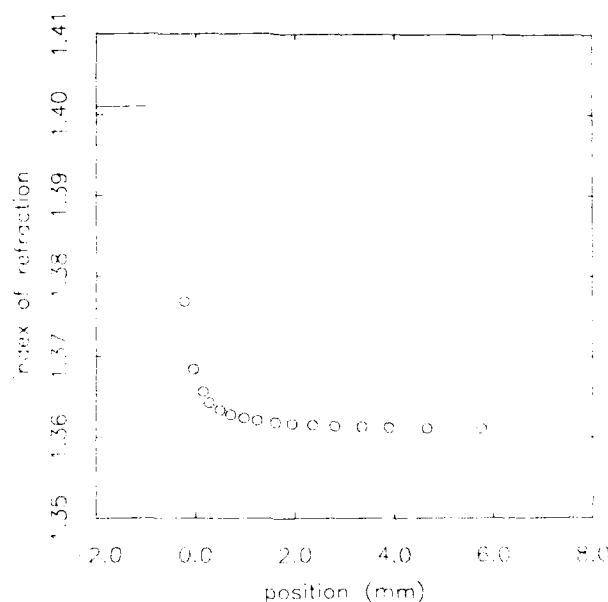


Figure 18.1. (a)  $N_2$  adsorption-desorption isotherm obtained by the SAW technique for a film prepared from the weakly branched precursor. (b) Corresponding  $N_2$  adsorption-desorption isotherm for a bulk, monolithic gel prepared from identical precursors as in a [12].

1. The brief deposition time combined with a low condensation rate allows little further condensation to occur during deposition.
2. The weakly branched, compliant polymers are able to interpenetrate and rearrange themselves to progressively denser configurations in response to the evaporating solvent.
3. Because the extent of condensation remains low, the compliant films are further compressed at the final stage of drying by the capillary pressure, which can now be enormous (1–2 kbar, Chapter 16) due to the preceding shrinkage that reduces the effective pore size to molecular dimensions.

This collapse is illustrated by the refractive index profile of a drying film determined from imaging ellipsometry: Figure 18.2 shows a narrow region near the drying front where the index suddenly increases.

The importance of the brief time scale of the film deposition process compared to the bulk gel process is illustrated in Fig. 18.1b, which shows the  $N_2$  adsorption–desorption isotherm of a monolithic gel prepared from the identical silicate precursors used for the film (Fig. 18.1a). The monolithic sample, which was gelled and dried over a period of several months, becomes much more highly condensed (stiffer) at an earlier stage of the drying process. Therefore, it shrinks less during the initial stage of drying, where it is completely filled with liquid, causing the capillary pressure during the final stage of shrinkage to be



**Figure 18.2.** Index of refraction of a drying sol–gel film versus position on the substrate determined by imaging ellipsometry. The drying line is at approximately  $x = 0$ . The solid and dotted line at  $y = 1.401$  indicates the refractive index of the dry film.

reduced due to the larger effective pore size. In addition the resistance to the capillary pressure is increased due to the increased stiffness. The result is a less dense, microporous gel as indicated by the large amount of adsorption at low  $N_2$  pressures characteristic of a type I isotherm [14]. This result contrasts dramatically with the dense films formed from the same precursors on a much shorter time scale.

### 18.3.2. Strongly Branched System

The strongly branched system deposited at pH 3.4 exhibits a reciprocal relationship between precursor size and refractive index, for example, films deposited from solutions containing progressively larger-sized polymeric precursors (obtained by aging at 50°C) exhibit progressively lower refractive indices (see Table 18.1). Because for mass fractals, density,  $\rho$ , decreases radially as

$$\rho \sim 1/r^{(3-D)} \quad (2)$$

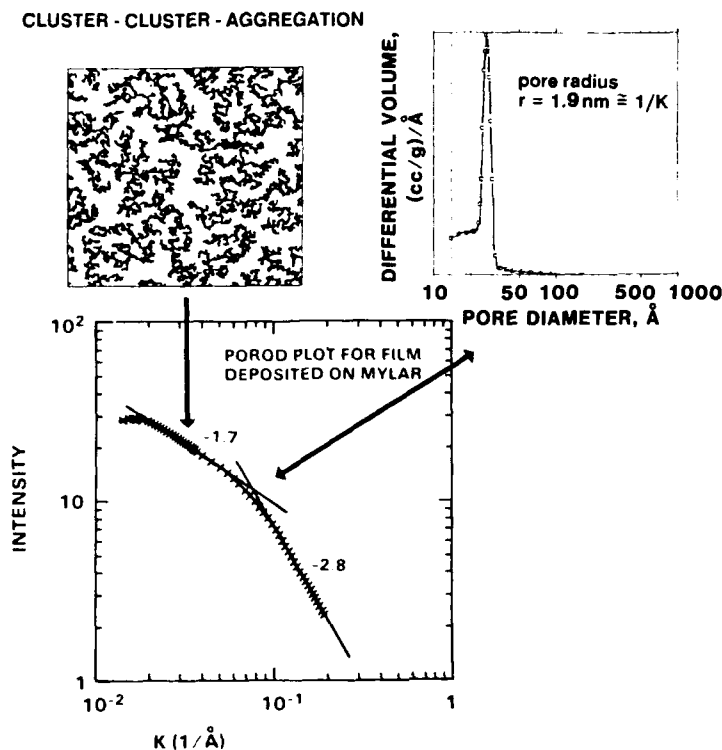
this behavior is consistent with an assemblage of mutually opaque mass fractal clusters: The porosity of an assemblage of clusters should increase with cluster size (assuming that the clusters do not completely collapse). The Porod plot of a film prepared from precursors aged for 14 days (Fig. 18.3) is composed of two limited power law regions corresponding to  $D = 1.7$  and  $D = 2.8$  separated by a transition region ( $K^{-1} \sim 1.7$  to 1.3 nm). The corresponding pore size distribution obtained from the SAW desorption isotherm (Fig. 18.3, inset) indicates that the transition occurs at about the mean pore radius,  $\sim 1.9$  nm. The SAXS and pore size data suggest that the individuals clusters ( $D = 2.4$ ) are compacted during deposition due to the capillary pressure, causing  $D$  to increase to 2.8 on length scales  $< 1.3$  nm. The  $D$  values of 1.7 is consistent with simulations of transport-limited cluster-cluster aggregation (Fig. 18.3). This suggests that on length scales greater than  $\sim 1.7$  nm the compacted clusters are aggregated

TABLE 18.1. Porosity versus Aging Conditions for the Weakly-Branched Precursor<sup>a</sup>

Sample	Refractive Index	Porosity Adsorption $N_2$	Median Pore Radius (nm)	Surface Area ( $m^2/g$ )
Unaged	1.45	0	$< 0.2$	1.2-1.9
3 days	1.31	16	1.5	146
1 week	1.25	24	1.6	220
2 weeks	1.21	33	1.9	263
3 weeks <sup>b</sup>	1.18	52	3.0	245

<sup>a</sup>Aged at 50°C and pH 3.2 for the indicated times prior to deposition by dipping

<sup>b</sup>The 3-week sample was gelled and reliquified ultrasonically prior to deposition.



**Figure 18.3.** SAXS Porod plot of a film deposited from the strongly branched system after 2 weeks of aging. Slopes corresponding to  $D = 2.8$  and  $D = 1.7$  indicate compaction on short length scales ( $< 1.4 \text{ nm}$ ) and cluster-cluster aggregation on longer length scales. The crossover occurs at approximately the mean pore size,  $1.9 \text{ nm}$ .

creating interconnected porosity with "throat" radii  $\sim 1.9 \text{ nm}$ . We speculate that the aggregation process appears to be transport limited rather than reaction limited ( $D = 2.1$ ), because the rapidly increasing viscosity "freezes in" a non-equilibrium configuration.

Based on this aggregation model, it is expected that the pore size should increase with cluster size. Table 18.1 shows that the mean pore radius determined from the desorption isotherms by standard calculation procedures [15] increases from  $< 0.2$  to  $> 3.1 \text{ nm}$  with the duration of aging at  $50^\circ\text{C}$  prior to deposition. The isotherm obtained for the film prepared from unaged precursors is a type II isotherm indicative of a nonporous film ( $r < 0.2 \text{ nm}$ , the kinetic radius of  $\text{N}_2$ , and  $S = 1.2 \text{ cm}^2/\text{cm}^2$ , approximately the geometric area of the film surface). This suggests that due to the small effective pore size the film is collapsed during the last stage of deposition by the high capillary pressure. Larger, opaque clusters presumably increase the effective pore size causing the capillary pressure to decrease, resulting in more porous films. For example, Fig.

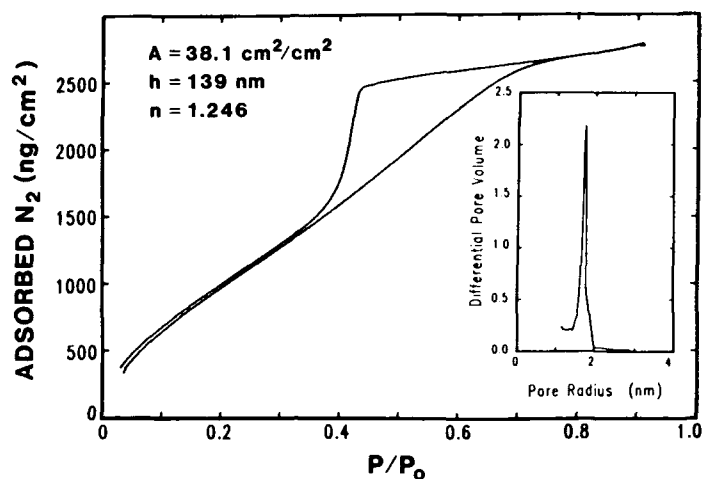


Figure 18.4. Type IV  $N_2$  adsorption-desorption isotherm obtained for a film prepared from the strongly branched system after 1 week of aging. Inset: Pore size distribution determined from the desorption branch.

18.4 shows the  $N_2$  adsorption-desorption isotherm obtained from the 1-week-aged precursor. It is a type IV isotherm characteristic of a mesoporous solid [14]. The surface area has increased to  $220 \text{ m}^2/\text{g}$  (Table 18.1), and the pore size distribution (Fig. 18.4, inset) is narrow and centered at  $\sim 1.6 \text{ nm}$ .

Table 18.1 clearly shows a correlation between pore volume (or refractive index) and pore size: Pore volume increases (refractive index decreases) with pore size as a consequence of the fractal model described above. Unfortunately this does not allow the preparation of films with large volumes of extremely small pores. However, because precursor aging times less than 3 days result in refractive indices that vary between 1.31 and 1.45, according to the above correlation, an advantage of this process should be the preparation of microporous films with pore radii ranging from 0.2 to 1.6 nm, sizes of interest for sensors and gas separations. SAW studies of these films are currently in progress.

As described above, a condition for mutual opacity of mass fractal objects is condensation reactions at points of intersection. Therefore, a reduction in the condensation rate should reduce opacity, resulting in denser films. This hypothesis was tested by depositing 1-week-aged precursors at pH values ranging from about 3.2 to 1.2. In situ FTIR reflectance microscopy (Fig. 18.5) shows that at pH 3.2 condensation reactions, characterized by increased relative intensity and broadening of the Si-O asymmetric stretching vibration centered at  $1180 \text{ cm}^{-1}$ , accompany film deposition. Figure 18.6 shows that the refractive index increases as the pH is reduced below pH 3.2 by additions of 2 M HCl immediately prior to deposition. Equivalent additions of  $H_2O$  cause no consistent changes in refractive index. This result suggests that HCl additions reduce the condensation rate facilitating interpenetration and contributing to

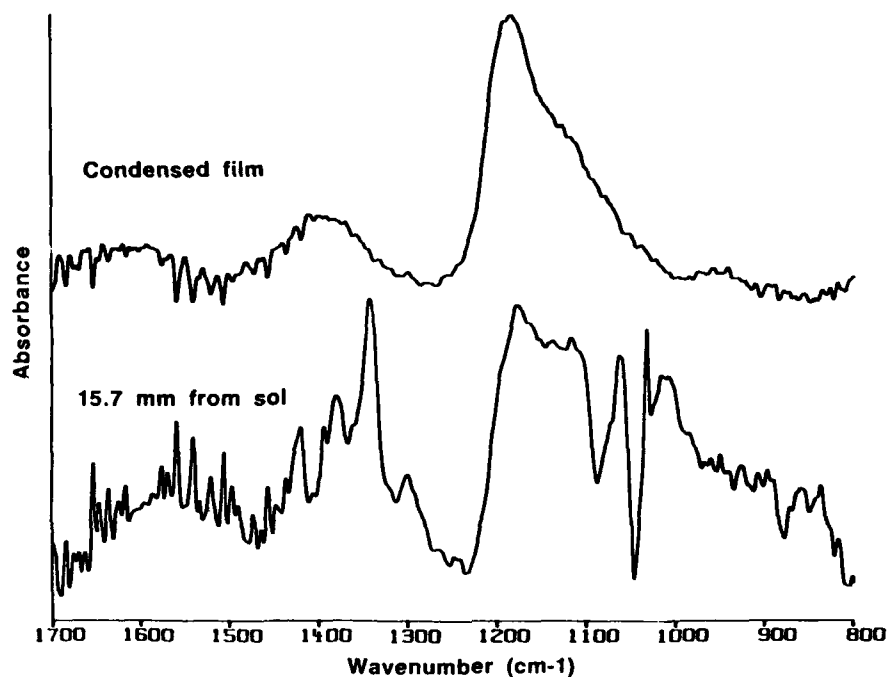


Figure 18.5. FTIR reflection spectra obtained in situ at positions 15.7 mm above the coating bath and  $>2$  cm above the coating bath (corresponding to a dried film).

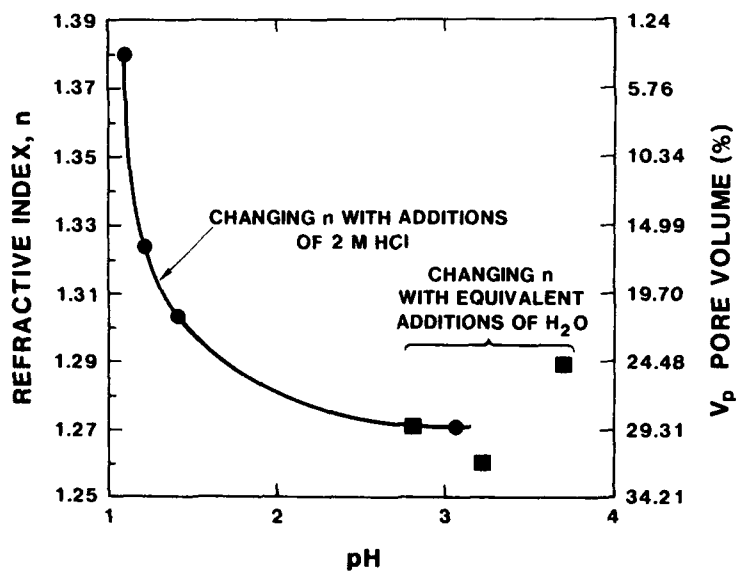


Figure 18.6. Refractive index and pore volume for films prepared from the strongly branched system after about 1 week of aging versus the deposition pH achieved by additions of 2 M HCl (aqueous). Squares denote equivalent additions of water.

compliance.<sup>†</sup> As described above, both factors promote compaction of the film. By analogy to the correlation between refractive index and pore size shown in Table 18.1, changes in the relative rates of condensation and evaporation during deposition should provide an alternate method of pore size control utilizing a single solution aging condition.

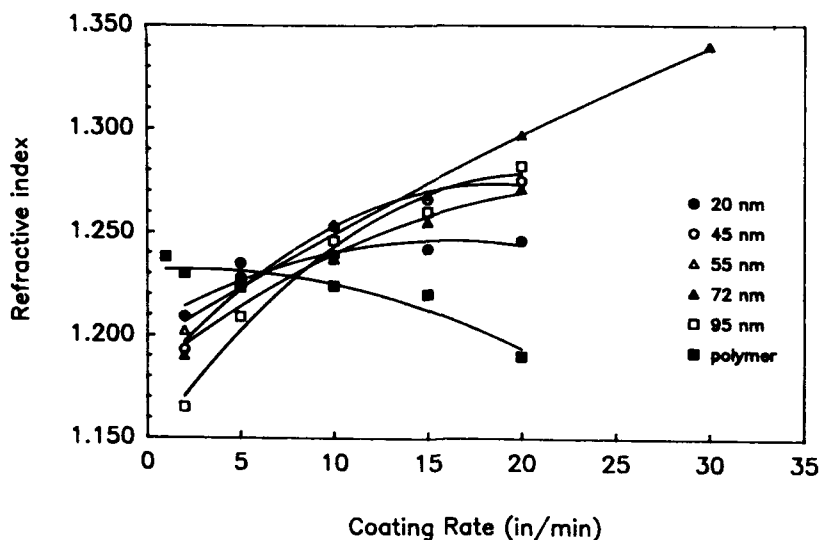
### 18.3.3. Particulate Films

Using opaque, monosized, particulate precursors, the porosity is controlled by the particle size and extent of aggregation or ordering. Our previous work [2] has shown that aggregation and deposition of silicate spheres at pH 7, where the silica condensation rate is maximized, results in films with porosities exceeding 65% compared to a minimum of 25% corresponding to face-centered-cubic or hexagonal close packing. This high porosity is created in a manner similar to that described for the strongly branched system in Section 18.3.2: Consistent with the concept of mutual opacity (Eq. 1), aggregation results in fractal clusters ( $D = 2.1$ ) that do not interpenetrate due to the large  $D$  and the high condensation rate. In addition, the capillary pressure is reduced, because the effective pore size is approximately the aggregate size. At comparable coating rates, deposition of the particles at pH 11 where they are mutually repulsive [6] (Chapter 6) causes the porosity to decrease to about 42%. SAXS studies [2] indicate that under these conditions aggregation is avoided, presumably due to repulsive forces, and a liquidlike structure is frozen in at the final stage of drying. Figure 18.7 shows that at high pH a further decrease in the pore volume (increase in the refractive index) occurs as the coating rate is increased. For example, increasing the coating rate from 2 to 30 in./min (5 to 76.2 cm/min) causes the refractive index of the film prepared from 55-nm particles to increase from 1.2 to 1.34, corresponding to a reduction in  $V_p$  from 52 to 24%. For base concentrations exceeding 0.001 M, this trend of increasing refractive index with coating rate is observed for all silicate particles we have investigated (particle diameters  $\approx 20$ –95 nm, see Fig. 18.7). By comparison the weakly branched and strongly branched systems deposited at lower pH show a slight trend of decreasing refractive index with coating rate (e.g., polymer sample in Fig. 18.7), because there is a greater time for condensation reactions to occur.

Our present interpretations of these trends of changing refractive index with coating rate are based on the relative rates of condensation and concentration (via solvent evaporation) and/or the possibility of shear-induced alignment. Because drying occurs exclusively from the film/vapor interface, which is independent of the film thickness, and higher coating rates produce thicker films, thick films take longer to dry than thin films. Normally, when the condensation rate is finite, longer drying times allow additional crosslinking to occur, leading to more porous gels. This is well illustrated by the comparison of thin films and monoliths in Fig. 18.1 and explains the trend of decreasing

<sup>†</sup> A similar effect would be obtained if HCl promoted depolymerization; however, the dissolution rate of silica is minimized in this pH range [6].



Coating Rate Dependence of  $n$ 

**Figure 18.7.** Coating rate dependence of the refractive index for films prepared from a series of monosized particulate precursors (particle diameters = 20 to 95 nm) deposited at  $\sim$  pH 11 compared to the coating rate dependence of refractive index for films prepared from the strongly branched system after 2 weeks of aging (denoted polymer).

refractive index with coating rate (polymer sample, Fig. 18.7). However if the particles are mutually repulsive (condensation rate = 0), longer drying times provide the necessary time for particle ordering leading to denser films. In addition, based on molecular dynamics calculations [16], it is expected that increased shear rates achieved by higher coating speeds will aid the ordering process. From the standpoint of pore size control, ordered packings of monosized particles should provide precise control of throat sizes defined by the interstice created by three touching spheres, providing a means of achieving large pores with narrow size distributions.

#### 18.4. SUMMARY

The porosity of sol-gel thin films prepared by dipping depends on the precursor structure, the relative rates of condensation and evaporation (or concentration) during deposition, and the coating rate. Using three different classes of precursors, we have demonstrated that the porosity of sol-gel thin films can be varied over wide ranges. Weakly branched precursors deposited under conditions where the condensation rate is low result in dense films with pore radii less than the kinetic radius of  $N_2$ . Strongly branched, compact precursors

exhibit variable porosities ( $V_p = 0$  to  $> 50\%$ ,  $r = 0$  to  $3.0$  nm,  $S = 1-245$  m<sup>2</sup>/g) that depend on the precursor size and the deposition conditions. Monosized particulate precursors appear to order when applied at high coating rates, providing a potential method for achieving rather large pore sizes with very narrow size distributions.

### ACKNOWLEDGMENTS

The authors acknowledge S. T. Reed for assistance in film formation and deposition and A. J. Ricco and S. J. Martin for contributions to the SAW measurements.

### REFERENCES

1. B. B. Mandelbrot, *Fractals, Form, and Chance*, Freeman, San Francisco (1977).
2. C. J. Brinker, A. J. Hurd, and K. J. Ward, in: J. D. Mackenzie and D. R. Ulrich, Eds., *Ultrastructure Processing of Advanced Ceramics*, p. 223, Wiley, New York (1988).
3. B. B. Mandelbrot, *The Fractal Geometry of Nature*, Freeman, San Francisco (1982).
4. P. G. de Gennes, *Phys. Today*, **36**, 33-39 (1983).
5. T. A. Witten and M. E. Gates, *Science*, **232**, 1607 (1986).
6. R. K. Iler, *The Chemistry of Silica*, Wiley, New York (1979).
7. C. J. Brinker, K. D. Keefer, D. W. Schaefer, R. A. Assink, B. D. Kay, and C. S. Ashley, *J. Non-Cryst. Solids*, **63**, 45 (1984).
8. C. S. Ashley and S. T. Reed, Report SAND84-0662 Sandia National Laboratories (1984) (available from NTIS).
9. W. Stöber, A. Fink, and E. Bohn, *J. Colloid Interface Sci.*, **26**, 62 (1968).
10. G. Porod, *Kolloid Z.*, **124**, 83 (1951).
11. A. J. Hurd and C. J. Brinker, *J. Phys.*, **47**, 1017 (1988).
12. K. J. Ward, unpublished observations.
13. G. C. Frye, A. J. Ricco, S. J. Martin, and C. J. Brinker, in: C. J. Brinker, D. E. Clark, and D. R. Ulrich, Eds., *Better Ceramics Through Chemistry*, Vol. III, *Mater. Res. Soc. Symp. Proc.*, 349 (1988).
14. S. J. Gregg and K. S. W. Sing, *Adsorption, Surface Area and Porosity*, Academic Press, New York (1982).
15. S. Lowell and J. E. Shields, *Powder Surface Area and Porosity*, Chapman & Hall, New York (1984).
16. J. H. Simmons, R. K. Mohr, and C. J. Montrose, *J. Appl. Physics*, **53**, 4075 (1982).

## SOL-GEL PROCESSING OF OXYCARBIDE GLASSES AND GLASS MATRIX COMPOSITES

H. ZHANG AND C. G. PANTANO

### 19.1. INTRODUCTION

In earlier studies, the thermochemical interactions between carbon fibers and silicate glass matrices were evaluated [1]. It was found that at high temperatures, the predominant reactions between the glass matrix and carbon fibers produce CO, CO<sub>2</sub>, and SiO gases. These reactions are greatly enhanced if the glass matrix composition contains reducible oxides such as Nb<sub>2</sub>O<sub>5</sub> or MoO<sub>3</sub>. In these cases, it could be shown that significant degradation of the fiber surfaces occurs, and moreover, solid phase reaction products including Nb-carbide and Mo-carbide eventually form at the interface [2]. If excessive, these interphases lead to a measurable increase in the interfacial shear strength and, correspondingly, a decrease in the strength and fracture toughness of the composite.

On the basis of these observations, it is proposed that the interface reactions can be limited if *chemically reduced* glass matrices are used in the composite fabrication, that is, glasses whose redox potential has been equilibrated with carbon. In this way, a great deal of latitude would exist in the time and temperature schedule for composite processing. Moreover, the high-temperature strength of the composite could — for a variety of reasons — be improved. The limited interface reactivity should prevent degradation of the

*Ultrastructure Processing of Advanced Materials.*

Edited by Donald R. Uhlmann and Donald R. Ulrich (deceased).

ISBN 0-471-52986-9 © 1992 John Wiley & Sons, Inc.

fibers during service at elevated temperatures. Also, the carbon-coating glass matrix would oxidize to a degree and thereby limit the oxidation rate of the fibers. Finally, the presence of carbon and/or carbide in the glass matrix will reduce the crystallization rate of the glass. In general, though, the ability to control the interfaces through the redox potential of the glass matrix phase would represent a new approach to tailoring the interface properties in composites. One way to reduce the oxidation state of the glass is to substitute carbon for oxygen in the silicate network, that is, to create an *oxycarbide* network.

We have already developed a sol-gel method for the synthesis of ternary silicon-oxycarbide (Si-O-C) glasses [3]. The solutions are prepared using organometallic silanes that contain one unhydrolyzable alkyl group. In this way, carbon can be retained in the gel, and most importantly, it is covalently bonded to silicon. The gel can then be processed in an inert atmosphere to create a carbon-containing X-ray amorphous *black glass*. In the case of  $\text{SiO}_2$ , it has been shown that up to 18% carbon can be incorporated into the dense glass.  $^{29}\text{Si}$  magic angle spinning-nuclear magnetic resonance (MAS-NMR) verifies that 50–60% of the silicon atoms in the glass are bonded directly to one  $[\text{SiCO}_{3/2}]$  or two  $[\text{SiC}_2\text{O}_{2/2}]$  carbon atoms.  $^{13}\text{C}$ -NMR reveals that there is also some free carbon in the glass. But the creation of the oxycarbide network is the significant observation. Although other investigators have discussed the synthesis of carbon-containing glasses [4–7], this study provided the first direct verification of Si-C ligands in the dense black glass.

The sol-gel approach is certainly advantageous, and perhaps critical, to the synthesis of oxycarbide glass. However, the gelation and hot pressing characteristics of the ternary Si-O-C system are not yet suitable for carbon fiber-reinforced composite fabrication. On the other hand, we have a well-developed sol-gel method for the synthesis of borosilicate glasses and carbon fiber-reinforced borosilicate glass composites [8] and, further, possess a data base of microstructural, interface, and mechanical properties. Thus, it is ideally suited for evaluating the effects of carbon additions to the matrix glass composition. In this Chapter, the synthesis and characterization of these borosilicate/oxycarbide glasses are described, and the temperature-dependent strength behavior of carbon fiber reinforced *borosilicate/oxycarbide* glass composites is reported.

## 19.2. SYNTHESIS OF GLASSES AND COMPOSITES

The borosilicate glass is nominally of the Pyrex (CGW 7740) composition:  $81\text{SiO}_2$ ,  $13\text{B}_2\text{O}_3$ ,  $4\text{Na}_2\text{O}$ , and  $2\text{Al}_2\text{O}_3$ . The alkoxide precursors used in the sol-gel syntheses of the *oxide* glass are tetramethoxysilane (TMOS), trimethylborate, aluminum *sec*-butoxide, and sodium acetate. In the oxycarbide, carbon is introduced by replacing one-half of the TMOS with methyl-trimethoxysilane. An equimolar mixture of these two silanes are hydrolyzed for 2 hr at  $60^\circ\text{C}$  in methanol that contains one-third the water required for complete hydrolysis of

the methoxy groups. Subsequently, stepwise additions of the B, Al, and Na precursors are added. Then, an excess of water is introduced to drive the hydrolysis to completion. The resulting solution is clear and is typically of pH 5. The gelation of this solution requires about 4 hr at 80°C. They are aged and dried further at 80°C to obtain clear, stiff gels. The black glass is obtained after a heat treatment of the gel at 800°C in argon.

Although the sol and gel can be processed to yield a glass frit for conventional composite fabrication, the solutions were used to pre-pregnate carbon fiber paper directly [8]. It was found that these solutions exhibited a strong tendency to wet and impregnate the carbon fiber paper. The carbon fiber paper (Celion-International Paper Co.) was cut and stacked in a mold, and then a measured volume of solution was introduced. An independent measure of the effective glass yield (after processing the solution through to a dense glass) permits a reasonably accurate control of the volume fraction of fiber in the final composite.

Here, composites with 25 vol% fibers were fabricated. The molds containing the fiber paper and solution were covered and held overnight at 80°C to effect the gelation. These preforms were then aged and dried at 80°C for 8 days. Before hot pressing, the preforms were heat treated at 600°C in argon for 30 min. The hot pressing was accomplished in vacuum at 1200°C under 1000 lb/in.<sup>2</sup> pressure. The heat-treated preforms were stacked in the die, and after reaching ~800°C, the pressure was applied. The composites were then heated rapidly and held for only a very short time at the maximum temperature of ~1250°C. The pressure was maintained until the system cooled to <700°C.

### 19.3. CHARACTERIZATION OF THE GLASSES

The carbon contents of the solution, gel and glass are presented in Table 19.1, the data obtained for a ternary silicon oxycarbide [3] is shown for comparison. It can be seen that the methyl groups are, in fact, retained in the gel. This is further verified by the <sup>29</sup>Si-MAS-NMR spectra in Fig. 19.1a. It shows the presence of methyl groups bonded directly to Si and the absence of Si-methoxy

TABLE 19.1. Carbon Contents<sup>a</sup> of Solutions, Gel, and Glass

	Borosilicate	Silica
Total carbon in solution (calculated)	14.7	35
Carbon in gel (calculated) <sup>b</sup>	7.2	16
Carbon in gel (measured)	9.2	14
Carbon in glass (measured)	3.2	12

<sup>a</sup>LECO carbon analyzer.

<sup>b</sup>Assumes all methoxy groups are hydrolyzed.

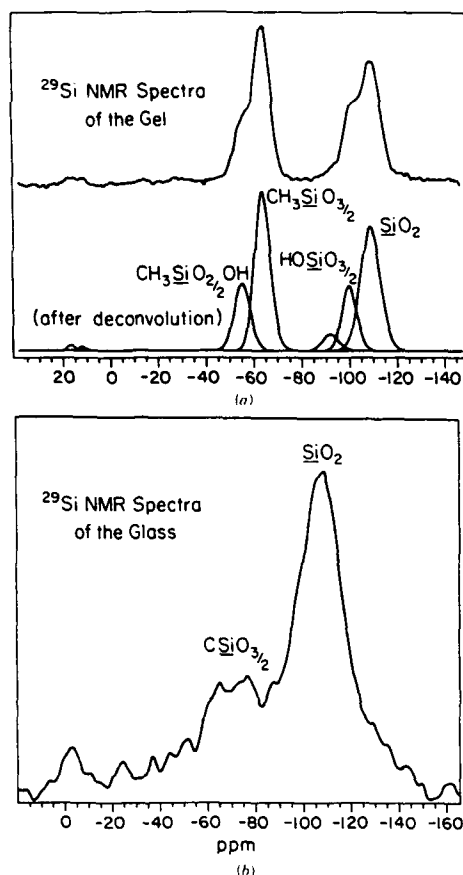


Figure 19.1.  $^{29}\text{Si}$ -MAS-NMR spectra of the (a) borosilicate/oxycarbide gel and, (b) borosilicate/oxycarbide glass obtained after an 800 C heat-treatment of the gel in argon.

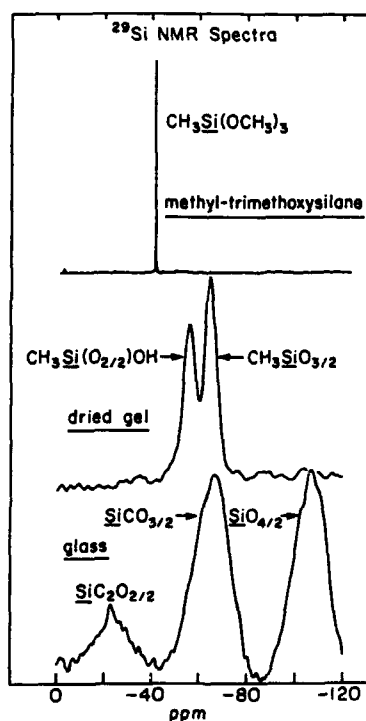
groups. These peak assignments are based upon the study of simpler Si-O-C gels [3] (Fig. 19.2) and NMR spectra published in the literature [9]. In the ternary silicon-oxycarbide gel, there is one methyl group for every silicon atom (lines at  $\sim 50$  and  $60$  ppm). This is because methyl-trimethoxysilane was the only silica precursor, and the methyl ligand is not susceptible to hydrolysis/polymerization.

In the case of the borosilicate, additional lines due to silica and/or silicate are observed at  $90$ ,  $100$ , and  $110$  ppm. The silica precursor in the borosilicate was a 50-50 mixture of methyl-trimethoxysilane and TMOS. Thus, one-half of the silicon atoms have a methyl group and three oxygens (the lines at  $50$ - $70$  ppm) and the other half of the silicon atoms are bonded to four oxygens (the lines at  $90$ - $110$  ppm). The integrated intensity ratio of these two sets of lines is consistent with the initial 50-50 solution composition. The deconvolution of these peaks reveals whether the oxygens bonded to the silicon are bridging or hydroxylated.

It should be noted that the line at  $\sim 100$  ppm could be due to  $\text{CH}_3\text{OSiO}_{3/2}$  or  $\text{OHSiO}_{3/2}$ , but  $^{13}\text{C}$ -NMR spectra verified the absence of any methoxy groups ( $\text{CH}_3\text{O}$ ) in the gels.

Figure 19.1b shows the  $^{29}\text{Si}$ -NMR spectra of the borosilicate/oxycarbide glass. The presence of Si-C ligands in the glass is indicated by the line at  $\sim 70$  ppm. In contrast to the Si-O-C glasses (Fig. 19.2), however, Si atoms with only one carbon ligand ( $\text{CSiO}_{3/2}$ ) are observed. The ternary glasses showed the additional presence of Si atoms with two carbon ligands ( $\text{C}_2\text{SiO}_{2/2}$ ) at  $\sim 35$  ppm. Moreover, the carbon analyses in Table 19.1 reveal a substantial loss of carbon — approximately 65% — during conversion of the borosilicate gel to glass. In contrast, the ternary Si-O-C gels lost only 15% of the carbon during the gel-to-glass conversion. It is likely that the other constituents in this glass ( $\text{B}_2\text{O}_3$ ,  $\text{Al}_2\text{O}_3$ , and  $\text{Na}_2\text{O}$ ) catalyze the oxidation of the Si-C bonds and thereby lead to the evolution of CO or  $\text{CO}_2$ —even in the argon atmosphere.

Figure 19.3 compares the densification behaviors of the borosilicate *oxide* and the borosilicate *oxycarbide* gels. The expected density of the borosilicate glass is approximately  $2.2 \text{ g/cm}^3$ . It can be seen that this value is reached after a



**Figure 19.2.**  $^{29}\text{Si}$ -MAS-NMR spectra of a ternary (Si-O-C) silicon oxycarbide prepared using a methyltrimethoxysilane precursor, the glass was obtained after a  $900^\circ\text{C}$  heat-treatment of the gel in argon.

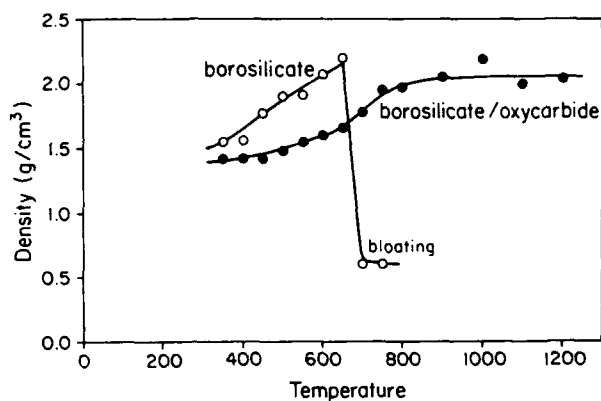


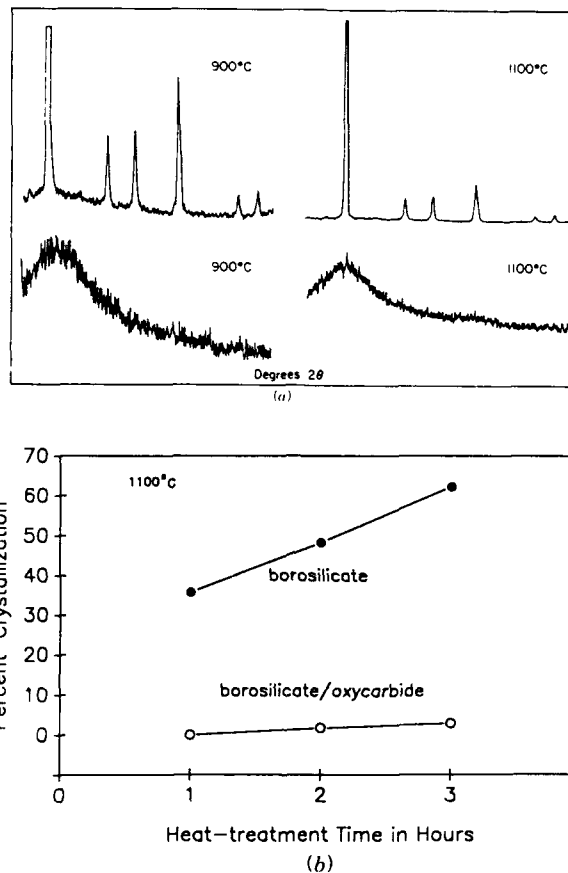
Figure 19.3. The densification behavior of borosilicate and borosilicate/oxycarbide gels in argon; each data point represents one hour of sintering.

1-hr heat treatment of the gel at 650°C. At higher temperatures, bloating of the glass occurs due to the water trapped in the gel. The borosilicate/oxycarbide gel requires a higher temperature to exhibit any densification. The theoretical density of the borosilicate/oxycarbide glass is not known, but is expected to be slightly less than 2.2 g/cm<sup>3</sup> because of the carbon substitution for oxygen. More importantly, though, bloating is not observed in the oxycarbide—at least at temperatures up to 1200°C. These observations are consistent with effects of a carbon substitution in the glass network.

The most important influence of the carbon observed in this study concerned the crystallization behavior. Figure 19.4a shows the X-ray diffraction patterns of the borosilicate and borosilicate/oxycarbide glasses after heat treatments at 900°C and 1100°C for 1 hr in argon. There is no measurable crystallization of the oxycarbide, whereas the oxide glass is almost completely devitrified at 1100°C. A semiquantitative analysis (using the method of internal standards) showed that the oxide begins to crystallize at 800°C, whereas the onset of the crystallization in the oxycarbide is shifted to >1100°C. The rate of crystallization is considerably greater for the borosilicate than for the borosilicate/oxycarbide; this is shown in Fig. 19.4b. Chi [5] and Larsen et al. [6] also observed an effect of carbon upon the crystallization of silica glasses. The mechanism through which the carbon additions influence the crystallization behavior is not fully understood. There is certainly an effect of viscosity upon the kinetics, but the thermodynamic effects of the carbon substitution are unknown.

Finally, the contact angle of the borosilicate and borosilicate/oxycarbide glasses on the carbon fibers was measured. The carbon fibers were dip-coated in the solutions and then heat treated in argon at ~1200°C to create microsessile drops. Scanning electron microscopy (SEM) micrographs show a clear difference in the wetting behavior of the oxide and oxycarbides. The borosilicate is essentially nonwetting and exhibits a contact angle of ~90°. The





**Figure 19.4.** (a) X-ray diffraction patterns of the borosilicate (upper) and borosilicate/oxycarbide (lower) glasses after 2 hours in argon. (b) The kinetics of crystallization of the borosilicate and borosilicate/oxycarbide at 1100°C in argon; semi-quantitative analysis using the methods of internal standards.

borosilicate/oxycarbide spreads on the fibers and exhibits a contact angle of  $\leq 45^\circ$ .

#### 19.4. STRENGTH BEHAVIOR OF OXYCARBIDE MATRIX COMPOSITES

The room temperature mechanical properties of the oxycarbide matrix composites were somewhat inferior to the standard oxide matrix materials. The data in Table 19.2 show a two- to threefold decrease in the flexural strength and fracture toughness. It was expected that a loss of room temperature fracture toughness would occur in this system. The better wetting of oxycarbide glass on

TABLE 19.2. Room Temperature Mechanical Properties of Carbon Fiber-Reinforced Glass Composites<sup>a</sup>

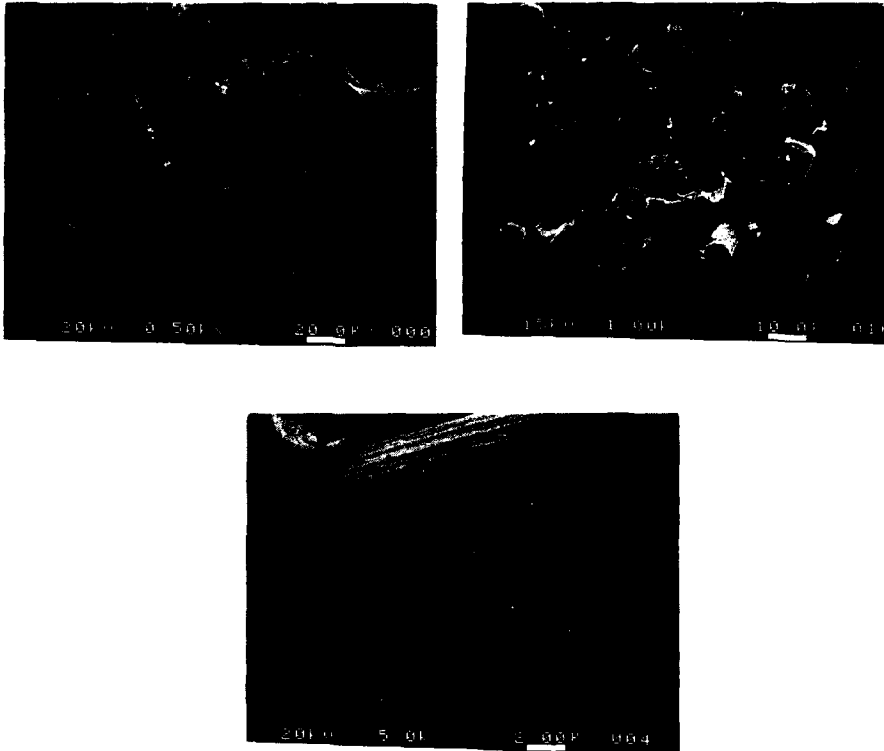
	Three-point Flexural Strength (MPa)		Fracture Toughness (MPa · m <sup>1/2</sup> )	
	Flatwise	Edgewise	Flatwise	Edgewise
Borosilicate	336	350	7.28	9.15
Borosilicate/oxycarbide without heat treatment	112.5	103.4	2.69	3.03
in air				
with 300°C heat treatment	196.3	172.2	5.57	4.98
in air				

<sup>a</sup>All composites contain 25% v/o Celion fiber.

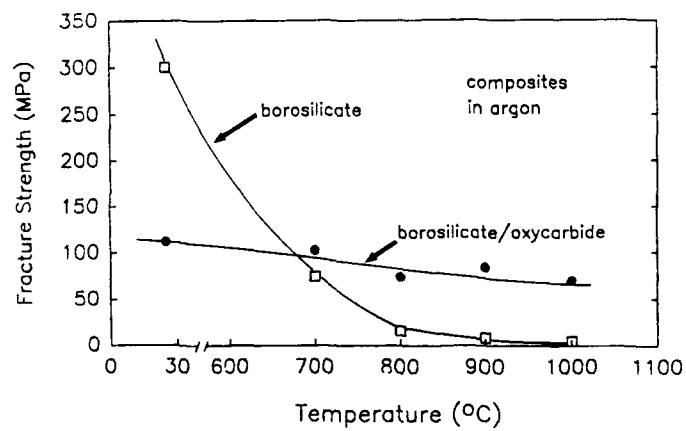
the carbon fibers enhances the fiber/matrix adhesion, and this limits debonding and fiber pullout. However, the magnitude of the effect was far greater than expected. It was suspected that volatiles in the composite preforms, which could not be removed during the argon treatment at 600°C, were responsible, in part, for the poor performance. Any volatiles that can oxidize the fibers will cause a decrease in their strength. Thus, additional composites were prepared and these were heat treated at 300°C in air before the 600°C argon treatment. It can be seen (Table 19.2) that this led to a nearly twofold improvement in the room temperature properties. It is not yet known how much further improvement in the room temperature properties can be expected. Larsen et al. [6] used a black glass matrix in SiC fiber-reinforced composites, and they also found the room temperature properties to be very sensitive to the processing. More experience in the processing of these highly reduced glasses is required.

The SEM micrographs in Fig. 19.5 show the fracture surfaces of the oxycarbide matrix composites tested at room temperature. Most obvious is the absence of any significant degree of fiber pullout. Nevertheless, the higher magnification images show that fiber/matrix debonding does occur and, further, that the fibers have not been etched or degraded in any way to interactions with the glass matrix. However, in many regions, a granular residue associated with the matrix phase adheres to fiber surfaces. This is generally not observed in the oxide matrix composites. This undoubtedly contributes to an increase in the interfacial shear strength. If the enhanced adhesion in this system occurs without any degradation of the fiber strength, one would expect an increase in the composite strength at the expense of fracture toughness. This was the effect anticipated, but clearly, an increase in strength has not yet been realized.

On the other hand, the use of an oxycarbide matrix in these composites does enhance the high-temperature performance of the composites. Figure 19.6 compares the flexural strength of the borosilicate composites and the



**Figure 19.5.** SEM micrographs of the room temperature fracture surface of a carbon fiber reinforced borosilicate/oxy carbide glass matrix composite.



**Figure 19.6.** Temperature dependence of the 3-point flexural strength of carbon-fiber reinforced borosilicate and borosilicate/oxy carbide glass matrix composites in argon.

borosilicate/oxycarbide composites. The tests were performed in argon over the temperature range 700–1000°C. It is clear that the oxide matrix composite undergoes a significant loss in strength in this temperature range. The borosilicate/oxycarbide glass appears to retain its strength—albeit low—up to 1000°C. The fractured specimens were examined in the SEM, and the differences could be attributed directly to the crystallization resistance of the borosilicate/oxycarbide.

### 19.5. SUMMARY

It has been shown that borosilicate/oxycarbide glass can be synthesized using a sol-gel approach. The resistance of the glass to bloating and crystallization is increased by the carbon incorporation, and this enhances the high-temperature strength behavior of carbon fiber-reinforced composites. This is the most advantageous effect of the oxycarbide matrix. Whereas 80–90% of the carbon in ternary silica-oxycarbide gels is retained during the gel-to-glass conversion, only 30–40% is maintained in the borosilicate. This suggests that other glass compositions, or the ternary Si–O–C, should be developed to increase the oxycarbide content of the glass matrix in composites. Moreover, further study of the interface chemistry of these oxycarbide glasses with carbon fibers and with silicon carbide fibers is warranted.

### ACKNOWLEDGMENT

The authors gratefully acknowledge the Office of Naval Research (ONR N00014-55-C-0332 and N00014-87-K-0247) for their support of this research.

### REFERENCES

1. P. Benson, K. E. Spear, and C. G. Pantano, Thermochemical analysis of interface reactions in carbon fiber reinforced glass matrix composites, in: J. A. Pask and A. G. Evans, Eds., *Ceramic Microstructures '86*, pp. 415–426, Plenum, New York (1987).
2. W. K. Tredway, K. M. Prewo, and C. G. Pantano, *Carbon*, **27**, 717–727 (1989).
3. H. Zhang and C. G. Pantano, *J. Am. Ceram. Soc.*, **73**, 958–963 (1990).
4. C. F. Smith and W. B. Crandall, U.S. Patent No. 3,378,431, 1968.
5. F. K. Chi, *Ceramic Sci. Eng. Proc.*, **4**, 704–717 (1983).
6. D. C. Larsen et al., Silicon Carbide Fiber Reinforced Black Glass Matrix Composites, AFWAL-TR-83-4134, 1986.
7. J. Homeny, G. G. Nelson, and S. H. Risbud, *J. Am. Ceramic Soc.*, **71**, 386–390 (1988).
8. D. Qi and C. G. Pantano, Sol/Gel processing of carbon fiber reinforced glass matrix in: J. D. Mackenzie and D. R. Ulrich, Eds., *Ultrastructure Processing of Advanced Ceramics*, pp. 635–649, Wiley, New York (1988).
9. J. Lipowitz, H. A. Freeman, R. T. Chen, and E. R. Prack, *Advan. Ceramic Mater.*, **2**, 121–128 (1987).

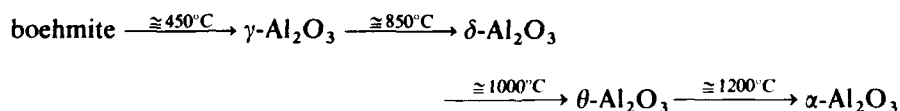
## SEEDED TRANSFORMATION OF ALUMINUM CHLOROHYDRATE GELS

J. M. BOULTON, S. SUBRAMONEY, AND D. R. UHLMANN

### 20.1. INTRODUCTION

The basic aluminum chloride, aluminum chlorohydrate, has the nominal formula,  $\text{Al}_2(\text{OH})_5\text{Cl} \cdot 2\text{H}_2\text{O}$ . The high alumina equivalent of aluminum chlorohydrate makes it suitable for ceramic applications. It is currently used in the manufacture of ceramic fibers [1, 2]. Aluminum chlorohydrate has a formal degree of hydrolysis (OH/Al ratio) of 2.5. The exact composition of highly hydrolyzed aqueous aluminum chloride solutions depends on factors such as aging. The principal species are polymeric, although smaller amounts of monomers and dimers also exist. The polymeric components have been identified as  $[\text{AlO}_4\text{Al}_{12}(\text{OH})_{24}(\text{OH}_2)_{12}]^{7+}$  (designated  $\text{Al}_{13}^{7+}$ ) and higher-molecular-weight polymers, either structurally related to  $\text{Al}_{13}^{7+}$  or with a layer structure, similar to that of gibbsite,  $\gamma\text{-Al}(\text{OH})_3$  [3-7].

The beneficial effects of  $\alpha\text{-Al}_2\text{O}_3$  seeding in boehmite,  $\gamma\text{-AlOOH}$ , gels has been well demonstrated [8-15]. Boehmite transforms to  $\alpha\text{-Al}_2\text{O}_3$  via the following reaction series:



*Ultrastructure Processing of Advanced Materials.*

Edited by Donald R. Uhlmann and Donald R. Ulrich (deceased).

ISBN 0-471-52986-9 © 1992 John Wiley & Sons, Inc.

On seeding, each  $\alpha$ - $\text{Al}_2\text{O}_3$  particle can provide a multiple nucleation site for the  $\theta$ - to  $\alpha$ - $\text{Al}_2\text{O}_3$  transition. Boehmite seeded with approximately 1.5 wt %  $\alpha$ - $\text{Al}_2\text{O}_3$  exhibits a reduction in the activation energy for  $\alpha$ - $\text{Al}_2\text{O}_3$  formation by 71 kJ/mol, a lowering in the transformation temperature by as much as 170°C and the development of a submicrometer, aggregate-free microstructure that sinters to full density at 1200°C [8, 9].

In this Chapter, the effects of  $\alpha$ - $\text{Al}_2\text{O}_3$  seeding in amorphous gels prepared from aluminum chlorohydrate are evaluated.

## 20.2. EXPERIMENTAL

Aluminum chlorohydrate (10.0 g, equivalent to 0.046 mol of  $\text{Al}_2\text{O}_3$ ) (Micro-Dry Super Ultrafine, Reheis Chemical Co., Berkeley Heights, N.J.) was dissolved in distilled water (20 ml) to give a clear solution.  $\alpha$ - $\text{Al}_2\text{O}_3$ , with an ultimate particle size of 0.15  $\mu\text{m}$  (0.2345 g, 0.0023 mol) (Baikalox SM-8, Baikowski Corp., Charlotte, N.C.) was then added to give a seeding level of 5 mol %  $\alpha$ - $\text{Al}_2\text{O}_3$ /mol  $\text{Al}_2\text{O}_3$  derived from aluminum chlorohydrate. Sonication was applied at this stage to aid in the dispersion of the  $\alpha$ - $\text{Al}_2\text{O}_3$  seed particles. The solution was dehydratively gelled by exposure to the atmosphere and sonication overnight at 60°C. After drying the gel at 60°C for 24 hr, gel fragments approximately 5 mm in diameter were obtained. Samples of the gel were then fired at 500, 700, and 900°C for 2-, 4-, and 8-hr soak periods using a heating/cooling rate of 5°C/min in all cases.

The efficacy of  $\alpha$ - $\text{Al}_2\text{O}_3$  seeding was determined by a quantitative X-ray diffraction technique using quartz as an internal standard. The weight fraction of  $\alpha$ - $\text{Al}_2\text{O}_3$  in the fired gels was determined by comparing the relative integrated intensities of the (102) reflection of  $\alpha$ - $\text{Al}_2\text{O}_3$  and the (110) reflection of quartz to an  $\alpha$ - $\text{Al}_2\text{O}_3$ -quartz calibration curve. Fracture surfaces of samples were investigated by scanning electron microscopy.

## 20.3. RESULTS AND DISCUSSION

Unseeded aluminum chlorohydrate gels showed a similar phase development as boehmite on firing. With 2-hr soak periods, transitional  $\text{Al}_2\text{O}_3$  phases were detected between 500 and 1000°C, and  $\alpha$ - $\text{Al}_2\text{O}_3$  began to crystallize at approximately 1000°C. On firing to 1100°C,  $\alpha$ - $\text{Al}_2\text{O}_3$  was the only phase detected.

Seeding had a dramatic effect on the transformation to  $\alpha$ - $\text{Al}_2\text{O}_3$ . The weight fractions of  $\alpha$ - $\text{Al}_2\text{O}_3$  in both seeded and unseeded fired gels are given in Table 20.1. On firing to 500°C for 2 hr, 23.8 wt %  $\alpha$ - $\text{Al}_2\text{O}_3$  (after subtracting the seed percent) had been formed in the gel. In comparison, only 17.5 wt %  $\alpha$ - $\text{Al}_2\text{O}_3$  had been formed in the unseeded gel on firing at the much higher temperature of 900°C for the much longer time of 8 hr. With the seeded gels, it can be seen that

TABLE 20.1. Conversion to  $\alpha$ -Al<sub>2</sub>O<sub>3</sub> on Firing Aluminum Chlorohydrate Gels

Temperature (°C)	Time (hr)	Weight percent $\alpha$ -Al <sub>2</sub> O <sub>3</sub>		
		Unseeded	Seeded	
			Total $\alpha$ -Al <sub>2</sub> O <sub>3</sub>	$\alpha$ -Al <sub>2</sub> O <sub>3</sub> Formed in Gel
500	2	—	27.4	23.8
	4	—	33.7	30.4
	8	—	46.1	43.4
700	2	—	38.4	35.3
	4	—	47.2	44.6
	8	—	64.8	63.0
900	2	—	62.8	60.9
	4	—	72.4	71.0
	8	17.5	88.9	88.3

the fraction crystallized increases both with increasing temperature and with increasing time at temperature.

The seeding level investigated in these experiments is equivalent to 5 mol%  $\alpha$ -Al<sub>2</sub>O<sub>3</sub>/mol Al<sub>2</sub>O<sub>3</sub> derived from the aluminum chlorohydrate. This equates to approximately  $3 \times 10^{13}$  seed particles/cm<sup>3</sup>  $\theta$ -Al<sub>2</sub>O<sub>3</sub> derived from the aluminum chlorohydrate. As can be seen in Fig. 20.1, which shows a fracture surface of a seeded, dried gel, the  $\alpha$ -Al<sub>2</sub>O<sub>3</sub> seed particles are well dispersed throughout the amorphous gel network, although in some instances agglomeration of the seeds had occurred. The rapid crystallization of  $\alpha$ -Al<sub>2</sub>O<sub>3</sub> on firing was accompanied

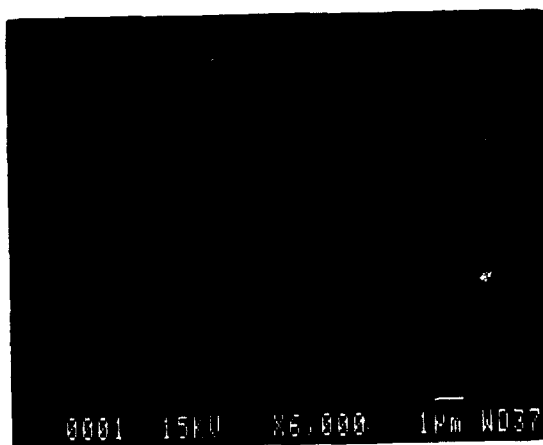


Figure 20.1. SEM micrograph of the fracture surface of a seeded, dried gel (bar = 1  $\mu$ m).

by remarkable growth of the seed particles as indicated by scanning electron micrograph observations. Micrographs of fracture surfaces of seeded gels fired at 500 and 700°C for 4 hr are shown in Figs. 20.2 and 20.3. As seen in Fig. 20.2, the average diameter of the seeds has grown to approximately  $0.3\text{ }\mu\text{m}$ , indicating a significant epitaxial effect. In Fig. 20.4, the fracture surface of an unseeded gel fired at 700°C for 4 hr is shown. A comparison of Figs. 20.3 and 20.4 illustrates the effect of seeding on microstructural development.



Figure 20.2. SEM micrograph of the fracture surface of a seeded gel fired at 500°C for 4hr (bar =  $1\text{ }\mu\text{m}$ ).



Figure 20.3. SEM micrograph of the fracture surface of a seeded gel fired at 700°C for 4hr (bar =  $1\text{ }\mu\text{m}$ ).



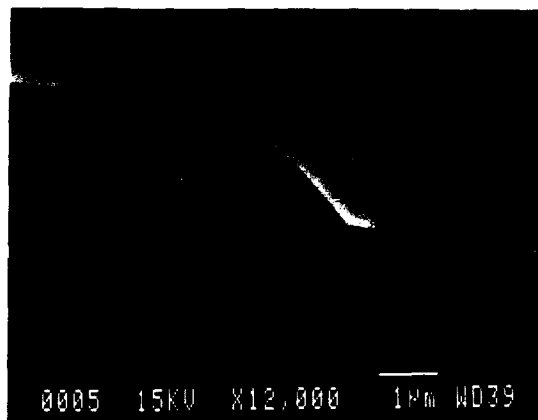


Figure 20.4. SEM micrograph of the fracture surface of an unseeded gel fired at 700°C for 4 hr (bar = 1 µm).

## 20.4. CONCLUSION

Seeding aluminum chlorohydrate gels with fine  $\alpha$ -Al<sub>2</sub>O<sub>3</sub> particles has been shown to enhance greatly the conversion of the amorphous gels to  $\alpha$ -Al<sub>2</sub>O<sub>3</sub>.

## ACKNOWLEDGMENTS

Financial support for the present work was provided by E. I. du Pont de Nemours and Company and by the Air Force Office of Scientific Research. This support is gratefully acknowledged.

## REFERENCES

1. L. E. Seufert, U.S. Patent 3808015, April 30, 1974 (to E. I. du Pont de Nemours and Co.).
2. M. J. Morton, J. D. Birchall, and J. E. Cassidy, British Patent 1360197, June 19, 1970 (to I.C.I. Ltd.).
3. J. W. Akitt and A. Farthing, *J. Chem. Soc., Dalton Trans.*, 1606 (1981).
4. J. W. Akitt, A. Farthing, and O. W. Howarth, *J. Chem. Soc., Dalton Trans.*, 1609 (1981).
5. J. W. Akitt and A. Farthing, *J. Chem. Soc., Dalton Trans.*, 1617 (1981).
6. J. W. Akitt and A. Farthing, *J. Chem. Soc., Dalton Trans.*, 1625 (1981).
7. D. Z. Denney and P. H. Hsu, *Clay Clay Minerals*, **34**, 604 (1986).
8. M. Kumagai and G. L. Messing, *J. Am. Ceram. Soc.*, **68**, 500 (1985).
9. R. A. Shelleman, G. L. Messing, and M. Kumagai, *J. Non-Cryst. Solids*, **82**, 277 (1986).
10. R. A. Shelleman and G. L. Messing, *J. Am. Ceram. Soc.*, **71**, 317 (1988).
11. M. Kumagai and G. L. Messing, *J. Am. Ceram. Soc.*, **67**, C-230 (1984).

12. G. L. Messing, M. Kumagai, R. A. Shelleman, and J. L. McArdle, in: L. L. Hench and D. R. Ulrich, Eds., *Science of Ceramic Chemical Processing*, pp. 259-271, Wiley, New York (1986).
13. W. A. Yarbrough and R. Roy, *J. Mater. Res.*, **2**, 494 (1987).
14. Y. Suwa, S. Komarneni, and R. Roy, *J. Mater. Sci. Lett.*, **5**, 21 (1986).
15. Y. Suwa, R. Roy, and S. Komarneni, *Mater. Sci. Eng.*, **83**, 151 (1986).

## PHOTOELECTROCHEMICAL DEPOSITION OF THALLIUM(III) OXIDE THIN FILMS ONTO *n*-SILICON

JAY A. SWITZER, RICHARD J. PHILLIPS,  
AND MICHAEL J. SHANE

### 21.1. INTRODUCTION

Thallium(III) oxide is a degenerate *n*-type semiconductor with a bandgap of 1.4 eV [1–4]. The oxide has a room-temperature resistivity of 70  $\mu\text{ohm-cm}$ , majority carrier mobility of 105  $\text{cm}^2/\text{Vsec}$ , and carrier concentration of  $7 \times 10^{20} \text{ cm}^{-3}$  [2, 3]. The 1.4-eV optical transition is indirect, and the material does not absorb light appreciably until the first direct transition at 2.2 eV [4].

We have previously exploited the high optical transparency and electrical conductivity of thallium(III) oxide in the fabrication of a heterojunction SIS-type thallium(III) oxide/*n*-silicon photovoltaic cell [5, 6]. The efficiency of the photovoltaic cell was 11% with 75.3  $\text{mW/cm}^2$  natural sunlight, and the short-circuit quantum efficiency at 800 nm was 97%. The thallium(III) oxide/*n*-silicon heterojunction was shown to have a barrier height of 0.96 V and a diode quality factor of 1.2 [5].

In this Chapter, the photoelectrochemical *direct writing* of thallic oxide films onto *n*-silicon is explored in more detail. The effects of concentration, potential, irradiance, and wavelength of the microstructure of electrochemically and photoelectrochemically deposited thallium(III) oxide films are presented.

*Ultrastructure Processing of Advanced Materials.*

Edited by Donald R. Uhlmann and Donald R. Ulrich (deceased).

ISBN 0-471-52986-9 © 1992 John Wiley & Sons, Inc.

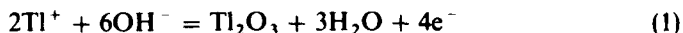
## 21.2. EXPERIMENTAL

Current-potential curves and electrodepositions were run with a Stonehart BC 1200 potentiostat/galvanostat, Princeton Applied Research (PAR) Model 175 universal programmer, PAR Model 379 digital coulometer, and Hewlett-Packard Model HP 7047A XY recorder. Single-crystal (100) wafers of semiconductor-grade *n*-silicon were obtained from Monsanto. The wafers were doped with phosphorous by the manufacturer to a volume resistivity of 2.1–2.4  $\Omega$ -cm. Back ohmic contacts were made either with Ga-In eutectic or by evaporating a thin film of aluminum onto a cooled silicon substrate. The wafers were exposed to the aqueous electrolyte using the PAR Model K105 flat specimen holder, and they were etched in aqueous 10% HF for 5 min prior to photoelectrochemical deposition. The semiconductor electrodes were irradiated with an Oriel Model 6431 250-W quartz tungsten-halogen source. Melles Griot 10-nm bandwidth interference filters were used for monochromatic light experiments. Irradiances were measured with an Eppley Model E6 thermopile radiometer. Scanning electron microscopy was done on the JEOL 35CF scanning electron microscope.

## 21.3. RESULTS AND DISCUSSION

### 21.3.1. Electrochemical Deposition of Thallium(III) Oxide Films

We have previously deposited ceramic films either by effecting a redox change in metal ion precursors or by electrogenerating base [7, 8]. In the present study the redox change method is used, since the thallium(I) ion is oxidized to thallium(III) oxide according to Eq. 1. The standard reduction potential for the reverse of Eq. 1 is 0.02 V versus NHE or –0.22 V versus the standard calomel (SCE) reference electrode.



Current potential curves for the electrodeposition of  $\text{Tl}_2\text{O}_3$  onto a platinum electrode are shown in Fig. 21.1 for various thallium ion concentrations. The curves have a potential-dependent or activation-controlled region and a potential-independent or mass-transport-limited region. The potential-dependent current follows approximately a Butler-Volmer or Tafel exponential dependence on potential. The mass-transport-limited current is independent of potential, but is a direct function of concentration, electrode area, and mass transport mechanism (i.e., diffusion, convection, or migration).

The microstructure of the film is dependent on whether the electrodeposition is run at activation-controlled or mass-transport-limited potentials. Dense columnar films are formed at lower activation-controlled potentials. We have previously shown that the films grow with cube faces parallel to the electrode

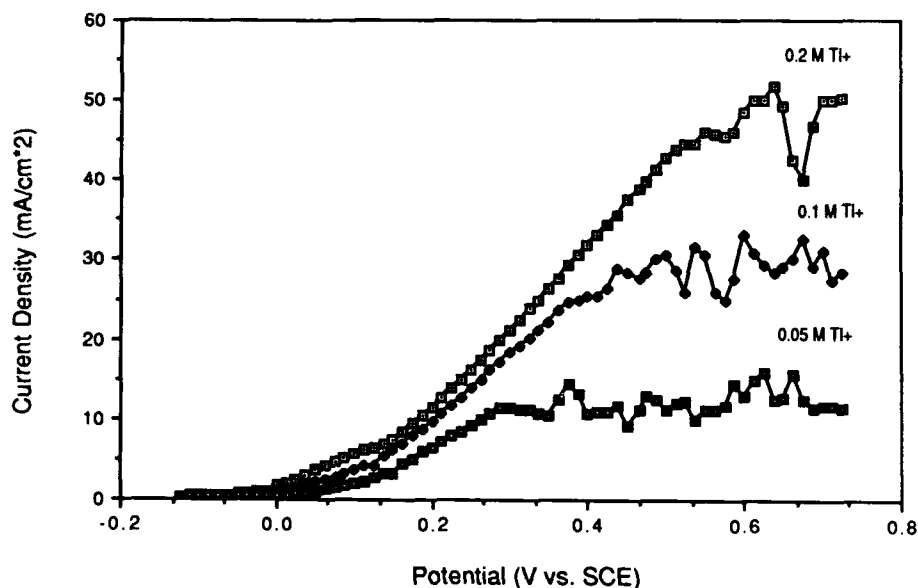
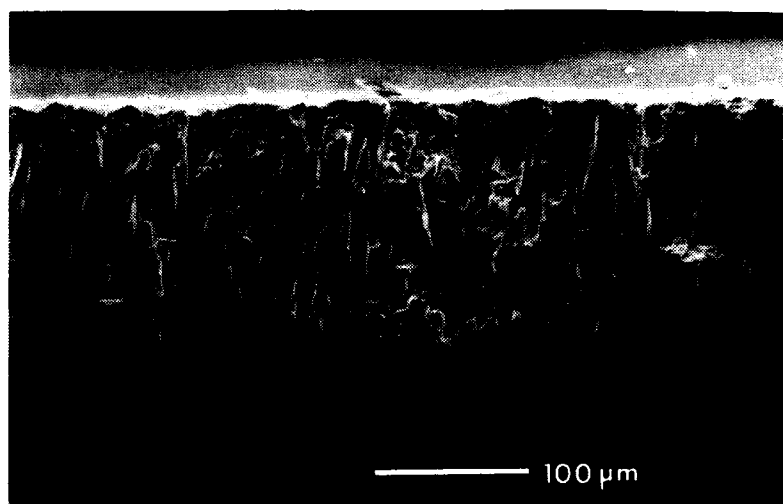


Figure 21.1. Current-potential curves for electrodeposition of thallium(III) oxide onto platinum as function of thallous ion concentration. Stirred alkaline solution (1.0 M NaOH); 20 mV/sec scan rate.

surface, since the (400), (600), and (800) reflections in the X-ray diffraction pattern were anomalously intense [7]. Wirtz and Siebert have shown that films of thallium(III) oxide grown by vapor-transport grew fastest along the  $\langle 111 \rangle$  directions [9]. The 170- $\mu\text{m}$ -thick thallium(III) oxide film in Fig. 21.2 was galvanostatically grown on a 430 stainless-steel substrate from an alkaline 0.5 M  $\text{Tl}^+$  solution at a current density of 10 mA/cm<sup>2</sup>. Dense columnar films can be deposited at currents below the mass-transport limit with thicknesses ranging from 0.1  $\mu\text{m}$  to several hundred micrometers. This is in sharp contrast with sol-gel processing, in which only thin films can be deposited. As shown in Table 21.1, the current efficiency for films grown at 10 mA/cm<sup>2</sup> for various thickness is approximately  $103 \pm 2\%$ . The current efficiency was determined gravimetrically, and the thicknesses were calculated from the anodic coulombs by assuming a density of 10.2 g/cm<sup>3</sup>.

Thallium(III) oxide films deposited at mass-transport-limited currents tend to assume a dendritic microstructure. The currents are noisy in the mass-transport region, and they are independent of potential. The noise is apparently due to the changing electrode area and current distribution during the dendrite formation, since mass-transport-limited currents for homogeneous solution redox reactions are not noisy. The scanning electron micrograph of dendritic thallium(III) is shown in Fig. 21.3.



**Figure 21.2.** Scanning electron micrograph of a cross section of thallium(III) oxide thick film grown at  $10 \text{ mA/cm}^2$  on a 430 stainless-steel substrate. Stirred alkaline solution ( $1.0 \text{ M NaOH}$ ,  $0.5 \text{ M Tl}^+$ ). Marker on micrograph is  $100 \mu\text{m}$ .

### 21.3.2. Photoelectrochemical Deposition of Thallium(III) Oxide Films onto *n*-Silicon

Semiconductor electrodes tend to form rectifying junctions with solutions due to the energetic mismatch of the Fermi level of the semiconductor and the electrochemical potential of the solution. In general, *n*-type semiconductors are rectifiers towards anodic processes, and *p*-type semiconductors are rectifiers toward cathodic processes [10]. In this study, thallium(III) oxide is photoelectrochemically deposited onto *n*-silicon in an anodic process. Photons of energy greater than the bandgap of *n*-silicon produce electron-hole pairs, and

**TABLE 21.1. Current Efficiency for Thallium(III) Oxide Electrodeposition**

Anodic Coulombs	Thallium(III) Oxide ( $\mu\text{mol}$ )	Calculated Thickness ( $\mu\text{m}$ )	Current Efficiency (%)
1	2.63	1.2	101
5	13.79	60	106
10	26.79	12	102
50	132.9	60	103

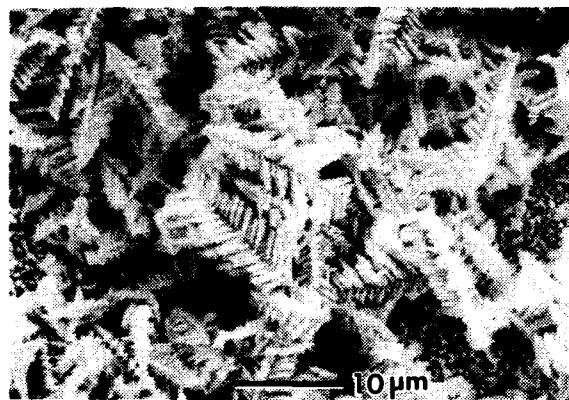


Figure 21.3. Scanning electron micrograph of dendritic thallium(III) oxide grown with mass-transport limited currents on a 430 stainless-steel substrate. Marker on micrograph is  $10\ \mu\text{m}$ .

the photogenerated holes are driven to the surface by the electric field in the depletion region.

The photocurrent-potential curves are shown in Fig. 21.4 for  $n$ -Si in alkaline  $0.2\ \text{M}\ \text{Tl}^+$  for various tungsten-halogen irradiances. The potential-independent portions of the curves are photon-flux limited at lower irradiances, but become mass-transport limited at high irradiance. The curves are smooth when the reaction is photon-flux limited and become noisy at the mass-transport limit of

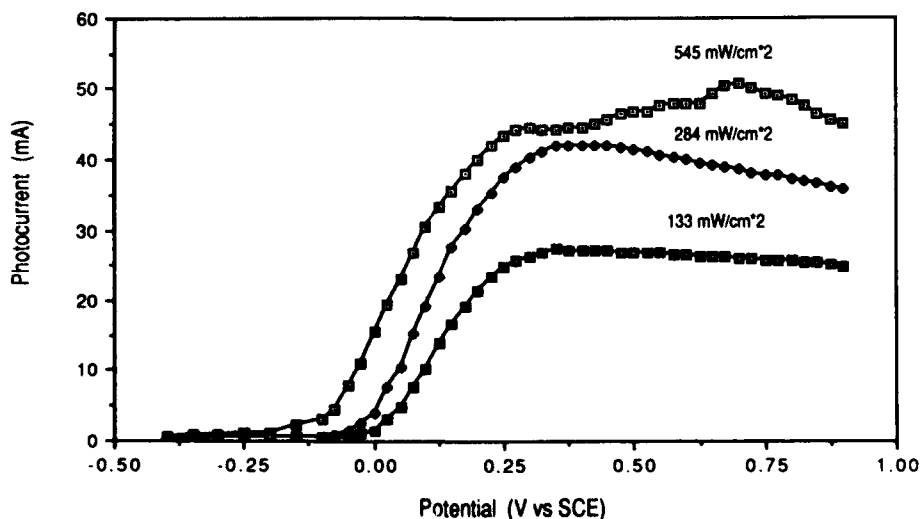
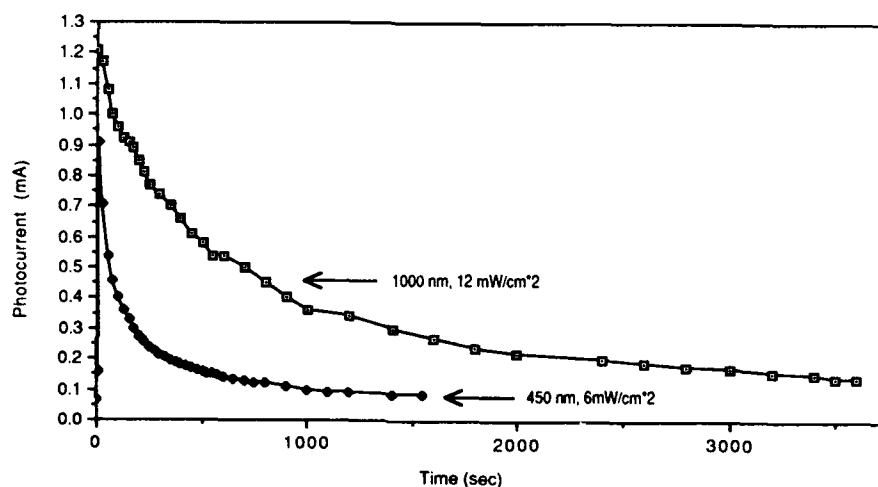


Figure 21.4. Photocurrent-potential curves of thallium(III) oxide deposition onto  $n$ -Si substrate for three irradiances ( $\text{mW}/\text{cm}^2$ ) from a tungsten-halogen light source. Stirred alkaline solution ( $1.0\ \text{M}\ \text{NaOH}$ ,  $0.2\ \text{M}\ \text{Tl}^+$ );  $50\ \text{mV}/\text{sec}$  scan rate.



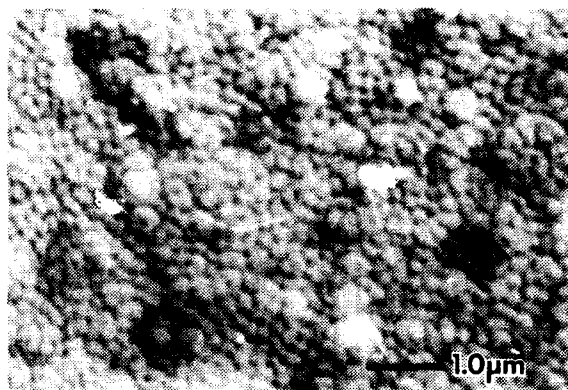
**Figure 21.5.** Photocurrent-time curves for thallium(III) oxide deposition onto *n*-Si substrate for 1000- and 450-nm light. Potentiostated at +0.5 V versus SCE. Stirred alkaline solution (1.0 M NaOH, 0.2 M  $\text{Ti}^{3+}$ ). Initial irradiation with 3000 mW/cm<sup>2</sup> tungsten-halogen light to 0.025 C/cm<sup>2</sup>.

about 50 mA/cm<sup>2</sup>. The photocurrents decrease slightly in the photon-flux-limited regions of the curves, because the photoelectrochemically deposited thallium(III) oxide attenuates the light.

Photocurrent-time curves for an *n*-Si electrode potentiostated at +0.5 V versus SCE in alkaline 0.5 M thallos acetate are shown in Fig. 21.5 for both 1000- and 450-nm monochromatic light. The photocurrent decreases much more rapidly for the 450 nm light, because the first direct transition for thallium(III) oxide is 2.2 eV (564 nm), and the oxide attenuates the light strongly at shorter wavelengths. The 1000-nm light has a high enough energy (1.24 eV) to generate electron-hole pairs in the silicon, but it is not attenuated appreciably by the thallium(III) oxide. The scanning electron micrograph of the film that was grown by irradiation with 450-nm light is shown in Fig. 21.6. The electrode was irradiated with 6.8 mW/cm<sup>2</sup> light for a total time of 42 mins and coverage of 0.5 C/cm<sup>2</sup>. The film is fairly uniform and is composed of small 0.2- $\mu\text{m}$  spheres. The thickness is approximately equal to the sphere diameters. Hence, the photoelectrochemical deposition is "turned off" through light attenuation after the electrode is covered with a thin film. Much thicker films can be grown by irradiating with longer-wavelength monochromatic light or broadband radiation containing a large long-wavelength component.

We have observed in the photoelectrochemical deposition of hundreds of thallium(III) oxide films that the most uniform thin ( $\sim 0.1\text{-}\mu\text{m}$ ) films of thallium(III) oxide are deposited when the *n*-silicon is initially irradiated with a short pulse of high intensity light. The pulse apparently promotes the instantaneous nucleation of a high density of thallium(III) oxide nuclei. Hence, both of





**Figure 21.6.** Scanning electron micrograph of thallium(III) oxide film grown with 450-nm light at an irradiance of  $6.8 \text{ mW/cm}^2$ . Substrate is *n*-Si. Potentiostated at  $+0.5 \text{ V}$  versus SCE. Initial irradiation with  $3000 \text{ mW/cm}^2$  tungsten-halogen light to  $0.025 \text{ C/cm}^2$ . Stirred alkaline solution ( $1.0 \text{ M NaOH}$ ,  $0.2 \text{ M Tl}^+$ ). Marker on micrograph is  $1.0 \mu\text{m}$ .

the electrodes in Fig. 21.5 were initially irradiated with a  $3000 \text{ mW/cm}^2$  pulse of tungsten-halogen light. The pulse resulted in a  $0.03 \text{ C/cm}^2$  coverage of small ( $<0.1 \mu\text{m}$ ) spherical nuclei on the surface, which grew together to form a continuous film during the subsequent lower-intensity irradiation. Films that were not nucleated at high irradiance tended to be nonuniform, with widely varying grain sizes. More details on the nucleation and growth of very thin thallium(III) oxide films will be presented in a future article.

### ACKNOWLEDGMENTS

The authors gratefully acknowledge the donation of electrochemical and photonic instrumentation by Unocal Corporation and the assistance of George M. McManus with the scanning electron microscopy.

### REFERENCES

1. A. W. Sleight, J. L. Gillson, and B. L. Chamberland, *Mater. Res. Bull.*, **5**, 807 (1970).
2. V. N. Shukla and G. P. Wirtz, *J. Am. Ceram. Soc.*, **60**, 253 (1977); **60**, 259 (1977).
3. G. P. Wirtz, C. J. Yu, and R. W. Doser, *J. Am. Ceram. Soc.*, **64**, 269 (1981).
4. H. P. Geserich, *Phys. Status Solid.*, **25**, 741 (1968).
5. J. A. Switzer, *J. Electrochem. Soc.*, **133**, 722 (1986).
6. J. A. Switzer, U.S. Patents 4,492,811 (Jan. 8, 1985); 4,495,046 (Jan. 22, 1985); 4,521,499 (June 4, 1985); 4,592,807 (June 3, 1986); 4,626,322 (Dec. 2, 1986); and 4,608,750 (Sept. 2, 1986).

7. J. A. Switzer, *Am. Ceram. Soc. Bull.*, **66** 1521 (1987).
8. J. A. Switzer and R. J. Phillips, in: C. J. Brinker, D. E. Clark, and D. R. Ulrich, Eds., *Better Ceramics Through Chemistry*, Vol. III, *Mater. Res. Soc. Symp. Proc.*, **121**, 111-114 (1988).
9. G. P. Wirtz and D. C. Siebert, *J. Cryst. Growth*, **32**, 274 (1976).
10. J. A. Switzer, *J. Electrochem. Soc.*, **136**, 1009 (1989).

## **22**

# **REAL TIME MONITORING OF SILICA GEL DRYING BEHAVIOR**

**M. J. R. WILSON AND L. L. HENCH**

### **22.1. INTRODUCTION**

One of the main difficulties in monitoring changes during the drying of gels is that the "as formed" gel is extremely sensitive to physical contact. Any device contacting the gel may affect drying behavior by altering the surface temperature, causing inhomogeneous evaporation and development of differential stresses that can lead to cracking.

In this apparatus, optical means are used to measure changes in thickness and diameter of a gel and the stresses that develop during drying. Weight change is measured simultaneously enabling density and pore volume to be calculated.

The gel is suspended within a drying chamber contained within an oven. Both the drying chamber and the oven are equipped with windows to provide 360° viewing of the sample. The windows allow transmission of polarized light through the sample and also side illumination. An automatic 35-mm camera is used to record the dimensions of the gel (by careful use of mirrors) and the balance readout at any time interval, from 1 sec to 120 hr. An automatic data collection system records temperature at up to eight locations within the drying chamber in order to confirm temperature homogeneity. Temperature control is provided by means of a (Micristar) ramp and soak controller.

*Ultrastructure Processing of Advanced Materials.*

Edited by Donald R. Uhlmann and Donald R. Ulrich (deceased).

ISBN 0-471-52986-9 © 1992 John Wiley & Sons, Inc.

## 22.2. EXPERIMENTAL APPARATUS

The apparatus is shown in detail in Fig. 22.1. Evaporation rate is controlled by both temperature and by two vapor outlets, one of which is variable. Details are shown in the inset of Fig. 22.1. The camera records the sample dimensions on high-resolution 35-mm slides that afford a four- to five-times magnification of the sample.

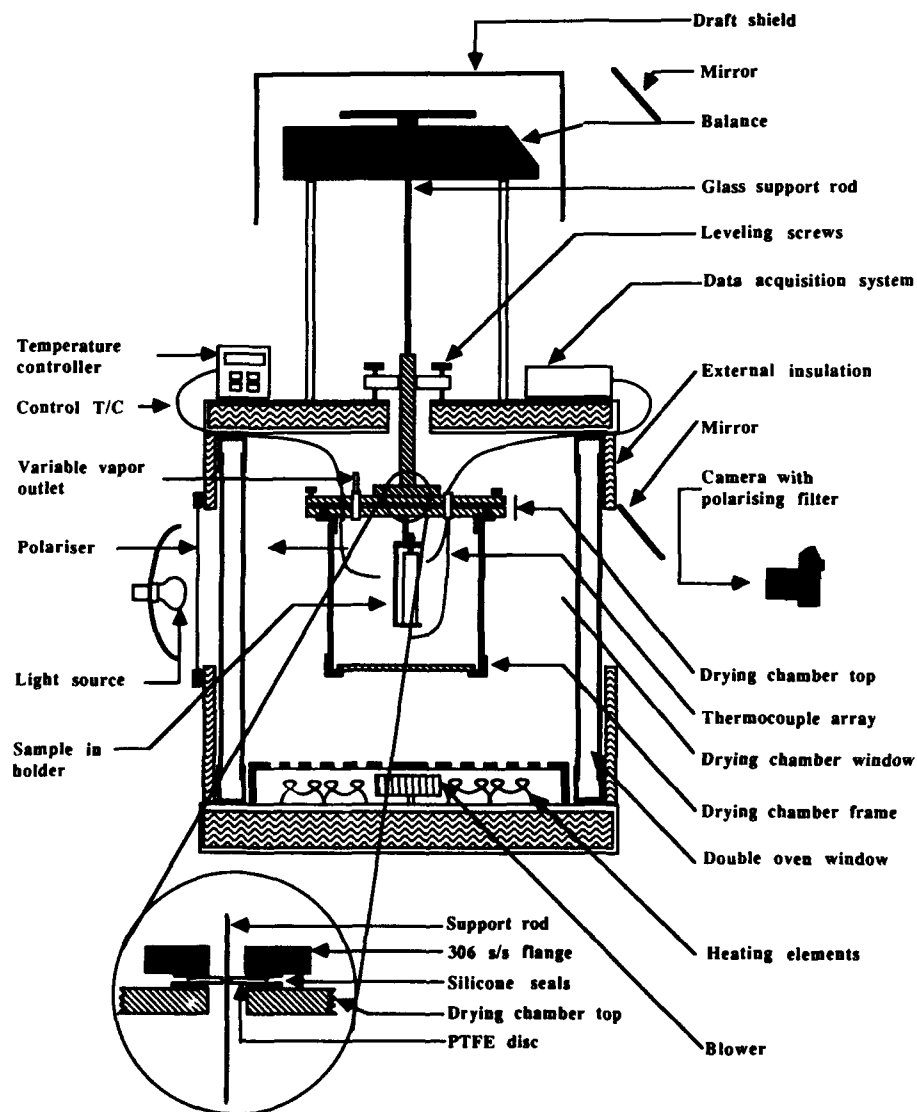


Figure 22.1. Experimental apparatus for real-time monitoring of silica gel drying behavior.

The gels 22 and 25 used in this study were made by adding 1 mol of tetramethyloxysilane to 16.17 mol of water containing 0.089 mol of nitric acid at pH  $\sim 1.5$ . After stirring for 10 min, the resulting sol was chilled to 20°C and cast into a 110-mm-diameter polymethylpentene mold. Gelation occurred in 55 hr at 23°C and was followed by aging for 3 months at 22–25°C. The aged gel was removed from its mold and placed on edge on the sample holder. The drying chamber was sealed and the wet weight recorded. The drying chamber was heated to 110°C at a rate of 5°C/hr. The gel was maintained at 110°C  $\pm$  0.5°C until no further changes in weight or dimension occurred, this was about 135 hr for gel 25.

### 22.3. RESULTS

The data collected are weight, diameter, thickness, birefringence, transparency (or opacity), and temperature. These data are shown in Fig. 22.2 for a 99.3-mm-diameter, 21.2-mm-thick silica gel monolith (gel 25) with an initial density of 1.077 g/cm<sup>3</sup>. The sequence of photographs (1 to 10) in Fig. 22.2a show the appearance of the gel at points marked on Fig. 22.2. Figure 22.3 shows the equivalent data for a similar monolith 99.4 mm in diameter and 19.4 mm thick with an initial density of 1.080 g/cm<sup>3</sup> (gel 22).

The pore volume can be calculated by

$$V_p = V_b - V_s$$

where  $V_b$  is the bulk volume, calculated from the sample thickness and diameter, and  $V_s$  is the volume of the network, calculated from knowledge of the amount of SiO<sub>2</sub> in the sample (from the amount of alkoxide used) and assuming a structural density of 2.11 g/cm<sup>3</sup> for the acid-catalyzed gels used (Chapter 11). The time dependence of the pore volume is shown for gel 25 in Fig. 22.4c. The change in the rate of weight loss and density is shown in Figs. 22.4a and 22.4b. Figure 22.5 shows the comparative (log) loss rates for both samples. During the rise in temperature the gel expands slightly up to  $\sim 70^\circ\text{C}$  after which evaporative losses begin to dominate and the gel rapidly loses both weight and volume (stage 1). This first stage of drying accounts for over 80% of the total weight loss and almost 100% of the total volume loss while taking only 30% of the total drying time. The end of this stage coincides with the maximum observed density of 1.48 g/cm<sup>3</sup>. This value corresponds to the calculated density of the dry gel with the pores completely full of pore liquid.

After shrinkage stops, the rate of evaporation slows and assumes a linear relationship with time (Fig. 22.4a). This stage (stage 2) accounts for 11% of the total weight loss and about 35% of the total drying time. Shortly after entering this stage the gel turns opaque (photographs 5 to 10), first at the edges, progressing linearly toward the center. It is normally during this opaque stage that the gel breaks, if sufficient stress or defects are present (Chapter 15). Some

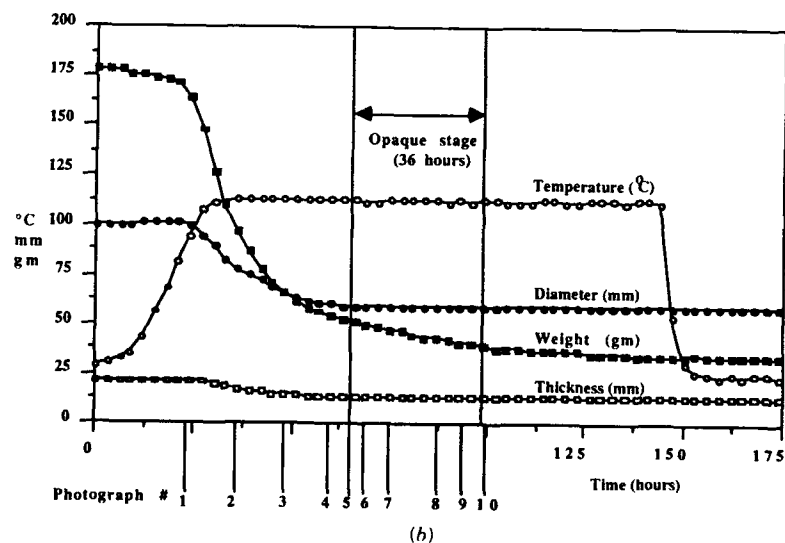
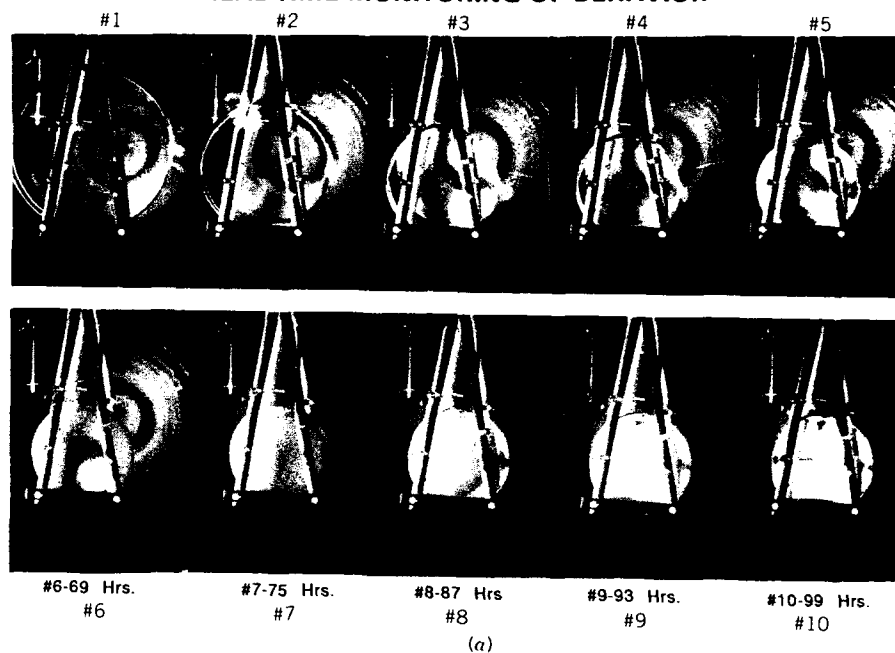


Figure 22.2. Drying behavior of silica gel as a function of time (gel 25).

further shrinkage ( $\sim 1\%$  linear) is observed during this stage, although the gel subsequently expands to its previous size as transparency is regained. At the end of this stage, the gel is within 5% of the theoretical weight of silica formed in the original hydrolysis and subsequent polycondensation. Further soaking at  $110^\circ\text{C}$  reduces the weight to within 2.2% of the theoretical value, but at a very reduced rate. This final stage (stage 3), leading to equilibrium, accounts for the remaining

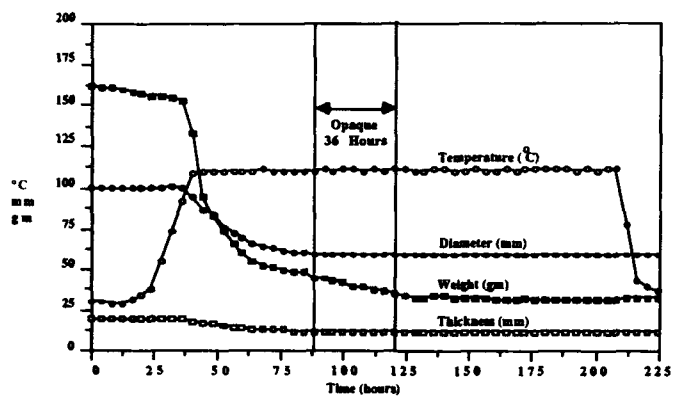


Figure 22.3. Drying behavior of silica gel as a function of time (gel 22).

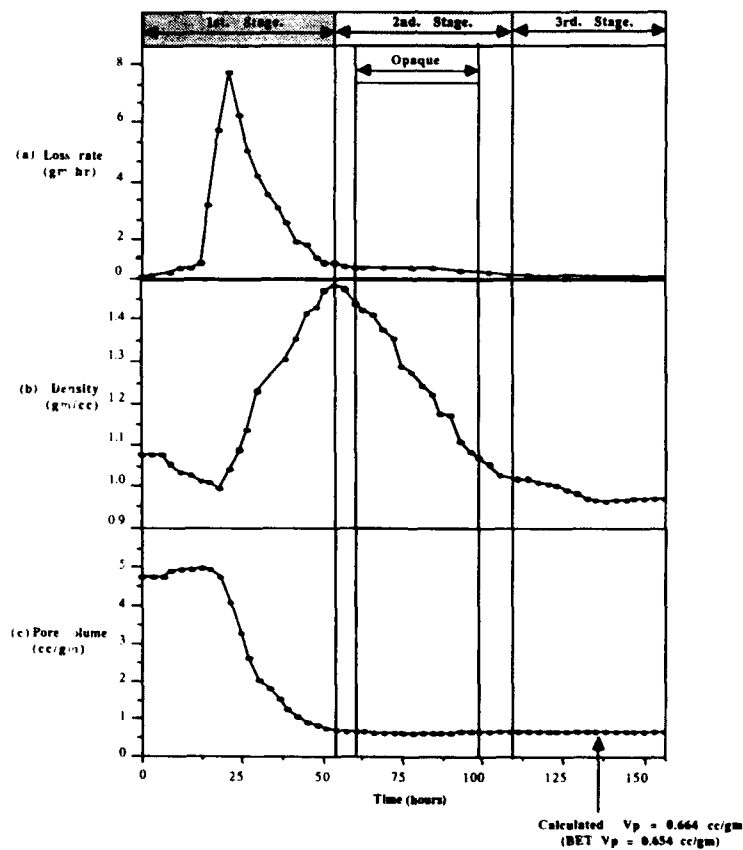


Figure 22.4. Time dependence of (a) rate of weight loss (b) density and (c) pore volume for gel 25.

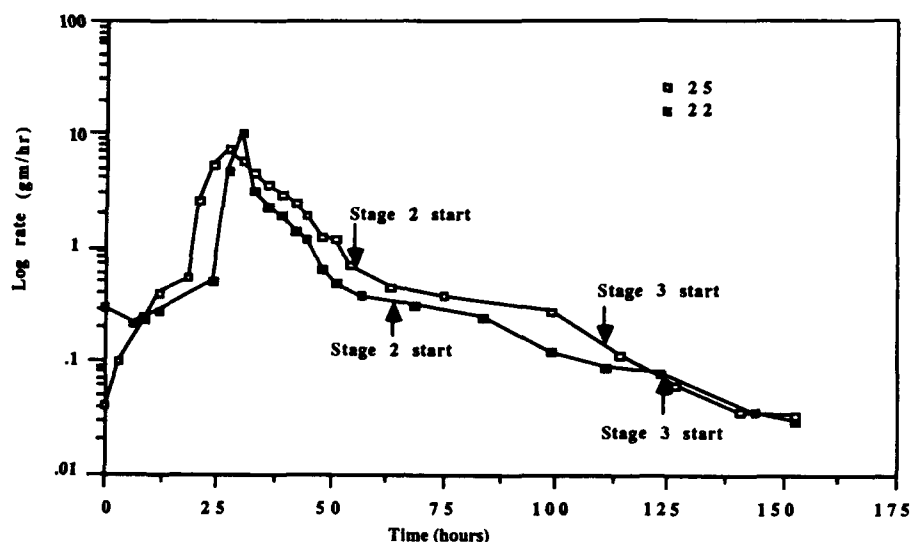


Figure 22.5. Comparative (log) loss rates for gel 22 and gel 25.

drying time. The aged gel consists, by volume, of 91% pore liquid (35% methanol/65% water at pH ~1.5) and 9% solid phase. The 110°C dry gel, in contrast, consists of 42% solid phase, 57% open porosity, and 1% adsorbed moisture. The Brunaur-Emmett-Teller data give an average pore radius of 23.1 Å, a surface area of 566 m<sup>2</sup>, and a pore volume of 0.654 cm<sup>3</sup>/g for gel 25, compared to a pore radius of 23.8 Å, a surface area of 581 m<sup>2</sup>, and a pore volume of 0.692 cm<sup>3</sup> for gel 22.

## 22.4. DISCUSSION

The drying process consists of three stages:

- Stage 1.* During which the greatest changes in volume weight and structure occur.
- Stage 2.* In which changes in weight and volume are small, but large changes in optical characteristics are seen.
- Stage 3.* In which there are no further dimensional changes, but there is a progressive loss of weight to the minimum attainable value.

The physical changes that occur during these stages are shown in Fig. 22.4. In stage 1, the rise in temperature is accompanied by the rapid increase in the loss rate seen in Fig. 22.4a and Fig. 22.5. The rise in temperature is also responsible for the small increase in pore volume seen in Fig. 22.4c due to thermal expansion



of the enclosed pore liquid. The drop in density seen in Fig. 22.4b can only be partially attributed to this expansion. The minimum density observed occurs slightly before the peak loss rate. The volume loss does not equal the volume of evaporated pore liquid, but follows closely behind suggesting that the evaporation rate is greater than the maximum strain rate of the gel and that pore emptying is occurring. As the evaporative forces begin to dominate, the gel begins to shrink rapidly, resulting in an increased packing density of the solid phase, further polycondensation (formation of new Si-O bonds) and a rise in density, modulus, and viscosity of the solid phase. The shrinkage is accompanied by a nonlinear decrease in the loss rate, which may be due to decreasing surface area and pore radius. This structural change would create a dry surface layer through which vapor must diffuse to reach the surface. A decrease in the strain rate of the gel or a combination of these factors may also be involved in producing the observed rates. The maximum density corresponds to the point at which shrinkage stops and the meniscus is at the surface. This is the point where the resistance to shrinkage becomes greater than the applied stress, and the meniscus penetrates the interior of the gel. This marks the beginning of stage 2. Once this occurs the loss rate progressively slows as the liquid vapor interface moves toward the center. The opacity seen during stage 2 is due to this interface. Shaw [1] suggests that this phenomenon is caused by light scattering from isolated pores (or groups of pores) of such a dimension that they are able to scatter light. The data obtained during stage 2 indicate an increase in open porosity from 0.012 to 0.364 cm<sup>3</sup>/g during the opaque transition, thus supporting Shaw's scattering theory. The start of stage 3 occurs when the loss rate again drops. The division between stages 2 and 3 is not as well defined as that between 1 and 2, but can be seen clearly in Fig. 22.5.

A small level of stress birefringence appears to be present throughout the whole process. However during stage 1 the position and motion of the stress generated isogyres is difficult to monitor. During the opaque stage the birefringence is obscured by the scattering. On completing the opaque stage the stress birefringence becomes sufficiently strong to lead to the formation of the biaxial optical figure of the two curved isogyres and the Maltese cross optical figure seen in Fig. 22.2a(8-10). For further analysis of this stress birefringence data see Ref. 4.

The presence of differing drying rates for silica gels has been noted by Zarzycki [3], although long drying times (~400 hr) were required to preserve monolithicity. Dwivedi [4] reported that the water loss during drying of alumina gels takes place in two stages, although cracking occurred during the drying process. The detailed drying data presented herein on uncracked monoliths shows three identifiable stages of drying. These three stages are consistent with the constant rate period (stage 1), the first falling rate period (stage 2), and second rate period (stage 3), discussed by Scherer and Brinker [5]. For further discussion of the differences between stage 1, as determined herein and the constant rate period, see Ref. 2.

## 22.5. CONCLUSIONS

The apparatus described is capable of accurately monitoring the physical and optical changes that occur while drying large monolithic gels. The data show that the drying process consists of three distinct phases.

*Stage 1.* Initial gel expansion is followed by rapid loss of weight and volume.

*Stage 2.* When shrinkage ceases, the gel turns opaque to transmitted light and undergoes a small and temporary reduction in volume. During this second stage the rate of weight loss becomes linear.

*Stage 3.* The rate of loss falls to a lower value. The third stage takes considerable time, but results in a gel within  $\sim 2\%$  of theoretical dry weight at  $110^{\circ}\text{C}$ .

## ACKNOWLEDGMENT

The authors are grateful to the U.S. Air Force Office of Scientific Research under Contract AFOSR F49620-88-C-0073 for supporting this work.

## REFERENCES

1. T. M. Shaw, in: *Better Ceramics Through Chemistry, Mat. Res. Soc. Symp. Proc.*, **73** (1986), 215.
2. M. J. R. Wilson, Drying Kinetics of Pure Silica Xerogels, Master Thesis, University of Florida (1989).
3. J. Zarzycki, in: *Ultrastructure Processing of Ceramics, Glasses, and Composites*, p. 27, Wiley, New York (1984).
4. R. K. Dwivedi, *J. Mater. Sci. Lett.*, **5**, 373 (1986).
5. G. W. Scherer and C. J. Brinker, *Sol-Gel Science*, Academic Press, New York, 1989.

## PART 3

---

### **Powders, Films, and Monoliths**

## THE SCIENCE OF ULTRAFINE POWDERS: WELL-DEFINED COMPOSITE AND COATED PARTICLES

EGON MATIJEVIĆ

### 23.1. INTRODUCTION

The importance of fine particles in different areas of ceramic science has been generally recognized and amply documented. The workers in the field have also realized that for numerous applications monodispersed powders are advantageous and often essential in order to impart a specific property to a product and to assure the reproducibility of the latter. In addition to uniformity in size, particle shape often plays an important role. In summary, optical, magnetic, electric, sintering, adsorptive, adhesive, and other characteristics of ceramic materials may depend in a sensitive manner on the size and shape of the powder constituents from which such products are made.

In view of the significance of fine particles, it is no surprise that much effort has been invested into methods for the preparation of well-defined colloids, especially of inorganic compounds of interest to ceramists. The results of these studies have been summarized in several recent review articles [1-7]. Indeed, a large number of dispersions are now available, consisting of uniform particles of different compositions and morphologies.

*Ultrastructure Processing of Advanced Materials.*

Edited by Donald R. Uhlmann and Donald R. Ulrich (deceased).

ISBN 0-471-52986-9 © 1992 John Wiley & Sons, Inc.

For many uses, solids of mixed composition are desirable. Such materials can be of fixed stoichiometry, or they may have a variable internal composition, both with respect to anions and/or cations. It is quite feasible to greatly affect properties of a given matter by doping it with smaller or larger quantities of another compound.

A different type of composite particles consists of cores coated with layers of a solid of dissimilar chemical composition. In producing such powders, it is possible to modify their characteristics and processes based on surface interactions. Furthermore, in case where costly materials are of interest, one may utilize inexpensive (and inert) cores and coat them with the precious reactant.

In all mixed systems described above, it is usually desirable to carefully control the internal and/or surface structural and chemical constitution in addition to particle morphology and size.

This Chapter describes preparations of some *monodispersed* fine powders in different described categories. Examples are offered of crystalline or amorphous solids of exact or variable stoichiometry, as well as of coated particles. Some of the properties are described, and problems that need to be resolved are indicated.

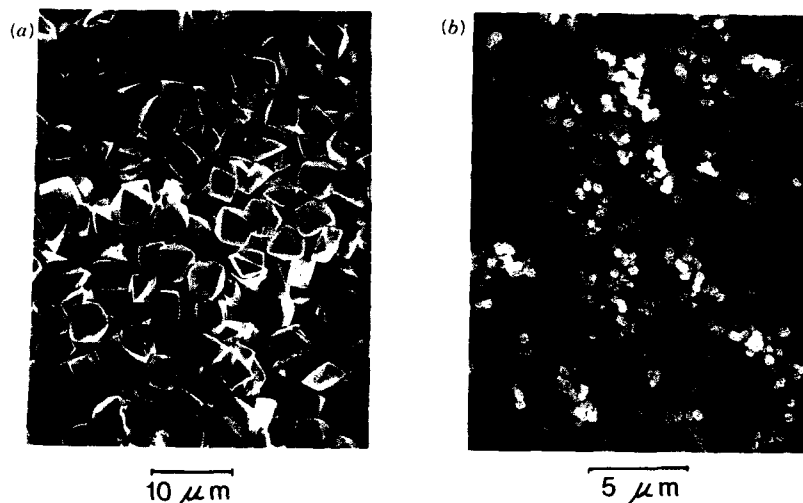
### 23.2. UNIFORM PARTICLES OF FIXED STOICHIOMETRY

A typical example of colloidal crystals of fixed chemical composition is given in Fig. 23.1a, which shows hexagonal alunite,  $\text{Fe}_3(\text{SO}_4)_2(\text{OH}) \cdot 2\text{H}_2\text{O}$ , particles prepared by forced hydrolysis of ferric sulfate solutions [8]. In this case, the solids of a well-defined habitus contain one cation and two anions in exact ratios. The structure is further confirmed by the X-ray diffraction analysis. The speciation of the solution in which the precipitation took place revealed the complexes that acted as precursors to the solid phase formation [9].

A different case is illustrated by the scanning electron micrograph in Fig. 23.1b, which represents a colloidal magnetite,  $\text{Fe}_3\text{O}_4$ , powder. This material contains both  $\text{Fe}^{2+}$  and  $\text{Fe}^{3+}$  and its composition can be written as  $\text{Fe(II)O} \cdot \text{Fe}_2(\text{III})\text{O}_3$ . The particles were obtained by crystallization from a ferrous hydroxide gel in the presence of a mild oxidizing agent [10]. The special aspect of this example is the difficulty in reconciling the spherical shape with the crystallinity of the precipitate. Indeed, it was clearly demonstrated that the particles are not single crystals, but that they consist of a large number of tiny subunits. This finding poses an intriguing question as to why a huge number of very small particles aggregate into *uniform* large spheres?

There are a number of analogous examples where perfectly smooth spheres obtained by precipitation from homogeneous solutions exhibit distinct X-ray patterns of known minerals or other crystals, such as hematite [11] or  $\text{CeO}_2$  [12]. It was possible to document that in all these cases the particles were built up of identical spherulites of  $\sim 30 \text{ \AA}$  in size.

Finely dispersed solids containing two different metals in fixed ratios are



**Figure 23.1.** (a) Scanning electron micrograph (SEM) of alunite,  $\text{Fe}_3(\text{SO}_4)_2(\text{OH}) \cdot 2\text{H}_2\text{O}$ , particles obtained by aging at 80°C for 1.5 hr a solution of  $0.18 \text{ mol/dm}^3$   $\text{Fe}(\text{NO}_3)_3$  and  $0.27 \text{ mol/dm}^3$   $(\text{NH}_4)_2\text{SO}_4$  [8, 9]. (b) Transmission electron micrograph (TEM) of magnetite,  $\text{Fe}_3\text{O}_4$ , particles obtained by aging at 90°C for 4 hr a  $\text{Fe}(\text{OH})_2$  gel ( $2.5 \times 10^{-2} \text{ mol/dm}^3$ ) with excess  $\text{FeSO}_4$  ( $3 \times 10^{-2} \text{ mol/dm}^3$ ) [10].

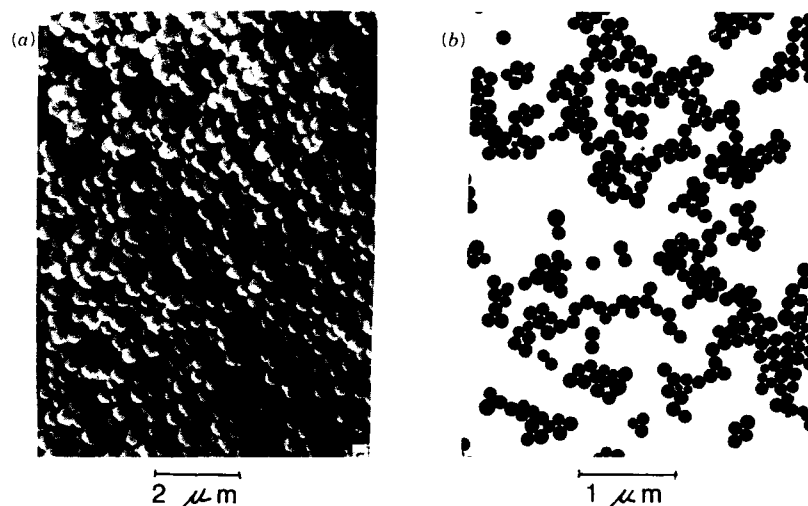
illustrated by Ba-titanate and Pb-niobate (Fig. 23.2). These powders were obtained by controlled decomposition of complex solutes of both metals in the presence of an oxidizing agent [13, 14]. Again, the particles are perfectly spherical, although the correct stoichiometric composition is established only after a given reaction (particle growth) time (Fig. 23.3).

Precipitation can often be aided by the addition of organic molecules, such as urea or formamide that decompose under the influence of temperature and/or pH and release different ions. Depending on the solubility of respective products, aging of salt solutions in the presence of urea can yield either metal oxides or basic carbonates. Under certain conditions, also metal amino carbonates can be obtained, as is exemplified with yttrium (Fig. 23.4) [15].

### 23.3. UNIFORM PARTICLES OF MIXED VARIABLE COMPOSITION

It is quite feasible to coprecipitate dispersions of narrow size distribution from solutions containing more than one metal salt. In such cases, the composition of the solid phase should vary in some manner as the ratio of concentrations of dissolved electrolytes is altered.

Figure 23.5 shows two such powders, consisting of mixed Ce(III)–Y(III) and La(III)–Cu(II) basic carbonates, respectively [15, 16].



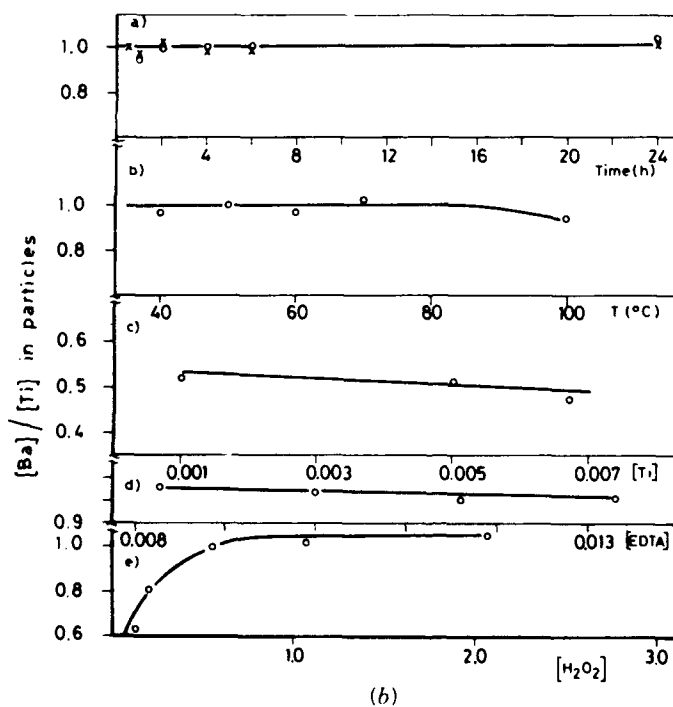
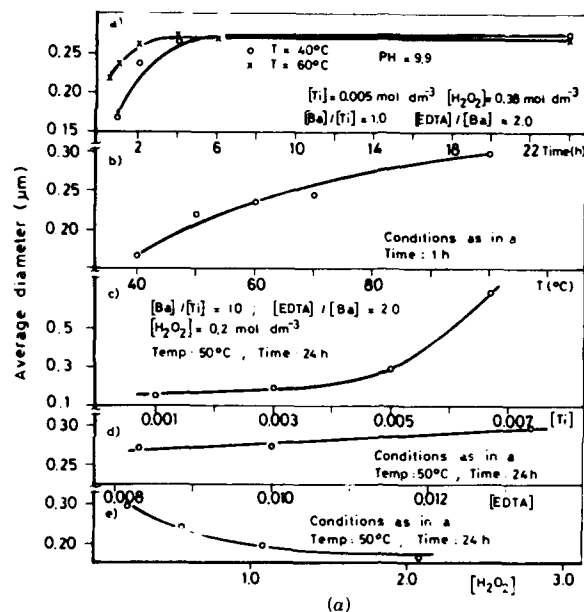
**Figure 23.2.** (a) SEM of barium titanate,  $\text{BaTiO}_3$ , particles obtained by aging at  $60^\circ\text{C}$  for 2 hr a solution of  $5.0 \times 10^{-3} \text{ mol/dm}^3$   $\text{Ti(IV)-isopropoxide}$ ,  $\text{Ti(i-OPr)}_4$ ,  $1.0 \times 10^{-2} \text{ mol/dm}^3$   $\text{Na}_2\text{H}_2\text{-ethylenediaminetetraacetic acid}$ ,  $5.0 \times 10^{-3} \text{ mol/dm}^3$   $\text{BaCl}_2$  and  $0.38 \text{ mol/dm}^3$   $\text{H}_2\text{O}_2$  [13]. (b). TEM of lead niobate,  $\text{Pb}_2\text{Nb}_2\text{O}_7$ , particles obtained by aging at  $70^\circ\text{C}$  for 5 hr a solution  $6 \times 10^{-3} \text{ mol/dm}^3$   $\text{Pb(NO}_3)_2$ ,  $4.0 \times 10^{-3} \text{ mol/dm}^3$   $\text{NbCl}_5$ ,  $1.0 \times 10^{-3} \text{ mol/dm}^3$   $\text{Na}_2\text{HNTA}$ , and  $2.2 \text{ mol/dm}^3$   $\text{H}_2\text{O}_2$ .

There are two fundamental questions that need to be answered with respect to such mixed systems. The first is the relationship between the molar ratios of reactants (cations or anions) in solution and in the solid phase precipitated from the latter. The second question is the internal homogeneity of individual particles, such as whether the components are uniformly distributed within the solid or if the surface and bulk composition differs.

In systems studied so far, it seems that the overall content in terms of the molar ratio of two cations in the precipitate correlated well with that in the solution. For example, the chemical analysis of  $\text{Ce(III)-Y(III)}$  basic carbonate particles yielded formulas  $\text{Y}_{0.75}\text{Ce}_{0.25}(\text{OH})\text{CO}_3 \cdot \text{H}_2\text{O}$  and  $\text{Y}_{0.25}\text{Ce}_{0.75}(\text{OH})\text{CO}_3 \cdot \text{H}_2\text{O}$  when precipitated in solutions of molar ratios  $[\text{Y(NO}_3)_3]/[\text{Ce(NO}_3)_3]$  of 3 and 0.33 respectively. Analogous results were obtained with the  $\text{La(III)-Cu(II)}$  and  $\text{Y(III)-Cu(II)}$  mixed solids.

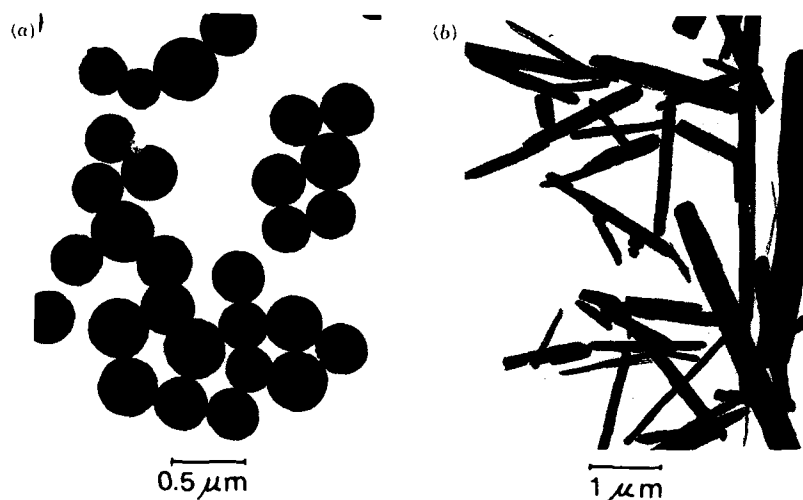
As far as the internal composition is concerned, evidence indicates that the constituent cations are not evenly distributed throughout the particles. Figure 23.6 shows that the ratio of  $\text{Cu(II)}$  to either  $\text{Y(III)}$  or  $\text{La(III)}$  changes with the time of the precipitation process. Obviously, in both examples the solids are at first enriched in copper, but the ratio of  $\text{Cu(II)}$  to the lanthanides changes as the particles grow [16].

Nickel ferrites prepared by crystallization from gels [17] offer another example of internal inhomogeneity. Figure 23.7 displays electrokinetic mobilities as a function of the pH of three solid samples in which the  $[\text{Ni}]/[\text{Fe}]$

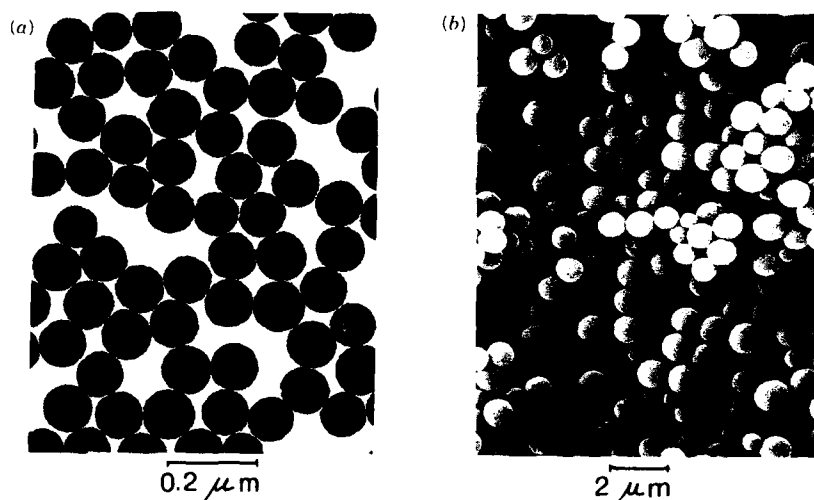


**Figure 23.3.** (a) Variation of the average diameter of barium titanate particles, as illustrated in Fig. 23.2a, as a function of (a) time, (b) temperature, (c) concentration of Ti(*i*-OPr)<sub>4</sub>, (d) concentration of ethylenediaminetetraacetic acid, and (e) concentration of H<sub>2</sub>O<sub>2</sub> with other parameters being constant at values indicated in the figure. (b) Variation of the molar ratio [Ba]/[Ti] in the solids as a function of the same parameters and conditions indicated in a [13].

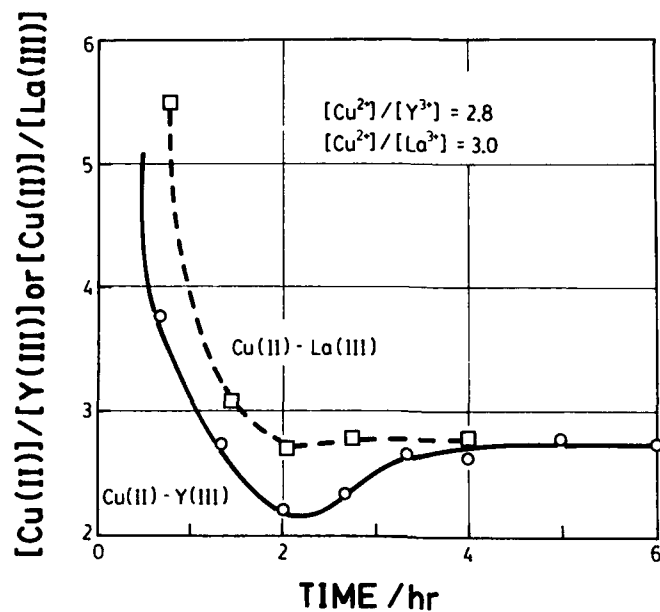




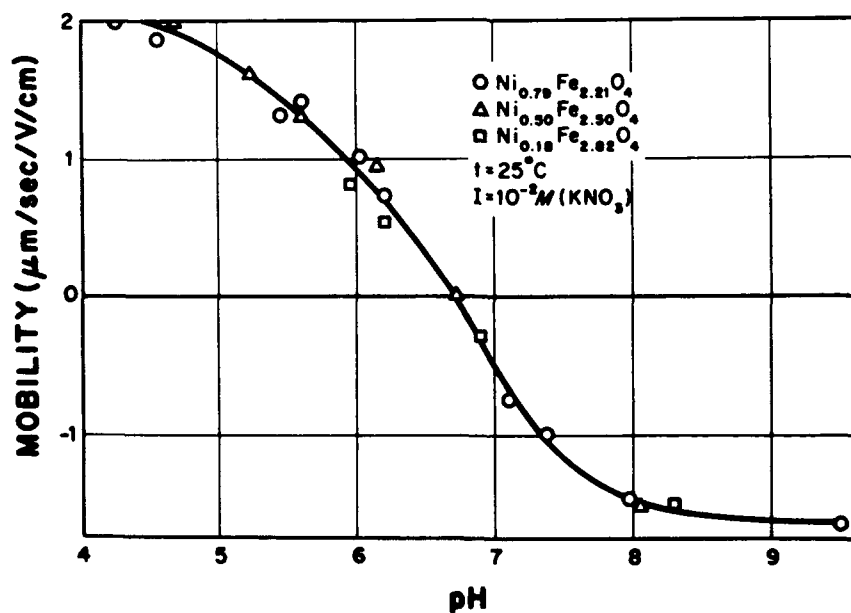
**Figure 23.4.** (a) TEM of yttrium basic carbonate,  $\text{Y(OH)CO}_3$ , particles obtained by aging at  $85^\circ\text{C}$  for 3 hr a solution of  $1.6 \times 10^{-2} \text{ mol/dm}^3$   $\text{Y(NO}_3)_3$  and  $0.33 \text{ mol/dm}^3$  urea [15]. (b) TEM of yttrium ammine carbonate,  $\text{Y}_2(\text{CO}_3)_3 \cdot \text{NH} \cdot 3\text{H}_2\text{O}$ , particles obtained by aging at  $110^\circ\text{C}$  for 20 hr a solution of  $3.0 \times 10^{-2} \text{ mol/dm}^3$   $\text{YCl}_3$  and  $3.3 \text{ mol/dm}^3$  urea [15].



**Figure 23.5.** (a) TEM of mixed Y(III)/Ce(III) basic carbonate particles obtained by aging at  $90^\circ\text{C}$  for 25 hr a solution of  $5.0 \times 10^{-3} \text{ mol/dm}^3$   $\text{Y(NO}_3)_3$ ,  $1.5 \times 10^{-2} \text{ mol/dm}^3$   $\text{Ce(NO}_3)_3$ , and  $0.5 \text{ mol/dm}^3$  urea [15]. (b) SEM of mixed La(III)/Cu(II) basic carbonate particles obtained by aging at  $90^\circ\text{C}$  for 4 hr a solution of  $8 \times 10^{-3} \text{ mol/dm}^3$   $\text{La(NO}_3)_3$ ,  $8.0 \times 10^{-3} \text{ mol/dm}^3$   $\text{Cu(NO}_3)_2$ , and  $0.2 \text{ mol/dm}^3$  urea [14].



**Figure 23.6.** The change of  $[Cu(II)]/[Y(III)]$  or  $[Cu(II)]/[La(III)]$  in particles as a function of time of aging at 90°C for the following solutions: —,  $8.0 \times 10^{-3}$  mol/dm<sup>3</sup>  $Y(NO_3)_3$ , 0.4 mol/dm<sup>3</sup> urea, and  $[Cu^{2+}]/[Y^{3+}] = 2.8$ ; ---,  $8.0 \times 10^{-3}$  mol/dm<sup>3</sup>  $La(NO_3)_3$ , 0.5 mol/dm<sup>3</sup> urea, and  $[Cu^{2+}]/[La^{3+}] = 3.0$  [16].



**Figure 23.7.** Electrophoretic mobilities of aqueous dispersions of nickel ferrite particles of varying chemical composition as a function of pH [17].

ratio differs, yet all data fall on the same curve. Because the isoelectric points of nickel oxide and iron oxide are not the same, one would expect samples of nickel ferrite of varying overall composition to exhibit different surface electrokinetic characteristics, yet no such effect is observed. Again, it is evident that the content in cations at the surface and in the bulk differs.

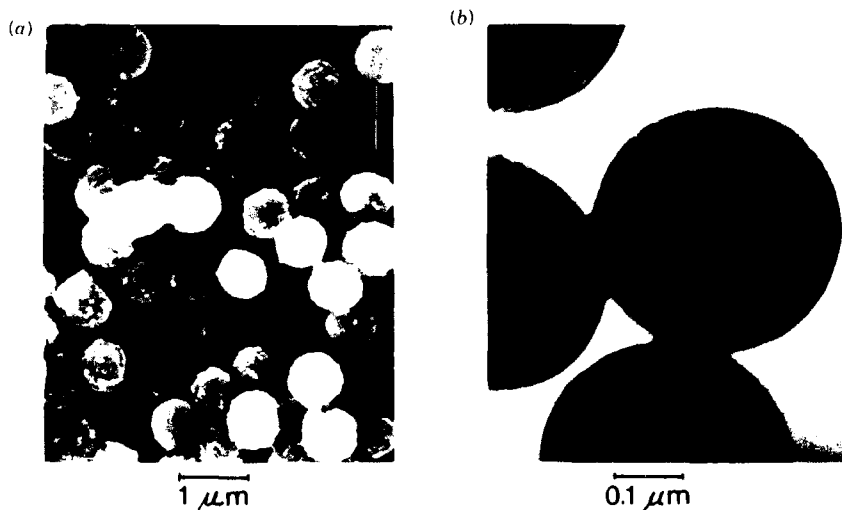
Such findings can be used advantageously when the more active metal (e.g., in catalytic applications) is preferentially located in the surface layer, responsible for interfacial reactions.

### 23.4. COATED PARTICLES

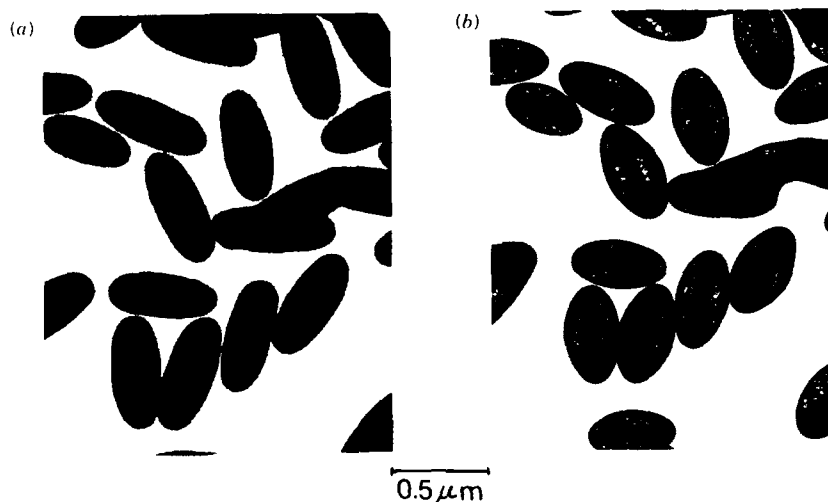
The deposition of one kind of material on cores of a different chemical composition can be achieved by various means including adsorption, adhesion, precipitation, and surface reactions. Examples of these procedures will be offered below.

One obvious approach to envelop a particle with another material is to deposit a finely dispersed matter on the surface of another solid. Such a process will be governed by general principles valid for particle adhesion, whereby the sign and the magnitude of the potential on interacting surfaces, ionic strength, relative particle size, and number concentration play a decisive role. Once right conditions are established, it is indeed possible to coat cores with monolayers or multilayers of other particles [18, 19].

The electron micrograph in Fig. 23.8a shows silica particles covered by



**Figure 23.8.** (a) SEM of silica particles coated with hematite particles obtained by aging at 100 °C for 24 hr a dispersion containing 35 mg/dm<sup>3</sup> of SiO<sub>2</sub> (0.75 μm in diameter), 1 × 10<sup>-3</sup> mol/dm<sup>3</sup> HCl, and 2.0 × 10<sup>-3</sup> mol/dm<sup>3</sup> FeCl<sub>3</sub>. (b) TEM of ovalbumin-coated chromium hydroxide particles.



**Figure 23.9.** (a) TEM of spindle-type hematite,  $\alpha\text{-Fe}_2\text{O}_3$ , particles coated with yttrium basic carbonate,  $\text{Y(OH)CO}_3$ , obtained by aging at  $90^\circ\text{C}$  for 2 hr a suspension of  $1.0 \times 10^{-2} \text{ mol/dm}^3$   $\alpha\text{-Fe}_2\text{O}_3$  in the presence of  $5.0 \times 10^{-3} \text{ mol/dm}^3$   $\text{Y(NO}_3)_3$  and  $1.8 \text{ mol/dm}^3$  urea. (b) The same particles exposed to a high-intensity electron beam to show the core and coating [22].

hematite. In this case, the coating material was produced in situ by hydrolysis of a ferric salt solution in the presence of silica and subsequently deposited on the latter. Similarly, titania particles could be coated by iron oxides using an analogous procedure [19]. The nature of the outer layer could be altered by proper chemical treatment. For example, by using a mild reducing agent, the hematite coating was transformed to magnetite [20].

In another case, colloidal silica was adsorbed on latex in a monolayer arrangement. The measured number of adhered silica particles per polymer particle agreed well with that calculated from the theory of interaction of unlike spheres [18].

Figure 23.8b shows chromium hydroxide particles coated with ovalbumin. It is evident that by a proper adjustment of the pH in order to conveniently adjust the charge on both reactants the metal oxide can be covered by a uniform layer of the protein [21].

Forced hydrolysis of metal ions can be used to coat preformed solid particles with inorganic layers of varying thickness. Figure 23.9 displays elongated hematite ( $\alpha\text{-Fe}_2\text{O}_3$ ) cores covered with yttrium basic carbonate. In this example, the spindle-type cores are added to a solution containing the yttrium salt and urea, and the dispersion is then aged at an elevated temperature [22].

Using variations of this procedure, coatings of other inorganic compounds on different cores were successfully produced. Thus, aluminum (hydrated) oxide was deposited on titania, iron oxide, and chromium hydroxide [23], or hematite was coated with chromium hydroxide [24] and zirconia [25].

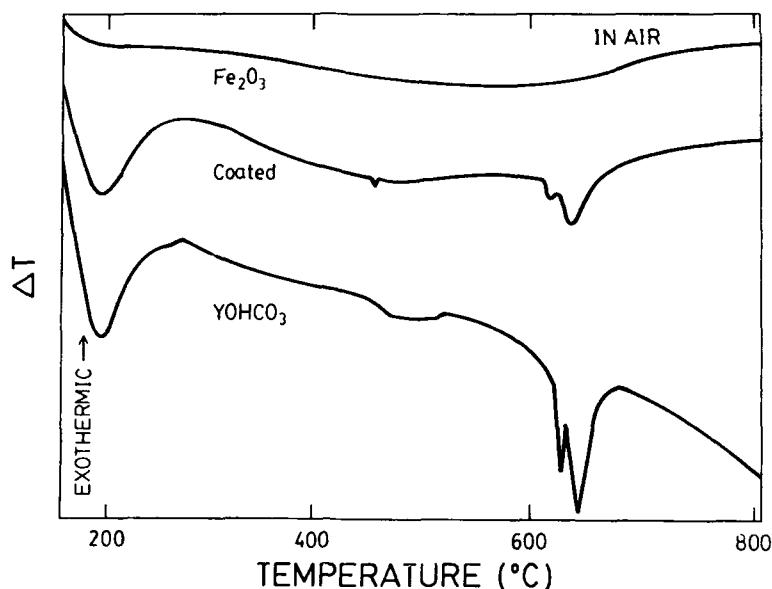


Figure 23.10. Differential thermal analysis curves for  $\alpha$ - $\text{Fe}_2\text{O}_3$ ,  $\text{Y}(\text{OH})\text{CO}_3$ , and  $\alpha$ - $\text{Fe}_2\text{O}_3$  coated with  $\text{Y}(\text{OH})\text{CO}_3$ .

Different measurements have confirmed that, as far as surface properties are concerned, the coated particles show characteristics of the material in the outer layer. For illustration, Fig. 23.10 compares differential thermal analysis curves for particles shown in Fig. 23.9 and for core and coating material alone. Obviously, the coated dispersion displays the same characteristics as the outer layer when the latter material is precipitated separately. Infrared and electrokinetic measurements confirm the same effect, that is, the covered particles behave as if they were made of the coated material only.

### 23.5. CONCLUSION

In this chapter we have demonstrated that dispersions of composite particles of different properties, yet uniform in size and shape, can be obtained by precipitation from solutions or by phase transformation. Although the feasibility of the production of such materials has now been established, there are a number of problems that need to be resolved. Topics of special interest are

1. The control and predictability of particle morphology.
2. The relationship of the composition of particles consisting of chemically different ionic compounds to the concentration of the reactants in solutions in which these solids are generated.

3. The homogeneity of the composite particles.
4. The control of the thickness and the permeability of the surface layer of coated particles.

Solving these problems would greatly enhance our understanding of composite systems and lead to the production of new materials of well-defined and unique properties.

### ACKNOWLEDGMENT

This study was supported by the Air Force Contract F49620-85-C-0142.

### REFERENCES

1. E. Matijević, *Pure Appl. Chem.*, **60**, 1479 (1988).
2. E. Matijević, *Chim. Ind. (Milan)*, **70**, 98 (1988).
3. E. Matijević, in: S. D. Mackenzie and D. R. Ulrich, Eds., *Ultrastructure Processing of Advanced Ceramics*, p. 429, Wiley-Interscience, New York (1988).
4. E. Matijević, *Langmuir*, **2**, 12 (1986).
5. E. Matijević, *Annu. Rev. Mater. Sci.*, **15**, 483 (1985).
6. T. Sugimoto, *Adv. Colloid Interface Sci.*, **28**, 65 (1987).
7. M. Haruta and B. Delmon, *J. Chim. Phys.*, **83**, 859 (1986).
8. E. Matijević, R. S. Sapieszko, and J. B. Melville, *J. Colloid Interface Sci.*, **50**, 567 (1975).
9. R. S. Sapieszko, R. C. Patel, and E. Matijević, *J. Phys. Chem.*, **81**, 1061 (1977).
10. T. Sugimoto and E. Matijević, *J. Colloid Interface Sci.*, **74**, 227 (1980).
11. E. Matijević and P. Scheiner, *J. Colloid Interface Sci.*, **63**, 509 (1978).
12. W. P. Hsu, L. Rönnquist, and E. Matijević, *Langmuir*, **4**, 31 (1988).
13. P. Gherardi and E. Matijević, *Colloids Surf.*, **32**, 257 (1988).
14. M. J. Kim and E. Matijević, *Chem. Mater.*, **1**, 363 (1989).
15. B. Aiken, W. P. Hsu, and E. Matijević, *J. Am. Ceram. Soc.*, **71**, 854 (1988).
16. F. Ribot, S. Kratochvil, and E. Matijević, *J. Mater. Res.*, **4**, 1123 (1989).
17. A. E. Regazzoni and E. Matijević, *Corrosion*, **38**, 212 (1982).
18. A. Bleier and E. Matijević, *J. Chem. Soc., Faraday Trans. I*, **74**, 1346 (1978).
19. P. Gherardi and E. Matijević, *J. Colloid Interface Sci.*, **109**, 57 (1986).
20. E. Matijević and P. Gherardi, U.S. Patent 4,675,251, June 23, 1987.
21. J. Johnson and E. Matijević, *Colloid Polymer Sci.*, in press.
22. B. Aiken and E. Matijević, *J. Colloid Interface Sci.*, **26**, 645 (1988).
23. S. Kratochvil and E. Matijević, *Adv. Ceram. Mater.*, **2**, 798 (1987).
24. A. Garg and E. Matijević, *Langmuir*, **4**, 38 (1988).
25. A. Garg and E. Matijević, *J. Colloid Interface Sci.*, **126**, 243 (1988).

## 24

# PREPARATION OF NARROW-SIZE-DISTRIBUTION BOROSILICATE POWDERS BY ALKOXIDE HYDROLYSIS

L. V. JANAVICIUS, E. A. BARRINGER, A. B. HARDY  
H. K. BOWEN, AND J. DYNYS

### 24.1. INTRODUCTION

The recent literature contains many examples of ceramic powder synthesis from metal alkoxides, because high-purity, reactive powders can be prepared and, in some cases, the morphology of the powder can be controlled to produce narrow size distribution, unagglomerated, spherical particles [1,2]. Processing these powders can increase the uniformity and density of both the green body and the sintered body [3], and can also reduce the sintering temperature [4]. Most synthesis techniques for controlling the particle morphology were developed for single alkoxide systems, and it has been difficult to extend these methods to mixed alkoxide systems, particularly when the reaction rates of the alkoxides differ substantially.

This Chapter describes a method for preparing narrow size distribution, spherical, unagglomerated particles containing up to 28 wt% boron oxide by hydrolyzing boron and silicon alkoxides. Borosilicate formation was studied both to develop a technique for controlling the hydrolysis of alkoxides with very

*Ultrastructure Processing of Advanced Materials.*

Edited by Donald R. Uhlmann and Donald R. Ulrich (deceased).

ISBN 0-471-52986-9 © 1992 John Wiley & Sons, Inc.

different reaction kinetics and because several borosilicate properties make it a potentially useful electronic substrate material. Overall and relative concentrations of the alkoxides were varied to study their effects on the particle size and morphology, boron content, and reaction rates. In addition, borosilicate powder properties are described.

## 24.2. EXPERIMENTAL PROCEDURE

All chemicals and solvents were filtered through 0.2- $\mu$ m filters before use. Tetraethylorthosilicate [TEOS;  $\text{Si}(\text{OC}_2\text{H}_5)_4$ ] (Alfa Chemical Co., Danvers, Mass.) was partially hydrolyzed by adding ammonium hydroxide to a dilute solution of TEOS in ethanol and stirring for 1 hr. The ammonium hydroxide was the water source, and the concentration was adjusted so that the molar concentration of water was twice that of the TEOS. Tri-*n*-butyl borate [TBB;  $\text{B}(\text{OC}_4\text{H}_9)_3$ ] (Alfa Chemical Co.) was then added to the TEOS solution, and the solution was stirred for 30 min. No visible precipitation was observed in this precursor solution.

The alkoxide solution was then rapidly poured into a second solution of ammonium hydroxide (water source, overall  $\text{H}_2\text{O}$  concentration = 4.75 M) in ethanol. The TEOS concentrations used in the hydrolysis reactions varied from 0.01 to 0.20 M. The TBB was added in proportion to the TEOS concentration, and TBB to TEOS molar ratios ranged from 0.1:1 to 2:1. Particle nucleation, as evidenced by an increase in turbidity, was observed within several minutes after mixing; the solutions were usually opaque after 15 min. Solution turbidity during the reaction was monitored using a photocell. Relative reaction rates were estimated from the change in turbidity with time. The dispersions were stirred (magnetic stirrer) for 24 hr to ensure complete particle growth. The powders were washed by centrifugally sedimenting the powder, decanting the supernatant, and redispersing in either water or ethanol. This procedure was repeated two times. Powders were dried overnight at 125°C in a vacuum oven and then stored in a desiccator.

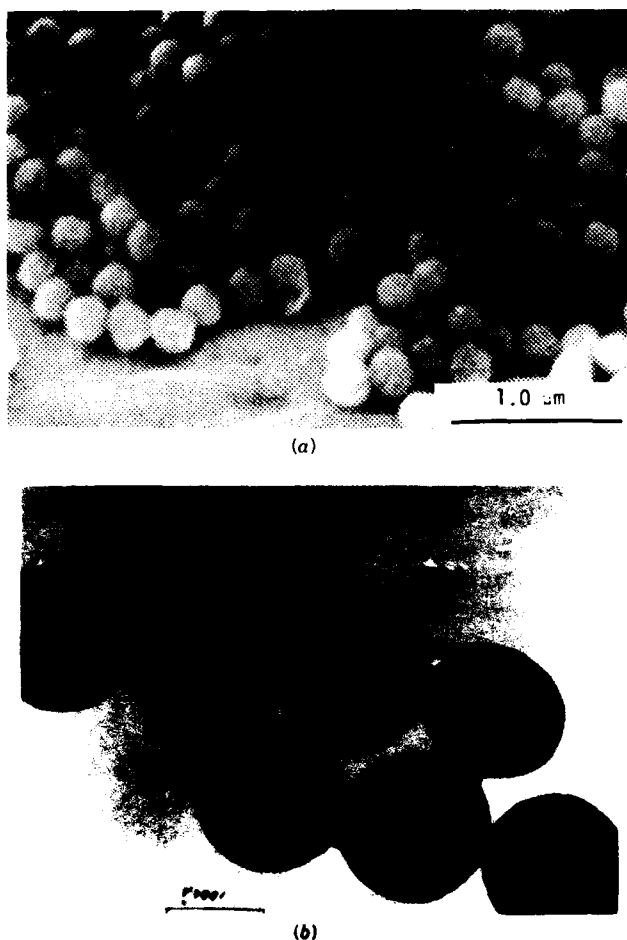
Boron content in the powders was measured by inductively coupled plasma emission spectroscopy (ICP) (Jarrell-Ash Model 1160, Jarrell-Ash Co., Waltham, Mass.). Thermal gravimetric analysis (TGA) and differential thermal analysis (DTA) measurements were made simultaneously using a heating rate of 10°C/min in air (Netzsch, Exton, Pa). Powder morphology was examined using scanning electron microscopy (SEM) (Cambridge Stereoscope, Cambridge, England) and transmission electron microscopy (TEM) (Phillips EM300, Phillips, Ltd., Holland). Particle sizes were determined by photon correlation (Coulter Electronics, Inc., Hialeah, Fla.) or by using SEM micrographs and a digitizer (error ~ 10%). Powder surface areas were measured using single point Brunaur-Emmett-Teller (BET) analysis (powders were outgassed at 300°C for 2 hr) (Quantachrome Quantasorb, Quantachrome Corp., Syosset, N.Y.). Density was measured using a helium gas stereopycnometer (samples were



outgassed for 3 hr at 80°C in a vacuum oven) (Quantachrome Model SPY-2, Quantachrome Corp.).

### 24.3. RESULTS

The bososilicate powder morphology was dependent on both the alkoxide concentration and the boron alkoxide to silicon alkoxide ratio. In order to form spherical, unagglomerated particles with a narrow size distribution at high boron-to-silicon alkoxide ratios (B:Si alkoxide ratios up to 1.0), it was necessary to use low (0.01 M TEOS) alkoxide concentrations. At this concentration the yield was  $\sim 0.7$  g/liter reaction solution. Figure 24.1 shows a typical powder



**Figure 24.1.** Powder prepared from a 1:1 boron-to-silicon alkoxide ratio at 0.01 M TEOS. (a) SEM micrograph. (b) TEM micrograph.



**Figure 24.2.** SEM micrograph of powder prepared from a 1:1 boron-to-silicon alkoxide ratio at 0.20 *M* TEOS.

formed using 0.01 *M* TEOS and a 1:1 boron-to-silicon alkoxide ratio. The TEOS concentration could be increased to 0.05 *M* and the desired morphology retained by decreasing the boron to silicon alkoxide ratio to 0.1. When high alkoxide concentrations were combined with high boron-to-silicon alkoxide ratios, the powders contained large aggregates of spherical particles and loose flocs of tiny ( $d < 0.1 \mu\text{m}$ ), agglomerated particles as shown in Fig. 24.2.

Within the conditions that resulted in narrow size distribution powders (0.01 *M*), the average particle size increased from 0.085 to 0.16  $\mu\text{m}$  as the boron-to-silicon alkoxide ratio was increased from 0.1 to 1.0. Similarly when the boron-to-silicon alkoxide ratio was fixed, an increase in alkoxide concentration led to an increase in the average particle diameter. Monitoring the reaction turbidity indicated that increasing the boron alkoxide concentration increased the reaction rate: as the boron-to-silicon alkoxide ratio was increased from 0.1 to 0.67, the particle formation rate increased approximately threefold.

Boron content of unwashed powders increased with increasing boron-to-silicon ratios, and for a given boron-to-silicon alkoxide ratio was relatively independent of the alkoxide concentration. Narrow size distribution powders ( $0.17 \pm 0.03 \mu\text{m}$ ) were formed that contained up to 8.9 wt % boron (28.6 wt %  $\text{B}_2\text{O}_3$ ). Boron content in unwashed powders was systematically less than that predicted from the boron alkoxide concentration. After washing, particularly with water, the boron content of powders formed with high boron-to-silicon ratios dropped dramatically. Boron loss was reduced by washing with ethanol, and washed powders containing up to 6.6 wt % boron (21 wt %  $\text{B}_2\text{O}_3$ ) were formed. Boron content results are summarized in Fig. 24.3.

Surface area measurements for the narrow size distribution powders (e.g., 0.01 *M* TEOS;  $\text{B}:\text{Si} \leq 1$ ) showed a good correspondence between the equivalent diameter,  $d$ , calculated from the surface area,  $S$  ( $d = 6/\rho S$ ) and the average

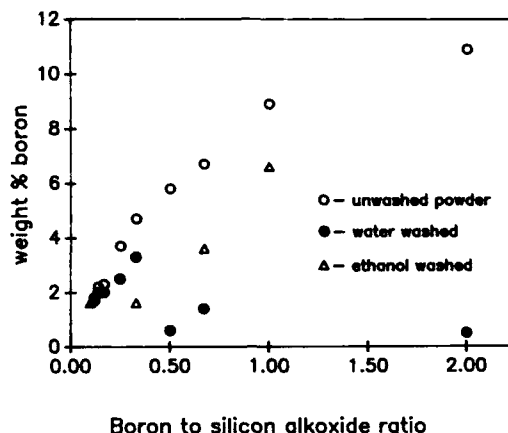


Figure 24.3. Boron content as a function of the boron-to-silicon alkoxide ratio and the washing procedure.

diameter measured by photon correlation and SEM. Powders prepared with high B:Si alkoxide ratios at high alkoxide concentrations had higher surface areas, which corresponded to the small ( $d < 0.1 \mu\text{m}$ ) precipitates observed by SEM. Powder density measurements showed that the powders had an average density of  $\sim 1.9 \text{ g/cm}^3$  (theoretical density,  $\sim 2.2 \text{ g/cm}^3$ ). X-ray analysis showed that the powders were amorphous.

TGA and DTA curves for powders prepared at different B:Si ratios are shown in Figs. 24.4 and 24.5. The TGA traces show that as the boron concentration in the powders increased, the weight loss also increased. DTA curves showed endothermic peaks at  $\sim 200$  and  $300^\circ\text{C}$  and an exothermic peak at  $450^\circ\text{C}$ . The  $300^\circ\text{C}$  peak decreased with decreasing boron concentration.

#### 24.4. DISCUSSION

Because boron alkoxides hydrolyze faster than TEOS, it is typical, in forming alkoxide-derived borosilicate gels, to add the boron alkoxide to partially hydrolyzed TEOS [5-7]. Presumably the boron alkoxide then reacts with silanol groups to form a boron-silicon alkoxide, which, when hydrolyzed, forms powder containing a homogeneous distribution of boron and silicon. Similarly, in this work TBB was added to partially hydrolyzed TEOS to form a boron-silicon alkoxide precursor. It was hypothesized that it would be easier to control the precipitation of a single bimetallic complex rather than two alkoxides with different reaction rates.

Borosilicate powders were then precipitated following a procedure similar to that used to form silica powders from pure TEOS. By using the boron-silicon alkoxide it was possible to increase the  $\text{B}_2\text{O}_3$  content in narrow size distribution

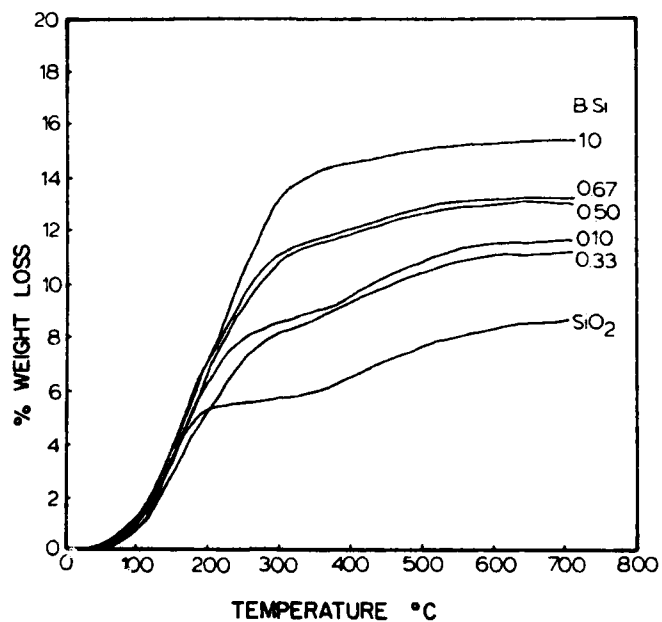


Figure 20.4. TGA curves of precipitated SiO<sub>2</sub> and borosilicate powders made with various B:Si alkoxide ratios at 0.01 M TEOS.

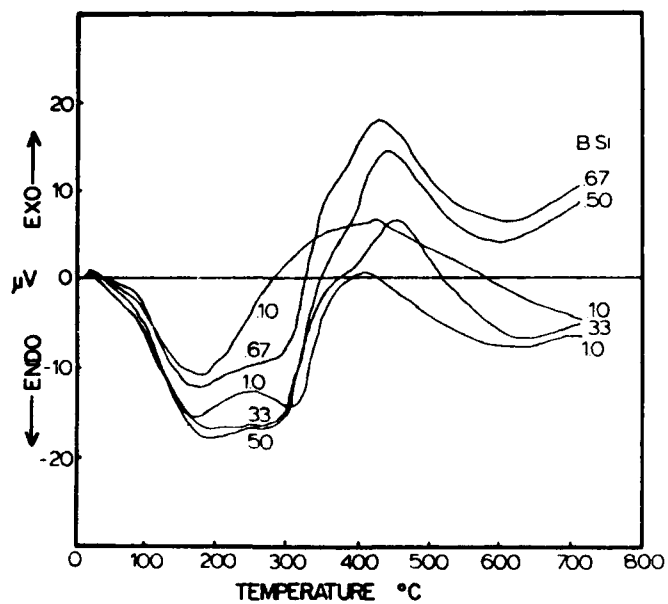


Figure 24.5. DTA curves of powders made with different B:Si alkoxide ratios at 0.10 M TEOS.

powders from a previously reported maximum of 2.45 wt % [8] to 28.6 wt %. Addition of boron alkoxide to the TEOS affected the particle formation kinetics as evidenced by the increase in the rate of particle formation. It also appeared to disturb the stability of the growing particles so that it was necessary to use very dilute solutions (compared to the pure silica system) to form narrow size distribution particles.

It has been found in borosilicate gels that when high boron-to-silicon alkoxide ratios ( $> 20$  mol %  $B_2O_3$  [6]) are used, not all the boron alkoxide is incorporated into the complex and that the excess boron alkoxide reacts to form orthoboric acid,  $H_3BO_3$  [6,9]. Boric acid has a relatively high solubility in water and ethanol (6.35 and 5.56 g/100 ml, respectively) [10]. The unstoichiometric recovery of boron, especially at high boron-to-silicon alkoxide ratios, and the loss of boron as the powders were washed could indicate that some of the boron alkoxide hydrolyzed independently to form boric acid. In addition, DTA results showed a peak at  $300^\circ C$ , the temperature at which boric acid decomposes to the oxide [10], which increased in intensity with increasing boron concentration. This also suggests that some of the boron alkoxide might precipitate as boric acid. Boron loss was reduced in this work either by not washing the powder or by washing in ethanol.

Density measurements showed that the powders were not completely dense—the particles had a density of about 85% theoretical, indicating that there was some internal porosity. However, the close agreement between diameters calculated from surface area measurements and those measured by SEM and photon correlation indicated that after heating to  $300^\circ C$  the particle surfaces were smooth and that there was little accessible internal porosity. Low temperature weight loss ( $< 250^\circ C$ ) indicated that the powders as prepared probably contained physisorbed water, hydroxide groups, and unreacted alkoxy groups.

## 24.5. SUMMARY

It was shown that narrow size distribution powders with submicrometer diameters could be formed either by working with very dilute solutions or by using low boron-to-silicon alkoxide ratios. Narrow size distribution powders were formed with a range of boron concentrations up to 8.9 wt % in unwashed powders and up to 6.6 wt % in ethanol-washed powders. Boron content increased with increasing boron to silicon alkoxide ratios in both unwashed powders and in ethanol-washed powders. The powders as formed were amorphous and porous and lost 10–15 wt % upon heating to  $1000^\circ C$ .

## ACKNOWLEDGMENTS

A portion of this work was performed at IBM/East Fishkill. In addition, the authors gratefully acknowledge the support of the Semiconductor Research Corporation.

## REFERENCES

1. R. H. Heistand II, Y. Oguri, H. Okamura, W. C. Moffatt, B. Novich, E. A. Barringer, and H. K. Bowen, in: L. L. Hench and D. R. Ulrich, Eds., *Science of Ceramic Chemical Processing*, Wiley, New York (1986), pp. 482-496.
2. B. Fegley and E. A. Barringer, in: C. J. Brinker, D. E. Clark, and D. R. Ulrich, Eds., *Better Ceramics Through Chemistry, Mater. Research Soc. Symp.*, **32** (1984), pp. 187-197.
3. E. A. Barringer, The Synthesis, Interfacial Electrochemistry, Ordering and Sintering of Monodisperse Titanium Oxide Powders, Ph.D. Dissertation, MIT (1983).
4. W. H. Rhodes, *J. Am. Ceram. Soc.*, **64**, 19-22 (1981).
5. B. E. Yoldas, *J. Mater. Sci.*, **14**, 1843-1849 (1979).
6. M. Nogami and Y. Moriya, *J. Non-Cryst. Solids*, **48**, 359-366 (1982).
7. B. Kumar, *Mater. Res. Bull.*, **19**, 331-338 (1984).
8. N. J. Jubb, The Processing of Boron-Doped Monodispers  $\text{SiO}_2$  Particles, M.S. Thesis, MIT (1982).
9. D. C. Bradley, R. C. Mehrotra, and D. P. Gaur, *Metal Alkoxides*, Academic Press, New York (1978).
10. R. C. Weast, Ed., *Handbook of Chemistry and Physics*, 64th ed., CRC Press Inc., Boca Raton, Fla. (1983).

## SYNTHESIS AND PROCESSING OF ALKALINE EARTH METAL, TITANATE GELS, POWDERS, AND THIN FILMS

PRADEEP P. PHULE AND SUBHASH H. RISBUD

### 25.1. INTRODUCTION

Alkaline earth titanates (e.g.,  $\text{BaTiO}_3$ ,  $\text{SrTiO}_3$ , and  $\text{CaTiO}_3$ ) are technologically important materials widely used for the manufacture of electronic components such as multilayer ceramic capacitors, thermistors, and so on. Conventional mixing and firing approaches can lead to inhomogeneous, impure, and multiphase ceramic powders that are undesirable for capacitor, thermistor, ferroelectric, and electrooptic applications. In recent years, considerable research effort has been directed toward the development of high-purity, ultrafine, stoichiometric doped and undoped titanate powders. The synthesis of  $\text{BaTiO}_3$  from organometallic compounds has been actively pursued in recent work at several laboratories [1-9]. Many of the alkoxide-based techniques reported in the earlier literature made use of extremely moisture sensitive, difficult-to-handle, and expensive precursors. Due to the high moisture sensitivity of the alkoxides, precipitation of barium hydroxide and hydrous titania can occur easily during the sol-gel processing of  $\text{BaTiO}_3$ . Barium precursors can also easily react with atmospheric carbon dioxide to form insoluble  $\text{BaCO}_3$ .

The primary objective of this work was to develop and use moisture-

---

*Ultrastructure Processing of Advanced Materials.*

Edited by Donald R. Uhlmann and Donald R. Ulrich (deceased).

ISBN 0-471-52986-9 © 1992 John Wiley & Sons, Inc.

insensitive, easy-to-handle, and relatively inexpensive precursors to prepare gels, powders, and thin films of barium and other alkaline earth titanates.

## 25.2. EXPERIMENTAL PROCEDURE

The details of the preparation of powders and gels have been discussed in our previous publications [1-4]. Therefore, we will recapitulate only some salient aspects of the experimental procedures.

### 25.2.1. Sol-Precipitation Synthesis

Titanium(IV) isopropoxide was reacted with excess glacial acetic acid (HOAC/Ti  $\approx$  10) to obtain a titanyl acylate precursor, which upon addition of small amounts of water formed a white precipitate. On continued addition of deionized water, a clear sol of hydrolyzed titanyl acylate was formed. Appropriate amount of barium acetate/carbonate was added to obtain a stoichiometric sol. Separately, a highly alkaline (pH 13.5) NaOH solution was prepared and maintained at desired temperature (85-100°C). On gradual addition of the barium acetate-titanyl acylate sol to the alkaline NaOH solution resulted in direct formation of crystalline, ultrafine BaTiO<sub>3</sub> powders. After aging, the precipitate was dried and washed with distilled water. Heat treatment of powders was also conducted at 900-1000°C to obtain BaTiO<sub>3</sub> powders with a tetragonal crystal structure.

### 25.2.2. Sol-Gel Process

Titanium isopropoxide, dissolved in isopropanol, was reacted with glacial acetic acid to obtain the titanyl acylate precursor. A concentrated barium acetate solution ( $\approx$  1 M) was then added to the acylate while stirring the mixture. The sol was then cast into petri dishes to form monolithic gels. The as-prepared gels were dried and calcined to obtain crystalline high-purity BaTiO<sub>3</sub> powders. The as-prepared and heat-treated gels and powders were characterized using thermogravimetric analysis, X-ray diffraction, scanning electron microscopy, transmission electron microscopy, and other characterization techniques.

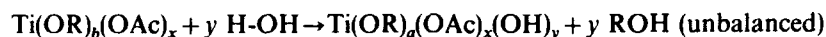
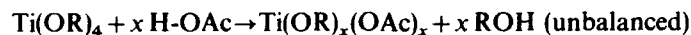
## 25.3. RESULTS AND DISCUSSION

### 25.3.1. Mechanisms for Formation of Gels and Powders

The successful formation of amorphous BaTiO<sub>3</sub> gels is attributed to the molecular modification of titanium alkoxides by glacial acetic acid [10-12]. Based upon this and other studies reported recently in the literature, we can

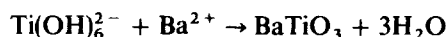
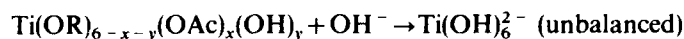


propose the following reactions:



Livage and Henry [12] have also recently presented a simple predictive model based on electronegativity changes to help explain modification of titanium alkoxides by acetic acid. Livage and co-workers have reported that the chemical modification of titanium alkoxides is accompanied by a change in tetrahedral to octahedral coordination of titanium ion (Chapter 3). The exact stoichiometry of these reactions has not yet been determined. Polycondensation of hydrolyzed titanyl acylate results in formation of amorphous  $\text{BaTiO}_3$  gels.

In the sol-precipitation process, a different mechanism may be operative. We believe that under highly alkaline acidic conditions ( $\text{pH} > 13$ ) the hydrolyzed titanium acylate is modified further to a titanium hydroxy complex. This titanium hydroxy complex then probably undergoes an acid-base reaction with the  $\text{Ba}^{2+}$  to form crystalline  $\text{BaTiO}_3$  directly,



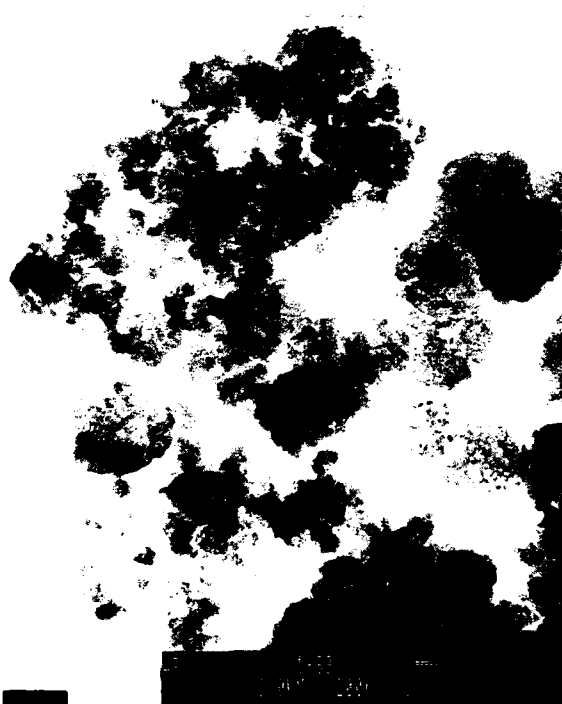
Choice of titanium precursor is important. Wilson et al. [5] have shown that use of  $\text{TiCl}_4$  instead of a molecularly modified titanium alkoxide, under otherwise identical conditions, results in a precipitate that is not  $\text{BaTiO}_3$ . According to the recent results of Riman [13], the mechanism for sol-precipitated  $\text{SrTiO}_3$  powders appears to be the crystallization of amorphous hydrous oxide and/or hydrothermal reactions [14]. Similar possibilities exist in the synthesis sol-precipitated  $\text{BaTiO}_3$  powders and will be examined in our future work. In the sol-precipitation scheme other water-soluble barium precursors such as barium hydroxide can also be used. However, barium carbonate/acetate is preferred, because it is relatively inexpensive.

### 25.3.2. Powder Morphology

The oven-dried gels were mildly ground to obtain bright white, amorphous gel powders. On calcination, crystalline  $\text{BaTiO}_3$  powders with particle size in the range  $1\text{--}4 \mu\text{m}$  were obtained (Fig. 25.1). The relatively larger particle size of the gel-derived powders is probably due to the exothermic reactions occurring during the calcination treatment. The as-prepared powders obtained by sol-precipitation technique consisted of ultrafine primary particles (Fig. 25.2). On calcination tetragonal powders with larger particle size were obtained due to the sintering of the primary particles of the original powders (Fig. 25.3).



**Figure 25.1.** Crystalline BaTiO<sub>3</sub> powders obtained from amorphous barium titanate gels (left bar = 1 μm).



**Figure 25.2.** Crystalline, ultrafine BaTiO<sub>3</sub> powders obtained using sol-precipitation technique.



Figure 25.3. Morphology of sol-precipitated powders after calcination at 950°C, 24 hr (bar = 1  $\mu\text{m}$ ).

### 25.3.3. Microstructure and Electrical Properties

The gel powders calcined at lower temperatures ( $\leq 700^\circ\text{C}$ ) were found to contain a small amount of carbon (0.1–0.5%) predominantly as  $\text{BaCO}_3$  [2–4] due to which relatively low-density (70%) ceramics were obtained. On increasing the calcination temperature to  $1000^\circ\text{C}$  no carbonate carbon was detected and relatively dense ( $\approx 90\%$ ) ceramics were obtained on sintering. The improvement in the dielectric constant of the fired ceramics on increasing the gel calcination temperature is evident from the data presented in Fig. 25.4.

The sol-precipitated powders appeared to be cubic in the as-prepared form and were calcined at  $900\text{--}1000^\circ\text{C}$  to obtain tetragonal crystal structure. The calcined powders were sintered to obtain dense ceramics (92–96%). Figure 25.5 shows the microstructure of the as-fired ceramic showing predominance of large grains (10–25  $\mu\text{m}$ ) with some small grains (1–5  $\mu\text{m}$ ). The room temperature dielectric constant and dielectric loss factor ( $\tan \delta$ ) were 1000 and 0.01, respectively. These properties are comparable to undoped, high-purity  $\text{BaTiO}_3$  with a similar grain size distribution obtained by other routes.

### 25.3.4. Considerations for Future Work

The  $\text{BaTiO}_3$  powders prepared in this work using the sol-precipitation technique were ultrafine ( $\approx 10\text{ nm}$ ) and apparently cubic in structure. Calcination treatments ( $900\text{--}1000^\circ\text{C}$ ) employed with a view to obtaining powders with a tetragonal crystal structure resulted in an increase in the average primary particle size. Recent transmission electron microscopy results reported by Eichorst, Howard, and Payne have shown that such nanosized  $\text{BaTiO}_3$  particles have a twinned tetragonal crystal structure. Continuing research efforts should be directed toward establishing the precise crystal structure and presence of domains in these particles. The role of residual hydroxyl ion content in relation

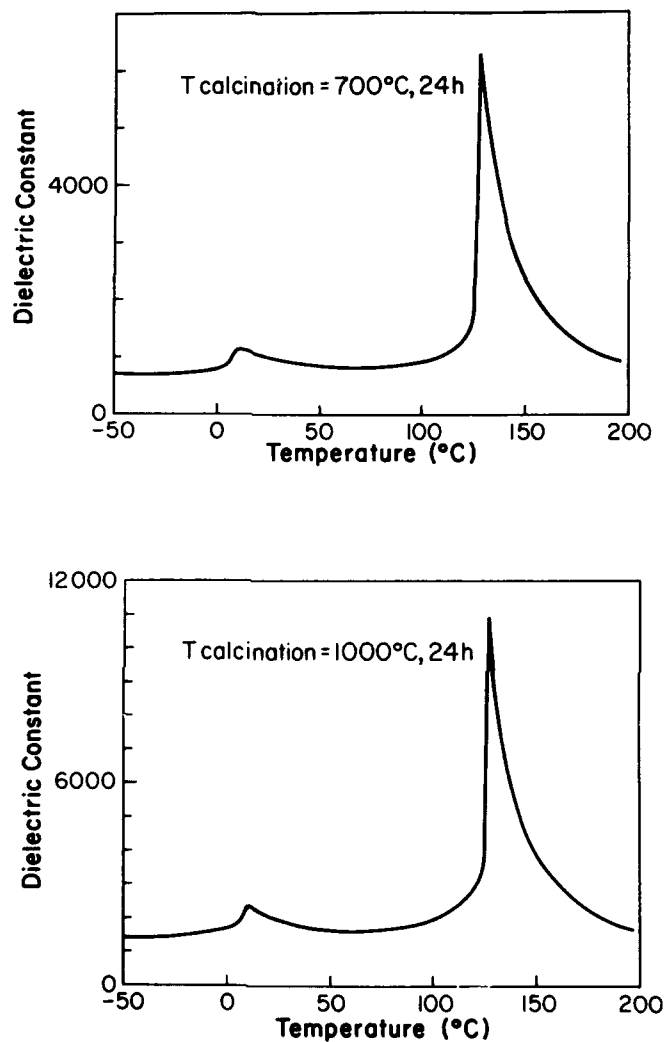
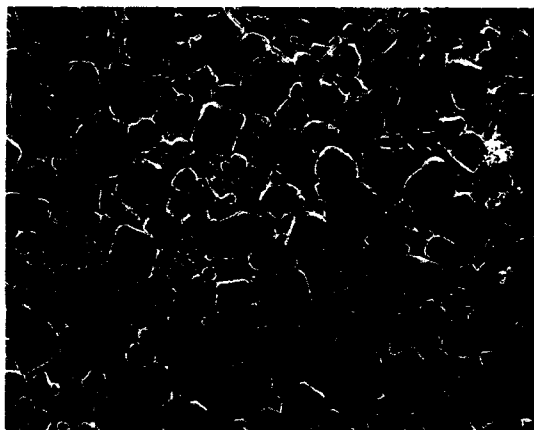


Figure 25.4. Effect of gel calcination temperature on dielectric constant of sintered BaTiO<sub>3</sub> ceramics.

to the cubic/tetragonal transformation is also important [14] and should be examined.

Because the as-precipitated powders are ultrafine ( $\approx 10$  nm), they have potential for densification at lower temperatures (e.g.,  $\approx 1000^\circ\text{C}$ ). Future efforts should explore the possibility of reducing the presence of agglomerates in the as-precipitated powders and the direct preparation of fine-grained, dense BaTiO<sub>3</sub> ceramics from these precipitated powders.



**Figure 25.5.** Microstructure of dense, high-purity BaTiO<sub>3</sub> ceramics derived using calcined sol-precipitated powders (200 $\times$ ).

## 25.4. CONCLUSIONS

This work has shown the applicability of molecularly modified titanium alkoxides for the preparation of BaTiO<sub>3</sub> gels and powders. Mohallem and Aegerter [7] have used this approach to obtain thin BaTiO<sub>3</sub> films from the stoichiometric sol. The advantages of this approach are the use of water soluble and relatively inexpensive precursors. Wilson et al. [5] have optimized the addition conditions and sequence for the sol-precipitation route in order to avoid application of external heat. The sol-gel and sol-precipitation processes have the potential for use in preparation of more complex formulations of alkaline earth titanates with tailored dielectric properties. Future research should be directed toward studying other applications of the precursors reported here as well as development of other novel precursors that would offer significant technological advantages.

## REFERENCES

1. P. P. Phule and S. H. Risbud, *J. Mater. Sci.*, **25**, 1169 (1990).
2. P. P. Phule and S. H. Risbud, submitted for publication.
3. P. P. Phule and S. H. Risbud, in: *Better Ceramics Through Chemistry. Mater. Res. Soc. Symp. Proc.*, **121**, 275 (1988).
4. P. P. Phule and S. H. Risbud, *Adv. Ceramic Mater.*, **3**, 183 (1988).
5. J. M. Wilson, D. L. Coller, and S. Venkatramani, U.S. Patent 4, 670, 243 (1987).
6. G. Tomandl, H. Rosch, and A. Stiegelschmitt, in: *Better Ceramics Through Chemistry. Mater. Res. Soc. Symp. Proc.*, **121**, 281 (1988).

7. N. D. S. Mohallem and M. A. Aegerter, in: *Better Ceramics Through Chemistry. Mater. Res. Soc. Symp. Proc.*, **121**, 515 (1988).
8. F. Chaput and J. P. Boilot, *Mater. Sci. Monogr.*, **38B**, 1459 (1987).
9. A. Mossett, I. Luneau-Gautier, J. Galy, P. Strehlow, and H. Schmidt, *J. Non-Cryst. Solids*, **100**, 339 (1988).
10. S. Doeuff, M. Henry, C. Sanchez, and J. Livage, *J. Non-Cryst. Solids*, **100**, 206 (1988).
11. C. Sanchez, F. Babonneau, S. Doeuff, and A. Leautic, in: J. D. Mackenzie and D. R. Ulrich, Eds., *Ultrastructure Processing of Advanced Ceramic Materials*, p. 77, Wiley, New York (1988).
12. J. Livage and M. Henry, in: J. D. Mackenzie and D. R. Ulrich, Eds., *Ultrastructure Processing of Advanced Ceramic Materials*, p. 183, Wiley, New York (1988).
13. R. Riman, personal communication, Rutgers University (1989).
14. R. Vivekandan, S. Philip, and T. R. N. Kutty, *Mater. Res. Bull.*, **22**, 99 (1986).

## FORMATION OF $V_2O_5$ GELS FROM VANADYL ALKOXIDES

HIROSHI HIRASHIMA, KOSAKU TSUKIMI,  
AND REIKI MURATAKE

### 26.1. INTRODUCTION

$V_2O_5$  gels containing  $H_2O$  are known to be highly conductive and anisotropic semiconductors with layerlike structure [1]. It has been previously reported that  $V_2O_5$  gels could be obtained from vanadyl alkoxides [2, 3]. Physical properties of  $V_2O_5$  gels and gel coatings, prepared by dip coating, have been also reported [4]. Electrical conductivity of the gel coatings increased with the addition of  $Li_2O$  or  $Na_2O$ , and scratch hardness was improved with addition of  $TiO_2$ . The gel coatings less than 10 nm in thickness were optically anisotropic, and  $V_2O_5$  polymers seemed to be oriented [5]. In this Chapter, formation process and structure of  $V_2O_5$  gels have been investigated.

### 26.2. EXPERIMENTAL PROCEDURES

$VO(OR)_3$ ,  $R = C_2H_5$ ,  $i-C_3H_7$ , and  $n-C_4H_9$ , was hydrolyzed in ROH solutions at room temperature.  $HCl$ ,  $HNO_3$ ,  $H_2SO_4$ , or  $NH_4OH$  was added to the solutions as catalyst. Activity of  $H^+$  ion,  $a_{H^+}$ , in the solutions was measured by a pH meter using an electrode for organic solutions, and  $-\log[a_{H^+}]$  is described as pH in

*Ultrastructure Processing of Advanced Materials.*

Edited by Donald R. Uhlmann and Donald R. Ulrich (deceased).

ISBN 0-471-52986-9 © 1992 John Wiley & Sons, Inc.

this paper. The gels and the precipitates were dried at room temperature under a vacuum and were pulverized using an agate mortar. The fraction of reduced V ion was determined by wet chemical analysis [4]. The wet gels were peptized in ethanol with an ultrasonic vibrator and were placed on collodion films for transmission electron microscopy observation. Gel coatings on glass substrates were prepared from the peptized gels or the sols by dip coating. Infrared absorption spectra of the dried gels (xerogels) were measured by KBr disk method. X-ray diffraction of the xerogels and the gel coatings was measured by step counting,  $0.2^\circ$  and 200 sec each step, using a graphite monochromator and  $CuK\alpha$ . X-ray photoelectron spectra of the gels were also measured.

### 26.3. RESULTS AND DISCUSSION

Condition for the gel formation without catalyst have been previously reported by the authors [5]. Monolithic gels could be obtained without catalyst or with acidic catalysts when  $pH \leq 2.2$ . Effect of acid species on gel formation was not observed. Syneresis was observed during aging when  $pH < 1$ . Gellike precipitates are shown in Fig. 26.2. Absorption peaks attributed to residual alkoxy group were hardly observed for the xerogels obtained in acidic and short with addition of acidic catalysts and were thick and long with addition of  $NH_4OH$ . Infrared absorption spectra of the xerogels and the dried precipitates are shown in Fig. 26.2. Absorption peaks attributed to residual or alkoxyl group were hardly observed for the xerogels obtained in acidic solutions. However, strong absorption near  $1400$  and  $1000\text{ cm}^{-1}$ , attributed to O-H and C-O in alcohol, respectively, were observed for the precipitates

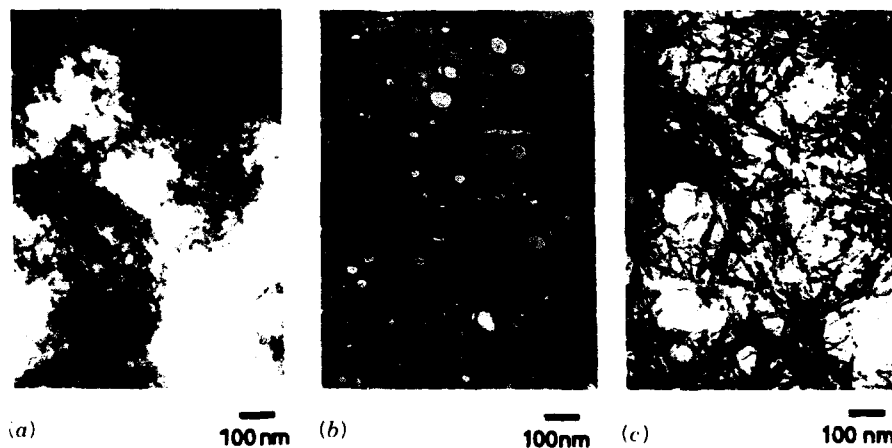


Figure 26.1. Transmission electron microscopy photographs of  $V_2O_5$  gels from  $VO(OC_2H_5)_3$  hydrolyzed (a) with HCl ( $[HCl]/[VO(OC_2H_5)_3] = \frac{1}{2}$ ), (b) without catalyst, and (c) with  $NH_4OH$  ( $[NH_4OH]/[VO(OC_2H_5)_3] = \frac{1}{2}$ ).



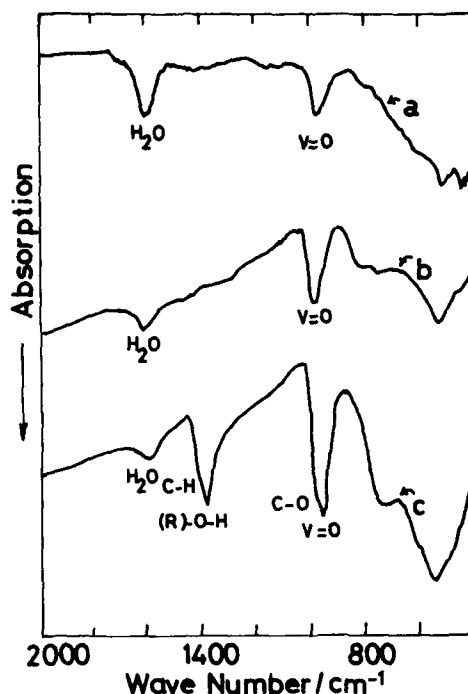


Figure 26.2. Infrared absorption spectra of  $V_2O_5$  xerogels from  $VO(OC_2H_5)_3$  hydrolyzed (a) with HCl, (b) without catalyst, and (c) with  $NH_4OH$ .

obtained with addition of  $NH_4OH$ . These results indicate that the hydrolysis proceeds rapidly in acidic solutions. Monolithic gels were obtained in a few seconds from  $VO(OC_2H_5)_3$ , and about 1 min from  $VO(O n-C_4H_9)_3$ , when  $[VO(OR)_3]/[ROH] = 1/75$  in mol and  $[H_2O]/[VO(OR)_3] = 15$  in mol. In these cases, the gels were red or orange at first, and the color changed to dark green in several hours. This suggests that reduction of  $V^{5+}$  to  $V^{4+}$  proceeds during aging of the gels [6]. When  $VO(O i-C_3H_7)_3$  was used as the starting material, green gellike precipitates were obtained in 24 hr, but monolithic gel could not be obtained. The rate of gel formation decreased in the following order;  $C_2H_5 > n-C_4H_9 > i-C_3H_7$ . This result is similar to gel formation of silica from Si-alkoxides [7].

Examples of X-ray diffraction patterns for the powders and coatings of  $V_2O_5 \cdot nH_2O$  xerogels,  $n \cong 3$ , are shown in Fig. 26.3. Most of the broad peaks of the coatings could be indexed as (00l), as reported for the hydrated  $V_2O_5$  gel coating from metavanadate solutions [1]. However, several peaks other than (00l) peaks were observed for the powders (closed circles in Fig. 26.3). These results indicate that the fiber-like polymers have three-dimensionally ordered structure and that the polymers orient in the coatings.

$O_{1s}$  peaks of X-ray photoelectron spectra are considered to consist of at least

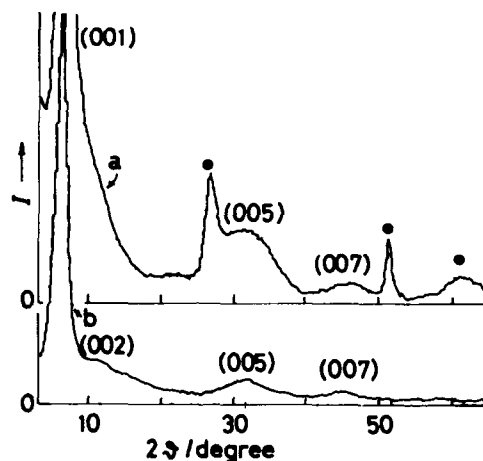


Figure 26.3. X-ray diffraction patterns of  $V_2O_5 \cdot nH_2O$  xerogels,  $n \approx 3$ . (a) Powder, (b) coating.

two peaks, as shown in Fig. 26.4. The difference of binding energies between these two peaks is about 1.7 eV, which is almost the same as the difference between the peaks of bridging oxygen and nonbridging oxygen or double-bonded oxygen in silicate and phosphate glasses [8].  $O_{1s}$  spectra of vanadate glasses containing more than 50 mol %  $V_2O_5$ , which was considered to have vanadate network [9], are similar to those of the  $V_2O_5$  gels, as shown in Fig. 26.4b. Therefore, the coordination state of oxygen in the gels can be considered to be similar to that in vanadate glasses. The values of the chemical shift of  $V_{2p_{1/2}}$  and  $V_{2p_{3/2}}$  peaks of  $V_2O_5$  gels, about 4 to 5 eV, were between those

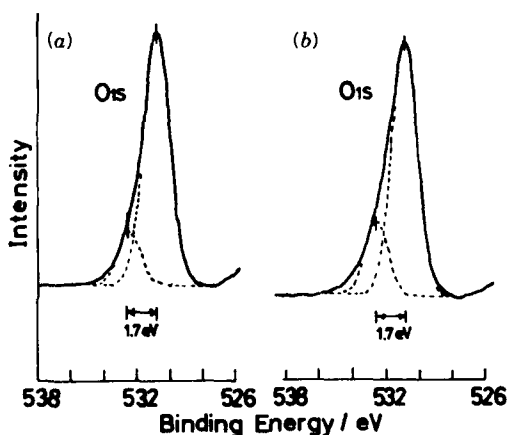


Figure 26.4.  $O_{1s}$  peaks of X-ray photoelectron spectra of  $V_2O_5$  (a) xerogel coating and (b)  $70V_2O_5 \cdot 25TeO_2 \cdot 5Fe_2O_3$  glass.

reported for  $V_2O_5$  and  $V_6O_{13}$  crystals [10]. These results indicate that the gels contain  $V^{4+}$ . The fraction of reduced V ion,  $[V^{4+}]/[V_{total}]$ , of the gels was determined to be about 0.15 by wet chemical analysis. The chemical shift of these peaks seems to be dominantly affected by oxidation state of V ions, and it was difficult to discuss the coordination state of  $V^{4+}$  and  $V^{5+}$  in the gels from the measurement of X-ray photoelectron spectra.

## 26.4. CONCLUSIONS

Gel formation process and the structure of  $V_2O_5$  gels from  $VO(OR)_3$  have been investigated, and the following results have been obtained.

1. Monolithic gels can be obtained from  $VO(OC_2H_5)_3$  without catalyst or with acidic catalysts when  $pH \leq 2.2$ .
2. The rate of gel formation decreases in the following order:  $C_2H_5 > n-C_4H_9 > i-C_3H_7$ .
3. The gels consist of fiberlike thin polymers less than 10 nm in diameter. The polymers obtained with acidic catalysts are thin and short.
4.  $O_{1s}$  spectra of X-ray photoelectron spectra of the gels consist of at least two peaks and are similar to those of vanadate glasses.

## REFERENCES

1. J. Livage, in C. J. Brinker, D. E. Clark, and D. R. Ulrich, Eds., *Better Ceramics Through Chemistry. Mater. Res. Soc. Symp. Proc.*, 125 (1984).
2. H. Hirashima, T. Koyama, and T. Yoshida, *Yogyo-Kyokai-Shi*, **93**, 554 (1985).
3. C. Sanchez, N. Nabavi, and F. Taulelle, in: C. J. Brinker, D. E. Clark, and D. R. Ulrich, Eds., *Better Ceramics Through Chemistry*, Vol. III, *Mater. Res. Soc. Symp. Proc.*, 93 (1988).
4. H. Hirashima, S. Kamimura, and R. Muratake, *J. Non-Cryst. Solids*, **100**, 394 (1988).
5. H. Hirashima and S. Kamimura, in: C. J. Brinker, D. E. Clark, and D. R. Ulrich, Eds., *Better Ceramics Through Chemistry*, Vol. III, *Mater. Res. Soc. Symp. Proc.*, 779 (1988).
6. H. Hirashima, K. Tsukimi, and R. Muratake, *Nippon-Seramikkusu-Kyokai-Gakujutsu-Ronbun-Shi (J. Ceramic Soc. Japan)*, **97**, 235 (1989).
7. C. J. Brinker, *J. Non-Cryst. Solids*, **100**, 31 (1988).
8. B. Brückner, H. U. Chun, H. Goretzki, and M. Samet, *J. Non-Cryst. Solids*, **42**, 49 (1980).
9. H. Hirashima, H. Kurokawa, K. Mizobuchi, and T. Yoshida, *Glastech. Ber.*, **61**, 151 (1988).
10. F. Werfel, G. Drager, and U. Berg, *Cryst. Res. Technol.*, **16**, 119 (1981).

## PROPERTIES OF ALKALI SILICATE GELS AND THEIR SINTERED FUSED SILICA GLASSES

ROBERT D. SHOUP

The alkali silicate gelation process has demonstrated an ability to produce large intricate monolithic fused silica shapes that have properties approaching those of Corning's Code 7940, which is produced by a flame oxidation process. The pore structure of these gels was found to be broader than originally disclosed, suggesting that the matrix is composed of flocculated aggregates that yield pores between 0.1 and 1.0  $\mu\text{m}$ . This open network readily permits permeation of gases during presintering stages to remove unwanted species such as hydroxyl groups, alkali metal oxides, and transition metal oxides that are common to commercial precursor materials. Generation of purer starting materials has demonstrated that this process can produce glass with improved UV and infrared transmission.

### 27.1. INTRODUCTION

It has been reported that colloidal silica sols in combination with potassium silicate and a hydrolytic reagent such as formamide produced controlled pore size (10 to 300 nm) silica gels [1, 2]. These structures in the pore diameter range of 100 to 300 nm possessed sufficient bond strength to resist capillary forces

*Ultrastructure Processing of Advanced Materials.*

Edited by Donald R. Uhlmann and Donald R. Ulrich (deceased).

ISBN 0-471-52986-9 © 1992 John Wiley & Sons, Inc.

involved with rapid (minutes to hours) water removal in a microwave oven. Large pore structures and the ability to rapidly dry large monolithic shapes without generating cracks differentiates this gelation process from the alkoxide sol-gel route that is receiving so much attention [3-7]. The latter gels are characterized by very small pore structures, generally below about 300 Å diameter.

The preferred pore diameter range for generating large monolithic structures that are capable of being sintered to fused silica is about 200 to 250 nm [8]. These pore size distributions were considered to be very uniform (based on mercury porosimeter data), but more recent studies by workers at Rutgers University [9,10] show internal voids that approach 1  $\mu\text{m}$  in diameter. Subsequent follow-up studies on precursor gel solutions with varying solids contents support these findings and are reported here. Despite the broader distribution of pore sizes, the monolithic gels sinter readily to dense glass with very few inclusions, either bubbles or crystalline particles.

Advances in forming near-net-shape structures have been made both in direct casting of shapes (Figs. 27.1 and 27.2) and in machining of shapes from gel blanks (Fig. 27.3). Machining either by milling or water jet processes can be done rapidly in the green gel state, for example, the  $33 \times 5\text{-cm}^2$ -thick blank in Fig. 27.3 was machined in less than 2 hr. Blanks up to 20 cm thick have been gelled, machined, and sintered. Figure 27.4 shows a subscale low expansion fused silica mirror that was fabricated by frit bonding a 15-cm-diameter  $\times$  2.5-cm-deep gel glass core to a planar gel glass faceplate.

The purity of the glass is a function of the basic raw materials used to produce the gels, the chemical dealkalization (rinsing baths) of the green structure, and the thermal exposure of the porous structure prior to its densification. Even without improved purity, the fused silica gel glass demonstrated properties (CTE, strength, homogeneity, etc.) that are adequate for reflective optics.

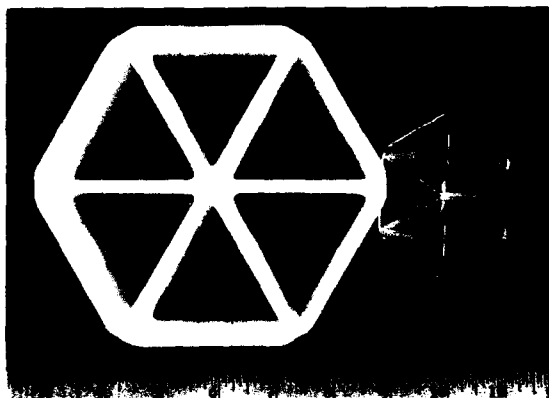


Figure 27.1. A 15-cm molded casting and 7.6-cm sintered glass core.

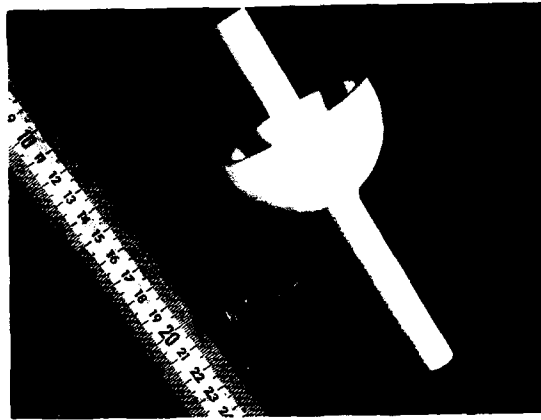


Figure 27.2. A  $15.5 \times 26\text{-cm}^2$ -diameter molded casting and  $9 \times 4\text{-cm}^2$ -diameter sintered glass shape.

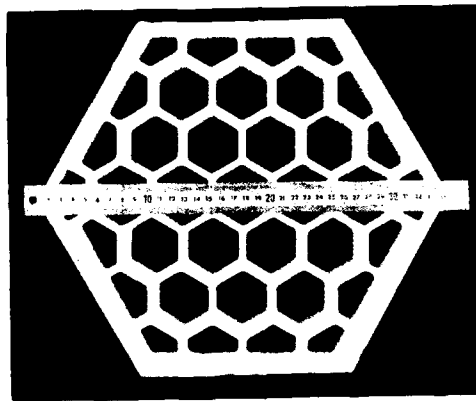


Figure 27.3. A  $35 \times 7.6\text{-cm}^2$ -deep machined green gel core.

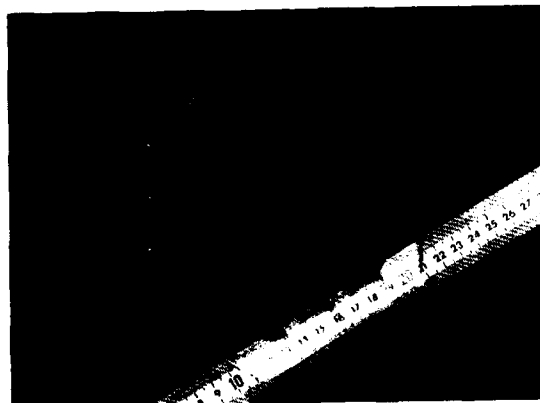


Figure 27.4. A  $15 \times 2.5\text{-cm}^2$ -deep fused silica gel glass core that was frit bonded to gel glass faceplate.

Significant progress was made in preparation of raw material and processing to achieve improved optical transmission in the UV and infrared.

## 27.2. EXPERIMENTAL PROCEDURE

The gel compositions that were used to produce the fused silica monoliths shown in Figs. 27.1 to 27.4 were the same as described in Ref. 8. Various water dilutions of the 90-g Kasil I (PQ Corp.), 10-g Ludox HS-40 (DuPont), and 10-g formamide reagent mix were used to generate the porous gels used in the porosimeter studies. The actual silica solids content of the precursor gel mixes were 17, 18, 19, and 20 wt%. The gels were dealkalized in two 10 wt% ammonium nitrate/distilled water baths, followed by three 10 wt% HCl/distilled water baths and finally by several distilled water baths, all heated to at least 70°C. After heating to 1000°C, scanning electron microscopy (SEM) data were obtained internally, whereas the porosimeter data were done by Porous Materials, Inc., Ithaca, New York.

Sintering after pretreatment to between 1000 and 1150°C was accomplished in a tungsten element vacuum furnace, either in inert gases (e.g., helium) or at reduced pressure, with rapid (30 to 50°C/min) heat-up rates to between 1720 and 1740°C and hold times of 10 to 30 min.

Physical property data on the glass, such as strength, annealing, and strain point temperatures, refractive index, expansion, infrared and UV transmission, and homogeneity, were obtained in Corning's testing facilities. Chemical composition such as trace metal analysis was also done internally.

The high-purity potassium silicate was made by two approaches. In one case, Degussa's OX-50 powder was dissolved in hot KOH solution, and in the second, either  $\text{SiCl}_4$  or tetraethylorthosilicate (TEOS) was hydrolyzed, washed free of HCl or ethanol, and then dissolved in the hot KOH solution to obtain the equivalent of Kasil I,  $\text{SiO}_2/\text{K}_2\text{O}$  ratio of 3.9.

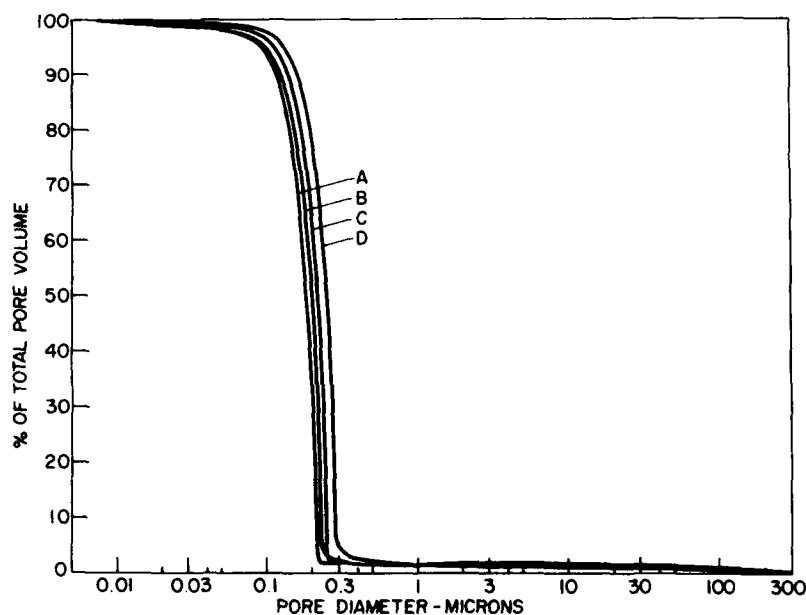
Chlorine drying experiments generally were run with 3 vol % chlorine in an oxygen-helium mixture. When chlorine was cut off, argon was substituted for the helium and chlorine.

## 27.3. RESULTS AND DISCUSSION

### 27.3.1. Pore Structure

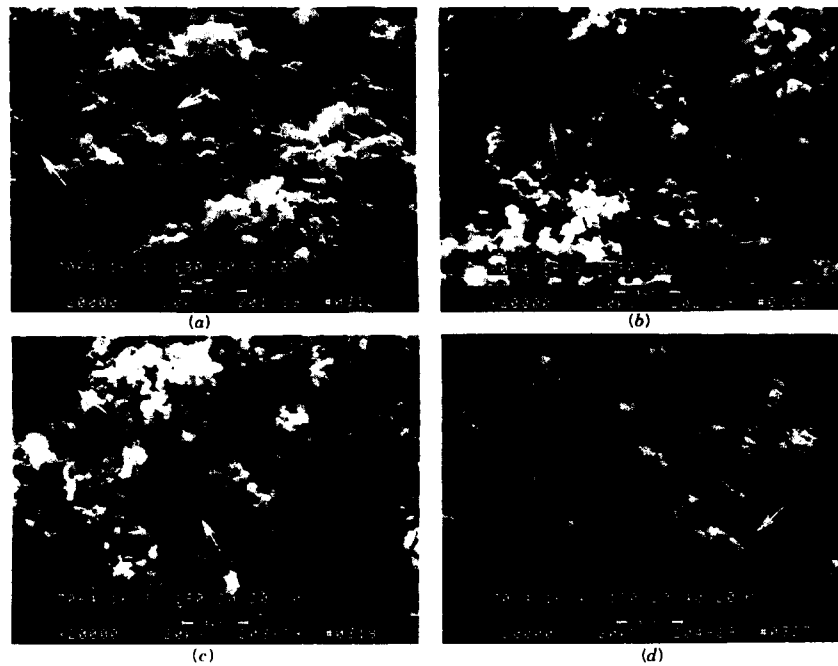
Some discrepancies existed in characterization of pore structure for the silicate gel structures. Differences in surface areas obtained by Brunaur-Emmett-Teller (BET) techniques vary substantially from those obtained by mercury porosimetry, assuming cylindrical capillary channels. The group at Rutgers University studied the problem by thorough evaluation of porosimetry and nitrogen absorption/desorption data [9], as well as ultramicrotomy of these gel

structures [10]. Their data indicated meso- and macropores with the latter approaching  $1\text{ }\mu\text{m}$  in diameter. It was decided to follow up on this work with a study on the compositions that are used to prepare the fused silica monoliths. Specifically, diluted versions of the composition yielding about 2000-Å-diameter pores were cast and measured by mercury intrusion and extrusion. If one only looks at the intrusion curve (Fig. 27.5), there appears to be a single, narrow pore size structure that increases with decrease in solids content of the precursor solution. Curve *A* represents 20%  $\text{SiO}_2$  solids in the precursor solution; *B*, 19%; *C*, 18%; and *D*, 17%, and they produce mean pore diameters of about 180, 200, 220, and 250 nm, respectively. However, careful examination of the SEMs (Figs. 27.6a–d) indicates that there are larger cavities (arrows). Because these are micrographs of freshly broken surfaces, one could speculate that these cavities might be the result of uneven fracture and pull out of excess material. For this reason, mercury extrusion curves were obtained (Fig. 27.7), and they all reveal a definite hysteresis effect. There is no direct measure of internal pore dimensions by a single extrusion test, but these curves, along with the SEM pictures, strongly suggest larger internal voids. Additional support of this reasoning is given in the surface area data obtained by mercury intrusion (Fig. 27.8). These curves suggest surface areas of about 27 (*A*), 36 (*B*), 42 (*C*), and 60 (*D*)  $\text{m}^2/\text{g}$ , whereas BET absorption predicts 16 (*A*), 22 (*B*), 25 (*C*), and 34 (*D*)  $\text{m}^2/\text{g}$ . One must conclude that the structure is more open than the uniform cylindrical

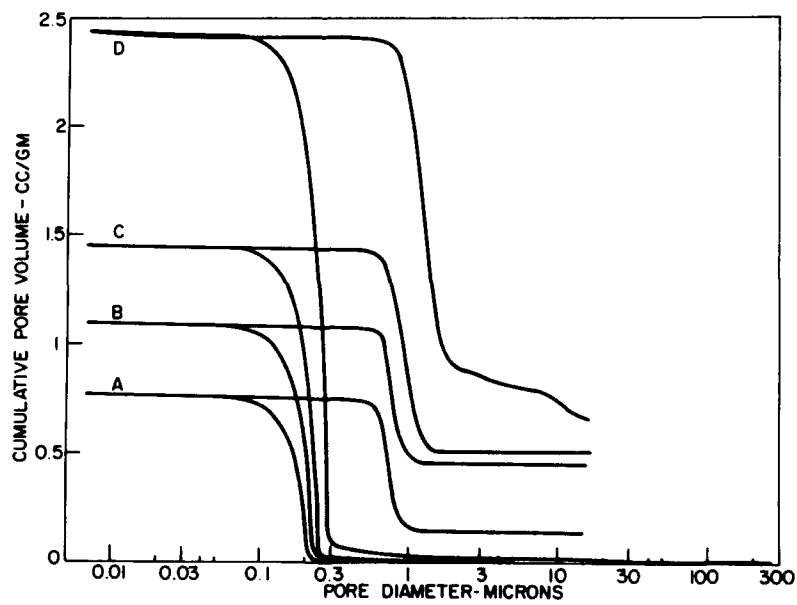


**Figure 27.5.** Mercury intrusion curves for ~200-nm pore gels: *A*, 20 wt % silica in precursor solution; *B*, 19 wt % silica; *C*, 18 wt % silica; *D*, 17 wt % silica.





**Figure 27.6.** SEM pictures of  $\sim 200$  nm pore gels shown in Fig. 27.5: (a) Curve A, (b) Curve B, (c) Curve C, (d) Curve D.



**Figure 27.7.** Intrusion/extension curves for  $\sim 200$ -nm gels shown in Figs. 27.5 and 27.6.

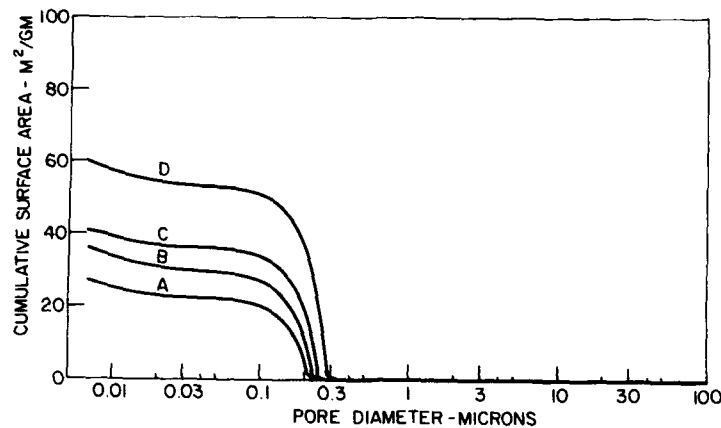


Figure 27.8. Surface area of gels in Figs. 27.5 to 27.7 obtained by mercury intrusion.

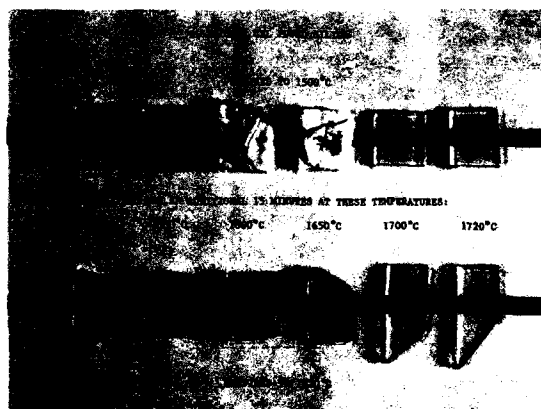
capillary structure that mercury intrusion assumes, and, whereas the pore neck may be about 200 nm, the internal cavities could be as large as 1  $\mu\text{m}$  in diameter. The suggestion by Cao, Gerhardt, and Wachtman [9] that the gel structure is formed by colloidal aggregates that flocculate and are firmly bonded together with additional monomeric silica from the "soluble" silicate is a reasonable one.

### 27.3.2. Processing and Glass Properties

Even using commercial raw materials such as Kasil 1 (potassium silicate) and Ludox HS-40 (colloidal silica sol) with their known contaminants, the silicate fused silica gel glass has good properties for reflective optics (see Table 27.1). To achieve these good properties despite low-level alkali and transition metal impurities, it is important to sinter fairly rapidly (30 to 50°C/min) through the cristobalite nucleation temperatures of 1500 to 1700°C. Figure 27.9 shows 1-in. glass samples cut from the same gel plate. The top row was sintered to total density at 1500°C, whereas the lower row was sintered at 1720°C. Subsequently, they were each fired for 15 min at the listed temperatures and examined by X-ray diffraction for crystalline inclusions. Obviously, the 1500°C samples exposed at 1600 and 1650°C crystallized dramatically. Even 1500°C for an additional 15 min showed a trace of crystallinity and 1550°C- and 1700°C-treated plates showed increased cristobalite formation. All the samples presintered at 1720°C remained crystal free after sintering for the additional times at the prescribed temperatures. This suggests that high-temperature sintering dissolved any cristobalite that may have been nucleated on the high-surface-area gel as the sample was heated. However, this could not occur in the 1500°C-pretreated glasses, so any nucleated crystals continued to grow when heated between 1500 and 1700°C.

TABLE 27.1. Fused Silica Gel<sup>a</sup> Glass Properties

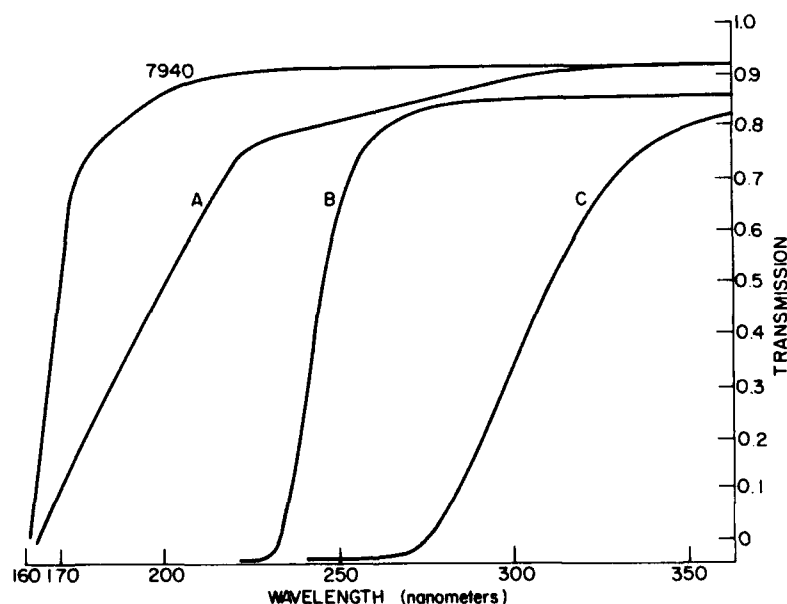
Property	
Annealing point (°C)	
No Cl <sub>2</sub>	1153
Cl <sub>2</sub> dried	1169
Strain point (°C)	
No Cl <sub>2</sub>	1042
Cl <sub>2</sub> dried	1063
Expansion coefficient (300°C)	$5.7 \times 10^{-7}$
Specific gravity (g/cm <sup>3</sup> )	2.204
Modules of rupture (psi)	
Abraded	~ 8,000
Unabraded	~ 14,000
Refractive index	
$n_f(486 \mu\text{m})$	1.463
$n_d(589 \mu\text{m})$	1.458
$n_c(656 \mu\text{m})$	1.456
Homogeneity	$1-3 \times 10^{-6}$
$\beta$ OH (ppm H <sub>2</sub> O)	
No Cl <sub>2</sub>	30-100
Cl <sub>2</sub> dried	<1

<sup>a</sup>Commercial raw materials.

**Figure 27.9.** Sintered gel glasses cut from the same gel plate; top-row samples presintered to 1500°C then exposed for 15 min at temperatures from 1500 to 1700°C. Bottom-row samples were presintered to 1720°C before equivalent thermal treatment as the top row.

Optical transmission spectra in the UV wavelength region show the effect of absorbing species in these gel glasses. Figure 27.10 shows spectra of gel glasses prepared under different sintering conditions and from different raw material bases. Curves *B* and *C* were obtained from gel glasses prepared from commercial reagents, but the improved transmission of *B* was due to removal of transition metals during chlorine exposure at 1150°C before final densification. There probably can be more improvement by changing the thermal cycle, but it is also clear that some transition metal impurities are more difficult to remove than others (e.g., Ti), and there will be a limit to this effect. Curve *A* demonstrates a better approach to increasing the gel glass transmission in the UV region. It was obtained from a gel glass generated from potassium silicate that was prepared by dissolving high-purity silica, such as freshly hydrolyzed TEOS,  $\text{SiCl}_4$ , or flamed soots (Cab-O-Sil or Degussa), in high-purity KOH. Whereas these gel glasses have improved transmission, the overall process has not yet been optimized.

In the infrared region from 2500 to 4500 nm, the effect of different thermal processes can be observed for a few gel glasses (Fig. 27.11). Curve *A* was a well dried ( $\text{Cl}_2$  atm) gel glass that showed less than 1 ppm  $\text{H}_2\text{O}$  retention. Curve *B* was  $\text{Cl}_2$  dried, but it was not sintered immediately after  $\text{Cl}_2$  exposure, so it picked up about 20 ppm  $\text{H}_2\text{O}$ . Curve *C* was not  $\text{Cl}_2$  dried, but was sintered under vacuum (70 ppm  $\text{H}_2\text{O}$ ). Curve *D* also was not  $\text{Cl}_2$  dried, and it was consolidated in flowing helium (140 ppm  $\text{H}_2\text{O}$ ). These data indicate that water



**Figure 27.10.** UV spectra of gel glasses compared to Corning Code 7940; *A*, high-purity gel glass; *B*, commercial raw materials glass pretreated in chlorine; *C*, same as *B* but not pretreated in chlorine.

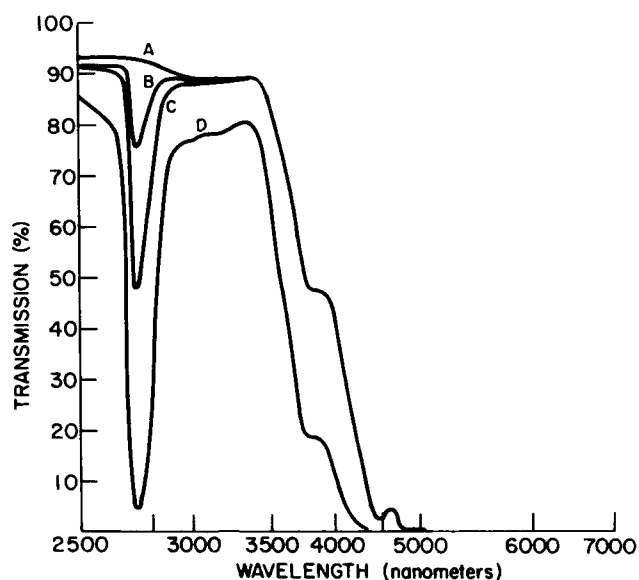


Figure 27.11. Infrared spectra of silicate gel glasses exposed to different thermal processes: A, well dried by chlorine treatment; B, chlorine treated, but not sintered immediately; C, sintered in vacuum furnace (no  $\text{Cl}_2$ ); D, sintered in flowing helium (no  $\text{Cl}_2$ ).

retention is dependent on sintering atmosphere, and care must be taken to control conditions in order to achieve reproducible results.

An effort was made to determine the temperatures that were required to effectively remove water and other metal impurities by chlorine atmospheres. Table 27.2 and Fig. 27.12 combine to demonstrate the effect of temperature on metal and water removal from the porous structures when they were exposed to 3% chlorine at 600 to 900°C for at least 10 hr. Although some authors [11] describe water removal in chlorine atmospheres at temperatures as low as 700°C, at these conditions neither water or metal species were removed until

TABLE 27.2. Effect of Temperature on  $\text{Cl}_2$  Purification of Gel Glass

Temperature of $\text{Cl}_2$ <sup>a</sup> Exposure		Impurities (ppm)			
Curve	(°C)	$\text{H}_2\text{O}$	Fe	Na	K
A	600	35	80	6.3	66
B	700	41	77	8.9	71
C	800	35	77	8.5	75
D	900	<1	4	0.4	27

<sup>a</sup>3%  $\text{Cl}_2$  in  $\text{He}/\text{O}_2$ .

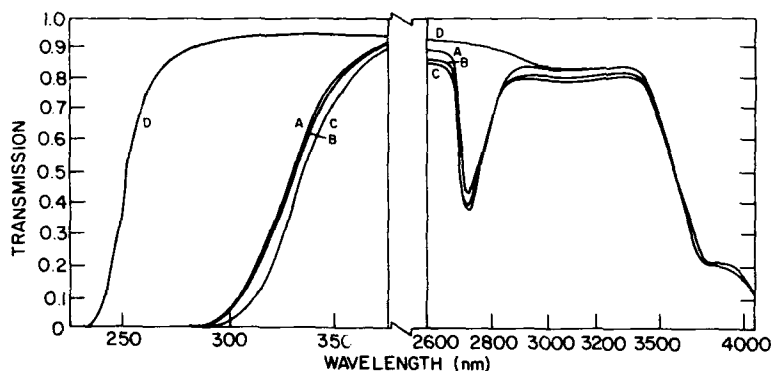


Figure 27.12. UV and infrared spectra of gel glasses exposed to chlorine atmosphere at different temperatures: A, 600°C; B, 700°C; C, 800°C; D, 900°C.

900°C. However, at 900°C there was a dramatic decrease in alkali, iron, and water, which was accompanied by the expected improvement in transmission in the UV and infrared regions of the spectra. Although it may be too much to expect to duplicate Code 7940 glass purity, these studies indicate that materials and processes can produce significant improvement in optical transmission of silicate gel glass.

## 27.4. CONCLUSIONS

Potassium silicate/colloidal silica-based gels have demonstrated their capability to produce intricate geometric gel shapes, either by direct near-net-shape casting or by their machineability from solid green gel blanks. The open pore structure is considered to be broader in pore size than originally disclosed. The preferred pore diameter of about 200 to 250 nm is now considered to have internal voids as large as 1  $\mu\text{m}$ , and the 200-nm size only represents the pore neck as observed by mercury intrusion techniques. Formation of the larger voids can be associated with flocculated aggregates of colloidal silica particles.

Fused silica gel glasses consolidated from large monolithic gels have glass properties comparable to Corning's Code 7940 with respect to low expansion reflective optics. Because of the nature of the raw material source for alkali silicates (inexpensive sands), sufficient transition metal impurities are carried over into the glass to reduce their UV transmission. Preparation of high-purity potassium silicates by dissolution of high-purity silica in KOH-yielded gels, which, when subjected to  $\text{Cl}_2$  atmospheres before consolidation, sintered to glasses that have dramatically improved UV and infrared transmission. Water and metal species were reduced from hundreds of parts per million to less than 10 ppm, and in some cases less than 1 ppm.

## REFERENCES

1. R. D. Shoup, in: *Colloid and Interface Science*, Vol. 3, p. 63, Academic Press, New York (1976).
2. R. D. Shoup and W. J. Wein, U.S. Patent 4,059,658 (Corning Glass) (1977).
3. L. L. Hench, in: *Science of Ceramic Chemical Processing*, pp. 52-64, Wiley, New York (1986).
4. L. C. Klein, *Annu. Rev. Mater. Sci.*, **15**, 277-248 (1985).
5. C. J. Brinker, K. D. Keefer, D. Schaefer, R. A. Assink, B. D. Kay, and C. S. Ashley, *J. Non-Cryst. Solids*, **63**, 45 (1984).
6. B. E. Yoldas, *J. Non-Cryst. Solids*, **51**, 105-121 (1982).
7. H. Dislich, *Angew. Chem.*, **10**(6), 363-370 (1971).
8. R. D. Shoup, in: *Ultrastructure Processing of Advanced Ceramics*, pp. 347-354, Wiley, New York (1988).
9. W. Cao, R. Gerhardt, and J. B. Wachtman, Jr., *J. Am. Ceram. Soc.*, **71**(12), 1108-1113 (1988).
10. H. M. Kerch, R. A. Gerhardt, and J. L. Grazul, *J. Am. Ceram. Soc.*, **73**(8), 2228-2237 (1990).
11. T. E. Elmer, *J. Am. Ceram. Soc.*, **64**(3), 150-154 (1981).

## EFFECTS OF ULTRASTRUCTURE ON ELASTIC AND THERMAL PROPERTIES OF GLASS

NAOHIRO SOGA

### 28.1. INTRODUCTION

In order to discuss the effect of *ultrastructure* on the physical properties of matter, one has to define the term or level of ultrastructure. According to the definition of the previous Ultrastructure Processing Conferences, the *ultrastructure* level is considered to be the range of somewhere between molecular and submicron dimensions, that is, in the range of 10 to 1000 Å [1]. Porous glasses, derived by the phase separation process of alkali-borosilicate glasses or by the sol-gel process of silicon alkoxides, and nanocomposites containing nanosize SiC or Si<sub>3</sub>N<sub>4</sub> particles in Al<sub>2</sub>O<sub>3</sub> are typical examples of materials with ultrastructure. If one considers the 10-Å size voids, many network-forming compounds have an open space of such size within their networks, as exemplified by a group of zeolites used for a molecular sieve. In these compounds, the size of ultrastructure level voids is affected by both the coordination state of network-forming cations and the connecting way of oxygen-polyhedra surrounding these cations.

Elastic moduli and thermal expansivity are typical physical properties that involve the change in volume, one with respect to pressure and the other to temperature. Thus, they depend upon the forces between atoms or ions in solids,

*Ultrastructure Processing of Advanced Materials.*

Edited by Donald R. Uhlmann and Donald R. Ulrich (deceased).

ISBN 0-471-52986-9 © 1992 John Wiley & Sons, Inc.



so that it should be possible, in principle, to relate these properties to the bond strength of constituent atoms or ions. In the past, a good correlation between them has been observed for a number of solids, particularly metals or alkali halides [2]. However, the correlation becomes poor for the silicates having network structure, because the change in bonding angle also appears under stress due to the existence of open space. Furthermore, the low frequency modes are observed, which have the wavelength in the range of several to ten times the interatomic spacing. Thus, the elastic and thermal properties are sometimes affected differently by the change in such nanolevel pores within the networks.

As for the glassy state, the short range ordering of atoms or ions is usually regarded similar to that in the crystalline state having the same chemical composition. The advantage of glassy state is the easiness of changing physical properties widely and continuously by choosing an appropriate preparation condition or chemical composition. From the similarity in short-range order between the glassy and crystalline states, one can predict reasonably well the change in elastic moduli caused by substitution of one network-modifying ion for another in an isomorphous series based on packing considerations, bond energy, and/or the interaction of network-forming and network-modifying ions [3-7]. However, because of difficulty in changing network structure without introducing some network modifiers by normal ceramic or glass-making processes, little data exist to discuss the effect of middle-range structural change on elastic moduli and thermal expansivity.

Recently, various new techniques have come into use to produce novel materials that could not be realized by any conventional ceramic- or glass-making process. They include the ultrahigh-pressure application, rapid quenching of molten state, reactive and nonreactive vapor deposition, precipitation from liquid solutions, and heat treatment of gels among others. In many cases, the short-range order of the products made by such new processes either in an amorphous or crystalline state is similar to those made by the conventional method [8], but their middle-range orders or crystal structures are different because polyhedra of different types sometimes coexist, and they are connected in a nonequilibrium manner when quenched from a high energetic state.

In the past few years, the author and his associates have been trying to accumulate systematic data of elastic moduli and thermal expansivity for network-modified glasses with a hope to find a way to molecular engineering of amorphous materials by means of substitution of constituent atoms or ions. This Chapter summarizes some of the results obtained so far.

## 28.2. EFFECT OF ULTRASTRUCTURE-LEVEL VOIDS ON PHYSICAL PROPERTIES

In two-phase composite systems, the overall elastic modulus or thermal expansivity is intermediate between the two end components, and a number of theoretical, semiempirical, and empirical analytical expressions have been

proposed to express the change in these properties as a function of fractional volumes of two components [9, 10]. For the simplest case of a porous material, the thermal expansivity is hardly affected by porosity so far as it has a continuous matrix phase. On the other hand, its elastic moduli change with pore volume [11–15] as well as shape. If one assumes penny-shape pores, the elastic moduli decrease drastically with increasing the aspect ratio [16–18]. The effect of cylindrical pores on Young's modulus has been predicted to be much lower than that of spherical pores (19–20). The experimental data by Warren [21] for highly porous perlite with millimeter-size pores were found to fall between the upper and lower bounds predicted based on the calculation of Hashin and Rosen [19] as shown in Fig. 28.1. Recently, Young's moduli of porous silica with ultrastructure-level pores derived by the sol-gel method became available [22, 23], and these data are plotted also in Fig. 28.1. All the data fall between the boundaries predicted by the model.

Silica takes different polymorphs with three-dimensional framework composed of rigid  $\text{SiO}_4$  molecules joined by a flexible Si–O–Si bridge. This flexibility allows the tetrahedra to tilt or twist with respect to one another. Because the Si–O bond is very strong, a significant expansion or contraction observed for some polymorphs of silica is attributed largely to the change in tilting or twisting of  $\text{SiO}_4$  tetrahedra [24], and thus the change in apparent density reflects the change in void or open space within three-dimensional framework. Such an open space can be varied by the densification process.

$\text{SiO}_2$  glass was densified by a high-pressure MA-8 apparatus composed of eight cubic WC anvils at pressure up to 80 kbar as and temperature up to 920°C [25]. By this apparatus, it was possible to obtain the densified glasses having no crack, because the pressure was very close to the hydrostatic

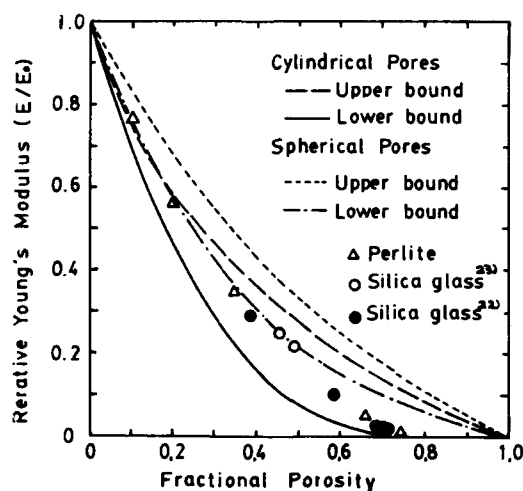


Figure 28.1. Relationship between relative Young's modulus and porosity for porous materials.

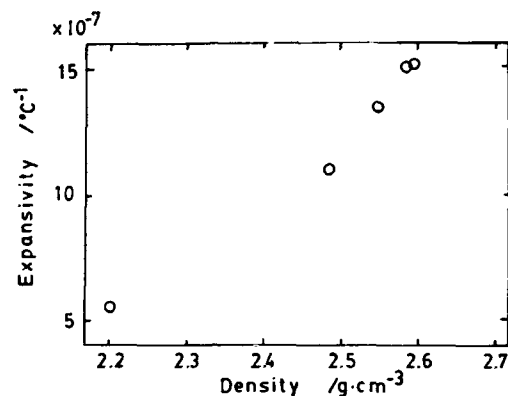


Figure 28.2. Expansivity of densified silica glass as a function of density.

condition. Their elastic moduli were determined by using the cube resonance method capable of measuring the shear wave velocity and Poisson's ratio of small-size specimens [26]. The results are shown in Fig. 28.2 as a function of density. The thermal expansivity was determined by a specially made dilatometer equipped with a very sensitive displacement transducer. The average thermal expansion coefficients from room temperature to 250°C for the densified glasses are shown in Fig. 28.3 as a function of density. Clearly, both the

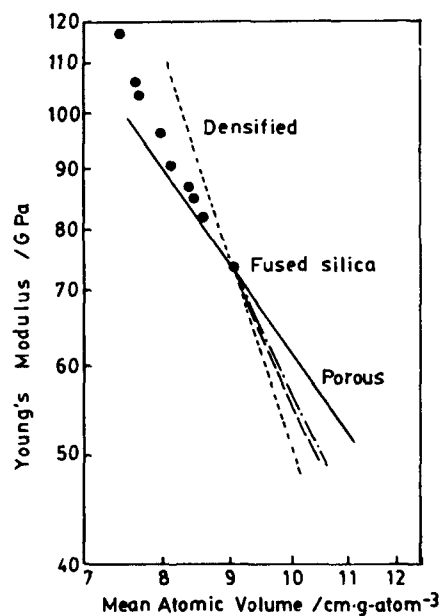
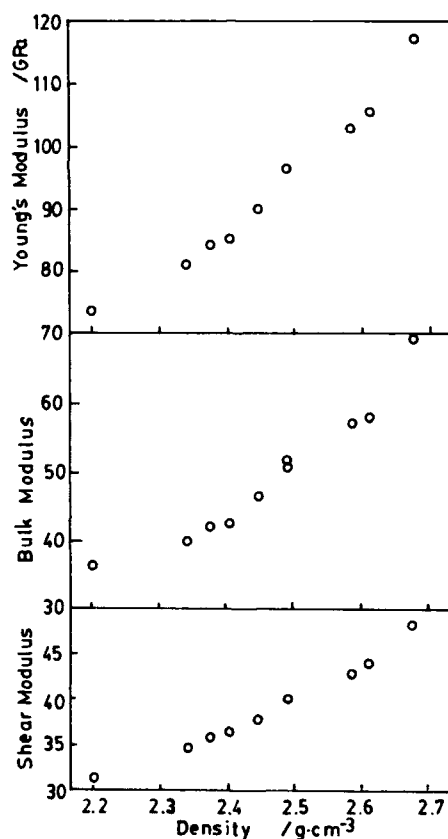


Figure 28.3. Elastic moduli of densified silica glass as a function of density.

elastic moduli and thermal expansion coefficient increased with densification in contrast to the tendency of a normal close-packed solids. If the interatomic bond strength governs the elastic moduli and thermal expansion of a solid, it is expected that the elastic moduli increase with densification, while the thermal expansivity decreases. The results of infrared spectra, chemical shift of X-ray emission spectra, molar refractivity, and other available measurements indicated no change in coordination state of Si in the densified glass. So, such an anomalous tendency of densified fused silica is associated with the change in bonding angle or connecting way of  $\text{SiO}_4$  tetrahedra.

As described above, the Young's modulus of a porous solid with a fixed porosity is independent of pore size provided all the pores have the same geometry. Because the void or open space within the three-dimensional framework of untreated or densified fused silica is expected to be nanolevel, it is interesting to see whether the same theoretical consideration is applicable to such a small-scale pore. Figure 28.4 shows the Young's modulus-volume



**Figure 28.4.** Young's modulus of densified silica glass as a function of mean atomic volume. The lines are the same as those shown in Fig. 28.3.

relationship for the densified glass in log-log plot. Also given are the predictions based on the models of spherical and cylindrical pores by Hashin and Rosen [19]. Clearly, the slope of the densified glass is close to the lower bound of spherical pores and the upper bound of cylindrical pores. This is understandable, because voids in glass structure are not exactly the closed pores, but connected to other voids with holes less than the diameter of voids. Such a rearrangement in void structure does not affect so much on the lattice vibration of the three-dimensional network, but because of more constrained state of Si-O-Si bridge in the densified glass, the glass expands more to release the stress when heated in comparison with the untreated fused silica.

### 28.3. EFFECT OF SUBSTITUTION OF $\text{SiO}_4$ TETRAHEDRA BY DIFFERENT TYPE TETRAHEDRA

The nanolevel voids discussed above can be changed by substituting tetrahedra of different types to  $\text{SiO}_4$  tetrahedra. Such substitution is difficult to carry out by a conventional melting method, but by using RF sputtering method, one can introduce different cations in the network. It has been postulated that the substitution of Si by Al, Ga, B, Ge, and Zn in the tetrahedron barely affect the thermal expansion of  $\text{SiO}_2$  glass [27]. The recent results revealed that Ti ions take the four-coordinated state up to 12 mol % in amorphous  $\text{SiO}_2$  films [28]. The effect of  $\text{TiO}_2$  addition on thermal expansivity is to decrease the expansivity considerably as shown in Fig. 28.5. The thermal expansivity of amorphous  $\text{TiO}_2$ - $\text{SiO}_2$  films become negative with increasing  $\text{TiO}_2$ . The same effect was observed for the melt-derived glasses [29] or sol-gel-derived glasses [30]. The tilting or twisting of Si-O-Si (or Ti) bridging is certainly responsible for the enhanced negative thermal expansivity of amorphous  $\text{TiO}_2$ - $\text{SiO}_2$  films, but the

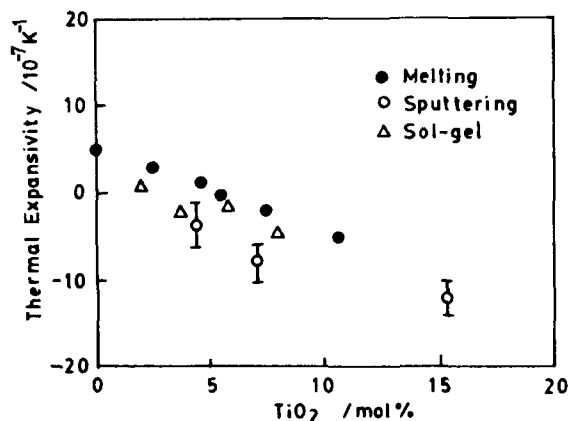


Figure 28.5. Thermal expansivity of  $\text{TiO}_2$ -containing silica glass made by different methods.

effect of the easiness of such tilting or twisting on elastic moduli has not been examined yet.

The analogy between diamond and cubic boron nitride (CBN), as well as that between  $\text{SiO}_2$  and  $\text{AlPO}_4$ , has been discussed. Because of the heterogeneous network of CBN or  $\text{AlPO}_4$  against the homogeneous network of diamond or  $\text{SiO}_2$ , one expects different thermal and elastic behaviors. The thermal expansivity of CBN has been found to be not so much different from that of diamond, whereas its elastic moduli are much lower than those of diamond.

Recently, an attempt was made by the RF sputtering method to fabricate amorphous  $\text{AlPO}_4$  films, which could not be made by an ordinary melting method because of the tendency of  $\text{AlPO}_4$  to decompose into  $\text{Al}_2\text{O}_3$  and  $\text{P}_2\text{O}_5$  at high temperatures, and its physical properties were determined [31, 32]. As shown in Table 28.1 the thermal expansivity of amorphous  $\text{AlPO}_4$  was found to be comparable to that of fused silica, as in the case of isomorphous crystals. However, the Young's modulus of  $\text{AlPO}_4$  was about 30% lower than that of  $\text{SiO}_2$ . This result is analogous to the decrease in bulk moduli of  $\alpha$ -quartz-type  $\text{AlPO}_4$  from  $\alpha$ -quartz or the decrease in hardness of CBN from diamond. In  $\text{AlPO}_4$ , the Al-O bond length is 1.739 Å longer than that of P-O bonds (1.516 Å). The higher ionicity of Al-O bonds can cause  $\text{AlO}_4$  tetrahedra to take a more closed-pack structure of  $\text{AlO}_6$ , as observed in amorphous alumina where the average coordination number of Al is about 5 [33]. It is considered that such a difference in tetrahedron size between  $\text{AlO}_4$  and  $\text{PO}_4$  as well as a tendency of Al to take a high coordination state enhances the tilting or twisting motion of tetrahedra, and thus the overall volume change takes place more easily than the case of  $\text{SiO}_4$  tetrahedra assembly.

#### 28.4. EFFECT OF CHANGE IN ANIONS IN GLASS NETWORK

The nanolevel voids within the three-dimensional frameworks of fused silica can be modified by changing oxygen to other anions. From the electrostatic point of

TABLE 28.1. Physical Properties of  $\text{SiO}_2$  and  $\text{AlPO}_4$

	$\text{AlPO}_4$		$\text{SiO}_2$	
	Berlinite	Amorphous	$\alpha$ -Quartz	Amorphous
Bulk modulus (GPa)	29.3	30	37.7	37
Density ( $\text{g/cm}^3$ )	2.618	2.25	2.655	2.20
Refractive index	$n_e = 1.529$ $n_o = 1.519$	1.462	1.544 1.535	1.458
Thermal expansion coefficient	$\alpha_a = 15.9$ $\alpha_c = 9.7$	0.5	16.1 4.1	0.5

view, the substitution of oxygen ions by monovalent anions such as F ions should decrease the bond strength, and the substitution by tri- or four-valent anions should increase the bond strength. As described above, both thermal and elastic properties of silica are affected more by the change in Si-O-Si bridging angle than by the bond strength within the tetrahedron. So, such substitution may give different effects on elastic and thermal properties depending upon the restricting degree of the motion of  $\text{SiO}_4$  tetrahedra.

Monovalent anions introduced in place of oxygen ions certainly decrease the average bond strength of the glass, but also break the Si-O-Si bridging, affecting the displacement of other tetrahedra. F-doped silica of optical fiber grade were obtained from Sumitomo Electric Company and made into a cube suitable for the cube resonance method. The thermal expansivity was also measured for comparison. The results are summarized in Table 28.2, along with the temperature derivatives of elastic moduli. Although the elastic moduli decreased with F content as expected, the thermal expansion coefficient remained almost unchanged. Furthermore, the anomalous elastic behavior of fused silica, which is the positive temperature coefficients of elastic moduli, is enhanced by F doping. This means that the anomaly inherited in fused silica is not released by breaking the bridging oxygen bonds by F ions, because the nanolevel voids or open space in the network responsible for the change in bridging angle still exist.

At this moment, it is difficult to replace oxygen in amorphous silica by nitrogen or carbon, although it has been postulated that nitrogen or carbon have an ability to bond three or four silicons in the glass network, as in the cases of  $\text{Si}_3\text{N}_4$  and  $\text{SiC}$ , and increase mechanical properties considerably due to more tightly crosslinked structures than found in fused silica. A number of evidences have been given for multicomponent oxynitride glasses [34, 35]. A noteworthy one is that of oxycarbide glasses in the Mg-Al-Si-O-C systems by Homeny, Nelson, and Risbud [36]. By utilizing respective oxides and SiC powders, they were able to obtain the glasses containing carbon content up to 0.37 mol %. The density increase for the highest C-containing glass was about 4%, accompanied with 12% increase in Young's modulus, 11% increase in shear modulus, and 17% increase in hardness. Their other data of oxynitride glasses show the increase of density and Young's modulus by 0.84% and 4.0%, respectively, when substituted

TABLE 28.2. Physical Properties of F-Doped Silica

F content (wt %)	0	0.8	3.2
Density ( $\text{g/cm}^3$ )	2.204	2.198	2.179
Young's modulus (Y) (GPa)	74.6	72.5	59.3
Shear modulus (G) (GPa)	31.7	31.1	24.9
Bulk modulus (K) (GPa)	38.4	36.2	31.6
Thermal expansivity ( $\times 10^7/^\circ\text{C}$ )	4.34	3.40	2.76
$(dG/dT)/G$ ( $\times 10^4/^\circ\text{C}$ )	1.20	1.50	2.09
$(dK/dT)/K$ ( $\times 10^4/^\circ\text{C}$ )	2.76	3.29	4.14

by 1 mol % of nitrogen. These changes gives almost the same Young's modulus-volume relationship for the densified glasses in Fig. 28.6.

A large amount of nitrogen can be incorporated into binary  $\text{CaO-SiO}_2$  glasses by using  $\text{Si}_3\text{N}_4$  [37]. The changes in physical properties induced by the substitution of oxygen by nitrogen for calcium metasilicate glasses given in Figs. 28.7 and 28.8 was not so much different from the values given by others. These binary or ternary oxide glasses behave in a normal thermal fashion like crystals because of a large amount of network-modifying cations exist, thus depressing the contribution of the bending, tilting, or twisting motion of  $\text{SiO}_4$  tetrahedra to the overall change in physical properties. Consequently, the increase in bond strength introduced by other constituents is reflected directly to the physical properties. This is why the data of the thermal expansion coefficient show a normal behavior, that is, a tendency to decrease with increasing density or elasticity and approach the value of  $\text{Si}_3\text{N}_4$ . As for the elastic moduli, calcium metasilicate glasses also contain an open space or voids in their glass structure and may give an influence in elastic behavior as in the case of the pore-matrix composite system. The Young modulus-volume relationship for this series of glasses shows that this is the case.

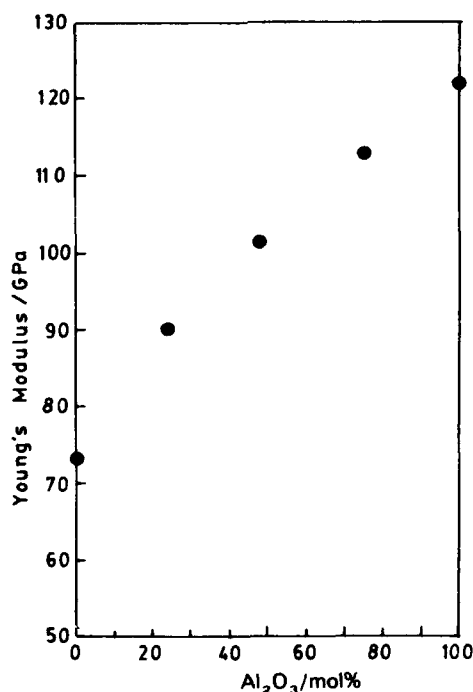


Figure 28.6. Young's modulus of amorphous films in a  $\text{SiO}_2\text{-Al}_2\text{O}_3$  system.



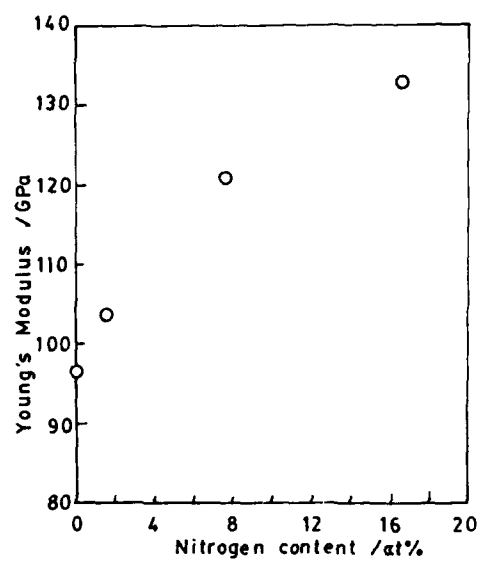


Figure 28.7. Young's modulus of  $\text{CaSiO}_3$  glass containing nitrogen.

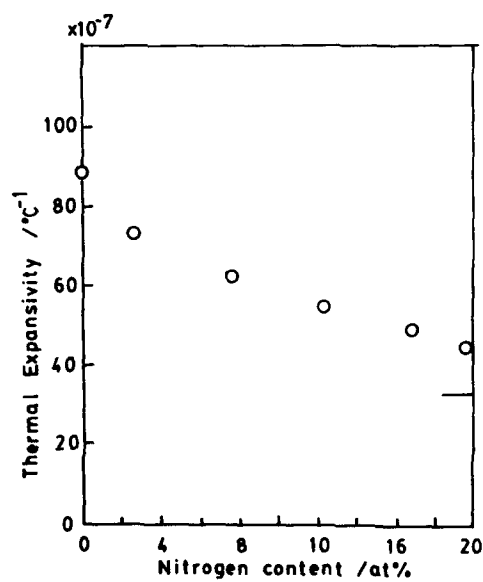


Figure 28.8. Thermal expansivity of  $\text{CaSiO}_3$  glass containing nitrogen.

## REFERENCES

1. J. D. Mackenzie and D. R. Ulrich, *Ultrastructure Processing of Advanced Ceramics*, Wiley, New York (1988).
2. M. Born and K. Huang, *Dynamic Theory of Crystal Lattices*, Oxford Univ. Press, Oxford (1954).
3. A. Dietzel, *Naturwissenschaften*, **29**, 537-547 (1941).
4. A. Makishima and J. D. Mackenzie, *J. Non-Cryst. Solids*, **12**, 35-45 (1973).
5. N. Soga, *J. Non-Cryst. Solids*, **52**, 365-375 (1982); **73**, 305-313 (1985).
6. M. R. DeGuire and S. D. Brown, *J. Am. Ceramic Soc.*, **67**, 270-273 (1984).
7. P. M. Halleck, R. E. Pacalo, and E. K. Graham, *J. Non-Cryst. Solids*, **86**, 190-203 (1986).
8. N. Soga and T. Hanada, *Diffusion and Defect Data*, **53-54**, 265-276 (1987).
9. J. B. Wachtman, Jr., *Mechanical and Thermal Properties of Ceramics*, NBS Spec. Publ. No. 303, pp. 139-168 (1968).
10. Z. Hashin and S. Shtrikman, *J. Mech. Phys. Solids*, **10**, 335-342 (1962).
11. J. K. Mackenzie, *Proc. Phys. Soc., London, Ser. B*, **63**, 2-11 (1950).
12. R. M. Spriggs, *J. Am. Ceramic Soc.*, **44**, 628-629 (1961).
13. D. P. H. Hasselman, *J. Am. Ceramic Soc.*, **45**, 453-453 (1962).
14. J. Wang, *J. Mater. Sci.*, **19**, 801-814 (1984).
15. K. K. Phani and S. K. Niyogi, *J. Am. Ceramic Soc.*, **70**, 632-636 (1987).
16. R. J. O'Connell and B. Budiansky, *J. Geophys. Res.*, **79**, 5412-5426 (1974).
17. N. Soga, H. Mizutani, H. Spetzler, and R. J. Martin III, *J. Geophys. Res.*, **83**, 4451-4458 (1978).
18. H. Banno, *Ceram. Bull.*, **66**, 1332-1337 (1987).
19. Z. Hashin and B. W. Rosen, *J. Appl. Mech.*, **2**, 223 (1965).
20. D. P. H. Hasselman and R. M. Fulrath, in: R. M. Fulrath and J. A. Pask, Eds., *Ceramic Microstructures*, pp. 343-378, Wiley, New York (1968).
21. N. Warren, *J. Geophys. Res.*, **74**, 713-719 (1969).
22. T. Adachi, M. Okada, H. Kozuka, and S. Sakka, in: *Proc. 1988 Annual Meeting of Japan Ceramic Society*, 276 (1988).
23. N. Soga, K. Nakanishi, K. Hirao, and T. Kawano, to be published.
24. D. Taylor, *Br. Ceramic Trans. J.*, **84**, 129-134 (1984).
25. T. Goto and N. Soga, *J. Japan. Soc. Powder Powder Metallurgy*, **29**, 8-12 (1982).
26. T. Goto, T. Hanada, and N. Soga, *J. Soc. Mater. Sci. Japan*, **32**, 1264-1268 (1983).
27. A. A. Lisenkov, *Fiz. Khim. Stekla*, **12**, 198-205 (1986).
28. T. Hanada and N. Soga, *J. Am. Ceramic Soc.*, **65**, C-84-86 (1982).
29. P. C. Schultz, *J. Am. Ceramic Soc.*, **59**, 214-219 (1976).
30. K. Kamiya and S. Sakka, *J. Non-Cryst. Solids*, **52**, 357-363 (1982).
31. T. Hanada, T. Kano, and N. Soga, *J. Ceramic Soc. Japan*, **97**, 279-283 (1989).
32. T. Hanada, Y. Bessyo, and N. Soga, *J. Non-Cryst. Solids*, **113**, 213-220 (1989).
33. T. Hanada, T. Aikawa, and N. Soga, *J. Am. Ceramic Soc.*, **67**, 52-56 (1984).
34. D. R. Messier and R. D. Gleisner, *J. Am. Ceramic Soc.*, **71**, 422-425 (1988).
35. M. Rajaram and D. E. Day, *J. Am. Ceramic Soc.*, **70**, 203-207 (1987).
36. J. Homeny, G. G. Nelson, and S. H. Risbud, *J. Am. Ceramic Soc.*, **71**, 386-390 (1988).
37. T. Hanada, N. Ueda, and N. Soga, *J. Ceramic Soc. Japan*, **96**, 284-291 (1988).

## DETERMINATION OF THE SKELETAL DENSITY OF SILICA GELS FROM WIDE-ANGLE X-RAY DIFFRACTION

L. ESQUIVIAS, C. BARRERA-SOLANO,  
N. de La ROSA-FOX, F. L. CUMBRERA, AND J. ZARZYCKI

### 29.1. INTRODUCTION

In recent years there has evolved a growing interest in new techniques for solventless hydrolysis [1–3]. One of these consists of submitting a mixture of tetraethoxysilane (TEOS) +  $H_2O$  to the action of ultrasound. These very dense sonogels show important textural differences from similar gels obtained in alcoholic solution [4–7] that make them potential candidates for improved low-shrinkage matrices for ceramic–ceramic composites.

From a structural point of view, no noticeable changes in silicon coordination may be expected in silica aerogels with respect to bulk vitreous silica. Because of the defects on the pore–matrix interface, the short-range order may be affected by the texture of gels, which depends on the preparation conditions [8]. These defects are highly reactive, and water molecules form silanol sites with surface atoms. The presence of hydroxyls implies a slight elongation in the adjacent Si–O bond lengths [9], and small variations in the short-range order of the gel may occur depending on the method of preparation. Here the results of an X-ray radial distribution function (RDF) analysis of a sonogel and gel prepared in alcoholic solution are reported.

*Ultrastructure Processing of Advanced Materials.*

Edited by Donald R. Uhlmann and Donald R. Ulrich (deceased).

ISBN 0-471-52986-9 © 1992 John Wiley & Sons, Inc.

Recently, a controversy has risen over the skeletal density of the elementary particles that form the gel and values that range from  $0.2 \text{ g/cm}^3$  to that of the bulk solid  $2.2 \text{ g/cm}^3$  [10–14]. Results depend on resolution of the method of measuring and on the scale at which the density is measured.

Wide-angle X-ray diffraction offers a possible method of measuring the skeletal density with a resolution of the order of the X-ray wavelength, because the Fourier transform of the interference function implicitly involves this parameter. Problems arise because of spurious oscillations appearing in the transformed function due to the lack of high-angle data. They are not entirely smoothed out by usual extrapolation methods, making it impossible to accurately determine the density.

In this Chapter an evaluation of this parameter is carried out for a sonogel and a gel obtained in alcoholic solution by the maximum entropy method (MEM) [15]. This method finds the RDF of an arrangement of atoms as the one corresponding to the atomic distribution of maximum entropy compatible with the accessible data and density. Thus, it allows the evaluation of the skeletal density at the scale of several angstroms.

## 29.2. EXPERIMENTAL

The hydrolysis of TEOS (Fluka), was obtained by subjecting a mixture of TEOS and water to ultrasonic radiation [4]. TEOS was hydrolyzed using 4 mol  $\text{H}_2\text{O}$ /mol TEOS. The pH of the mixture was adjusted to close to 2 by the addition of 12 N HCl to the water of hydrolysis and measured 30–60 sec after the onset of the application. In the following SG is used to designate the sonogel and CG the corresponding classic gel (obtained with a dilution of 3.4 mol alcohol/mol TEOS). The liquids were kept in hermetic containers under isothermal conditions at  $50^\circ\text{C}$  until gelation.

Humid gels were dried by hypercritical evacuation [16] of the residual products (to a large extent, ethanol). For the autoclave treatment, the critical conditions were  $P = 190$  bars,  $T = 320^\circ\text{C}$ . Apparent densities,  $d_a$ , were measured by mercury volumetry and specific surfaces,  $S'$ , by Brunaur–Emmett–Teller using nitrogen. The aerogels were submitted to an oxidation treatment in oxygen at  $500^\circ\text{C}$  for 5 hr followed by a dehydration treatment in  $\text{CCl}_4$  at  $500^\circ\text{C}$  for 8 hr.

The obtained aerogels and commercial vitreous silica were ground to fine powders ( $< 40 \mu$ ) and compacted by pressure into bricks of approximately  $20 \times 20 \times 1 \text{ mm}^3$  from which X-ray diffraction intensities were measured on a D500 Siemens diffractometer equipped with conventional Bragg–Brentano geometry and a Mo anode. The Mo  $K_\alpha$  line ( $\lambda = 0.71069 \text{ \AA}$ ) was selected by means of a bent graphite monochromator in the diffracted beam.

Four series of data were collected in the interval  $5.6^\circ < 2\theta < 110^\circ$ . From  $5.6^\circ$  to  $70^\circ$ , step sizes of  $(2\Delta\theta) = 0.2^\circ$  were used and from  $70^\circ$  to  $110^\circ$  steps of  $(2\Delta\theta) = 0.5^\circ$  were used. Pulses were counted using a scintillation counter, the

number of counts never being less than 2000. Mean values of those measured in each observation were assigned to that position.

Data were corrected for background, polarization, and multiple scattering [17] and normalized into electronic units by the high-angle method [18, 19], and then the Compton scattering was subtracted.

## 29.3. RESULTS AND DISCUSSION

### 29.3.1. Description of the Results

Figure 29.1 shows the spectra of X-ray diffraction intensities for both investigated gels and vitreous silica as a function of the scattering vector modulus  $s = 4\pi/\lambda \cdot \sin \theta$ . The low order of atomic arrangement inside the elementary particles with regard to V-SiO<sub>2</sub> is obvious from the lower scattering maxima and shift of these maxima toward higher  $S$  values. Other features are the absence of a characteristic vitreous silica shoulder between 2.2 and 2.7/Å [20] and a significant drastic increase in depth of the minimum located at 6/Å in the gel pattern, clearly observed in the interference function  $s \cdot i(s)$  (Fig. 29.2).

$$F(s) = s \cdot i(s) \quad \text{and} \quad i(s) = \frac{I_{\text{eu}} - \sum x_i f_i^2}{(\sum x_i f_i)^2}$$

where  $x_i$  and  $f_i$  are, respectively, the atomic fraction and atomic amplitude of the  $i$  element, which is  $i = \text{Si, O}$ .  $I_{\text{eu}}$  represents the resulting intensity in electronic units after corrections. The RDF is calculated as

$$4\pi r^2 \rho(r) = 4\pi r^2 \rho_0 + rG(r) \quad (1)$$

where  $\rho_0$  and  $\rho(r)$  represent, respectively, the mean atomic distribution and the local atomic density.  $G(r)$  stands for the Fourier transform of the interference function,

$$G(r) = \int_0^{s_{\text{max}}} F(s) \sin(sr) ds$$

Data were extended until  $s_{\text{max}} = 40/\text{Å}$  by the method proposed by D'Anjou and Sanz [21].

The reduced radial distribution functions,  $rG(r)$ , are represented in Fig. 29.3. This function shows the difference between the RDF and the one describing a distribution with a uniform local density  $\rho_0$ , each peak corresponding to a coordination sphere.

A correspondence between homologous peaks of the  $rG(r)$  of bulk silica and that of SG can be discerned until the value of  $r$  becomes around 11 Å:CG. Beyond these distances the characteristic short-range order of vitreous silica is

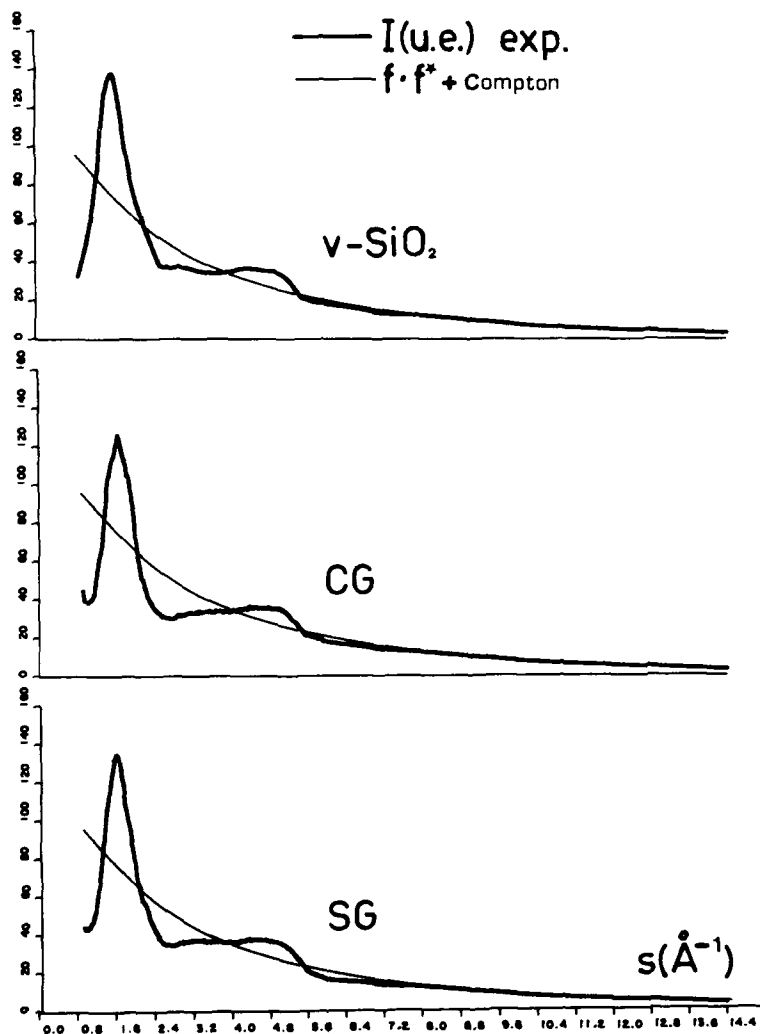


Figure 29.1. X-ray diffraction patterns of vitreous silica, CG, and SG samples after corrections and normalized in electronic units.

broken. It can be interpreted as evidence of the different size of the elementary particles that build up the gels. Thus, the sonogels are formed by appreciably smaller particles than the classic gel.

The first peak of  $rG(r)$  of gels are found slightly shifted toward a higher  $r$  value than that of vitreous silica. The differences in shape and width of the second peak of gels'  $rG(r)$  in comparison with that of the bulk silica point out a distortion of the characteristic tetrahedral silica network. The positions of higher order maxima are also shifted toward higher values to an amount that

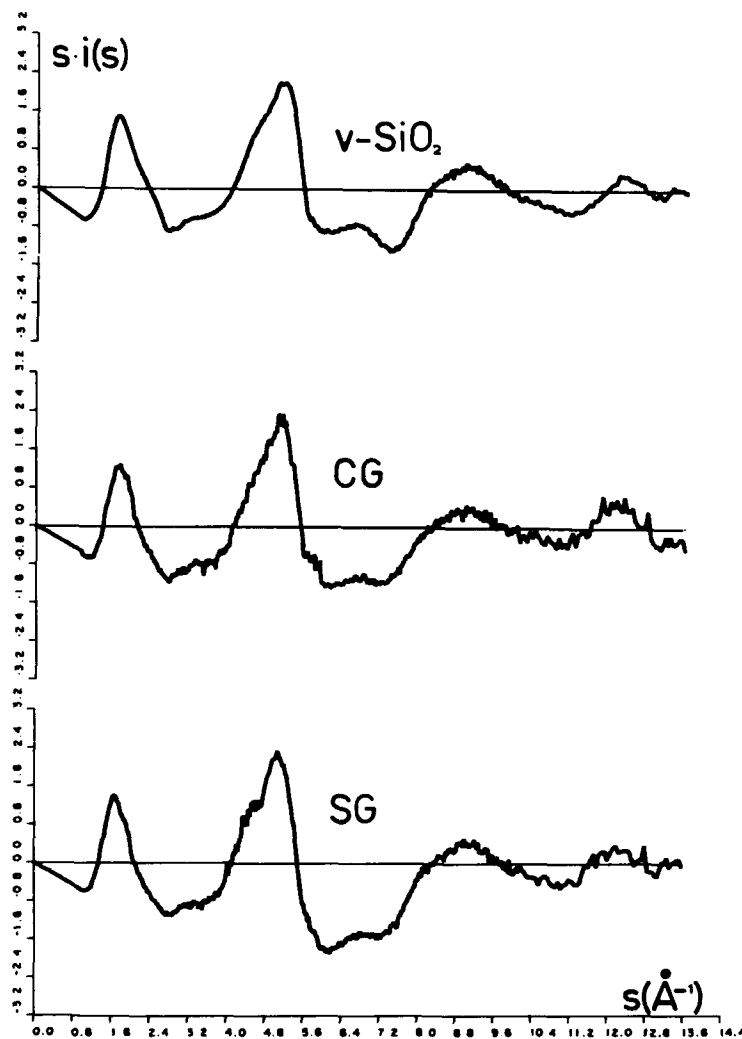
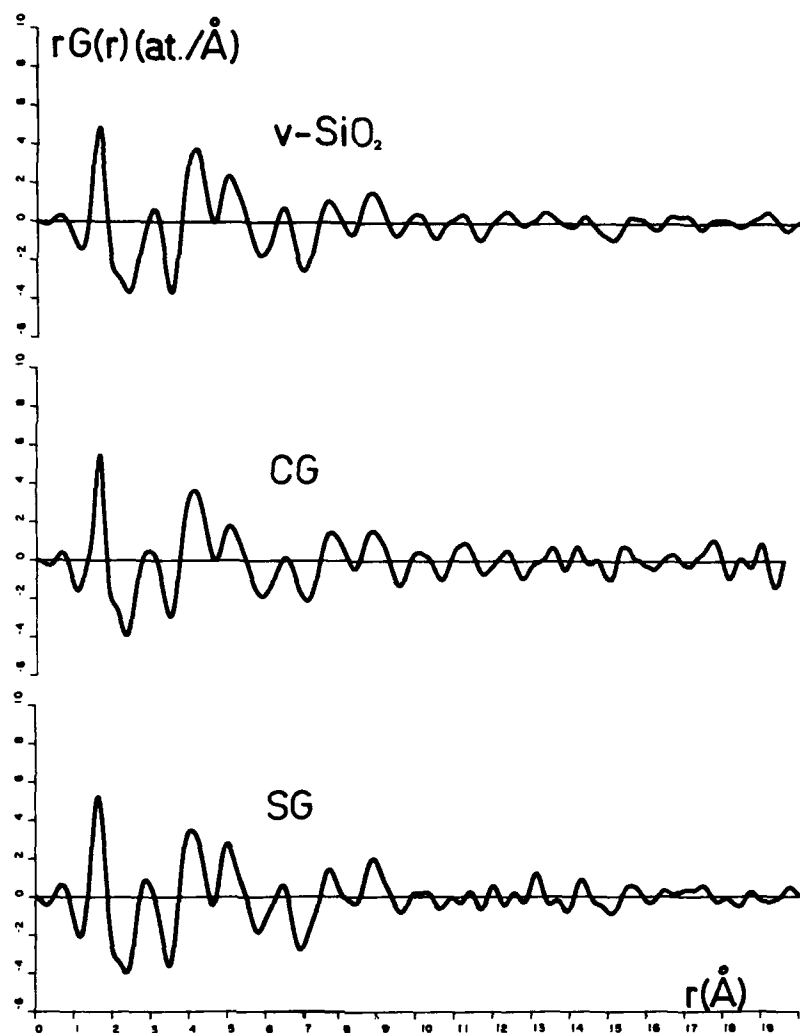


Figure 29.2. Interference functions of vitreous silica, CG, and SG.

increases with  $r$ , which could indicate a skeletal density value somewhat smaller than  $2.2 \text{ g/cm}^3$ .

### 29.3.2. Determination of the Skeletal Densities

An approach to determine the skeletal density of gels may be obtained by taking into consideration that for  $r$  smaller than the minimal first neighbor's length  $rG(r)$  must be equal to  $-4\pi r^2 \rho_0$ . Unfortunately, unwanted ripples in this zone make this method useless.



**Figure 29.3.** Reduced RDFs of vitreous silica, CG, and SG. It can be observed that in the gel patterns, beyond a certain  $r$ , the short-range order of vitreous silica is lost.

Recently, Wei [15] proposed the use of the maximum entropy method to obtain the correlation function in the direct space, because it is free from the drawbacks attached to other methods. In this method the strategy consists of obtaining the RDF that maximizes the system's entropy compatible with the experimentally accessible data and avoids any arbitrary assumption over inaccessible data.



The entropy  $S$  of a structure with spherical symmetry composed by  $N$  scattering centers distributed over  $M$  spherical shells of volume  $4\pi r_j^2 \Delta r$  is

$$S = CN \ln N - C \sum 4\pi r_j^2 \Delta r \cdot \rho(r_j) \ln \rho(r_j)$$

$C$  being a constant and  $\rho(r_j)$  the radial density of scattering centres in the  $j$  shell. The experimental constraints set up an  $(L + 1)$  system of equations:

$$\sum 4\pi r_j^2 \rho(r_j) \sum 4\pi r_j^2 \rho_0$$

for the macroscopic density, besides the  $L$  equations

$$\sum 4\pi r_j^2 [\rho(r_j) - \rho_0] \sin c(r_j s_l) \cdot \Delta r = i(s_l), \quad l = 1, 2, \dots, L$$

which corresponds to the Fourier inversion in the  $L$  known values of the structure factor  $i(s)$ , and  $\sin c(x) = \sin x/x$ .

The problem may be satisfactorily solved by means of the Lagrange multipliers leading to the result

$$\rho(r_j) = \exp[-1 - \mu_0 - \mu_1 \sin c(r_j s_1)]$$

where  $\mu_0, \mu_1, \dots$  are the unknowns to be evaluated. In this case the highly nonlinear system is solved numerically by means of an algorithm based on the Newton method [22], with the initial values  $\mu_0 = 1 - \ln \rho_0$  and  $\mu_1 = 0$  for  $l = 1, \dots, L$ . Typical CPU times range between 3 and 5 min.

This procedure allows for a reliable estimate of the materials' real macroscopic density. In fact, the  $\mu_0 = -1 - \ln \rho_0$ . Lagrange multiplier is an adjustable parameter of the problem. On this basis, values of  $0.0630 + 0.0005$  atoms/ $\text{\AA}^3$  ( $2.09 + 0.02$  g/cm $^3$ , in macroscopic terms) and  $0.0660 + 0.0005$  atoms/ $\text{\AA}^3$  ( $2.19 + 0.02$  g/cm $^3$ ) were found for both gels and bulk silica glass, respectively.

#### 29.3.4. Textural Characteristics

Specific porous volume calculated as

$$V_p = \frac{1}{d_a} - \frac{1}{d_s}$$

where  $d_s$  is the skeletal density, are shown in Table 29.1 together with other derived textural macroscopic quantities;  $V_p/S'$  values are included as a reference of the average pore size. These values agree with the smaller size of sonogel particles, because small particles give rise to small pores that have a more important surface/volume ratio and a small porous volume.

TABLE 29.1. Textural Characteristics of Gels

	$d_a$ (g/cm <sup>3</sup> )	$S'$ (m <sup>2</sup> /g)	$S'd_a$ (m <sup>2</sup> /cm <sup>3</sup> )	$V_p$ (cm <sup>3</sup> /g)	$V_p/S'$ (Å)
Classic gel	0.30	745	223	2.85	38.3
Sonogel	0.98	634	621	0.54	8.5

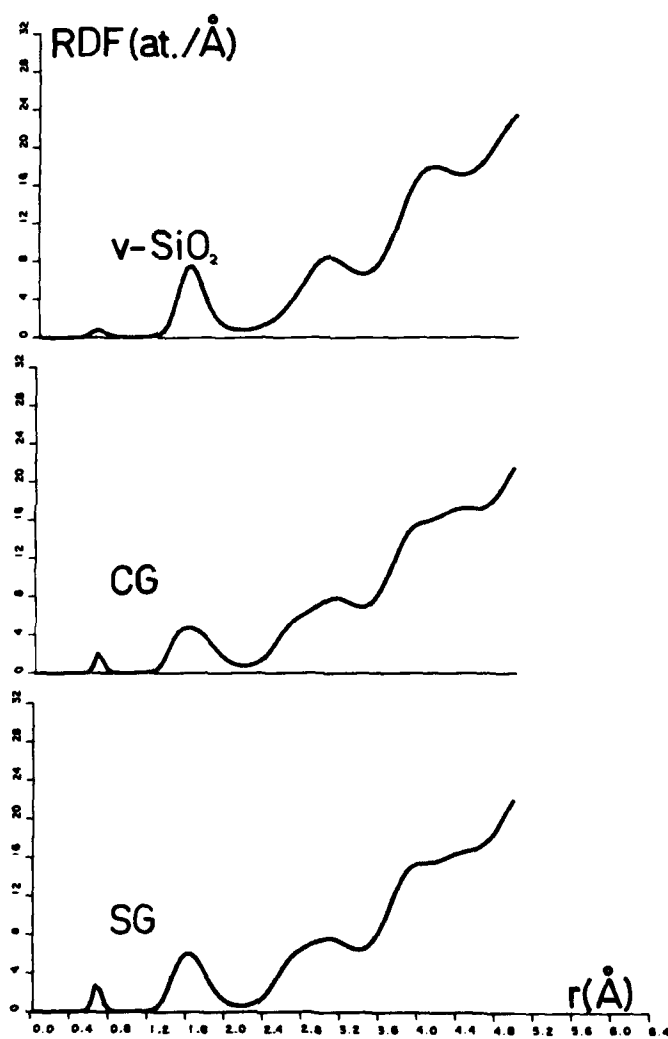


Figure 29.4. RDFs of vitreous silica, CG, and SG calculated from the maximum entropy method.

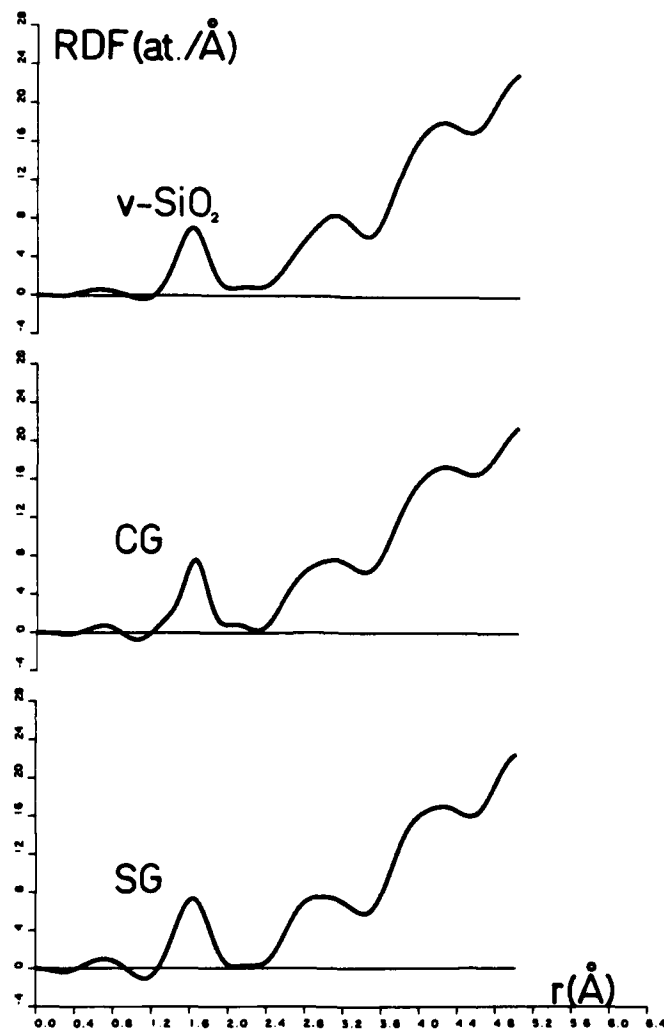


Figure 29.5. RDFs of vitreous silica, CG, and SG resulting from the substitution in Eq. 1 of the calculated densities.

#### 29.3.4. Short-range Order of Gels

The area under the first maximum is related to the average number of atoms in the first sphere of coordination by [23]

$$A = \frac{1}{(\sum x_i Z_i)^2} \sum \sum x_i Z_i Z_j n_{ij}$$

$Z_i$  being the atomic number of the  $i$  element ( $i = \text{Si, O}$ ).  $n_{ij}$  is the averaged number of  $j$  atoms in the first coordination sphere of an  $i$ -type atom.

The  $n_{ij}$  parameters can be calculated from the formulated hypotheses. Therefore, for vitreous silica  $n_{11} = 0$ ,  $n_{12} = 4$ ,  $n_{21} = 2$ , and  $n_{22} = 0$ , which yields  $A = 2.99$  atoms.

In Figs. 29.4 and 29.5 are represented the RDFs calculated from MEM and those resulting from the substitution in Eq. 1 of the calculated densities. Table 29.2 accounts for the main structural parameters.

The lower value of the density may be attributed to the presence of hydroxyls, that is, to say Si-O nonbridging bonds, standard distance of which is 1.54 Å [9]. This causes a slight shift in the adjacent bridging Si-O bond length (Table 29.2), as well as a broadening of the first peak and a distortion of tetrahedra arrangement as is reflected in the shape of the second peak in each of the gel RDFs (Figs. 29.4 and 29.5).

The  $[\text{SiO}_4]$  tetrahedral structure is preserved in both gels by taking into consideration the area below the first peak, although the presence of nonbonded oxygen might cause a lowering of the average coordination, in particular in CG.

## 29.4. CONCLUSIONS

Skeletal densities of aerogels prepared by two different methods were determined with a high resolution by means of a wide-angle X-ray diffraction experiment.

Both gels are formed by elementary particles of density 2.09 g/cm<sup>3</sup>. The size of the sonogel particles is appreciably smaller than that of the classic gel, which explains the high apparent density and microporosity of those aerogels.

**TABLE 29.2. Structural Parameters Deduced from the Radial Distribution Functions Resulting from the Extrapolation of Data Described in Ref. 21 and Applying the Wei Method [15]**

	Area (atoms)	First Peak Position (Å)	Second Peak Position (Å)
Silica			
Extrapolation of data	2.99	1.61	3.10
Wei method	2.90	1.59	3.05
Classic gel			
Extrapolation of data	2.87	1.64	3.08
Wei method	2.66	1.68	2.90
Sonogel			
Extrapolation of data	2.97	1.64	3.10
Wei method	2.77	1.68	3.05

The short-range order is affected by the surface defects yielding a longer average bond length and a distortion in the tetrahedral vitreous silica network.

### ACKNOWLEDGMENT

This work has been supported by Project PB86-0225 of the CICYT (Spain).

### REFERENCES

1. M. Tarasevich, *Am. Ceramic Bull.*, **63**, 500 (1984).
2. W. M. Jones and D. B. Fischbach, *J. Non-Cryst. Solids*, **101**, 123 (1988).
3. J. W. Fleming and S. A. Fleming, presented at the MRS Spring Meeting, Kend, Nev., April 5-9, 1988.
4. L. Esquivias and J. Zarzycki in: M. D. Baró and N. Clavaguera, Eds., *Current Topics on Non-crystalline Solids, Proc. 1st International Workshop on Non-Crystalline Solids, San Feliu de Guixols, Spain, 26-30 May 1986*, World Scientific, Singapore (1986).
5. L. Esquivias and J. Zarzycki, presented at the 3rd International Conference on Ultrastructure Processing of Ceramics, Glasses and Composites, San Diego, Calif., February 23-27, 1987.
6. N. de la Rosa-Fox, L. Esquivias, and J. Zarzycki, *Diffusion Defect Data*, **53-54**, 363 (1987).
7. N. de la Rosa-Fox, L. Esquivias, and J. Zarzycki, presented at the 2nd International Symposium on Aerogels, Montpellier, France, September 21-23, 1988.
8. J. Zarzycki, in: D. R. Uhlmann and N. J. Kreidl, Eds., *Glass Science and Technology*, Vol. 2, pp. 209-245, Academic Press, New York (1984).
9. S. H. Garofalini, *Diffusion Defect Data*, **53-54**, 21 (1987).
10. M. W. Colby, A. Osaka, and J. D. Mackenzie, *J. Non-Cryst. Solids*, **82**, 37 (1986).
11. M. Nogami and Y. Moriya, *J. Non-Cryst. Solids*, **37**, 191 (1980).
12. C. A. M. Mulder, G. van Leeuwen-Stienstra, J. G. van Lierop, and J. P. Woerdman, *J. Non-Cryst. Solids*, **82**, 148 (1986).
13. A. F. Craievich, M. Aegerter, D. I. Dos Santos, T. Woigner, and J. Zarzycki, *J. Non-Cryst. Solids*, **86**, 394 (1986).
14. T. Woigner and J. Phalippou, *J. Non-Cryst. Solids*, **93**, 17 (1987).
15. W. Wei, *J. Non-Cryst. Solids*, **81**, 239 (1986).
16. J. Zarzycki, M. Prassas, and J. Phalippou, *J. Mater. Sci.*, **17**, 3371 (1982).
17. B. E. Warren and R. L. Mozzi, *Acta Crystallogr.*, **21**, 459 (1966).
18. F. Hajdu, *Acta Crystallogr., Sect. A*, **28**, 250 (1972).
19. G. Pálinkás and T. Radnai, *Acta Crystallogr., Sect. A*, **32**, 666 (1976).
20. Th. Gerber and B. Himmel, *J. Non-Cryst. Solids*, **83**, 324 (1986).
21. A. D'Anjou and F. Sanz, *J. Non-Cryst. Solids*, **28**, 319 (1978).
22. J. More, B. Garbow, and K. Hillstrom, User Guide for Minpack-1, National Laboratory Report ANL-80-74, Argonne, Ill. (1980).
23. B. E. Warren, *X-Ray Diffraction*, Addison-Wesley, Reading, Mass. (1969).

## MODULUS OF RUPTURE FOR ROOM-TEMPERATURE GELS DERIVED FROM METHYLTRIMETHOXSILANE

GEORGE E. WHEELER AND SANDRA A. FLEMING

### 30.1. INTRODUCTION

Since the nineteenth-century, attempts have been made to preserve stone sculpture and monuments with alkoxysilanes. In fact, only 15 years after the synthesis of tetraethoxysilane (TEOS) by von Ebelman in 1846 [1], von Hoffmann [2] suggested that it might be exploited as a preservative for the deteriorating stonework of the then recently reclad Houses of Parliament in London. This suggestion, however, bore little fruit for more than 100 years. Bailey and Schaffer [3] summarized the century of futility in 1964,

... all organized trials known to have been made with it [i.e., TEOS], including those of A. P. Laurie who patented its use, have been discouraging. On stone of reasonably good quality it has had no apparent effect, good or bad. On stone of relatively poor quality its use has been followed by scaling of the treated surfaces.

Although the last 20 years have witnessed advances in the use of alkoxysilanes as consolidants for stone [4-7], the results of any individual treatment are still neither predictable nor consistent. Among the reasons for this

---

*Ultrastructure Processing of Advanced Materials.*

Edited by Donald R. Uhlmann and Donald R. Ulrich (deceased).

ISBN 0-471-52986-9 © 1992 John Wiley & Sons, Inc.

fact is that a fundamental understanding of these consolidants is lacking. The work presented here is an attempt to explore one of these fundamental properties, namely, modulus of rupture (MOR) for gels derived from methyltrimethoxysilane (MTMOS) at room temperature.

### 30.2. SAMPLE PREPARATION AND TESTING

Gels were prepared from 4:1 molar proportions of distilled water to MTMOS<sup>†</sup> and either 200-proof dehydrated punctilious ethanol or high-performance liquid chromatography-grade 2-propanol as the solvent. The molar proportions of solvent to MTMOS ranged from 1.5 to 3.0:1. A volume of 100 ml of each mixture was allowed to react in an open polypropylene container at ambient laboratory relative humidity and temperature (on average 32.4% and 26.3°C, respectively, for the period in question). The containers were left open to mimic field application conditions. Samples of neat MTMOS and neat ethyltrimethoxysilane (ETMOS) were also allowed to react under the same conditions. Each of the above-mentioned mixtures conduced to rigid monoliths with masses from between 9% and 33% of the original liquids.

The components and proportions were arrived at through extensive testing. For open systems it was determined that uncracked monoliths of reasonable strength could not be prepared at room temperature with either tetramethoxy- or tetraethoxysilane. Neither could these monoliths be prepared with molar proportions of water to MTMOS greater than 7:1. Solvents with high vapor pressures such as acetone (231 mm Hg at 25°C [8]; all vapor pressures are taken from Ref. 8) or methanol (127 mm Hg) produced extensive cracking. Solvents with lower vapor pressures such as methylcellosolve (9.7 mm Hg) or ethylcellosolve (5.3 mm Hg) produced only weak gels. Solvents such as *t*-butanol or 2-pentanol did not have adequate cosolvency for the water and the MTMOS. Ethanol (59.0 mm Hg) and 2-propanol (43.3 mm Hg) gave monoliths consistently when molar proportions of water to MTMOS between 2 and 4:1 were employed. All mixtures were uncatalyzed: Bases in general produced cracking, and acids are incompatible with calcite-containing stones such as marbles, limestones, and calcareous sandstones from which so much of our sculpture and architecture have been constructed.

All mixtures were slow to gel taking from 1 to 2 weeks. The gels were aged under ambient conditions for approximately 5 months. At that time the monoliths were cut into small "planks" measuring approximately  $53 \times 3.0 \times 2.0 \text{ mm}^3$  with a diamond wafering saw and a petroleum-based lubricating fluid.

Following the procedure and using the apparatus of Pardenek, Fleming, and

<sup>†</sup>Materials and manufacturers: methyltrimethoxysilane, Dow Corning Corporation, Z6070; ethyltrimethoxysilane, Petrarch Systems, E6382; ethanol, USI Chemicals Co.; 2-propanol, Aldrich Chemical Co., 27,049-0; ISOCUT lapping fluid, Buehler LTD, 11-193-032; ISOMET low-speed saw, Buehler LTD, 11-1180. The two alkyltrimethoxysilanes were distilled directly before use.

Klein [9], each sample was stressed until rupture in a three-point bend configuration in accordance with ASTM c674-81. The operative equation for samples of rectangular cross section is

$$M = 3PL/2bd^2$$

where  $M$  = modulus of rupture  
 $P$  = load at rupture  
 $L$  = distance between supports  
 $b$  = width of specimen  
 $d$  = thickness of specimen

A minimum of five samples for each mixture type was tested with the exception of ETMOS for which there was only three samples.

### 30.3. RESULTS AND DISCUSSION

The MORs for the various gels are found in Table 30.1. It is clear from the table that the concentration of solvent in the original mixture affects the MOR. For ethanol, the modulus decreases with the increase in the solvent concentration, that is, with more solvent in the pores of the gel, there is less opportunity for the condensation reactions to occur that would stiffen the gel. For 2-propanol the effect is the same, but more dramatic. In moving from 2.0 to 3.0 mol of solvent per mole of MTMOS, the modulus decreases by over 32 MPa. It was expected that the 4.0:2.0 2-propanol gel would be weaker than the same gel prepared with ethanol. It might be argued that more solvent would escape in the ethanol gel due to that solvent's higher vapor pressure. However, the average MOR is about

TABLE 30.1. Modulus of Rupture for Gels Derived from Methyltrimethoxysilane

Sample Water: MTMOS <sup>a</sup> : Solvent (molar proportions)	Modulus of Rupture (MPa)	Standard Deviation
4.0: 1: 1.5 (EtOH)	52.6	4.40
4.0: 1: 2.0 (EtOH)	48.8	2.95
4.0: 1: 2.5 (EtOH)	43.6	3.13
4.0: 1: 2.0 (2-propanol)	53.0	13.5
4.0: 1: 3.0 (2-propanol)	20.8	1.09
Neat MTMOS	57.5	5.82
Neat ETMOS	36	n.d.

<sup>a</sup>Abbreviations used: MTMOS, methyltrimethoxysilane; ETMOS, ethyltrimethoxysilane.



4 MPa higher for 2-propanol, although the standard deviation for these gels is high.

The highest MOR is obtained for neat MTMOS, that is, with no solvent and no water added. The MTMOS will hydrolyze with atmospheric moisture and ultimately produce a gel. It has been shown that the nature of these gels is strongly dependent on the ambient relative humidity and that in general the amount of gel is lower and the strength of the gel is greater at lower relative humidities [10]. The mass of the gel formed in this way is as low as 9% of the original mass of MTMOS and can be even lower when reacted within porous media such as stones [11]. This low mass return would necessitate multiple treatments for adequate consolidation. Neat ETMOS on the other hand has over a 30% mass retention while its MOR is lower by approximately 29 MPa. ETMOS gels also have greater flexibility, and this flexibility may prove to be an added advantage for a consolidant.

### 30.4. CONCLUSIONS

The test results indicate that reducing the solvent concentration to lower levels improves the MORs of these room-temperature gels derived from MTMOS. There is a delicate balance between too great a volatility of solvent, which can crack the gel during drying, and too low a volatility of the solvent, which thereby inhibits condensation in the gel. MTMOS gels retain a flexible network during drying and can produce strong, uncracked monoliths under conditions not possible for gels derived from tetraalkoxysilanes. Proportions of water to MTMOS (between 2 and 4:1) more in keeping with good film or fiber formation also produce better monoliths. Further work is being pursued in examining other mechanical properties of these gels such as elastic modulus and viscosity.

### REFERENCES

1. J. J. von Ebelmann, *Ann. Chem. Pharm.*, **57**, 334 (1846).
2. A. W. von Hoffman, *The Builder*, **19**, 103 (1861).
3. T. A. Bailey and R. J. Schaffer, *Report on Stone Preservation Experiments*, Ancient Monuments Branch, Ministry of Public Works, London, (1964).
4. S. Z. Lewin, *The Treatment of Stone*, p. 139, Centro per la conservazione delle sculture all'aperto, Bologna (1971).
5. K. Hempel and A. Moncrieff, *The Conservation of Stone I*, p. 319, Centro per la conservazione dell sculture all'aperto, Bologna (1976).
6. E. Bosch, M. Roth, and K. Gogolok, U.S. Patent 3,955,988 (1976).
7. J. Larson, in: *Fourth International Congress on Deterioration and Preservation of Stone*, p. 219, University of Louisville, Louisville, Ky. (1983).
8. J. A. Riddick, W. B. Bunger, and T. K. Sakano, *Organic Solvents*, Wiley, New York (1986).

## REFERENCES

331

9. S. Pardenek, J. Fleming, and L. Klein, *Ultrastructure Processing of Advanced Ceramics*, p. 379, Wiley, New York (1988).
10. A. E. Charola, G. E. Wheeler, and G. G. Freund, *Adhesives and Consolidants*, p. 177, IIC, London (1984).
11. S. Bradley, in: *Fifth International Congress on the Deterioration and Preservation of Stone*, p. 759, Presses Polytechniques Romandes, Lausanne (1985).

## SOL-GEL-DERIVED TITANIA-SILICA GEL-GLASSES

YEU-CHYI CHENG AND LARRY L. HENCH

### 31.1. INTRODUCTION

TiO<sub>2</sub>-SiO<sub>2</sub> glasses are of significant technical importance due to their unusual thermal expansion behavior. The linear thermal expansion coefficient decreases with increasing titania content, with zero expansion in the range of 7-8 wt % TiO<sub>2</sub> [1, 2]. Conventionally, the titania-doped silica glasses, produced either by melting or by flame hydrolysis, are difficult to prepare as large, transparent, homogeneous single-phase materials. Recently, the sol-gel technique has been successfully used to prepare glasses at a relatively lower temperature. Yoldas [3] and Kamiya and Sakka [4, 5] have shown that it is possible to prepare titania-silica glasses through this route, which involves hydrolyzing liquid metal alkoxides and subsequently heating the gel to produce a vitreous glass.

It is concluded from X-ray diffraction [6] and infrared analysis [7, 8] that the titanium ions are in tetrahedral coordination in the TiO<sub>2</sub>-SiO<sub>2</sub> glass system with up to 10.5 wt % TiO<sub>2</sub>. Also, these glasses are built up of a homogeneous network in which each TiO<sub>4</sub> tetrahedron is linked to four SiO<sub>4</sub> tetrahedra.

The objectives of this investigation are (1) to study the effect of atmosphere on the densification of the TiO<sub>2</sub>-SiO<sub>2</sub> monoliths, (2) to determine the physical properties as a function of densification temperature, and (3) to investigate the effect of densification on the coordination of titanium ions in the monolith throughout densification using Fourier transform infrared spectroscopy.

*Ultrastructure Processing of Advanced Materials.*

Edited by Donald R. Uhlmann and Donald R. Ulrich (deceased).

ISBN 0-471-52986-9 © 1992 John Wiley & Sons, Inc.

### 31.2. EXPERIMENTAL PROCEDURES

The monolithic titania-silica gels were prepared as previously reported by a prehydrolysis method using nitric acid as the catalyst [9]. Titanium isopropoxide (TIP) and silicon tetramethylorthosilicate (TMOS) were used as the alkoxide precursors. The sol was prepared by adding one-fourth of the stoichiometric amount of water into the desired amount of TMOS, followed by the addition of TIP under vigorous stirring. Additional water was then added to complete gelation after sufficient mixing. The gels were cast in polyethylene containers, aged at 75°C for 2 days, and slowly heated from room temperature to 170°C in 4 days. Discs of  $3 \times 1 \text{ cm}^2$  and rods of  $2 \times 9 \text{ cm}^2$  were obtained.

The gels were densified by conventional sintering in both ambient static and controlled dried air atmosphere. A heating rate of 50°C/hr below 600°C was used to remove physisorbed water and organics on the surface of the gel. The humidity in the ambient static air ranged from 65 to 80%. In the controlled dried air atmosphere, the water content was less than 6 ppm.

The surface area, average pore radius, and pore volume were determined by the  $\text{N}_2$  adsorption Brunaur-Emmett-Teller method using a Quantachrome Autosorb-6 sorption system [10]. Diamond pyramid hardness numbers were obtained using Micro Hardness Tester (Leco Co., Warrendale, PA) with a load of 100 g for 12 sec. Densities of the gel-glasses were determined using mercury and helium pycnometry (Quantachrome, MPY-1, Syosset, N.Y.).

### 31.3. RESULTS

Figure 31.1 plots the change of bulk density as a function of densification temperature for gels with different titania content. Below 700°C, the bulk density increases as temperature increases regardless of sintering atmosphere. Figure 31.2 shows the increase in skeletal density for 3, 5, and 8% titania-silica glasses

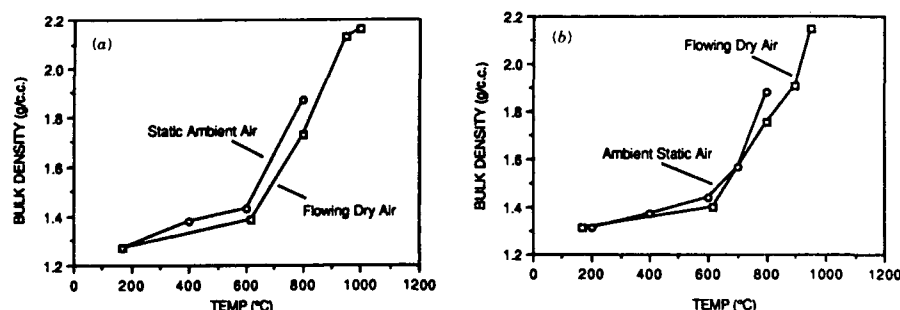


Figure 31.1. Bulk density as a function of densification temperature for gels with different titania content (a) 3%  $\text{TiO}_2$  (b) 5%  $\text{TiO}_2$ .

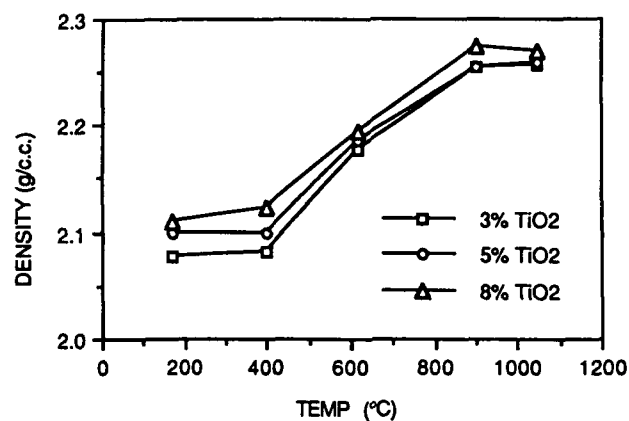


Figure 31.2. Skeletal density of titania-silica glasses as a function of sintering temperature.

as a function of sintering temperature. All the samples were ground into fine powder and treated in dried air atmosphere at the desired temperature for 2 hr.

The infrared spectra of the titania-silica gel-glasses are shown in Fig. 31.3. The intensity of the bands at 460, 945, and  $1050\text{ cm}^{-1}$  increase with successive increase in temperature. In addition, the peak maxima shift toward higher wavenumbers as the densification temperature increases.

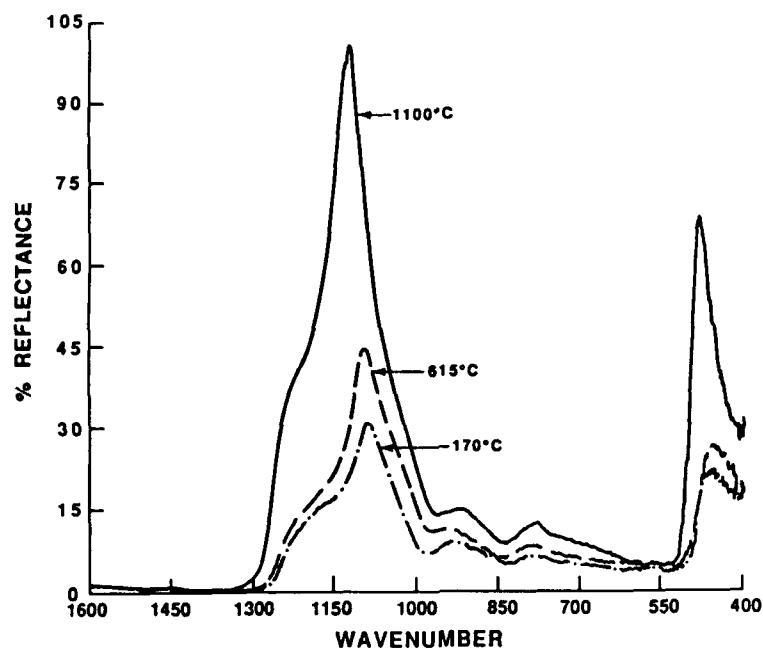


Figure 31.3. Infrared spectra for 3% titania-silica gel-glass.

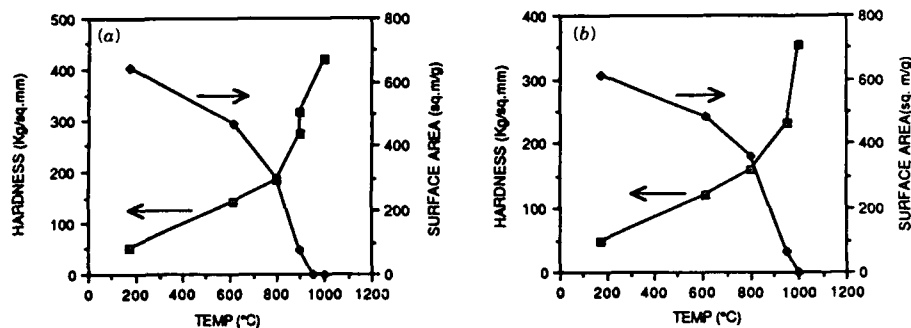


Figure 31.4. The effect of processing temperature on the hardness and surface area of titania-silica gel-glasses (a) 3%TiO<sub>2</sub> (b) 7%TiO<sub>2</sub>.

Figures 31.4 and 31.5 illustrate the effect of processing temperature on the physical properties of titania-silica gel-glasses when sintered in flowing dry air. The change of linear dimension, weight loss, and skeletal density as a function of temperature for 5% titania-silica gel-glass is shown in Fig. 31.6.

### 31.4. DISCUSSION

All the physical properties determined in this study, that is, microhardness, specific surface area, pore radius, pore volume, and bulk density, show no significant changes below 600°C regardless of TiO<sub>2</sub> content. Above 600°C, these properties change rapidly with temperature. However, there is about 6% shrinkage when the dried titania-silica gels are heated to 600°C for all the compositions studied. Gel shrinkage can be attributed to four mechanisms: (1) capillary contraction, (2) condensation-polymerization, (3) structural relaxat-

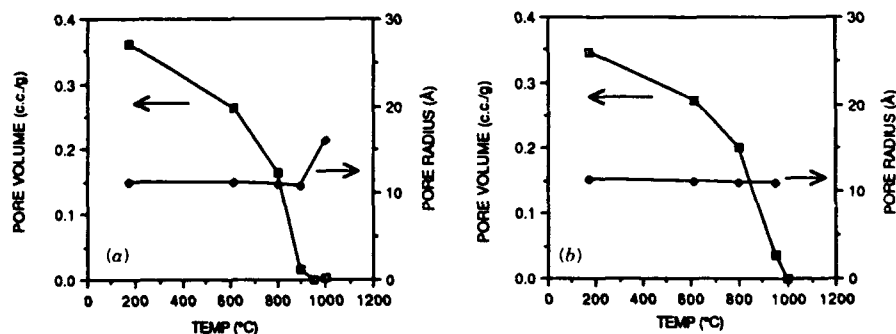


Figure 31.5. The effect of processing temperature on the pore volume and pore radius of titania-silica gel-glasses (a) 3%TiO<sub>2</sub> (b) 7%TiO<sub>2</sub>.

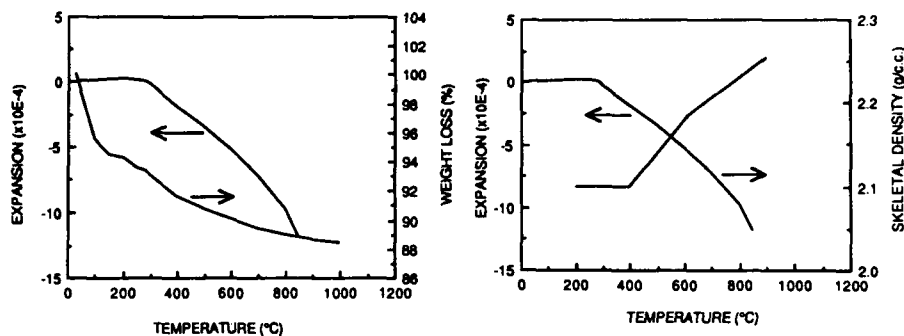


Figure 31.6. The change of linear dimension, weight loss and skeletal density as a function of temperature for a 5% titania-silica gel-glass.

ion, and (4) viscous sintering [11]. Below 400°C, the skeletal density of the gels is essentially constant (see Fig. 31.2) with 10% weight loss in this temperature regime as indicated by thermogravimetric analysis results (see Fig. 31.6). This weight loss is attributed to the desorption of water molecules and pyrolysis of the gels. Thus, shrinkage in this temperature range is attributed to condensation reactions,  $\text{Si-OH} + \text{HO-Si} \rightarrow \text{Si-O-Si} + \text{H}_2\text{O}$ , which result in a more rigid network and increases the bulk density and microhardness.

At higher temperature (<600°C), structural rearrangement or structural relaxation takes place due to available thermal energy, which results in the decrease of the excess free volume. This is confirmed by the increase of the skeletal density as shown in Fig. 31.2. Thus, both condensation and structural relaxation contribute to the shrinkage observed. In addition, the network structure is further strengthened as indicated in Fig. 31.3. The infrared peak at  $1050\text{ cm}^{-1}$ , attributed to the antisymmetric Si-O stretching mode within the  $\text{SiO}_4$  tetrahedra, and the peak at  $460\text{ cm}^{-1}$ , attributed to the bending mode of O-Si-O within tetrahedra and Si-O-Si between tetrahedra, are shifted toward higher wavenumbers, suggesting higher force constant for the vibrations. The vibrational band associated with  $\text{TiO}_4$  tetrahedra is obtained at  $945\text{ cm}^{-1}$ , as reported in the literature [8, 9].

It is observed that gels sintered under ambient static atmosphere all bloated at a temperature above 800°C. On the other hand, sintering conducted under a dried air atmosphere showed no sign of bloating at a temperature of 1000°C. This is presumed to be due to the lower water content of gels sintered in dried air atmosphere. Densification of silica glass increases with increasing OH content [12]. Consequently, densification starts earlier for gels with higher water content, as in the case of static ambient atmosphere, and bloating is observed, because pores are closed before water can be thermally desorbed.

There is no question that gels with higher titania content are more difficult to sinter. Because the size of the  $\text{Ti}^{4+}$  ion is larger than that of  $\text{Si}^{4+}$ , it is expected that as  $\text{Ti}^{4+}$  enters the glass network, both bond angle and bond length are

affected. Greigor et al. [13] and Morikawa et al. [14] have shown a Ti-O-Si bond angle of  $159^\circ$  and a Ti-O distance of 1.80 to 1.86 Å compared to the  $152^\circ$  Si-O-Si bond angle and 1.6-Å Si-O bond distance. Thus, the network structure "opens up" upon titania addition. The increase in densification of the  $\text{TiO}_2$ - $\text{SiO}_2$  glasses thus may be attributed to the introduction of more easily deformed Ti-O-Si bonds, which increase the ease of structural rearrangement.

### 31.5. CONCLUSIONS

Large, monolithic  $\text{TiO}_2$ - $\text{SiO}_2$  gel-glasses were produced using organometallic sol-gel technology. The physical properties of the gel-glasses do not change significantly below  $600^\circ\text{C}$  in either an ambient static or controlled dried air atmosphere. Above  $600^\circ\text{C}$ , the properties change rapidly with densification temperature. Bloating of the samples was observed when sintering was carried out in ambient static, but not in controlled dried air atmosphere. This was attributed to the difference in the water content of the samples, which resulted in the difference in densification rates. The network structure is strengthened as densification temperature increases, as indicated by the increase in the wavenumbers of infrared vibration peak. The vibrational band associated with  $\text{TiO}_4$  tetrahedra is obtained at  $945\text{ cm}^{-1}$ . The increase in densification with increasing titania concentration is explained in terms of the weaker nature of the Ti-O-Si bond, increasing the ease of structural rearrangement as titania content increases.

### ACKNOWLEDGMENT

Financial support from AFOSR Contract F49620-88-C-0073 is greatly appreciated.

### REFERENCES

1. P. C. Schultz and H. T. Smyth, *Amorphous Materials*, Wiley, New York (1972).
2. P. C. Schultz, *J. Am. Ceramic Soc.*, **59**, 214 (1976).
3. B. E. Yoldas, *J. Non-Cryst. Solids*, **38-39**, 81 (1980).
4. K. Kamiya and S. Sakka, *J. Mater. Sci.*, **15**, 2937 (1980).
5. K. Kamiya and S. Sakka, *J. Non-Cryst. Solids*, **32**, 357 (1982).
6. D. L. Evans, *J. Am. Ceramic Soc.*, **53**, 418 (1970).
7. K. Kusabiraki, *J. Non-Cryst. Solids*, **79**, 208 (1986).
8. H. R. Chandrasekhar and M. Chandrasekhar, *Solid State Comm.*, **31**, 329 (1979).
9. Y. C. Cheng and L. L. Hench, presented at the MRS spring meeting, Reno, Nev., April 5-9, 1988.
10. S. Wallace and L. L. Hench, in: L. L. Hench and D. R. Ulrich, Eds., *Science of Ceramic Chemical Processing* p. 148, Wiley, New York (1986).



11. C. J. Brinker and G. W. Scherer, *J. Non-Cryst. Solids*, **70**, 301 (1985).
12. J. Arndt, *J. Am. Chem. Soc.*, **52**, 285 (1969).
13. R. B. Gregor, F. W. Lytle, D. R. Sandstrom, J. Wong, and P. Schultz, *J. Non-Cryst. Solids*, **55**, 27 (1983).
14. H. Morikawa, T. Osuka, F. Marumo, A. Yasumori, and M. Yamane, *J. Non-Cryst. Solids*, **82**, 97 (1986).

## PART 4

---

# **Composites Including Organic-Modified Ceramics**

## 32

# CONVENTIONAL AND MOLECULAR COMPOSITES—PAST, PRESENT, AND FUTURE

W. WADE ADAMS AND SATISH KUMAR

### 32.1. INTRODUCTION

Advanced fiber-reinforced composite materials are here to stay in aerospace applications; they are no longer laboratory curiosities or trial materials forced upon the design engineer. The fraction of the structural weight of modern military aircraft composed of advanced composites is rapidly increasing, with aircraft of over 50% already flying. In civilian aviation, the Beechcraft STARSHIP exemplifies the (nearly) 100% advanced composite airplane. This dramatic increase in usage is due to a number of factors, including increased user confidence, demonstrated performance over time, and greatly improved property levels. Much of the impetus in the United States has come from the Air Force Materials Laboratory's programs seeking to advance the state of the art, but the growing willingness on the part of the defense aerospace contractors (airframe manufacturers) to incorporate composite technology comes from performance and economic factors. Research and development in advanced fiber-reinforced composites is driven by defense needs, but the total aerospace and military use of composites is only 1.5% by weight of the total worldwide use of composite materials (Fig. 32.1) [1]. However, the cost of aerospace composites is nearly half that of all composite materials. This Chapter will review

*Ultrastructure Processing of Advanced Materials.*

Edited by Donald R. Uhlmann and Donald R. Ulrich (deceased).

ISBN 0-471-52986-9 © 1992 John Wiley & Sons, Inc.

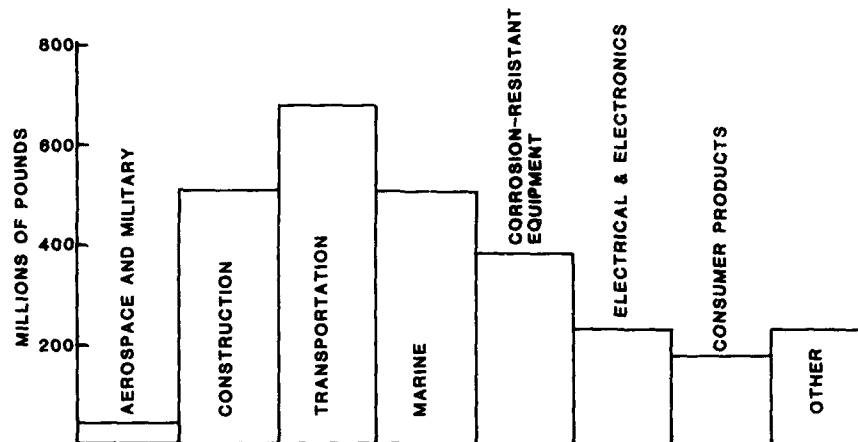


Figure 32.1. 1988 world-wide composites use [1].

progress in the area of conventional and advanced composites using polymeric or carbon-reinforcing fibers with thermoset or thermoplastic matrix resins. Lower performance materials such as glass/polyester composites are only included for comparison.

Currently, experimental polymeric fibers have tensile stiffness (modulus) and strength approaching 50 and 1 mpsi, respectively, with a theoretical tensile modulus of about 100 mpsi [2]. Commercial pitch-based carbon fibers with tensile modulus of up to 130 mpsi have a tensile strength of 570 kpsi. Commercial polyacrylonitrile (PAN)-based carbon fibers are available with tensile strength of up to 1 mpsi or with modulus of 80 mpsi. However, the full benefits of high fiber strength and modulus have not been utilized in structural applications, because all polymeric fibers and the high modulus carbon fibers have poor axial compressive strength [3].

Thermoset and thermoplastic matrix resins are now available with service temperatures in excess of 500°F. Developments in high-temperature matrix resins have reached the stage that further improvements in the matrix thermal stability alone are not useful unless accompanied by increased thermooxidative stability of the fiber and its surface finish. Variations in electrical and thermal conductivity of composites are useful for a number of potential applications, including radar transparency, de-icing applications on aerospace structures, and electromagnetic shielding.

The recently evolved *molecular composite concept* uses a rigid-rod polymer to reinforce a flexible matrix polymer at the molecular level in a manner analogous to a macroscopic fiber-reinforced composite [4]. Molecular composites have potential advantages over conventional fiber-reinforced composites.

Conventional composites can have poor adhesion between the fiber and matrix and invariably have a mismatch in thermal expansion coefficients (CTE) between fiber and matrix. The problem of weak interface and mismatch in CTE is likely to be eliminated in molecular composites due to molecular level mixing. The possibility also exists for achieving even better properties from synergistic effects because of molecular level mixing.

### 32.2. FIBERS

The field of high-performance fibers for use in composites continues to make rapid progress. Commercial fibers currently being used in advanced composites include carbon (T300, T1000, P100), glass, boron, SiC, alumina, aramid (Kevlar), and extended-chain polyethylene (Spectra), whose specific properties are shown in Fig. 32.2. Significant property improvements continue to be made in many of these commercial fibers.

Carbon fibers were invented approximately simultaneously in England and the United States by Sir Joseph Swan and Thomas Edison, respectively, in the 1860s. The intended application was not structural, but electrical in nature, and filaments made by carbonizing bamboo or cotton thread were used widely in electric Ediswan lamps until replaced by tungsten wire in the 1920s (for interesting reviews of this early history, see Refs. 5 and 6 and references cited therein). Glass fibers were used with polyester matrix resins in World War II for fiberglass composite radomes, leading to a very popular postwar industry for shaped structures, such as boat hulls and pools. However, the weight penalty of glass-fiber composites led scientists to continue research into higher specific property fibers. In the early 1960s, Watt at the Royal Aircraft Establishment produced the first high performance carbon fiber from PAN precursor fiber, which accelerated interest in carbon fibers and helped spawn an active industry in England, Japan, and the United States, mostly focused on structural aircraft applications [6]. Currently PAN-based carbon fibers with tensile strength as high as 1 mpsi (with modulus of 35–42 mpsi) and modulus as high as 80 mpsi (with tensile strength of 500 kpsi) are commercially available. Pitch-based carbon fibers are available with a tensile modulus of over 120 mpsi and tensile strength of 550 kpsi [3]. Although extremes in modulus and strength have been achieved, a better balance of both properties is still sought.

The early synthetic fibers (e.g., nylon and polyester) were useful only for low-temperature applications (typically less than 100°C). Compared to other structural materials of that time these early fibers were also characterized by relatively low mechanical properties, significant viscoelasticity, and poor environmental and chemical resistance. Poly(paraphenylene terephthalamide) (PPTA) was the first polymeric fiber to be developed and commercialized (as

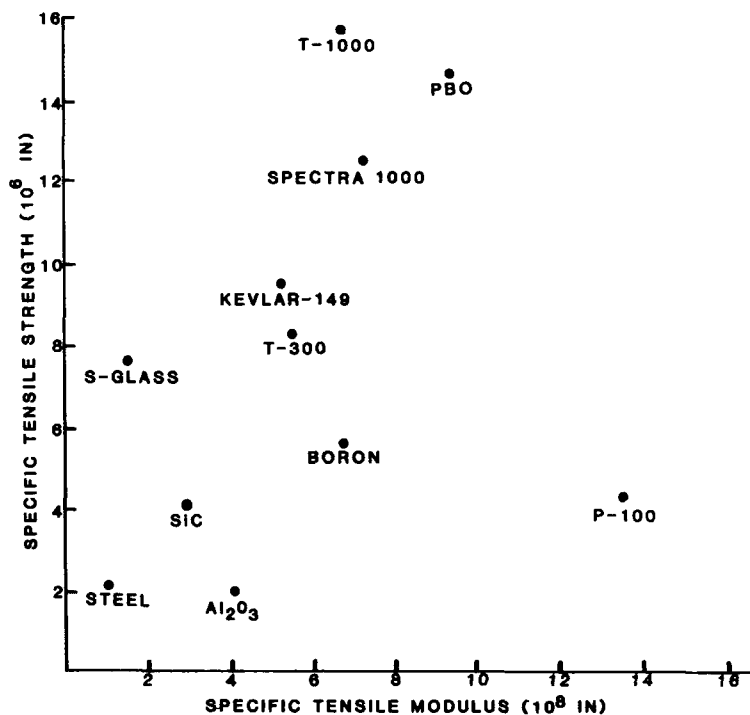


Figure 32.2. Fiber specific properties.

Kevlar in 1970), with high thermal stability, good mechanical properties, and good resistance to chemicals and environmental conditions [7]. These *aramid* fibers have found composite applications including projectile-proof armor and filament-wound pressure tanks. With recent advancements in processing technology, it is now possible to prepare polyethylene fibers in the extended molecular chain conformation, characterized by high modulus and high tensile strength, but these fibers (such as Spectra) are still limited to low-temperature applications (less than 130°C) [8]. The new aromatic heterocyclic rigid-rod polymer fiber PBO has exceptionally high thermal stability (onset of degradation, 600–700°C), excellent environmental and chemical resistance, and a good balance of mechanical properties (40- to 50-mpsi modulus, 500- to 850-ksi strength) [2].

The full potential benefits of high fiber strength and stiffness are not being currently realized in structural composites. This is because the improvements in fiber stiffness and strength are not associated with an improvement in the key composite property for aerospace structural applications, namely, axial com-

pressive strength. With the exception of 35- to 42-mpsi modulus PAN-based carbon fiber, axial composite compressive strength is limited due to poor fiber axial compressive strength as evidenced by fiber buckling failure [3].

Similarly, achievements of high stiffness and strength in organic polymeric fibers, such as Kevlar and PBO, have yielded only limited benefits in composites, because all current polymeric fibers have a compressive strength of less than about 70 kpsi. In the past, significant research efforts have focused on understanding and improving the tensile strength and modulus of materials in general and of high-performance fibers in particular. However, it is only recently that the research and development issues related to increasing the compressive strength of high-performance fibers have begun to be addressed in greater depth. Improvements in the compressive strength of polymeric and carbon fibers would be a major breakthrough in both fiber and composite technology. Such issues take added importance when material requirements for advanced projects such as vertical takeoff and landing aircraft or ultra lightweight structures are considered [9]. Fiber electrical properties and thermal conductivity are also currently of interest. For radar transparency, low electrical conductivity materials are preferred, and in this regard polymeric fibers are useful. However, for a host of other applications such as electromagnetic interference shielding, aircraft de-icing, and lightning strike-tolerant aircraft, high electrical conductivity is desirable. Therefore research efforts are in two diverse directions—to increase and to decrease electrical conductivity—while maintaining or improving the mechanical properties. To increase conductivity, carbon fibers have even been coated with various metals. Intercalation of pitch-based carbon fibers is also being pursued for increased conductivity. For example, intercalation of the high-modulus pitch-based P100 fiber with Br is reported to have increased its axial fiber electrical conductivity by a factor of 5 with almost no change in mechanical properties [10].

Active areas of research in high-performance polymeric and carbon fibers for composites are highlighted in Table 32.1 (see Ref. 11 for an overview of high-performance fibers).

**TABLE 32.1. Fibers—Future Research Areas**

- 
- Very high modulus
  - Very high strength
  - Balanced high strength and modulus
  - Improved compressive strength
  - Variations in electrical conductivity
  - Variations in thermal expansion coefficients
  - Thermooxidative stability—fiber and finish
-

TABLE 32.2. Matrix Resins

	$T_G (T_M)$ (°C)	Process Temperature (°C)	Tensile Strength (kpsi)	Tensile Modulus (kpsi)	Fracture Energy ( $G_{IC}$ ) (in.-lb/in. <sup>2</sup> )
Polyetheretherketone	143(343)	400	15	450	<23
Polyphenylene sulfide	90(290)	343	12	630	
Polyamideimide (Torlon)	275	400	9	670	19
Polyetherimide (ULTEM 1000)	217	343	15	430	19
Polyimide (AVIMID K-III)	251	350	15	550	11
Polysulfone (UDEL P-1700)	190	300	10	360	14
Polyarylsulfone (RADEL A400)	220	330	10	310	20

Source: Adapted from Ref. 14.



### 32.3. MATRIX MATERIALS

The two types of polymeric matrix materials (resins) used in composites are thermosets (TS) and thermoplastics (TP). In high-performance composites, epoxy is the oldest and most common thermosetting matrix in current use and is available with service temperature of over 350°F. Other newer TS's of current interest are the bismaleimides (BMI) and the acetylene-terminated (AT) resins. Polypropylene, polyamides, and polycarbonate are examples of the common TP matrices at the lower end of the temperature performance scale. PEEK (polyetheretherketone) and PPS (polyphenylenesulfide) are examples of the current high-performance TP matrices (see Refs. 12–14 for overview of matrix resins). New developments in high-temperature TP's are becoming very useful for high-performance, high-temperature composites for aerospace applications. Some of the TP matrix resins available today and their properties are listed in Table 32.2. This list is by no means complete, and further development continues.

Compared to the composites using thermosetting matrices, composites using TP matrices offer some advantages and some disadvantages. Advantages include superior damage tolerance and interlaminar fracture toughness (although new heterogeneously toughened TS's are vastly improved), indefinite prepreg life, and ease of forming odd-shaped parts by using processes such as thermoforming. Because of the flow properties, composites using TP matrices may in some cases be reprocessed and may offer easier repairability. Disadvantages of TP's are difficulty in making uniform prepregs (because of high viscosity), necessitating very high processing temperatures, and the possibility of creep, although creep in composites is drastically reduced from creep in the TP matrix alone. A list of comparative attributes is shown in Table 32.3.

### 32.4. COMPOSITES

People have long used structural composites: Straw-reinforced mud for house construction offers adequate mechanical properties and is cheap and repairable, and processing training is easy! Although it is commonly believed that advanced composites date from the 1960s, the first documented use of a composite in the air was a flax fiber-reinforced phenolic resin composite called *Gordon Aerolite*, which was tested at Duxford, Cambridge, in 1937 [5]. Development work continued on the concept, not just because of possible weight savings, but also because of potential shortages of metals during the war. Paper/phenolic trailing edge skins were tested in 1941–1942, but the bombers sent to North Africa all suffered cracks, and the ones kept in England wrinkled during the wet winter [5].

The first primary aircraft structural application was a glass fiber-reinforced

TABLE 32.3. Comparison of Thermoset and Thermoplastic Matrices

Property	Thermosets	Thermoplastics
Matrix formulation	Complex	Simple
Melt viscosity	Very low	High
Fiber wetting	Easy	Difficult
Prepreg handling	Good	None/fair
Prepreg stability	Poor	Excellent
Processing cycle	Long	Short to long
Processing temperature/pressure	Low to moderate	High
Fabrication cost	High	Low (potentially)
Solvent resistance	Excellent	Poor to good
Environmental resistance	Fair	Good
Repairability	Poor	Good
Recyclable	No	Yes
Impact resistance	Poor to good	Good
Property data base	Good	Fair

Source: Adapted from Ref. 14.

phenolic resin composite fuselage on the BT-15, tested at Wright Field (now Wright-Patterson Air Force Base) during World War II [15]. Composites have featured prominently in aircraft research and development activities ever since, although actually replacing metal airplane structural components with composites has been a slow and sometimes painful process. The extent to which aerospace composites have succeeded is shown by the Federal Aviation Administration's recent certification of the first commercial civilian aircraft whose structure is made completely from composites, the Beechcraft STARSHIP [16].

Modern composites evolved from chopped-fiber reinforcement (as in fiber-glass), and typical properties of chopped-fiber composites are listed in Table 32.4. These are used today for sheet molding compound (SMC) for automotive applications, sports equipment, boat hulls, and so on. In chopped-fiber composites, the full reinforcement potential of the fiber for mechanical properties is not realized due to the low aspect ratio (length to diameter) and low volume fraction of fibers, but chopped-fiber composites can be made isotropic with random orientation of the fibers.

Significantly higher mechanical properties are achieved with continuous fiber-reinforced composites, the focus of most advanced composite activity. Advanced composites manufacturing is through unidirectional and multidirectional laminates. First, a prepreg is formed, which is a sheet made from a thin layer of unidirectional fibers impregnated with a matrix resin. Next, prepreg sheets are "laid up" into layers of specified arrangements, for example, a unidirectional laminate has all fibers in the same direction, whereas a "quasi-

TABLE 32.4. Properties of Chopped Fiber Composites (40 wt %)

System	Epoxy Glass	Epoxy Carbon	Nylon 66 Carbon	Nylon 66 Aramid	PPS Glass	PPS Carbon	PES Carbon	PEEK Carbon	PEEK Ni- Carbon
Density (g/cm <sup>3</sup> )	1.90	1.50	1.33	1.24	1.67	1.46	1.52	1.46	1.64
Tensile strength (kpsi)	35	30	36	17 <sup>a</sup>	20	26	31	39	28
Tensile modulus (mpsi)			4.2	1.2	2.0	4.8	3.5	4.4	3.4
Flexural strength (kpsi)	85	54	52	22	30	40	42	54	38
Flexural modulus (mpsi)	4.2	7.2	3.4	0.95	1.6	4.1	3.2	3.2	2.6
Compressive strength (kpsi)	42	36	25	21	25				
Ixod impact strength (ft-lb/in)			1.6	1.6	1.4	1.2	1.4	1.7	1.2
Electrical resistivity (ohm-cm)	7.5 × 10 <sup>14</sup>		30		10 <sup>16</sup>	30		30	0.1

<sup>a</sup>Ultimate tensile strength.

Source: Adapted from Ref. 17.

Abbreviations: PPS, polyphenylenesulfide; PES, polyethersulfone; PEEK, polyetheretherketone.

isotropic" laminate might have layers alternating by  $0^\circ$ ,  $-45^\circ$ ,  $+45^\circ$ ,  $90^\circ$  rotation of the fiber direction in the plane of the laminate. Finally, the laminate is consolidated by heat and pressure to distribute the resin uniformly among the fibers and to cure it chemically. This process is expensive for complex-shaped parts, amounting to 70% of the total cost of the part [18]. Forming of complex parts from laminates can create weak joints, and delamination can also be a problem.

Textile technology (braiding, knitting, and weaving) is playing a key role now in some structural composites manufacturing methods. Nearly final-shaped fabrics are made either from reinforcing fibers alone (to be injected with resin later) or with commingled fibers (both reinforcing and TP) in the near net-shape mold [19]. For composites made from woven fiber preforms, the damage tolerance throughout the part comes from fibers. At the joints in a laminated composite part damage tolerance mostly comes from the resin.

The properties of various laminates employing different fibers and matrices are listed in Tables 32.5, 32.6, and 32.7. For all matrices, translation of fiber modulus into composite modulus nearly follows a volume fraction rule of mixtures. For composite tensile strength, however, fiber tensile strength is not as efficiently translated. The biggest difference between TS matrix (epoxy) and TP matrix composites is in fracture toughness, where TP's are up to an order of magnitude tougher than simple TS's.

High-temperature resistance is another area of importance for composites and fibers. Until recently thermooxidative stability of carbon-fiber composites has been limited due to matrix thermal stability limitations. However, the development of high-temperature-resistant matrix resins has reached the stage where further improvements in matrix thermal stability alone will not be sufficient. Recent research shows that a composite of PMR-15 resin with epoxy-sized (coated) carbon fiber has a useful life of about 2500 hr at  $550^\circ\text{F}$ . At this temperature, debonding at the resin-fiber interface (presumably due to coeffi-

TABLE 32.5. Carbon Fiber/Epoxy Unidirectional Composite Properties

Fiber	T300	T50	T650	T1000	P55	P100
Tensile (brittle resin)						
Strength (kpsi)	270	190	350	500	105	165
Modulus (kpsi)	20	35	25	23	34	70
Tensile (ductile resin)						
Strength (kpsi)	310	205	445	550	130	175
Modulus (mpsi)	20	35	25	34	70	
Compression						
Strength (kpsi)	250	140	240	245	70	40
Modulus (mpsi)	18	34	22	28	73	

Sources: Adapted from Refs. 20 and 21.

TABLE 32.6. Unidirectional Composite Properties

	XAS/M-ATB (AF-8)		XAS/M-ATS (AF-20)		Celion ST/NARMCO 5245C		Celion 6000/BMI H795E	
	Strength (kpsi)	Modulus (kpsi)	Strength (kpsi)	Modulus (mpsi)	Strength (kpsi)	Modulus (mpsi)	Strength (kpsi)	Modulus (mpsi)
Tension								
-67°F	330	21	285	21	350	22		
RT	320	21	300	20	360	21	205	17
200°F					355	21	185 <sup>a</sup>	18 <sup>a</sup>
Flexure								
RT	260	18	275	18			265	17
450°F	160	16	110	17			180 <sup>a</sup>	17 <sup>a</sup>
425°F/wet	114	16	46	8				
Compression								
RT	180	22	185	19	240	21	200	18
200°F					225	21		
450°F	105		71	18			115 <sup>a</sup>	17 <sup>a</sup>
425°F/wet	105		35	18				
$G_{IC}$ (in.-lb/in. <sup>2</sup> )		1.8		3.7				2.0

Sources: Adopted from Refs. 22 and 23.

Note: ATB and ATS are acetylene-terminated resins developed at the Air Force Materials Laboratory [22]. XAS and Celion are PAN-based carbon fibers developed by Courtaulds and BASF, respectively. NARMCO and H795E are bismaleimide (BMI) matrix resins.

TABLE 32.7. Unidirectional Fiber/Thermoplastic Composite Properties

Resin	Fiber	Tensile Strength (kpsi)	Tensile Modulus (mpsi)	Compressive Strength (kpsi)	$G_c$ (in.-lb/in. <sup>2</sup> )
PEEK (APC2) <sup>a</sup>	AS-4	325	20	155	10.7
APC (HTX) <sup>a</sup>	AS-4		20	165	12.7
PEKK <sup>a</sup>	AS-4			200	5.7
PPS <sup>b</sup>	AS-4	240	20	95	5.1
TORLON-C <sup>c</sup>	C-6000	200	21	200	10.0
ULTEM 1000 <sup>d</sup>	AS-4		20		6.1
AVIMID K-III <sup>e</sup>	IM-6				9.7
UDEL P1700 <sup>f</sup>	AS	195	19	150	7.7
J-2 <sup>g</sup>	Kevlar 49	190	11	40	

Source: Adapted from Ref. 14.

Abbreviations used: PEEK, polyetheretherketone; APC/HTX: PEKK, PPS, polyphenylenesulfide.

<sup>a</sup>Both PEEK and APC (HTX) are different grades of PEEK, poly(aryletheretherketone).

<sup>b</sup>Polyphenylenesulfide

<sup>c</sup>Poly(amideimide)

<sup>d</sup>Poly(etherimide)

<sup>e</sup>Polyimide

<sup>f</sup>Polysulfone

<sup>g</sup>Poly(arylamide)

cient of thermal expansion mismatch between fiber and matrix) was a major problem, which subsequently allowed fiber oxidation [24]. This calls for improvements in the thermooxidative stability to not only the fiber, but also its finish coating.

A comparison of the mechanical properties of TP/CF composites with TS/CF composites indicates that the axial compressive strength of all the TP/CF composites is consistently lower than for TS/CF composites. For example, TS/CF axial compressive strength (using the high compressive strength carbon fibers) is generally reported in the range of 200–240 kpsi, whereas for the same carbon fibers the TP/CF composites exhibit an axial compressive strength of 95–200 kpsi (95 kpsi was reported with PPS and 200 kpsi was reported with PEEK, the fiber in both cases was AS-4) [14]. Other mechanical properties for TP/CF composites, such as flexural strength, flexural modulus, short-beam shear strength, fracture toughness, and longitudinal and transverse properties are good. However, this is a very general statement considering the large number of TP matrices available with wide variations in properties. Observation of lower properties (for example, flexural strength of 187 kpsi, transverse tensile strength of 4.6 kpsi for PPS/AS-4 composite) [14] appears to be the exception rather than the rule for the TP/CF composites.

In making these comparisons, however, a couple of points should be kept in mind: (1) the processing technology of TP/CF composites lags that of TS/CF composites and (2) the property data base of the TP/CF composites is limited compared to that of the TS/CF composites.

Low compressive strength of the TP/CF composites can be attributed to a number of factors, including fiber matrix interfacial strength, and matrix modulus. However, in this regard processing temperature differences between thermosetting resins (generally lower than 350°F) and high-performance TP's (650°–850°F) may also be responsible. This is because of differences in the coefficient of thermal expansion between the fiber and the matrix, which causes residual compressive stresses in the fibers after lamination. These stresses are higher in high-performance TP/CF composites than in TS/CF composites because of the higher processing temperatures. The higher residual compressive stresses in the fiber may result in the lower observed compressive strength in TP/CF composites. Resin morphology changes may also be a contributing factor that has not been thoroughly explored.

It has now been established that the high-temperature TP/CF composites have desirable mechanical properties and offer toughness, some possibility of reprocessing and reforming of parts, and in some cases easier repairability. However, work continues for achieving uniformity in processing, for minimizing the fiber residual stresses from high-temperature processing, for other processing optimizations such as the fiber–matrix interfacial strength improvement, and for process innovations such as diaphragm forming. Also, for design considerations, a more extensive data base will have to be developed for TP composites.

TABLE 32.8. Mechanical Properties of Rigid-Rod Molecular Composites [26]

Material	Tensile Modulus (measured)		Tensile Modulus (predicted)		Tensile Strength		Elongation (%)
	GPa	(mpsi)	GPa	(mpsi)	GPa	(kpsi)	
PBZT FIBER	300	(43)	615	(88)	3.0	(430)	1.6
30% PBZT/70% AB-PBI <sup>a</sup> molecular composite							
Spun fiber	120	(17)	184	(26)	1.3	(190)	1.4
Spun film	88	(13)	87	(12)	0.92	(130)	2.4
(quasi isotropic)							

Source: Adapted from Ref. 26.

<sup>a</sup>(AB-PBI is an aromatic heterocyclic semiflexible matrix polymer).



### 32.5. MOLECULAR COMPOSITES

Significant problems with conventional fiber-reinforced composites include mismatch of CTE between the fiber (often negative along the fiber) and the matrix (usually large and positive). In thermal processing and in actual use, adhesion between fiber and matrix can be adversely affected by this mismatch. These detrimental interface problems spawned a new concept in composites. The rigid-rod molecular composite was conceived in 1969 as a homogenous mixture of rigid polymer molecules and flexible matrix polymers, where reinforcement occurred at the molecular level [4]. The molecular composite does not have macroscopic interfaces and may offer synergistic effects in other properties as well, such as temperature or solvent resistance, due in part to the peculiar nature of the true rigid-rod polymer molecule. This development was predicated on availability of true rigid-rod molecules that had very high-chain modulus, due to aligned covalent chemical bonds with very limited rotational flexibility [25], and excellent chemical, environmental, and thermal resistance due to their aromatic heterocyclic chemical backbone. Development activity has concentrated on improving processability of these systems, both with TP matrix polymers and TS's, but commercial materials are not yet available. Properties of the initial molecular composites are listed in Table 32.8 [26] for comparison to conventional composites in Tables 32.5 and 32.6.

### 32.6. THE FUTURE

Significant growth is expected in advanced composites over the next decade. Some of the factors which are expected to govern the growth [27] are listed in Table 32.9.

We have already seen that confidence is rapidly improving, especially because the tremendous investment in processing technology and for making better fibers and matrices has resulted in high-quality composites. However, cost often remains very high, but is expected to decrease with increased production volume. The lack of more extensive use of composites in many applications (e.g., in medical applications) is attributed to a number of reasons including the lack of skilled technical personnel in the field. A quadrupling of advanced composites

**TABLE 32.9. Advanced Composites Significant Factors for Future Growth**

- 
- User confidence
  - Improvement in processing technology
  - Material quality
  - Cost
  - Composites education/training
  - Government funding
-

use over the next decade will produce critical shortages of skilled composite personnel at all levels unless training programs are also expanded.

Exciting new uses of composites are on the horizon. The Air Force's Project Forecast II identified ultralightweight structures as a major need for further research and development activity, primary to be met by composite materials approaches [28]. Building further on that concept, multifunctional materials is the concept of incorporating different (unique) attributes of one or more into a design that can perform multiple functions. One example, the *smart skin*, is a desirable future technology [29]. It is expected that future aircraft composite skin will have built-in antennae, sensors, avionics, and de-icing capabilities. This will not only reduce the aircraft's weight, but will also improve the aerodynamics.

Smart composites are also being developed as a means for sophisticated nondestructive testing. Optical fibers embedded into the composites during manufacturing are used for this purpose. Smart composites are initially being used for self-determination of fracture, fatigue, crack growth, and delamination. A number of other variables including pressure, vibration, temperature, and strain can also be measured.

The concept of adaptable wing structure, flexible ship hulls, and variable response sports equipment opens up a whole new area in composite manufacturing technology. This will also require redesigning the entire structure or entire system rather than just replacing individual (metal) parts with composites, as has so often been done in the past. The ability to process molecular composites in large scale offers even more flexibility in designing more adaptive structures. If molecular composites can be developed with even better properties, less weight, and higher reliability than conventional advanced fiber-reinforced composites, then the concept of concurrent engineering becomes a reality, where we can optimize materials, design, manufacturing, and supportability simultaneously. We may even some day see composite aircraft design (molecular composites?) that truly mimics mother nature—airplane wings as flexible as a bird's wings!

## ACKNOWLEDGMENTS

The authors gratefully acknowledged many useful discussions with guidance from Tobey Cordell and Captain David Curliss of the Structural Materials Branch, Materials Laboratory, in the preparation of this paper.

## REFERENCES

1. Composites Institute, Society of the Plastics Industry, as quoted by Ann Thayer in *Chem. Eng. News*, p. 16 (October 10, 1988).
2. W. W. Adams and R. K. Eby, *Mater. Res. Soc. Bull.*, **12**, 22-26 (1987).

3. S. Kumar and T. E. Helminiak, in: W. W. Adams, D. E. McLemore, and R. K. Eby, Eds., *The Materials Science and Engineering of Rigid-Rod Polymers*, Materials Research Society Proceedings 134, p. 363.
4. T. E. Helminiak, Reinforcement of Polymeric Matrices with Rigid-Rod Macromolecules, presented at the Biennial Symposium, American Chemical Society, San Diego, Calif. (1988).
5. J. E. Gordon, *The Science of Structures and Materials*, Scientific American Books, New York (1988).
6. R. Bacon and C. T. Moss, in: R. B. Seymour and G. S. Kirshenbaum, Eds., *High Performance Polymers: Their Origin and Development*, pp. 341-353, Elsevier, New York (1986).
7. S. Kwolek, U.S. Patent No. 3,600,356 (1971).
8. H. W. Chang and G. C. Weedon, *Polymer News*, **12**, 102 (1986).
9. V. Wiggotsky, *Plastics Eng.*, pp. 25-32 (October 1988).
10. D. A. Jaworske, R. D. Vannucci, and R. Zinolabedini, *J. Composite Mater.*, **21**, 580 (1987).
11. A. J. Klein, *Adv. Composites*, pp. 32-44 (May-June 1988).
12. *Modern Plastics Encyclopedia*, pp. 19-98 (1985-1986).
13. J. King, M. Chaudhari, and G. DiSalvo, in: *32nd International SAMPE Symposium Proceedings*, pp. 59-67 (1987).
14. N. J. Johnston and P. M. Hergenrother, in: *32nd International SAMPE Symposium Proceedings*, pp. 1400-1412 (1987).
15. G. B. Rheinfank and W. A. Norman, Army Air Forces Technical Report No. 5159, November 8, 1944.
16. *Adv. Composites*, p. 59 (July-August 1988).
17. *Mater. Eng.*, p. 235 (December 1986).
18. Kline & Co., Inc., quoted in *Adv. Composites*, p. 12 (July-August 1988).
19. *Adv. Mater. Processes*, pp. 59-66 (January 1989).
20. I. M. Kowalski, in: *32nd International SAMPE Symposium Proceedings*, p. 953 (April 1987).
21. S. Wamane, T. Hiramatsu, and T. Higuchi, in: *32nd International SAMPE Symposium Proceedings*, p. 1928 (April 1987).
22. P. A. Steiner, J. Browne, M. J. Blair, and J. M. McKillen, in: *32nd International SAMPE Symposium Proceedings*, p. 807 (April 1987).
23. H. D. Stengenberger et al., in: *32nd International SAMPE Symposium Proceedings*, p. 1054 (April 1987).
24. C. H. Sheppard, *SAMPE Quart.*, 1988.
25. S. G. Wierschke, in: W. W. Adams, D. E. McLemore, and R. K. Eby, Eds., *The Materials Science and Engineering of Rigid-Rod Polymers*, Materials Research Society Proceedings 134, p. 313.
26. S. Krause, in: W. W. Adams, D. E. McLemore, and R. K. Eby, Eds., *The Materials Science and Engineering of Rigid-Rod Polymers*, Materials Research Society Proceedings 134, p. 511.
27. S. Witzler, *Adv. Composites*, pp. 62-66 (January-February 1989).
28. J. W. Canan, USAF in the 21st Century, *Air Force Magazine*, **69**, 47 (1986).
29. L. Leonard, *Adv. Composites*, p. 47 (March-April 1989).

## STRUCTURE-PROPERTY RELATIONSHIPS IN SILICA-SILOXANE MOLECULAR COMPOSITES

DALE W. SCHAEFER, J. E. MARK, L. JIAN, C.-C. SUN,  
D. W. MCCARTHY, C.-Y. JIANG, Y.-P. NING,  
AND STEVE SPOONER

### 33.1. INTRODUCTION

Although it is widely recognized that multiphase materials dispersed at the 100-Å level offer unprecedented opportunity to enhance material properties, successful techniques for achieving these so-called molecular composites (MC's) are limited. In the absence of systematic relationships between synthetic protocol, structure, and properties, it is difficult to optimize these materials. Even for conventional composites, for example, the properties (ramification, stiffness, interfacial properties, etc.) of the ideal filler are not well established.

Two factors have limited the understanding of the microstructure of complex phase-separated materials: the absence of unambiguous methods for characterizing structure and the lack of reasonable models to predict structure based on chemical and physical parameters. Substantial progress, however, has been made in both these areas because of advances in instrumentation, advances in the interpretation of scattering from disordered systems, and advances in

*Ultrastructure Processing of Advanced Materials.*


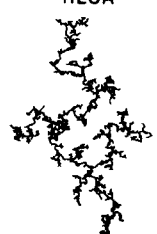
Edited by Donald R. Uhlmann and Donald R. Ulrich (deceased).

ISBN 0-471-52986-9 © 1992 John Wiley & Sons, Inc.

development of simple models for complex disorderly growth processes. We attempt to build on these advances to enhance our understanding of composites.

We investigate the relationship between synthesis, structure, and properties of silica-filled siloxane rubbers. Based on insights from kinetic growth models and known results for solution polymerization of silicon alkoxides, we develop synthetic schemes designed to generate fillers of varying degree of ramification. With the aid of fractal geometry, we infer relevant aspects of the filler structure from small-angle X-ray (SAXS) and small-angle neutron scattering (SANS). We demonstrate that filler structure does indeed depend on synthetic protocol. From the observed correlations between structure and mechanical properties, we speculate on the nature of the optimum filler for increased toughness in silicone elastomers.

Fractal concepts will aid in tracing filler structure to polymerization processes. The strategy is to map growth processes in precursor phases onto fractal kinetic growth models like those shown in Fig. 33.1. These computer-simulated two-dimensional structures result from simple rules (typically governing mass transport and accretion) that characterize growth processes occurring far from equilibrium. In solution, the polymerization of silicon alkoxides can mimic these models, suggesting that filler structure of silica-filled siloxanes could be controlled through polymerization protocol. Kinetic growth models like Fig. 33.1 as well as fractal geometry play an important role in our methodology. To

	REACTION-LIMITED
MONOMER-CLUSTER	EDEN  $D = 3.00$ (a)
CLUSTER-CLUSTER	RLCA  $D = 2.09$ (b)

**Figure 33.1.** Simulations of kinetic models in the reaction-limited regime. (a) A compact Eden cluster that arises by reaction-limited monomer cluster growth. (b) The cluster-cluster analogue. (Courtesy of Paul Meakin.)

successfully establish the link between synthesis, structure, and properties, it is necessary to understand these concepts as well as small-angle scattering (SAS).

### 33.2. FRACTAL GEOMETRY

Fractal geometry [1-3] is a natural description for disordered objects ranging from macromolecules to the earth's surface. These objects often display *dilation symmetry*, which means they look geometrically self-similar under transformation of scale such as changing the magnification of a microscope.

Structures like those in Fig. 33.1 can be simply characterized with single parameter  $D$ , the fractal dimension. The fractal dimension is defined as the exponent that relates the mass,  $M$ , of an object to its size  $R$ :

$$M \sim R^D \quad (1)$$

Note that Eq. 1 also applies to normal Euclidean objects such as rods, disks, and spheres for which the exponent  $D$  is equal to 1, 2, and 3, consistent with the common notion of dimensionality. For fractal objects, however, the exponent need not be integral.

Objects like the cluster in Fig. 33.1a are described by Eq. 1 and are called mass fractals of which polymers are a prime example [2]. By contrast, surface fractals are uniformly dense (that is, colloidal,  $D = 3$ , as opposed to polymeric), but have a rough surface. Surface fractals share the self-similarity property, however, in the sense that if surface is magnified, its geometric features do not change. Mathematically surface self-similarity is represented by an analog of Eq. 1,

$$S \sim R^{D_s} \quad (2)$$

where  $S$  is the surface area, and  $D_s$  is the surface fractal dimension. Note that for a smooth object,  $D_s = 2$  consistent with the notation that a smooth surface is two-dimensional. For fractally rough surfaces, however,  $D_s$  varies between 2 and 3, so  $D_s$  is a measure of roughness. In the near surface region, the cluster in Fig. 33.1b obeys Eq. 2, but is said to be self-affine rather than self-similar because of the finite thickness of the rough layer.

### 33.3. SMALL-ANGLE SCATTERING

Fractals can be characterized by scattering techniques [4]. An incident beam (light, neutrons, or X-rays) impinges on a sample, and the angular dependence of the scattered intensity is measured. For fractal objects, the intensity profile has a power-law dependence when plotted versus the magnitude of the wavevector  $K$ ,

$$I \sim K^{-2D+D_s} \quad (3)$$

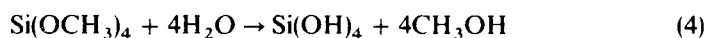
The quantity  $P = -2D + D_s$  is called the *Porod slope*. Through Bragg's law, the parameter  $K$  can be related to a characteristic length  $L$  and the scattering angle  $\theta$  ( $K = 2\pi/L = 4\pi\lambda^{-1} \sin \theta/2$ ), where  $\lambda$  is a wavelength. By scanning  $\theta$ , one effectively studies an object on different length scales determined by  $K^{-1}$ . With a combination of light, X-ray, and neutron scattering, it is possible to probe scales between 1 Å and 1 μm.

Although one must be cognizant of exceptions to general rules, it is usually possible to distinguish structures by the exponent [3, 4] in Eq. 3. Polymeric (mass fractals where  $D_s = D$ ) precursors yield scattering curves with slopes between  $-1$  and  $-3$ , whereas smooth colloids give slopes of  $-4$ . Rough colloids give slopes between  $-3$  and  $-4$ . Strong power-law polydispersity can alter these rules somewhat [4].

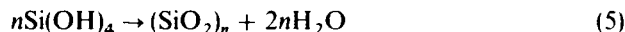
Occasionally, Porod slopes steeper than  $-4$  are observed corresponding to  $D_s < 2$  in Eq. 3. This behavior has been observed for surfactant-coated colloidal particles, and these layers are referred to as *subfractal interfaces* [5].  $D_s < 2$  corresponds to surface roughness whose amplitude diminishes with distance (along or perpendicular to the surface) in a power-law fashion. It is not clear why some interfacial layers follow this description.

In general we say the structure becomes more ramified or dispersed as one starts with a compact uniformly dense object ( $D = 3$ ,  $D_s = 2$ ) and roughens the surface ( $D = 3$ ,  $D_s > 2$ ) to produce a rough colloid. Further ramification leads to a mass fractal or branched polymer with  $D = D_s < 3$ .

The analysis of SAS curves, using the Porod slope, is illustrated in Fig. 33.2, which shows data on silicate systems solution polymerized under a variety of conditions [6, 7]. Polymerization takes place in two stages, the first of which is hydrolysis,



Silicic acid,  $\text{Si}(\text{OH})_4$ , then condenses to yield  $\text{SiO}_2$ ,



In Fig. 33.2 polymerization conditions differ in catalysis (acid versus base), polymerization protocol (single stage versus two stage), water/silicon ratio  $W$ , and monomer constitution [TMOS, TEOS,  $\text{Si}(\text{OH})_4$ ]. The data show that polymers are produced under acid catalysis, two-stage polymerization, and low  $W$ . Colloidal particles, with rough or smooth surfaces, are produced with base catalysis when  $W$  is about 4.

It was data like Fig. 33.2 that led us to investigate filler structure in in situ polymerized MC's. Although we qualitatively observe the same trends in MC's as in solution (greater ramification and lower  $D$  at lower pH), classical compact nonfractal structures are the rule in MC, whereas they are the exception in solution.

Self-similarity cannot extend to all length scales. Certainly a lower cutoff will

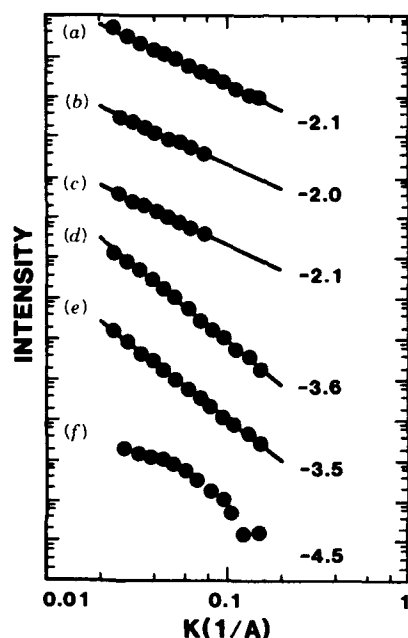


Figure 33.2. SAXS curves [18] for alkoxides polymerized in solution. (a) TMOS, acid catalyzed. (b) TEOS, two stage, acid/base. (c) TEOS, two stage, base/base. (d) 1.6 M TEOS, 0.01 N NaOH,  $W = 4$ . (e) 1.6 M TMOS, 0.01 N NaOH,  $W = 4$ . (f) 0.2%  $\text{Si(OH)}_4$  polymerized at  $\text{pH} \approx 8.5$ .

be found at the dimension of the monomer unit. For independent clusters, the upper cutoff is the mean cluster radius,  $R_g$ . A break occurs in the scattering profiles at  $KR_g \approx 1$ . One typically extracts  $R_g$  from the scattering profiles by Guinier analysis of plots of the log intensity versus  $K^2$ . The initial slope gives  $R_g$ , the Guinier radius.

### 33.4. COMPACT FILLERS AT HIGH pH

To investigate the structure of fillers precipitated at high pH, we prepared samples following Mark and Ning [8]. Vinyl-terminated polydimethyl siloxane (PDMS) was first endlinked with  $\text{Si}[\text{OSi}(\text{CH}_3)_2]_4$ . The resulting networks were leached for several days in tetrahydrofuran (THF). Strips of the rubber were then swelled to equilibrium with tetraethoxysiloxane (TEOS). The swollen strips were placed in a 25% aqueous ethylamine solution for 0.25 to 4 hr. From weight gain, filler weight percent varied from 2.6 to 53%.

Dramatic reinforcement is observed in the above materials. Figure 33.3 is a Mooney–Rivlin plot of the reduced stress (modulus) versus reciprocal elongation. The increased modulus over the unfilled rubber as well as the upturn at



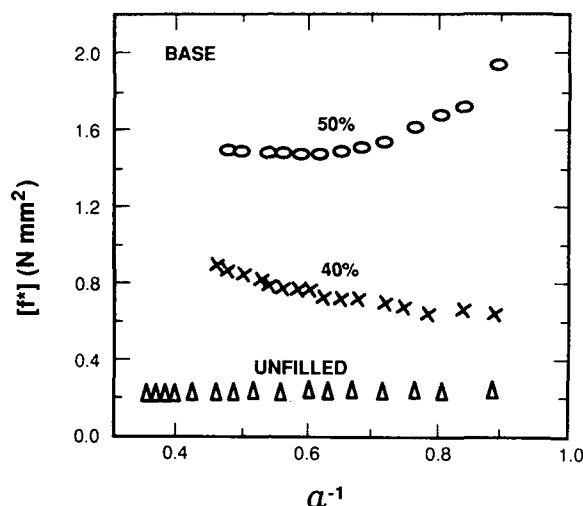


Figure 33.3. Mooney-Rivlin plots for silica/siloxane molecular composites prepared at pH 11 by two-step synthesis in which the PDMS is first endlinked and then swollen with a polymerizable alkoxide.

high elongation indicate increased strength and toughness with minimal loss of extensibility.

SANS data (Fig. 33.4) on these materials indicate the presence of aggregates of uniformly dense particulates. The data for  $Q > 0.01 \text{ \AA}^{-1}$  show that the particles are uniformly dense ( $D = 3$ ) and grow at constant number density. The steep portion of the curves have a slope somewhat less than  $-4$  indicating a nondistinct interfacial profile.

At small  $Q$ , an upturn is seen in the data indicative of structure on scales beyond the resolution of our instrument. Limiting slopes near  $-4$  indicate that the larger clusters are uniformly dense. It should be noted that the upturn scales with the size of the primary particles as illustrated by Fig. 33.5 where the background-subtracted data are plotted in scaled form ( $I_0/\text{concentration}$ ) versus  $KR_g$ . The data nearly fall on top of one another indicating that there is only one scaling length in the system.

The relationship between  $I_0$  and  $R_g$  shows that particles above  $100 \text{ \AA}$  are not fully dense. Since  $I_0/c$  is proportional to  $M$  in Eq. 1, the slope of  $\log I_0/c$  versus  $R_g$  should have a slope of 3 for compact growth. Figure 33.6 shows that this relationship is obeyed only for  $R_g > 100 \text{ \AA}$ . Particles  $< 100 \text{ \AA}$  are more compact. Given assumptions concerning the nature of the second phase incorporated into the larger particles, the mean silica density could be extracted from the data.

We conclude that growth under strongly basic conditions and large excess  $\text{H}_2\text{O}$  produces uniformly dense particles. These particles appear to be clustered into larger units that also appear to be uniformly dense and nonfractal.

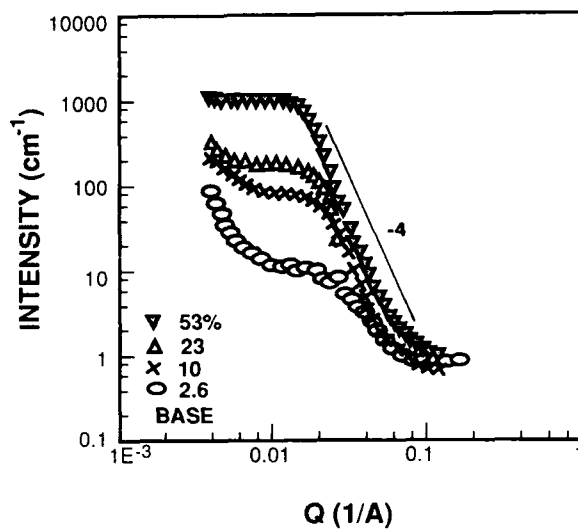


Figure 33.4. SANS and SAXS data on networks similar to Fig. 33.3. Only the 10% sample is SAXS data.

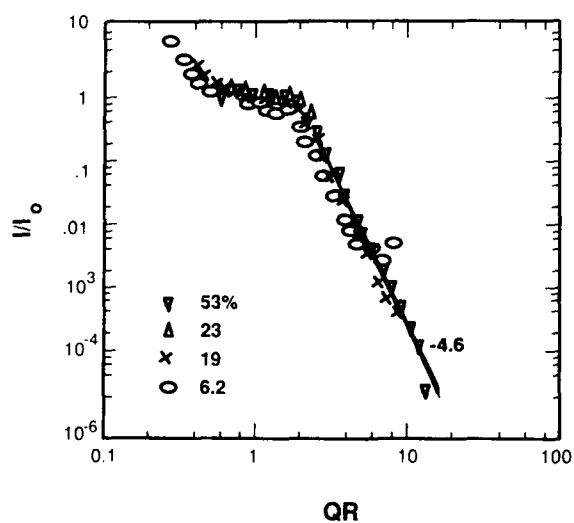
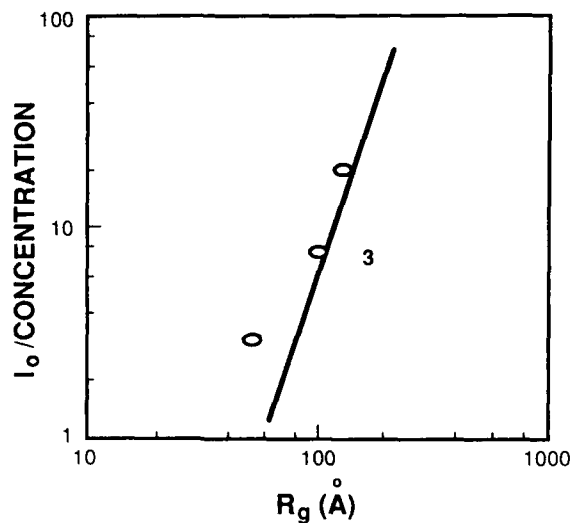
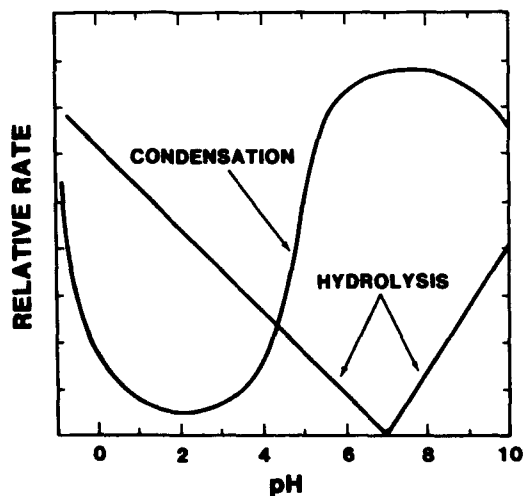


Figure 33.5. Scaled background-subtracted data from Fig. 33.4. The limiting slope of  $-4.6$  indicates an interfacial layer of intermediate contrast between the filler and matrix.



**Figure 33.6.** Intensity in the plateau region of Fig. 33.5 versus the Guinier radius. The limiting slope of 3 indicates uniformly dense particles with  $D = 3$ . Data on 10% sample are not included. In the absence of detailed knowledge of the composition of the phases, it is impossible to correct for differences in contrast in SAXS and SANS experiments.



**Figure 33.7.** Schematic representation of the rate of important reactions for silicates.

Figure 33.7 shows the pH dependence of the relevant chemical processes active in silica polymerization [5]. The diagram is schematic at best and is only meant to indicate that in strongly basic solution, silica is somewhat soluble and that both hydrolysis and condensation of alkoxides are relatively facile. At high pH we reckon that fully hydrolyzed silicic acid polymerizes close to equilibrium. The fact that silica is soluble means that conventional nucleation and growth takes place to yield uniformly dense, nonfractal particles. Because growth takes place in an incompatible matrix, it is not surprising that the particles are not fully dense. Presumably particles larger than the mean distance between crosslinks in the parent elastomer must either dispose of the unwanted chains at the advancing interface or somehow incorporate them in the interior. The former could account for the observed interfacial region and the latter for the noncompact nature of larger particles.

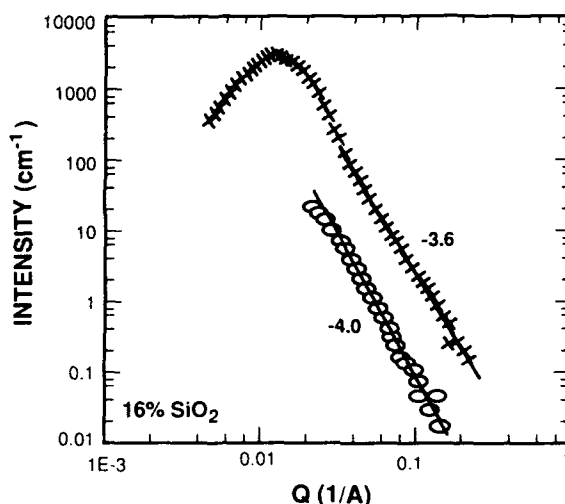
The growth of fillers under basic conditions is directly analogous to the growth of compact particles via the Stober process [9] for the production of colloidal silica. The analogy is confirmed by the similarity of the scattering curves in Fig. 33.2*f* and 33.5.

### 33.5. SPINODAL DECOMPOSITION

While experimenting on strategies for the production of ramified fillers, we stumbled on a synthetic protocol that we believe produces a bicontinuous macroscopic interpenetrating network of silica and siloxane. The scattering data and mechanical properties suggest that the operative mechanism is spinodal decomposition before or during polymerization.

The sample was also prepared by a two-stage process [10]. Hydroxy-terminated PDMS ( $M_n = 1.8 \times 10^4$ ) was first endlinked with a stoichiometric amount of TEOS using 1% stannous-2-ethyl hexanoate as a catalyst. The resulting elastomer was then leached in THF and swollen to equilibrium with TEOS. A slab of the material was then placed in a desiccator saturated with water vapor at 25°C. Anhydrous ammonia was then flowed through the system for 10 min. Ammonia flow was halted after 10 min, and polymerization proceeded for 2 days. The resulting material was cloudy and brittle even though the silica content was only 16%.

Figure 33.8 compares SAXS and SANS data on the ammonia vapor-catalyzed material. The observed peak as well as the brittle nature of the material suggest that the filler cannot consist of isolated particles, but must form a silica continuous network. Berk [11] has recently shown that phase separation via spinodal decomposition leads to a bicontinuous network and a peak in the structure factor. It seems that ammonia induces phase separation in the fluid TEOS as polymerization proceeds. The PDMS network restricts growth of the unstable Fourier components of the concentration fluctuation spectrum.



**Figure 33.8.** SAXS and SANS data for two-step composites polymerized by anhydrous ammonia vapor.

Polymerization then freezes in the spinodal pattern. The limiting slopes between  $-3.5$  and  $-4$  indicate possible surface roughness.

It should be noted that nucleation and growth can also lead to peaks in the scattering profile as the particles begin to overlap and interfere with each other [13, 14]. The absence of peaks in Fig. 33.4 at much higher filler concentration, however, coupled with the brittle nature of the sample leads us to reject this interpretation.

### 33.6. STRATEGIES FOR RAMIFIED FILLERS

In the experiments described above, the silica surfaces are to first approximation smooth. It seemed to us reasonable that the synthesis of fractally rough particles might enhance the bonding between phases and improve toughness. Reference to Fig. 33.7 shows that in solution polymerized alkoxides become increasingly ramified as the pH is lowered and as the water/silicon ratio is lowered [7]. Near neutral pH, Fig. 33.2 implies that polymerization is strongly hydrolysis-limited and silica is highly insoluble. Under these conditions, Schaefer et al. [15] argue that mass-fractal clusters with  $D = 2.5$  are generated by a growth model called *kinetic percolation*. At lower pH, hydrolysis is fast compared to condensation, and reaction-limited cluster aggregation leads to polymeric clusters with  $D = 2.1$ . Under basic conditions, fractally rough clusters are found in alkoxide solutions. Keefer and Schaefer [16] argue that they are produced by poisoned Eden growth, a variation of the monomer cluster growth model in Fig. 33.1a.

Although we did observe a transition to mass-fractal fillers on lowering the

pH at low loading, we found that smooth particulates were always found at silica concentrations needed for effective reinforcement. Figure 33.9, for example, shows neutrally polymerized TEOS in swollen networks ( $M = 1.8 \times 10^5$ ). Then the TEOS-swollen networks were immersed in 1/1 ethanol/water solutions for 12 hr. Loading is quite light particularly for thin samples, because the TEOS leaches out before the slow hydrolysis reaction occurs. Although the fillers are far from polymeric, the limiting slope of the 0.17% data is consistent with fractally rough particles. Unfortunately, the limited extent of the power-law region precludes definitive conclusions. Data presented below on acid-catalyzed systems suggest that at any reasonable loading, the fillers would be structurally very similar to the uniformly dense smooth particles described above.

In 5% acetic acid solutions, ramified fillers are found in much higher concentration. Figure 33.10 shows data at 17 and 24 wt% filler. At 17% we find structures with  $D = 2.9 \pm 0.4$ , implying a maximally dense polymer or a maximally rough colloid ( $D = D_s = 3$ ). At higher loading, the domains are smooth with an interfacial layer identical to that found under base catalysis. Once again, the apparent power-law regimes of the data are quite limited.

Mooney-Rivlin analysis of the mechanical properties as a function of pH are shown in Fig. 33.11 at roughly the same filler concentration. Although there is little difference in effectiveness, it is clear that modulus increases with pH, whereas maximum extensibility decreases with pH. Intuitively, these trends seem reasonable in view of the trend to more ramified polymeric structures at lower pH.

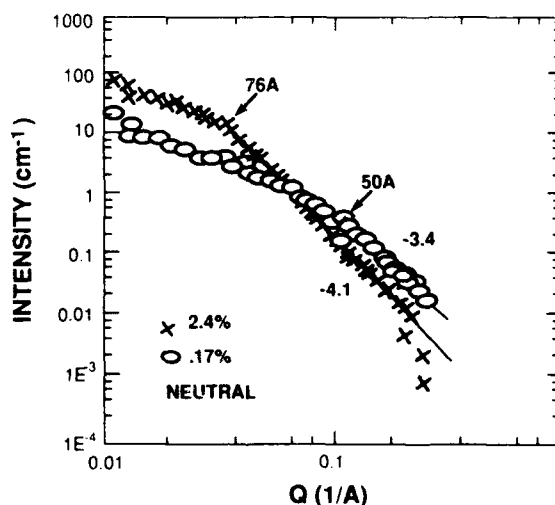


Figure 33.9. SAXS data for two-step composites polymerized in neutral alcohol solution.

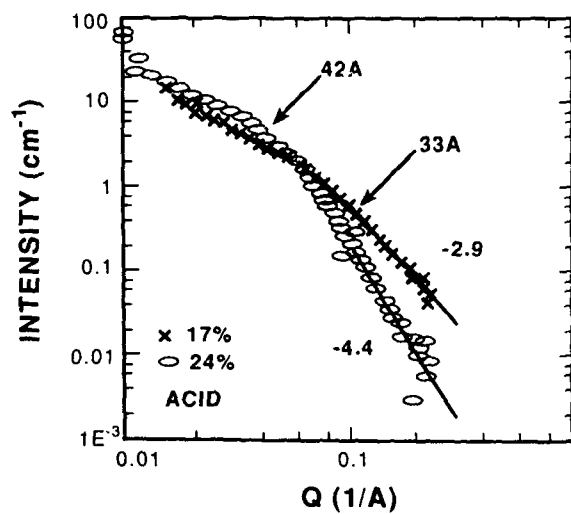


Figure 33.10. SAXS data for two-step composites polymerized in acidic solution.

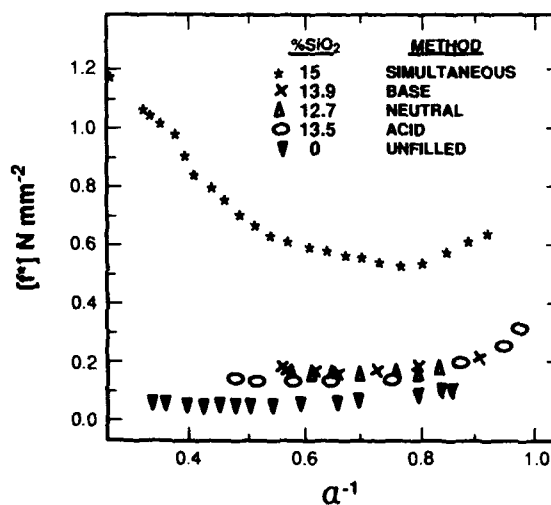


Figure 33.11. Mooney Rivlin plot of stress-strain data for both two-step and simultaneously polymerized composites.

## 33.7. POLYMERIC BICONTINUOUS NETWORKS

Work by Mark, Jiang, and Tang [17] shows that the best reinforcement is achieved when the endlinking and filler polymerization reactions are carried out simultaneously. Figure 33.11, for example, shows that both the modulus and maximum extensibility increase, giving dramatic improvement in the ultimate strength and energy required for rupture. SAXS data on these materials reveal a novel filler structure consisting of a bicontinuous structure in which the filler network is polymeric on short-length scales.

Simultaneously cured and filled networks are starting with hydroxy-terminated PDMS with  $M = 2.1 \times 10^4$ . The catalysts employed, dibutyltin diacetate and stannous 2-ethyl hexanoate, were present at 1.0 and 1.7 wt%, respectively, relative to PDMS. The homogeneous mixtures including varying amounts of TEOS were allowed to react in humid air for 3 days. The resulting clear networks were extracted in THF, but the sol fractions were minimal.

The scattering profiles for two samples (10 and 14 wt % filler) are compared to the unfilled PDMS in Fig. 33.12. We interpret the peak in the curve to indicate a bicontinuous network similar to the ammonia-catalyzed system depicted in Fig. 33.8. The high  $Q$  region of the curve, however, reveals that the substructure of the bicontinuous network is itself a network. The system is an interpenetrating network where the 100-Å backbone is a flexible branched silicate. The structure of the silicate network is insensitive to loading, but the core diameter of the super interpenetrating network increases with loading.

It is interesting to note the extensive scattering from the unfilled network. A

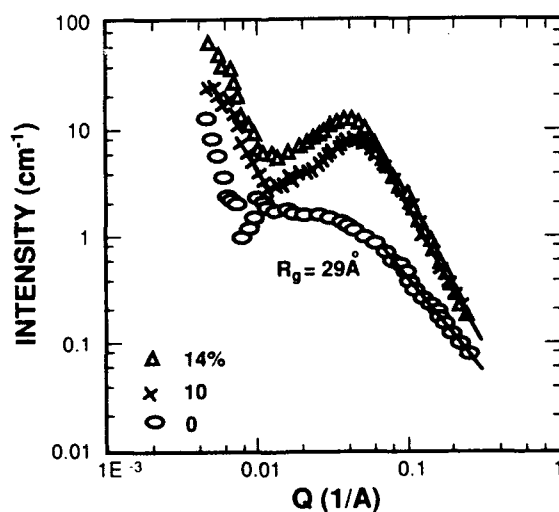


Figure 33.12. SAXS data for simultaneously polymerized composites.



Debye-like function is observed with a radius of gyration of 29 Å, not unreasonable for the distance between network branchpoints. Presumably the strong density fluctuations indicated by this curve provide a template on which phase separation develops in this system.

This system shows considerable scattering at small  $Q$  in both the filled and unfilled state. It is likely that this scattering is due to imperfections such as dust or trapped bubbles.

### 33.8. CONCLUSION

We conclude that a variety of different filler morphologies can be realized in silica/siloxane molecular composites. The rule at high-filler loading is porous, but uniformly dense particulates. In some cases, interfacial layers are observed and are presumably due to PDMS expelled from the growing particles. At neutral and acidic pHs, some filler ramification (dispersion) is achieved, but the truly branched polymer structure found in solution polymerized alkoxides are not realized at any reasonable filler loading. As filler ramification increases, so does maximum extensibility. Ultimate strength decreases with filler ramification for particulate fillers.

By far the best performance is achieved through simultaneous curing and filling. Based on SAXS data, we postulate the existence of a super interpenetrating network or bicontinuous array of PDMS and silicate polymers. In these systems good ultimate strength is achieved because of the continuous nature of the filler network. Maximum extensibility is enhanced because of polymeric mass-fractal character of the silicate phase.

We also studied a bicontinuous system in which the silica phase is rigid and uniformly dense. In this case a brittle material results, consistent with the nonpolymeric nature of the filler. Taken in total, our results indicate that ramified fillers are desirable only if a continuous, nonparticulate minority phase can be achieved.

### REFERENCES

1. B. B. Mandelbrot, *The Fractal Geometry of Nature*, Freeman, San Francisco (1982).
2. P. Meakin, in: C. Domb and J. L. Laibowitz, Eds., *Phase Transitions and Critical Phenomena*, *Adv. Colloid Interface Sci.*, **12**, 1 (1988).
3. D. W. Schaefer, *Bull. Mater. Res. Soc.*, **13**(2), 22 (1988).
4. J. E. Martin and A. J. Hurd, *J. Appl. Cryst.*, **20**, 61 (1987).
5. D. W. Schaefer et al., in: J. R. Banavar, J. Koplik, and K. W. Winkler, Eds., *Physics and Chemistry of Porous Media*, Vol. II, *Am. Inst. Phys. Conf. Proc.*, **154**, 63 (1987).
6. E. K. Iler, *The Chemistry of Silica*, Wiley-Interscience, New York, (1979).
7. D. W. Schaefer and K. D. Keefer, in: C. J. Brinker, D. E. Clark, and D. R. Ulrich, Eds., *Better Ceramics Through Chemistry*, Vol. II, *Mater. Res. Soc. Symp. Proc.*, **73**, 277 (1986).

8. J. E. Mark and Y.-P. Ning, *Polymer Bull.*, **12**, 413 (1984).
9. W. Stober, A. Fink, and E. Bohn, *J. Colloid Interface Sci.*, **26**, 62 (1968).
10. C.-Y. Jiang and J. E. Mark, *Makromol. Chem.*, **185**, 2609 (1984).
11. N. F. Berk, *Phys. Rev. Lett.*, **58**, 2718 (1987).
12. M. A. Liorente and J. E. Mark, *Macromolecules*, **13**, 681 (1980).
13. W. Haller and P. B. Macedo, *Phys. Chem. Glasses*, **9**, 153 (1968).
14. D. W. Schaefer, B. C. Bunker, and J. P. Wilcoxon, *Phil. Trans. R. Soc., Ser. A*, **423**, 35 (1989).
15. D. W. Schaefer, A. J. Hurd, J. E. Martin, and A. Glines, in preparation.
16. K. D. Keefer and D. W. Schaefer, *Phys. Rev. Lett.*, **56**, 2376 (1986).
17. J. E. Mark, C.-Y. Jiang, and M.-Y. Tang, *Macromolecules*, **17**, 2613 (1984).
18. D. W. Schaefer, *Science*, **243**, 1023 (1989).

## PREPARATION OF (Pb<sub>0.5</sub>Bi<sub>0.5</sub>)(Ti<sub>0.5</sub>Fe<sub>0.5</sub>)O<sub>3</sub> CERAMIC POWDER FROM METAL ORGANIC PRECURSORS FOR 0-3 CERAMIC- POLYMER COMPOSITES

K. H. HAN, R. E. RIMAN, AND A. SAFARI

### 34.1. INTRODUCTION

During the past few years, a number of investigators have examined piezoelectric ceramic-polymer composites with different connectivity patterns [1-3]. One of the simplest types has a 0-3 connectivity pattern. In this case, the ceramic powder has no physical particle-particle contacts because the polymer phase is a matrix. This type of composite is easy to fabricate and also amenable to mass production.

In most of the earlier work on 0-3 composites, lead zirconate titanate (PZT) or PbTiO<sub>3</sub>-based powder was used as the ceramic filler material [4-9]. In general, chemical preparation routes have resulted in the preparation of materials with improved properties. Recently it was shown by Giniewicz [10] that the PbTiO<sub>3</sub>-BiFeO<sub>3</sub> solid solution with a composition near the morphotropic phase boundary results in a better piezoelectric filler material for 0-3 composites than pure PbTiO<sub>3</sub> because of its extremely large structural anisotropy.

---

*Ultrastructure Processing of Advanced Materials.*  
Edited by Donald R. Uhlmann and Donald R. Ulrich (deceased).  
ISBN 0-471-52986-9 © 1992 John Wiley & Sons, Inc.

In this study,  $(\text{Pb}_{0.5}\text{Bi}_{0.5})(\text{Ti}_{0.5}\text{Fe}_{0.5})\text{O}_3$  powders were prepared by a *liquid mix* technique known as the *Pechini method* [11, 12]. The liquid mix method consists of the following three steps:

1. Preparation of clear, homogeneous metal solutions using  $\alpha$ -hydroxycarboxylic acids (e.g., citric acid) to form metal chelates with various metal cations.
2. Evaporation of solutions to form rigid polymer resins via polyesterification with a polyhydroxy alcohol (e.g., ethylene glycol) and carboxylic acid group functionalities.
3. Calcination of solid resins to form ceramic powders.

Powders obtained from this process were incorporated into the Eccogel polymer to form 0-3 composites. Piezoelectric and dielectric properties were measured.

## 34.2. EXPERIMENTAL PROCEDURE

### 34.2.1. Powder Preparation

As Table 34.1 reveals, when citric acid solutions were employed, it was not possible to codissolve all four types of cations. In particular, the bismuth salt

TABLE 34.1. Cosolubility of Various Metal Salts in Liquid Mix Solutions

Metal Cation	Metal Salts	Citric Acid Solution <sup>a</sup>	Ammonium Citrate Solution
Lead	PbO	Insoluble	Soluble
	Pb(OH) <sub>2</sub>	Insoluble	<sup>b</sup>
	PbCO <sub>3</sub>	Soluble	<sup>b</sup>
Iron	Fe <sub>2</sub> O <sub>3</sub>	Insoluble	<sup>b</sup>
	FeO(OH)	Insoluble	<sup>b</sup>
	Fe <sub>2</sub> O <sub>3</sub> · xH <sub>2</sub> O	Soluble	Soluble
Bismuth	(BiO) <sub>2</sub> CO <sub>3</sub>	Insoluble	Soluble
	Bi <sub>2</sub> O <sub>3</sub>	Insoluble	<sup>b</sup>
	Bi <sub>2</sub> O <sub>3</sub> · xH <sub>2</sub> O	Insoluble	Soluble
	Bi(OH) <sub>3</sub>	Insoluble	<sup>b</sup>
	Bi(C <sub>6</sub> H <sub>5</sub> O <sub>7</sub> )	Insoluble	Soluble
Titanium	Ti(O- <i>i</i> -Pr) <sub>4</sub>	Soluble	Soluble
	Ti(O- <i>n</i> -Bu) <sub>4</sub>	Soluble	Soluble

<sup>a</sup>Saturated citric acid solutions.

<sup>b</sup>Not investigated.

was typically the component that was insoluble. However, when ammonia is titrated into a citric acid solution, ammonium citrate complexes formed that were capable of solubilizing all four cations. The precursors typically used as sources of ions were  $\text{Ti}(\text{O-}i\text{-Pr})_4$  (Fisher Scientific Co., Springfield, N.J.), freshly precipitated hydrous iron oxide,  $\text{PbCO}_3$  (Fisher Scientific Co.), and a commercially available 50 wt % aqueous bismuth ammonium citrate solution (Pfaltz & Bauer Inc., Waterbury, Conn.).

A molar ratio of 1:1 Pb:Ti cation solutions were prepared by the stoichiometric addition of  $\text{PbCO}_3$  to a 0.776 M titanium citrate solution [250 ml  $\text{Ti}(\text{O-}i\text{-Pr})_4$ , 400 g citric acid, and 500 ml ethylene glycol (Fisher Scientific Co.), 60°C]. Iron citrate solutions, 0.250 M, (320 g citric acid and 350 ml  $\text{H}_2\text{O}$ ) were prepared by dissolution of wet water-washed hydrated oxide ( $\sim 79$  g on the basis of  $\text{Fe}_2\text{O}_3$ ) precipitated from an aqueous iron nitrate solution (Fisher Scientific Co.) adjusted to a pH 6-7 with ammonium hydroxide (Fisher Scientific Co.). The liquid mix solution was prepared with the above precursors and the bismuth ammonium citrate solution (0.502 M) as shown in Fig. 34.1. All pH adjustments were made with ammonium hydroxide. Stock solutions were prepared as assayed gravimetrically using a procedure described by Mulder [13] for bismuth and iron cation solutions and a classical oxide ignition technique for titanium. The liquid mix solution was prepared with a cation stoichiometry corresponding to  $(\text{Pb}_{0.5}\text{Bi}_{0.5})(\text{Ti}_{0.5}\text{Fe}_{0.5})\text{O}_3$  and a pH in the range of 6-7. This solution was diluted with ethylene glycol to a concentration of  $\sim 0.7$  M. Polymerization of the four component solution and evaporation of volatile constituents was conducted as described by Pechini [12].

Calcination was accomplished in two steps. The metal organic resin was decomposed by slowly heating at 2°C/min to 600°C in air with a 1-hr soak in a flat combustion boat. This was followed by 1- to 1.5-hr 800, 900, and 1000°C heat treatments in air in a covered alumina crucible with a subsequent quenching in air to produce a dark red powder.

#### 34.2.2. Powder Characterization

Thermogravimetric (TGA) and differential thermal analyses (DTA) were performed on the solid resin at a heating rate of 5°C/min from room temperature to 1100°C (1090B Thermal Analyzer, du Pont de Nemours, Wilmington, Del.) The calcined powders were characterized with X-ray diffraction to determine both the phase and lattice parameters. A Guinier camera was used to measure the lattice parameters using a least-square refinement of the unit cell dimensions over a  $2\theta$  range of 20-60° using a silicon powder as an internal standard. The chemical composition was examined by inductively coupled plasma (ICP) spectroscopy (Perkin Elmer, Model No. 6500, Norwalk, Conn.). The particle size, surface area, and morphology of the powders were also characterized using scanning electron microscopy (SEM, Amray, Model No. 1200, Bedford, Mass.), X-ray photosedimentation (Micromeritics, Model No. 5000, Norcross, Ga.),

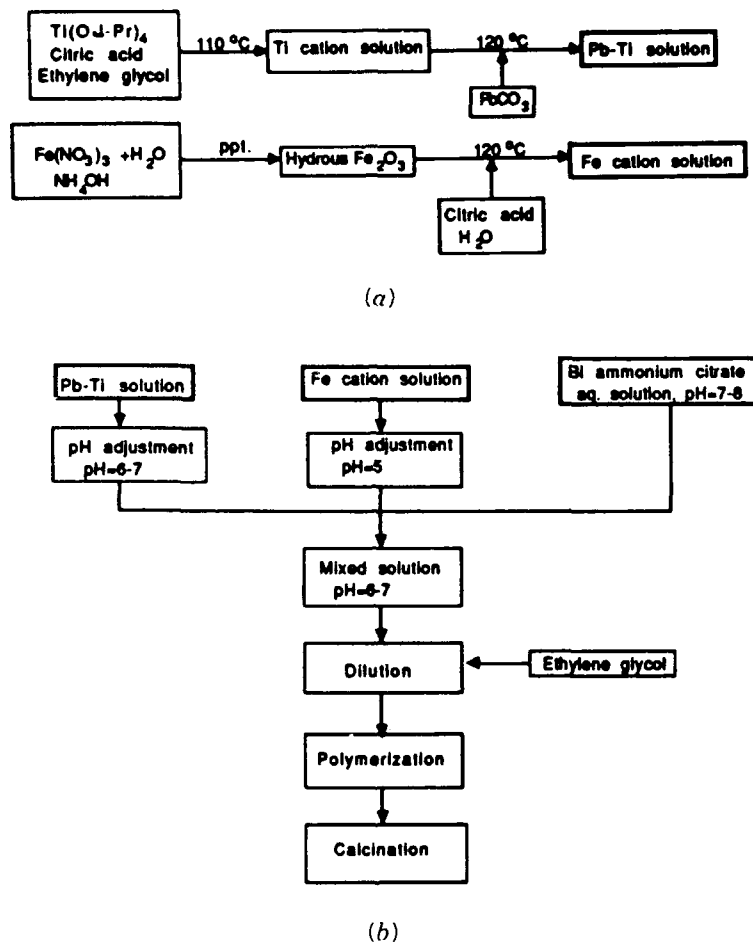


Figure 34.1. Powder synthesis route (a) precursor solution preparation; (b) "liquid mix" process.

and single-point nitrogen adsorption analysis (Quantachrome QS-10, Syosset, N.Y.).

### 34.2.3. Composite Preparation and Property Measurement

The  $(\text{Pb}, \text{Bi}) (\text{Ti}, \text{Fe})\text{O}_3$  powder was dispersed in Eccogel polymer 1365-80 (Emerson and Cuming, Dewey and Almy, Chemical Division, Canton, Mass.) with a solids loading of 65 vol% and prepared as described by Safari et al. [9]. The samples were poled in silicone oil bath at  $80^\circ\text{C}$  with a direct current field of 80–100 kV cm for 15 min. The capacitance and dissipation factors were measured at 1 kHz using a Hewlett-Packard 4194A impedance/gain phase analyzer (Palo Alto, Calif.). The  $d_{33}$  coefficients were measured dynamically using a piezo

$d_{33}$ -Meter (Channel Products Inc., Berlincourt, Chesterland, Ohio) at a frequency of 100 Hz.

### 34.3. RESULTS AND DISCUSSION

The chemical composition of lead titanate–bismuth ferrite powder was characterized with ICP, TGA, DTA, and X-ray diffraction as shown in Table 34.2. The close agreement between the measured cation concentration and theoretical value indicates that a powder with the desired stoichiometry was prepared. The calcination conditions were based on thermal analysis and X-ray diffraction data. In general, decomposition of organic species was complete above 375°C with a large exothermic peak at  $\sim 300^\circ\text{C}$ . Although no crystallization temperature was detected with DTA, X-ray diffraction showed that an oxide perovskite phase appears at a temperature as low as 500°C. This temperature is 100°C lower than what has been observed for the preparation of this material using conventional powder processing routes.

Heat-treatment studies summarized in Fig. 34.2 and Table 34.2 reveal the manner in which the tetragonal phase forms. Below 900°C, the pseudocubic phase was observed along with a trace amount of  $\text{PbO}_{1.57}$  impurity phase. A pure tetragonal phase began to form at 900°C as shown by the apparent peak splitting, which is more well defined at 1000°C. This temperature is 100°C lower than the conventional powder processing technique reported by Giniewicz [10].

TABLE 34.2. Summary of Powder Characteristics

Calcination temperature (1 hr) ( $^\circ\text{C}$ )	600	
Heat-treatment temperature (1 hr) ( $^\circ\text{C}$ )	1000	
Lattice parameters (tetragonal) <sup>a</sup>	$a = 3.847 \text{ \AA}$ $c = 4.388 \text{ \AA}$ , $c/a = 1.141$	
X-ray density ( $\text{g}/\text{cm}^3$ )	7.88	
Sedigraph mean particle size ( $\mu\text{m}$ )	3.5	
Brunauer–Emmett–Teller particle size ( $\mu\text{m}$ )	4.2 (0.18 $\text{m}^2/\text{g}$ )	
Morphology	Equiaxed	

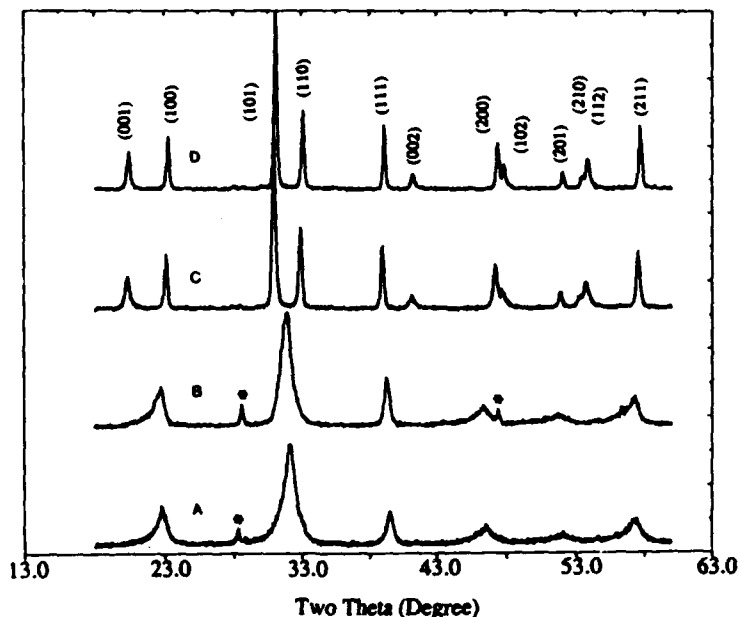
  

Stoichiometry <sup>b</sup> (wt %)	Measured	Calculated <sup>c</sup>
Pb	33.7	33.64
Ti	8.24	7.77
Bi	33.6	33.93
Fe	9.77	9.07

<sup>a</sup>900°C heat treatment for 1 hr:  $a = 3.849 \text{ \AA}$ ,  $c = 4.387 \text{ \AA}$ ,  $c/a = 1.134$ .

<sup>b</sup>950°C heat treatment for 1.5 hr, 600°C calcination, 1 hr.

<sup>c</sup>Based on  $(\text{Pb}_{0.5}\text{Bi}_{0.5})(\text{Ti}_{0.5}\text{Fe}_{0.5})\text{O}_3$ .



\* = PbO<sub>1.57</sub> peak

Figure 34.2. Room temperature X-ray diffraction traces of (Pb,Bi)(Ti,Fe)O<sub>3</sub> after (a) 600°C calcination, 1 hr and successive heat treatments for 1 hr at (b) 800, (c) 900, and (d) 1000°C.

Lattice parameter determinations, consistent with previously reported work [10], indicate that  $c/a$  ratio increases slightly as the heat-treatment temperature increases from 900 to 1000°C. A  $c/a$  ratio of 1.141 indicates that PbTiO<sub>3</sub>-BiFeO<sub>3</sub> solid solution is a very promising material as the filler material for 0-3 piezoelectric composites [10].

After heat treatment, the calcined powders were quenched to room temperature in air. Upon quenching, SEM examination revealed that the powders developed an equiaxed faceted morphology. Relatively good agreement between particle sizes measured with SEM, photosedimentation, and nitrogen adsorption indicates that a disperse powder has been prepared without the need for comminution as typically required for conventional powder processing [10]. Other characteristics are summarized in Table 34.2. This behavior is due to structural anisotropy developed during cooling through the Curie temperature ( $\sim 660^\circ\text{C}$ ) [10]. Differential thermal expansion between the  $a$  and  $c$  axis develops stresses capable of causing intergranular fracture of primary particles to produce secondary particles. This feature makes it difficult to produce dense ceramics, but is very useful in 0-3 ceramic-polymer composites where maximum particle dispersion is desired.

0-3 composites prepared with the powder exhibit a piezoelectric charge



coefficient,  $d_{33}$ , of 28 pC/N, dielectric constant,  $k$ , of 20, dissipation factor of 2%, and a voltage coefficient,  $g_{33}$ , of  $158 \times 10^{-3}$  Vm/N. These properties are comparable with those of composites loaded with powders prepared via mixed oxide methods, but far less than those of composites incorporating Mn-doped (Pb, Bi)(Ti, Fe)O<sub>3</sub> as a filler material [10]. This is probably due to a deficiency of oxygen that can impart  $n$ -type conductivity in the ceramic filler by reduction of transition metals. Such increases make the composite more resistant to poling and lead to low  $d_{33}$  values. In addition, other factors due to the lack of process optimization such as voids and microcracks create poling complications due to dielectric breakdown. In addition to optimizing the process, synthetic work for (Pb, Bi)(Ti, Fe)O<sub>3</sub> ceramic powders will continue by doping Mn<sup>4+</sup> ions in an attempt to reduce the conductivity of ceramic powder and thus make poling composites more effective.

#### 34.4. CONCLUSIONS

(Pb<sub>0.5</sub>Bi<sub>0.5</sub>)(Ti<sub>0.5</sub>Fe<sub>0.5</sub>)O<sub>3</sub> ceramic powders were prepared successfully by a modified liquid mix method that utilized ammonium citrate rather than citrate complexes. Disperse, equiaxed, tetragonal 3–4 μm powder of a controlled stoichiometry resulted with heat treatments as low as 1000°C, which is 100°C lower than required for conventional processing, without the need for a comminution step. The powders were used to produce 0–3 ceramic–polymer composites with a  $g_{33}$  of  $158 \times 10^{-3}$  Vm/N, which is comparable with that of composites filled with powders made by conventional powder processing.

#### ACKNOWLEDGMENTS

We gratefully acknowledge the financial assistance of the Center for Ceramic Research for support of this research. Furthermore, we thank Dr. L. Grahl-Madsen for her useful comments on this manuscript.

#### REFERENCES

1. R. E. Newnham, D. P. Skinner, and L. E. Cross, *Mater. Res. Bull.*, **13**, 525 (1978).
2. R. E. Newnham, L. J. Bowen, K. A. Klicker, and L. E. Cross, *Mater. Eng.*, **112**, 93 (1980).
3. R. E. Newnham, A. Safari, G. Sa Gong, and J. Ginieswicz, in: *Proceedings of IEEE Ultrasonic Symposium*, p. 501, Institute of Electric and Electronic Engineers, New York, (1984).
4. T. Katayama, *Seramikkusu*, **14**(3), 209–214 (1979).
5. L. A. Pauer, *IEEE Int. Conf. Res.*, 1–5 (1973).
6. W. B. Harrison, in: *Proceedings of the Workshop on Sonar Transducer Materials*, pp. 257–268, Naval Research Laboratory (1976), Arlington, VA.
7. H. Banno, *Japan. J. Appl. Phys. Suppl.*, **22**, 67–69 (1983).

8. D. L. Monroe, J. B. Blum, and A. Safari, *Ferroelectric Lett.*, **5**, 39 (1986).
9. A. Safari, Y. H. Lee, A. Halliyal, and R. H. Newham, *Am. Ceram. Soc. Bull.*, **66**(4), 668 (1987).
10. J. Giniewicz, M. S. Thesis, Pennsylvania State University (1985), "(Pb, Bi)(Ti, Fe)O<sub>3</sub>/polymer (0-3) composite materials for hydrophone applications".
11. M. Pechini, U.S. Patent No. 3, 330, 697 (July 11, 1967).
12. M. Pechini, Canadian Patent No. 832, 365 (June 20, 1970).
13. B. J. Mulder, *Ceramic Bull.*, **49**(11), 990 (1970).

## SOL-GEL SYNTHESIS OF ALUMINA-ZIRCONIA AND MULLITE-ZIRCONIA

J. M. BOULTON, S. SUBRAMONEY, AND D. R. UHLMANN

### 35.1. INTRODUCTION

There is considerable interest in transformation-toughened ceramics, such as  $\text{Al}_2\text{O}_3$ - $\text{ZrO}_2$  and mullite- $\text{ZrO}_2$ . Optimum toughening is obtained with dense, uniform fine-grained microstructures. In addition, retention of  $\text{ZrO}_2$  in the metastable, tetragonal phase is necessary for stress-induced transformation. Retention requires the  $\text{ZrO}_2$  grain size to be less than  $0.5\text{--}0.8\text{ }\mu\text{m}$  [1-6]. Above the critical size, monoclinic  $\text{ZrO}_2$  prevails.

A variety of wet chemical procedures have been investigated for preparing  $\text{Al}_2\text{O}_3$ - $\text{ZrO}_2$  composites. These include evaporative decomposition of an  $\alpha$ - $\text{Al}_2\text{O}_3$ - $\text{ZrO}(\text{NO}_3)_2$  slurry [7]; hydrolysis of  $\text{Zr}(\text{O}-n\text{-Pr})_4$  in a dispersion of  $\alpha$ - $\text{Al}_2\text{O}_3$  [8]; colloidal processing [9-11] coprecipitation, spray-drying or spray-ICP of aqueous sols or solutions [12-14] and sol-gel processing using alkoxides [15-17]. Debsikdar prepared  $80\text{Al}_2\text{O}_3 \cdot 20\text{ZrO}_2$  (wt) powders by complexing  $\text{Al}(\text{O}^i\text{Bu})_3$  with 2,4-pentanedione, partially hydrolyzing this complex, reacting with  $\text{Zr}(\text{O}-n\text{-Pr})_4$ , followed by further hydrolysis [17].

Less attention has been paid to the preparation of mullite- $\text{ZrO}_2$  composites. These have been prepared by conventional sintering [18, 19], from  $\text{ZrSiO}_4$  and  $\text{Al}_2\text{O}_3$  [20], from glass powders [21], and reaction of  $\text{Al}_2\text{O}_3$  and  $\text{SiO}_2$  sols prepared from alkoxides and  $\text{ZrO}_2$  powder [22].

In this study, a similar approach to that of Debsikdar has been used to

*Ultrastructure Processing of Advanced Materials.*

Edited by Donald R. Uhlmann and Donald R. Ulrich (deceased).

ISBN 0-471-52986-9 © 1992 John Wiley & Sons, Inc.

prepare  $\text{Al}_2\text{O}_3\text{-ZrO}_2$  gels from a chelated aluminum alkoxide. Three compositions have been investigated:  $95\text{Al}_2\text{O}_3\text{-5ZrO}_2$  (wt);  $80\text{Al}_2\text{O}_3\text{-20ZrO}_2$  (wt), and  $57.4\text{Al}_2\text{O}_3\text{-42.6ZrO}_2$  (wt). The last is the eutectic composition in the  $\text{Al}_2\text{O}_3\text{-ZrO}_2$  system. This approach was then extended to prepare a mullite + 15 wt%  $\text{ZrO}_2$  composition.

## 35.2. EXPERIMENTAL

Gels were prepared from commercially available aikoxides (Alfa Products, Danvers, Mass.). These were aluminum di(isopropoxide) acetoacetic ester chelate,  $\text{Zr}(\text{O-}i\text{-Pr})_4$ , and  $\text{Si}(\text{OEt})_4$ . The following synthetic procedures were used.

### 35.2.1. $57.4\text{Al}_2\text{O}_3\text{-42.6ZrO}_2$

$\text{Al}(\text{O-}i\text{-Pr})_2\text{C}_6\text{H}_9\text{O}_3$  (0.011 mol), 3.00 g, was added to 10 ml of *i*-PrOH in an inert atmosphere. The aluminum alkoxide was partially hydrolyzed by the addition of 0.20 ml 0.15 M aqueous HCl in 5 ml of *i*-PrOH giving the ratio 1 mol Al-alkoxide:1 mol  $\text{H}_2\text{O}$ . After 30 min 1.100 g of  $\text{Zr}(\text{O-}i\text{-Pr})_4$  (0.003 mol) in 10 ml of *i*-PrOH was added. After stirring for an additional 30 min, a final hydrolysis was carried out. A solution of 0.45 ml of 0.15 M aqueous HCl and 5 ml of *i*-PrOH was added giving the ratios 1 mol Al-alkoxide:1 mol  $\text{H}_2\text{O}$  and 1 mol Zr-alkoxide:4 mol  $\text{H}_2\text{O}$ . The resulting clear solution was poured into polypropylene beakers, loosely covered with foil, and allowed to gel. This took several days at ambient temperature. Drying of the resultant gel at  $60^\circ\text{C}$  gave clear, pale yellow, gel fragments ~3 mm in diameter.

### 35.2.2. $80\text{Al}_2\text{O}_3\text{-20ZrO}_2$

A gel was prepared as above, but using 0.371 g of  $\text{Zr}(\text{O-}i\text{-Pr})_4$  (0.001 mol) and 0.28 ml of 0.15 M aqueous HCl in the final hydrolysis.

### 35.2.3. $95\text{Al}_2\text{O}_3\text{-5ZrO}_2$

A gel was prepared as above, but using 0.078 g of  $\text{Zr}(\text{O-}i\text{-Pr})_4$  (0.0002 mol) and 0.21 ml of 0.15 M aqueous HCl in the final hydrolysis.

### 35.2.4. $3\text{Al}_2\text{O}_3\text{-2SiO}_2 + 15\text{ wt \% ZrO}_2$

$\text{Al}(\text{O-}i\text{-Pr})_2\text{C}_6\text{H}_9\text{O}_3$ , 3.00 g, was reacted with 0.3097 g of  $\text{Zr}(\text{O-}i\text{-Pr})_4$  (0.001 mol) as described above. A prehydrolyzed solution of  $\text{Si}(\text{OEt})_4$  was then added. This consisted of 0.7595 g of  $\text{Si}(\text{OEt})_4$  (0.004 mol), 3.8 ml of *i*-PrOH, and 0.13 ml of 0.15 M aqueous HCl giving the molar ratio 1 mol  $\text{Si}(\text{OEt})_4$ :2 mol  $\text{H}_2\text{O}$ . The solution was stirred at ambient temperature for 30 min prior to its addition to effect prehydrolysis.

The reaction mixture was stirred for 30 min, and then a final hydrolysis was

carried out. This consisted of adding 0.40 ml of 0.15 *M* aqueous HCl in 5 ml *i*-PrOH giving the ratios 1 mol Al-alkoxide: 1 mol H<sub>2</sub>O, 1 mol Zr-alkoxide: 4 mol H<sub>2</sub>O and 1 mol Si-alkoxide: 2 mol H<sub>2</sub>O. Subsequent gelation and drying gave clear, pale yellow, gel fragments.

Samples of dried gels were fired in air using a 2-hr soak and a heating/cooling rate of 5°C/min. In the case of the mullite-ZrO<sub>2</sub> gel, firing led to undesirable blackening due to residual alkoxide groups. This was eliminated by prefiring the gel in O<sub>2</sub> to 700°C at 1°C/min. Fracture surfaces of gel pieces were investigated by scanning electron microscopy (SEM) and EDS. Samples were also analyzed by X-ray diffraction (XRD); before being fired they were ground to a fine powder. Grinding was not conducted after heat treatment to avoid the stress-induced transformation of tetragonal ZrO<sub>2</sub>. The ratio of tetragonal to monoclinic ZrO<sub>2</sub> was determined from the integrated intensities of the tetragonal (111) and the monoclinic (111) and (11 $\bar{1}$ ) peaks [23].

### 35.3. RESULTS AND DISCUSSION

For the Al<sub>2</sub>O<sub>3</sub>-ZrO<sub>2</sub> gels, XRD indicated the  $\theta \rightarrow \alpha$ -Al<sub>2</sub>O<sub>3</sub> transition occurred at  $\sim 1100^\circ\text{C}$  (see Table 35.1). This is considerably higher than for an Al<sub>2</sub>O<sub>3</sub> gel prepared from Al(O-*i*-Pr)<sub>2</sub>C<sub>6</sub>H<sub>5</sub>O<sub>3</sub>, where the transition occurred at  $\sim 900^\circ\text{C}$ , and  $\alpha$ -Al<sub>2</sub>O<sub>3</sub> was the only phase observed after firing at 950°C for 2 hr. A similar retardation of phase development on the introduction of ZrO<sub>2</sub> has been reported by Pugar and Morgan [16]. In their case a 90Al<sub>2</sub>O<sub>3</sub>-10ZrO<sub>2</sub> (vol. %) gel from Al(O-*s*-Bu)<sub>3</sub> and Zr(O-*n*-Pr)<sub>4</sub> gave  $\alpha$ -Al<sub>2</sub>O<sub>3</sub> at  $\sim 1050^\circ\text{C}$ , whereas in the pure Al<sub>2</sub>O<sub>3</sub> material the transition to  $\alpha$ -occurred at 850°C and was essentially complete at 1100°C.

In the present work, the relative amount of ZrO<sub>2</sub> was also found to be an important factor in phase development. With 95Al<sub>2</sub>O<sub>3</sub>-5ZrO<sub>2</sub>, well-developed  $\alpha$ -Al<sub>2</sub>O<sub>3</sub> was observed at 1200°C; but this was observed only on firing to 1300°C for the 57.4Al<sub>2</sub>O<sub>3</sub>-42.6ZrO<sub>2</sub> composition. Also observed for the latter composition, a high concentration of ZrO<sub>2</sub> inhibited the formation of transitional

TABLE 35.1. Crystalline Phases Detected in Fired Gels

Temperature (°C)	95Al <sub>2</sub> O <sub>3</sub> -5ZrO <sub>2</sub>	80Al <sub>2</sub> O <sub>3</sub> -20ZrO <sub>2</sub>	57.4Al <sub>2</sub> O <sub>3</sub> -42.6ZrO <sub>2</sub>	Mullite-15ZrO <sub>2</sub>
900	$\gamma$	$\gamma$	Amorphous	M
1000	$\gamma$ , $\theta$	$\gamma$ , ZT	ZT	M, ZT
1100	$\gamma$ , $\theta$	$\gamma$ , $\theta$ , $\alpha$	$\gamma$ , $\theta$ , $\alpha$	M, ZT
	$\alpha$ , ZT	ZT, ZM	ZT, ZM	
1200	$\alpha$ , ZT, ZM	$\alpha$ , ZT, ZM	$\theta$ , $\alpha$ , ZT, ZM	M, ZT
1300	$\alpha$ , ZT, ZM	$\alpha$ , ZT, ZM	$\alpha$ , ZT, ZM	M, ZT
1400	$\alpha$ , ZT, ZM	$\alpha$ , ZT, ZM	$\alpha$ , ZT, ZM	M, ZT

Abbreviations used:  $\gamma$ ,  $\gamma$ -Al<sub>2</sub>O<sub>3</sub>;  $\theta$ ,  $\theta$ -Al<sub>2</sub>O<sub>3</sub>;  $\alpha$ ,  $\alpha$ -Al<sub>2</sub>O<sub>3</sub>; ZT, tetragonal ZrO<sub>2</sub>; ZM, monoclinic ZrO<sub>2</sub>; M, mullite.

$\text{Al}_2\text{O}_3$  phases. No crystalline  $\text{Al}_2\text{O}_3$  ( $\gamma$ ,  $\theta$ , or  $\alpha$ ) was formed until  $1100^\circ\text{C}$ . Broad peaks corresponding to the (111) reflection of tetragonal  $\text{ZrO}_2$  were apparent in the high  $\text{ZrO}_2$  content gels at  $1000^\circ\text{C}$ , that is, before the  $\gamma \rightarrow \theta$ - $\text{Al}_2\text{O}_3$  transition. It has been postulated by Pugar and Morgan [16] that in materials derived from alkoxides zirconium is incorporated into the  $\gamma$ - $\text{Al}_2\text{O}_3$  network and is precipitated out during the  $\gamma \rightarrow \theta$  transformation. The  $\text{ZrO}_2$  particles then exhibit rapid growth as the  $\text{Al}_2\text{O}_3$  transforms from  $\theta \rightarrow \alpha$ . However, Debsikdar [17] observed tetragonal  $\text{ZrO}_2$  before the  $\gamma \rightarrow \theta$  transformation in materials prepared by a different synthetic procedure. Our results concur with the latter finding; however, rapid growth in the size and number of the  $\text{ZrO}_2$  particles was observed at  $1200^\circ\text{C}$  indicated by the (111) reflection becoming sharp and well defined with an increased integrated intensity.

The  $\text{ZrO}_2$  phase was principally the tetragonal form in all the samples and firing temperatures studied here; only minor amounts ( $< 5$  wt %) of monoclinic  $\text{ZrO}_2$  were detected. In all cases, the amounts of tetragonal  $\text{ZrO}_2$  and  $\alpha$ - $\text{Al}_2\text{O}_3$  crystallized increased substantially on firing between  $1100$  and  $1400^\circ\text{C}$ . For example, in the  $80\text{Al}_2\text{O}_3$ - $20\text{ZrO}_2$  material, the integrated intensity of the (111) reflection of tetragonal  $\text{ZrO}_2$  increased by a factor of 1.6 and that of the (012) reflection of  $\alpha$ - $\text{Al}_2\text{O}_3$  by a factor of 4.5 between  $1100$  and  $1400^\circ\text{C}$ .

For the mullite- $\text{ZrO}_2$  gel, poorly crystalline mullite was observed at  $900^\circ\text{C}$ ; at  $1000^\circ\text{C}$  the mullite was well crystallized. Very weak reflections corresponding to tetragonal  $\text{ZrO}_2$  were detected at  $1000^\circ\text{C}$ , and the  $\text{ZrO}_2$  was well crystallized at  $1300^\circ\text{C}$ . No monoclinic  $\text{ZrO}_2$  was detected by XRD in any of the samples investigated here.

Fracture surfaces of fired gels were investigated by SEM in the back-scattered mode. Indistinct microstructures with a lack of  $\text{ZrO}_2$ -rich areas were observed at  $1200^\circ\text{C}$ . However, in samples fired at  $1400^\circ\text{C}$ , well-defined microstructures were observed. Representative micrographs are shown in Figs. 35.1 to 35.4. At

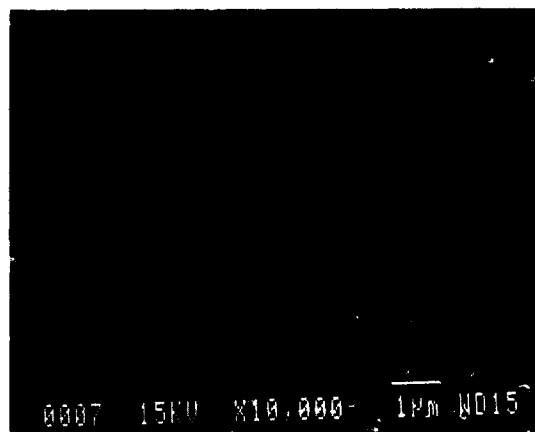


Figure 35.1. Microstructure of  $95\text{Al}_2\text{O}_3$ - $5\text{ZrO}_2$  fired at  $1400^\circ\text{C}$  (bar =  $1\mu\text{m}$ ).

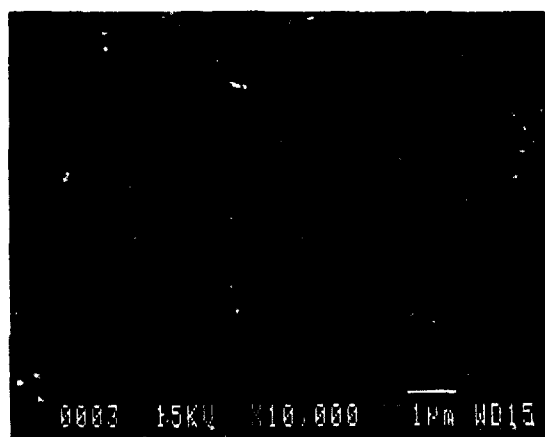
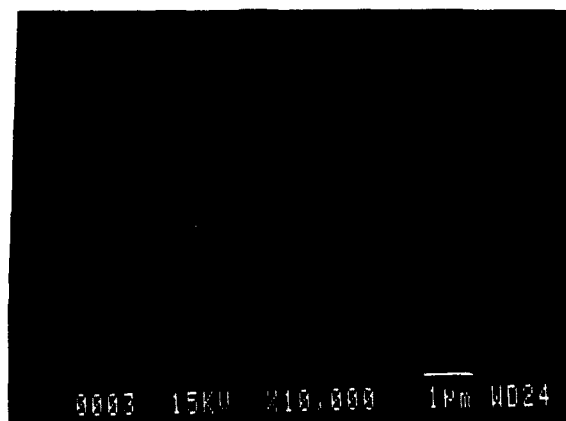
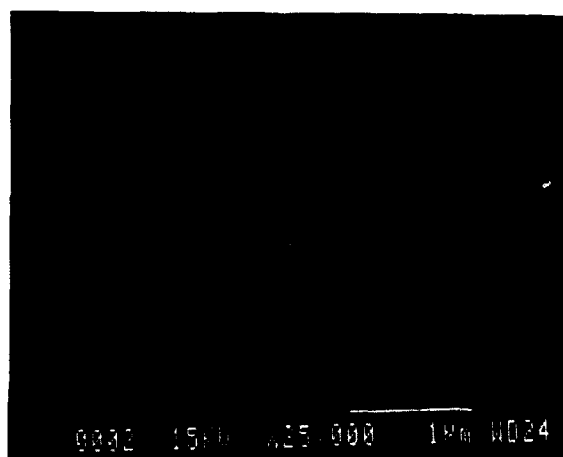


Figure 35.2. Microstructure of 80Al<sub>2</sub>O<sub>3</sub>-20ZrO<sub>2</sub> fired at 1400°C (bar = 1 μm).



(a) × 10000



(b) × 25000

Figure 35.3. Microstructure of 57.4Al<sub>2</sub>O<sub>3</sub>-42.6ZrO<sub>2</sub> fired at 1400°C at different magnifications [bar = 1 μm in both (a) and (b)].



Figure 35.4. Microstructure of mullite-15ZrO<sub>2</sub> fired at 1400°C (bar = 1 μm).

this temperature, the samples appeared dense and virtually pore-free within the resolution limits of the SEM. Tetragonal-ZrO<sub>2</sub> particles (light areas in the micrographs) were well dispersed throughout the ceramic matrices. For 95Al<sub>2</sub>O<sub>3</sub>-5ZrO<sub>2</sub>, the ZrO<sub>2</sub> was intergranular, principally at three- but also at two- and four-grain boundaries. With higher ZrO<sub>2</sub> concentrations, the ZrO<sub>2</sub> was both inter- or intragranular. Coarsening of the ZrO<sub>2</sub> particles was observed with increasing concentration, ranging from 0.05 μm for the 95Al<sub>2</sub>O<sub>3</sub>-5ZrO<sub>2</sub> material to 0.4 μm for the 57.4 Al<sub>2</sub>O<sub>3</sub>-42.6ZrO<sub>2</sub> material. A similar increase in size of the matrix α-Al<sub>2</sub>O<sub>3</sub> grains (dark regions) was noted. The grain size ranged from ~0.5 to 1.5 μm for the low ZrO<sub>2</sub> content to ~5 μm for the high ZrO<sub>2</sub> content materials. Interestingly, no eutecticlike structure was observed in the 57.4Al<sub>2</sub>O<sub>3</sub>-42.6ZrO<sub>2</sub> sample. With the mullite-ZrO<sub>2</sub> material, fine tetragonal ZrO<sub>2</sub> particles were dispersed throughout the mullite matrix, both inter- and intragranular.

### 35.4. CONCLUSION

Dense Al<sub>2</sub>O<sub>3</sub> and mullite-tetragonal ZrO<sub>2</sub> composites have been successfully prepared by an all-alkoxide route.

### ACKNOWLEDGMENTS

Financial support for the present work was provided by E. I. du Pont de Nemours and Company and by the Air Force Office of Scientific Research. This support is gratefully acknowledged.



## REFERENCES

1. N. Claussen, *J. Am. Ceramic Soc.*, **59**, 49 (1976).
2. D. J. Green, *J. Am. Ceramic Soc.* **65**, 610 (1982).
3. F. F. Lange, *J. Mater. Sci.*, **17**, 225 (1982).
4. F. F. Lange and D. J. Green, in: A. H. Heuer and L. W. Hobbs, Eds., *Advances in Ceramics*, Vol. 3, pp. 217-225, The American Ceramic Society, Columbus, Ohio (1981).
5. R. C. Garvie, *J. Mater. Sci. Lett.*, **3**, 315 (1984).
6. A. H. Heuer, *J. Am. Ceramic Soc.*, **65**, 642 (1982).
7. D. W. Sproson and G. L. Messing, *J. Am. Ceramic Soc.*, **67**, C-92 (1984).
8. B. Fegley, P. White, and H. K. Bowen, *J. Am. Ceramic Soc.*, **68**, C-60 (1985).
9. F. F. Lange, B. I. Davis, and E. Wright, *J. Am. Ceramic Soc.*, **69**, 66 (1986).
10. S. Baik, A. Bleier, and P. F. Becher, in: C. J. Brinker, D. E. Clark and D. R. Ulrich, Eds., *Better Ceramics Through Chemistry*, Vol. II, *Mater. Res. Soc.*, **73**, 791-800 (1986).
11. I. A. Askay, F. F. Lange, and B. I. Davies, *J. Am. Ceramic Soc.*, **66**, C-190 (1983).
12. Y. Murase, E. Kako, and K. Diamon, *J. Am. Ceramic Soc.*, **69**, 83 (1986).
13. N. Claussen, *J. Am. Ceramic Soc.*, **61**, 85 (1978).
14. M. Kagawa, M. Kikuchi, Y. Syano, and T. Nagae, *J. Am. Ceramic Soc.*, **66**, 751 (1983).
15. H. Yoshimatsu, T. Yabuki, and H. Kawasaki, *J. Non-Cryst. Solids*, **100**, 413 (1988).
16. E. A. Pugar and P. E. D. Morgan, *J. Am. Ceramic Soc.*, **69**, C-120 (1986).
17. J. C. Debsikdar, *J. Mater. Sci.*, **22**, 2237 (1987).
18. S. Prochazka, J. S. Wallace, and N. Claussen, *J. Am. Ceramic Soc.*, **66**, C-125 (1983).
19. J. S. Moya and M. I. Osendi, *J. Mater. Sci.*, **19**, 2909 (1984).
20. G. Orange, G. Fantozzi, F. Cambier, C. Leglud, M. R. Anseau, and A. Leriche, *J. Mater. Sci.*, **20**, 2533 (1985).
21. R. McPherson, *J. Am. Ceramic Soc.*, **69**, 297 (1986).
22. Q.-M. Yuan, J.-Q. Tan, J.-Y. Shen, X.-H. Zhu, and Z.-F. Yang, *J. Am. Ceramic Soc.*, **69**, 268 (1986).
23. R. C. Garvie and P. S. Nicholson, *J. Am. Ceramic Soc.*, **55**, 303 (1972).

## DENSIFICATION OF SILICA-CUBIC BORON NITRIDE COMPOSITES: I

AZAR NAZERI-ESHGHI AND J. D. MACKENZIE

### 36.1. INTRODUCTION

Cubic boron nitride (CBN) is second only to diamond in hardness. CBN is a highly desirable filler in ceramic-matrix composites. The sol-gel route to prepare CBN-containing composites is apparently a desirable process. However, achieving full densification is a major problem encountered in the fabrication of particulate-reinforced composites as the concentration of the filler is increased. Indeed, the effect of inhomogeneities on the densification of ceramic powders has been the subject of many studies and presents a practical problem in the fabrication of ceramic-matrix composites. These inhomogeneities that may occur as bimodal powder compacts or as inclusions with different sintering rates than the matrix have been investigated theoretically and experimentally [1-4]. On the other hand, in the sol-gel technology, drying and sintering of wet gels to monolithic dense-shaped bodies have been two of the biggest obstacles to the widespread industrial use of this process [5, 6].

Although there has been a considerable number of studies done on sol-gel-based composites, no systematic study on the drying and sintering of these composites has been reported. The present work is a preliminary study of ongoing research on the effect of CBN inclusions on the densification of silica-CBN composites. This study is aimed at the investigation of this phenomena by

*Ultrastructure Processing of Advanced Materials.*  
Edited by Donald R. Uhlmann and Donald R. Ulrich (deceased).  
ISBN 0-471-52986-9 © 1992 John Wiley & Sons, Inc.

the systematic measurement of the linear shrinkage as a function of temperature at a constant rate of heating. Due to the complex mechanisms of drying and unexpected behavior of these gel composites below the viscous flow region, only the temperature range between 20 and 940°C is discussed.

### 36.2. EXPERIMENTAL

Silica matrices of the composites were prepared by a 4:4:1 ratio of ethanol, water, and tetraethoxysilane (TEOS), respectively. Different volume percent of CBN from 0 to 40% and three different particle sizes of 0-1, 2-4, and 6-12  $\mu\text{m}$  were incorporated in the silica solution. CBN grains (obtained from GE Superabrasives; BZN-I-MP, Worthington, Ohio) had a bell-shaped size distribution and irregular shapes as shown in an electron micrograph in Fig. 36.1. Hydrofluoric acid (0.05 mol) was added to the TEOS solution containing CBN particles. Solution was stirred with a magnetic stirrer up to a few minutes before complete gellation (the gradual increase in the viscosity results in uniform dispersion of the CBN particles in the gel matrix). Viscous solution was cast into test tubes 75 mm long and 15 mm in diameter. Samples 12.7 mm long and 9.4 mm in diameter were cut with parallel ends for continuous dilatometric shrinkage measurements in an Orton automatic recording dilatometer. Both bulk and apparent densities were measured by using Archimedes's principle and soaking the samples overnight in the distilled water. Differential thermal (DTA) and thermogravimetric analyses (TGA) of the samples were obtained by a Perkin-Elmer 1700 DTA system.



Figure 36.1. Scanning electron micrograph of 6 to 12- $\mu\text{m}$  CBN particles.

### 36.3. RESULTS AND DISCUSSION

DTA of the silica matrix shows that evaporation of physically adsorbed water and the burnout of organics happen below 460°C. TGA of the silica at the same heating rate of 3°C/min shows that the weight loss continues long after 460°C, due to chemically adsorbed water and perhaps some residual organics still trapped in the matrix. Isothermal hold at 460°C showed that most of the organic burnout happens in the first 10 min of the heat treatment. The constant heating rate of the composites with different volume loading of CBN showed four different regions of shrinkage. In a typical curve, shown in Fig. 36.2, the shrinkage rate at low temperatures is slow until a certain temperature is reached where the shrinkage rate increases abruptly. Next, there is a well-defined plateau and then another sharp increase in shrinkage, which is associated with the viscous flow of the matrix. This report is limited to the results and discussion of the temperature region just below the viscous flow regime. Linear shrinkage of the composites with CBN particles of 2–4  $\mu\text{m}$  with different volume percent of inclusions is shown in Fig. 36.3. The increase in particle volume percent shifts the second region of the shrinkage curve to higher temperatures. Unexpectedly, the amount of total shrinkage increases for higher volume percent of CBN.

When the particle size of the CBN is changed, the amount of shrinkage and

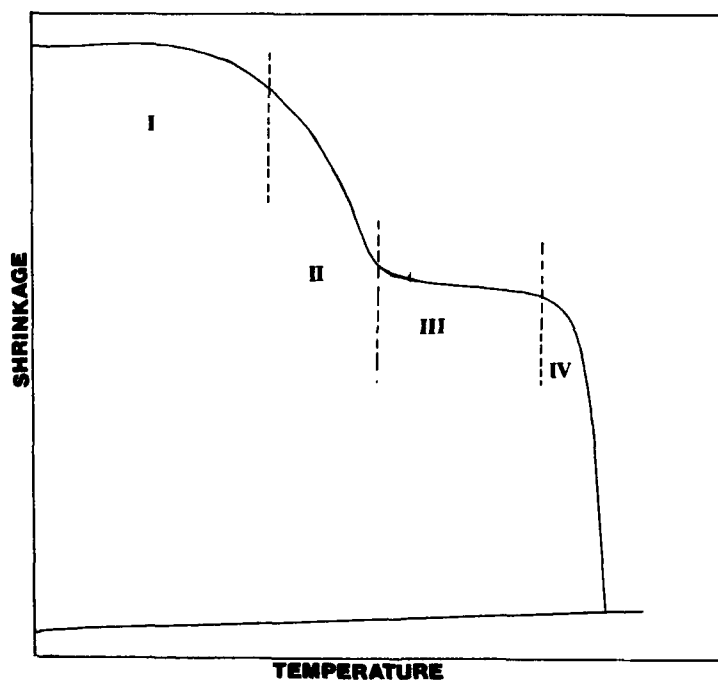


Figure 36.2. Linear shrinkage versus temperature for a typical silica-CBN composite.

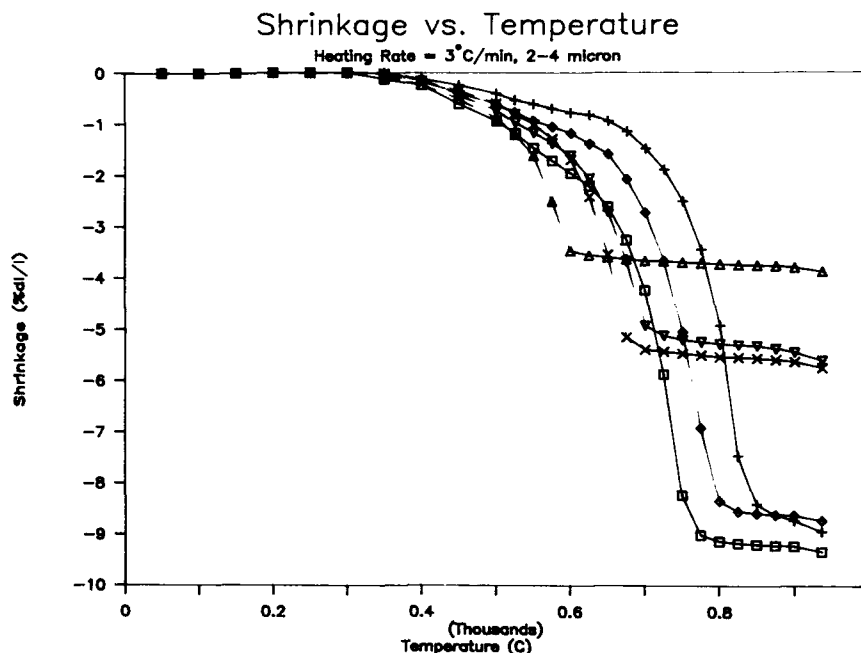


Figure 36.3. Linear shrinkage versus temperature at constant-rate heating of 3 C/min for different volume loading of CBN.  $\Delta$ , pure silica; x, 6.6 vol %;  $\triangle$ , 13.7 vol %;  $\square$ , 21.3 vol %;  $\diamond$ , 29.7 vol. %; +, 38.8 vol. %.

the temperature range of each stage of shrinkage change drastically, especially at higher concentration of inclusions. With 6.6% CBN incorporated in the composite, there is little difference in the shrinkage or temperature shift, although small changes are observed (Fig. 36.4). However, when the volume percent of CBN is increased to 21.3%, sharp differences in the shape of the shrinkage curve is observed for different particle sizes. For the samples of 0 to 1- $\mu$ m CBN, the plateau of the third region disappears and only 2% shrinkage is observed up to  $\sim 900^\circ\text{C}$  (Fig. 36.5). To investigate if the sharp shrinkage in the second region of the shrinkage curve is due to the organic burnout, two samples of 6.6 and 21.3% CBN were heat-treated at  $460^\circ\text{C}$  prior to the run in the dilatometer. Figure 36.6 shows that despite the previous thermal history of the two gels, all four gels still go through a sharp shrinkage.

Tables 36.1 to 36.3 present the apparent and bulk densities of the samples with 2-4  $\mu$ m CBN at different temperatures (bulk density is based on the volume of the solid and the closed and open pores). As seen in Table 36.1, the apparent density of the silica gel dried at  $100^\circ\text{C}$  is very high; an indication of high skeleton density in the gel (the increase in the apparent and bulk densities with the increase in volume percent of CBN) is due to the higher density of CBN versus

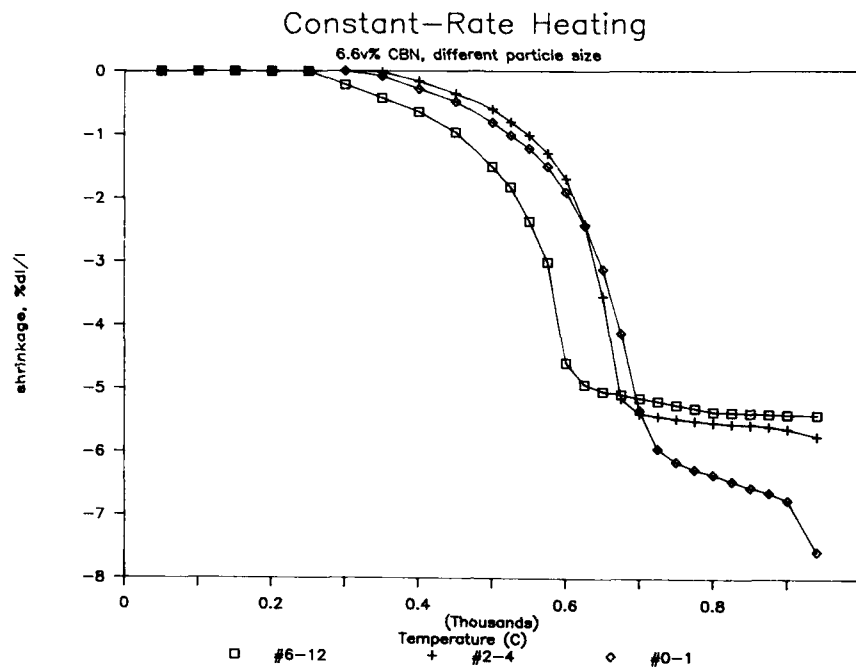


Figure 36.4. Linear shrinkage of composites with 6.6% CBN of different particle sizes.

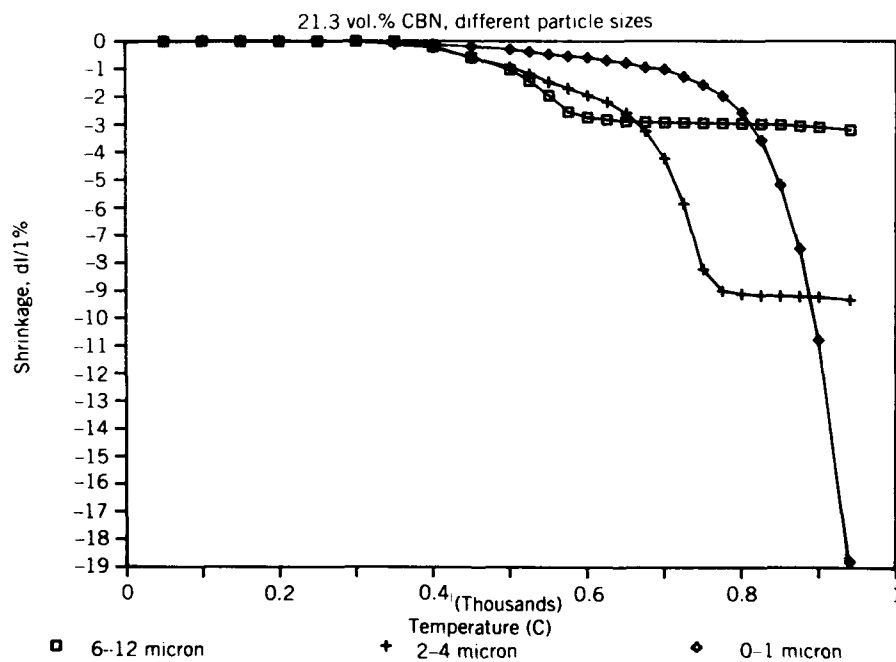
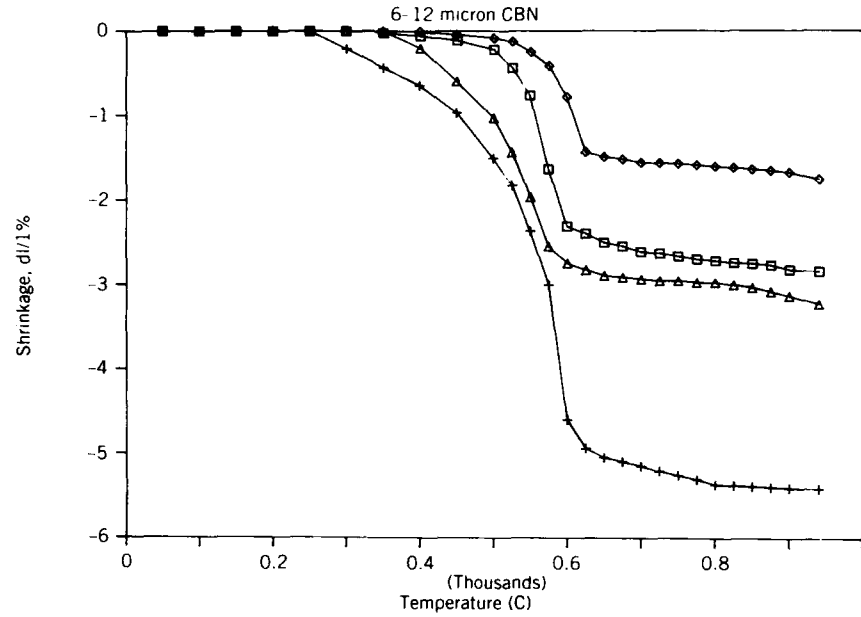


Figure 36.5. Linear shrinkage of composites with 21.3% CBN of different particle sizes.



**Figure 36.6.** Linear shrinkage of composites with different thermal history. +, 6.6 vol% not preheated;  $\Delta$ , 21.3 vol%, not preheated;  $\square$ , 6.6 vol%, preheated to 460°C;  $\diamond$  21.3 vol%, preheated to 460°C.

silica. The pore volume per gram of composite was calculated using the bulk and apparent densities in the following equation:

$$V_p(\text{cm}^3/\text{g}) = \frac{1}{d_{(\text{bulk})}} - \frac{1}{d_{(\text{apparent})}}$$

**TABLE 36.1.** Density and Porosity of Silica-CBN Composites Dried at 100°C

CBN Volume %	Bulk Density (g/cm <sup>3</sup> )	Apparent Density (g/cm <sup>3</sup> )	Porosity (%)	Composite Pore Volume/ (cm <sup>3</sup> /g)	Silica Pore Volume (cm <sup>3</sup> /g)
0.0	0.48	2.18	78	1.65	1.65
6.6	0.55	2.24	75	1.37	1.52
13.7	0.58	2.39	76	1.31	1.77
21.3	0.65	2.45	73	1.13	1.61
29.7	0.71	2.56	72	1.01	1.68
38.8	0.83	2.68	69	0.83	1.66

**TABLE 36.2. Density and Porosity of Silica-CBN Composites Heated to 450°C for 3 Hours**

CBN Volume %	Bulk Density (g/cm <sup>3</sup> )	Apparent Density (g/cm <sup>3</sup> )	Porosity (%)	Composite Pore Volume/ (cm <sup>3</sup> /g)	Silica Pore Volume (cm <sup>3</sup> /g)
0.0	0.50	2.18	76	1.54	1.54
6.6	0.58	2.25	75	1.28	1.37
13.7	0.60	2.32	75	1.27	1.43
21.3	0.67	2.34	72	1.07	1.35
29.7	0.75	2.53	72	0.94	1.33
38.8	0.85	2.65	71	0.80	1.29

These values were then normalized for the silica matrix. The pore volume in the silica matrix, as expected, was constant for all the composites of different volume percent of CBN. Table 36.2 gives the results for density measurements after an isothermal soak at 460°C. Linear shrinkage from 20 to 460°C is between 0.5 and 1.5%, and the changes in apparent densities are nominal. However, there has been a measurable increase in the bulk density, which is the result of bulk densification. The density measurement after the constant heating rate to 940°C showed both skeletal and bulk densification. At this stage the pore volume in the silica matrix was reduced as the concentration of the CBN increased. This is the result of larger shrinkage for higher concentrations of CBN as was seen in Fig. 36.3. Table 36.4 is a summary of the percentage shrinkage for all the tested composites.

The mechanisms of shrinkage at each stage are not formulated at the present time. Future experimental work on pore size and pore size distribution, surface

**TABLE 36.3. Density and Porosity of Silica-CBN Composites Heated from 20-940°C at 3°C/min**

CBN Volume %	Bulk Density (g/cm <sup>3</sup> )	Apparent Density (g/cm <sup>3</sup> )	Porosity (%)	Composite Pore Volume/ (cm <sup>3</sup> /g)	Silica Pore Volume (cm <sup>3</sup> /g)
0.0	0.55	2.22	77	1.51	1.51
6.6	0.58	2.31	75	1.29	1.43
13.7	0.70	2.4	62	1.01	1.17
21.3	0.85	2.54	66	0.78	1.11
29.7	0.93	2.61	64	0.55	0.92
38.8	1.16	2.69	57	0.49	0.98



TABLE 36.4. Linear Shrinkage of Silica-CBN Composites at Constant Heating Rate of 3°C/min from 20-940°C

CBN Volume (%)	% Linear Shrinkage		
	Particle Size of CBN		
	9 $\mu$	3 $\mu$	0.5 $\mu$
0.0	—	3.9	—
6.6	5.4	5.8	7.6
13.7	—	5.6	—
21.3	3.1	9.3	18.8
29.7	—	8.7	—
38.8	—	8.9	—

area, and isothermal shrinkage in the viscous flow regime is expected to help determine the mechanisms.

### 36.4. SUMMARY

Silica-CBN composites of different volume loadings were prepared through sol-gel processing. Dilatometric shrinkage of these composites at the temperature range between 20 and 940°C was measured. Large differences in the amount and temperature of shrinkage were observed with change in CBN volume loading. Also, considerable differences in shrinkage resulted as the particle size of the CBN was changed. The effect of the thermal history of the composites on the shrinkage behavior showed that the abrupt shrinkage of the matrix is completely related to organic burnout.

### ACKNOWLEDGMENT

The authors are grateful to the Air Force Office of Scientific Research, Directorate of Chemical and Atmospheric Sciences, for their support of this work.

### REFERENCES

1. A. G. Evans, *J. Am. Ceramic Soc.*, **69**, 102 (1986).
2. C. H. Hsueh, A. G. Evans, and R. M. McMeeking, *J. Am. Ceramic Soc.*, **69**, C-64 (1986).
3. M. N. Rahaman and L. C. DeJonghe, *J. Am. Ceramic Soc.*, **70**, C-348 (1987).
4. G. W. Scherer, *J. Am. Ceramic Soc.*, **70**, 719 (1987).
5. C. J. Brinke, G. W. Scherer, and E. P. Roth, *J. Non-Cryst. Solids*, **72**, 345 (1985).
6. G. W. Scherer, *J. Non-Cryst. Solids*, **100**, 77 (1988).

## MECHANICAL BEHAVIOR OF (POLY)METHYLMETHACRYLATE- IMPREGNATED SILICA GELS

B. ABRAMOFF AND L. C. KLEIN

### 36.1. INTRODUCTION

Only a handful of studies have reported mechanical properties of sol-gel-processed silica. These include alcogels [1], aerogels [2, 3], xerogels [4, 5], and colloidal gels [6]. For alcogels, aerogels, and colloidal gels, Young's modulus and strength have been measured. For silica xerogels from silicon alkoxides, elastic constants and strength have been measured. A typical value for Young's modulus is about 10 GPa, and a typical strength is 20 MPa [4]. The elastic constants of xerogels are found to be sensitive to relative humidity. To lessen the sensitivity to moisture without increasing the weight substantially, it is possible to impregnate the xerogel with (poly)methylmethacrylate (PMMA) and, at the same time, maintain optical transparency [7].

Silica xerogel monoliths have been infiltrated with PMMA and other glassy polymers [7, 8]. Processing of the xerogels involved catalysis with HF and firing to 800°C. The resulting xerogels were 33% porous and had a median pore diameter of 10 nm. The porous gels were infiltrated with monomer solutions and polymerized in situ. The resulting composites consisted of two fully percolating phases, a silica matrix and an organic polymer impregnant. The measured Young's modulus was about 30 GPa [8].

The silica/PMMA composite can be used to encapsulate electrooptically

*Ultrastructure Processing of Advanced Materials.*

Edited by Donald R. Uhlmann and Donald R. Ulrich (deceased).

ISBN 0-471-52986-9 © 1992 John Wiley & Sons, Inc.

active organic compounds such as 2-methyl-4-nitroaniline (MNA). Electro-optical de Kerr effect and solid-state deuterium nuclear magnetic resonance (NMR) measurements were made [9]. In comparison to conventional optical cells, silica/PMMA composites had better optical quality and retained dimensional stability to about 90°C. The composites were abrasion resistant and could be machined to complex shapes.

Following this concept, the question is whether or not it is possible to have a composite with a lower density and finer texture for improved toughness. Ideally, all processing should be at room temperature instead of at 800°C for heat treatment. Monolithic xerogels that are 50% porous with a median pore diameter of 2 nm [10] were used to prepare composites without high-temperature treatment.

### 37.2. EXPERIMENTAL TECHNIQUES

Silica xerogels were prepared from a solution of tetraethylorthosilicate (TEOS), distilled deionized water, and ethanol. Equal volumes of distilled TEOS and ethanol were used. The molar ratio of water:TEOS was 16 [10]. The solution was catalyzed with 0.1 M HNO<sub>3</sub> and was stirred for 30 min. Polystyrene tubes were filled with 10 ml of the solution. Samples were gelled in an oven for 7 days at 50°C and then at 70°C for 10 days. Next, the tubes were uncovered and dried in lots of 100 at 50°C for 14 days. Xerogels were removed from the tubes and dried 2 more days at 50°C. Finally, the gels were outgassed 24 h at 250°C to remove physically adsorbed species.

A monomer solution of 1 g benzoyl peroxide (97%) catalyst/100 ml MMA (methylmethacrylate, inhibited) was prepared (Aldrich Chemicals, Milwaukee, Wisc.). After outgassing, each xerogel was immediately immersed in a borosilicate vial containing 11 ml of the monomer solution (I). The solution was allowed to infiltrate for 2 hr, and then the sealed vials were polymerized 7 days in a cabinet with longwave UV illumination (II). The cabinet had a UV intensity of about 2000  $\mu\text{W}/\text{cm}^2$ , a temperature 3°C above ambient, and a fan to dissipate heat from the vials. After polymerization, the vials were destructively removed, and the PMMA-surrounded composites were treated at 200°C in a mechanical convection oven for 30 min (III). This is a temperature about 100°C above the glass transition temperature of bulk PMMA and is also high enough to promote a moderate rate of depolymerization. Immediately after removal from the oven, the now rubbery and bloated PMMA shells were removed by hand to recover net shape composites (IV). These steps (I–IV) are shown schematically in Fig. 37.1.

Density and porosity were measured using Archimedes method. Density was determined in freshly boiled deionized water. Before immersion in water, silica matrices were exposed to ambient conditions for 2 days to prevent explosion. The open porosity of the silica matrix was measured with methanol, ethanol,

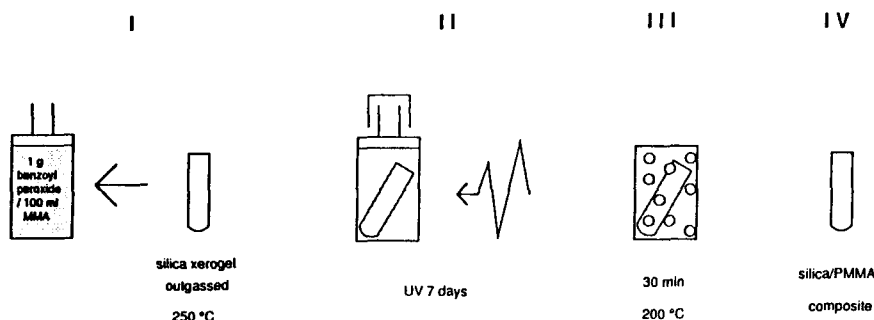


Figure 37.1. Schematic of silica xerogel impregnation with PMMA.

and MMA monomer solution. Five samples were measured for each test, and immersion time with all solvents was 24 hr. Surface area, pore size distribution and pore shape were measured using nitrogen sorption on the Omnisorp 360 (Omicron Technology, Berkeley Heights, N.J.). After outgassing 24 hr at 250°C, monolithic xerogels were outgassed 2 hr at 250°C under vacuum in the unit before analysis.

Strength measurements were made by the four-point flexure technique. The flexure fixture had a support span of 2.540 cm (1.000 in.) and a load span of 1.270 cm (0.500 in.). A gear-driven Instron materials testing machine with a 1000-lb load cell was used. Crosshead speeds were 0.05 cm/min (0.02 in./min) for silica and silica/PMMA and 5.08 cm/min (2.0 in./min) for PMMA. The rapid strain rate for PMMA was necessary to prevent elastic deformation. Silica samples were measured before and after outgassing. Composite samples were measured fresh within 1 hr of recovery from the PMMA and also after exposure to ambient conditions for 14 days. Water adsorption in PMMA was only on the order of 0.1% even after exposure. Sample test sets numbered 50 for silica and silica/PMMA and 20 for PMMA.

Elastic constants were measured with ultrasonic NDE. Transducers used in the pitch/catch mode for longitudinal and transverse wave velocities were 5 MHz WC50-5 and 2MHz SDB25-2 (Ultran Laboratories, State College, Pa.). For each test, five samples were measured. Materials were ground dry on two sides to produce test samples of about 4 mm thickness. Silica samples were measured within 3 min of outgassing and with less than 0.5% water adsorption. Composites were measured fresh. Young's modulus,  $E$ , and shear modulus,  $G$ , were calculated directly from the longitudinal wave velocities,  $v_L$ , transverse wave velocities,  $v_T$ , and bulk densities,  $\rho$ , according to

$$E = [3\rho v_L^2 - 4\rho v_T^2] / [(v_L/v_T)^2 - 1] \quad (1)$$

$$G = \rho v_T^2 \quad (2)$$

Poisson's ratio,  $n$ , and bulk modulus,  $K$ , were then determined from relations

$$n = E/2G - 1 \quad (3)$$

$$K = E/3(1 - 2n) \quad (4)$$

### 37.3. RESULTS

Silica samples were roughly cylindrical in shape with some tapering from top to bottom. The diameter at the center of the outgassed matrixes and composites was 5.60 mm and the length was about 33 mm. Linear shrinkage of the gel due to outgassing was 2.2%. Nitrogen adsorption and desorption yielded information on pore size and texture. The surface area of the matrix was 900 m<sup>2</sup>/g. Porosity was almost completely microporous (less than 2.0 nm in diameter) and cylindrical in shape.

Table 37.1 summarizes physical characteristics. Listed are bulk densities and open porosities. Assuming no closed porosity to methanol or ethanol gives a skeletal density about 2.27 g/cm<sup>3</sup>. The open porosity in MMA was 52.5% compared to 53.4% in methanol and ethanol. The composite was 94% theoretical density and 8.5% calculated total porosity. The total weight gain during infiltration followed by polymerization was 50%.

Table 37.2 lists elastic properties of the materials. Included are the longitudinal and transverse wave velocities, Young's modulus, shear modulus, bulk modulus, and Poisson's ratio.

Figure 37.2 shows the strength distributions of each set of 50 samples as represented by the two-parameter Weibull analysis [11]. Values of the mean strength, Weibull modulus, and correlation coefficient are listed in Table 37.3. Water adsorption for silica was 26% during the testing at 50% relative humidity. Water adsorption for aged composites was 1.2% during the testing at 20% relative humidity. Outgassing of the xerogels led to a small increase in strength and a widening of the distribution. Aging of the composite led to a slight decrease in strength.

TABLE 37.1. Physical Characteristics

	Bulk density (g/cm <sup>3</sup> )	Porosity (%)
Silica xerogel	1.06	53.4%
Silica/PMMA	1.59	8.5%
PMMA	1.18	—

Abbreviation used: PMMA, (poly)methylmethacrylate.

TABLE 37.2. Elastic Properties

	$v_L$ (km/sec)	$v_t$ (km/sec)	$E$ (GPa)	$G$ (GPa)	$K$ (GPa)	$n$
Silica xerogel	2.25	1.40	4.9	2.1	2.6	0.18
Silica/PMMA	3.19	1.87	14.0	5.6	8.9	0.24
PMMA	2.69	1.37	5.8	2.2	5.6	0.33

Abbreviation used: PMMA, (poly)methylmethacrylate.

### 37.4. DISCUSSION

The heat treatment at 200°C served two purposes. First, the treatment allowed extraction of net shape composites. Additionally, the treatment relieved some stresses that developed from expansion of PMMA during the last stages of

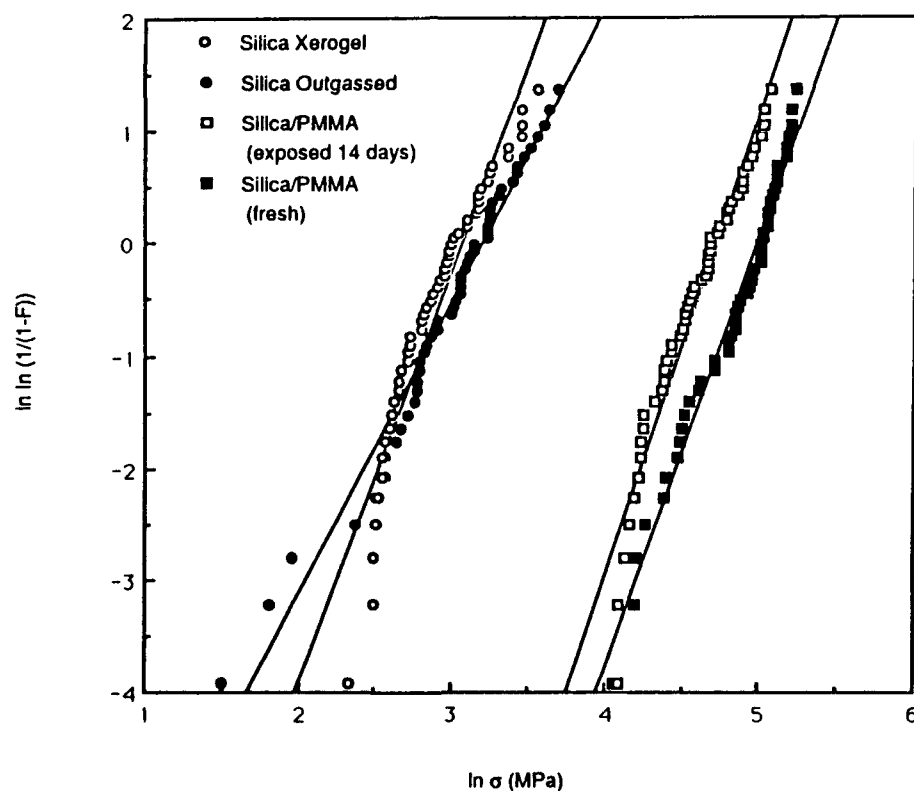


Figure 37.2. Strength distribution of the samples.

TABLE 37.3. Strengths

	Strength MPa	Weibull Modulus	$R^2$
Silica xerogel	19.3	3.7	0.91
Silica xerogel (outgassed)	21.6	2.6	0.97
Silica/PMMA (fresh)	132	3.9	0.98
Silica/PMMA (exposed 14 days)	102	4.1	0.95
PMMA	119	8.9	0.97

Abbreviations used: PMMA, (poly)methylmethacrylate.

polymerization. This expansion of the thick shell was enough to break the borosilicate vials after a few days of polymerization.

Although composites were lightweight and optically transparent, they were only 94% dense. Attainment of 100% theoretical density was limited primarily by resistance to infiltration during polymerization. In bulk, MMA densifies from 0.94 to 1.18 g/cm<sup>3</sup> during polymerization. However, as the average molecular weight of the monomer solution increases during polymerization, it becomes increasingly difficult for the monomer monomers to infiltrate the matrix. Because of the very fine size of the silica microporosity, about 1% of the matrix volume is not impregnable by even the initial monomer solution. Previously, it was determined that the PMMA in the composite contains a larger concentration of residual MMA than bulk PMMA [9].

Outgassing of the silica xerogels tended to increase strength slightly and widen the distribution. The strengthening may be attributed to some condensation of hydroxyls on the silica surface and the widening of the distribution is likely due to some damage to the surface. Although the use of different strain rates and surface conditions prevents direct comparison, it appears that the strength of the composites is similar to bulk PMMA, with a somewhat wider distribution in strengths for the composites. This indicates preexisting matrix flaws are not healed by impregnation or that new flaws are introduced by impregnation. Adsorption of water may decrease the strength of composites slightly due to corrosion of siloxane bonds of the silica matrix. Nevertheless, the water adsorption of the composites is negligible compared to adsorption for the xerogels without impregnation. The impregnated xerogel offers mechanical stability for longer exposure times.

## ACKNOWLEDGMENT

The financial support of the Office of Naval Research under Contract N00014-87-K-0529 is greatly appreciated.

## REFERENCES

1. S. A. Pardenek, J. W. Fleming, and L. C. Klein, in: Eds., C. J. Brinker, D. E. Clark, and D. R. Ulrich, *Better Ceramics Through Chemistry*, Vol. III, *Mater. Res. Soc. Symp. Proc.*, **88**, 73 (1988).
2. T. Woignier, J. Pelous, J. Phalippou, R. Vacher, and E. Courtens, *J. Non-Cryst. Solids*, **95/96**, 1197 (1987).
3. T. Woignier and J. Phalippou, *J. Non-Cryst. Solids*, **100**, 404 (1988).
4. M. J. Murtagh, E. K. Graham, and C. G. Pantano, *J. Am. Ceramic Soc.*, **69**, 775 (1986).
5. S. C. Park and L. L. Hence, in: Eds., L. L. Hence and D. R. Ulrich, *Science of Ceramic Chemical Processing*, p. 168. Wiley, New York (1986).
6. D. Ashkin, R. A. Haber, and J. B. Wachtman, *J. Am. Ceramic Soc.*, **73**, 3376 (1990).
7. E. J. A. Pope and J. D. Mackenzie, in: Eds., C. J. Brinker, D. E. Clark, and D. R. Ulrich, *Better Ceramics Through Chemistry*, Vol. II, *Mater. Res. Soc. Symp. Proc.*, **73**, 809 (1986).
8. E. J. A. Pope and J. D. Mackenzie, in: *32nd International SAMPE Symposium*, p. 760 (1987).
9. T. M. Che, R. V. Carney, G. Khanarian, R. A. Keosian, and M. Borzo, *J. Non-Cryst. Solids*, **102**, 280 (1988).
10. L. C. Klein, T. A. Gallo, and G. J. Garvey, *J. Non-Cryst. Solids*, **63**, 23 (1984).
11. S. B. Batdorf, in: Eds., R. C. Bradt, D. P. H. Hasselman, and F. F. Lange, *Fracture Mechanics of Ceramics*, Vol. 3, *Flaws and Testing*, p. 1, Plenum, New York (1978).



## ORGANICALLY MODIFIED CERAMICS—MATERIALS WITH “HISTORY” OR “FUTURE”?

H. SCHMIDT

### 38.1. INTRODUCTION

If one wants to answer the question of the future of a group of materials, one first has to look into its history. The combination of materials with different properties in order to gain new properties is an old objective of researchers concerned with material development. There are numerous examples for composites, and the tendency during the last decade shows that the unit size of the composite phases is decreasing continuously. If the unit size reaches the nanometer range, mechanical mixture of the different components becomes impossible. Other methods like vapor deposition or chemical routes have to be chosen. The sol-gel process is a suitable way to synthesize ceramic precursors like gels with the desired composition at low temperatures. These mostly amorphous materials can have different structures or microstructures, where two extremes are the *polymer type* (Fig. 38.1a) and the *colloidal type* (Fig. 38.1b). It depends on composition and reaction conditions, which type will be obtained, and which combinations are possible. The low processing temperature allows to incorporate organics, which can have different functions, depending on their type and the way they are linked to the organic network. Figure 38.2 illustrates some general possibilities. Organics can act as network modifiers and network

*Ultrastructure Processing of Advanced Materials.*

Edited by Donald R. Uhlmann and Donald R. Ulrich (deceased).

ISBN 0-471-52986-9 © 1992 John Wiley & Sons, Inc.

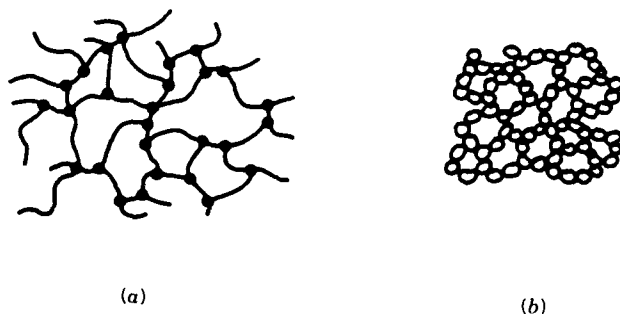


Figure 38.1. Two different types of ceramic gels. (a) Polymer type; (b) colloidal type.

formers. They can add special functions as a consequence of their chemical nature. Because there exists a large variety of organic groupings, the number of variations is almost endless. In order to bring some systematics into the jungle, it is necessary to develop some rules in the sense of structure to property or component to property relation. The size of organic and inorganic or inorganic and mixed organic-inorganic phases is not included in this structural con-

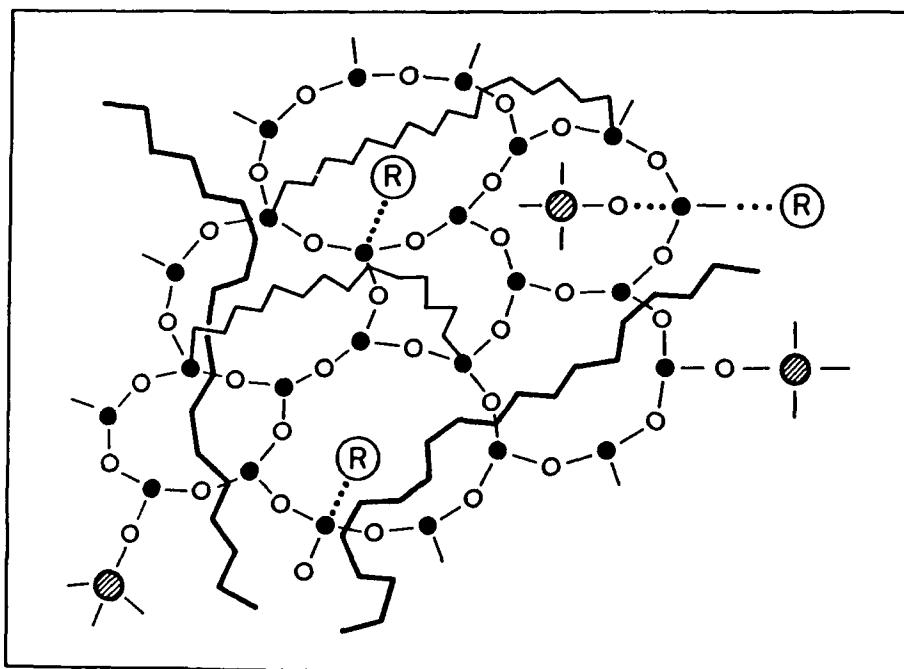


Figure 38.2. Possible structures of organic-inorganic polymers.  $\circ = \text{O}$ ;  $\bullet = \text{Si}$ ;  $\circ = \text{inorganic heteroatom}$ ;  $\sim = \text{organic chain}$ .

sideration. Because the building up process starts with molecules, due to their reactivity differences separation or arrangement effects are possible.

The Si atom offers a convenient method to link organics via a  $\equiv\text{Si}-\text{C}\equiv$  bond covalently to an inorganic backbone, if at least one  $\equiv\text{Si}-\text{O}-$  bond is present at the same Si atom, because the  $\equiv\text{Si}-\text{C}\equiv$  bond is pretty stable under ambient conditions. With other network formers, like Ti or Al, other coupling principles are necessary if a chemical bond to the organic part is desired. Complex formation (e.g., by chelating ligands) is one, ionic bonds (e.g., to organic acid ions) are another possibility.

The sol-gel process plays the dominant role for the synthesis, because it is the most important and a very flexible method to synthesize inorganic polymer networks at low temperatures. For reactions of the organic grouping, the wide knowledge of organic chemistry can be used. However, very often it is necessary to develop new routes, because the simple transformation of known reactions into different media or other reaction conditions very often is not possible. Principles of reactions by sol-gel chemistry are published elsewhere, as well as reactions of organic groups [1-6] and will only be partially discussed in this Chapter.

### 38.2. GENERAL ASPECTS OF INORGANIC-ORGANIC POLYMERS

The question has to be answered, what are the reasons for investigating or synthesizing organically modified inorganic polymers or inorganically modified organic polymers? There is at least one very simple reason: The scientific curiosity for what comes out by "mixing" together organics and inorganics on a nano or even molecular level. Behind this "simple" one, a lot of other reasons exist like the question, which sizes of the different phases are possible? or can the sizes be tailored? which properties can be obtained? or is a tailoring possible similar to a molecular engineering? and, of course, can new materials lead to new applications?

It is important to get an overview over the major influences of different components, for example, the inorganic groupings on the one hand and the organic groupings on the other hand. If one starts this consideration with examples of inorganic network or gel formers as "inorganics," like  $\text{SiO}_2$ ,  $\text{Al}_2\text{O}_3$ , or  $\text{TiO}_2$ , one should expect chemical, optical, or mechanical properties related to these materials as bulk materials (glasses or ceramics). If one starts the consideration from the organic polymeric side, for example, with polyethyleneoxide (PEO), polymethylmethacrylate (PMMA), or polyethylene (PE), one should expect properties related to these properties like high thermal expansion, low  $T_g$  values, softness, low densities, and low  $n_D$  values. In addition to this, the influence of chemical functions, for example, by organofunctional groupings, is a third parameter, because its effect on the material properties depends on the structure, or on the arrangement of these groups in the structure or their

interaction with the rest of the network. the network. Figure 38.3 is an attempt to show the connections between the main components and the influenced parameters. The question that arises is whether or not it is possible to tailor desired properties based on an experimental knowledge of the influence of different components.

### 38.3. PROPERTIES, COMPOSITION, AND STRUCTURES

The path of different developments of organically modified ceramics (ORMOCERs) showed us that in various cases properties could be predicted, that is, that new properties expected from the different elements (in this case, the element is a component, grouping, reaction condition, or similar) could be obtained. Other cases show that new unexpected properties are achieved. In the following, this will be demonstrated with a few examples.

#### 38.3.1. Reactivity of Substituted Si Esters

As described above, for the introduction of organic groupings into an inorganic network a convenient way is the use of organoalkoxysilanes. The advantage of this type of molecules is that there is yet one assembling given: The organic group is covalently linked to an inorganic network former. In a cocondensation process together with other alkoxides, the organic phase only can be separated

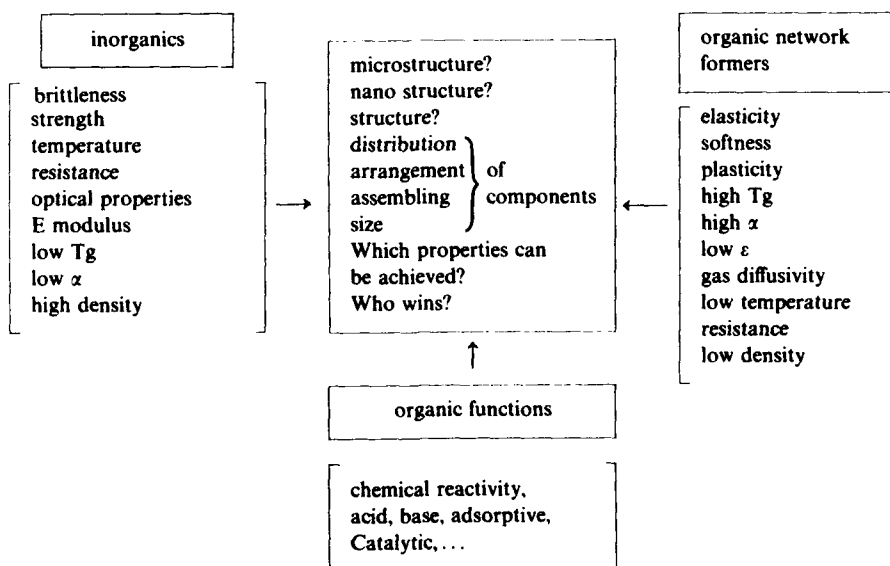


Figure 38.3. Possible influences of different components on ORMOCER properties.

from the inorganic one by including one partially inorganic network forming unit, but in this case various arrangements are possible (Fig. 38.4).

In Fig. 38.5, an example for a structure development according to step III is given.

The  $H_2O$  adsorption isotherm leads to the conclusion that the inside of the pores is covered to a great deal with hydrophobic  $CH_3$  groups from the  $CH_3-Si\equiv$  unit. This self-assembling reaction can be explained by the fact that during the hydrolysis and condensation process, where a maximum of OH groups appears, a separation effect takes place into  $SiO_{n/3}(OH)_{4-n}$  and  $CH_3SiO_{n/2}(OH)_{3-n}$  phases. This leads to the conclusion that hydrolysis and condensation rates should be different for the two different species, as one has expected anyway. As shown elsewhere [7], the hydrolysis rates actually are different, the striking point, however, is that hydrolysis of  $\equiv Si-R$  group-containing silanes decreases almost linearly with increasing content of OH groups (Fig. 38.6).

This fact can be interpreted with the assumption of an increasing difficulty of the  $OH^-$  ion to substitution reaction due to the +I effect of the alkyl groups. In this case, the proton catalyzed mechanism is the only possible one (Fig. 38.7). This means, that based on rate differences, inhomogeneities occur, regardless of whether they are desired or not. Because the means for rate control are limited, especially if one wants to equilibrate hydrolysis and condensation rates of several components, one has to look for other reactions to overcome rate difference-based disadvantages for structure controlling. Yoldas [8] has pointed

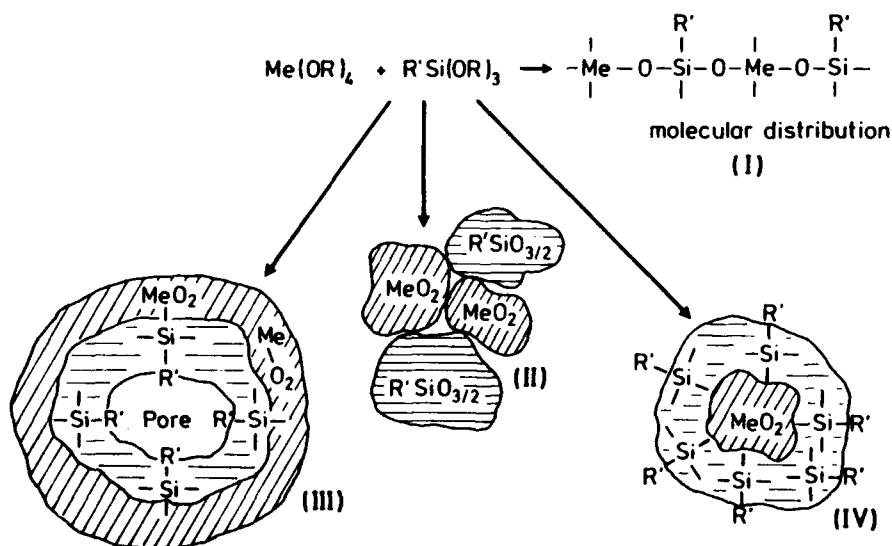


Figure 38.4. Some examples for different arrangements of inorganic-organic composites by sol-gel reactions.

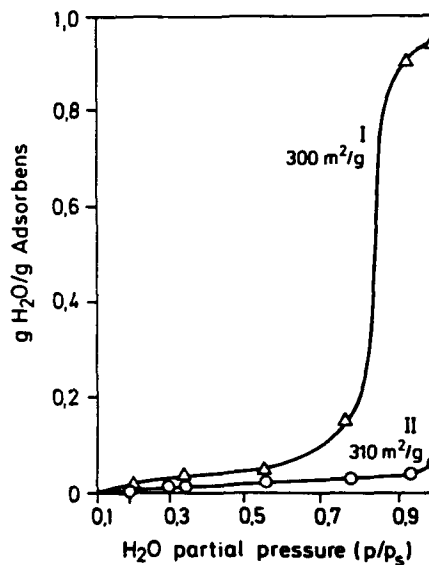


Figure 38.5. H<sub>2</sub>O adsorption isotherm (25°C) of amino group containing SiO<sub>2</sub> gel (I) compared to (CH<sub>3</sub>)SiO<sub>3/2</sub>:SiO<sub>2</sub> = 4:6 gel (II).

out that by a fixation of one species to an already formed polymeric network, phase separation can be avoided or, as shown in Ref. 2, the so-called CCC (chemically controlled condensation) reaction can be applied successfully. The latter one allows control of the unit size as shown in Ref. 9 and keeps it small enough to cause light scattering and to exclude optical application. This was shown on a polymer based on SiO<sub>2</sub>/TiO<sub>2</sub>/SiO<sub>3/2</sub> epoxy. With chemical

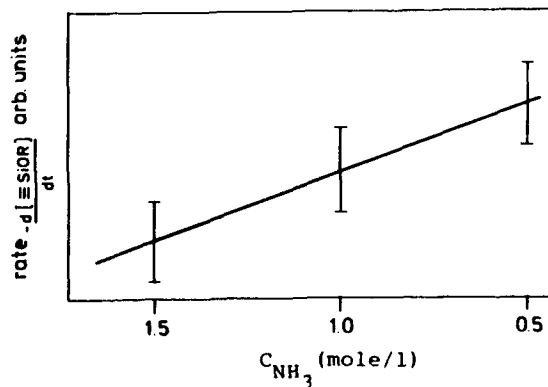


Figure 38.6. Dependence of hydrolysis rate of (CH<sub>3</sub>)<sub>2</sub>Si(OC<sub>2</sub>H<sub>5</sub>)<sub>2</sub> on NH<sub>3</sub> content: H<sub>2</sub>O:OR stoichiometry = 1:4; 50 vol % ethanol as solvent; 25°C.

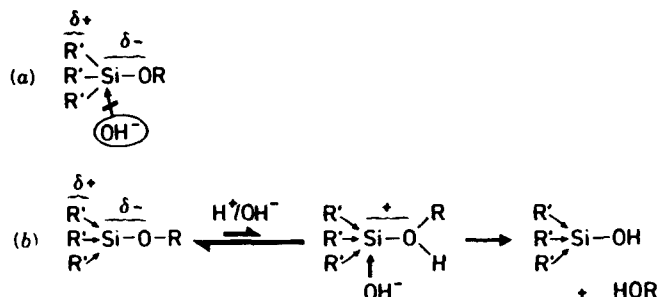
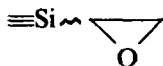


Figure 38.7. Proposed mechanism for the base-catalyzed hydrolysis of substituted silanes.

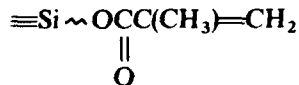
processing reactions like these, it is possible to incorporate substituted esters of various types into inorganic networks avoiding separation effects, and it is possible to tailor phase sizes if necessary.

### 38.3.2. Combination of Properties

Following are examples for the combination of properties. As described elsewhere [10], a contact lens material has been developed. The basic considerations of this material development resulted from *molecular* considerations of different structural units. For oxygen diffusion, a siliconelike unit having a  $\equiv\text{Si}-\text{CH}_2-\text{CH}_2-$  grouping was chosen. For hydrophilicity (low wetting angle), a  $-\text{CH}_2\text{OH}$  group was considered to be suitable. However, the combination of these functional silanes in a sol-gel process led to a reesterification reaction of the  $\equiv\text{Si}(\text{CH}_2)_n\text{OH}$  to the  $\equiv\text{Si}-\text{R}$  by destroying the hydrophilic  $-\text{CH}_2\text{OH}$  groups. Therefore, the



group was chosen, and the ring opening was performed *after* the condensation. Now, the combination led to oxygen permeation and hydrophilicity, but the mechanical properties were poor, and the material was porous. The introduction of  $\text{Ti}(\text{OR})_4$  as a condensation catalyst led to dense, but extremely brittle material, which was not machinable to lenses. To reduce brittleness and increase flexibility,



was introduced, which was polymerized with methylmethacrylate (MMA). Now, mechanical properties were sufficient, but wettability decreased. The sub-

group	expected function	obtained function
$\equiv \text{Si}-\text{CH}_2\text{CH}_2-$ (I)	good oxygen permeation	→ good
$\equiv \text{Si}-\text{CH}_2\text{CH}_2-\text{OH}$ (II)	good wettability	→ poor
$\equiv \text{Si} \sim \text{Si} \rightarrow \equiv \text{Si} \sim \underset{\text{OH}}{\underset{ }{\text{CH}}}-\underset{\text{OH}}{\underset{ }{\text{CH}}}-\text{CH}_2$ (III)	good wettability	→ good
$\equiv \text{Si}$ -organics (I-III)	good flexibility	→ poor
$[\text{SiO}_4]^{4-}$	good strength	→ poor
$[\text{TiO}_4]^{4-}$	good densification behavior	→ good
$\equiv \text{Si} \sim \underset{\text{O}}{\underset{  }{\text{C}}}-\text{C}(\text{CH}_3)=\text{CH}_2$ + MMA	high flexibility	→ good
HEMA	good wettability	→ good
unexpected		strength increase scratch resistance low density (=1.3)

<sup>a</sup>These materials were prepared from  $\text{Si}(\text{OCH}_3)_4$ ,  $\text{Ti}(\text{OC}_2\text{H}_5)_4$ ,  $(\text{CH}_3\text{O})_3\text{Si}(\text{CH}_2)_2\text{OCH}_2\text{CHCH}_2\text{O}$ ,  $(\text{CH}_3\text{O})_3\text{Si}(\text{CH}_2)_2\text{OCOC}(\text{CH}_3)=\text{CH}_2$ , and MMA by a sol-gel process according to Ref. 10.

Table 38.1 shows that the molecular tailoring is possible, but it only works if the structure formation can be controlled. For example, the strength of the inorganic network could not be transformed into the composite at the low processing temperatures of  $<130^{\circ}\text{C}$ , whereas the flexibility of PPMA (polymethylmethacrylate) polymeric chains could be. The wettability of  $\text{CH}_2\text{OH}$  groups could not be transferred; the glycol groups acted as wetting groups if present. Ti in these composites seems to be present in a coordinated state (Fig. 38.8).

In this case, a photoelectronic property of the bulk could be transferred



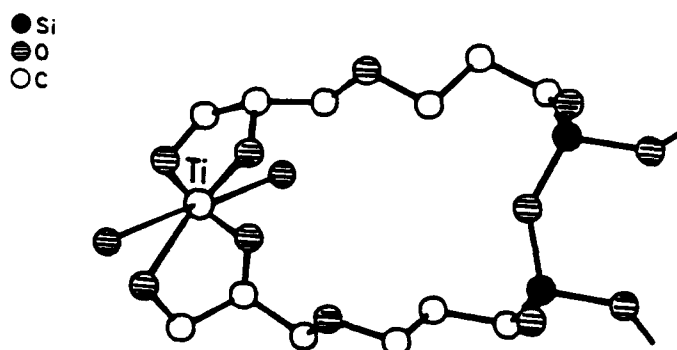


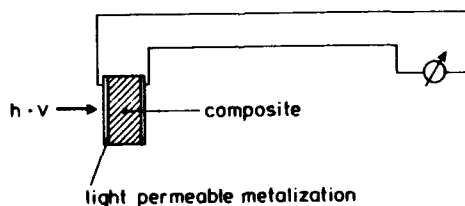
Figure 38.8. Coordination of Ti according to Ref. 11.

unexpectedly into a molecular composite. The disadvantage of this property is a reduced UV stability of these composites. This led to investigations to substitute Ti by Al or Zr. With Zr only weak photoactivity was observed, and with Al no photoactivity was observed. One-to-one substitution of Ti by Al led to an unexpected drastic increase of brittleness and scratch resistance of coatings [9] and to an increase of UV stability by the factor of  $>20$ ! Because structural evaluation is still under investigation, a structure-property relationship is not yet known. However, the consequence of these findings is an enlarged field of applications for outdoor purposes.

Due to the high costs of precursors, the main applications presently consist of coatings. Therefore, a variety of coating materials have been prepared. The main point in this case is the control of viscosity and curing behavior of the coated materials. The control of viscosity can be carried out according to two different mechanisms:

1. Partial hydrolysis and condensation (sol-gel control).
2. Control of the polymerization mechanisms of the organic grouping.

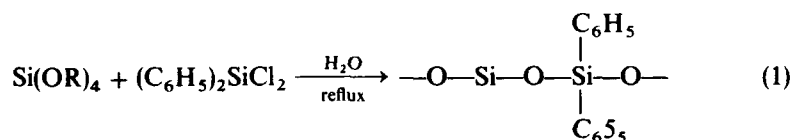
The main fields of application are hard coatings and soft materials like plastics, soft metals, paper wood, and even glass and ceramics.


 Figure 38.9. Device for detecting the  $[\text{TiO}_4]^{4-}$  redox reaction in a composite according to Table 38.1.

For coating application, in most cases the addition of a third function is necessary, for example, reduction of  $\text{H}_2\text{O}$  permeation is required. This can be achieved by the introduction of groupings with hydrophobic properties, such as  $\equiv\text{Si}(\text{CH}_2)_2\text{CH}_3$ . The effect of this group in a scratch-resistant coating reduces the  $\text{H}_2\text{O}$  permeability to about 10% of the original permeability and makes this coating applicable as a scratch and corrosion protective coating on brass and aluminum.

The scratch-resistant properties of these materials could be maintained. The Al-based materials including polymerized epoxy and propyl groups show an excellent adhesion on metalized glass surfaces and a chemical and mechanical protection of the metal layer (Fig. 38.10), which otherwise would be chemically and mechanically unstable.

Investigations of the  $-\text{C}_6\text{H}_5$  groups was carried out for reasons of the high thermal stability of the  $\equiv\text{Si}-\text{C}\equiv$  bond in aryl-substituted silanes. With  $(\text{C}_6\text{H}_5)_2\text{Si}=\text{}$  groupings it was possible to synthesize materials in combination with  $\text{Si}(\text{OR})_4$  or  $\text{Ti}(\text{OR})_4$  as precursors, which have temperature stabilities up to  $350^\circ\text{C}$  [ $(\text{C}_6\text{H}_5)_2\text{SiO}:\text{MeO}_2 \approx 2:1$ , (Eq. 1)] [12].



However, these materials remain soluble in toluene or ethyl acetate. The infrared spectra of these materials show a surprising high OH content [13], even after 8 hr curing at  $250^\circ\text{C}$ . Traces of KOH reduce the OH content almost to zero. With fillers, like graphite or mica, high-temperature-resistant coatings ( $500^\circ\text{C}$  in air) can be prepared. However, the surprising effect is the perfect *adhesion* of this system to glass surfaces and its *thermoplasticity*. Both properties had not been expected and were not described in literature. Based on these findings various adhesives could be developed. The introduction of the  $=\text{SiCH}_3(\text{CH}=\text{CH}_2)$  group permitted to cure these materials by a radical polymerization without losing the good adhesive properties. The base-catalyzed sol-gel processing

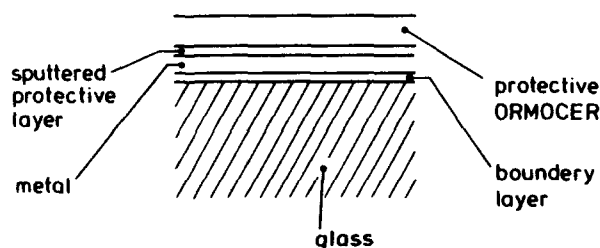


Figure 38.10. ORMOCER protection of metalized glasses.

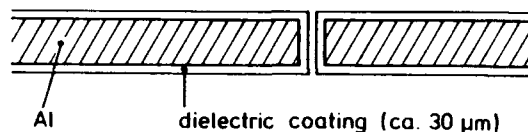


Figure 38.11. Metal core, printed circuit board.

combined with a high-temperature ( $280^{\circ}\text{C}$ ) curing under vacuum allowed the OH group content to be reduced to very low levels so that permittivity constants ( $\epsilon$ ) around 2.7 were possible. These types of coatings have been developed for metal core techniques for novel, printed circuit boards (Fig. 38.11) [14].

In order to make these materials depositable by electrophoretic deposition for the coating of sharp edges (cataphoretic coating), a third function in the form of electric charges had to be added. The cocondensation of  $\approx 5 \text{ mol}\%$  of  $-\text{NH}_2$  groups [from  $(\text{RO})_3\text{Si}\sim\text{NH}_2$ ] and the preparation of a stable emulsion led to a system that allowed a cataphoretic coating (Fig. 38.12).

After coating, a UV curing based on the vinyl group polymerization can be applied. Probably due to the low OH content and the additional organic crosslinking, a new unexpected property was found: These materials are very stable against bases, which is very unusual for silicate-based materials. In order to attack the surface, a 40% KOH solution at  $50^{\circ}\text{C}$  is necessary. The combination of low  $\epsilon$ , low OH content, good thermal stability (280 to  $300^{\circ}\text{C}$ ), and high chemical stability make these groups a good candidate for micro-electronic application.

Another interesting question relates to the problem of the effect of the combination of two different basic properties of organic polymeric "networks" (linear and flexible) on the one hand and of inorganic network (stiff, brittle, and

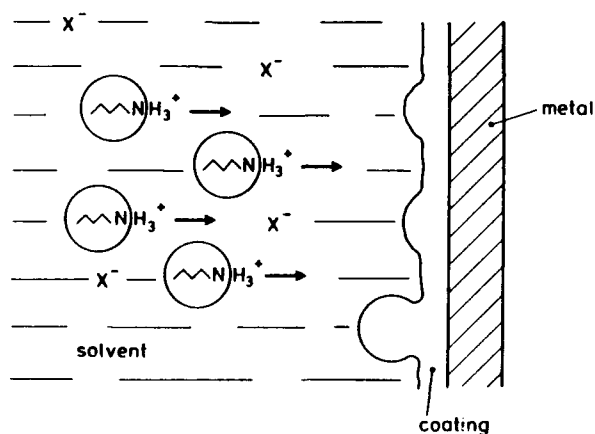


Figure 38.12. Scheme of the electrophoretic deposition process.

three-dimensionally crosslinked) on the other if these networks are not covalently bond, but exist independently of each other. In one example, the experiment was carried out with a soluble polymer (ethylvinyl acetate copolymer, EVA) and 50 wt%  $\text{TiO}_2$  were added to a 5% solution of EVA in toluene (Fig. 38.13) [3]. In this case, the change of EVA properties was drastic as well as of the properties of  $\text{TiO}_2$ . The used EVA was soft and plastically deformable.  $\text{Ti(OR)}_4$  under the applied reaction conditions would have formed a white powder. The "new" polymer is elastic, and the tensile strength is up to  $\approx 20$  MPa. Phase separation is difficult to be detected, but scanning electron microscopy indicates a range of  $\approx 20$  to 50 nm. It is surprising that despite its high  $\text{TiO}_2$  content an elastic material results. The material was used for the coating of polypropylene, creating a sterilizable surface for medical use.

The combination of properties was investigated with a series of other examples. As a general rule, in most cases very interesting properties could be obtained, but the case of a "linear" addition of properties is the exception. For example, density does not follow the inorganic and organic increments: the density, even with high inorganic contents, remains low (Fig. 38.14). This shows that the oxygen chains or groupings govern density by chain movement or rotation, and an "open" structure results. Another example is the thermal expansion coefficient as a function of the numbers of Si-C bonds, which is given in Ref. 15.

### 38.4. MATERIALS

Numerous materials have been developed. One can distinguish between different groups of materials according to their properties or structures.

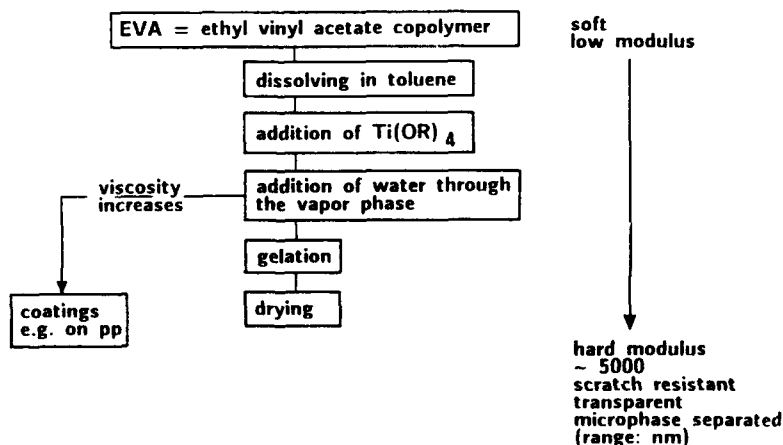


Figure 38.13. Scheme of the preparation of  $\text{TiO}_2$ /EVA copolymer.

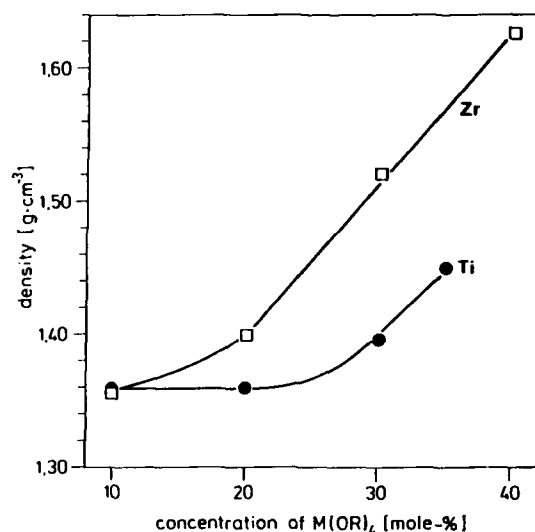


Figure 38.14. The density of ORMOCERS.

#### 38.4.1. Porous Materials

They are characterized by a high content of inorganic network formers. The properties are influenced by composition and reaction parameters: It is possible to tailor microstructure (pore size from 4 nm to several micrometers can be established). The organic groupings can be used for special chemical properties, such as complexation of metals, acid or basic properties, hydrophobic or hydrophilic properties, selective adsorption, and surfaces with chemical links for covalent coupling of biochemical compounds. Some applications resulting from these general properties are various adsorbents for gas- and liquid-phase adsorption, membranes, carriers for catalysts and enzymes, sensors, ion exchangers, and materials for chromatography.

#### 38.4.2. Thermoplastic Materials

They are characterized by high contents of the  $(C_6H_5)_2SiO$  unit. With the addition of other network formers, the thermal properties can be varied [12]; with organics, mechanical properties and processing properties, as well as chemical properties, can be varied. Introduction of olefinic groupings (e.g., vinyl, allyl, or methacryl) can lead to photocurable behavior. Tailoring of  $\equiv SiOH$  or  $\equiv SiOR$  group contents leads to good adhesive properties on inorganic surfaces. Applications for these groups are adhesives, protective coatings, dielectrics for microelectronic application (structurizable coatings for packaging and housing), and ion conductive materials ( $H^+$ ,  $Li^+$ ).

### 38.4.3. Hard Materials

This group is characterized by inorganic network formers like Ti, Al, Zr, or Sn and polymerizable grouping bonds to Si ( $\equiv\text{Si}\sim\text{R}$ ). R = methacryl, epoxy. Hardness and antiabrasive properties result from the inorganic backbone in combination with some flexibility by the organic polymer. The adaption to various substrates (metal and polymers) is possible, and other functions can be added by other organic groupings or fillers. Bulk materials can be prepared in the form of plates or rods, which can be machined to parts. Examples for applications are hard coatings, protective coatings, lubricating coatings, and lenses.

### 38.4.4. Interpenetrating Networks

This type is characterized by the fact that no chemical bond exists between the inorganic and organic backbone, whereas in the Sections 38.4.1 and 38.4.2 described materials the distribution of organics and inorganics can be controlled by the sol-gel reaction, in the latter type of materials the distribution reaction is controlled by a "phase formation" reaction, leading to phase separation effects. The chemistry, therefore, has to be investigated thoroughly, and not much data concerning inorganic-organic sol-gel techniques are available [16]. Applications are, for example, reinforcement of polymers on a nanosized level or creating new functions in polymers.

## 38.5. CONCLUSION AND FUTURE

The conclusion that can be drawn from the available data is that a tailoring of properties can be done successfully only in combination with the reaction control. It seems to be possible to predict functions from the properties of the used units, but it is rather difficult to predict the structure development based on the reactivities of the component in a complex environment. Based on sufficient experience, this tailoring is a combination of predictable basic features and an unknown part to be solved permanently.

Because there are huge numbers of parameters resulting from composition and reaction conditions, the field is only scratched. Important questions like structure formation mechanisms or size effects of the different phases are only investigated in a few examples. So, despite already having a short history, the future of the inorganic composite material will be interesting and exciting.

## REFERENCES

1. H. Schmidt, *Mater. Res. Soc. Symp. Proc.*, **32**, 327 (1984).
2. H. Schmidt and B. Seiferling, *Mater. Res. Soc. Symp. Proc.*, **73**, 739 (1986).
3. H. Schmidt, *ACS Symposium Series*, No. 360, 333 (1988).

4. H. Schmidt, *Proceedings of the Symposium Material-forschung 1988, September 12-14, 1988, Hamm, ed.*: Forschungszentrum Jülich, Projektträgerschaft Rohstoffforschung, Vol. 1, 1988, 722.
5. H. Schmidt, in: Eds., P. Picozzi, S. Santucci, P. Boattini, L. Massarelli, and V. Scopa, *Proceedings of the European Meeting on Inorganic Coatings on Glass September 5-9, 1988, L'Aquila*, p. 131 (1988).
6. H. Schmidt, in: *Proceedings of the Journées "Verre et Lumière," November 24-25, 1988, Brussels*, *Rivista della Stazione Sperimentale del Vetro* **1**, 149 (1989).
7. H. Schmidt, H. Scholze, and A. Kaiser, *J. Non-Cryst. Solids*, **63**, 1 (1984).
8. B. E. Yoldas, *Appl. Optics*, **21**, 2960 (1982).
9. H. Schmidt, B. Seiferling, G. Philipp, and K. Deichmann, in: J. D. Mackenzie and D. R. Ulrich, Eds., *Ultrastructure Processing of Advanced Ceramics*, p. 651, Wiley, New York (1988).
10. G. Philipp and H. Schmidt, *J. Non-Cryst. Solids*, **63**, 261 (1984).
11. I. Gautier-Luneau, Ph.D. thesis, L'Université Paul Sabatier de Toulouse (Sciences) (March 1988).
12. H. Schmidt, H. Scholze, and G. Tünker, *J. Non-Cryst. Solids*, **80**, 557 (1986).
13. H. Schmidt, G. Philipp, H. Patzelt, and H. Scholze, *Collected Papers, XIV International Congress on Glass*, Vol. II, p. 429 (1986).
14. H. Schmidt, *DVS-Berichte*, **110**, 54 (1988).
15. H. Scholze and P. Strehlow, *Wiss. Ztschr. Friedrich-Schiller-Univ. Jena, Naturwiss. R.*, **36**, 753 (1987).
16. G. L. Wilkes, B. Orler, and H. H. Huang, *Polym. Prepr.*, **26**, 300 (1985).

## 39

# STRUCTURE-PROPERTY STUDY OF HYBRID MATERIALS INCORPORATING ORGANIC OLIGOMERS INTO SOL-GEL SYSTEMS

H. HUANG, R. H. GLASER, A. B. BRENNAN,  
D. RODRIGUES, AND G. L. WILKES

### 39.1. INTRODUCTION

The sol-gel reaction has been studied extensively in the last two decades to principally produce new inorganic materials for the modern world of technology. One important advantage of this relatively new reaction route is that some multicomponent systems (mainly combinations of inorganic species) can be produced by this route yet are not possible by a fusion method [1, 2]. This feature has since fostered a new area of material research.

Within the last decade, a new concept has emerged that utilizes this sol-gel reaction as a bridging technique to produce hybrid materials combining inorganic moieties with organic species [3-15]. One form of these hybrid systems is produced by using organic group-substituted metal alkoxides. Desired properties can thus be obtained by choosing appropriate organic groups, for example, a hydroxyl group for higher hydrophilicity or an epoxide group for better abrasion resistance [3-5]. Another approach of producing

*Ultrastructure Processing of Advanced Materials.*

Edited by Donald R. Uhlmann and Donald R. Ulrich (deceased).

ISBN 0-471-52986-9 © 1992 John Wiley & Sons, Inc.



hybrid materials is to use functionalized organic species. The basic concept is that during the buildup of the network resulting from the condensation of the hydrolysis products of metal alkoxides appropriately functionalized organic (or potentially organic/inorganic) moieties that can also undergo the same condensation reaction as the hydrolyzed metal alkoxides are also incorporated. This approach can lead to either an alloylike material if molecular dispersion is obtained or, in other cases, more of a microphase morphological texture.

In the last few years, several new hybrid systems utilizing the concept of functionalized oligomers have been prepared in the authors' laboratory. Depending on the type of oligomer and metal alkoxide, the composition, and type of catalyst, the final materials displayed different structure and properties. In this Chapter, the basic concept of producing these hybrid systems will be reviewed and the corresponding structure–property behavior will be discussed.

### 39.2. TEOS–PDMS HYBRID MATERIALS

As alluded to earlier, modification of the general sol–gel reaction has been employed to prepare hybrid (*ceramers*) materials incorporating appropriately functionalized oligomeric species. One of the first examples of such systems prepared in our laboratory was to incorporate low-molecular-weight (550–1700) poly(dimethyl siloxane) (PDMS) oligomers terminally functionalized with silanol groups into a tetraethoxysilane (TEOS) network [7]. It was demonstrated that these materials, when analyzed for structural features, tended to indicate some degree of very localized phase separation of the PDMS component, but that the dispersion of the oligomer into the alkoxide-based material was enhanced by higher levels of acid catalyst. A higher acid catalyst content would promote a higher rate of hydrolysis thereby providing a greater concentration of hydrolysis products of TEOS to react with the silanol-functionalized oligomers. This resulted in a better dispersion of the oligomer. Proof of this has been presented based on small angle X-ray scattering (SAXS) measurements in conjunction with dynamic mechanical measurements [8, 9] and more recently using solid state nuclear magnetic resonance (NMR) investigations [10]. As an example, Fig. 39.1 shows the ratio of loss to storage modulus ( $\tan \delta$ ) in the dynamic mechanical spectra of a series of materials made with a 1700 (g/mol) silanol-terminated PDMS and TEOS as a function of acid catalyst content. [With regard to the sample nomenclature used in Fig. 39.1, TEOS(48)-PDMS(1700)-50-0.045-80C indicates that the material was prepared with 48 wt % of TEOS, 52 wt % of the functionalized oligomer (PDMS in this case) with 1700 (g/mol), 50% stoichiometric amount of water for the hydrolysis reaction, a molar ratio of HCl/TEOS of 0.045 and a reaction temperature of 80°C. This nomenclature system will be used throughout this Chapter.]

Inspecting the  $\tan \delta$  data in Fig. 39.1, one notes that as the acid catalyst content increases, the glass transition region (dispersion) associated with the

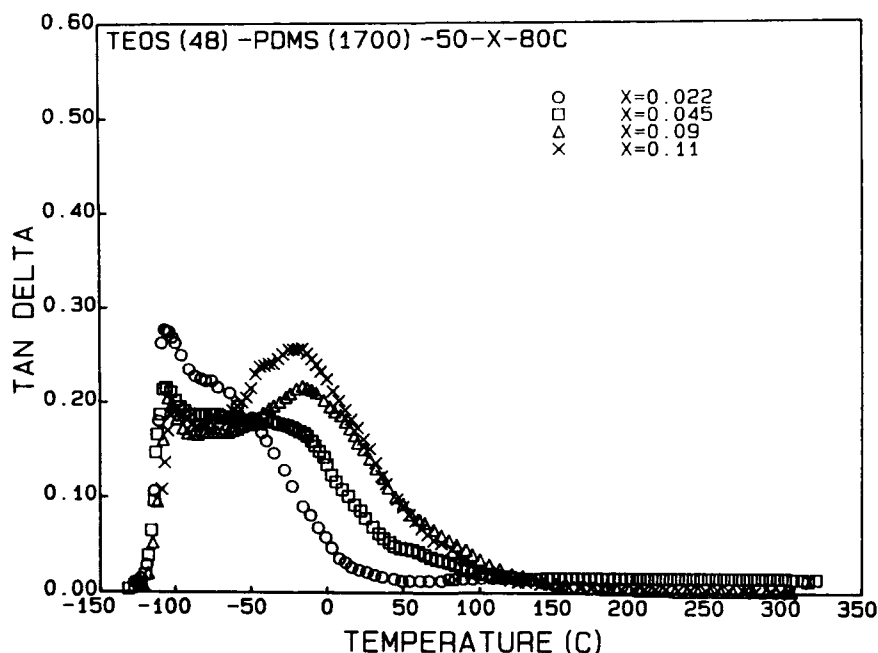
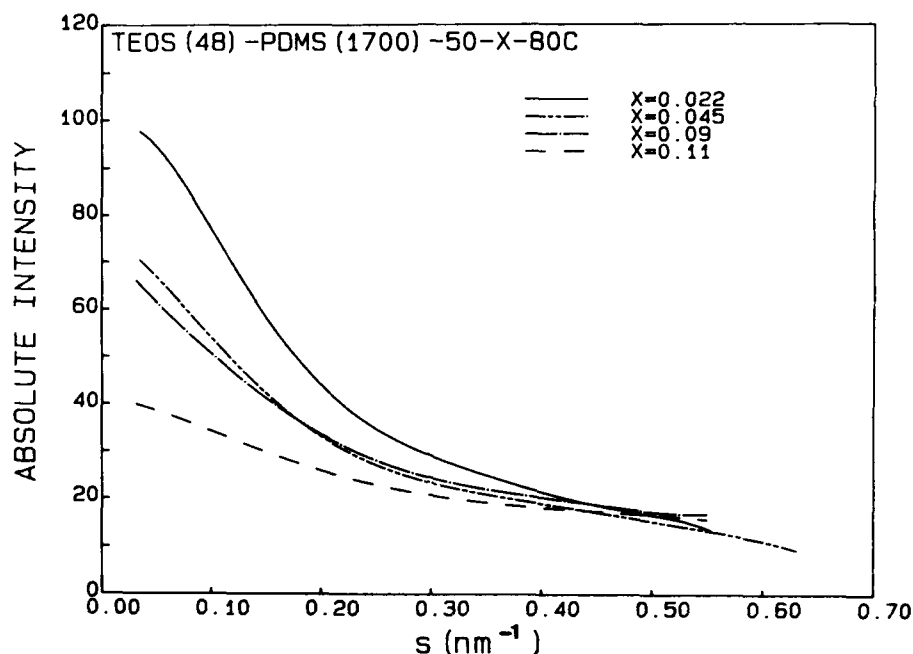


Figure 39.1. Effect of acid catalyst (HCl) content on the temperature dependence of the dynamic mechanical parameter  $\tan \delta$  for a series of TEOS(48)-PDMS(1700)-50-X-80C materials. See text for sample nomenclature. (Reproduced with permission from Ref. 8.)

general PDMS oligomer is highly broadened ( $T_g$  of pure PDMS is approximately  $-120^\circ\text{C}$ ). This broadening to considerably higher temperatures indicates restrictions on molecular mobility, which indirectly suggests further oligomeric dispersion into the more immobile crosslinked condensation products of the TEOS components. Figure 39.2 provides a series of SAXS scans from these same materials. In Fig. 39.2, the variable  $s$  is an angular-dependent parameter defined as  $(2/\lambda)\sin(\theta/2)$ , where  $\theta$  is the radial scattering angle and  $\lambda$  is the wavelength of X ray (nm). The normalized intensity is represented in Fig. 39.2 by  $I(s)$ . The magnitude of scattering in these scans (as indicated by the area under the scattering curves) suggests progressively more homogeneous materials with increasing catalyst, that is, the scattering approaches very low levels as acid content increases. An invariant analysis of these same SAXS scans gives further support to this conclusion [8].

NMR and Raman data have indicated nearly equivalent levels of hydrolysis for all of these systems thereby suggesting that comparisons of the general SAXS intensity profiles of these materials indeed provides a comparative indication of increasing homogeneity (better mixing) of the TEOS and siloxane components as acid catalyst content increases. Further indications of systematic effects on mechanical response with chemical composition have been presented elsewhere [8–10].



**Figure 39.2.** SAXS profiles for TEOS(48)-PDMS(1700)-50-80C materials with different levels of acid catalyst. (Reproduced with permission from Ref. 8.)

### 39.3. TEOS-PTMO HYBRID MATERIALS

Another approach used in our studies has been to incorporate oligomeric species whose chemistry contrasts to that of the metal alkoxide—the latter often based on silicon. In particular, we have utilized triethoxysilane (tri-EOS)-functionalized poly(tetramethyleneoxide) (PTMO) oligomers rather than the earlier discussed silanol-terminated PDMS oligomers. These functionalized PTMO systems have been prepared with a variety of molecular weights and then reacted with TEOS or TMOS [11, 12]. Indeed, the functionalized PTMO oligomers provide good reactivity with the hydrolysis products of the metal alkoxide, but at the same time tend to form a local phase separation or “microdomain structure” somewhat similar to the segmented or block polymers familiar to the polymer chemist [16]. A distinct indication of this local phase separation is provided by Fig. 39.3, which illustrates the SAXS intensity profiles. One notes that in these profiles, there is a distinct maxima (although somewhat broadened due to the nature of slit smearing) that strongly indicates a correlation distance over which somewhat periodic fluctuations in electron density occur. We have found that such a shoulder or pseudo-Bragg peak appears in the PTMO-based systems, whereas it is absent in the PDMS-containing hybrid materials discussed earlier.

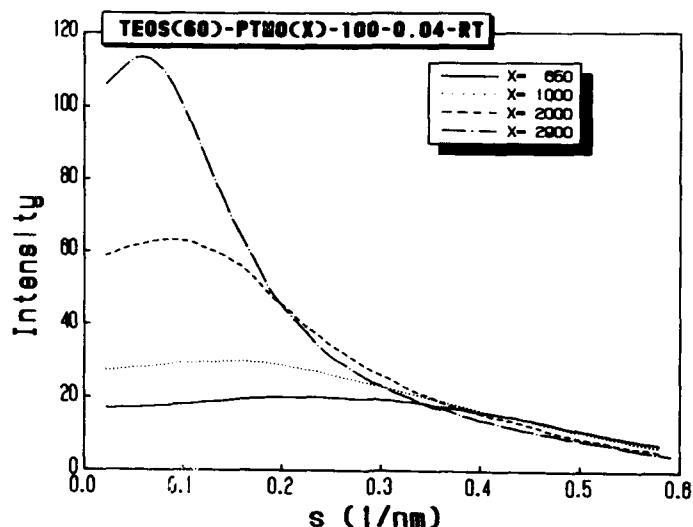
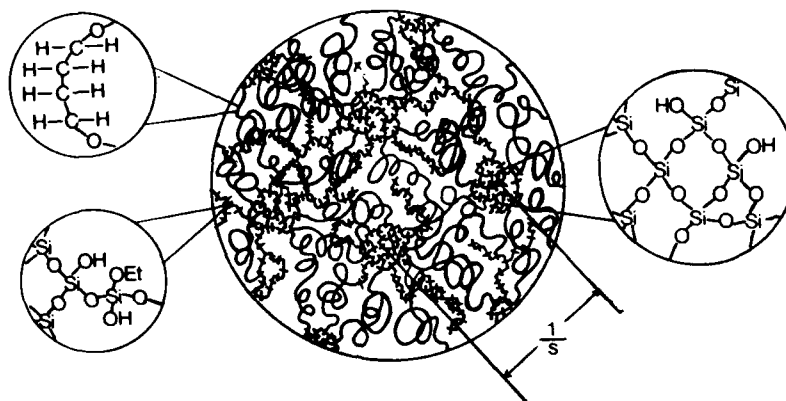


Figure 39.3. Effect of PTMO oligomer molecular weight on the SAXS profiles of a TEOS(60)-PTMO(X)-100-0.04-RT system.

Analysis of these SAXS profiles suggest that this correlation distance (ca.  $1/s$ , see Fig. 39.3) or "average" periodicity in electron density fluctuations is on the order of 10 nm. This length is not unreasonable when the general chain or coil dimensions of the PTMO oligomers are taken into account along with the size of clusters that may form from the partially condensed hydrolysis products of TEOS [11]. An oversimplified model based on the interpretation of the mechanical data in conjunction with the SAXS results is provided in Fig. 39.4. This highly schematic model indicates that there are systematic compositional variations in the materials that occur over a correlation distance given approximately by the value  $1/s$ , an indicator of a pseudo-Bragg spacing. It is viewed that the general matrix is richer in PTMO composition, although not in pure form due to its broadened and raised glass transition response, whereas the more dispersed regions have a higher composition of the condensation products of the TEOS species. Further details regarding the justification for this model can be found elsewhere [11].

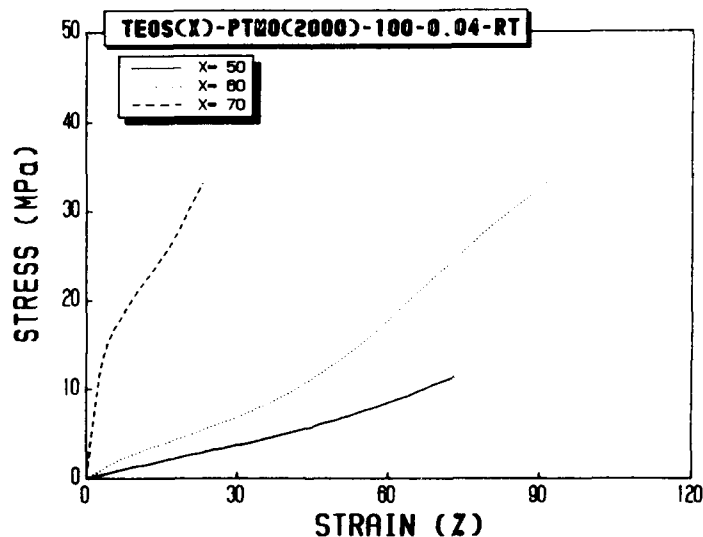
An additional important point to note is that in contrast to the materials prepared using the dimethyl siloxane oligomers, the PTMO-containing materials typically provide a much more enhanced mechanical response [8, 11]. An indication of this is shown in Fig. 39.5, which illustrates three examples of the stress-strain behavior of materials prepared with various TEOS contents and functionalized PTMO (2000 g/mol) at constant water and acid contents. The strain to break ranges from several percent to over 100% whereas the tensile strength may be as high as 30 MPa. By contrast, under equivalent test conditions, the tensile strength measured for materials incorporating PDMS-



**Figure 39.4.** Proposed model of the local morphological structure in the PTMO-TEOS hybrid systems where  $1/s$  is an estimate of the correlation distance (Reproduced with permission from Ref. 11.)

functionalized oligomers terminated with single silanol groups never exceeded 6 MPa with the strain at break typically being less than 20% [8]. This indicates that the additional links provided by the tri-EOS groups result in a considerable enhancement in mechanical properties at least from a structural point of view.

The PTMO-containing materials, we have noted, tend to display a glass transition dispersion that is greatly broadened and raised above that of the pure PTMO component (pure PTMO of reasonable molecular weight displays a



**Figure 39.5.** Effect of TEOS content ( $X$ ) on the stress-strain behavior of a series of TEOS( $X$ )-PTMO(2000)-100-0.04-RT materials.

glass transition temperature of about  $-75^{\circ}\text{C}$  [17]). Figures 39.6a and b show the dynamic mechanical behavior ( $E'$  and  $\tan\delta$ ) for a series of PTMO-containing materials as a function of TEOS content. The data in Fig. 39.6a particularly give an indication of the systematic change in mechanical behavior as restrictions on the mobility of the PTMO oligomers occurs as the result of a greater metal alkoxide content. As either Fig. 39.6a or b indicates, the glass transition dispersion behavior of the PTMO oligomers and the general overall modulus temperature response varies quite dramatically with changing TEOS content. Indeed, one notes that at 10% TEOS addition, the general softening or glass transition response of the network prepared by the sol-gel approach is rather typical of pure PTMO. In fact, there is even an enhancement of modulus in the range of  $-50^{\circ}\text{C}$ . This rise is caused by partial crystallization of the oligomers, a common response of PTMO oligomers in this molecular weight range [11]. Subsequent melting of these crystals occurs at about  $-25^{\circ}\text{C}$ . However, as the TEOS content increases above 30%, not only is the glass transition dispersion broadened and shifted to higher temperatures, but the inducement of crystallizability (indicated by a rise in modulus following the glass transition) is completely eliminated. This lack of crystallizability is without doubt due to restrictions caused by the presence of the TEOS-based components interacting with the PTMO oligomers.

#### 39.4. MULTIFUNCTIONAL PTMO-CONTAINING HYBRID MATERIALS

Another hybrid system that was prepared and studied in our laboratory has been based on TEOS and PTMO possessing multiple functional groups. Unlike the previous systems in which PTMO was endcapped with tri-EOS groups, these higher molecular weight oligomers possess various numbers of tri-EOS groups along the backbone of the chain. The procedure of synthesizing these multifunctional compounds is discussed elsewhere [13]. The additional functional groups were expected to help the incorporation of these organic species into orthosilicate network and assist compatibility during the sol-gel reaction. Most importantly, if this approach of multiple functional groups was successful, other higher-molecular-weight species could be considered in the future. This would significantly raise the versatility of this organic modified sol-gel route.

To illustrate the effectiveness of this addition of functional groups, the stress-strain curves for a series of samples made with PTMO possessing two to five tri-EOS groups are shown in Fig. 39.7. One notes that the range of elongation at break is considerably higher than those shown by the endcapped PTMO(2000) materials (recall Fig. 39.5), which seems reasonable, because the molecular weight is higher in this case. The elongation at break decreases as the average number of tri-EOS groups decreases. The tensile strength is also much higher for these materials than for the analogous PTMO(2000) systems. In fact, it reaches 150 MPa for the sample with only two tri-EOS groups (i.e., tri-EOS terminated).

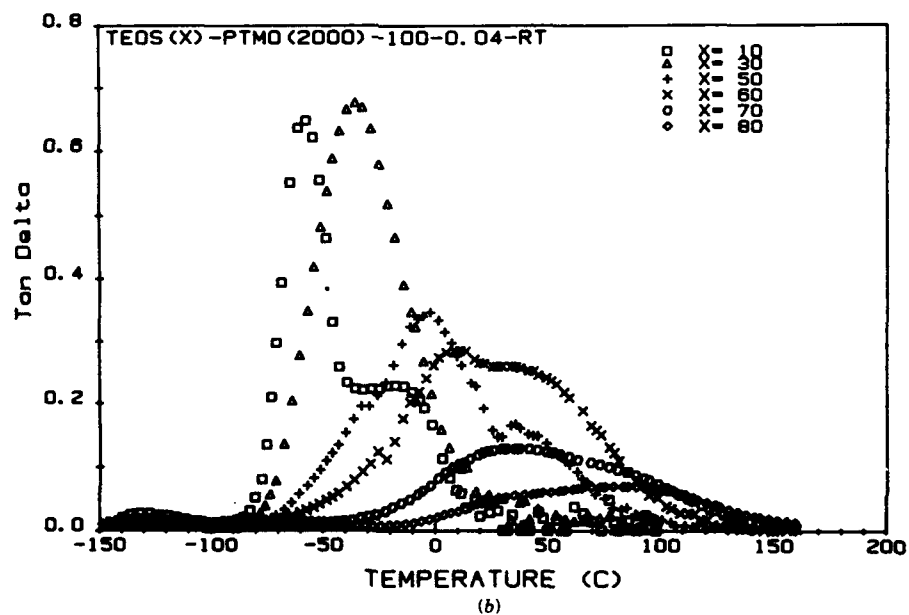
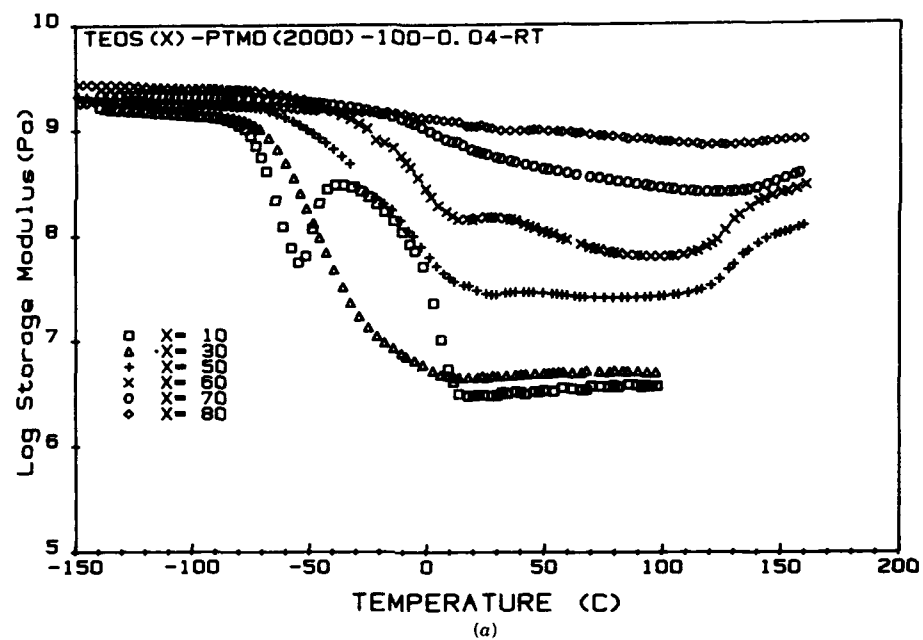


Figure 39.6. Effect of TEOS content (X) on the dynamic mechanical behavior of a series of TEOS(X)-PTMO(2000)-100-0.04-RT materials: (a) storage modulus, and (b)  $\tan \delta$ .

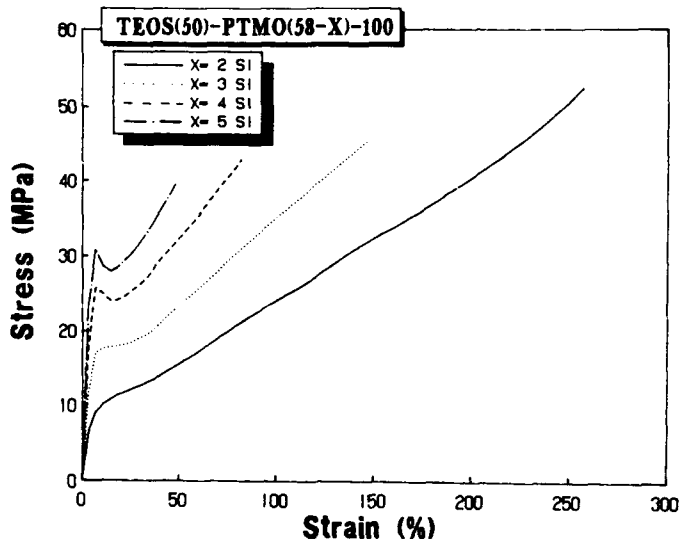


Figure 39.7. Effect of number of functional groups on the stress-strain behavior of a series of TEOS(50)-PTMO(58-X)-100-0.04-RT.

This relatively high strength along with high strain at break makes these materials more attractive in terms of practical applications. The initial modulus of these materials increases with the number of tri-EOS groups on PTMO. In fact, the value of Young's modulus reaches  $10^9$  Pa for the sample made with five functional groups. Another important feature to note is that as the average number of tri-EOS groups increases to four and higher, a yield point is clearly shown, and the yield stress increases with the number of tri-EOS groups. This observation of a yield point and increasing modulus strongly suggests that the material has become more glasslike as the concentration of the tri-EOS group increases. This point was further justified by the dynamic mechanical experiments (data not given), which shows that the glass transition temperature for the PTMO species was much higher than ambient temperature [13]. This suggests that the polymer chains are basically in the glassy state while deformed, and this explained the high modulus values observed. It is also important to mention that from the SAXS results, the general structure for these new systems may still be interpreted by the morphological model suggested above (see Fig. 39.4).

### 39.5. TITANIUM-CONTAINING HYBRID MATERIALS

Mixed metal alkoxide systems are also of interest as a means of creating additional hybrid systems. However, recognition of the large differences in their hydrolysis/condensation rates is crucial. One way to overcome large differences in the reactivity of two metal alkoxide species is to employ a chemically



controlled condensation (CCC) procedure first proposed by Schmidt et al. [4]. In this method the hydrolysis of the fast reacting alkoxide species is slowly initiated by the controlled release of water from the esterification of an organic acid with an alcohol. The starting reaction mixture contains only the reacting alkoxides and the chosen acid/alcohol system—no water. Once the fast-reacting alkoxide has been partially hydrolyzed and condensed, water is added to complete the overall reaction and incorporate the slower-reacting alkoxide (such as TEOS).

A different method has been used by Parkhurst et al. to incorporate titanium ethoxide into TEOS-based silica gels [18]. In this procedure the TEOS species is allowed to partially hydrolyze and condense in the presence of an acid catalyst and water before the fast-reacting titanium ethoxide is added. Once introduced, the titanium ethoxide quickly hydrolyzes and condenses into the preexisting "immature" TEOS-based network rather than precipitating as titanium dioxide.

In our laboratory, we have developed a hybrid procedure that employs aspects of both of these methods in order to incorporate titanium isopropoxide into TEOS-based gels that contain functionalized oligomeric species of either PTMO or PDMS. In our approach, the TEOS moiety as well as the tri-EOS-endcapped PTMO or silanol-terminated PDMS species are partially hydrolyzed and condensed using a CCC system of glacial acetic acid and isopropanol—no water. The titanium isopropoxide is added at a later time; the entire system is, thereafter, gently heated (refluxed) to facilitate the completion of the hydrolysis and condensation reactions. We have found, using this method, that very transparent materials can be produced [11, 14]. This indicates a good dispersion of the titanium species, at least on a size scale distinctly smaller than the wavelength of light.

From the SAXS and dynamic mechanical measurements, the general structure of these titanium-containing materials is similar to those of the TEOS/PTMO systems. However, the modulus tends to be higher for these mixed alkoxide systems. This may be partially due to the fact that titanium tends to catalyze the condensation reaction and produce a network with a somewhat higher degree of reaction [11]. Currently, work is being undertaken to explore other types of alkoxide mixtures; the results will be reported in the near future.

### 39.6. OTHER NEW APPROACHES

Besides all the systems just discussed, several other approaches have been taken to produce new hybrid systems. The first one to mention is the TEOS-poly(ether ketone) (PEK) systems. Although detail is not to be discussed here, it is important to point out that oligomeric species that are glassy in pure form at ambient conditions can also be incorporated into sol-gel network systems in addition to those possessing a more rubberlike backbone such as PDMS or the PTMO components discussed earlier. Indeed, materials incorporating tri-EOS-

functionalized PEK oligomers (which possess a "pure"  $T_g$  of the order of 180°C) have been successfully made through a sol-gel reaction with TEOS. The limitations on the extent of reaction (crosslinking) in such a system due to the more glasslike or stiffer oligomer are clearly much greater than those imposed by the broadened  $T_g$  behavior of the PTMO discussed earlier. The level of network development can be extremely restricted as vitrification is approached through molecular weight buildup in a similar fashion as has been explained by Gillham for common glassy network systems, such as epoxies [19]. A thermal treatment of such materials allows further curing, which results in network enhancement thereby raising mechanical integrity and glass transition behavior accordingly. Studies concerning materials made by the incorporation of tri-EOS-functionalized PEK oligomers with TEOS have been reported elsewhere [15]. In brief, their structure is of a similar microdomain type morphology as occurs in the PTMO-functionalized oligomers addressed earlier.

Another approach that is currently being undertaken in our laboratory is to use a polymeric acid as the catalyst for the modified sol-gel reactions, as reported in the literature, the sol-gel reaction can be catalyzed by any number of acids or bases. There are numerous polymers that have been modified, or exist naturally, with specific groups that impart an acidic or basic functionality. The use of this type of polymer in the sol-gel reaction would hopefully impart a means of controlling the rheology of the system. This should enhance the processing of these hybrid materials in terms of fiber drawing, dip coating, and so on.

The first polymer-based catalyst investigated for the "ceramer" in our laboratory is poly(styrene sulfonic acid) (PSS). The dynamic mechanical properties of these hybrid materials catalyzed with PSS, as a function of the initial concentration of TEOS, are shown in Fig. 39.8. The observed behavior follows the same trends as the HCl-catalyzed hybrid materials in terms of showing both an increase in  $T_g$  and an increase in the rubbery modulus with higher concentrations of TEOS. These data demonstrate the feasibility of using a polymeric acid for the sol-gel reactions. Other polymeric acids are currently being evaluated by the authors.

All the systems discussed above were cured under ambient conditions. To further investigate the processing aspect of these new hybrid materials, microwave curing was also considered. Microwaved samples were prepared in a manner identical with that of their oven-cured counterparts; the chief exception being that they were placed in a carefully designed cylindrical microwave cavity and heated due to the microwave absorption of the materials. These microwave-cured samples were stiff and transparent.

Two days after the samples were prepared by microwave curing, the stress-strain properties were measured. The results are shown in Fig. 39.9. Samples cured to 70°C using both oven and microwaves show very low modulus, stress at break, but very high extensions at break. The attainment of a high extent of reaction is hindered by the rapid evaporation of solvent from the reaction mixture thereby constraining the molecules and trapping them in an unreacted

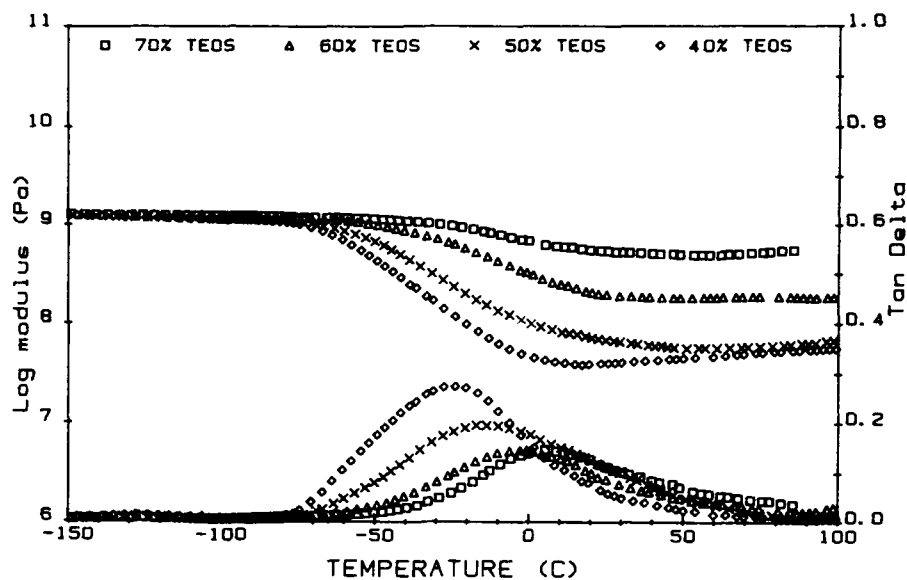


Figure 39.8. Dynamic mechanical behavior of hybrid materials catalyzed with poly(styrene sulfonic acid) as a function of TEOS content. The initial composition is TEOS(X)-PTMO(2000)-100-0.0143 poly(styrene sulfonic acid).

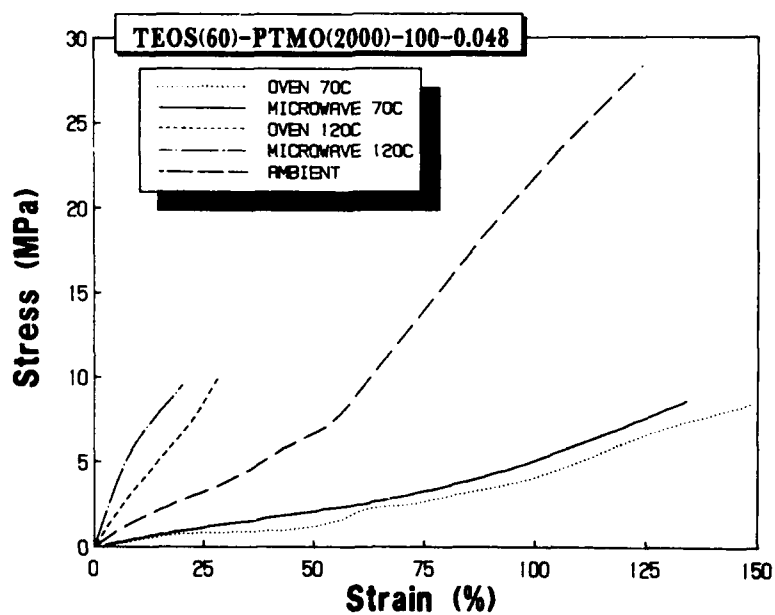


Figure 39.9. Stress-strain behavior of hybrid materials of TEOS(60)-PTMO(2000)-100-0.048 cured under various conditions.

state. The manifestation of this kinetic effect limits diffusion and the resulting mixture of a relatively unreacted glass phase and entrapped polymer gives a highly elastomeric final product. This diffusion limitation can be overcome by elevating the temperature, and the additional molecular mobility gained when cured at 120°C helps further the extent of reaction. Samples reacted at the higher temperature show a higher modulus. However, there is now a tremendous difference between the moduli of the oven cured and the microwaved sample. This effect can be explained partly in terms of the coupling that occurs between microwaves and the polar reactants and partly by the above-mentioned phenomenon of additional energy necessary to overcome diffusion limitations. Also shown in Fig. 39.9 is a stress-strain curve for a room temperature-cured sample. The higher modulus may be attributed to a higher extent of reaction due to slow solvent evaporation and, therefore, higher mobility of the reactive groups. More work in this novel area of sol-gel processing is currently undergoing in our laboratory.

### 39.7. CONCLUSIONS

It has been demonstrated in our laboratory that by utilizing the sol-gel reaction scheme hybrid systems can be prepared with a potentially wide range of properties depending on the choice of metal alkoxide and functionalized oligomer accordingly. The authors believe this approach to prepare new and novel materials is in its stages of infancy and will, with time, lead to useful applications of such systems whether they be for structural, electronic-related materials, new catalyst supports, or porous supports for chromatographic applications. Many of these topics have not been discussed here, but with a little forethought, one should realize that the range of chemistry available for producing such hybrid organic/inorganic-related systems is immense. It is hoped that the novel approach will stimulate new research and, eventually, lead to the development of some new materials.

### ACKNOWLEDGMENTS

The authors would like to acknowledge the partial financial support of this work through the Office of Naval Research, the Akzo Corporation, and the Johnson & Johnson Foundation.

### REFERENCES

1. H. Dislich, *Angew. Chem. Int. Ed. Engl.*, **10**(6), 363 (1971).
2. B. E. Yoldas, *J. Mater. Sci.*, **12**, 1203 (1977).
3. H. Schmidt, *Mater. Res. Soc. Symp. Proc.*, **32**, 327 (1984).

#### 438 STRUCTURE—PROPERTY STUDY OF HYBRID MATERIALS

4. H. Schmidt and B. Seiferling, *Mater. Res. Soc. Symp. Proc.*, **73**, 739 (1986).
5. G. Philipp and H. Schmidt, *J. Non-Cryst. Solids*, **63**, 283 (1984).
6. J. E. Mark, C. Y. Jiang, and M. Y. Tang, *Macromolecules*, **17**, 2613 (1984).
7. G. L. Wilkes, B. Orler, and H. Huang, *Polym. Prep.*, **26**(2), 300 (1985).
8. H. Huang, B. Orler, and G. L. Wilkes, *Macromolecules*, **20**(6), 1322 (1987).
9. H. Huang, R. H. Glaser, and G. L. Wilkes, *Polym. Prep.*, **28**(1), 434 (1987).
10. R. H. Glaser, G. L. Wilkes, and C. E. Bronnimann, *J. Non-Cryst. Solids*, **113**, 73 (1989).
11. H. Huang, R. H. Glaser, and G. L. Wilkes, *ACS Symposium Series*, **360**, 354 (1987).
12. H. Huang, and G. L. Wilkes, *Polym. Bull.*, **18**, 455 (1987).
13. H. Huang, G. L. Wilkes, and J. G. Carlson, *Polymer*, **30**, 1 (1989).
14. R. H. Glaser and G. L. Wilkes, *Polym. Bull.*, **19**, 51 (1988).
15. J. L. Noell, D. K. Mohanty, and G. L. Wilkes, *J. Appl. Polym. Sci.*, **40**, 1177 (1990).
16. T. Hashimoto, M. Shibayama, M. Fujimura and H. Kawai, *Memoirs of the Faculty of Engineering*, p. 43, Kyoto University, (1981).
17. R. E. Wetton and G. Allen, *Polymer*, **7**, 331 (1966).
18. C. S. Parkhurst, L. A. Doyle, L. A. Silverman, S. Singh, M. P. Anderson, D. McClurg, G. E. Wnek, and D. R. Uhlmann, *Mater. Res. Soc. Symp. Proc.*, **73**, 769 (1986).
19. J. K. Gillham, *Polym. Eng. Sci.*, **19**(10), 676 (1979).

## STRUCTURE - PROPERTY INVESTIGATIONS IN HEAT-TREATED POLYQUINOLINE FIBERS

S. SUBRAMONEY, D. R. UHLMANN,  
M. FEATHERSTONE, G. C. BERRY, A. PARKER,  
J. TSANG, AND J. K. STILLE

### 40.1. INTRODUCTION

Macromolecular composites, that is, polymeric materials where rigid rod molecules reinforce flexible coil or semiflexible coil molecules, have generated a considerable amount of interest as future aerospace materials. Such composites have been processed to date by two principal means: blending of the individual polymers in a common solvent followed by extrusion and coagulation to prevent any form of phase separation and synthesizing a block copolymer composed of flexible coil and rigid rod block segments [1]. As in conventional composite materials, it is essential to have a high aspect ratio of the reinforcing polymer chains in order to achieve optimum mechanical properties. It has been demonstrated that substantial improvements in mechanical properties can be obtained by heat treatment of the molecular composites [2-6]. In the present study, fibers and films of a molecular composite of two polyquinolines, one of which is a rigid rod (a) and the other more flexible (b), were processed as both blends and blocks and were subjected to heat treatment procedures under different temperature and tension conditions. Changes in mechanical properties

*Ultrastructure Processing of Advanced Materials.*

Edited by Donald R. Uhlmann and Donald R. Ulrich (deceased).

ISBN 0-471-52986-9 © 1992 John Wiley & Sons, Inc.

and morphological features due to heat treatment are presented in subsections that follow.

## 40.2. EXPERIMENTAL PROCEDURES

The high-molecular-weight rigid rod (a) and flexible coil (b) polyquinolines were synthesized by the solution polymerization of bis(ketomethylene) and bis(*o*-aminoketones) monomers [1]. The following types of fibers were obtained by dry-jet wet spinning techniques utilizing equipment at the Materials Laboratory, Wright Patterson Air Force Base:

1. Pure rigid rod (a).
2. 45/55 blend of rigid rod (a) to flexible coil (b) (by weight).
3. DP50 block copolymer (50/50 by weight of a to b).

The fibers were heat-treated under conditions listed in Tables 40.1 to 40.3 in a three-zone tube furnace using an inert argon atmosphere. The fibers were heat-treated for either a short duration of 5 min (implying that the procedure was terminated immediately following the initial burst of fiber elongation) or for a long duration (12 hr). The short treatment was to prevent any form of fiber degradation due to prolonged exposure to high temperatures.

TABLE 40.1. Rigid Rod Polyquinoline Fibers

Heat Treatment Parameters			Mechanical Properties		
Temperature (°C)	Time (min)	Tension (Mpa)	Modulus (Gpa)	Strength (Mpa)	Elongation (%)
	As spun		12.9	392	5.7
445	5	30	27.3	701	3.4
445	5	50	43.6	726	2.8
475	5	30	49.7	881	2.0

TABLE 40.2. 45/55 Blend Fibers of Rigid Rod/Flexible Coil Polyquinolines

Heat Treatment Parameters			Mechanical Properties		
Temperature (°C)	Time (min)	Tension (Mpa)	Modulus (Gpa)	Strength (Mpa)	Elongation (%)
	As spun		4.2	162	33
240	720	18	9.7	295	3.4
290	720	18	12.6	373	4.7

TABLE 40.3. Polyquinoline DP50 Block Copolymer Fibers (50/50 by Weight)

Heat Treatment Parameters			Mechanical Properties		
Temperature (°C)	Time (min)	Tension (Mpa)	Modulus (Gpa)	Strength (Mpa)	Elongation (%)
	As spun		5.5	212	50
290	720	54	23.2	486	3.1
290	720	85	30.1	611	2.0
290	5	190	23.4	512	2.8
420	720	85	42.1	335	1.2

Tensile mechanical properties of the different heat-treated fibers were evaluated using procedures outlined in ASTM-D3379 [7]. To determine the effect of the heat treatment on the lateral coherence size, typical  $2\theta$  equitorial scans were carried out using a conventional X-ray diffractometer. Freeze-fractured surfaces of the heat-treated fibers were compared to those of the as-spun fibers by scanning electron microscopy (SEM) to determine orientation effects. Results of the various studies will be discussed.

### 40.3. RESULTS AND DISCUSSION

#### 40.3.1. Rigid Rod Polyquinoline Fibers (a)

Fibers of a were heat-treated at a temperature above the suggested  $T_g$  of 420°C. Fibers heat-treated for the longer duration degraded to a severe extent and were quite brittle. On the other hand, fibers subjected to the short-term treatment showed good improvement in mechanical properties as a function of tension during heat treatment with approximate increases in the tensile modulus and strength by factors of 4 and 2, respectively. A fiber of a was also heat-treated at close to its melting point (about 480°C) to determine if melting and drawing caused substantial orientation. Table 40.1 illustrates the results for the rigid rod fibers.

Whereas the short-term treatment at 445°C resulted in no fiber degradation, degradation (as shown by fiber shattering during tensile testing) was observed in a few of the fiber segments heat-treated at 475°C.

#### 40.3.2. 45/55 Blend Fibers of (a) to (b)

The as-spun blend fibers were brittle in the transverse direction (as during bending) and, hence, were difficult to handle during the heat treatment



procedures. Heat treatment of the fibers at a temperature below the  $T_g$  of the flexible coil (b) resulted in modest improvements in mechanical properties. Heat treatment at a temperature above the  $T_g$  of b caused more substantial property improvements. Table 40.2 illustrates the results of the mechanical tests for the blend fibers.

It is possible that further improvements in properties of the blend fibers could be obtained under higher tension conditions by heat treatment at temperatures above the  $T_g$  of b, causing better orientation of the elements of a. Higher tensions during heat treatment were not possible due to the brittle nature of these fibers.

#### 40.3.3. DP50 Block Copolymer Fibers

Long-term heat treatment of the block copolymer fibers at fairly low temperatures and high-tension conditions leads to substantial improvements in properties without fiber degradation. This is shown by improvements in the tensile modulus and strength by factors of about 6 and 3, respectively. This indicates that reorientation of the reinforcing elements is obtained at temperatures only modestly above the  $T_g$  of b. Short-term heat treatments under higher tensions, however, does not appear to be as beneficial for improved mechanical properties. Higher-temperature treatments, close to the supposed  $T_g$  of a, for long durations causes the block copolymer fibers to become brittle. Results from the heat treatment studies are summarized in Table 40.3.

Results from the equatorial X-ray diffraction studies to determine the effect of heat treatment on the lateral coherence sizes of the different fibers are summarized in Table 40.4. Corrections for instrumental broadening for the operating conditions used were made using hexamethylenetetramine (with its 4.968-Å spacing diffraction peak at  $2\theta = 17.84^\circ$ ) as a standard. The crystallite sizes as a function of heat treatment temperature and the values of the  $d$ -spacings for the different fibers are presented in Table 40.4.

TABLE 40.4. Lattice Spacing and Apparent Crystallite Sizes Estimated from X-ray Diffraction Data

Fiber	$d$ -spacing (Å)	Processing Condition	Crystallite Size (Å)
Rigid rod (a)	7.396, 3.375	As spun	15
		HT 445°C	26
45/55 blend	7.369, 4.037	As spun	12
		HT 290°C	23
DP50	7.557, 4.037	As spun	16
		HT 290°C	21
		HT 420°C	30

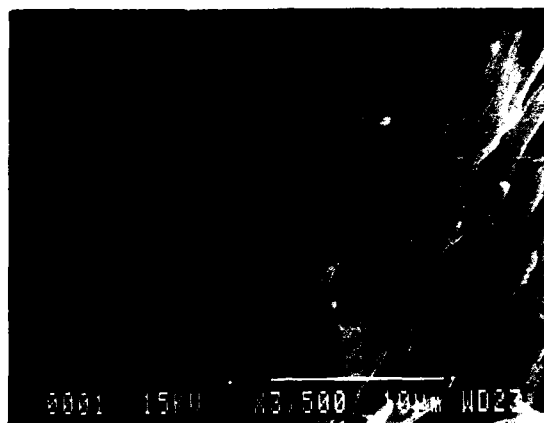


Figure 40.1. SEM of the freeze-fractured surface of a DP50 block copolymer fiber.

It can be observed that heat treatment of the different fibers at elevated temperatures leads to marginal increases in the lateral coherence size. The ratio of  $d_1/d_2$  for the three fibers is also approximately equal to  $\sqrt{3}$ , indicating that these fibers consist of hexagonally packed cylinders [8]. Further X-ray diffraction data are necessary for confirming the molecular structure of these polyquinoline fibers.

SEM of the heat-treated fibers showed considerable alignment in the fibers, as indicated by the freeze-fractured surface of a DP50 block copolymer fiber in Fig. 40.1. This micrograph also shows a significant void content in the fibers. It is expected that the mechanical properties of these fibers would have been substantially higher if the fibers had been free of voids.

#### 40.4. CONCLUSIONS

The heat treatment processing of as-spun fibers of rigid rod, blend, and block copolymer polyquinoline fibers shows significant enhancement of tensile mechanical properties due to considerable improvement in alignment of the fibers, as well as an improvement in the lateral molecular order of the molecules. Comparison of the values in Tables 40.2 and 40.3 clearly indicates that the improvement in properties in the block fibers obtained by the heat treatment processing is significantly better than in the blend fibers. This result could be attributed to the lack of phase separation in the block copolymer fibers. Higher heat treatment temperatures and longer heating schedules lead to obvious degradation of the fibers.

### ACKNOWLEDGMENTS

This research was supported by a grant from DARPA and the Air Force Office of Scientific Research. This support is gratefully acknowledged. The authors thank Dr. Hoe Chuah of the Air Force Materials Laboratory for guidance in the fiber spinning operations.

### REFERENCES

1. J. K. Stille, A. Parker, J. Tsang, G. C. Berry, M. Featherstone, D. R. Uhlmann, S. Subramoney, and Wen-li Wu, *Contemp. Top. Polym. Sci.*, ed. W. M. Culbertson, Plenum, New York (1989) p. 43.
2. W. F. Hwang, D. R. Wiff, C. L. Benner, and T. E. Helminiak, *J. Macromol. Sci., Phys.*, **B22**, 231 (1983).
3. S. J. Krause, T. Haddock, G. E. Price, P. G. Lenhert, J. F. O'Brien, T. E. Helminiak, and W. W. Adams, *J. Polym. Sci. Polym. Phys. Edn.*, **24**, 1991 (1986).
4. J. R. Minter, K. Shimamura, and E. L. Thomas, *J. Mater. Sci.*, **16**, 3303 (1981).
5. S. R. Allen, R. J. Farris, and E. L. Thomas, *J. Mater. Sci.*, **20**, 2727 (1985).
6. S. R. Allen, R. J. Farris, and E. L. Thomas, *J. Mater. Sci.*, **20**, 4583 (1985).
7. ASTM D3379-75, Test Method for Tensile Strength and Young's Modulus for High-Modulus, Single-Filament Materials, **15.03**.
8. W. W. Adams, L. V. Azaroff, and A. K. Kulshreshtha, *Z. Kryst.*, **150**, 321 (1979).

## **PART 5**

# **Optical and Electrical Applications**

## RECENT OPTICAL STUDIES OF THE LOCAL ENVIRONMENT OF RARE EARTH IONS IN GLASS

MARVIN J. WEBER

### 41.1. INTRODUCTION

Rare earths may be present in a glass as a major component, playing the role of a network modifier cation or being important for glass formation, or they may be present as dilute impurities, constituting a minor defect in an otherwise normal continuous random network. In either case knowledge of the local environment of the rare earth is of both scientific and technological interest. The symmetry and bonding at the rare earth site and how they vary with the chemical composition of the glass and from site to site throughout the glass are essential to a detailed understanding of the atomic-scale structure of glass. In addition, because rare earths are used for many luminescence and quantum electronic applications, such knowledge can also lead to the ability to tailor glass compositions to optimize specific optical properties.

Optical spectroscopy is an excellent tool to investigate the local fields and interactions at rare earth sites in glass. In general a spectroscopist can measure the frequency (wavelength), intensity (average or time dependent), polarization, and phase of the radiation. All of these have been exploited in the study of rare earths in glass. The advent of laser techniques—fluorescence line narrowing, spectral hole burning, and coherent optical transients—has greatly expanded

---

*Ultrastructure Processing of Advanced Materials.*

Edited by Donald R. Uhlmann and Donald R. Ulrich (deceased).

ISBN 0-471-52986-9 © 1992 John Wiley & Sons, Inc.

our arsenal of steady-state and transient spectroscopic tools and has led to unique site selective capabilities. These techniques are applicable to many fluorescing species (e.g., transition metal ions, post-transition group ions, and organic dyes) and to many materials (e.g., inorganic and organic crystals and glasses, glass ceramics, and insulating phases of high-temperature superconductors), but nowhere have they been more successfully exploited than for rare earths in glasses.

Although optical studies of rare earths in glass go back many decades [1], their application to new glasses and the development of new laser techniques continue to demonstrate the value and versatility of such studies [2-5]. Several reviews of laser spectroscopy applied to the investigation of the local structure of rare earths in glass have been published in the past few years [6-9]. Here we survey some selected examples of recent advances involving both conventional and laser spectroscopy to illustrate the continued usefulness and possible future directions of optical studies.

## 41.2. SPECTROSCOPIC PROPERTIES OF RARE EARTHS

Optical spectra of trivalent rare earths arise from transitions between energy levels within the ground  $4f^n$  electronic configuration and between levels of the  $4f$  and higher-lying  $5d$  configurations. The Hamiltonian for the  $4f$  electrons is

$$H = H_{el} + H_{so} + V, \quad (1)$$

where  $H_{el}$  is the electrostatic interaction of the electrons,  $H_{so}$  is the spin-orbit interaction, and  $V$  is the crystal field potential at the rare earth due to its environment [10]. The outer  $5s$  and  $5p$  electrons of the rare earth reduce the field acting on the  $4f$  electrons. Thus, for trivalent rare earth ions,  $H_{el} \gg H_{so} \gg V$ . The strengths of the electrostatic repulsion and spin-orbit terms are given by the Slater integrals or Racah parameters and the spin-orbit constant, respectively. These terms cause large energy level separations of  $\sim 10^3 - 10^4 \text{ cm}^{-1}$ . When a rare earth is in a solid, the Racah and spin-orbit parameters are reduced from their free-ion values because of the nephelauxetic (cloud expanding) effect on the  $4f$  shell electrons. The observed shift of energy levels from their free-ion values is a measure of the degree of covalent bonding between the rare earth and its ligands.

The local field at a rare earth site in a glass is described by expanding the potential  $V$  in terms of tensor operator components  $C_q^{(k)}$  that transform as spherical harmonics. Thus,

$$V = \sum_{k,q,i} B_q^k [C_q^{(k)}]_i \quad (2)$$

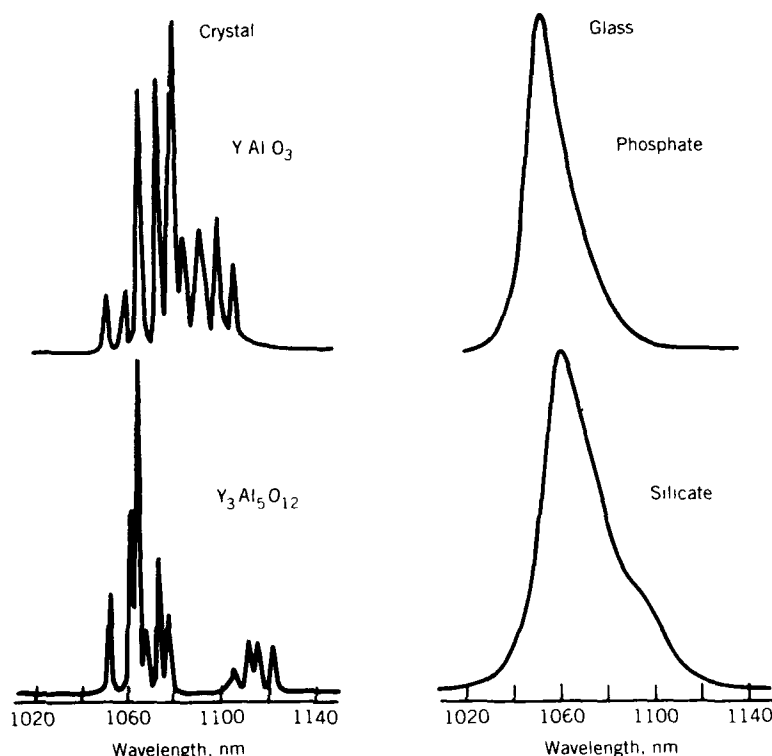
where the  $B_q^k$  are crystal-field parameters involving products of geometric factors and radial integrals, and the summation  $i$  is over all electrons of interest. The

different crystal-field components are a measure of the symmetry and strength of the local field. The number and type of terms in the above summation are determined by the site group symmetry. There is no symmetry at the rare earth in a glass, hence, the site symmetry is  $C_1$ , therefore, all terms are allowed. Because d electrons have angular momentum  $l = 3$ ,  $k$  is limited to values  $\leq 6$  by a triangle rule for allowed matrix elements. The even- $k$  terms in the above sum remove the degeneracy of the free-ion  $J$  states and cause crystalline Stark splittings of  $\sim 10^2 \text{ cm}^{-1}$ . The odd- $k$  terms admix states of different parity and make normally forbidden electric-dipole transitions between states of the  $4f^n$  configuration possible. Because of the small natural (homogeneous) linewidth of rare earth f-f transitions, lines corresponding to transitions between individual Stark levels can usually be resolved for crystalline materials at room temperature. For a disordered medium such as a glass, however, site-to-site variations in the local field result in a distribution of energy level splittings and of radiative and nonradiative transition probabilities. This is evident from the large, inhomogeneously broadened optical linewidths and non-single-exponential excited state decays observed in rare earth spectroscopy.

### 41.3. OPTICAL SPECTROSCOPY

A distinguishing feature of the optical spectra of rare earths in glasses compared to crystals is inhomogeneous line broadening. Figure 41.1 shows the  $^4F_{3/2} \rightarrow ^4I_{11/2}$  fluorescence spectra of  $\text{Nd}^{3+}$  impurities at room temperature in four oxide hosts. At the left are spectra for two crystals of the  $\text{Y}_2\text{O}_3\text{-Al}_2\text{O}_3$  system, the 1:1 perovskite and the 3:5 garnet compounds. Although the two crystals are composed of the same chemical elements, different arrangements of ions about  $\text{Nd}^{3+}$  produce different crystal-field splittings and resulting 12-line Stark spectra. In a random glass network containing  $N$   $\text{Nd}^{3+}$  ions, there will be  $N$  physically different environments. The superposition of spectra from these sites yields an inhomogeneously broadened spectrum, usually with little evidence of the underlying Stark splitting. This is illustrated for the phosphate and silicate glasses at the right in Fig. 41.1. There are small differences in the shape and effective width and in the peak position of the fluorescence bands for the two glasses. These reflect differences in the overall extent and distribution of Stark splittings, in radiative transition probabilities, and in the degree of covalent bonding of the rare earth.

How the above properties are affected by changing the glass composition, either the glass network former or network modifier ions, can be observed more clearly by examining transitions between a single pair of energy levels. Particularly useful absorption lines are the  $^7F_0 \rightarrow ^5D_0$  transition of  $\text{Eu}^{3+}$  and the  $^4I_{9/2} \rightarrow ^2P_{1/2}$  transition of  $\text{Nd}^{3+}$  at liquid He temperatures, where only the lowest Stark level of the  $^4I_{9/2}$  state is populated. The latter transition for several oxide (silicate, borate, and phosphate), fluoride, and oxyfluoride glasses shows, for example, a near-Gaussian or slightly skewed spectral distribution in all cases,



**Figure 41.1.** Comparison of the  $^4F_{3/2} \rightarrow ^4I_{11/2}$  fluorescence spectra of  $Nd^{3+}$  (1%) in different oxide crystals and glasses at 300 K.

however, the peaks of the distributions are shifted to longer wavelengths for the more covalently bonded borate and silicate glasses [11]. In addition, the widths of the distribution are narrower for the phosphate and fluoroberyllate glasses, indicating a weaker or less varied crystal field, but is very wide for a fluorophosphate glass, suggesting a mixed-anion coordination.

Recently Soga and co-workers [12] examined the effects of densification on the fluorescence spectra and local structure of  $Eu^{3+}$  in borate glasses. Hydrostatic pressures up to 6 GPa were applied at various temperatures from 250 to 900°C and the peak position and inhomogeneous linewidth of the  $^5D_0 \rightarrow ^7F_0$  fluorescence were monitored. The results indicate that the role of hydrostatic pressure is first to eliminate atomic scale voids usually appearing when glasses are quenched from high temperatures and then to increase the fluctuation of local fields around  $Eu^{3+}$  due to the distortion of the glass network accompanied by larger variations of bond length and angle in the densified glass. The latter features were also evident from changes in the Eu–O pair distribution functions for normal and densified glass structures simulated using molecular dynamics.



Spectral intensities can also be used to detect changes in local structure. Because the line strength involves radial integrals of the  $4f$  wave functions, it is a measure of the covalency of the rare earth bond. Trivalent europium is a particular convenient ion to study because the  ${}^7F_1 \rightarrow {}^5D_0$  transition is magnetic-dipole allowed and therefore is independent of the local field (except for possible small  $J$ -state mixing), whereas the  ${}^7F_0 \rightarrow {}^5D_2$  and  ${}^5D_0 \rightarrow {}^7F_2$  transitions are electric-dipole allowed by crystal-field admixing of opposite parity states and therefore strongly dependent on the  $B^{k\text{-odd}}$  terms in the local field. Because only the low-order  $k = 1$  and  $k = 3$  terms of Eq. 2 enter into transitions between  $J = 0$  and  $J = 2$  states, these transitions are very sensitive to site asymmetries. An earlier study of  $\text{Eu}^{3+}$  in simple  $\text{BeF}_2$  glass and in a  $\text{NaF}-\text{BeF}_2$  glass showed that the electric-dipole intensities were greatly reduced in the latter glass indicating a weaker and/or more symmetric local field. The reduced spectral intensities correlated with reductions in the second-order (axial) crystal-field parameters determined from the splitting of the  ${}^4F_{3/2}$  state of  $\text{Nd}^{3+}$  in the same glass [13].

In contrast to the behavior in the beryllium fluoride glasses, the  ${}^5D_0 \rightarrow {}^7F_2/{}^5D_0 \rightarrow {}^7F_1$  intensity ratio for a series of  $\text{Eu}^{3+}$ -doped  $(100-x)\text{B}_2\text{O}_3-x\text{Na}_2\text{O}$  glasses grew as the  $\text{Na}_2\text{O}$  content was increased to  $\sim 25$  mol % [14]. This was interpreted as an increase in the asymmetry of the  $\text{Eu}^{3+}$  site. At higher  $\text{Na}_2\text{O}$  concentrations, the intensity ratio was almost independent of composition; this was attributed to an increased  $\text{Eu}-\text{O}$  bond covalency accompanied by a higher site symmetry. Qualitatively, these effects are a consequence of the two-dimensional versus three-dimensional character of the  $\text{BO}_3$  and  $\text{BO}_4$  network formers, which change with increasing Na content.

#### 41.3.1. Glass Ceramics and Crystallization

As shown in Fig. 41.1, there is a striking difference between the optical spectra of a rare earth in a crystal and in a glass. The presence or absence of Stark structure and inhomogeneous broadening can be used as a simple indicator of an ordered or disordered environment and of which phase or phases of a glass ceramic the rare earth resides. More than 15 years ago  $\text{Nd}^{3+}$  laser action was reported in glass ceramics [15]. The emission spectra, however, was similar to that of the silicate glass in Fig. 41.1 indicating that the rare earth was in a glassy phase. This is reasonable because the crystalline phase of, for example, a lithium aluminosilicate glass ceramics does not have an appropriate site for incorporating a large, trivalent rare earth. This is not the case for europium-containing phosphotungstate glass ceramic where both inhomogeneously broadened glass-like and sharp crystallike  $\text{Eu}^{3+}$  fluorescence lines have been observed [16, 17]. The latter spectra was identical to that of crystalline  $\text{EuPO}_4$ . A more complicated  $\text{Na}_2\text{O}-\text{CaO}-\text{Al}_2\text{O}_3-\text{TiO}_2-\text{SiO}_2$  glass ceramic has been studied by Capobianco et al. [18]. By carefully comparing the  $\text{Eu}^{3+}$  fluorescence spectrum with that for a sphene ceramic ( $\text{CaTiSiO}_5$ ), they established that the majority of  $\text{Eu}^{3+}$  ions resided in two sites of microcrystalline sphene embedded in a sodium

aluminosilicate glass and that about 12% of the ions were present in the glassy phase. Additional studies of  $\text{Eu}^{3+}$  partitioning in sphene glass ceramics has been made by Belliveau et al. [19].

Crystallization in zirconium–barium–lanthanum–aluminum fluoride glass has been investigated using  $\text{Ho}^{3+}$  and  $\text{Er}^{3+}$  as optical probes [20]. From observed changes in the spectra, the glass was found to undergo rapid devitrification around 640 K. A temperature-dependent incubation time for the crystallization was also found. After devitrification,  $\text{Er}^{3+}$  exhibits a single exponential fluorescence decay (compared to a slightly nonexponential decay before), another indication of a single site symmetry and field strength. Additional studies of crystallization in fluorozirconate glasses have been made using the  $^1\text{D}_2 \rightarrow ^3\text{H}_4$  fluorescence of  $\text{Pr}^{3+}$  as a probe. In these studies two different types of microcrystals were found corresponding to two different structural arrangements. Measurements of Pr–Pr crossrelaxation were also made and fitted to a model for a fractal distribution of fluorescing ions. Heat treatment at a temperature slightly higher than  $T_g$  decreased the dimensionality governing the crossrelaxation [21].

#### 41.3.2. Silica

Because of its many attractive physical and chemical properties, people have been adding rare earths to silica for more than a half-century [22]. It is difficult, however, to incorporate large quantities of lanthanide ions into the rigid, covalently bonded tetrahedral  $\text{SiO}_2$  glass network homogeneously. In melted fused silica, for example, crystallization occurs at lanthanide concentrations of  $\lesssim 0.1$  mol% [23]. At higher concentrations, Nd is not accepted homogeneously, but rather as some type of Nd-silicate cluster embedded in a glass matrix. Thus the early demonstrations of laser action in silica [24] were done with  $\text{Nd}^{3+}$  concentrations much lower than those used in silicate laser glasses (typically  $\sim 1$  mol%).

To the rare earth glass spectroscopist, the optical absorption and emission spectra of isolated  $\text{Nd}^{3+}$  ions in silica are extraordinary. Compared to the emission spectra in Fig. 41.1, the fluorescence of Nd-doped  $\text{SiO}_2$  glass is shifted to longer wavelengths and is much broader [25]. The first feature indicates a greater degree of covalent bonding in simple  $\text{SiO}_2$  compared to multicomponent silicate, phosphate, or other oxide glasses; the second feature indicates a stronger local field strength and or more site-to-site variations in the field. In addition, the Judd–Ofelt spectral intensity parameters for  $\text{Nd}^{3+}$  show that the lower-order terms in the local field expansion are larger for  $\text{SiO}_2$  than for silicate glasses indicating a more asymmetric coordination environment [26]. A similar behavior is observed for rare earths in simple  $\text{BeF}_2$  vis-a-vis multicomponent fluoroberyllate glass [13].

It is possible to incorporate greater quantities of rare earths into  $\text{SiO}_2$  without phase separation if another component such as  $\text{Al}_2\text{O}_3$  or  $\text{P}_2\text{O}_5$  is added

simultaneously [23, 27]. When the ratio of additive to rare earth is  $> 1$ , optical transitions are shifted to shorter wavelengths and have narrower effective linewidths more typical of those for an oxide glass. The  $\text{Nd}^{3+}$  and codopant ions must therefore be in close proximity with the codopants providing a modified environment and a less disordered coordination shell. The spectra are inhomogeneously broadened, thus although there is not a random distribution of rare earths and codopants, there are still site-to-site variations.

Similar behavior has been observed from studies of f-d transitions of  $\text{Ce}^{3+}$ . For phosphorus codoping, the spectra, were shifted to shorter wavelengths [28]. In contrast, codoping with fluorine, had no effect on the spectra from which it was concluded that fluorine neither becomes incorporated into nor influences the coordination of anions around cerium ions [29].

In Nd-doped silica prepared by plasma-torch chemical vapor deposition, it was found that some of the Nd ions cluster, thereby providing their own modified environment and a shifted, narrowed optical spectrum. That Nd clustering occurred was evident from the very fast fluorescence decay times of the shifted spectrum [30]. [When two  $\text{Nd}^{3+}$  ions become close together ( $< 1$  nm), they can interact by a electric multipole process resulting in pairs of nonradiative transitions that shorten the  ${}^4\text{F}_{3/2}$  lifetime.] The clustered spectra were inhomogeneously broadened with no evidence of order. In contrast, Ainslie et al. [31] observed  $\text{Nd}^{3+}$  emission consisting of a superposition of glasslike and crystallike spectra for Nd concentrations approaching 1 mol % in phosphorus codoped silica. Thus the relative number of isolated and modified Nd environments in silica depends upon both the rare earth and codopant ion concentrations.

There has been several efforts in recent years to incorporate rare earths into  $\text{SiO}_2$  prepared by sol-gel techniques. This synthesis method presents additional variations in local environments that can be probed by rare earth spectroscopy. The fluorescence from  $\text{Eu}^{3+}$  in silica gel glass has been used as a probe for cation binding and for changes in cage symmetry during gel dehydration [32]. Structural modifications occurring during the gel-to-glass transformation were readily apparent from changes in the relative intensities of the  ${}^5\text{D}_0 \rightarrow {}^7\text{F}_1$  and  ${}^5\text{D}_0 \rightarrow {}^7\text{F}_2$  emission bands. From the optical spectra one can follow the release of trapped solvents as the drying proceeds upon heating and the participation of europium cations in the continuous polymerization-condensation reaction.

Neodymium has been incorporated into sol-gel  $\text{SiO}_2$  at concentrations up to 5 wt % without crystallization [33]. Comparative studies of the spectra of sol-gel and melted silica containing 0.5 wt %  $\text{Nd}_2\text{O}_3$  show that they can be identical [34]. The Nd fluorescence decay shows no fast component due to clustering, however, the lifetime may be shortened if the water content is not reduced to very low concentrations during the drying and densification process. Comparing absorption spectra for a dried porous gel and a fully densified silica glass showed that the presence of large quantities of OH or other solvents in the  $\text{Nd}^{3+}$  coordination environment shifts the optical spectra from that observed for

isolated Nd ions [33]. Clustering or crystallization occurring during the sol-gel process has also been detected from the appearance of sharp lines in the absorption spectra [34].

Measurements of the location, shape, and width of optical spectra and of excited state lifetimes provide evidence of rare earth clustering, the presence of water and other additives in the immediate vicinity of rare earths, and how these properties vary with silica preparation and processing. While this information is interesting and useful, we do not have a detailed picture of the near neighbor coordination environments of rare earth ions in silica nor how they differ from those in silicate glasses. Thus many intriguing questions remain.

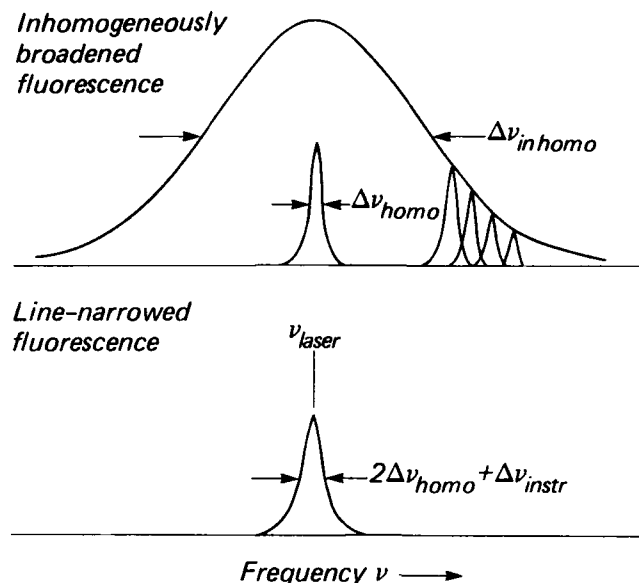
#### 41.4. LASER SPECTROSCOPY

##### 41.4.1. Fluorescence Line Narrowing

If a broadband optical source is used to excite fluorescence, all ions are subject to being excited, and an inhomogeneously broadened emission line such as shown at the top of Fig. 41.2 is obtained. If, instead, a laser is used for excitation, only those ions resonant with the laser frequency are excited. The fluorescence from this subset of ions, if observed in a time short compared to any spectral crossrelaxation of excitation to other ions, will be narrowed as shown at the bottom of Fig. 41.2. Using a tunable laser, isochromats throughout the entire energy distribution can be probed selectively. The number of spectroscopically different isochromats that can be observed depends upon the ratio of the homogeneous to inhomogeneous linewidths. For rare earths, because of their narrow homogeneous linewidths at low temperatures, this number can easily be  $> 10^6$ .

Fluorescence line narrowing (FLN) has been used to investigate site-to-site variations in rare earth energy levels, linewidths, radiative and nonradiative transition probabilities, and energy transfer between ions in different environments. These results have been the subject of several reviews [6-9]. Brecher and Riseberg [35], in their pioneering FLN studies of  $\text{Eu}^{3+}$  in oxide and fluoride [36] glasses, determined for the first time the even-order crystal-field parameters  $B_q^k$  and their variations throughout the glass. They then related these results to geometric distortions of the nearest-neighbor oxygen coordination shell using simple point charges to calculate the local field strengths. Different structural models were needed to account for the different FLN spectra observed for silicate and fluoroberyllate glasses. Although these studies are instructive in eliminating many structure from consideration, there is no uniqueness theorem to prove that the proposed structures are the only ones that can explain the observed spectra.

Recently Berville and Simkin [37] have performed similar measurements and crystal-field parameter determinations for  $\text{Eu}^{3+}$  in sodium aluminosilicate and titanosilicate glasses. From the similarity of the FLN spectra for various



**Figure 41.2.** Principles of inhomogeneous broadening and laser-induced fluorescence line narrowing. Top, inhomogeneously broadened line profile; bottom, resonant laser-excited fluorescence.  $\Delta\nu_{\text{homo}}$ ,  $\Delta\nu_{\text{inhomo}}$ , and  $\Delta\nu_{\text{instr}}$  are the homogeneous, inhomogeneous, and instrumentation linewidths.

oxide glasses, they suggest that the rare earth forms a quasi-molecular complex with the oxygen in glass network. Because in all cases the optical spectra are inhomogeneously broadened, there must be a distribution of local fields associated with these complexes.

FLN spectra has also been recorded for  $\text{Eu}^{3+}$  in fluorozirconate glasses [38]. Based on the appearance of more than the three Stark components expected for the  $^5\text{D}_0 \rightarrow ^7\text{F}_1$  transition and other evidence, the authors propose that there are two major types of sites in these glasses which overlap within the total inhomogeneous band profile. (Durville et al. [39] have reported a secondary peak in the  $^7\text{F}_0 \rightarrow ^5\text{D}_0$  absorption band for  $\text{Eu}^{3+}$  in a lithium aluminosilicate glass, again suggesting two major types of sites. A corresponding feature, however, is not observed in the  $^4\text{I}_{9/2}(1) \rightarrow ^2\text{P}_{1/2}$  absorption band of  $\text{Nd}^{3+}$  [11].) Extra peaks and a continuum fluorescence background are frequently observed in the FLN spectra of  $\text{Eu}^{3+}$ . Belliveau and Simkin [37] have analyzed this problem and concluded that phonon-assisted transitions occurring on the high energy side of the asymmetric  $\text{Eu}^{3+} \ ^7\text{F}_0 \rightarrow ^5\text{D}_0$  excitation band account for the observed extra peaks and intensity in their spectra. The coincidence of excitation wavelengths for phonon-assisted transitions of one group of sites and for zero-phonon transitions of another group of sites is one of a number of accidental degeneracies that can give rise to residual inhomogeneous broadening observed in nonresonant FLN spectra [6]. Strictly speaking, laser spectroscopy is energy selective rather than site selective.

As discussed in previous reviews [6, 7], FLN spectroscopy of  $\text{Eu}^{3+}$ -doped alkali borate glasses reveals structural changes that occur with increasing alkali content. Recent studies [40] of the site-to-site variations of the  ${}^7\text{F}_1$  splitting and the  ${}^5\text{D}_0$  lifetime show continuous variations of these parameters for low ( $<25$  mol %) alkali content. This was attributed to the flexibility of the two-dimensional character of the B–O sublattice at these alkali concentrations. At higher alkali content, the parameters become almost composition independent which was taken as evidence for a more pronounced three-dimensional character of the B–O network. Phase separation in  $(100-x)\text{B}_2\text{O}_3-x\text{Na}_2\text{O}$  glasses was also investigated. Thermal treatment led to a narrowing of the  ${}^5\text{D}_0 \rightarrow {}^7\text{F}_1$  splitting implying that  $\text{Eu}^{3+}$  ions segregated in the sodium-poor phase.

The detailed information about crystal field parameters that can be obtained from FLN spectroscopy provides a critical test of local structures for rare earths predicted by Monte Carlo [41] and molecular dynamics [42] methods. Computer-simulated structures are dependent on the adequacy of the interionic potentials used and are subject to artificial structural disorder introduced because of the extremely fast effective cooling rates employed. Nevertheless, many general features of observed optical spectra are in reasonable agreement with simulated structures [13]. Hirao and Soga [43] have simulated  $\text{Eu}^{3+}$ -doped sodium borate glasses and found that the inhomogeneous linewidth of the  ${}^5\text{D}_0 \rightarrow {}^7\text{F}_2$  emission peak varied with sodium content with a maximum at 18 mol %  $\text{Na}_2\text{O}$ . This result agreed well with their laser-induced fluorescence data, thereby further validating the meaningfulness of simulated structures. Another prediction of molecular dynamics simulations, an increased average rare earth coordination number when alkali ions are added to fluoroberyllate glasses [42], has recently been confirmed by extended X-ray absorption fine structure measurements [44].

#### 41.4.2. Homogeneous Optical Linewidths

As shown in Fig. 41.2, the homogeneous linewidth of rare earth transitions in glass can be measured using resonant fluorescence line narrowing. One of the earliest discoveries of FLN spectroscopy was that the magnitude and temperature dependence of rare earth linewidths in glasses at low temperatures differed significantly from those of the same ion in a crystal. Similar observations have been made for fluorescing molecules in organic glass. The phenomenon has now been observed for a large number of fluorescing species in a wide variety of inorganic and organic glasses using FLN and spectral hole burning in the frequency domain and optical dephasing in the time domain (coherent transients and photon echoes). The homogeneous linewidths of rare earths in glass also vary with excitation energy [39]. All of these experiments are reviewed in a special issue of the *Journal of Luminescence* [45].

After the initial observation of anomalous low-temperature optical linewidths in glass, the question immediately arose whether this was related to two-

level systems (TLS) and atomic tunneling modes and, if so, how. The existence of TLS, in which two quasi-equilibrium structural configurations of ions are separated by small energy barriers of varying heights, had been invoked a few years earlier to account phenomenologically for the anomalous heat capacity and conductivity of amorphous systems at very low temperatures. Because in optical studies one usually measures electronic transitions of centers that have been deliberately introduced into the solid, it is not always clear whether one is probing intrinsic two-level systems, some perturbation thereof, or TLS associated with the dopant. Experimental evidence for specific TLS structures has been obtained from studies of several model disordered systems (see Ref. 45, p. iv). Thus far, however, no really cogent explanation for the microscopic structure of TLS and the nature of the low-frequency excitations thought to be responsible for the anomalous thermal properties and optical linewidths of amorphous solids has yet emerged.

#### 41.4.3. Hole Burning and Refractive Index Gratings

Two additional rare earth optical phenomena in glass arising from the use of lasers and attributed to some as yet not well-defined local structural change or modification are the creation of long-lived spectral holes and laser-induced refractive index gratings. A common feature of spectral hole burning is photostimulation of some process that depletes or displaces in frequency the optical absorption or emission associated with those sites in an inhomogeneous spectral distribution that are in resonance with an irradiating laser. Saturation, photochemical, and photophysical processes can cause hole burning [8]. In photophysical hole burning the photo product is redistributed within the inhomogeneous absorption band profile and appears as a decrease (hole) at the frequency of the laser and as an increase (antihole) at frequencies off resonance. Holes in the spectra of rare earth ions in silicate glasses have been burned with continuous wave dye lasers having intensities of  $\sim 1 \text{ W/cm}^2$  [46]. Exposure times ranged from 10 sec to 10 min for samples at liquid helium temperatures with hole depths growing to  $\sim 10\%$  of the total absorption. There was also clearly a distribution of hole burning efficiencies [47]. If the glasses were kept in the dark at low temperatures, holes persisted many hours after cessation of irradiation with no profile change. The hole was attributed to an optically induced rearrangement of the local glass structure resulting in a decrease of the number of ions resonant with the laser and corresponding increase elsewhere within the inhomogeneously broadened band. The nature of the structural rearrangement of the rare earth environment has not been defined.

Laser-induced refractive index changes have been observed in various glasses under varying experimental conditions and the results attributed to bond rearrangements associated with trapped exciton effects [48]. When  $\text{Eu}^{3+}$ -doped glasses are resonantly excited, two types of laser-induced gratings are formed: a transient population grating associated with excited  $\text{Eu}^{3+}$  ions and a holo-

graphic grating that is permanent at room temperature, but can be erased either thermally or optically [49]. Studies using four-wave mixing processes have shown that whereas silicate and phosphate glass hosts produce permanent gratings very efficiently, no gratings have yet been observed for borate, germanate, or fluoride glasses [50]. Changing the network modifier ions can vary the grating signal intensity. The strength of the grating is also proportional to the rare earth concentration, however saturation can occur [51]. A two-level model involving an asymmetric double-minima potential well has been used to describe the formation of permanent, laser-induced grating. In this model the rare earth ions play a major role by providing the high-energy local modes phonons required to produce a structural modification of the glass host.

### 41.5. DILUTION NARROWED SPECTROSCOPY

Thus far the optical properties of rare earths in different sites in glass have been resolved spectrally by selective excitation. By sufficient dilution of the rare earth impurities and the use of laser excitation and sensitive detection, it may also be possible to resolve different sites spatially. The possibility of performing optical experiments with only a few (one to ten) fluorescing atoms was demonstrated recently for a  $\text{CaF}_2$  crystal doped with  $10^{-9}$  mol %  $\text{Sm}^{3+}$  [51]. The laser was focused into an excitation volume of  $\sim 20 \mu\text{m}^3$  containing, for the most dilute sample studied, an average of only five Sm atoms.

Yen [53] has applied this approach to glass using a single-mode silica fiber very lightly doped with  $\text{Nd}^{3+}$ . A ring laser excited the fiber perpendicular to the fiber axis and the  $^4\text{F}_{3/2}$  fluorescence emerging at the end of the fiber was monitored. At low temperatures the fluorescence excitation spectra exhibited many narrowed features that were attributed to a random sampling of a small distribution of glass sites. Shifting the excitation to another region of the fiber yielded a spectra with different narrowed features. This technique opens the prospect of isolating a single ion in a glass and providing detailed information about site-to-site variations in local environments without the complications of accidental degeneracies. Improvements in detection sensitivity and the technique are needed to realize this possibility, however, at higher doping levels, spatial compositional variations on a more macroscopic scale (volumes with dimensions  $\geq \mu\text{m}^3$ ) could easily be investigated using this technique.

### ACKNOWLEDGMENT

This work was performed under the auspices of the U.S. Department of Energy by the Lawrence Livermore National Laboratory under Contract W-7405-ENG-48.



## REFERENCES

1. J. Wong and C. A. Angell, *Glass Structure by Spectroscopy*, Marcel-Dekker, New York (1976).
2. W. M. Yen and P. M. Selzer, Eds., *Laser Spectroscopy of Solids*, Springer-Verlag, Berlin (1981).
3. I. Zchokke, Ed., *Optical Spectroscopy of Glasses*, Reidel, Amsterdam (1986).
4. A. A. Kaplyanskii and R. M. Macfarlane, Eds., *Spectroscopy of Solids Containing Rare Earths*, North-Holland, Amsterdam (1987).
5. W. M. Yen, Ed., *Laser Spectroscopy of Solids II*, Springer-Verlag, Berlin (1989).
6. M. J. Weber, in: Eds., W. M. Yen and P. M. Selzer, *Laser Spectroscopy of Solids*, p. 189, Springer-Verlag, Berlin (1981).
7. G. Boulon, M. Bouderbala, and J. Seriot, *J. Less-Common Metals*, **112**, 41 (1985).
8. M. J. Weber, *Bull. Am. Ceramic Soc.*, **64**, 1439 (1986).
9. G. Boulon, *Mater. Chem. Phys.*, **16**, 301 (1987).
10. S. Hufner, *Optical Spectra of Transition and Rare Earth Compounds*, Academic Press, New York (1978).
11. C. Brecher, L. A. Riseberg, and M. J. Weber, *Phys. Rev. B*, **18**, 5799 (1978).
12. N. Soga, K. Kirao, M. Yoshimoto, and H. Yamamoto, *J. Appl. Phys.*, **63**, 4451 (1988).
13. M. J. Weber and S. A. Brawer, *J. Non-Cryst. Solids*, **52**, 312 (1982).
14. M. Zahir, R. Olazcuaga, C. Parent, G. Le Flem, and P. Hagemuller, *J. Non-Cryst. Solids*, **69**, 221 (1985).
15. G. Müller and N. Neuroth, *J. Appl. Phys.*, **44**, 2315 (1972); C. F. Rapp and J. Chrysoschoos, *J. Mater. Sci.*, **7**, 1090 (1972); *J. Phys. Chem.* **77**, 1016 (1973).
16. H. Mack, G. Boulon, and R. Reisfeld, *J. Lumin.* **24/25**, 111 (1981).
17. F. Durville, G. Boulon, R. Reisfeld, H. Mack, and C. K. Jorgensen, *Chem. Phys. Lett.*, **102**, 393 (1983).
18. J. A. Capobianco, T. F. Belliveau, G. Lord, D. J. Simkin, J. Tait, and P. J. Hayward, *Phys. Rev. B*, **34**, 4204 (1986).
19. T. F. Belliveau, D. J. Simkin, J. Tait, and P. J. Hayward, unpublished.
20. K. Tanimura, M. D. Shinn, and W. A. Sibley, *Phys. Rev. B*, **30**, 2439 (1984).
21. M. Ferrari, E. Duval, A. Boyrivent, A. Boukenter, and J. L. Adam, *J. Non-Cryst. Solids*, **99**, 210 (1988).
22. R. W. Wood, *Phys. Rev.*, **38**, 487 (1931).
23. E. I. Galant, B. S. Gorovaya, E. L. Demskaya, Yu. N. Kondrat'ev, M. P. Golubovskaya, A. K. Przhevuskii, T. I. Prokhorova, and M. I. Tolstoi, *Fiz. Khim. Stekla*, **2**, 438 (1976).
24. J. Stone and C. A. Burrus, *Appl. Phys. Lett.*, **23**, 388 (1973); E. I. Galant, Yu. N. Kondrat'ev, A. K. Przhevuskii, T. I. Prokhorova, M. N. Tolstoi, and V. N. Shapovalev, *Zh. ETF Pis. Red.*, **18**, 635 (1973).
25. A. V. Amosov, V. K. Zakharov, G. T. Petroskii, T. I. Prokhorova, and D. M. Yudin, *Z. Prikl. Spektrosk.*, **11**, 742 (1969).
26. R. R. Jacobs and M. J. Weber, *IEEE J. Quantum Electron.*, **QE-12**, 102 (1976).
27. K. Arai, H. Namikawa, K. Kumata, T. Honda, Y. Ishii, and T. Handa, *J. Appl. Phys.*, **59**, 3430 (1986).
28. Y. Ishii, K. Arai, H. Namikawa, M. Tanaka, A. Negishi, and T. Handa, *J. Am. Ceramic Soc.*, **70**, 72 (1987).
29. H. Imai, K. Arai, Y. Fujino, Y. Ishii, and H. Namikawa, *Phys. Chem. Glasses*, **29**, 54 (1988).
30. H. Namikawa, K. Arai, K. Kumata, Y. Ishii, and H. Tanaka, *Japan J. Appl. Phys.*, **21**, L360 (1982); K. Arai, H. Namikawa, K. Kumata, Y. Ishii, H. Tanaka, and I. Iida, *Japan J. Appl. Phys.*, **22**, L367 (1983).

31. B. J. Ainslie, S. P. Craig, S. T. Davey, D. J. Barber, J. R. Taylor, and A. S. L. Gomes, *J. Mater. Sci. Lett.*, **6**, 1361 (1987).
32. D. Levy, R. Reisfeld, and D. Avnir, *Chem. Phys. Lett.*, **109**, 593 (1984).
33. E. J. A. Pope and J. D. Mackenzie, *J. Non-Cryst. Solids*, **106**, 236 (1988).
34. E. J. A. Pope, J. D. MacKenzie, M. Shinn, and M. J. Weber, unpublished.
35. C. Brecher and L. Z. Riseberg, *Phys. Rev.*, **13**, 81 (1976).
36. C. Brecher and L. A. Riseberg, *Phys. Rev. B*, **21**, 2607 (1980).
37. T. F. Belliveau and D. J. Simkin, *J. Non-Cryst. Solids*, **110**, 127 (1989).
38. J. L. Adam, V. Poncon, J. Lucas, and G. Boulon, *J. Non-Cryst. Solids*, **91**, 191 (1987).
39. F. M. Durville, G. S. Dixon, and R. C. Powell, *J. Lumin.*, **36**, 221 (1987).
40. M. Zahir, C. Parent, R. Olazcuaga, G. Le Flem, and P. Hagenmuller, *J. Non-Cryst. Solids*, **81**, 53 (1986).
41. S. A. Brawer and M. J. Weber, *Phys. Rev. Lett.*, **45**, 460 (1980).
42. S. A. Brawer and M. J. Weber, *J. Chem. Phys.*, **75**, 3522 (1981).
43. K. Hirao and N. Soga, *J. Am. Ceramic Soc.*, **68**, 515 (1985).
44. E. Larson, M. Weber, and J. Wong, submitted for publication.
45. *J. Lumin.*, **36**, 179–329 (1987).
46. R. M. Macfarlane and R. M. Shelby, *Opt. Commun.*, **45**, 46 (1983).
47. R. M. Macfarlane and R. M. Shelby, in: P. A. Fleury and B. Golding, Eds., *Coherence and Energy Transfer in Glasses*, Plenum, New York (1984).
48. F. M. Durville, E. G. Behrens, and R. C. Powell, *Phys. Rev. B*, **34**, 4213 (1986) and references cited therein.
49. E. G. Behrens, F. M. Durville, and R. C. Powell, *Opt. Lett.*, **11**, 653 (1986).
50. R. C. Powell, E. G. Behrens, and F. M. Durville, in: W. M. Yen, Ed., *Dynamical Processes in Disordered Systems*, Trans-Tech Publ., Aedermannsdorf (1989).
51. E. G. Behrens, F. M. Durville, R. C. Powell, and D. H. Blackburn, *Phys. Rev. B*, **39**, 6076 (1989).
52. R. Lange, W. Grill, and W. Martenssen, *Europhys. Lett.*, **6**, 499 (1988).
53. W. M. Yen, *SPIE Proc.*, **1033**, 83 (1988).

## NONLINEAR OPTICAL PROCESSES IN POLYMERS AND SOL-GEL GLASS COMPOSITES

PARAS N. PRASAD

### 42.1. INTRODUCTION

Nonlinear optical processes will play an important role in the newly emerging technology of photonics. The area of photonics is a new frontier of science and technology that is capturing the imagination of scientists and engineers worldwide because of its potential applications to many areas of present and future technologies. Photonics is the analog of electronics where photons instead of electrons are used to carry information. Applications range from fiber-optic communication and link to optical computing and other optical processing of information and images [1,2]. In addition, the photonics technology can also be used for new applications not provided by electronics. One example is sensor protection (or even eye protection) against laser threats. To emphasize the importance of photonics, other terms such as light wave technology and optical circuitry have also been used. Nonlinear optical processes provide important functions of frequency conversion (like frequency doubling to increase the density of data storage), light control by electric field, and even all optical processes such as light control by light.

Utilizing these manifestations of optical nonlinearities, one can build devices such as frequency converters, light modulators, all optical switches, optical logic,

---

*Ultrastructure Processing of Advanced Materials.*

Edited by Donald R. Uhlmann and Donald R. Ulrich (deceased).

ISBN 0-471-52986-9 © 1992 John Wiley & Sons, Inc.

optical memory storage, and optical limiters. The technology of photonics with devices using nonlinear optical processes offer many advantages; among them the most important ones are

1. The gain in speed of signal processing.
2. Three-dimensional connectivity (optical neural network) to produce smaller integrated optical chips.
3. No electrical and magnetic interference.
4. Compatibility with fiber-optics link.

## 42.2. BACKGROUND

Nonlinear optical processes can conveniently be viewed as dielectric phenomena. For a linear dielectric, application of an electric field polarizes the medium to produce a polarization  $P$ , which is linearly proportional to the applied field, the proportionality constant  $\chi^{(1)}$  being the linear susceptibility. The response is also described by a dielectric constant  $\epsilon$ . If the electric field is due to an optical field, then the response is also described by a refractive index  $n$ . For a plane wave propagation

$$E = E_0(z, t) = E_0 \cos(kz - \omega t) \text{ or } \frac{1}{2}[E_0 e^{i(\omega t - kz)} + cc] \quad (1)$$

The refractive index  $n$ , the wave vector  $k = n\omega/c$ , and the phase velocity  $v = c/n$  are all independent of the field strength  $E$ .

For a nonlinear dielectric one has the polarization [3]

$$\begin{aligned} P &= \chi^{(1)} \cdot E + \chi^{(2)} : EE + \chi^{(3)} : EEE + \text{higher order terms} \\ &= \chi_{\text{eff}} \cdot E \end{aligned} \quad (2)$$

$\chi_{\text{eff}}$ , the effective susceptibility, now depends on the field strength  $E$ . Therefore at optical frequencies,  $n$ ,  $k$ , and  $v$  are all dependent on  $E$ .  $\chi^{(2)}$  and  $\chi^{(3)}$  are the second- and third-order nonlinear optical susceptibilities. Two important manifestations of optical nonlinearities are harmonic generation and refractive index modulation by electric and optical fields. Their origin can conveniently be explained by considering a plane wave propagation through the nonlinear medium. The polarization is then given by

$$\begin{aligned} P &= \chi^{(1)} E_0 \cos \alpha + \chi^{(2)} E_0^2 \cos^2 \alpha + \chi^{(3)} E_0^3 \cos^3 \alpha \\ &= \chi^{(1)} E_0 \cos \alpha + \frac{1}{2} \chi^{(2)} E_0^2 (\cos 2\alpha + 1) + \chi^{(3)} E_0^3 \left[ \frac{3}{4} \cos \alpha + \frac{1}{4} \cos 3\alpha \right] \end{aligned} \quad (3)$$

where  $\alpha = (kz - \omega t)$ . Equation 3 shows that due to nonlinear optical effects, higher frequency components ( $2\alpha$  and  $3\alpha$  terms) are generated that describe higher harmonic generation; examples being second-harmonic generation due to  $\chi^{(2)}$  terms and third-harmonic generation due to  $\chi^{(3)}$  terms. In addition, the

$\chi^{(3)}$  terms leads to a term with  $\cos \alpha$  that describes the intensity dependence of refractive index. The dependence of refractive index on the electric field actually consists of two terms: (1) one derived from  $\chi^{(2)}$  that is linearly dependent on  $E$  and describes the electrooptic effect, also known as *Pockels effect*, in which the application of electric field modulates the refractive index and (2) that derived from  $\chi^{(3)}$ , which is quadratically dependent on  $E$  and hence linearly dependent on  $I$ , which describes the Kerr effect. It is the latter that provides a mechanism for light control by light because an intense beam can be used to change the refractive index of the medium and influence either its own propagation or propagation of another beam of different or same frequency.

Nonlinear optical materials can be classified in two different categories:

1. Molecular materials that consist of chemically bonded molecular units interacting in the bulk through weak van der Waals interactions. For these classes of materials, the optical nonlinearity is primarily derived from the molecular structure. One can define microscopic nonlinear coefficients  $\beta$  and  $\gamma$ , which are the molecular equivalents of the bulk susceptibilities  $\chi^{(2)}$  and  $\chi^{(3)}$ . Examples of molecular materials are organic crystals and polymers [4].

2. Covalent and ionic bulk materials, where the optical nonlinearity is a bulk effect. The examples of this class of materials are most inorganic systems, multiple quantum well semiconductors, and inorganic photorefractive crystals [5].

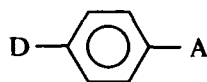
The molecular materials are emerging as an important class of materials because they provide flexibility to tailor their molecular structure and use molecular engineering to maximize the optical nonlinearity [4].

Although potential technological opportunities have provided the main impetus for the development of this area, there are also tremendous challenges for fundamental research in this field. A basic understanding of relationship between molecular structure and microscopic optical nonlinearity is still very limited. This understanding has to be sufficiently developed before one can take full advantage of the tailorability of molecular structures to enhance optical nonlinearity. Then problems involving cooperative effects, intermolecular charge transfer, and the nature of local fields are key issues in understanding the relation between microscopic and bulk nonlinearities. The dynamics of excitations and resonance effects on optical nonlinearity; the effect of quantum confinements of excitations, and the role of some excitations such as solitons, polarons, and bipolarons in polymeric structures are other relevant topics that need to be investigated.

### 42.3. STRUCTURAL REQUIREMENTS FOR SECOND- AND THIRD-ORDER OPTICAL NONLINEARITIES

Although our theoretical understanding of the relationship between the structure and the microscopic optical nonlinearity is rather limited, some features of structural requirements for nonlinear optical molecular materials

have been identified [4, 6]. Because  $\chi^{(2)}$  and the corresponding microscopic coefficient  $\beta$  are third-rank tensors, in order for them to be nonvanishing the molecular structure must be noncentrosymmetric. An asymmetric charge distribution in a molecular structure is found to enhance  $\beta$ .



In the above structure,  $D$  and  $A$  represent the electron-donating and accepting groups, respectively, which are separated by a  $\pi$  structure (aromatic ring in the above example). Even with a nonzero  $\beta$  structure, one needs to have a noncentrosymmetric bulk structure to achieve  $\chi^{(2)} \neq 0$ . To recognize inadequacies in our understanding of optical nonlinearities, it is to be noted that we are investigating several systems in our laboratory that do not conform to the above structure, but exhibit large  $\chi^{(2)}$ . Examples are  $\text{CH}_3\text{I}$ :sulfur and  $\text{CH}_3\text{I}$ :hexamethylenetetramine complexes that do not have  $\pi$  electrons or typical electron donor and acceptor groups.

The  $\chi^{(2)}$  organic systems do not necessarily require polymeric structures. Consequently, an important group of organic materials for  $\chi^{(2)}$  processes are organic crystals of relatively small molecules. It should be pointed out that one does not need crystallinity in order to have nonvanishing  $\chi^{(2)}$ . Simply a noncentrosymmetric ordering of dipoles in an otherwise noncrystalline medium (such as a glass, an amorphous polymer, or a Langmuir-Blodgett film) is sufficient to produce nonvanishing  $\chi^{(2)}$ , provided  $\beta \neq 0$ . In Langmuir-Blodgett multilayer films such a noncentrosymmetric ordering can be generated by so-called X- or Z-type depositions or by using an alternate layer structure. In a glassy medium or a polymer, a noncentrosymmetric ordering of dipoles can be created by electric field poling of the medium in a more fluid state (e.g., before gelation in a sol-gel-processed glass or by heating a polymer to near its glass temperature). Among the polymeric structures, side-chain liquid crystalline polymers are becoming recognized as an important group of  $\chi^{(2)}$  materials where a nonlinear optically active group (with  $\beta \neq 0$ ) is attached to the polymer backbone through flexible spacers [4]. Such polymers are easier to pole and also offer considerable flexibility for molecular engineering. In addition, we have found that some liquid crystalline polymers can also be deposited as Langmuir-Blodgett films, which may be useful for some device structures [7].

Structural requirements for  $\chi^{(3)}$  systems are different from that for  $\chi^{(2)}$  materials [4]. Organic structures with extensive  $\pi$  conjugation exhibit large  $\gamma$  (the molecular analog of  $\chi^{(3)}$ ). These structures do not have to be noncentrosymmetric, because  $\gamma$  is a fourth-rank tensor. Conjugated polymers provide a molecular frame for extensive conjugation and have, therefore, emerged as the dominant group of  $\chi^{(3)}$  organic materials [4]. Examples of conjugated polymers are polydiacetylenes, poly-*p*-phenylene vinylene (PPV), and polythiophenes. Our work has revealed that all conjugated polymers do not show the same effective delocalization in relation to optical nonlinearity. Therefore, in addition

to being a conjugated polymeric structure, it must provide effective delocalization. In a sequentially built structure, we have found that the  $\pi$ -delocalization effect on  $\gamma$  is more effective for the thiophene oligomers than it is for the benzene oligomers [8]. The largest component of the  $\gamma$  tensor is along the conjugation direction. Therefore, even though no order in the bulk is required for  $\chi^{(3)} \neq 0$ , a uniaxially oriented bulk in which all conjugated polymeric chains align in the same direction will have a large  $\chi^{(3)}$  value compared to that in a truly amorphous form of the same polymer. Our study of  $\chi^{(3)}$  measurements in stretch-oriented polymers as discussed below confirms this prediction. Finally, to increase the number density, these polymeric chains must pack closely so that  $\chi^{(3)}$  is maximized.

From the above discussion, it is apparent that amorphous polymeric or glassy structures are more suitable as media for third-order nonlinear optical processes. Interest recently has shifted considerably to the third-order processes, because they provide mechanisms for all optical switching and all optical signal processing.

#### 42.4. MEASUREMENT OF THIRD-ORDER OPTICAL NONLINEARITY

Our research program focuses heavily on the study of third-order nonlinear optical processes. We measure the third-order optical nonlinearity by a variety of methods. The method most frequently used in our laboratory is that of degenerate four-wave mixing (DFWM). In this method two beams  $I_1$  and  $I_3$  are crossed at an angle. The third beam  $I_2$  is incident as counterpropagating to  $I_1$ , the nonlinear polarization generates a fourth beam  $I_4$ , the signal, which is produced in a direction counterpropagating to  $I_3$ . Because all waves are of the same optical frequency, this method utilizing the interaction of four waves is called *degenerate four-wave mixing*. The signal is proportional to the square of  $\chi^{(3)}(-\omega; \omega, -\omega, \omega)$ . This notation for  $\chi^{(3)}$  simply represents the frequencies of the four waves, the negative sign implying the phase conjugate nature (counterpropagation). Because  $\chi^{(3)}$  shows a dispersion behavior the specification of frequencies of waves is appropriate. This value of  $\chi^{(3)}$  directly relates to the intensity-dependent refractive index coefficient  $n_2$  at  $\omega$ , which is an important device parameter. Furthermore, the DFWM arrangement also provides information on the time response of the optical nonlinearity ( $n_2$ ).

To conceptually understand this feature, one often uses a dynamic grating picture. In this picture, beams  $I_1$  and  $I_3$  interfere in a material to set up an intensity grating. The material's nonlinear response leads to a refractive index grating. This index grating in the nonresonant case is due to the  $n_2 I$  term. In the resonant case, the refractive index change is due to excited state species or due to local heating (thermally induced refractive index change). Furthermore, this local periodic heating also leads to a corresponding density grating, setting up an ultrasonic (strain) wave grating. Now if beam  $I_2$  is incident on this grating, it

is Bragg-diffracted from this grating to generate beam  $I_4$  in the phase-matched direction. The delay of beam  $I_2$  with respect to beams  $I_1$  and  $I_3$  can conveniently probe the dynamic behavior of this grating and provide information on the time response of the optical nonlinearity.

The ultrasonic phonon grating time behavior can be used to obtain information on the mechanical properties (elastic constants) of the medium, even though this time response is too slow for optical signal processing. Our work on stretch-oriented polymers has shown that the ultrasonic phonon grating provides a convenient method of obtaining both the longitudinal and shear components of the elastic constant tensor [9, 10].

In order to identify the mechanism of optical nonlinearity generating a four-wave mixing response, one should utilize the shortest laser pulse accessible because some resonant nonlinearities have a subpicosecond response time. In our laboratory, we use subpicosecond laser pulses. One laser system used for DFWM is shown in Fig. 42.1. A colliding pulse mode-locked (CPM) dye laser pumped by an argon ion laser is amplified in a multipass dye amplifier pumped by a copper vapor laser, which runs at 8 KHz. The amplified pulses are  $\sim 80$  fsec with a pulse energy of  $\sim 10 \mu\text{J}$ . The beam is split in three parts with an independently adjustable delay for each beam. Then a backward wave counter-propagating geometry is used in which the backward beam delay is scanned to obtain the time response.

Table 42.1 lists the nonresonant  $\chi^{(3)}$  values of some of the polymers investigated in our laboratory. It should be emphasized that for conjugated polymers, it is difficult to define a truly nonresonant (optically transparent) wavelength region because there are always residual absorptions. A practical definition of the nonresonant region may be the wavelength at which the absorption coefficient  $\alpha \leq 10 \text{ cm}^{-1}$ . A promising polymer is PPV. We have investigated the behavior of this polymer both in unoriented (as cast) films as well as in various stretch-oriented forms [11]. Figure 42.2 shows a representative plot of the DFWM signal as a function of orientation of the film with respect to the vertical polarization used for the laser beams. The  $\chi^{(3)}$  value is highly anisotropic, being the largest along the draw direction in the uniaxially stretched film. This result confirms that the largest component of the  $\chi^{(3)}$  tensor (and the  $\gamma$  tensor) is along the chain direction, because in an uniaxially stretched film the polymer chains preferentially orient along the draw direction. The solid curve is a theoretical fit using a simple model of transformation of a fourth-rank tensor  $[\chi^{(3)}]$  from a film-based coordinate system to a laboratory coordinate system, which defines the polarizations of the laser beams. The solid curve adequately describes the observed anisotropy and hence confirms the fourth-rank tensor property of  $\chi^{(3)}$ .

We have also investigated the behavior of resonant optical nonlinearities [12]. Here the excited state dynamics plays an important role in determining the optical nonlinearity and its time response. The resonant nonlinearity is sufficiently large in some cases like phthalocyanines so that the DFWM signal can



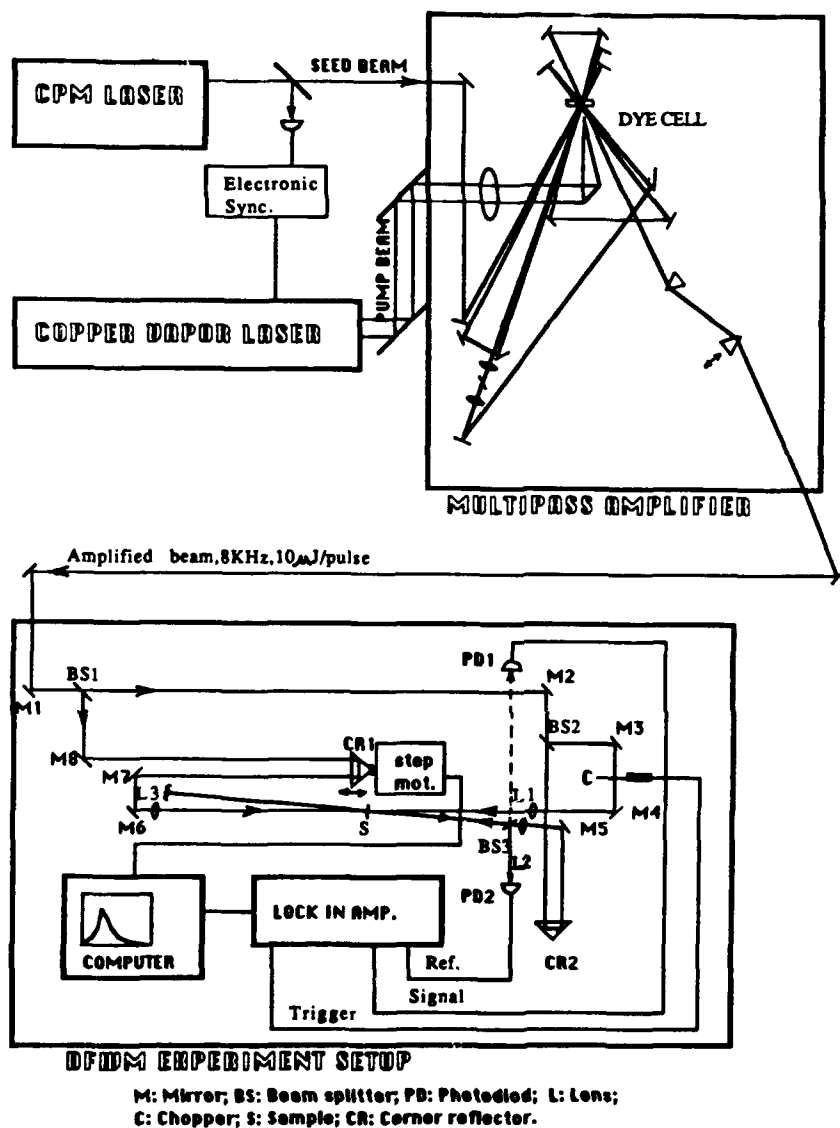
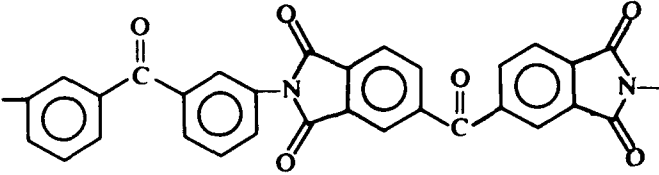
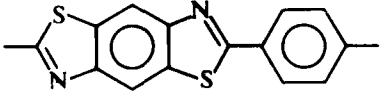
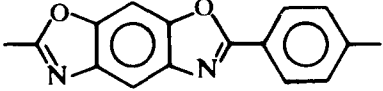
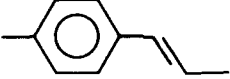
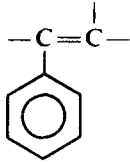
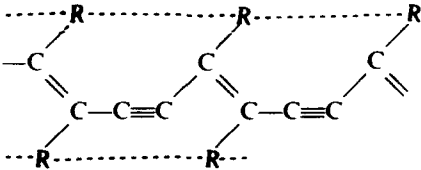
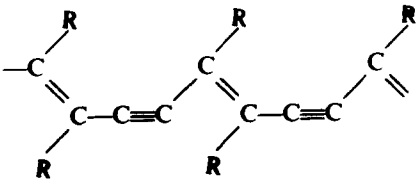
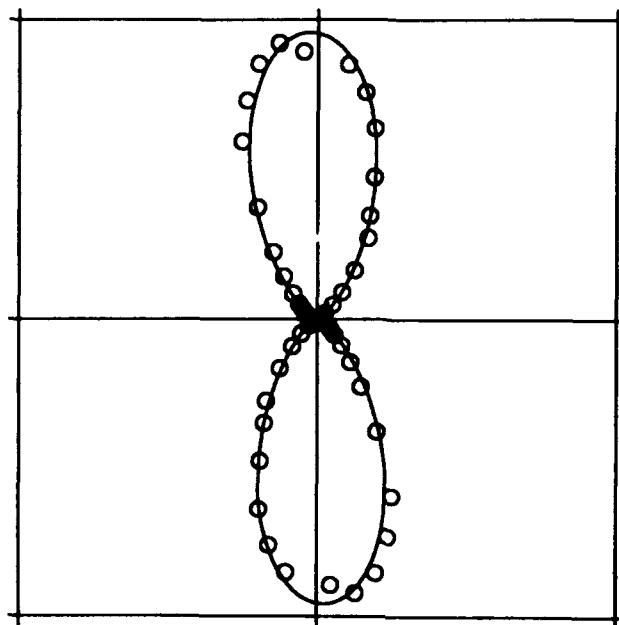


Figure 42.1. Schematics of the amplified colliding pulse mode-locked laser system used for femtosecond degenerate four-wave mixing.

be observed even from a monolayer thick (30 Å) Langmuir-Blodgett film [13]. The response time varies from subpicoseconds to hundreds of picoseconds, determined by the excited state relaxation processes. However, compared to inorganic systems, such as multiple quantum well semiconductors, the resonance enhancement is not large in organic materials.

TABLE 42.1.  $\chi^{(3)}$  Values of Various Polymers

Systems	Repeat Structures	$\chi_{1111}^{(3)}$ at $\lambda = 602$ nm (esu)
LARC-TPI		$-2 \times 10^{-12}$
PBT		$-10^{-11}$
PBO		$-10^{-11}$
Poly- <i>p</i> -phenylenevinylene		$-4 \times 10^{-10}$
Poly-phenyl acetylene		$5 \times 10^{-11}$
Poly- <i>n</i> -BCMU Red		$5 \times 10^{-11}$
Yellow		$3 \times 10^{-10}$
	$R = (\text{CH}_2)_n - \text{O} - \text{C}(=\text{O}) - \text{NH} - \text{CH}_2\text{COO}(\text{CH}_2)_3\text{CH}_3$	$2.5 \times 10^{-11}$



**Figure 42.2.** Polar plot of the degenerate four-wave mixing signal as a function of the film rotation in a 10:1 uniaxially stretch-oriented poly-*p*-phenylenevinylene film. The vertical axis is the draw direction.

## 42.5. DEVICE NEEDS

Devices for all-optical switching are based on utilization of an intensity-dependent phase shift. This phase shift is derived from  $n_2$ , the nonlinear (intensity dependent) refractive index coefficient. Based on our measurements, a typical value for  $n_2 = 10^{-7} \text{ cm}^2/\text{MW}$ . The phase shift is given as

$$\Delta\phi = \frac{n_2 I L}{\lambda}$$

If one needs a phase shift of  $\pi$ , the above value of  $n_2$  for an intensity of 100 MW/cm<sup>2</sup> at  $\lambda = 1 \mu\text{m}$  would require a path length of 1 cm. Due to diffraction effects, it is not possible to maintain high power density for this path length. Hence, one needs to use an optical waveguide structure [2]. For high optical throughput in the optical waveguide, one would need  $\alpha L \leq 1$ , where  $\alpha$  is the waveguide loss and  $L$  is the length of the nonlinear interaction region of the device. For  $L = 1 \text{ cm}$ , it yields  $\alpha \leq 1 \text{ cm}^{-1}$ , which means that the medium should have a very low optical loss due to absorption and scattering, the latter derived from refractive index inhomogeneities. This stringent requirement clearly rules out resonant nonlinear processes for polymers. Furthermore, one

would be limited to waveguide devices of polymers that yield high optical quality (low  $\alpha$ ) films and fibers. This is not easy to achieve in conjugated polymers due to the presence of defects, domain structures, and a distribution of conjugation lengths. After a great deal of effort on improving processing conditions, our first success was a waveguide of polyamic acid for which  $\alpha \ll 1 \text{ cm}^{-1}$ , but  $\chi^{(3)}$  is only  $\sim 10^{-12}$  esu which is low [14]. We have looked at nonlinear optical processes in this waveguide and observed that due to the change of refractive index induced by intensity changes, the coupling angle is different at low and high input intensities (a grating coupling arrangement was used). Suppose the coupling angle is kept as the one optimized at low power. Then as the input intensity increases, this angle detunes producing a limiter action behavior in the output-input relation. It also leads to a drop in the coupling efficiency defined by the ratio  $I_{\text{out}}/I_{\text{in}}$ . This is what we observe.

We have investigated the waveguiding characteristics of the polymer PPV for which the  $\chi^{(3)}$  value is  $> 10^{-10}$  esu, more than two orders of magnitude larger than that for the polyamic acid. PPV is also a very unusual material because even in the as-cast film, the refractive indices for the TE and TM modes are different. The material is highly birefringent, because the chains due to their rigid structures prefer to lie in the plane of the film. The losses are high, being much higher for the TE mode, which limits the propagation to less than 1 mm.

Let us now examine the needs of a nonlinear optical device from the materials point of view. There are two components in a *photonic material*. One is the active component, which ideally should have the largest nonlinear coefficient. The other component is a photonic medium, the requirements for which (such as refractive index and optical losses) are determined by a specific device structure. The biggest materials research problem is to optimize both. An ideal situation, of course, is when the active components alone form the photonic medium. However, such situations are not always achievable. Hence, one looks for composite materials in which an active component of high optical nonlinearity is dispersed at the ultrastructure level within a photonic medium made of a component that provides excellent optical quality.

#### 42.6. THEORETICAL AND EXPERIMENTAL STUDIES OF SEQUENTIALLY BUILT AND SYSTEMATICALLY DERIVATIZED COMPOUNDS

Recognizing the two important needs that are (1) to maximize optical nonlinearity of the active components and (2) to design photonic media of high optical throughput, we have developed a comprehensive program at SUNY at Buffalo in this area. To fulfil the need to understand what structures will allow enhancement of optical nonlinearity, we have coupled ab initio theoretical calculations of optical nonlinearity with synthesis of sequentially built and systematically derivatized model compounds and the measurement of their optical nonlinearities. For the second objective that is to optimize the photonic

media, we have worked on materials processing for devices and their needs. Hence, we are also involved in device physics. An advantage of having a comprehensive program is an interactive feedback that leads to optimization and cross-correlation at each stage.

Now I would like to discuss very briefly our efforts to understand microscopic optical nonlinearities. An expression similar to the expansion of the bulk polarization as a function of the applied field can be written for the induced dipole moment. Naturally, the nonlinear term  $\gamma$ , for example, is the third derivative of the induced dipole moment with respect to the applied field. Also, using the Stark energy analyses one can write the nonlinear term  $\beta$  (and  $\gamma$ ) as a sum over all excited terms involving transition dipoles and permanent dipoles, similar to what one does for polarizability. Consequently, the two theoretical approaches are (1) the derivative method and (2) the sum-over-states method. We have used the derivative method at the *ab initio* level [15]. We correlate the predictions of these calculations with measurements on systematically derivatized and sequentially built model compounds. Some conclusions of our theoretical computations are as follows:

1. The choice of basis functions, particularly the inclusion of diffuse polarization functions, is important in the calculation of  $\beta$  and  $\gamma$ .
2.  $\pi$ -electron contribution to optical nonlinearity dominates.
3.  $\pi$ -electron delocalization (conjugation effect) increases  $\gamma$  significantly exhibiting a  $N^3$  to  $N^4$  power dependence with respect to the number of repeat units  $N$  in a sequentially built oligomeric structure.
4. For nonresonant cases,  $\gamma$  is positive.

One group of sequentially built structures is the thiophene oligomers and related derivatized structures that we have synthesized and experimentally investigated. The agreement with theoretical predictions appears to be satisfactory [16]. Another group of systematically derivatized model compounds that relate to rigid-rod aromatic heterocyclic polymers have been synthesized by Bruce Reinhardt of the Air Force Wright Aeronautical Laboratory, Polymer Branch. These measurements, when correlated with the structural variations, have provided us with useful insight into molecular engineering of new structures with large optical nonlinearity.

#### 42.7. NONLINEAR OPTICAL DEVICE PROCESSES

In relation to devices our work focuses on the study of device processes of optical switching, optical bistability, optical limiter action, and light modulation. We have demonstrated the optical bistability behavior in a quasi-waveguide interferometric configuration [17]. We have also seen an optical limiter action behavior in an optical waveguide as discussed above [14]. Another device process we have been studying utilizes a hollow core fiber filled

with a nonlinear optical material [18]. Again one very serious limitation to device studies is the optical quality of materials.

#### 42.8. A NOVEL POLYMER: SOL-GEL COMPOSITE FOR NONLINEAR OPTICS

Because of its low loss, a glass is an excellent photonic medium in the form of either fibers or films. Hence sol-gel processing can be expected to play an important role for fabrication of device structures for photonics. However, the glass by itself has very low optical nonlinearity. In order to use the sol-gel processing for developing nonlinear photonic media one can take two different approaches:

1. One can derivatize the sol-gel precursor to put a nonlinear functional group as a part of the structure. This approach is more useful for placing small molecular units and hence more suitable for second-order nonlinear functional groups.
2. One can use a sol-gel-processed composite material that consists of a sol-gel-processed glass doped with a nonlinear optical material. The nonlinear optical component can be a conjugated polymer.

A practical problem is miscibility of the two components. Generally, at higher concentrations phase separation occurs. We have been successful in producing a novel composite of the sol-gel-processed silica and the PPV polymer, which also forms promising waveguiding films with significantly improved optical quality [19]. The optical losses are so low that even for a TE mode one can achieve propagation distances of more than 2 cm at 1.06  $\mu\text{m}$ . We have obtained the Raman spectra of the composite in a waveguide configuration. The observed Raman spectra in the C=C region shows two bands that are due to the aromatic ring mode and the olefinic double bond. The frequencies for these modes in the composite are the same as that seen for pure PPV. Hence, the effective  $\pi$ -conjugation for the polymer in the composite is quite comparable to what exists in the pure PPV material. We have conducted the DFWM study of this composite using ultrashort amplified pulses of < 100 fsec from the amplified CPM laser system discussed above. A response time limited by the laser pulse width is observed. The value of  $\chi^{(3)}$  depends on the relative composition and is  $\geq 5 \times 10^{-11}$  esu.

#### 42.9. FUTURE DIRECTIONS OF RESEARCH

To conclude, a discussion of future direction of research is appropriate. In my opinion the following areas need to be developed:

1. Improvement of our microscopic understanding of optical nonlinearity.

For this purpose theoretical and experimental studies of sequentially built, and systematically derivatized structures are needed.

2. Increase of data base. Even though more studies are being reported on the measurement of third-order optical nonlinearities, the data base is still limited. We need input from syntheses of novel structures and measurements of optical nonlinearities on them.

3. Finally, materials research. This is a very important direction of future research. The work in this area will focus on developing new composites, designing processing schemes to improve optical quality, properly characterizing the ultrastructures of these materials, and fabricating various device structures.

This is a highly active and truly multidisciplinary area with exciting opportunities for materials scientists. One can expect significant developments to occur in the near future.

### ACKNOWLEDGMENTS

This work was supported by the Defense Initiative Organization, the Office of Innovative Science and Technology; the Air Force Office of Scientific Research, Directorate of Chemical Sciences; and the Air Force Wright Aeronautical Laboratory through Contracts F4962087C0097 and F4962087C0042.

I acknowledge valuable collaborations with Professor F. E. Karasz of University of Massachusetts, Professor G. I. Stegman of University of Arizona, and Dr. B. Reinhardt of Air Force Wright Aeronautical Laboratory, Polymer Branch. Valuable help and encouragement of Dr. D. R. Ulrich of Air Force Office of Scientific Research is also acknowledged. Finally, my thanks go to my research group members, Dr. J. Swiatkiewicz, Dr. R. Burzynski, Dr. M. Samoc, Dr. A. Samoc, Dr. E. Perrin, Dr. K. Wijekoon, Dr. B. P. Singh, Ms. P. Chopra, Mr. Y. Pang, Mr. J. C. Wung, and Mr. M. T. Zhao whose research efforts have contributed to this Chapter.

### REFERENCES

1. B. Clymer and S. A. Collins, *J. Opt. Eng.*, **24**, 74 (1985).
2. G. I. Stegman, *Thin Solid Films*, **152**, 231 (1987).
3. Y. R. Shen, *The Principles of Nonlinear Optics*, Wiley, New York (1984).
4. P. N. Prasad and D. R. Ulrich, Eds., *Nonlinear Optical and Electroactive Polymers*, Plenum, New York (1988).
5. H. Haug, Ed., *Optical Nonlinearities and Instabilities in Semiconductors*, Academic Press, London (1988).
6. D. J. Williams, Ed., *Nonlinear Optical Properties of Organic and Polymeric Materials*, American Chemical Society, Washington, D.C. (1983).
7. M. M. Carpenter, P. N. Prasad, and A. C. Griffin, *Thin Solid Films*, **161**, 315 (1988).

8. M. T. Zhao, M. Samoc, B. P. Singh, and P. N. Prasad, *J. Phys. Chem.* **93**, 7916 (1989).
9. D. N. Rao, Y. Pang, R. Burzynski, and P. N. Prasad, *Macromolecules*, **22**, 985 (1989).
10. R. Burzynski, Y. Pang, D. N. Rao, and P. N. Prasad, *Polymer*, **30**, 1247 (1989).
11. B. P. Singh, P. N. Prasad, and F. E. Karasz, *Polymer*, **29**, 1940 (1988).
12. P. N. Prasad, J. Swiatkiewicz, and J. Pflieger, *Mol. Cryst. Liq. Cryst.*, **160**, 53 (1988).
13. P. N. Prasad, M. K. Casstevens, J. Pflieger, and P. Logsdon, in: Symposium on Multifunctional Materials, *PWIE Proc.*, **878**, 106 (1988).
14. R. Burzynski, B. P. Singh, P. N. Prasad, R. Zanoni, and G. I. Stegeman, *Appl. Phys. Lett.*, **53**, 2011 (1988).
15. P. Chopra, L. Carlacchi, H. F. King, and P. N. Prasad, *J. Phys. Chem.*, **93**, 7120 (1989).
16. M. T. Zhao, B. P. Singh, and P. N. Prasad, *J. Chem. Phys.*, **89**, 5535 (1988).
17. B. P. Singh and P. N. Prasad, *J. Opt. Soc. Am.*, **B5**, 453 (1988).
18. G. S. He and P. N. Prasad, *Phys. Rev.*, **A41**, 2687 (1990).
19. J. C. Wung, Y. Pang, P. N. Prasad, and F. E. Karasz, *Polymer*, **32**, 605 (1991).



## PHASE CHANGE MATERIALS FOR OPTICAL DATA STORAGE

DUNBAR P. BIRNIE III

### 43.1. INTRODUCTION

The present review of the status of phase change optical memory concentrates on advances that have been made in the past 10 years. Because much of the research has involved laser melting of thin semiconductor films, this review will draw heavily from a related field: laser processing of semiconductor devices. Both fields have high-intensity laser beams incident on the surface of semiconductor materials. These sometimes cause melting or amorphization and are also used to heal damaged amorphous layers present from other processes (such as ion implantation). Much understanding has been achieved in this area, and it may be applicable to the present topic.

Optical memory systems have been under consideration for many years. This has resulted primarily from the much higher storage densities that can be achieved in comparison to magnetic storage systems. Optical memory systems are limited in their storage density by the diffraction of the laser light that is used for reading and writing. For lasers that are easily available, this translates to a bit size of about 1  $\mu\text{m}$  in diameter.

These optical memory systems are of primary interest for the computer industry. In this application, *memory* implies that the system is erasable or cyclable. This is in contrast to the audio compact disks that store information digitally, but are read-only. For digital computer applications, two stable states must be available, and it must be possible to switch rapidly between the two states at will.

---

*Ultrastructure Processing of Advanced Materials.*  
Edited by Donald R. Uhlmann and Donald R. Ulrich (deceased).  
ISBN 0-471-52986-9 © 1992 John Wiley & Sons, Inc.

Three distinct different functions must be used for these optical memory systems: read, write, and erase. These three functions must be achievable optically. The *read* function is typically performed at lowest laser power, where it will have the least effect on the bit state. The *write* and *erase* functions are very similar; *write* implies causing a 1 to be marked on the disk, whereas *erase* implies causing a 0 to be marked on the disk. These are usually performed by having different power and laser duration, as discussed later.

Many types of materials systems have been investigated for use as optical memory. These range from the common magnetooptic (MO) memory [1-5] and phase change materials [most references] to semiconductor-metal transitions [6-9], ferroelectric [10], elastomeric [11], photodichroic [12-14], photochromic [14], optical hole burning [15], surface texture change [16], and possibly others [16-21]. Many of these systems are considered novelties, and only the first two systems are presently considered viable for reversible applications. The MO memory systems are advanced enough that they are now being marketed in Japan and will be included in the new Stephen Jobs computer, the NeXT [22]. The phase change memory systems under consideration must compete with these MO systems; the phase change systems have several specific advantages that can be utilized, such as optical path simplicity and media stability.

MO memory operates by sensing the polarization rotation of the incident beam through the Kerr effect. The amount of Kerr rotation is usually on the order of  $1^\circ$  only. This decreases signal-to-noise (S/N) ratio and makes for complex optics in the optical head design. (For more information on MO media refer to Refs. 1-5.)

Phase change systems rely on the intensity of reflected light to signal either a 0 or a 1. The intensity depends on the optical constants of the material phase of the film (either amorphous or crystalline). This type of system is attractive, because simpler optical head design is possible. For many systems, there is good optical contrast between the crystalline and the amorphous phases, yielding a good S/N.

In general, both the MO and the phase change media are more preferably designed in a reflective mode. This has two benefits. First, double-sided disks can be used. Second, the alignment of the optics is far simpler; transmission systems would require two heads that would both have to be servo-ed and aligned simultaneously.

The following section describes the typical design of phase change optical memory systems. Further sections describe more detail about experimental observation techniques and compositions that have been investigated.

### 43.2. PHASE CHANGE OPTICAL MEMORY SYSTEMS

A phase change system usually contains a multilayer, pregrooved disk. The laser used for the read-write-erase operations is a diode laser that runs in the range of 800 nm. Part of the reflected signal is used to sense both focus and tracking

operations and thereby run servos. The remainder of the signal is interpreted as data.

The multilayer disk usually contains many different components. There is the active film, where most of the laser light is absorbed and the phase transformation occurs. A thick substrate is used as a support for the multilayer above; this is commonly glass or a polymer such as (poly)methylmethacrylate. Other films can be utilized for a variety of different functions. Films may be placed between the substrate and the active medium or as overcoating layers. These may enhance reflectivity, change thermal conductivity, provide environmental protection, or even provide more strongly absorbing layers. Often these different layers are optimized in combination to achieve the largest contrast between the amorphous and the crystalline phases [23–25]. This typically takes advantage of optical interference effects that are disrupted when the optical constants change.

The diode lasers used in these systems are attractive because the output power can be easily controlled by monitoring the injection current into the diode. Usually, systems are designed such that only one wavelength is used. Otherwise, more than one laser would be required in a system; each of the lasers would have to be independently focused onto the same area, a large undesirable increase in complexity.

One constraint on the active phase change film is that it be strongly absorbing at the wavelength that is generated by the diode laser. The energy that is absorbed by the material is used to melt the material, controllably leaving either amorphous or crystalline material. Large absorption coefficients are usually obtained by band-to-band-type absorptions in a direct band gap-type material (note that the band gap must be small enough to couple well with the semiconductor diode laser output). Therefore small band gap semiconductors are of interest for phase change optical data storage systems. With a strongly absorbing material (having a small penetration depth), the disks are usually designed with films that are also very thin. This means that melting usually occurs completely through the material to the substrate. As discussed below, this may have some advantages for controlling the potential phase transformation processes that occur. Typical film thicknesses range from 300 to 1000 Å, depending on the optical design of the multilayer.

### 43.3. PHASE TRANSFORMATION CONTROL

For an optical data storage system the only requirement is that there be two easily distinguishable states that can be reversibly changed using the laser. Literature observation generally shows that we want materials that have a crystalline background so that the amorphous regions become 1s [26]. This is an indirect result of the laser having a Gaussian intensity profile. This radial function of intensity translates directly into a Gaussian temperature distribution deposited by the laser. This temperature distribution interacts with important temperatures that describe the phase transformation processes in materials. The

temperatures of interest are the melting temperature ( $T_m$ ), the crystallization temperature ( $T_x$ ), and the glass transition temperature ( $T_g$ ).  $T_g$  is of somewhat less importance than the first two as described below.

The material in the active film must be raised above  $T_m$  if the material is to be left in the amorphous state.  $T_m$  is usually a smooth function of composition; alloy mixtures of elements can be used to tailor its  $T_m$ . This melting temperature must be significantly above room temperature because the written film must be stable over long periods of time between writing cycles. From the molten state, either crystalline or amorphous materials can result. This depends on a competition between heat removal and crystal nucleation and growth.

The crystallization temperature,  $T_x$ , is the temperature that an amorphous (or liquid) phase must be raised to cause crystallization. This is important because the amorphous spots must be erased back to the crystalline state. This temperature is related to the glass transition temperature,  $T_g$ .  $T_g$  is the temperature, upon heating, where an amorphous material starts to become fluid and therefore able to rearrange its configuration (and potentially crystallize). Heating an amorphous material above  $T_g$  is necessary, but not sufficient to cause crystallization. For crystallization to occur, often nucleation must occur. Nucleation events depend on local defects, such as interfaces that may serve as heterogeneous nucleation sites, and on thermodynamic properties of the materials, such as interfacial tensions and transformation energy. Heating to  $T_m$  is not required for crystallization, but heating above the crystallization temperature is required.

As a general rule, materials that are good glass formers, such as silicate glasses, will have a ratio of  $T_x$  to  $T_m$  (in degrees Kelvin) of about 2:3. And, poor glass formers, such as most metals and elemental semiconductors, will have a ratio of about 1:2. One qualitative distinction is that the silicate glasses (usually good glass formers) must have rotation of  $\text{SiO}_4$  tetrahedra for the crystallization front to advance. But, elemental materials (usually poor glass formers) only require an atom jump for attachment. This makes it more difficult to make these materials amorphous. For the optical memory application, the crystallization and amorphization are happening so rapidly that we must consider primarily poor glass formers as candidate materials.

For memory application, it will be necessary for both crystalline and amorphous regions to remain stable over long periods of time (10 years or so). To achieve this level of stability, it will be necessary to have a crystallization temperature of about 150°C. With this  $T_x$  and using the ratio of 1:2, interesting materials will have a melting temperature of about 550 to 600°C [27].

The difference between the write and the erase cycle can be described as writing at high power with short durations and erasing with medium powers for medium durations. The first profile causes melting and then quenching into the amorphous state by rapid conduction of the heat into the substrate material. The second profile raises the amorphous material above its crystallization temperature and holds it there until crystallization occurs.

This format for using the crystallization temperature to erase and the melting

temperature to write seems more favorable than simply using two different pulse shapes that both raise the temperature above the melting temperature, but cool at different rates. The different cooling rates achievable are probably still within an order of magnitude of each other [28]. Therefore the ability to control crystallization would require much better overall control of the system.

The phase transformation must also happen in a very short period of time. To have the most control over the data storage process it is desirable to have direct-read-after-write (DRAW) type of behavior. This means that the crystallization or amorphization must occur while the spot is under the laser beam. Then the spot can be verified immediately; if a write error has occurred, then rewriting can be attempted. This means that the crystallization must occur within about 300 nsec. And, if the crystallization time were even less, then the disk rotation speed could be increased.

The amorphization occurs whenever the melted material cools fast enough to prevent crystal growth into the spot area. The crystal growth may or may not require nucleation events to occur depending on the type of background that the material retains. Reported cooling rates for amorphization are in the range of  $10^9$  to  $10^{10}$ /sec. At these cooling rates, the material remains hot for between 100 nsec and 1  $\mu$ sec.

These cooling rates are obtained for two reasons. First, the active films are very thin, which sets up very steep temperature gradients. This drives the very rapid heat removal. The other reason for the rapid heat removal is that the absorption coefficient of typical materials is very large, usually larger than  $10^5 \text{ cm}^{-1}$ . This means that the light is absorbed preferentially at the surface. This also gives a very steep temperature gradient that drives the heat flow. For an absorption coefficient of  $10^5 \text{ cm}^{-1}$ , the laser power is absorbed to a  $1/e$  depth of  $1/\alpha = 10^{-5} \text{ cm}$  or 1000 Å. The temperature gradient will be most enhanced at the interface with a nonabsorbing material (the substrate) that remains unaffected by the laser light.

Then, in the absence of nucleation, the very rapid cooling rate can cause the material to be frozen into an amorphous state. Usually nucleation sites are prevented in the area of the melted spot by having the melting proceed all the way through the film to the substrate material. Then the only sites for crystal growth are at the perimeter of the melted spot [29]. It may be possible that the interface between the melt and the substrate could be a preferred, heterogeneous, nucleation site. However, it is probably easier to freeze the melt if no nucleation occurs at that surface; the crystallization front would then have to move about 10 times as far across the thin disk-shaped spot, rather than just the thickness of the spot. Typical micrographs bear out this interpretation of the nucleation and crystal growth [25, 30–35]. Frequently, there is a radial appearance to the spot, and often there are only a few grains per spot. Differences in growth velocity with crystal direction may account for the texture. Fast growth directions will dominate, even though there may be many tiny nucleation sites at the perimeter.

Note that the liquid–solid interfacial velocity must be large enough to

have the spot transform in the requisite amount of time. If the transformation must traverse the radius of a diffraction limited spot in 100 nsec, then the crystallization velocity must be about 5 m/sec. Observed crystallization velocities are about 2 m/sec for Te films [29] and 10 m/sec for Si [36]. These crystallization velocities are still much slower than ultimate physical limits. Usually, the most rapid crystallization velocity would be at the velocity of sound. For the Te-alloy-based materials, we are still about two orders of magnitude slower than this rate. If long-range diffusion is required for the interface to move, then the crystallization velocity will be reduced significantly.

For practical optical memory application, it will be desirable to have *direct overwrite* [37, 38]. The writing process would be optimized if the writing worked equally well whether the starting material was previously written with 0 or 1. The two temperature profiles described above could have this behavior. The writing pulse that raises the temperature above  $T_m$  must melt both the amorphous and the crystalline phases. Then upon cooling, the melt will be quenched into the amorphous state. Also, the erasing pulse that raises the temperature to somewhere above  $T_x$ , but below  $T_m$  will cause crystallization if the previous state was amorphous. However, if the previous state was crystalline, then nothing will happen, because the melting temperature has not been reached. Therefore, this type of system would yield the proper phases independent of the starting phase.

For fast, reversible optical memory, the phase transformation characteristics must be carefully controlled. Factors that may be used to control the phase transformation are film thickness, composition, substrate material (and therefore its thermal conductivity and other properties), and other multilayer component choices. The next section covers experimental techniques that have been very valuable in characterizing the phase transformation processes that are active in these materials.

#### 43.4. CHARACTERIZATION TOOLS

Many different techniques have been used to increase the understanding of phase change optical memory materials. These include transmission electron microscopy (TEM), differential thermal analysis (DTA), reflectivity, conductivity, and thermal modeling. Some of these techniques will be briefly reviewed and discussed.

TEM has been very useful in determining the starting and resultant microstructures in these materials. Active films are typically on the order of 1000 Å thick, which makes them quite attractive for TEM observation, because they are already thin enough for electron transparency. Using this examination technique, it is difficult to differentiate features that vary as a function of depth through the quite thin film; all of the depth features are compressed into two dimensions. This makes it very difficult to assess different aspects of the phase transformation process, such as nucleation location or growth directions.

Alternately, with significant expertise, it is possible to make transections that make a cross section through all layers of the optical memory stack [39–42]. This enables a closer view of the crystal morphology that exists in different written states of the film. Because the size of the written spot is on the order of  $1\text{ }\mu\text{m}$ , it is difficult to make a cross section that goes through the center of a bit. This technique is more useful in looking at films that have had large area illumination or where tracks have been uniformly written as stripes. These different geometries of sample preparation necessitate different write profiles, it is not guaranteed that the morphology will be representative of the status in stored bits. The transections have been useful in analyzing optical data storage materials and other related laser–material interactions, such as laser processing of implanted semiconductors.

The electron microscopy observations described above can only look at the morphology either before or after the interaction of the laser with the material. Other techniques can give information that describes the laser interaction with the disk as a function of time. These use rapid optical or electrical measurement of the relevant film during the illumination.

One of the most useful techniques is to monitor the reflected light from the surface as a function of time, light flux, beam size, and so on. Some parameters control the extent of the light profile. Other parameters are mediated by the materials properties, such as phase (liquid or solid), temperature, thermal conductivity, and heat of fusion.

Another transient measurement technique is to measure the lateral conductivity of a thin film under the influence of laser radiation [29, 34, 36, 43–45]. Parallel electrical contacts are deposited on the surface of the active thin film semiconductor. A rectangular area between the two contacts is illuminated with very high-intensity laser light. Because high total powers are required to melt rather large areas, excimer laser light can be used. Care must be taken that the illumination is very uniform across the rectangular area and zero beyond that area. The signal is the change in the resistance between the two leads.

The basic assumption is that there is uniform illumination. This causes a uniform thermal profile; when melting occurs, the solid–liquid interface moves parallel to the surface of the sample. During heating, the interface moves inward. Later, as heat is conducted away from the surface, material solidifies and the interface moves back out to the surface. Because the liquid and the solid have different electrical conductivity, the total conductivity will change as a function of the location of the solid–liquid interface. Another factor that must be considered is that the laser light has greater than the band gap energy (which is why it absorbs so strongly). This absorption creates electron-hole pairs. These, in turn create a significant amount of photoconductivity. The fraction of the signal due to photoconductive processes can easily be determined at lower laser fluences where no melting occurs. This can also be used to determine the intensity profile of the illuminating laser radiation [34, 43].

The melting and freezing velocities can be determined using the change in conductivity with time. These calculations should take into account the

changing properties of the three different phases (liquid, crystal, and solid amorphous) as a function of temperature. For Te, the melting velocity peaked at 8 m/sec and the freezing velocity peaked at about 2 m/sec [29, 34]. It should be noted that these peak interface velocities are functions of the geometry of the multilayer thin film stack; they also depend on the thermal conduction behavior of nearby layers of material.

This technique is best used when coupled with careful heat flow calculations. The above-mentioned materials properties as a function of temperature, the thermal conductivities, and the heat of melting of the solid should all be included in the analysis.

The above technique is by definition planar. This is only a crude approximation of the melting and freezing operation that occurs during writing a single bit of information. The written bit is a pancake shape and the typical beam profile is Gaussian, which causes nonplanar aspects of the melting and freezing profile. Radial heat conduction may be very important; this cannot be observed in the above planar melting experiment. Also, the previously cited observations of the microstructure seem to show that the crystallization front comes radially inward rather than from the bottom layer.

To complicate matters further, the system is not really completely radially symmetric. This is due to the rotation of the disk. Because heat is always flowing away from the currently illuminated region, some heat is conducted forward into the area that will be illuminated next. This creates a *bow-wave effect*. The extent of this effect depends on the rate of rotation and the thermal conductivity of the material, etc.

Realistic simulation of the operation of these memory materials can be achieved in both static and dynamic testers. These use focused laser illumination to melt and observe spots of the material. The static tester uses small "coupons" of simulated disk material and studies it with various illumination sequences. This can be used to evaluate cyclability. It can also be used to measure melting, crystallization, and amorphization thresholds in the material. Typically a static tester is accompanied by an X-Y stage so that new areas of material may be brought under the laser.

A *dynamic tester* is one that has an actual spinning disk. This is even more realistic. This can be used to make areal evaluations of the quality and uniformity of the desposited material. Various deposition techniques can exhibit nonuniformities, in thickness or composition. These nonuniformities and other deposition flaws can be mapped using a dynamic tester. The dynamic tester has an added level of complexity in that the focusing servo for the laser must be more complex to allow for the variations in height with disk rotation. The dynamic tester must also have a full optical head with the ability to seek particular tracks and must be able to follow that track around during disk revolution.

For both types of disk tester, it is necessary to be able to control the laser power and duration for read, write, and erase operations. Also, the reflected signal must be sensed to determine the final state of the material. Then, the write



and erase sensitivity and the cycling and phase transformation behavior can be determined.

These disk testers give the only realistic measure of the phase transformation kinetics of the system being measured. The results found in these measurements can be plotted on a phase transformation kinetics (PTK) diagram [27, 32, 45, 46]. The PTK diagram is a map of what happens to the active film as a function of laser power and pulse duration. Note that each graph is applicable for only one specific stack geometry and active material. The PTK diagram must be determined for a variety of conditions so that the stack parameters may be optimized; active film thickness, dielectric thickness, and substrate thermal conductivity all play integral roles in determining the kinetics that can be achieved.

Several regions are found in typical PTK diagrams. At very low powers or short durations, nothing happens to the film, independent of whether it starts amorphous or crystalline. At very high powers and durations ablation will occur. At high power and short duration melting and amorphization occur. At low power and long duration crystallization occurs. The crystallization can occur two ways, either with or without melting. The amorphous phase need not be raised above the melting point to crystallize. However, for amorphization, the material *must* be melted and then cooled rapidly.

The PTK diagram can be used to determine the minimum crystallization speed of the material. This occurs as a "nose" of the crystallization region that extends to the lowest values of laser duration that still achieve crystallization. Typically, this single laser pulse duration can be used for all three operations by only changing the laser power. The movement of this nose with Ge addition into a Te-Ge alloy shows the change in crystallization rate [27, 32, 45]. As more Ge is added, the nose moves to longer and longer times. This has been interpreted as an increase in crosslinking of the amorphous and liquid structures. In this particular case the addition of Ge makes the system too slow for reasonable applicability. However, the Ge addition does achieve a different goal, increased stability at room temperature. Continually, the stability and the sensitivity of optical data storage materials must be weighed and countered to optimize memory systems.

Two slow heating techniques can be used to determine the bulk melting and crystallization behavior. These are DTA and hot-stage microscopy. Both of these operate on large regions of material that are at room temperature. Upon heating, DTA senses phase transformations such as melting or crystallization; melting is endothermic, and crystallization is exothermic. These two temperatures are of interest for determining the stability and longevity of the film, as discussed above. The hot-stage microscopy can be used to actually observe the crystallization or melting, in situ. Nucleation frequencies, growth rates, and crystal morphologies can be determined. Unfortunately, the heating rate is not comparable to that which is found under laser illumination. This makes it difficult to extrapolate up to realistic laser melting or crystallization rates and morphologies.

Another approach that has not been extensively utilized is to measure thermal effects using thin film thermocouples [47, 48]. Thin films of two dissimilar metals are deposited in contact with each other. This thermocouple can be placed at any interface in the optical memory stack. Any two different metals can be used; the specific choice will determine the temperature dependence of the voltage generated. Because the intersection of the metal layer changes the thermal properties of the stack, careful thermal modeling must usually be performed to back out the laser heating data [47, 49–51]. The new layer has its own heat capacity, thermal conductivity, and so on. Care must also be taken that the small size of the metal films does not change the voltage that is generated by the couple [52] or that the small geometry does not cause interfering impedance. In general, the thickness of the metal layers should be small in relation to the thickness of the other layers in the stack.

### 43.5. PHASE CHANGE MEDIA LIMITATIONS

Many different systems have been studied. These include Te, Te-alloyed with Ge, Sn, Se, Sb, and other elements [25, 46, 53, 54]; suboxides of Te, Ge, Sn, and so on [30, 55–57]; and semiconducting compounds such as GeTe [44, 58], InSb [59, 60], InP [59], GeSe [58], GaAs [59], GeSe<sub>2</sub> [61, 62], Sb<sub>2</sub>Te<sub>3</sub> [24], Sb<sub>2</sub>Se<sub>3</sub> [24, 57], Sb<sub>2</sub>Se [63], and In<sub>3</sub>SbTe<sub>2</sub> [46]. Each of these compositions has different drawbacks. Pure Te is unstable at room temperature; the amorphous phase crystallizes too easily. Tellurium alloys are typically too slow; once significant additions have been made to stabilize the Te these also make the crystallization more difficult. Many of these alloys and suboxides are found to not be cyclable. This cyclability problem is discussed below. Compound materials suffer from similar limitations. Some crystallize slowly as a result of the large viscosity of the amorphous phase [58]. Others have sensitivity or cyclability problems.

Current limitations can be summarized in three words: sensitivity, stability, and cyclability. Sensitivity refers to the need for very rapid phase transformation. Then only very short laser pulses are needed to write and erase. It would be desirable to have this be near 100 nsec. Stability implies that *both* amorphous and crystalline states remain fixed over long periods of time. Typical design shelf lives are 10 years at some elevated temperature like 50°C or so. To have the amorphous phase crystallize, the temperature must be raised above  $T_x$ . Therefore, good lifetimes can be obtained with  $T_x$  around 150°C. Cyclability pertains to the useful lifetime; for computer applications, it will be reasonable to have a million cycles without significant degradation of the optical and response properties.

The sensitivity of a material is determined by a variety of materials properties, some of which can be controlled by variations in composition. These variables are absorption coefficient ( $\alpha$ ), thermal conductivity, heat of fusion, heat capacity

( $C_p$ ),  $T_m$ ,  $T_x$ , and  $T_g$ . Other factors, such as the multilayer stack geometry and coherent interference effects, can influence the sensitivity of a disk system. These factors can be interrelated: The sensitivity of a film is based on first melting it and then amorphizing it. The melting requires a certain amount of energy per unit volume. The amorphization requires a critical cooling rate to bypass crystallization. If a smaller volume of material is melted during the writing process, then the material can be considered more sensitive. This smaller volume is most likely to occur if the material has a very large absorption coefficient. Then the light cannot penetrate very far; the incident light is concentrated at the surface and causes only surface melting. The amount of energy required to melt depends on  $T_m$ ,  $C_p$ , and the heat of fusion. The temperature profile and cooling behavior can be quite complicated when the multilayer stack is considered. However, most of these properties are simple bulk materials; it may be possible to screen materials before actual testing occurs.

Media stability is determined by factors that control the change from the metastable amorphous state to the stable crystalline state. These include the diffusivity in the glass,  $T_g$ , the free energy change on crystallization, and other factors. Usually there are already locations of crystalline material adjacent to the amorphous spot. Thus no nucleation events are required to drive the recrystallization process. Note that this is the same process that is operative during erasure, however, this crystallization occurs at higher temperature where the kinetics are more rapid. The classic example of a material that is not stable enough is Te, which is known to undergo recrystallization at room temperature. Many of the alloying elements that are added into Te are then thought to be "glass formers" and increase the amount of crosslinking in the amorphous phase.

Cyclability is determined by other factors, it may be related to chemical interactions, either within the active material itself or with protective dielectric layers. The discussion above has shown how it is useful to have a material with a relatively high (500–600°C) melting temperature to ensure that the crystallization temperature is high enough. This means that to get amorphization, the entire spot must be melted and then quenched. But, the laser has a Gaussian intensity profile, which creates a Gaussian temperature profile in the material. For rapid pulses, this Gaussian injection is only partly mitigated by the thermal diffusivity in the active material [64]. This can generate temperatures in the molten spot that far exceed the melting temperature of the active film. This can cause chemical interactions between the active material and the adjacent materials. The interaction with one of the layers may be exacerbated by the fact that the energy is preferentially absorbed at one surface of the material (depending on which side the laser is on).

Another aspect of material interaction that can cause irreversible changes in the material with time is composition segregation. Many of the systems that have been investigated are ternary alloys that would be multiphasic at equilibrium [65, 66]. When crystallization occurs, it is often not of the same

composition as the amorphous matrix. Then, when crystallization occurs, some of the constituents can be rejected by the crystallization front, causing partitioning of species in the initially homogeneous system. One unsatisfactory aspect is that this requires long range diffusion for the solid-liquid interface to advance. This can make this transformation slower. It also means that care must be taken to rehomogenize the system when melting to amorphize. This aspect of chemical segregation has led some researchers to seek congruently melting stoichiometric compounds for optical memory media [58].

This chemical segregation with solid-liquid interface motion has been observed in the nonstoichiometric In-Sb system [60]. The published micrographs show peripheral crystallization of InSb only, followed by Sb and InSb crystallization in from edge. The Sb and InSb are each in rather large crystals; significant atomic diffusion was required to cause this separation.

This chemical segregation is related to the solute redistribution phenomena that are observed in semiconductor processing with lasers [49, 67, 68]. Supersaturated solute atoms are rejected by the growing interface and end up concentrated at the surface of the material. Studies in semiconductor processing have shown a variation in the segregation coefficient with interface velocity [67, 69]. This could be an important factor in most alloyed memory media, because the alloying elements are seldom below their solubility limits in the parent crystalline phase.

Other factors can play a role in cyclability problems. Crystal nuclei, or *embryos*, can exist after melting of the material. These can cause different crystallization cycles to occur with different speed [46, 54]. This can be partly dealt with by preannealing the disk above  $T_x$  before use. Also, mechanical fatigue is known to be a problem because of the large change in volume on crystallization for some materials.

Another factor that affects media quality is the intrinsic media noise. This arises from reflectivity variations with location. This can arise due to differences in the composition, thickness, surface finish, and crystalline state. One contribution to media noise is differences in reflectivity with crystal orientation. All noncubic crystal symmetries exhibit differences in optical properties with orientation. Then, in the crystalline state, the reflectivity can change simply because the crystal morphology in the film has changed. This becomes a significant problem when the crystal size becomes close to the laser spot size. Below this limit many small crystallites with random orientations (if they indeed are random) then cause a homogenization of the signal. This observation has led to stronger interest in cubic materials for optical memory media [58]. These materials will have no reflectivity variation with orientation and hence also no variation with grain size.

Many of these problems are being addressed by various researchers. The current studies seem to indicate that favorable materials for optical data storage would be strongly absorbing, have a cubic crystal structure, and be a congruently melting stoichiometric compound that melts around 500°C. This is a difficult combination to achieve entirely, and materials may be found that work well without meeting this whole shopping list.

### 43.6. FUTURE RESEARCH DIRECTIONS

Many frontiers exist in this research area. Novel approaches exist that remain to be fully explored. These directions have the opportunity of revolutionizing optical data storage in many ways. New systems are possible that may address problems that exist with current systems. Also, there is abundant room for further exploration and improvement of the known systems.

New materials are currently being sought that can meet the design criteria described above [70]. Stoichiometric oxide materials are being investigated due to their superior environmental stability in comparison to present Te-based alloys. Several transition metal oxides seem to have favorable absorption, melting, and phase diagram characteristics.

New mechanisms for causing contrast should also be investigated. These may include nonthermal processes, such as photonucleation and crystallization [61, 71, 72], and light-driven oxidation reduction processes through electron-hole pair generation and separation [73–75]. Photonucleation studies to date have not separated thermal effects from the bond breaking or carrier creation aspects. Other mechanisms may still arise that can act without melting. These may be related to the spectral process of photochemical hole burning, which can now only be performed at cryogenic temperatures.

Another frontier is in the area of modeling and understanding of rapid nucleation and growth in these film systems. This modeling will include comparison between heterogeneous and homogeneous nucleation types. The nucleation will be influenced by the thin film geometry. This may lead to variations in the texture of resultant films. And, understanding of the crystal growth mechanisms must be advanced. This must be related to better understanding of the solid-liquid interface morphology and possible atomic attachment processes from the liquid. Another related area is to see whether *explosive crystallization*, which has been observed in some semiconductor systems [40, 76], can be utilized for causing rapid erasure of amorphous spots.

One final area that will certainly attract profuse activity is in thin film processing technology. This can lead to more uniform, higher quality, active, and passive layers in the optical memory stack. Better-quality films may be able to resist pinhole formation. It may also be possible to engineer layers that are more inert to chemical interactions with other layers and to make layers that are more impervious to penetration by moisture or oxygen [77]. For some of these materials, sol-gel processing may be useful in obtaining better quality films. This technique is ideal for preparation of films in the range of 1000 Å thick and can achieve very good levels of uniformity, both physically and chemically.

### 43.7. CONCLUSION

Phase change materials have great potential for application to the optical memory area. This Chapter has reviewed progress that has been made on these materials and has shown the wide range of directions that could bear fruit in

future research efforts. New materials systems and improved design and quality control can achieve a better optical memory system and allow the introduction of phase change optical memory into the marketplace.

### ACKNOWLEDGMENTS

I am grateful for many valuable discussions with Martin Chen, Ernesto Marinero, and Kurt Rubin of IBM who have illustrated to me many aspects of phase change optical memory. I apologize in advance for any unwitting inaccuracy in summarizing the literature. Finally, I am deeply indebted to Mike Weinberg and Brian Zelinski for many fruitful discussions in this area.

### REFERENCES

1. G. Bate, *IEEE Trans. Mag.*, **MAG-23**, 156-161 (1978).
2. D. Chen, *Proc. SPIE*, **38** 9 (1973).
3. Y. Mimura, N. Imamura, and T. Kobayashi; *Japan. J. Appl. Phys.*, **15** (1976) 933.
4. S. Matsushita, K. Sunago, and Y. Sakurai; *Japan J. Appl. Phys.*, **15** (1976) 713.
5. Y. Togami, *IEEE Trans. Mag.*, **MAG-18** (1982) 1233.
6. R. M. Walser and M. F. Becker, in: S. D. Ferris, H. J. Leamy, and J. M. Poate, Eds., *Laser-Solid Interactions and Laser Processing*, AIP Conference Proceedings 50, pp. 117-122. (1978).
7. D. D. Ecen, *Opt. Eng.*, **20** (1981) 377-378.
8. M. Fukuma, S. Zembutsu, and S. Miyazawa, *Appl. Optics*, **22** (1983) 265-268.
9. W. E. Case, J. L. Smith, and D. D. Eden, *SPIE*, **420** (1983) 168-172.
10. S. E. Cummins, *Proc. IEEE*, **50** (1967), pp. 1536-1537.
11. W. S. Colburn and E. N. Tompkins, *Appl. Opt.*, **13** (1974) 2034.
12. C.-K. Wu, *SPIE*, **200** (1979) 39-50.
13. C.-K. Wu, *Opt. Eng.*, **19** (1980) 769-776.
14. L. M. Ralston, *SPIE*, **420** (1983) 186-193.
15. G. C. Gjorklund, W. E. Moerner, et al., in: *Optical Data Storage*, OSA ThC-D5-1 (1984).
16. V. B. Jipson and K. Y. Ahn, *Solid State Technol.*, **27**, p. 141 (1984).
17. R. A. Bartolini, *SPIE*, **123**, (1977) 2-9.
18. M. R. Tubbs and G. E. Scrivener, in: R. J. Cox, Ed., *Non-silver Photographic Processes*, Academic Press, New York (1975).
19. A. A. Litwak, and B. W. Stryj, *SPIE*, **420** (1983), 178-185.
20. M. C. Gupta, *J. Mater. Res.*, **3**, 1187-1195 (1988).
21. T. Igo and Y. Toyoshima, *J. Non-Cryst. Solids*, **11**, 304-308 (1973).
22. G. R. Knight, in: *Optical Data Storage 1989 Technical Digest*, p. xx WD1-1, Los Angeles.
23. D. Strand, *Proc. SID*, **24**, 25-27 (1983).
24. K. Watanabe, N. Sato, and S. Miyaoka, *J. Appl. Phys.*, **54** 1256-1260 (1983).
25. C. J. van der Poel et al., *J. Appl. Phys.*, **59** 1819-1821 (1986).
26. B. A. J. Jacobs, *Vacuum*, **35** 445-446 (1985).
27. K. A. Rubin, personal communication, Aug. 1988.

28. N. Gotoh et al., in: *Optical Data Storage 1989 Technical Digest*, pp. TuA3-1-TuA3-4, Los Angeles (1989).
29. W. Pamler and E. E. Marinero, *J. Appl. Phys.*, **61**, 2294-2300 (1987).
30. M. Takenaga and N. Yamada et al., *SPIE*, **420**, 173-177 (1983).
31. D. Strand, *Opt. Eng.*, **20**, 379-381 (1981).
32. R. Barton and K. A. Rubin, in: H. Kurz, G. L. Olson, and J. M. Poate, Eds., *Beam-Solid Interactions and Phase Transformations*, MRS Vol. 51, pp. 303-308, (1986).
33. C. Ortiz, K. A. Rubin, and S. Ajuria, *J. Mater. Res.*, **3**, 1196-1200 (1988).
34. E. E. Marinero, in: M. O. Thompson, S. T. Picraux, and J. S. Williams, Eds., *Beam-Solid Interactions and Transient Processes*, MRS Vol. 74, pp. 237-250 (1987).
35. J. Feinleib, J. deNeufville, S. C. Moss, and S. R. Ovshinsky, *Appl. Phys. Lett.*, **18** (1971) 254-257.
36. M. O. Thompson and G. J. Galvin, in: J. Narayan, W. L. Brown, and R. A. Lemons, Eds., *Laser-Solid Interactions and Transient Thermal Processing of Materials*, MRS Vol. 13, pp. 57-67 (1983).
37. T. Nishida et al., *Appl. Phys. Lett.*, **50**, 667-669 (1987).
38. Y. Sato et al., in: *Optical Data Storage 1989 Technical Digest*, pp. TuA2-1-TuA2-4 (1989).
39. W. Pamler, E. E. Marinero, and M. Chen, *Phys. Rev. B.*, **33**, 5736-5743 (1986).
40. J. J. P. Bruines, R. P. M. van Hal, B. H. Koek, M. P. A. Fiegers, and H. M. J. Boots, in: M. O. Thompson, S. T. Picraux, and J. S. Williams, Eds., *Beam-Solid Interactions and Transient Processes*, MRS Vol. 74, pp. 91-102 (1987).
41. A. G. Cullis, in: D. K. Biegelsen, G. A. Rozgonyi, and C. V. Shank, Eds., *Energy Beam-Solid Interactions and Transient Thermal Processing 1984*, MRS Vol. 35, pp. 15-24 (1985).
42. D. H. Lowndes, G. E. Jellison, Jr., R. F. Wood, S. J. Pennycook, and R. W. Carpenter, in: D. K. Biegelsen, G. A. Rozgonyi, and C. V. Shank, Eds., *Energy-Solid Interactions and Transient Thermal Processing 1984*, MRS Vol. 35, pp. 102-106 (1985).
43. E. E. Marinero, W. Palmer, and M. Chen, in: H. Kurz, G. L. Olson, and J. M. Poate, Eds., *Beam-Solid Interactions and Phase Transformations*, MRS Vol. 51, pp. 289-296 (1986).
44. E. Huber and E. E. Marinero, in: M. O. Thompson, S. T. Picraux, and J. S. Williams, Eds., *Beam-Solid Interactions and Transient Processes*, MRS Vol. 74, pp. 257-261 (1987).
45. P. S. Peercy and M. O. Thompson, in: D. K. Biegelsen, G. A. Rozgonyi, and C. V. Shank, Eds., *Energy Beam-Solid Interactions and Transient Thermal Processing 1984*, MRS Vol. 35, pp. 53-64 (1985).
45. K. A. Rubin, R. W. Barton, M. Chen, V. B. Jipson, and D. Rugar, *Appl. Phys. Lett.*, **50**, 1488-1490 (1987).
46. Y. Maeda et al., *J. Appl. Phys.*, **64**, 1715-1719 (1988).
47. T. T. Kostas, T. H. Baum, and P. B. Comita, in: V. M. Donnelly, I. P. Herman, and M. Hirose, Eds., *Photon, Beam, and Plasma Stimulated Chemical Processes at Surfaces*, MRS Vol. 75, pp. 57-63 (1987).
48. P. Baeri, S. U. Campisano, E. Rimini, and J. P. Zhang, *Appl. Phys. Lett.*, **45**, 298-400 (1984).
49. P. Baeri, in: *Laser-Solid Interactions and Transient Thermal Processing of Materials*, MRS, Pittsburgh, pp. 157-170 (1983).
50. C. M. Surko, A. L. Simons, D. H. Auston, J. A. Golovchenko, and R. E. Slusher, in: D. Ferris, H. J. Leamy, and J. M. Poate, Eds., *Laser-Solid Interactions and Laser Processing*, AIP Conference Proceedings 50, pp. 155-159 (1978).
51. P. Kivits, R. De Bont, and P. Zalm, *Appl. Phys.*, **24**, 273-278 (1981).
52. K. L. Chopra, S. K. Bahl, and M. R. Randlett, *J. Appl. Phys.*, **39** 1525 (1968).
53. M. Chen, K. A. Rubin, V. Marrello, U. G. Gerber, and V. J. Jipson, *Appl. Phys. Lett.*, **46**, 734-736 (1985).

54. R. T. Young, D. Strand, J. Gonzalez-Hernandez, and S. R. Ovshinsky, *J. Appl. Phys.*, **60**, 4319-4322 (1986).
55. N. Akahira, T. Ohta, N. Yamada, M. Takenaga, and T. Yamashita, *SPIE*, **329**, 195-201 (1982).
56. M. Takenaga, N. Yamada et al., *J. Appl. Phys.*, **54**, 5376-5380 (1983).
57. M. Takenaga and M. Mikoda, in: Y. Hamakawa, Ed., *Amorphous Semiconductor Technologies and Devices*, Elsevier, Amsterdam, pp. 266-282 (1984).
58. M. Chen, K. A. Rubin, and R. W. Barton, *Appl. Phys. Lett.*, **49**, 502-504 (1986).
59. G. Fuxi and W. Hao, *SPIE*, **529**, 51-54 (1985).
60. Y. Goto, K. Utsumi, A. Ushioda, I. Tsugawa, and N. Koshino, in: M. O. Thompson, S. T. Picraux, and J. S. Williams, Eds., *Beam-Solid Interactions and Transient Processes*, MRS Vol. 74, pp. 251-256 (1987).
61. E. Haro, Z. S. Xu, et al., *Phys. Rev. B*, **32**, 969-979 (1985).
62. E. Haro, M. Balkanski, G. F. Espinosa, and J. C. Phillips, in: D. K. Biegelsen, G. A. Rozgonyi, and C. V. Shank, Eds., *Energy Beam-solid Interactions and Transient Thermal Processing 1984*, MRS Vol. 35, pp. 193-198 (1985).
63. R. Barton, C. R. Davis, K. Rubin, and G. Lim, *Appl. Phys. Lett.*, **48**, 1255-1257 (1986).
64. V. B. Jipson and C. R. Jones, *J. Vac. Sci. Technol.*, **18**, 105-109 (1981).
65. T. Ohta, M. Takenaga, N. Akahira, and T. Yamashita, *J. Appl. Phys.*, **53**, 8497-8500 (1982).
66. R. J. von Gutfeld and P. Chaudhari, *J. Appl. Phys.*, **43**, 4688 (1972).
67. C. W. White, in: *Laser-Solid Interactions and Transient Thermal Processing of Materials*, pp. 145-155 (1983).
68. J. M. Poate, *J. Phys.*, **41**, suppl. Colloque 4, pp. C4,1-5 (1980).
69. S. U. Campisano, in: D. K. Biegelsen, G. A. Rozgonyi, and C. V. Shank, Eds., *Energy Beam-solid Interactions and Transient Thermal Processing 1984*, MRS Vol. 35, pp. 145-151 (1985).
70. D. P. Birnie et al., work in progress.
71. R. J. von Gutfeld, *Appl. Phys. Lett.*, **22**, 257-258 (1973).
72. M. Okuda, T. Matsushita, and A. Suzuki, in: E. Gerlach and P. Grosse, Eds., *The Physics of Selenium and Tellurium*, pp. 270-272 (1979).
73. R. M. Osgood, Jr., in: V. M. Donnelly, I. P. Herman, and M. Hirose, Eds., *Photon. Beam, and Plasma Stimulated Chemical Processes at Surfaces*, MRS Vol. 75, pp. 3-15 (1987).
74. F. A. Houle, *Chem. Phys. Lett.*, **95**, 5-8 (1983).
75. C. I. H. Ashby and R. M. Biefeld, *Appl. Phys. Lett.*, **47**, 62-63 (1985).
76. C. E. Wickersham, G. Bajor, and J. E. Greene, *Solid State Comm.*, **27**, 17-20 (1978).
77. T. K. Hatwar, S. C. Shin, and D. G. Stinson, *IEEE Trans. Mag.*, **MAG-22**, 946-948 (1986).



## STRUCTURE-DEPENDENT OPTICAL PROPERTIES OF COMPOSITE MATERIALS

B. G. POTTER, E. M. CLAUSEN,  
C. J. SIMMONS, AND J. H. SIMMONS

### 44.1. INTRODUCTION

Although there are many kinds of microstructures that can influence the optical properties of materials, this Chapter will concentrate primarily on microstructures involving semiconductors in composites formed with an insulating matrix. This class of materials offers great promise in the study of quantum-size effects on the electronic band structure and the related optical properties of isolated semiconductor crystallites. Cadmium sulfide crystals as small as 0.4 nm have been produced in a zeolite matrix [1], and a wide variety of II to VI semiconductors ranging in size from 1 to 100 nm have been crystallized from a glass matrix [2–7] or in a variety of solutions by arrested precipitation [8–10].

The fundamental process of interest is the modification of the semiconductor's bulk electronic structure and the eventual decomposition of the energy bands into discrete, localized states as the crystal size is reduced and the number of atoms contributing to the formation of the band structure drops. Briefly, as the semiconductor size is decreased, the wavefunctions of its carriers become limited to the borders of the crystal and undergo significant distortion from the boundary conditions imposed by this interface. Because optical characteristics

*Ultrastructure Processing of Advanced Materials.*

Edited by Donald R. Uhlmann and Donald R. Ulrich (deceased).

ISBN 0-471-52986-9 © 1992 John Wiley & Sons, Inc.

arise from the electronic band structure, they can be used to measure the resulting size-dependent changes in the allowed state energies. The presence of a large semiconductor-insulator interfacial area can also provide a greater proportion of trapping defect sites than found in the bulk semiconductor. This property could significantly influence excited state lifetimes.

Semiconductor-glass composites also have the potential to exhibit a strong third-order optical nonlinearity resulting from a wide variety of processes including electron-hole plasma, band filling, and absorption saturation. These mechanisms, to be described below, can be enhanced by some of the characteristics found in the semiconductor-glass composites. For example, confinement-induced band splitting into more localized states can reduce intraband scattering thus inhibiting renormalization effects and allowing more efficient filling of states to achieve transition blocking. An increased exciton binding energy observed in these structures could furnish a saturable level for third-order nonlinearities even at room temperature. The isolating properties of the glass matrix could also be used to reduce cross talk between adjacent nonlinear optical elements in a multidimensional array by limiting carrier diffusion.

## 44.2. PAST RESEARCH

### 44.2.1. Bulk Semiconductor Properties

The semiconductors of primary interest for glass composite applications are the II to VI compounds. Between ZnS and CdTe, they cover a band gap energy range from 3.8 down to 1.5 eV. Inclusion of Pb increases the range to 0.19 eV for PbTe.

Absorption and reflectivity measurements can be used to furnish valuable information about the electronic band structure of the semiconductors. Additional insight into the nature of exciton complexes and defect states existing in the band gap can be obtained using photoluminescence (PL) measurements [11]. At high incident radiation intensities, however, the properties measured by these techniques can be significantly altered in the bulk semiconductor. The accompanying third-order optical nonlinearities primarily result from absorption of the incident radiation and subsequent redistribution of occupied carrier states within the electronic band structure of the material.

High carrier densities in the conduction band (free carriers) can result in a number of effects, which may occur concurrently, each of which furnishes some sort of absorptive change and thus a refractive index variation over that observed under lower incident intensities. One major mechanism involves the excitation of carriers into the conduction band and their almost immediate relaxation to the band edge via phonon-assisted intraband scattering. This results in the eventual occupation of the lowest allowed states of the conduction band. This *band filling effect* blocks further optical transitions near the band

edge, reducing the absorption coefficient in that frequency range. A corresponding change in the refractive index is associated with the effect.

A second free carrier population-related mechanism is associated with Coulombic interactions occurring within the excited ensemble. Electrostatic screening of electron-hole interactions at high carrier densities can actually cause a decrease in energy of the single-particle states that compose the band continuum. This causes the band gap to narrow with increasing incident intensity and accompanying free carrier density. Again, the resulting *renormalization effect* leads to a variation in the absorption coefficient and refractive index seen at frequencies near the band gap of the material.

Transition saturation effects similar in nature to the band filling mechanism discussed above are also possible using the exciton state. Tests on bulk single crystals of CdS by Dagenais and Sharfin [12] have shown a high refractive index nonlinearity under very low incident powers (10–1000 W/m<sup>2</sup>) at 2 K by means of a resonant saturation of the  $I_2$ -bound exciton. However, unlike the band edge effects, exciton resonance saturation effects require very low temperatures. This is due to the low binding energy of the exciton in comparison to the thermal energy of the free carriers. Quantum confinement effects, associated with a reduction of the semiconductor crystal to sizes below the exciton Bohr orbit, increase the exciton binding energy and the electronic band gap. It is this mechanism that may furnish the means to sufficiently increase the exciton binding energy, thus yielding optically nonlinear behavior based on the saturation of exciton resonances at elevated temperatures.

#### 44.2.2. Quantum Confinement (QC) Effects

A theoretical analysis of the effect of size confinement on the electronic band structure of semiconductors has been presented by numerous authors. Efros and Efros [13], Brus [8], and Nair et al. [14] present analytical models for the effect of a shrinking infinite potential well on the exciton and band-edge energies and on the associated optical properties of isolated semiconductor crystals, or *quantum dots*, as they are popularly called. They show that exciton and band edge energies vary proportionally with the inverse square of the crystal size. The interband absorption threshold energy is calculated through an evaluation of transition probabilities at two extremes: crystal size,  $2R$ , smaller than the hole Bohr diameter,  $2a_h$ , and crystal size greater than the electron Bohr diameter,  $2a_e$ , [13].

$$\begin{aligned} \hbar\omega_0 &= E_g + \frac{\hbar^2\pi^2}{2\mu R^2} \quad \text{where } \frac{1}{\mu} = \frac{1}{m_e} + \frac{1}{m_h} \quad \text{and } R < a_h < a_e \\ \hbar\omega_0 &= E_g - E_{ex} + \frac{\hbar^2\pi^2}{2MR^2} \quad \text{where } M = m_e + m_h \quad \text{and } R > a_e > a_h \quad (1) \end{aligned}$$

where  $m_{e(h)}$  = effective mass of the electron (hole)  
 $\mu$  = exciton reduced mass  
 $E_g$  = bulk band gap energy  
 $E_{ex}$  = bulk exciton binding energy.

Therefore, in the extremes of small and large crystal sizes, the dependence of band gap and exciton energies on the inverse square crystal size follows a slope equal to an effective inverse mass,  $M_{eff}$ . At large crystal sizes and near the exciton Bohr radius,  $a_0$ , the electron-hole Coulomb interaction dominates and only the translational motion of the exciton is actually confined with little if any distortion of the individual electron and hole orbits. In this case the effective mass is the exciton translational mass ( $M$ ) and the quantum confinement effect is relatively weak. Results presented elsewhere [7] show that this process dominates from  $0.8a_0$  to  $10.0a_0$  corresponding to crystal radii of 2.0 to 25.0 nm in CdS, where  $a_0$  is the exciton Bohr radius, at 2.6 nm. These sizes are well above the electronic Bohr radius (1.6 nm).

The treatment of crystal sizes between the asymptotic limit of the bulk and the hole Bohr radii incorporates both a variational calculus approach on the unperturbed wave function and a numerical integration of the various components of the exciton energy to take into account a partial shielding of the electron-hole Coulomb interaction by the potential well [8, 13]. The proposed *variational calculus approach* [14], however gives a strong underestimate of the Coulomb coupling of the electron and hole ground state energy in CdS-glass composites at crystal sizes equal to and greater than the exciton diameter [7]. The numerical approach [8] could not be tested by following the size dependence in semiconductor-glass composites. However, it appears to describe well the quantum size effects for CdS crystallites 2.2 to 3.8 nm in size, precipitated in isopropanol and acetonitrile [10]. It should be noted at this point that the crystals formed in the semiconductor-glass composite appear rectangular in shape and show little structural distortion, whereas those from the CdS-isopropanol solution are spherical, indicating a strong interfacial tension and consequent surface distortion.

In the regime of sizes below the hole Bohr radius, Efros and Efros [13] show that the effective mass is the exciton reduced mass. This corresponds to an uncorrelated motion of the electron and hole and leads to a very strong quantum confinement effect. Studies of CdS crystals by Ekimov et al. [5] and Ekimov et al. [4] over the range 1.2 to 40 nm show an intermediate value of effective mass near the free-electron value. Studies with CuCl also produced an effective mass slope intermediate between the reduced mass (uncorrelated motion) and translational mass (rigid particle motion) of the excitons. A comparison of the size dependence of two asymptotic behaviors of quantum confinement calculated by Efros and Efros [13] with the variational approach of Nair et al. [14] and with the absorption threshold of a glass composite containing pure CdS crystallites of different sizes in the range  $0.8a_0$  to  $10a_0$  is shown in Fig. 44.1.

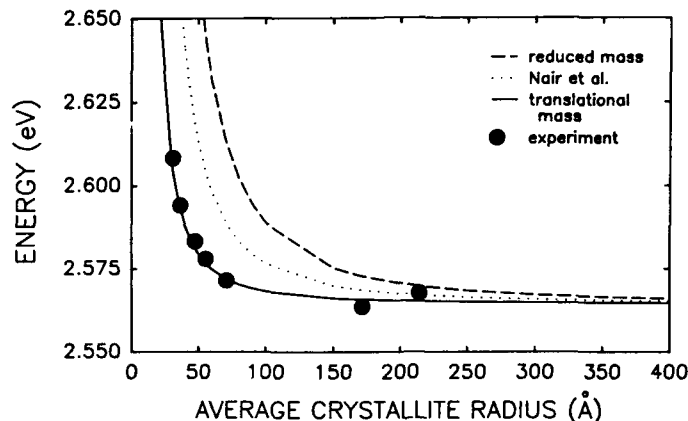


Figure 44.1. Threshold absorption energy plotted as a function of average microstructure size for various theoretical quantum confinement regimes and for CdS-glass composite data [7].

A comparison of these models with much of the existing measurements on semiconductor alloys, such as  $\text{CdS}_x\text{Se}_{1-x}$ , is not possible due to the difficulty of separating variations in band edge energies resulting from size confinement and those resulting from alloying changes during crystal growth. It seems reasonable to assume that since the sulfur ion is more mobile in the glass than selenium, the smaller crystals will be richer in sulfur and therefore have a larger shift in band gap energy due to stoichiometric considerations. This is often confused with quantum confinement effects. Moreover, measurements conducted on a commercial  $\text{CdS}_x\text{Se}_{1-x}$  filter glass [15] have shown a continuing shift in absorption threshold energy with increasing heat treatment time despite a lack of further growth in the crystal size as shown by microstructure studies.

Alloying effects should be expected between any components of the semiconductor-glass mixture. They are most pronounced between S, Se, and Te and between Zn and Cd. In both cases the ion with the greater diffusion coefficient in the glass will exhibit a larger band gap energy when present in the semiconductor. Recent measurements have shown that under special circumstances alloying of CdS with CdO is a possibility that should be suspected [16].

Alloying effects would not present a problem in analysis if measurements of the actual exciton binding energy were available. These measurements, however, are difficult to obtain because of the need to specify the band edge energy accurately and independently from the exciton energies.

#### 44.2.3. Nonlinear Optical Characteristics

Numerous studies have been conducted on the linear and nonlinear optical properties of both commercially available and experimental semiconductor-glass composites [17-25]. The results show that the mechanisms observed vary with experimental method, excitation source wavelength and time resolution of

the test. Degenerate four-wave mixing (DFWM) measurements on modified commercial  $\text{CdS}_x\text{Se}_{1-x}$  filter glasses have focused on phase conjugation characteristics and indicate the dominance of a band filling mechanism in the steady-state and dynamic optical nonlinear behavior of these materials.

Jain and Lind [17], Yao et al. [18], and Roussignol et al. [19–21] examined Corning and Schott glasses with a variety of cutoff wavelengths corresponding to  $x$  values of 0.7 to 0.9 in  $\text{CdS}_x\text{Se}_{1-x}$ . DFWM reflectivity measurements just under the cutoff wavelength (530 nm) exhibited a significant saturation due to either higher-order susceptibility effects or the onset of free carrier absorption [17]. Time-resolved photoluminescence measurements using 30-psec pulses at 532 nm exhibited carrier recombination times ranging from 80 to 27 psec for incident powers of 5 to 40  $\text{MW}/\text{cm}^2$ , respectively [18]. Longer pulse measurements (10 ns in the range 560–595 nm) exhibited a decrease in conjugate signal intensity with time above an apparent threshold energy fluence of about  $0.5 \text{ mJ}/\text{cm}^2$  due to the formation of permanent volume gratings and eventual photochromiclike darkening of the glasses. The darkening effect appears to be necessary to produce carrier recombination times of the order seen (i.e., 50–100 psec), whereas fresh, undarkened samples exhibit transient grating decay times of tens of nanoseconds. The darkening process, more strongly evident in Schott glasses [21], is still the subject of investigation, although it seems to involve the saturation of trapping sites for photoexcited carriers, possibly at the glass–semiconductor interface.

A measurement of the frequency and intensity dependence of the third-order optical susceptibility ( $\chi^{(3)}$ ) and absorption [20] and comparison with theoretical predictions by various nonlinear mechanisms [26, 27] confirmed agreement of data with the Boltzmann-distributed band filling model. An examination of the frequency dependence of  $\chi^{(3)}$  through the band edge of the semiconductor–glass composite [21] showed no enhancement of the DFWM signal from the excitonic states. This result is somewhat consistent with the large size of crystallites present in these glasses and the relatively high temperature (300 K) of the measurements with respect to the exciton binding energies.

Pump-probe experiments and direct measurement of nonlinear index by Olbright et al. [22] revealed a sharpening of the band edge and an observable shift to higher energies indicative of a band filling effect in both conduction and valence band states that blocks further transitions in this frequency range. This is accompanied by a change in sign of the nonlinear refractive index from negative below the band gap to positive above it. An elegant measurement technique developed by Finlayson et al. [28] employs a Mach–Zehnder interferometric setup to simultaneously examine the absorption saturation and refractive index change in a waveguide geometry. Their results confirm the band filling interpretation.

Femtosecond carrier relaxation studies at relatively low pulse energies performed on undarkened Schott filter glasses [29] revealed electron-hole recombination times of 80–100 psec in contrast to the nanosecond times observed by Roussignol et al. [20]. Fluences used were well below the darkening

thresholds defined by Roussignol et al. These differences indicate that the nature of trapping sites may vary between glasses or that several recombination processes may be possible with a sample-to-sample variation of the dominating processes.

To summarize, we have seen that the nonlinear optical studies of commercial semiconductor-glass composites appear to support a band filling interpretation of the microscopic mechanisms controlling the steady-state and dynamic optical nonlinear behavior. At high incident intensities, significant carrier densities modify the linear dielectric function through carrier thermalization and filling of near band edge states. Decay time constants of this population seem to vary with glass composition and past exposure to high dosages of radiant energy. Recombination times in the picosecond, nanosecond, and even microsecond [30] ranges have been reported. It appears most likely that shallow carrier traps, whose identity is not yet fully understood, play a major role in the recombination process and therefore degree of filling.

Because most of the measurements were conducted on relatively large crystallites with broad crystal size distributions and at room temperature, none of these studies appear to have addressed the exciton confinement effect most prevalent in these kinds of materials. In addition, speculation about the source of the rapid recombination mechanism leads one inexorably to the semiconductor-glass interface and its associated high density of defect traps. A simple test of this hypothesis would be to compare decay times and band filling effects in two samples of the same composition and different size, thus having different crystal surface-to-volume ratio.

### 44.3. CURRENT RESEARCH

#### 44.3.1. Fabrication of Semiconductor-Glass Composites

The ideal semiconductor-glass composite would consist of a single-compound semiconductor whose size can be varied, but yet can maintain a very narrow distribution of crystal sizes. It should also have oriented crystals so as to yield narrow exciton absorption peaks and a large exciton absorption cross section. Finally, the average crystallite size should be sufficiently smaller than the 1 s exciton Bohr radius to ensure that confinement-induced increases in exciton binding energy be at least 5 kT. Such shifts in the exciton energy would favor application of an absorption saturation mechanism at the exciton frequency to induce a nonlinear refractive index change at room temperature. GaAs multiple quantum well structures, for example, have exhibited distinct room temperature exciton-related absorption processes and nonlinearities [31].

For device applications, such as in nonlinear directional couplers, Stegeman et al. [32] have shown that a key material parameter is the ratio  $W = |\Delta n_{\text{sat}}|/2\lambda_0\alpha_0$ , where  $\Delta n_{\text{sat}}$  is the saturated value of the nonlinear refractive index change,  $\lambda_0$ , the free space wavelength of the incident light; and  $\alpha_0$ , the

linear absorption coefficient of the material. Wright et al. [33], using coupled-mode theory and a two-level saturable nonlinearity, showed that the figure of merit parameter for incident light below the band gap energy favors semiconductors with low gap energies.

Different approaches have been followed to fabricate semiconductor-glass composites. Commercially available crown glass compositions are susceptible to phase separation. They generally contain zinc and cadmium and sufficient iron to form permanent defect traps. The sulfur, selenium, and tellurium ions oxidize easily to compounds with low sublimation temperatures, therefore, it is difficult to keep them in solution in the glass at high concentrations (i.e., greater than 0.1 to 0.5 vol %). It is generally believed that crystal concentrations can best be raised by alloying several of the anions. Single anion semiconductors are thus more difficult to form.

We were able to obtain single-anion compound semiconductors in zinc-free calcium-crown glasses from Lee Cook at Schott Technologies [34]. An investigation of this material showed that because of the high-temperature precipitation of CdS, it was difficult to fabricate a homogeneous glass without precipitated crystals. The heat treatments conducted led to crystal growth by a classical diffusion-controlled ripening process [7]. This guaranteed that the size distributions thus obtained had a 35% width at half maximum about the average size. Measurements of critical nucleus size yielded 20 Å as the minimum obtainable radius [7].

Borelli and Luong [35] used a gas-phase reaction of thiourea and selenourea with metal chlorides ( $\text{CdCl}_2$  and  $\text{ZnCl}_2$ ) deposited within the pores of unconsolidated Vycor to produce semiconductor deposits within the glass. CdS crystals were thus formed, measured by electron microscopy to be 4–5 nm, yet they showed no shift in absorption edge. CdSe crystals by contrast showed a 0.3-eV edge shift for crystals presumed to be less than 2 nm. PbS and PbSe crystals exhibited considerably larger shifts.

Wang and Mahler [36] synthesized CdS crystallites 5 nm in diameter in Nafion polymer films and PbS clusters from single molecule to 15 nm in an ethylene methacrylic acid copolymer. Absorption bleaching of the excitonic transition resulted from interface-trapped carriers. Bleaching efficiencies were sufficiently high that a single electron-hole trapped pair could bleach the excitonic absorption of the entire CdS cluster.

$(\text{CdS})_4$  clusters were produced in a zeolite matrix [1]. These were found to interact in groups to form superclusters. Room temperature optical absorption data showed the largest shift in band edge absorption observed in such materials, with a band edge near 300 nm for the  $(\text{CdS})_4$  clusters and near 400 nm for the superclusters.

Clausen and Simmons [16] used an RF sputtering method to develop thin films of CdS-glass composites with 2–50 wt % CdS and crystal sizes ranging from 2 to 40 nm. Pure CdS films were also formed to test the fabrication technique. Structures could be varied from amorphous to columnar to epitaxial character. Annealed films showed a stoichiometric CdS composition with a high



degree of epitaxial orientation. A comparison of optical properties with single crystal platelets is shown in the subsequent section.

More complex porous glass fabrication techniques and sol-gel processing techniques are currently under study.

#### 44.3.2. Effect of Crystal Size

Let us now examine the effect of crystal size on the optical properties of semiconductor-glass composites. Our research has concentrated on studies of a calcium-crown glass containing pure cadmium sulfide crystallites and a more typical commercial crown glass containing zinc and  $\text{CdS}_x\text{Se}_{1-x}$  crystals. Microstructure size measurements on the alloy as a function of heat treatment time revealed that the S:Se stoichiometry of the precipitated crystals varies during the heat treatment by increasing Se content at longer times.

Measurements of optical absorption and PL of the pure CdS-containing glasses are shown in Figs. 44.2 and 44.3 for samples with different crystal sizes at 10 K. The absorption measurements clearly show the presence of an exciton absorption feature and an absorption shelf going into the band edge absorption for the material. The PL spectra show a sharper peak in the blue followed by a lower frequency broad recombination band. The sharp peak shows a clear decrease in frequency for longer heat treatments. The peak position for the sharp PL feature and the energy of the absorption shelf (AS) are plotted against inverse square microstructure size in Fig. 44.4 for the CdS glasses.

The data show a linear dependence of both properties on the inverse square crystal size for the CdS-doped glasses. The PL peak from these composites has often been interpreted as band-edge luminescence, however, an examination of

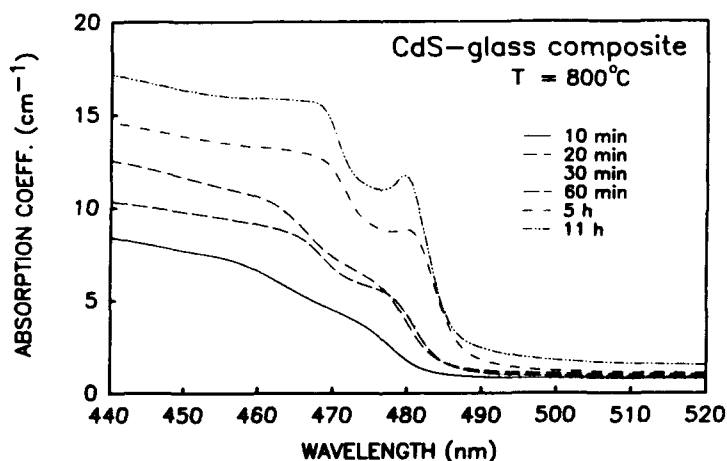


Figure 44.2. Optical absorption spectra, taken at an ambient temperature of 10 K, of CdS-glass composites heat-treated at 800°C for varying time durations.

## 500 OPTICAL PROPERTIES OF COMPOSITE MATERIALS

resonant Raman scattering in these glasses strongly suggests that the PL peak corresponds to an exciton recombination. Figure 44.5 shows a comparison of PL data from the CdS-glass composite at 9.8 and 104.7 K. The sharp peaks visible on top of the broader luminescence peak correspond to the fundamental and higher harmonics of the LO-phonon Raman scattering spectrum from the

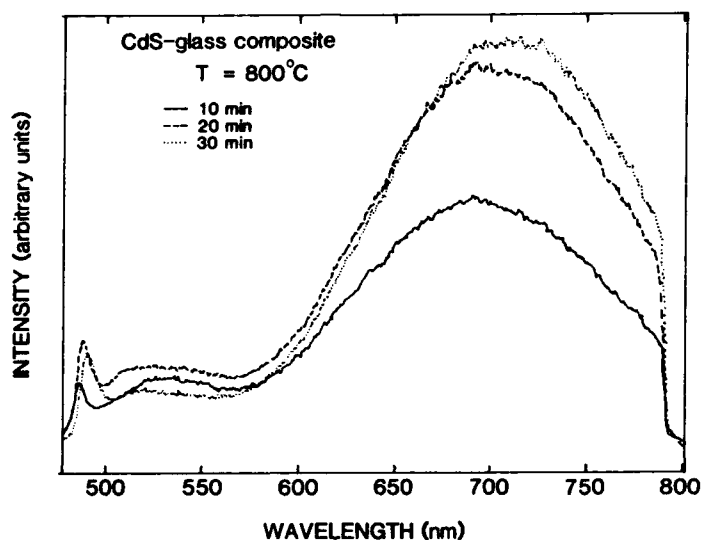


Figure 44.3. Low-temperature (10 K) PL spectra collected from CdS-glass composites heat-treated at 800°C for 10, 20, and 30 min.

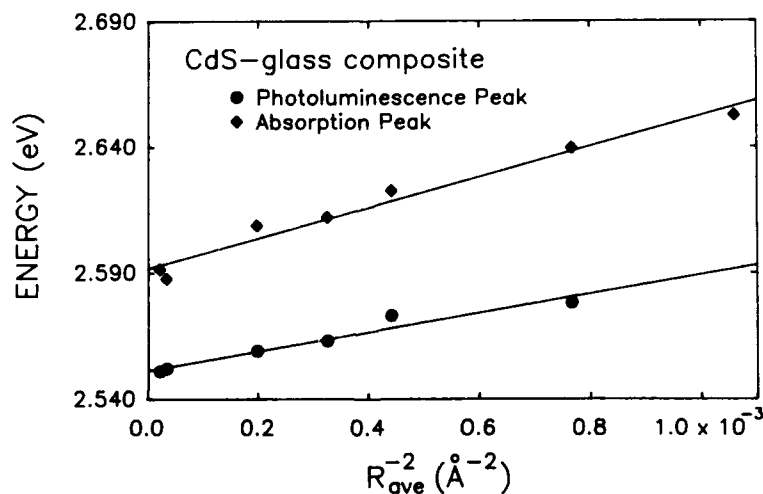
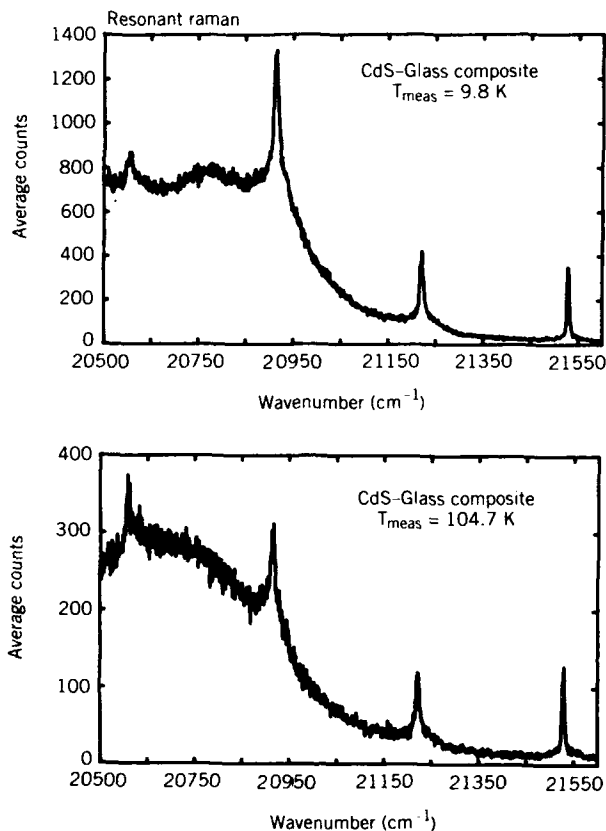


Figure 44.4. Energy positions of the PL and absorption peaks observed at 10 K for the CdS-glass composites as a function of inverse average crystallite radius squared.



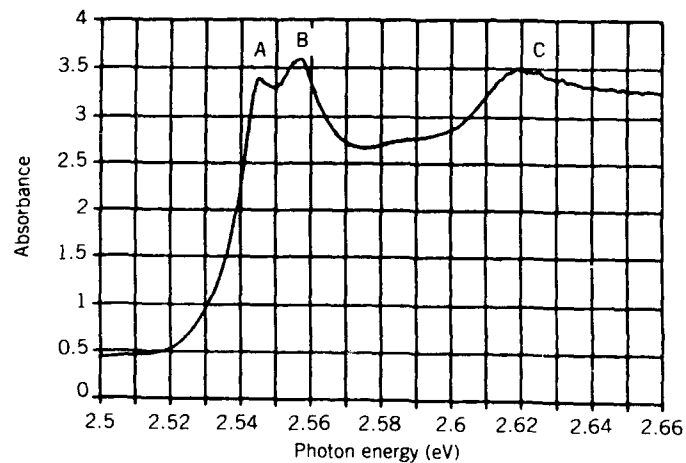
**Figure 44.5.** PL spectra obtained at 9.8 K and 104.7 K from a CdS-glass composite subjected to a 800°C heat treatment for 10 min. The spectra show four LO-phonon harmonics superimposed on the broader PL peak.

CdS crystallites. A comparison of the relative intensities of the overtone peaks reveals a large enhancement in scattering amplitude when a particular overtone overlaps the PL peak. Figure 44.5 shows how the enhancement of the various overtones shifts from the third to the fourth harmonic as the luminescence band moves to a lower energy with increasing temperature. This resonant process suggests the presence of underlying exciton luminescence processes in the PL peak, which serve as intermediate states in the resonant Raman process [37].

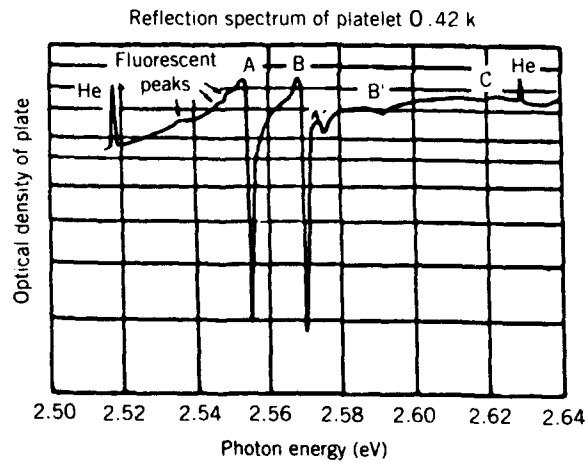
Figure 44.6 shows a comparison of the absorption behavior from a single crystal platelet of CdS with that from an RF-sputtered epitaxial CdS film grown on a silica substrate. Both exhibit the excitonic features corresponding to the A, B, and C excitons. This result demonstrates that the RF sputtering technique used is able to yield high quality CdS crystals. As described earlier, the same procedure was used to deposit CdS-glass composites containing from 5 to 50 wt% CdS. Figure 44.7 shows the absorption spectra for three films with

## 502 OPTICAL PROPERTIES OF COMPOSITE MATERIALS

5 wt % CdS in a glass matrix deposited under similar conditions, two with subsequent heat treatment. The as-deposited film is denoted by curve 1. Curves 2 and 3 correspond to heat treatments of 10 min and 8 hr at 650°C, respectively. The crystal sizes range from 0.4 to 5.0 to 40 nm, respectively, for curves 1 to 3. An examination of the change in threshold absorption energy with the inverse average crystal size squared shows that QC effects again appear as translational confinement of a highly correlated electron-hole pair down to crystal sizes of  $0.4a_0$ .

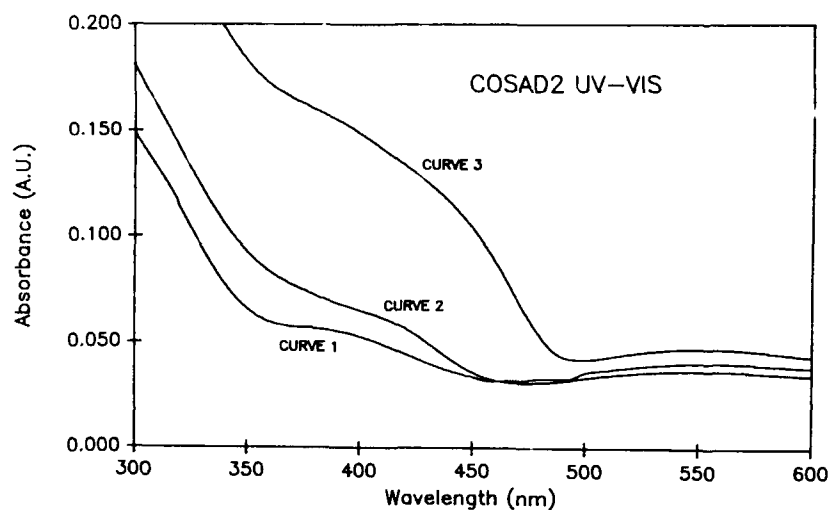


(a)



(b)

**Figure 44.6.** Absorption and reflectance spectra taken at low temperature for (a) an RF-sputtered CdS thin film on silica and (b) a CdS bulk platelet, respectively.



**Figure 44.7.** Absorption spectra collected from 5 wt% glass thin films subjected to differing postdeposition heat treatments. The as-deposited film is shown by curve 1, whereas curves 2 and 3 correspond to treatments of 10 min and 8 hr at 650°C, respectively.

#### 44.3.3. Discussion

The optical behavior of quantum confined semiconductors, as shown in the Introduction, may be delineated into two main regimes leading to the asymptotic behavior modeled by Efros and Efros [13]. It is instructive to remember that in these regimes, the quantum well boundary serves to reduce the apparent Coulomb interaction between the electron and hole due to a more rapid increase in their individual kinetic energies with crystal size reduction. Therefore the two regimes are differentiated by the degree of correlated motion of the individual components of the exciton. Previous results on CdS-glass composites [7], discussed above showed that in the size range  $0.4a_0$  to  $10a_0$ , where  $a_0$  is the exciton ground state Bohr radius, the quantum confinement effect on the exciton acts through the translational mass and the electron-hole motion remains strongly correlated.

Schmitt-Rink et al. [38] have examined the effect of size on the nonlinear optical properties of confined semiconductors which they call *quantum dots* (QD). These are defined as structures smaller than the exciton Bohr diameter yet large enough to ensure the validity of the effective mass approximation, that is, they restrict themselves to the range of sizes where the bulk crystal structure is not effectively distorted, therefore, the minimum size QD must cover at least several lattice constants. This requirement disqualifies most of the commercial filter glasses, because the isolated crystallites are too large. Wang's doped

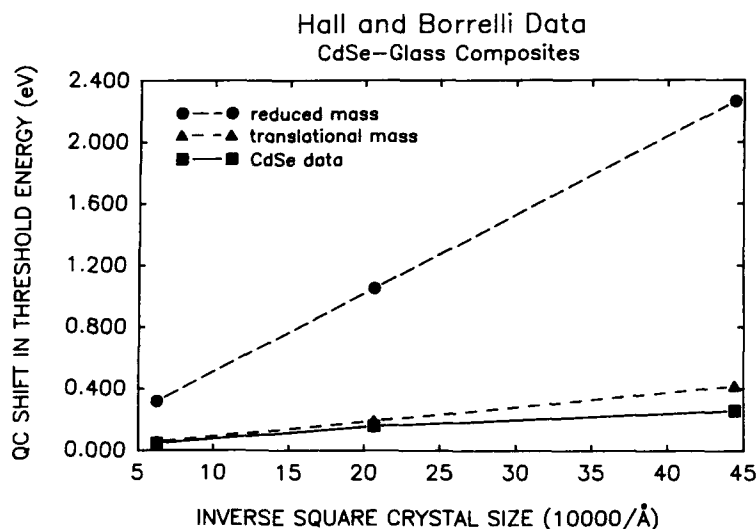
zeolites, in the other extreme, fail to satisfy the criteria, because the crystals are too small.

Schmitt-Rink's treatment assumes that in the selected size range, the Coulomb interaction between electrons and holes may be either neglected or treated as a perturbation since the confinement effects scale as  $R^{-2}$ , whereas the Coulomb interaction scales as  $R^{-1}$ . The electronic structure of QD's undergo a split of conduction and valence bands into discrete energy levels. This splitting leads to the disappearance of temperature-dependent, phonon-assisted absorption processes due to a reduced availability of states whose energy separation is less than the energy of a phonon. The only nonlinear absorption mechanism remaining is state filling, and the observed effect is that of nonlinear absorption saturation of the lowest QD transition, as in a two-level system.

From our CdS-glass studies, it seems that neglecting the Coulomb interaction requires a reduction of the upper limit of the crystal size range well below the exciton ground state Bohr radius. A fit of Borrelli's CdSe data [2] to the Efros-Efros treatment (Fig. 44.8) shows that even at crystal sizes  $0.3 a_0$  the coulomb interaction dominates the exciton's electronic structure. This severely restricts the applicable range of treatments based on uncorrelated motion of carriers.

Banyai and Koch [39] treated the case of larger semiconductor crystallites ( $3 a_0$  to  $7 a_0$ ). They find this in this size range, the screening of the Coulomb interaction due to free carriers leads to an increase in the exciton Bohr radius. This, in turn, changes the size difference between the exciton and the crystallites, which changes the degree of confinement and thus achieves the same effect as a reduction in average crystallite size, that is a confinement-related blue shift. High free carrier densities therefore can lead to an additional blue-shift in the exciton energy beyond that of spatial confinement. This blue shift results in a nonlinear decrease in absorption below the band edge within the frequency range of the linear exciton absorption. The critical electron-hole density necessary to achieve a significant blue shift in the exciton resonance of CdS is predicted to be about 60% of the Mott density of the bulk material [39]. At the Mott density, there exists a large probability of exciton wavefunction overlap due to the high density of electron-hole pairs present. This destabilizes the excitons with respect to an electron-hole plasma allowing band gap renormalization effects to reduce the band gap an amount sufficient to annihilate exciton absorption transitions. An estimate of the necessary power required to reach 60% of Mott density in the CdS crystallites of the composites, based on their measured absorption [7], is found to be about  $20 \text{ kW/cm}^2$ . Thus, following this treatment, saturation mechanisms may only be observed at incident powers below that value if excitation-dependent blue shifts of the exciton resonance are to be avoided.

Although we have had well-characterized CdS-glass composite samples, which clearly exhibited quantum confinement effects, it has not been possible, so far, to conduct exciton saturation measurements due to the scarcity



**Figure 44.8.** The predicted quantum-confinement shift in absorption threshold energy as a function of the inverse square crystallite size is presented for the extreme crystal size regimes given by Efros and Efros [13] and data of Hall and Borrelli [40] for CdSe-glass composites.

of tunable laser sources at the high energies corresponding to low-temperature, quantum-confined, CdS excitons (2.57 to 2.65 eV). However, Hall and Borrelli conducted room temperature absorption measurements at wavelengths roughly equal to an apparent excitonic feature in the absorption spectrum of quantum confined CdSe crystals [40]. Measurements of absorption on glasses with crystal radii from below  $0.3 a_0$  to  $0.5 a_0$  showed a measurable saturation for the larger crystal size only (near  $0.5 a_0$ ) and no noticeable saturation for the smaller crystallites (less than  $0.3 a_0$ ). The authors speculate that the observed decrease in nonlinear absorption with increased quantum confinement may result from a reduced electron-hole recombination time at these sizes. Thus, although, a potential enhancement of the spectral weight of the quantumly confined state is anticipated [38], the increased rate of recombination makes band filling much more difficult. Recombination time measurements are promised. However, the authors note that the powers used reached as high as  $2 \text{ GW/cm}^2$ . At these levels, it seems reasonable to also consider the effect of free carrier plasma as discussed above.

In closing it seems instructive to examine various reported QC effects by means of the observed shift in absorption threshold, according to the treatment of Efros and Efros [13]. An examination of the shift in absorption threshold against inverse square microstructure size for data from CdS- and CdSe-containing glasses reveals that, except for the CdS measurements of Ekimov et al. [4], all threshold energy shifts follow closely a QC effect only on the

translational motion of the exciton. This is indicative of a dominating electron-hole coulomb interaction and a weak confinement process. These results suggest that the composites made to date with crystal size-to-exciton Bohr diameter ratios as low as 0.3 do not satisfy the Schmitt-Rink et al. [38] requirement for a QD where electron-hole Coulomb interactions may be neglected. This means that optical measurements on these materials should not be expected to exhibit a splitting of bands or optical transitions between essentially single-particle eigenstates. For these effects and the expected high nonlinear optical coefficients accompanying them, additional fabrication studies will be required to more precisely control the microstructure of semiconductor-glass composites.

### ACKNOWLEDGMENTS

The current research is support by DARPA under Grant MDA-972-B5-J1006, the past work was supported in part by AFOSR under Grant AFOSR84-0395, and one of us (B.G.P.) received partial support under an AT&T Graduate Fellowship.

### REFERENCES

1. Y. Wang and N. Herron, *J. Phys. Chem.*, **91** 257 (1987).
2. N. F. Borrelli, D. W. Hall, H. J. Holland, and D. W. Smith, *J. Appl. Phys.*, **61**, 5399 (1987).
3. J. Warnock and D. D. Awschalom, *Phys. Rev. B*, **32**, 5529 (1985).
4. A. I. Ekimov, A. A. Onushchenko, A. G. Plyukhin, and Al. L. Efros, *Sov. Phys. JETP*, **61**, 891 (1985).
5. A. I. Ekimov and A. A. Onushchenko, *Sov. Phys. Semicond.*, **16**, 775 (1982).
6. Y. Fuyu and J. M. Parker, *Mater. Lett.*, **6**, 233 (1988).
7. B. G. Potter and J. H. Simmons, *Phys. Rev. B*, **37**, 10838 (1988).
8. L. E. Brus, *J. Chem. Phys.*, **79**, 5566 (1983); *J. Lumin.*, **31/32**, 381 (1984).
9. H. Weller, H. M. Schmidt, U. Koch, A. Fojtik, S. Baral, A. Henglein, W. Kunath, K. Weiss, and E. Dieman, *Chem. Phys. Lett.*, **124**, 557 (1986).
10. R. Rossetti, J. L. Ellison, J. M. Gibson, and L. E. Brus, *J. Chem. Phys.*, **80**, 4464 (1984).
11. D. C. Reynolds and T. C. Collins, *Excitons: Their Properties and Uses*, Academic Press, New York (1981).
12. M. Dagenais and W. F. Sharfin, *Appl. Phys. Lett.*, **46**, 230 (1985).
13. Al. L. Efros and A. L. Efros, *Sov. Phys. Semicond.*, **16**, 772 (1982).
14. S. V. Nair, S. Sinha, and K. C. Rustagi, *Phys. Rev. B*, **35**, 4098 (1987).
15. B. G. Potter, Quantum Size Effects on the Optical Properties of CdS and CdS/Se-Glass Composites Master's Thesis, University of Florida (1987).
16. E. C. Clausen and J. H. Simmons, *J. Appl. Phys.*, **68**, 1218 (1990).
17. R. K. Jain and R. C. Lind, *J. Opt. Soc. Am.*, **73**, 647 (1983).
18. S. S. Yao, C. Karaguleff, A. Gabel, R. Fortenberry, C. T. Seaton, and G. I. Stegeman, *Appl. Phys. Lett.*, **46**, 801 (1986).



19. P. Roussignol, D. Ricard, K. C. Rustagi, and C. Flytzanis, *Opt. Commun.*, **55**, 143 (1985).
20. P. Roussignol, D. Ricard, J. Lukasik, and C. Flytzanis, *J. Opt. Soc. Am. B*, **4**, 5 (1987).
21. P. Roussignol, D. Ricard, and C. Flytzanis, *Appl. Phys. A*, **44**, 285 (1987).
22. G. R. Olbright, N. Peyghambarian, S. W. Koch, and L. Banyai, *Opt. Lett.*, **12**, 413 (1987).
23. K. C. Rustagi and C. Flytzanis, *Opt. Lett.*, **9**, 344 (1984).
24. B. Danielzik, K. Natterman, and D. von der Linde, *Appl. Phys. B*, **38**, 31 (1985).
25. F. Henneberger, U. Woggon, J. Puls, and Ch. Spiegelberg, *Appl. Phys. B*, **46**, 19 (1988).
26. B. S. Wherrett and N. A. Higgins, *Proc. R. Soc. London, Ser. A* **379**, 67 (1982).
27. R. K. Jain and M. B. Klein, Chapter 10, pp. 307-416, in: R. A. Fisher, Ed., *Optical Phase Conjugation*, Academic Press, New York (1983).
28. N. Finlayson, W. C. Banyai, C. T. Seaton, G. I. Stegeman, M. O'Neill, T. J. Cullen, and C. N. Ironside, *J. Opt. Soc. Am. B*, **B6**, 675 (1989).
29. M. C. Nuss, W. Zinth, and W. Kaiser, *Appl. Phys. Lett.*, **49**, 1717 (1986).
30. J. T. Remillard and D. G. Steel, *Opt. Lett.*, **13**, 30 (1988).
31. D. S. Chemla, D. A. B. Miller, P. W. Smith, A. C. Gossard, and W. Wiegmann, *IEEE J. Quant. Electron.*, **QE-20**, 265 (1984).
32. G. I. Stegeman, C. T. Seaton, C. N. Ironside, T. Cullen, and A. C. Walker, *Appl. Phys. Lett.*, **50**, 1035 (1987).
33. E. M. Wright, S. W. Koch, J. E. Ehrlich, C. T. Seaton, and G. I. Stegeman, *Appl. Phys. Lett.*, **52**, 2127 (1988).
34. Glass samples were supplied by Mr. Lee Cook of Schott Glass technologies, Duryea, Pa.
35. N. F. Borrelli and J. C. Luong, presented at the International Symposium on the Techniques of Optoelectronics, November 16-20, 1987, Cannes, France.
36. Y. Wang and W. Mahler, *Opt. Commun.*, **61**, 233 (1987).
37. R. C. C. Leite, J. F. Scott, and T. C. Damen, *Phys. Rev. Lett.*, **22**, 780 (1969).
38. S. Schmitt-Rink, D. A. B. Miller, and D. S. Chemla, *Phys. Rev. B*, **35**, 8113 (1987).
39. L. Banyai and S. W. Koch, *Phys. Rev. Lett.*, **57**, 2722 (1986).
40. D. W. Hall and N. F. Borrelli, *J. Opt. Soc. Am. B*, **5**, 1650 (1988).

## GRADIENT-INDEX MATERIALS BY THE SOL-GEL PROCESS

MASAYUKI YAMANE

### 45.1. INTRODUCTION

A gradient-index (GRIN) glass having a continuous variation in refractive index has attracted great interest. Its application to a wide variety of optical and optoelectronic devices, such as the element for lens array of a photocopier, connector, attenuator, directional coupler, switch, or isolator in optical communication systems, is rapidly spreading [1-4].

The most popular GRIN lens used in these fields is a rod-shaped microlens of a few millimeters in diameter with the radial refractive index profile, which is given by

$$\begin{aligned} [n(r)]^2 &= n_0^2[1 - (gr)^2 + h_4(gr)^4 + h_6(gr)^6 + \dots] \\ &\approx n_0^2[1 - g^2r^2] \end{aligned} \quad (1)$$

where  $n_0$  is the refractive index at the center axis;  $r$  is the radial distance from the rod center axis; and  $g$ ,  $h_4$ , and  $h_6$  are constants. The factor  $g$  is sometimes called the *focusing factor* [5, 6].

Using a GRIN lens of this type called a *r-GRIN lens*, a collimated light can be focused, and a diverging light can be collimated like a concave lens even with flat surfaces.

---

*Ultrastructure Processing of Advanced Materials.*  
 Edited by Donald R. Uhlmann and Donald R. Ulrich (deceased).  
 ISBN 0-471-52986-9 © 1992 John Wiley & Sons, Inc.

One of the important parameters for the r-GRIN lens is the  $\Delta n$ , the difference in the refractive index between the center and perimeter of the rod. The  $\Delta n$  is related to a numerical aperture ( $NA$ ) by Eq. 2:

$$NA = (n_0)^{1/2} gR = (2n_0 \Delta n)^{1/2} \quad (2)$$

where  $R$  is the radius of the lens.

The brightness of the lens system is proportional to the square of the numerical aperture. The resolving power of the lens is proportional to the inverse of the numerical aperture. The values of the numerical aperture required for the GRIN lenses for various applications are shown in Table 45.1 along with other requirements [7].

The use of r-GRIN lenses in optical systems for cameras, binoculars, and so on provide many advantages over homogeneous glass. These advantages include greater simplicity by reduction of the total number of optical elements in a system and improved performance [8]. At the present time, however, the lack of suitable materials limits the development and application of gradient-index optics. The drawbacks of currently available materials include small size and a limited variety of optical characteristics, such as index profile dispersion and base index of refraction.

The sol-gel process is potentially advantageous over conventional methods in the production of large-size GRIN lens with a broad variety of index-modifying cations, although the techniques have not yet been established.

In this Chapter two important routes by the sol-gel process to the GRIN lens, which begin with the formation of precursor gels by introducing the index-modifying cations in the form of (1) metal alkoxide and (2) aqueous metal salt solution, will be reviewed along with the conventional methods.

**TABLE 45.1. Characteristics Required of GRIN Rod Lenses for Various Applications**

Application	Numerical Aperture	Index Profile	Others
Pickup for Video disk	0.5-0.6	Extremely low aberration	Large diameter
Digital audio disk	0.3-0.4		
Imaging system			
Endoscope	0.3	Low aberration	
Lens array	0.1-0.3	Low aberration	Low cost
Fiber system	0.2-0.5	Low loss	

## 45.2. CONVENTIONAL METHODS OF FABRICATION OF GRIN ROD LENS

### 45.2.1. The Ion-Exchange Method

Most of the currently available r-GRIN lenses are manufactured by the ion-exchange method in which  $\text{Tl}^+$  or  $\text{Cs}^+$  contained in a glass rod as an index-modifying ion is exchanged with  $\text{K}^+$  by immersing the glass in a  $\text{K}^+$ -containing fused salt bath [9]. This method is good for the precise control of the profile of refractive index and gives material of large  $\Delta n$ . However, the maximum diameter of the rod lens produced by this method has been only a few millimeters or even less due to the small diffusion coefficient of  $\text{Tl}^+$  or  $\text{Cs}^+$  in a glass, that is, about  $5 \times 10^{-14} \text{ m}^2/\text{sec}$ .

### 45.2.2. The Molecular Stuffing Method

The molecular stuffing method, which was developed by J. H. Simmons et al. [10], in principle includes the stuffing of aqueous solution of  $\text{TlNO}_3$  or  $\text{CsNO}_3$  in a Vycor-type porous glass, subsequent partial unstuffing of dopant ion, and sintering the rod into a pore-free glass. This method is good for the preparation of the lens with a large diameter. However, the process to form a porous glass rod of a uniform pore distribution is very complicated. Moreover, the maximum value of  $\Delta n$  is limited due to the limited amount of index-modifying cation that can be introduced in the pores of the glass.

### 45.2.3. The Double-Ion-Exchange Method

The double-ion-exchange, or ion-stuffing, method, which was recently developed by Ohmi et al. [11], includes the total replacement of  $\text{Na}^+$  ions in a Na-containing glass rod with  $\text{Ag}^+$  ions in a fused salt bath of  $\text{AgNO}_3$  and the partial exchange of  $\text{Ag}^+$  ions with  $\text{Na}^+$  ions in a fused salt bath containing  $\text{NaNO}_3$ . The method is good for the preparation of GRIN rods with diameters larger than 10 mm. However, it still takes long time, about 2 months for 10-mm-diameter rods. Moreover, the reduction of  $\Delta n$  with the increase in lens diameter is inevitable. Therefore, the production of GRIN rods with large diameters and large  $\Delta n$ 's may not be expected.

## 45.3. FABRICATION OF GRIN ROD LENS BY SOL-GEL PROCESS

### 45.3.1. The GRIN Rod from Metal Alkoxide as the Source of the Index-Modifying Cation

A method for making a GRIN rod lens was developed by Shingyouchi et al. [12]. It was done by preparing a wet gel using tetramethylorthosilicate (TMOS)

and tetraethylorthogermanate  $[\text{Ge}(\text{OEt})_4]$  as starting materials and subsequently leaching a part of the Ge component out of the gel followed by drying and sintering the gel.

This method was extended to the titanium-silica system by the same researchers [13] and later to ternary and quaternary systems by the group at the University of Rochester [14]. The process in this method is relatively simple as shown in Fig. 45.1 and good for the preparation of large-sized lens with a precisely controlled profile of refractive index, although the conditions to produce materials of large  $\Delta n$  must be elaborated.

First, TMOS is combined with  $\text{Ge}(\text{OEt})_4$ , ethanol, EtOH, water, and hydrochloric acid. The mixture forms a gel in which germanium was incorporated in the network structure building up the gel particle along with silicon. The gel is placed in water to leach out some of the germanium component. The gel then is washed in methanol to fix the germanium concentration gradient and then is dried and sintered into gradient index glass [12].

Shingyouchi et al. also used titanium to replace germanium as index-modifying cation and leached out some of the titanium with 10 wt % HCl aqueous solution. Typical molar ratio compositions of the precursor solutions were  $0.7\text{TMOS}/0.3\text{Ge}(\text{OEt})_4/2\text{H}_2\text{O}/4\text{EtOH}$  for the  $\text{GeO}_2\text{-SiO}_2$  system and  $0.85\text{TMOS}/0.15\text{Ti}(\text{O-}n\text{-Bu})_4/4\text{H}_2\text{O}/4.5n\text{-PrOH}$  for the  $\text{TiO}_2\text{-SiO}_2$  system [12-13].

In both germanium- and titanium-containing gels, the leaching was considered to proceed, in principle, by a diffusion-controlled process rather than a

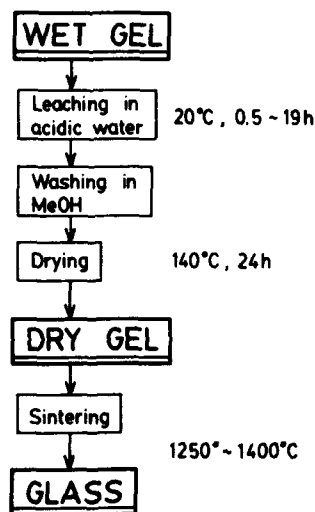


Figure 45.1. Flow chart for the GRIN preparation by the partial leaching of the index-modifying cation from a gel.

reaction-controlled one. Only germanium or titanium was detected in the solution after leaching [15–17].

The resulting glass of  $\text{TiO}_2$ – $\text{SiO}_2$  system obtained from a wet gel of about 6 mm in diameter and 30 mm in length by leaching for 20 hr and sintering the dry gel at  $1200^\circ\text{C}$  was a rod of about 2 mm in diameter with the refractive index at the center axis of 1.491 and a  $\Delta n$  of 0.013,  $NA = 0.197$  [13, 16, 17].

The concentrations of  $\text{TiO}_2$  at the center axis and the perimeter were about 7 mol % and 3 mol %, respectively, whereas the concentration of  $\text{TiO}_2$  in the original gel was 15 mol % [16]. This suggests that the concentration of the index-modifying cation decreased noticeably during leaching not only at the perimeter, but also at the center.

Caldwell [14] extensively studied the preparation of GRIN glass rods from gels of ternary and quaternary systems using techniques similar to that of Shingyouchi et al. The systems investigated were  $\text{TiO}_2$ – $\text{Al}_2\text{O}_3$ – $\text{SiO}_2$ ,  $\text{TiO}_2$ – $\text{B}_2\text{O}_3$ – $\text{SiO}_2$ ,  $\text{TiO}_2$ – $\text{Al}_2\text{O}_3$ – $\text{B}_2\text{O}_3$ – $\text{SiO}_2$ ,  $\text{TiO}_2$ – $\text{GeO}_2$ – $\text{Al}_2\text{O}_3$ – $\text{SiO}_2$ ,  $\text{ZrO}_2$ – $\text{B}_2\text{O}_3$ – $\text{SiO}_2$ ,  $\text{ZrO}_2$ – $\text{GeO}_2$ – $\text{SiO}_2$ , and  $\text{ZrO}_2$ – $\text{B}_2\text{O}_3$ – $\text{Al}_2\text{O}_3$ – $\text{SiO}_2$ .

$\text{Zr}^{4+}$  and  $\text{Ti}^{4+}$  were the index-modifying cations.  $\text{Al}_2\text{O}_3$ ,  $\text{B}_2\text{O}_3$ , or  $\text{GeO}_2$  was introduced as a gel modifier to eliminate the problems inherent in a binary system, such as bloating and/or crystallization during sintering.

Typical molar ratio compositions studied of  $\text{TiO}_2$ – $\text{Al}_2\text{O}_3$ – $\text{SiO}_2$  system were the following:  $\text{TiO}_2:\text{AlO}_{3/2}:\text{SiO}_2 = 0.10:0.09:0.81$ ,  $0.10:0.10:0.80$ ,  $0.10:0.20:0.70$ ,  $0.05:0.20:0.75$ ,  $0.05:0.15:0.80$ ,  $0.05:0.10:0.85$ ,  $0.10:0.15:0.75$ ,  $0.10:0.05:0.85$ ,  $0.15:0.10:0.75$ ,  $0.15:0.05:0.80$ ,  $0.20:0.05:0.75$ . Titanium, aluminum, and silicon were introduced in the form of titanium isopropoxide,  $(\text{Ti}(\text{O}-i\text{-Pr})_4)$ , Al chelate, and TMOS, respectively.

Most of the GRIN glass rods reported were about 4.5 mm in diameter with a  $\Delta n$  of about 0.013. Some of the rods had  $\Delta n$ 's of about 0.03 with a similar diameter, and some had  $\Delta n$ 's of 0.007, but those diameters were as large as 8 mm. The time necessary to fabricate the GRIN rod was 5 to 7 days.

Caldwell [14] investigated the effect of leaching time on the index profile on the 15-mm-diameter  $\text{TiO}_2$ – $\text{Al}_2\text{O}_3$ – $\text{SiO}_2$  gel soaked in 3 mol/liter  $\text{H}_2\text{SO}_4$  aqueous solution. The index profile of the eventual GRIN rod became close to parabolic after 4–5 hr, and thereafter,  $\Delta n$  decreased as the leaching time continued. The change in  $\Delta n$  with leaching time is shown in Fig. 45.2.

Taking this result and the fact reported by Shingyouchi et al. [16] that the concentration of  $\text{TiO}_2$  at the center remarkably decreased during leaching into consideration, the elaboration of the minimum leaching time to attain the parabolic concentration profile for a gel of given composition and size is essential in this method in order to produce the GRIN rod with a large  $\Delta n$ . The other factors to be taken into consideration for the purpose of GRIN manufacture by this method include

1. The gel composition from the point of maximum amount of index-modifying cation and gel-modifying cations (if any) that can be introduced without fracture and/or devitrification during sintering.

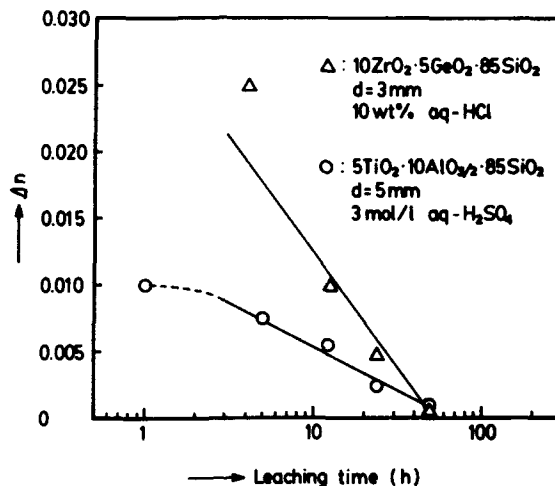


Figure 45.2. Change in  $\Delta n$  of a GRIN rod lens with leaching time with  $\text{Ti}^{4+}$  or  $\text{Zr}^{4+}$  from wet gel.

## 2. The kind and concentration of acid to be used for leaching.

The gel composition is also related to the fracturing of eventual glass due to stress attributed to the difference in thermal expansion coefficients at the center and perimeter.

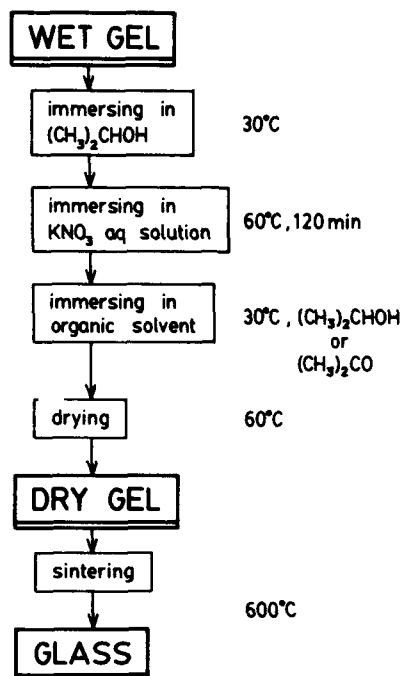
### 45.3.2. The Method to Use a Metal Salt Aqueous Solution as the Source for Index-Modifying Cation

A method for making a GRIN rod lens from a wet gel prepared by using lead acetate as the source for index-modifying cation was developed by this author's group [18, 19]. The method includes

1. Gel formation by the introduction of aqueous solution of lead into an alkoxy-derived silica sol.
2. Interdiffusion of  $\text{Pb}^{2+}$  with  $\text{K}^+$  in aqueous solution of potassium nitrate.
3. Drying and sintering of the gel, as shown in Fig. 45.3.

The potential advantage of this method over others include

1. The ability to introduce a large amount of index-modifying cation, such as lead, thus enabling the production of a GRIN rod with a large  $\Delta n$ .
2. The ability to introduce a broad variety of index-modifying cations.
3. The ability to prepare a material of uniform thermal expansion coefficient through the center axis to the perimeter of the rod, thus avoiding the stress buildup.



**Figure 45.3.** Schematic drawing of the process for GRIN preparation using a metal salt aqueous solution as the source for the index-modifying cation.

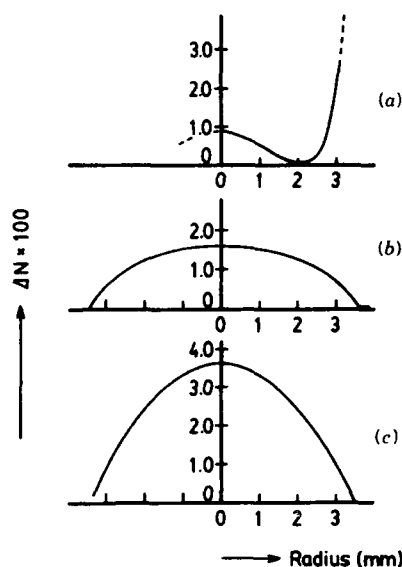
The biggest drawback of this method is the complicated procedure to control the index profile. In this method, the index-modifying cation that is introduced in the form of metal salt aqueous solution is not incorporated in the network structure of the gel, but stays in the liquid phase of the wet gel and easily migrates toward the gel surface upon removal of water, which is the main component of the liquid filling the micropores of the gel [20].

One of the ways to reduce the migration of the cation is to replace water in the pores with an organic solvent to which the cation salt can dissolve only slightly. These organic solvents include acetone and *iso*-propanol in the case of lead acetate.

Figure 45.4 demonstrates the effect of the replacement of water with organic solvent in the gel of 20PbO/5B<sub>2</sub>O<sub>3</sub>/75SiO<sub>2</sub> (mol %). The curves in Fig. 45.4 show the profile of refractive index of GRIN glasses obtained from gels dried (1) without replacement of water, (2) after the replacement with *iso*-propanol, and (3) after the replacement with acetone, respectively. It is obvious from these curves that the migration of Pb<sup>2+</sup> is remarkably reduced by the replacement of water with acetone.

Both the  $\Delta n$  in Fig. 45.4c and the  $NA$ , estimated by assuming the refractive index at the center axis,  $n_0$ , to be 1.5, are compared with those of GRIN rod





**Figure 45.4.** Profile of the refractive index of GRIN glass rods prepared from Pb-containing tels by various procedures. (a) Dried without replacement of water; (b) dried after the replacement of water with *iso*-propanol; (c) dried after the replacement of water with acetone.

lenses of other methods in Table 45.2. It is shown in the table that the gel formation using aqueous Pb-acetate solution is advantageous over the method starting with Ti- or Ge-alkoxide in order to manufacture GRIN rods of large numerical aperture, although the value is much smaller than that expected from the composition of the precursor sol. The improvement of the  $\Delta n$  and numerical aperture will be possible if the mixture of *iso*-propanol and water is used for the  $\text{KNO}_3$  bath for the interdiffusion of  $\text{Pb}^{2+}$  and  $\text{K}^+$ .

One of the important factors to be taken into consideration in the manufacture of GRIN by the sol-gel process starting with an aqueous metal salt solution is the maximum size of the gel that can be handled without deformation or fracturing throughout the process. The preparation of GRIN rods with both large diameters and length is obviously favorable from an economical viewpoint. However, a wet gel of multicomponent system is often very soft and easily deforms during drying by its own weight, resulting in the distortion of the concentration profile of the index-modifying cation.

Although a detailed investigation has not been made yet, the maximum size of the Pb-containing GRIN rod that can be obtained by natural drying is expected to be 7 to 8 mm in diameter and 20 to 25 mm in length. The diameter of 7 to 8 mm is large enough for the application in the fields shown in Table 45.1, but is far from satisfactory for the application to an optical system, such as cameras and binoculars. Therefore, the establishment of the drying conditions of a large wet gel by a hypercritical evacuation technique is the urgent necessity in this process.

Table 45.2. Comparison of the Characteristics of GRIN Rod Lenses by Various Methods

Method	Rod Diameter (mm)	$\Delta n$	Numerical Aperture	Manufacturing Time (approx. days)	Ref. No.
Ion exchange	2	0.1	0.5	30	5
Molecular stuffing	3.2	0.021 <sup>a</sup>	0.25	7	5
Double	9.7	0.037	0.44	60	5
ion exchange	12.5	0.018	0.25	>60	5
Sol-gel	4.7	0.014	0.2	7	14
(leaching)	8.1	0.007	0.15 <sup>b</sup>	7	14
Sol-gel (aqueous solution)	7	0.037	0.34 <sup>b</sup>	10	19

<sup>a</sup>Estimated from the curve in Ref. 5.<sup>b</sup>Estimated assuming  $n_0$  to be 1.5.

## REFERENCES

1. D. T. Moore, *Photoionics Spectra*, p. 71 (March 1987).
2. W. J. Tolmison, *Appl. Opt.*, **19**, 1127 (1980).
3. K. Sono, T. Yamasaki, and T. Kishimoto, *Laser Focus*, p. 70 (February 1981).
4. M. Kawazu and Y. Ogura, *Appl. Opt.*, **19**, 1105 (1980).
5. Y. Asahara and A. J. Ikushima, *Optoelectronics*, **3**, 1 (1988).
6. K. Nishizawa, *Japan. J. Opt.*, **16**, 189 (1987).
7. S. Ohmi and Y. Asahara, *Newglass Technol.*, **4**, 2 (1984).
8. L. G. Atkinson, S. N. House-Walter, D. T. Moore, D. P. Ryan, and J. M. Stagaman, *Appl. Opt.*, **21**, 993 (1982).
9. H. Kita, I. Kitano, T. Uchida, and M. Furukawa, *J. Am. Ceramic Soc.*, **54**, 321 (1971).
10. J. H. Simmons, R. H. Mohr, D. C. Tran, P. B. Macedo, and J. A. Litovitz, *Appl. Opt.*, **18**, 2732 (1979).
11. S. Ohmi, H. Sakai, Y. Asahara, Y. Yoneda, and T. Izumitani, *Appl. Opt.*, **27**, 496 (1988).
12. K. Shingyouchi, S. Konishi, K. Susa, and I. Matsuyama, *Electron. Lett.*, **22**, 99 (1986).
13. K. Shingyouchi, S. Konishi, K. Susa, and I. Matsuyama, *Electron. Lett.*, **22**, 1109 (1986).
14. J. B. Caldwell, Ph.D. Thesis, Institute of Optics, University of Rochester, 1989.
15. K. Shingyouchi and A. Makishima, *J. Am. Ceramic Soc.*, **71**, c-82 (1988).
16. K. Shingyouchi, A. Makishima, M. Tutumi, S. Takenouchi, and S. Konishi, *J. Non-Cryst. Solids*, **100**, 383 (1988).
17. S. Konishi, K. Shingyouchi, and A. Makishima, *J. Non-Cryst. Solids*, **100**, 511 (1988).
18. M. Yamane, J. B. Caldwell, and D. T. Moore, *J. Non-Cryst. Solids*, **85**, 244 (1986). M. Yamane, J. B. Caldwell, and D. T. Moore, in: C. J. Brinker, D. E. Clark and D. R. Ulrich, Eds., *Better Ceramics Through Chemistry*, Vol. II, North-Holland, Amsterdam p. 765, (1986).
19. M. Yamane, H. Kawazoe, A. Yasumori, and T. Takahashi, *J. Non-Cryst. Solids*, **100**, 506 (1988).
20. M. Yamane, H. Kawazoe, A. Yasumori, and T. Takahashi, *J. Non-Cryst. Solids*, **99**, 160 (1988).

## LASER BEHAVIOR AND NONLINEAR OPTICAL PROPERTIES IN ORGANIC DYE-DOPED SOL-GEL MATERIALS

E. T. KNOBBE, B. BUNN, P. D. FUQUA, F. NISHIDA,  
AND J. I. ZINK

### 46.1. INTRODUCTION

There are numerous organic molecules available that possess desirable properties for laser and nonlinear optical applications. Finding suitable host materials for these organics is problematic, and in the case of laser dyes, devices have been primarily restricted to liquid-state applications. Attempts have been made to fabricate solid-state organic dye materials using polymeric hosts. These hosts, however, have been shown to be inherently lacking in mechanical and thermal properties, photostability, and refractive index uniformity. Inorganic glasses, on the other hand, do possess extremely good optical, thermal, and chemical stability. Unfortunately, typical melt glasses require processing temperatures that would cause the rapid decomposition of most organic species. Sol-gel processing offers a low-temperature alternative to the synthesis of oxide-based transparent materials. Sol-gel precursor solutions allow for room temperature dissolution of optically active organic molecules. This step is followed by low-temperature polymerization, which does not require strong redox conditions or reactive initiators. The sol-gel method has been previously proposed as a

---

*Ultrastructure Processing of Advanced Materials.*

Edited by Donald R. Uhlmann and Donald R. Ulrich (deceased).

ISBN 0-471-52986-9 © 1992 John Wiley & Sons, Inc.

## 520 LASER BEHAVIOR AND NONLINEAR OPTICAL PROPERTIES

technique for synthesizing optical materials [1], but relatively little work on the relevant optical properties has been reported.

The present Chapter reviews our recent results involving the use of the sol-gel process to prepare solid-state dye laser materials and thin films, that exhibit nonlinear optical effects. Two different host materials were investigated; silica gels based on the hydrolysis of tetraethoxysilane (TEOS) and composite silica-acrylate gels based upon hydrolysis of tetramethoxysilane (TMOS) and an organically modified silicate (ORMOSIL). The latter approach incorporates an organic monomer and produces an organic-inorganic matrix with phase mixture occurring at the molecular level. Optical gain was determined during the sol-gel transition and subsequent aging of gels containing coumarin and rhodamine dyes. High-gain values were obtained, and laser oscillation was easily achieved with these materials. ORMOSIL gels appear to be a particularly promising host material as they exhibit high gain in the fully dried state and, when doped with an appropriate nonlinear organic molecule, demonstrate relatively efficient resonance enhanced third-order effects.

### 46.2. REVIEW OF RELATED PUBLICATIONS

Several researchers have explored the synthesis and fundamental properties of gels doped with organic molecules [1-8]. The work regarding optical properties seems to have developed in two different directions. One direction for this work has been to use the organic species as luminescent probes. This approach is based on the well-known characteristic of specific organics regarding alterations of their optical properties in response to changes in local chemical and structural environments. By adding these molecules to gels, the resulting spectroscopic investigations have provided substantial insight regarding selected aspects of gel chemistry such as polarity [3], pH [3, 7], and local water content [7, 9]. Other molecular probes were found to be responsive to the structural aspects of the gel including gel microstructure [3] and rigidity [10]. A second direction for the work has been to explore the prospects for using dye-doped gels for optical device applications. The approach involves adding specific molecules to the host material in order to produce particular optical effects. The work to date suggests that the resulting materials may possess a number of potential applications. Suitably doped gels have been shown to exhibit highly efficient luminescence [1], photochemical hole burning [4], photochromism [12], and tunable laser action [13-16]. The latter behavior has been reported with rhodamine 6G in bulk silica gels [13-15] and in alumina-based thin films [16]. The gel matrix possesses a number of other desirable features for optical materials including enhanced photostability and good matrix isolation characteristics [2]. The availability of solid-state tunable laser based on laser dyes incorporated into photochemically stable host materials is of substantial interest to the optical community.

### 46.3. EXPERIMENTAL METHODS

#### 46.3.1. Measurement of Optical Gain Characteristics

Optical gain measurements are extremely useful because they represent a sensitive probe of the chemical environment as well as provide a definitive measure of the gain characteristics of the medium. It is well known that changes in local chemistry can have a substantial effect on the stable oscillation region of dye laser molecules that would cause the gain curve envelope to be shifted and the bandwidth to narrow or broaden. Thus, by determining the gain characteristics during the gelation and aging stages, there is an opportunity to establish how these processes influence optical gain. These results are of obvious importance regarding the development of solid-state tunable lasers.

Optical gain measurements were performed by inserting the sample of interest into the amplifier cell of a nitrogen pumped tunable dye laser. The system used was a PTI Model PL 202, having a pump pulse width of approximately 500 psec (full width at half-maximum, FWHM) at a repetition rate of 2 Hz. The primary oscillator cell held an ethanol solution of the same dye at the same concentration as in the gel sample. A reverse-biased pin photodiode was used to measure spectral variations in the amplitudes of each of the following: probe signal ( $S$ ) generated by the primary oscillator cell, fluorescence emission from the amplifier cell ( $F$ ), amplified spontaneous emission ( $ASE$ ), and total signal gain ( $G_t$ ). The stimulated gain ( $G_s$ ) due to the sample in the amplifier cell was calculated as follows:

$$G_s = (G_t - F - ASE)/S \quad (1)$$

The sample in the amplifier cell consisted of either a sol-gel-derived material or a reference ethanol solution. Both types of samples were contained in quartz cuvettes and could be readily substituted. In this way, the gain values for sol-gel-derived samples were accurately compared to those for reference solutions of the dye at the same concentration.

Laser oscillation bandwidths were determined by positioning the samples into a transversely pumped optical resonator. The experimental arrangement was analogous to that reported in earlier publications [14, 15]. Samples were pumped at the 308-nm output of a XeCl excimer laser at 0.1 to 2 mJ per 20-ns pulse and a repetition rate of 1 to 5 Hz. Spectral output was measured using an OMA detector array in conjunction with a one-third meter grating monochromator. As with the gain measurements, the outputs obtained with dyedoped gel samples were compared to those of the same dye in ethanol solutions.

#### 46.3.2. Synthesis and Chemistry

The silica matrix gels were derived using the sonogel method [17]. The initial sol was composed of a 3/1/0.01 molar ratio of water/TEOS/HCl catalyst. Dye was immediately dissolved into the resultant single-phase solution, which possessed

## 522 LASER BEHAVIOR AND NONLINEAR OPTICAL PROPERTIES

an initial pH of 3. Condensation and polymerization of the silica gels were carried out in covered transparent quartz cuvettes. The samples gelled in approximately 2 days and were then aged at room temperature for various periods of time. Solid rods were obtained from samples that were prepared and slowly dried in acrylic cuvettes. The dye concentrations ranged from  $3.4 \times 10^{-3}$  to  $5.9 \times 10^{-3}$  mol/liter.

Composite ORMOSIL gels were synthesized according to the methods described by Capozzi [18] and Schmidt [19]. The initial precursor solution was composed of a 1/1/1/3.5 molar ratio of TMOS/methylmethacrylate (MMA)/3-(trimethoxysilyl)propylmethacrylate (TMSPM)/0.04 N HCl in a homogeneous solution. After one day at room temperature, the dye was dissolved into the sol and the solution was placed into acrylic cuvettes. The doped ORMSIL was kept uncovered at room temperature for about 3 days, until approximately one-half of the initial volume had evaporated. A significant increase in the viscosity of the gel was apparent at that stage of the polymerization reaction. The lost volume is believed to be due to removal of methanol, which is formed as a product of the hydrolysis of TMOS. Starting dye concentrations in the ORMOSIL solutions were  $1.7 \times 10^{-3}$  and  $2 \times 10^{-3}$  mol/liter for coumarin 153 and rhodamine 6G, respectively. Following the 3-day prepolymerization step, the samples were placed in an oven at 55°C for 2 weeks. During the first week, the viscous sol became a rigid gel. The second week of heating promoted complete product formation and allowed residual solvent to volatilize.

## 46.4. RESULTS

### 46.4.1. Optical Gain Experiments

The spectral gain envelopes for coumarin 153 in an ethanol solution and in silica gels are shown in Fig. 46.1. The gel samples were aged for 1 day and for 11 days. The gel that was aged for 1 day is quite similar to that of the reference solution. At that stage, there was little apparent differences between the chemical environments of the ethanol solvent and the sol-gel matrix despite the fact that gelation had occurred. Prior to gelation, the two gain curves were essentially indistinguishable. After 11 days of aging, however, the two spectra had become distinctly different. The gel had begun to shrink and to expel solvent. It is estimated that the gel had undergone a net volume shrinkage of 5%. Figure 46.1 shows that a sizeable 19-nm red shift had occurred in the peak of the gain curve. It is significant to note, however, that aging produced very little reduction in the peak gain of the system. Thus, it is possible to obtain high values of optical gain in a well-aged gel matrix. The red shift is consistent with what is expected from the local chemical changes that are known to occur in the solution-filled pores. During the aging process, condensation of the hydrolyzed species produces additional water that enters the solvent phase. Jones et al. [11] have shown that

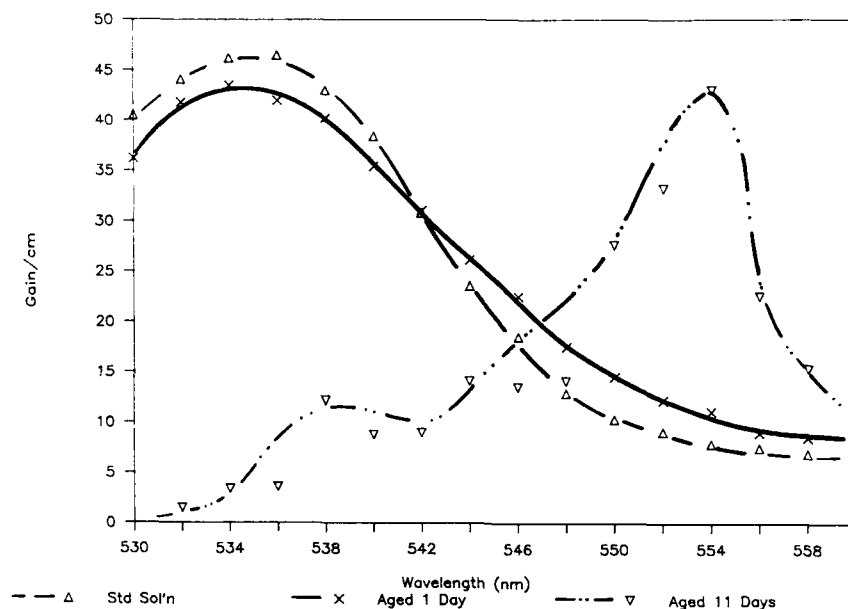


Figure 46.1. Spectral gain envelope for coumarin 153 in ethanol and aged gels.

coumarin dyes in ethanol-water solutions exhibited red shifts of some 11 nm compared to pure ethanol. The rhodamine 6G samples exhibit somewhat similar results, although these materials are susceptible to dimerization of the dye molecule. Thus, the gelled rhodamine 6G materials exhibited reduced gain values as well as increased losses in the short wavelength portion of the spectrum.

The ORMOSIL composite matrix was found to possess good optical properties. Coumarin 153-doped ORMOSIL gel proved to have gain characteristics very similar to those of the ethanolic solution, as seen in Fig. 46.2. Although the peak gain value had diminished slightly, the overall spectral gain curve had become significantly broader. This result indicates the development of an enhancement in the broadband tunability of the solid-state laser material with respect to the reference liquid-phase laser medium. These gain characteristics for the coumarin-doped ORMOSIL are extremely promising for tunable laser applications. In contrast, the rhodamine-doped ORMOSIL gels showed no optical gain. At a final concentration of approximately  $4 \times 10^{-3}$  mol/liter, dimerization of the active species appeared to be a major source of absorptive and scattering losses. Thus, the rhodamine 6G-doped ORMOSIL host exhibited only lossy behavior over the range of oscillation for the primary cell. Table 46.1 summarizes the spectral gain profile characteristics for both the reference and gel-derived samples.

## 524 LASER BEHAVIOR AND NONLINEAR OPTICAL PROPERTIES

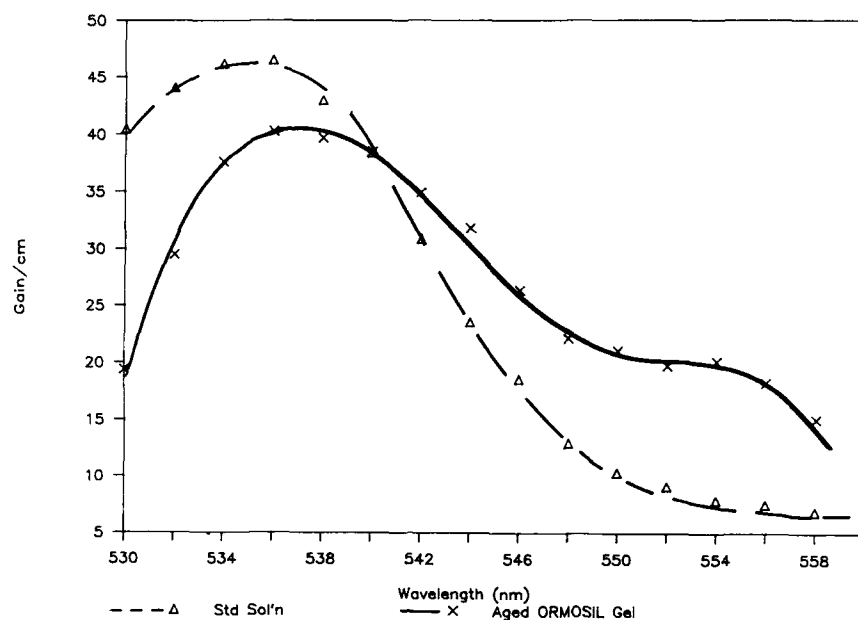


Figure 46.2. Spectral gain envelope for coumarin 153 in ethanol and in dried ORMOSIL gel.

TABLE 46.1. Spectral Gain Characteristics of Doped Gels

Dye	Medium	Maximum Gain ( $G_s$ ) ( $\text{cm}^{-1}$ )	Peak Wavelength (nm)
Coumarin 153 ( $3.4 \times 10^{-3}$ mol/liter)	EtOH solution	47	535
	Aged 1 day	43	534
	Aged 4 days	40	550
	Aged 11 days	41	554
	Ormosil (14 days)	40	537
Rhodamine 6G ( $4.0 \times 10^{-3}$ mol/liter)	EtOH solution	45	585
	Aged 1 day	40	585
	Aged 4 days	31	587
	Aged 11 days	10	590
	Ormosil (14 days)	NA	NA

Abbreviation used: NA, not applicable.



#### 46.4.2. Laser Oscillation Experiments

Laser oscillation was obtained in several coumarin-doped gels. The data shown in Fig. 46.3 and in Table 46.2 are for gels that were aged for 1 week. The spectral output of the free running ethanol solution contains a great deal of structure, partially due to etalon effects at the cuvette wall interfaces. The peak emission is centered about 542 nm, having a FWHM oscillation band of 13 nm. The full spectral oscillation range was 25 nm, from 529 to 554 nm. Figure 46.3 also shows that there is a significant red shift in the fluorescence spectrum of aged silica gels containing coumarin 153. The doped sonogel, aged for 1 week, had a peak emission centered at 558 nm. FWHM bandwidth of 13 nm, and demonstrated fundamental oscillation from 545 to 572 nm in the free-running cavity. The primary amplitude structure seen in Fig. 46.3 is believed to be caused by hole burning in the inhomogeneously broadened gain profile, due to strong interactions with the charged silica matrix. Table 46.2 includes the results for silica gels made with all three coumarin dyes: 1, 102, and 153. The values reported for gels are for samples that were aged for 1 week at room temperature.

As in the gain experiment, all of the dye-doped gels exhibited a red shift in peak fluorescence. The reasons for this red shift are associated with the chemical changes during aging as discussed previously. In two of the three samples (coumarin 1 and coumarin 153), the total range of oscillation was increased in

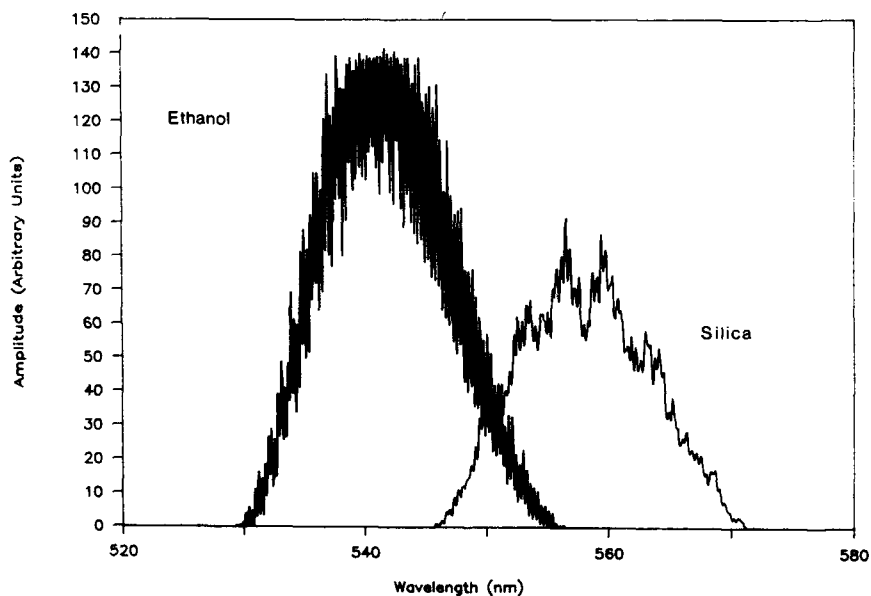


Figure 46.3. Spectral output of free-running lasers; coumarin in ethanol and coumarin in aged silica gel.

## 526 LASER BEHAVIOR AND NONLINEAR OPTICAL PROPERTIES

TABLE 46.2. Spectral Output of Excimer-Pumped Laser Resonator

Dye	Medium	Peak (nm)	Full Width at Half-Maximum (nm)	Oscillation Range (nm)
Coumarin 1	( $4.0 \times 10^{-3}$ mol/liter)			
	EtOH solution	438	7	432–446
	Gel, aged	444	10	433–457
Coumarin 102	( $5.9 \times 10^{-3}$ mol/liter)			
	EtOH solution	475	8	468–483
	Gel, aged	491	6	487–495
Coumarin 153	( $3.4 \times 10^{-3}$ mol/liter)			
	EtOH solution	542	13	529–554
	Gel, aged	558	13	545–572
Rhodamine B	( $1 \times 10^{-3}$ mol/liter)			
	Gel, fully dried	618	4	612–620

the gel even though peak amplitude was lower for all of the aged gel samples. This is indicative of strong–matrix interactions, demonstrating the importance of tailoring the local environment of matrix to suit the requirements of the optically active organic species.

Laser oscillation studies for partially dried and completely dried gels have also been performed. Coumarin 153, which had lost approximately 50% of its solvent continued to exhibit laser action, although its tuning range was more limited (13 nm). Partially dried silica gels containing coumarin dyes 1 and 102 also exhibited laser oscillation with reduced tuning ranges of 6 and 8 nm, respectively. Fully dried, solid samples of dye-doped gels show good to excellent luminescence. Achieving laser action from a xerogel rod, however, is difficult because of problems in obtaining optically polished surfaces. Despite the current limitation in obtaining polished samples, laser action from a solid rod of rhodamine B-doped silica gel was observed. The solventless silica rod had a peak laser emission wavelength of 618 nm and had a free running spectral range of 10 nm. In general, the prospects are very good for achieving laser oscillation with other solid, doped rods.

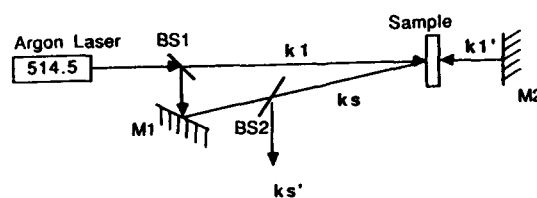
The question of photostability of entrapped dye molecules is an issue that has yet to be fully explored. Avnir et al. [1] found that dye-doped sol–gel materials exhibited enhanced photostability. The present results are qualitatively consistent with their findings. The aged, dye-doped silica and ormosil gels exhibited no visible bleaching subsequent to either the gain or oscillation measurements. The rhodamine B-doped xerogel, however, appeared to degrade somewhat with increasing ultraviolet excitation. Further studies are required in order to more completely establish the photostability characteristics of doped gel matrices.

#### 46.4.3. Resonance-Enhanced Nonlinear Optical Properties

Films suitable for degenerate four-wave mixing (DFWM) experiments were modeled after the work published by Fujiwara and Nakagawa [20]. In our study, methyl red was dissolved into an ORMOSIL solution, as described in an earlier section. The starting concentration of the dye in the sol was  $2 \times 10^{-3}$  mol/liter. The solution was then coated onto glass slides by standard spinning techniques, forming a film approximately  $5 \mu\text{m}$  thick. The films were prepolymerized uncovered at room temperature for 2 days. They were then baked, uncovered, in an oven at  $55^\circ\text{C}$  for 5 days in order to drive the polymerization reaction to completion.

Resonance-enhanced DFWM can be measured in isotropic media using relatively low-power, continuous wave (CW), single-mode laser sources. For this reason, it is one of the more easily observed of the nonlinear optical phenomena. In materials such as methyl red-doped films, a thermal grating, formed by absorption of the pump signals by the dye, scatters the probe beam as a phase conjugate signal. Thus, the mixing of  $\omega$ ,  $\omega$ , and  $-\omega$  signals generates a third-order nonlinear response ( $\omega$ ). Resonance-enhanced nonlinear optical characterization of dye-doped thin films was accomplished by positioning the sample in the DFWM system shown in Fig. 46.4. The pump/probe source used was a Spectra Physics Model 2020 CW argon ion laser with an internally housed etalon. The counterpropagating  $k_1$  and  $k_1'$  beams were generated by retroreflection from a high-reflection efficiency dielectric mirror. The beam splitters used were selected to give approximately 1:1:1 beam ratios between  $k_1(\omega)$ ,  $k_1'(-\omega)$ , and  $k_s(\omega)$ . A portion of the diffracted-phase conjugate signal,  $k_s'(\omega)$ , was reflected into a detector by the beam splitter, BS2. The angle between the  $k_1$  and  $k_s$  pump and probe beams was  $9^\circ$ , resulting in a transmission grating spacing of approximately  $3 \mu\text{m}$  when constructed with a 514.5-nm source.

Scattering of the probe signals by the gratings developed in the ORMOSIL films produced a visible phase conjugate output signal. Peak diffraction



BS = Beam Splitter

M = Mirror

$$k_s' = -k_s + k_1 + k_1' = -k_s$$

Figure 46.4. Schematic of experimental arrangement for DFWM.

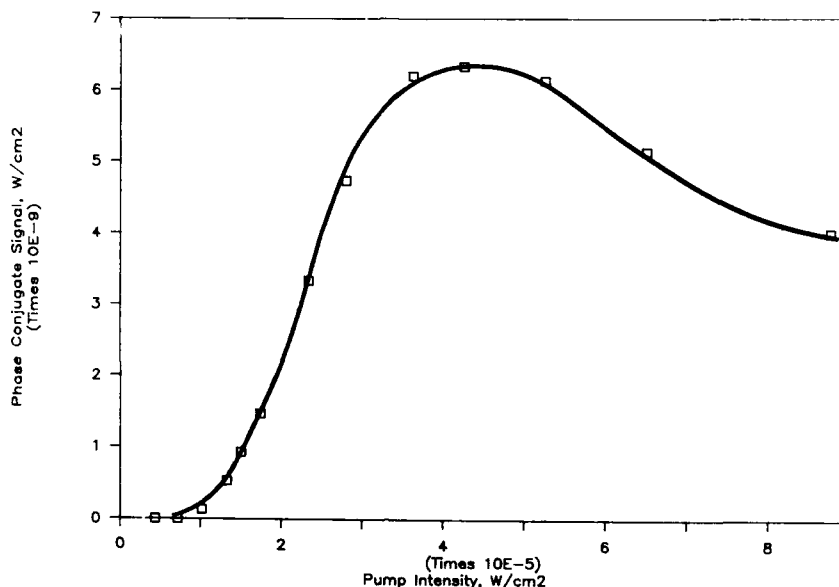


Figure 46.5. DFWM response for thin films of methyl red/ORMOSIL gels.

efficiencies on the order of  $1 \times 10^{-4}$  for CW-pumped methyl red were in good agreement with prior results [20]. A plot of the phase conjugate signal as a function of pump-probe intensity is given in Fig. 46.5. Sonogel-derived films containing a similar concentration of methyl red did not produce a detectable phase conjugate signal. The saturation behavior at higher pump levels in the ORMOSIL composite is indicative of the thermal nature of the grating, arising from methyl red's strong absorption at 514.5 nm.

#### 46.5. CONCLUSIONS AND SUMMARY

Sol-gel-derived silica and organically modified silicate composite gels show considerable promise as media for optical gain and nonlinear optical effects. Although silica gels eventually cracked as they retracted from the quartz cuvette walls during drying, they exhibited very strong laser behavior in a standard optical resonator and even demonstrated broadened spectral oscillation bandwidth. The gain curves of dye-doped silica gels exhibited a red shift in the peak gain wavelength with aging, but with little loss in the peak gain of coumarin-doped materials. Rhodamine 6G-doped samples were limited by losses arising from dimerization of the active species. Dye-doped ORMOSILS exhibited particularly promising behavior. A completely dried ORMOSIL composite gel doped with coumarin 153 gave a spectral gain curve very similar to that of the ethanol control solution. It is believed that MMA monomer bound

into the rigid backbone functionally solvates the organic dye molecules, while at the same time giving improved mechanical properties to the gel matrix. The ORMOSIL film containing methyl red dye demonstrated relatively efficient resonance-enhanced third-order effects. Phase conjugation via DFWM from a CW argon ion laser was observed at pump intensities as low as  $1 \times 10^{-5} \text{ W/cm}^2$ .

### ACKNOWLEDGMENTS

The authors appreciate the helpful discussions with Dr. Robert Devine and Professor Oscar Stafsudd. We are grateful for the support of this work by the National Science Foundation (DMR 87-06010).

### REFERENCES

1. D. Avnir, V. R. Kaufman, and R. Reisfeld, *J. Non-Cryst. Solids*, **74**, 395 (1985).
2. D. Avnir, D. Levy and R. Reisfeld, *J. Phys. Chem.*, **88**, 5956 (1984).
3. V. Kaufman and D. Avnir, *Langmuir*, **2**, 717 (1986).
4. T. Tani, H. Namikawa, K. Arai, and A. Makishima, *J. Appl. Phys.*, **58**, 3559 (1985).
5. A. Makishima and T. Tani, *J. Am. Ceramic Soc.*, **69**, 72 (1986).
6. E. J. A. Pope and J. D. Mackenzie, *Mater. Res. Soc. Bull.*, **12**, 29 (1987).
7. V. R. Kaufman, D. Avnir, D. Pines-Jojanski, and D. Huppert, *J. Non-Cryst. Solids*, **99**, 379 (1988).
8. D. I. Santos, M. A. Aegerter, C. H. Brito Cruz, M. Scarparo, and J. Zarzycki, *J. Non-Cryst. Solids*, **82**, 165 (1986).
9. J. C. Pouxviel, B. Dunn, and J. I. Zink, *J. Phys. Chem.*, **93**, 2134 (1989).
10. J. M. McKiernan, J. C. Pouxviel, B. Dunn, and J. I. Zink, *J. Phys. Chem.*, **93**, 2129 (1989).
11. G. Jones, W. R. Jackson, and A. M. Helpert, *Chem. Phys. Lett.*, **72**, 391 (1980).
12. D. Levy and D. Avnir, *J. Phys. Chem.*, **92**, 4737 (1988).
13. G. B. Altshuler et al., *Opt. Spectrosc. (USSR)*, **62**, 709 (1987).
14. B. Dunn, E. Knobbe, J. M. McKiernan, J. C. Pouxviel, and J. I. Zink, in: C. J. Brinker, D. E. Clarke, and D. R. Ulrich, *Better Ceramics Through Chemistry*, Vol. III.
15. E. T. Knobbe, J. D. Barrie, B. Dunn, and O. M. Stafsudd, submitted for publication.
16. Y. Kobayashi, Y. Kurokawa and Y. Imai, *J. Non-Cryst. Solids*, **105**, 198 (1988).
17. L. Esquivias and J. Zarzycki, in: J. D. Mackenzie and D. R. Ulrich, Eds., *Proceedings of the Third International Conference on Ultrastructure Processing*, pp. 255-270, Wiley, New York (1981).
18. C. A. Capozzi and L. D. Pye, *Proc. SPIE*, **970**, 135 (1988).
19. H. Schmidt and B. Seiferling, *Mater. Res. Soc. Symp. Proc.*, **73**, 739 (1986).
20. H. Fujiwara and K. Nakagawa, *Optics Comm.*, **66**, 307 (1988).

## OPTICAL PROPERTIES OF ARTIFICIALLY STRUCTURED METALS

CHARLES M. FALCO, J. M. SLAUGHTER,  
AND B. N. ENGEL

### 47.1. INTRODUCTION

Exploitation of modern vacuum technology and vapor deposition techniques for the synthesis of nearly flawless semiconductor superlattices has been highly successful [1]. The exponential growth in research on molecular beam epitaxy (MBE)-grown semiconductors can partially be attributed to the large number of practical devices arising from this research. Although research on metallic multilayers, superlattices, and other artificially structured metals dates back over 15 years, only recently has it reached the point where a number of emerging practical applications are beginning to drive the research in a similar fashion as is the case for semiconductors. Two examples of such applications for artificially structured metals are optics for soft X-rays [2, 3] and materials for magnetooptic data recording [4–6]. The emergence of additional such applications should continue to stimulate research in this field and should mean a strong future for both basic and applied research on metallic superlattices and other thin film structures.

In the case of artificially layered materials made partially or completely of metallic components, the absence of strong covalent bonding makes the growth of high-quality crystals more difficult than for semiconductors. However,

---

*Ultrastructure Processing of Advanced Materials.*

Edited by Donald R. Uhlmann and Donald R. Ulrich (deceased).

ISBN 0-471-52986-9 © 1992 John Wiley & Sons, Inc.

although highly perfect layers are required for semiconductors in order to exhibit phenomena of interest, it is important to realize that metals can tolerate greater levels of structural and chemical imperfections and still exhibit useful properties. Many physical properties of metals are not strongly affected by a less than perfect material, whereas semiconductor properties are seriously degraded by defects, impurities, and so on.

Although it is more difficult to grow a "perfect" metal crystal than it is a perfect semiconductor crystal, at the same time it is usually less important. For example, the multilayer mirrors for soft X-rays produced to date have polycrystalline and amorphous layers. Sputtering and evaporation techniques have been successful in producing these mirrors with precisely controlled layer thicknesses. Such mirrors can have very high reflectances for wavelengths greater than 100 Å [7]. Multilayers with desirable magnetooptic properties have been successfully produced by the same techniques.

However, for certain materials and physical properties great care must be taken in the fabrication of the metallic film. For example, the superconducting properties of Nb-containing superlattices are degraded by oxygen contamination. Because Nb is a strong oxygen getter, UHV and/or high deposition rates are required to keep oxygen contamination negligible in the growing film. In the case of X-ray mirrors designed for wavelengths  $\lambda < 80$  Å, the interfacial roughness inherent in amorphous and polycrystalline layers reduces the reflectance to such a degree that the mirrors often are not useful. It is for this wavelength region that MBE growth of X-ray multilayers may prove essential in the future.

## 47.2. MULTILAYER OPTICS FOR SOFT X-RAYS

### 47.2.1. Introduction

As discussed earlier, advances in microfabrication technology have made possible the development of multilayer thin films with near-atomic perfection. Coupled with the increasing availability of synchrotron light sources, this has generated a revival of interest in reflective X-ray optics, in particular for the soft X-ray regime [8]. The soft X-ray spectral region can be considered to lie between the "hard" X rays ( $\lambda < 10$  Å), conventionally used for materials analysis and medical radiology, and the vacuum ultraviolet ( $\lambda > 500$  Å).

Multilayer-based soft X-ray imaging devices can be extremely useful in many areas, such as astronomy, plasma diagnostics, and synchrotron optics. The high spatial resolution that can be expected is also of much interest in microelectronics fabrication. It has been estimated that by 1997 there will be 175 commercial synchrotron radiation sources dedicated to producing integrated circuits by X-ray lithography [9]. The high resolution is also important for microscopy with the additional advantage that live cells are observable with soft X-rays without the need for staining or processing. Mirrors and beam splitters

are needed for soft X-ray laser resonator cavities. Development of such lasers would generate a large number of additional applications requiring optical elements. Unfortunately, at X-ray wavelengths the refractive index approaches unity for every material. As a consequence, very little reflection or refraction occurs at any surface, as Röntgen himself found. In addition, absorption of X rays by all materials is significant. Thus, conventional lenses or mirrors are not possible at these wavelengths.

Because of the small normal-incidence reflectivity of all materials in the soft X-ray and X-UV regions of the electromagnetic spectrum, optical systems must be either grazing-incidence or based on interference or diffraction phenomena (multilayers or Fresnel zone plates [10]). Unlike grazing-incidence optics, these latter two phenomena allow for normal-incidence use. This geometry makes possible larger apertures for a given size device plus the avoidance of the severe aberrations, astigmatism in particular, associated with grazing incidence optics. Crystals have been used for a long time as optical elements for hard X-rays. Many attempts to fabricate artificial crystals as *Bragg reflectors* for soft X-rays have been made throughout this century [11]. More recently, and from a different perspective, multilayer structures were suggested by Spiller [12] with the specific aim of producing near-normal-incidence optical elements. Positive results were obtained soon thereafter [13].

Multilayers for this spectral region consist of layers of high-absorption materials separated by spacer layers of low-absorption materials. The nodes of the standing wave that result from interference of the incident and reflected waves are located within the high-absorption material. In accordance with an analog of Bragg's condition, for a many-period structure of this type, at a given incidence angle a particular wavelength will be selectively reflected *and* transmitted through the structure.

Because of the very small thicknesses of the layers required ( $< 100 \text{ \AA}$ ), very fine deposition control is necessary. Also, information about the microstructure of the films has to be taken into account, since the optical constants depend strongly on it in the X-UV region [14].

The choice of the pair of materials in a reflecting multilayer is primarily a compromise between pairs with the greatest difference in refractive indices and materials with the lowest absorptances [15]. However, other factors also must be taken into account. For example, the difficulty with which the materials can be deposited in the very thin layers required and the interfacial stability and microroughness that will result for the given pair of materials. The latter is often not known in advance.

Very high reflectances can be predicted for ideal multilayer structures in the soft X-ray region [16]. However, actual structures can deviate strongly from the ideal model. Film materials are not generally homogeneous, but can contain impurities and microvoids. The microstructure of the films depends on growth conditions. Oxidation and compound formation also can occur. The most important deviation from ideal multilayers is caused by interfaces that are not atomically sharp, but show diffusion and microroughness. All of these film



characteristics will affect the optical properties of the materials. Diffusion enhances transmission at the interfaces, reducing reflection, while (due to absorption) there is no compensating increase in the effective number of layers contributing to reflection.

Microroughness at the interfaces causes scattering losses. Such losses in multilayers for soft X rays are usually included in an *ad hoc* manner during the recursive calculation of reflectance [17]. This is accomplished by multiplying the reflectance amplitude coefficient for a given interface by the square root of the exponential decay factor

$$\exp \left[ - \frac{4\pi\sigma \sin \theta}{\lambda} \right]^2$$

where  $\sigma$  is the root mean square roughness value, and  $\theta$  is the glancing angle. This factor appears in diffraction theory of X-rays or neutrons by crystals when accounting for the effects of thermal motion of atoms in the lattice [18]. The same factor appears in the scalar treatment of electromagnetic wave scattering by single rough surfaces [19]. The computational scheme used to account for scattering losses in multilayers also can be modified to account for reflectance losses due to interdiffusion [20].

Any fabrication method for soft X-ray multilayers must meet rather demanding criteria, because layer thicknesses range from approximately 200 Å to a few angstroms. Angstrom-level constant deviations from the design thicknesses will displace the wavelength of peak reflectance. Random thickness errors of each layer of the order of 1% will produce nonnegligible reduction in reflectance.

In general, it is desirable to keep contamination and oxidation of the layers as low as possible. Damage to the sample surface during fabrication must be avoided, because it will increase microroughness. To date, multilayer reflectors for soft X-rays have been fabricated by electron-beam evaporation [21], sputtering [22], and laser evaporation [23]. These techniques can produce amorphous or polycrystalline layers with precisely controlled thicknesses and very low impurity levels. The major problem, particularly for small-layer thicknesses, is the lack of control over the interface roughness and microstructural properties.

#### 47.2.2. Fabry-Perot Interferometer for Soft X-Rays

We describe in this section preliminary results obtained with a Mo/Si Fabry-Perot etalon designed to work at near-normal incidence with 125-Å radiation. This spectral region is of interest, because it corresponds to the L-shell absorption edge of the spacer material (Si). For photon energies just below this L-edge, Si exhibits low absorptance, making it a suitable candidate as a spacer.

A Fabry-Perot interferometer is basically a pair of face-to-face semitransparent coatings separated by a transparent spacer. If the coatings are of high reflectivity, sharp interference lines will be observed at the output. The

sharpening of the lines is due to multiple-beam interference. If the spacer has a thickness that cannot be changed, then the interferometer is referred to as an etalon [24].

One of the samples was studied with grazing-incidence X-ray diffraction using 1.54-Å radiation. Fitting these data yields an interfacial roughness parameter for all interior layers of 6.25 Å. Similar Mo/Si samples produced in our sputtering system have been studied by transmission electron microscopy (TEM) [25]. The TEM images indicate that the Mo layers are polycrystalline with grains 100 to 300 Å wide and 30 Å thick with evidence for twinning in some grains. The Si is amorphous.

A plot of reflectivity as a function of photon energy (in eV) for an etalon sample deposited on float glass is shown in Fig. 47.1 [25]. Interference effects between the two reflectors, through the spacer, are clearly demonstrated. Using information obtained from characterization results, we have calculated theoretical curves. The theoretical curve corresponding to Fig. 47.1 is shown in Fig. 47.2. There is a good qualitative agreement between the calculated and measured results, but quantitative deviations exist. While characterization efforts on these samples are not completed, we do not expect dramatic changes of the calculated curves. We also have calculated the reflectivity of a 15-layer Mo/Si reflector with identical characteristics to those of the end mirrors assumed for Fig. 47.2. Figure 47.3 shows plot of the single mirror results

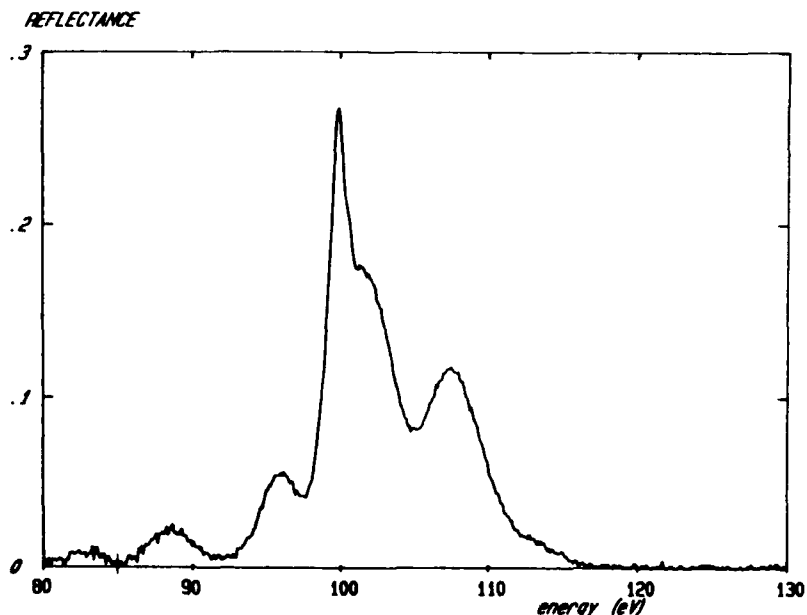


Figure 47.1. Measured reflectance at  $10^\circ$  from normal. The peak at 100 eV corresponds to  $\lambda = 124 \text{ Å}$ .

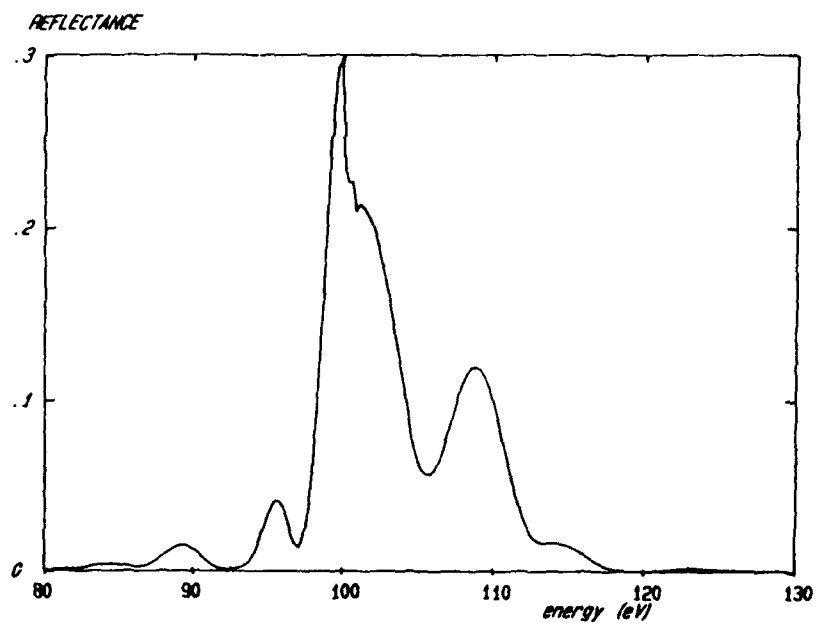


Figure 47.2. Calculated reflectance at 10° from normal. The calculation includes the effect of interfacial roughness.

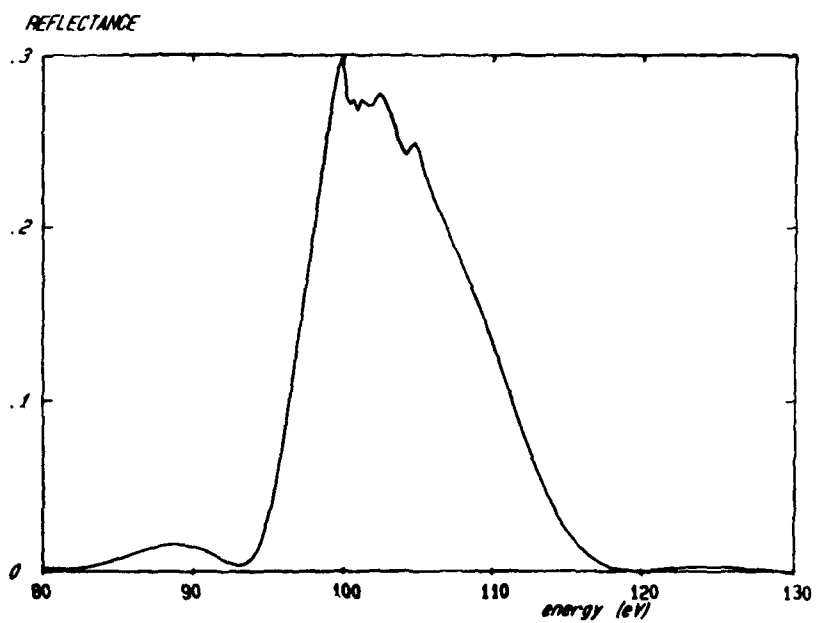


Figure 47.3. Calculated reflectance at 10° from normal for a 15-layer stack multiplied by 2. The calculation includes the effect of interfacial roughness. Note that this curve forms a rough envelope for Fig. 47.2.

multiplied by a factor of 2. This curve forms an approximate envelope for Fig. 47.2. After comparing Figs. 47.2 and 47.3, it is possible to appreciate interference minima and maxima more clearly.

It is apparent that the asymmetry of the reflectance maximum at 100 eV is the result of the coincidence of an interference maximum with a sharp feature in the behavior of the refractive index of Si. The resulting measured full width at half maximum (FWHM) of this peak is 6 Å; however, due to the effect of the absorption edge this result is not a simple property of the etalon. The intrinsic FWHM of the structure for energies below the Si L-edge may be as small as 2 Å. The measured peak reflectance at a 10° angle of incidence from the normal was 27%. Because the mirror was designed for normal incidence, this represents a lower limit on the actual value of the reflectance.

#### 47.2.3. Molecular Beam Epitaxy

MBE is a promising fabrication technique that has not previously been applied to multilayer X-ray optical coatings. This technique could allow the fabrication of essentially roughness-free interfaces in soft X-ray multilayers, substantially improving reflectances. With state-of-the-art MBE deposition methods, it is possible to reduce contamination and oxidation to negligible levels. In addition, the possibility of fabricating thousands of layers with the required tolerances would allow structures designed for the most difficult part of the soft X-ray spectrum,  $\lambda < 40$  Å.

MBE may make possible fabrication of fully crystalline multilayers. These could withstand the effects of high-intensity radiation much better than polycrystalline or amorphous ones, because recrystallization could not occur. Recrystallization can greatly increase surface roughness or even destroy the layered structure in a multilayer, as has recently been shown by Ziegler et al. [26] for carbon/metal multilayers.

The requirements for a MBE machine capable of producing such multilayers are different than for a GaAs machine. Some of the materials commonly used for X-ray optics are C or Si as the spacer and W, Mo, or another refractory metal as the high-absorption material. An MBE system for X-ray optics must be able to deposit these materials as well as a variety of other metals. Because the materials of interest have high melting points, MBE systems based on the new generation of Si MBE machines, such as the machine shown in Fig. 47.4, also are well suited to produce soft X-ray optics.

### 47.3. MAGNETOOPTICAL PROPERTIES OF ARTIFICIALLY LAYERED MATERIALS

#### 47.3.1. Introduction

The study of the magnetooptical properties of artificially layered magnetic thin films has seen increased activity in recent years as a result of the economic and technological feasibility of data storage media produced from these materials

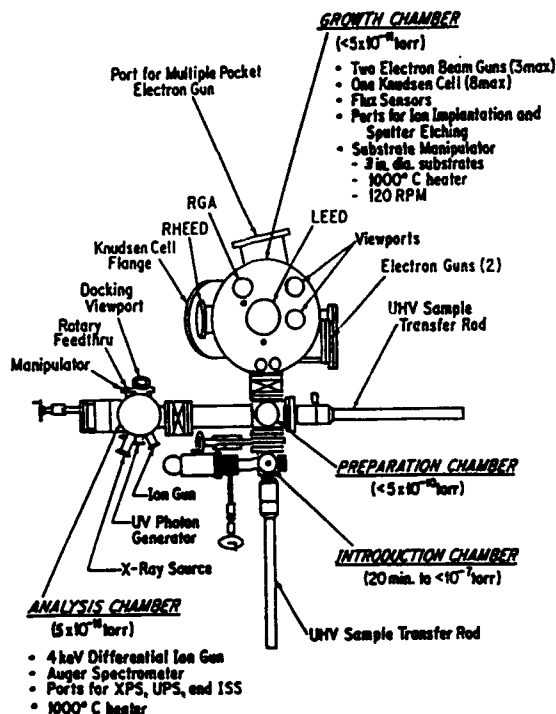


Figure 47.4. Schematic diagram of the silicon/metals MBE system used for epitaxial growth of silicon and refractory metals for X-ray optics (Perkin-Elmer Model 433S).

[27]. The emphasis of this section will be to discuss the differing effects and enhancements that these magnetic multilayers possess over those of bulk material and single-layer thin films.

Briefly, the term *magneto-optical* refers to the interaction of light with localized magnetic fields. One of the most commonly studied manifestations of this interaction is the Kerr effect. In the Kerr effect, linearly polarized light undergoes a rotation of its polarization upon reflection from a magnetic material. This rotation angle is proportional to the component of magnetization that is aligned with the direction of propagation. A parallel field yields a clockwise rotation, and conversely, an antiparallel field produces a counter-clockwise rotation. It is therefore possible to determine the magnetic state of a material by optical means. Schemes for magnetic storage of data and subsequent readout using the Kerr effect have been devised [20].

#### 47.3.2. Choice of Materials

From a technological standpoint, interest in magneto-optical multilayers has centered on two areas. Certain combinations of materials, such as Fe/Cu, exhibit [29] an enhanced Kerr rotation over certain optical frequencies when compared

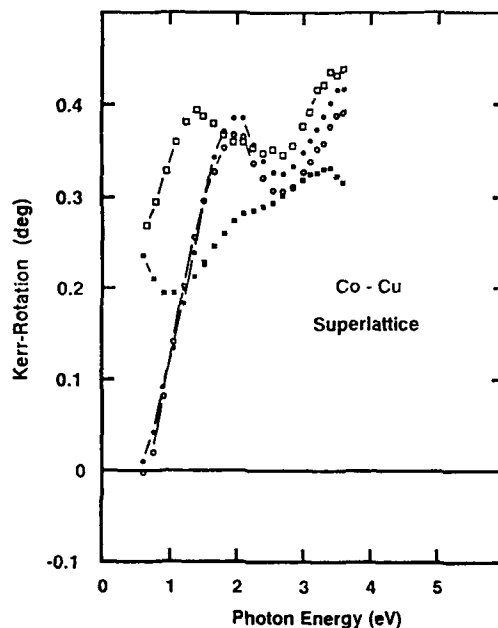
to pure Fe films. This enhancement can increase the signal-to-noise ratio of any data storage device. The other area of interest, although not necessarily distinct from the previous, is the observation of perpendicular magnetic anisotropy in certain material combinations such as Pd/Co multilayered films [30]. For the majority of thin films, the shape anisotropy tends to drive the magnetic easy axis into the plane of the film. With these newly discovered multilayered systems, the easy axis is normal to the plane, giving the possibility of much higher densities for magnetooptical recording.

### 47.3.3. Kerr Effect

The variation of the Kerr effect in multilayered materials can be divided into two groups. First, the choice of materials and their adjacent proximity in the multilayer stack can alter the magnetic and electronic behavior relative to bulk or single thin films. This effect is independent of layer period as evidenced in bilayer films. Second, the multilayer period can affect the magnetooptical properties as a result of the previously discussed proximity effects at the interfaces and from purely interference effects. In many systems, constructive interference of the reflected light from the individual layer interfaces can enhance the Kerr rotation signal [31]. This easily can be distinguished from intrinsic effects by any dependence on the angle of incidence [32]. The noninterference effects show a layer period dependence of the Kerr response independent of the incident angle and thus can be treated in the context of a homogeneous medium with different effective optical and magnetooptical constants as in the first group.

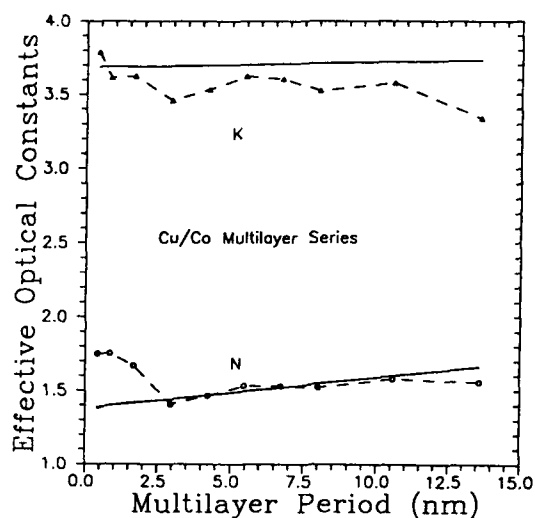
In the search for enhanced Kerr effect materials, large rotations were found in  $\text{UAs}_x\text{Se}_{1-x}$ ,  $\text{TmS}$ ,  $\text{TmSe}$ , and  $\text{Tm}_{1-x}\text{Eu}_x\text{Se}$  [33]. A relation of this enhancement with the plasma edge splitting of the conduction electrons was studied by Reim et al. [34]. Recently, a model was introduced by Feil and Haas [35] that explained the Kerr enhancement as resulting from a change in the dielectric constant due to the plasma resonance of the free-charge carriers. In a recent experiment, Katayama et al. [29] performed Kerr rotation spectroscopic measurements on a series of Fe/Cu bilayers. A pronounced enhancement was found at 560 nm corresponding to the plasma frequency of the conduction electrons of the Cu. The peak in the Kerr rotation reaches a maximum at a Fe thickness of 13 nm and then moves toward the longer wavelength side and decreases with the increase of Fe layer thickness. At the maximum, the enhancement is as high as a factor of 2 over that of bulk Fe. The authors effectively model this behavior by numerical calculation with the optical constants of Fe and Cu. Figure 47.5 displays the wavelength dependence of the Kerr rotation in a series of Co/Cu multilayers. Slight enhancement can be seen at the plasma frequency of Cu as in the Fe/Cu experiment. Exploitation of this effect by the choice of appropriate nonmagnetic materials as spacers in the multilayer stack clearly can improve data storage media.

It was demonstrated in the previously described experiments that the change

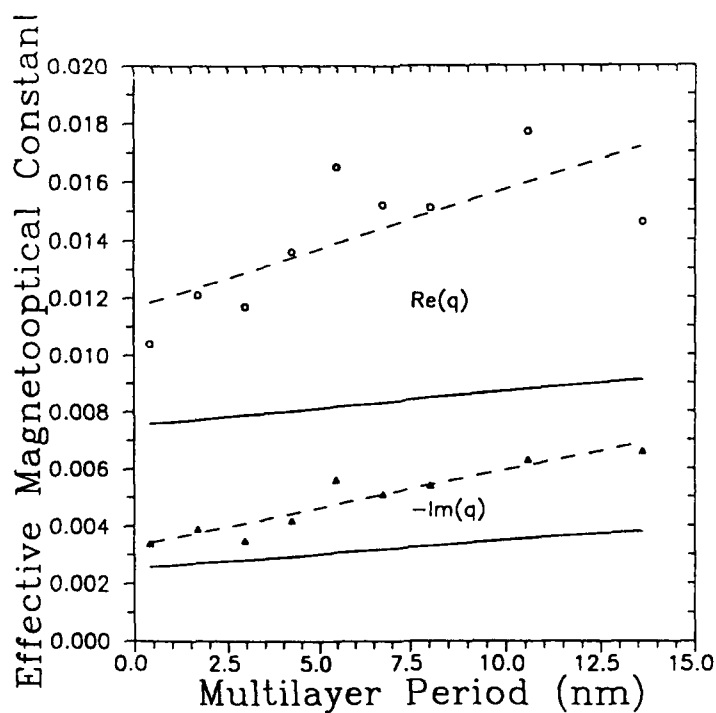


**Figure 47.5.** Wavelength dependence of Kerr rotation for Co/Cu multilayers. Open squares 2900 Å of pure Co; closed squares 72 Å Co/7 Å Cu,  $N = 8$ ; open circles, 73 Å Co/47 Å Cu,  $N = 8$ ; Closed circles, 72 Å Co/111 Å Cu,  $N = 8$ .

in the optical constants near the plasma resonance strongly affects the Kerr rotation. It is not clear, however, that the concept of a changing effective optical constant is legitimate in the case of multilayers where interference effects could dominate. An experiment to test whether a series of Cu/Co multilayers could be treated as a homogeneous medium in the context of optical response was recently performed by Deeter et al. [36]. Both the effective optical and magneto-optical constants were measured at 633 nm. Analysis of optical constants using both a homogeneous medium and exact multilayer model gives reasonable agreement indicating a lack of interference effects (see Fig. 47.6). However, for periods less than about 2.5 nm, there appears to be a definite increase in the experimentally determined values of  $n$  and  $k$ , which is not predicted by the theoretical calculations. One interesting result can be seen in Fig. 47.7 where both the real and imaginary effective magneto-optical constants are plotted versus the multilayer period. An enhancement in the overall magnitude of the constants above that predicted by theory is observed. In addition, the rate of increase with period is greater than that of the theory. An understanding of these phenomena not only provides for interesting physics, but technologically useful materials as well.



**Figure 47.6.** The dependence of the effective optical constants on the Cu/Co multilayer period. Theoretical values based on the bulk optical constants of Cu and Co are indicated by the solid lines.



**Figure 47.7.** The dependence of the effective real and imaginary parts of the magneto-optical constant ( $q$ ) on the Cu/Co multilayer period. Theoretical values based on the bulk optical constants of Cu and Co are indicated by the solid lines. The dashed lines are linear least-squares fits to the experimental data.



#### 47.4. SUMMARY

This Chapter has described two very different and potentially useful areas of research on artificially structured metals. Modern techniques allow an impressive amount of control in the growth and characterization of these multilayered systems. In the development of X-ray optics, controlled growth on the atomic level using the techniques of MBE is crucial for the elimination of interface roughness, which is extremely detrimental to reflectivity. In the area of magnetooptics, the observed Kerr effect enhancement and interface-induced magnetic anisotropy are interesting fundamental physics problems with obvious commercial benefits. Artificially layered materials hold great promise for future developments and studies of interesting phenomena in unique materials under very controlled conditions.

#### ACKNOWLEDGMENTS

The authors are pleased to acknowledge Professor Felix Fernandez, Patrick Kearney, Dr. Anna Lampis, and Dean Schultz for contributions to the X-ray optics effort and Merrit Deeter, Craig England, Professor Dror Sarid, and Robert Van Leeuwen for magnetooptics. This work is funded by the Air Force Office of Scientific Research Contract AFOSR-88-0010, by the AFOSR/ARO Joint Services Optics Program Contract F49620-88-C-0009, and by the University of Arizona's Optical Data Storage Center.

#### REFERENCES

1. See, for example, Chapter 6 by L. Esaki and Chapter 8 by G. H. Dohler of *The Technology and Physics of Molecular Beam Epitaxy*, E. H. Parker, Ed., Plenum, New York (1985).
2. See various articles in Multilayer Structures and Laboratory X-Ray Laser Research. *Procl. SPIE*, **688**, (1986).
3. See various articles in "Soft X-Ray Optics and Technology. *Proc. SPIE*, in press.
4. N. L. Sato, *Appl. Phys.*, **59**, 2514 (1986).
5. W. R. Bennett, D. C. Person, and C. M. Falco, in *Proceedings of the 4th Topical Meeting on Optical Data Storage*, Optical Society of America, Technical Digest Series, **10**, 127 (1987).
6. M. Tanaka, H. Yuzurihara, and T. Tokita, *IEEE Trans. on Magn.*, **26**, 1549 (1990).
7. Felix E. Fernandez, Charles M. Falco, P. Dhez, A. Khandar-Shahabad, L. Nevot, B. Pardo, J. Corno, and B. Vidal, *Appl. Phys. Lett.*, **51**, 880 (1987).
8. See various articles in *X-Ray Multilayers for Diffractometers, Monochromators, and Spectrometers*, F. E. Christensen, Ed., *Proc. SPIE*, **984** (1988).
9. A. Yanoff as quoted in: G. P. Williams, *Synchrotron Rad. News*, **1**, 21 (1988).
10. A. V. Baez, *J. Opt. Soc. Am.*, **42**, 756, (1952); *J. Opt. Soc. Am.*, **51**, 405 (1961).
11. J. H. Underwood and T. W. Barbee, *AIP Conf. Proc.*, **75**, 170 (1981).
12. E. Spiller, *Appl. Phys. Lett.*, **20**, 365 (1972).
13. See various articles in *AIP Conf. Proc.*, **75** (1981).

14. B. L. Henke and E. S. Ebisu, *Adv. X-Ray Anal.*, **17**, (1974) 152.
15. E. Spiller, *Appl. Opt.*, **15**, 2333 (1976).
16. A. E. Rosenbluth, Ph.D. Dissertation, University of Rochester (1983).
17. B. Vidal and P. Vincent, *Appl. Opt.*, **23**, 1794 (1984).
18. R. W. James, *The Optical Principles of the Diffraction of X-Rays*, Bell, London (1948).
19. P. Beckmann and A. Spizzichino, *The Scattering of Electromagnetic Waves from Rough Surfaces*, Pergamon, Oxford (1963).
20. E. Spiller and A. E. Rosenbluth, *Opt. Eng.*, **25**, 954 (1986).
21. E. Spiller, *AIP Conf. Proc.*, **75**, 124 (1981).
22. T. W. Barbee, *AIP Conf. Proc.*, **75**, 131 (1981).
23. S. V. Gaponov, E. S. Gluskin, S. A. Guser, B. M. Luskin, and N. N. Salashchenko, *Opt. Commun.*, **38**, 7 (1981).
24. M. Born and E. Wolf, *Principles of Optics*, 6th ed., p. 330, Pergamon Press, Oxford (1986).
25. F. E. Fernandez, C. Riedel, A. Smith, B. Edwards, B. Lai, F. Cerrina, M. G. Lagally, M. J. Carr, A. D. Romig, Jr., J. Corno, L. Nevot, B. Pardo, J. M. Slaughter, and C. M. Falco, in *X-Ray Multilayers for Diffractometers, Monochromators, and Spectrometers. Proc. SPIE*, **984**, 256 (1988).
26. E. Ziegler et al., *Appl. Phys. Lett.*, **48**, 1354 (1986).
27. G. A. N. Connell, *J. Magn. Magn. Mater.* **54-57**, 1561 (1986).
28. M. Kryder, *J. Appl. Phys.*, **57**, 3913 (1985).
29. T. Katayama, Y. Suzuki, H. Awano, Y. Nishihara, and N. Koshizuka, *Phys. Rev. Lett.*, **60**, 1426 (1988).
30. P. F. Carcia, A. D. Meinhalt, and A. Sunaetal, *Appl. Phys. Lett.*, **47**, 178 (1985).
31. P. Bernstein and C. Gueugnon, *IEEE Trans. Mag.*, **MAG-21**, 1613 (1985).
32. D. O. Smith, *Opt. Act.*, **12**, 13 (1965).
33. W. Reim, O. E. Hüsser, J. Schoenes, E. Kaldis, and P. Wachter, *J. Appl. Phys.*, **55**, 2155 (1984).
34. W. Reim, J. Schoenes, and O. Vogt, *Phys. Rev. B*, **29**, 3252 (1984).
35. H. Feil and C. Haas, *Phys. Rev. Lett.*, **58**, 65 (1987).
36. M. N. Deeter, D. Sarid, C. D. England, W. R. Bennett, and C. M. Falco, in press.

## SOL-GEL SYNTHESIS OF PLANAR OPTICAL WAVEGUIDES AND INTEGRATED COMPONENTS

RONALD L. RONCONE, LAURA A. WELLER-BROPHY,  
AND BRIAN J. J. ZELINSKI

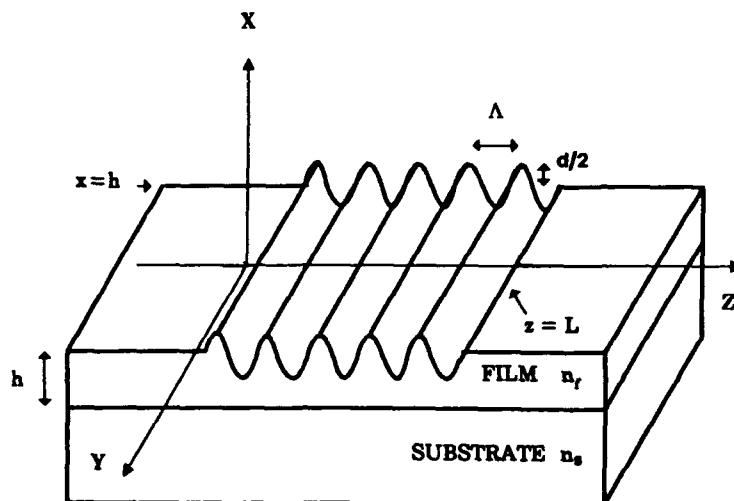
### 48.1. INTRODUCTION

The low-loss interconnection of optical fibers, planar waveguides, laser diodes, and optical detectors is a central issue in the successful development and routine implementation of fiber optic networks and integrated optic circuits. Surface corrugation waveguide gratings such as that illustrated schematically in Fig. 48.1 have been demonstrated successfully as efficient and rugged interconnects between planar waveguides and external optical components, sources, and detectors. In addition, waveguide gratings can provide very efficient coupling (near 100%) between guided-wave components, detectors, and diode lasers in planar integrated optic circuits, such as wavelength division multiplexers [1] and magneto-optic read/write heads [2].

The grating couplers required for the efficient interconnection of planar waveguides, laser sources, and optical fibers typically are written directly by electron beam into suitable waveguide or resist materials [3]. Such processes are quite time-consuming (greater than 1 hr of write time for each grating component) and typically are limited to the production of grating components with apertures no larger than 1 mm<sup>2</sup>. Given these limitations of the electron-beam

---

*Ultrastructure Processing of Advanced Materials.*  
Edited by Donald R. Uhlmann and Donald R. Ulrich (deceased).  
ISBN 0-471-52986-9 © 1992 John Wiley & Sons, Inc.



**Figure 48.1.** Illustration of the planar waveguide with surface-relief grating coupler. The parameters  $h$ ,  $d$ ,  $L$ , and  $\Lambda$  denote film thickness, corrugation peak-to-trough depth, grating length, and grating period, respectively. Typical values for these parameters are  $h = 0.2 \mu\text{m}$ ,  $d = 50 \text{ nm}$ ,  $L = 1\text{--}5 \text{ mm}$ , and  $\Lambda = 0.3\text{--}2 \mu\text{m}$ . The rulings of the grating may assume more complex shapes and orientations given the exact function of the grating coupler.

process, a number of other techniques have been proposed for the fabrication of waveguide gratings. These include standard lithographic and holographic methods, waveguide holography, and pattern embossing in sol-gel films. Of these various fabrication techniques, only the last encompasses both the deposition of the thin-film waveguide as well as the generation of complex grating patterns.

The application of the sol-gel process to the fabrication of step-index planar waveguides was first reported by Ulrich and Weber in 1972 [4]. Using a commercially available sol-gel solution, they fabricated lead-silica waveguiding films of refractive index 1.646 and thickness  $0.9 \mu\text{m}$ . The attenuation of the guided  $\text{TE}_0$  mode was measured to be  $0.3 \text{ dB/cm}$  at  $\lambda = 1.064 \mu\text{m}$ . The sol-gel process also has been used by Lukosz and Tiefenthaler [5] and Heuberger and Lukosz [6] in the fabrication of  $\text{SiO}_2\text{--TiO}_2$  waveguiding films. The refractive indices of the resulting films were readily varied between 1.6 and 1.9 through adjustment of the relative amounts of the liquid precursors used. The waveguides were reported to have losses of less than  $1 \text{ dB/cm}$  in the visible portion of the spectrum. Similar results have been obtained in our laboratories using premixed  $\text{SiO}_2\text{--TiO}_2$  solutions manufactured by Emulsitone [7].

The introduction of a surface deformation at the sol-gel film/air interface typically is done prior to heat treatment. At this stage, it is likely that the porous structure of the film allows the surface to be deformed simply by embossing. Investigations of this technique have been reported by Lukosz and Tiefenthaler

in 1983 [5] and Heuberger and Lukosz in 1986 [6]. Surface-relief gratings having 1200, 2400, and 3600 lines/mm were fabricated on  $\text{SiO}_2\text{-TiO}_2$  waveguides using the sol-gel process in combination with an embossing technique. Following heat treatment of the embossed films, it was found that the gratings experienced a shrinkage of approximately 75% in depth with no lateral shrinkage noted. Final peak-to-trough grating depths were on the order of 5 nm.

The shrinkage of surface-relief patterns embossed into  $\text{B}_2\text{O}_3\text{-SiO}_2$  sol-gel films more recently has been addressed by Tohge et al. [8]. Through the addition of varying amounts of polyethylene glycol (PEG), it was possible to control the degree of film shrinkage to between 30 and 70% of the original thickness. Gratings were fabricated having 500 lines/mm with final peak-to-trough depths on the order of 50 nm.

In this Chapter, we report on the experimental characterization of the shrinkage of surface-relief gratings embossed in  $\text{SiO}_2\text{-TiO}_2$  thin film waveguides as a function of heat treatment. In the work reported here, we focus our attention on premixed  $\text{SiO}_2\text{-TiO}_2$  solutions available from Emulsitone. We have found that such solutions, although not developed for use as optical waveguides, can successfully produce low-loss ( $< 1$  dB/cm) planar waveguides incorporating embossed surface-relief features. The procedures used in the fabrication of the planar waveguides and embossed surface-corrugation gratings are described in section 48.2.

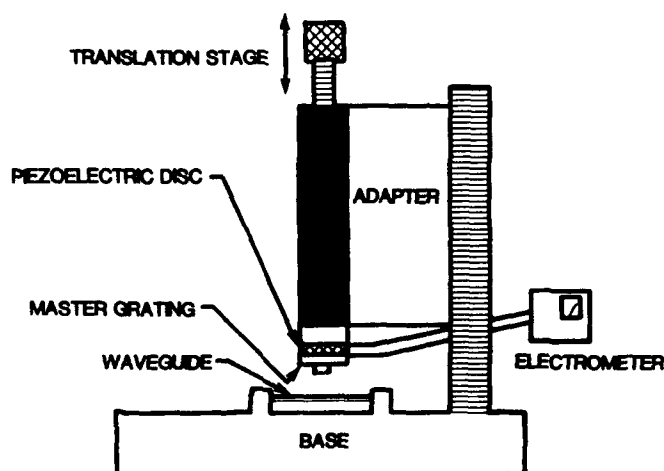
The shrinkage of the embossed features is measured optically by monitoring the diffraction efficiency of the surface-corrugation gratings at various stages throughout the heat treatment. As described in sections 48.3 and 48.4, we found the lateral dimension of the grating to remain constant after heating to  $500^\circ\text{C}$ , with the grating depth shrinking to approximately 57% of its pre-heat-treatment depth. Embossed surface-relief gratings of 625 lines/mm with final peak-to-trough depths ranging from 13 to 20 nm were successfully fabricated on densified  $\text{SiO}_2\text{-TiO}_2$  planar waveguides.

## 48.2. WAVEGUIDE FABRICATION AND EMBOSSING PROCEDURES

Sol-gel thin films are deposited using a static-flood, spin-coat technique. Standard microscope slide substrates are carefully cleaned prior to solution-deposition. The slides initially are rinsed in deionized (DI) water to remove gross particulates. Following this rinse, they are placed in a solution of DI water and Micro cleaner (International Products Corp., Trenton, N.J.); this removes most of the remaining particulates. Surface films are removed by gently rubbing the glass surfaces with a gloved finger and rinsing several times with fresh DI water. This surface film removal is completed with a 5-min sonic cleaning in a mixture of DI water and Micro. After several thorough rinses with DI water, the slides again are sonic cleaned in a 95% ethanol solution for an additional 5 min. The final step in the cleaning process is a bake at  $200^\circ\text{C}$  for 30 min to remove all

residual traces of water and ethanol. After cooling to room temperature, the substrates are ready for sol-gel film deposition. The microscope slides are mounted into a customized chuck (Headway Research Corp.), consisting of a 4-in.-diameter plate with a depression into which the slide is inserted. In this position, the surface of the slide and chuck are coplanar. Approximately 2 ml of sol-gel solution (Emulsitone type A titaniumsilica film) is deposited onto the stationary slide, flooding the slide/chuck surface. The chuck is ramped immediately to between 1000 and 1500 rpm, with the piece spun for 1 to 4 min. This spin-coat procedure is carried out in a Class 1000 environment and a typical relative humidity of 25%. Coatings deposited in this environment usually demonstrate unwanted adhesion of the master grating during the subsequent emboss procedure. It was found that the addition of approximately 1 in. of water in the base of the spin bowl raises the relative humidity during the spin-coat deposition and significantly reduces the adhesion of the master to the film surface. It is possible that this increase in relative humidity increases crosslinking in the film, reducing the reactivity of the sol-gel interface with the aluminized grating master. The use of this spin-coat procedure produces thin-film layers with final densified thicknesses of approximately 120 nm, with a refractive index of  $1.80 \pm 0.03$  at  $\lambda = 632.8$  nm. Such thin-film waveguides support the lowest-order TE- and TM-guided modes, with losses on the order of 1 dB/cm [7].

Immediately following spin-coating, the porous films are placed in the embossing apparatus, illustrated schematically in Fig. 48.2. The master grating, a commercially available aluminized blazed grating with a  $1.66\text{-}\mu\text{m}$  period, is lowered into contact with the film surface. A piezoelectric disc sandwiched



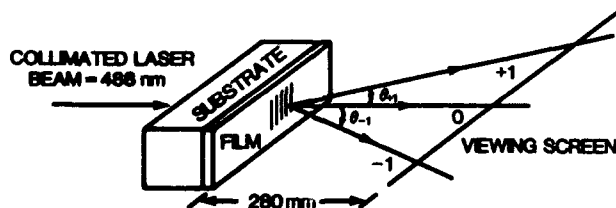
**Figure 48.2.** Schematic of embossing apparatus. The master grating of 625 lines/mm is pressed into a spin-coated waveguiding film. The voltage output of the piezoelectric disc is converted to embossing pressure.

between the master grating and the translation stage senses the pressure with which the grating is pressed into the planar waveguide. This disc produces a voltage that is proportional to the pressure applied over the  $3 \times 3\text{-mm}^2$  surface area of the grating master. The voltage is converted easily to pressure given the physical and materials parameters of the piezoelectric element; the actual pressures used during the embossing procedure ranged from  $2 \times 10^6$  to  $5 \times 10^6 \text{ N/m}^2$ . Embossing times ranged from 1 to 6 min, producing no reproducible difference in the final depth of the embossed surface-relief pattern.

Following the embossing procedure, the depth and periodicity of surface-relief grating pattern imparted to the film are evaluated optically through measurement of the grating diffraction efficiencies with the gratings used in transmission. This measurement procedure is described in section 48.3. After evaluation, the patterned films are placed into a Transtemp muffle furnace with the temperature ramped at  $5.7^\circ\text{C/min}$  to a final soak temperature of  $200^\circ\text{C}$ . The slides are baked at this temperature for 60 min and allowed to cool in the furnace at a rate of  $3.8^\circ\text{C/min}$ . The grating depth and period are remeasured optically at this point to monitor the degree of pattern shrinkage following the low-temperature bake. The films are returned to the cool furnace with the temperature ramped at  $12^\circ\text{C/min}$  to a soak temperature of  $500^\circ\text{C}$ . The films are baked at this temperature for 25 min and left in the furnace to cool to room temperature at a ramp rate of  $8^\circ\text{C/min}$ . After cooling the grating period and depth are measured one final time to assess total pattern shrinkage.

### 48.3. OPTICAL EVALUATION

The modulation depths and periods of the embossed surface-relief gratings were monitored through measurements of the grating diffraction efficiencies with the samples used in transmission. These measurements were made as illustrated in Fig. 48.3. The collimated, *p*-polarized beam of a 488-nm Ar laser source, normally incident to the substrate and slightly underfilling the grating region, is diffracted by the surface corrugation grating into a number of orders. The



**Figure 48.3.** Diagram of the experimental setup used to measure grating period and diffraction efficiency. A collimated Ar laser beam, incident normal to the substrate, fills the grating region and is diffracted into a number of orders. The angular separation of the zero-order and the plus and minus first orders is represented by  $\theta_{+1}$  and  $\theta_{-1}$ .

grating period is determined by measuring the angular distribution of the diffracted light. With  $\lambda = 488$  nm, and first-order diffraction lobes measured at  $\theta_{+1} = 17.49^\circ$  and  $\theta_{-1} = 16.72^\circ$ , the average grating period is found to be  $1.66 \mu\text{m}$  using the grating equation  $\Lambda \sin \theta = m\lambda$ . It was found that the grating period remained unchanged throughout the fabrication procedure with no measurable lateral shrinkage.

Shrinkage in the depth of the grating was monitored through the measurement of grating diffraction efficiencies at various stages of heat treatment. Diffraction efficiencies are determined by dividing the measured optical power in the plus and minus diffracted orders by the power incident on the grating in the film layer. The incident power in the film layer is approximated as  $P_i = P_0(1 - R_1)(1 - R_2)$ , where  $P_0$  is the power incident at the substrate, and  $R_1$  and  $R_2$  are the intensity reflection coefficients of the substrate/air and substrate/film interfaces. This approximation neglects coherent interactions between multiple reflections in the substrate material and film layer. With the refractive indices of the substrate and film measured to be  $n_s = 1.51$  and  $n_f = 1.8$  at  $\lambda = 632.8$  nm, the power incident in the film layer is approximated by  $P_i = 0.951P_0$ .

By assuming an approximately sinusoidal grating modulation, the peak-to-trough grating modulation depth can be calculated from

$$d = \frac{\sqrt{\eta_{\pm 1}} \lambda \sqrt{2}}{|\bar{d}_{l+1}|(n_f - n_c)2\pi} \quad (1)$$

where  $d$  is the grating modulation depth,  $n_f$  and  $n_c$  are the film and cover indices,  $\lambda$  is the wavelength,  $\eta$  is the diffraction efficiency of the first diffracted orders, and  $|\bar{d}_{l+1}|$  is the first-order Fourier coefficient describing the surface corrugation [6]. For sinusoidal corrugations this factor is equal to 0.5.

As the master grating consisted of blazed rather than sinusoidal corrugations, the plus and minus first-order diffraction efficiencies were not equal, with the ratio  $\eta_{+1}/\eta_{-1}$  varying from 0.59 to 0.77. Rather than calculate the grating modulation depth corresponding to each diffracted order, we have used the average of the two first-order diffraction efficiencies in this calculation. This is done in order to average the influence of the grating shape on the calculation of the grating depth. In later studies, the influence of grating shape will be more closely monitored.

#### 48.4. EXPERIMENTAL RESULTS AND DISCUSSION

Table 48.1 displays the spin-coating and embossing times, average diffraction efficiencies, and peak-to-trough grating modulations depths for 10 samples. The grating period remained fixed at  $1.6 \mu\text{m}$  throughout all stages of heat treatment. All 10 samples were embossed using pressures from  $2 \times 10^6$  to  $5 \times 10^6$  N/m<sup>2</sup>. Although the measured data indicate that embossing times may



TABLE 48.1. Averaged Diffraction Efficiencies Measured Prior to Heat Treatment ( $\eta_0$ ), After the 200°C Bake ( $\eta_{200}$ ), and After the Full Heat Treatment ( $\eta_{500}$ )

Sample	Spin Time (min)	Emboss Time (min)	$\eta_0$	$\eta_{200}$	$\eta_{500}$
1	2	2	<sup>a</sup>	0.00255	0.00152
2	2	2	<sup>a</sup>	0.00195	0.00156
3	2	2	<sup>a</sup>	0.00354	0.00263
4	2	6	<sup>a</sup>	0.00353	0.00281
5	2	1	<sup>a</sup>	0.00229	0.00145
6	2	3	0.00615	0.00283	0.00206
7	2	2	0.00610	0.00265	0.00203
8	4	1	0.00355	0.00177	0.00118
9	4	3	0.00503	0.00230	0.00177
10	2	2	0.00415	0.00194	0.00123

<sup>a</sup>Quantities correspond to diffraction efficiency measurements taken in the presence of spurious room light. These measurements are not included here.

influence the grating diffraction efficiencies, more data are needed to formulate a reliable correlation. The embossing pressures, which were not accurately recorded for each sample, and the spin time may also influence the quality of the grating replication and thus the grating efficiencies. Future work will investigate each of these factors.

The measured data in Table 48.1 are used to calculate peak-to-trough grating depths using Eq. 1. Uncertainties of  $\pm 0.0003$  in the average diffraction efficiencies (arising from measurement of optical powers) correspond to uncertainties of  $\pm 0.75$  nm in the calculated grating depths. The rather large range of grating depths over the 10 samples may be due to the variations in embossing times, embossing pressures, and the spin times, as noted above. The shrinkage factors simply are ratios of the grating depths at the various stages of heat processing with  $SF_{a/b} = d_a/d_b$ . The calculated results are shown in Table 48.2. The average shrinkage factors for the last five samples are  $SF_{200/0} = 0.680$ ,  $SF_{500/200} = 0.843$ , and  $SF_{500/0} = 0.573$ . These values provide an indication of the shrinkage rates occurring during each phase of the heat processing.

In addition to the gratings embossed in Emulsitone sol-gel films, one grating was fabricated in an  $\text{SiO}_2$ - $\text{TiO}_2$  solution developed by Dale et al. from the Department of Materials Science and Engineering, University of Arizona [9]. The sol-gel material was filtered to  $0.2\ \mu\text{m}$  and spin-coated onto a glass substrate at 1000 rpm. The same aluminized grating used in the previous embossing trials was again employed as the master with a 3-min embossing time. Heat treatments were the same as described above. The first-order diffraction efficiencies of the fully heat-processed gratings/films were  $\eta_{+1} = 1.92\%$  and  $\eta_{-1} = 2.16\%$  with the average value of  $2.04\%$ . These initial data indicate that the final embossed grating had a peak-to-trough depth of

TABLE 48.2. Calculated Peak-to-Trough Grating Depths Using the Data from Table 48.1

Sample	$d_0$ (nm)	$d_{200}$ (nm)	$d_{500}$ (nm)	$SF_{200/0}$	$SF_{500/200}$	$SF_{500/0}$
1	<i>b</i>	19.37	14.95	<i>b</i>	0.772	<i>b</i>
2	<i>b</i>	16.92	15.15	<i>b</i>	0.895	<i>b</i>
3	<i>b</i>	22.82	19.65	<i>b</i>	0.861	<i>b</i>
4	<i>b</i>	22.77	20.31	<i>b</i>	0.892	<i>b</i>
5	<i>b</i>	18.35	14.60	<i>b</i>	0.796	<i>b</i>
6	30.08	20.39	17.41	0.678	0.854	0.579
7	29.96	19.74	17.26	0.659	0.874	0.576
8	22.85	16.11	13.18	0.705	0.818	0.577
9	27.26	18.39	16.11	0.675	0.876	0.591
10	24.71	16.87	13.42	0.683	0.795	0.543

<sup>b</sup>Quantities correspond to diffraction efficiency measurements taken in the presence of spurious room light. These measurements are not included here.

approximately 39 nm. The synthesis of this sol-gel solution is currently being modified to produce very low-loss waveguiding films while preserving the film embossibility.

## 48.5. CONCLUSION

This Chapter has described the embossing of surface-relief gratings of 625 lines/mm into  $\text{SiO}_2$ - $\text{TiO}_2$  dielectric, step-index, planar optical waveguides through the use of a sol-gel process. The fully heat-processed gratings exhibit peak-to-trough depths ranging from 13 to 20 nm, with approximately 57% shrinkage relative to the grating depths prior to heat treatment. The grating period remains constant through heat processing.

Although the bulk of the data presented here is for a commercially available sol-gel solution, we have obtained very encouraging preliminary results on waveguides and embossed gratings fabricated using solutions synthesized on site. These customized solutions promise the control over refractive index, chemical purity, film losses, and embossibility that cannot be achieved using commercially available solutions. Although much remains to be done in understanding and optimizing waveguide losses, film embossibility, and the mechanisms driving them, the sol-gel process offers a flexible and economically attractive alternative to conventional techniques for the fabrication of optical waveguides incorporating surface-relief integrated optic components.

## ACKNOWLEDGMENTS

This work has been supported by the Optical Data Storage Center at the Optical Sciences Center of the University of Arizona. We wish to acknowledge the Headway Research Corporation for their generous donation of a customized, automated, spin-deposition system. We also thank Mr. Walter Dunkel for his assistance in sample preparation.

## REFERENCES

1. J. D. Spear-Zino, R. R. Rice, J. K. Powers, D. A. Bryan, and D. G. Hall, *Proc. SPIE*, **239**, 293 (1980).
2. S. Ura, T. Suhara, H. Nishihara, and J. Koyama, *J. Lightwave Technol.*, **LT-4**, 913-918 (1986).
3. Y. Handa, T. Suhara, H. Nishihara, and J. Koyama, *Appl. Opt.*, **19**, 2842 (1980).
4. R. Ulrich and H. P. Weber, *Appl. Opt.*, **11**, 428-434 (1972).
5. W. Lukosz and K. Tiefenthaler, *Opt. Lett.*, **8**, 537-539 (1983).
6. K. Heuberger and W. Lukosz, *Appl. Opt.*, **25**, 1499-1504 (1986).
7. L. Weller-Brophy, B. Zelinski, and R. Roncone, Sol-gel waveguide and grating fabrication, in: *Optical Data Storage Center, September 15, 1988 Quarterly Report*, pp. 68-75, Optical Sciences Center, University of Arizona.
8. N. Tohge, A. Matsuda, T. Minami, Y. Matsuno, S. Datayame, and Y. Ikeda, *J. Non-Cryst. Solids*, **100**, 501-505 (1988).
9. G. W. Dale, H. H. Fox, B. J. J. Zelinski and L. A. Weller-Brophy, Better Ceramics Through Chemistry IV, ed. B. J. J. Zelinski, C. J. Brinker, D. E. Clark and D. R. Ulrich, *Mater. Res. Soc. Symp. Proc.*, **180**, 371 (1990).

## CHEMICAL SYNTHESIS OF LANTHANUM SESQUISULFIDE POWDERS FOR INFRARED OPTICAL APPLICATIONS

PRASHANT N. KUMTA AND SUBHASH H. RISBUD

### 49.1. INTRODUCTION

The application of infrared radiation for detection of low-temperature objects is the basis for the need for optical windows that can transmit all the way into the far infrared region. The spectral emittance curves from a black body follow the familiar Wien's displacement law and show that to detect objects at room temperature the 8 to 14- $\mu\text{m}$  infrared window is most suitable [1]. These requirements are the foundation for the major interest in the fabrication of materials that transmit in the infrared wavelength range and thus play a major role in the development of future target acquisition and weapon aiming devices, surveillance equipment, alerting devices, and missile homing seekers [2]. Materials for these applications require erosion resistance, high hardness and strength with good thermal shock resistance. Oxides possess the required mechanical properties because of the strong M-O bond, but are limited in infrared transmission due to the high fundamental vibration frequencies (especially when M is a light element) giving rise to absorption in the range of 8-12  $\mu\text{m}$ . A massive anion is desirable to promote infrared transmission

*Ultrastructure Processing of Advanced Materials.*

Edited by Donald R. Uhlmann and Donald R. Ulrich (deceased).

ISBN 0-471-52986-9 © 1992 John Wiley & Sons, Inc.

requiring a search for nonoxide ceramics [3,4]. Table 49.1 lists the currently interesting infrared materials.

A materials study to find an advanced optical window material better than ZnS for the 8 to 12- $\mu$ m airborne application led to the understanding that the alkaline earth-rare earth ternary compounds of the formula  $AB_2S_4$  (particularly  $CaLa_2S_4$ ) would be ideal candidate materials for far infrared applications. Preliminary studies had indicated materials in this group had good transmission up to 14  $\mu$ m, low free-electron absorption, and high melting point and formed in the cubic symmetry ( $Th_3P_4$  type). The large coefficient of thermal expansion of  $CaLa_2S_4$  ( $14.7 \times 10^{-6}/^\circ C$ ) makes this material inferior compared to ZnS, although its hardness and Young's modulus are better than those of ZnS, suggesting a better performance in rain erosion environments (see Table 49.1). Savage et al. [5] worked on the solid solution region in the phase diagram between  $CaLa_2S_3$  and  $La_2S_3$  with the hope of finding other infrared-transmitting compositions. In their work, they found that increasing the amount of  $La_2S_3$  the materials gave the same infrared transmission with a lower thermal expansion coefficient material. Table 49.1 shows the properties reported for  $\beta$ - $La_2S_3$ . As can be seen, the  $\beta$ - $La_2S_3$  transmits only up to 10  $\mu$ m being an oxysulfide. These data suggest that  $La_2S_3$  has the potential to be an infrared material if the cubic ( $\gamma$ ) form can be obtained as shown in our recent work [6]. Takeshita et al. [7] have also shown that  $\gamma$ -phase lanthanum sulfide solid solution alloys can be made by direct combination of stoichiometric amounts of lanthanum metal and elemental sulfur in a quartz ampoule at low temperatures ( $< 800^\circ C$ ). The reaction product thus obtained was the low-temperature  $\alpha$  phase. This  $\alpha$ -phase powder was then ground and mixed with  $LaH_3$  prepared by hydriding the lanthanum metal. The mixture of  $LaH_3$  and  $La_2S_3$  was then heated under a pressure of 6000 psi at  $1450^\circ C$  for 2 hr to give the desired  $\gamma$  phase

TABLE 49.1. Some Properties of Currently Interesting Infrared Materials

Material	Transmission Range ( $\mu$ m)	Thermal Expansion ( $10^{-6}/^\circ C$ )	Melting Point ( $^\circ C$ )	Hardness (kg/mm <sup>2</sup> )	Young's Modulus (GPa)
ZnS <sup>a</sup>	0.5-12	7.5	1700	250	75
ZnSe <sup>a</sup>	0.6-14	7.6	1520	100	60
Ge <sup>a</sup>	2-16	6.0	936	700	100
Si <sup>a</sup>	1-10	4.0	1420	1150	190
GaAs <sup>a</sup>	1-16	5.7	1240	750	85
GaLa <sub>2</sub> S <sub>4</sub> <sup>a</sup>	0.5-14	15.0	1800	600	96
$\beta$ -La <sub>2</sub> S <sub>3</sub> <sup>b</sup>	0.5-10	10.0	2100	670	—
$\gamma$ -La <sub>2</sub> S <sub>3</sub>	—	—	2100	—	—

<sup>a</sup>Values from Ref. 13.

<sup>b</sup>Value from Ref. 14.

in a densification method known as the *pressure-assisted reaction sintering*. The optical properties of dense ceramics pressed from these powders were not reported in the work of Takeshita et al. In the present work various synthesis routes for the preparation of binary lanthanum sesquisulfides are presented. The focus is primarily on low-temperature synthesis of cubic  $\gamma$ - $\text{La}_2\text{S}_3$  powders for eventual fabrication of optically transmitting infrared material.

## 49.2. EXPERIMENTAL PROCEDURE

Three different processing routes were attempted in the preparation of single-phase lanthanum sulfide. All the three routes consisted of first precipitating the amorphous precursor either at room temperature or at 130°C followed by heat treatment in hydrogen sulfide at 1000°C. The procedures followed for the three powders are labeled type 1, type 2, and type 3, respectively, in the following.

*Type 1.* This procedure consisted of preparing a 0.02 *M* solution of lanthanum alkoxide (Alfa Products, Mass.) in dry benzene obtained using standard analytical distillation procedures. Sulfidization of the resultant clear solution was carried out at room temperature by bubbling hydrogen sulfide into the alkoxide solution. The effect of hydrogen sulfide is seen immediately when the clear solution becomes turbid. The reaction was allowed to proceed for about 2 hr to ensure complete precipitation. The resultant powders, pale yellow in color, were washed repeatedly in benzene and carbon disulfide and then dried in a nitrogen atmosphere to ensure evaporation of the solvents. Figure 49.1 shows the schematic of the processing steps.

*Type 2.* In this procedure lanthanum nitrate hexahydrate (Alfa Products) was dissolved in propylene carbonate, followed by the addition of *tert*-butyl sulfide as the sulfidizing agent. Refluxing of the entire solution at a temperature of 130°C for about 2.5 hr resulted in the formation of pale yellow powders that were filtered and collected.

*Type 3.* In this process, lanthanum alkoxide (Strem Chemicals, Dexter Industrial Park, Mass.) was obtained in solution in dry toluene obtained by following standard distillation procedures. To this solution *tert*-butyl sulfide was added as the sulfidizing agent, and the entire reaction was allowed to proceed for 24 hr. Precipitation occurs at a temperature of 130°C, the product appearing light brown in color. The resultant powder was collected by filtering. Figure 49.2 shows the schematic of these two processes.

Heat treatment of the as-prepared powders was performed in an atmosphere of  $\text{H}_2\text{S}$ . Chemical analyses of the as-prepared type 1 powders conducted by Galbraith Laboratories (Knoxville, Tenn.) indicated the presence of La, S, and hydrocarbons and oxygen was estimated as the balance. Types 2 and 3 precursor powders were not analyzed chemically and were directly subjected to

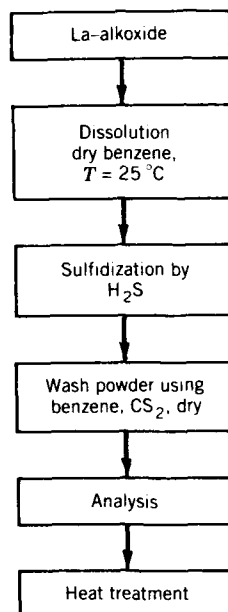


Figure 49.1. Schematic flow chart for type 1 powders.

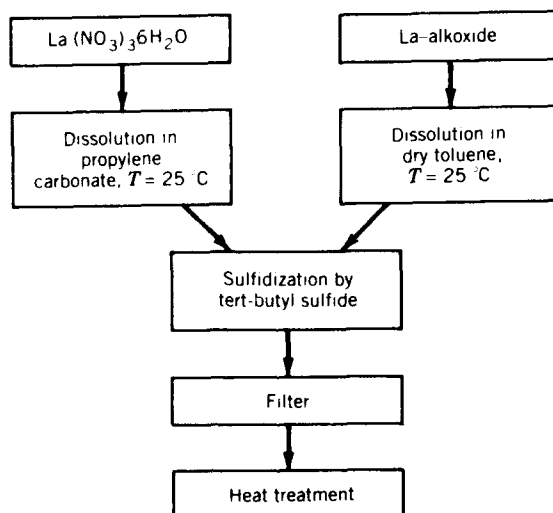


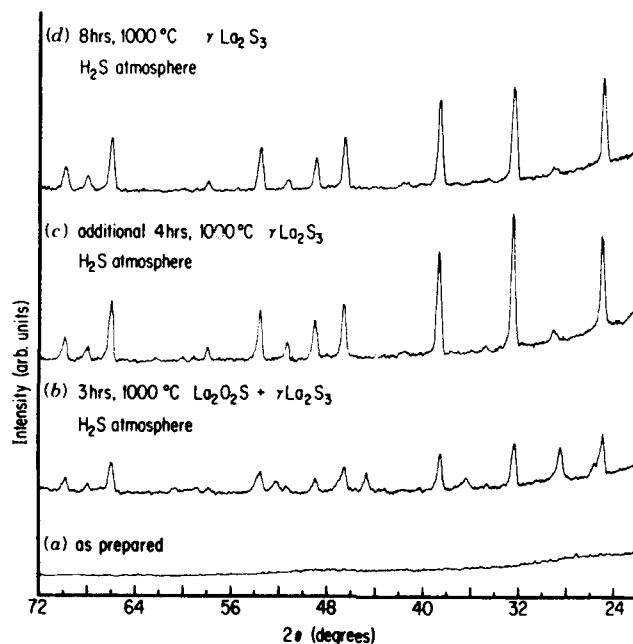
Figure 49.2. Schematic flow chart for types 2 and 3 powders.

heat treatment in order to study the phase development. Sulfidization of the as-prepared precursors was conducted in a horizontal tube furnace, following the procedure outlined by Schevciw and White [8], by heating for 8 hr in flowing  $H_2S$ . At the end of the  $H_2S$  treatment, the powders were characterized by X-ray diffraction (XRD), scanning electron microscopy, and bulk chemical analyses.

### 49.3. RESULTS AND DISCUSSION

After sulfidization for 8 hr, the type 1 powders resulted in the formation of single-phase  $\gamma\text{-La}_2\text{S}_3$ , the cubic phase of lanthanum sulfide. When sulfidized for a period of only 3 hr, the powders consisted of  $\text{La}_2\text{O}_2\text{S}$  and  $\gamma\text{-La}_2\text{S}_3$ . On further heat treatment, single-phase  $\gamma\text{-La}_2\text{S}_3$  was obtained as shown by the XRD pattern [9]. Figure 49.3 shows the XRD patterns showing the phase transformation occurring during heat treatment for type 1 powders.

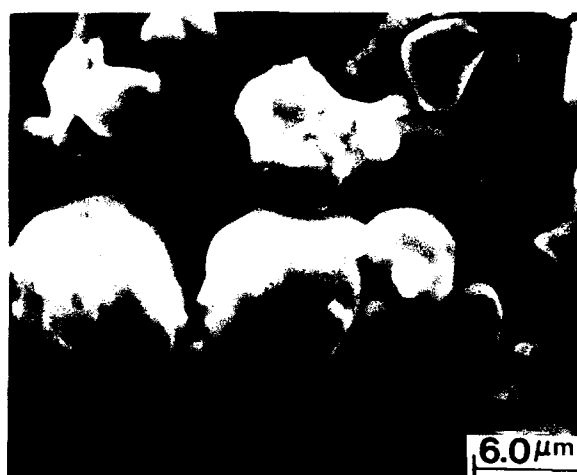
The as-prepared powders in all three cases were amorphous. The formation of mixed phases on initial heat treatment for 3 hr could be speculated to be due to three possible reaction mechanisms: (1) formation of a mixture of oxysulfide and  $\gamma\text{-La}_2\text{S}_3$  (2) conversion of the oxysulfide to  $\gamma\text{-La}_2\text{S}_3$  in the presence of  $H_2S$  catalyzed by the amorphous precursor, or (3) reaction of the oxysulfide and  $\gamma\text{-La}_2\text{S}_3$  with unreacted precursor to form cubic lanthanum sulfide.



**Figure 49.3.** XRD patterns showing the phase transformation of type 1 precursor after heat-treating in  $H_2S$ . Patterns c and d are identical to those in Ref. 9.



The morphology of the transformed  $\gamma\text{-La}_2\text{S}_3$  powders was studied by observing the particles under the scanning electron microscope. Figures 49.4a and b are micrographs of the heat-treated, transformed  $\gamma\text{-La}_2\text{S}_3$  powders. The figures show the powders to be clusters of particles with a size of the order of  $1\text{--}3\text{ }\mu\text{m}$ . It is interesting to observe that some of the particles exhibit rounded edges, and in Fig. 49.4b a distinct roundedness is seen at the neck of the two particles. This suggests that during heat treatment there is an amorphous to



(a)



(b)

**Figure 49.4.** Scanning electron micrographs showing (a) clusters of  $\gamma\text{-La}_2\text{S}_3$  powders and (b) the morphology of two  $\gamma\text{-La}_2\text{S}_3$  particles in contact.

crystalline transition, leading to a possible occurrence of viscous flow of the amorphous precursor particles. The presence of such viscous flow would play a major role in the sinterability of these particles. Chemical analyses of the heat-treated powders are shown in Table 49.2, which shows the analysis obtained on the heat-treated powder and the theoretical analyses for lanthanum sulfide. Good agreement is seen for the metal and sulfur analysis with theoretical weight contents. There is also a substantial reduction in the hydrocarbon content after heat treatment.

In the case of the types 2 and 3 powders, XRD of the heat-treated powders did not result in the formation of  $\gamma$ - $\text{La}_2\text{S}_3$ ; instead a polymorph of lanthanum sulfide whose XRD pattern matched the powder diffraction file [10] was formed. This may be the intermediate  $\beta$  form of  $\text{La}_2\text{S}_3$ . Lanthanum sulfide exists in three different polymorphs:  $\alpha$ ,  $\beta$ , and  $\gamma$ .  $\alpha$ - $\text{La}_2\text{S}_3$  is the low-temperature form possessing the orthorhombic structure that transforms reversibly to the  $\beta$ , the tetragonal form at  $900^\circ\text{C}$ , which in turn transforms to  $\gamma$ , the cubic form at  $1300^\circ\text{C}$ . The intermediate  $\beta$  phase of  $\text{La}_2\text{S}_3$  is essentially an oxysulfide of the form  $\text{La}_{10}\text{S}_{14}\text{O}_x\text{S}_{1-x}$  [11].

Thus, we see that the nature of the precursor seems to play a major role in the transformations of the lanthanum sulfide or oxysulfide powders to the cubic form. Also, the nature of the starting chemical compound, the environment in which it is in solution, and the sulfidizing agent all seem to play a significant role in the formation of the desired cubic phase for infrared transmission.  $\beta$ - $\text{La}_2\text{S}_3$  being an oxysulfide only transmits to  $10\text{ }\mu\text{m}$ . Further, it is interesting to note that the nature of the alkoxide also seems to affect the initial sulfidization. Experiments involving room temperature precipitation using the alkoxide obtained from Strem Chemicals did not result in a powder similar to the one obtained using the alkoxide obtained from Alfa even though all the experimental conditions were identical. Furthermore, heat treatment of this precursor

TABLE 49.2. Chemical Analysis of As-Prepared Precursor and  $\text{La}_2\text{S}_3$  from the Heat-Treated Precursor

Element	As-Prepared Precursors (wt %)		$\text{La}_2\text{S}_3$	
	Type 1 <sup>a</sup>	Type 2 <sup>b</sup>	Observed	Theoretical
La	$50.0 \pm 2$	$50.77 \pm 2$	$74.31 \pm 2$	74.32
S	$8.50 \pm 0.5$	$5.36 \pm 0.5$	$25.71 \pm 0.5$	25.68
C	$5.96 \pm 0.01$	$6.54 \pm 0.01$	$0.05 \pm 0.01$	—
H	$1.79 \pm 0.01$	$2.56 \pm 0.01$	$<0.02 \pm 0.01$	—
O	33.7 <sup>c</sup>	34.77 <sup>c</sup>	Not analyzed	—

<sup>a</sup>Precursor obtained using alkoxide from Alfa Products.

<sup>b</sup>Precursor obtained using alkoxide from Strem Chemicals.

<sup>c</sup>By difference.

in  $\text{H}_2\text{S}$  resulted in a pattern identical to types 2 and 3 powders. This, therefore, leads us to believe that the starting chemicals, the purity, and the actual metal-oxygen-hydrocarbon ratio of the alkoxide seem to have an important bearing on the formation of the cubic phase ( $\gamma\text{-La}_2\text{S}_3$ ). The hydrocarbon content of the initial alkoxide affects the amount of hydrocarbon retained in the precursor as well as in the final transformed powders. This can be clearly seen in the precursor obtained by precipitation at room temperature using the alkoxide from Strem Chemicals. The chemical analysis for the precursor is shown in Table 49.2. The analysis clearly shows a larger percentage of hydrocarbon compared to the precursor obtained using the alkoxide purchased from Alfa Products. There is also less sulfur in the precursor, which may be attributed to the probable prehydrolysis of the alkoxide. The subsequent sulfidization with hydrogen sulfide assisting the completion of the hydrolysis reaction of the alkoxide and consequently limited the amount of sulfur in the precursor [12].

As a result, there is the formation of some amounts of the corresponding oxide in addition to the oxysulfide, which is seen upon heat-treating the precursor in an argon atmosphere. Thus, it can be said that the nature of the alkoxide plays an important role in the formation of the desired precursor. Nevertheless, the success of the type 1 powder offers several advantages in comparison with the existing EDS process. The amorphous state and the final size of the precursor increases the reactivity of the powders, thereby leading to reduction in the sulfidization times [6]. This would also reduce the subsequent grain growth in densified ceramics prepared from these powders.

#### 49.4. CONCLUSION

Sulfide compounds form an important class of materials that can be used for infrared windows. Rare earth sesquisulfide powders having the cubic ( $\text{Th}_3\text{P}_4$ ) structure show promise as potential infrared materials better than  $\text{CaLa}_2\text{S}_4$ . Low-temperature processing and structure control require a careful choice of reagents and the starting materials. The nature of the material and the nature of the precursor have an important bearing on the phase formation of lanthanum sulfide ceramic powders.

#### REFERENCES

1. J. A. Savage, *Infrared Optical Materials and Their Antireflection Coatings*, p. 3, Adam Hilger Ltd., London (1985).
2. J. A. Savage and K. J. Marsh, in: S. Musikant, Ed., *Emerging Optical Materials. Proc. SPIE*, **297**, 35 (1981).
3. P. E. D. Morgan and M. S. Koutsoutis, *Mater. Res. Bull.*, **22**, 617-621 (1987).
4. D. W. Roy, in: S. Musikant, Ed., *Emerging Optical Materials. Proc. SPIE*, **297**, 24 (1981).
5. J. A. Savage, K. L. Lewis, B. E. Kinsman, A. R. Wilson, and R. Riddle, in: R. W. Schwartz, Ed., *Infrared and Optical Transmitting Materials. Proc. SPIE*, **683**, 79 (1986).

6. P. N. Kumta and S. H. Risbud, *Mater. Sci. Eng. B*, **B2**, 281 (1989).
7. T. Takeshita, K. A. Gschneidner, Jr., and B. J. Beaudry, *J. Appl. Phys.*, **57**, 4633 (1985).
8. O. Schevciw and W. B. White, *Mater. Res. Bull.*, **18**, 1059 (1983).
9. Powder Diffraction File, Joint Committee on Powder Diffraction Standards, International Center for Diffraction Data, Swarthmore, Pa. (1973), Card 25-1041.
10. Powder Diffraction File, Joint Committee on Powder Diffraction Standards, International Center for Diffraction Data, Swarthmore, Pa. (1968), Card 22-645.
11. P. Besancon, D. Carre, P. Laruelle and J. Flahaut, in: P. E. Field, Ed., in: *Proceedings of the 9th Rare Earth Research Conference, Va.*, Vol. 1, p. 113, (1971).
12. L. Hench, private communication, 1989.
13. Paul Klocek, *Mater. Res. Bull.*, **41** (1986).
14. K. L. Lewis, J. A. Savage, K. J. Marsh, and A. P. C. Jones, in: S. Musikant, Ed., *Emerging Optical Materials. Proc. SPIE*, **400**, 21 (1983).

# **FABRICATION OF SUPERCONDUCTING OXIDE- COATING FILMS AND FIBERS BY THE SOL-GEL METHOD**

**SUMIO SAKKA AND HIROMITSU KOZUKA**

## **50.1. INTRODUCTION**

Since the discovery of (La, Ba)CuO<sub>4</sub> high-temperature superconducting oxide by Bednorz and Müller [1], many efforts have been made to study the physics of high- $T_c$  superconducting oxides, the development of new high- $T_c$  materials, and the manufacture of high- $T_c$  ceramics. The high- $T_c$  materials do not necessarily best demonstrate the potential properties when they are fabricated in practical shapes, and therefore many improvements are required.

From the application point of view, wires that may consist of a thick fiber or a bundle of fibers and wirelike substrates coated with superconducting oxides are important. People are trying to fabricate such wires through deposition via gas phase and extrusion of ceramics into wires. The sol-gel process may be one of the candidates for wire formation.

In this Chapter, a review has been made on the present state of the art in the field of sol-gel preparation of superconducting fibers and coating films. It will be shown that at present there are many serious problems to be solved in order to obtain satisfactory coating films and fibers by the sol-gel method.

*Ultrastructure Processing of Advanced Materials.*

Edited by Donald R. Uhlmann and Donald R. Ulrich (deceased).

ISBN 0-471-52986-9 © 1992 John Wiley & Sons, Inc.

## 50.2. SIGNIFICANCE OF THE SOL-GEL METHOD AS APPLIED TO THE FABRICATION OF HIGH- $T_c$ SUPERCONDUCTING CERAMICS

There are a number of superconducting oxides [1-8] as shown in Table 50.1. Among them, superconductors of the systems Y-Ba-Cu-O [4], Bi-Sr-Ca-Cu-O [5], and Tl-Ba-Ca-Cu-O [6] are promising candidates for applications at present.

It is known [9-11] that generally the sol-gel method is suitable for making shapes from oxides, because this method is usually based on the hydrolysis and polycondensation of starting substances. When this method is applied to superconducting oxides, however, the problems particular to superconducting oxide ceramics have to be discussed. Table 50.2 shows such problems with an example of  $\text{YBa}_2\text{Cu}_3\text{O}_{7-\delta}$  ceramics. In order to achieve better superconducting properties, that is, higher  $T_c$  (end) and  $J_c$ , the ceramics must be well sintered with the single superconducting phase. This requires higher sintering temperatures. However, the sintering temperature available is limited by the decomposition of the crystalline phase. Also, oxidation of  $\text{Cu}^{2+}$  ions to  $\text{Cu}^{3+}$  ions requires lower heating temperatures. In short, superconducting ceramics should be fabricated at temperatures as low as possible.

Bearing this in mind, the significance of sol-gel method as applied to high- $T_c$  ceramics is considered. Fine particles formed in the solution would lead to lower sintering temperatures, which are favorable for avoiding decomposition and preserving the oxidized state. Homogeneous mixing at the start would lead to the precipitation of pure, uniform crystals, which should be important for the occurrence of superconductivity. Another important advantage of the sol-gel method is possibility of forming fibers and coating films from the solution at low temperatures near room temperature. This is very important because such forming may not be easy with other methods than the sol-gel method.

Two examples showing the above advantage of the sol-gel method will be

TABLE 50.1. Superconducting Oxides

Oxide	Critical Temperature		Year	Authors
	$T_c$ (K)			
$\text{LiTi}_2\text{O}_4$	13.7		1973	Johnson et al. [2]
$\text{BaPb}_{0.75}\text{Bi}_{0.25}\text{O}_3$	13		1975	Sleight et al. [3]
$(\text{La}, \text{Ba})_2\text{CuO}_4$	30		1986	Bednorz and Müller [1]
$(\text{La}_{0.92}\text{Sr}_{0.08})_2\text{CuO}_x$	37		1986	Uchida et al. [4]
$\text{YBa}_2\text{Cu}_3\text{O}_{7-\delta}^a$	94		1987	Wu et al. [5]
$\text{Bi}_2\text{Sr}_2\text{Ca}_2\text{Cu}_3\text{O}_{10}$	104		1988	Maeda et al. [6]
$\text{Tl}_2\text{Ba}_2\text{Ca}_2\text{Cu}_3\text{O}_{10}$	120, 80		1988	Sheng and Hermann [7]
$\text{Ba}_{0.7}\text{K}_{0.3}\text{BiO}_{2.91}$	30		1988	Cava et al. [8]

<sup>a</sup>Y can be replaced by rare earths.

TABLE 50.2. Problems in Developing Superconducting Ceramics of  $\text{YBa}_2\text{Cu}_3\text{O}_{7-\delta}$ 

Problem	Requirement	Method for Solving Problems
Crystalline phase for occurrence of superconductivity	Single superconducting phase	Lower heating temperature than that of decomposition of the phase
Sintering for better superconducting properties <sup>a</sup>	Well-sintered ceramics	High sintering temperature
Crystal growth for occurrence of superconductivity	Larger sizes of crystal	High heating temperature
Oxidation of $\text{Cu}^{2+}$ to $\text{Cu}^{3+}$	$\delta < 0.5$	Heating in oxidizing atmosphere at lower temperatures

<sup>a</sup>Higher  $T_c(\text{end})$ , critical temperature for zero resistivity. Higher  $J_c$ , critical current.

cited. Comparison of the X-ray diffraction patterns of Y–Ba–Cu–O materials derived from gels consisting of metal acetates heated at a rate of 5°C/min to 750, 800, and 910°C, respectively, and kept at each temperature for 19 h [13] with that of the material made by solid-state reaction of conventional raw materials indicates that the sol–gel method gives  $\text{YBa}_2\text{Cu}_3\text{O}_{7-\delta}$  crystalline phase at 750°C, whereas the solid-state reaction does not give  $\text{YBa}_2\text{Cu}_3\text{O}_{7-\delta}$  phase.

Shibata et al. [14] made superconducting  $\text{YBa}_2\text{Cu}_3\text{O}_{7-\delta}$  ceramics from the pellet consisting of fine particles precipitated from the butanol solution of alkoxides  $\text{Y}(\text{n-OC}_4\text{H}_9)_3$ ,  $\text{Ba}(\text{n-OC}_4\text{H}_9)_2$ , and  $\text{Cu}(\text{n-OC}_4\text{H}_9)_2$ . They indicate that the sintering temperature decreases from 950°C for the conventional powder mixture to 800 to 900°C for the alkoxy-derived powder. The decrease in formation and sintering temperatures can be attributed to homogeneous, fine-natured particles in the sol–gel processing. It should be noted that Sakka [13] and Shibata et al. [14] obtained a  $T_c(\text{end})$  of about 90 K for bulk  $\text{YBa}_2\text{Cu}_3\text{O}_{7-\delta}$  ceramics.

Hirano et al. [15] obtained a single-phase  $\text{YBa}_2\text{Cu}_3\text{O}_{7-\delta}$  crystalline phase at 750°C, while the solid-state reaction does not form  $\text{YBa}_2\text{Cu}_3\text{O}_{7-\delta}$  phase at this temperature.

### 50.3. SUPERCONDUCTING COATING FILMS PREPARED BY THE SOL–GEL METHOD

#### 50.3.1. Sol–Gel Coating Films Reported

In a sol–gel coating, a substrate is coated with solutions at near room temperature and heated to 700 to 950°C so that the film might show superconducting properties.

Table 50.3 summarizes coating films prepared by the sol-gel method. It is seen that organic salts, metal alkoxides, and inorganic salts can be used as starting substances. The chemical composition of a substrate has to be selected, so that the reaction between the film and the substrate might be minimized. Yttria-stabilized zirconia (YSZ) ceramics and MgO single crystals are suitable as substrates. Heating up to 900 to 950°C will generally give the coating films that have  $T_c(\text{end})$  at 56 to 90 K.

Here, consideration will be given to the thickness of the film. It has been shown [12] for  $\text{SiO}_2$  [29],  $\text{TiO}_2$  [11], and  $\text{BaTiO}_3$  [30], which are brittle throughout the process from near room temperature to a maximum heating temperature, the thickness for one application should be very thin, approximately 0.1  $\mu\text{m}$ . On the other hand, for the films listed in Table 50.3, the thickness for one application can be as thick as more than 1  $\mu\text{m}$ . This larger thickness is achieved by softening of the coating film at about 200 to 500°C, which makes it possible to cover the surface of the substrate without much stress.

Table 50.3 shows that Bi-Sr-Ca-Cu-O coating films are also prepared by the sol-gel method.

### 50.3.2. An Example of the $\text{YBa}_2\text{Cu}_3\text{O}_{7-\delta}$ Coating Film

A detailed explanation will be given of example No. 7 in Table 50.3, which is the present authors' route [22, 31]. The starting solution consists of Ba-, Y-, and Cu-alkoxides.  $\text{Ba}(\text{OCH}_3)_2$  is made by putting pieces of Ba metal into methanol.  $\text{Y}(\text{n-OC}_4\text{H}_9)_3$  in xylene is dissolved in methanol-triethanolamine. Triethanolamine is added for dissolving Cu-alkoxide, which is not soluble in alcohol-water solvents. A homogeneous, dark-blue-colored starting solution containing the three kinds of alkoxides is dropped on a YSZ substrate. After drying, the coating film is heated at 800°C for 5 min. This coating procedure consisting of dipping, drying, and heating at 800°C is repeated 5 to 10 times to increase the film thickness so that the superconductivity may appear. One coating procedure gives about a 1.5- $\mu\text{m}$  thick film. When the film thickness is smaller than 5  $\mu\text{m}$ , superconductivity is not observed after annealing. This is attributed to the deviation of the composition of the film near the surface of the substrate. Thicker films might not be affected by the composition deviation.

Finally, the ceramic film is annealed in  $\text{O}_2$  at 800°C for 60 to 80 hr and cooled in the furnace. The annealing and slow cooling induce superconductivity by providing the film with oxygen, which is required for producing pertinent superconducting  $\text{YBa}_2\text{Cu}_3\text{O}_{7-\delta}$  crystals, where  $\delta$  is small.

The resistivity-temperature relationship for a 7- $\mu\text{m}$ -thick film prepared by the sol-gel method shows  $T_c(\text{onset})$  and  $T_c(\text{end})$  at 98 K and 56 K, respectively. The grain size of  $\text{YBa}_2\text{Cu}_3\text{O}_{7-\delta}$  crystals in the film is about 1  $\mu\text{m}$  in diameter, and the film displays a pretty well-sintered microstructure.

The observation of the heating process indicates that the film is formed during heating at 200 to 500°C, which means that the softened materials cover the substrate after decomposition of the constituent and volatilization of gases,



TABLE 50.3. Superconducting Coating Films Prepared by the Sol-Gel Method

Superconductor	Starting Substances	Solvent	Method of Application	Substrate	Film Thickness ( $\mu\text{m}$ )	Heating ( $^{\circ}\text{C}$ )	$T_c$ (K)	Orientation	Author
							Onset	End	
$\text{YBa}_2\text{Cu}_3\text{O}_{7-x}$	Metal carboxylates								
	1. Y-stearate, Ba- and Cu-naphthates	<i>n</i> -Butanol	Dripping	YSZ	1-3	800	90	60	Kumagai et al. [16]
	2. 2-Ethylhexanoates	Toluene	Dripping	YSZ	10	900	100	82	Nasu et al. [17]
	3. 2-Ethylhexanoates	Chloroform	Spin coat	MgO	1.4	990	80	77	Cross et al. [18]
	4. Neodecanoates, octanoates	Xylene	Spin coat	Si wafer	0.1-1	800	98	80	Davison et al. [19]
	5. Acetates	Water	Spin coat	MgO	0.16	990	80	58	Rice et al. [20]
	6. Citrates	Ethylene glycol	Spin coat	$\text{SiTiO}_3$ (single)	0.5	800-900	60		Chang et al. [21]
	Metal alkoxide								
	7. Y- <i>n</i> -butoxide, Ba- and Cu-methoxides	Methanol, triethanolamine	Dripping	YSZ	1.5-7	800	98	56	Monde et al. [22]
	8. Y- and Ba-methoxyethoxides, Cu-ethoxide	Methoxyethanol, toluene	Dip coat	Si (single)	0.15-1.0	700	(40)		Kramer et al. [23]
	9. <i>n</i> -Butoxide	<i>n</i> -Butanol, water	Pasting	YSZ	5-10	920-950			Shibata et al. [15]
	10. Ethoxides	Organic solvents	Dip coat	YSZ	5-10	950	96	80-90	Tatsumisago et al. [24]
	Inorganic salt								
	11. Nitrates	Nitric acid, water, ethanol	Spray	YSZ		930-950	95	89	Cooper et al. [25]
$\text{Bi-Sr-Ca-Cu-O}$ ( $\text{BiSrCaCu}_2\text{O}_x$ )	12. Nitrates	Toluene	Dripping	YSZ		900	93	63	Nasu et al. [26]
	13. Bi-2-ethylhexanoate, Sr-cyclohexanecarboxylate, Ca- and Cu-2-ethylhexanoates	Organic solvents	Spin coat	MgO (single)	2	800-900	100	84	Agostinelli et al. [27]
	14. 2-Ethylhexanoates	Toluene	Dripping	YSZ	10	950-980	97	79	Nasu et al. [28]

Abbreviation used: YSZ, yttria-stabilized zirconia.

in contrast with the films  $\text{SiO}_2$ ,  $\text{BaTiO}_3$ , and  $\text{TiO}_2$ , which stay brittle during heating. It is assumed that the softening would cause adherence of a thicker film to the substrate, because there is no large shrinkage at solidification of the film.

#### 50.4. SUPERCONDUCTING FIBERS PREPARED BY THE SOL-GEL METHOD

There are several ways for preparing wires or fibers of superconducting ceramics. Extruding a pipe containing sintered ceramics into a wire [32, 33] is extensively studied, and the result is not satisfactory yet. One thinks of formation of glass fibers from a glass-forming melt of the superconducting oxide compositions and crystallization of the fibers [34]. This is possible only when fibers can be drawn from the melt. If drawing from the melt is not possible, one has to use a special method of forming wires, for example, pumping up the melt into silica tubes [35]. Another way of forming fibers is to utilize the sol-gel method in which gel fibers are drawn from a sol changed into superconducting ceramic fibers by heating, which will be discussed here.

##### 50.4.1. Sol-gel Fibers Reported

Attempts to make superconducting ceramic fibers by the sol-gel method are summarized in Table 50.4. In general, a viscous solution is prepared by dissolving viscosity-increasing agents, such as polyvinylalcohol (No. 2 in Table 50.4) and methacrylic acid (No. 5) into solutions of pertinent metals or by reacting homogeneous solutions containing pertinent metals such as acetates or alkoxides, into viscous drawable solutions (Nos. 2-4 and 6-8).

The superconducting ceramic fibers obtained so far are mechanically brittle and characterized by relatively low  $T_c(\text{end})$  at present. This might result from the use of organic method compounds as starting substances, which are not decomposed by hydrolysis into oxide skeletons in the solution, but give out gases when heated at temperatures higher than  $200^\circ\text{C}$ , resulting in porous ceramic fibers with rough surface.

It is expected that metal alkoxides are hydrolyzed and polycondensed into oxide skeletons if water is used as solvent. The alkoxides of copper that is required for preparing  $\text{YBa}_2\text{Cu}_3\text{O}_{7-\delta}$  and  $\text{Bi-Sr-Ca-Cu-O}$  superconducting oxides, however, are not usually dissolved in an alcohol-water solution. Therefore, alkanolamines that dissolve copper alkoxides are used. It is suspected that in such cases metal alkoxides dissolved in alkanolamine-alcohol solutions may not be decomposed into oxides in solutions.

##### 50.4.2. An Example of a $\text{YBa}_2\text{Cu}_3\text{O}_{7-\delta}$ Fiber

Our experience in fabrication of  $\text{YBa}_2\text{Cu}_3\text{O}_{7-\delta}$  will be described [37-39]. The first requirement for preparation of ceramic fibers is to find starting solutions

TABLE 50.4. Superconducting Fibers Prepared by the Sol-Gel Method

Superconductor	Starting Substances	Solvent	Diameter of fiber	$T_c$ (K)			Author
				Heating	Onset	End	
YBa <sub>2</sub> Cu <sub>3</sub> O <sub>7-x</sub>	1. Y <sub>2</sub> O <sub>3</sub> , BaCO <sub>3</sub> , CuO	Water, <sup>a</sup> PVA	20 $\mu$ m	950°C, 5 h			Goto et al. [36]
	2. Y-, Ba-, and Cu-acetates	Water		950°C, 5 h			Goto et al. [36]
	3. Y-, Ba-, and Cu-acetates	Water	10 $\mu$ m - 1 mm	900°C, 950°C	90	73	Sakka et al. [37-39]
	4. Y-, Ba-, and Cu-acetates	Diethylenetriamine	100 $\mu$ m	950°C	90	80	Uchikawa et al. [40]
	5. Nitrates, reaction with methacrylic acid	Water	(Wire)	900°C			Pope and Mackenzie [41]
	6. Y-, Ba- and Cu-iso-propoxides	Isopropanol		950°C, 3 hr	90		Zheng et al. [42]
	7. Y-, Ba-alkoxides, Cu-acetate	2-Propanol, dimethylformamide	10 $\mu$ m - 1 mm	900-950°C	92 <sup>b</sup>		Masuda and Tateishi [43]
Bi-Ca-Sr-Cu-O system	8. Bi-, Ca-, Sr-, and Cu-acetates	Water, tartaric acid		835-845°C			Zhuang et al. [44]

<sup>a</sup>Extrusion.<sup>b</sup>Magnetic susceptibility measurement.

that become drawable after reactions of the compounds in the solution. Not all viscous solutions are spinnable.

In view of successful fiber drawing from metal alkoxide solutions, one would think of a triethanolamine-methanol solution [22] of Y-, Ba-, and Cu-alkoxides as candidates for fiber drawing. It has turned out that this solution that was used in coating does not exhibit spinnability during reaction. Thus, metal acetates have been found to work as starting substances.

An aqueous solution of the composition Y:Ba:Cu equal to 1:2:3 in moles is prepared by dissolving  $\text{Y}(\text{CH}_3\text{COO})_3 \cdot 4\text{H}_2\text{O}$ ,  $\text{Ba}(\text{CH}_3\text{COO})_2$ , and  $\text{Cu}(\text{CH}_3\text{COO})_2$  in distilled water. The solution remains homogeneous even after concentration when the pH of the solution is adjusted to  $6 \pm 0.1$  with the addition of ammonia water. The solution is kept in a beaker without a cover at 60 to 80°C to concentrate. The solution remains transparent upon concentrating and becomes viscous in about 3 days, when the volume of the solution decreases to about 10% of the initial one. Drawing from the viscous solution by putting a glass rod and drawing it up gives gel fibers more than 50 cm long as shown in Fig. 50.1.

Gel fibers are converted to ceramic fibers by heating in air from room temperature to 900 to 950°C at a rate of 5°C/min, keeping there for 5 hr and cooling down to room temperature in the furnace. Figure 50.2 shows the fine and black ceramic fibers thus obtained. The fibers are hollow and rough on the surface, and accordingly, they are fragile. The ceramic fibers of about 1 mm diameter thus obtained have a  $T_c(\text{end})$  at 60 to 75 K depending on the heating temperature. It is noticed that the value of  $T_c(\text{end})$  is not sufficiently high compared with  $T_c(\text{end}) = 90 \text{ K}$  found for well-sintered, oxidized  $\text{YBa}_2\text{Cu}_3\text{O}_{7-\delta}$  ceramics.

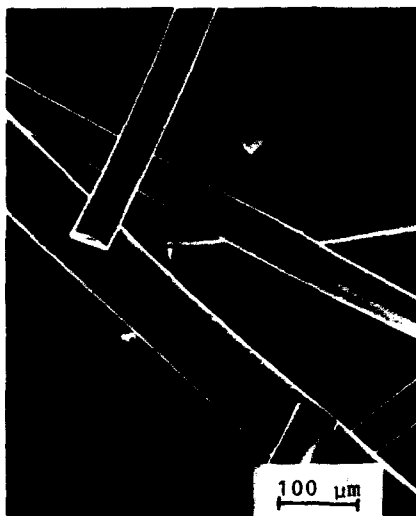


Figure 50.1. A scanning electron micrograph of the Y-Ba-Cu-O gel fibers [39].

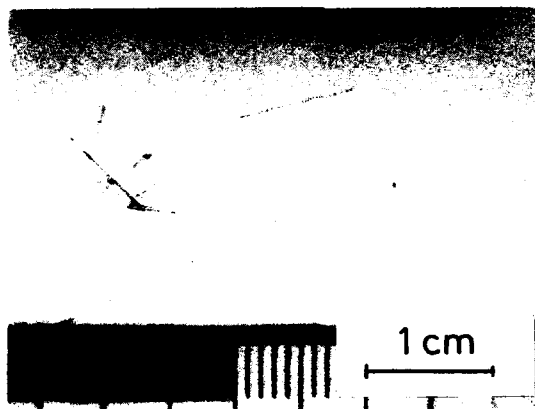


Figure 50.2. Y-Ba-Cu-O ceramic fibers prepared by heating the gel fibers up to 910°C at a rate of 5 °C/min.

The mechanically fragile nature and lower  $T_c$  values of the resultant ceramics may be attributed to the decomposition of components of gel fibers during their heating. It is assumed from the infrared spectra that gel skeletons consist of associated metal acetates and not of metal oxide. Accordingly, the decomposition of acetate skeletons to metal and oxide fine particles occurs when the gel is heated to 200 to 400°C, as shown in thermal analysis curves in Fig. 50.3. This indicates that a large volume of gases is given out around 200 to 400°C where the gel is softened. This will result in formation of small and large pores, a part of which remains at high temperatures for sintering, giving a coarse surface and porous microstructure. These may be the cause for fragility and a lower  $T_c$ .

Masuda and Tateishi [43] partially improved this situation by replacing  $Y(CH_3COO)_3$  by  $Y(O \cdot i-C_3H_7)_3$  and  $Ba(CH_3COO)_2$  by  $Ba(OC_2H_5)_2$  and

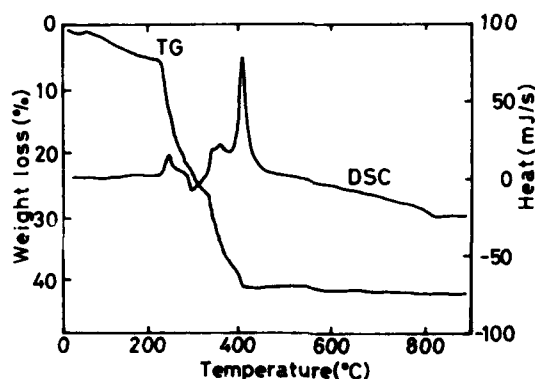


Figure 50.3. DSC and TG curves of the Y-Ba-Cu-O gel derived from the aqueous solution of metal acetates.

increasing the oxide concentration of the solution. Because  $\text{Cu}(\text{CH}_3\text{COO})_2$  could not be replaced by copper alkoxide, however, problems due to the decomposition of acetate were not completely solved.

### 50.5. FUTURE WORKS ON THE APPLICATION OF THE SOL-GEL METHOD TO SUPERCONDUCTORS

It has been shown that coating films and fibers of superconducting oxides can be made by the sol-gel method. Much improvement is required, however, for developing better materials. Problems specific to coating films and fibers will be discussed in 50.5.1 and 50.5.2, respectively.

#### 50.5.1. The Future of Superconducting Coating Film

Many attempts have been made to prepare  $\text{YBa}_2\text{Cu}_3\text{O}_{7-\delta}$  coating films by the sol-gel methods as shown in Table 50.3. However, sol-gel-derived coating films show relatively low  $T_c$  and  $J_c$  compared with those prepared by vapor-phase deposition [45]. These serious problems may arise from the difficulty in sintering films at lower temperatures. High-temperature sintering causes the reaction of components, especially BaO, with the substrate in the case of  $\text{YBa}_2\text{Cu}_3\text{O}_{7-\delta}$  [46], resulting in the deviation of the film composition from the desired one. This reaction may be partially removed by the discovery of nonreactive substrates.

Low-temperature sintering may be suppressed by (1) the formation of pores due to gases produced by the decomposition of starting compounds around 200 to 400°C and (2) the formation of  $\text{BaCO}_3$ , which persists at high temperatures. In order to avoid these, the starting compounds have to be found, that may form oxide skeletons in solutions and gels before heating, and/or the heating conditions have to be modified.

The formation of  $\text{BaCO}_3$  is inevitable in the case of  $\text{YBa}_2\text{Cu}_3\text{O}_{7-\delta}$ , when organic compounds (Table 50.3) are used as starting compounds, because they contain a CO source. Even with nitrates, carbon dioxide comes into the reaction system from air if the sol-gel reaction is carried out in air. Bi-Ca-Sr-Cu-O superconductors may be free from the formation of  $\text{BaCO}_3$ .

Another method of improvement may come from the formation of superconducting oxide film with appropriate orientation [47]. With those improvements, coating films with better superconducting properties will be made by the sol-gel method in the future.

#### 50.5.2. The Future of Superconducting Fibers

Most of the problems encountered in superconducting coating films of  $\text{YBa}_2\text{Cu}_3\text{O}_{7-\delta}$  are shared by superconducting fibers, and one can refer to section 50.5.1 for the solution of the problems.

The most serious problems particular to fibers are softening and bloating at around 200 to 400°C during heating of gel fibers, due to melting and decomposition, respectively, of organic materials composing gel fibers. The softening makes it difficult to keep the shape of the gel fibers during heating. The bloating causes rough surfaces and the hollow nature of the fibers and very much lowers the mechanical strength of the fibers. Modification of the heat treatment condition or findings of new drawable solutions is required for the fabrication of better superconducting fibers.

Attempts are being made to draw fibers of the Bi-Ca-Sr-Cu-O system using the sol-gel method.

### 50.6. CONCLUSION

It has been shown that the sol-gel method is suitable for preparing superconducting oxide-coating films and fibers, but has many serious problems. A large effort has to be made in order to solve the problems for fabricating high-performance coating films and fibers.

### REFERENCES

1. J. G. Bednorz and K. A. Müller, *Z. Phys.*, **B64**, 189 (1986).
2. D. C. Johnson, H. Prakash, W. H. Zachariasen, and R. Viswanathan, *Mater. Res. Bull.*, **8**, 777 (1973).
3. A. W. Sleight, J. L. Galson, and P. E. Bierstedt, *Solid State Commun.*, **17**, 27 (1985).
4. S. Uchida, H. Takagi, K. Kitazawa, and S. Tanaka, *Japan. J. Appl. Phys.*, **26**, L1 (1987).
5. M. K. Wu, J. R. Ashburn, C. J. Torng, P. H. Hor, R. L. Meng, L. Gao, Z. J. Hung, Y. Q. Wang, and C. W. Chu, *Phys. Rev. Lett.*, **58**, 908 (1987).
6. H. Maeda, Y. Tanaka, M. Fukutani, and T. Asano, *Japan. J. Appl. Phys.*, **27**, L209 (1988).
7. Z. Z. Sheng and A. M. Hermann, *Nature*, **322**, 55 (1988).
8. R. J. Cava, B. Batlogg, J. J. Krajewski, R. Farris, L. W. Rupp, A. E. White, K. Short, W. F. Peck, and T. Kometani, *Nature*, **322**, 814 (1988).
9. S. Sakka, in: M. Tomozawa and R. Doremus, Eds., *Treatise on Materials Science and Technology* 22, Vol. III, Glass, Academic Press, New York (1982).
10. S. Sakka, in: *Proceedings of the 1st International Conference on Advances in the Fusion of Glass*, Alfred University, Alfred, N.Y., June 14-17, 1988, pp. 2.1-2.27, The American Ceramic Society (1988).
11. S. Sakka, in: M. Zeldin, K. J. Wynne, and H. R. Allcock, Eds., *Inorganic and Organometallic Polymers*, ACS Symposium Series 360, pp. 345-353, American Chemical Society, Washington, D.C. (1988).
12. S. Sakka and H. Kozuka, *J. Non-Crystal. Solids*, **100**, 142 (1988).
13. S. Sakka, presented at the Materials Research Society International Meeting on Advanced Materials, Tokyo, May 30-June 3, 1988.
14. S. Shibata, T. Kitagawa, H. Okazaki, T. Kimura, and T. Murakami, *Japan. J. Appl. Phys.*, **27**, L53 (1988).

15. S. Hirano, T. Hayashi, M. Miura, and H. Asanaga, presented at the Autumn Meeting of the Association of Powder and Powder Metallurgy, Tokyo, May 17, 1988.
16. T. Kumagai, H. Yokota, K. Kawaguchi, W. Kondo, and S. Mizuta, *Chem. Lett.*, 1646 (1987).
17. H. Nasu, S. Makida, T. Imura, and Y. Osaka, *J. Mater. Sci. Lett.*, 7, 858 (1988).
18. M. E. Cross, M. Hong, S. H. Liou, and P. K. Gallagher, *Mater. Res. Soc. Symp. Proc.*, 99, 731 (1988).
19. W. W. Davison, S. G. Shyu, and R. C. Buchanan, *Mater. Res. Soc. Symp. Proc.*, 99, 289 (1988).
20. C. E. Rice, R. B. van Dover, and G. J. Fisanick, *Appl. Phys. Lett.*, 51, 1842 (1987).
21. Y.-M. Chiang, S. L. Furcone, J. A. S. Ikeda, and S. A. Rudman, *Mater. Res. Soc. Symp. Proc.*, 99, 307 (1988).
22. T. Monde, H. Kozuka, and S. Sakka, *Chem. Lett.*, 287 (1988).
23. S. Kramer, K. Wu, and G. Kordas, *Mater. Res. Soc. Symp. Proc.*, 99, 323 (1988).
24. M. Tatsumisago, H. Sato, and T. Minami, *Chem. Express*, 3, 311 (1988).
25. E. I. Cooper, M. A. Frisch, E. A. Giess, A. Gupta, B. W. Hussey, E. J. M. O'Sullivan, S. I. Raider, and G. J. Scilla, *Mater. Res. Soc. Symp. Proc.*, 99, 165 (1988).
26. H. Nasu, S. Makida, T. Imura, and Y. Osaka, in: *High Temperature Superconductors*, Vol. II, p. 101, D. W. Capone II, W. H. Butler, B. Batlogg, and C. W. Chu, Eds., *Materials Research Society, Pittsburg* (1988).
27. J. A. Agostinelli, G. R. Paz-Pujalt, and A. K. Mehrotra, *Physica*, C156, 208 (1988).
28. H. Nasu, S. Makida, Y. Ibara, T. Kato, T. Imura, and Y. Osaka, *Japan. J. Appl. Phys.*, 27, L536 (1988).
29. Y. Yamamoto, K. Kamiya, and S. Sakka, *Yogyo-Kyokai-Shi*, 90, 328 (1982).
30. S. Sakka and T. Kokubo, *Japan. J. Appl. Phys.*, 22 (Suppl. 22-2), 3 (1983).
31. T. Monde and S. Sakka, presented at the Materials Research Society International Meeting on Advanced Materials, Tokyo, May 30-June 3, 1988.
32. S. Jin, R. C. Sherwood, R. B. van Dover, T. H. Tiefel, and D. W. Johnson, *Appl. Phys. Lett.*, 51, 203 (1987).
33. Y. Yamada, N. Fukushima, S. Nakayama, H. Yoshino, and S. Murase, *Japan. J. Appl. Phys.*, 26, L865 (1987).
34. T. Komatsu, R. Sato, K. Imai, K. Matusita, and T. Yamashita, *Japan. J. Appl. Phys.*, 27, L550 (1988).
35. Y. Abe, H. Hosono, M. Osoe, J. Iwase, and Y. Kubo, *Appl. Phys. Lett.*, 53, 1341 (1988).
36. T. Goto, I. Horiba, M. Kada, and M. Tsujihara, *Japan. J. Appl. Phys.*, 26 (Suppl. 26-3), 1211 (1987).
37. S. Sakka, H. Kozuka, and T. Umeda, *J. Ceramic Soc. Japan*, 96, 468 (1988).
38. T. Umeda, H. Kozuka, and S. Sakka, *Adv. Ceramic Mater.*, 3, 520 (1988).
39. H. Kozuka, T. Umeda, J. S. Jin, and S. Sakka, *Mater. Res. Soc. Symp. Proc.*, 121, 639 (1988).
40. F. Uchikawa, Haixing Zheng, K. C. Chen and J. D. Mackenzie, in: D. W. Capone II, W. H. Butler, B. Batlogg, and C. W. Chu, Eds., *High Temperature Superconductors*, Vol. II, p. 89, *Materials Research Society, Pittsburg* (1988).
41. E. J. A. Pope and J. D. Mackenzie, in: D. W. Capone II, W. H. Butler, B. Batlogg, and C. W. Chu, Eds., *High Temperature Superconductors*, Vol. II, p. 97, *Materials Research Society, Pittsburg* (1988).
42. H. Zheng, K. C. Chen, and J. D. Mackenzie, in: D. W. Capone II, W. H. Butler, B. Batlogg, and C. W. Chu, Eds., *High-Temperature Superconductors*, Vol. II, p. 93, *Materials Research Society, Pittsburg* (1988).
43. Y. Masuda and T. Tateishi, *J. Jpn. Soc. Powd. and Powd. Metal*, 35, 865 (1988).
44. H. R. Zhuang, H. Kozuka and S. Sakka, *Jpn. J. Appl. Phys.*, 28, L1805 (1989).



## REFERENCES

577

45. T. Terashima, K. Iijima, K. Yamamoto, Y. Bando, and T. Mazaki, *Japan. J. Appl. Phys.*, **27**, L91 (1988).
46. H. Koinuma, K. Kukuda, T. Hashimoto and K. Fueki, *Japan. J. Appl. Phys.*, **27**, L1216 (1988).
47. S. Hirano and K. Kato, *Adv. Ceramic Mater.*, **3**, 503 (1988).

## SUPERCONDUCTIVITY AND MICROSTRUCTURE IN LEAD-SUBSTITUTED Bi-Sr-Ca-Cu-O CERAMICS

HUNG C. LING

### 51.1. INTRODUCTION

Since the discovery of high- $T_c$  superconductors in the layered perovskite system of  $(\text{La, Ba})_2\text{CuO}_4$  [1] with  $T_c$  about 40 K, three other perovskite systems have been synthesized with  $T_c$  above the liquid nitrogen temperature of 77 K. They are  $\text{YBa}_2\text{Cu}_3\text{O}_{7-x}$  [2, 3],  $\text{Bi}-(\text{Sr, Ca})-\text{Cu}-\text{O}$  [4, 5], and  $\text{Tl}-(\text{Ba, Ca})-\text{Cu}-\text{O}$  [6–8].  $\text{YBa}_2\text{Cu}_3\text{O}_{7-x}$  has a  $T_c$  of about 90 to 95 K. A number of superconducting phases have been identified in the Bi and Tl systems, one of which has a  $T_c$  exceeding 100 K. In this Chapter, I shall focus the discussion on the  $\text{Bi}-(\text{Sr, Cu})-\text{Cu}-\text{O}$  system.

Maeda et al. [4] reported that a nominal composition of  $\text{BiSrCaCu}_2\text{O}_y$ , (1112) exhibited a drop in electrical resistance at about 105 K, but with a low-temperature resistance “tail.” The zero resistance temperature was between 70 and 80 K. A superconducting phase having a composition of  $\text{Bi}_4(\text{Sr, Ca})_6\text{Cu}_4\text{O}_{16+x}$  and a  $T_c$  of 85 K was reported by Tarascon et al. [9]. When heated for a long time near the melting temperature, the 85 K material produced a phase with a zero-resistance  $T_c$  above 100 K, sometimes as high as

*Ultrastructure Processing of Advanced Materials.*

Edited by Donald R. Uhlmann and Donald R. Ulrich (deceased).

ISBN 0-471-52986-9 © 1992 John Wiley & Sons, Inc.

107 K [10]. Hazen et al. [11] also studied the crystal structures of multiphase samples in the Bi-Sr-Ca-Cu-O system and concluded that the 90 K phase† has a composition near  $\text{Bi}_2\text{Sr}_2\text{Ca}_1\text{Cu}_2\text{O}_9$ . The 105 K phase has been identified as having a composition of  $\text{Bi}_2\text{Sr}_2\text{Ca}_2\text{Cu}_3\text{O}_y$  (abbreviated as 2223).

From the crystal chemistry point of view, the Bi-Sr-Ca-Cu-O and the Tl-Ba-Ca-Cu-O systems conform to the same layered perovskite structure. The compositions have a general formula of  $A_m\text{B}_2\text{Ca}_{n-1}\text{Cu}_n\text{O}_y$ , where  $A = \text{Bi}$  or  $\text{Tl}$ ;  $B = \text{Sr}$  or  $\text{Ba}$ ;  $m = 1$  or  $2$ ; and  $n = 1, 2$ , and  $3$ . The majority of work reported in the literature so far is on compositions with  $m = 2$ . The approximate  $T_c$ 's associated with these structures and the simplified stacking sequence are listed in Table 51.1. With the same number of stacking layers, the Tl system shows a higher  $T_c$  than the corresponding Bi system. The highest  $T_c$  of 125 K was observed in the  $\text{Tl}_2\text{Ba}_2\text{Ca}_2\text{Cu}_3\text{O}_y$  system [7].

Although a substantial volume of work has been published on the Bi system [4, 5, 9-18], it is equally clear that there is not a single optimum processing method to achieve 100% transition at the higher  $T_c$ . Many researchers were not able to achieve a resistance drop at the 105 K transition in their samples, even following the "recipe" processing used by other groups. Furthermore, the low  $T_c$

TABLE 51.1.  $T_c$  in the Bi and Tl Systems

Bi: Sr: Ca: Cu	$T_c$ (K)	Tl: Ba: Ca: Cu
2 2 0 1	20	
2 2 1 2	80	2 2 0 1
2 2 2 3	105	2 2 1 2
	125	2 2 2 3
2 2 0 1	2 2 1 2	2 2 2 3
$\text{Bi}_2\text{O}_2$	$\text{Bi}_2\text{O}_2$	$\text{Bi}_2\text{O}_2$
SrO	SrO	SrO
$\text{CuO}_2$	$\text{CuO}_2$	$\text{CuO}_2$
SrO	CaO	CaO
$\text{Bi}_2\text{O}_2$	$\text{CuO}_2$	$\text{CuO}_2$
	SrO	CaO
	$\text{Bi}_2\text{O}_2$	$\text{CuO}_2$
		SrO
		$\text{Bi}_2\text{O}_2$

†We have to be careful about the use of a  $T_c$  temperature to describe the low  $T_c$  transition in the Bi system, because it depends on how individuals defined  $T_c$  and whether any resistance tail was taken into account. Therefore, we shall treat any reported  $50\text{ K} < T_c < 90\text{ K}$  as referring to the low  $T_c$  transition.

transition at 85 K may have a resistance tail that only reaches zero resistance at temperatures far below 80 K. Thus, both the proportion of high  $T_c$  transition to low  $T_c$  transition and the  $T(R = 0)$  point are very sensitive to the starting compositions and the heat treatment conditions. A summary of the compositions, processing conditions, and major results from "earlier" publications are listed in Table 51.2. In view of the output of papers, this table is by no means inclusive of all the studies that have been performed. From this table, it is obvious that attempts to synthesize a single high  $T_c$  phase have involved large variations in the starting compositions and the processing conditions (calcination, sintering, and atmospheres).

One common route to produce some drop in the resistance near 105 K has been to perform prolonged sintering or annealing of several hundred hours near the melting temperature. Some researchers also reported that excess Ca and Cu enhanced the formation of the high  $T_c$  phase, with the disadvantage of forming CuO- or Ca-rich impurity phases. A second method is to partially substitute Bi by Pb. Some degree of solid solution is to be expected, since  $\text{BaPb}_{1-x}\text{Bi}_x\text{O}_3$  is a superconducting oxide with a  $T_c$  of 12 K [19]. Sunshine et al. [20] measured 10% Meissner effect starting at 107 K in a multiphase sample, but the Pb concentration was not reported. Since then, other reports have indicated that the addition of Pb to the Bi system increased the volume fraction of the high  $T_c$  phase [21–24]. Table 51.3 lists the compositions, processing conditions, and the results of some published papers. With the further addition of a lanthanide, such as Y or La, a new family of cuprate superconductors with a  $T_c < 68$  K was found [25], with a formula of  $\text{Pb}_2\text{Sr}_2\text{ACu}_3\text{O}_{8+\delta}$ , where A is the lanthanide.

In order to understand the effect of Pb substitution and sintering conditions on the superconducting transitions in the Bi system, systematic variation in the controlling parameters becomes necessary. This Chapter discusses the results obtained from starting compositions of  $\text{BiSrCaCu}_2\text{O}_y$  and  $\text{Bi}_2\text{Ca}_2\text{Sr}_2\text{Cu}_3\text{O}_y$ .

## 51.2. EXPERIMENTAL

We used a base composition of either  $\text{BiSrCaCu}_2\text{O}_y$  or  $\text{Bi}_2\text{Sr}_2\text{Ca}_2\text{Cu}_3\text{O}_y$ . In addition, Pb was substituted for Bi in atomic percents between 2 and 75 to form a series of compositions  $\text{Bi}_{1-x}\text{Pb}_x\text{SrCaCu}_2\text{O}_y$  or  $(\text{Bi}_{1-x}\text{Pb}_x)_2\text{Sr}_2\text{Ca}_2\text{Cu}_3\text{O}_y$ . Ceramic powders were mixed from  $\text{Bi}_2\text{O}_3$ ,  $\text{PbO}$ ,  $\text{SrCO}_3$ , and  $\text{CuO}$  in the appropriate ratios and milled in 1-liter polyethylene bottles with  $\text{ZrO}_2$  balls and de-ionized water for 4 hr. The slurry was filtered and dried at 110°C for 16 hr. The dried mix was granulated through 20-mesh screen and calcined in open  $\text{ZrO}_2$  boats at 850°C for 4 hr (or at 800°C for 16 hr). After crushing the calcined powders with a mortar and pestle, rectangular bar samples (1.27 cm long and 0.318 cm wide) were pressed under a pressure of 165.4 MN (24,000 psi). Sintering was between 875°C and 890°C in a flowing oxygen atmosphere or at 840°C in air. The heating and cooling rates were maintained constant at 400°C/hr.

Electrical resistance versus temperature was measured using a four-point

**TABLE 51.2. Literature Survey on Bi-Sr-Ca-Cu-O System**

References	Bi:Sr:Ca:Cu	Conditions	Results
Maeda et al. [4]	1:1:1:2	880°C, 20 min + 872°C, 9 hr, air or O <sub>2</sub> furnace cooled	$T_c(\text{extrapolated}) = 105 \text{ K}$
Togano et al. [13]	1:1:1:2	800°C, 12 hr, calcined 820–870°C air	Multiphase with high and low $T_c$ for thinner samples, optimum temperature was lower
Takayama-Muromachi et al. [14]	Various	800°C, 24 hr, 850°C several days, 880°C several days	High $T_c$ peak at $2\phi = 4.8^\circ$ $c = 37 \text{ \AA}$
Tanaka et al. [12]	1:u:v:w	800–890°C, 10–12 hr	High resistive state if rapid cooled, low $T_c$ state affected by heat treatment and composition, optimum temperature 865–880°C, air
Endo et al. [15]	1:1:3:4	870°C, air 870°C, 0.02 atm O <sub>2</sub> 870°C, 0.1 atm O <sub>2</sub> 870°C, 0.4 and 0.6 atm O <sub>2</sub>	Ca <sub>2</sub> CuO <sub>3</sub> + CuO 2201 + Ca <sub>2</sub> CuO <sub>3</sub> low $T_c$ 2212 increased, 2201 + Ca <sub>2</sub> CuO <sub>3</sub> + CuO decreased 2212 disappeared
Mizuno, et al. [25]	2:2:6:8	880–900°C >0.2 atm O <sub>2</sub> 800°C, 24 hr + 870°C, 24–120 hr	More high $T_c$ phase
Hazen et al. [11]	1:1:1:1 1:1:1:3		Multiphase, $T_c$ phase near 2122 structure Cell $5.41 \times 5.44 \times 30.78 \text{ \AA}$
Tarascon et al. [10]	4:3:3:4  4:3+x:3-x:6	800–900°C, O <sub>2</sub> ground	Single phase at 865 ± 10°C, easier to get 4334 from 4336, multiphase phase if $x > \pm 0.5$ , low $T_c$ has 2212 structure, argon anneal lowers $T_c$
Sunshine et al. [20]	2.2:2:0.8:2	Annealing near melting temperature Single crystal	110 K phase appeared $T(R=0) = 84 \text{ K}$ , susceptibility began at 84 K
Subramanian et al. [8]	Various  Single crystal	700–900°C, 12–36 hr air  From 2:2:1:3 mixture, 850–900°C, 3h hr 840–885°C	Bi <sub>2</sub> Sr <sub>3-2x</sub> Ca <sub>x</sub> Cu <sub>2</sub> O <sub>8+y</sub> , 85 < $T_c$ < 95 K, slow cool and quench similar $T(R=0) = 90 \text{ K}$
Grader et al. [18]	2:3-x:x:2:8+δ		Single phase for 1.25 < x < 2.0, low $T_c$ onset near 70–89 K
Honda et al. [27]	1:1-x:1-x:2 K <sub>2x</sub>	845–880°C, 36 hr, air	Grain growth

TABLE 51.3. Literature Survey on Bi-Pb-Sr-Ca-Cu-O System

Reference	Bi:Pb:Sr:Ca:Cu	Conditions	Results
Endo et al. [16]	0.8:0.2:0.8:1:1.4	828°C, 36 hr, low O <sub>2</sub> (1/13 atm) 842°C, 84 hr, low O <sub>2</sub>	Single-phase high $T_c$ (from nitrates) Some Ca <sub>2</sub> PbO <sub>4</sub> (from solid state), cell $a = b = 5.396$ Å, $c = 37.18$ Å Pure 110 K phase near 2223
Koyama et al. [24]	Various	830–843°C, 36–84 hr low O <sub>2</sub>	best composition
Yamada et al. [22]	1.84:0.34:1.91:2.03:3.06 (1-x:x) <sub>2</sub> :2:2:3 $x = 0, 0.3, 0.5$	850°C, 10 hr, calcined 850°C, 165, 200, 300 hr	$T_c > 100$ K, porous samples Multiple phase, weak pinning at 77 and 4 K
Mizuno et al. [21]	2:x:2:2:3 $x = 0.2-0.6$	800°C, 24 hr + 855°C, 24–120 hr, air Slow cool	Multiphase, Pb lowers optimum temp
Mizuno et al. [25]	2:x:2:2:3 $x = 0.2, 0.4, 0.6$	855°C, 120 hr	More high $T_c$ at $x = 0.6$ sharper peaks
Kijima, et al. [23]	2:y:2:x-1:x $x = 2-8$ $y = 0-1.0$	800°C, 24 hr, calcined	Ca <sub>2</sub> CuO <sub>3</sub> + CuO + Ca <sub>2</sub> PbO <sub>4</sub>

technique, with a constant current of 100 mA. We adopted  $R < 10^{-6} \Omega$  as the criterion of zero resistance. The Meissner effect (magnetic susceptibility) was measured at 13 Hz under a bias field of 1 G. Scanning electron microscopy (SEM) and energy dispersive X-ray analysis (EDX) of fractured samples were performed on AMRAY 1000 SEM and a Tracor-Northern TN2000 EDX system. Powder X-ray diffraction was performed on an automated Phillips Diffractometer.

### 51.3. RESULTS AND DISCUSSION

#### 51.3.1. X-Ray Diffraction

In the 1112 or 2223 compositions, the X-ray diffraction patterns of the sintered samples can be indexed to the 2212 structure given by the powder X-ray diffraction patterns in Onoda et al. [17] and Hazen et al. [11]. There was no unknown peaks with intensity greater than 2% of the highest intensity peak. In the 50% Pb-modified 1112 and 2223 compositions, there was a peak at  $2\theta = 17.7^\circ$  ( $d = 5.1$  Å), which can be attributed to Ca<sub>2</sub>PbO<sub>4</sub>. It is interesting to note that when the calcination was at 800°C for 16 hr, the intensity of this peak was one-half to two-thirds lower than when the calcination was at 850°C for 4 hr. Some optimization of the calcination condition, such as prereaction of certain starting materials, may be helpful in decreasing further the formation of

the  $\text{Ca}_2\text{PbO}_4$  phase. This technique has been found to be useful in eliminating the pyrochlore phase from the relaxor dielectrics.

Other than the existence of all the X-ray diffraction peaks, there are some significant differences in the X-ray patterns from the as-sintered surfaces due to the two calcination conditions used. In general, calcination at  $850^\circ\text{C}$  (condition A) resulted in samples with preferred (001) orientation on the surface. For example, the ratio of  $I_{(008)}/I_{(115)}$  was 2.70 in 1112A and 2.24 in 2223A, compared to 0.47 in 1112B and 0.44 in 2223B. The ratio was 0.48 in the reference powder X-ray pattern [17]. Similar differences were observed in the (00100) and (00120) intensities. The enhancement in the preferred orientation was still present in the 50% Pb-modified compositions, although to a smaller degree. For example, the ratio of  $I_{(008)}/I_{(115)}$  was 0.55 in 1112A (50% Pb) and 1.21 in 2223A (50% Pb) compared to 0.37 in 1112B (50% Pb) and 0.31 in 2223B (50% Pb).

Because current transport in the superconducting phase is largest in the  $a$ - $b$  plane in the layered perovskite structure, single-crystal or preferred orientation with the (001) axis normal to the current carrying direction will increase the critical current density. In our experiments, it was found that calcination at  $850^\circ\text{C}$  resulted in sintered samples with fourfold to sixfold enhancement ( $I_{(008)}/I_{(115)}$ ) in the (001) orientation on the sample surfaces in the 1112 and 2223 compositions. The enhancement was two to three times in the 50% Pb-modified 2223 composition. It is likely that such an effect will persist when very thin layers of the appropriate powders, prepared by thick film techniques, are sintered on various substrates. Although the underlying reasons for the preferred orientation effect is not clear, our results show that small changes in the processing conditions can lead to interesting and potentially useful fabrication techniques for making oriented superconducting films.

### 51.3.2. Electrical Resistance and the Meissner Effect

The room temperature resistivity as a function of the Pb concentration is shown in Table 51.4. The resistivity of the nominal composition of 2223 was 2 to  $6 \times 10^{-3} \Omega\text{-cm}$  in the entire sintering temperature range investigated. After substituting Bi with Pb, the resistivity did not vary between 0 and 25% Pb, but increased to  $16 \times 10^{-3} \Omega\text{-cm}$  at 50% Pb if sintering was below the liquidus/solidus line, such as at  $875^\circ\text{C}$ . Just above this line, such as at  $890^\circ\text{C}$ , the resistivity increased from  $3\text{--}4 \times 10^{-3} \Omega\text{-cm}$  at 0–5% Pb to  $10.7 \times 10^{-3} \Omega\text{-cm}$  at 10% Pb, to  $15.9 \times 10^{-3} \Omega\text{-cm}$  at 15% Pb, and to  $20\text{--}26 \times 10^{-3} \Omega\text{-cm}$  at 50% Pb. The increase in the resistivity with Pb concentration when sintered above the liquidus line is probably due to the greater distribution of Pb-containing insulating phase in the grain boundaries. As shall be discussed later, a large value of the room temperature resistivity is correlated with a "semiconducting" normal state resistance behavior, which is consistent with the existence of an insulating layer.

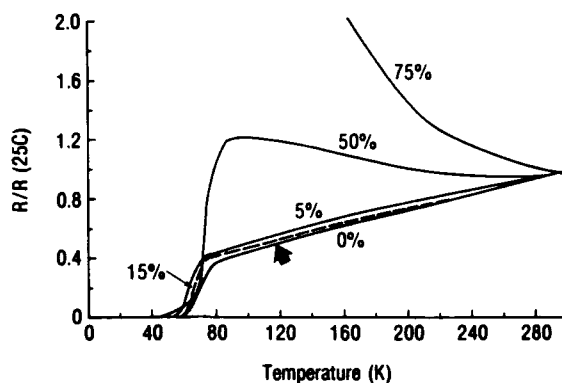
Prolonged annealing of the samples after sintering at  $890^\circ\text{C}$  reduced the resistivity in the 50% Pb composition, from  $16\text{--}22 \times 10^{-3}$  to  $5\text{--}10 \times 10^{-3} \Omega\text{-cm}$ .

TABLE 51.4. Room Temperature Resistivity as a Function of Sintering Condition in Oxygen<sup>a</sup>

Firing No.	Condition	Room Temperature Resistivity							
		0% Pb	2% Pb	5% Pb	10% Pb	15% Pb	25% Pb	50% Pb	
639A	925°C, 4 hr						51.9		
643A/644A	910°C, 4 hr	12.3					19.8		
642A	900°C, 4 hr	3.42					32.4		
632B	890°C, 48 hr	3.7					5.0		
674A/649A	890°C, 12 hr	4.67	3.13	3.38	10.7	15.9	20.5	26.0	
652A	890°C, 12 hr	4.15					21.3	22.1	
637B	890°C, 12 hr	2.21					4.90	20.5	
651B	890°C, 12 hr	3.25					4.69	9.93	
	+880°C, 80 hr								
657A	890°C, 12 hr	3.64					7.09	5.42	
	+875°C, 120 hr								
655A	890°C, 12 hr	2.87					8.97	7.31	
	+850°C, 80 hr								
653A	890°C, 12 hr,	8.50					200.2	176.0	
	quenched								
654A	875°C, 12 hr	4.79					6.00	16.10	
647/648/650A	875°C, 2 hr	6.07	4.03	6.1	4.4	5.1	N/A	19.7	

<sup>a</sup>2223 compositions  $\rho \times 10^{-3} \Omega\text{-cm}$ .





**Figure 51.1.** Relative change in resistance with temperature as a function of % Pb (samples sintered at 875°C, 2 hr in oxygen).

This reduction in the resistivity is likely linked to the elimination of excess Pb from the grain boundaries. Further, this excess Pb may diffuse into the superconducting grains in the sintered compact and partially substitute for Bi. The compositional change in the superconducting phase could produce changes in the normal state property, such as the resistance change with temperature, and in the superconducting property, such as  $T(R = 0)$ .

Figure 51.1 shows the resistance-versus-temperature curves for samples sintered at 875°C for 2 hr. Samples containing 0 to 25% Pb exhibited the metallic behavior of linearly decreasing resistance with temperature in the normal state. The slope was determined to be  $2.72 \times 10^{-3}$  per degree K. The onset of resistance drop occurred between 80 and 74 K, with  $T(R = 0)$  between 61 and 46 K. For the nominal 2223 composition,  $T(R = 0)$  was 57.7 K, and there was a slight change in slope beginning at 120 K (indicated by the arrow). However, there was not a noticeable drop in  $R$  in this temperature range. The 50% Pb composition had a high room temperature resistivity of  $20 \times 10^{-3} \Omega\text{-cm}$  and showed a semiconducting normal state resistance. The onset of resistance drop was estimated from the zero slope of the curve to be 95 K. Although an extrapolation of the resistance drop would indicate 60 K as the zero resistance temperature, there was a tail at lower temperature and the  $R = 0$  temperature was reached only at  $T = 46$  K. The 75% Pb composition did not have the superconducting transition and was semiconducting down to 4 K. Increasing the sintering time to 12 hr did not alter the  $R$  vs  $T$  curves nor  $T(R = 0)$ . Figure 51.2 shows the data for three compositions: 0, 25, and 50% Pb. Both the 0 and 25% Pb compositions had "metallic" normal state resistivity behavior, whereas the 50% Pb was semiconducting. The change in slope at 120 K was more apparent in the 2223 composition, but the other compositions still did not show this change.

At a higher sintering temperature of 890°C for 12 hr, there was a gradual

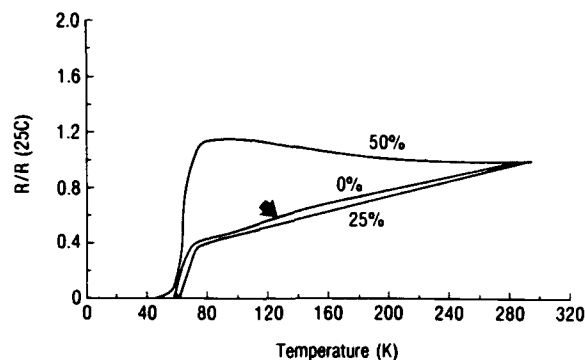


Figure 51.2. Relative change of resistance with temperature for 0%, 25% and 50% Pb composition (samples sintered at 875°C, 12 hr in oxygen).

change in the normal state resistance behavior with composition. The 0 to 5% Pb compositions were metallic while the 75% Pb composition was still semiconducting down to 4 K. At 10, 15, 25, and 50% Pb concentration, the normal state resistance was almost independent of temperature. This is shown in Fig. 51.3. Each curve was comprised of two regions: a metallic behavior with a positive slope ( $1.7 \times 10^{-4}/\text{K}$ ) in the high-temperature region ( $> 240 \text{ K}$ ) and a semiconducting region with a negative slope between 200 K and  $T_c$ . The positive and negative slopes nearly canceled each other, resulting in a flat region between 240 and 200 K. In this series of Pb-substituted compositions, the classification of the normal state behavior coincided with the room temperature resistivity behavior described earlier. It is reasonable to assume that at temperatures slightly higher than the liquidus/solidus line, a low-melting Pb compound(s) may have formed as an insulating grain boundary layer, increasing the room

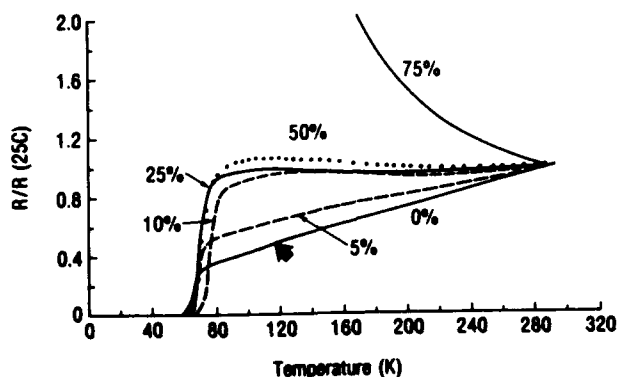
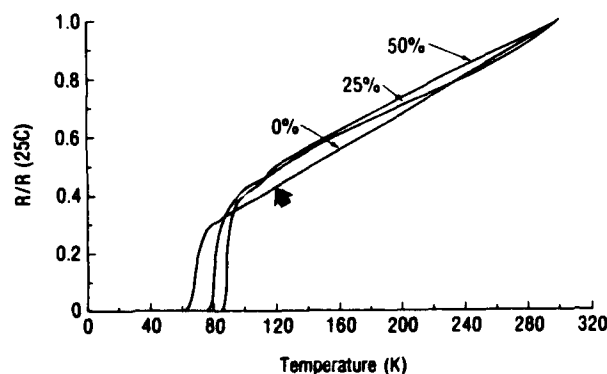


Figure 51.3. Relative change of resistance with temperature as a function of % Pb (samples sintered at 890°C, 12 hr in oxygen).

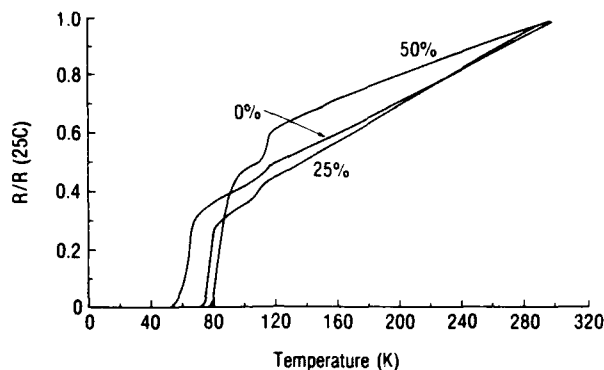
temperature resistivity and giving rise to the semiconducting behavior. The  $T(R = 0)$  temperatures occurred between 65 and 55 K and the slope change at 105 K was only noticed in the 2223 composition.

Because it was reported in the literature that long annealing times were beneficial in establishing the higher-temperature superconducting transition, we performed three annealing schedules after the 12-hr sintering at 890°C: (1) 850°C for 80 hr, (2) 875°C for 120 hr, and (3) 880°C for 80 hr, and the data for (2) and (3) are shown in Figs. 51.4 and 51.5, respectively. Two important features are immediately noted. The slope change at 105 K in the 2223 composition has developed into a step decrease in the 50% Pb composition in Fig. 51.4. A bigger drop in  $R$  was observed after annealing at 880°C (Fig. 51.5), with the percentage decrease in  $R$ ,  $\Delta R/R(105\text{ K})$ , determined to be 8.8% in 2223, 13.2% in the 25% Pb composition, and 13.4% in the 50% Pb composition. The results associated with the 105 K transition are summarized in Table 51.5. The second feature was the shifting of the low  $T_c$  transition from 57.5 K in the pure 2223 system to 78.2 K in 25% Pb and to 78.3 K in the 50% Pb-substituted composition. The differences in  $\Delta R/R(105\text{ K})$  and  $T(R = 0)$  between 25 and 50% Pb concentration is within the experimental accuracy.

The increase in the low  $T_c$  transition with the addition of 25 and 50% Pb was observed at several sintering and annealing conditions. There was only a small change from 55–60 K in the 2223 to 62–65 K in the 25 and 50% Pb composition after sintering at 890°C for 12 hr. However, subsequent annealing increased  $T(R = 0)$  significantly (Table 51.5). Although annealing did not change the  $T(R = 0)$  in the 2223 composition, the increase was about 10 K at 850°C for 80 hr and 15–20 K at the higher annealing temperatures and longer times. It could be that long annealing resulted in more Pb substitution and/or better ordering in the lattice positions of the superconducting phase, leading to the higher  $T(R = 0)$  point.



**Figure 51.4.** Relative change of resistance with temperature for 0%, 25%, and 50% Pb compositions (samples sintered at 890°C, 12h + 875°C, 120 hr in oxygen) to show the step decrease in  $R$  near 105 K in the 50% Pb composition and the increase in  $T(R = 0)$  with Pb concentration.



**Figure 51.5.** Relative change in resistance with temperature for 0%, 25%, and 50% Pb compositions (samples sintered at 890°C, 12 hr + 880°C, 80 hr in oxygen) to show the step decrease in  $R$  near 105 K in three compositions and the increase in  $T(R = 0)$  with Pb concentration.

**TABLE 51.5.** Temperature of Zero Resistance (K) as a Function of Sintering Condition

Firing No.	Condition	Temperature of Zero Resistance (K)		
		0% Pb	25% Pb	50% Pb
639A	925°C, 4 hr	< 39	69	
643/644A	910°C, 4 hr	70	69.5	
642A	900°C, 4 hr	65.8	67.1	
638B	890°C, 48 hr	55.3	62.7	
674A	890°C, 12 hr	55.0	63.5	63
652A	890°C, 12 hr	60.4	63	65
637B	890°C, 12 hr	54.2	61.8	63.0
651B	890°C, 12 hr	57.5	78.2	78.3
	+ 880°C, 80 hr			
657A	890°C, 12 hr	62.3	76.6	86
	+ 875°C, 120 hr			
655A	890°C, 12 hr	59.1	69.8	70
	+ 850°C, 80 hr			
653A	890°C, 12 hr, quenched	54.5	< 4	< 4
654A	875°C, 12 hr	58.4	62.2	46.0
647/648A	875°C, 2 hr	57.7	N/A	46.0

Abbreviation used: N/A, not applicable.

The samples exhibiting the largest  $\Delta R/R$  at 105 K were measured for their Meissner effect. Figure 51.6 shows the susceptibility of two samples of the 50% Pb concentration from the same sintering run: 890°C, 12 hr + 880°C, 80 hr. There was no discernable drop in susceptibility near 105 K, although a change in slope with temperature can be noted. Both samples began to display the susceptibility drop at 93 K, which continued to decrease to 77 K, the lower temperature limit of measurement. Therefore, the low  $T_c$  transition in our samples is a bulk superconductivity effect.

Although the samples sintered in oxygen did not exhibit a large resistance decrease near 105 K, sintering in air at lower temperatures have produced a  $\Delta R/R$  of greater than 60% near 105 K and a Meissner effect was measured, in addition to the Meissner effect associated with the low  $T_c$  transition. Figures 51.7a and b show the resistance-versus-temperature curves for powders calcined at 850°C 4 hr (condition A) and 800°C 16 h (condition B), respectively. The sintering condition was at 840°C for 10, 80, 120, or 180 hr. In both cases, the resistance decrease near the high  $T_c$  transition increased with the sintering time between 10 and 120 hr, with a maximum decrease of about 60%. At a longer sintering time of 180 hr, the normal state resistance became semiconducting. However, the high  $T_c$  phase was still present, as evidenced by the step decrease in resistance near 120 K. Figure 51.8 shows the magnetic susceptibility measurements, with an onset temperature of 115 K. The magnitude of the susceptibility signal, normalized by the sample weight, increased with the sintering time from 10 to 120 hr. This is in accordance with the trend observed in the electrical resistance. However, the magnitude of the susceptibility signal near the high  $T_c$  transition was small compared to the low  $T_c$  transition. Thus, the high  $T_c$  phase was still a minor portion in our samples.

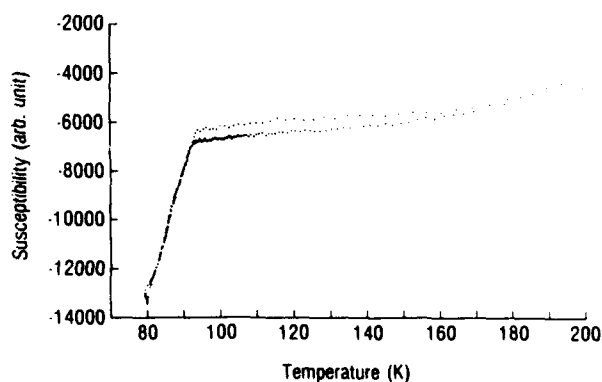
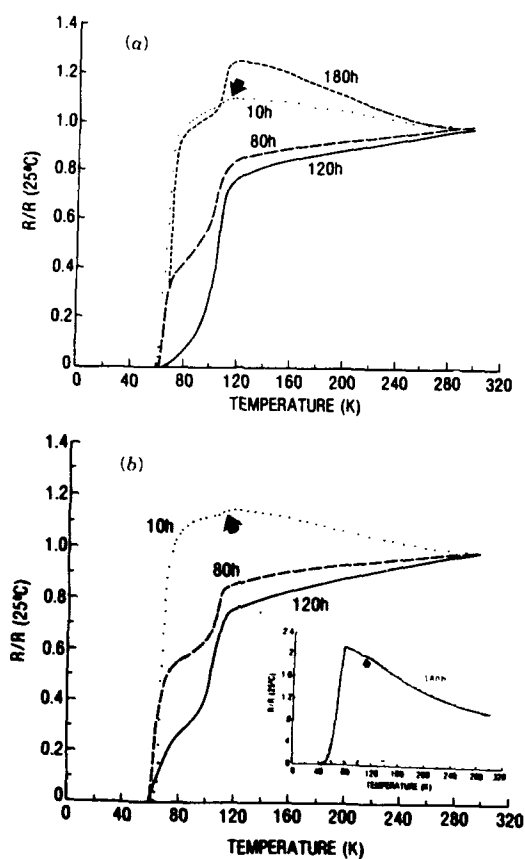
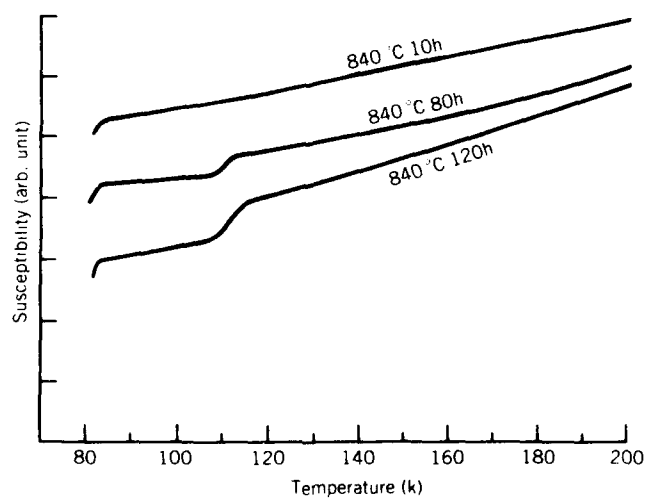


Figure 51.6. Magnetic susceptibility (normalized to sample weight) versus temperature in two samples sintered at 890°C, 12 hr + 880°C, 80 hr in oxygen.



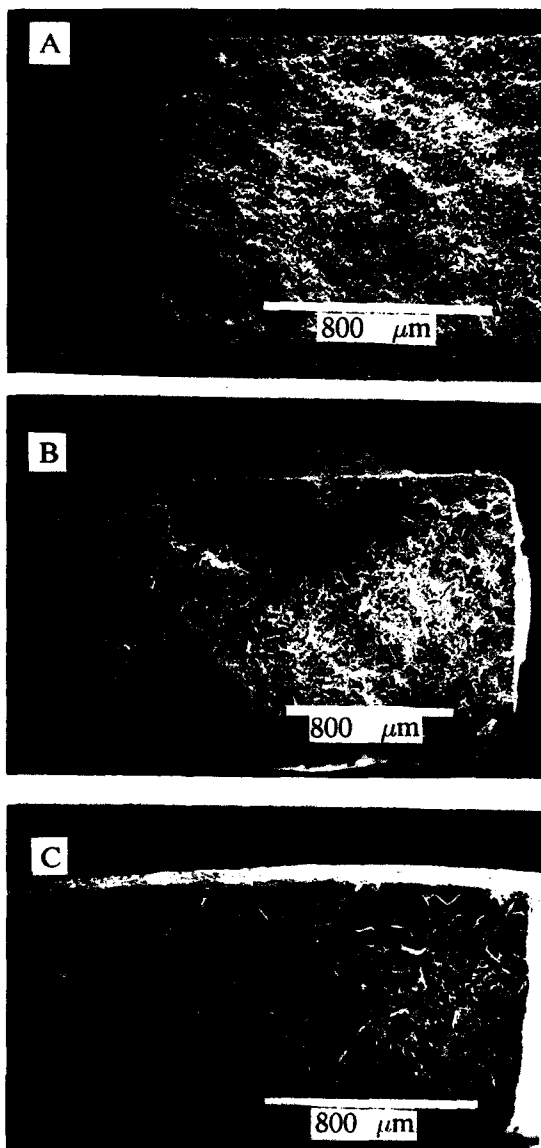
**Figure 51.7.** Relative change in resistance with temperature for 50% Pb composition (a) calcined at  $850^\circ\text{C}$  4 hr and (b) calcined at  $800^\circ\text{C}$  16 hr. Samples were sintered at  $840^\circ\text{C}$  for 10, 80, 120, or 180 hr in air.



**Figure 51.8.** Magnetic susceptibility (normalized to sample weight) versus temperature in a 50% Pb composition calcined at  $850^\circ\text{C}$  4 hr and sintered at  $840^\circ\text{C}$  in air for 10, 80, and 120 hrs.

## 51.3.3. Microstructures

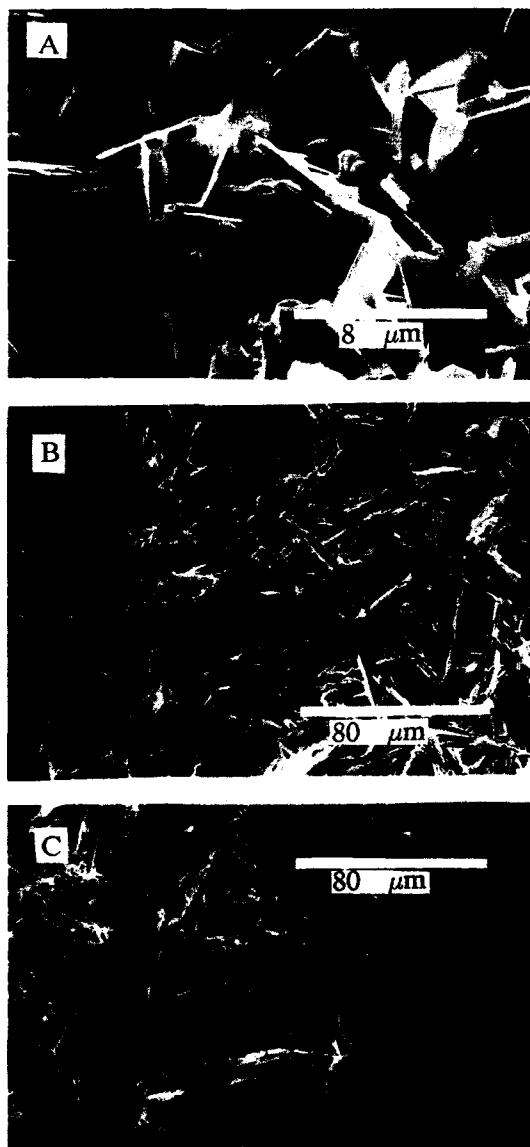
Figure 51.9 shows a low magnification view of the fracture surfaces of 0, 25, and 50% Pb compositions sintered at 890°C, 12 hr + 880°C, 80 hr in O<sub>2</sub>. The 0% Pb composition exhibited a uniform microstructure, with many voids dispersed throughout the matrix (Fig. 51.9a). There was much less porosity in the 25 and



**Figure 51.9.** Low-magnification SEM micrographs of fracture surfaces of (a) 0% Pb, (b) 25% Pb, and (c) 50% Pb compositions (samples sintered at 890°C, 12 hr + 880°C, 80 hr in oxygen).

50% Pb compositions, due to a lower melting temperature in these two compositions (Figs. 51.9*b* and *c*). An outstanding feature in these micrographs was the large plates, which formed winglike or starlike shapes in some areas.

At higher magnification, the 0% Pb composition consisted of an aggregate of small, thin platelets (Fig. 51.10*a*) generally described as "mica"-like. The platelets were about 5  $\mu\text{m}$  in one dimension and less than 0.6  $\mu\text{m}$  thick. The poor



**Figure 51.10.** High-magnification SEM micrographs of fracture surfaces of (a) 0% Pb, (b) 25% Pb, and (c) 50% Pb compositions (samples sintered at 890°C, 12 hr + 880°C, 80 hr in oxygen).



packing of these platelets resulted in no densification of this composition even when sintered within  $5^\circ$  of the melting temperature. At the 25% Pb composition, the plates were much larger in size, with a dimension of about  $50\text{ }\mu\text{m}$  and thickness reaching  $3\text{--}4\text{ }\mu\text{m}$ . Figure 51.10*b* shows a mixture of plate edges and flat surfaces. The "wing" shape cluster of plates suggests a cooperative growth mechanism that may minimize the total strain of the cluster during the growth process. Figure 51.10*c* shows that somewhat larger plate size was attained in the 50% Pb composition. There was also more areas of small grains, which was identified to be Pb-rich by EDX.

A region in Fig. 51.10*b* (25% Pb) was further magnified in Fig. 51.11, and qualitative measurements by EDX were carried out to determine the elemental concentration in the small-grain area, the flat surface, and the edge of the plates. In the small-grain area (*a*), approximate equal intensities of Pb and Bi were measured. On the flat surface (*b*) and along the edge (*c*) of the plates, the Pb intensity was about one-half to one-quarter of the Bi intensity, respectively. Because these areas constituted the superconducting phase, the data demonstrated that a substantial concentration of Pb had substituted for Bi in this phase. The compositional modification by Pb increased the  $T(R = 0)$  temperature, which was observed after long annealing.

#### 51.4. CONCLUSIONS

1. In the nominal 1112 and 2223 compositions that we had prepared, the normal state behavior was "metallic." A maximum drop in resistance of 8.8% was observed near the 105 K transition in samples after long annealing. The zero-resistance temperature varied between 54 and 62 K if the sintering temperature was close to or below the liquidus/solidus line ( $\leq 890^\circ\text{C}$ ) in oxygen. The addition of Pb, up to 50% of the Bi concentration, enhanced the formation of the 105 K superconducting phase in an oxygen-sintering atmosphere such that a resistance decrease of 14% was measured near 105 K. However, the volume fraction of the 105 K phase was still too small to be detectable by the Meissner measurement.

2. In the Pb-containing compositions, the  $T(R = 0)$  temperature was increased by 10–20 K after long annealing from 57–62 K to 70–86 K. We suggest that this was due to the incorporation of substantial amount of Pb into the superconducting phase, as the EDX data showed.

3. The Pb addition also enhanced the growth of the superconducting plates and improved the packing of these plates to produce a more dense compact after sintering. The size of the plates increased from  $5 \times 5 \times 0.6\text{ }\mu\text{m}^3$  in the nominal 2223 composition to  $50 \times 50 \times 4\text{ }\mu\text{m}^3$  in the 25–50% Pb compositions. To avoid excess Pb-containing phases being retained in the matrix, our data suggest a maximum Pb concentration of 25% in the starting composition.

4. Sintering in air at a lower temperature of 840°C, just below the melting temperature, increased the volume fraction of the high  $T_c$  phase to a maximum at a sintering time of about 120 hr. Longer sintering times (180 hr) produced a semiconducting normal state and decreased the fraction of the high  $T_c$  phase.

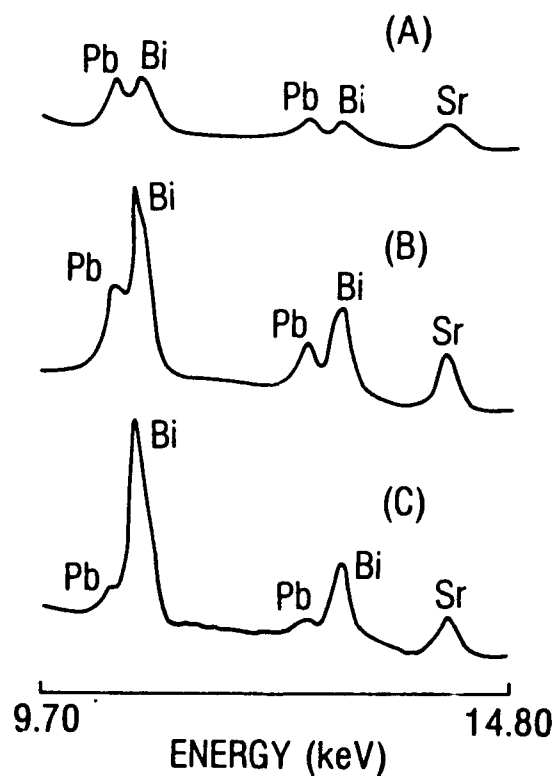
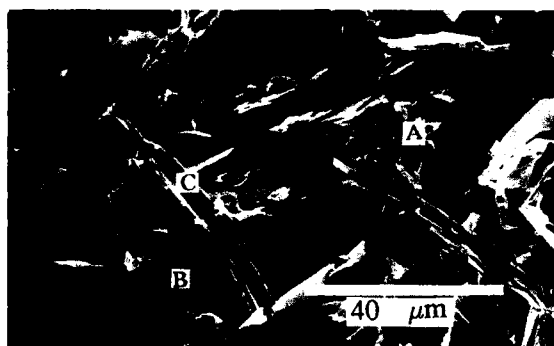


Figure 51.11. High-magnification SEM micrograph of a region in Fig. 10(b) and the corresponding EDX spectrum of (a) a small-grain area, (b) a flat surface, and (c) an edge of the plates.

## ACKNOWLEDGMENTS

The author thanked Dean Holmes for assistance in sample preparation, R. E. Woods for SEM work, A. Karp for assistance in setting up the apparatus for measuring the Meissner effect, and E. L. Smith and R. F. Roberts for critical reading of the manuscript.

## REFERENCES

1. J. G. Bednorz and K. A. Muller, *Z. Phys. B*, **64**, 189 (1986).
2. M. K. Wu, J. R. Asburn, C. J. Torng, P. H. Hor, R. L. Meng, L. Gao, Z. J. Haang, Y. Q. Wang, and C. W. Chu, *Phys. Rev. Lett.*, **58**, 908 (1987).
3. R. J. Cava, R. B. van Dover, B. Batlogg, and E. A. Reitman, *Phys. Rev. Lett.*, **58**, 408 (1987).
4. H. Maeda, Y. Tanaka, M. Fukutomi, and T. Asano, *Japan. J. Appl. Phys.*, **27**, L209 (1988).
5. C. W. Chu et al., *Phys. Rev. Lett.*, **60**, 941-943 (1988).
6. Z. Z. Sheng and A. M. Hermann, *Nature*, **332**, 55-58 (1988).
7. S. S. P. Parkin, V. Y. Lee, E. M. Engler, A. I. Nazzari, T. C. Huang, G. Gorman, R. Savoy, and R. Beyers, *Phys. Rev. Lett.*, **60**, 2539-2542 (1988).
8. M. A. Subramanian, C. C. Torardi, J. C. Calabrese, J. Gopalakrishnan, K. J. Morrissey, T. R. Askew, R. B. Flippen, U. Chowdhry, and A. W. Slight, *Science*, **239**, 1015 (1988).
9. J. M. Tarascon, Y. LePage, P. Bardoux, B. G. Bagley, L. H. Greene, W. R. McKinnon, G. W. Hull, M. Giroud, and D. M. Hwang, *Phys. Rev. B*, **37**, 9382 (1988).
10. J. M. Tarascon, Y. LePage, L. H. Greene, B. G. Bagley, P. Bardoux, D. M. Hwang, G. W. Hull, W. R. McKinnon and M. Giroud, *Phys. Rev. B*, **38**, 2504 (1988).
11. R. M. Hazen et al., *Phys. Rev. Lett.*, **60**, 1174-1177 (1988).
12. Y. Tanaka, M. Fukutomi, T. Asano, and H. Maeda, *Japan J. Appl. Phys.*, **27**, L548-549 (1988).
13. K. Togano, H. Kumakura, H. Maeda, K. Takahashi, and M. Nakao, *Japan. J. Appl. Phys.*, **27**, L323-324 (1988).
14. E. Takayama-Muromachi, Y. Uchida, Y. Matsui, M. Onoda, and K. Kato, *Japan. J. Appl. Phys.*, **27**, L556-558 (1988).
15. H. Endo, J. Tsuchiya, N. Kijima, A. Sumiyama, M. Mizuno, and Y. Oguri, *Japan. J. Appl. Phys.*, **27**, L1906-1909 (1988).
16. U. Endo, S. Koyama, and T. Kawai, *Japan. J. Appl. Phys.*, **27**, L1476-1479 (1988).
17. M. Onoda, A. Yamamoto, E. Takayama-Muromachi, and S. Takekawa, *Japan. J. Appl. Phys.*, **27**, L833-836 (1988).
18. G. S. Grader, E. M. Gyorgy, P. K. Gallagher, H. M. O'Bryan, D. W. Johnson, Jr., S. A. Sunshine, S. M. Zahurak, S. Jin, and R. C. Sherwood, private communication, 1988.
19. A. W. Slight, J. L. Gillson, and P. E. Bierstedt, *Solid State Comm.*, **17**, 27-30 (1975).
20. S. A. Sunshine et al., *Phys. Rev. B*, **38**, 893 (1988).
21. M. Mizuno, H. Endo, J. Tsuchiya, N. Kijima, A. Sumiyama, and Y. Oguri, *Japan. J. Appl. Phys.*, **27**, L1225-1227 (1988).
22. Y. Yamada, S. Murase, M. Koizumi, M. Tanaka, D. Ito, S. Takeno, I. Suzuki, and S. Nakamura, in: *Proceedings of ISS'88, Nagoya, Japan*, Springer-Verlag, Tokyo (1989).
23. N. Kijima, H. Endo, J. Tsuchiya, A. Sumiyama, M. Mizuno, and Y. Oguri, *Japan. J. Appl. Phys.*, **27**, L1852-1855 (1988).

## REFERENCES

597

24. S. Koyama, U. Endo, and T. Kawai, *Japan. J. Appl. Phys.*, **27**, L186 (1988).
25. M. Mizuno, H. Endo, J. Tsuchiya, preprint, Matsubishi Kasei Corp.
26. R. J. Cava et al., *Nature*, **336**, 211-214 (1988).
27. Honda et al., *Japan. J. Appl. Phys.*, **27**, L545 (1988).

## ULTRASTRUCTURE PROCESSING OF CERAMICS IN ELECTRONICS PACKAGING

H. T. SAWHILL

### 52.1. INTRODUCTION

The trend toward microcircuits with higher electrical densities that operate at faster speeds with higher-wattage IC chips is placing increased demands on ceramic thick-film and tape dielectric systems. These pastes and tapes are mixtures of inorganic powders with organic vehicles formulated for required rheological properties. Multilayer interconnects are fabricated using a sequential print/fire process or by cofiring a prelaminated assembly. The control and reproducibility of microstructural development in these ceramic system components is central to providing the desired performance and reliability.

This Chapter focuses on the processing modifications and microstructural and materials issues involved in designing ceramic systems for more stringent performance and reliability. The Chapter is divided into three sections: thick-film and tape dielectrics, thick-film resistors, and multilayer fabrication. For each case, general performance and reliability trends are described followed by discussions of structure property relations in these systems. Each section ends with some anticipated processing modifications in response to changing performance and reliability needs

---

*Ultrastructure Processing of Advanced Materials.*  
Edited by Donald R. Uhlmann and Donald R. Ulrich (deceased).  
ISBN 0-471-52986-9 © 1992 John Wiley & Sons, Inc.

## 52.2. GENERAL TRENDS IN THICK-FILM AND TAPE DIELECTRICS

Dielectrics function as insulators to isolate signal lines, ground planes, and passive and active components. Hermeticity and resistance to electrochemical migration is paramount for reliability in environments encompassing a range of humidity, temperature, and electrical bias conditions. Trends continue toward longer-term operation under more severe environments. Common industry standards for reliability include high-humidity bias (85°C, 85% relative humidity, 5 V direct current,) and high bias and temperature testing (150°C, 200 V dc) [1].

Low-transmission delay times needed for high switching speeds require a combination of high conductivity metallization for signal lines and low dielectric constant for the dielectrics. Thermal expansion values of the dielectric are typically matched closely to 96% alumina to allow thick-film processing on these substrates or utilization of alumina-based chip carriers. A trend toward direct Si chip attachment to multilayers is prompting designs of tape dielectrics with thermal coefficient of expansion (*TCE*) values close to Si. Higher-wattage chips are requiring more sophisticated thermal management of packages to dissipate the added heat.

### 52.2.1. Structure-Property Relations in Dielectrics

Thick-film technology and tape dielectric systems designed for use with high conductivity metallizations (viz., Au, Ag, Cu) utilize processing temperatures of 850 to 1050°C. Dielectrics designed for this temperature range typically have microstructure comprizing both crystalline and noncrystalline phases. Two general approaches are used: crystalline filler powders added to glass powders in the formulation or crystalline phases precipitated during the firing process. Physical properties of the dielectric are related to the distribution of the different phases in the composite.

Dielectric constant (*k*), *TCE*, and thermal conductivity (*k<sub>th</sub>*) of a dielectric composite can be considered volume average quantities. The composite values for each can be approximated as follows:

$$K^m = \sum v_i K_i^m$$

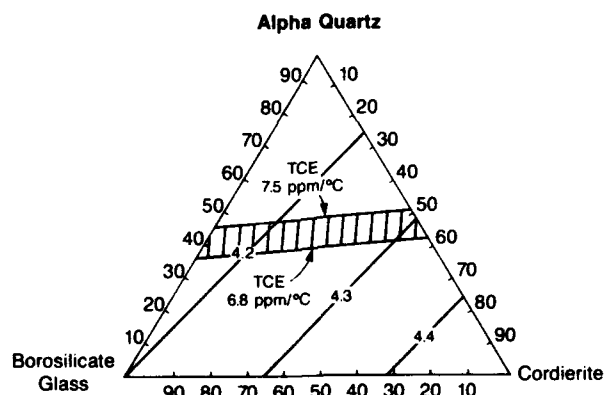
where *v<sub>i</sub>* is the weighted volume fraction of phase *i*, *K<sub>i</sub>* is the specific property of this phase, and *m* is an exponent that depends on the spacial distribution of the different phases [2]. Thus the overall bulk property of the composite is a sum of the weighted volume fraction properties of the constituent phases. Limiting cases of *m* = -1 for parallel, *m* = +1 for series behavior, and *m* = 0 for log mixing rules are commonly cited examples. Weighting factors include elastic constant for TCEs, as an example. The exponent *m* depends on the distribution of phases, their relative sizes, and so on. Variations of this general form can

provide improved second-order approximations, but the point is that these properties can be predicted fairly accurately if the phase distribution in the fired composite is known. With these algebraic structure-property relations, it is possible to generate diagrams such as Fig. 52.1, which shows a map of dielectric constant and *TCE* values for a three-component system [3]. A similar graph for thermal conductivity (in plane) versus dielectric constant (out of plane) is shown in Fig. 52.2; typical property ranges provided by different material systems are indicated [4].

The precision of the prediction depends on how well phase relations in the fired microstructure correspond to parameters chosen for the model. Take, for example, a 50/50 v/o quartz/glass composite with a *TCE* of 7.0 that is properly *TCE* matched with the substrate to be nonbowing. If the quartz particles are 1  $\mu\text{m}$  in radius, and 500 Å of the outer surface dissolves in the glass during processing, the overall composite *TCE* will change from 7.0 to 6.4. The bowing of a 25- $\mu\text{m}$  dielectric on a substrate of 25 mil (635  $\mu\text{m}$ ) thickness with a 600°C temperature change ( $\sim$  from  $T_g$  of glass to room temperature), is calculated to be 16 mils (406  $\mu\text{m}$ ) on a 4-in. (101 mm) substrate. The typical allowance for bowing is less than 10 mils (254  $\mu\text{m}$ ) for this size substrate under these conditions. Consequently, reactivity of fillers with the glass matrix is often an important issue for proper control of *TCE* of dielectrics. Similarly, for crystallizable glasses, consistency of crystallization endpoints is important to meet both dielectric constant and *TCE* specifications.

### 52.2.2. Reliability of Dielectrics

Leakage current is one method used to measure hermeticity of dielectrics layers [5]. A relation between the failure rate in thick-film dielectrics and leakage current is shown in Fig. 52.3. Porosity pathways or microcracks through the



**Figure 52.1.** Dielectric constant map of mixtures of  $\alpha$ -quartz, cordierite, and a borosilicate glass (Corning 7070). The band indicates compositions with a thermal expansion compatibility (TEC) with  $\text{Al}_2\text{O}_3$ . (Data from Ref. 3.)

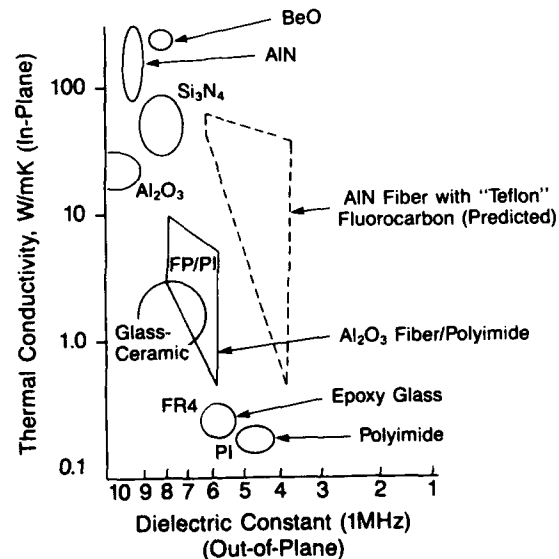


Figure 52.2. A map of thermal conductivity (in plane) and dielectric constant (out of plane) for different electronic packaging materials. (Data from Ref. 4.)

dielectric are common sources of high leakage currents. The microcracks can result from different *TCEs* of surrounding materials or thermal shock [6, 7], whereas porosity can result from pinholes during printing or casting or from incomplete sintering. For ceramic-filled glass systems, densification is largely controlled by glass viscosity and wetting behavior. Nonwettable fillers lead to considerable porosity in these composites as illustrated by the models shown in Fig. 52.4 [8].

For nonreactive systems with wettable fillers, the intermediate state of

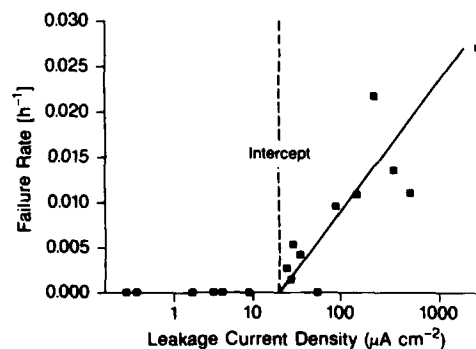
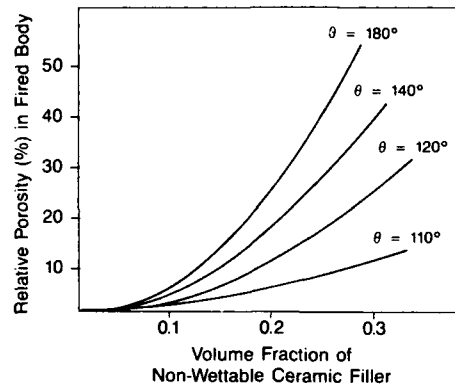


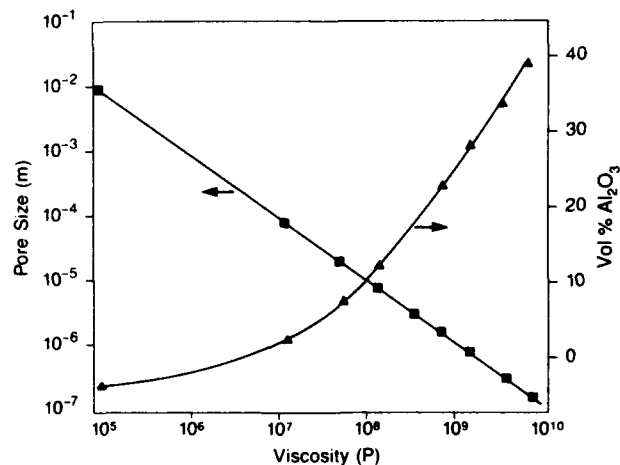
Figure 52.3. Correlation of accelerated life test. Failure rate and electrolytic hermeticity test data. (Data from Ref. 5.)





**Figure 52.4.** Predicted porosity values of fired glass-filled composites as a function of volume fraction of filler. The effect of wetting angle of the glass on the particulate filler is indicated. (Data from Ref. 8.)

sintering involves particle rearrangement and a balance between particles pulled into liquid regions and particles pulled into pore spaces [9]. Porosity remaining in the final stage of sintering is removed at rates related to the composite viscosity, which can be orders of magnitude higher than the viscosity of the glass alone. Calculations of the largest pores that can be removed during a 1-hr firing cycle at 850°C in the final-stage sintering of glass-filled composites versus  $\text{Al}_2\text{O}_3$  filler loading are shown in Fig. 52.5 [10]. The kinetics of wetting have been shown to depend on glass viscosity and geometric factors as well [11].



**Figure 52.5.** The largest pore size that can be removed during a 1-hr firing cycle at 850°C is indicated as a function of slurry viscosity. The influence of volume percent  $\text{Al}_2\text{O}_3$  filler on the slurry viscosity is indicated on the second axis. (Data from Ref. 10.)

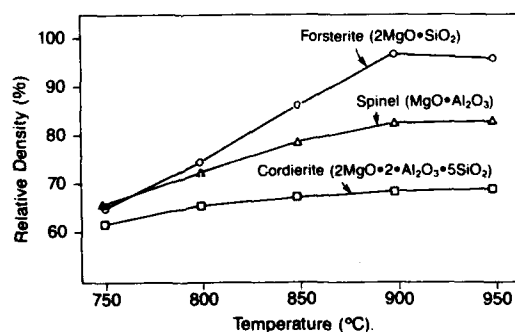
The least well-understood factor at this time is the reactivity of glass with fillers. An example is shown in Fig. 52.6 where densification is a strong function of the filler used [12]. Other more extreme examples of filler reactivity have also been reported [13]. Quartz filler is a common example where wetting angles  $>90^\circ\text{C}$  are measured, but full composite densification is possible due to reactivity with the glass matrix. For crystallizable glass systems, the densification must precede crystallization to assure reproducible and hermetic microstructures. Assuring reproducibility of these densification and crystallization processes poses a considerable challenge to materials designers.

### 52.2.3. Future Trends in Dielectric Materials

There is a clear trend toward more demanding hermeticity and reliability requirements, lower dielectric constants, *TCE* control, and greater processing latitude. These trends are fueling efforts to provide improved materials, processes, and fundamental understanding of controlling microstructural factors. New glass chemistries with greater resistance to electrochemical migration, crystallizable glasses with designed densification/crystallization behavior, particle size optimization, and surface modification of powders are likely to be part of development efforts for thick-film and tape dielectrics. Improvements in process modeling will come with better understanding of the electrochemical migration, sintering, and crystallization processes and better-defined materials, reactions, and interactions during firing and aging.

## 52.3. GENERAL TRENDS IN THICK-FILM RESISTORS

A general trend for thick-film resistors is higher tolerances, improved stability of a wide range of performance requirements, and expanded capabilities at very high and low resistance values. More demanding performance of resistance,



**Figure 52.6.** Effect of various ceramic fillers on the relative density of fired glass-filled composites. The component ratios are glass, 40 w/o;  $\text{Al}_2\text{O}_3$ , 35 w/o; and filler additive, 25 w/o. (Data from Ref. 12.)

temperature coefficient of resistance (*TCR*), short-term overload voltage (*STOL*), noise, and laser trim stability continue to pose challenges in materials design.

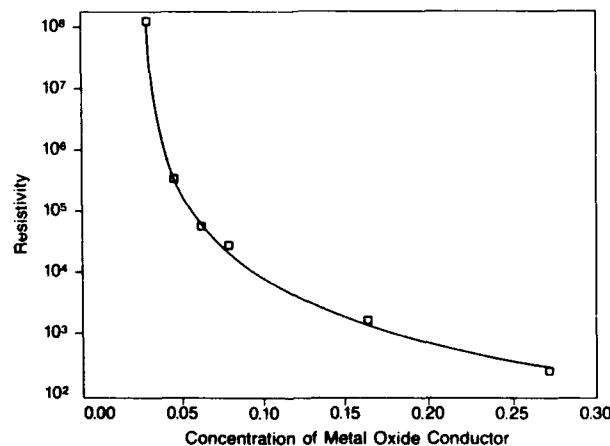
### 52.3.1. Structure-Property Relations in Thick-Film Resistors

Thick-film resistors consist of a conductive oxide phase and a glass phase to allow processing at temperatures in the 850°C range [14]. The general relationship between conductive phase loading and resistivity (*R*) is shown in Fig. 52.7 [15].

This percolative type behavior can be described using an equation of the following general form:

$$R = R_s(x - x_c)^\beta$$

where *x* is the volume fraction of conductive oxide, *x<sub>c</sub>* is the critical volume fraction below which the resistor is effectively insulating, *R<sub>s</sub>* is a constant, and *β* is the critical exponent. For the case of regular mixtures of identical-size conductive and nonconductive spheres, the critical volume fraction is 0.15 [16]. This critical volume fraction varies to some degree with the packing coordination of the chosen model, but neither cubic packing nor random packing models account for the low values of *x<sub>c</sub>* reported for thick-film resistors (viz.,  $0.02 \leq x_c \leq 0.1$ ) [15]. Recent work with different-sized, silver-coated glass spheres has shown that particle size differences of the order of 5 between nonconductive and conductive spheres led to *x<sub>c</sub>* values as low as 0.05 [17]. This particle size effect is supported by experimental findings [18] of *x<sub>c</sub>* values of



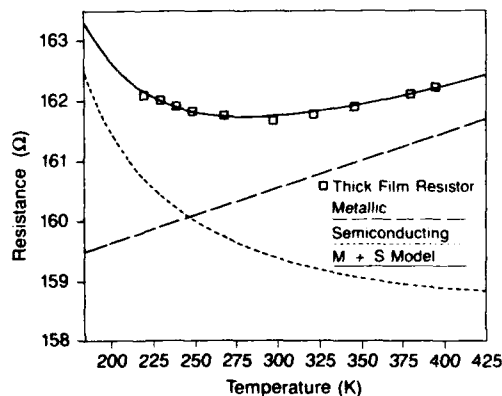
**Figure 52.7.** Experimental sheet resistivity data ( $\Omega/\square$ ) versus volume fraction conducting phase in thick-film resistors. The curve shown was calculated using the formula  $R = R_s(x - x_c)^{-\beta}$ . (Data from Ref. 15.)

0.149 and 0.0715 for  $\text{RuO}_2$  particle size values of 10 and 300 nm, respectively, in combination with 1.6- $\mu\text{m}$  size glass particles.

The significance of the critical exponent for thick-film resistors is not well understood. Values of  $\beta$  between 1 and 2 are characteristic of percolative systems [15]. Some reports conclude that the critical exponent is independent of conductive particle size (for a given glass particle size) with values close to 2 [15]. Other reports [18] indicate differences of over 100% in this critical exponent with differences in conductive particle size, with values considerably higher than 2 ( $3 < \beta < 7$  [19],  $\beta = 4.5$  [20]).

The numerical value of  $R_s$  can be thought of as a constant for a given resistor system, but in general, its relation to the intrinsic conductivity of the conducting oxide is not predictable on any a priori basis. Thus, in contrast to the volume average properties of dielectrics described in the previous section, a knowledge of the phase distribution for a thick-film resistor allows only a very coarse approximation of its properties; resistance values could easily be in error by an order of magnitude using volume average approximations. The reason for this lies in the nature of the conduction paths.

There are several experimental reports that suggest the conduction pathway in thick-film resistors are made of chains of conducting particles with insulating or semiconductive barriers between the conducting oxide particles: Samples of thick-film resistors that were etched to remove the glass and refired to consolidate conducting chains were observed to increase in conductivity by three or four orders of magnitude [21]. The sensitivity of resistance to strain is quite large [22]. The characteristic temperature coefficient of resistance (TCR) behavior can be modeled (see Fig. 52.8) in a first-order approximation by combining the temperature dependence of a metal and the temperature dependence of a semiconductor. In addition, the  $R$  and  $TCR$  values are affected by processing parameters, such as heating rate, firing time, and firing temper-



**Figure 52.8.** Resistance value ( $\Omega$ ), of a thick film resistor as a function of temperature. The M&S model is the sum of the metallic and semiconducting curves.

ature [23]. All the observations cited above support a picture of rate-limited conduction by electron tunneling across thin semiconducting barriers separating conductive oxide particles.

There are varying beliefs concerning the specific details of the tunneling barriers. Several factors complicate the generalization of their behavior. First, there are competitive processes of sintering and wetting in operation during firing. Ostwald ripening of the conductive phase has been documented [24], and particle sizes, glass viscosity, and processing variables (time, heating rate, and temperature) can each strongly influence the resulting property of the resistor [25]. Second, small amounts of oxide modifiers (*TCR* drivers) are known to dramatically shift *R* and *TCR* values, and results depend strongly on the modifier route used (oxide particles vs oxide doping of the glass). It is generally believed these effects are the result from modifications of the electronic structure of the tunneling barrier and not from differences in tunneling distances. However, this has not been substantiated by critical experimentation at sufficiently high resolution levels to preclude the effects of special distribution of component phases.

#### 52.3.2. Future Trends in Thick-Film Resistors

The trends discussed in thick-film resistors are fueling efforts to provide pastes with rheological properties with better print definition and improved dispersions to provide more reproducible microstructures and improved tolerance values. These improvements are especially important on the high-end resistivity members, because such a small amount of conducting oxide is present. Surface modification of powders and greater control of particle sizes should lead to advantages in improved reproducibility and increased process latitude. New conductive oxide, glass, and *TCR* drivers could provide greater process latitude and product performance. An improved understanding of the variables governing the behavior of tunneling barriers would facilitate the development of thick-film resistors with higher voltage stability and lower noise properties.

### 52.4. GENERAL TRENDS IN MULTILAYER CERAMIC PACKAGING

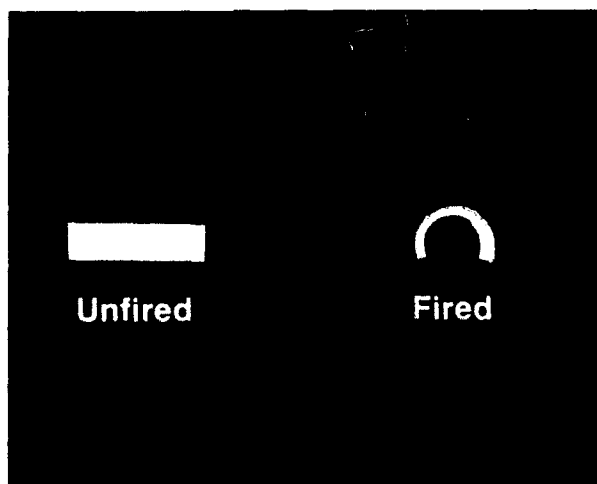
Multilayer design allows dramatic increases in circuit density. Cofiring is being examined in fabrication of thick-film multilayers to reduce the number of processing steps. Cofired tape dielectric systems continue to grow with a trend toward larger areas and higher layer count multichip packages [26]. Low-temperature cofired material systems provide the opportunity for integration of buried passives in cofired packages. Examples of buried passives include resistors, capacitors, varistors, inductors, piezoelectrics, and thermistors. The flexibility of tape processing is providing opportunities to use tape materials as

structural components to design multiteared cavities and rims with internal circuitry.

#### 52.4.1. Cosintering in Multilayers Ceramic Packages

Multilayer fabrication with tape systems requires sintering compatibility between dielectric, conductor, and passive components. In contrast to stress associated with mismatches in *TCEs* of these different materials, stresses associated with cosintering can be greater by orders of magnitude. An example is shown in Fig. 52.9 in which a metalized tape has undergone cosintering stresses that resulted in sufficient bowing to form a semicircle from the once-flat sample [27]. Calculations indicate that 0.035 in. (0.89 mm) of bowing would be predicted if all the *TCE* mismatch (15 ppm/°C) was accommodated through relief by bowing [28]. In contrast, a *TCE* mismatch of 170 ppm/°C would be required to cause the degree of bowing present in Fig. 52.9.

Sinter-forging studies have shown that sintering rate of filled glass dielectrics can be described using models based on viscous flow [29]. Independent activation energies measured from isothermal and nonisothermal sinter-forging studies are in good agreement [30]. The case for the metallic conductors is quite different. Poor agreement is found between activation energies obtained from isothermal and nonisothermal cases and the discrepancy is largely attributed to grain growth effects [30]. The shrinkage rate and overall shrinkage of the multilayer does not always lie between those of the dielectric and metal conductor, as illustrated in Fig. 52.10. Quantification of this behavior remains a topic of research.



**Figure 52.9.** Bowing of a cofired metallized dielectric tape as a result of cosintering stresses during firing. (Data from Ref. 27.)

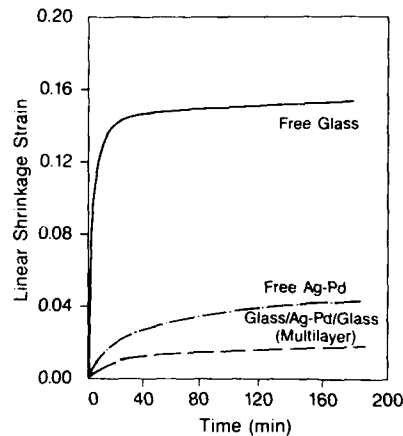


Figure 52.10. Isothermal sintering of glass/metal/glass multilayer film and individual films of Ag-Pd and glass. (Courtesy of R. Raj, Cornell University.)

Despite a lack of full quantitative modeling, material suppliers have been able to formulate materials for cosintering compatibility, largely by utilization of particle size control and sintering modifiers. Examples of cofired multilayer test circuits fabricated with three different conductor metallurgies are shown in Fig. 52.11.

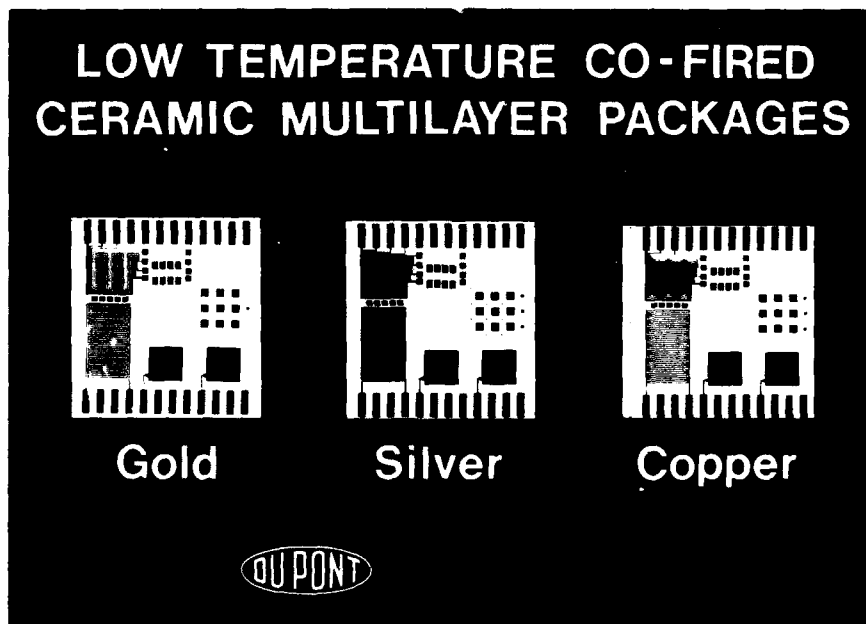


Figure 52.11. Circuit test patterns fabricated with cofired tape dielectric system with three different conductor metallurgies.

Incorporation of passive components within multilayer packages poses additional complexity. The electrical performance of passives is considerably more sensitive to microstructure variations than conductors or dielectrics, for example, the large resistivity variations of thick-film resistors to process conditions and particle size effects described in the previous section. Buried resistors that sinter faster than the dielectric result in blisters, whereas those sintering slower, bow or delaminate [13]. Similar defects have been reported for buried capacitor materials [31]. Materials suppliers continue to formulate materials for cosintering compatibility, again largely by utilization of particle size control, glass viscosity control, and sintering modifiers.

#### 52.4.2. Future Trends in Multilayer Ceramic Packaging

As the demand for larger layer area and higher layer count multilayers continues, cosintering compatibility among different component materials grows in importance. The development of more active powders, for example, by solution synthesis, will provide flexibility in accommodating the cosintering requirements. Finer lines and vias will likely result from integration of photoimageable technologies. The need for flexible processing and improved performance continues to drive research and development efforts in dispersion and particle size refinements.

### REFERENCES

1. C. R. S. Needes, K. M. Nair, and M. V. Coleman, in: *IMC 1988 Proceedings, Tokyo, May 25-27*, pp. 219-227 (1988).
2. W. D. Kingery, H. K. Bowen, and D. R. Uhlmann, *Introduction to Ceramics*, pp. 604, 636, 947, Wiley, New York (1976).
3. D. M. Maddox, S. R. Gurkovich, J. A. Olenick, and K. M. Mason, *Ceramic Eng. Sci. Proc.*, **9**, 1567-1578 (1988).
4. J. D. Bolt and R. H. French, *Advan. Mater. Proc.*, **134**, 32-35 (1988).
5. C. R. S. Needes and D. P. Button, in: *Proceedings of the 35th Electronic Components Conference, Washington, DC, May 20-22, 1985*, pp. 505-511.
6. A. G. Evans and M. Ruhle, in: A. G. Evans, Ed., *Ceramic Contining Systems*, Chap. V, Noyes Publications, Park Ridge, N.J. (1986).
7. P. L. Kirby and A. Owens, *Microelectron. J.*, **14**(5), 35-41 (1983).
8. V. C. Ducamp, *Thermodynamic Aspects of Sintering in Glass and Glass-Ceramic Powder Compacts*, M. S. Thesis, Cornell University, (1988).
9. K. G. Ewsuk, in: G. L. Messing, E. R. Vuller, and H. Hausner, Eds., *Ceramic Powder Science, Part B, Ceramic Transactions*, Vol. 1, pp. 969-977, American Ceramics Society, Westerville, Oh., (1988).
10. K. G. Ewsuk, presented at the Annual Ceramic Society Meeting, Indianapolis, Ind, April 1989.
11. M. Denesuk, J. P. Cronin, T. J. Gudgel, B. J. J. Zelinski, and N. Kriedl, and D. R. Uhlmann, presented at the Glass Division Meeting of American Ceramics Society, November 1988, Tuscon, Ariz.



12. K. Kawakami, M. Takabatake, T. Minowa, J. Chiba, and M. Sasaki, *Multilayer Ceramic Devices*, pp. 95–102, American Ceramic Society, Westerville, Oh., (1986).
13. H. T. Sawhill, *Ceramic Eng. Sci. Proc.*, **9**, 1603–1617 (1988).
14. J. R. Larry, R. M. Rosenberg, and R. O. Uhler, *IEEE Trans. CHMT-3*(2), 211–225 (1980).
15. P. F. Carcia, A. Ferretti and A. Suna, *J. Appl. Phys.*, **53**, 5282–5288 (1982).
16. H. Scher and R. Zallen, *J. Chem. Phys.*, **53**, 3759–3761 (1970).
17. L. Oger, J. P. Troadec, D. Bideau, J. A. Dodds, and M. J. Powell, *Powder Technol.*, **46**, 133–140 (1986).
18. A. Szpytma and A. Kusy, *Thin Solid Films*, **121**, 263–270 (1984).
19. G. E. Pike, in: *AIP Conference Proceedings: Electr. Transp. Opt. Prop. Inhomogeneous Media*, **40**, pp. 366–371 (1978).
20. W. H. DeJeu, R. W. J. Geuskens, and G. E. Pike, *J. Appl. Phys.*, **52**, 4128–4134 (1981).
21. G. E. Pike and C. H. Seager, *J. Appl. Phys.*, **48**, 5152–5169 (1977).
22. C. Canali, D. Malavasi, B. Morten, M. Prudenziati, and A. Taroni, *J. Appl. Phys.*, **51**, 3282–3288 (1980).
23. J. Lee and R. W. Vest, in: *Electron Component Conference, 33rd, Orlando Fla, IEEE Trans. Components, Hybride and Manufacturing Technol.*, **CHMT-6**(4), 430–435 (1983).
24. A. N. Prahbu and R. W. Vest, *Mater. Sci. Res.*, **10**, 399–408 (1975).
25. T. Inokuma, Y. Taketa, and M. Haradome, *IEEE Trans. Components, Hybrids Manufact. Technol.*, **CHMT-8**(3), 372–373 (1985).
26. H. C. Bhedwar, H. T. Sawhill, D. H. Scheiber, S. Kawasaki and E. A. Kemp, *Proceedings of the 5th International Microelectronics Conference* (published by Int. Soc. Hybrid Microelectron., Tokyo, Japan, pp. 89–97, 1988).
27. K. R. Mikeska, presented at the Annual American Ceramics Society Meeting, Cincinnati, Ohio, April 1988.
28. J. H. Lauchner, R. L. Cook and A. I. Andrews, *J. Am. Ceramics Soc.*, **39**(8), 1956, pp. 288–292.
29. G. W. Scherer, *J. Am. Ceramics Soc.*, **67**(1), 709–715 (1984).
30. G. W. Scherer, presented at the Annual American Ceramics Society Meeting, Cincinnati, Ohio, 1988.
31. K. Utsumi, Y. Shimada, T. Ikeda, and H. Takamizawa, *Ferroelectrics*, **68**(1–4), 157–179 (1986).

## SYNTHESIS, CHARACTERIZATION, AND APPLICATIONS OF LEAD AND BARIUM TITANATE MATERIALS PREPARED BY THE SOL-GEL METHOD

M. A. AEGERTER, Y. CHARBOUILLOT,  
N. MOHALLEM, AND L. H. DE GODOY

### 53.1. INTRODUCTION

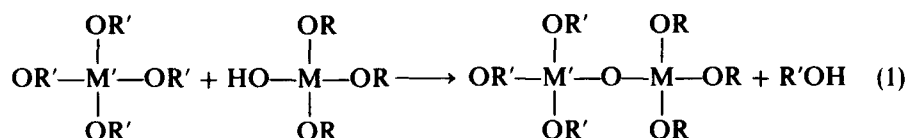
The fabrication of high-quality ceramic materials and devices has received much attention in the recent years. The chemical methods appear very attractive as they offer potential advantages over the traditional mixed-oxide routes. In particular the purity, the chemical homogeneity, and particle size characteristics may be enhanced by adopting these processing techniques. These methods may also lower considerably the ceramic processing temperatures and therefore facilitate their integration with semiconductor devices, microelectronic packaging, integrated optics devices, and so on. This will include thin- or thick-layer devices and multilayer configuration. On the other hand, the preparation of submicron powders with well-defined and controlled granulation may lead to the obtention of better and more reliable ceramics with reproducible characteristics.

---

*Ultrastructure Processing of Advanced Materials.*  
Edited by Donald R. Uhlmann and Donald R. Ulrich (deceased).  
ISBN 0-471-52986-9 © 1992 John Wiley & Sons, Inc.

In this Chapter we review the studies realized during the last decade using the sol-gel route for obtaining lead and barium titanate-derived materials in the form of gels, powders, and films. We first discuss the relative merits and problems of the different chemical processes used for the preparation of adequate precursors and for which two basic methods can be visualized:

1. A multicomponent alkoxide can be prepared by reacting a combination of single alkoxide. The reaction of a partially hydrolized alkoxide of species M with another alkoxide of species M' forms a double alkoxide and an alcohol:



This method requires alkoxides of both species and an understanding of their relative rates of hydrolysis and reaction products.

2. A soluble salt, such as a nitrate or acetate, can be added to a single or a complex alkoxide. An understanding of the solution and reaction chemistry of the species is important to determine the nature and the structure of these complex alkoxides and to obtain a stable sol.

We also discuss how to obtain specific sols from these precursors in order to prepare specific products such as gels, powders, and films. Finally, the physical properties of these materials obtained either in the amorphous or crystalline form are presented, and possible applications of high technological relevance are mentioned.

## 53.2. LEAD TITANATE-DERIVED MATERIALS

Pure lead titanate has not proved to be an important technological material when prepared via conventional processing procedures. However, it is the base constituent of important electrical ceramics, such as lead zirconium titanate and PLZT. Its synthesis in a thin-film form of high optical quality and high refraction index may be fundamental for the development of electronic and optical devices.

### 53.2.1. Precursors and Sols Preparations

The first preparation of  $\text{PbTiO}_3$  precursor was made by Gurkovich and Blum [1] through the reaction of lead acetate,  $\text{Pb}(\text{C}_2\text{H}_3\text{O}_2)_2$ , dissolved in methoxyethanol,  $\text{C}_3\text{H}_6\text{O}_2$  with titanium isopropoxide,  $\text{Ti}(\text{OC}_3\text{H}_7)_4$ . The synthesis process was rather complicated, and the final product highly viscous with high moisture reactivity. Sols were prepared by dissolving this complex in methoxyethanol (1 : 7 ratio volume), introducing the water of hydrolysis as a solution of

methoxyethanol and water (2:1 ratio) with 0.002 mol  $\text{HNO}_3$ /mol water added. Gelation occurred in a few minutes, and transparent gels were obtained after drying at  $34^\circ\text{C}$  for 2 to 3 weeks. Tetragonal  $\text{PbTiO}_3$  was reported after firing at  $600^\circ\text{C}$ .

The precursor preparation process was later modified by Budd et al. [2, 3] who recognized, through gas chromatography analysis, the occurrence of an exchange reaction between the titanium alkoxide and the methoxyethanol:



where  $\text{R}' = i\text{-C}_3\text{H}_7$  and  $\text{R} = \text{CH}_3\text{OCH}_2\text{CH}_2$ . The titanium methoxyethoxide prepared in this way at  $125^\circ\text{C}$  was then combined with a 2-methoxyethanol solution of dehydrated lead acetate, reacted and concentrated by repeated vacuum distillations. Sols for gel formation and thin-film preparation were prepared by combining equal volume of the stock solution with a solution of water-catalyst (acid or base)-methoxyethanol to give 0.5 M gel. Stable sols were obtained for a  $[\text{H}_2\text{O}]/[\text{PbTiO}_3]$  ratio smaller than 1.5. For higher ratios, gelation occurred in a few minutes with a rate increasing with the water amount and pH.

We propose an easier method particularly useful to prepare precursor sol for obtaining dense material in film form. It is based on the chemical modification of titanium isopropoxide  $\text{Ti}(\text{O-}i\text{-Pr})_4$  by acetylacetone ( $\text{AcacH}$ ), a rather strong chelating ligand and stabilizing agent [4-6]. The preparation of the complex alkoxide is described by the exothermic reaction [7]



The yellow and homogeneous solution is mixed for 30 min until its temperature lowers to  $25^\circ\text{C}$ . A solution of lead acetate,  $\text{Pb}(\text{OAc})_2 \cdot 3\text{H}_2\text{O}$  in acetic acid (concentration 720 g/liter) is then added under 30 min of stirring. This sol does not exhibit gelation or precipitation for at least 6 months. Its color, however, changes from clear yellow to orange in a few days indicating either an evolution of the Ti complexation or a change in the particles size. Both precursor sols can be mixed in any proportion to prepare lead titanate material of other compositions (Table 53.1).

TABLE 53.1. Typical Composition for the Preparation of  $\text{PbTiO}_3$  and  $\text{TiO}_2$ -0.25 $\text{PbO}$  Sol

Product	<i>i</i> -PrOH (ml)	Acetylacetone (ml)	$\text{Ti}(\text{O-}i\text{-Pr})_4$ (ml)	Pb-Acetate Solution (ml)	pH
$\text{PbTiO}_3$	40	3	4	7.24	4.7
$\text{TiO}_2$ -0.25 $\text{PbO}$	40	3	4	1.81	5.7

### 53.2.2. Gel to Ceramic Conversion

Whatever is the process of sol preparation, the dried gels are amorphous to X-rays up to  $\sim 400^\circ\text{C}$ . Their structure shows, however, differences analogous to those found for  $\text{SiO}_2$  gels: Acidic gels have fibrous morphology with entanglements of more linear and less crosslinked species capable after drying of polymeric rearrangement into microcrystalline regions. The spatial repartition of Pb and Ti was found homogeneous. On the contrary, basic gels have a coarse texture and a more highly condensed structure and inhomogeneous cations distribution [3, 8]. These materials crystallize directly into a  $\text{PbTiO}_3$  perovskite structure with crystallite sizes of 225 to 450 Å; the transition temperature is lower than that found in conventional processes and depends on the time of the heat treatment (typically  $425^\circ\text{C}$  after 600 min) [9]. The heat of crystallization for the basic gel is higher than for acid gel, and the reaction rate is given by the Arrhenius law  $K = \exp(-E_a/kT)$ , with  $E_a \sim 63 \text{ kcal/mol}$  and  $\nu = 1.72 \times 10^5 \text{ sec}^{-1}$  [9]. No structural and thermal characterizations are yet reported for films.

### 53.2.3. Properties and Applications

Some dielectric properties have been reported by Budd et al. [3] who found that partially ordered acid gels have a higher dielectric constant ( $\epsilon' \sim 36\text{--}40$ ) than base-catalyzed gels ( $\epsilon' \sim 28\text{--}32$ ) and that  $\epsilon'$  is smaller for the crystalline material. The most interesting characteristics are related to the optical properties of thin films. Figure 53.1 shows the evolution of the refractive index as a function of the processing conditions [3]. Acidic film heated to  $300^\circ\text{C}$  have a higher value than corresponding base-catalyzed film, consistent with the concept of polymeric rearrangement leading to a denser structure.

The amorphous films obtained by us by a dip-coating technique and densified in air at  $460^\circ\text{C}$  for 15 min have outstanding optical quality when withdrawn at a speed of 5 to 13 cm/min whatever is the ambient humidity. Their index of refraction,  $n \simeq 2.05$ , is, however, slightly smaller. Due to the easiness and the long shelf life of the sol preparation, the  $\text{PbTiO}_3$  and  $\text{TiO}_2\text{--PbO}$  amorphous films are perfect candidates for the preparation of reflective coating (up to 45%) with flat characteristics in the visible or near infrared region (Fig. 53.2). The films deposited on glass have a lower index of refraction because of the diffusion of Na ions from the substrate during the heat treatment.

The fabrication of passive optical devices using the sol-gel method is simple and inexpensive. It is advantageous as the method allows the choice of index of refraction and the thickness of the layers. Hermann and Wildmann [10] have shown the feasibility of the method by fabricating planar optical waveguides using  $\text{SiO}_2\text{--TiO}_2$  Lipicoat Merck solution. Using a rutile prism coupler, a He-Ne laser beam was successfully coupled to a thin planar  $\text{TiO}_2\text{--}0.25\text{PbO}$  film  $0.82 \mu\text{m}$  thick deposited on a common glass substrate. Figure 53.3 shows the schematic arrangement and the dispersion relation of the thickness versus the

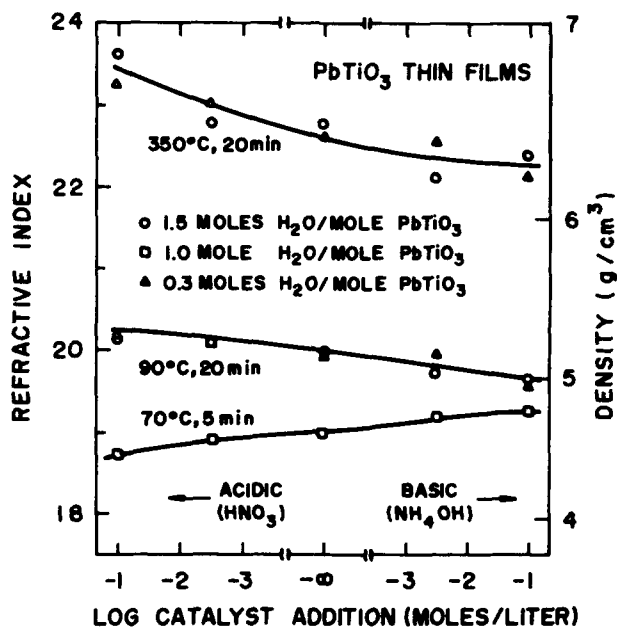


Figure 53.1. The refractive index for amorphous  $\text{PbTiO}_3$  thin films prepared by the sol-gel process as a function of the processing conditions from Ref. 3.

effective mode numbers  $N_m = n_p \sin(\epsilon + \arcsin(\sin \alpha / n_p))$  [11] for the TE modes only. The values measured experimentally are in good agreement (Table 53.2).

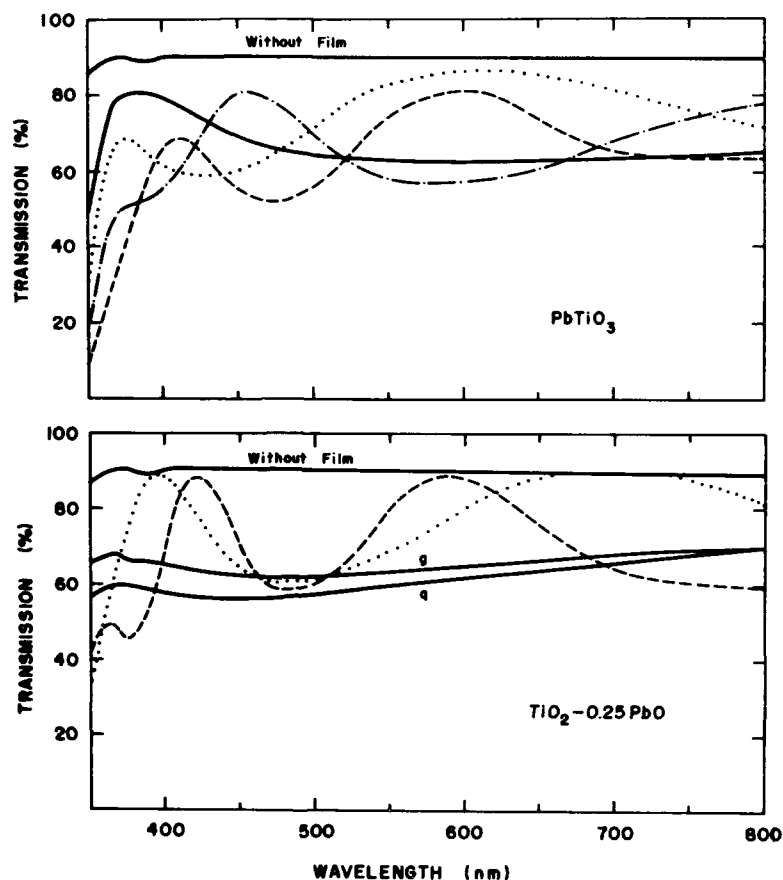
These results are extremely promising and open a new field of application as the layers were prepared without special substrate cleaning, solution filtration, and clean room facilities and confirm the high optical quality of these lead titanate-derived films.

Embossing techniques used in integrated optics to fabricate surface-relief gratings and channel waveguides would be another promising possibility. The technique was first developed for hard and resistant  $\text{SiO}_2$ - $\text{TiO}_2$  sol-gel film

TABLE 53.2. Experimental Values of  $\alpha$  and  $N_m$ <sup>a</sup>

$\text{TE}_m$	$\alpha$	$N_m$
$\text{TE}_0$	$18^\circ 38'$	2.12
$\text{TE}_1$	$11^\circ 12'$	2.04
$\text{TE}_2$	$-0^\circ 45'$	1.89
$\text{TE}_3$	Not observed	

<sup>a</sup>See also Fig. 53.3.



**Figure 53.2.** Transmission spectra of films deposited on both faces of common glass substrate. Each layer is heat treated at 460°C for 15 min. (Top)  $\text{PbTiO}_3$ : —, one layer; ···, two layers; ---, three layers; - · -, four layers. Each layer has a thickness  $t \sim 72$  nm. (Bottom)  $\text{TiO}_2-0.25\text{PbO}$ : q, one layer on  $\alpha$ -quartz,  $t = 51$  nm,  $n = 2.19$ ; g, one layer on glass,  $t = 55$  nm,  $n = 2.10$ ; ···, three layers,  $t = 170$  nm,  $n = 2.13$ ; - · -, five layers,  $t = 280$  nm,  $n = 2.17$ .

(Liquicoat ZLI 1686, Merck) by Lukosz et al. [12, 13] and more recently by Tohge et al. for  $\text{SiO}_2$  film [14]. The technique involves the pressing of a dry film against an aluminized reflective grating or stamper followed by baking at 500°C. The replica may function as an input or output grating coupler, Bragg reflector, pregrooves of optical memory disk, or any other optical device that requires an engraved pattern. Recently, using a microprocessor-controlled dipping arm to withdraw a  $\text{SiO}_2$ - $\text{TiO}_2$  film from the solution with varying speeds, Hewak and Lit [15] fabricated tapered and lenslike waveguides. The successful and easier preparation of thin lead titanate film of high optical quality combined with their high refractive index is without any doubt a good candidate for future research and applications in this optical field.

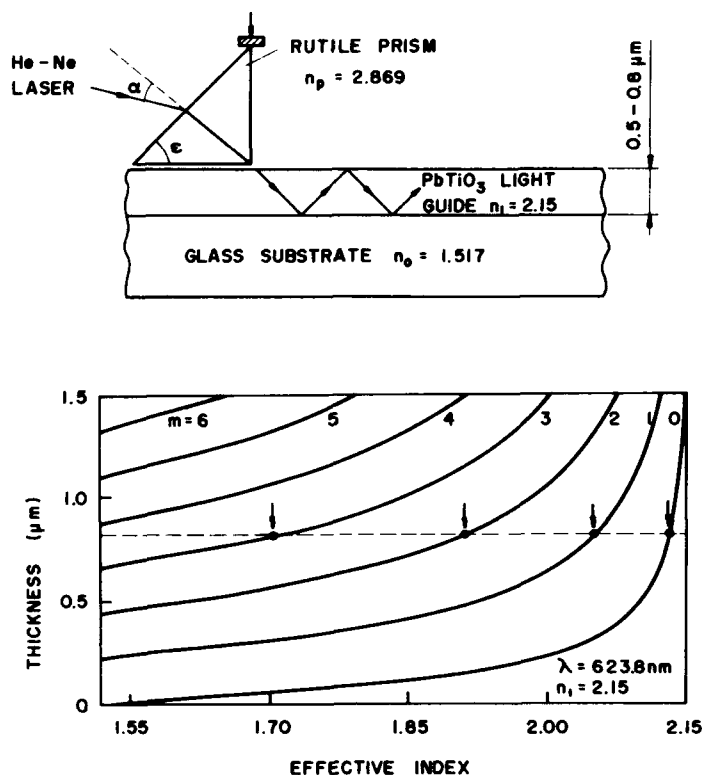


Figure 53.3. (Top) The prism coupler method to couple the He-Ne laser light beam to a  $\text{TiO}_2$ -0.25PbO planar waveguide. (Bottom) The dispersion relation for a  $\text{TiO}_2$ -0.25PbO waveguide ( $n_1 = 2.15$  at  $\lambda = 623.8 \text{ nm}$ ) deposited on a glass substrate ( $n_0 = 1.517$ ) showing the various effective modes obtained as a function of the film thickness. The dashed line refers to a film  $0.82 \mu\text{m}$  thick (15 layers) measured experimentally (see Table 53.2).

### 53.3. BARIUM TITANATE-DERIVED MATERIAL

Several compounds in the  $\text{BaO-TiO}_2$  system are known to be technologically important electroceramics.  $\text{BaTiO}_3$  is a dielectric ceramic widely used in the manufacture of capacitors.  $\text{BaTi}_4\text{O}_9$  and  $\text{Ba}_2\text{Ti}_9\text{O}_{20}$  have interesting properties for microwave applications (filters, etc). However, the conventional processing of these materials relies on relatively high temperature ( $1100$ – $1300^\circ\text{C}$ ). It is therefore not surprising to find several sol-gel studies in the literature, because the use of organometallic compounds allows in principle a low-temperature preparation and processing of homogeneous thin films and powders without the undesirable impurities, such as  $\text{Al}_2\text{O}_3$ ,  $\text{SiO}_2$ , S, and P, which have deleterious effects on the electrical properties of these ceramics.



### 53.3.1. Precursors, Sols, and Gel-to-Ceramic Conversion

#### 53.3.1.1. Preparation Using Two Alkoxides

In their pioneering work, Mazdidasni et al. [16, 17] prepared  $\text{BaTiO}_3$  powder by the simultaneous hydrolytic decomposition of high-purity titanium tertiary amyloxyde  $\text{Ti}(\text{OC}_5\text{H}_{11})_4$  and barium bisisopropoxide,  $\text{Ba}(\text{OC}_3\text{H}_7)_3$ . The stoichiometric mixture of both alkoxides was refluxed for 24 hr. After adding dropwise water and isopropyl alcohol, they obtained a barium titanate hydroxide precipitate, which after washing and drying at  $50^\circ\text{C}$  gave a  $>99.98\%$  pure  $\text{BaTiO}_3$  power of 50- to  $150\text{-}\text{\AA}$  size. Doping with Sc, and Ln oxide was prepared by the addition of the respective isopropoxides. The powders were calcined at  $500^\circ\text{C}$  for 30 min, ground, and then cold pressed. Sintering of compact bodies was done in air at 1300 to  $1500^\circ\text{C}$  for 1 hr.

Thin films have been prepared by Yanovskaya et al. [18] by hydrolytic decomposition of alcoholic solution of  $\text{Ba}(\text{OEt})_2$  and  $\text{Ti}(\text{OEt})_4$ . These solutions are highly sensitive to moisture and carbon dioxide; the formation of the amorphous product is thought to arise from the hydrolysis of the  $\text{BaTi}(\text{OEt})_6$  complex. Crystallization into  $\text{BaTiO}_3$  occurred around  $700^\circ\text{C}$ , and several polytitanates such as  $\text{Ba}_2\text{TiO}_4$ ,  $\text{BaTi}_2\text{O}_5$ , and  $\text{BaTiO}_7$ , were observed at higher annealing temperatures.

Rehspringer [19] prepared  $\text{BaTiO}_3$  powders by mixing the same ethoxides in the presence of a large excess of alcoholic water (400%). The reaction led to the formation of very fine amorphous powder ( $\sim 30\text{ nm}$ ) already aggregated. Crystallization occurred at  $\sim 700^\circ\text{C}$ . Monolithic gels [19, 20] were obtained by controlling the chemical reactions of hydrolysis and polycondensation by working at lower temperatures ( $\sim -45$  to  $0^\circ\text{C}$ ). After drying, the gels can be transformed at  $725^\circ\text{C}$  into a glassy matrix containing small egg-shaped  $\text{BaTiO}_3$  crystals.

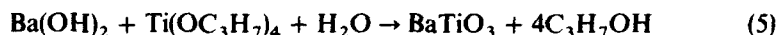
#### 53.3.1.2. Preparation Using BaO and Ti-Alkoxide

Ritter et al. [21] proposed a novel and inexpensive technique that uses technical grade BaO to prepare a barium extract under argon atmosphere; this compound is thought to be a 1:1 mixture of  $\text{Ba}(\text{OC}_2\text{H}_5)_2$  and  $(\text{C}_2\text{H}_5\text{O})\text{Ba}_2\text{O}$  and has been used in the preparation of barium polytitanates by reaction with titanium isopropoxide, ethanol, and water. The powder that resulted was separated by centrifugation, washed, and finally dried. The method was used to prepare and characterize various polytitanates such as  $\text{Ba}_2\text{TiO}_4$  (2:1),  $\text{BaTiO}_3$  (1:1),  $\text{Ba}_6\text{Ti}_{17}\text{O}_{40}$  (6:17),  $\text{Ba}_4\text{Ti}_{13}\text{O}_{30}$  (4:13),  $\text{BaTi}_4\text{O}_9$  (1:4),  $\text{Ba}_2\text{Ti}_9\text{O}_{20}$  (2:9),  $\text{BaTi}_5\text{O}_{11}$  (1:5), and  $\text{BaTi}_6\text{O}_{13}$  (1:6).

#### 53.3.1.3. Preparation Using $\text{Ba}(\text{OH})_2$

Flaschen [22] proposed an aqueous synthesis of  $\text{BaTiO}_3$  by the dropwise addition of tetrapropyl titanate into a degassed water solution of barium

hydroxide (pH 11 to 14). This technique was found useful for introducing desirable impurities and for the partial substitution of barium. The process is simple and is summarized as follows:



The same process was later used by Dosch [23] to prepare thin film on Si, Ni, and Ti substrates.

#### **53.3.1.4. Preparation Using Ba-Carbonate and Ti-Alkoxide**

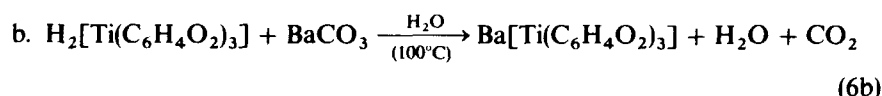
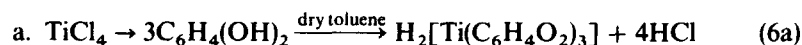
Salze et al. [24] prepared powders with the following reaction: Titanium was introduced in the form of Ti-isopropoxide dissolved in ethylene glycol and citric acid at 80 to 100°C. The clear, and water-soluble complex is not yet known. Barium was introduced as a solution of carbonate dissolved in citric acid at 80°C. The final solution is clear, water soluble, and stable; a polymer can be obtained by heating at 160°C, which after elimination of the organic fractions is pyrolyzed in air. Crystalline BaTiO<sub>3</sub> is noted around 550°C together with BaCO<sub>3</sub> and other polytitanates. The power is composed of small plates 10 μm thick made up of clusters of BaTiO<sub>3</sub> (~0.5 μm) associated with very small crystallites (20–40 nm).

#### **53.3.1.5. Preparation Using Ba-Acetate and Ti-Alkoxide**

This novel method is quite interesting, because it allows the preparation of powders and thin films from simple chemical polymerization between inexpensive and moisture-insensitive materials. The process involves the mixing at room temperature of a solution of Ti-isopropoxide in isopropanol [25–27] or Ti-ethoxide [28, 29] with an aqueous solution of Ba-acetate (molar ratio 1:1). Acetic acid and/or acetylacetone are also added in order to avoid precipitation. These sols are relatively stable and gel in a few days. The white opaque gels transform into powder when dried at 100°C. Thin films can be prepared by the dip-coating technique at a withdrawal speed 6 to 20 cm/min for a sol viscosity of 2.5 to 4 cP. For both products, crystallization starts around 550 to 600°C. The evolution of the local structure of the Ba–Ti environment of the complex has been studied by Mosset et al. [28] by the large-angle X-ray scattering method. They showed that for  $T < 250^\circ\text{C}$ , Ba<sub>4</sub>(HC<sub>3</sub>COO)<sub>8</sub> units are associated to Ti<sub>3</sub> and Ti<sub>6</sub> complex molecules. Pyrolysis of the organic ligands with Ba–O–Ti bonds breaking occurs between 250 and 400°C. The presence of BaCO<sub>3</sub> around 400°C and a theoretical analysis of the radial distribution function, which excludes BaO, BaTi<sub>4</sub>O<sub>9</sub>, and Ba<sub>2</sub>TiO<sub>4</sub> as precursors, indicate that BaTiO<sub>3</sub> is probably formed by a BaCO<sub>3</sub>–TiO<sub>2</sub> reaction. Gels dried hypercritically at 280°C, 200 bars, and analyzed by transmission electron microscopy (TEM) and X-ray diffraction showed a needle structure composed of crystalline barium acetate and titanium oxide. In this case, pure BaTiO<sub>3</sub> was only observed after heat treatment at 900°C [25].

**53.3.1.6. Another Preparation**

Ali et al. [30, 31] have recently developed a promising new route to synthesize titanate compound powders from catecholate complexes through the following reactions:



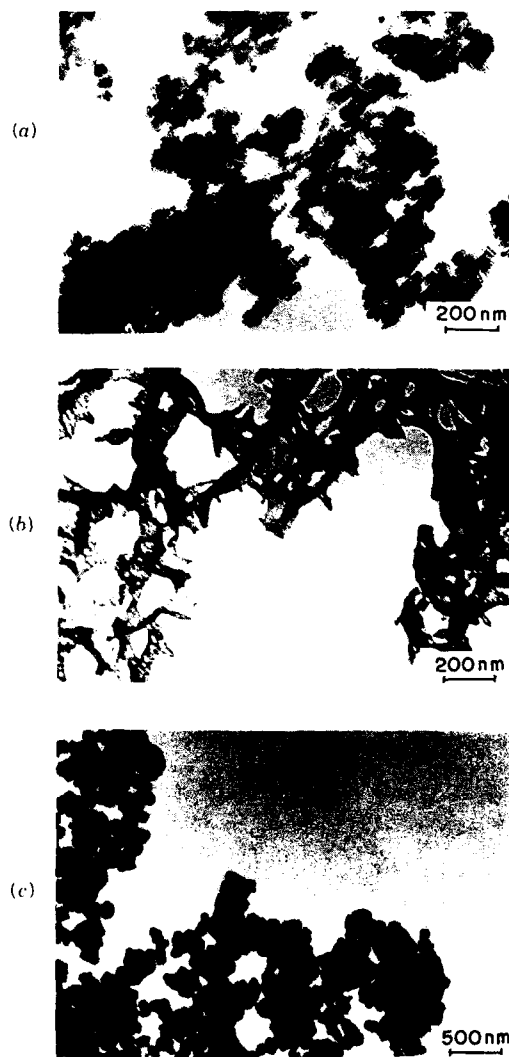
After removing the unreacted carbonate phases by filtration, this sol was freeze-dried to isolate the complex in solid form and transformed by calcination at  $600^\circ\text{C}$ ,  $>1$  hr into a crystalline  $\text{BaTiO}_3$  fine powder.

**53.3.2. Gels, Powders, and Films Characterization**

Most of the available characterization of the Ba-titanate-derived materials was obtained by X-ray diffraction and TEM studies. Differences in alkoxide precursor, hydrolysis and polycondensation conditions, and drying and calcination conditions have an important effect on the polymeric structure and subsequent ceramic microstructure. It is therefore difficult to synthesize the results.

Whatever is the precursor preparation the " $\text{BaTiO}_3$ " initial product is amorphous, but the structure of the chemical complex is not well known; when calcined at  $500$  to  $600^\circ\text{C}$ , it transforms into crystalline  $\text{BaTiO}_3$  with a tetragonal structure. Adapting the stoichiometry, it is possible to obtain other Ba-Ti compositions. At this stage the powders are usually composed of fine particles in the range of  $5$  to  $10$  nm agglomerated in  $<1\text{-}\mu\text{m}$  clusters and are considered  $>99.9\%$  pure. Calcination at a higher temperature increases the grains size and the powder density, but no other polytitanates are observed. Figure 53.4 shows as an example TEM micrographies of  $\text{BaTiO}_3$  powders prepared with the Ba-acetate-Ti-isopropoxide precursor method under different pH and drying conditions; the powders have been later calcined at  $700^\circ\text{C}$  during  $4$  hr. The figure illustrates the complexity and the dependence of the structure on the processing conditions that can have a definite influence on the sintered ceramics microstructure and physical properties.

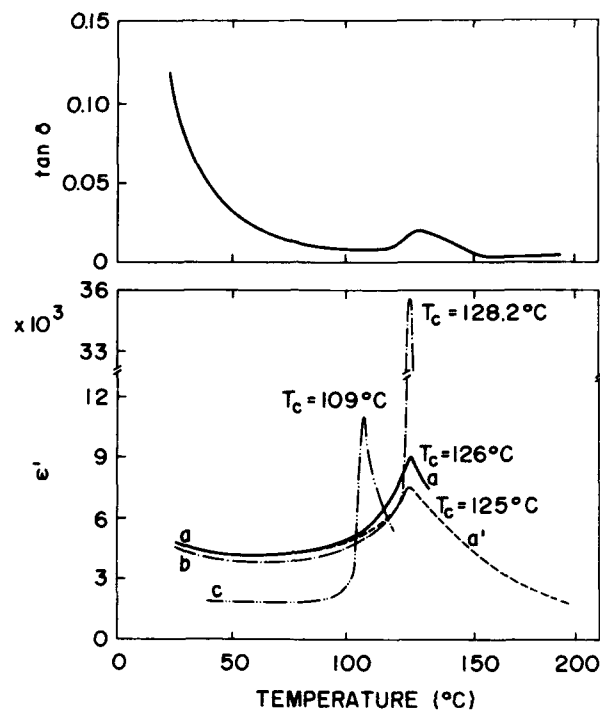
Interesting dielectric characteristics are obtained after sintering at an elevated temperature, but no systematic study has been done yet to find out the best processing conditions. At this stage the density is close to the theoretical one [16, 17], and the ceramics structure presents virtually no internal and grain boundary porosity [16, 17]. Figure 53.5 shows typical results of  $\epsilon'$  and  $\tan\delta$  obtained by us, Mazdiyasi and Brown [17], and Martens [32]. The overall behavior is analogous for all systems. Our sintered material has the highest dielectric constant at room temperature, but the Curie point is not as sharp as



**Figure 53.4.** BaTiO<sub>3</sub> powders structure obtained by the Ba-acetate–Ti-isopropoxide method (see section 53.3.1.5) and calcined at 700°C for 2 hr: (a) Sol prepared at pH 4.3 and dried at 100°C; (b) sol prepared at pH 9.4 and dried at 100°C; (c) sol prepared at pH 4.3 and hypercritically dried at 280°C, 200 bars.

the other two and the maximum value of  $\epsilon'$  is lower than that found by Mazdiyasni and Brown. This broadening may be due to the presence of regions with a different  $T_c$ , defects that inhibit the domain wall movements, or grain size effects.

The highest Curie temperature of these materials agrees with the value found for a single crystal [33]. The lower value obtained for the Martens material is



**Figure 53.5.** The dielectric constant and dissipation factor measured as a function of temperature of pure  $\text{BaTiO}_3$  ceramics prepared with *a* and *a'*, powder obtained from the Ba-acetate-Ti-isopropoxide mixture (see Section 53.3.1.5) calcined at  $700^\circ\text{C}$  and sintered at  $1350^\circ\text{C}$ , 2 hr (*a'*) and 5 hr (*a*) ( $f = 10\text{ KHz}$ ); *b*, powder obtained from Ba and Ti-alkoxide mixture (see section 53.3.1.1), calcined at  $50^\circ\text{C}$  and sintered at  $1350^\circ\text{C}$ , 1 hr (data from [17]); *c*, powder obtained by Martens [32] and sintered at  $1325^\circ\text{C}$ , 4 hr (precursor preparation and processing not available).

due to the high reported percentage of SrO impurity (2.3 wt %, [32]). Above  $T_c$  our measurements are consistent with a Curie-Weiss behavior,  $\epsilon' = C/(T - T_0)$ , where  $C = 5.3 \times 10^6^\circ\text{C}$  and  $T_0 = 88^\circ\text{C}$ . In all cases the  $\tan \delta$  behavior is normal with a small discontinuity at the Curie point. Phule and Risbud [27] have also reported that the powder calcined at  $700^\circ\text{C}$  and sintered at  $1350^\circ\text{C}$  for 6 hr have a dielectric constant of 4000.

Until now and in spite of its fundamental technological importance for the preparation of multilayer capacitors,  $\text{BaTiO}_3$  obtained in thin-film form has been poorly characterized. A dense amorphous single layer 30 to 120 nm thick with an index of refraction  $n = 2.0$  can be deposited by the dip-coating technique on glass,  $\alpha\text{-SiO}_2$ , and metallic substrates. Thick layers can be prepared by repeating the process. According to X-ray diffraction and differential thermal and thermogravimetric results, crystallization into tetragonal  $\text{BaTiO}_3$  structure occurs in the temperature range  $450$  to  $500^\circ\text{C}$  [23, 25] or  $700^\circ\text{C}$  [18]. Annealing

at a higher temperature only increases the grain sizes, and no other titanates have been reported. Amorphous films have an electrical breakdown strength of the order of  $9 \times 10^6$  V/cm, which is greater than that of crystalline films  $\sim 10^5$  V/cm. The values, however, are dependent of the substrate material [18, 23]. Manifestation of ferroelectric properties have only been reported after a heat treatment at  $800^\circ\text{C}$  where sufficient a grain size of  $0.1 \mu\text{m}$  has been obtained. Higher temperatures increase the grain size, but is accompanied by film cracking and the formation of cavities. The dielectric response is poor ( $\epsilon' \sim 50\text{--}80$ ,  $\tan \delta \sim 2\text{--}3$ ) and shows a broad Curie point at  $118^\circ\text{C}$  with little increase of the dielectric constant [18].

#### 53.4. CONCLUSION

Sol-gel processing of lead and barium titanate materials is possible, and various precursor preparation recipes are now available and have been reviewed. These materials can be better obtained in the form of gels, powders, and films. Amorphous products are obtained at low temperatures, but their chemical compositions and their thermal evolution are usually not known with certainty. Basic and arduous work is still necessary in order to elucidate these processes.

All the materials crystallized at relatively low temperatures ( $500\text{--}700^\circ\text{C}$ ). The transition temperatures depend mainly of the precursor preparation and the processing conditions. However, interesting dielectric properties seem only obtainable at temperatures close to those used in conventional processes, but no detailed and systematic studies have yet been reported to optimize the processing conditions.

The sol-gel process definitively lowers the temperature of formation of pure lead and barium titanate-derived materials, but it is not proven at all that devices having physical characteristics similar or better to those obtained today by conventional processes can be prepared by this method.

The most interesting results are reported for amorphous thin films densified at low temperatures:  $\text{BaTiO}_3$  films present good electric insulation properties, and lead titanate films are promising systems for optical applications and passive integrated-optical devices fabrication.

#### ACKNOWLEDGMENTS

Research was supported by FAPESP, FINEP, CNPq, and the Secretary for Science, Technology and Economic Development of the State of São Paulo, Brazil. One of us (Y.C.) is grateful to the Ministère des Affaires Étrangères for a VSNA scholarship.

## REFERENCES

1. S. R. Gurkovich and J. B. Blum, in: L. Hench and D. Ulrich, Eds., *Ultrastructure Processing of Ceramics, Glasses and Composites*, p. 152, Wiley, New York (1984).
2. K. D. Budd, S. K. Dey, and D. A. Payne, *Proc. Br. Ceramic Soc.*, **36**, 107 (1985).
3. K. D. Budd, S. K. Dey, and D. A. Payne, in: C. J. Brinker, D. E. Clark, and D. R. Ulrich, Eds., *Better Ceramics Through Chemistry*, Vol. III, *Mater. Res. Soc. Symp. Proc.*, **73**, 711 (1986).
4. C. Sanchez, in: *Précurseurs Moléculaires de Matériaux Inorganiques Procédés sol-gel, Proceedings CNRS (France) Greco*, **93** (1987).
5. C. Sanchez, J. Livage, M. Henry, and F. Babonneau, *J. Non-Cryst. Solids*, **100**, 65 (1988).
6. C. Sanchez, F. Babonneau, S. Doeuff, and A. Léaustic, in: J. D. Mackenzie et al., Eds., *Ultrastructure Processing of Advanced Ceramics*, Wiley, New York (1988).
7. A. Yamamoto and S. Kambara, *J. Am. Chem. Soc.*, **79**, 4344 (1957).
8. S. K. Dey, K. D. Budd, and D. A. Payne, *J. Am. Ceramic Soc.*, **70**, C295 (1987).
9. R. W. Schwartz and D. A. Payne, in: C. J. Brinker, D. E. Clark, and D. R. Ulrich, Eds., *Better Ceramics Through Chemistry*, Vol. III, *Mater. Res. Soc. Symp. Proc.*, **121**, 199 (1988).
10. P. P. Hermann and D. Wildmann, *IEEE J. Quantum Electron.*, **QE-19**, 1735 (1983).
11. D. Ulrich and R. Torge, *Appl. Opt.*, **12**, 2901 (1973).
12. W. Lukosz and K. Tiefenthaler, *Opt. Lett.*, **8**, 537 (1983).
13. K. Heuberger and W. Lukosz, *Appl. Opt.*, **25**, 1499 (1986).
14. N. Tohge, A. Matsuda, T. Minami, Y. Matsuno, S. Katayama, and Y. Ikeda, *J. Non-Cryst. Solids*, **100**, 501 (1988).
15. D. W. Hewak and J. W. Lit, *Appl. Opt.*, **27**, 4562 (1988).
16. K. S. Mazdiyasni, R. T. Dolloff, and J. S. Smith, *J. Am. Ceramic Soc.*, **52**, 523 (1969).
17. K. S. Mazdiyasni and L. M. Brown, *J. Am. Ceramic Soc.*, **55**, 633 (1972); **54**, 534 (1971).
18. M. I. Yanovskaya, N. Ya. Turova, E. P. Turevskaya, A. V. Novoselova, Y. N. Venetsev, S. I. Sagitov, and E. M. Soboleva, *Inorg. Mater.*, **17**, 221 (1981).
19. J. L. Rehspringer, in: *Précurseurs Moléculaires de Matériaux Inorganiques, Procédés sol-gel, Proceedings CNRS (France) Greco*, **93**, III-5 (1987).
20. J. L. Rehspringer, P. Poix, and J. C. Bernier, *J. Non-Cryst. Solids*, **82**, 286 (1980).
21. J. J. Ritter, R. S. Roth, and J. E. Blendell, *J. Am. Ceramic Soc.*, **69**, 155 (1986).
22. S. S. Flaschen, *J. Am. Chem. Soc.*, **77**, 6194 (1955).
23. R. G. Dosch, in: C. J. Brinker, D. E. Clark, and D. R. Ulrich, Eds., *Better Ceramics Through Chemistry*, Vol. I, *Mater. Res. Soc. Symp. Proc.*, **32**, 157 (1984).
24. H. Salze, B. Dubois, C. Proust, and P. Odier, in: *Précurseurs Moléculaires de Matériaux Inorganiques, Procédés sol-gel, Proceedings CNRS (France) Greco*, **93**, III.6 (1987).
25. N. D. S. Mohallem and M. A. Aegerter, in: C. J. Brinker, D. E. Clark, and D. R. Ulrich, Eds., *Better Ceramics Through Chemistry*, Vol. III, *Mater. Res. Soc. Symp. Proc.*, **121**, 515 (1988).
26. P. P. Phule and S. H. Risbud, in: C. J. Brinker, D. E. Clark, and D. R. Ulrich, Eds., *Better Ceramics Through Chemistry*, Vol. III, *Mater. Res. Soc. Symp. Proc.*, **121**, 275 (1988).
27. P. P. Phule and S. H. Risbud, *Adv. Ceramic Mater.*, **3**, 183 (1988).
28. A. Mosset, I. Gauthier-Luneau, J. Galy, P. Strehlow, and H. Schmidt, *J. Non-Cryst. Solids*, **100**, 339 (1988).
29. G. Tomandl, H. Rösch, and A. Stiegelschmitt, in: C. J. Brinker, D. E. Clark, and D. R. Ulrich, Eds., *Better Ceramics Through Chemistry*, Vol. III, *Mater. Res. Soc. Symp. Proc.*, **121**, 281 (1988).
30. N. J. Ali and S. J. Milne, *Br. Ceramic Trans. J.*, **86**, 113 (1987).

## REFERENCES

627

31. N. J. Ali, J. Bultitude, L. A. Xue, and S. J. Milne, in: C. J. Brinker, D. E. Clark, and D. R. Ulrich, Eds., *Better Ceramics Through Chemistry*, Vol. III, *Mater. Res. Soc. Symp. Proc.*, **121**, 269 (1988).
32. G. Martens, Solvay Co., private communication. The precursor fabrication process is not known.
33. C. J. Johnson, *Appl. Phys. Lett.*, **7**, 221 (1965).



## A NOVEL PROCESS FOR FABRICATION OF Bi—Ca—Sr—Cu—O HIGH- $T_c$ SUPERCONDUCTORS—A GLASS-TO-CERAMIC PROCESS

HAIXING ZHENG AND J. D. MACKENZIE

### 54.1. INTRODUCTION

The subsequent discoveries of high- $T_c$  superconducting ceramics, La—Ba—Cu—O [1], Y—Ba—Cu—O [2,3], Bi—Ca—Sr—Cu—O [4], and Tl—Ca—Cu—O [5], have opened an era of technology through the use of low-cost liquid nitrogen as a cooling agent. Since then, extensive research has been stimulated for the application of high- $T_c$  superconductors. The practical application of the high- $T_c$  superconducting ceramics mandates (1) the ceramics with high critical current density  $J_c$  at high magnetic field and (2) fabrication of specific shapes of the ceramics: wires, tapes, and films. Scientists have used various processes for fabrication of high- $T_c$  superconducting ceramics. However, none of these processes work ideally for these high- $T_c$  superconducting ceramics yet. The main reasons include:

1. Random distribution of the superconducting crystals, because these new crystals are anisotropic.
2. Impurities (nonsuperconducting phases and porosity) existing among the superconducting grains.

*Ultrastructure Processing of Advanced Materials.*

Edited by Donald R. Uhlmann and Donald R. Ulrich (deceased).

ISBN 0-471-52986-9 © 1992 John Wiley & Sons, Inc.

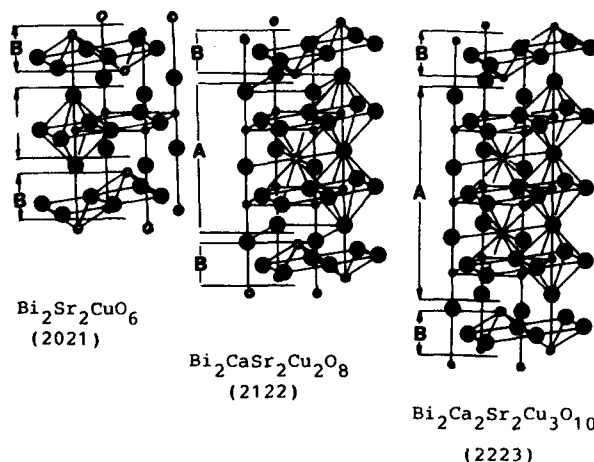
3. Difficulties in fabrication of specific shapes, for example, wires and fibers.
4. Brittleness and inflexibility of the superconducting materials.

The Bi-Ca-Sr-Cu-O high- $T_c$  superconducting system possesses the high  $T_c$  (110 K) and nontoxicity as compared to other high- $T_c$  superconducting systems, such as  $\text{LnBa}_2\text{Cu}_3\text{O}_{7-x}$  ( $T_c \sim 90$  K) and  $\text{Tl-Ba-Ca-Cu-O}$  ( $T_c \sim 125$  K, but is toxic). There are three superconducting phases, 110 K ( $\text{Bi}_2\text{Ca}_2\text{Sr}_2\text{Cu}_3\text{O}_y$ ), 75 K phase ( $\text{Bi}_2\text{CaSr}_2\text{Cu}_2\text{O}_y$ ), and 20 K phase ( $\text{Bi}_2\text{Sr}_2\text{CuO}_y$ ), which consist of three Cu-O layers, two Cu-O layers, and one Cu-O layer, respectively (Fig. 54.1). The intergrowth problem of the 110 K, 75 K, and 20 K phases [6], however, degrades the advantages of the Bi-Ca-Sr-Cu-O high- $T_c$  superconducting system. Much effort has been placed on this problem [7].

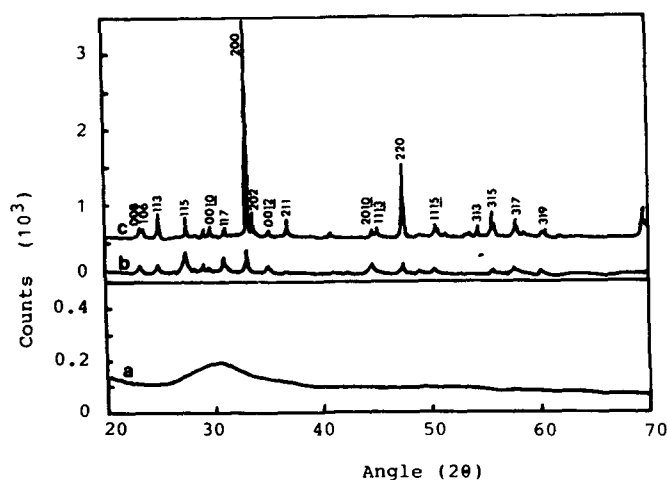
Last year, a novel and promising process for the fabrication of high- $T_c$  Bi-Ca-Sr-Cu-O superconductors—a glass-to-ceramic process—was investigated by several groups [8–11]. In this Chapter, the systematic experimental results on the glass-forming range, glass structure, crystallization, preferred orientation of superconducting crystals, mechanical strength, and the formation of 110 K superconducting phase will be reported. The potential of this process also will be discussed.

#### 54.2. $\text{Bi}_4\text{Ca}_3\text{Sr}_3\text{Cu}_4\text{O}_{16}$ SUPERCONDUCTING CERAMICS BY THE GLASS-TO-CERAMIC ROUTE [8]

$\text{Bi}_4\text{Ca}_3\text{Sr}_3\text{Cu}_4\text{O}_{16}$  glass is prepared by melting  $\text{Bi}_2\text{O}_3$ ,  $\text{CaCO}_3$ ,  $\text{SrCO}_3$ , and  $\text{CuO}$  in an alumina or platinum crucible at 950 to 1100°C for 15 to 60 min and then quenching the melt between two brass plates. The X-ray diffraction pattern



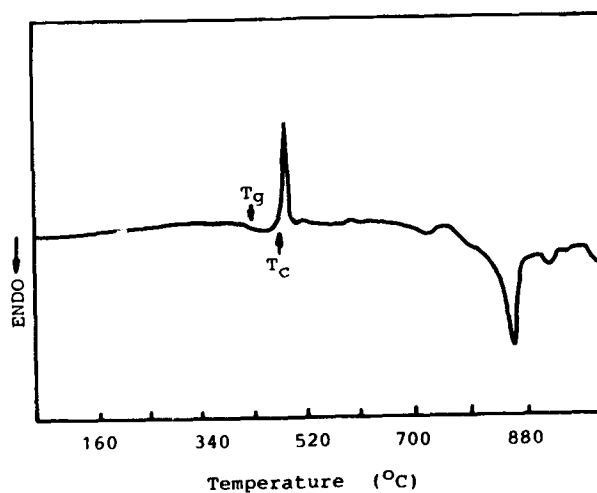
**Figure 54.1.** The unit cells of superconducting crystals:  $\text{Bi}_2\text{Sr}_2\text{CuO}_y$ , (2021),  $\text{Bi}_2\text{CaSr}_2\text{Cu}_3\text{O}_y$ , (2122), and  $\text{Bi}_2\text{Ca}_2\text{Sr}_2\text{Cu}_3\text{O}_y$ , (2223).



**Figure 54.2.** X-ray diffraction patterns of (a)  $\text{Bi}_4\text{Ca}_3\text{Sr}_3\text{Cu}_4\text{O}_{16}$  glass, (b) glass ceramic powder and (c) glass ceramic bulk.

of the quenched  $\text{Bi}_4\text{Ca}_3\text{Sr}_3\text{Cu}_4\text{O}_{16}$  sample (Fig. 54.2a) shows a glass characteristic. The glass transition temperature ( $T_g$ ), the crystallization temperature ( $T_c$ ), and the liquidus temperature of  $\text{Bi}_4\text{Ca}_3\text{Sr}_3\text{Cu}_4\text{O}_{16}$  glass (as shown in Fig. 54.3) are about  $434^\circ\text{C}$ ,  $478^\circ\text{C}$ , and  $833^\circ\text{C}$ , respectively, and its density is  $5.73 \text{ g/cm}^3$ .

When  $\text{Bi}_4\text{Ca}_3\text{Sr}_3\text{Cu}_4\text{O}_{16}$  glass is annealed at  $800^\circ\text{C}$  in air, it crystallizes (Figs. 54.2b and c). X-ray diffraction shows that the crystal phase,  $\text{Bi}_4\text{Ca}_3\text{Sr}_3\text{Cu}_4\text{O}_{16}$



**Figure 54.3.** Differential thermal analysis of  $\text{Bi}_4\text{Ca}_3\text{Sr}_3\text{Cu}_4\text{O}_{16}$  glass (heating rate,  $10^\circ\text{C/min}$ ).

( $T_c \sim 75$  K), is superconducting. The observed density of  $\text{Bi}_4\text{Ca}_3\text{Sr}_3\text{Cu}_4\text{O}_{16}$  glass ceramics is  $6.25 \text{ g/cm}^3$ . Because the calculated density is  $6.35 \text{ g/cm}^3$  for  $\text{Bi}_4\text{Ca}_3\text{Sr}_3\text{Cu}_4\text{O}_{16}$  crystal,  $\text{Bi}_4\text{Ca}_3\text{Sr}_3\text{Cu}_4\text{O}_{16}$  glass ceramic is about 98.5% ( $= 6.25/6.35$ ) dense.

Figure 54.4 is the photo of a  $\text{Bi}_4\text{Ca}_3\text{Sr}_3\text{Cu}_4\text{O}_{16}$  superconducting rod and ring fabricated by the glass-to-ceramic route. The compressive strength and the Vicker's hardness of the superconductors by the glass-to-ceramic process are  $2 \times 10^4$  psi and  $600 \text{ kg/mm}^2$ , respectively. The dependence of the relative resistance of  $\text{Bi}_4\text{Ca}_3\text{Sr}_3\text{Cu}_4\text{O}_{16}$  glass ceramic on temperature after the heat treatment at  $750^\circ\text{C}$  for 20 hr in air is shown in Fig. 54.5.  $\text{Bi}_4\text{Ca}_3\text{Sr}_3\text{Cu}_4\text{O}_{16}$  glass ceramic is superconducting with an onset transition temperature of about 100 K and zero resistivity at 75 K.

### 54.3. THE GLASS-FORMING RANGE AND GLASS STRUCTURE OF $\text{BiO}_{1.5}\text{-CuO-Ca}_{0.5}\text{Sr}_{0.5}\text{O}$ SYSTEM [12]

The glass-forming region of  $\text{BiO}_{1.5}\text{-CuO-Ca}_{0.5}\text{Sr}_{0.5}\text{O}$  system has been determined by melting batches of 5 g and then quenching the melt between two brass plates (Fig. 54.6). The glass-forming range for each component is almost equal, that is,  $20 \text{ mol } \% < \text{BiO}_{1.5}, \text{CuO}, \text{Ca}_{0.5}\text{Sr}_{0.5}\text{O} < 50 \text{ mol } \%$ . The area circled by a dash line in Fig. 54.6 comprises the composition that forms more stable glasses, because all these glasses have  $(T_x - T_g) > 45^\circ\text{C}$ .

$\text{Bi}_2\text{O}_3$  is a conditional glass-forming oxide, that is, in the presence of strong polarizing cations such as  $\text{Si}^{4+}$  ions, bismuth ions can reduce their coordination number (6) from  $[\text{BiO}_6]$  octahedra and form glass network in the  $[\text{BiO}_3]$  pyramidal units. The infrared spectra of Bi-Ca-Sr-Cu-O glasses (glass composition listed in Table 54.1) is shown in Fig. 54.7. There are four vibration bands, 840, 620, 500, and  $300 \text{ cm}^{-1}$  in SC1 and Bi4 glasses, which are assigned to



Figure 54.4. A  $\text{Bi}_4\text{Ca}_3\text{Sr}_3\text{Cu}_4\text{O}_{16}$  superconducting rod and tube fabricated by the glass-to-ceramic process.

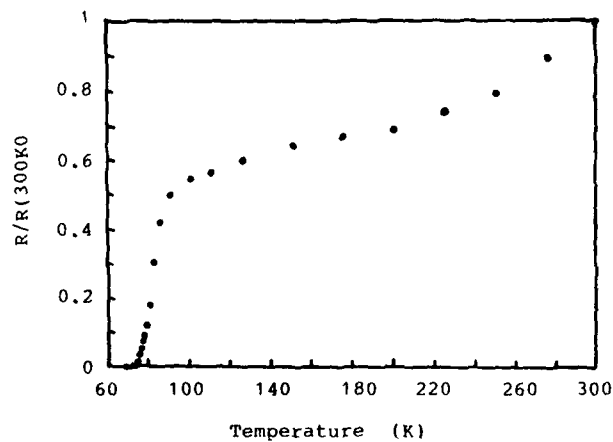


Figure 54.5. Electrical resistance of  $\text{Bi}_4\text{Ca}_3\text{Sr}_3\text{Cu}_4\text{O}_{16}$  superconducting ceramics on temperature.

the vibrations of  $[\text{BiO}_3]$  pyramidal units [13]. By decreasing the relative amount of  $\text{Ca}^{2+}$  or  $\text{Sr}^{2+}$  ions (or increasing  $\text{Bi}^{3+}$  ions), the number of vibration bands of Bi1,0 and SC2 glasses reduce to two (Fig. 54.7), which implies that  $[\text{BiO}_3]$  pyramidal units transform to  $[\text{BiO}_6]$  octahedra units, that is,  $\text{Bi}^{3+}$  ions become glass network modifiers. This causes loosening or shortening of the glass network [12], therefore decreasing  $T_g$  of glasses.

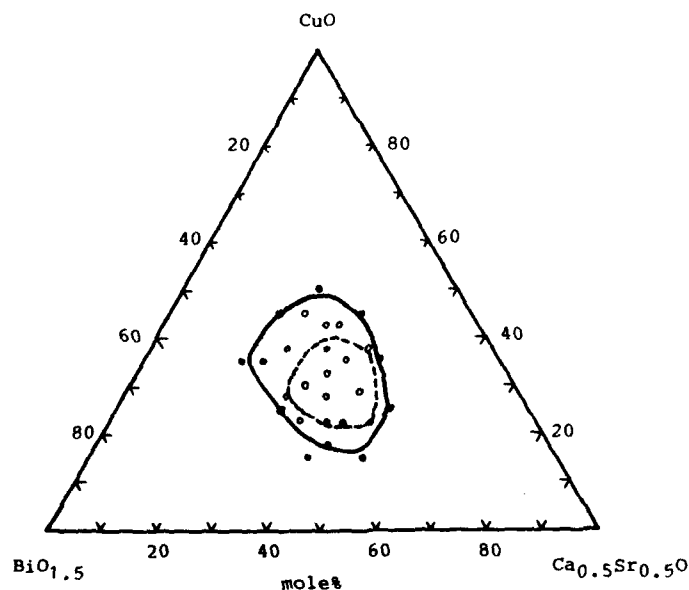


Figure 54.6. The glass-forming range of  $\text{BiO}_{1.5}$ - $\text{CuO}$ - $\text{Ca}_{0.5}\text{Sr}_{0.5}\text{O}$  system. O, glass, ●, partially crystallized glass.

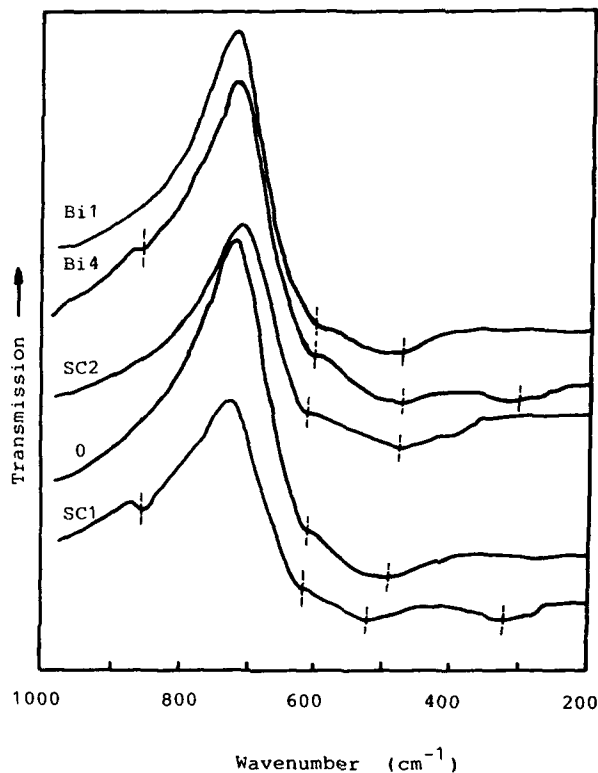


Figure 54.7. Infrared transmittance of Bi-Ca-Sr-Cu-O glasses.

#### 54.4. CRYSTALLIZATION OF Bi-Ca-Sr-Cu-O GLASSES

The knowledge of crystallization of Bi-Ca-Sr-Cu-O glass plays a key role in the prepared high quality of Bi-Ca-Sr-Cu-O high- $T_c$  superconductors. Figure 54.8 is the X-ray diffraction patterns of  $\text{Bi}_4\text{Ca}_3\text{Sr}_3\text{Cu}_4\text{O}_{16}$  glass heat treated at 475, 512 and 585°C for 1 hr. These temperatures correspond to the crystallization peaks of the differential scanning calorimetry run at 10°C/min of scan heating rate. The X-ray diffraction results show that the 75 K ( $\text{Bi}_2\text{CaSr}_2\text{Cu}_2\text{O}_8$ ) crystallizes at above 550°C, and the nonsuperconducting phases crystallizes out at low temperature. These results agree with the neutron diffraction results, which show that the 75 K phase emerges at > 550°C [14].

Depending on the glass composition, the number of crystallization peaks ranges from one to four below 550°C (Table 54.1). The X-ray diffraction patterns of glasses heat treated at 450°C are similar to that of the  $\text{Bi}_2\text{Sr}_2\text{CuO}_6$  phase, which has one copper layer with  $T_c < 22$  K [15]. This implies that the glass structure is closer to the structure of the  $\text{Bi}_2\text{Sr}_2\text{CuO}_6$  phase than that of the  $\text{Bi}_2\text{CaSr}_2\text{Cu}_2\text{O}_8$  phase or  $\text{Bi}_2\text{Ca}_2\text{Sr}_2\text{Cu}_3\text{O}_9$  phase.

TABLE 54.1. Glass Composition and Properties of the Bi-Ca-Sr-Cu-O System

No.	Composition (mol %)			Density (g/cm <sup>3</sup> )	$T_g$ (°C)	$T_i$ (°C)
	BiO <sub>1.5</sub>	CuO	Ca <sub>0.5</sub> Sr <sub>0.5</sub> O			
Bi1	42.5	27.5	30.0	6.6045	370	430, 480, 508
Bi2	37.5	30.0	32.5	6.4839	385	441, 539
0	32.5	32.5	35.0	6.2875	396	450
Bi3	27.5	35.0	37.5	6.1372	402	457
Bi4	22.5	37.5	40.0	5.9474	401	450, 468, 500
Cu1	27.5	42.5	30.0	6.2884	386	435, 440, 474
Cu2	30.0	37.5	32.5	6.2756	390	443, 475
0	32.5	32.5	35.0	6.2875	396	450
Cu3	35.0	27.5	37.5	6.3312	400	453
Cu4	37.5	22.5	40.0	6.4039	408	456
SC1	28.6	28.6	42.8	5.7702	410	458, 476, 482, 509
0	32.5	32.5	35.0	6.2875	396	450
SC2	37.5	37.5	25.0	6.7726	361	402, 433, 445

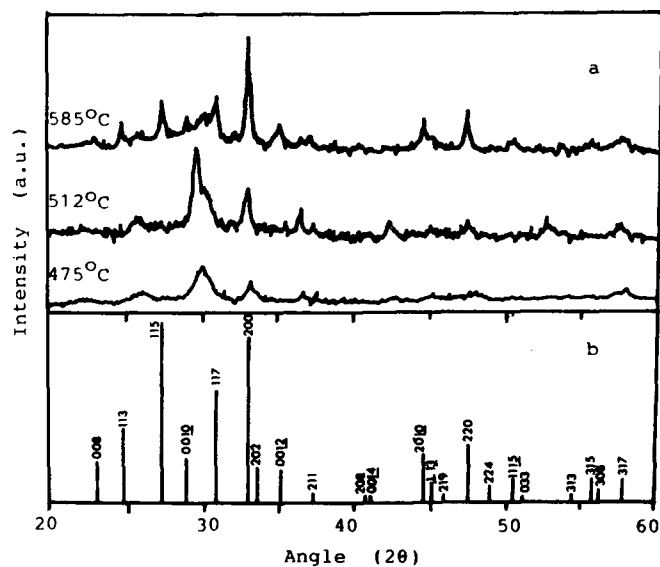
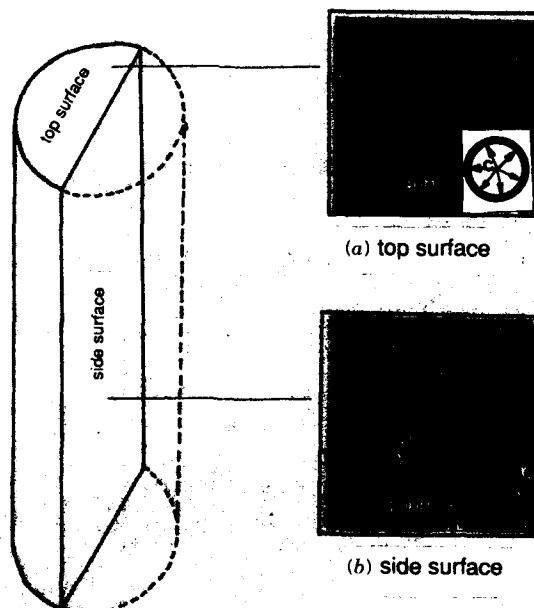


Figure 54.8. (a) X-ray diffraction patterns of Bi<sub>4</sub>Ca<sub>3</sub>Sr<sub>3</sub>Cu<sub>4</sub>O<sub>16</sub> glasses heat treated at a different temperature for 1 hr. (b) A standard X-ray diffraction pattern of the high- $T_c$  superconducting Bi<sub>2</sub>CaSr<sub>2</sub>Cu<sub>2</sub>O<sub>y</sub> crystal phase.

### 54.5. PREFERRED ORIENTATION OF SUPERCONDUCTING CRYSTALS

Preparation of superconducting ceramics with highly preferred orientation is a basic element for obtaining high critical current density  $J_c$ . Several techniques can be applied to orientate the crystal phases [16, 17]. Figure 54.2 shows the X-ray diffraction patterns of  $\text{Bi}_4\text{Ca}_3\text{Sr}_3\text{Cu}_4\text{O}_{16}$  glass ceramic bulk (c) and powder ground from the bulk (b). As shown, the X-ray diffraction peaks of the bulk solid at  $20^\circ$ ,  $25^\circ$ ,  $33^\circ$ ,  $37^\circ$ ,  $47^\circ$ ,  $54^\circ$ ,  $56^\circ$ , and  $58^\circ$ , which correspond to (113), (200), (211), (220), (313), (315), and (317) crystal planes of the  $\text{Bi}_2(\text{Ca}, \text{Sr})_3\text{Cu}_2\text{O}_x$  crystals, are enhanced, especially for the  $33^\circ$  and  $37^\circ$  peaks. Because all these enhanced peaks come from the atom planes parallel, or nearly parallel, to the  $c$  axis of  $\text{Bi}_4\text{Ca}_3\text{Sr}_3\text{Cu}_4\text{O}_{16}$  crystal, this enhancement of the diffraction peaks indicates  $c$ -axis preferred orientation of the  $\text{Bi}_4\text{Ca}_3\text{Sr}_3\text{Cu}_4\text{O}_{16}$  crystals in the bulk sample.

Figure 54.9 shows the microstructure of Bi-Ca-Sr-Cu-O superconducting ceramic rods derived from glasses. The microstructure of the top surface (polished and then etched) of the glass rods (Fig. 54.9a) consists of 75 K superconducting crystals with the  $c$  axis parallel to the surface. Therefore the microstructure of the side surface (polished and then etched) should be made of the crystal plane with the  $c$  axis perpendicular to the axis of the rods. A scanning electron micrograph (SEM) of the side surface section (Fig. 54.9b) illustrates exactly the same microstructure.



**Figure 54.9.** A superconducting rod with highly preferred-orientation microstructure. (a) An SEM of the top surface. (b) An SEM of the side surface.



## 54.6. DOPING EFFECTS

In order to prepare high-quality Bi-Ca-Sr-Cu-O superconductors, chemical doping of 1.5 wt % PbO,  $P_2O_5$ ,  $Al_2O_3$ ,  $B_2O_3$ ,  $Ga_2O_3$ , and  $SiO_2$  in  $Bi_2Ca_2Sr_2Cu_3O_{10}$  glass ceramics have been investigated. Table 54.2 lists the effects of doping on the superconductivity. Except for  $Ga_2O_3$ ,  $Bi_2Ca_2Sr_2Cu_3O_y$  ceramics with all other dopants show the superconductivity.

Typical Bi-Ca-Sr-Cu-O superconducting ceramics (e.g.,  $Bi_2Ca_2Sr_2Cu_3O_{10}$  ceramics) have three steps of resistance drop: the first small drop at 120 K, the second major drop at 85 K, and the last drop at 70 K (Fig. 54.10) due to the intergrowth of the three superconducting phases. With 1.5 wt %  $P_2O_5$  doping in  $Bi_2Ca_2Sr_2Cu_3O_{10}$  ceramics derived from glasses, the sample only has one drop starting at 90 K and ending at 81 K. Overdoping of  $P_2O_5$  lowers zero resistance temperature back to 60 K. The critical current density  $J_c$  of  $Bi_2Ca_2Sr_2Cu_3O_{10}$  with 1.5 wt %  $P_2O_5$  doping is in excess of 500 A/cm<sup>2</sup> at 77 K in a zero magnetic field. All these experimental results indicate that  $P_2O_5$  doping helps the prevention of the intergrowth. The mechanism of  $P_2O_5$  doping is being investigated.

The most effective doping is PbO. Research has shown that the substitution of PbO for  $Bi_2O_3$  can dramatically increase the amount of 110 K phase [7]. The X-ray diffraction pattern of  $Bi_{1.84}Pb_{0.34}Ca_2Sr_2Cu_4O_y$  glass tapes heat treated at 842°C for 5 days (Fig. 54.11) clearly shows that the main phase is the 110 K phase. The electrical resistivity measurement (Fig. 54.12) shows the zero resistance of  $Bi_{1.84}Pb_{0.34}Ca_2Sr_2Cu_4O_y$  glass ceramic tapes at 100 K, which agree with the X-ray diffraction results. However, the critical current density  $J_c$  is only 20 A/cm<sup>2</sup> at 77 K in zero magnetic field, which may be due to the existence of a major second phase in the sample. Further work on preparing pure 110 K phase is being carried on in our laboratory.

TABLE 54.2. 1.5 wt % Dopants in  $Bi_2Ca_2Sr_2Cu_3O_{10}$  Glass Ceramics

Doping Oxide	Melting Temperature (°C)	Superconducting Transition Temperature (K)	
		Onset	Zero Resistance
—	1100	90	60
PbO	1100	115	52
$P_2O_5$	> 1300	100	81
$Al_2O_3$	1100	100	68
$Ga_2O_3$	1100	Semiconducting	
$B_2O_3$	1100	100	66
$SiO_2$	1100	90	26

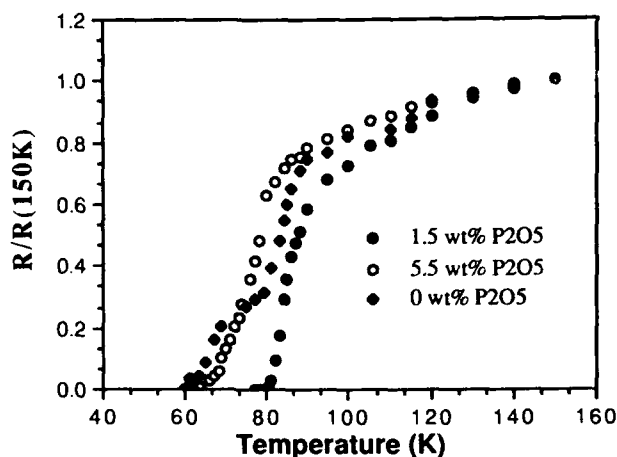


Fig. 54.10. The effect of  $P_2O_5$  doping in  $Bi_2Ca_2Sr_2Cu_3O_y$  glass-crystallized ceramics on superconductivity.

#### 54.7. SUMMARY AND FUTURE WORK

Preparation of high- $T_c$  Bi-Ca-Sr-Cu-O superconductors by the glass-to-ceramic route has been systematically investigated. The Bi-Ca-Sr-Cu-O system has a relatively large glass-forming region, but the formed glasses easily crystallize due to low-dimensional  $[BiO_3]$  glass network. The glass transition temperature ( $T_g$ ) and the first crystallization temperature ( $T_x$ ) of Bi-Ca-Sr-Cu-O glasses are about  $390^\circ C$  and  $450^\circ C$ , respectively. The 75 K superconducting phase only crystallizes at  $>550^\circ C$  from the glasses. Because Bi-Ca-Sr-Cu-O superconducting ceramics prepared by the glass-to-ceramic process are pore-

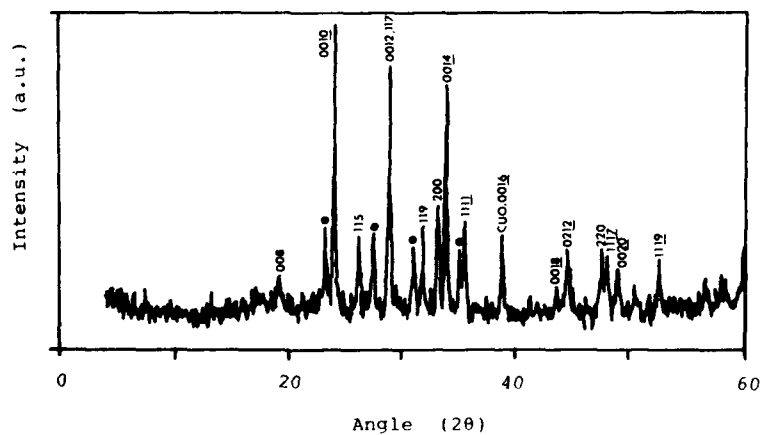
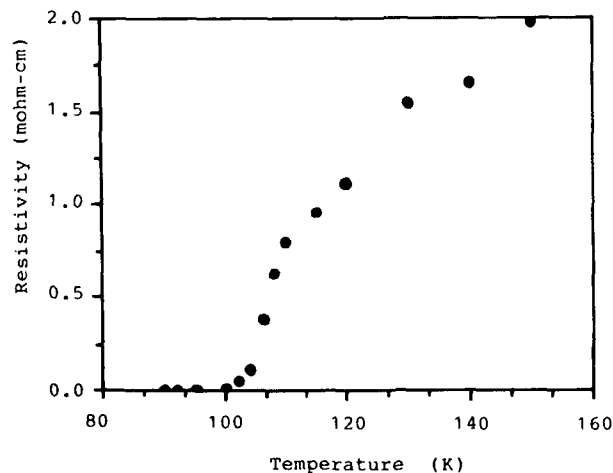


Figure 54.11. An X-ray diffraction pattern of  $Bi_{1.84}Pb_{0.34}Ca_2Sr_2Cu_4O_y$  glass tapes fired at  $842^\circ C$  for 120 hr in the atmosphere of Ar +  $O_2$ . (hkl), 110 K phase; ●, 75 K phase.



**Figure 54.12.** Electrical conductivity of  $\text{Bi}_{1.84}\text{Pb}_{0.34}\text{Ca}_2\text{Sr}_2\text{Cu}_4\text{O}_y$  lglass tapes fired at  $842^\circ\text{C}$  for 120 hr in the atmosphere of Ar and  $\text{O}_2$ .

free, they show superior mechanical properties having compressive strength of  $2 \times 10^4$  psi and Vicker's hardness of  $600 \text{ kg/cm}^2$ .

By doping 1.5 wt %  $\text{P}_2\text{O}_5$ ,  $\text{Bi}_2\text{Ca}_2\text{Sr}_2\text{Cu}_3\text{O}_y$  ceramics have zero resistance at 81 K and the critical current density in excess of  $500 \text{ A/cm}^2$  at 77 K in a zero magnetic field. By substitution of PbO for  $\text{Bi}_2\text{O}_3$ , the 110 K superconducting phase in the ceramics with starting a composition of  $\text{Bi}_{1.84}\text{Pb}_{0.34}\text{Ca}_2\text{Sr}_2\text{Cu}_4\text{O}_y$  becomes primary and the ceramics show zero resistance at 100 K.

Because the ceramics transformed from glasses are 100% dense, microstructure controllable, and easily made into any shape, the fabrication of Bi-Ca-Sr-Cu-O high- $T_c$  superconductors by the glass-to-ceramic process is very promising. However, because of the intergrowth problem, the 110 K superconductors with high critical current density  $J_c$  still have not been prepared; and because of the low viscosity of the Bi-Ca-Sr-Cu-O glass melts, various shapes of Bi-Ca-Sr-Cu-O high- $T_c$  superconductors are not so easily fabricated. Therefore, future work should be concentrated on (1) learning the way to prepare the superconducting ceramics with a single 110 K phase, and (2) inventing new techniques to fabricate the low viscosity of the glass melts into various useful forms.

### ACKNOWLEDGMENT

The authors wish to thank Patrick Lin, Ren Xu, and E. Pope for assistance. This work was supported by the Strategic Defense Initiative Organization and the Air Force Office of Scientific Research, Directorate of Chemical and Atmosphere Science.

## REFERENCES

1. J. G. Bednorz and K. A. Muller, *Z. Phys. B*, **64**, 189 (1986).
2. M. K. Wu, J. R. Ashburn, C. J. Torng, P. H. Hor, R. J. Meng, L. Gao, Z. J. Huang, Y. Q. Wang, and C. W. Chu, *Phys. Rev. Lett.*, **58**, 908 (1987).
3. Z. Zhao et al., *Kexue Tongbao*, No. 6 (1987).
4. H. Maeda, Y. Tanaka, M. Fukutomi, and T. Asano, *Japan. J. Appl. Phys.*, **27**, L209 (1988).
5. Z. Z. Sheng and A. M. Hermann, *Nature*, **332**, 138 (1988).
6. Y. Matsui, H. Maeda, Y. Tanaka, E. Takayama-Maromachi, S. Takekawa, and S. Horiuchi, *Japan. J. Appl. Phys.*, **27**, L827 (1988).
7. U. Endo, S. Koyama, and T. Kawai, *Japan. J. Appl. Phys.*, **27**, L1476 (1988).
8. H. Zheng and J. D. Mackenzie, *Phys. Rev. B.*, **38**, 7166 (1988).
9. T. Komatsu, R. Sato, K. Imai, K. Matusita, and T. Yamashita, *Japan. J. Appl. Phys.*, **27**, L550 (1988).
10. D. G. Hinks, L. Soderholm, D. W. Capone II, B. Dabrowski, A. W. Mitchell, and D. Shi, *Appl. Phys. Lett.*, **53**, 423 (1988).
11. H. Garzon, J. G. Beedy, and L. D. Raistrick, *Appl. Phys. Lett.*, **53**, 805 (1988).
12. A. Bishay and C. Maghrabi, *Phys. Chem. Glasses*, **10**, 1 (1969).
13. H. Zheng, R. Xu, and J. D. Mackenzie, *J. Mater. Res.*, **4**, 911 (1989).
14. A. C. Wright, private communication, 1988.
15. C. Michael, M. Hervieu, M. M. Borel, et al., *Z. Phys. B.*, **68**, 421 (1987).
16. D. I. H. Atkinson and P. W. McMillan, *J. Mater. Sci.*, **12**, 443 (1977).
17. A. Maries and P. S. Rogers, *Nature (Lond.)*, **256**, 401 (1975).

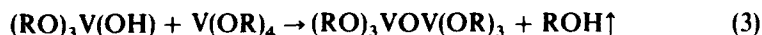
## SOL-GEL GROWTH OF VANADIUM DIOXIDE PHASE TRANSITION MATERIALS

K. R. SPECK, H. S.-W. HU,  
R. A. MURPHY, AND R. S. POTEMBER

### 55.1. INTRODUCTION

Vanadium dioxide,  $\text{VO}_2$ , has been studied extensively over the past 30 years, because it undergoes a thermally induced semiconductor-to-metal phase transition near  $68^\circ\text{C}$ . Pronounced and reversible changes in the optical, electrical, and magnetic properties of  $\text{VO}_2$  occur as it is cycled through the transition temperature [1–3].

Vanadium tetraalkoxides have been used to make  $\text{VO}_2$  by the sol-gel process [4, 5]. As in other alkoxide systems, the formation of vanadium dioxide occurs through hydrolysis and condensation. The vanadium alkoxide first reacts with water from the solvent and the atmosphere (Eq. 1). Condensation proceeds by either a water-producing reaction (Eq. 2) or an alcohol-producing reaction (Eq. 3).



*Ultrastructure Processing of Advanced Materials.*

Edited by Donald R. Uhlmann and Donald R. Ulrich (deceased).

ISBN 0-471-52986-9 © 1992 John Wiley & Sons, Inc.

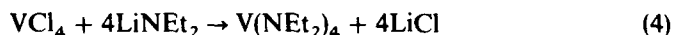
These reactions may be monitored by various analytical techniques [6, 7].

Powders and films obtained by the sol-gel process are usually amorphous and highly porous and contain residual organics. These amorphous materials must be heated for crystallization and densification. Differential scanning calorimetry (DSC) was used to study the crystallization of gel-derived powder and to identify temperatures at which volatiles are lost. Thermogravimetric analysis (TGA) was used to monitor the removal of residual organics, the evolution of alkyl species not replaced during hydrolysis, and dehydration of the powder. The temperature at which organics and water are eliminated was also determined by Fourier transform infrared spectroscopy (FTIR). FTIR spectra were taken of  $\text{VO}_2$  sol-gel films on silicon to identify the temperatures at which volatiles are liberated.

The sol-gel process has been used to deposit doped vanadium dioxide films [5, 8]. Substitutional impurity ions or dopants are known to have a large effect on the phase transition of  $\text{VO}_2$  [3, 8]. Ions with a valence greater than the tetravalent vanadium ( $\text{Nb}^{5+}$ ,  $\text{W}^{6+}$ , and  $\text{Mo}^{6+}$ ) cause the transition to occur at progressively lower temperatures as the impurity ion concentration increases, with tungsten having the largest effect per atomic percent added. Doping was effected by the addition of other transition metal alkoxides or salts, such as nitrates, oxalates, acetates, or chlorides, to the initial sol.

## 55.2. EXPERIMENTAL

Vanadium(IV) tetrakis(*t*-butoxide),  $\text{V}(\text{O}-t\text{-Bu})_4$ , was originally synthesized by Bradley and Mehta [9] in a two-step reaction scheme (Eqs. 4 and 5), which involved the alcoholysis of vanadium tetrakis(diethylamide).



Razuvaev et al. [10] employed a one-step synthesis of the tertiary butyl derivative, which involved reacting  $\text{VCl}_4$  with  $\text{LiO}-t\text{-Bu}$  in petroleum ether.

We have recently reported [5] a new reaction scheme for the synthesis of vanadium tetrakis(*t*-butoxide) based on a variation of the Razuvaev procedure. Potassium *t*-butoxide was reacted with vanadium tetrachloride in methylene chloride (Eq. 6).



The reaction was performed in a moisture-free nitrogen atmosphere to prevent subsequent oxidation and hydrolysis. Methylene chloride was dried over activated alumina, then distilled from calcium hydride. A solution of vanadium tetrachloride (13.2 g) (Atomergic) dissolved in methylene chloride (50 ml) was

added dropwise to a suspension of potassium *t*-butoxide (50 g) (Aldrich) in  $\text{CH}_2\text{Cl}_2$  (150 ml) while stirring at  $-78^\circ\text{C}$ . Precipitated by-product KCl was then filtered off under  $\text{N}_2$ . The methylene chloride was evaporated off in vacuo and  $\sim 3$  g of the product was collected by vacuum distillation (12.8%).

The thermal analysis was done on a PerkinElmer DSC-4 and TGS-2. A small amount of water was added to a solution of the tetraalkoxide. A brown precipitate formed. The precipitate was placed into an aluminum pan and heated under flowing nitrogen. FTIR spectra of  $\text{VO}_2$  sol-gel films on *n*-type silicon wafers (Silicon Casting, Inc.) were taken on a Mattson Sirius 100 FTIR after each 10-min heat treatment of 100 to  $600^\circ\text{C}$ .

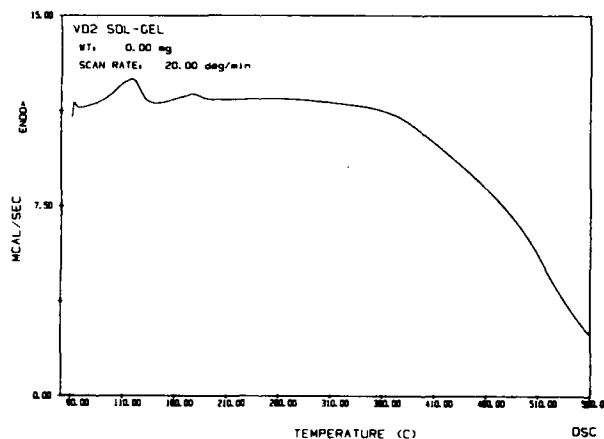
Vanadium dioxide sol-gel films were deposited from a solution of the vanadium tetraalkoxide in isopropanol (Aldrich, high-performance liquid chromatography grade). Solutions were adjusted to contain 2 to 5% vanadium dioxide by weight. Doped films were made by combining solutions of the vanadium alkoxide with solutions of tungsten or molybdenum(VI) tetrachloride oxide (Alfa). Films were deposited on Corning 7059 barium borosilicate glass slides and MRC superstrates alumina substrates by either dip coating or spin coating. The thickness of each individual layer of the dip-coated films was dependent on the concentration of the solution, the withdrawl rate (1 mm/sec), and the number of times the slide was dip-coated. Sol concentration and spinning rate (5000 rpm) controlled the thickness of spin-coated films. Thicker films were made by applying additional coatings. Each layer was dried at  $200^\circ\text{C}$  in air to remove organics and water from the film before recoating. The amorphous olive-green films were heated at  $500^\circ\text{C}$  for 10 min under nitrogen to achieve dehydration, residual solvent removal, and crystallization.

The electrical and optical properties of the gel-derived vanadium dioxide films were measured while they were heated through the transition temperature. The experimental setup was the same as previously described [4, 5], which allowed for the concurrent measurement of electrical resistance and optical transmission versus temperature. The thickness of each film was determined using a Sloan Dektak profilometer, and the microstructure was examined by a JEOL 840A SEM.

### 55.3. RESULTS

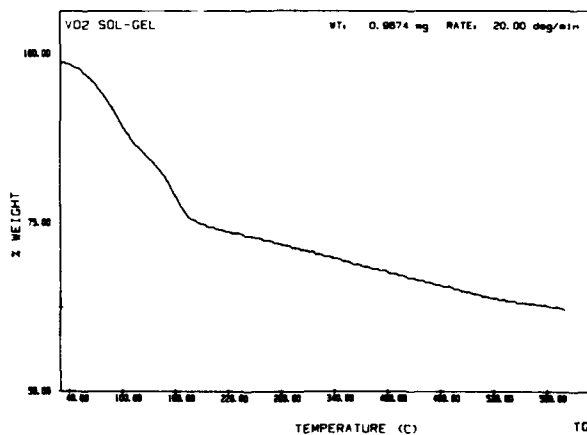
A typical DSC plot for a  $\text{VO}_2$  sol-gel is shown in Fig. 55.1. The initial weight of the sample was 3.4 mg. The heating rate was  $20^\circ\text{C}/\text{min}$ . Three exothermic peaks appeared, the first peak (below  $100^\circ\text{C}$ ) was attributed to organic and solvent removal, and the second peak (between 100 to  $200^\circ\text{C}$ ) was attributed to loss of  $\text{H}_2\text{O}$  and other contaminants. Crystallization of the powder was seen as exothermic reaction in DSC ( $350^\circ\text{C}$  and above).

The TGA plot in Fig. 55.2 shows three areas of weight loss. The first area (below  $100^\circ\text{C}$ ) was attributed to alcohol evaporation. The second area (100 to  $160^\circ\text{C}$ ) was most likely due to a combination of water evaporation along with

Figure 55.1. DSC plot for a  $\text{VO}_2$  gel.

residual organic removal. Above  $160^\circ\text{C}$ , the slow process of  $-\text{OH}$  removal as water is evident. Weight loss did not appear to level off until  $500^\circ\text{C}$ . The initial weight of the sample was  $0.9674\text{ mg}$  and the heating rate,  $20^\circ\text{C}/\text{min}$ .

The infrared spectra shown in Fig. 55.3 supports the thermal analysis. The top curve was taken directly after film deposition. The most noticeable features in the spectra are the wide  $\text{O}-\text{H}$  band centered at  $3334\text{ cm}^{-1}$  and the molecular water peak at  $1624\text{ cm}^{-1}$ . The spectra also showed a  $-\text{CH}_3$  band at  $2976\text{ cm}^{-1}$  and a  $\text{C}-\text{O}$  band at  $981\text{ cm}^{-1}$ . After a 10-min heat treatment at  $100^\circ\text{C}$  in air, there was a noticeable decrease in each of these four peaks. The  $-\text{CH}_3$ ,  $\text{H}_2\text{O}$ , and  $\text{C}-\text{O}$  bands became indistinguishable after the  $200^\circ\text{C}$  heat treatment in air. Heat

Figure 55.2. A TGA plot for a  $\text{VO}_2$  gel.



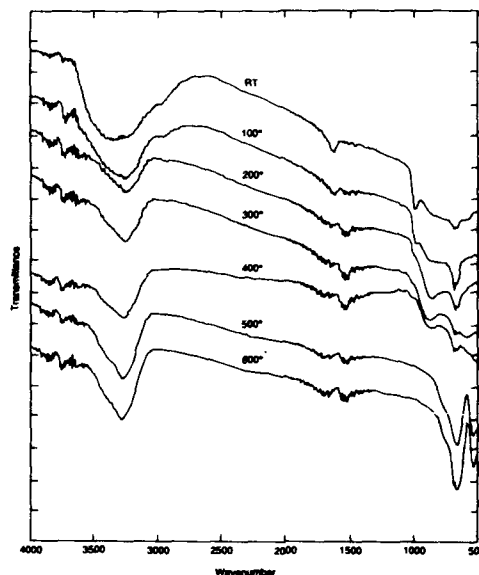


Figure 55.3. Infrared spectra of a  $\text{VO}_2$  gel.

treatments above  $200^\circ\text{C}$  were done under nitrogen to prevent oxidation to  $\text{V}_2\text{O}_5$ . The O–H peak remained intense after the  $600^\circ\text{C}$  heat treatment.

The most interesting aspect of the infrared study was the increased definition of the peaks between  $500$  to  $1000\text{ cm}^{-1}$ , which became more distinguished as  $\text{VO}_2$  crystallization proceeds. The peak at  $649\text{ cm}^{-1}$  was assigned to V–O–V stretching, whereas a band at  $523\text{ cm}^{-1}$  was attributed to lattice vibrations [11]. At  $200^\circ\text{C}$ , a peak at  $849\text{ cm}^{-1}$  (V=O) became apparent, and its disappearance after the  $500^\circ\text{C}$  heat treatment indicated some  $\text{V}^{5+}$  in the untreated film.

Electrical and optical switching were observed in sol–gel-derived  $\text{VO}_2$  films as they were cycled through the transition temperature. Electrical resistance decreased by two to three orders of magnitude at a switching temperature of  $68^\circ\text{C}$ . The resistive ratio and switching temperature observed was typical for  $\text{VO}_2$  thin films prepared on glass and alumina substrates by other techniques [6, 12]. Switching occurred over a narrow range of temperatures, with a heating–cooling hysteresis of about  $10^\circ\text{C}$  being characteristic of these films. The results obtained for a  $\text{V}_{0.99}\text{W}_{0.01}\text{O}_2$  are shown in Fig. 55.4. It was assumed that the concentration of the dopant in the film was the same as that in solution. The resistance decreased more than two orders of magnitude in this film. The transition temperature, taken as the inflection point of the heating curve, is near  $50^\circ\text{C}$ .

The transmission changes observed between  $400$  and  $2500\text{ nm}$  are consistent with that reported for  $\text{V}_{1-x}\text{M}_x\text{O}_2$  [2, 6]. The near-infrared transmission of  $\text{VO}_2$  on glass abruptly decreased at the transition temperature. The transmission at  $2400\text{ nm}$  versus temperature for a  $\text{V}_{0.99}\text{W}_{0.01}\text{O}_2$  is shown in Fig. 55.5.

## 646 VANADIUM DIOXIDE PHASE TRANSITION MATERIALS

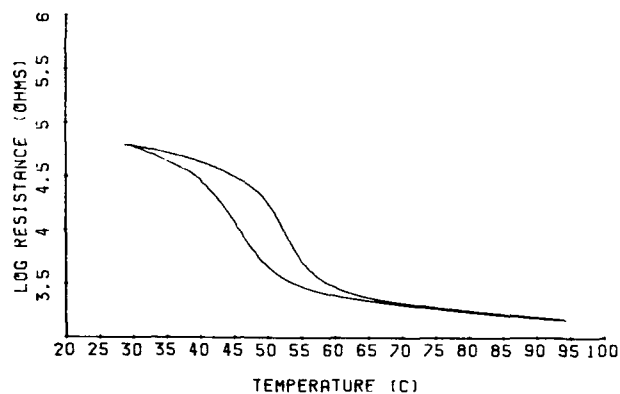


Figure 55.4. Temperature dependence of electrical resistance for a  $V_{0.99}W_{0.01}O_2$  film 100 nm thick on glass.

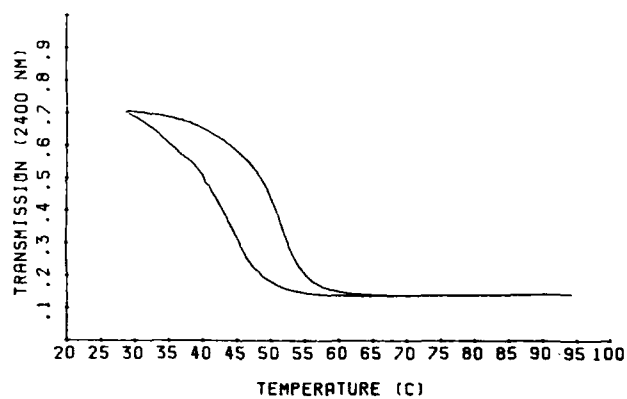


Figure 55.5. Temperature dependence of transmission at 2400 nm for a  $V_{0.99}W_{0.01}O_2$  film 100 nm thick on glass.

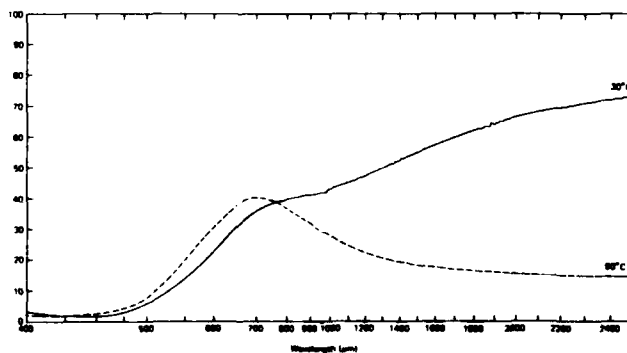


Figure 55.6. Transmission of  $V_{0.99}W_{0.01}O_2$  film 100 nm thick on glass above and below the transition temperature.

The switched and unswitched transmission spectra shown in Fig. 55.6 are typical for the 1% tungsten doped gel-derived films [6].

Although the dopant ions greatly influence the transition temperature, they have little effect on the observed spectral transmission of the film.

#### 55.4. CONCLUSION

Vanadium dioxide films were deposited from vanadium tetrakis(*t*-butoxide) by the sol-gel process. The electrical and optical properties of these films are comparable to that observed in vanadium dioxide grown by other deposition techniques. The sol-gel process provides a versatile way of making doped vanadium dioxide-based devices. The technique permits mixing of the constituents in solution at the molecular level.

#### ACKNOWLEDGMENTS

This work was supported by DARPA/AFSOF and Wright-Patterson Air Force Base.

#### REFERENCES

1. F. J. Morin, *Phys. Rev. Lett.*, **3**, 34 (1959).
2. H. W. Verleur, A. S. Barker, Jr., and C. N. Berlund, *Phys. Rev.*, **1972**, 788 (1968).
3. J. B. Goodenough, *J. Solid State Chem.*, **3**, 490 (1971).
4. K. R. Speck, H. S.-W. Hu, M. E. Sherwin, and R. S. Potember, *Thin Solid Films*, **165**, 317 (1988).
5. K. R. Speck, H. S.-W. Hu, R. A. Murphy, and R. S. Potember, *Mater. Res. Soc. Symp. Proc.*, **121**, 667 (1988).
6. H. Schmidt, H. Scholze, and A. Kaiser, *J. Non-Cryst. Solids*, **48**, 65 (1982).
7. K. C. Chen, A. Jahan, and J. D. Mackenzie, *Mater. Res. Soc. Symp. Proc.*, **73**, 731 (1986).
8. C. B. Greenberg, *Thin Solid Films*, **110**, 73 (1983).
9. D. C. Bradley and M. L. Mehta, *Can. J. Chem.*, **40**, 1183 (1962).
10. G. A. Ruzuevaev, V. N. Latyaeva, V. V. Drobotenkov, A. N. Linyova, L. I. Vishinskaya, and V. K. Ckerkasov, *J. Organomet. Chem.*, **131**, 43 (1977).
11. V. A. Perelyaev, V. I. Miller, L. A. Perelyaeva, N. E. Grebenshchikova, G. P. Shveikin, and A. K. Chirkov, *Russ. J. Inorg. Chem.*, **22**, 1267 (1977).
12. G. A. Rozgonyi and D. H. Hensler, *J. Vac. Sci. Technol.*, **5**, 194 (1968).

## **PART 6**

# **Organometallic Precursors, Polymers, and Aerogels**

## TRANSITION METAL-CATALYZED ROUTES TO POLYSILANE POLYMERS

H.-G. WOO AND T. D. TILLEY

### 56.1. INTRODUCTION

Polysilane polymers,  $(-\text{SiRR}'-)_n$ , represent a class of inorganic polymers that have been known for some time, but their novel chemical properties and potential applications were not appreciated until rather recently. The first polysilane,  $(-\text{SiMe}_2-)_n$ , was described by Burkhard in 1949 as an intractable white solid [1]. More recent synthetic and physical studies, particularly by West and co-workers, have revealed that these polymers have unusual properties that suggest a number of technological applications [2]. A rather small HOMO-LUMO gap for the  $\sigma$ -bonding framework of the polysilanes results in interesting electronic properties. For example, ultraviolet (UV) radiation causes depolymerization reactions with Si-Si bond scission, allowing polysilanes to serve as photoinitiators for radical polymerizations [3]. This property also makes polysilanes attractive candidates for photoresist materials [2, 4]. Other applications for polysilanes as photoconductors [5], dopable semiconductors [6], and nonlinear optical materials [7] have been reported.

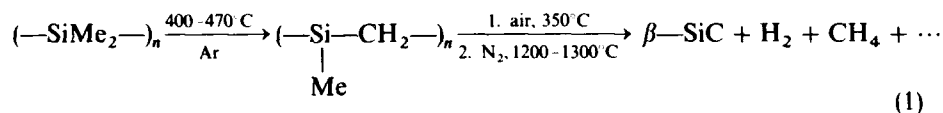
Much of the current interest in polysilanes stems from their ability to serve as preceramic polymers. In work pioneered by Yajima, it was shown that poly(dimethylsilylene) undergoes thermolysis to polycarbosilanes, which can be

*Ultrastructure Processing of Advanced Materials.*

Edited by Donald R. Uhlmann and Donald R. Ulrich (deceased).

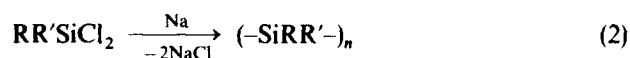
ISBN 0-471-52986-9 © 1992 John Wiley & Sons, Inc.

spun into fibers that are pyrolyzed at high temperature to a  $\beta$ -SiC (Eq. 1) [8].

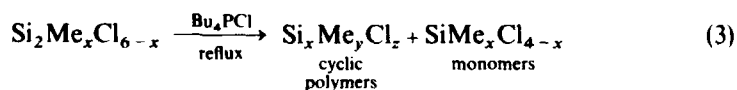


The resulting high-strength silicon carbide fibers are now sold commercially. Further improvements in this technology can be made by modification of the polymer structure. West and Mazdiyasni have shown that copolymers of the type  $(\text{—SiMe}_2\text{—})_n(\text{—SiMePh—})_m$ , or *polysilastyrene*, are more tractable and can be formed into fibers and films. These films can be crosslinked by UV irradiation and then converted directly to silicon carbide by thermolysis at higher temperature [2, 9, 10].

Development of polysilane chemistry would not be possible without a practical synthetic route to the polymers. Such a preparative method is provided by the Wurtz-type coupling of dichlorosilanes by sodium metal in a hydrocarbon solvent (Eq. 2) [2].



Although this method has served well for defining the applications mentioned above, it suffers from some important limitations that discourage commercial development. These include problems associated with handling large quantities of molten alkali metals and difficulties in controlling polymer molecular weights and molecular weight distributions. In addition, the highly reducing conditions for this reaction preclude direct introduction of many functional groups into the polymer chain. An alternative synthesis is based on a redistribution of chlorosilanes to low-molecular-weight, cyclic polysilanes (Eq. 3) that can be converted to silicon carbide on thermolysis [11].



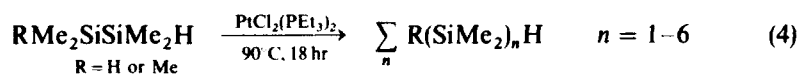
Given the potential for polysilanes in a number of applications, it would be beneficial to have alternative routes that allow more flexibility with respect to the polymer structures that can be generated. An appealing approach that has appeared feasible for some time is a coordination polymerization route based on a transition metal catalyst. The advantages of such a polymerization reaction can be readily appreciated by considering the impact of Ziegler–Natta polymerizations on the polyolefins industry. Such a dehydrogenative condensation of hydrosilanes would theoretically provide a clean route to polysilanes with hydrogen as the only side product. Control of chemical factors at the reacting metal center could result in the ability to manipulate polymer properties such as

chain length and tacticity. Recent progress in development of this area has been reported, most notably by Harrod and co-workers in Canada [12]. Our group is generally interested in early transition metal silicon chemistry, and the use of this chemistry for obtaining novel ceramic precursors. Recently we have turned our attention to reaction chemistry relevant to catalytic pathways to polysilane polymers. This work has resulted in a new mechanistic model that could influence development of this area.

## 56.2. TRANSITION METAL-MEDIATED Si-Si BOND FORMATION

Organosilanes display a rich reaction chemistry toward transition metal species, and many types of metal-mediated Si-X bond-forming and bond-breaking processes have been identified [13, 14]. In particular, silane compounds with Si-H bonds undergo a number of transformations in the presence of transition metal complexes are active toward Si-Si bond-forming processes. The first therefore has the potential to provide more sophisticated approaches to synthetic methodology for silicon-based materials. Given the fact that Si-H and Si-Si bond activations by transition metal complexes are well known, it seems quite possible that this reaction chemistry could be productively channeled into formation of polysilane chains. Of course, this requires some knowledge of how metal complexes and silicon species interact at a mechanistic level, but despite the large number of known metal silyl derivatives, such detailed studies are for the most part unavailable.

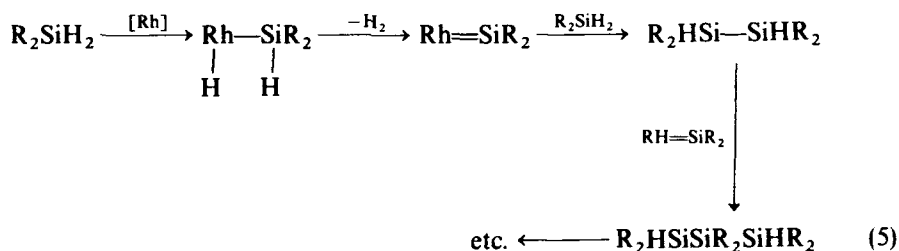
For some time it has been known that certain platinum-metal (late transition metal) complexes are active toward Si-Si bond-forming processes. The first report of such a reaction appeared in 1970. This reaction, which corresponds to a Si-H/Si-Si redistribution process, utilizes a platinum catalyst at a slightly elevated temperature (Eq. 4) [15].



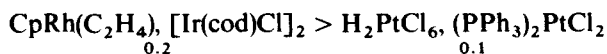
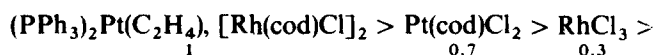
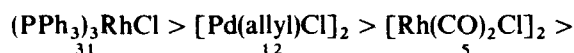
Later work by these authors involving trapping reactions with alkynes presented circumstantial evidence that implicated a  $\text{Pt}=\text{SiMe}_2$  silylene intermediate in the above reaction [16]. Palladium complexes catalyze Si-Si/Si-Si redistribution reactions that also form new Si-Si bonds [17].

Wilkinson's catalyst,  $(\text{PPh}_3)_3\text{RhCl}$ , also appears to be reactive toward Si-Si bond-forming redistribution reaction. The initial report of use of this catalyst by Ojima et al. [18] described low conversions of the monosilanes  $\text{PhMeSiH}_2$ ,  $\text{Ph}_2\text{SiH}_2$ , and  $\text{Et}_2\text{SiH}_2$  to mixtures of mono-, di-, and trisilanes. Again, a metal-bound silylene intermediate was proposed as the key species involved in Si-Si

bond formation, and it was suggested that this intermediate is formed by an  $\alpha$ -abstraction process that eliminates hydrogen (Eq. 5) [18].



Corey et al. [19] found that  $(\text{PPh}_3)_3\text{RhCl}$  also produced di- and trisilanes from the secondary silane 9,10-dihydro-9-silaanthracene, and Lappert and Maskell [20] has reported the catalytic conversion of  $\text{Ph}_2\text{SiH}_2$  to hydrogen and  $\text{Ph}_2\text{HSiSiHPh}_2$  with the rhodium carbene complex (cyclooctadiene)- $\text{C}(\text{RhCNMeCH}_2\text{CH}_2\text{NMe})$  as catalyst. Interestingly, Vaska's complex  $(\text{PPh}_3)_2(\text{CO})\text{IrCl}$  catalyzed redistribution of  $\text{PhMeSiH}_2$ , but only to other monosilanes [21]. Brown-Wensley [22] investigated a number of platinum metal catalysts for the dimerization of diethylsilane and found the following ordering of activities (with relative reactivities):

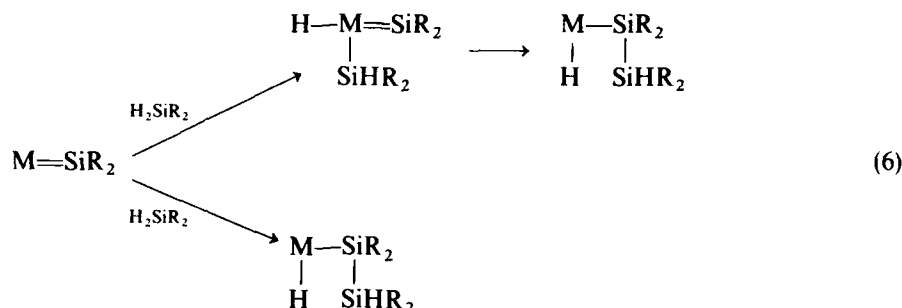


In addition it was observed that, with respect to the monosilanes, reactivities follow the order  $\text{RSiH}_3 > \text{R}_2\text{SiH}_2 > \text{R}_3\text{SiH}$  [22]. Generally tertiary silanes  $\text{R}_3\text{SiH}$  are unreactive, but a recent report by Tanaka et al. [2] describes the dehydrogenative condensation of  $\text{Me}_2\text{PhSiH}$  to the disilane  $(\text{Me}_2\text{PhSi})_2$  with platinum catalysts.

It is therefore well established that late transition metal complexes, particularly of rhodium, are active in dehydrogenative Si—Si bond formation from hydrosilanes. However, chain growth does not proceed beyond the small oligomer stage. It is difficult to evaluate the potential for this area, because the mechanisms by which these reactions operate are unknown. In some cases metal silylene intermediates are proposed, and this seems reasonable, because silylene units are being incorporated into a polysilane chain via activation by a metal. Such species would presumably participate in Si—Si bond formation via

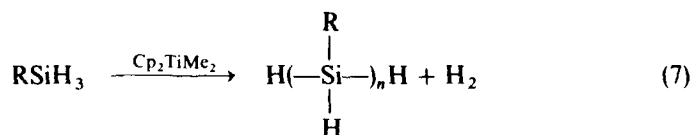


migrations at the metal center or by direct addition to the  $M=Si$  double bond (Eq. 6).



Recently the first few transition metal silylene complexes have been reported, but these species all have a Lewis base (usually a solvent molecule) coordinated to the metal-bound silicon [24–26]. Hopefully future work will produce base-free silylene complexes and evaluate their reactivity toward silanes. Note that for the coupling reaction reported by Tanaka et al. [23], silylene intermediates seem unlikely.

Although the research summarized above is not encouraging with respect to production of high polymers with transition metal catalysts, more recent work by Harrod and co-workers has produced an important breakthrough. This work showed that early transition metal metallocene derivatives of titanium and zirconium are active catalysts for the dehydrogenative coupling of primary silanes  $RSiH_3$  to polysilanes (Eq. 7,  $Cp = \eta^5-C_5H_5$ ) [12, 27–32].

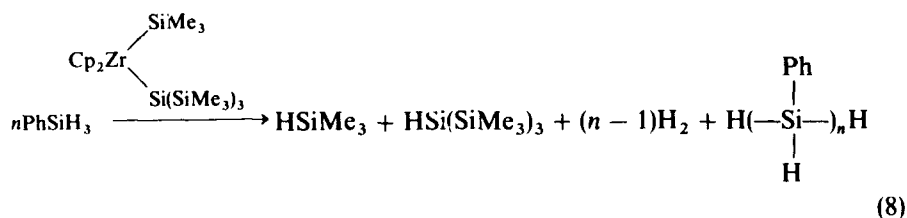


Polymers isolated from the titanium-catalyzed reactions are linear and atactic, with an average degree of polymerization of ca. 10 and narrow polydispersities. Analogous zirconium catalysts give chains with up to 20 Si atoms. Interestingly, the polymer mixtures obtained have bimodal molecular weight distributions, which may imply two polymerization processes. These coupling reactions are more selective than the rhodium-based ones, in that no side products from redistribution are formed. Although primary hydrosilanes are generally reactive toward this polymerization, secondary and tertiary hydrosilanes are not, and the polymerization rates are very sensitive to steric factors. In some cases coupling of secondary silanes to the corresponding disilanes has been observed. Addition of olefins suppresses the evolution of hydrogen and increases the polymerization rate.

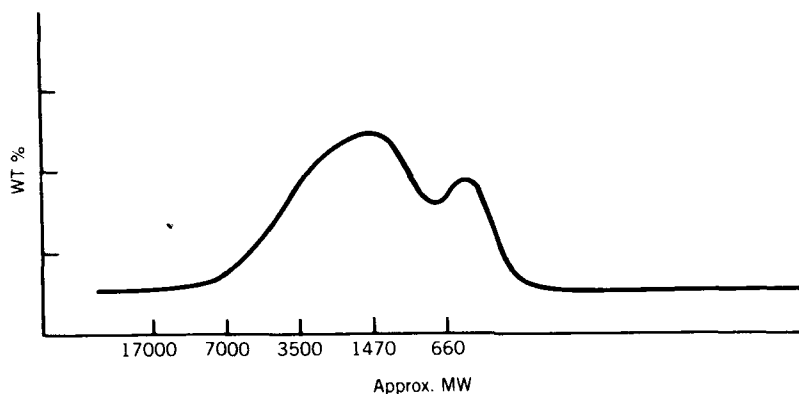
There is complex, but interesting chemistry that accompanies these polymerization reactions. Induction periods lasting from a few seconds to a few hours are reported, and a number of species have been identified in solution. For the titanium-based catalyst, titanium species in solution appear to be undergoing monomer-dimer equilibria and redox reactions. The complexes  $[\text{Cp}_2\text{TiH}]_2(\mu\text{-H})$ ,  $\text{Cp}_2\text{Ti}(\mu\text{-H})(\mu\text{-SiHPh})\text{TiCp}_2$ , and  $\text{Cp}_2\text{Ti}(\mu\text{-SiHPh})_2\text{TiCp}_2$  have been isolated from solution, but these species do not appear to be directly involved in the catalysis [28]. Mechanistic proposals have focused on the intermediacy of a titanium silylene complex, formed via an  $\alpha$ -abstraction process analogous to the one shown in Eq. 5 [12, 28, 30, 32]. This proposal seemed reasonable since silylene-extrusion products are observed in the reaction mixtures, and since the metal centers are acting to add silylene units to a growing polymer chain. Such mechanisms also can account for the fact that secondary and tertiary silanes are much less reactive.

### 56.3. GROUP 4 SILYL COMPLEXES AS CATALYST PRECURSORS FOR THE DEHYDROGENATIVE POLYMERIZATION OF SILANES

Our group's interest in the chemistry of early transition metal M-Si bonds has led us to synthesize and study a number of Zr-Si- and Hf-Si-bonded compounds [33]. In light of Harrod's reports of silane polymerization chemistry with related species, we began an investigation into the interaction of our silyl complexes with silanes. A survey of this reaction chemistry quickly revealed that certain early metal silyl complexes were very efficient catalyst precursors for the dehydrogenative coupling of primary silanes such as  $\text{PhSiH}_3$  to polysilanes [34]. In the best cases these reactions are extremely rapid and produce polysilanes that appear to be similar to those reported by Harrod, based on comparison of spectroscopic and gel permeation chromatography data. A representative reaction is shown in Eq. 8.



Monitoring this reaction at low  $\text{PhSiH}_3$  concentration by  $^1\text{H}$  nuclear magnetic resonance (NMR) spectroscopy showed that  $\text{HSiMe}_3$  and then  $\text{HSi}(\text{SiMe}_3)_3$  were produced sequentially before significant amounts of polymer were detected. Polymers obtained by such reactions show bimodal molecular weight distributions as reported by Harrod [12]. A typical gpc trace is shown in



**Figure 56.1.** Gel permeation chromatographic trace of  $[\text{SiHPh}]_n$  polymer, obtained with  $\text{Cp}_2\text{Zr}[\text{Si}(\text{SiMe}_3)_3]\text{SiMe}_3$  catalyst and  $\text{PhSiH}_3$  monomer. Molecular weights on the graph are based on polystyrene standards.

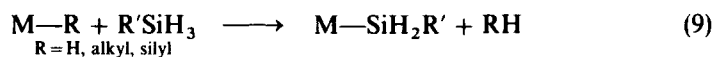
Fig. 56.1. These preliminary experiments suggest that the polymer molecular weight distributions and polydispersities are to some degree a function of the catalyst used. Early transition metal silyl complexes therefore show promise as effective catalysts for this polymerization.

Some early transition metal silyl complexes exhibit low activities. For example,  $\text{Cp}^*\text{Zr}[\text{Si}(\text{SiMe}_3)_3]\text{Cl}_2$  ( $\text{Cp}^* = \eta^5\text{-C}_5\text{Me}_5$ ) is totally inactive, and  $\text{Cp}_2\text{Ti}(\text{SiMe}_3)\text{Cl}$  only dimerizes  $\text{PhSiH}_3$  stoichiometrically. The tantalum silyl  $\text{Cp}^*\text{Ta}(\text{SiMe}_3)\text{Cl}_3$  also dimerizes phenylsilane, and this reaction is accompanied by clean formation of  $\text{HSiMe}_3$  and the hydride  $[\text{Cp}^*\text{TaHCl}_3]_n$ . Generally, we have observed that halide substituents at the metal inhibit silane coupling dramatically. Also, as expected, hafnium complexes react more sluggishly than analogous zirconium ones.

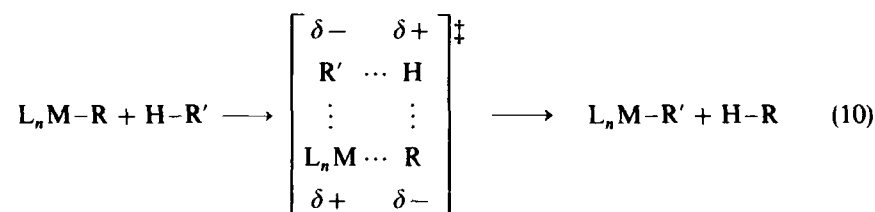
#### 56.4. PROPOSAL OF A MECHANISM

A major goal of studies in this area is development of catalysts that will allow control of chain length and in particular production of high polymers. The key to advancement toward this goal is elucidation of the mechanism(s) by which the polymerization reaction operates. Our approach to this problem includes the study of slow catalysts that allow observation of reacting intermediates. This entails use of factors mentioned above, namely, chloro substitution at the metal center and the fact that hafnium derivatives react more slowly and yield more stable complexes. Initially our investigations concentrated on reactions that model initiation steps, and later we turned to reactivity designed to model propagation reactions.

A reasonable assumption is that the catalyst precursors initially interact with silane via a hydrogen-transfer reaction of the type shown in Eq. 9.



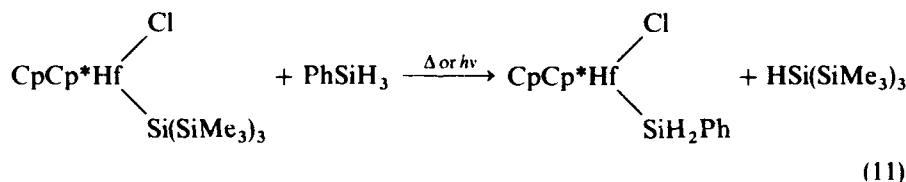
It seemed to us that such reactions probably occur via  $\sigma$ -bond metathesis reactions involving four-centered transition states [35]. Such reactions have recently been observed for related early transition metal, lanthanide, and actinide complexes in their reactions with hydrocarbons (Eq. 10) [35–40].



$\text{R}, \text{R}' = \text{H, alkyl, alkenyl, aryl}$

$\text{L}_n\text{M} = \text{Cp}_2^*\text{Sc, Cp}_2^*\text{Y, Cp}_2^*\text{Lu,}[(\text{Me}_3\text{Si})_2\text{N}]_3\text{U, Cp}_2^*(\text{X})\text{Th, Cp}_2^*(\text{X})\text{U, etc.}$

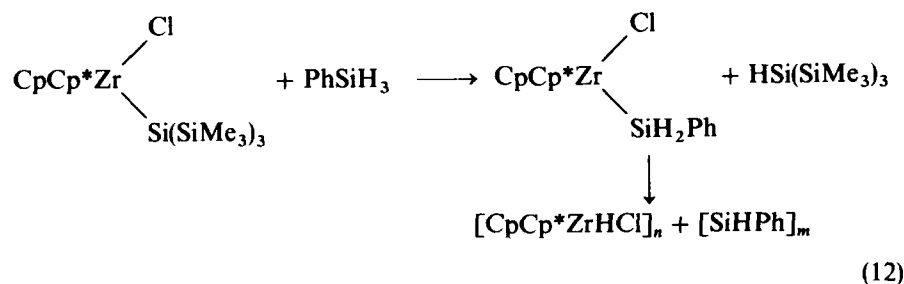
A reaction of this type involving a metal silyl complex and a primary silane is shown in Eq. 11. This reaction proceeds cleanly to the  $\text{Hf}-\text{SiH}_2\text{Ph}$  species shown.



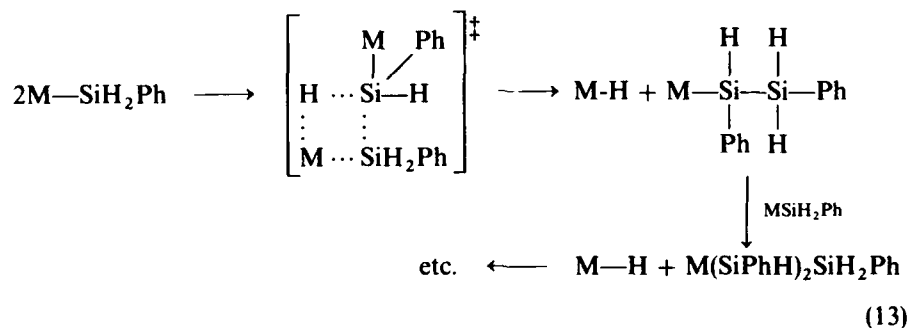
This yellow crystalline compound was isolated and completely characterized by elemental analysis and NMR and infrared spectroscopy. The reaction occurs in the dark, but it is greatly accelerated in the presence of fluorescent room light. A number of new hafnium silyl derivatives have been obtained by reaction of  $\text{CpCp}^*\text{Hf}[\text{Si}(\text{SiMe}_3)_3]\text{Cl}$  with 1 equiv. of a primary or secondary silane ( $\text{RSiH}_3$ ,  $\text{R} = \text{Ph, } p\text{-MeC}_6\text{H}_4, 2,4,6\text{-Me}_3\text{C}_6\text{H}_2, \text{CH}_2\text{Ph, and } c\text{-C}_6\text{H}_{11}$ ;  $\text{Ph}_2\text{SiH}_2$ ;  $\text{PhMeSiH}_2$ ). These reactions are quantitative by  $^1\text{H}$ -NMR spectroscopy, and isolated yields range from 65 to 75%. This appears to be the only general method for synthesis of  $d^0$  metal silyl complexes with  $\text{Si}-\text{H}$  bonds [41, 42]. A kinetic study demonstrated that the thermal (dark) reaction in Eq. 11 is a second-order process and first order in both hafnium complex and silane. Significantly, the activation parameters for this process [ $\Delta H^\ddagger = 16.4$  (7) kcal/mol;  $\Delta S^\ddagger = -27$ (2) eu] and the kinetic isotope effect [ $k_{\text{H}}/k_{\text{D}} = 2.5$  (1)] are in close agreement with values previously observed for  $\sigma$ -bond metathesis reactions [35–40]. A related

process was observed in the reaction of the hydride  $[\text{CpCp}^*\text{HfHCl}]_n$  with phenylsilane. This reaction slowly yields the silyl  $\text{CpCp}^*\text{Hf}(\text{SiH}_2\text{Ph})\text{Cl}$  and hydrogen as major products, presumably via a four-center transition state.

Having obtained a stable monomeric derivative with a primary silyl group, we began to examine the chemistry of this compound for a clue as to how  $\text{M}-\text{SiH}_2\text{R}$  species react or rearrange to deliver  $\text{RSiH}$  silylene units to a polymer chain. The zirconium primary silyl complex  $\text{CpCp}^*\text{Zr}(\text{SiH}_2\text{Ph})\text{Cl}$  may be generated clearly in solution by a reaction analogous to that shown in Eq. 11, but the product is unstable, decomposing to a zirconium hydride and polysilane (Eq. 12).



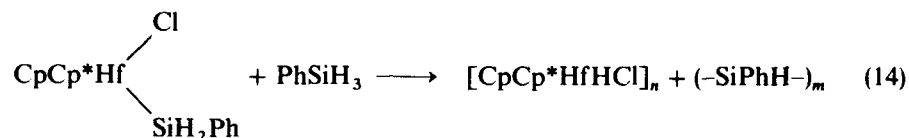
To examine this process in more detail, we studied the kinetics of the thermal decomposition of  $\text{CpCp}^*\text{Hf}(\text{SiH}_2\text{Ph})\text{Cl}$ . This compound decomposes by a second-order rate law,  $\text{rate} = k[\text{CpCp}^*\text{Hf}(\text{SiH}_2\text{Ph})\text{Cl}]^2$ , with  $\Delta H^\ddagger = 19.5$  (3) kcal/mol and  $\Delta S^\ddagger = -21$  (1) eu, to the hafnium hydride and  $(-\text{SiPhH}-)_n$  polymer. Again, a four-center transition state is implicated, and we propose that Si-Si bond formation occurs via the process shown in Eq. 13.



This result was somewhat surprising, because related studies with analogous hydrocarbons indicated that there was a strong preference for hydrogen to be in the  $\beta$  position of the four-center transition state, because the orbital that it uses in bonding is more nondirectional [35]. Generally, results of our reactivity studies have shown that silicon readily participates in four-centered reactions, where  $\text{M}-\text{Si}$ ,  $\text{M}-\text{H}$ ,  $\text{Si}-\text{H}$ , and  $\text{Si}-\text{Si}$  bonds are involved [34]. To test for the possible intermediacy of silylene intermediates, the decomposition of

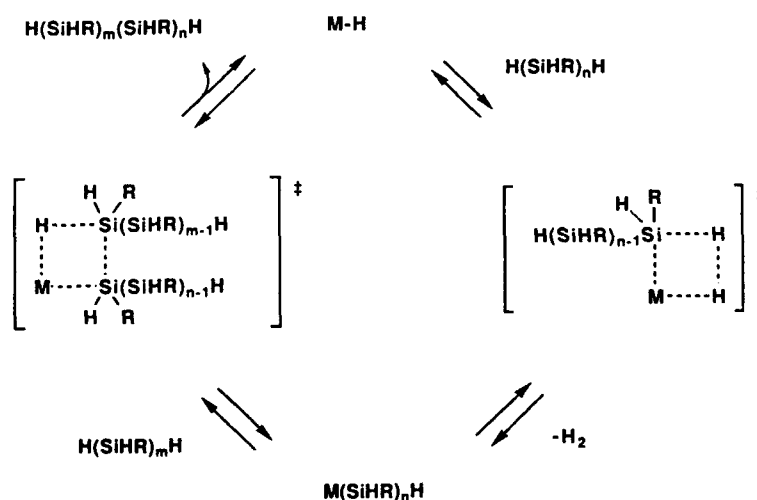
$\text{CpCp}^*\text{Hf}(\text{SiH}_2\text{Ph})\text{Cl}$  was carried out in the presence of good silylene traps:  $\text{HSiEt}_3$ ,  $(\text{c-C}_6\text{H}_{11})\text{SiH}_3$ ,  $\text{Ph}_2\text{SiH}_2$ , and  $\text{PhMeSiH}_2$ . The presence of these traps did not effect the rate of decomposition.

A Si-Si bond forming reaction that we believe to be more relevant to the polymerization mechanism is shown in Eq. 14.



This reaction yields the same products observed in the thermal decomposition of  $\text{CpCp}^*\text{Hf}(\text{SiH}_2\text{Ph})\text{Cl}$ , but it is significantly faster. Under pseudo-first-order conditions with excess  $\text{PhSiH}_3$ , disappearance of  $\text{CpCp}^*\text{Hf}(\text{SiH}_2\text{Ph})\text{Cl}$  is first order in both reactants. The isotope effect for this process at  $70^\circ\text{C}$  is 2.7(2) [34].

With the above observations, it is now straightforward to write a mechanism for chain propagation based on  $\sigma$ -bond metathesis processes (Fig. 56.2). We believe that the active species in the cycle is a metal hydride species that interacts predominately with the sterically less crowded  $-\text{SiH}_2\text{R}$  end group of a polymer chain. This introduces a polysilyl group into the metal coordination sphere. Chain growth then occurs via Si-Si bond-forming  $\sigma$ -bond metathesis. Note that the chain growth step releases polymer, regenerating the metal hydride. This mechanism explains the stringent steric requirements that are observed for catalysts and silane monomers, because the four-center transition states will be



**Figure 56.2.** A mechanism for dehydrogenative silane polymerization by an early transition metal catalyst precursor.

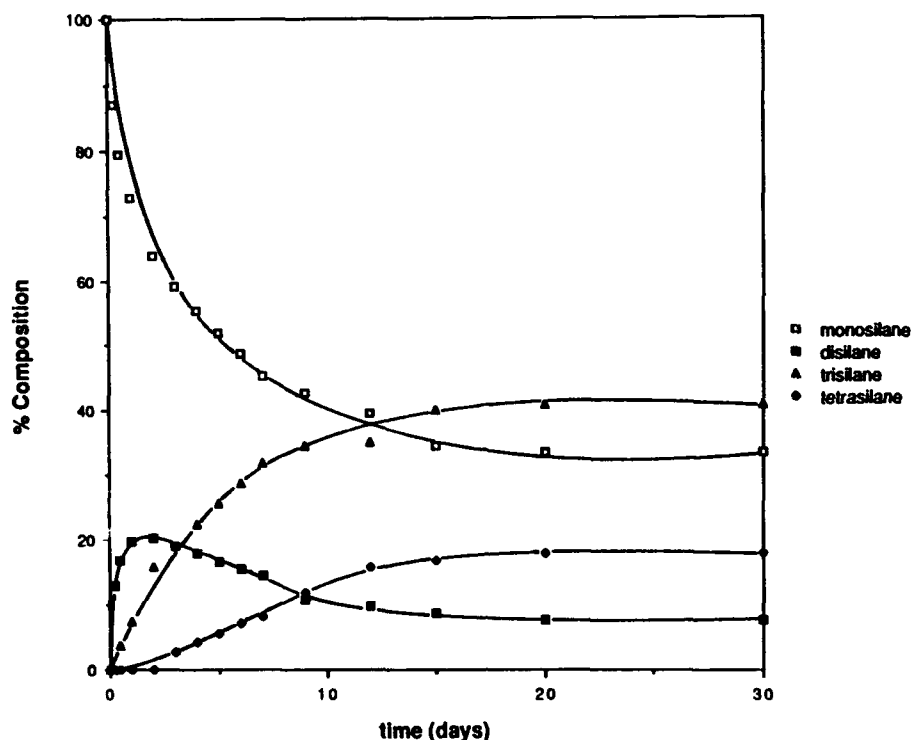


Figure 56.3. Concentrations of various silane species in the coupling of  $\text{PhSiH}_3$  as catalyzed by  $\text{Cp}_2^*\text{HfH}_2$ . Monitored by  $^1\text{H}$ -NMR in benzene- $d_6$ .

inherently quite crowded. We believe that steric constraints are such that one of the reacting silanes in a cycle must be primary ( $n$  or  $m = 1$ ), resulting in chain growths of only one Si per cycle.

Using model reactions, we have been able to detect the expected intermediates for the proposed mechanism. One such intermediate,  $\text{CpCp}^*\text{Hf}(\text{SiHPhSiH}_2\text{Ph})\text{Cl}$ , was prepared from  $\text{CpCp}^*\text{Hf}[\text{SiMe}_3]_3\text{Cl}$  and  $\text{PhH}_2\text{SiSiH}_2\text{Ph}$  and isolated as a mixture of two diastereomers. This species was then identified (by  $^1\text{H}$ -NMR spectroscopy) in the slow oligomerization of  $\text{PhSiH}_3$  by  $\text{CpCp}^*\text{Hf}(\text{SiH}_2\text{Ph})\text{Cl}$ . The addition of 2 equiv of  $\text{PhSiH}_3$  to  $\text{CpCp}^*\text{Hf}(\text{SiH}_2\text{Ph})\text{Cl}$  resulted in a slow reaction that after 24 hr (33% conversion) yielded  $[\text{CpCp}^*\text{HfHCl}]_n$ ,  $\text{CpCp}^*\text{Hf}(\text{SiHPhSiH}_2\text{Ph})\text{Cl}$ ,  $\text{PhH}_2\text{Si}-\text{SiH}_2\text{Ph}$ , and  $\text{PhH}_2\text{Si}-\text{SiHPh}-\text{SiH}_2\text{Ph}$ . The latter three silicon-containing products were formed in a ratio of ca. 3:2:3. Free, oligomeric silanes have been observed in coupling reactions with  $\text{Cp}_2^*\text{HfH}_2$  as catalyst. Presumably because of steric hindrance at the reacting metal center, this hafnium hydride couples Si-H bonds very slowly. This allows observation of the conversion of  $\text{PhSiH}_3$  to disilane, which is more slowly followed by the appearance of trisilane and, finally, a species that we believe to be the tetrasilane (Fig. 56.3). Note that after

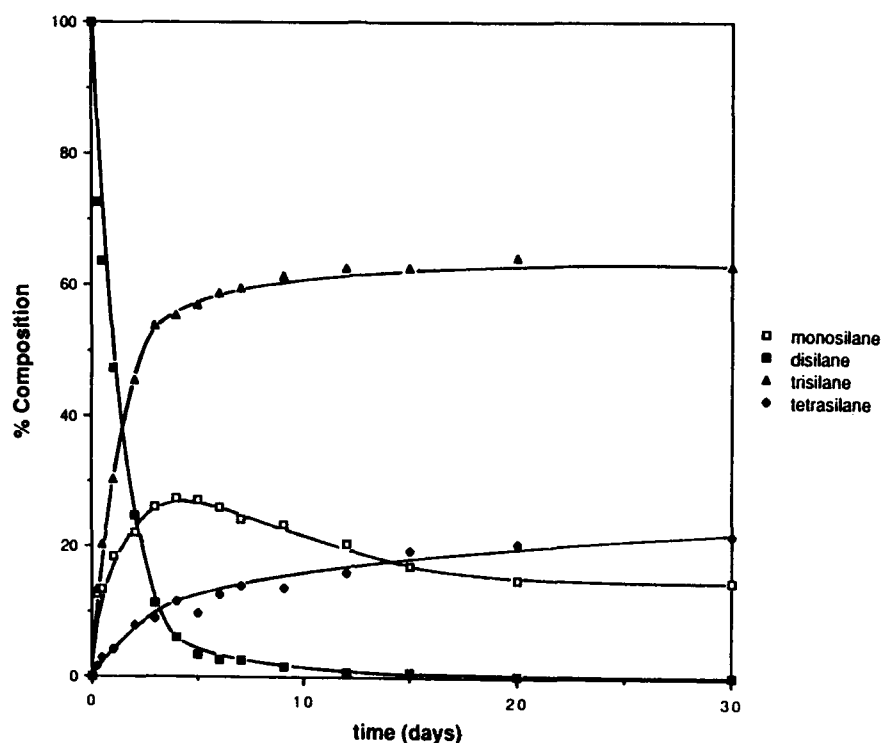


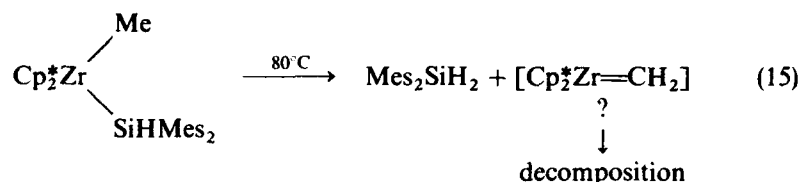
Figure 56.4. Concentrations of various silane species in the coupling of  $\text{PhH}_2\text{SiSiH}_2\text{Ph}$  as catalyzed by  $\text{Cp}_2^*\text{HfH}_2$ . Monitored by  $^1\text{H-NMR}$  in benzene- $d_6$ .

the relatively rapid appearance of disilane, monosilane and disilane are consumed at roughly the same rate. Figure 56.4, which gives the time dependence of silane concentrations in the reaction between excess disilane and hafnium catalyst, shows that Si-Si bond cleavage can be an important competing process. These reactions with  $\text{Cp}_2^*\text{HfH}_2$  were carried out in a closed system (sealed NMR tubes) [34].

Some of our results are relevant to the possible intermediacy of a metal silylene complex,  $\text{M}=\text{Si}(\text{R})\text{H}$ , in these polymerization reactions. First, the chloro complexes  $\text{CpCp}^*\text{M}[\text{Si}(\text{SiMe}_3)_3]\text{Cl}$  are catalysts for dehydrogenative silane polymerizations, and the polymerization reaction quantitatively converts these complexes to the corresponding hydrides,  $[\text{CpCp}^*\text{MHCl}]_n$  [34]. The polymerizations therefore appear to require use of only one  $\sigma$  bond at the metal center (note that formation and reactions of a silylene complex would require involvement of two  $\sigma$  bonds). Furthermore if silylene complexes are formed by an  $\alpha$  abstraction, this should be observed in isolated complexes of the type  $\text{M}(\text{SiHRR}')\text{R}''$  ( $\text{R}, \text{R}', \text{R}'' = \text{alkyl}, \text{H}$ ). We have isolated a few mixed alkyl/silyl complexes with Si-H bonds, but have not observed decomposition reactions consistent with  $\alpha$  abstraction from silicon. In fact in one case, decomposition was



seen to proceed by abstraction of hydrogen from the alkyl group by the silyl ligand (Eq. 15, Mes = 2,4,6-Me<sub>3</sub>C<sub>6</sub>H<sub>2</sub>).



The free silane is formed quantitatively in this reaction, along with unidentified zirconium products. Significantly, no methane was detected (by <sup>1</sup>H-NMR and gas chromatography) [42]. Given our observations of chemistry relevant to the polymerization reaction and the lack of precedent for silylene complexes of the early transition metals, metal silylenes do not appear to be likely intermediates in these polymerization reactions.

## 56.5. CONCLUSIONS

The results described above present evidence for a mechanism for the transition metal-catalyzed dehydrogenative polymerization of silanes [34]. This mechanism explains many aspects of the polymerization reaction, including steric requirements of the catalyst and substrate. Basic features of the mechanism are that it (1) requires a coordinatively unsaturated metal hydride catalyst, (2) involves σ-bond metathesis reactions with four-center transition states, and (3) each catalytic cycle involves formation of a metal silyl derivative and free polymer. This appears to be a new polymerization mechanism and is unusual in that a transition metal complex mediates a step-polymerization reaction. This feature of the mechanism explains the relatively short chain lengths that are obtained and indicates that the chain lengths are limited only by the extent of reaction. Future investigations may therefore prove that it is possible to modify reaction conditions and/or catalyst to favor a greater extent of reaction and higher polymer molecular weight.

Our proposal of a mechanism for the polymerization reaction is based largely on the zirconium and hafnium metallocene systems that we have investigated. Clearly there are more mechanistic tests that need to be applied. Also, there are obvious differences between the reactions catalyzed by zirconium or hafnium silyl complexes and those catalyzed by titanium alkyl complexes. It is therefore by no means clear that the titanium catalyst is operating by the same mechanism. However, we suggest that the mechanism described here deserves serious consideration for all dehydrogenative silane coupling reactions involving early transition metal catalysts and that major differences between catalysts may be attributed primarily to differences in initiation and side reactions.

It is hoped that the mechanism presented here will aid in the development of

polysilane chemistry by providing new and useful synthetic pathways. This mechanism provides significant information that can be used in the design of new and better catalysts. We believe that the prognosis is very good and that this synthetic route may prove to be quite useful in the future. Silane coupling reactions can potentially lead to a number of new silicon-containing polymers that have useful properties as electronic and structural materials.

## REFERENCES

1. C. A. Burkhard, *J. Am. Chem. Soc.*, **71**, 963 (1949).
2. R. West, *J. Organomet. Chem.*, **300**, 327 (1986).
3. R. West, A. R. Wolff, and D. J. Peterson, *J. Rad. Curing*, **13**, 35 (1986).
4. P. Trefonas III, R. West, and R. D. Miller, *J. Am. Chem. Soc.*, **107**, 2737 (1985); L. A. Harrah and J. M. Zeigler, *Macromolecules*, **20**, 601 (1987).
5. R. G. Kepler, J. M. Zeigler, L. A. Harrah, and S. R. Kurtz, *Bull. Am. Phys. Soc.*, **28**, 362 (1983).
6. R. West, L. D. David, P. I. Djurovich, K. L. Stearley, K. S. V. Srinivasan, and H. Yu, *J. Am. Chem. Soc.*, **103**, 7352 (1981).
7. F. Kajzar, J. Messier, and C. Rosilio, *J. Appl. Phys.*, **60**, 3040 (1986).
8. S. Yajima, J. Hayashi, and M. Omori, *Nature*, **261**, 683 (1976); S. Yajima, *Am. Ceramic Soc. Bull.*, **62**, 893 (1983).
9. K. S. Mazdhyasni, R. West, and L. D. David, *J. Am. Ceramic Soc.*, **61**, 504 (1978).
10. R. West, in: L. L. Hench and D. R. Ulrich, Eds., *Ultrastructure Processing of Ceramics, Glasses, and Composites*, Chap. 19, p. 235, Wiley-Interscience, New York, (1984).
11. R. H. Ganey, J. H. Gaul, Jr., and T. K. Hilty, *Organometallics*, **2**, 859 (1983).
12. J. F. Harrod, in: M. Zeldin, K. J. Wynne, and H. R. Allcock, Eds., *Inorganic and Organometallic Polymers*, ACS Symposium Series 360, Chap. 7, p. 89, American Chemical Society, Washington, D.C., (1988).
13. B. J. Aylett, *Adv. Inorg. Chem. Radiochem.*, **25**, 1 (1982).
14. T. D. Tilley, in: S. Patai and Z. Rappoport, Eds., *The Chemistry of Organosilicon Compounds*, Chap. 24, p. 1415, Wiley, New York, (1989).
15. K. Yamamoto, H. Okinoshima, and M. Kumada, *J. Organomet. Chem.*, **23**, C7 (1970).
16. K. Yamamoto, H. Okinoshima, and M. Kumada, *J. Organomet. Chem.*, **27**, C31 (1971).
17. K. Tamao, T. Hayashi, and M. Kumada, *J. Organomet. Chem.*, **114**, C19 (1976); H. Sakurai, Y. Kamiyama, and Y. Nakadaira, *J. Organomet. Chem.*, **131**, 147 (1977).
18. I. Ojima, S. I. Inaba, T. Kogure, and Y. Nagai, *J. Organomet. Chem.*, **55**, C7 (1973).
19. J. Y. Corey, L. S. Chang, and E. R. Corey, *Organometallics*, **6**, 1595 (1987).
20. M. F. Lappert, and R. K. Maskell, *J. Organomet. Chem.*, **264**, 217 (1984).
21. M. D. Curtis and P. S. Epstein, *Adv. Organomet. Chem.*, **19**, 213 (1981).
22. K. A. Brown-Wensley, *Organometallics*, **6**, 1590 (1987).
23. M. Tanaka, T. Kobayashi, T. Hayashi, and T. Sakakura, *Appl. Organomet. Chem.*, **2**, 91 (1988).
24. D. A. Straus, T. D. Tilley, A. L. Rheingold, and S. J. Geib, *J. Am. Chem. Soc.*, **109**, 5872 (1987).
25. C. Zybill and G. Müller, *Angew. Chem. Int. Ed. Engl.*, **26**, 669 (1987).
26. K. Ueno, H. Tobita, M. Shimoi, and H. Ogino, *J. Am. Chem. Soc.*, **110**, 4092 (1988).
27. C. Aitken, J. F. Harrod, and E. Samuel, *J. Organomet. Chem.*, **279**, C11 (1985).
28. C. T. Aitken, J. F. Harrod, and E. Samuel, *J. Am. Chem. Soc.*, **108**, 4059 (1986).

29. C. Aitken, J. F. Harrod, and E. Samuel, *Can. J. Chem.*, **64**, 1677 (1986).
30. C. Aitken, J. F. Harrod, and U. S. Gill, *Can. J. Chem.*, **65**, 1804 (1987).
31. J. F. Harrod, *Polym. Preprints*, **28**, 403 (1987).
32. J. F. Harrod and S. S. Yun, *Organometallics*, **6**, 1381 (1987).
33. J. Arnold, T. D. Tilley, A. L. Rheingold, S. J. Geib, and A. M. Arif, *J. Am. Chem. Soc.*, **111**, 149 (1989); F. H. Elsner, T. D. Tilley, A. L. Rheingold, and S. J. Geib, *J. Organomet. Chem.*, **358**, 169 (1988); J. Arnold, D. M. Roddick, T. D. Tilley, A. L. Rheingold, and S. J. Geib, *Inorg. Chem.*, **27**, 3510 (1988), and references in the above.
34. H.-G. Woo and T. D. Tilley, *J. Am. Chem. Soc.*, **111**, 8043 (1989).
35. M. E. Thompson, S. M. Baxter, A. R. Bulls, B. J. Burger, M. C. Nolan, B. D. Santarsiero, W. P. Schaefer, and J. E. Bercaw, *J. Am. Chem. Soc.*, **109**, 203 (1987).
36. S. L. Latesky, A. K. McMullen, I. P. Rothwell, and J. C. Huffman, *J. Am. Chem. Soc.*, **107**, 5981 (1985).
37. P. L. Watson, *J. Am. Chem. Soc.*, **105**, 6491 (1983).
38. J. W. Bruno, T. J. Marks, and V. W. Day, *J. Am. Chem. Soc.*, **104**, 7357 (1982).
39. K. H. den Haan, Y. Wielstra, and J. H. Teuben, *Organometallics*, **6**, 2053 (1987).
40. S. J. Simpson, H. W. Turner, and R. A. Andersen, *Inorg. Chem.*, **20**, 2991 (1981).
41. H.-G. Woo and T. D. Tilley, *J. Am. Chem. Soc.*, **111**, 3757 (1989).
42. D. M. Roddick, R. H. Heyn, and T. D. Tilley, *Organometallics*, **8**, 324 (1989).

## POLYCARBOSILANES AS SILICON CARBIDE PRECURSORS

DIETMAR SEYFERTH AND HEINRICH LANG

### 57.1. INTRODUCTION

Since Yajima and his co-workers developed the first polymeric precursors for silicon carbide [1], there has been much interest in organosilicon polymers whose pyrolysis gives ceramic materials with a high content of silicon carbide [2]. Among known organosilicon polymers that might be considered as potentially useful SiC precursors, the linear polycarbosilane,  $[(CH_3)_2SiCH_2]_n$ , is of interest [3]. Polymers of this kind, of relatively low molecular weight, have been prepared by active metal condensation of  $ClCH_2Si(CH_3)_2Cl$  [4], but material of considerably higher molecular weight could be prepared by transition metal complex-initiated ring-opening polymerization of 1,1,3,3-tetramethyl-1,3-disilacyclobutane, 1 [5]. Studies of the properties of such polycarbosilanes [5, 6] did not result in any useful applications. In particular, they are not useful as SiC precursors, their pyrolysis in a stream of argon to 1000°C leaving little or no ceramic residue. In spite of this defect, the  $[(CH_3)_2SiCH_2]_n$  polymers have been of continued interest as SiC precursors, because they are the type of polymer, linear and, in part, of high molecular weight, that should serve well in the preparation of fibers. However, it is obvious that the  $[(CH_3)_2SiCH_2]_n$  polymers will have to be modified by appropriate

*Ultrastructure Processing of Advanced Materials.*

Edited by Donald R. Uhlmann and Donald R. Ulrich (deceased).

ISBN 0-471-52986-9 © 1992 John Wiley & Sons, Inc.

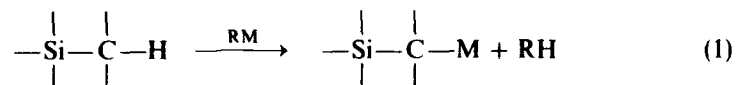
chemistry so that their pyrolysis will give high ceramic yields. (Ceramic yield = weight of pyrolysis residue  $\times$  100/weight of material pyrolyzed.)

One approach to such chemical modification of the  $[(CH_3)_2SiCH_2]_n$  polymers with this objective in mind was reported by Bacqué and co-workers [7]. Utilizing known Si-C bond cleavage chemistry, they treated a  $[(CH_3)_2SiCH_2]_n$  polymer fraction of molecular weight 250,000 with the  $(CH_3)_3SiCl/AlCl_3$  reagent. Their goal, the selective cleavage of one of the two methyl groups on silicon to give  $[CH_3(Cl)SiCH_2]_n$ , was realized. However, extensive Si-CH<sub>2</sub> cleavage occurred as well, and the molecular weight of their product was only 2300. Nevertheless, the  $[CH_3(Cl)SiCH_2]_n$  polymer was reduced to  $[CH_3(H)SiCH_2]_n$  material, which would, as a result of its reactive Si-H functionality, give SiC in high ceramic yield on pyrolysis. However, such was not the case: Thermal crosslinking via the Si-H functionality apparently did not occur, and pyrolysis of  $[CH_3(H)SiCH_2]_n$  gave a ceramic residue in only 5% yield [8].

We have shown that catalyzed hydrosilylations involving organosilicon polymers containing a multiplicity of Si-H functions, including those containing  $[R(H)SiCH_2]$  as the major repeat unit, and organosilicon compounds, both cyclic and polymeric, containing Si-CH=CH<sub>2</sub> functionality would give useful preceramic polymers [9]. With a suitable choice of reactants, a crosslinked (and still soluble) polymer whose pyrolysis gives a high yield of a ceramic material with a Si/C ratio of close to unity could be obtained. However, we were interested in alternative approaches for the successful utilization of  $[(CH_3)_2SiCH_2]_n$  polymers as preceramic materials. We report here one such approach.

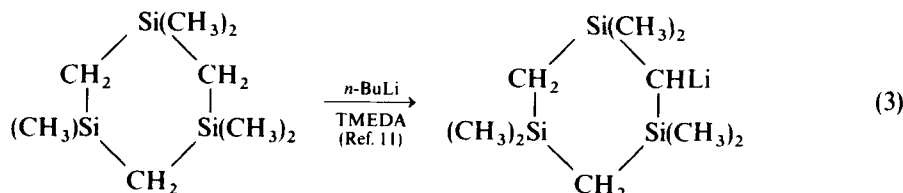
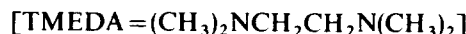
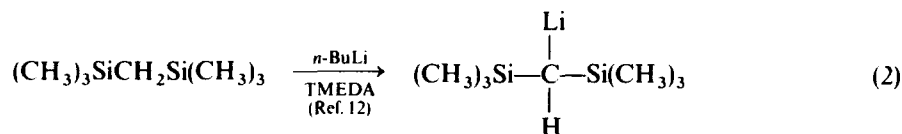
## 57.2. RESULTS AND DISCUSSION

Although at first sight  $[(CH_3)_2SiCH_2]_n$  polycarbosilanes contain no useful functionality for further chemical modification, one may make use of the fact that methylsilyl groups activate adjacent C-H bonds toward deprotonation by strong bases (Eq. 1) [10].



Studies by Fritz and co-workers [11] and by Gröbel and Seebach [12] have shown that methylene bridges between two silicon atoms are more readily deprotonated by strong organometallic bases than are methyl groups bonded to a single silicon atom. Equations 2 and 3 give a few examples. In the case of the trisilacyclohexane further metalation did not occur at 20°C even when an excess

of metalation reagent was used.

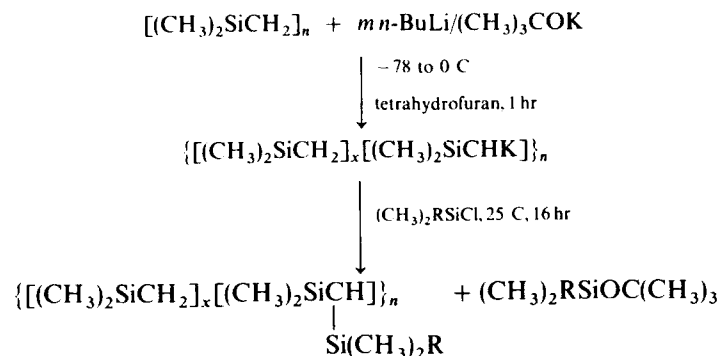


Our own model chemistry studies [13] of the metalation of  $(\text{CH}_3)_3\text{SiCH}_2\text{Si}(\text{CH}_3)_3$ ,  $(\text{CH}_3)_3\text{SiCH}_2\text{Si}(\text{CH}_3)_2\text{CH}_2\text{Si}(\text{CH}_3)_3$ , and cyclo- $[(\text{CH}_3)_2\text{SiCH}_2]_3$  using several organoalkali bases ( $t\text{-BuLi} \cdot \text{TMEDA}$ ,  $\text{sec-BuLi} \cdot \text{TMEDA}$ ,  $n\text{-BuLi}/t\text{-BuOK}$ ) showed the last of these to be especially effective in the metalation of  $\text{SiCH}_2\text{Si}$  groups. This reagent reacted rapidly with these carbosilanes even at  $-70^\circ\text{C}$  in tetrahydrofuran (THF) solution. Accordingly, we have studied the metalation of the  $[(\text{CH}_3)_3\text{SiCH}_2]_n$  polymers by the  $n\text{-BuLi}/t\text{-BuOK}$  reagent.

The  $[(\text{CH}_3)_3\text{SiCH}_2]_n$  polymer was prepared by  $\text{H}_2\text{PtCl}_6 \cdot 6\text{H}_2\text{O}$ -catalyzed ring-opening polymerization of 1,1,3,3-tetramethyl-1,3-disilacyclobutane using a procedure described by Levin and Carmichael [5]. It was isolated in the form of colorless, rubbery material that began to flow on standing. According to gel permeation chromatography (GPC) (in toluene solution, polystyrene standard), it contains three fractions: two in the 1000- to 3000-dalton range and one (very broad GPC peak) in the 50,000- to 200,000-dalton range, with the low-molecular-weight components being the major ones by far. By cryoscopy in benzene, the "molecular weight" was 2018.

The metalations of the  $[(\text{CH}_3)_2\text{SiCH}_2]_n$  polymer thus prepared were carried out as follows: The polymer was dissolved in THF, and the solution was cooled to  $-78^\circ\text{C}$ . Potassium *tert*-butoxide then was added and subsequently the same molar quantity of  $n$ -butyllithium in pentane. An immediate color change to yellow/yellow-orange (due to the  $n\text{-BuLi}/(\text{CH}_3)_3\text{COK}$  interaction, according to a control experiment) occurred. After the reaction mixture had been allowed to warm to  $0^\circ\text{C}$  over the course of an hour, the chlorosilane  $[(\text{CH}_3)_2\text{HSiCl}$ ,  $(\text{CH}_3)_2(\text{CH}_2=\text{CH})\text{SiCl}$ , etc.] was added (Scheme 57.1). Ratios of base: $(\text{CH}_3)_2\text{SiCH}_2$  of 1:6, 1:2, 1:1, 2:1, 3:1, and 5:1 were used in these experiments. There was no correspondence of these ratios with the degree of metalation. When the indicated base: $(\text{CH}_3)_2\text{SiCH}_2$  ratio was 1:6,  $x$  in the formula of the silylated product (Scheme 57.1) was about 15. When it was 1:2,  $x$

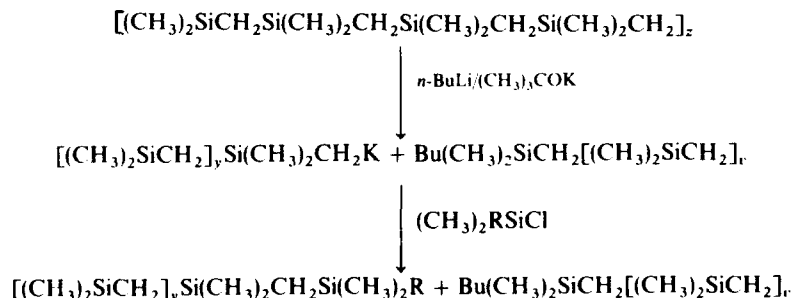
670 POLYCARBOSILANES AS SILICON CARBIDE PRECURSORS



Scheme 57.1.

was about 9. A base:  $(\text{CH}_3)_2\text{SiCH}_2$  ratio of 1 was optimum: About every fourth  $(\text{CH}_3)_2\text{SiCH}_2$  unit was metalated ( $x = 3$ ). Use of an excess of  $n\text{-BuLi}/(\text{CH}_3)_3\text{COK}$  base reagent, according to cryoscopic molecular weight measurements and complications in the product proton nuclear magnetic resonance (NMR) spectra, appears to lead to chain cleavage, most likely via nucleophilic attack by  $n\text{-BuK}$  at silicon (Scheme 57.2). Such a process will lower the average molecular weight (as was observed) and, through introduction of  $n$ -butyl groups and  $(\text{CH}_3)_2\text{RSi}$  groups on terminal sites, will result in more complicated NMR spectra in the aliphatic C-H region. Even in the case of 1:1 reactions there was some limited Si-C cleavage, based on these experimental criteria.

All further experiments were carried out using an  $n\text{-BuLi}/(\text{CH}_3)_3\text{COK}$  base-to- $(\text{CH}_3)_2\text{SiCH}_2$  ratio of 1. After reaction of the metalated polycarbosilane with the respective  $(\text{CH}_3)_2\text{RSiCl}$ , all volatiles were removed under high vacuum, and the residue was extracted with benzene/hexane mixtures. The silylation products were isolated by vacuum evaporation of the extracts as viscous oils (more



Scheme 57.2.

mobile than the starting polycarbosilane) that are soluble in benzene, toluene, dichloromethane, and chloroform. The yields of these products based on charged  $[(\text{CH}_3)_2\text{SiCH}_2]_n$  were in the 92 to 98% range.

That only every fourth  $(\text{CH}_3)_2\text{SiCH}_2$  unit of the polycarbosilane is metalated can be understood in terms of charge dispersal from the metalated, negatively charged carbon atom along the  $(\text{Si}-\text{C})_n$  chain (polarization and inductive effects), which becomes sufficiently attenuated by the time the fourth  $\text{CH}_2$  group is reached.

Thermogravimetric analysis (TGA) of the starting  $[(\text{CH}_3)_2\text{SiCH}_2]_n$  polycarbosilane and of  $\{[(\text{CH}_3)_2\text{SiCH}_2]_3[(\text{CH}_3)_2\text{SiCH}(\text{SiCH}_3)_2\text{CH}=\text{CH}_2]\}_n$  was obtained (to 1000°C under argon). The starting polycarbosilane is thermally stable to about 350°C, at which point rapid decomposition, which is complete at around 675°C, begins. No ceramic residue remains. The TGA of the silyl-substituted polymer shows a two-stage decomposition process: an initial 25% weight loss between 80°C and 240°C, followed by a rapid weight loss, which leaves about a 2% ceramic residue weight between 450°C and 625°C. The silylated polymers obtained using  $(\text{CH}_3)_2\text{HSiCl}$  and  $(\text{CH}_3)_3\text{SiCl}$  gave a ceramic yield of zero (TGA to 1000°C, 10°C/min, under argon).

The introduction of  $(\text{CH}_3)_2\text{HSi}$  and  $(\text{CH}_3)_2(\text{CH}_2=\text{CH})\text{Si}$  groups into the polycarbosilane as substituents on the methylene carbon atoms provides the means for crosslinking reactions, which can result in an increase in the ceramic yield on pyrolysis. One might expect that a hydrosilylation reaction involving the  $(\text{CH}_3)_2\text{HSi}$  groups on one polymer chain and the  $(\text{CH}_3)_2(\text{CH}_2=\text{CH})\text{Si}$  groups on another might give a hybrid polymer whose pyrolysis would give a greatly enhanced ceramic yield (compared with the negligible ceramic yields obtained with the component polymers alone). This, however, was not the case. Such reactions of ca. 1.5 M-eq of the  $(\text{CH}_3)_2\text{HSi}$ -substituted polycarbosilane with 1 eq of the  $(\text{CH}_3)_2(\text{CH}_2=\text{CH})\text{Si}$ -substituted polycarbosilane, using either AIBN or  $\text{H}_2\text{PtCl}_6 \cdot 6\text{H}_2\text{O}$  as a catalyst, did not proceed to high conversion, possibly as a result of steric factors, and the resulting materials isolated by removal of volatiles and column chromatography (silica gel) gave only very low ceramic yields on pyrolysis to 1000°C under argon.

If this interchain crosslinking by means of catalyzed hydrosilylation been successful, then the resulting polymer still would have presented problems: its pyrolysis (under argon) would be expected to give a ceramic residue containing a high content of elemental carbon in addition to the desired SiC.

These problems of low ceramic yield and the formation of elemental carbon in large amounts in the pyrolysis of the polycarbosilane were successfully addressed by another hybrid polymer approach. In earlier work, we [14] (and independently by Brown-Wensley and Sinclair [15]) had studied the sodium condensation of  $\text{CH}_3\text{SiHCl}_2$ . In THF solvent, this reaction gave a solid, THF-soluble polysilane of composition  $[(\text{CH}_3\text{SiH})_{0.4}(\text{CH}_3\text{Si})_{0.6}]_n$ , that is about 60% of the Si-H bonds had reacted with the sodium, generating crosslinking sites in which a silicon atom is bonded to three other silicon atoms. As a result of this extensive crosslinking, pyrolysis of this polysilane to 1000°C under argon gave a



fairly good (ca. 60%) ceramic yield. However, this 40% weight loss includes loss of many of the methyl groups (such as  $\text{CH}_4$ ), and the residue had a composition (by analysis) of 1.0 SiC + 0.5 Si on a molar basis (equivalent to 26 wt % of elemental Si). The liquid polysilane,  $[(\text{CH}_3\text{SiH})_x(\text{CH}_3\text{Si})_y]_n$  ( $x = \sim 0.65$  to  $0.85$ ;  $y = \sim 0.35$  to  $0.15$ ) obtained by sodium condensation of  $\text{CH}_3\text{SiHCl}_2$  when the solvent system used is about 6 vol of hexane + 1 vol of THF is less highly crosslinked and its pyrolysis gave a ceramic yield of only 15 to 20%, again of composition of about 1.0 SiC + 0.5 Si.

However, this defect of these polysilanes, the formation of free silicon on pyrolysis, can be used to good advantage. In the present instance, we can make use of their abundant Si-H functionality in a hydrosilylation reaction with the vinyl-substituted polycarbosilane,  $\{[(\text{CH}_3)_2\text{SiCH}_2]_3[(\text{CH}_3)_2\text{SiCH}(\text{Si}(\text{CH}_3)_2-\text{CH}=\text{CH}_2)]\}_n$ , catalyzed by AIBN in refluxing benzene solution. A molar ratio of the polysilane to the vinyl-substituted polycarbosilane of 1.5 gave a new organosilicon polymer whose pyrolysis gave a 54% ceramic yield. When this molar ratio was 4.0, the ceramic yields obtained on pyrolysis to  $1000^\circ\text{C}$  under argon was 68%; the composition of the solid residue was 91% by weight SiC, 9% C. Increasing this molar ratio of the two polymers to 7.5 gave a new organosilicon polymer via the hydrosilylation crosslinking process whose pyrolysis gave by analysis a mixture containing 94% by weight of SiC and only 6 wt % of carbon. Such hybrid polymers thus are good candidates for further studies aimed at developing useful applications.

The Yajima (Nicalon) polycarbosilane is not a simple linear polymer, but appears to be a crosslinked material of complicated structure [16]. The main component repeat units are  $[\text{CH}_3(\text{H})\text{SiCH}_2]$  and  $[(\text{CH}_3)_2\text{SiCH}_2]$ , with the former predominating. Pyrolysis of the uncured polymer under argon generally gives a 55 to 60% yield of a ceramic material that contains substantial amounts of free carbon in addition to SiC. We have been able to upgrade the Nicalon polycarbosilane by means of the reaction sequence: metalation with the  $n\text{-BuLi}/(\text{CH}_3)_3\text{COK}$  reagent, reaction of the metalated polymer with  $(\text{CH}_3)_2(\text{CH}_2=\text{CH})\text{SiCl}$  to produce a "vinyl-Nicalon," and, finally, hydrosilylation of the latter with the liquid polysilane,  $[(\text{CH}_3\text{SiH})_x(\text{CH}_3\text{Si})_y]_n$ , to give a new hybrid organosilicon polymer. In this way we have been able to obtain crosslinked polycarbosilanes whose pyrolysis under argon left a ceramic residue in good (65–85%) yield, which, if the right ratio of the two polymers is used, can be 98% by weight SiC, with only 2% excess carbon.

Because of the expense of the  $n\text{-BuLi}/(\text{CH}_3)_3\text{COK}$  reagent and its relative inefficiency in metalating  $[(\text{CH}_3)_2\text{SiCH}_2]_n$ , the approach described here may not be very practical. However, the results described here show very clearly that polymers that are at first sight useless as precursors for ceramics can be converted to useful preceramic materials by means of chemistry appropriate to their composition. However, attainment of high ceramic yield on pyrolysis and correct elemental composition represent only the beginning of what will be a long and, usually, difficult course of collaborative study by the chemist and the

ceramist if a ceramic precursor that will be useful in the real world is to be developed.

### ACKNOWLEDGMENT

The authors are grateful to the U.S. Air Force Office of Scientific Research (AFSC), Directorate of Chemical and Atmospheric Sciences, for generous support of this research.

### REFERENCES

1. S. Yajima, *Am. Ceramic Soc. Bull.*, **62**, 893 (1983).
2. C. L. Schilling, Jr., J. P. Wesson, and T. C. Williams, *Am. Ceramic Soc. Bull.*, **62**, 912 (1983); R. West, L. D. David, P. I. Djurovich, and H. Yu, *Am. Ceramic Soc. Bull.*, **62**, 899 (1983); J. Lipowitz, G. E. LeGrow, T. F. Lim, and N. Langley, *Ceramic Eng. Sci. Proc.*, **9**, 931 (1988); D. A. White, S. M. Oleff, R. D. Boyer, P. A. Budinger, and J. R. Fox, *Adv. Ceramic Mater.*, **2**, 45 (1987).
3. D. Seyferth, in: M. Zeldin, K. J. Wynne, and H. R. Allcock, Eds., *Inorganic and Organometallic Polymers*, ACS Symposium Series 360, pp. 21-42, American Chemical Society, Washington, D.C. (1988).
4. J. T. Goodwin, Jr., U.S. patent 2,483,972 (October 2, 1949); *Chem. Abstr.* **44**, 2011e (1950); J. T. Goodwin, Jr., U.S. patent 2,607,791 (1952); *Chem. Abstr.*, **48**, 13732 (1954).
5. N. S. Nametkin, V. M. Vdovin, and P. L. Grinberg, *Izv. Akad. Nauk SSSR, Ser. Khim.*, 1123 (1964); D. R. Weyenberg and L. E. Nelson, *J. Org. Chem.*, **30**, 2618 (1965); W. A. Kriner, *J. Polym. Sci., Part A-1*, **4**, 444 (1966); W. R. Bamford, J. C. Lovie, and J. A. C. Watt, *J. Chem. Soc. C*, 1136 (1966); G. Levin and J. B. Carmichael, *J. Polymer Sci., Part A-1*, **1** (1968); N. S. Nametkin, N. V. Ushakov, and V. M. Vodvin, *Vysokomolekul. Soedin.*, **1**, 29 (1971); V. S. Poletaev, V. M. Vdovin, and N. S. Nametkin, *Dokl. Akad. Nauk SSSR*, **203**, 1324 (1973); V. S. Poletaev, V. M. Vdovin, and N. S. Nametkin, *Dokl. Akad. Nauk SSSR*, **208**, 1112 (1973).
6. J. H. Ko and J. L. Mark, *Macromolecules*, **8**, 869 (1975); J. L. Mark and J. H. Ko, *Macromolecules*, **8**, 874 (1975); M. A. Llorente, J. L. Mark, and E. Siaz, *J. Polym. Sci., Polym. Phys. Ed.*, **21**, 1173 (1983); V. Galiatsatos and J. L. Mark, *Polym. Preprints*, **28**, 258 (1987).
7. E. Bacqué, J.-P. Pillot, M. Birot, and J. Dunoguès, *Macromolecules*, **21**, 30 (1988).
8. E. Bacqué, J.-P. Pillot, M. Birot, and J. Dunoguès, *Macromolecules*, **21**, 34 (1988).
9. D. Seyferth and Y.-F. Yu, U.S. patent 4,650,837 (February 17, 1987).
10. W. P. Weber, *Silicon Reagents in Organic Synthesis*, Chap. 6, Springer, Berlin (1983).
11. G. Fritz, J. Neutzner, and H. Volk, *Z. Anorg. Allg. Chem.*, **497**, 21 (1983).
12. B. T. Gröbel and D. Seebach, *Chem. Ber.*, **110**, 852 (1977).
13. D. Seyferth and H. Lang, unpublished work.
14. T. G. Wood, Ph.D. Thesis, Massachusetts Institute of Technology (1984); D. Seyferth and Y.-F. Yu, in: D. L. Cocke and A. Clearfield, Eds., *Design of New Materials*, pp. 73-94, Plenum, New York (1987).
15. K. A. Brown-Wensley and R. A. Sinclair, U.S. patents 4,537,942 (August 27, 1985) and 4,611,035 (September 9, 1986).
16. Y. Hasegawa and K. Okamura, *J. Mater. Sci.*, **21**, 321 (1986).

## PREPARATION OF ALUMINUM NITRIDE FIBERS

JOHN D. BOLT

### 58.1. INTRODUCTION

Aluminum nitride (AlN) has received considerable attention as a micro-electronic packaging substrate because of its high thermal conductivity, similar thermal expansion to silicon, and moderate dielectric constant. As fibers, AlN would be particularly attractive for enhancing the thermal conductivity of composites. Previously, we demonstrated the usefulness of alumina fibers in polymer matrices for electronics packaging (dielectric materials) to enhance thermal conductivity and lower thermal expansion while maintaining low dielectric constants [1]. Candidate materials for new fibers included diamond, cubic, and hexagonal BN, SiC, AlN, and BeO. Of these, AlN possessed a good combination of properties and feasibility of fiber preparation. In addition, aluminum nitride's high modulus, low CTE, creep resistance, and strength retention at high temperature make AlN fibers potentially useful in structural ceramic, metal, and glass matrix composites.

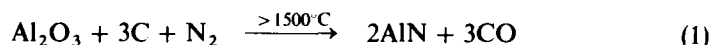
*Ultrastructure Processing of Advanced Materials.*

Edited by Donald R. Uhlmann and Donald R. Ulrich (deceased).

ISBN 0-471-52986-9 © 1992 John Wiley & Sons, Inc.

## 58.2. ALUMINUM NITRIDE FIBERS BY CARBOTHERMAL REDUCTION

AlN is prepared by several routes, direct nitridation of metal, carbothermal reduction of alumina in nitrogen, and various inorganic and organometallic reactions. The carbothermal reduction route, Eq. 1, is widely used in preparation of AlN powders [2-7].



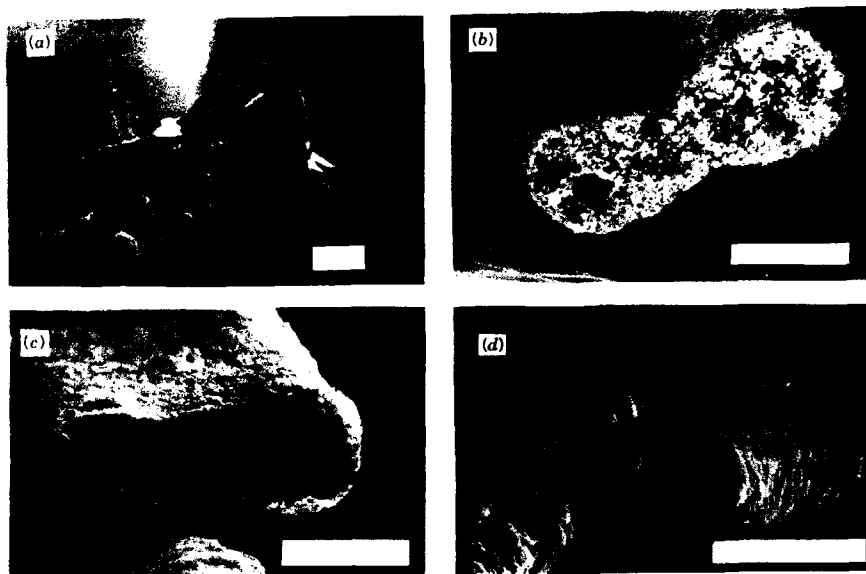
To prepare AlN fibers we wanted precursor fibers containing an intimate mixture of carbon and alumina or their precursors, which would transform to AlN fibers by Eq. 1. Patent references to such a process include spinning fibers containing aluminum dicarboxylates [8] or mixtures of  $\text{Al}_2(\text{OH})_5\text{Cl}$  and polyvinyl alcohol [9, 10]. We prepared the carbon-alumina fibers by dispersing submicron alumina in two well-known precursors to carbon fibers, polyacrylonitrile (PAN) and petroleum pitch.

PAN-alumina slurries suitable for spinning fibers were prepared by ball milling alumina in dimethylformamide (DMF) containing small amounts of PAN as a dispersing aid and subsequently adding the bulk of the PAN. For wet spinning into 60:40 DMF:water, a typical slurry contained 74% DMF, 14.3%  $\text{Al}_2\text{O}_3$ , and 11.7% PAN by weight. For dry spinning a typical slurry contained 55.9% DMF, 24%  $\text{Al}_2\text{O}_3$ , 0.3%  $\text{Y}_2\text{O}_3$ , and 19.8% PAN by weight. In dry spinning, dispersions were extruded at 0.5 ml/min per hole at 90°C into a vertical column at 150°C (average), and fibers were wound up at 132 m/min. Fibers were further drawn five times in boiling water, then oxidatively stabilized in air by heating from 200 to 280°C at 1°C/min. Subsequently, fibers were carbonized and nitrided by heating in a graphite resistance furnace in nitrogen to 1650°C, then sintered by further heating to between 1700 and 1850°C.

Spinnable dispersions of alumina in petroleum pitch were prepared by ball milling alumina,  $\text{Y}_2\text{O}_3$ , and oleic acid in tetrahydrofuran, adding an isotropic pitch (Ashland Aerocarb), and evaporating the solvent. Addition of high-molecular-weight polystyrene enhanced spinnability. A dispersion containing 54.4%  $\text{Al}_2\text{O}_3$ , 35% pitch, 9.1% polystyrene (molecular weight, 250,000), 1% oleic acid, and 0.5%  $\text{Y}_2\text{O}_3$  was melt spun at 210°C. Fibers were oxidatively stabilized in air by heating at 0.5°C/min to 265°C, then carbonized, nitrided, and sintered as for PAN-alumina fibers above.

Figure 58.1 is a series of micrographs at several stages in the conversion of PAN-alumina fibers to AlN fibers. The dog bone-shaped fiber cross section is typical of dry-spun PAN. In conversion of the PAN to carbon, fibers densified to a composite fiber of  $\text{Al}_2\text{O}_3$  particles in a carbon matrix. After nitridation the microstructure consisted of uniform submicron particles, typical of carbothermally prepared AlN. These sintered to dense, polycrystalline fibers with grain sizes from 1 to 3  $\mu\text{m}$ .

Sintering aids were essential in obtaining dense fibers; in their absence AlN particles did not sinter, but continued to coarsen at progressively greater



**Figure 58.1.** (a) Dry-spun PAN-alumina fibers undrawn. (b) Carbon-alumina fibers. (c) AlN fibers after carbothermal reduction. (d) AlN fibers after carbon removal and sintering. All scale bars = 10  $\mu\text{m}$ .

temperature and times. Typical sintering aids were used such as  $\text{CaO}$  and  $\text{Y}_2\text{O}_3$  [11, 12]. These were added either as oxides in the original dispersion of  $\text{Al}_2\text{O}_3$  or by applying solutions of the metal nitrates subsequent to nitridation.

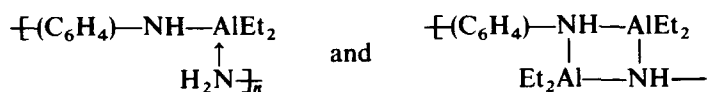
Control of the carbon-to- $\text{Al}_2\text{O}_3$  ratio was particularly important for reproducible sintered fibers. Carbon yield from PAN and pitch was determined thermogravimetrically. However, precise control of carbon was necessary to prevent excessive grain growth enhanced by oxide phases. With a deficiency of carbon, aluminum oxynitride ( $\gamma\text{-Al}_{27}\text{O}_{33}\text{N}_5$  [13]) formed above 1600°C. With excess carbon, fibers did not sinter, and  $\text{Y}_2\text{O}_3$  was reduced to YN, as detected by X-ray diffraction. In preparation of AlN powder, it has been reported that an excess of carbon is necessary to completely convert  $\text{Al}_2\text{O}_3$  to AlN optimally at a C: $\text{Al}_2\text{O}_3$  molar ratio of 4.2 [4, 6]. However, we found a ratio of 3.3 was sufficient, perhaps due to the intimate mixture of C and  $\text{Al}_2\text{O}_3$  and the easy exchange of gases within fiber bundles. Excess carbon was burned out in air at 600 to 650°C prior to sintering.

### 58.3. ORGANOMETALLIC ROUTES TO AlN FIBERS

Impurities such as O, Si, and some transition metals are known to degrade the thermal conductivity of AlN [14, 15]. We pursued organometallic routes to AlN fibers based on our experience producing high-purity  $\text{Al}_2\text{O}_3$  from triethylaluminum [16].

### 58.3.1. Precursor Polymers from Alkylaluminums and Aromatic Amines

Initially we prepared a soluble, infusible polymer from triethylaluminum ( $\text{Et}_3\text{Al}$ ) and *p*-phenylenediamine [17]. Highly viscous solutions were obtained in ratios of diamine to alkyl aluminum of 1:1 and 1:2. Yield, volume of gas evolved, elemental analysis, and  $^1\text{H}$  nuclear magnetic resonance (NMR) were consistent with the loss of one ethane from each  $\text{Et}_3\text{Al}$ . These simplified polymer structures are proposed:



Polymers from a variety of aromatic di-, tri-, and tetraamines and alkyl aluminums were prepared. After pyrolysis in  $\text{N}_2$  or Ar, residues of about 60% contained Al and N in stoichiometric amount, confirming AlN detected in X-ray powder patterns. However, substantial carbon remained, 38 to 60%. Fibers hand-pulled from concentrated solutions retained their shape when pyrolyzed. Pyrolysis in ammonia led to lower carbon contents, but tended to depolymerize the precursor.

### 58.3.2. Precursor Polymer from Diethylaluminum Amide

Tebbe found a simpler method that gave a thermoplastic organoaluminum precursor [18, 19]. Diethylaluminum amide polymerized in the presence of alkyl aluminums to give products with a typical empirical formula,  $(\text{EtAlNH})_{0.15}(\text{Et}_2\text{AlNH}_2)_{0.85}$  based on ethane evolved and elemental analysis.  $^{15}\text{N}$ -NMR data suggested the presence of AlN groups in the polymer [20]. More detailed definition of the polymer structure is in progress.

The organoaluminum precursor could be melt spun above  $100^\circ\text{C}$ , cured, and pyrolyzed in ammonia, converting to a stoichiometric, high-surface-area, crystalline AlN by  $400^\circ\text{C}$  [21, 22]. At subsequently higher temperatures the microstructures evolved by particle coarsening and finally sintering to fully dense AlN with submicron grains. In contrast to fibers produced by carbothermal reduction or to conventional AlN ceramics, sintering aids were unnecessary. However, in attempts to prepare rigorously oxygen-free samples, we found that trace oxygen is necessary for sintering, although at substantially lower levels than in conventional powder processing of AlN.

Properties of AlN fibers made from the thermoplastic organoaluminum precursor are summarized in Table 58.1. Thermal conductivity is three times that of the best available ceramic fibers from  $\alpha$ -alumina and ten times that of aluminosilicate fibers. Other properties are comparable to bulk AlN.

**TABLE 58.1. Properties of Aluminum Nitride Fibers: Comparisons to Literature Values for Monolithic AlN and to  $\alpha$ -Alumina Fibers**

	AlN Fibers	Bulk AlN (Literature Value)	$\alpha$ -Al <sub>2</sub> O <sub>3</sub> Fibers (Fiber FP)
Thermal conductivity (W/m K) at room temperature	82	40–285	27
(oxygen content, %)	(0.5–1.0)	(0.03–3.6) <sup>a</sup>	
Coefficient of thermal expansion (ppm/°C) (50–400°C)	4.6	4.5	7.3
Dielectric constant at 1 MHz	8.2	8.8	10.5
Tensile strength (MPa) (6.4 mm gauge)	340	(440) <sup>b</sup>	1500
Density (g/cm <sup>3</sup> )	3.14–3.32	3.25	3.9
Grain size ( $\mu$ m)	0.3–0.8	3–5	0.4
Diameter ( $\mu$ m)	8–25	—	20

<sup>a</sup>Refs. 15, 25.

<sup>b</sup>Three-point bend, Ref. 26.

#### 58.4. OTHER ROUTES TO AlN FIBERS

AlN fibers by direct nitridation of short aluminum fibers have been reported [10], but no properties were given. Whiskers (acicular single crystals) of AlN have been prepared by numerous routes, all of which proceed through volatile intermediates [23]. Tensile strengths up to 7 GPa were reported [24], but no thermal conductivity data are available.

#### 58.5. SUMMARY

Two methods were demonstrated for preparing AlN fibers. Carbothermal reduction of carbon precursor fibers containing dispersed alumina produced AlN fibers from inexpensive raw materials. Sintering required mixed metal oxide liquid phases. Organoaluminum precursor polymers could be melt spun and converted to AlN. Sintering required oxygen, but additional metallic cations were unnecessary.

## REFERENCES

1. D. P. Button, B. A. Yost, R. J. French, W. Y. Hsu, J. D. Bolt, M. A. Subramanian, H.-M. Zhang, R. E. Giedd, A. J. Whittaker and D. G. Onn, in: W. Young, and M. F. Yan, Eds., *Advances in Ceramics*, Vol. 26, American Ceramics Society, Columbus, Oh, pp. 353-374 (1989).
2. O. Serpek, German Patent 181,991 (1905).
3. T. Sakai and M. Iwata, *Yogyo Kyokaishi*, **82**, 181 (1975).
4. W. I. Li, L. P. Huang, X. Z. Huang, G. Kuang, S. H. Tan, S. R. Fwu, and T. S. Yen, in: P. Vincenzini, Ed., *Ceramic Powders*, p. 403, Elsevier, Amsterdam (1983).
5. T. Ya. Kosolapova, D. S. Yakovleva, G. S. Olenik, T. S. Bartnitskaya, N. P. Tel'nikova, and I. I. Timofeeva, *Sov. Powder Metal.*, **23**, 829 (1984). [English trans.]
6. P. Lefort, F. Marty, G. Ado, and M. Billy, *Rev. Chim. Miner.*, **22**, 534 (1986).
7. M. Mitomo and Y. Yoshioka, *Adv. Ceramic Mater.*, **2**, 253 (1987).
8. G. Winter, M. Mansmann, and H. Zirngibl, U.S. Patent 4,010,233 (1977).
9. Y. Oguri, M. Awata and H. Endo, U.S. Patent 4,761,388 (1988).
10. T. Konno, Japanese Patent Application Publ. Kokai, 61-124626 (1986).
11. S. Prochazka and C. F. Bobik, *Mater. Sci. Res.*, **13**, 321 (1980).
12. K. Komeya, *Ceramic Bull.*, **63**, 1158 (1984).
13. J. W. McCauley and N. D. Corbin, in: F. L. Riley, Ed., *Progress in Nitrogen Ceramics*, p. 111, Nijhoff, The Hague (1983).
14. N. Kuramoto, H. Taniguchi, Y. Numata, and I. Aso, *Yogyo Kyokaishi*, **93**, 517 (1985).
15. G. A. Slack, R. A. Tanzilli, R. O. Pohl and J. W. Vandersnade, *J. Phys. Chem. Solids*, **48**, 641 (1987).
16. F. N. Tebbe, P. A. Morris, R. H. French, U. Chowdhry, and R. L. Coble, *J. Am. Ceramic Soc.*, **71**, C204 (1988).
17. J. D. Bolt and F. N. Tebbe, U.S. Patent 4,740,574 (1988).
18. F. N. Tebbe, U.S. Patent 4,696,968 (1987).
19. F. N. Tebbe, J. D. Bolt, R. J. Young, O. R. Van Buskirk, W. Mahler, G. S. Reddy and U. Chowdhry in: H. M. O'Bryan, K. Niwa, W. Young, and M. F. Yan, Eds., *Advances in Ceramics*, Vol. 26, American Ceramics Society, Columbus, Oh, pp. 63-68 (1989).
20. R. T. Baker, J. D. Bolt, G. S. Reddy, D. C. Roe, R. H. Staley, F. N. Tebbe, and A. J. Vega, *Mater. Res. Soc. Symp. Proc.*, **121**, 471 (1988).
21. J. D. Bolt and F. N. Tebbe, in: H. M. O'Bryan, K. Niwa, W. Young, and M. F. Yan, Eds., *Advances in Ceramics*, Vol. 26, American Ceramics Society, Columbus, Ohio, pp. 69-76 (1989).
22. J. D. Bolt and F. N. Tebbe, *Mater. Res. Soc. Symp. Proc.*, **108**, 337 (1988).
23. W. Kleber and H.-D. Witzke, *Z. Kristall.*, **116**, 126 (1961).
24. V. N. Gribkov, V. A. Silaev, and E. L. Umantsev, *Izvestiya Akad. Nauk SSSR, Neorganicheskie Materialy*, **13**, 1775 (1977).
25. G. A. Slack, *J. Phys. Chem. Solids*, **34**, 321 (1973).
26. M. Billy and J. Mexmain, *Fachberichte*, **118**, 245 (1985).



## STRUCTURE-REACTIVITY RELATIONSHIPS OF POLYSILAZANE PRECERAMICS

KAY A. YOUNGDAHL, JEFFREY A. RAHN,  
RICHARD M. LAINE, RICHARD A. KENNISH,  
AND GILBERT A. BALAVOINE

### 59.1. INTRODUCTION

Nonoxide ceramics, such as silicon nitride ( $\text{Si}_3\text{N}_4$ ), boron nitride (BN), and silicon carbide (SiC), have much to offer in the way of high hardness and high structural stability. However, considerable expense is often associated with their preparation and transformation into finished products.

Coatings of  $\text{Si}_3\text{N}_4$ , SiC, and BN are currently produced by physical or chemical vapor deposition. These methods are both equipment and energy intensive; therefore, the development of inexpensive methods for the synthesis and fabrication of nonoxide ceramic coatings is needed. Fibers are also of interest because of their potential utility in ceramic and metal matrix composites.

Polysilazanes have received renewed interest since their discovery [1] in the 1920s as precursors to  $\text{Si}_3\text{N}_4$ . However, little is known about their high temperature reaction chemistry. In order for polysilazanes to become useful precursors, questions need to be addressed and answers provided concerning the

*Ultrastructure Processing of Advanced Materials.*

Edited by Donald R. Uhlmann and Donald R. Ulrich (deceased).

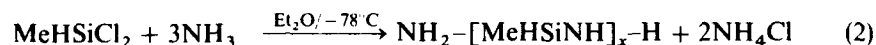
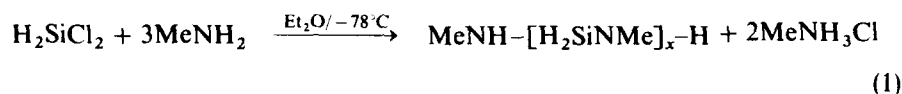
ISBN 0-471-52986-9 © 1992 John Wiley & Sons, Inc.

types of catalysts needed to provide controlled polymer structures. Also, one must determine what chemical and microstructural changes occur in the precursor during pyrolysis in the range of 200 to 900°C and at what temperature intermediate (e.g., 400–600°C) products begin to resemble the target ceramic products.

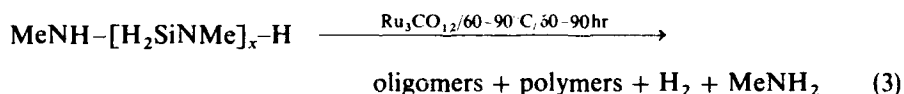
This Chapter will concentrate on the pyrolysis studies of the precursor polysilazanes,  $-\text{[H}_2\text{SiNMe]}_x-$  and  $-\text{[MeHSiNH]}_x-$ , and will show how ceramic product selectivity is controlled by molecular structure. The experimental details of the work reported here will be described in detail elsewhere [2].

## 59.2. DISCUSSION AND RESULTS

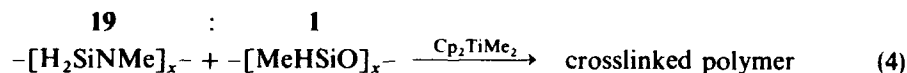
The two polysilazane oligomers,  $-\text{[H}_2\text{SiNMe]}_x-$  and  $-\text{[MeHSiNH]}_x-$ , are prepared by ammonolysis or aminolysis (reactions 1 and 2). The termini are  $\text{MeNH-}$  and  $\text{NH}_2-$ , respectively.



As we have previously shown [3–5], it is possible to treat these oligomers with a ruthenium catalyst derived from  $\text{Ru}_3(\text{CO})_{12}$  to form higher-molecular-weight oligomers and polymers (reaction 3).



However, we would like to reduce or even eliminate the dependence on ruthenium catalysts, as well as find catalysts that will increase the rate of the current catalytic process and improve control of the polysilazane rheology. We have succeeded in eliminating the need for ruthenium as shown in reaction 4:



Thermogravimetric analysis (TGA) and bulk pyrolysis studies on  $-\text{[H}_2\text{SiNMe]}_x-$  and  $-\text{[MeHSiNH]}_x-$  prepared via reaction 3 give the same results under nitrogen or argon. Likewise, ceramic yields and products do not change even when heating schedules are varied between 1 and 10°C/min. The apparent ceramic products obtained from pyrolysis of  $-\text{[H}_2\text{SiNMe]}_x-$  are silicon nitride and carbon, whereas pyrolysis of  $-\text{[MeHSiNH]}_x-$  leads to the formation of SiC in addition to  $\text{Si}_3\text{N}_4$  and carbon.

Figures 59.1 and 59.2 provide information about pyrolytic weight losses

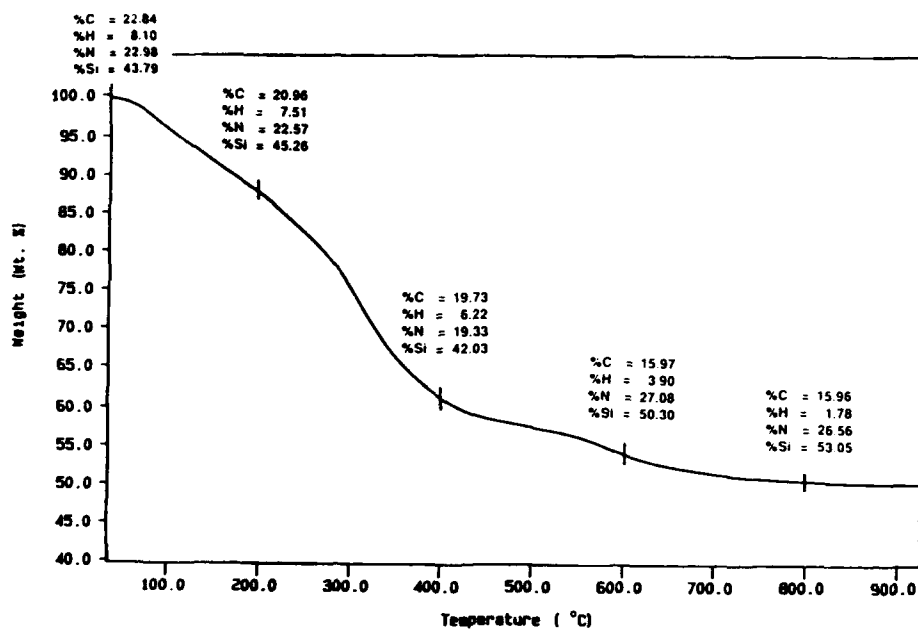


Figure 59.1. TGA and chemical analyses for  $-[\text{MeHSiNH}]_x-$  at 25, 200, 400, 600, and 800°C (pyrolyzed in nitrogen at a heating rate of 5°C/min).

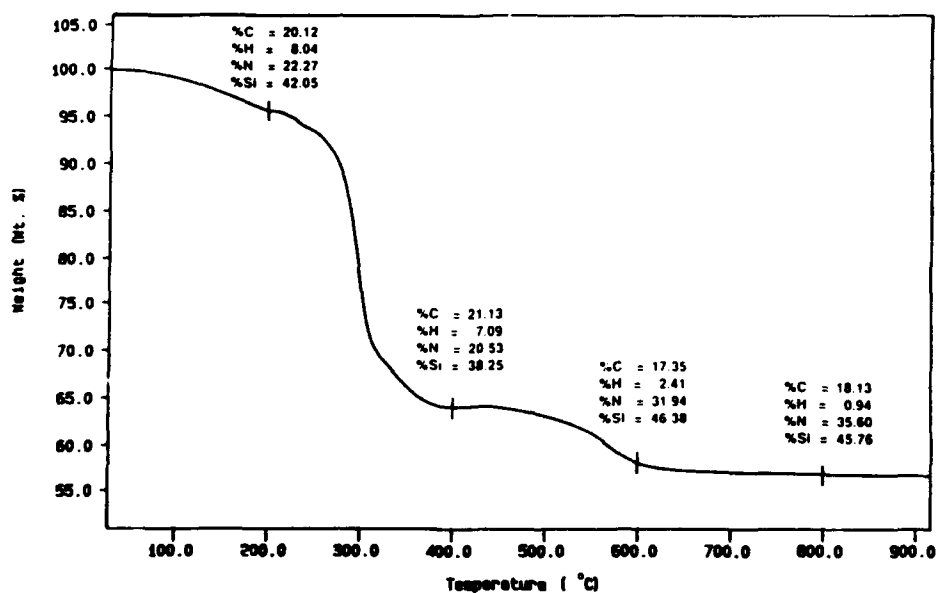


Figure 59.2. TGA and chemical analyses for  $-[\text{H}_2\text{SiNMe}]_x-$  at 25, 200, 400, 600, and 800°C (pyrolyzed in nitrogen at a heating rate of 5°C/min).

(TGA curves) for  $-\text{[H}_2\text{SiNMe]}_x-$  and  $-\text{[MeHSiNH]}_x-$  and the chemical compositions of the intermediate materials at selected temperatures. If considered together with Figures 59.3 and 59.4, one obtains a reasonable picture of the chemical changes that occur as each precursor first undergoes extensive crosslinking followed by decomposition into an amorphous ceramic product.

At temperatures up to 400°C, the chemical compositions of the two polymers evolve slowly; however, the diffuse reflectance infrared Fourier transform (DRIFT) spectra (Figs. 59.3 and 59.4) show that significant changes occur in the chemical structure. The bands due to Si-H bonds ( $\sim 2200\text{ cm}^{-1}$ ) in both polymers decrease relative to the bands of the fingerprint region ( $< 1300\text{ cm}^{-1}$ ) and broadening is observed in both the C-H ( $\sim 3000\text{ cm}^{-1}$ ) and N-H

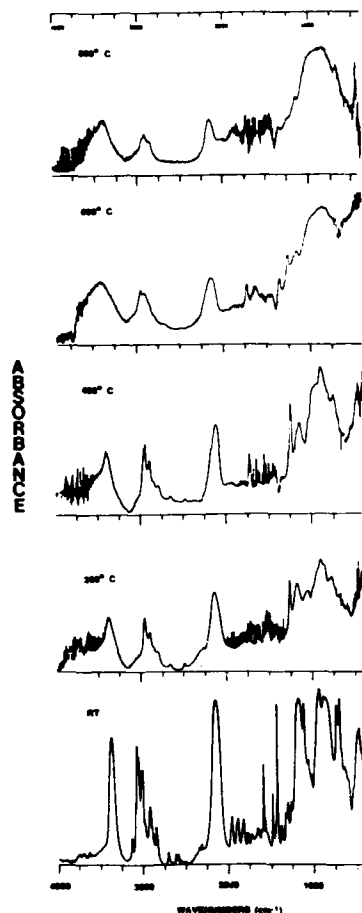


Figure 59.3. DRIFT spectra for  $-\text{[MeHSiNH]}_x-$  at 25, 200, 400, 600 and 800°C (pyrolyzed in nitrogen at a heating rate of 5°C/min).

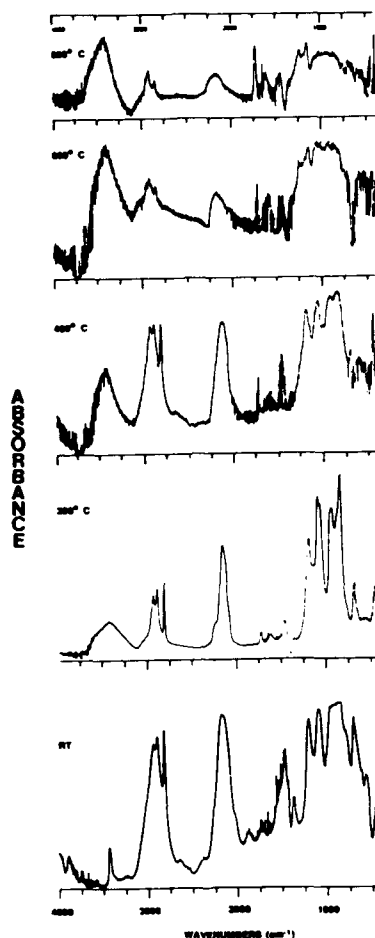


Figure 59.4. DRIFT spectra for  $-\text{[H}_2\text{SiNMe]}_x-$  at 25, 200, 400, 600, and 800°C (pyrolyzed in nitrogen at a heating rate of 5°C/min).

( $3450\text{ cm}^{-1}$ ) regions. These changes are most likely a result of crosslinking, which restricts the movement of the polymer chains, causing the infrared bands to broaden as various polymer segments are frozen in different conformations.

There is significant weight loss in both polymers over the temperature range from 200 to 400°C with little change in composition. Examination of the DRIFT spectra shows that the N-H band increases in intensity relative to C-H and Si-H bands, which suggests that either Si-N or C-N bonds are being broken and subsequent hydrogen abstraction is leading to formation of new N-H bonds. We suggest that this cleavage takes place during polymer fragmentation resulting in the observed weight loss.

At 400°C, both intermediates still retain structural and compositional

features resembling the precursors. However, by 600°C, the composition of both intermediates resembles the end product even though the hydrogen content is high. This temperature region is important in that the product obtained has qualities associated with the initial polymer (e.g., flexibility) as well as properties associated with the ceramic product (e.g., oxidation resistance).

### 59.3. CONCLUSIONS

Transition metal catalysts may be used to polymerize  $-\text{[H}_2\text{SiNMe]}_x-$  and  $-\text{[MeHSiNH]}_x-$  oligomeric silazanes, thereby increasing the molecular weight. The ceramic yield of the product is a function of the precursor molecular weight, whereas the ceramic composition of the product is influenced by the precursor structure.

The transformation into ceramic products can be monitored by FTIR, TGA, and chemical analysis. The 400 to 600°C temperature region may prove to be very important, because the intermediates produced at this stage have properties befitting both a polymer and a ceramic.

### ACKNOWLEDGMENTS

We would like to thank the Strategic Defense Sciences Offices and the Office of Naval Research through Contract N00014-88-k-305 for generous and continuing support for this work.

### REFERENCES

1. A Stock and K. Smieski, *Ber. Dt. Chem. Ges.*, **54**, 740 (1921).
2. R. M. Laine, F. Babonneau, J. A. Rahn, Z-F. Zhang and K. A. Youngdahl, *37th Sagamore Army Mat. Res. Conf. Proc.* D. J. Viechnicki Ed., Publ. Dept. of the Army, pp. 159-169 (1991).
3. R. M. Laine, Y. D. Blum, R. D. Hamlin, and A. Chow, in: D. J. Mackenzie and D. R. Ulrich, Eds., *Ultrastructure Processing of Ceramics, Glasses and Composites*, Vol. II, Wiley, NY, p. 761 (1988).
4. A. W. Chow, R. D. Hamlin, Y. D. Blum, and R. M. Laine, *J. Polym. Sci. C*, **26**, 103 (1988).
5. K. B. Schwartz, D. J. Rowecliffe, Y. D. Blum, and R. M. Laine, in: C. J. Brinker, D. E. Clark, and D. R. Ulrich, Eds., *Better Ceramics Through Chemistry*, Vol. II, *Mater. Res. Soc. Symp. Proc.*, **73**, 407-412 (1986).

## MULTIFUNCTIONAL MACROMOLECULAR MATERIALS

A. BUCKLEY, G. W. CALUNDANN,  
L. F. CHARBONNEAU, AND A. J. EAST

### 60.1. INTRODUCTION

Multifunctional macromolecules are a new concept in polymeric materials. They are polymeric organic structures that combine desirable physical and mechanical properties with one or more functional properties such as electrical conductivity or novel optical properties. Historically, the evolution of synthetic organic molecules was concerned with their function long before polymers and their mechanical properties were recognized. The earliest use of processed organic molecules were probably soaps, alkali metal salts of long chain fatty acids derived by heating animal fats with crude alkali, such as potash. Turpentine was extracted from pine resin for use as a solvent, whereas other essential oils have been used as perfumes and fragrances since Biblical times. Technology existed for the extraction and processing of such materials long before their chemical natures were properly understood. Midway through the 19th century, the infant science of organic chemistry matured quickly along with rapid expansion of technology in areas such as dyestuffs and pigments, textile auxiliaries, pharmaceuticals, and photographic chemicals. In the 20th century this growth has accelerated as new drugs, insecticides, herbicides, and synthetic hormones have been developed.

*Ultrastructure Processing of Advanced Materials.*

Edited by Donald R. Uhlmann and Donald R. Ulrich (deceased).

ISBN 0-471-52986-9 © 1992 John Wiley & Sons, Inc.

The history of structural polymeric organic molecules is briefer, but intensely varied. The discovery of nitrocellulose by Schöbein in 1845 and its subsequent development into two widely differing commercial products, nitrocellulose silk for textiles by Chardonnet in 1889 and Xylonite for molding into billiard balls by the Hyatt brothers in 1872, were the harbingers of a flood of new synthetic materials: Bakelite, rayon, cellulose acetate, nylon, poly(vinylchloride), polyethylene, polyesters, polyacetals, polyimides, epoxies, polyurethanes, polysulfones, and so on right up to today's latest polymers, PEEK and ordered polymers, such as Kevlar and Vectra. All these materials are characterized by specific mechanical and physical properties, and their usefulness depends on the correct balance of such properties. Until Staudinger and Carothers recognized and established on the concept of rigorous macromolecular structure in the 1920 to 1930 period, there was no hope of scientific understanding of the true relationship between mechanical property and molecular structure. However, over the last 50 years, great strides have been made in this direction, so that it is now possible to predict in advance, solely from its molecular structure, the mechanical properties of a new polymer with some degree of confidence. At the same time, as polymer science itself has developed, macromolecules have been synthesized able to withstand increasingly harsh physical environments (Fig. 60.1).

## **60.2. FUNCTIONALITY IN POLYMERS**

For more than a century polymers have been regarded primarily as structural materials, but not there is growing awareness of their utility as functional materials in the same sense that small molecules are useful. Some examples of functionality in polymers are shown in Fig. 60.2.

Drug delivery systems are an area of great interest, and many different polymers have been used, all characterized by an ability to degrade or erode under physiological conditions so as to release a drug into the body at a controlled and predictable rate. Specialized polymers are used in semipermeable membranes of value in desalination, purification of peptides, and food processing. The electronics industry could not have reached its present state of reliability and miniaturization without the specialized photoresist resins employed in microlithography of integrated circuits. Electrically conductive polymers have been widely investigated: Several fairly satisfactory materials now exist, such as polyacetylene, polyaniline, and polypyrrole, although as yet none combine the conductivity, environmental stability, and ease of fabrication of metallic conductors. Certain polymers, notably poly(vinylidene fluoride) and copolymers of vinylidene dicyanide and vinyl acetate, show unique piezo and pyroelectrical properties. Thanks to sophisticated polymer engineering, optical data recording and storage on polymer discs or tapes are possible: One specialized area, compact disc digital sound recordings, have become widely popular consumer items because of their compact size and extraordinary quality



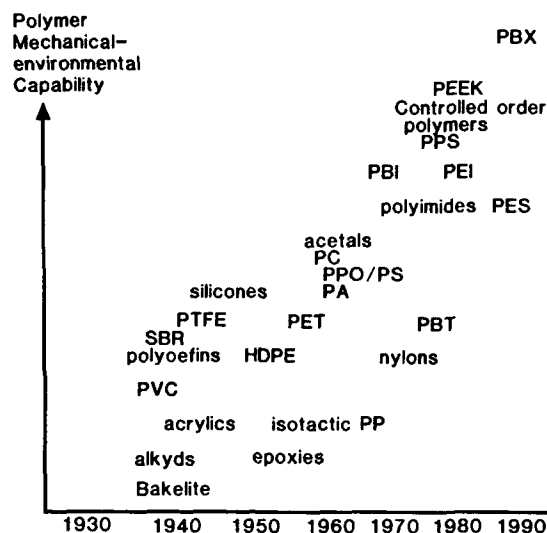


Figure 60.1. Historical development of structural polymers.

of sound reproduction. The development of optical transmission of information with laser light has led recently to intense activity in the field of polymeric nonlinear optical (NLO) materials, which hold promise of ease of fabrication and rapid response speeds unobtainable with previously known inorganic crystal NLO materials.

### 60.2.1. Specific Functional Polymers

Three types of functional polymers are worth discussing in more detail. These are electrically conductive polymers, piezo/pyroelectric polymers, and NLO-active polymers. These properties are amenable to combination with desirable

#### Examples...

- Drug delivery
- Selective separation
- Microlithography
- Electrical conductivity
- Piezo/pyroelectricity
- Optical data storage
- Nonlinear optical activity

Figure 60.2. Examples of functionality in polymers.

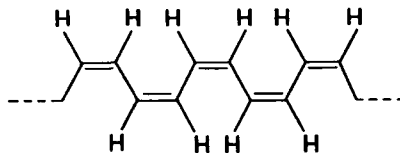


Figure 60.3. The structure of *cis*-polyacetylene.

structure/mechanical properties in ways that may lead to unique and valuable multifunctional macromolecules.

### 60.2.2. Conductive Polymers

Polymers in general are electrical insulators with resistivities in the range of  $10^{14}$  to  $10^{18} \Omega\text{-cm}$ , but polymers with systems of conjugated double bonds behave more as semiconductors (resistivities around  $10^1$  to  $10^8 \Omega\text{-cm}$ ) and by suitable doping can be made to approach metals in conductivity. However, the dopants are frequently extremely strong acids, such as arsenic pentafluoride, or free alkali metals, and there are very few conductive polymer systems that are thermally and oxidatively stable and thus easily handled.

#### 60.2.2.1. Polyacetylene

The most intensively investigated polymer is polyacetylene made by a Ziegler/Natta polymerization of acetylene gas according to Ito et al.'s [1] method. Both *cis* (Fig. 60.3) and *trans* (Fig. 60.4) forms are known and the all-*trans* form is the more thermodynamically stable and has a higher conductivity,  $10^{-5} \text{ S/cm}$  compared with  $10^{-9} \text{ S/cm}$  for the all-*cis* form [2]. Flexible films can be produced that are capable of being stretched two or three times by direct gas/solid polymerization, but because the polymer is insoluble and infusible, it is difficult to fabricate into shaped articles. By doping with *p*- or *n*-type dopants, high conductivity is obtained. *p*-type dopants are bromine, iodine, or  $\text{AsF}_5$ , whereas *n*-type dopants are metallic cations from lithium, sodium, or potassium usually applied as the naphthalide radical ion. *p*-type dopants give conductivities up to  $3000 \text{ S/cm}$  ( $0.003 \Omega\text{-cm}$ ), but all doped polyacetylene materials must be kept under anaerobic conditions [3].

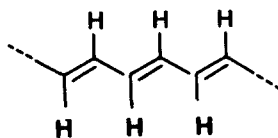


Figure 60.4. The structure of *trans*-polyacetylene.

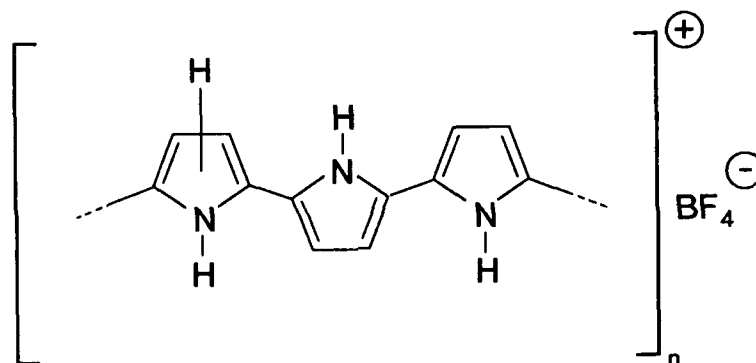


Figure 60.5. The structure of polypyrrole (cation form).

#### 60.2.2.2. Polypyrrole

This is the only polymeric conductor that is air stable. It is made by an electrochemical oxidative coupling of pyrrole in a special cell using noble metal electrodes and acetonitrile as an electrolyte [4]. Thin, bronze-colored films may be thus deposited on the platinum anode, which can be peeled off and are tough and flexible. The structure is shown in Fig. 60.5. As made, the film (which is amorphous) has a conductivity of 30 to 100 S/cm and is stable to air at ambient conditions. Thermogravimetric analysis shows it to be stable up to 300°C. The conductivity appears to be due to a cationic oxidized form: Reducing this electrochemically gives the neutral polypyrrole, which has a resistivity of  $10^{10} \Omega\text{-cm}$ . Reoxidation with silver or ferric ions or HF vapor generates a conductive film again, whereas treatment of the as-made film with  $\text{AsF}_5$  has no effect on conductivity.

#### 60.2.2.3. Polyaniline

The latest conductive polymer is polyaniline, first described by MacDiarmid [5] in 1984. Aniline has been known to give dark polymeric substances on oxidation for over a century. Recently the controlled oxidative coupling, either with persulfate in dilute hydrochloric acid or electrochemically using platinum electrodes in aqueous acid, such as  $\text{HBF}_4$ , has given a well-defined polymer whose structure (Fig. 60.6) is believed to be a polyquinone-imine salt.

The conductive cationic form is green, and electrochemical reduction gives the yellow nonconducting form, which is believed to be a poly(*p*-phenylene diamine). The conductive film can be cast from dimethyl sulfoxide solution as a film, but this is very brittle. Polyaniline has been used in lightweight rechargeable cells.

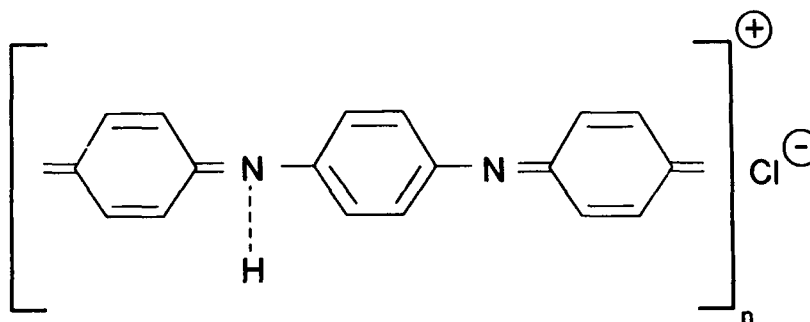


Figure 60.6. The structure of polyaniline (cation form).

### 60.2.3. Piezoelectric and Pyroelectric Polymers

Piezoelectricity was discovered about 100 years ago by the Curies. Quartz crystals produce an electrical charge when deformed mechanically; shortly afterward they found the same crystals also generate a charge when heated, and this was called *pyroelectricity*. Some crystals possess ferroelectric properties, so-called by analogy with ferromagnetic materials, and have spontaneous permanent electric dipoles that may be aligned by an external field with hysteresis effects and a Curie temperature exactly like a magnet. All these materials are dielectrics, but although all ferroelectrics are also pyro and piezoelectrics, the converse is not true (see Fig. 60.7).

Only those crystals that have a noncentrosymmetric structure can show piezoelectricity. Those crystals that develop spontaneous polarization are

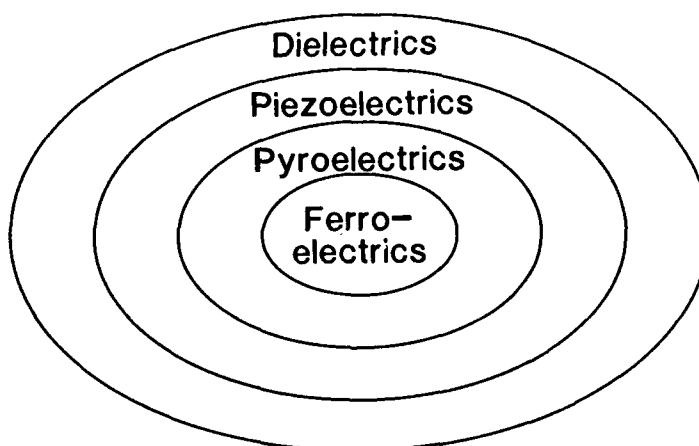


Figure 60.7. Hierarchy of dielectric properties of materials.

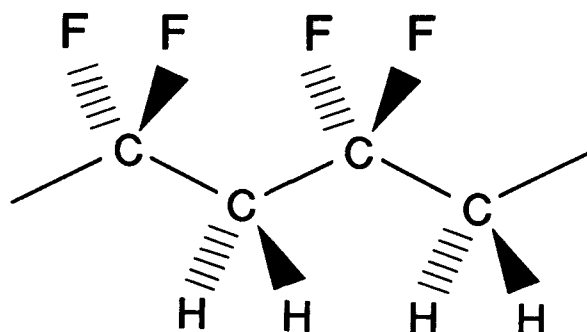


Figure 60.8. The structure of PVDF.

ferroelectric. Piezoelectric crystal transducers are widely used in ultrasonic applications, but in the 1960s it was found that certain polymers that had polarizable bonds could be induced to show piezoelectric behavior if "poled" in a strong field. The best by far was poly(vinylidene fluoride) (PVDF) (see Fig. 60.8). Later, the regularly alternating copolymer of vinylidene cyanide and vinyl acetate (PVDCN-PVA) (Fig. 60.9) was shown by Miyata et al. [6] to show the same effect, while Newton and co-workers [7] have worked on films from odd-numbered nylon polymers, such as nylon-7 and nylon-11, which also have piezoelectric properties.

All these polymers can be induced to show piezoelectric effects, because they possess polarizable or dipolar units and exist in a noncentrosymmetric structure. That is why only odd-numbered nylons show the effect; the interchain hydrogen bonds in nylons place strong constraints on molecular conformation and while the even-numbered nylons effectively cancel out their dipoles, in the case of the odd-numbered series the dipoles tend to line up all in the same direction (Fig. 60.10).

PVDF is semicrystalline (50/50 crystalline/amorphous) and has strongly

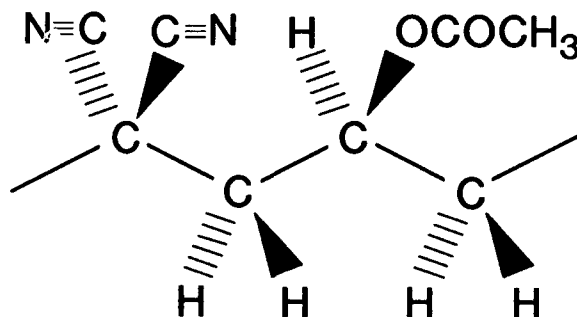


Figure 60.9. The structure of PVDCN-PVA alternating copolymer.

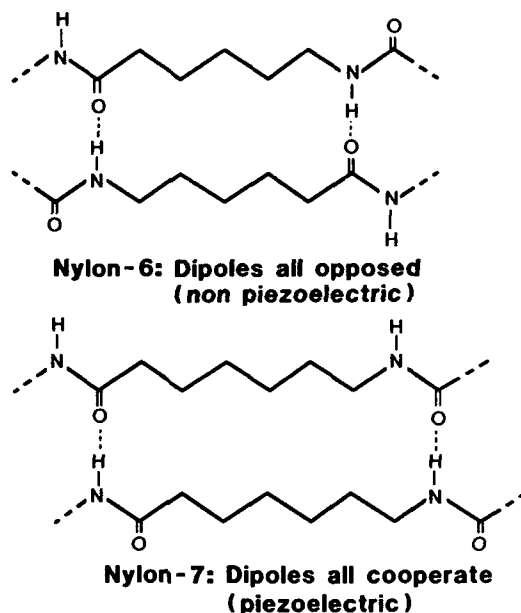


Figure 60.10. The structures of odd and even nylons.

dipolar carbon fluorine bonds. It exists in four crystalline forms, called *I*, *II*, *III*, and *IIP* forms. They are produced by different processing conditions and are intraconvertible. Form *I* is the most useful for piezoelectric films. The film is poled by subjecting the stretched film to a strong electrical field at 80 to 120°C and cooling the film in the applied field. Intense fields will pole the material at room temperature if applied in very short bursts; otherwise dielectric breakdown will occur.

#### 60.2.4. Nonlinear Optical Polymers

The third type of novel functional polymers are those that show NLO properties. This is another function of a dielectric material possessing polarizable bonds and is concerned with their response to an intense electromagnetic field such as that produced by the intense light of a laser. The molecular polarization in an applied field is the sum of the permanent dipole moment, plus the polarizability factor  $\alpha$  and higher terms involving  $\beta$  and  $\gamma$ , which are called the *second-* and *third-order hyperpolarizabilities*.

$$M\mu = M\mu(\rho) + \alpha E + \beta E^2 + \gamma E^3 + \dots$$

At normal light intensities, the higher terms are negligible in importance, but this is not so at the intensities produced with laser light. Hence nonlinear

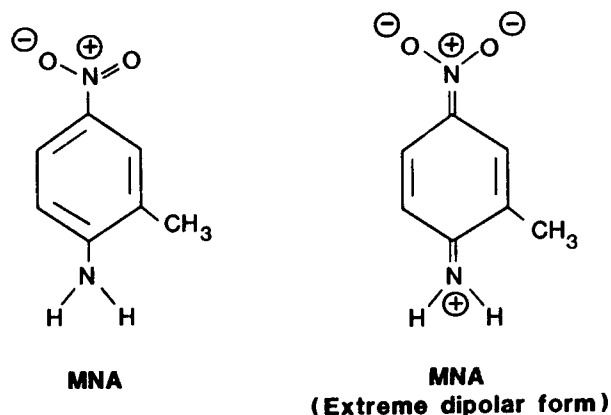


Figure 60.11. The structure of MNA.

response, such as frequency doubling, are observable. The rapid growth in information transmission via optoelectronic devices and modulated laser light has given rise to great activity in the NLO field. As in the case of the piezoelectrics, the first NLO materials known were organic and inorganic crystals. For a specific second-order effect ( $\beta$ ) the material must have a *noncentrosymmetric* structure. Because crystals are difficult to fabricate, Hoechst Celanese has been engaged in a program to develop NLO-active polymers that can be readily fabricated into useful NLO devices.

To obtain a high  $\beta$  the first requisite is a long straight planar molecule with a conjugated system of double bonds and a large dipole moment, usually achieved by having electron-rich and electron-deficient molecular groupings at opposite ends of the conjugated system. A classical example is the molecule 2-methyl-4-nitroaniline (MNA) shown in Fig. 60.11.

However, the correct chromophore alone is not sufficient; there must be an absence of any centrosymmetric structure. Certain NLO-active organic molecules do in fact crystallize in a noncentrosymmetric structure; others that ought to be NLO active crystallize with a symmetrical structure. Organic crystals are seriously lacking in mechanical properties and do not lend themselves to fabrication techniques. One way of making a polymeric NLO material is to dissolve a suitable chromophoric molecule in a glassy polymer matrix. However, the usefulness of this approach is limited by the concentration of the chromophore obtainable without phase separation and subsequent loss of optical clarity. At Hoechst Celanese Science and Technology Company we have used side-chain liquid crystal polymers (LCP) to obtain the desired balance of properties. The molecular requirements for NLO-active chromophores are similar in many respects (for example, molecular shape) with those for mesogenic units. Hence, it was argued that a side-chain LCP (SCLCP) with NLO-active mesogens ought to give a high concentration of active chromophores, which would tend to spontaneously adopt preferred alignment due to their mesogenic nature.

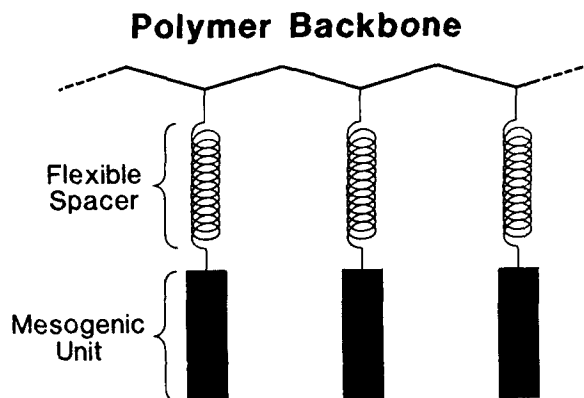


Figure 60.12. The structure of a typical SCLCP.

whereas external poling would further enhance the perfection of this alignment. The generalized schematic structure is due to Finkelmann and Rehage [8] and Ringsdorf et al. [9]. It has a flexible polymer backbone with pendant mesogens hanging from it, which, in turn, are molecularly decoupled from the polymer backbone by a flexible spacer group (Fig. 60.12).

SC LCPs can exist in most of the mesophase states that molecule mesogens exhibit and nematic, smectic-A, smectic-C, and cholesteric phases have all been observed. Typical examples of NLO-active polymers emerging from these

$n$	Phase	$T_G(^{\circ}\text{C})$	$T_{cl}(^{\circ}\text{C})$
2	I	-	-
3	N	85	100
5	N	45	72
6	N	40	64
8	N	35	75
11	S <sub>A</sub>	20	95
12	S <sub>A</sub>	10	30

$$\left[ \text{CH}_2 - \underset{\begin{array}{c} | \\ \text{C=O} \\ | \\ \text{O} \\ | \\ (\text{CH}_2)_n \\ | \\ \text{O} \\ | \\ \text{C}_6\text{H}_4 \\ | \\ \text{C}_6\text{H}_4 \\ | \\ \text{NO}_2 \end{array}}{\text{C}} \begin{array}{c} | \\ \text{CH}_3 \end{array} \right]_x$$

I = Isotropic  
N = Nematic  
S = Smectic  
 $T_G$  = Glass Temperature  
 $T_{cl}$  = Clearing Temperature (LC  $\rightarrow$  Isotropic)

Figure 60.13. The structure of an NLO polymer.



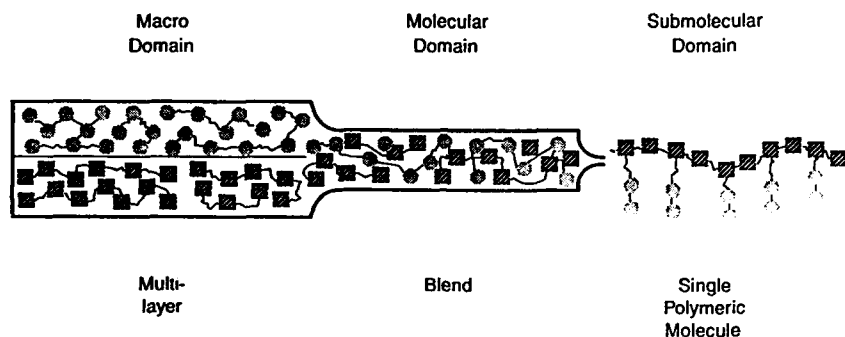


Figure 60.14. A multifunctionality diagram.

studies [10] are the polymethacrylates from 4-(hydroxy-alkoxy)-4'-nitro-biphenyls (Fig. 60.13) with varying lengths of side chains from C2–C12.

By systematic variation of the structure shown in Fig. 60.13, the type of mesophase structure produced can be manipulated. Thus short side chains (C2 to C3) give isotropic polymers: There is not enough molecular decoupling from the backbone to allow mesophase order to develop, and the polymer is glassy. Medium-length side chains (e.g., C6) give nematic polymers, whereas longer chains still, C8 to C12, exhibit smectic structures. Each of these phase structures has specific optical properties and molecular order that are capable of exploitation in devices.

By comparing the NLO activity of the polymer with model compounds having the same electronic structure (i.e., the same chromophore), it has been shown that attaching the chromophore to a polymer backbone makes little difference to its NLO activity. For NLO-active polymers it is the electronic structure of the individual units that gives rise to the NLO effect; the polymer backbone simply adds the important attributes of ease of fabrication and dimensional stability, factors notably lacking in organic crystals. This is in sharp contrast to the situation extant in piezoelectric and pyroelectric polymers, where the desired effect is only observed in a macromolecular structure.

#### 60.2.5. Multifunctional Combinations

There are a number of scale levels at which functionalities can be combined, ranging from discrete layers through compatible polymer blends to specific copolymers that combine the functionalities in one molecule. This is shown schematically in Fig. 60.14. All of these structures have potential depending on the degree of interaction desirable. Multilayer Langmuir-Blodgett films, where alternate layers exhibit different functional response, should also be considered in this context.

### 60.3. CONCLUSIONS

It has been shown that many functionalities can be incorporated individually into macromolecular structures and that the thermomechanical properties and ease of fabrication of these materials can be used to advantage. It should now be possible to incorporate a multiplicity of functionalities into a macromolecular structure either by attaching different functional units onto one polymer backbone or by using techniques of polymer blending and alloying to combine separate functional polymers into one macromolecular assembly. Because the three types of functionality discussed here all involve polar groupings and movement of polar groupings generates electronic interactions, novel "cross-talk" effects should be detectable in such mixed-functionality polymers. The blending of multifunctional units whichever way it is accomplished will lead to significant weight savings in active systems, and it is reasonable to extrapolate the concept to structural materials with added functionalities for a variety of novel end uses.

### ACKNOWLEDGMENTS

This work is being sponsored by the Air Force Office of Scientific Research (AFSOR) under Contract F49620-87-C-0109. The U.S. Government is authorized to reproduce and distribute reprints for governmental purposes notwithstanding any copyright notation hereon.

### REFERENCES

1. I. Ito, H. Shirakawa, and S. Ikeda, *J. Polym. sci., Polym. Chem. Ed.*, **12**, 11 (1974).
2. [ Ito, H. Shirakawa, and S. Ikeda, *J. Polym. Sci., Polym. Chem. Ed.*, **13**, 1943 (1975).
3. C. K. Chiang, C. R. Fincher, Y. W. Parks, A. J. Heeger, H. Shirakawa, E. J. Louis, S. C. Gau, and A. G. MacDiarmid, *Phys. Rev. Lett.*, **39**, 1098 (1977).
4. A. F. Diaz, K. K. Kanazawa, and G. P. Gardini, *J. Chem. Commun.*, **635** (1979).
5. A. G. MacDiarmid, *Chem. Eng. News*, **38** (September 1984).
6. S. Miyata, M. Yoshikawa, S. Takawa, and M. Ko, *Polym. J. (Tokyo)*, **12**(12), 857 (1980).
7. B. A. Newman, P. Chen, K. D. Pae, and J. I. Scheinbein, *J. Appl. Phys.*, **51**(10), 5161 (1980).
8. H. Finkelman and G. Rehage, *Makromol. Chem. Rapid Commun.*, **1**, 31 (1980).
9. H. Ringsdorf and A. Schneller, *Br. Polym. J.*, **13**, 43 (1981).
10. R. N. DeMartino, E-W. Choe, G. Khanarian, D. Haas, and T. Leslie, G. V. Nelson, J. Stamatoff, D. Stuetz, C. C. Teng, and H-N. Yoon, presented at the 193rd National Meeting of the American Chemical Society, Denver, Colo., April 1987.

# 61

## THE MICROSTRUCTURE OF AEROGELS AND ITS EFFECT ON PROPERTIES

J. FRICKE

### 61.1. INTRODUCTION

Aerogels [1] are sol-gel-derived, supercritically dried materials with densities between about 50 and 500 kg/m<sup>3</sup>, corresponding to porosities of 98 to 80%. The pore structure extends from the range of 1 to 100 nm [2] and thus displays micro-, meso-, and macroporosity. As many solid-state properties drastically change with porosity, aerogels can be expected to be quite unusual materials: Most striking are,

The clear transparency of properly made SiO<sub>2</sub> aerogels, even if their porosity is as high as 98%.

The extremely low sound velocity, which can be as small as 100 m/sec [3].

The low thermal conductivity, which is reduced by a factor of several hundred, compared to nonporous silica glass [4].

The exceptionally large specific heat at low temperatures [5], which is caused by the high vibrational density of states in the frequency range of 1 to 1000 GHz [6].

The large specific surface area in the order of about 500 to 1000 m<sup>2</sup>/g [7].

---

*Ultrastructure Processing of Advanced Materials.*

Edited by Donald R. Uhlmann and Donald R. Ulrich (deceased).

ISBN 0-471-52986-9 © 1992 John Wiley & Sons, Inc.

Aerogels were first made by S. S. Kistler [8] in 1931. Progress in the gelation and drying procedures was stimulated by efforts to use aerogels as catalytic substrates [9] and in Čerenkov counters [10–12]. More recently aerogels were recognized as valuable materials for transparent thermal insulations in windows and modified Trombe wall systems [4, 13].

In the following overview I want to discuss some of the exceptional properties of  $\text{SiO}_2$  aerogels and analyze correlations between properties and mass density as well as structural characteristics.

## 61.2. OPTICAL PROPERTIES

High-quality aerogel tiles made from tetramethylorthosilicate (TMOS) are mainly Rayleigh scatterers and therefore show a more or less isotropic scattering pattern if probed with visible light. Systematic scattering investigations using light [14] and X-rays [15] show that the correlation length, which is a measure of the largest building units in the  $\text{SiO}_2$  network,

Increases with decreasing density for aerogels made under the same conditions, for example, pH value (Fig. 61.1).

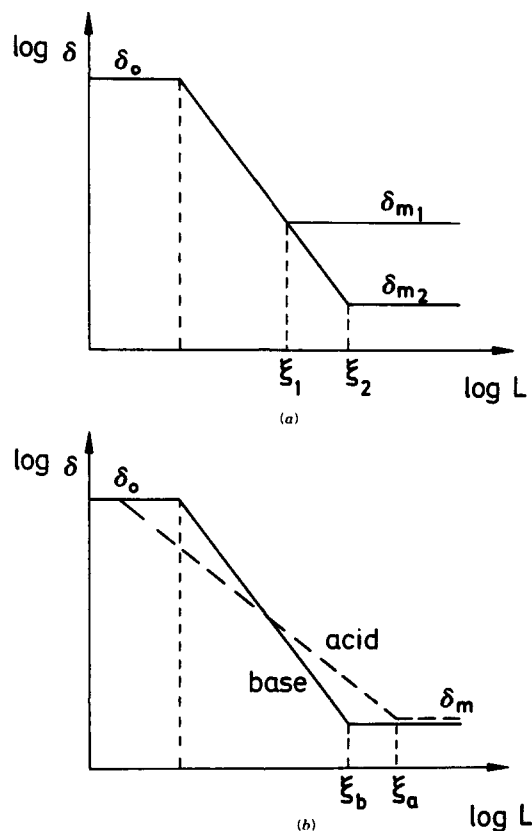
Is larger for acid- than for base-catalyzed aerogels for a given density (Fig. 61.1). Base-catalyzed aerogels thus are preferable for optical applications, where high transparency is required.

The index of refraction  $n$  of aerogels is basically a function of density  $\delta$ :  $n - 1 = b \cdot \delta$ , where the constant  $b$  somehow depends on the size of the network-forming particles  $d$ , the number  $z$  of OH groups per Si atom of the inner surface of the network, and the wavelength  $\lambda$  [16]. For  $\lambda = 663 \text{ nm}$ ,  $d = 4 \text{ nm}$  and  $z = 2$  (0) one expects  $b = 2.05 \times 10^{-4}$  ( $1.9 \times 10^{-4}$ )  $\text{m}^3/\text{kg}$ ; experimentally one derives  $b = 2.1 \times 10^{-4} \text{ m}^3/\text{kg}$  for base-catalyzed aerogels [16].

The small value of  $n$  and its variation with density promoted the fabrication and use of monolithic aerogels in Čerenkov counters [10–12]. If sintered, aerogels can cover the range  $n - 1 = 8 \times 10^{-3} \dots 0.4$  and thus allow the determination of particle energies  $E$  in the relativistic range  $E/m_0 = 1 \dots 8$ , where  $m_0$  is the rest mass (Fig. 61.2). A modern application is the use of aerogel counters in balloon flights, which are performed for the detection of stratospheric particle showers [17].

## 61.3. MECHANICAL PROPERTIES

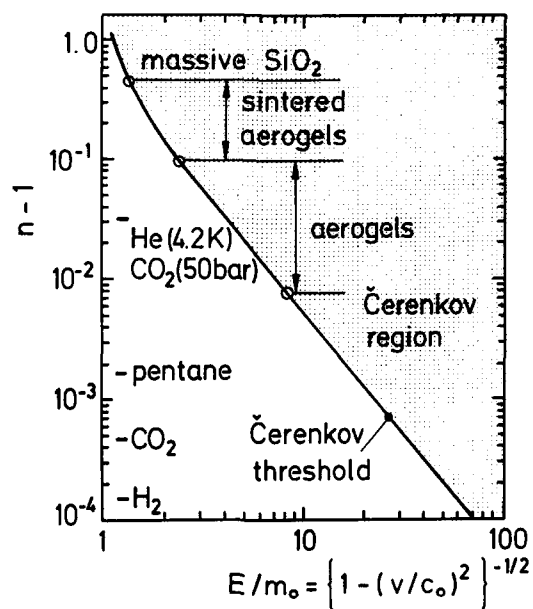
Longitudinal sound velocities  $v_l$  in the order of 100 m/sec (Fig. 61.3) and a Young's modulus  $Y$  (Fig. 61.4) as low as  $5 \times 10^5 \text{ N/m}^2$  are the consequences of the extremely tenuous structure of low-density aerogels. Sound propagation occurs along the skeleton, as can be demonstrated by evacuation. The influence



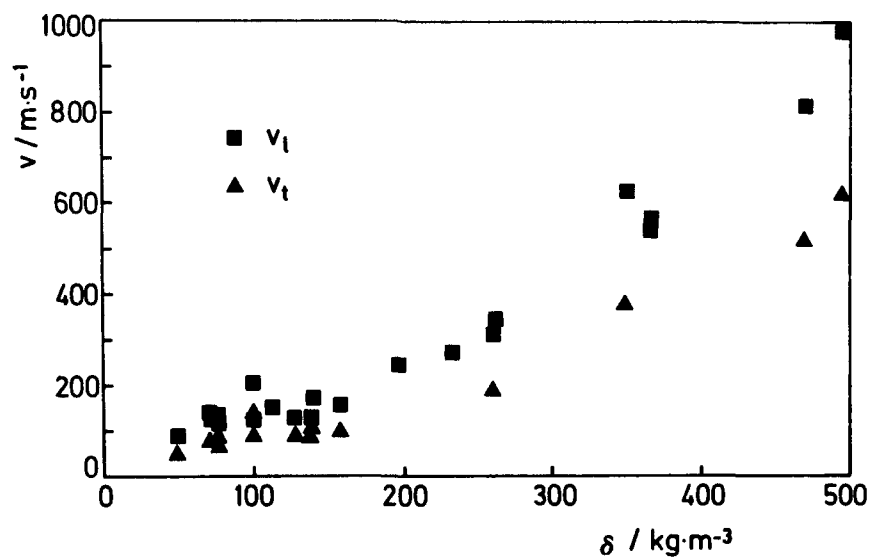
**Figure 61.1.** Variation of density  $\delta$  with scale length  $L$  schematically; this double-log plot shows that upon an increase of  $L$  the density drops from the skeletal density  $\delta_0$  toward the macroscopic density  $\delta_m$ . The straight slopes, used for reasons of simplicity, do not imply that aerogels are necessarily fractals. (a) Aerogels with smaller densities display larger correlation length  $\xi$  than those with higher densities. (b) Acid-catalyzed aerogels tend to have a larger correlation length  $\xi_a$  than base-catalyzed aerogels of equal density ( $\xi_b$ ).

of the enclosed air on the elastic constants is in the percentage range [8]. If the density is varied, approximate scaling of elastic properties is observed; the derived scaling exponent  $\alpha$  ranges from 2.9 to 3.6, depending on the density range analyzed. Surprising is the decrease of elastic constants by nearly 20% upon external uniaxial stress with loads of  $6 \times 10^4 \text{ N/m}^2$ . This effect was explained by a "knee-bending" deformation of the microstructure [19].

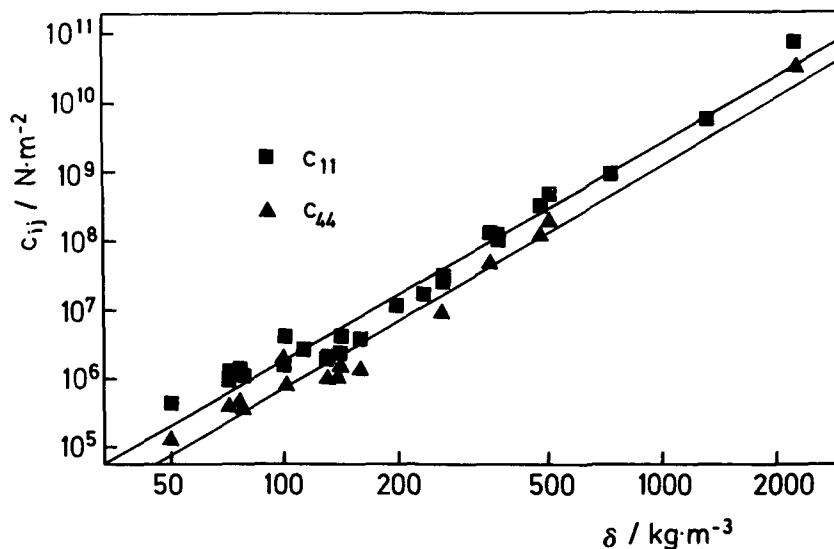
Another unusual consequence of external stress is creeping. A constant stress of  $3 \times 10^3 \text{ N/m}^2$  leads to creeping with exponential decrease in velocity; larger stress ( $6 \times 10^4 \text{ N/m}^2$ ) causes runaway creeping with relative shrinkages in length of about  $10^{-4} \text{ h}^{-1}$  [19]. This phenomenon possibly can be explained in terms of water-induced glass cracking. Sintering allows densification of the aerogel



**Figure 61.2.** Excess of index of refraction over 1 versus reduced energy  $E/m_0$  of relativistic elementary particles, where  $m_0$  is the rest mass. The full line is the Čerenkov threshold. Aerogels and sintered aerogels cover a  $E/m_0$  range not covered by other solid materials [16].

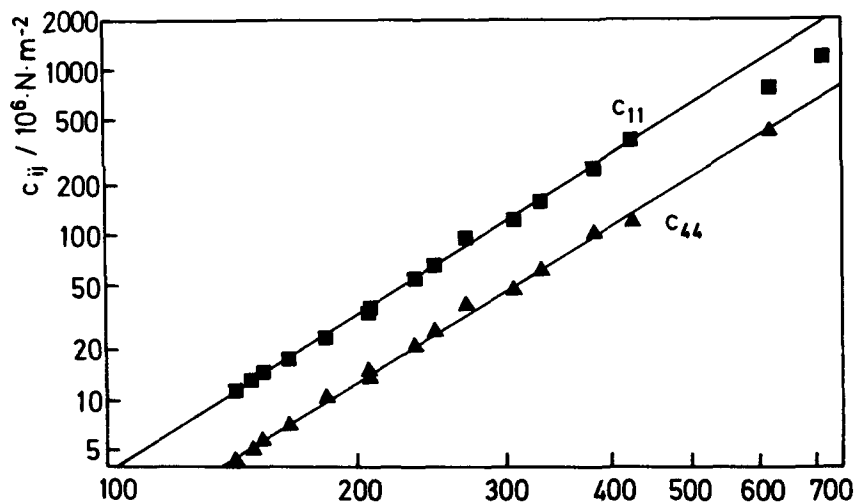


**Figure 61.3.** Longitudinal and transverse sound velocity  $v_l$  and  $v_t$ , respectively, versus density  $\delta$  of aerogels [18].



**Figure 61.4.** Elastic constants  $c_{11}$  and  $c_{44}$  versus density of aerogels, silica gels (xerogels), and vitreous silica. The plotted straight lines belong to a scaling exponent  $\alpha \approx (3.2 \pm 0.15)$  [18].

network. As was shown recently, viscous flow occurs already at temperatures as low as  $750^\circ\text{C}$  [18]. Sintering activation energies are in the range of 2.0 to 2.5 eV. Overall, sintered aerogels show the same scaling of elastic constants with density as unsintered aerogels. The only difference is that for a given density sintered aerogels have elastic constants that are about twice as large as for unsintered aerogels [18] (Fig. 61.5). As elastic properties of aerogels can be varied over



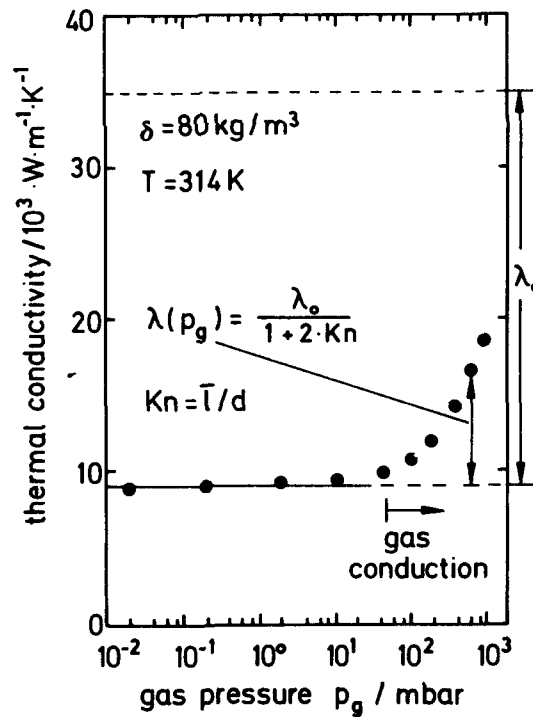
**Figure 61.5.** Elastic constants versus density for sintered aerogels [18].

several orders of magnitude, their application as impedance matching layers in ultrasonic transducers has been proposed [3].

#### 61.4. THERMAL TRANSPORT

As Kistler already knew [20], monolithic aerogels have thermal conductivities in the order of  $\lambda \approx 0.02 \text{ W/m.K}$ . If evacuated, values of  $\lambda \approx 0.01 \text{ W/m.K}$  are obtained. As we have shown earlier [21], the air pressure-induced change in the thermal conductivity occurs above  $p_{\text{gas}} \approx 50 \text{ mbar}$  (Fig. 61.6). This allows the derivation of a medium pore size in the order of 100 nm.

The heat transfer in evacuated aerogels is caused by solid conduction via the tenuous skeleton and by radiative transport. Infrared extinction is provided by absorption, which is strong above wavelengths of  $\Lambda \approx 7 \mu\text{m}$ . Thus aerogels block thermal radiation effectively for temperatures around 300 K [22].



**Figure 61.6.** Thermal conductivity of a 80 kg/m<sup>3</sup> aerogel tile at about 300 K as a function of gas pressure [21].  $\lambda_0$  is the thermal conductivity of nonconvecting air; the gaseous conductivity  $\lambda(p_{\text{gas}})$  within the porous aerogel body can be described by the Knudsen formula, given in the figure. The Knudsen number  $Kn = \bar{l}/d$  is determined by the ratio of the mean free path  $\bar{l}$  of the gas particles and the pore diameter  $d$ .



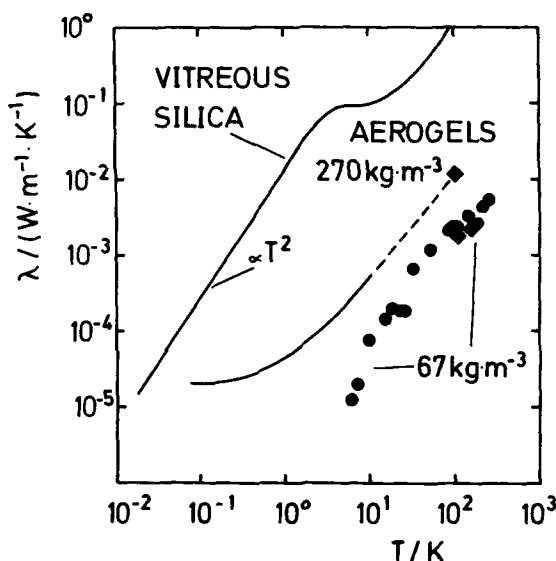


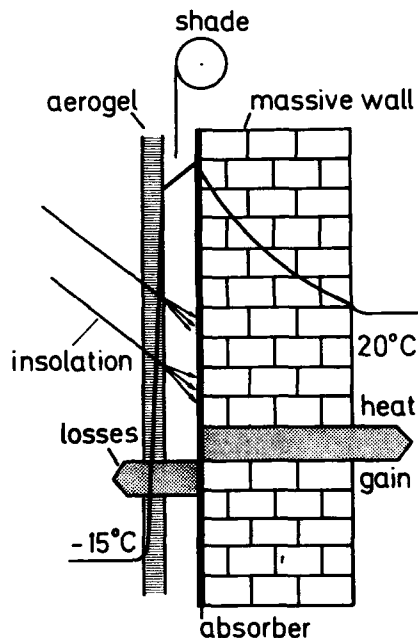
Figure 61.7. Thermal conductivity of silica glass [25] and two aerogels with density of 270 [24] and 70 kg/m<sup>3</sup> [26] versus temperature. For the latter for 100 K a conductivity of about 10<sup>-3</sup> W/m.K can be estimated if Eq. 1 is used.

The solid conduction of aerogels is reduced by a factor of about 10<sup>3</sup> compared to vitreous silica. Recent measurements (Fig. 61.7) show that this holds for temperatures as low as 1 K [23,24]. One reason for the reduced thermal transport is the low density of the network; another is the many "detours" the phonons have taken in order to travel from one side of the specimen to the other. Phenomenologically the thermal conductivity can be described by the phonon diffusion model [23]. The conductivity of silica glass  $\lambda_0$  and of aerogel  $\lambda_{ae}$ , according to this model, are coupled via the densities  $\delta_0$  and  $\delta_{ae}$  as well as the macroscopic sound velocities  $v_0$  and  $v_{ae}$ :

$$\lambda_{ae} = \lambda_0 \frac{\delta_{ae}}{\delta_0} \cdot \frac{v_{ae}}{v_0} \quad (1)$$

That this equation gives rough estimate on  $\lambda_{ae}$  for  $T > 1$  K can be seen from Fig. 61.7. On the other hand, it was surprising to learn that Eq. 1 allows the prediction of the room temperature conductivity of powdery insulation materials quite accurately from sound velocity measurements [27].

I do not want to close this Chapter without mentioning that the small thermal conductivity of aerogels in combination with their high transparency makes these materials excellent transparent thermal insulators. The principle employed in several experimental setups for passive usage of solar energy as well as in a real two-family house in Ardon, Switzerland, can be seen in Fig. 61.8. The



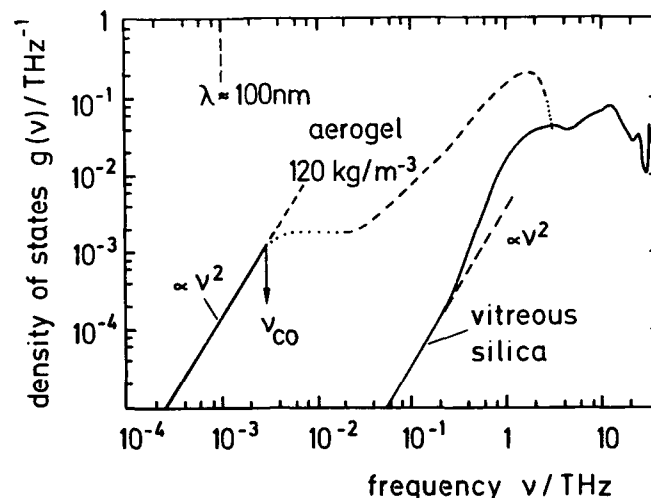
**Figure 61.8.** Transparent house wall insulation using a superinsulating aerogel-filled glass pane system in front of a massive wall with dark surface.

energy consumption for heating purposes in the prototype house is exceptionally low, that is, about 300 liters of oil per year [28].

Other possible applications for aerogels are in windows, solar storage collectors (which can be operated without use of antifreezing agents), and covers for solar ponds.

### 61.5. DYNAMICS OF AEROGELS

Heat capacity as well as thermal conductivity are strongly influenced by the dependence of the vibrational density of states (DOS)  $g(\nu)$  on frequency  $\nu$ . The DOS is a measure of how many modes can be excited within a certain frequency interval. For a Debye solid,  $g(\nu) \propto \nu^2$  holds. In the Debye DOS range, the excitations represent propagating modes. Due to the small sound velocity  $v$ , the DOS, which is proportional to  $\nu^{-3}$  in the Debye range, is expected to be a factor of about  $10^5$  larger for aerogels than for vitreous silica. The DOS dependence on frequency, determined from inelastic neutron scattering [29], can be seen in Fig. 61.9. Although for vitreous silica the total DOS is larger than the Debye DOS above 0.3 THz, which has been attributed to two-level excitations, the opposite is true for aerogels: Above a crossover frequency  $\nu_{co} \approx 2$  GHz, the total DOS is



**Figure 61.9.** Vibrational density of states of vitreous silica and an aerogel versus frequency determined from inelastic neutron scattering [29].

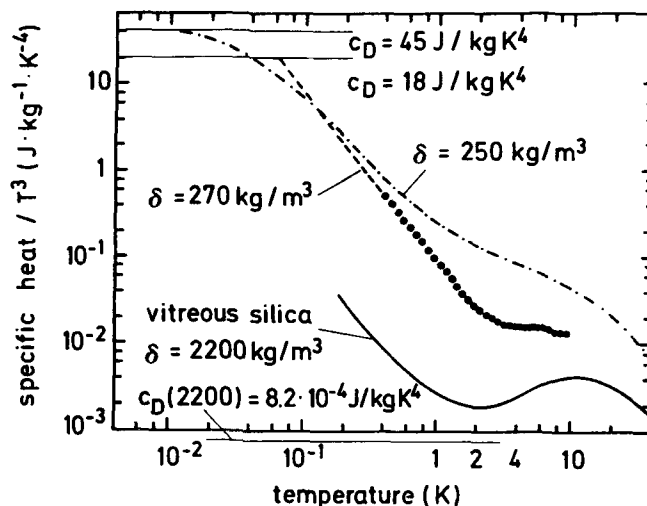
below the Debye DOS. This is plausible, as above  $\nu_{co}$ , the porous structure between 100 and 1 nm is probed—a size range where material is “missing”—and thus are also modes. A strong increase in the DOS spectrum is again observed above 30 GHz, when modes within the spherelike aerogel building blocks are excited.

The large excess in the DOS of aerogels has important consequences for the specific heat  $c$  (Fig. 61.10) at low temperatures [5, 29]: Below 10 K for vitreous silica,  $c$  is dominated by the two-level modes, which completely “bury” the Debye contributions; for aerogels,  $c/T^3$  strongly rises with decreasing temperature, but still is far below the Debye value at the lowest temperatures investigated.

Likewise, the thermal conductivity of aerogels is influenced by the dependence of DOS on frequency. The interpretation here, however, is more complicated than for the specific heat. A consistent picture is not yet at hand. We are convinced, though, that only the high energy modes around and above 1 THz can contribute significantly to the solid thermal transport [30].

## 61.6. SURFACE AREA

Aerogels are microstructured materials and thus have huge specific surface areas in the range  $A_s \approx 500$  to  $1000 \text{ m}^2/\text{g}$  [7]. Upon density variation,  $A_s$  does not change characteristically; even air-dried xerogels with densities around  $800 \text{ kg/m}^3$  have surface areas that are comparable with those of aerogels. We



**Figure 61.10.** Specific heat  $c/T^3$  of vitreous silica [25] and aerogels with densities  $\delta = 250$  and  $270 \text{ kg/m}^3$  versus temperature  $T$ ;  $c_D$  are the corresponding Debye values. ●●●, measurements from [5]; ---, calculations from DOS [29].

conclude that the specific surface area is a quantity that is not systematically correlated with porosity.

## 61.7. CONCLUSIONS

Mechanical and acoustical properties as well as the dynamic and thermal behavior of aerogels are strongly influenced by the tenuous structure. A detailed understanding of these low-density materials can be expected to be at hand in the near future.

## ACKNOWLEDGMENTS

This work, Report E21-0289-2(1989), was supported by the German Ministry of Research and Technology (BMFT). I would like to thank Dr. G. Poelz, DESY, Hamburg, as well as Dr. S. Henning, Airglass, Staffanstorp, Sweden, for generously providing aerogel tiles.

## REFERENCES

1. J. Fricke, Ed., in *Springer Proceedings in Physics*, Vol. 6, *Aerogels*, Springer, Heidelberg (1986).
2. J. Fricke and G. Reichenauer, *J. Non-Cryst. Solids*, **95/96**, 1135 (1987).
3. M. Gronauer and J. Fricke, *Acustica*, **59**, 177 (1986).

4. J. Fricke, in: J. Fricke, Ed., *Aerogels, Springer Proceedings in Physics*, Vol. 6, p. 94, Springer, Heidelberg (1986).
5. R. Calemczuk, A. M. de Goer, B. Salce, and R. Maynard, in: A. C. Anderson and J. P. Wolfe, Eds., *Phonon Scattering in Condensed Matter V, Solid State Sciences*, Vol. 68, p. 26, Springer, Heidelberg, (1986).
6. G. Reichenauer, U. Buchenau, and J. Fricke, presented at the 2nd International Symposium on Aerogels, University of Montpellier, September 1988.
7. C. A. M. Mulder and J. G. van Lierop, in: J. Fricke, Ed., *Aerogels, Springer Proceedings in Physics*, Vol. 6, p. 68, Springer, Heidelberg (1986).
8. S. S. Kistler, *Nature*, **127**, 741 (1931).
9. S. J. Teichner, G. A. Nicholaon, M. A. Vicarini, and G. E. E. Gardes, *Adv. Colloid Interf. Sci.*, **5**, 245 (1976).
10. M. Cantin, M. Casse, L. Koch, R. Jouan, P. Mestran, D. Roussel, F. Bonnin, J. Moutel, and S. J. Teichner, *Nucl. Instr. Methods*, **118**, 177 (1974).
11. G. Poelz and R. Riethmüller, *Preparation of Silica Aerogel for Čerenkov Counters*, DESY 81-055 (1981).
12. S. Henning and L. Svensson, *Phys. Scripta*, **23**, 697 (1981).
13. A. Goetzberger and V. Wittwer, in: J. Fricke, Ed., *Aerogels, Springer Proceedings in Physics*, Vol. 6, p. 84, Springer, Heidelberg (1986).
14. A. Beck, O. Gelsen, P. Wang, and J. Fricke, presented at the 2nd International Symposium on Aerogels, University of Montpellier, September 1988.
15. R. Vacher, T. Woignier, J. Phalippou, J. Pelous, and E. Courtens, presented at the 2nd International Symposium on Aerogels, University of Montpellier, September 1988.
16. G. Poelz, in: J. Fricke, Ed., *Aerogels, Springer Proceedings in Physics*, Vol. 6, p. 176, Springer, Heidelberg (1986).
17. I. L. Rasmussen, presented at the 2nd International Symposium on Aerogels, University of Montpellier, September 1988.
18. J. Gross, R. Goswin, G. Reichenauer, and J. Fricke, presented at the 2nd International Symposium on Aerogels, University of Montpellier, September 1988.
19. J. Gross, G. Reichenauer, and J. Fricke, *J. Phys. D*, **21**, 1447 (1988).
20. S. S. Kistler and A. G. Caldwell, *Industr. Eng. Chem.*, **26**, 658 (1934).
21. D. Büttner, R. Caps, U. Heinemann, E. Hümmer, A. Kadur, and J. Fricke, *Solar Energy*, **40**, 13 (1988).
22. R. Caps and J. Fricke, in: J. Fricke, Ed., *Aerogels, Springer Proceedings in Physics*, Vol. 6, p. 110, Springer, Heidelberg (1986).
23. J. Fricke, E. Hümmer, H.-J. Morper, and P. Scheuerpflug, presented at the 2nd International Symposium on Aerogels, University of Montpellier, September 1988.
24. R. Maynard, R. Calemczuk, A. M. de Goer, B. Salce, J. Bon, E. Bonjour, and A. Bouret, presented at the 2nd International Symposium on Aerogels, University of Montpellier, September 1988.
25. R. C. Zeller and R. O. Pohl, *Phys. Rev.*, **B4**, 2029 (1971).
26. J. Fricke, H.-J. Morper, and P. Scheuerpflug, 21st International Thermal Conductivity Conference, Lexington Ky, October 1989.
27. O. Nilsson, G. Rüschenpöhler, J. Gross, and J. Fricke, presented at the *Porous Media-Correlation between Thermal Conductivity* 11th European Conference on Thermophysics Properties, Umea, Sweden, June 1988.
28. Novakov, Report on the Cité Solaire, Ardon Switzerland, at the 2nd International Workshop on Transparent Insulations, Freiburg, March 1988.
29. G. Reichenauer, J. Fricke, and U. Bucheau, *Europhys. Lett.*, in press.
30. H.-J. Morper, Diplom Thesis, University Würzburg (1989).

## AEROGELS AND XEROGELS FROM ORGANIC PRECURSORS

RICHARD W. PEKALA

### 62.1. INTRODUCTION

The hydrolysis and condensation of metal alkoxides is the common synthetic route for the formation of aerogels and xerogels [1–3]. This sol–gel technique permits the formation of ceramics and glasses with new compositions and homogeneity that is superior to the high-temperature processing of powders. The high surface areas, low densities, ultrafine pore/cell size, and controllable microstructure of these materials make them attractive for applications, such as membranes, catalyst supports, insulators, and electrodes [4–6].

Although sol–gel chemistry has been primarily utilized to form inorganic materials, we have been interested in organic synthesis that proceed through a sol–gel transition. One particularly promising reaction involves the polycondensation of resorcinol (1,3-dihydroxybenzene) with formaldehyde in a dilute, aqueous solution. In this polymerization, resorcinol serves as a trifunctional monomer capable of electrophilic aromatic substitution in the 2, 4, and/or 6-ring positions. This monomer is particularly reactive because of the electron donating and *o,p* directing effects of the hydroxyl groups. The substituted resorcinol rings condense with each other to form 30 to 150-Å “clusters” in solution. The size of the clusters is regulated by the catalyst concentration in the resorcinol–formaldehyde (RF) solution. The clusters possess surface functional groups (e.g.,  $-\text{CH}_2\text{OH}$ ) that can further react to form a gel.

*Ultrastructure Processing of Advanced Materials.*

Edited by Donald R. Uhlmann and Donald R. Ulrich (deceased).

ISBN 0-471-52986-9 © 1992 John Wiley & Sons, Inc.

The RF gels are exchanged into an organic solvent and supercritically dried to form organic aerogels. If the solvent is slowly evaporated from the gels, substantial shrinkage results and a xerogel is formed. The RF aerogels and xerogels can be further processed at high temperatures in an inert atmosphere to form glassy carbon. The structure and properties of RF and carbon aerogels/xerogels will be discussed in this Chapter.

## 62.2. EXPERIMENTAL

The production of RF aerogels has been described previously [7-9]. Briefly, resorcinol and formaldehyde are mixed in deionized and distilled water at a 1:2 molar ratio, respectively. Sodium carbonate is then added as a base catalyst. The solution is poured into glass vials or ampules, which are then sealed. The polymerization is continued for 7 days at 85 to 95°C. The water-filled gels are then exposed to a dilute acid solution to further enhance crosslinking. The gels undergo a noticeable increase in modulus during this procedure. Supercritical extraction is performed with carbon dioxide after the gels have been exchanged into a compatible organic solvent.

RF aerogels are red in color and transparent. Pyrolysis of these aerogels is performed in a three-zone Lindberg furnace (Model 54657-S) at a ramp rate of 1°C/min to 1075°C in a nitrogen atmosphere. The samples are held at this temperature for 3 hr and then allowed to cool to room temperature in approximately 24 hr. The carbonized aerogels are opaque and black in color. Pyrolysis leads to volumetric shrinkages of 65 to 75% with an accompanying mass loss of ~50%.

## 62.3. RESULTS AND DISCUSSION

The microstructure of RF and carbon aerogels/xerogels was examined by scanning electron microscopy. Figure 62.1 shows that both types of aerogel have an open cell structure with continuous porosity. The observed cell/pore size is less than 1000 Å in each case. The corresponding xerogels show a collapsed structure composed of aggregated particles with diameters of 100 to 300 Å.

In a fashion similar to silica aerogels, the microstructure and properties of RF aerogels are controlled by the amount of catalyst in the polymerization. Because the pH of the RF solution changes as the polymerization proceeds, all formulations are referenced by the [Resorcinol]/[catalyst] (R/C) ratio in the mixture. R/C ratios of 50 to 300, corresponding to an initial pH range of ~6.0 to 7.5, provide an acceptable region in which gels can be formed. Outside of this range, precipitates are usually formed.

The R/C ratio manifests itself in the density and surface area of the aerogels. Figure 62.2 shows the final density of both carbon and RF aerogels made from solutions containing 5% solids, but varying R/C ratios. In the case of the RF

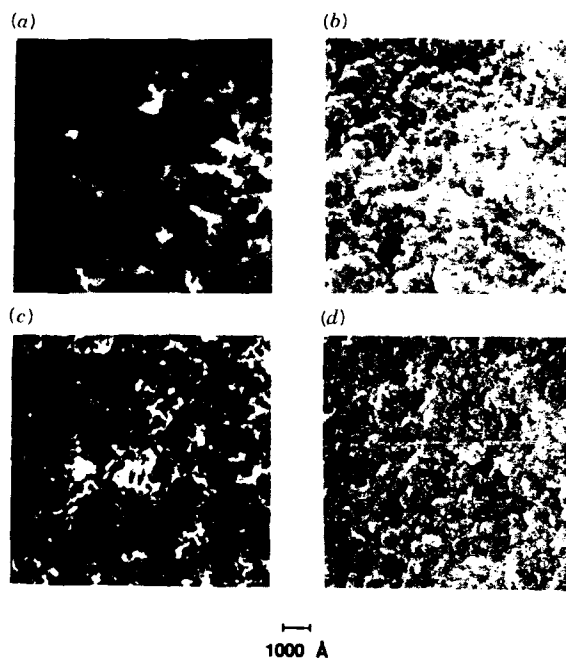


Figure 62.1. Scanning electron micrographs of (a) RF aerogel, (b) RF xerogel, (c) carbonized aerogel, and (d) carbonized xerogel.

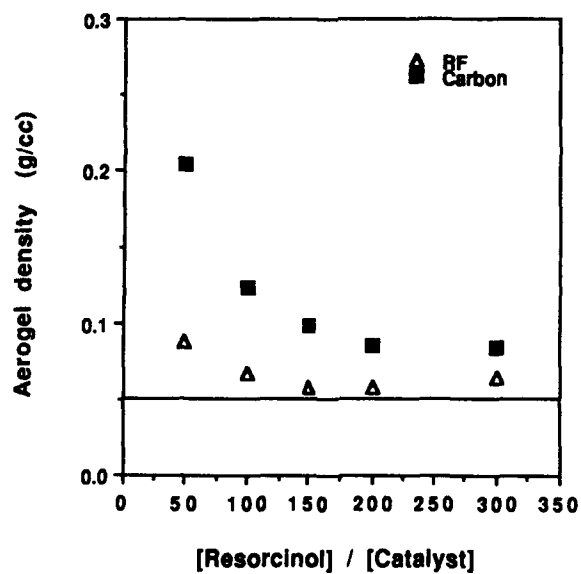


Figure 62.2. Final density of RF and carbon aerogels as a function of the R/C ratio. All formulations at 5% solids.



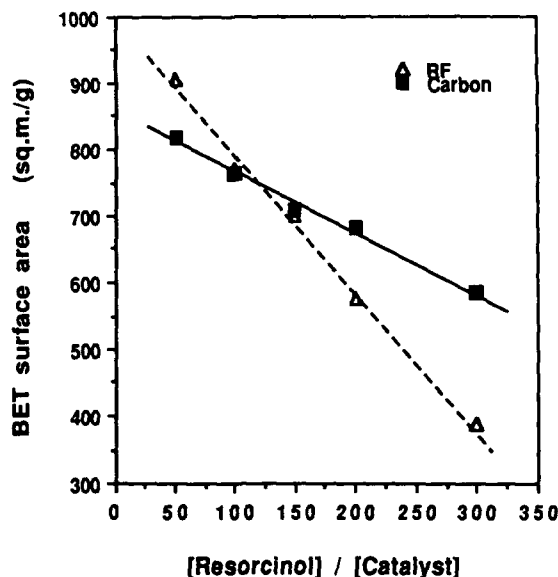


Figure 62.3. BET surface areas of RF and carbon aerogels as a function of the R/C ratio.

aerogels, substantial shrinkage occurs during supercritical drying at low R/C values (i.e., high catalyst concentrations), and the aerogels have densities much higher than their theoretical values. At R/C ratios greater than 150, the density of the RF aerogels begins to plateau at a value that is approximately 15% higher than the theoretical value.

If the RF aerogels are carbonized, a density effect that depends upon the R/C ratio is still observed. In all cases, the percent mass loss is approximately the same, and differences in volumetric shrinkage determine the density of the carbonized aerogels. RF aerogels prepared at low R/C ratios undergo the largest amounts of shrinkage during carbonization. The density increase, relative to that of the starting RF aerogel, varies from ~35 to ~130% over the accessible range of R/C ratios.

The Brunaur-Emmett-Teller (BET) surface areas of the above aerogels were measured. Figure 62.3 shows an inverse relationship between the R/C ratio and the surface area of both RF and carbon aerogels. The surface areas of the RF aerogels range from 350 to 950 m<sup>2</sup>/g and display a strong dependence upon the R/C ratio. In contrast, the surface areas of the carbonized aerogels range from 550 to 850 m<sup>2</sup>/g and show less of a dependence upon the R/C ratio.

RF and carbon xerogels dried from an aquagel with an R/C value of 200 had surface areas of 415 and 495 m<sup>2</sup>/g, respectively. These values are smaller than the corresponding aerogels, and they show the effects of collapse and aggregation during evaporation of water from the gel.

An explanation of the dependence of aerogel densities and surface areas upon

the R/C ratio was thought to involve chemical differences. For example, the degree of crosslinking in the bulk polymer might affect gel shrinkage during supercritical drying. In order to test this hypothesis, solid state  $^{13}\text{C}$  nuclear magnetic resonance spectra of RF aerogels synthesized at  $R/C = 50$  and  $R/C = 200$  were obtained. Figure 62.4 shows that the aerogels are virtually identical and that chemical differences within the bulk polymer cannot explain the above data.

Differences in microstructure were observed for RF aerogels by transmission electron microscopy (TEM). Figure 62.5 shows that the fundamental particle/bead size increases in proportion to the R/C ratio. These morphological differences are responsible for the variation of density and surface area with the R/C ratio.

From the measured specific surface areas and the aerogel densities, a surface area per unit volume ( $SA/V$ ) was determined. A theoretical value of  $SA/V$  was then calculated from bead diameters measured in the TEM photos. In the latter calculation, the aerogel microstructure was modeled as a series of interconnected, monodisperse beads. The beads were assumed to be solid with a density of 1 g/m. Table 62.1 shows good agreement between the two methods of obtaining  $SA/V$ . In addition, the data suggest that the interconnected beads are near full density.

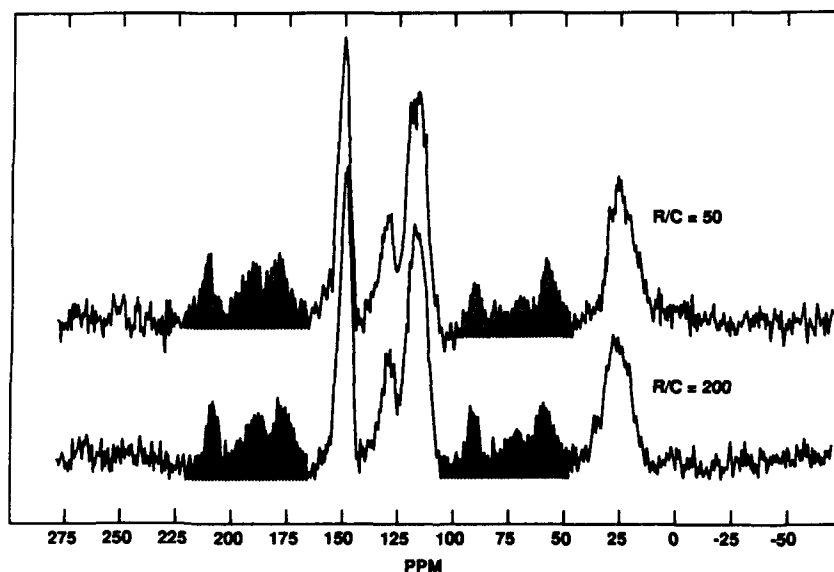


Figure 62.4. CPMAS  $^{13}\text{C}$  NMR spectra of RF aerogels synthesized at two different catalyst concentrations. Cross-hatched areas represent spinning side bands.

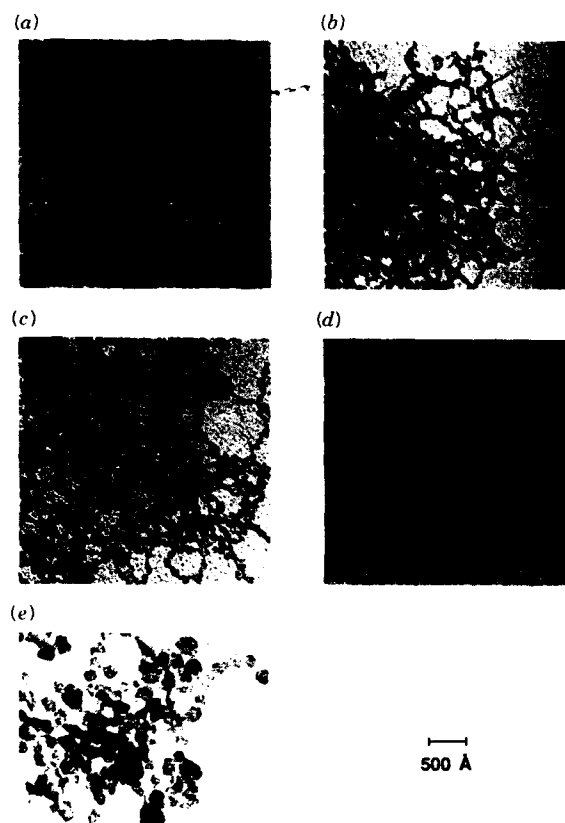


Figure 62.5. Transmission electron micrographs of RF aerogels synthesized at different catalyst concentrations  $\rho/C$  equals (a) 50 (b) 100 (c) 150 (d) 200, and (e) 300.

TABLE 62.1. Resorcinol-Formaldehyde Aerogels

Target density (g/cc)	Actual density (g/cc)	[Res] / [Cat]	Surface area (m <sup>2</sup> /g)	Measured SA/Volume (m <sup>2</sup> /cc)	TEM bead radius (Å)	Theoretical SA / Volume (m <sup>2</sup> /cc)
.050	.068	50	905	80	*	----
.050	.067	100	769	52	*	----
.050	.057	150	699	40	42	41
.050	.057	200	577	33	59	29
.050	.064	300	389	25	84	23

\* Could not be measured from available TEM photos

## 62.4. CONCLUSIONS

The polycondensation of resorcinol with formaldehyde under alkaline conditions follows a sol-gel pathway in which polymer clusters crosslink to form gels. These gels are then dried to form organic aerogels or xerogels. The structure and properties of these new materials are controlled through modifications of the polymerization conditions and/or heat treatment at high temperatures.

## ACKNOWLEDGMENT

Work performed under the auspices of the U.S. Department of Energy by Lawrence Livermore National Laboratory under Contract W-7405-ENG-48.

## REFERENCES

1. J. Fricke, Ed., *Aerogels*, Springer-Verlag, New York (1986).
2. S. J. Teichner, G. A. Nicolaon, M. A. Vicarini, and G. E. E. Gardes, *Adv. Coll. Interf. Sci.*, **5**, 245 (1976).
3. C. J. Brinker, D. E. Clark, and D. R. Ulrich, Eds., *Better Ceramics Through Chemistry*, Vol. II, Materials Research Society, Pittsburgh, (1986).
4. G. M. Pajonk and S. J. Teichner, in: J. Fricke, Ed., *Aerogels*, p. 193, Springer-Verlag, New York (1986).
5. J. Fricke, *J. Non-Cryst. Solids*, **100**, 169 (1988).
6. J. Fricke, *Sci. Am.*, **258**(5), 92 (1988).
7. R. W. Pekala and R. E. Stone, *ACS Polym. Preprints*, **29**(1), 204 (1988).
8. R. W. Pekala, *J. Mater. Sci.*, **24**, 3221 (1989).
9. R. W. Pekala and F. M. Kong, *J. de Physique, Coll. Suppl.* **50**(4), C4-33 (1989).

# INDEX

- Abrasives, 130
- Acetic acid, 24, 70, 278
- Acetylacetone, 28, 615
- Aerogels:
  - carbon, 712
  - organic, 712
  - SiO<sub>2</sub>, 316, 699
- Alkaline earth titanates, 277
- Alkali silicate, 291
- Alkoxides, *see also specific types*
  - chemical properties, 5, 26
  - complexing agents for, 26
  - double, 5, 87, 620
  - physical properties, 6
  - structure, 6
  - synthesis, 4
  - volatility, 9
- Al<sub>2</sub>O<sub>3</sub>, 180, 190, 233, 303, 345, 603
- Alumina-zirconia, 385
- Aluminum alkoxides, 6, 28, 224, 385
- Aluminum cations, 38
- Aluminum chlorohydrate, 233, 676
- Aluminum nitride, 675
- Aluminum phosphate, 309
- Ammonia, 53
- Aqueous precursors, 28
- Aramid, 345
- Artificially structured metals, 531
- Band filling effect, 492
- Barium acetate, 278, 621
- Barium alkoxides, 568, 620
- Barium titanate, 125, 156, 259, 277, 613
- Beads, 131
- Beryllium fluoride, 451
- Bi-Ca-Sr-Cu-O, *see* Superconductors
- Bioceramics, 152
- Biological materials, 150
- Biomimetic processing, 149
- Birefringence, 253
- Boehmite, 62, 233
- Boric acid, 275
- Boron alkoxides, 224, 270
- Boron nitride, 130, 309, 393, 675, 681
- Borosilicates, 224, 269
- Brunaur-Emmett-Teller method, 270, 295, 334
- Cadmium sulfide, 491
- Calcium metasilicate, 311
- Calorimetry, 77
- Capillary forces, 182
- Carbon fibers, 225, 345
- Carbothermal reduction, 676
- Cavitation, 137
- CdS, 493
- CdTe, 492
- Ceramic yield, 668
- Cerenkov counters, 700
- Cerium basic carbonate, 260
- Chelation, 615
- Chemically controlled condensation, 414, 434
- Chromium hydroxide, 265
- Coatings, *see* Films
- Coefficient of thermal expansion, 171, 298, 306, 333, 345, 420, 600, 675
- Colloids, 25, 58, 103, 213, 257, 294, 363
  - boehmite, 60
  - Ludox colloidal SiO<sub>2</sub>, 60
- Complexation, 6, 23, 47, 279, 411, 615
  - anions, 31
- Composite engineering, 207

- Composites, 130, 149, 176, 201, 223, 304, 343, 361, 377, 393, 401, 409, 439, 472, 491, 675
- Condensation, 24, 47, 80, 97, 215, 337, 413, 434
- olation, 24
- oxolation, 24
- Conductive polymers, 690
- Continuity equation, 191
- Copper alkoxides, 568
- Co-sintering of multilayer ceramics, 608
- Coumarin, 522
- Critical stress intensity,  $K_{IC}$ , 140
- Cryogenic TEM, 57
- Darcy's Law, 185
- Degenerate four-wave mixing, 465, 496, 527
- Densification of composites, 393
- Derjaguin - Landau - Verwey - Overbeek (DLVO) Theory, 103, 182
- Dielectrics, 600, 616
- Diethylaluminum amide, 678
- Diffusive transport, 188
- Dilution narrowed spectroscopy, 458
- Dimethyldiacetoxysilane, 96
- Dimethyldimethoxysilane, 91
- Drying, 166, 179, 247
- stress, 192
- Drying chemical control additives, 140
- Dyes, 19, 176, 519
- Elastic constants, 404, 703
- Electrical switching, 645
- Electrokinetic sonic amplitude, 71
- Electrophoretic deposition, 419
- Embossing, 547, 617
- Ethyltrimethoxysilane, 328
- Fabry - Perot interferometer, 534
- Ferrites, 260
- Fibers, 152, 208, 225, 345, 439, 570, 652, 675, 681
- Fillers, 126, 365, 602
- Films, 211, 239, 264, 286, 308, 418, 464, 477, 503, 531, 548, 567, 616, 643, 681
- Fluorescent line narrowing, 454
- Fluorescent probes, 19
- Fluoride, 13, 24, 51, 310, 401
- Formaldehyde, 711
- Formamide, 53, 259
- Fractal geometry, 17, 211, 363
- Fracture, 193
- Fresnel lens, 173
- Functional polymers, 689
- Gelation, 19, 60, 69, 103, 117, 138
- Gels:
- density, 142, 334
- modulus, 143
- fracture surface energy, 144
- Germanium alkoxides, 78, 512
- Glass-to-ceramic process, 629
- Glycerol, 141
- Gradient index, 509
- Gratings, 457, 547
- $H_2S$ , 558
- Hole burning, 457
- Homogeneity, 168
- Hückel molecular orbital calculations, 111
- Hydrolysis, 15, 24, 69, 80, 91, 135, 287, 413
- Hydrosilylation, 671
- Hydroxymethylmethacrylate, 416
- Hypervalent silicon complexes, 47
- Integrated optics, 545
- Intermediate neglect of differential overlap (INDO), 111
- Interpenetrating networks, 373, 422
- Ion conduction, 421
- Ion exchange, 511
- Iron oxides, 265
- Kerr effect, 463, 476, 539
- Langmuir - Blodgett films, 462, 697
- Lanthanum alkoxides, 7, 557
- Lanthanum sesquisulfide, 555
- Laser behavior, 519
- Laser densification, 176
- Laser oscillation, 525
- Laser spectroscopy, 454
- Lead acetate, 516, 613
- Lead niobate, 259
- Lead titanate, 377, 613
- waveguides, 618
- Liquid crystal polymers, 695
- Liquid transport, 185
- Lithium alkoxides, 90
- Lithium niobate, 87
- Lithium niobium alkoxides, 88
- Magnetite, 150, 258
- Magneto-optics, 476, 537
- Mechanical properties, 123, 139, 152, 194, 229, 298, 303, 329, 345, 365, 401, 426, 440, 700
- Meissner effect, 584
- Metalation, 669

- Metallization, 600  
2-Methoxyethanol, 88  
Methylmethacrylate, 402, 415, 522  
Methyltriethoxysilane, 327  
Methyltrimethoxysilane, 224  
MgO substrates, 568  
Microwave curing, 435  
Microwave drying, 165  
Modulus of rupture, 329  
Moisture potential, *see* Moisture stress  
Moisture stress, 184  
Molecular beam epitaxy, 531  
Molecular composites, 344, 357, 361, 439  
Molecular orbital calculations, 48, 112  
Molecular stuffing, 511  
Mooney-Rivlin plots, 366, 372  
Mullite-zirconia, 385  
Multifunctional macromolecules, 687  
Multilayer ceramic packaging, 607  
Multilayer optics, 532  
  
Na<sub>2</sub>O-SiO<sub>2</sub>, 117  
Neodymium, 453  
Nickel ferrites, 260  
Niobium alkoxides, 89  
Non-linear optics, 156, 176, 402, 461, 495, 519, 694  
    polymers, 468  
NMR spectroscopy, 6, 15, 28, 88, 97, 225, 427, 670, 678  
  
Optical composites, 156, 176, 402, 472, 491  
Optical data storage, 475  
Optical gain, 521  
Optical polymers, 174  
Optical spectroscopy, 449  
Optical switching, 645  
Optical windows, 555  
Organically modified ceramics, 95, 327, 361, 401, 409, 425, 472, 520  
Osmosis, 180  
Oxycarbide glasses, 224, 310  
Oxynitride glasses, 311  
  
Packaging, 599, 675  
Partial charge method, 25  
(Pb<sub>0.5</sub>Bi<sub>0.5</sub>)(Ti<sub>0.5</sub>Fe<sub>0.5</sub>)O<sub>3</sub>, 377  
PbO-SiO<sub>2</sub>, 546  
Pechini method, 379  
Perlite, 305  
Petroleum pitch, 676  
pH, 69  
Phase change materials, 475, 641  
  
Phase separation, 201  
Phase transformation, 477  
Phase transformation kinetics (PTK) diagram, 483  
Phosphates, 30  
Photocatalysis, 416  
Photocurrent, 243  
Photoelectrochemical deposition, 239  
Photoluminescence, 500  
Photostability, 526  
Photovoltaic cells, 239  
Piezoelectrics, 380, 692  
Piezoelectric coefficient:  
    *d*<sub>33</sub>, 380  
    *g*<sub>33</sub>, 380  
Poling, 380, 464  
Polyacetylene, 690  
Polyacrylonitrile, 676  
Polyaniline, 691  
Polycarbosilanes, 667  
Polydiacetylenes, 464  
Polydimethylsiloxane, 96, 365, 426  
Polyetherketone, 349, 434  
Polyethylene, 345, 411  
Polyethylene oxide, 411  
Polyethylvinyl acetate, 420  
Polymethylmethacrylate, 49, 401, 411  
Polyphenylenesulfide, 349  
Poly-*p*-phenylvinylene, 464  
Polypyrrole, 691  
Polysilastyrene, 652  
Polystyrenesulfonic acid, 435  
Polytetramethylene oxide, 428  
Polyquinoline, 439  
Polysilanes, 651, 671  
Polysilazanes, 681  
Polythiophenes, 464  
Polyvinylidene fluoride, 688  
Porosity, 17, 123, 136, 162, 182, 211, 249, 294, 305, 321, 334, 421  
    macropores, 131  
    structure, 294  
Powders, 257, 269, 277, 379, 555, 613  
    coated powders, 264  
Pre-ceramic polymers, 122, 651, 667, 677, 681  
Preferred orientation, 153, 240, 584, 636  
Pyroelectricity, 692  
  
Quantum confinement, 463, 491  
Quantum dots, 504  
  
Raman spectroscopy, 16, 427, 472, 500  
Rare earth ions, 447

- Refractive index, 516
- Reliability of dielectrics, 601
- Resistors, 604
- Resorcinol, 711
- Rhodamine, 522
- Rod-like particles, 201
- Ruthenium oxide, 606
  
- Salt solutions, 125, 126, 378
- SAW, 213
- Second-harmonic generation, *see* Non-linear optics
- Seeding, 233
- Semi-conductors, 239, 285, 475, 492, 641
- Silanol polymerization, 47
- Silica, 13, 60, 69, 78, 111, 128, 135, 159, 186, 213, 247, 264, 291, 305, 315, 361, 393, 402, 426, 452, 699
  - Cl<sub>2</sub> treatment, 300
  - clusters, 111
  - colloidal, 62, 294
  - F-doped, 310
  - homogeneity, 168
  - optics, 117, 159, 291
  - porous, 111, 174, 218, 294
  - purity, 170
  - radial distribution functions, 320
  - sheet, 128
  - skeletal density, 315
  - types, 160-163
  - uv cut-off, 111, 170, 299
- Silica titania, 95, 125, 136, 308, 333, 512, 546, 616
- Silicic acid, 48
- Silicon carbide, 303, 345, 652, 667, 681
- Silicon nitride, 303, 681
- Silicon oxycarbide, 224
- Silicon tetrachloride, 294
- Silylation, 670
- Sintering aids, 676
- Skeletal density, 183, 315, 336
- Small angle scattering, 14, 213, 363, 426
- Smart composite, 358
- Sodium acetate, 224
- Sodium fluoride, 13
- Soft x-rays, 532
- Sonocatalysis, 135
- Sonogels, 135, 316, 521
- Spinodal decomposition, 369
- Stober process, 58, 213, 369
- Structure-property relationships, 600
- Sulfates, 34
- Sulfidization, 557
  
- Superabrasive disc, 130
- Superconductors:
  - Bi-Ca-Sr-Cu-O, 566, 579, 629:
    - fibers, 571
    - glass to ceramic process, 629
    - lead doped, 579, 637
    - microstructure, 592
    - preferred orientation, 584
  - YBa<sub>2</sub>Cu<sub>3</sub>O<sub>x</sub>, 129, 566:
    - fibers, 129, 570
    - films, 568
- Supercritical drying, 712
- Syneresis, 122, 135, 181, 286
  
- Tetraethoxysilane, 57, 69, 78, 135, 187, 270, 294, 315, 327, 364, 386, 394, 402, 426, 520
  - acid catalyst, 69, 80
  - base catalyst, 83
- Tetraethylorthogermanate, *see* Germanium alkoxides
- Tetramethoxysilane, 13, 69, 135, 224, 249, 334, 364, 428, 511, 520, 700
- Thallium (III) oxide films, 239
- Thermal transport, 704
- Thermoplasticity, 421
- Thick-film resistors, 604
- Third-harmonic generation, *see* Non-linear optics
- TiO<sub>2</sub>, 27
- Titanium alkoxides, 7, 26, 96, 155, 260, 278, 334, 378, 415, 434, 512, 614
- Tl<sub>2</sub>O<sub>3</sub>, 239
- Toughening, 153
- Transformation toughening, 385
- Transition metal catalysts, 681
- Triethylaluminum, 678
- Trimethoxysilylpropylmethacrylate, 522
  
- Ultrahomogeneity, 121
- Ultrasonic radiation, 135, 316
  
- Vanadium alkoxides, 641
- Vanadium dioxide films, 646
- Vanadyl alkoxides, 285
- Viscoelastic properties, 139
- VO<sub>2</sub>, 641
- V<sub>2</sub>O<sub>5</sub>, 285
- Voids, 304
  
- Waveguides, 176, 469, 545, 616
- Wetting, 228
- Whiskers, 208, 679
- Wide angle X-ray diffraction, 315



- Wilkinson's catalyst, 653
- Xerogels, 401
- X-ray photoelectron spectra (XPS), 288
- $\text{YBa}_2\text{Cu}_3\text{O}_x$ , *see* Superconductors
- Young's Modulus, 303
- Yttria-stabilized zirconia substrates, 568
- Yttrium alkoxides, 568
- Yttrium basic carbonate, 260
- Zirconia, 33, 131, 265, 385
- Zirconium alkoxides, 10, 28, 132, 385
- Zirconyl cation, 31
- ZnS, 492, 556